ATOMIC AND MOLECULAR COLLISIONS

by

MALCOLM ANTHONY DAVIS FLUENDY

A

THESIS
SUBMITTED FOR THE DEGREE

of

DOCTOR OF SCIENCE

FACULTY OF SCIENCE
UNIVERSITY OF EDINBURGH
JULY 1981

CONTENTS

STATEMENT BY THE CANDIDATE

The nature of the experimental research described in this thesis has often required the collaboration of other workers. The candidate's contribution to the work submitted in this thesis may be summarised as follows:

In publications 2,3,5,7,8,10,11,12,13,14,16,18,21, 22,23,24,25,27,28,29,30,31,32,33,34,35,36 and 37 the candidate was either solely responsible or played the leading role in the design, execution and analysis of the work, in some cases with the assistance of research students working under his supervision.

In publications 1,4,6,9,15,17 and 26 the work was carried through in equal collaboration with one or more of the co-authors.

Finally, in publications 19 and 20 the candidate played a lesser role.

Preface and Acknowledgements

The work presented in this thesis has been carried out at the Universities of Harvard (Mass.), Edinburgh and Florida (Cainesville). None of the publications have been submitted by the candidate for any other degree. The papers describe research investigations performed by the author alone or in collaboration with the co-authors named or by research students directed by the author.

It is a pleasure to acknowledge my debt to the many colleagues and collaborators who have been so generous with their help, advice and enthusiasm. In particular, I wish to thank Professor Dudley Herschbach for initiating me into the "Heroic Age" of crossed molecular beam research and Dr. Kenneth Lawley without whose help, sage advice and collaboration this work would have been impossible.

Generous support from the Science Research Council and the North Atlantic Treaty Organisation is acknowledged.

LIST OF PUBLICATIONS SUBMITTED

---

with E. B. Smith,

1) "The Application of Monte Carlo Methods to Physiochemical Problems", Quart. Revs., 16, 241, (1962)

2) "Recombination Detector for Atomic Hydrogen Beams", Rev. Sci. Instr., 35, 1606, (1964).

3) "Magnetic Velocity Selector for Hydrogen Atom Beams using an Unfolding Technique", J. Sci. Instr., 42, 489, (1965).

with A. R. Blyth and K. P. Lawley,

4) "Molecular Beam Scattering", Quart. Revs., 20, 465, (1966).

with R. M. Martin, E. E. Muschlitz Jr. and D. R.Herschbach,

5)"Hydrogen Atom Scattering; Velocity dependence of Total Cross Section for Scattering from Rare Gases,Hydrogen and Hydrocarbons",J. Chem. Phys., 46, 2172, (1967).

with L. T. Cowley and K. P. Lawley,

6) "Small Angle Scattering from Crossed Sodium and Potassium Beams", Trans. Farad. Soc., 65, 2027, (1969).

with L. T. Cowley, K. P. Lawley and D. S. Horne,

7) "A Crossed Molecular Beam Apparatus and Associated Computer Programmes for the Measurement of Differential Scattering Cross Sections", J. Sci. Instr., 2, 1021, (1969).

with L. T. Cowley and K. P. Lawley,

8) "A Radial Disk Velocity Selector for Molecular Beams", Rev. Sci. Instr., 41, 666, (1970)

with D. S. Horne, K. P. Lawley and A. W. Morris,

9) "Elastic Scattering of Alkali Atoms from Iodine Atoms and Molecules at Thermal Energies", Mol. Phys., 19, 659, (1970)

10) "Monte Carlo Methods" in "Markov Chains and Monte Carlo Calculations in Polymer Science" Ed. G. Lowry, Marcel Dekker, New York (1970)

11) "Molecular Scattering", Ann. Rept. on Chemistry, 67A, 151, (1970)

with B. S. Duchart and K. P. Lawley,

12) "Angular Scattering of Superthermal K by I_2", Chem.Phys. Letters, 14, 129, (1971).

with B. S. Duchart and K. P. Lawley,

13) "Angular Scattering of Superthermal Potassium by Hg and I_2" Proc. VII ICPEAC, Amsterdam, 549, (1971).

with E. C. Darwall and K. P. Lawley,

14) "Elastic Differential Scattering of Metastable Mercury Hg 6 $^3P_2$ from K and Hg", Entropie, 42, 162, (1971).

with K. P. Lawley,

15) "Potential Energy Surfaces", Essays in Chemistry, 5, 25, Academic Press.

with K. P. Lawley and T. A. Davidson,

16) "The Scattering of Metastable Mercury Atoms", Disc. Farad. Div. Chem. Soc., 55, 158, (1973).

with K. P. Lawley,

17) "Chemical Applications of Molecular Beam Scattering", Chapman and Hall, 450 pages, 1974

with D. R. McDonald and K. P. Lawley,

18) "Monte Carlo Simulation of K/I_2 Collisions at Superthermal Energies" Proc. VIII ICPEAC, Belgrade, 1973, 56.

with J. R. Reddington and K. P. Lawley,

19) "Two state calculations on the collisions of Alkali Metal and Halogen Atoms at Superthermal Energies",Proc. 4th Int. Conf. on Molecular Beams, Cannes, 1973.

with I. H. Kerr and K. P. Lawley,

20) "Atomic Scattering from Heavy P-State Atoms:Role of Depolarisation", Mol. Phys. 28, 69, (1974).

with I. H. Kerr, K. P. Lawley and J. M. McCall,

21) "Differential Scattering Cross Sections in the eV Region: the K/Ar ground state potential",J. Phys. B., 8, L190, (1975).

with I. H. Kerr, D. R. McDonald and K. P Lawley,

22) "K/I_2 Collision at Superthermal Energies", Chem. Phys., 13, 425 (1975).

with I. H. Kerr, J. M. McCall and D. Munro,

23) "On-line Computer Control of an Atomic Beam Scattering Experiment", Proceeding of Conf. on "On-line Computing" 1201, (1975), I.E.E.Inst. of Phys., London.

with J. Costello and K. P. Lawley,

24) "The Scattering of $Hg(6\,^3P_2)$ by CO, N_2 and CO_2 ",Disc. Farad. Div. Chem. Soc., 62, 291, (1977).

with T. A. Davidson, J. Costello and K. P. Lawley,

25) "The Elastic Scattering of Slow Electronically Excited Mercury Atoms from the Alkali Metals and Neon: the Interatomic Potentials",J. Phys. B., 10, 1523. (1977)

with E. E. Muschlitz,

26) "Velocity Dependence of Vibrational Branching Ratios in Electronic Energy Transfer" Chem. Phys. Lett., 42, 103, (1976).

27) "Reactive Scattering of Molecular Beams", Contemp. Physics, 16, 147, (1975)

with K. P. Lawley, J. M. McCall and C. Sholeen,

28) "K/CH_3I Inelastic Scattering", Disc. Farad. Div. Chem. Soc., 62, 149, (1977).

with J. M. McCall,

29) "Signal Enhancement by Velocity Modulation in Time of Flight Analysis of Atomic and Molecular Beam Scattering", J. Phys. E., 11, 631, (1978).

with K. P. Lawley, J. M. McCall, C. Sholeen and D. Sutton,

30) "Electronic Excitation in Potentially Reactive Atom-Molecule Collisions", Disc. Farad. Div. Chem. Soc., 67, 41, (1979).

with K. P. Lawley and D. Sutton,

31) "Electronic Excitation into Repulsive states by K/CH_3I Collisions", Disc. Farad. Div. Chem. Soc., 67, 116, (1979).

with D. Sutton

32) "On the Absence of Electronic Excitation in K/Br_2 Collisions", Disc. Farad. Div. Chem. Soc., 67, 343, (1979).

with K. P. Lawley and G. W. Black,

33) "Monte Carlo Calculations including Surface Hopping for K/CH_3I", Disc. Farad. Div. Chem. Soc., 67, 118, (1979).

with F. Castano, K. P. Lawley, C. Sholeen and D.Sutton,

34) "Electronic Excitation in Potassium Alkyl Iodide Collisions", Chem. Phys. Letts., 65, 26, (1979).

with D. Sutton and G. W. Black,

35) "Electronic Excitation and Energy Transfer in Potassium/Nitrogen Molecule Collisions", Chem. Phys. Letts., 69, 260, (1980).

with K. P. Lawley, C. Sholeen and D. Sutton,

36) "Electronic Excitation in Potassium/Alkyl Halide Collisions - The Electron Harpoon", Mol. Phys., 42, 1, (1981).

with G. W. Black,

37) "Electronic and Vibrational Excitation in K+SF Collisions", Proceedings of the VIII International Symposium on Molecular Beams, Cannes, 223, (1981)

DISCUSSION

1. INTRODUCTION.

All chemical change occurs as a result of collisions: in some cases highly complex, involving the interactions of solvated species, in others relatively simple as in a diatomic photo-dissociation. Despite this fundamental importance, until the 1960's there was little effort on the part of chemists to study the collision itself. Despite some isolated early work (A) and a clear perception of the important goals in this field (B) it appears that technical difficulties were too severe to make the area attractive to chemists. It was thus left to a Physicist, P. B. Moon (C)*, (almost inadvertently, as a by-product of other work) to make the first direct studies of wide chemical significance. A study using "Crossed

* The author will always be grateful to his tutor and later supervisor, Mr. R. P. Bell, for first drawing his attention to this paper during the course of a tutorial.

Molecular Beams " of the reactive process:

$$K + CCl_4 \Rightarrow KCl + CCl_3$$

in which it was possible not only to estimate the velocity dependence but uniquely the angular distribution of the product molecules. Information which leads naturally to an interpretation in terms of the actual trajectories of the individual atoms during the collision.

In practice this work attracted little interest at the time and it was left to other groups notably that of D. R. Herschbach, J. Ross and E. F. Greene, and Sheldon Datz to generate the modern field of "Molecular Dynamics" in which detailed knowledge and understanding of the trajectories and potential surfaces followed during the collision is sought.

The rapid progress seen in this field since this time is a result of two factors, both technical. The first lies in the dramatic improvement in vacuum and electronic techniques, spilling over from work in elementary particle and nuclear physics. This advance, coupled with the availability to chemists of sufficient technical resources to exploit them, was of fundamental importance. In parallel with this experimental progress and of almost

equal consequence, it became possible to use fast digital computers to model the molecular collisions studied experimentally. These "Monte Carlo" (1,10) computations provided great physical insight into the experimental data; it is clear that by itself each would have been of much less significance.

This thesis is concerned with studying the most intimate details of molecular collisions, especially those preceeding or occurring during chemical reaction. For this purpose crossed molecular beam experiments provide a unique tool. As already discussed, technical innovation has played an important part in this field and molecular beam collision research remains technique rather than conceptually limited. Improvements in beam intensity and resolution bring yet more processes under the microscope provided by the technique. For this reason considerable attention will be paid to experimental developments in this thesis.

Atomic and molecular collisions take place over a range of 10^{-9} m and have a lifetime of 10^{-11} - 10^{-15} s, though considerably longer-lived "complexes" or "resonances" can sometimes occur. Information as to the mechanics of the

collision in this "black box" region can only be obtained by varying the input conditions in as controlled a fashion as possible and observing - again with as much detail as possible - the long time, long distance (in molecular terms) output. The available information reaches its theoretical quantum limit in the fully state-resolved, energy selected differential cross section in which the incident state "i" and exit state "e" are fully determined. In almost all systems involving chemical species, the available number of states is so large relative to the available beam intensity that this quantum-limited level of information is unlikely ever to be available. (This limit may usefully be signalling that at least partially classical models will be appropriate for understanding chemical collision systems.) Since the resolution will inevitably be limited, it is of key importance in experiments to select the appropriate parameters for study so that the best diagnostic information about the collision can be obtained.

In conceptualising the collision problem it is usual to divide it into two parts - the potential surface and the trajectories followed by the atoms over this surface. This separation is, of course, just the Born-Oppenheimer

approximation strictly valid only in the limit of stationary atoms! The description of systems in motion will thus raise some questions as to the electronic adiabaticity of the collision. For weak departures from electronic adiabaticity a useful description of such systems can be obtained by considering the motion as occurring over a manifold of surfaces with transitions possible between the surfaces. For more extreme cases the separation into surface and trajectory may be less useful. In this thesis attention is primarily - but not exclusively - directed at atom/molecule systems and in particular those which involve reactive molecules. Information on both the intermolecular potential surface and the trajectories of the atoms is obtained. The consequences of the breakdown in the Born-Oppenheimer approximation are explored and interpreted in terms of electron dynamics.

It is shown that:

1) Total and differential elastic cross sections provide information on potentials even for complex systems in which several surfaces are accessible. Thus it was possible to obtain information on the $^3\Sigma$ surface in

alkali metal diatomics even though the $^1\Sigma$ surface is also populated in the collision.

2) The same technique can be used to study very short-lived, highly energetic species such as the excited mercury atom, $6\,^3P_2$. Potentials for its interaction with a number of different atoms have been measured and in favourable cases it was possible to extract information about all the surfaces populated. It was shown that this excited state of mercury was reasonably stable to atomic collisions, the metastable electron configuration showing little mixing with otherwise accessible states. In sharp contrast, collisions with molecular systems were strongly inelastic though it was still possible to estimate effective central potentials for these systems.

3) A suitable choice of initial collision conditions greatly simplifies the form of the trajectories followed in reactive collisions. In particular fast collisions scattering to small angles are especially convenient probes and with this technique direct evidence for the involvement of ionic intermediates in many systems has been obtained. Competing adiabatic behaviour has been demonstrated and coupling matrix elements estimated.

4) The dynamics of vibronic excitation in alkali metal/molecule collisions can be described in terms of diabatic electronic motion, and quantitative models incorporating known intramolecular and negative ion potentials produce excellent agreement with experiment. A start has been made on extending this model to the very highly excited electronic states which are also observed experimentally.

2. ELASTIC SYSTEMS

A complete description is available in either quantum or classical mechanics for collisions between particles interacting only by central, range dependent forces. Such collisions are necessarily elastic. Some atomic systems, notably the rare gases at low collision energies, (well below their lowest excitation energies) fall into this class. For systems such as these, quantum effects are substantial (unlike the bulk properties of these gases) and strong quantum effects are observed (4,15). In particular, the characteristic attractive/repulsive form of the interatomic potential leads to spectacular interference effects in the total and differential cross sections. Apart from the intrinsic interest of these features, such as rainbows, glories, resonances etc. (17), it is possible to "invert" the observed cross sections to obtain information on the intermolecular potential. In principle, cross section data contains sufficient information to reconstruct completely the potential over the potential region explored by the trajectory. Unfortunately, limitations in resolution and precision

usually mean that only partial information can be extracted as to the potential over a limited range or as to some key feature of the potential.

Accurate mapping of the potential over a significant range thus requires high resolution cross section measurements over an equally extended collision energy. Such measurements have been largely limited to the rare gases. For many systems of more chemical interest the method is limited by the multiplicity of different molecular states which emerge from asymptotically degenerate states of the individual species. In some cases the resulting ambiguity can be resolved by state-selected scattering experiments, more frequently so many states are involved (as in the collision of heavy molecules) that the collision can more usefully be described in terms of an average or effective potential. The derived "potential" is then valid only over a limited range. There is thus a dichotomy between very accurate measurements leading to a full mapping of the potential for a small number of simple systems and a less precise but perhaps more chemically interesting investigation of more complex molecular systems.

The hydrogen atom illustrates this dichotomy: it plays a

direct role in much main stream chemistry interacting with many species including large organic molecules. At the same time it is the most fundamental chemical species offering in its collision processes with simple atoms or molecules the best testing ground for full "ab initio" quantum calculations. It is the logical starting point for our investigation.

The requirements for direct experimental work on H atom collisions using the molecular beam technique include a suitable source for the atoms, a velocity selector capable of producing an approximately mono-energetic beam, a scattering target and a suitably sensitive and specific detector for the scattered H atoms. The whole must be contained in a vacuum environment in which the mean free path for the atoms is much greater than any apparatus dimensions.

Ground state H atoms can be prepared by thermal dissociation at 2700 K, a superior technique to the alternative RF or microwave discharge method which is less well-defined and can produce various excited species in addition to the atoms. A suitable source of this type was developed(5). H atoms can be detected in low

concentrations either by mass spectrometric means or by calorimetrically measuring the heat liberated by their atomic recombinations. In practice, mass spectrometry is difficult because of the large background signals present at mass no. 1 while the initial ionization process depends on the density of the H atoms and is less effective at high atom velocities. In contrast, a bolometer detector responds directly to the atom flux and can be very specific for H atoms. A sensitive device of this type was developed for this work from a thin platinum film bolometer (2) and proved extremely convenient in use.

The usual mechanical rotating disc pattern of molecular beam velocity selectors are unsuitable for use with very fast atom beams, since mechanical engineering restrictions limit their rotation speed. For these experiments, a magnetic selection technique was developed using the deflection of the paramagnetic atoms in a strong magnetic field gradient (3).

The sensitivity of the apparatus was such that quantum limited total cross sections could be measured over a velocity range of $3 - 11 \times 10^5$ cm s^{-1}. The systems studied included the interactions of H atoms with the rare gases,

H and a number of saturated and unsaturated hydrocarbons. It was possible to estimate potential parameters for these systems and to compare the results with various empirical correlations (5).

More accurate estimations of potential surfaces require measurements of the differential elastic cross section since such data more sensitively reflect, via the appropriate mapping of impact parameters onto scattering angle, the range dependence of the potential. Unfortunately such measurements are intrinsically more difficult since the scattered signal is very much weaker than that measured in the total cross section experiments.

The alkali metals offered an interesting prospect in this direction since it was known that "hot wire" surface ionisation provided a very sensitive detector for them. However, the two spin states of these atoms, degenerate in zero H fields, correlate with two different potential surfaces $^1\Sigma$ and $^3\Sigma$. Some information on the rather strongly bonding $^1\Sigma$ was available from the spectroscopy of the dimer while the $^3\Sigma$ was expected to be much less strongly bound. This system thus appeared a promising one

in which to explore the use of differential cross sections in realistic chemical systems where more than one potential surface was involved. These systems were also of interest in that calculations suggested that higher order, quadrupole/quadrupole dispersion forces might be unusually important.

Interference between motion in different regions of impact parameters space, which nevertheless exits at the same scattering angle contains potential information. The angular frequency, $\Delta\theta$, of the resulting oscillations in the scattering intensity will be:

$$\Delta\theta \sim \pi\hbar/\mu V a$$

where μ and V are the reduced mass and centre of mass velocity of the system and "a" is the "grating spacing". The highest frequency thus corresponds to the effective range of the potential. For typical atomic systems at thermal energies $\Delta\theta_{MAX} \sim 0.2^{\circ}$, determining the design value for the angular resolution in an experiment. The energy resolution, $\Delta E/E$, required in the collision can be obtained similarly. Since any feature "i" is located by (D)

$$E\theta_i \sim C\varepsilon$$

where ε is the potential well depth and C is a constant, we obtain:

$$\frac{\Delta E}{E} = \frac{C\varepsilon}{\Delta\theta E}$$

and from estimates of the potential range and well depth we can obtain design requirements for the experiment. For the shallow $^3\Sigma$ potential $\Delta\theta \sim 0.2^\circ$ and $\frac{\Delta E}{E} \sim 10\%$ are suitable; in contrast at this energy resolution the structure arising from the much deeper well of the $^1\Sigma$ surface will be substantially washed out. The contribution of the surface to the observed structure will be further diminished by the degeneracy weighting of the collisions - for unselected beams three quarters of the collisions will follow the triplet surface, one quarter the singlet. Overall a substantial separation of the features arising from the two surface may be expected.

The requirements for apparatus resolution reached above were rather severe and it was clear that very low scattered signals would result. As a consequence particular attention was given to this aspect of the design and a number of novel features were developed. The different alkali metal species were distinguished by following a standard "hot wire" ionizing detector with a

four pole mass filter. The ions on exit from the four pole field were detected on an electron multiplier, discriminated and counted into a gated scaler system, the gates operating in synchronism with the modulation of one of the molecular beams. Counts were thus accumulated in either "signal + noise" or "noise" categories enabling scattering from the background gas to be eliminated. It was further necessary to interchange the scalers between these duties so as to remove any biasing in the collection.

The scalers were read directly onto paper tape together with other experimental variables such as the scattering angle. The paper tape was processed subsequently by computer, a substantial suite of programs being developed for this purpose.

This technique was very succesful - albeit on the first occasion it was used to collect significant experimental data (with L. T. Cowley) it was realised that it was necessary to operate two switches at 5-second intervals throughout the experiment - a period of 24 hours in the event! A simple automation scheme was rapidly developed

to circumvent this problem.

Further gains in signal intensity were achieved by designing a novel pattern of velocity selector having a very short path length (8). The complete system and associated computer programs are described elsewhere (7). With hindsight we can see that these new features were all successful; however the beam sources and associated pumping arrangements, although of the then current "effusive" pattern, were less successful. The design now current based on a hydrodynamic rather than a molecular expansion provides a much greater beam flux though at a considerably greater cost and complexity in pumping arrangements. Further difficulties were caused by the commercial shaft position encoders used to measure the scattering angle. Several versions from different manufacturers were used but all proved unreliable in the vacuum environment of this experiment - a trivial but damaging failure.

Using this equipment, measurements of the very small angle quantum undulations in the cross section for the NaK system (6) yielded values of Rm=5.6A and $\varepsilon = 2 \times 10^{-21}$ J for

the position and well depth in their $^3\Sigma$ potential. Unfortunately the available beam intensity was insufficient to allow measurements at this resolution to be extended over the wider range of angles needed to probe the repulsive part of the potential. However, the experiment was very sensitive to the long range features in the potential surface.

To capitalise on this sensitivity to the interactions occurring in grazing collisions it was decided to study a reactive system, $K + I_2$. This was thought to proceed at large impact parameters by electron transfer at an avoided potential crossing; the subsequent motion of the ions yielding the ionic product $KI(E)$. Measurements of the non-reactive scattering from impact parameters sampling the region of the supposed avoided crossing would be particularly sensitive to this mechanism. In nuclear physics the "cloudy crystal ball" model has been used to describe such elastic scattering from collisions of reactive species and it was possible to develop a similar description for K/I_2. The parameters in such a model are the black sphere radius, ie the range below which trajectories are swallowed to disappear for ever as reactants, its opacity and the form of the elastic

potential exterior to the black sphere.

Measurements made on this system using the apparatus described were compared with a range of model calculations (9). Clear evidence for the sudden onset of a strongly attractive - presumably coulombic - potential was found but it was shown that such electron transfer was not invariably followed by chemical reaction, even though the motion was substantially over the electronically adiabatic surface. Similar measurements at much higher collision velocities further confirmed this observation (12,13) though they also revealed a greater degree of electronically diabatic behaviour as expected from the faster collision velocity.

3. COLLISIONS WITH ELECTRONICALLY EXCITED ATOMS.

The collisions just described (and those to be discussed in the final section) explore the adiabaticity of motion over the ground state surface of the collision system. Interactions between this state and other electronically excited states at thermal collision energies are relatively sparse and usually at most one other such state can be substantially involved due to energy conservation restrictions, if for no other reason. In contrast, in collisions involving a highly excited species very many exit channels are available even for collisions with thermal velocities and the extent of electronic adiabaticity in the collision becomes of central importance.

The crossed beam technique is particularly powerful in studying such very non Boltzmann situations ie translationally cold collisions between internally very hot species since the absence of collisions in the beam

prevents equilibration. The lifetimes of electronically excited species range from 10^{-9} s upwards depending on their coupling to the radiation field. In such a time an atom would have a high probability of making a collision in a beam target of normal density and in experiments of this type the collisions zone for the two beams and the excitation process would all occur in the same region of space. It is more convenient, however, to use a longer lived metastable species. Quite a number of such states are known (F), including particularly states of atomic hydrogen and the rare gases in which a single electron is promoted into an outer s orbital: other species have a more complex electronic structure. The mercury atom $6\,^3P_2$ states are a particularly interesting example in which the outer shell is 6s and lies 6-7 eV above ground. The chemistry of metastable mercury has been extensively studied over many years, while it is also interesting in that this state has a permanent quadrupole moment. Beams of the Hg $6\,^3P_2$ states had previously been prepared by workers interested in molecular beam resonance spectroscopy (G) and although the intensities required for scattering experiments using crossed beams are much greater than are needed for spectroscopy this seemed a promising start.

Work to develop suitable sources and detectors for this species was begun in collaboration with Professor R. M. Martin of the University of California at Santa Barbara. The new devices were to be incorporated in the existing Edinburgh machine; while at Santa Barbara measurements of the photon emission arising from molecular systems colliding with the metastable atoms were to be studied.

A metastable beam source using a magnetically collimated, intense electron beam to excite a ground state mercury beam was developed. This source used efficient oxide cathodes in the electron gun and capillary array structures to produce a well collimated atom beam. It proved reliable and stable in operation though the velocity range of the metastables produced was very limited. The metastable atoms were detected on a clean potassium surface (coated in situ) by Auger electron ejection, the ejected electron being detected via a channel electron multiplier and the usual gated scalers/paper tape arrangements.

The detector proved sensitive and stable in operation but became noisy in the presence of halogen containing

molecules - presumably because of chemi-ionisation processes occuring on the potassium surface. Despite U.H.V. differential pumping for the detector region experiments with molecules of this type were difficult.

The $Hg\,^3P_2$ level contains a number of discrete states $^3P_0$ $^3P_1$ and $^3P_2$ together with their appropriate magnetic sublevels. The $^3P_1$ metastable has a lifetime of 10^{-7} s and because of the dimensions of the apparatus could be entirely neglected. The $^3P_0$ and $^3P_2$ states on the other hand are all long lived. Calculations suggested that our electron bombardment source would produce each state with equal efficiency, though the detector would probably be most sensitive to the $^3P_2$ state. However, especially near threshold, substantial polorisation effects can occur, and it was necessary to characterise the beam. A 'two wire' inhomogeneous magnetic field was used for this purpose and it was shown that all the $^3P_2$ magnetic states were equally populated while the $^3P_0$ formed less than 5% of the detected beam and could be neglected. In principle, it would have been advantageous to conduct the scattering experiment with such a state selected beam but the available beam intensity was insufficient. Experiments using this apparatus thus populated several molecular

states of the collision system and in interpreting the results it was always necessary to untangle the separate contributions of the various states.

Collisions of the Hg metastable with alkali atoms provide a good test of electronic adiabaticity since energetically all the discrete states of the alkalis together with several eV of ionisation continuum are accessible. Reorientation or M_J changing collisions are also possible though computations (20) suggested that this process would be relatively unimportant in the potential range likely to be sampled in these experiments.

Experiments with the alkali metals revealed differential cross sections with strong oscillatory structure - up to nineteen interference oscillations being revealed in the sodium case (14,16). With this detail it was possible to distinguish contributions from all three molecular states evolving in the collisions. The structure was a typical supernumerary rainbow pattern and it was inverted to obtain the long range behaviour of the potentials with some confidence (25). Most interestingly the envelope of the differential cross section showed the behaviour expected for potentials with an R^{-6} range dependence. There

was no evidence for any quenching of the electronic excitation in the collision region explored by these experiments implying a substantial electronic adiabicity. Experiments with the rare gas Neon revealed a similar absence of quenching, though in this case the potential inversion was less satisfactory due to ambiguities in the assignment of the structure in the cross section to particular molecular states.

In experiments with the molecular systems N_2, CO and CO_2 supernumerary rainbow structure was again clearly visible enabling some potential information to be extracted. However the envelope containing these differential cross sections fell off much more rapidly with scattering angle than expected for elastic scattering from an R^{-6} potential. These collisions were known to be electronically inelastic (H) and a number of potential models incorporating an absorption term to represent the electronic quenching were explored. It was not possible to make an entirely unambiguous interpretation, but it was clear that electronically inelastic behaviour was occurring at long ranges on the attractive branch of the potential. Furthermore, the angular period of the observed interference structure indicated a potential bowl much

broader and more strongly attractive than expected for a dispersion force potential - possibly associated with a contribution from the excited ion pair state, eg. Hg^{*+}/N_2^-. N_2 has an unfavourable electron affinity at its equilibrium distance but this becomes markedly more favourable as the N_2 bond extends. The slow moving thermal Hg^* atom would provide ample time for such a stretch to occur in these collisions (24).

A similar contrast was observed in experiments scattering the metastable from an unsaturated hydrocarbon propene and the saturated analogue propane. In this case the structure was insufficiently resolved to obtain potential information but the strong fall-off in scattered intensity with scattering angle, characteristic of absorption in the elastic channel was clearly visible in the scattering from the unsaturated but not from the saturated hydrocarbon. This change parallels the chemical activity of the unsaturated species in forming charge transfer species.

Thus in the systems studied the metastable quenching process appears to be initiated by a sudden change in the potential surface. It is tempting to identify this change in the alkali metal systems, with an abrupt electron transfer or 'harpoon'.(27)

4) INELASTIC COLLISIONS.

As was already clear from the experiments described sudden, substantial electron transfer frequently appears to be the initial step in inelastic processes such as chemical reaction or electronic energy quenching. Study of the elastic scattering from such systems yields useful information but by no means affords the best probe. For this purpose an experiment with the following characteristics would be more suitable:.

(i) A collision velocity variable over a range encompassing at its lower end adiabatic electronic behaviour and extending to velocities high enough for substantial diabatic effects to occur. If this diabatic behaviour occurs at an intermolecular distance Rc the requirement will be for velocities such that:

$$\frac{\text{time for electron to move distance Rc}}{\text{time for nuclei to move } \Delta Rc \text{ at Rc}} \sim 1$$

For typical molecular systems a collision velocity in the range 10^4 - 10^5 ms would be appropriate.

(ii) A collision lifetime variable about the vibrational

period of the molecule so that the role of internal motion in the electronic rearrangement can be explored. Again this requirement depends upon the vibrational modes of interest but collision lifetimes from 10^{-12} - 10^{-15} s would bracket the change from collisions slow with respect to vibration to those in which the molecular geometry was frozen during the period of the collision.

(iii) A simple trajectory throughout the collision so that the range dependence of the process can be obtained unambiguously from the angular distribution.

(iv) As much state selective detail about the exit species from the collision as possible so as to provide the maximum information for comparison with model calculations.

These requirements can conveniently be met by studying collisions between transitionally fast species so that the required lifetimes (paragraphs (i) and (ii)) can be achieved. The range of interactions involved in chemical processes can then be sampled by confining observations to small scattering angles, since collisions scattering to the same value of $E\theta$= collision energy x scattering angle (known as the reduced scattering angle) can be shown to probe the same potential region (D). The grazing

collisions required for this work then also provide the very simple, almost straight line, trajectories required for easy inversion.

Collisions involving molecular species at these collision velocities, corresponding to energies in the 10 - 1000eV range had been little studied. In comparison with thermal collision energies an enormous range of exit channels were open including several ionization continua, dissociation and the discrete states of electronic and vibration/rotation excitation. It was thus essential to assess the relative importance of such processes before proceeding further with experimental work.

It was anticipated that the electronic behaviour in these systems would be substantially adiabatic except in regions where several potential surfaces were in close proximity and it was possible to satisfy locally the Massey criterion, $\Delta E \Delta R / \hbar v \sim 1$ Indeed the velocities planned for the experiment were designed to fulfill this requirement. On the other hand the resulting atom trajectories described during and subsequent to the collision were much less easy to foresee. It was necessary to gain some understanding of these effects before proceeding with the

design of an experiment.

Molecular dynamics or Monte Carlo methods provide an excellent tool for this purpose (18,22). Exploratory computations were made using this technique for the typical system K + I_2 . It was found that in the collision conditions of interest, ie high velocity, narrow scattering angle and with E_T in the range suitable for probing the potential crossing regions, rather simple collision dynamics prevailed with almost elastic behaviour dominating the scattering. For most processes, including vibrational/rotational inelastic behaviour, it was found that a simple two-body description of the collision provided excellent agreement with the detailed computations. There appeared, indeed, to be a "window" in the region of scattering needed to probe the electronic non-adiabatic behaviour within which the collision dynamics were especially simple. This prediction was confirmed, as we shall see later, in the very first experiments made in this region on the K/I_2 system.

The experimental realisation of this program posed a number of difficulties. The substantial collision velocities required, corresponding to collision energies

in the 50 - 200eV range, could only be achieved by electrostatic methods, ie acceleration of the beam material as ions in an electric field followed by their neutralisation to yield fast atoms. At high collision velocities density dependent detectors, such as mass spectrometers, have a very low efficiency and a flux sensitive device was essential. The species suitable for use in the beam were thus limited to the alkali metals or energetic metastables which could be both electrically accelerated and effectively detected on a suitable surface. Further constraints arose from the need to distinguish the different possible exit states. For a limited number of systems photon coincidence techniques might provide such information. The velocity change method, in which the transfer of energy from initial relative motion to internal energy can be determined from the associated change in relative velocity is, however, a more generally applicable technique. Since ion beams can readily be modulated, the time of flight (TOF) realisation of this approach, in which the fast beam is pulsed and the arrival time of the scattered material recorded, appeared an attractive option.

To obtain the necessary resolution using the TOF technique

beam gate times of the order 5 - 20 ns and a detector with a similar, or better, response time were required. It was also necessary for the energy spread in the beam to be minimal (< 0.2eV). These requirements seemed feasible in the case of alkali atoms since surface ionisation provides a copious source of ions on an equipotential surface with an energy spread expected to be limited to the surface temperature. The experimental concept was thus substantially symmetric with the sequence surface ionisation/acceleration/neutralisation/collision region/ flight region/surface ionisation detector.

Estimates of the expected signal rate for an experiment with this configuration indicated that extremely long counting times would be required. This was in part due to the unfavourable duty factor associated with the TOF technique. A narrow pulse is required to obtain the necessary energy loss resolution but its repetition rate must be low to avoid scrambling the various energy loss processes expected. In certain circumstances cross correlation techniques (I), in which a 50% mark-space random word modulation is imposed on the beam, can be used. However, such a strategy is not effective in recovering small inelastic signal peaks adjacent to a

larger peak ie exactly the type of signal expected in the proposed experiment. An alternative strategy was therefore adopted making better use of the density in phase space available to the experiment by velocity modulating the fast beam, with this technique duty factors of around 50% could be achieved. It was also possible by an extension of this technique to reduce the noise background in the time regions of interest in the experiment (29).

The data collected by this type of experiment is highly structured since observations are made with cross beam on and off and as a function of scattering angle, energy loss and collision energy. Collecting such data is a difficult and error prone task that must be carried out for many hours (if count rates are low) while the complexity of the data makes it impossible to provide much feed-back to the experimenter on the progress of the experiment.

In this situation a real time computer interfaced to the apparatus can be extremely valuable in both collecting the data, controlling the experiment and providing information eg time of flight spectra, angular variation, beam stability etc to the operator so that the performance can

monitored and optimised. This system is a natural extension of the non-interactive paper-tape data logging system used in the previous experiments which could only provide such feedback after completion of the experiment and subsequent off-line processing of the paper tape.

A system of this type including a susbstantial degree of automatic control and error detection was developed (23). The system operated in a concurrent foreground/background mode with the background process providing for the continuous monitoring and control of the experiment. The foreground process interacted with the experimenter to provide various updated displays of the data and performance of the apparatus.

The first scientific experiments with this apparatus were made on K/I_2, the system which had previously been the subject of a computational study. The measurements were initially of the total differential scattering cross section (13,21) but separate observations of the TOF spectra (32) showed that the scattering was > 98% elastic (with zero energy loss), in excellent accord with the model computations.

The angular dependence of the elastic cross sections revealed a sequence of supernumerary rainbow peaks in excellent agreement with those predicted from the K^+/I^- potential obtained from spectroscopic data. The experiment thus provided the most direct evidence for the electron harpoon mechanism in these collisions and confirmed that the dynamics were substantially two body in this scattering region as predicted by the computations. The overall envelope of the differential scattering was, however, substantially different from that expected from the $K^+ I^-$ potential alone, indicating a significant electronically diabatic contribution.

The comparison of these results, which were almost entirely elastic in the neutral exit channel, with those observed in the Ar metastable halogen molecule collisions (26) is particularly striking. The metastable atom produces substantial electron excitation of the halogen molecule. This difference in behaviour is probably a consequence of the very different location of the ion pair potential surface relative to the excited states in the two systems (32).

The importance of the ion pair surface was further

highlighted by preliminary experiments with alkyl halide molecules (28). Again there was a sharp contrast with the halogen molecule scattering and numerous discrete energy loss processes involving both atomic and molecular states were observed, a difference as marked as that displayed in the reactive channel of these systems which display stripping and recoil dynamics respectively.

The richness of the TOF spectra observed in the alkyl halide systems suggested that these methods would be especially informative in these sytems and a systematic study covering a range of collision energies and molecule species was undertaken.(30)

The experiments in this programme confirmed the important role of the "ion pair" state in these collisions. It was found that the observed processes could be divided into two classes. The first group comprised all those states that could be accessed via an ion pair in the ground state. These channels included electronic excitation of the potassium atom and vibrational excitation of the alkyl halide. Narrow angle onsets and vibrational energy losses increasing with the collision lifetime were seen. These observations were consistent with a mechanism involving

two successive electron transfers, into the molecule and then back to the potassium atom. The passage of the potassium ion between the two electron transfer points then, via the collision velocity, provided a stop-watch on the evolution of the molecular negative ion. Some information on the negative ion potential in the alkyl halide molecules is available (for configurations near that of the neutral molecule) and it was possible to make a classical model of the processes. In its full complexity such a model can include all the processes of importance via "surface hops" at the potential crossings. A model of this type has been developed (33) and it was shown that the region of the potential surfaces explored differed from that covered in thermal collisions, most notably because the C-X bond stretch was restricted by the short collision lifetime. To a good approximation, as expected from the earlier dynamical study the motion can be well described as a sequence of independent two body processes. With this simplification computation is much quicker, a range of potential surfaces can be explored and it was possible to derive a model for the system in good quantitative agreement with the observed cross sections, energy losses and other potential data available. Most notably it was found that the K^+ ion considerably

perturbed the CH_3I making the $2\sigma^*$ orbital occupied by the transferred electron markedly less antibonding in character. It was also possible to estimate the relative orientation dependence of the initial harpoon, collisions with the I end providing 70% of the inelastic behaviour (36).

The assignment of the higher energy loss processes was more difficult because of the large density of states but comparison of observations on different molecules CH_3I, C_3H_7I, CF_3I, CH_3Cl etc. with high energy electron scattering enabled a tentative assignment to be made. Again it was found (34) that an electron exchange could account for the observations, though now the orbitals into which the molecule captured the electron and from which an electron was subsequently recaptured were different. The nature of this intermediate state - an excited negative ion/resonance - is now less clear.

Intriguingly the energy loss of some processes, observed only in the methyl containing molecules, was seen to vary rapidly with collision lifetime. This variation and the limiting energy loss seen in fast collisions were in agreement with estimates for excitation in the methyl

group via an electron resonance in the C-H antibonding orbital (31,34). Further work is now in progress using deuterated compounds to explore this conjecture.

The collision systems K/N_2 which is non reactive at thermal energies, is of particular interest since it has been extensively investigated in the past by a variety of techniques. Most importantly in elucidating the dynamics are recent molecular beam measurements on the $Na(3\,^2P)/N_2$ channel (J) and ab initio computations for the potential surfaces operating (K). The K/N_2 system is particularly favourable for TOF investigation since the N_2 molecular states are well separated from those of excited potassium.

Experiments with these species showed considerable inelasticity in the $K4\,^2P/N_2$ V=3 exit channel in agreement with classical model calculations using the known N_2 and N_2' potentials (L). It was found that the considerable vibrational N_2 excitation produced concurrently with electronic excitation of the K atom was a very sensitive function of these potentials so that this "no parameter" fit was especially satisfying (35). In distinction to the alkyl halide systems, however, no concurrent vibrational inelasticity corresponding to electronically adiabatic

motion at both the inward and outward crossings was observed. This observation can be accounted for if the crossing probability decreases very sharply with N_2 distance. Unfortunately the N_2 and N_2' potentials yield identical (within experimental resolution) predictions for the analogous processes exciting as $K4^2P$ in the collision energy range explored so far. Further experiments over an extended energy range are required to confirm this interpretation.

To complete this series of experiments the system K/SF_6 was studied as an example of a system reacting via collision complex dynamics at thermal energies, again it was believed as a result of an initial electron transfer. The involvement of such an electron transfer had been supported by observations of ion production in these collisions. The cross section for this process rises rapidly from threshold and shows strong coupling with the vibrational excitation initially present in the SF_6 molecule.

The interpretation of TOF experiments is more difficult in this system since substantial vibrational excitation, and ambiguity as to vibrational or electronic assignment of

the observed energy losses are possible. The observed inelastic processes at 2.4 and 4.3 eV were, however, close to those calculated from the estimates of the SF_6^-/SF_5^- potentials for scattering in the $4\,^2S$ and $4\,^2P$ potassium states. Quite small adjustments to the long range form of the SF_6^- potential could produce excellent agreement with observations and it seems very probable that an electron exchange mechanism is again responsible for the collision dynamics.(37).

References

A) Kroger, Z. Physikal. Chem., 117,387, (1925)

B) Private Communication, I. Estermann, Cannes, 1971

C) T. H. Bull and P. B. Moon, Disc. Farad. Soc. 17, 54, (1954)

D) F. T. Smith, R. P. Marchi and K. G. Dedrick, Phys. Rev. 150, 79, (1966)

E) J. C. Magee, J. Chem. Phys. 8, 687, (1940)

F) E. E. Muschlitz Jr., Adv. Chem. Phys., 10, 171, (1966)

G) W. Lichten, Phys. Rev., 109, 1191, (1958)

H) G. Karl, P. Kruus, J. C. Polanyi and W. M. Smith, J. Chem. Phys., 46,244, (1967)

I) K. Skold, Nucl. Inst. and Meth., 63, 114, (1968)

J) I. V. Hertel, H. Hoffmann and K. A. Rost, J. Chem. Phys., 71, 674, (1979)

K) P. Habitz, Chem. Phys., 54, 131, (1980)

L) F. R. Gilmore, J. Quant. Spectrosc. Rad. Transfer, 5, 369, (1965)

1

THE APPLICATION OF MONTE CARLO METHODS TO PHYSICOCHEMICAL PROBLEMS

BY

M. A. D. FLUENDY and E. B. SMITH

Reprinted from Quarterly Reviews
1962, Vol. XVI, No. 3

London
The Chemical Society

QUARTERLY REVIEWS

THE APPLICATION OF MONTE CARLO METHODS TO PHYSICOCHEMICAL PROBLEMS

by M. A. D. FLUENDY† and E. B. SMITH

(PHYSICAL CHEMISTRY LABORATORY, OXFORD UNIVERSITY)

WITH the advent of fast electronic computers the Monte Carlo method has become a powerful tool in the hands of the theoretical chemist. Based on random sampling, it can be used to solve complex problems for which analytical methods are powerless, with an accuracy limited only by statistical considerations. In many physical problems the basic elements of the calculation may be fully understood but the general complexity prevents solution by standard means. For such problems the Monte Carlo method is particularly appropriate, whereas for simple calculations it is generally inefficient. As yet no general review of the applications of the method to problems of chemical interest has been available. Monte Carlo techniques have been used with some success in three fields of particular interest to chemists and these will be reviewed separately: (1) the properties of dense gases, liquids, and solids; (2) the configuration of macromolecules; and (3) order–disorder phenomena. In each of these the appropriate analytical theories will be surveyed and their conclusions compared with the results obtained by Monte Carlo methods. The Monte Carlo methods to be described generally involve the simulation of physical systems (in a purely mathematical sense), and the method is not markedly different, in principle, from the physical simulation of such systems. There have been frequent attempts to use physical models as molecular analogues in order to obtain a better understanding of molecular processes and the structure of matter. Ball bearings, seeds, and similar objects have all been used to study the distribution of molecules in liquids and metals, though, because of the practical difficulties, much of the work has been confined to two dimensions. Morrell and Hildebrand,[1] however, constructed a model liquid by means of gelatine balls, hardened by chemical treatment, in a matrix of liquid gelatine of the same density. The "molecular" distribution in this liquid was very similar to that observed in real liquids by *X*-ray diffraction studies.

† Present address: Department of Chemistry, University of California, Berkeley 4, California.

[1] W. E. Morrell and J. H. Hildebrand, *J. Chem. Phys.*, 1936, **4**, 224.

The Monte Carlo Method[2, 3]

The difficulty of devising appropriate mechanical models has severely limited the value of physical simulations of molecular systems. However, the availability of fast electronic computers has made it possible to design calculations involving essentially the same approach. The Monte Carlo technique is, in its essential and simplest form, an experimental study of a mathematical model of some physical process. Thus, if we wished at a game of chance to estimate our probable losses due to the "house percentage," we could proceed in several ways. The simplest, but probably most expensive, would be a direct appeal to experiment; as an alternative we could attempt to analyse the statistics of the game and perform a direct calculation. For all but the simplest games this would be prohibitively difficult. In such a case the statistical approach of the Monte Carlo method may be applied. From our knowledge of the rules of the game we can construct a directly analogous mathematical scheme, using random numbers to represent the fall of dice or the distribution of playing cards. We can then "play" a large number of games until the average house winnings converge, as closely as desired, to a steady value: the house percentage. With the aid of a fast electronic computer this apparently inefficient method may produce a satisfactory result in a comparatively short time. The Monte Carlo method involving such sampling procedures can be applied to a very wide range of problems. A trivial but instructive example is the integration,

$$\bar{y} = \int_0^A f(x)dx.$$

By choosing N specific values of x ($x_1, x_2 \ldots x_i \ldots x_n$,) at random we can compute

$$\hat{y} = \frac{A}{N}\sum_{i=1}^{i=N} f(x_i).$$

The accuracy of the estimate $\hat{y}$ of $\bar{y}$ will depend on both the number of samples of x_i considered and on the nature of the function $f(x)$. For example, if we wish to estimate $\hat{y} = \bar{y} \pm \epsilon$, with 95% certainty, the number of samples required (N) is given (when N is large) by

$$N = 3{\cdot}84 \text{ var } (\hat{\bar{y}})/\epsilon^2.$$

The variance, var $(\hat{y})$, is defined as

$$\text{var } (\hat{y}) = \frac{1}{N}\left[\int_0^A f(x)^2 dx - \bar{y}^2\right].$$

[2] Monte Carlo Method, U.S. Dept. of Commerce, National Bureau of Standards, Applied Maths., Vol. XII.

[3] Symposium on Monte Carlo Methods (1954), University of Florida, John Wiley and Sons Inc., New York.

The efficiency of the method in the solution of any given problem will depend on the variance, and the key to the use of the Monte Carlo method is the devising of sampling schemes which will produce a small variance and so converge rapidly. Basically most methods of variance reduction presuppose some approximate knowledge of the final answer so that each sample may be classed according to the size of its contribution. Samples are chosen, not at random, but from some other probability function which is nowhere zero and varies so that the probability of picking a sample is greatest in the region of most importance. Samples selected in this manner are weighted (by the inverse probability of selection) to obtain an unbiased final value.

An example of both the Monte Carlo method and of the power of variance-reduction techniques in a very simple case is the determination of the area of a quadrant of a circle (Fig. 1). The simplest way would be to

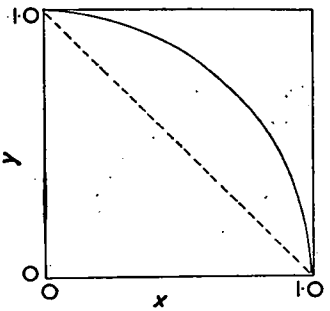

FIG. 1. *Quadrant of a circle, of which the area can be determined by both Monte Carlo and variance-reduction techniques.*

sample pairs of x_i and y_i randomly from 0 to 1, estimating the fraction of total points within the quadrant by using the condition:

$$x_i^2 + y_i^2 \leqslant 1.$$

The ratio of such samples to the total number would give the area. In this case the variance may be shown to be $0{\cdot}17/N$. A superior method would involve sampling only x randomly from 0 to 1 to evaluate the integral

$$\int_0^1 (1 - x^2)^{\frac{1}{2}} dx \approx \frac{1}{N} \sum_{i=1}^{i=N} (1 - x_i^2)^{\frac{1}{2}}$$

The variance is now

$$\text{var}\,(\hat{y}) = \frac{1}{N}\left[\int_0^1 (1 - x^2)dx - (\pi/4)^2\right] = 0{\cdot}05/N.$$

This method would be three times as efficient as the previous one if th computing time per iteration were unchanged—an assumption which is n more than approximately true. Had only those points lying above the 1, diagonal been considered, and the area of the segment been estimated, variance as low as $0{\cdot}015/N$ could be obtained. In more complicate problems even greater savings can sometimes be attained. The evaluatio of a simple integral of this type would never be carried out by a Mont Carlo method since, even if an analytical procedure were unavailable, systematic numerical quadrature would be very much more efficient However, for multiple integrations of four or more dimensions the Mont Carlo method is usually more powerful.

The Monte Carlo method has been used in two somewhat different type of problem. The first class comprises those problems to which, in principle a numerical method could be applied but is impracticable owing to com putational difficulties. High-order multiple integrations are a typica example. The second type of application is in the solution of statistica problems for which no concise mathematical formulation is available bu only a set of rules for forming a population from which samples may b drawn. In the physical world there are many problems for which a goo conceptual model of the individual events is available but in which th complex statistical nature of their interactions precludes any simpl solution. This situation is particularly common in chemistry where th behaviour of dense gases and liquids, the structure of polymers, and order-disorder phenomena in the solid state and many similar problems hav defied any quantitative understanding. The Monte Carlo method ca therefore be expected to find considerable application in chemical problems The remainder of this Review is concerned with the several attempts tha have already been made to use Monte Carlo techniques to solve suc problems. The three main areas are discussed separately. The recen applications of the method to the theory of absolute reaction rates ar also reviewed.

The States of Matter

One of the most general problems which occur in physical chemistr is the evaluation of bulk properties of matter in terms of the forces actin between molecules (and *vice versa*). The problem in general cannot b solved; thus no adequate theoretical prediction of the properties of liquid or dense gases is possible. In the first place, we lack precise knowledge o the forces between molecules. The Lennard-Jones intermolecular potentia is generally considered adequate for the inert gases but it is an over simplification when applied to more complicated molecules. Nevertheless even if an accurate knowledge of the forces between molecules wer available, the major difficulty would still remain, that is, the purel statistical problem of accounting for the mutual interactions of larg numbers of molecules. The properties of a molecular system can b

xpressed in terms of the partition function which, for a classical system, s given by

$$Z_N = \frac{1}{N!h^{3N}} \int \ldots \int \exp(-E/kT)\, dq_1 \ldots dq_{3N}, dp_1, \ldots .dp_{3N},$$

where p and q are the conjugate momenta and co-ordinates. The contribution of the kinetic energy can be evaluated by direct integration, but the ontribution of the potential energy is not so easily evaluated. The so-alled configurational integral may be written:

$$Q_N = \frac{1}{N!} \int \ldots \int \exp[-U(q)/kT]\, dq_1 \ldots dq_{3N},$$

where $U(q)$ is a function of all co-ordinates. As, in general, this integration annot be performed, most theories attempt to simplify it by approximating he relation between the potential energy of the system and the co-rdinates of the molecules. Thus the potential energy might be expressed s a function of the co-ordinates of a few molecules only. The derived hermodynamic properties are valid only so far as the initial assumptions re valid.

Two such approaches are of particular interest. At low densities the quation of state of a gas can be expressed in terms of a series of virial oefficients

$$PV/RT = 1 + B(T)/V + C(T)/V^2 + \ldots\ldots$$

The second virial coefficient, $B(T)$, is related to the relative co-ordinates of wo (spherically symmetrical) molecules by the equation

$$B(T) = -2\pi N \int_0^\infty [\exp(-U(r)/RT) - 1] r^2 dr,$$

where r is the separation of the molecular centres. If the variation of the ntermolecular potential energy $U(r)$ with r is known, $B(T)$ can be evalu-ted. At high densities the cell (or free-volume) theory has been used xtensively with moderate success. A reference molecule is considered to nove in a potential field produced by its neighbours which are assumed to e fixed on lattice sites. The method is not very satisfactory for liquids but t has been the basis of a large amount of research.

The Monte Carlo method differs fundamentally from theories of this ype as no attempt is made to simplify the configurational integral.[4] If the orces acting between molecules are known it is possible to sample the onfigurations of a large number of molecules and so evaluate the con-igurational integral with an accuracy limited only by statistical considera-ions. The assumption of the pairwise additive nature of the intermolecular

[4] I. Z. Fisher, *Soviet Physics Review*, 1960, 2, 783.

energy is an approximation common to most analytical and Monte Carl methods. The simplest type of Monte Carlo procedure would sample th configurations generated by a number of molecules placed at random in regular volume.[5] The total energy of the system could be calculated from knowledge of the form of the intermolecular potential, enabling eac overall configuration to be weighted by the appropriate Boltzmann facto The value of any equilibrium property can then be obtained by averagin over sufficient configurations. The limitation of this approach is tha except at the lowest densities, any randomly constructed molecula distribution is likely to be an extremely improbable one. Thus, in the cas of hard-sphere molecules, an acceptable non-overlapping configuration almost impossible to generate by this method at densities greater than thos appropriate to the dilute gas.

The Monte Carlo method of Metropolis, Rosenbluth, Rosenbluth, Telle and Teller.[6]—A more powerful method was devised by Metropolis *et al* The molecules are confined to a rectangular or cubic space by period boundary conditions which in effect give rise to an infinite space made up o unit translations of the basic cell. It is considered that at least 32 or 6 molecules in the basic cell are required to give an adequate picture of th condensed states of matter. Initially the molecules are distributed on lattice and new configurations are generated by moving one molecule at time. In the case of hard-sphere molecules the theory takes a particularl simple form. If a move were such as to cause an overlap, the potenti energy would be infinite and the new configuration of the system woul have zero probability and need not be considered. In such a case the syste is returned to its original configuration. However, all configurations whi do not involve overlapping molecules are equally probable and contribu to the final average of any property. Each acceptable configuration analysed in terms of a pair distribution function, $g(r)$, of the molecules. Th function defines the number density of molecular centres at a distance from a reference molecule. Thus the number of molecular pairs which a separated by a distance r is $(N^2/2V)g(r)4\pi r^2 dr$. After many configuratio have been analysed the average pair distribution function is used to ca culate the thermodynamic properties in the usual manner. Thus, for har spheres,

$$PV/RT = 1 - (2\pi/3V)\,[g(\sigma)\sigma^3],$$

where σ is the diameter of the molecules and $g(\sigma)$ is the pair distributio function evaluated at the point of contact.

This method represents a great advance on the simple technique fir described, in which molecules are introduced randomly into an appro priate space. In place of a series of independent samples, each weighte

[5] B. J. Alder, S. P. Frankel, and V. A. Lewinson, *J. Chem. Phys.*, 1955, **23**, 417.
[6] Metropolis, Rosenbluth, Rosenbluth, Teller, and Teller, *J. Chem. Phys.*, 1953, **2** 1087.

by the appropriate Boltzmann factor, this method generates new configurations in such a way that the probability of their occurrence is proportional to the Boltzmann factor and then weights all configurations equally. This corresponds to the generation of a Markov chain with constant transition probabilities.[7] Since the outcome of any trial is not independent but depends on the outcome of the trial immediately before it, the probability of configuration E_k is no longer associated with a fixed probability p_k, but to every pair E_j, E_k there corresponds a conditional probability p_{jk}. Thus if E_j occurs then the probability that E_k follows is p_{jk}. The various probabilities form a matrix of transition probabilities. A series of trials obeying statistics of this form is called a Markov chain. The absolute probability $a_k^{(n)}$, of state E_k after n steps starting from E_j can be expressed

$$a_k^{(n)} = \sum_j a_j \, p_{jk}^{(n)},$$

where a_j is the probability that E_j occurs in the initial trial. $a_k^{(n)}$ should be independent of a_j if n is large. This is the case if $p_{jk}^{(n)}$ converges to a finite limit independent of j. This is usually so if no periodicities occur. States which have a mean finite recurrence time but are not periodic are called ergodic states, and for a stationary distribution to occur all states must be ergodic. All such states can be attained from every other state. For such a system there is a stationary distribution which is unique and tends, as n gets large, to become independent of the initial state.

In a classical molecular system each state occurs with a frequency proportional to the Boltzmann factor for that state. The commonly used transition probabilities are given by:[8]

$$\left.\begin{aligned} p_{jk} &= A_{jk} && U_k \leqslant U_j \\ &= A_{jk} \exp[-(U_k - U_j)/kT]; && U_k > U_j \end{aligned}\right\} k \neq j;$$

$$p_{jj} = 1 - \sum_{j \neq k} p_{jk},$$

A_{jk} is only non-zero when the two states differ only in the co-ordinates of one molecule. A further restriction is that A_{jk} is zero if the move is such as to take the molecule a distance greater than that defined by an arbitrary fixed parameter, a condition which is included to increase the probability that moves will be acceptable. This parameter determines the rate of convergence of the method but not the final average. In the case of hard spheres the above conditions reduce to

$$\begin{aligned} p_{jk} &= A_{jk}; && U_k = 0; \\ p_{jk} &= 0; && U_k = \infty. \end{aligned}$$

[7] W. Feller, "Probability Theory and Its Applications," John Wiley and Sons Inc., New York, 1950, Ch. 15.

[8] W. W. Wood and F. R. Parker, *J. Chem. Phys.*, 1957, 27, 720.

The theory, together with many computational details, has been given by Wood *et al.*[8,9]

Molecular Dynamics.—The Monte Carlo method of Metropolis *et al.* is concerned only with the equilibrium properties of molecular systems, and the moves which the molecules undergo are not associated with real time but only with an arbitrary computer time. However, it is possible to solve with any required accuracy the simultaneous classical equations of motion of a number of molecules—this explicit simulation technique has been called molecular dynamics.[10,11] The molecules are again confined to cubic or rectangular boxes by periodic boundary conditions. To start with, the molecules are given equal kinetic energies with velocities in random directions, and after each collision the new velocities of the interacting molecules are calculated. The number of collisions as a function of time and the sum of the momentum changes, are recorded to enable the collision rate and the pressure to be evaluated. This extension to transport properties represents a great advance in simulation techniques and enables a wide range of problems of a kinetic nature to be tackled.

Hard-sphere Systems.—Hard spheres exerting no attraction on each other are the simplest type of molecular model; consequently the properties of systems of such molecules are of particular interest. The potential is defined

$$U(r) = \infty; r \leqslant \sigma;$$
$$U(r) = 0; r > \sigma;$$

where σ is the collision diameter of the molecule. Before simulation calculations were undertaken it was a matter of controversy whether such systems could undergo phase transitions. The majority of studies have involved hard sphere molecules in two or three dimensions.*[12–15] Fig. 2 illustrates the Monte Carlo equation of state for three-dimensional hard sphere systems and those predicted by various theories. Not unexpectedly the virial expansion provides an adequate model for the low-density results, whereas the cell theory is in poor agreement at all except the very highest densities. The most interesting feature of the Monte Carlo results is the phase transition which is observed in hard-sphere systems. The transition is between the fluid and the solid phase and, despite the absence of attractive forces, both phases are well defined. The Plate illustrates the change in the molecular motions in a system of hard spheres that ha

* "Two-dimensional hard spheres" are more properly called hard discs.

[9] W. W. Wood and J. D. Jacobson, Proc. Western Joint Computer Conference, San Francisco, California, 1959, p. 261.
[10] T. Wainwright and B. J. Alder, *Nuovo Cimento Suppl.*, 1958, **6**, 116.
[11] B. J. Alder and T. W. Wainwright, *J. Chem. Phys.*, 1959, **31**, 459.
[12] M. N. Rosenbluth and A. W. Rosenbluth, *J. Chem. Phys.*, 1954, **22**, 881.
[13] W. W. Wood and J. D. Jacobson, *J. Chem. Phys.*, 1957, **27**, 1207.
[14] B. J. Alder and T. Wainwright, *J. Chem. Phys.*, 1957, **27**, 1208.
[15] B. J. Alder and T. Wainwright, *J. Chem. Phys.*, 1960, **33**, 1439.

pontaneously undergone a transition from the fluid to the solid phase vith no change in density. The photographs were obtained by following he molecular trajectories for 3000 collisions, and using the method of nolecular dynamics. Hard-sphere systems undergo no gas–liquid transition nd behave like substances above their critical temperature. The simplest orm of intermolecular potential to give rise to all three states of matter is he square-well intermolecular potential which allows for molecular ttraction.

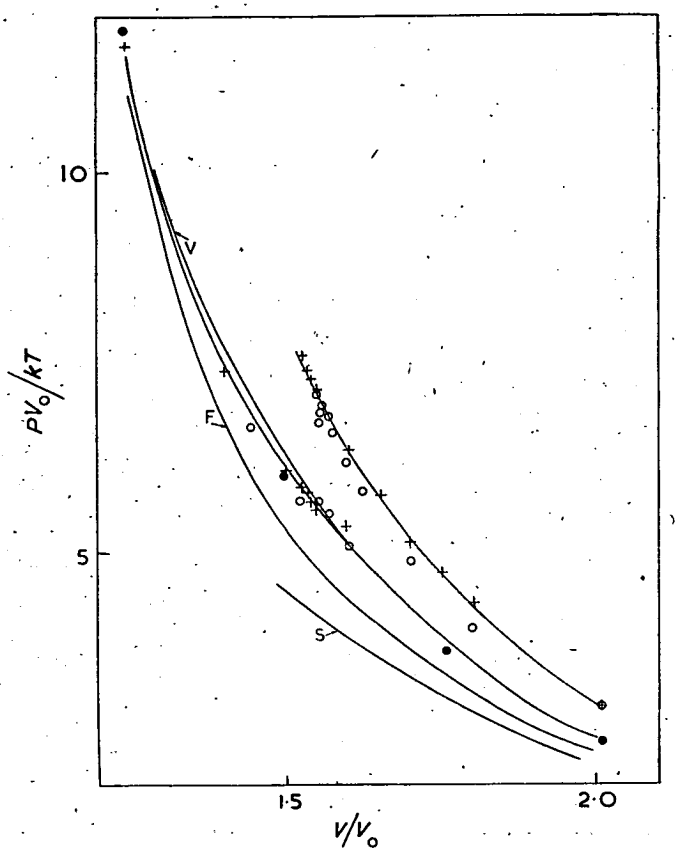

FIG. 2. *The equation of state for hard-spherical molecules.* The unlabelled solid curves represent the results obtained by molecular dynamics for system of 108 molecules. V_0 is the volume at close packing. The discontinuity at $V/V_0 \approx 1{\cdot}55$ is the fluid–solid phase transition. The predictions of various analytical methods are labelled: F, free-volume theory; V, virial expansion; S, superposition theory. Other symbols: + molecular dynamics for 32 molecules; O Monte Carlo results of Wood and Jacobson;[13] ● Monte Carlo results of Rosenbluth and Rosenbluth.[12]

(Reproduced, by permission, from ref. 13.)

Monte Carlo calculations have also been made on binary mixtures c hard-sphere molecules with a radius ratio 5:3.[16] Preliminary results showe that such systems undergo a contraction on mixing, and a feature of th results for such mixtures is that the cell model is found to be a somewha better approximation when used to predict changes on mixing than whe applied to the pure components. Further work is under way. Up t moderate densities the initial configuration of the mixture can be generate by distributing the two species randomly in a lattice. At high densities th problem of generating initial configurations is severe and special technique are required involving a gradual expansion of the radii of the molecules.[1] At these densities the results indicate that transitions between certain type of configuration become very improbable and the total number of state may be effectively divided into more than one class between which transi tions are extremely improbable. Wood, who has called this the quasi ergodic problem, has pointed out that under these conditions spuriou results will be attained.

The method of molecular dynamics has been applied to hard-spher systems, and the equilibrium properties obtained agree well with the mor recent Monte Carlo calculations. The phase transition was studied an found to be absent in systems of four or less molecules. Even with 50 molecules the two phases did not exist in the system simultaneously. Th fact that more than four molecules must be involved makes it unlikel that the transition can be studied by analytical means. A full investigatio of the dependence of the general thermodynamic properties on the numbe of molecules in the system has been made.[15] Thirty-two molecules give a reasonably adequate prediction of the equation of state in the fluid regio whereas at least 64 molecules are required at higher densities. An interestin feature of the results was the speed with which the Maxwellian velocit distribution was attained. Whereas configurational distributions are modified only very slowly, the equilibrium velocity distribution is reached after 2—4 collisions per molecule. The equilibrium collision rate is given b the Enskog theory with considerable accuracy at all densities,[18] but thi theory gives the self-diffusion coefficient correctly only in the fluid region. The exact results which have become available for this simple molecula model have already provided a stimulus to the development of analytical theories. Recently a new theory has been developed[19] which enables the equation of state of hard-sphere systems to be predicted with an accuracy never before attained. The use of the exact hard-sphere results as a basis for perturbation treatments of more realistic forms of intermolecular potential has also proved valuable.[20]

[16] E. B. Smith and K. R. Lea, *Nature*, 1960, **186**, 714.
[17] W. W. Wood, personal communication.
[18] J. O. Hirschfelder, C. F. Curtiss, and R. B. Bird, "Molecular Theory of Gases and Liquids," John Wiley and Sons Inc., New York, 1954, p. 634.
[19] H. Reiss, H. L. Frisch, and J. L. Lebowitz, *J. Chem. Phys.*, 1959, **31**, 369.
[20] E. B. Smith and B. J. Alder, *J. Chem. Phys.*, 1959, **30**, 1190.

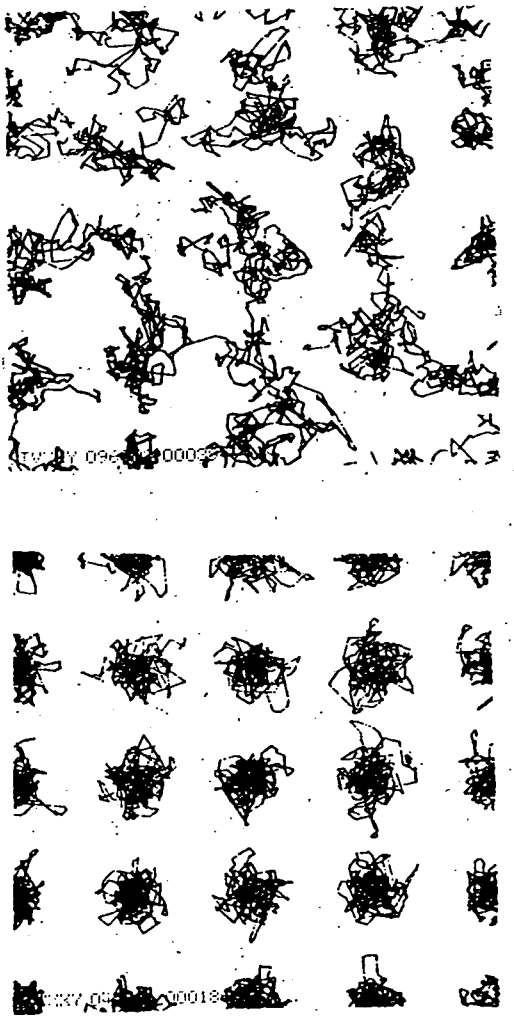

The phase transition in hard-sphere systems. The traces were made by a succession of positions in a 32-particle hard-sphere system as determined by the method of molecular dynamics. 3000 collisions (a) in the liquid phase, and (b) in the solid region. The solidification has taken place spontaneously as both systems are under identical conditions ($V/V_0 = 1{\cdot}525$).

(Reproduced by permission from Alder and Wainwright.[11])

Lennard-Jones Molecules.—The success of the method of Metropolis *et al.* with simple molecular systems led to its application to a more

realistic molecular model.[8] The Lennard-Jones intermolecular potentia

$$U(r) = 4\epsilon[(\sigma/r)^{12} - (\sigma/r)^{6}]$$

has been shown to be an adequate basis for the interpretation of th properties of the inert-gas molecules. The details of the calculation ar somewhat different from that designed for hard-sphere systems. Any con figuration j is changed to configuration k by moving one molecule. Th potential energies U_j and U_k are then evaluated; if $U_k \leqslant U_j$ the new con figuration is accepted. If $U_k > U_j$ then $\exp[-(U_k - U_j)/kT]$ is compare with a random number between 0 and 1, and, if the exponential is large the new configuration is accepted. If the reverse is true the original con figuration is retained. These conditions make the probability of any con figuration proportional to its Boltzmann factor. Because of the compara tively long-range nature of the Lennard-Jones forces the effect of distan neighbours was approximated in two ways, first, by assuming a lattic distribution and, secondly, by assuming a uniform distribution. The latte method proved satisfactory in most cases. The total potential energy o any configuration is estimated (for pairwise additive potentials) by

$$U = \tfrac{1}{2}\sum_{\substack{i=1 \\ i\neq j}}^{N}\sum_{j=1}^{N} U(r_{ij}).$$

The average potential energy over the Markov chain length gives th excess internal energy of the system. The excess heat capacity is calculate from the relation

$$C_v^E/\boldsymbol{R} = N[\langle(U/NkT)^2\rangle_{\text{av.}} - (U/NkT)^2],$$

and the equation of state from computations of the pair distribution func tion $g(r)$

$$\frac{PV}{\boldsymbol{RT}} = 1 - \frac{2\pi N^2}{3NkT}\int_0^{\infty} g(r)\frac{\mathrm{d}u}{\mathrm{d}r}\, r^3\mathrm{d}r.$$

The thermodynamic properties were calculated for Lennard-Jones molecules at the reduced temperature $kT/\epsilon = 2{\cdot}74$ and over a wide range o density to enable a comparison to be made with the experimental results of Michels *et al.*[21] and Bridgman[22] for argon at 55°C. Systems containing 32 and 108 molecules were studied and the results for both numbers were in good agreement. By using the potential parameters ϵ and σ, determined by Michels from a study of the second virial coefficient of argon, a com parison of the Monte Carlo and the experimental results can be made without the introduction of any adjustable parameters. As illustrated by Fig. 3 the Monte Carlo results and those of Michels from 150 to 2000 atm.

[21] A. Michels, H. Wijker, and H. Wijker, *Physica*, 1949, **15**, 627.
[22] P. W. Bridgman, *Proc. Amer. Acad. Arts Sci.*, 1935, **70**, 1.

re in excellent agreement but a discrepancy is evident between the alculations and Bridgman's results from 2000 to 15,000 atm. This may be ue to the inadequacy of the Lennard-Jones intermolecular potential at

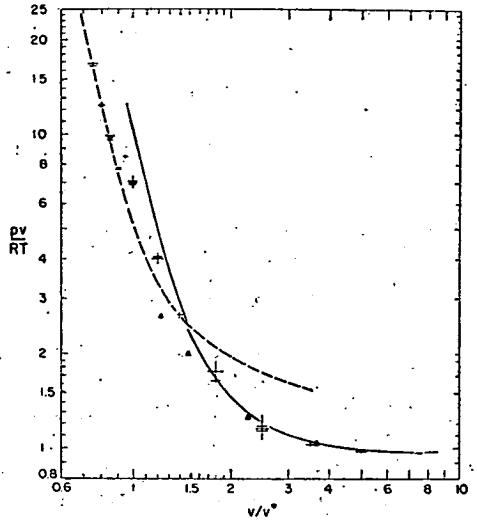

FIG. 3. *The equation of state of a system of Lennard-Jones molecules.* The crosses represent the Monte Carlo results. The upper solid curve represents Bridgman's results for argon at high pressures, and the lower one Michel's measurements up to 2000 atm. The broken curve is based on the results of the cell theory and the triangles on the superposition approximation. The discontinuity at $V/V^* \approx 1{\cdot}0$ is the phase transition. V^* is defined as $(\sqrt{2})N\sigma^3$, where σ is the collision diameter.

(Reproduced with permission from Wood and Parker.[6])

igh densities or to the fact that the pairwise additive potential approximaion is no longer valid. However, the facts that the Monte Carlo results provide a better continuation of Michels's results (whereas there is a discontinuity between these and Bridgman's), and that Bridgman's results for nitrogen, reported in the same paper, have disagreed with more recent equation-of-state determinations, suggest that the Monte Carlo results may be more accurate than the experimental results at high densities.

Order–Disorder Problems.

Many physical and chemical problems involve order–disorder processes on lattices. Superlattice transitions in alloys and the various co-operative transitions in many solid compounds are common examples. A theory of regular solutions has also been developed by using a lattice model. The general theory of order–disorder processes is appropriate to many similar phenomena.[23]

[23] E. A. Guggenheim, "Mixtures," Oxford University Press, London, 1952.

The simplest case involves two species A and B distributed on a lattice The total interaction energy can be written

$$U = N_{AA}\,\omega_{AA} + N_{BB}\,\omega_{BB} + N_{AB}\,\omega_{AB},$$

where $N_{\alpha\beta}$ is the number of $\alpha\beta$ neighbour pairs and $\omega_{\alpha\beta}$ is the interactio energy of α and β species. An interchange energy ω is defined as

$$\omega = \omega_{AB} - \tfrac{1}{2}\omega_{AA} - \tfrac{1}{2}\omega_{BB},$$

which represents the energy of formation of an AB pair. The total energ is clearly dependent on the distribution of A and B on the lattice, that is the degree of order present. The simplest treatment of this problem is t assume that the distribution is random despite the different energies o interaction. This has been called the zero-th approximation and was use by Bragg and Williams in their theory of superlattice transitions.[24] In th case of most liquid mixtures ω is positive and the tendency is toward phase separation, but for many metal alloys ω is negative and the tendenc to form unlike pairs leads to a regular array called a superlattice in whic the number of such pairs is maximum. Both tendencies are overcome b high temperatures, which favour random mixing, and definite transitio temperatures exist at which randomness overcomes the ordering tendency Such transitions are associated with a large rise in heat capacity. Th transition temperature (T_c) is given by

$$T_c = z\omega/2k$$

for the zero-th approximation, where z is the number of nearest neighbours More sophisticated approximations make some allowance for the fact tha the energy differences involved in the formation of various pair leads to non-random distribution. Thus Guggenheim suggested that a paralle with chemical equilibrium could be drawn and proposed

$$N_{AA}N_{BB}/(N_{AB})^2 = e^{2\omega/kT}/4.$$

This equation is the basis of the quasi-chemical theory which is a first-orde approximation. This theory gives

$$T_c = \omega/\{k \ln [z/(z-2)]\}.$$

Higher approximations are prohibitively difficult to evaluate by norma methods but the problem is most suitable for Monte Carlo study. Salsburg Jacobson, Fickett, and Wood[25] applied the Monte Carlo method to a two dimensional triangular lattice-gas (a lattice whose sites are only partl filled by interacting particles) for which an exact solution is available. Th co-ordination number of the lattice is 6 and the molecules interact onl

[24] W. L. Bragg and J. E. Williams, *Proc. Roy. Soc.*, 1934, *A*, **145**, 699; *ibid.*, 1935 *A*, **151**, 540.

[25] Z. W. Salsburg, J. D. Jacobson, W. Fickett, and W. W. Wood, *J. Chem. Phys.* 1959, **30**, 65.

ith nearest neighbours, the interaction giving rise to a pair energy ϵ. such particles are considered, distributed on M lattice sites. New configurations are generated by moving a "molecule" to an unoccupied site lected at random, and the system is contained by periodic boundary conitions. The details of the method are similar to that devised by Metropolis *al.* If the new configuration has a lower energy it is accepted. If not, the xponential of the energy difference is compared with a random number etween 0 and 1. An exponential greater than the random number leads the acceptance of the new configuration, otherwise the system is turned to its original state. Systems of from 8 to 98 molecules were udied on lattices for which 50% of the sites were occupied ($N/M = 0{\cdot}5$) a reduced temperature defined by

$$\exp(-\epsilon/kT) = 2.$$

he results were extrapolated to give values corresponding to an infinite umber of molecules. The ratio U/ϵ, that is, the ratio of the average internal nergy per molecule to that of a single pair interaction (or the average umber of nearest-neighbour bonds per molecule), was found to be 1·896. he value given by exact treatment[26] was 1·8938. About 500,000 configurations were considered in each case. A further study was made of the variation of the properties of the system with the fraction of sites occupied. The sults show the power of the Monte Carlo method in dealing with problems this type. In a similar study, Fosdick[27] considered a two-dimensional ttice, and for a 20 × 20 lattice rapid convergence was reported except ear the Curie point, but as yet only a preliminary notification of the search is available.

The Monte Carlo method has also been applied to more realistic lattices interest to metallurgists. Guttman[28] investigated order–disorder henomena in a body-cenrted cubic lattice containing two types of atom. e considered systems of from 256 to 1024 molecules at various composiion ratios. With $\omega_{AA} = \omega_{BB} = 0$, and $\omega = \omega_{AB}$, the total energy is ven by

$$U = -N_{AB}\,\omega,$$

here N_{AB} is the number of A–B interactions. The results for an infinite ystal are summarised in the annexed Table, together with the predictions various theoretical approximations. ρ_c represents the value of the short-nge order parameter at the transition temperature. ρ is defined by

$$\rho = \frac{N_{AB} - N_{AB\,(random)}}{N_{AB\,(perfect\ order)} - N_{AB\,(random)}}$$

[26] G. F. Newell and E. W. Montrose, *Rev. Mod. Phys.*, 1953, **25**, 353.
[27] L. D. Fosdick, *Bull. Amer. Phys. Soc.*, 1957, **2**, 239.
[28] L. Guttman, *J. Chem. Phys.*, 1961, **34**, 1024.

TABLE. *Comparison of the results for a* 1:1 *superlattice in a body-centr cubic lattice at the critical temperature.*[28]

Method	$kT_c/z\omega$	S_c/Nk	C_v/Nk	ρ_c
Bragg–Williams (zero-th order)	0·5	0·693	1·50	0
Quasi-chemical (1st order)	0·435	0·652	1·78	0·144
Domb[a]	0·385	0·548	(∞)	0·311
Monte Carlo	0·379	0·495	(∞)	0·418

[a]Domb, Changements de phases, Comp. rend. reunion ann. avec comm. therm dynamique, union intern. phys., Paris, 1952, p. 177.

The heat-capacity maximum in the region of order–disorder transitio reaches a maximum in an asymmetric manner. The Monte Carlo resul are in quite good agreement with the experimental heat capacities f $\beta_{Cu\text{-}Zn}$, considering the primitive nature of the model used. Guttma concludes that the power of such calculations lies, not so much in the fa that they can be adapted to give exact numerical solutions of these problen as in the insight they give towards the construction of a simple but adequa theoretical model.

Fosdick[29] investigated order–disorder phenomena in a A_3B alloy on face-centred cubic lattice, using a rather more sophisticated model. H defined interaction parameters

$$\omega^{(n)} = \tfrac{1}{2}\omega_{AA}{}^{(n)} + \tfrac{1}{2}\omega_{BB}{}^{(n)} - \omega_{AB}{}^{(n)},$$

where n refers to the order of the neighbour. Considering only first- ar second-nearest neighbours, two parameters are defined, $\omega^{(1)}$ ar $\lambda = \omega^{(2)}/\omega^{(1)}$, the latter representing the ratio of the interchange energi of the first and the second series of neighbours. Using systems of 5(lattice sites in $5 \times 5 \times 5$ unit-cell arrays, and with periodic bounda conditions, he studied the system when $\lambda = 0$, $-0{\cdot}25$, and $-0{\cdot}50$. Tl transition temperature at these values of λ is given by $kT_c/\omega^{(1)} = 1{\cdot}0$ 1·61, and 2·25, respectively. Taking $\lambda = -0{\cdot}25$, for the Cu_3Au syster $\omega^{(1)}$ is calculated to be 816 cal./mole, compared with values of 802 and 7 suggested by previous workers.

The Properties of Macromolecular Systems

The properties of high polymers of both natural and synthetic origin ha been of interest for many years. Their anomalous physical properties, su as viscosity, which is dependent on the shear rate, light scattering, and lon range elasticity have provided a challenge to theory. The aim of all work this field is to explain these macroscopic properties in terms of the detail molecular geometry of the long chains involved. Unfortunately a kno

[29] L. D. Fosdick, *Phys. Rev.*, 1959, **116**, 565.

edge of the molecular formula and geometry of a polymer in the normal hemical sense is not sufficient, since the properties of such molecules do epend directly, not upon the formal chemical structure, but upon the ctual configurations adopted by the polymer chains. In most work, the eometric properties of these chain configurations have been reported in erms of the average square distance between the ends of a chain of N nks, $<R_N^2>_{av}$. This quantity furnishes an indication of the size of the nolecule and can be used in the prediction of its viscous properties. For xample it has been suggested[30] for polymer solutions that

$$\eta_0 = K[<R_N^2>_{av}]^{\frac{3}{2}}/M,$$

where η_0 is the intrinsic viscosity, which is obtained by extrapolation to ero concentration and zero rate of shear, M is the molecular weight, and K a constant.

Thus the first step in any rigorous treatment of the properties of a nacromolecule must be the evaluation of the "average configuration," deally in terms of a probability density function (W) which defines the robability of finding a chain segment of the macromolecule in a given egion of space. This function being given, the problem is reduced to one n mechanics, albeit a very complex one. It is with the calculation of W hat we shall be concerned in the remainder of this discussion.

In principle it should be possible to calculate W exactly from a knowledge f the segment–segment interactions and the molecular geometry, but n practice the statistical complexity is too great. However, many approxinate methods have been devised. The simplest models[31,32] consider a olymer molecule as a long, freely jointed chain or random walk of equal teps, a model directly analogous to Brownian motion and for which the eometric properties can be determined exactly. Attempts have been made o improve this model by allowing for the effect of restricted rotation and ixed bond angles on the mean chain configuration. In the first such ttempt Kuhn[33] showed that the variations in end–end length due to these nolecular factors over a chain of many links could be dealt with by rouping several molecular links together to form a "statistical length." The actual molecular chain could then be replaced in the calculation by a hain made up of an equivalent number of freely jointed statistical lengths. The exact physical relation of the statistical length to the link length epends principally upon the intramolecular forces assumed in the calulation of Boltzmann weighting factors for each configuration.

An alternative method (*e.g.*, ref. 34) confines the chain segments to a attice, the tetrahedral diamond lattice being particularly suitable for use vhen discussing quadrivalent carbon chains. The relative probability for

[30] M. L. Huggins, *J. Phys. Chem.*, 1938, **42**, 911.
[31] E. Guth and H. Mark, *Akad. Wiss. Wien. Sitzungber.*, **IIb**, 1934, **143**, 445.
[32] W. Kuhn, *Kolloid Z.*, 1934, **68**, 2.
[33] W. Kuhn, *Kolloid Z.*, 1936, **76**, 258.
[34] R. P. Smith, *J. Chem. Phys.*, 1960, **33**, 876.

each possible step at every stage of the chains's growth is computed, as in th Kuhn model, by considering the Boltzmann weighting factor for the ste The random walk on a lattice is known as a Polya walk, and it is possibl as in the case of a walk in continuous space, to calculate the averag configuration of the chain. In general the theoretical calculations predi that a limit of the form

$$\lim_{N\to\infty} <R_N^2>_{\mathrm{av}} = Nl^2A$$

exists where l = the individual link length, and A is a constant dependin on the molecular properties of the chain. Unfortunately all calculatio based upon these types of model are deficient in one important respec No account is taken of the impossibility that two chain segments occup the same region of space. In other words no allowance is made for th "excluded volume".

The Problem of Excluded Volume.—Despite many attempts to in corporate this factor in calculations, only one exact result has bee obtained (on the limiting-step entropy for walks on a lattice).* In gener the theoretical treatments have given rise to widely divergent prediction Indeed it would be little exaggeration to say that all possible predictio as to the effect of excluded volume on chain configuration have been mad at one time or another. The difficulty seems to lie mainly in the math matical complexities associated with problems such as this in which th probability of any step depends directly, not only upon the immediate prior step, but upon all the previous steps

Rubin[35] in an ambitious attempt to secure a solution to the problem self-avoiding random walks in continuous space was able to show that was a bad approximation to neglect even high-order interactions (*i.e* interactions between segments separated by many chain links) and tha no useful approximate solution was likely to be found; however, he wa able to set an upper bound of 0·5 on ϵ in the empirical equation

$$\lim_{N\to\infty} <R_N^2>_{\mathrm{av}} = KN^{(1+\epsilon)}.$$

Flory and Fox[36] in a less fundamental approach assumed that the densit distribution of the excluded volume chain about a central reference poi was Gaussian in form but broadened by segment–segment interactio Thus $<R_N^2>_{\mathrm{av}} = <R_N^2>^{\circ}_{\mathrm{av}} A^2$, where $<R_N^2>^{\circ}_{\mathrm{av}}$ refers to the simp model involving no excluded volume corrections and A is an "expansio coefficient." From thermodynamic considerations they deduced tha $A^5 - A^3 = BN^{\frac{1}{2}}$ and that $<R_N^2>_{\mathrm{av}}/N$ increased with N. Unfortunatel

* The limiting step entropy dS_∞ for walks on a lattice is defined as

$$dS_\infty = k \log \lim_{N\to\infty} \left(\frac{\text{Number of allowed } n \text{ step walks}}{\text{Number of allowed } (n-1) \text{ step walks}} \right)$$

[35] R. J. Rubin, *J. Chem. Phys.*, 1952, **20**, 1940.
[36] P. J. Flory and T. G. Fox, jun., *J. Amer. Chem. Soc.*, 1951, **73**, 1904.

e approximations are of doubtful validity and it has been shown recently[37] at $(A^5 - A^3)/N^{\frac{1}{2}}$ is not constant but is an increasing function of A. ther workers[38] have used the simple unrestricted random walk as a first proximation and have attempted to allow for the effect of the excluded lume by incorporating additional "volume perturbation" terms in uations such as the differential Fokker–Planck equation which describes e distribution of end–end distances for simple random walks. However, e solution is very sensitive to the nature of the terms included and con- cting conclusions have been obtained.

Work on the other model of a polymer—the self-avoiding random walk a lattice (SARWL)—has followed a more purely mathematical course; e has been made of a method in which rigorous upper and lower bounds ϵ in the relation $\lim_{N\to\infty} <R_N^2>_{\text{av}} = KN^{(1+\epsilon)}$ are calculated, thus enabling e true value to be bracketed.[39] Unfortunately, it is not possible to produce very accurate estimate of ϵ in this way since the calculations become pro- bitively difficult if any but drastic simplifications are made. A method of rect enumeration has also been used in which the number of allowed nfigurations is counted directly.[40] The self-avoiding random walk has ovided the only exact theoretical result in the field. Hammersley and orton[41] were able to show that the limit $\mu = \lim_{N\to\infty} C_N/C_{N-1}$ exists for rtain lattices where C_N and C_{N-1} are the total numbers of N and $N - 1$ ep self-avoiding walks possible on the given lattice. The actual value of cannot yet be deduced mathematically but must be found experimentally. ne constant μ is often known as the attrition constant since it determines e probability that the SARWL will be disallowed at its next step owing an intersection. It is in fact related to the limiting-step entropy.

Monte Carlo Calculations.—The disagreement between the various proximate theoretical treatments of the chain-configuration problem ggests that none of them is entirely satisfactory. Unfortunately it is fficult to use experimental evidence to resolve this conflict since all the perimentally accessible quantities depend upon some bulk property nich, as yet, can only be related to the polymer configuration in a rather bitrary fashion. In this situation it would obviously be valuable to have me means of checking the accuracy of the theoretical prediction at some termediate stage. A Monte Carlo method is well suited to this purpose nce it can supply "experimental" information about chain configuration at would not otherwise be available.

An electronic computer can readily be programmed to generate a ttice model of a macromolecule by selecting, at random, steps along the

[37] M. Kurata, W. H. Stockmayer, and A. Roig, *J. Phys. Chem.*, 1960, **33**, 151.
[38] E. W. Montroll, *J. Chem. Phys.*, 1950, **18**, 734; J. J. Hermans, M. S. Klamkin, and Ullman, *J. Chem. Phys.*, 1952, **20**, 1360; H. M. James, *ibid.*, 1953, **21**, 1629.
[39] M. E. Fisher and M. F. Sykes, *Phys. Rev.*, 1959, **114**, 45.
[40] M. E. Fisher and B. J. Hiley, *J. Chem. Phys.*, 1961, **34**, 1253; 1961, **34**, 1531.
[41] J. M. Hammersley and K. W. Morton, *J. Roy. Stat. Soc.*, 1954, *B*, **16**, 1, 23.

lattice vectors, disregarding all chains which intersect. The "populatior of random walk self-avoiding chains so generated can then be used determine the various averages, such as end–end length, of theoretical ar practical interest.

The method used differs in one important respect from that applied the simulation of systems of hard-sphere molecules at high densities (as the equation of state investigations), where the new configurations we achieved by the random motion of the constituent molecules over cor paratively short distances. Thus there was a strong correlation between tl configurations at successive iterations, and the approach to equilibriu was, in some sense at least, kinetic. In the generation of model polym chains the packing density is much smaller (though this might not apply to polymer in a very unfavourable solvent or with strong intersegment a tractive forces) and it is consequently possible to generate entirely ne random configurations of the chain at each iteration (though we shall s later that in some cases greater efficiency can be achieved by retaining certain amount of the previous configuration). Thus the averaging carried out over a spatial or Gibbsian ensemble. This method of averagir has several advantages and in particular it should be noted that, if th method were not used, severe complications would arise due to the existen of certain classes of state—corresponding perhaps to knotted configuratio of the polymer chain—between which the probability of transition, whi not zero, would be very low. Thus the probability of the molecule "escaping" from this state during the "time" over which the averagir is carried out may be effectively zero. This type of behaviour is effective non-ergodic and convergence of the average to the true value for systen showing this behaviour cannot be expected in any reasonable computir time.

The first attempts to perform this type of calculation were made by Kir on simple punched-card equipment,[42] but most of the subsequent wo has been due to Wall and his co-workers.[43] All the investigations have be concerned with self-avoiding walks on various lattices, the tetrahedr being the most intensively studied. Interest has been focused mainly c the variation of the mean-square end–end length as a function of tl number of steps in the chain, although the radius of gyration, ring-closur probability, and limiting-step entropy have all been considered. It w found that for most two- and four-dimensional lattices the rat

[42] G. W. King, Monte Carlo Method, U.S. Dept. of Commerce, Nat. Bureau Standards, Appl. Maths., Vol. XII.

[43] F. T. Wall, L. A. Hiller, and D. J. Wheeler, *J. Chem. Phys.*, 1954, **22**, 1036; F. Wall and L. A. Hiller, *Ann. Rev. Phys. Chem.*, 1954, **5**, 267; M. N. Rosenbluth a A. W. Rosenbluth, *J. Chem. Phys.*, 1956, **23**, 356; F. T. Wall, L. A. Hiller, and W. Atchison, *ibid.*, 1955, **23**, 913; F. T. Wall, L. A. Hiller, and W. F. Atchison, *ibi* p. 2314; F. A. Cotton and F. E. Harris, *J. Phys. Chem.*, 1956, **60**, 1451; F. T. Wa L. A. Hiller, and W. F. Atchison, *J. Chem. Phys.*, 1957, **26**, 1742; F. T. Wall, R. Rubin, and I. M. Isaacson, *ibid.*, 1957, **27**, 186; F. T. Wall and J. J. Erpenbeck, *ibi* 1959, **30**, 634; G. S. Rushbrooke and J. Eve, *ibid.*, 1959, **31**, 1333; P. J. Marcer, D. Ph thesis, Oxford, 1960.

$\langle R_N^2 \rangle_{av}/N$ diverged and converged, respectively, as N increased. But for three-dimensional lattices of practical interest the trend of this ratio is less clear, and chains of greater length must be sampled. This is not easy, since, as the chain becomes longer, the probability of successfully adding a further step decreases. The probability that a step will be allowed was found[43] to decrease exponentially with increasing chain-length, *i.e.*,

if N_s = number of s step walks successful, and

N_0 = number of walks started,

then $N_s = N_0 \exp(-\lambda s)$,

where λ is called the attrition coefficient.

To counter this difficulty various "enrichment" procedures are used and much recent research has been concerned with developing satisfactory schemes for extending the chain lengths that can be sampled. One method, due to Wall and Erpenbeck,[43] utilises allowed chains of a certain length (say s steps) as a basis for the development of a number of longer chains so that a tree of such chains is produced (see Fig. 4). It can be seen that

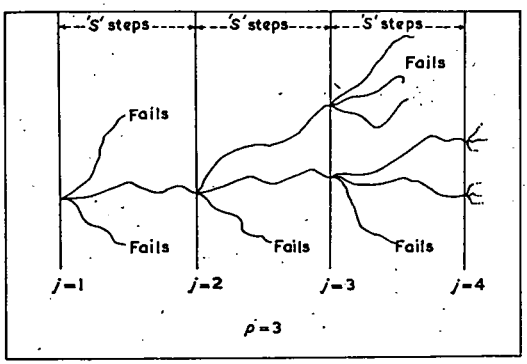

FIG. 4. *Chain enrichment by branching.*
If j is the number of levels at which branching occurs and p the number of branches started at each level, wasteful attrition or excess branching is minimised if $p = \exp(\lambda s)$ where λ is a constant and s the number of steps at each level.

wasteful branching or attrition is minimised when the number of walks started at each level is equal to the number of walks expected to fail within s steps.

A more sophisticated technique, devised by Marcer,[43] uses the branching procedure of Wall and Erpenbeck, but, instead of adding steps singly, whole sections of chain (40 step sections were in fact used) are added. These sections of self-avoiding chain are generated without difficulty by a straightforward Monte Carlo method. This technique is more efficient than the original Wall and Erpenbeck method since intersection within the

individual lengths is prevented and the overall chain attrition much r duced. With this method reasonably large samples of chains up to 20(links in length can be obtained. By these techniques a good knowledge the properties of self-avoiding chains has been built up.

The results for tetrahedral chains have been fitted to the relatio $\lim_{N\to\infty} <R_N^2>_{av} = KN^{(1+\epsilon)}$ (by analogy with the simple random-wa problem).

As longer chains have been sampled it has been found necessary t change the parameters, *e.g.*, for $N \approx 200$, $<R_N^2>_{av} = BN^{1.22}$ wa suggested; for $N \approx 800$, $<R_N^2>_{av} = B'N^{1.18}$ gave a better fit; fo $N \approx 2000$, $<R_N^2>_{av} = B''N^{1.13}$.

Most recently of all, Marcer has suggested that a relation of the for $\lim_{N\to\infty} <R_N^2>_{av} = KN\log N$ gives a better fit, both to his values for chai up to 2000 links in length and to the previous data due to Wall. The typic behaviour of some SARWL's is illustrated in Fig. 5. In the case of th three-dimensional lattice at least, the limiting behaviour has not bee reached and the plot is curved towards the log N axis.

Fig. 6 shows a comparison between the Monte Carlo results of Wa *et al.* and of Marcer, and some A factors determined by viscosity measure

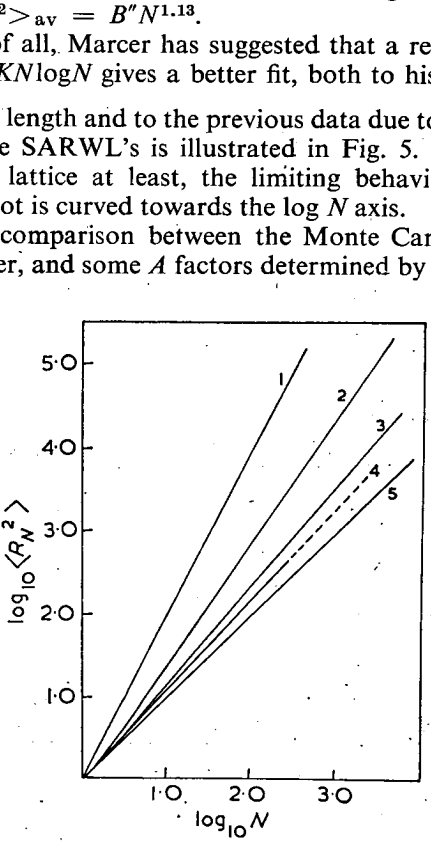

FIG. 5. *Typical behaviour of* $\langle R_N^2\rangle_{av}$ *for various types of lattice.*
(1) Self-avoiding random walk in one dimension (gradient = 2).
(2) Self-avoiding random walk on a two-dimensional square lattice.
(3) Self-avoiding random walk on a three-dimensional diamond lattice.
(4) Self-avoiding random walk on a typical four-dimensional lattice.
(5) Unrestricted random walk in three dimensions (gradient = 1).

(This Figure is based upon one given by Wall, Hiller, and Atchison.[43])

ments;[44] as can be seen, the Monte Carlo results conform quite well to the experimental values over the range of "A" values available and indeed suggest that even the comparatively primitive lattice model used in these

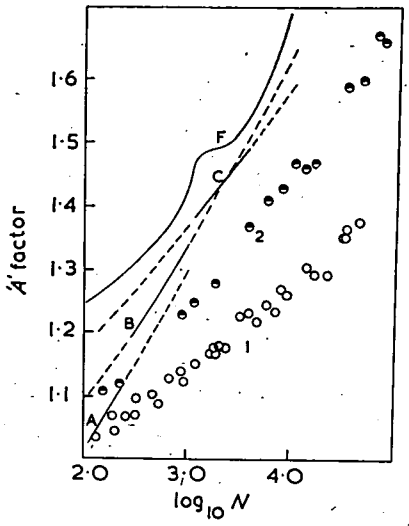

FIG. 6. *Comparison of "A" factors calculated from Monte Carlo results with factors obtained by viscosity measurements.*[47]

"A" factors from viscosity data for polyisobutenes: ○, at 20°C; ◓, in cyclohexane at 30°C.

Limiting dependence of A on N from Monte Carlo results:

A, Wall, Hiller, and Wheeler;[43] B, Wall and Erpenbeck;[43] C, Marcer.[43]

Curve F shows the value of A as calculated from the Flory relation $A^5 - A^3 = BN^{\frac{1}{2}}$, B being taken arbitrarily as 100 for this plot.

The A factors from viscosity measurements were computed by using the relation $A^3 = [\eta_0]/KM^{\frac{1}{2}}$.

While for the Monte Carlo results A was calculated as $A^2 = \langle R_N^2\rangle_{av}/\langle R_N^2\rangle^{\circ}_{av}$ where $\langle R_N^2\rangle^{\circ}_{av}$ was found by Tobolsky's method[34] using $E = 0{\cdot}8$ kcal. mole^{-1}.

calculations may form a reliable guide to the configuration of a polymer molecule. A more detailed comparision of theoretical and Monte Carlo results has been made by Kurata *et al.*[37]

Random Walks in Continuous Space.—The self-avoiding walk on a lattice is, of course, at best only an approximate model of the polymer molecule. A more realistic simulation would allow the walk to occur in continuous space and would incorporate as accurately as possible the various intramolecular-force fields. The application of a Monte Carlo method to a model of this type would correspond quite closely to the solution of the multidimensional integral formulated by Rubin. Naturally the greater mathematical complexity of this type of model will limit the

[44] P. J. Flory and W. R. Krigbaum, *J. Polymer Sci.*, 1953, **11**, 37.

chain lengths accessible to computation, but it is possible to compute end-to-end length distributions and other characteristic properties which can be compared with experimental observations of, for example, the transition-state enthalpy in cyclisation reactions.[45]

Computation of Absolute Reaction Rate

The theoretical calculation of absolute reaction rates has long been the subject of investigation but, at present, progress is severely limited by the mathematical difficulties of the transition-state theory. Briefly, this theory involves the calculation of a multidimensional surface describing the potential energy of the reacting system as a function of the position of all the nuclei. This, of course, in itself is an immensely difficult task but in simple cases such as the H_2–H reaction a reasonable approximation to the potential-energy surface can be constructed.

If equilibrium is assumed between the reactants and the so-called "activated complex" which exists in the neighbourhood of the saddle point in the potential-energy surface, it is possible to calculate the concentration of the complex in the system. The activated complex can suffer one of two fates; it may decompose to yield the original reactants, or reaction may occur with the formation of products. The fraction of such fruitful collisions is known as the "transmission coefficient." Thus, if the potential energy surface and the concentration of activated complex are known and the transmission coefficient can be calculated, our understanding of the reaction rate is complete.

The most elegant approach is the purely quantum-mechanical one in which the problem is regarded as the transmission of a wave packet through a potential-energy surface and a solution obtained by solving a time-dependent Schrödinger equation; unfortunately the mathematical difficulties of this method are at the moment almost prohibitive.[46]

An alternative procedure, possible in some cases, is to treat the assembly classically and, after computation of the potential-energy surface from quantum-mechanical considerations, to formulate the Hamiltonian equations of motion for the system of reacting nuclei. The track of all the nuclei can then be followed by solving these equations at successive short intervals of time, and hence the outcome of the collision, namely reaction or no reaction, can be determined.

Wall, Hiller, and Mazur[47] have used this procedure in an attempt to study the reaction, $H + H_2 \rightarrow H_2 + H$. In their method the positions of all the nuclei throughout the interaction are "plotted" on a cathode-ray screen and photographed at short intervals, plots similar to Fig. 7 being obtained. By repeating this procedure many times for different initial

[45] M. A. D. Fluendy, unpublished results.
[46] E. M. Mortensen and K. S. Pitzer, in "The Transition State," *Chem. Soc. Special Publ. No.* 16, 1962.
[47] F. T. Wall, L. A. Hiller, and J. Mazur, *J. Chem. Phys.*, 1958, **29**, 255; 1961, **35**, 1284

onditions of translational, vibrational, and rotational energy, it was ossible to determine the relation between these quantities and the robability of reaction. Though the results published so far are very

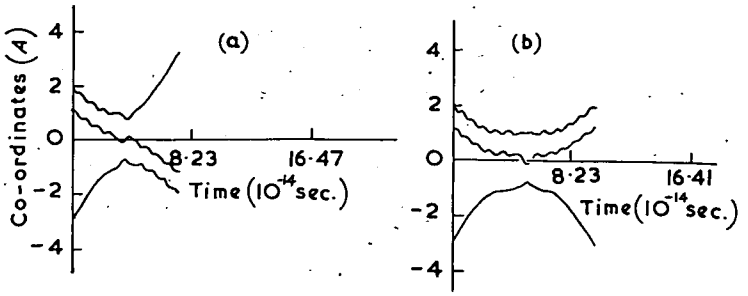

IG. 7. *The figures show the tracks of all the reacting nuclei in the reaction* $H + H_2 \rightarrow H_2 + H$.
A hydrogen atom is shown coming from the bottom of the diagram to collide with a ibrating hydrogen molecule (the top two tracks). For clarity collinear collisions are lustrated

(a) Reaction (b) No reaction

(Reproduced with permission from ref. 47.)

imited, it is apparent that the vibrational energy plays only a small part in ctivating the complex and that molecules with little or no rotational nergy are more likely to react with the colliding hydrogen atom.

Conclusion

From the preceding discussion it is clear that the Monte Carlo tech- iique can be applied to a wide range of physicochemical problems, where t can be used, not only to provide numerical results, but also to guide the ntuition in the construction of new theories. It must be remembered, owever, that it is expensive of computer time and therefore a method of he last resort which should only be used for tackling those problems for vhich analytical or conventional numerical methods are useless. What- ever the application of the method, it is essential that the fullest use be nade of any information available concerning the expected result, so that an efficient sampling scheme may be devised, since, in some cases, the computing time required to achieve a given accuracy may be reduced by several orders of magnitude by good sampling. Indeed, so important are he savings available that it may prove worthwhile to attempt to design a programme that would automatically optimise its sampling as the com- putation proceeded.

In fields outside chemistry the method has been shown to have wide applications. Successful applications range from scattering problems in nuclear physics to models of economic behaviour and the reorganisation of industrial stock piles. One thing seems certain; as electronic computers

of the present generation are replaced by new models (at least 100 time faster) the scope of the Monte Carlo method must increase. In particula the properties of systems involving long-range interactions, such a plasmas and electrolytic solutions, may be studied. The method may als find application in the investigation of extended gravitational systems surface-catalysis effects, the probability of knotting and similar topologica problems in long-chain polymers, and in quantum mechanics.

The authors thank Mr. R. P. Bell, F.R.S., for advice and encouragement and Dr. D. Handscomb for helpful comments on the manuscript.

PRINTED IN ENGLAND

THANET PRESS MARG

Reprinted from THE REVIEW OF SCIENTIFIC INSTRUMENTS, Vol. 35, No. 11, 1606, November 1964
Printed in U. S. A.

Recombination Detector for Atomic Hydrogen Beams*

M. A. D. FLUENDY

Department of Chemistry, Harvard University, Cambridge, Massachusetts

(Received 24 June 1964)

IT has been suggested by Estermann[1] that a bolometer might be used to detect beams of free radicals, and such a device was constructed by Reilly and Rabinovitch,[2] although with very limited success. In this note a bolometer detector is described which, when used with a phase sensitive amplifier, is capable of detecting a modulated H atom beam of 5×10^{10} atoms/cm^2/sec or greater. This simple detector functions by catalysing the recombination of H atoms, absorbed on the surface of a platinum strip, and detecting the temperature rise due to the liberated heat of recombination as a change in the resistance of the strip.

The bolometer[3] consists of a blackened metal case in which is supported the sensitive Pt ribbon. This ribbon is 0.65 cm long, 0.025 cm wide, and 0.1 μ thick with a resistance of $\approx 40\ \Omega$. The standard instrument is modified by leaving the surface of this ribbon in a "bright" condition rather than with the usual evaporated gold black finish and by removing the KBr window covering the strip. These alterations reduce the sensitivity of the device to infrared radiation by $\sim$50 times (when operated in a vacuum) and increase the catalytic activity of the Pt surface.

In the present application the modified bolometer is mounted in a vacuum chamber. The H atom beam to be detected is modulated at 10 cps by a chopper wheel and then allowed to strike the surface of the Pt strip. The signal, developed as an out-of-balance potential in a bridge circuit containing the Pt strip as one arm, is fed via a magnetically shielded cable to a 10-cps high gain tuned amplifier.[3] The signal is finally detected by a lock-in amplifier having an equivalent bandwidth of 0.2 cps. It has been found useful to incorporate a clipping circuit in this amplifier in order to minimize magnetically induced impulse noise, e.g. from control solenoids etc., which is particularly troublesome when long integrating times are used.

The detector should be operated in a well-trapped vacuum system since its catalytic activity is susceptible to poisoning; this condition is easily recognized since the detector will respond normally to infrared radiation but only weakly or not at all to an H atom beam. Poisoning can frequently be cured by passing a current of 12 mA through the Pt strip and pumping for up to 24 h, but may necessitate replacement of the strip.

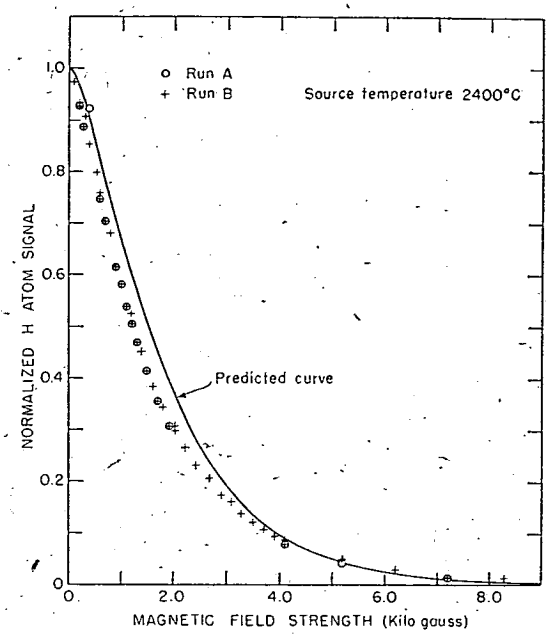

FIG. 1. Comparison of predicted and observed variation of H atom signal versus strength of the velocity selecting field.

When this detector was used to detect an H atom beam obtained from a thermal dissociation source equipped with a magnetic velocity selector, the variation in observed signal intensity with magnetic field strength was found to be consistent with a Maxwell-Boltzmann distribution of velocities among the atoms in the source at the measured temperature (see Fig. 1). The difficulties of temperature measurement at 3000°K prevent great accuracy, but these observations support the linearity of the detector response.[4] At high velocities ($\sim10^6$ cm/sec) the translational energy of the impinging H atoms becomes significant and it is necessary to include a correction for this effect.

It is anticipated that this detector will also be useful for beams other than H atoms, e.g. CH_3 radicals, which also recombine exothermally on a platinum surface.

* Support received from the U. S. Atomic Energy Commission, Division of Research, is gratefully acknowledged.

[1] I. Estermann, Rev. Mod. Phys. 18, 300 (1946).

[2] C. A. Reilly and B. S. Rabinovitch, J. Chem. Phys. 19, 248 (1951).

[3] Baird Associates Inc., Cambridge 38, Massachusetts (type AT3 bolometer and KW1 tuned amplifier).

[4] The linearity of a Pt catalytic H atom probe operated as a resistance thermometer in a flow system has also been confirmed [J. C. Greaves and J. W. Linnett, Trans. Faraday Soc. 55, 1338 (1959)].

Reprinted from the *Journal of Scientific Instruments*, Vol. 42, pp. 489–491, July 1965

A magnetic velocity selector for hydrogen atom beams using an unfolding technique

M. A. D. FLUENDY†
Department of Chemistry, Harvard University, Cambridge, Mass., U.S.A.
MS. received 11th March 1965

Abstract. A velocity selector for hydrogen atom beams using an inhomogeneous magnetic field is described. The transmission intensity as a function of field strength is calculated from the geometry of the system. The resulting Fredholm equation is then solved numerically to yield the intensity–velocity distribution in the beam.

Conventional rotating disk velocity selectors are for mundane reasons unsatisfactory for velocities much above 3×10^5 cm sec^{-1}. Thus for the velocity selection of thermal hydrogen atom beams, containing atoms moving at velocities up to 2×10^6 cm sec^{-1}, a magnetic method of velocity selection is attractive. Such devices have been used by Cohen and Ellet (1937), for velocity selection of a potassium beam and, more recently, by Bederson and Rubin (1962).

Basically all methods of magnetic velocity selection depend upon the acceleration produced by an inhomogeneous magnetic field on a neutral atom or molecule possessing a magnetic dipole moment (Ramsey 1956).

When a field of gradient $\partial H/\partial z$ is switched on, atoms of mass m and effective moment μ_{eff} will be deflected an amount $z(V)$ such that:

$$z(V) = \left(\frac{1}{2mV^2}\right)\mu_{\text{eff}} \frac{\partial H}{\partial z} (\text{length of field})^2 \qquad (1)$$

where V is the velocity of the atom.

Thus by passing a well-collimated beam through an inhomogenous field it can be split into components corresponding to the various magnetic substates. The case of hydrogen is particularly simple in that there are two such states (neglecting the small splittings produced by the nuclear spin) so that a deflection pattern, in which only one magnetic state can contribute to the intensity at any point, is produced. By scanning a detector across this pattern previous workers have been able to study the intensity at any given velocity. For scattering experiments where it is desired to transmit only a specified velocity into the experimental chamber a slit can be placed at the exit of the magnet, offset from the undeviated beam, so that the unwanted velocities may be filtered out. The velocity resolution of systems such as this is a function of the magnet length and the slit widths. Unfortunately slit widths much less than 0·05–0·025 mm are difficult to use with high temperature sources due to dimensional instabilities, hence for a given magnet length the resolution obtainable is limited. Operated in this mode the magnet and slit system described here had a resolution ($\Delta V/V$ half width) of approximately 20%. This mode is also disadvantageous in that only one spin state is transmitted —resulting in a loss of intensity by a factor of two.

In the method described below both spin states are transmitted and more information on the distribution of velocities can be obtained. The essential experimental arrangement is shown in figure 1; note that all the slits are set along the line of the undeviated beam. The electromagnet used in this work was designed by Herschbach and Herm (1962 unpublished). At zero field gradient the full beam intensity is transmitted and a velocity scan is made by observing the transmitted intensity as a function of the field gradient

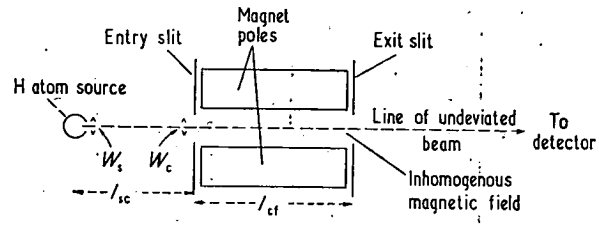

Figure 1. Arrangement of magnet and slits for velocity analysis of a hydrogen atom beam.

(which is readily varied by changing the magnet exciting current).

The observed transmitted intensity $I_{(H)\text{obs}}$ at field gradient H is then related to the distribution of velocities $I_{(V)}$ in the primary beam, by:

$$I_{(H)\text{obs}} = \int_0^\infty g(V, H) I_{(V)} dV \qquad (2)$$

where $g(V, H)$ is the transmission characteristic of the magnet and can be calculated from the geometry of the system.‡

‡ In the absence of a field the curve representing the intensity of the flux through the plane of the magnet exit slit is a trapezium. The width A of the flat top and B of the two skirts of this trapezium can be computed from:

$$A = \left\{W_c - (W_c - W_s)\frac{l_{cf}}{l_{sc}}\right\}$$

$$B = W_s \frac{l_{cf}}{l_{sc}}$$

where W_c = width of magnet entrance slit, l_{cf} = distance between magnet slits, W_s = width of atom source slit, l_{sc} = distance from source to magnet entrance slit. When a field gradient of $\partial H/\partial z$ G cm^{-1} is switched on each atom of velocity V is deflected by an amount

$$z(V) = \left(\frac{1}{2mV^2}\right)\mu\left(\frac{\partial H}{\partial z}\right) l_{cf}^2.$$

Each velocity thus gives rise to a trapezium of the calculated dimensions but displaced a distance z from its zero field position. The fractional transmission of a given velocity through the filter can therefore be calculated from the overlap between the magnet exit slit (normally of width A) and a trapezium of the appropriate width displaced a distance $z(V)$ from the zero field position. The transmission function for the system can therefore be constructed.

† Now at Department of Chemistry, University of Edinburgh.

The simplest approach to the solution of equation (2), which may be appropriate in some cases, is to assume $g(V, H)$ is a step function, i.e. that for each field strength there is a definite velocity below which essentially no hydrogen atoms are transmitted but above which the transmission is 100%. The signal due to a small range of velocities can then be obtained by subtracting the signals obtained at two closely spaced field strengths. The error introduced by this procedure may be gauged from figure 2 where the effective transmitted

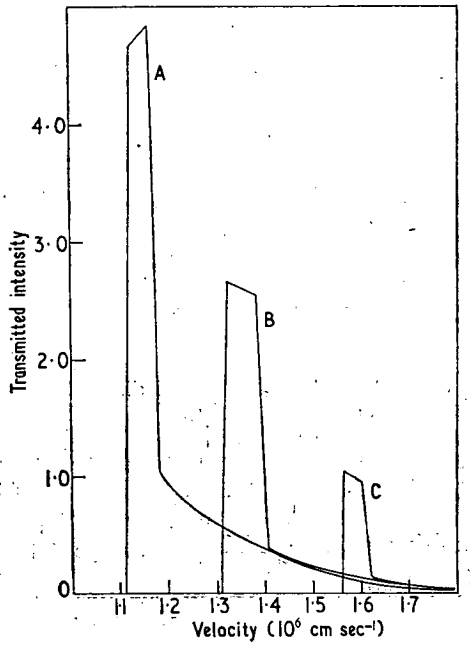

Figure 2. Transmitted intensity plotted against velocity calculated for the simple treatment of the linear slit arrangement. Curve A, H = 3010–3440 G; curve B, H = 4300–4720 G; curve C, H = 6010–6430 G. (Hydrogen atom source temperature 2700°C.)

band is plotted for several field strengths. At low velocities in particular this method can provide but poor resolution.

A more valid approach is to solve this equation accurately using the real transmission characteristic of the magnet. The equation (a Fredholm equation of the first kind), in many cases of physical interest, can be solved by numerical means (Fox 1962). In a successful process (D. L. Bunker 1964 private communication) the unknown function $I_{(V)}$ is expressed as an expansion of the form

$$I_{(V)} = \sum_{i=1}^{n} b_i F_{i(V)} \qquad (3)$$

where the $F_{i(V)}$ are any convenient functions and $n \simeq k^{1/2}$, k being the number of different field strengths at which observations of $I_{(H)}$ have been made.

The integrals

$$A_{(i,k)} = \int_0^\infty F_{i(V)} g_{(V,H_k)} dV$$

are then evaluated numerically and the $k \times n$ matrix:

$$\begin{aligned} I_{(1)} &= b_1 A_{(1,1)} + b_2 A_{(2,1)} + \ldots b_n A_{(n,1)} \\ &\vdots \\ I_{(k)} &= b_1 A_{(1,k)} + \ldots\ldots\ldots b_n A_{(n,k)} \end{aligned} \qquad (4)$$

solved for the b_i by a least squares regression. The values of $I_{(V)}$ can then be calculated from equation (3) by substituting the values of b_i which best satisfy the matrix equation (4).

The functions $F_{i(V)}$ either can be of a general nature, e.g. V^i, or, if a theoretical function is well established, the parameters can be fitted to this form. Figure 3 is a com-

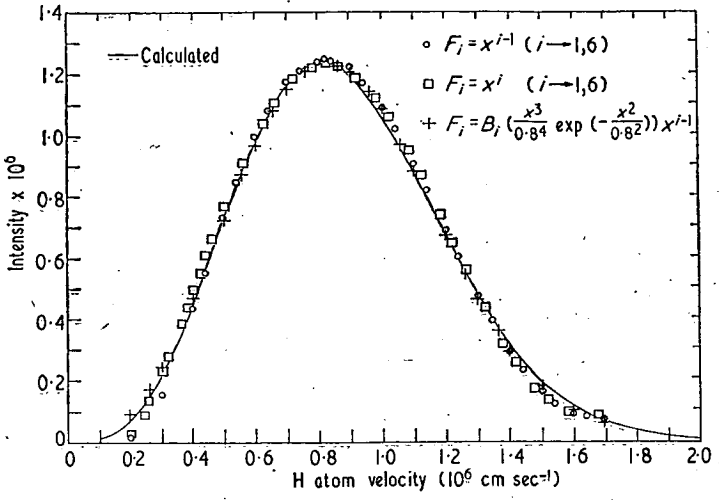

Figure 3. Comparison of the exact and numerical results obtained by solution of the Fredholm equation.

parison of the exact solution with the results obtained using this method and several different functions. The input data for this test were obtained by a forward calculation using an assumed $I_{(V)}$.

$$I_{(V)} = \frac{V^3}{(6{\cdot}64 \times 10^5)^4} \exp\left\{-\frac{V^2}{(6{\cdot}64 \times 10^5)^2}\right\}$$

was the expression actually used. A good fit was obtained for all three six-term expansions used. As expected the form most closely resembling the theoretical function, shown by crosses on the figure, provided a slightly better fit than the other expansions.

The resolution can no longer be simply defined in this mode of operation. The precision of the result depends upon (i) the accuracy with which the expansion, equation (3), can be made to fit the unknown form, and (ii) the number and precision of the observations of $I_{(H)}$. If a reliable theoretical form is used the uncertainty due to (i) will no longer arise.

Figure 4 shows a typical result obtained by applying the method to experimental (I, H) data obtained with a thermal beam of hydrogen atoms detected on a platinum strip bolometer (Fluendy 1964). The lower curve is corrected for the kinetic contribution to the signal and represents the hydrogen atom intensity as a function of velocity in the beam emerging from the oven.

In many experiments interest is concentrated on the perturbation in velocity distribution produced by some experimental intervention, e.g. scattering from a target gas. In such cases, once the distribution $I_{(V)}$ in the primary beam, has been established, the effect of the scattering process can be represented as:

$$I_{(H)\text{obs}} = \int_0^\infty \{I_{(V)} g(V, H)\} \sigma(V) dV \qquad (5)$$

where $\sigma(V)$ is the scattering function and everything within

the brackets is now known. An exactly analogous method of solution, possibly using different expansion functions, will thus lead to a solution for $\sigma(V)$.

This method of velocity selection might also be applicable to other cases. Thus, if a theoretical distribution of velocities for effusion from a molecular beam were assumed, velocity selection could be achieved by varying the oven temperature and solving the equation:

$$I_T = \int_0^\infty I_{(V,T)}\sigma(V)dV.$$

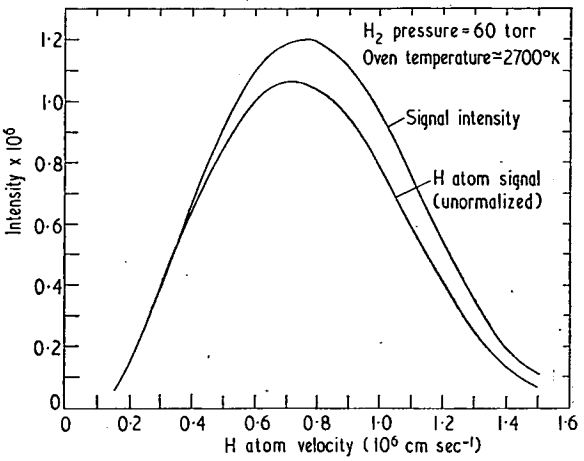

Figure 4. Experimental example showing the velocity distribution in a hydrogen atom beam obtained by solution of the Fredholm equation.

Acknowledgments

The author would like to thank Professor D. R. Herschbach and A. Fluendy for helpful discussions. Support received from the U.S. Atomic Energy Commission, Division of Research, is gratefully acknowledged.

References

BEDERSON, B., and RUBIN, K., 1962, *U.S. Atomic Energy Commission Technical Report* N.Y. 10, p. 117.

COHEN, V. W., and ELLET, A., 1937, *Phys. Rev.*, **52**, 502–8.

FLUENDY, M. A. D., 1964, *Rev. Sci. Instrum.*, **35**, 1606.

FOX, L. E., 1962, *Solution of Ordinary and Partial Differential Equations by Numerical Means* (Oxford: Pergamon).

RAMSEY, N. F., 1956, *Molecular Beams* (Oxford: Clarendon).

UNWIN BROTHERS LIMITED, WOKING AND LONDON (B4223)

4

MOLECULAR BEAM SCATTERING

BY

A. R. BLYTH, M. A. D. FLUENDY, and
K. P. LAWLEY

Reprinted from Quarterly Reviews
1966, Vol. XX, No. 3

London
The Chemical Society

MOLECULAR BEAM SCATTERING

By A. R. Blythe

(Imperial Chemical Industries Limited, Petrochemical and Polymer Laboratory, Runcorn)

and M. A. D. Fluendy and K. P. Lawley

(Department of Chemistry, University of Edinburgh)

1. Introduction

Processes occurring *via* atomic or molecular collisions are fundamental to chemistry. It is consequently somewhat surprising to see what a relatively small effort has been put into studying such collisions directly. Collisions may be divided into three broad categories: elastic, inelastic, and reactive. In elastic collisions, which normally predominate, the internal energy and quantum states of the collision partners remain unchanged and the only possible observable result is a change in the direction of their relative velocity vector, *i.e.*, an interchange of translational energy only. These elastic encounters are primarily responsible for the macroscopic properties of mass, momentum, and kinetic-energy transfer (diffusion, viscosity, and thermal conductivity). Inelastic collisions are those in which the quantum states of a particle are changed as a result of the collision and will, therefore, generally involve energy transfer between the internal modes of the particles. Reactive collisions comprise those in which chemical reaction occurs and thus, in general, will also involve a change in the mass of the particles. A knowledge of all three types of collision will be required if the details of chemical kinetics are to be successfully interpreted, though in this Review attention will be particularly directed to reactive collisions.

Molecular scattering experiments have enabled these collision processes to be studied without the difficulties of interpretation and inherent loss of detail associated with conventional experiments, where measurement of average properties over a wide distribution of incident energy and internal molecular states are made. Furthermore, in reactions involving a sequence of steps, one step can be isolated and studied.

A number of different experimental configurations[1] have been employed in these scattering experiments. In each case a well-pumped vacuum chamber (about 10^{-7} torr) provides the setting for the experiment. At these pressures the mean free path is many metres and well-defined beams of "molecules" (which in future will be taken to include atoms, free radicals, etc.) can be produced and their scattering either by another beam or by a suitable target investigated. In the arrangement shown in Fig. 1*a*, for example, a single beam of molecules is produced by the source *A*, collimated

[1] Fraser, "Molecular Rays", Cambridge Univ. Press, Cambridge, 1931; "Advances in Chemical Physics", ed. Ross, Wiley, New York, 1965, vol. X; Datz and Taylor in "Recent Research in Molecular Beams", ed. Estermann, Academic Press, New York, 1959, p. 157; Fite and Datz, *Ann. Rev. Phys. Chem.*, 1963, **14**, 61.

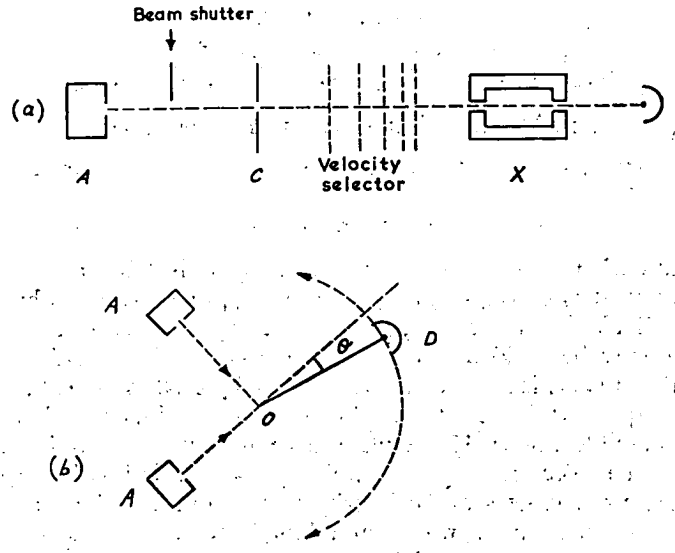

FIG. 1. *Schematic illustrations of molecular-beam experiments; (a) single beam for measuring total collision cross-sections for various velocities; (b) crossed-beams for measuring angular dependence of scattering intensity. θ is the angle of scattering in the laboratory co-ordinate system.*

by a set of slits at *C* and, after "monochromation" in the velocity selector (which transmits only a narrow range of velocities), passed through the scattering chamber *X* which contains an accurately known pressure of target gas. The beam is finally detected at *D*. The arrangement is thus exactly analogous to the measurement of optical density in a spectrophotometer and by observing the signal intensity recorded at *D* as a function of target-gas pressure, we can measure the total collision cross-section for the interaction of beam and target molecules. These simple arrangements are capable of considerable refinement, for example by selecting particular quantum states of the molecules in the primary beam. The limitation on the resolution and refinement of such selection experiments is at the moment set by the initial beam intensity and signal-to-noise ratio of the detector. An alternative configuration, Fig. 1*b*, uses two well collimated molecular beams arranged to intersect with a definite angle in the scattering centre *O*. The detector in this arrangement is no longer fixed but is rotated about *O*. In this class of experiment a great deal of additional information can be obtained since the angular distribution of scattered material can be measured. Once again the use of selectors is possible but the problems of intensity are much more severe, since the scattered flux will depend upon the product of the two beam intensities. Fortunately, very interesting information can be obtained in some cases with unselected beams. The range of experiments is at present very much dictated

by the techniques for generating and detecting molecular beams so that it is worth examining the experimental aspect more closely.

2. Experimental

(a) **Sources.**—The most usual source for molecular beams with energies in the thermal range is a small oven maintained at a well-stabilised temperature and provided with a narrow slit through which the molecules can effuse, and, after suitable collimation, form a beam. If the mean free path of molecules in the oven is larger than the slit width, there will be relatively few collisions in the beam and the intensity will be directly proportional to the number of molecules striking the area of the slit, *i.e.*, to the pressure. Unfortunately, we cannot increase the intensity of the beam indefinitely by increasing the pressure, since the onset of collisions in the region of the slit produces a cloud of molecules in front of the slit.[2] This cloud scatters and attenuates the beam. There is thus an optimum pressure and, correspondingly, a maximum beam intensity, available from sources of this type. The optimum pressure will be approximately that giving a mean free path comparable with the slit width of the oven. For a typical case, a beam 1 cm. high by 0·01 cm. wide, the conditions for effusive flow would require a mean free path in the oven of approximately 0·01 cm. $= 1/n\sigma 2^{\frac{1}{2}}$ where σ, the collision cross-section, might be of the order 10^{-13} cm.^{2}. The optimum pressure in the oven would then be about 0·03 torr. By kinetic theory the number of molecules striking a detector area A_d in the line of the primary beam but distant l_0 cm. from the source slit of area A_s is:

$$1{\cdot}12 \times 10^{22} A_s A_d p / l^2{}_0 (MT)^{\frac{1}{2}}$$

where M, T, and p are the molecular weight, temperature, and pressure of the beam material in the source. Thus primary beam intensities in conventionally sized machines are unlikely to exceed 10^{13} molecules/sec., corresponding in density to a gas at about 10^{-12} torr for normal molecular velocities.

Recently, in attempts to obtain higher beam intensities, some workers have used much greater pressures in their ovens, so that hydrodynamic flow occurs. Under these conditions a "Laval Nozzle",[3] in which the collisions between beam molecules serve to "focus" their translational energy in a forward direction, can be used to produce fast beams of very high intensity. Intensities 10^2—10^3 greater than those obtained by effusion are available. Such systems by virtue of the large mass flow require very high pumping speeds and are rather akin to hypersonic wind tunnels, and correspondingly expensive. So far they have not become available to chemists. Beams of condensable substances may offer more immediate scope, since relatively inexpensive cryogenic pumps can be used.

[2] Ramsey, "Molecular Beams", Oxford Univ. Press, Oxford, 1956; Smith "Molecular Beams", Methuen, London, 1955; Hasted, "Physics of Atomic Collisions", Butterworth, London, 1964.

[3] Valleau and Deckers, *Canad. J. Chem.*, 1964, **42**, 225.

Atomic and free-radical beams can be formed by effusion from suitable ovens in which dissociation has been brought about by familiar thermal or microwave–electric discharge methods, *e.g.*, hydrogen-atom beams of good intensity have been produced by thermal dissociation in a tungsten tube oven heated to 3000°K electrically.[4]

Very fast beams of neutral molecules have been produced by charge exchange in which, for example, a beam of A^+ ions with energies in the 10 ev range are fired through a chamber containing a suitable pressure of argon.[5] Since the cross-section for charge exchange is very much greater than that for momentum transfer a considerable fraction of the ions in the beam will be neutralised without being deflected from the beam. The final fast neutral beam is then obtained by deflecting away the remaining ions with an electric field.

(b) Velocity and State Selection.—It is obviously of interest to study collision processes as a function of the relative velocity and quantum states of each particle both before and after their encounter. In favourable cases this is now possible, though normally the sensitivity of the detector and beam intensity limit the resolution which would otherwise be obtainable.

The distribution of velocities in a molecular beam from an oven at T°K can be obtained from Maxwell's law. The number of molecules $N(v)$ with velocities between v and $v + \mathrm{d}v$ in directions within the solid angle $\mathrm{d}\omega$ defined by the beam is

$$N(v) = C(\mathrm{d}\omega/4\pi)v^2 \exp(-v^2M/2RT)\mathrm{d}v$$

But the number of molecules passing through the source slit is proportional to $vN(v)\ \mathrm{d}v$ molecules/cm.^{2}/sec. and thus the distribution of velocities in the beam is

$$I(v) = 2I_0\,(2RT/M)^{3/2}\ v^3 \exp(-v^2M/2RT) \text{ molecules/cm.}^2\text{/sec.}$$

(where I_0 is the total intensity of the beam, all velocities).

In principle, by varying the oven temperature and measuring the resultant signal after some velocity-dependent process has occurred it is possible to reconstruct the details of the velocity dependence. Unfortunately, for accurate results an excessively wide range of temperature is required, so that a more direct method of selection is needed. For velocity selection a mechanical method reminiscent of Fizeau's experiment to measure the velocity of light is most often used. The selector consists of a number (usually 5 or 6) of discs mounted on a shaft which can be rotated at an accurately known speed.[6] A series of equally spaced slots around the edge of each disc, mutually offset in successive discs, will then obstruct all but a small range of velocities, the transmitted velocity being determined by the

[4] Martin and Fluendy, *Rev. Sci. Instr.*, 1966, **36**, to be published.
[5] Devienne, Souquet, and Clapier, *Compt. rend.*, 1963, **256**, 233.
[6] Hostettler and Bernstein, *Rev. Sci. Instr.*, 1960, **31**, 872.

speed of rotation. Resolutions ($\Delta v/v$ half-intensity width) of 5% are commonly achieved.

The principle of the famous Stern–Gerlach experiment, in which a beam of atoms possessing a magnetic dipole is deflected by an inhomogeneous magnetic field, has also been used for velocity selection, since the deflection is a function of velocity. It is particularly suitable for fast moving projectiles such as hydrogen atoms for which the conventional type of selector would have to be very long.[7] For scattering experiments a system of offset slits is normally used to filter out unwanted velocities.

The deflection $x(v)$ produced by a given velocity v is

$$x(v) = \frac{1}{2\epsilon} \mu_{eff} \frac{\partial H}{\partial x} l^2$$

where l = length of field, $\partial H/\partial x$ = magnetic field gradient, ϵ = K.E. of molecules, $\mu_{eff} = Mg\mu_0$ (M can have values $-J, -J+1, \ldots J$; g is the Landé factor, and μ_0 is the Bohr magneton).

This procedure will also select the various angular momentum states of the atom. In a slightly different fashion an inhomogenous electric field can be used to select the rotational states of a molecule having a permanent electric dipole.[8]

Selection of both velocity and rotational states drastically reduces the intensity of the beam. In an effort to combat this, "lens systems" have been devised which will bring molecules with an electric or magnetic dipole moment to a focus and thus increase the effective area of the source.[2] Quadrupole fields have commonly been used because their field acts perpendicularly towards the central axis and increases with distance from this axis. The behaviour of polar diatomic molecules injected into the field is of two types. If $\mu_{eff} > 0$, *e.g.*, for the (J,M) states (0,0), (1,1), (2,2), *etc.*, the molecules are deflected away from the axis and are lost. However, if $\mu_{eff} < 0$, *e.g.*, for the states (1,0),(2,0), *etc.*, the molecules experience a restoring force proportional to their distance from, and directed towards, the central axis. As a result, they execute simple harmonic motion in the xy-plane. For a definite velocity in the z-direction all molecules in a particular rotational state return to the axis at the same half-wavelength position. By varying the voltage across the electrodes, molecules belonging to a state of chosen μ_{eff} can be focused on the detector. An obstacle is placed in the centre of the quadrupole field to shadow the detector against molecules which travel close to the axis and are therefore not much influenced by the field. For molecules with a large range of states there is a considerable degree of overlapping in the deflection pattern and very careful analysis is required if the results are to be unravelled.

Recently the construction of "molecular accelerators" has been started[9]

[7] Fluendy, *J. Sci. Instr.*, 1965, **42**, 489.
[8] Kramer and Bernstein, *J. Chem. Phys.*, 1965, **42**, 767.
[9] Wharton, personal communication, 1965.

in which suitably phased electrostatic radio frequency (R.F.) fields act upon the molecular dipole moment. They can accelerate highly dipolar molecules in states of specified μ_{eff} to translational energies in the region of 10 ev. These devices thus differ from the "passive" filters already discussed in that they transfer whole regions of phase space to a new energy region.

(c) **Detectors.**—The degree of refinement in the way of selection, etc., possible in the experiment is limited by our ability to detect the final signal. Thus while beam intensities are still limited by financial resources, detectors are a most critical part of a beam experiment.

Many different devices have been used or suggested for molecular-beam detection.[2] They can be conveniently divided into a few categories.

(i) *Chemical or condensation targets.* In these the beam molecules are collected and estimated by some chemical reaction, *e.g.*, a yellow MoO_3 target will show a blue trace of MoO_2 where exposed to atomic hydrogen. These methods are often sensitive but rarely metrical and definitely inconvenient. Recently methods using radioactive counting have seemed more promising.

(ii) *Pressure-measuring detectors.* In these the increase in pressure inside a small receiving vessel exposed *via* a narrow entry to the beam flux is measured. This is frequently by means of a hot-wire Pirani gauge or some form of ionisation gauge such as that due to Kingdon.[10] This type of detector is almost invariably used with some form of beam modulation so the zero drift and noise associated with pressure fluctuations in the main apparatus are minimised. Their chief advantage is the wide range of substances which can be detected in this manner.

(iii) *Thermal detectors.* Bolometers with a surface active as a catalyst can be used to detect beam molecules which react exothermally on their surface, *e.g.*, atomic hydrogen.[11] For very energetic beams the kinetic energy of the impinging molecules will yield sufficient heat.

(iv) *Ionisation methods.* These are perhaps the most important. Basically they involve the ionisation of the molecule followed by its measurement as an electric current through an electrometer or electron multiplier (possibly with a mass spectrometer intervening). In some cases the ionisation may be brought about very simply, *e.g.*, metastable $He(2S^1)$ will eject an electron on impact with a gold surface. The resulting current will then be a measure of the $He(2S^1)$ flux.

Surface ionisation detectors have been particularly widely used and are the most sensitive detectors available at present.[2] In these detectors the ionisation of molecules having a low work function (in practice largely the alkali metals and their compounds) is brought about by collision with a hot wire of high work function, typically tungsten (preferably of a type drawn

[10] Kingdon, *Phys. Rev.*, 1923, **21**, 408; Brooks, Thesis, Univ. of California, 1964.
[11] Fluendy, *Rev. Sci. Instr.*, 1964, **35**, 1606.

from a single crystal of the metal since this emits fewer alkali ions from internal impurities). This approach has been much extended by the use of differential surface ionisation[12] in which two wires, one of high and the other of rather lower work function, are used to distinguish between different species. An important example is the use of tungsten and platinum-alloy wires to differentiate between alkali metals and their halides. By using suitable temperatures and "ageing" treatment for the wires it is possible to arrange for the tungsten wire to ionise a very high proportion (about 90%) of the M and MX molecules striking it, while the platinum wire will only ionise the M plus a very small proportion of the MX molecules striking it. Thus by measuring the flux with both wires and making suitable calibrations the two fluxes can be distinguished. In a typical scattering experiment the currents measured range from 10^{-6} A in the main beam to $\sim 10^{-16}$ A. for some scattered products.

The hot-wire detector is unfortunately very limited in the range of molecules which it will detect. For other substances ionisation can in general be brought about by electron bombardment[13] (as in a mass spectrometer). A high density of electrons having energies in the 20—50 ev range are concentrated in the path of the beam. The resulting positive ions are passed into a mass spectrometer and the signal of the appropriate mass number observed. This method is considerably less sensitive than the hot wire since only approximately 1 in 10^2 or 10^3 of the molecules in the beam are ionised. Furthermore unless very low pressures are obtained in the detector region there is considerable noise from fragments of the background gas appearing at the relevant mass number. These drawbacks can to some extent be overcome by counting techniques in which the noise and signal can be integrated over long periods.

3. Interpretation of Results

The results of scattering experiments are normally reported in terms of "cross-sections" for particular processes. The area of these cross-sections is a measure of the relative probability of the process. For example consider the situation in which a stationary target molecule is exposed to a flux* of incident molecules.[14] The general differential cross-section $\sigma_{ij}(\omega)$ for scattering into an element of solid angle $d\omega$ accompanied by the change $i \rightarrow j$ is then defined by:

$$\sigma_{ij}(\omega)\, d\omega = \frac{\text{Number of molecules in state } j \text{ scattered per sec. into } d\omega}{\text{Intensity of incident molecules in state } i}$$

For molecules interacting with centrosymmetric forces (or for the average of many impacts with random orientations) there is complete symmetry

[12] Taylor and Datz, *J. Chem. Phys.*, 1955, **23**, 1711.
[13] Weiss, *Rev. Sci. Instr.*, 1961, **32**, 397.
[14] Goldstein, "Classical Mechanics", Addison Wesley, Reading, U.S.A., 1950.
* Flux = (Number density of molecules in beam) × (Velocity of molecules in beam).

about the incident direction, so $d\omega = 2\pi \sin\theta.d\theta$. θ is the scattering angle (between incident and scattered directions). All the information concerning the angular intensity of the scattering is therefore given by the differential cross-section $\sigma(\theta)$. By integrating over θ we obtain the total cross-section σ:

$$\sigma_{ij} = 2\pi \int_0^{\pi} \sigma_{ij}(\theta) \sin\theta.d\theta$$

The total cross-section is the effective area which the target molecule presents to the incident flux. The transmittance I/I_0 of a beam passing for distance l through a "static" target *gas* of number density n_B will be $\exp(-n_B l\sigma)$.

When the target molecules are not stationary, the treatment of results is more complicated. Experimental results are measured in laboratory co-ordinates with the origin at the apparatus scattering centre. For interpretation of results in terms of molecular collisions we must transform to centre-of-mass co-ordinates moving with the centre of mass because we are only interested in the *relative* kinematics of the colliding molecules.[14] Figure 2 shows the velocity vector (or Newton) diagram for the in-plane

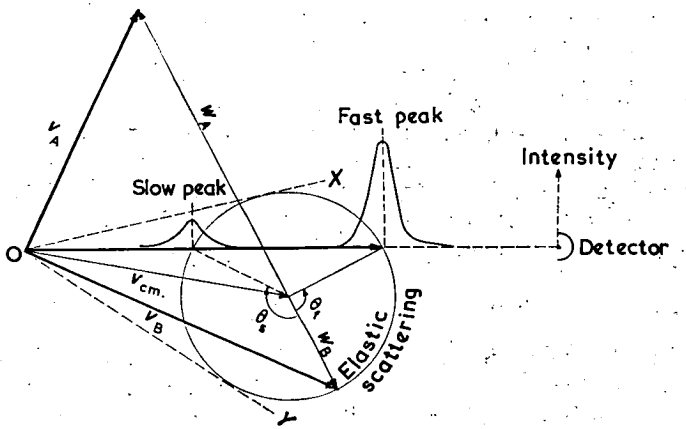

FIG. 2. *Newton diagram for scattering from two beams crossing at right angles. Elastic collision of particle* B *produces rotation of* w_B *(its relative velocity vector) about the tip of the centre-of-mass vector. For inelastic collisions in which energy is transferred to translational motion* w_B *would be increased in length as well as rotated.*

scattering of two particles A,B crossing at right angles. Beam particles A,B approach the centre of mass with relative velocities w_A, w_B whilst, as can be calculated from Newtonian mechanics, the centre of mass moves at constant velocity $v_{CM} = (m_A v_A + m_B v_B)/(m_A + m_B)$. The relative kinetic energy of the collision is $\frac{1}{2}\mu (v_A^2 + v_B^2)^{\frac{1}{2}}$ where μ is the reduced mass. During elastic collisions the relative velocities remain the same in magnitude but their directions are changed.* The locus of the termini of all

* For scattering in which reaction or energy transfer occurs the magnitude of the vector of scattered B may also change, and may also depend on the angle of scattering.

possible vectors of elastically scattered B is a circle of radius w_B. If $w_B < v_{CM}$ the scattered material is confined within the tangents OX, OY of the circle, and there are two relative velocity vectors for B scattered in a given direction: a "fast" component arises from scattering through the large centre-of-mass angle θ_F and a "slow" component arises from scattering through the small centre-of-mass angle θ_S. The angular distribution of scattering in the laboratory may thus be radically different from that in the centre-of-mass system. Experimental or laboratory cross-sections and angles have usually to be transformed into centre-of-mass co-ordinates.

In these co-ordinates the scattering problem is equivalent to that for a beam of particles scattered by a potential centred on a fixed target and theoretical interpretations are more easily made.

4. Elastic Scattering

The purely elastic scattering of molecules from spherically symmetric potentials is now rather well understood.[15] The total cross-section results normally show two distinct regions. At high energy the scattering is dominated by the short-range repulsive forces while at low energies the long-range dispersion effects are more important. Measurements of cross-sections for a range of velocities can be used to determine best-fit parameters in a suitable potential function. In particular, interference effects due to the de Broglie wavelength of the particles can often be observed at low energies and provide a very sensitive test for the potential function. In the angular scattering pattern a number of effects (not essentially quantum in origin) can operate to produce structure. Of particular interest is the "rainbow scattering" which can be associated with an extremum in the plot of deflection angle against impact parameter (Figure 3). The extremum is the result of a balance between effects of attractive and repulsive forces. The minimum in this function serves to concentrate extra intensity in the direction of the rainbow angle. Since this angle is primarily related to the ratio of incident kinetic energy to potential well depth an important parameter can be determined quite directly.

Elastic scattering results with good resolution are now becoming available and can be expected to provide our most accurate information about intermolecular potentials.

5. Inelastic and Reactive Scattering

In the field of chemical reactions, those of the type $A + B \rightarrow C + D$ have proved the most amenable to investigation by scattering experiments, since here relatively crude experiments yield much information.

In general, if the transformation of species i to species j (where i and j may be different internal states of the same compound *or* different chemical

[15] Bernstein, *Science*, 1964, **144**, 141.

species) proceeds by a bimolecular mechanism, then the usual kinetic rate constant, $k_{ij}(T)$, is given by

$$k_{ij}(T) = 2\pi \int_0^{\pi} \int_0^{\infty} v_r \sigma_{ij}(\theta, v_r) f(v_r, T) \mathrm{d}v_r \sin\theta . \mathrm{d}\theta$$

where $f(v_r,T)$ is the distribution of relative velocity v_r of the two participants at temperature T and θ is the angle of scattering (in centre-of-mass co-ordinates) resulting from the collision.

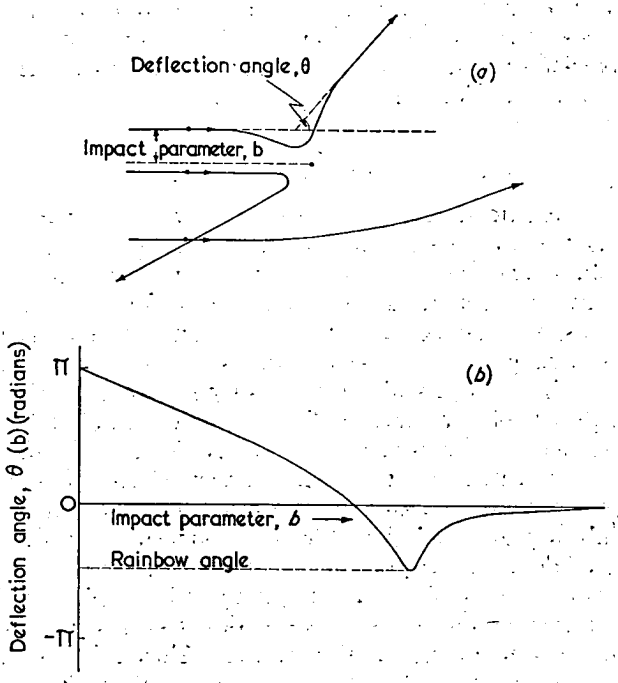

FIG. 3. *Elastic scattering by an intermolecular potential with both long-range attractive and short-range repulsive forces. (a) Trajectories of particles with various impact parameters, 'b'. Collisions with small b lead to scattering at wide angles and are dominated by the repulsive part of the potential. For collisions with large b the reverse is true. (b) Variation of deflection with impact parameter.*

In deriving a rate constant from measured cross-sections it is not normally necessary to measure differential cross-sections and the angular integration in the equation above is removed by using the appropriate total inelastic cross-section. However, there is as yet no experimental method for measuring such total cross-sections directly. Hitherto, chemical rate processes have been investigated through the rate constant k, usually a k that is a sum governing the formation of products in different rotational and vibrational states. The present state of molecular-beam work is that the angular dependence of $\sigma_{ij}(\theta,v_r)$ for a limited class of chemical reac-

tion is quite well established (and thus some relative total cross-sections are known), but that their velocity or energy dependence is as yet poorly defined, or known over only a small energy range. For this reason, rate constants cannot yet be reliably deduced from cross-sections. It may be noted that if the reaction is too fast, the Maxwellian velocity distribution will no longer hold and other processes then help to determine the overall rate of reaction. For this reason and because on integrating and averaging to obtain a total cross-section details of the angular and energy dependence of $\sigma_{ij}(\theta,v_r)$ are lost, the differential cross-section is of more fundamental interest than k_{ij} in examining a reactive system.

6. Energy-transfer Collisions

The crossed-beam technique is in principle capable of measuring $\sigma_{ij}(\theta,v_r)$ when i and j refer to different rotational or vibrational states of the same chemical species. To measure such an energy-transfer cross-section, the basic scattering experiment of Fig. 1 must be augmented either by measuring the velocity of one of the participants emerging from the collision or (for rotational energy transfer) by determining the rotational state of one of the colliding molecules before and after collision.

The two techniques are illustrated by the two types of experiment that have been performed in this area, namely the transfer of rotational energy in crossed beams of D_2 and K,[16] and rotational transitions in TlF induced by a variety of other molecules.[17] In the deuterium experiments (performed at only one angle of scattering) the conventional Newton diagram gives the velocity of the potassium to be expected from purely elastic scattering; atoms appearing at higher speeds are assumed to have gained extra recoil from rotational de-excitation of deuterium ($j = 2 \rightarrow 0$). Since the energy spacing of the rotational levels of deuterium is an appreciable fraction of the incident kinetic energy, the inelastically scattered potassium at any angle can be separated from elastically scattered potassium by velocity analysis. A small signal due to inelastically scattered potassium having the predicted velocity was observed, yielding a differential cross-section of 0·05 Å^2 per steradian (at $\theta = 108°$). Calculations indicate[18] that even in the system K–HCl total cross-sections less than 10 Å^2 are to be expected for transitions among the lowest rotational levels.

In the experiments of Bennewitz and Toennies using rotationally selected TlF, total cross-sections for a range of rotational transitions have been measured. Here, two separate quadrupole fields are used as selector and analyser. Only those molecules that suffer a specified change of J in the collision chamber are refocused and detected. The rotational levels are much more closely spaced than those of D_2 or HCl and the inelastic cross-

[16] Blythe, Grosser, and Bernstein, *J. Chem. Phys.*, 1964, **41**, 1917.
[17] Toennies in "Atomic Collision Processes", ed. McDowell, North-Holland Publishing Co., Amsterdam, 1963. p. 1113.
[18] Lawley and Ross, *J. Chem. Phys.*, 1965, **43**, 2943.

sections are consequently much larger. The observed results have been quantitatively interpreted using an intermolecular potential with an angle-dependent term which is consistent with the observed $\Delta J = \pm 1$ transitions. This type of experiment is one of the few that gives reliable information about the anisotropy in the potential.

The small cross-section to be expected for most collision-induced vibrational transitions makes it unlikely that beam methods will be useful in their investigation for some time to come.

7. Reactive Collisions

In the ideal scattering experiment designed to investigate a chemical reaction, the angular distribution in intensity of one of the scattering products and of one of the elastically scattered reactants is measured. The measurements are performed on mono-energetic beams of molecules in a selected rotational state and repeated for all quantum states of the reactants that are of interest. However, worthwhile velocity selection reduces the intensity of both incident beams by at least a factor of ten, so that subsequent rotational state selection, unless accompanied by efficient focusing, reduces the signal from reaction products almost below detection level. Also, and this is one of the gaps in the method, there is no way of analysing a beam of molecules into their vibrational states; in this respect the method is complementary to infrared emission methods,[19] where the vibrational state of a reaction product is known but not its translational energy. Fortunately, a great deal can be inferred about the nature of reactive collisions, especially the partition of energy in the products, by quite crude experiments using unselected beams.

There are two types of practical beam experiment. In the first the intensity of elastic scattering of one of the *unchanged* reactants (usually K or Cs) is measured as a function of angle.

Greene, Ross, and their co-workers[20] have investigated the elastic scattering of K from a variety of halogen-containing compounds, *e.g.*, the hydrogen halides, CH_3Br, and Br_2. In favourable cases (K–CH_3Br, K–HBr, K–HI) a scattering pattern of the general form shown in Fig. 4a was obtained. These experiments were performed with a detector sensitive only to K and the authors have interpreted the marked loss of intensity at large angles of scattering as due entirely to removal of K by reaction. By assuming that the elastic scattering at small angles (arising primarily from collisions with large impact parameters) is unaffected by the reactive process, the elastic potential parameters can be found. These parameters can then be used to predict the complete elastic scattering pattern in the absence of reaction. Thus, the total number of K atoms lost per second can be obtained by integration of the difference between predicted and

[19] Polanyi, *J. Chem. Phys.*, 1959, **31**, 1338.
[20] Beck, Greene, and Ross, *J. Chem. Phys.*, 1962, **37**, 2895; Ackermann, Greene, Moursund, and Ross, *J. Chem. Phys.*, 1964, **41**, 1183.

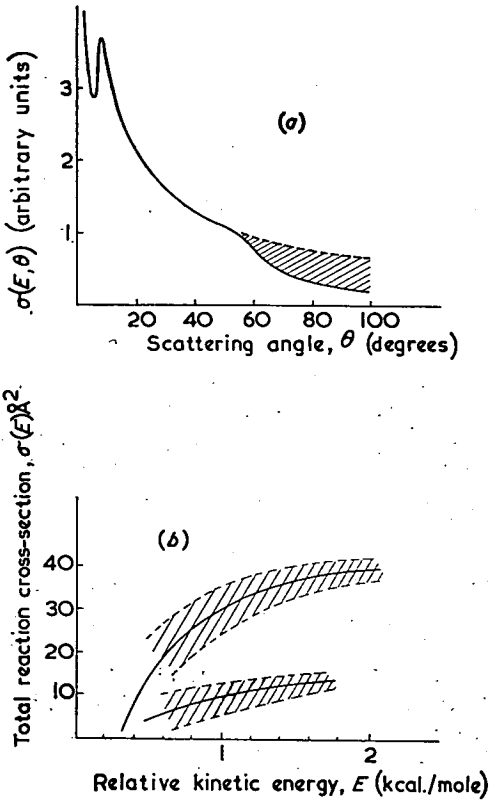

FIG. 4. *Experimental results for chemically reactive systems. (a) The general elastic scattering pattern for the system* K + HX. *The shaded area indicates the loss of* K *due to chemical reaction. (b) The energy-dependence of the total reaction cross-section for* K + CH_3 Br. *The shaded area indicates the spread of experimental results. The upper curve comes from the* K *loss method and the lower from direct measurement of* KBr.

observed signal. In order to obtain the absolute total reaction cross-section, the number of molecules lost per second must be divided by the incident flux of potassium atoms and the number of target molecules in the volume of intersection of the two beams. Absolute values are difficult to obtain, but relative values for different target molecules or for different incident energies can be measured to a precision of perhaps 20%.

In the case of K–BHr the product KBr has been detected in the same experiment and this constitutes the second, direct approach to measuring reaction cross-sections which we shall discuss in more detail later. In this reaction the value of σ_{react} obtained by the former indirect method is about 34 Å^2 (E_{rel} = 1 kcal./mole), while the direct method gives a value between three and eight times smaller than this depending on the experimental conditions. For the system K–HI the values obtained by the two methods are 31 Å^2 and 14 Å^2, respectively.

The cross-section obtained purely from observations of the scattering of K must be an upper limit since a decrease in scattered intensity at large angles could be also produced by a softening of the inner wall of the intermolecular potential, as an inspection of typical classical trajectories shows.

If the deficiency in scattered K at various angles (compared with that calculated by assuming a potential falling off with the sixth power of the distance) is plotted against the corresponding distances of closest approach, y, very similar curves are obtained over the whole range of experimental energies: anomalous scattering sets in below the same critical distance of closest approach in every case. This strongly suggests that in subtracting from a hypothetical, purely elastic scattering pattern a property of the potential energy surface has been obtained, but whether this property is due exclusively to reaction has yet to be settled. It being noted that the critical distance of closest approach in the K–HBr experiments corresponds almost exactly to the equilibrium K–Br distance in KBr, the potential energy $V(y)$ corresponding to the critical distance of closest approach is interpreted as the activation energy for reaction. [These critical values of $V(y)$ are all positive and thus two molecules starting from rest and moving together under the influence of their mutual attraction could never penetrate to the required separation.] This leads to the following values for the activation energies: K–HCl, 0·5 kcal./mole, K–HBr $<$ 0·4 kcal./mole, K–HI 0·2 kcal./mole.

In principle, activation energies can also be obtained simply from curves of total reaction cross-section σ plotted against relative kinetic energy E. Fig. 4b shows Greene and Ross's result for the K–HBr reaction, where a low threshold is discernable. More precise velocity selection of the reactant beams and better collimation are necessary before the threshold behaviour can be clarified and the activation energy accurately measured in this way. There is some evidence in the work of these authors of a second step appearing in $\sigma(E)$, possibly at a point where a new vibrational level of the product becomes accessible. The Arrhenius equation $k(T) \propto \exp(-E^*/kT)$ is broadly compatible with a variety of step-like $\sigma(E)$ functions.

In the second type of reactive scattering experiment, in which the angular distribution of one of the products is measured, the earlier experiments used unselected Maxwellian beams of alkali atoms and halides in order to keep the flux of the product high. An inspection of the Newton diagram for the K–HX system, Fig. 5a, indicates that because of the very small mass ratio of the products (m_H:m_{KX}) the potassium halide is largely concentrated near the centre-of-mass vector, leading to a high intensity of product in that direction. Thus, the integrated flux and hence the reaction cross-section can be measured more accurately than in, say, the systems K + CH_3I or K + Br_2 where the product is spread out over a larger solid angle Fig. 5b.

The reactions of Cs and K with the lower alkyl halides, and later with

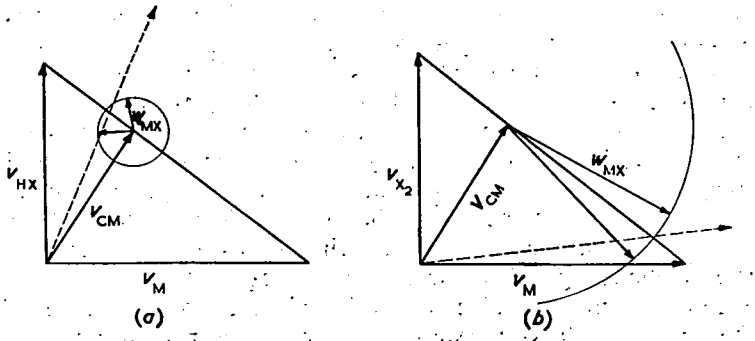

FIG. 5. *Newton diagrams for extreme types of reactive encounter. In (a) the product rebounds in the backward direction and there is a large change in reduced mass. In (b) the reaction is followed by forward scattering and there is little change in reduced mass. Only typical final relative velocity vectors of the detected products are shown and a broken line indicates the general direction in the laboratory in which maximum intensity of scattered product is observed.*

other small halogen-containing molecules,[21] have been investigated by Herschbach and his co-workers. Maxwellian beams were used in the earlier experiments and the angular distribution of the alkali halide measured. In some of the most recent experiments in this series, a magnetic field in front of the detector has been used to discriminate unambiguously between the paramagnetic alkali metals and their diamagnetic halides and the large reaction cross-sections reported for some of these systems have been confirmed.

The reaction cross-sections obtained (all for incident energies *ca.* 1 kcal./mole) range from *ca.* 10 Å^2 for the lower alkyl halides to $>$ 100 Å^2 for Cs–Br_2, K–Br_2, Cs–ICl, Cs–IBr, and Cs–I_2.[22,23] The results from about a dozen different systems seem to fall into two groups, those with large and those with small ($<$ 30 Å^2) reaction cross-sections, though it is perhaps accidental that relatively few intermediate cases have been found. Equally important, an analysis of the angular distribution of the scattered product also shows a division into two classes. In the first type, most of the alkali halide produced continues to travel roughly in the direction of the potassium beam; the angular distribution is strongly peaked between 5° and 20° in laboratory co-ordinates measured from the alkali-atom beam. This is in contrast to the reactions of small cross-sections, in which most of the alkali halide product is scattered backwards, *i.e.*, an observer travelling at the centre of mass would see the two reactants approaching from the left and from the right respectively, colliding at his point of observation, and the alkali halide formed returning roughly in the direction from which the

[21] Herschbach, *Discuss. Faraday Soc.*, 1962, **33**, 149; Wilson, Kwei, Norris, Herm, Birely, and Herschbach, *J. Chem. Phys.*, 1964, **41**, 1154.
[22] Datz and Minturn, *J. Chem. Phys.*, 1964, **41**, 1153.
[23] Helbing and Pauly, *Z. Physik*, 1964, **179**, 16; Gersing, Hundhausen, and Pauly, *Z. Physik*, 1963, **171**, 349.

alkali atoms came. It is also significant that no rainbow angle[23] is observed in the potassium scattering pattern in the large cross-section cases.

The general Newton diagram shows that the direction in which a scattered product is observed in the laboratory depends both on the angle through which the relative velocity vector is turned (the angle of scattering in relative co-ordinates), on the change in reduced mass, and on the change in length of *w i.e.*, on the final relative kinetic energy. In order for the scattering to be strongly peaked in the forward direction in the laboratory co-ordinate system, the angle of scattering θ must be small and the final relative kinetic energy of the same order of magnitude as the initial value. Since all the reactions studied are exothermic (*e.g.*, for K + RHal, $\Delta E \approx -20$ kcal./mole), the conservation of energy indicates that up to 90% of the heat of reaction goes into internal modes of the products. These conclusions are in keeping with other kinetic results, especially those from use of the sodium flame technique,[24] but in contrast to results from the study of the reactions of hydrogen atoms with the halogens by a flow technique.[25]

It has also been found by Herschbach[26] that there is no appreciable steric hindrance effect in going from methyl halide to butyl halide; this indicates a considerable orientating force in collisions of small impact parameter which line up the molecular partner in the required orientation for reaction. If this were not the case, then one would not expect the rapid rise of transition probability to almost unity with decreasing impact parameter found in the work of Greene and Ross.

Few experiments have been performed on reactive systems with measurement of the velocity of one of the product species. This is, of course, the most direct way of assessing the partition of energy between internal and translational modes and the use of a velocity selector on a product beam (if the primary beams are monoenergetic) does not result in the loss of intensity necessarily accompanying velocity selection of the primary beams.

The velocity distributions of KBr scattered from crossed-beams of velocity-selected K and thermal HBr and Br_2 have been measured by Grosser, Blythe, and Bernstein.[27] At any particular angle of observation the KBr velocity was found to be distributed about a well-defined maximum, the most probable velocity varying somewhat with the angle of observation. Should the latter effect remain after conversion to relative velocities, it might perhaps be due to the amount of energy taken up in rotational excitation of KBr changing with the angle of scattering. The result clearly emerged that the final kinetic energy was no more than 0·5 $\pm$ 0·5 kcal./mole greater than the initial relative kinetic energy, out of 5·1 kcal./mole liberated in reaction.

[24] Polanyi, "Atomic Reactions", Williams and Norgate, London, 1932.
[25] Airey, Getty, Polanyi, and Snelling, *J. Chem. Phys.*, 1964, **41**, 3255.
[26] Herschbach, *Applied Optics, Supple. 2 on Chemical Lasers*, 1965, p. 128.
[27] Grosser, Blythe, and Bernstein, *J. Chem. Phys.*, 1965, **43**, 1268; Grosser and Bernstein, *J. Chem. Phys.*, 1965, **43**, 1140.

Recently Moulton and Herschbach[27a] have further probed the energies and angular distributions of scattered product molecules using chemiluminescence. For example, vibrationally hot KBr^+, from crossed beams of $K + Br_2$, entered a second scattering chamber containing a Na cross-beam. Electronically excited K* atoms were generated by a chemical exchange process,

$$KBr^+ + Na \rightarrow K^* + NaBr,$$

and light emitted from K* was observed with a photomultiplier. Through this sort of experiment molecular beam scattering and infrared emission studies will eventually combine.

8. Models and Theories of Chemical Reaction

As a result of work with molecular beams, a certain amount is known about the details of a particular group of reactions, the reactions of potassium and cæsium with a variety of halides. The features of these reactions that any model must account for, at least qualitatively, are as follows: (i) Two rather distinct classes of reaction can be distinguished, "rebound" and "stripping" reactions. The former is characterised by small reaction cross-section (*ca.* 10 Å^2) and by backward scattering of alkali halide product, the latter by larger cross-section and by forward scattering. (ii) The energy released in the reaction goes almost entirely into internal modes of motion. (iii) All the reactions have activation energies less than 1 kcal./mole.

It is at once clear from the angular distributions observed that all the reactions studied proceed directly, not *via* a long-lived collision complex. If such a complex were formed, and its lifetime exceeded its period of rotation, then the Newton diagram shows that, depending on the change in reduced mass, a single (or possibly a double) peak symmetrically placed in the direction of the centre of mass or a very broad distribution of product without pronounced peaking would be observed. Further insight into the meaning of (i) above can be obtained by use of the ideas of elastic scattering. A large cross-section for an inelastic process means that a wide range of impact parameters is effective in inducing the change and there is a loose correlation between the strength of the ordinary intermolecular potential (as measured, for instance, by the Lennard-Jones parameter ϵ) and the choice between recoil and stripping mechanisms. The larger the intermolecular force, the more trajectories are drawn in to some critical distance of approach. Nevertheless, it is hard to escape the conclusion that a somewhat more specific effect is operating, and the occurrence of a charge-transfer mechanism was suggested many years ago in connection with the large cross-section observed in some sodium-flame experiments.[24] The ionisation energy and electron affinity of the two reactants may be such that even at

[27a] Moulton and Herschbach, *J. Chem. Phys.*, 1966, **44**, 3010.

a separation of *ca.* 10 Å the state of the colliding system rapidly changes from that of a molecular pair to a vibrationally excited ionic pair. From then on, Coulombic forces within the newly formed molecule take over and the reaction proceeds rapidly to completion. Considerations of angular momentum, together with the unusual nature of the potential-energy surface, seem to be responsible for the strong forward scattering.

Features (ii) and (iii) are also directly concerned with the nature of the potential-energy surface. If the system is regarded as moving over this surface in the course of reaction then the state of the products of an exothermic reaction depends upon the change in reduced mass accompanying reaction and upon the steepness of the entrance and exit valleys. This point has been discussed by Simons[28] and Polanyi[25] in contrasting the reaction of sodium atoms and hydrogen atoms.

The small activation energy observed in these reactions becomes a parameter to be used in the construction of potential-energy surfaces. These surfaces are then used in what is at the moment the most complete calculation of reaction rates, the Monte Carlo simulation method.[29] This method assumes that though the potential energy of interaction of reactants and products must be determined by quantum mechanics, the motion of the constituent atoms or groups through the force field obtained in this way can be found by classical mechanics. When the classical equations of motion are solved, the probability of reaction for the various impact parameters sampled is obtained, together with the angular distribution of the products and the classical degree of excitation of the products. These calculations were performed with the results of scattering experiments in mind, and some of the above features have been reproduced.

It is clear that molecular scattering measurements have a very considerable future in the study of chemical reactions. Up to the present the experiments have been confined to a rather narrow class of reaction. The mechanisms observed may thus not be very typical. In particular it can be expected that some reactions will proceed *via* relatively long-lived complexes. By analogy with nuclear reactions of the "compound nucleus" type it can be expected that the energy dependence of their reactive and elastic cross-sections will yield considerable information.

Improvements in technique can be expected to broaden the range of reactions in which the scattering products can be observed directly. Recently mass spectrometer detectors have been used in the determination of total cross-sections for the mutual scattering of the inert gases and of hydrogen and deuterium.[30] Nevertheless, for most reactions the reactive cross-section will remain too small for direct investigation. In

[28] Simons, *Nature*, 1960, **186**, 551.

[29] Bunker, *Scientific American*, 1964, **211**, 100; Karplus and Roff, *J. Chem. Phys.*, 1964, **41**, 1267; Kuntz. Nemeth, Polanyi, Rosner, and Young, *J. Chem. Phys.*, 1966, **44**, 1168.

[30] Buren, Feltgen, Gaide, Helbing, and Pauly, *Phys. Letters*, 1965, **18**, 282; Landorf and Mueller, *ibid.*, 1966, **19**, 658.

these cases the elastic scattering pattern (possibly of super-thermal beams) is capable of yielding considerable information about the potential surface accessible at the relative kinetic energy of the beams. By observing separately the mutual scattering of reactants and products the lower reaches of the entrance and exit valleys could be mapped.

PRINTED IN ENGLAND

THANET PRESS MARGATE

Reprinted from THE JOURNAL OF CHEMICAL PHYSICS, Vol. 46, No. 6, 2172-2181, 15 March 1967
Printed in U. S. A.

Hydrogen Atom Scattering: Velocity Dependence of Total Cross Section for Scattering from Rare Gases, Hydrogen, and Hydrocarbons

M. A. D. FLUENDY,* R. M. MARTIN,† E. E. MUSCHLITZ, JR.,‡ AND D. R. HERSCHBACH
Department of Chemistry, Harvard University, Cambridge, Massachusetts

(Received 31 October 1966)

An apparatus for scattering experiments with thermal energy hydrogen atom beams is described. The atoms are generated by dissociation of H_2 in a tungsten-tube furnace at ~2700°K, modulated by a mechanical chopper, and velocity selected by deflection in an inhomogeneous magnetic field. After passing through a scattering chamber containing the target gas, the atoms strike a platinum strip bolometer which functions as a catalytic recombination detector (capable of detecting an H beam of $\sim 5\times10^{10}$ atoms $cm^{-2}\cdot sec^{-1}$). Measurements of the velocity dependence of the total collision cross section in the range 3 to 11×10^5 cm/sec (equivalent to 0.05 to 0.5 eV) are given for scattering of H atoms from the rare gases, H_2, CH_4, C_2H_2, C_2H_4, C_2H_6, and $C(CH_3)_4$. The results show that throughout this range attractive r^{-6} interactions are still predominant for Xe, C_2H_4, and $C(CH_3)_4$ whereas repulsive interactions are dominant for most of the other gases. The data are compared with calculations based on the Lennard-Jones (n, 6) potential and with empirical correlations of van der Waals force constants.

SCATTERING experiments with hydrogen atoms are particularly inviting because of the prospect for detailed comparisons with electronic-structure theory.[1,2] However, because of the detection problem, H atom scattering in the thermal-energy range has been limited to a few exploratory studies, none with velocity selection.[3-6] This paper describes results obtained with an apparatus built around a simple catalytic recombination detector and a magnetic velocity selector. As compared with scattering work on other species,[7] these results are rather primitive and give only the velocity dependence of the total elastic scattering, but these data can be compared with theoretical calculations and empirical correlations to establish some of the main qualitative features of the interaction of H atoms with rare gases and simple hydrocarbons.

APPARATUS

Figure 1 gives a general view of the apparatus and Fig. 2 the beam geometry. The vacuum system consists of two differentially pumped chambers. One contains the H-atom oven (labeled D in Fig. 1) and is pumped through a water-cooled baffle by a 5-in.-diam oil diffusion pump. The other chamber (connected by a slit 0.40 mm wide by 1.0 cm high in Bulkhead F) contains the beam modulator (H), magnetic velocity selector (J), scattering box (M), and bolometer detector (P) and is pumped through a liquid-nitrogen-cooled baffle by a 7-in.-diam oil diffusion pump. The main chamber also contains a 15-liter liquid-nitrogen trap (not shown in Fig. 1) which supports a cold shield (R) that surrounds the scattering region. Typical ion gauge readings during an experiment are 1×10^{-4} torr in the oven chamber and 5×10^{-7} torr in the main chamber.

Hydrogen-Atom Oven

The H atoms are generated by thermal dissociation of H_2 in a tungsten tube furnace. In preliminary work, we used furnaces fashioned either by clamping together half-cylinders of tungsten formed by grinding[8,9] or by rolling up thin tungsten foil.[10] The use of a

* Present address: Department of Chemistry, University of Edinburgh, Scotland.

† National Institutes of Health Postdoctoral Fellow. Present address: Department of Chemistry, University of California, Santa Barbara, Calif.

‡ National Science Foundation Senior Postdoctoral Fellow. Permanent address: Department of Chemistry, University of Florida, Gainesville, Fla.

[1] See, for example, J. O. Hirschfelder, C. F. Curtiss, and R. B. Bird, *Molecular Theory of Gases and Liquids* (John Wiley & Sons, Inc., New York, 1954), p. 1050ff.

[2] Recent calculations include variation treatments of *repulsive forces* for H+He: (a) E. A. Mason, J. Ross, and P. N. Schatz, J. Chem. Phys. 25, 626 (1956); (b) H. S. Taylor and F. E. Harris, Mol. Phys. 7, 287 (1963); semiempirical estimates for H+Ne, H+Ar, $H+H_2$: (c) E. A. Mason and J. T. Vanderslice, J. Chem. Phys. 28, 1070 (1958); (d) 33, 492 (1960); perturbation calculations of *dispersion forces* for H+rare gases and $H+H_2$: (e) A. Dalgarno, Rev. Mod. Phys. 35, 522 (1963); (f) M. Karplus and H. J. Kolker, J. Chem. Phys. 41, 3955 (1964). Other papers are cited in these references and earlier work is reviewed in Ref. 1.

[3] E. G. Lunn and F. R. Bichowsky, Phys. Rev. 35, 671 (1930).

[4] H. Harrison, J. Chem. Phys. 37, 1164 (1962), found total cross sections of about 50 Å² for thermal beams of H scattered from He and H_2; also, variation of the H-beam temperature (which changed the average relative velocity from $7.5\text{–}9.2\times10^5$ cm/sec) indicated the velocity dependence is definitely weaker than would be expected for r^{-6} van der Waals forces.

[5] (a) W. L. Fite and R. T. Brackmann, in *Atomic Collision Processes*, M. R. C. McDowell, Ed. (North-Holland Publ. Co., Amsterdam, 1963), p. 955; J. Chem. Phys. 42, 4057 (1965); and (b) S. Datz and E. H. Taylor, *ibid.* 39, 1896 (1963), have reported preliminary work on reactive scattering of $H+D_2$ and $D+H_2$, respectively.

[6] I. Amdur and E. A. Mason, J. Chem. Phys. 25, 630 (1956), H+He; I. Amdur, M. C. Kells, and D. E. Davenport, *ibid.* 18, 1676 (1950) have reported high-energy (>100 eV) scattering experiments on $H+H_2$ which give information about the repulsive potential at distances within 1.2 Å.

[7] For reviews see (a) R. B. Bernstein, Science 144, 141 (1964); (b) H. Pauly and J. P. Toennies, Advan. At. Mol. Phys. 1, 195 (1965); (c) several articles in Advan. Chem. Phys. 10 (1966).

[8] W. E. Lamb, Jr., and R. C. Retherford, Phys. Rev. 79, 564 (1950); 81, 224 (1951).

[9] J. M. Hendrie, J. Chem. Phys. 22, 1503 (1954).

[10] W. L. Fite and R. T. Brackmann, Phys. Rev. 112, 1141 (1958).

magnetic velocity selector requires high intensity and stable, precise alignment however, and we found that much better results could be obtained with a furnace made from a solid tube. With this the beam intensity for the same background pressure in the oven chamber (1×10^{-4} torr) was increased at least fivefold, evidently by elimination of leakage of H_2. The tube is made[11] by drilling with a tungsten carbide drill a 3.0-mm-diam axial hole through a 5 cm length of 10-mm-diam swaged tungsten rod. The central 4 cm length of the tube is then ground down to 4.5 mm o.d., leaving shoulders of width about 0.5 cm on each end with the original diameter. A 0.05-mm slit 10 mm long is cut through the tube wall using an oil-immersion spark machine.[12] The tube is mounted vertically, with its shoulders inserted into water-cooled copper blocks. The H_2 gas is fed into the top end of the tube, which is rigidly clamped. The bottom end is blanked off and is free to slide between spring-loaded jaws which maintain thermal and electrical contact but allow thermal expansion. The copper mounting blocks are supported by a rigid framework (labeled D in Fig. 1) to prevent lateral strains from buckling the tungsten tube. This framework is mounted on a carriage which can be traversed by a micrometer screw (E) from outside the vacuum chamber so that the oven can be accurately positioned during operation. The tube is heated by passing a current of ~500 A at 6 V between the copper blocks. The operating temperature is usually in the range 2700°–3000°K (measured with a pyrometer) and the H_2 pressure is ~0.5 torr. The dissociation of H_2 is >60% in this range.[9] The operating lifetime of these ovens (provided the mounting is strain free) is limited by evaporation to ~300 h.

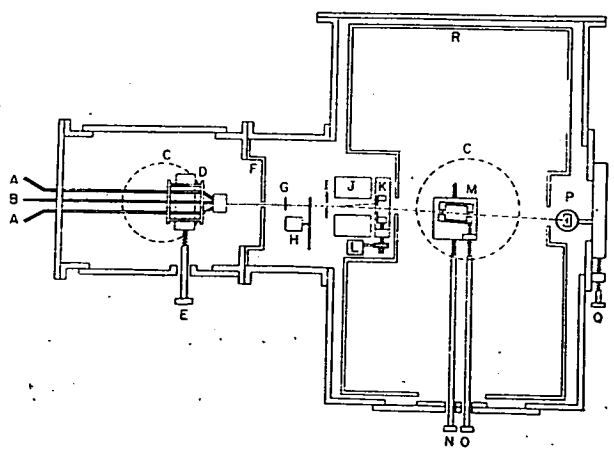

FIG. 1. Diagram (not to scale) of apparatus: (A) copper tubing ($\frac{1}{4}$ in. diam) supplying electric current and cooling water to tungsten oven; (B) H_2 supply tube; (C) oil diffusion pumps; (D) hydrogen oven and supporting framework; (E) traverse control for aligning oven; (F) water-cooled radiation shield separating chambers; (G) beam flag; (H) chopper wheel and motor; (I) magnet entrance slit; (J) deflecting magnet; (K) magnet exit slit; (L) motor for traversing magnet exit slit; (M) scattering chamber; (N) scattering chamber traverse control; (O) scattering-chamber rotation control; (P) bolometer detector; (Q) bolometer traverse control; (R) cold shields.

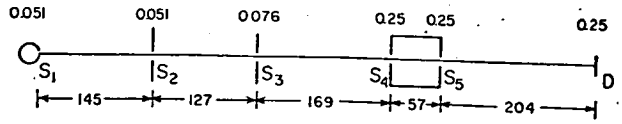

FIG. 2. Beam geometry. Slitwidths are shown above the beam line and distances between the elements are shown below (all in millimeters). S_1 denotes the oven slit, S_2 and S_3 the entrance and exit slits for the magnet, S_4 and S_5 the slits for the scattering chamber, and D the detector filament.

After entering the main chamber the beam is modulated, usually at 10 cps, by a rotating chopper disk (H) driven by a synchromous motor.[13] The chopper also interrupts a light beam at this point and thus provides a reference signal, via a phototransistor and amplifier, for phase-sensitive detection. The beam may also be interrupted by a mechanical flag (G).

Magnetic Velocity Selector

The inhomogeneous deflecting magnet (J) velocity selects the H atoms and also separates them from undissociated H_2 molecules and from most of the modulated infrared signal emitted by the oven. Magnetic velocity selection has occasionally been used for alkali atom beams,[14,15] although the customary rotating-disk selectors provide much better resolution. Above 2500°K the maximum intensity in the H atom velocity distribution[16] comes above 9×10^5 cm/sec, and with a mechanical selector it is difficult to go this high.[17]

The magnet used has the traditional "two-wire" pole-tip configuration,[18] with dimensions shown in Fig. 3, and is 11.6 cm in length. Details of construction and calibration have been given elsewhere.[19] The exciting current, up to 100 A, is provided by a transistorized, well-regulated dc power supply.[20] The maximum field

[11] We are much indebted to G. Pisiello, who devised this method of constructing the tungsten oven.

[12] Eleroda Model D1, Charmilles Engineering Works, Ltd., Inc., Geneva, Switzerland.

[13] Type SC, Globe Industries, Inc., Dayton, Ohio.

[14] V. W. Cohen and A. Ellet, Phys. Rev. 52, 502 (1937).

[15] (a) H. H. Brown, Jr., K. Lulla, and B. Bederson, in *Atomic Collision Processes*, M. R. C. McDowell, Ed. (North-Holland Publ. Co., Amsterdam, 1963), p. 921; (b) B. Bederson and K. Rubin, A.E.C. Tech. Rept. No. NYO-10, 117, New York University, 1962; (c) K. Lulla, H. H. Brown, and B. Bederson, Phys. Rev. 136, A1233 (1964).

[16] This refers to the intensity distribution transmitted by the selector (see Ref. 7), which has the form $v^4\exp(-v^2/\alpha^2)$ with maximum at $(2)^{\frac{1}{2}}\alpha$, where α is the most probable velocity in the oven.

[17] S. M. Trujillo, P. K. Rol, and E. W. Rothe, Rev. Sci. Instr. 33, 841 (1962).

[18] See, for example, N. F. Ramsey, *Molecular Beams* (Clarendon Press, Oxford, England, 1956), p. 400.

[19] R. R. Herm and D. R. Herschbach, UCRL Rept. 10526, Lawrence Radiation Laboratory, Berkeley, California, 1962.

[20] Regatran Series TO, Electronics Measurements Co. of Red Bank, Eatontown, N.J.

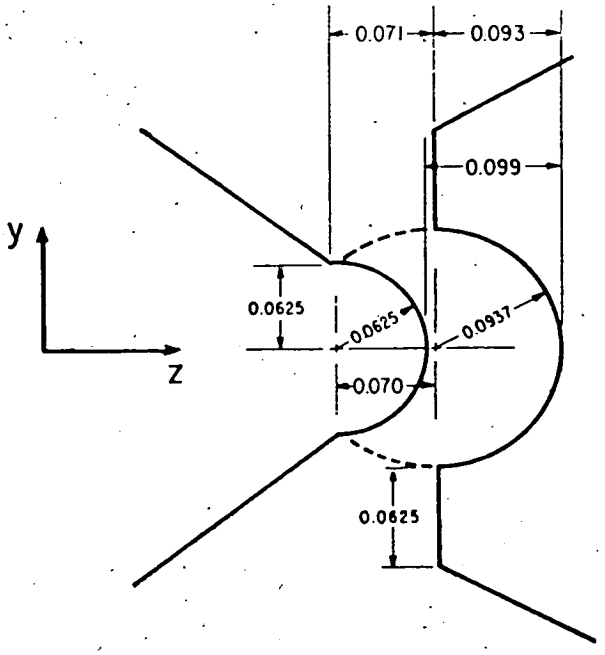

FIG. 3. End view of magnet pole tips (dimensions in inches).

is 15 kG and the field strength is linear with the exciting current up to 8 kG. In the part of the gap traversed by the beam the ratio of the field gradient to field is $(\partial H/\partial z)H^{-1}\sim 6$ cm^{-1}, as calculated from the pole-tip geometry. A fixed slit 0.051 mm wide and 3.0 mm high (I) collimates the beam at the entrance to the field and another slit 0.076 mm wide and 4.0 mm high (K) at the exit is mounted on a micrometer screw traverse (L) driven by a dc stepping motor.[21] This allows the position of the exit slit to be adjusted in increments of 0.0064 mm.

As indicated in Fig. 1, in operation the exit slit is offset from the original beam axis and thus transmits only one of the spin states (that deflected away from the convex pole tip) with a relatively narrow band of velocities (see Fig. 4). At the center of the slit the transmitted velocity is proportional to the square root of the magnet current (in the linear region) and inversely proportional to the square root of the slit offset, whereas the relative width of the transmitted velocity band, $\Delta v/v$, is one-half the ratio of the slit-width to the slit offset.[22] In the present experiments the velocity spectrum was always scanned (see Fig. 5) by varying the magnet current with the slitwidth and offset fixed.[23]

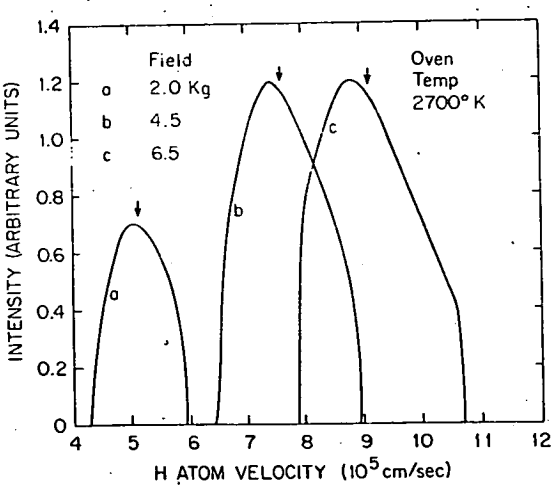

FIG. 4. Sample calculations of velocity bands for hydrogen atoms transmitted by the magnet for three values of the field strength (2.0, 4.5, and 6.5 kG, respectively, for Bands a, b, c). Arrows indicate the median velocity in each band (5.2, 7.7, and 9.2×10^5 cm/sec, respectively). The magnet exit slit is offset 0.020 cm and the temperature of the incident beam is 2700°K.

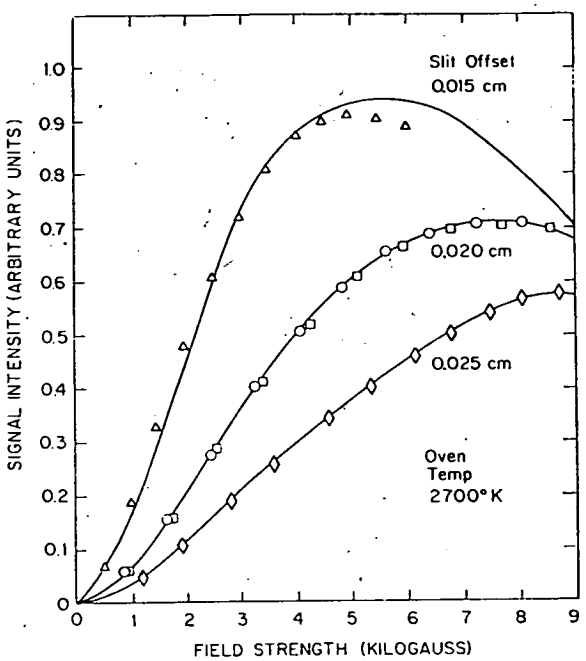

FIG. 5. Hydrogen atom signal intensity as a function of magnet field strength. The curves are calculated for three positions of the magnet exit slit and a beam temperature of 2700°K. The points (△, ○, □, ◇) are signals read on the bolometer detector in separate experiments, each normalized to the calculated curve.

[21] Slo-syn Type SS25, Superior Electric Co., Bristol, Conn.

[22] These are idealized relations, derived from the elementary deflection formulas given in Ref. 18, pp. 89–100, for the case in which the parent beam has negligible width. The computer program used for the velocity calibration and the calculation of Figs. 4 and 5 takes account of the (approximately trapezoidal) shape of the parent beam and also the slight variation in the field gradient with the position of the beam within the magnet gap. The essential features of this computation have been described in Refs. 15(b) and 23.

[23] An alternate mode of velocity analysis (not used here) is described by M. A. D. Fluendy, J. Sci. Instr. 42, 489 (1965). In this exit slit is not offset and the velocity spectrum is derived by applying an "unfolding" technique to measurements of the variation of the transmission with field strength. The results agreed closely with the velocity calibration obtained from Fig. 5.

The scattering chamber (M) is mounted on a side flange equipped with two control rods (N and O) which allow the chamber to be translated or rotated about its front slit so as to intercept the deflected beam. The chamber is made of stainless steel. The over-all beam path within the chamber is 57 mm, including entrance and exit canals each 12.7 mm long, 0.25 mm wide and 9.5 mm high. The target gas enters the chamber via a length of flexible copper bellows tubing which passes through the side flange and the gas pressure is regulated by a small variable leak.

Bolometer Detector

The detector (P) is a very thin Pt strip (10^{-3} mm thick, 0.25 mm wide, 6.5 mm long, resistance $\sim 40\ \Omega$), which apparently functions by catalyzing recombination of the incident H atoms. The heat liberated is detected as a change in resistance of the Pt strip which gives rise to an out-of-balance potential in a bridge circuit containing the strip as one arm. This detector is a slightly modified version of a commercial infrared bolometer.[24] The operating conditions and the associated electronics have been previously described.[25] Some difficulty was originally experienced[25] with drifts and loss of sensitivity to H atoms due to "poisoning" by surface contamination. However, this was eliminated by simply modifying the bridge circuit so as to pass 8 mA of dc current through the Pt strip (rather than the recommended[24] maximum of 4 mA).

The maximum sensitivity of the bolometer detector when used with beam modulation (10 cps) and lock-in amplification (equivalent bandwidth ~ 0.2 cps) is estimated[26,27] to be $\sim 10^{10}$–10^{11} atoms $cm^{-2} \cdot sec^{-1}$. This compares favorably with the estimated sensitivity for universal detectors using electron-bombardment ionization and mass analysis,[28] especially since the bolometer is much simpler and discriminates more sharply against the ambient H_2 and other background gases. The order of magnitude of the observed signals indicated that a large fraction of the incident H atoms was detected. For example, the largest signal obtained (80 V, with amplifier gain $\sim 3\times 10^7$) corresponds to $\sim 5\times 10^{-7}$ W or the heat of recombination of $\sim 5\times 10^{13}$ atoms $cm^{-2} \cdot sec^{-1}$. This is about the same as the flux at the detector calculated assuming effusive flow from the oven (with 10% of the H beam having the proper spin and velocity to be transmitted by the magnet).

PROCEDURE

The primary data for a run consist of bolometer readings taken at 10 settings of the magnet current, first with and then without the scattering gas present. A programmed switching device made the scan of the magnet current and data collection automatic. A single scan required 20–30 min. Before each run the scattering chamber pressure was adjusted to give 45%–55% attenuation of the H beam. This pressure was typically $\sim 10^{-3}$ torr, and the chamber temperature was 210°K. Many runs were made for each scattering gas (at least six, usually 10–20); the runs were simply repeated and averaged until the variation of the relative cross section with velocity appeared to be well established.

The velocity calibration was derived from a previous calibration of the field strength versus magnet current[19] and a computer program[23] which calculates the velocity distribution of transmitted H atoms as a function of the field strength, slit offset, and beam temperature, assuming effusive flow and a Maxwellian distribution within the oven. For the conditions used in most of the runs (field $\lesssim 8$ kG, slit offset $=0.020$ cm, $T=2700$°K), the calculated velocity resolution was $\Delta v/v \sim 27\%$, as illustrated in Fig. 4, and the mean H-atom velocity v (in 10^5 cm/sec) was related to the field strength $\mathcal{H}$ (in kilogauss) and the magnet current $\mathcal{I}$ (in amperes) by $v=3.623\mathcal{H}^{1/2}=1.61\mathcal{I}^{1/2}$. Despite this indirect means of establishing the velocity calibration, the magnet scans made without scattering gas show good agreement with the calculated velocity distribution, as illustrated in Fig. 5. Similar agreement was found in other experiments using the straight-through configuration.[23,29]

The relative H atom intensity was obtained by averaging the bolometer signals at each setting of the magnet current and subtracting the signal recorded at zero field. For the offset-slit configuration the zero-field signal is due entirely to the infrared background caused by oven light reflected from the magnet pole

[24] Type AT3 bolometer and KWl tuned amplifier, Baird Associates, Inc., Cambridge, Mass.

[25] M. A. D. Fluendy, Rev. Sci. Instr. 35, 1606 (1964).

[26] According to Ref. 24, the bolometer circuit output is 5 V/W of incident energy and the noise power in a 2-cps bandwidth is $\sim 5\times 10^{-10}$ W. Recombination of 2 H atoms/sec yields $\sim 3.5\times 10^{-19}$ W/atom. Thus, to give a signal-to-noise ratio of unity within a 0.2-cps bandwidth, $\sim 10^8$ atoms/sec must recombine on the strip (exposed area 0.016 cm^2), or $\sim 10^{10}$ atoms $cm^{-2} \cdot sec^{-1}$.

[27] Estimates of the recombination probability for H atoms on clean Pt range from $\sim 10\%$ to 100%; for a brief review see B. A. Thrush, in Progr. Reaction Kinetics 3, 63 (1965).

[28] See, for example: (a) R. Weiss, Rev. Sci. Instr. 32, 397 (1961); (b) H. G. Bennewitz and R. Wedemeyer, Z. Physik 172, 1 (1963); (c) G. O. Brink, Rev. Sci. Instr. 37, 857 (1966). The estimate given by Weiss (10-100 fold more optimistic than others) for an Ar beam (with background vacuum $\lesssim 3\times 10^{-9}$ torr) corresponds to a noise equivalent sensitivity of 2×10^8 atoms $cm^{-2} \cdot sec^{-1}$. For an H-atom beam the inefficiency of ionization and interfering background would be much more severe (cf. Refs. 4, 5) and the sensitivity is estimated to be no better than $\sim 10^{10}$ atoms $cm^{-2} \cdot sec^{-1}$ (even if the detector chamber vacuum were still $\sim 10^{-9}$ torr).

[29] As in Refs. 23 and 25, in calculating the curves of Fig. 5, we added the kinetic energy of impact (which reaches ~ 10 kcal/mole near the high end of the velocity range) to the heat of recombination. (51.5 kcal/mole per H atom). For the cross-section measurements no correction for the kinetic energy is required since it cancels from the intensity ratio I/I_0 at each fixed velocity.

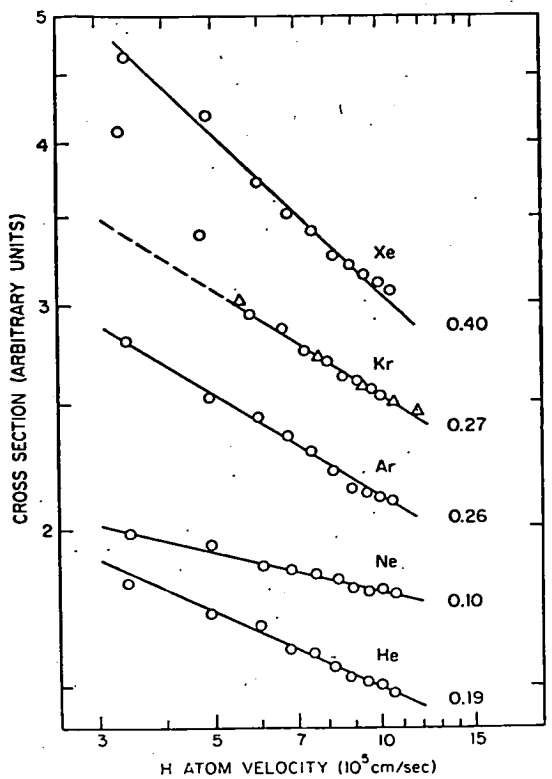

FIG. 6. Velocity dependence of scattering of hydrogen atoms from rare gases. Log$Q$ is plotted versus log$v$; values of the velocity derivative, $S=-\partial \log Q/\partial \log v$, corresponding to the straight lines shown are given at the right-hand side. For H+Kr several points obtained with the magnet exit slit offset by 0.015 cm rather than 0.020 cm are included (shown by △'s).

pieces. This background was usually 10%–30% as large as the maximum H atom signals but remained constant within <5% (independent of the magnet current or presence of scattering gas). The H-atom signal/noise ratio typically ranged from 1–2 for points taken at the lowest velocity with the attenuated beam to 60–80 for points taken in the 10^6-cm/sec region with the unattenuated beam.

As no attempt was made to determine absolute cross sections, the data give only the relative change in cross section with velocity. Thus, the relative cross section $Q=K\ \log(I_0/I)$, with K left as an undetermined constant and I/I_0 the ratio of H atom intensities with and without the scattering gas present.[30] Corrections[7,31] for thermal motion of the target gas were negligible, except for H_2 and He, because of the high velocity of the H beam. Also, according to the usual criteria,[7,32] the angular resolution in these experiments was sufficiently good to permit observation of the true velocity dependence as determined by the quantum limit of the small-angle scattering; this is primarily due to the kinematic leverage provided by the small mass of the H atom.

[30] Beer's law behavior was confirmed in auxiliary experiments carried out with a tenfold variation in the scattering-gas pressure. This offers further evidence for the linearity of the bolometer response (cf. Ref. 25).

[31] K. Berkling, R. Helbing, K. Kramer, H. Pauly, Ch. Schlier, and P. Toschek, Z. Physik 166, 406 (1962).

[32] F. von Busch, Z. Physik 193, 412 (1966). For our apparatus, the laboratory resolution angle as defined by Kusch is $\Theta_K=4.8'$ (nominal scattering angle for which 50% of the H atoms miss the detector).

RESULTS AND DISCUSSION

Figures 6–8 show the results, with the data for the various systems arbitrarily spaced along the ordinate scale for the purpose of comparison. The velocity dependence is characterized by the slope of these plots, or the logrithmic derivative, $S=-\partial \log Q/\partial \log v$. The value of S corresponding to the mean slope or the limiting slope at high velocity is indicated at the right for each system. The experimental uncertainty in S is about ± 0.03, as judged from comparison of replicate sets of runs.

Relation of Cross Section to Potential

The main qualitative features of $Q(v)$ are readily inferred from semiclassical-scattering theory.[7] The magnitude of the cross section is approximately $Q\simeq 2\pi b_0^2$, in terms of an impact parameter such that for $b\gtrsim b_0$ the scattering angle calculated from classical

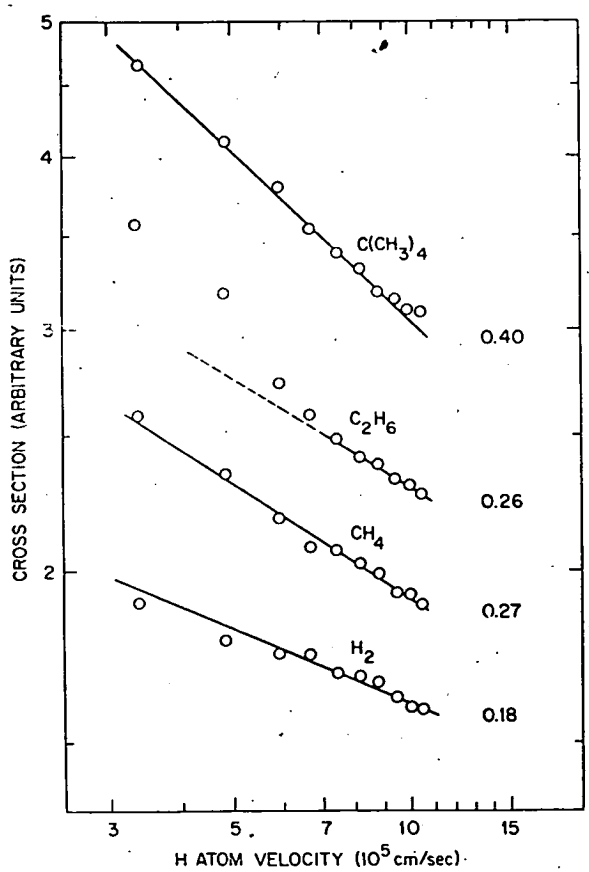

FIG. 7. Scattering of hydrogen atoms from molecular hydrogen, methane, ethane, and neopentane (notation as in Fig. 6).

mechanics becomes smaller than the transverse spreading of the particle's wave packet required by the uncertainty principle. For realistic intermolecular potentials this occurs where the semiclassical phase shift $\eta(b)$ drops below about $\frac{1}{2}$ rad. When the collision velocity is increased, the potential has less time to act, and the region in which the scattering is strong enough to be compatible with the uncertainty principle shifts to smaller distances. Thus, b_0 and the cross section decrease with increasing velocity at a rate which reflects the dependence of the potential on distance.

This behavior is illustrated in Fig. 9, which shows $Q(v)$ for Lennard-Jones $(n,6)$ potentials with $n=8$, 12, and 20 as calculated from the semiclassical Landau–Lifschitz approximation[33] (see the Appendix). Reduced variables are used, defined by $Q^*=Q/\pi r_m^2$ and $D=2\epsilon r_m/\hbar v$, where r_m is the radius of the potential minimum and ϵ its depth. For comparison, dashed lines are included to show the cross sections calculated for the separate terms of the potential; the velocity dependence is $v^{-2/5}$ for the r^{-6} term and $v^{-2/(n-1)}$ for the r^{-n} term.

At low reduced velocities ($D\gtrsim 3$), the critical impact parameter is considerably larger than the potential-well radius ($b_0\gtrsim 1.7r_m$) and $Q(v)$ is determined almost solely by the long-range attractive r^{-6} interaction.[34] At sufficiently high velocities ($D\lesssim 10^{-2}$), where the attractive interactions become too weak to satisfy the uncertainty principle, the critical impact parameter is appreciably less than the well radius ($b_0\lesssim 0.8r_m$) and $Q(v)$ is determined by the short-range repulsive wall. At intermediate velocities (near $D\simeq 1$, where $b_0\simeq r_m$), the cross section shows a steep transition region which is governed by the form of the potential well.

Qualitative Analysis of Data

The progression in $Q(v)$ seen in Fig. 6 is qualitatively similar to that found in scattering of other species from the rare gases.[35] For H+Xe the strength parameter ϵr_m is evidently large enough to make the attractive interaction dominant throughout the experimental velocity range. Since this requires $D\gtrsim 2$ or 3 for $v\lesssim 11\times 10^5$ cm/sec, we obtain a rough lower limit:

$$\epsilon r_m\gtrsim 10\text{–}20\times 10^{-22}\ \text{erg·cm}. \qquad (1a)$$

For H+Kr the $Q(v)$ shows pronounced curvature and hence appears to fall in the transition realm. Thus, $D\simeq 1$ for $v\simeq 3$ to 7×10^5 cm/sec and

$$\epsilon r_m\simeq 1.5\text{–}4\times 10^{-22}\ \text{erg·cm}. \qquad (1b)$$

For H+Ar, Ne, He the low slopes observed indicate the ϵr_m's are so small that repulsive interactions remain dominant even at the lowest experimental velocity. This requires $D\lesssim 1$ for $v\gtrsim 3\times 10^{-5}$ cm/sec and provides a rough upper limit:

$$\epsilon r_m\lesssim 2\times 10^{-22}\ \text{erg·cm}. \qquad (1c)$$

The same qualitative considerations apply for the molecules of Figs. 7 and 8. Since the electronic ground state is $^1\Sigma$ for all of these molecules the scattering involves only one potential curve and the leading term in the attractive part is again r^{-6}. A host of inelastic rotational, vibrational, and chemical transitions can occur. However, the range of impact parameters for which these inelastic processes become important is expected to be well inside the critical b_0 defined by the "pseudo two-body," spherically symmetric part of the

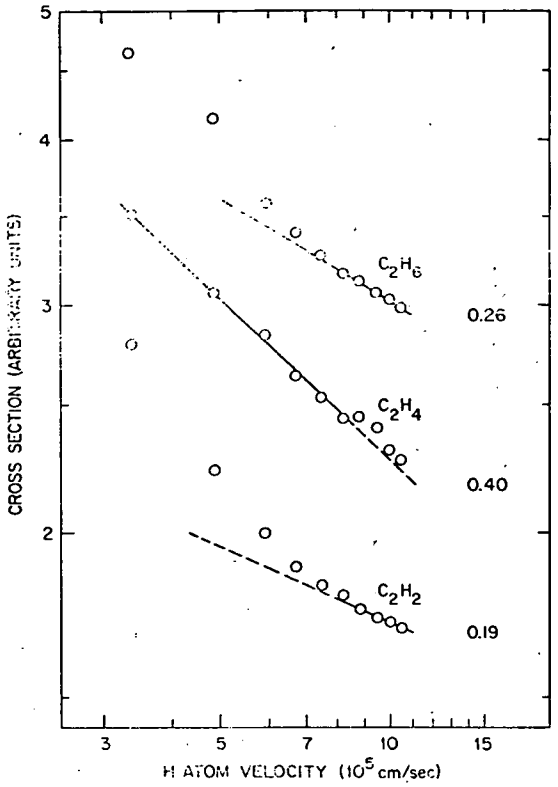

FIG. 8. Scattering of hydrogen atoms from acetylene, ethylene, and ethane (notation as in Fig. 6).

[33] L. D. Landau and E. N. Lifshitz, *Quantum Mechanics* (Pergamon Press, Ltd., London, 1958), p. 416.

[34] In the low-velocity realm there also appears an undulatory fine structure due to interference effects (see Fig. 9), and this offers the best available means to determine ϵr_m accurately (Refs. 7 and 35). However, the undulations are likely to blurred out entirely by our poor velocity resolution.

[35] (a) Li atoms: E. W. Rothe, P. K. Rol, and R. B. Bernstein, Phys. Rev. 130, 2333 (1963); (b) K atoms: D. Beck and H. J. Loesch, Z. Physik 195, 444 (1966); F. von Busch, H. J. Strunck, and C. Schlier, Phys. Letters 16, 268 (1965); (c) He atoms: R. Duren, R. Feltgen, R. Helbing, and H. Pauly, *ibid.* 18, 282 (1965); H. J. Beier, *ibid.* 18, 285 (1965); (d) H_2 molecules: R. Feltgen, W. Gaide, R. Helbing, and H. Pauly, *ibid.* 20, 501 (1966); (e) Metastable He atoms: E. W. Rothe, R. H. Neynaber, and S. M. Trujillo, J. Chem. Phys. 42, 3310 (1965).

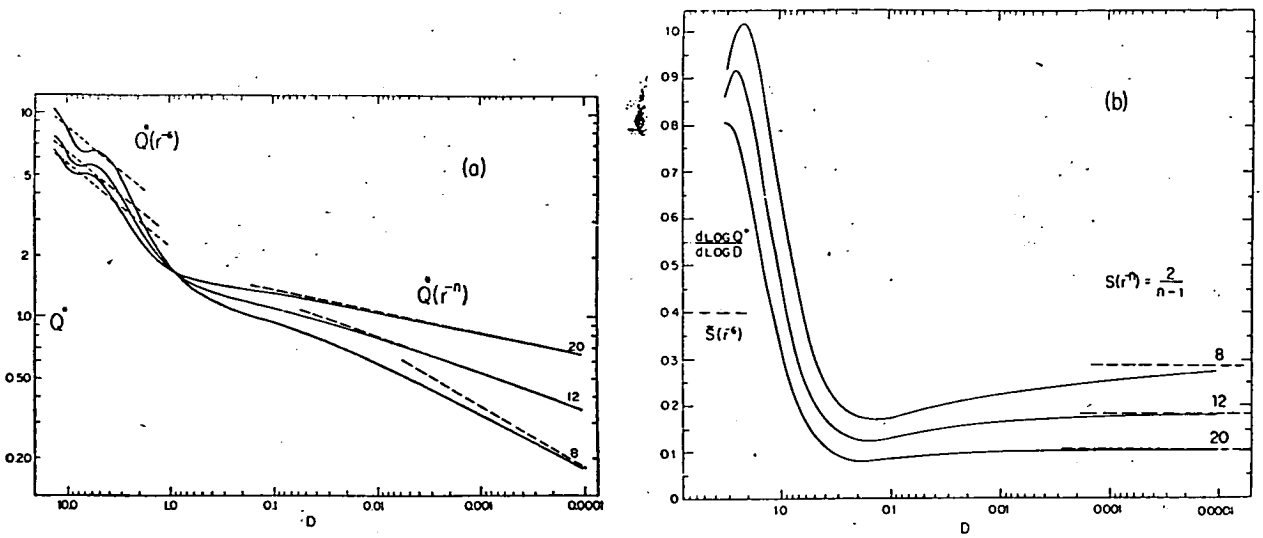

FIG. 9. Variation of (a) reduced cross section Q^* and (b) logrithmic velocity derivative S with reduced reciprocal velocity parameter D for the Lennard-Jones (n, 6) potential, with $n=8$, 12, and 20. The dashed lines show the results for the separate terms (r^{-n} and r^{-6}) of the potential.

potential (except perhaps at the highest velocities). Hence it is not surprising to find that the $Q(v)$ appear so similar to those for atom–atom systems of comparable size. The rough estimates given in Eq. (1) accordingly can also be assigned to (a) $H+C(CH_3)_4$ and C_2H_4; (b) $H+C_2H_6$ and C_2H_2; (c) $H+CH_4$ and H_2, respectively.

An alternative interpretation is possible for the systems assigned to the transition realm (H+Kr, C_2H_6, and C_2H_2). As indicated in Fig. 10, the data match fairly well the calculated transition behavior but could be attributed instead to undulatory fine structure[34] superposed on an $S=0.40$ slope. The velocity range covered is too narrow to indicate clearly the "wavelength" of this structure. However, calculations using formulas[7,35] based on the LJ (12,6) potential show that this interpretation would require $\epsilon r_m \simeq$ 15–35$\times 10^{-22}$ erg·cm for these systems. Except perhaps for $H+C_2H_6$, where the deviations from the $S=0.40$ line are rather small, this interpretation seems unlikely in view of our poor velocity resolution and our failure to observe undulatory structure for other systems that can definitely be assigned to the attractive realm (H+Xe and neopentane). Also, from results for other systems,[35] we would not expect to find both H+Xe and H+Kr in the attractive realm when H+Ar is in the repulsive realm.

For $H+C_2H_4$ the cross section shows a distinct "bump" in the region $v=8.5$–9.5×10^5 cm/sec (corresponding to 0.38–0.47 eV in the relative kinetic energy). This feature is well outside experimental scatter. It appeared consistently in sets of runs made several months apart and compared directly with concurrent runs on the H+Xe system. The bump could possibly be a Breit–Wigner resonance[36] associated with an excited state or decay channel of the ethyl radical but it may be merely a poorly resolved undulation of the usual kind.[35]

Firm conclusions about the form of the potential functions and values of the parameters must await experiments with a wider velocity range or higher resolution. However, the observed slopes for H+Ar and Ne indicate that the true potentials differ substantially from the customary LJ (12,6) model. This may be illustrated by comparison with Fig. 9(b).

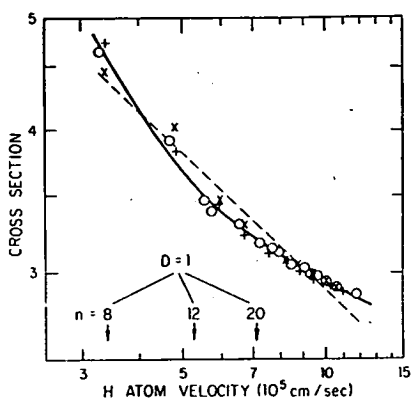

FIG. 10. Comparison of $Q(v)$ for systems assigned to the transition realm, H+Kr (○), C_2H_6 (×), and C_2H_2 (+). The solid curve shows the transition behavior calculated for a LJ (12, 6) potential with $D=1$ for $v=5.3\times 10^5$ cm/sec (corresponding to $\epsilon r_m = 2.8\times 10^{-22}$ erg·cm). Practically the same curve is obtained for LJ (8, 6) and (20, 6) potentials with $D=1$ for $v=3.4$ and 7.1×10^5 cm/sec, respectively. The dashed curve indicates the $S=0.40$ slope which would apply in the attractive realm.

[36] See, for example, Ref. 33, pp. 440–449.

For all of the systems studied we expect $\epsilon r_m > 0.1 \times 10^{-22}$ erg·cm (see Fig. 11), which corresponds to $D > 0.01$ for our velocity range. Thus, although we cannot assign the precise position along the D scale, the data for H+Ar, Ne, He, and H_2 evidently should be located near the region where the slope passes through a minimum. With allowance for experimental uncertainty of ± 0.03 in S, this implies that the slope found for H+Ar is too high to fit any LJ potential with $n \gtrsim 8$, whereas the very low slope found for H+Ne indicates a much higher index, nominally $n \gtrsim 15$. The slopes for H+He and H_2 are roughly compatible with $15 \gtrsim n \gtrsim 8$. The estimates found in Eq. (1) are intended to include some leeway for the uncertain form of the potential (but assume $n \sim 8$–20). The data were also compared in the same way with $Q(v)$ functions calculated[37] for Buckingham exp–6(α) potentials (with $\alpha = 10$–20), but no qualitatively significant differences from the LJ case appeared (again, for $D > 0.01$).

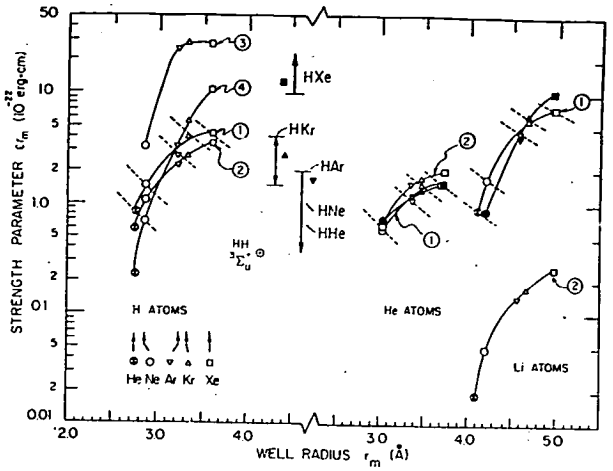

FIG. 11. Comparison of the strength parameters ϵr_m for scattering of H, He, and Li atoms from the rare gases. Solid symbols indicate results derived from experiments, open symbols results predicted from semiempirical correlations.

Correlation of Potential Parameters

In Fig. 11 the rough bounds on the strength parameter ϵr_m given in Eq. (1) are compared with parameters predicted from four semiempirical procedures and with the experimental results for scattering of He and Li atoms from rare gases.[35] A theoretical result[38] for the H+H interaction in the $^3\Sigma_u^+$ state is also included. The LJ (12,6) potential was assumed for both the semiempirical methods and the analysis[35] of the scattering data. Also, for the sake of consistency, the well radius r_m used for the abscissa was taken as the sum of effective atomic radii.[39] (The available scattering data are insensitive to r_m.) For the rare gases the radii were obtained from transport properties[40] and for H and Li from an empirical correlation[41] of van der Waals and bonding radii.[42] The procedures used to predict ϵr_m values are listed below (as numbered in Fig. 11).

(1) Theoretical values[26] of the dispersion force constant C for the leading term of the potential ($-C/r^6$) were used with the LJ (12,6) relation

$$C = 2\epsilon r_m^6. \tag{2}$$

The C's are expected to be accurate within ~10% (extrapolations had to be made for H and He with Kr and Xe) whereas Eq. (2) is found to hold within better than a factor of 2 for many like–like interactions.[43] Since the result obtained is quite sensitive to the choice of r_m, in Fig. 11 the range corresponding to a change of ± 0.20 A in r_m is indicated (dashed segments). This procedure gives very good agreement with the He scattering data and rough agreement with the Li data. However, it considerably underestimates the H+Xe interaction and probably overestimates H+Ar, Ne, He; thus, the trend in deviations indicated by the Li results appears to be amplified in the H-atom scattering.

(2) Johnston[44] has pointed out that an empirical correlation of spectroscopic vibrational force constants with bond length gives reasonable results when extended to van der Waals interactions of the rare gases. Force constants obtained from his correlation were used with the LJ (12,6) relation

$$F = 72\epsilon/r_m^2. \tag{3}$$

For the He and H interactions this gives results close to Method (1) but for Li it is more than an order-of-magnitude low.

(3) Since the vibrational force constants for all molecules containing an alkali atom are found to lie well above the correlation curves used by Johnston,[44] we "recalibrated" his method to fit the spectroscopic data for the ground $X\,^1\Sigma^+$ and first excited $A\,^1\Sigma^+$ states of the alkali hydrides.[45] For the $A\,^1\Sigma^+$ states the equilibrium bond lengths are very large (e.g., 2.60 Å for LiH, 3.87 Å for CsH) and thus no extrapolation is required to reach the van der Waals realm (e.g., the

[37] R. B. Bernstein, J. Chem. Phys. 38, 515 (1963).
[38] W. Kołos and L. Wolniewicz, J. Chem. Phys. 43, 2429 (1965).
[39] These radii are: He 1.44; Ne 1.55; Ar 1.92; Kr 2.02; Xe 2.29; H 1.30; Li 2.65; He* ($1s2s\,^3S$ state) 3.10; H_2 1.66 (in angstroms).
[40] Reference 1, p. 1212 of *Notes Added in Second Printing* (1964).
[41] J. O. Hirschfelder and M. A. Eliason, Ann. N.Y. Acad. Sci. 67, 451 (1957).
[42] J. C. Slater, J. Chem. Phys. 41, 3199 (1964).
[43] See, for example, (a) Ref. 1, p. 966; (b) W. Brandt, J. Chem. Phys. 24, 501 (1956); Discussions Faraday Soc. 40, 279 (1965).
[44] H. S. Johnston, J. Am. Chem. Soc. 86, 1643 (1964).
[45] For references, see Y. P. Varshni and R. C. Shukla, Rev. Mod. Phys. 35, 130 (1963).

estimated r_m value[39] is 2.7 Å for H+He, 3.6 A for H+Xe). However, the results obtained from this procedure are definitely much too high (except possibly for H+Xe).

(4) When plotted as $\log\epsilon$ versus r_m the data[7b] for scattering of alkali metals and metastable He atoms ($1s2s$ configuration) from rare gases fall on smooth curves, one curve for each rare gas (after slight adjustments to conform to our choice of standard radii[39]). Linear extrapolation of these curves provided another set of estimated ϵr_m's for H atom scattering. This comes closer to the experimental results than the other procedures.

For $H+H_2$, theoretical calculations[1,2] give $\epsilon r_m = 1.2\text{–}1.6\times10^{-22}$ erg·cm and Method (1) gives 1.8×10^{-22} erg·cm; thus, according to Eq. (1c), both are compatible with the experimental results.

For the hydrocarbon molecules, transport properties[40] indicate the like–like interactions are quite similar for CH_4 and Ar; for C_2H_2 and Kr; and for C_2H_4, C_2H_6, and Xe. This correspondence seems to carry over nicely to H-atom scattering (except possibly for $H+C_2H_6$, for which the proper interpretation of the data is uncertain). For $K+C(CH_3)_4$, rainbow scattering experiments[46] give $\epsilon=0.42$ kcal/mole. An extrapolation parallel to the curves of Method (4) predicts $\epsilon r_m \sim 15\text{–}20\times10^{-22}$ erg·cm for H scattering (with $r_m \simeq 4\text{–}6$ Å), consistent with the experimental bound given in Eq. (1a).

It is particularly interesting to note that in terms of the well depth the H+Xe interaction is appreciably stronger than Li+Xe. Thus, with $r_m \sim 3.6$ Å, Eq. (1a) gives as a lower bound $\epsilon \gtrsim 0.4\text{–}0.8$ kcal/mole for H+Xe, compared with ~0.2 kcal/mole[35a] for Li+Xe.

ACKNOWLEDGMENTS

The construction of several parts of the apparatus was carried out at the University of California, Berkeley, under the auspices of the Inorganic Materials Research Division of the Lawrence Radiation Laboratory and with support from the Division of Research, U. S. Atomic Energy Commission. We are greatly indebted to J. L. Kinsey and J. K. Cashion for their contributions to the early design and testing work. We wish to thank E. A. Gislason and Professor R. B. Bernstein for helpful discussions of the cross-section calculations. The completion of the apparatus and the experiments at Harvard were supported in part by the U. S. Atomic Energy Commission and in part by the National Science Foundation.

APPENDIX

The calculation given here extends the Landau–Lifschitz (LL) approximation[7,33] to a potential containing two inverse power terms,

$$V(r) = C_m r^{-m} + C_n r^{-n}. \tag{A1}$$

In the semiclassical formulation,[7] the cross section is an integral over the "target area" corresponding to a continuous distribution of impact parameters:

$$Q = \int_0^\infty |\, T(b)\,|^2\, d(\pi b^2). \tag{A2}$$

The weighting factor $|\,T(b)\,|^2 = 4\sin^2\eta(b)$ measures the strength of the scattering in terms of the phase shift function $\eta(b)$, which is in turn related to the classical angle of deflection via

$$\eta(b) = \tfrac{1}{2}k\int_b^\infty \Theta(b')\,db', \tag{A3}$$

where $1/k = \hbar/\mu v$ is the de Broglie wavelength. In the weak collision realm $\eta(b)$ may be calculated either from the Jeffreys–Born approximation or by use of (A3) with the classical small-angle formulas.[7] The result is

$$\eta(b) = -\tfrac{1}{2}K_m b^{-(m-1)} - \tfrac{1}{2}K_n b^{-(n-1)}, \tag{A4}$$

where

$$K_n = 2C_n f(n)/\hbar v,$$

$$f(n) = \tfrac{1}{2}\pi^{\frac{1}{2}}\Gamma(\tfrac{1}{2}n - \tfrac{1}{2})/\Gamma(\tfrac{1}{2}n).$$

The LL method consists of evaluating (A2) with the use of (A4) over the whole range of impact parameters. The formula (A4) is only valid for the region $b \gtrsim b_0$ in which $\eta(b) \lesssim \frac{1}{2}$ rad. However, this region essentially determines the magnitude of Q since $|\,T(b)\,|^2 \to 0$ very rapidly there. For the stronger collisions which occur at smaller impact parameters the actual form of $\eta(b)$ is unimportant.[33,47] There $\eta(b)$ is large so the weighting factor oscillates rapidly and in effect the target area is almost uniformly weighted by the random phase average, $|\,T(b)\,|^2 = 2$; this differs from the classical result, $T(b) = 1$, only because of shadow scattering. After integrating (A2) by parts, we find

$$Q = 2\pi K_m s I(s, t) + 2\pi K_n t' I(s', t'), \tag{A5}$$

where

$$I(s, t) = \int_0^\infty \sin(K_m x^s + K_n x^t)\,dx.$$

In the first term, $x = b^{-(m-3)}$ and

$$s = (m-1)/(m-3); \qquad t = (n-1)/(m-3).$$

In the second term, $x = b^{-(n-3)}$ and

$$s' = (m-1)/(n-3); \qquad t' = (n-1)/(n-3).$$

[46] E. F. Greene, A. L. Moursund, and J. Ross, Advan. Chem. Phys. 10, 135 (1966).

[47] R. B. Bernstein and K. H. Kramer, J. Chem. Phys. 38, 2507 (1963).

For $m<n$, we have $s<t$ and $s'<t'$ and the integrals may be evaluated from a series expansion,[48]

$$I(s,t)=t^{-1}\sum_{N=0}^{\infty}A_N(\alpha)K_m{}^N K_n{}^{-\alpha}, \qquad \text{(A6)}$$

where

$$A_N(\alpha)=[\Gamma(\alpha)\ \sin\tfrac{1}{2}\pi(\alpha-N)]/N!$$

and $\alpha=(Ns+1)/t$. Since this series is absolutely convergent, the calculation places no restrictions on (A1) except for $m<n$; negative values are allowed for either or both of the potential constants C_m and C_n.

For the Lennard-Jones (n,m) potential, the constants are related to the depth ϵ and radius r_m of the well by

$$C_m=-[n/(n-m)]\epsilon r_m{}^n, \qquad C_n=[m/(n-m)]\epsilon r_m{}^m.$$

In terms of the customary reduced units, $b^*=b/r_m$, $Q^*=Q/\pi r_m{}^2$, $D=2\epsilon r_m/\hbar v$, the result (A5) becomes

$$Q^*=2D\{-[n/(n-m)]f(m)sI^*(s,t) +[m/(n-m)]f(n)t'I^*(s',t')\}, \qquad \text{(A7)}$$

where the integrals $I^*(s,t)$ are evaluated from (A6) with K_m and K_n replaced by

$$K_m{}^*=K_m/r_m{}^{m-1}=[n/(n-m)]f(m)D,$$

$$K_n{}^*=K_n/r_m{}^{n-1}=[m/(n-m)]f(n)D.$$

At the high-velocity limit corresponding to $D\to 0$ (or for C_m or $K_m\to 0$) only the $N=0$ term of (A6) contributes and

$$Q^*=2\,|\,[n/(n-m)]f(n)D\,|^{2/(n-1)} \times\Gamma[(n-3)/(n-1)]\cos[\pi/(n-1)]. \qquad \text{(A8)}$$

The same formula with m and n interchanged is obtained from (A5) at the low-velocity limit where $D\to\infty$ (or for C_n or $K_n\to 0$). This is the original Landau–Lifschitz result for a potential with a single inverse power term.[33] Thus, the formula (A7) for the two-term potential is an expansion in powers of D about the high-velocity limit. The number of terms required increases rapidly as D increases or as $n-m$ decreases. For $D\lesssim 1.3$ and $m=6$, $n\gtrsim 8$ the first 30 terms are sufficient to obtain Q^* within 1%; for $D\simeq 13$ about 100 terms are required. The convergence is much more rapid with potentials for which C_m and C_n have the same sign. Stirling's approximation was used in the form

$$\ln\Gamma(z)=(z-\tfrac{1}{2})\ \ln z-z+\tfrac{1}{2}\ln(2\pi)+(12z)^{-1}-(360z^3)^{-1}$$

in evaluating terms with $N>30$.

For the high-velocity region ($D\lesssim 1$), Bernstein[37] has provided tables of the LJ$(n,6)$ cross sections derived from the Massey–Mohr (MM) approximation. Comparison with (A7) shows that at the high-velocity limit $\Delta=(Q_{\rm LL}{}^*-Q_{\rm MM}{}^*)/Q_{\rm LL}{}^*$ is 6.1%, 4.6%, and 3.0% for $n=8$, 12, 20, respectively. This is as expected from the results for one-term potentials, which indicate that the LL result is to be preferred (as it agrees within $\sim$0.5% with an "exact" partial-wave calculation for an r^{-12} potential).[47] At lower velocities, approaching the transition realm, Δ decreases appreciably and for $D\simeq 1$ it is $\lesssim 1\%$ for $n=8$–20. Several partial-wave calculations are now available for the LJ(12,6) potential[35,49] but in the region $D\lesssim 2$ these disagree by $\sim$5%, presumably due to truncation errors. The LL result is slightly ($\lesssim 3\%$) above these calculations. As expected, (A7) gives good results only for the mean cross section and does not accurately represent the undulatory structure which appears in the low-velocity region $D\gtrsim 3$. This would require the addition of further terms in (A4) to improve the approximation of the phase shift. However, accurate formulas for the undulations are already available.[50]

[48] D. Bierens de Haan, *Nouvelles Tables, D'Integrales Definies* (Hafner Publ. Co., New York, 1957), p. 108.

[49] R. Helbing, Ph.D. thesis, Bonn University, 1966.

[50] R. B. Bernstein and T. J. P. O'Brien, Discussions Faraday Soc. 40, 35 (1965), and papers cited therein.

Offprinted from the *Transactions of The Faraday Society*
No. 560, Vol. 65, Part 8, August, 1969

Small Angle Scattering from Crossed Sodium and Potassium Beams

BY L. T. COWLEY,* M. A. D. FLUENDY AND K. P. LAWLEY

Dept of Chemistry, University of Edinburgh, Edinburgh

Received 10*th January*, 1969

The small angle dependence of the differential cross-section for the elastic scattering of Na by K has been measured at relative velocitites from 936 to 1420 m sec^{-1} using a crossed-beam technique. Quantum undulations in the cross-sections were observed at laboratory angles less than 2° and their origin is discussed. The positions of the observed peaks together with a singlet potential obtained from spectroscopic data yield information on the long-range dispersion forces and the triplet potential. For the triplet potential with an assumed Lennard-Jones 8 : 6 form the best agreement found between observation and forward calculation yielded $\varepsilon = 2 \times 10^{-14}$ ergs and $r_m = 5{\cdot}6$ Å, though the fit is not perfect.

Colliding alkali metal atoms interact by a potential corresponding to either the singlet or the triplet molecular state. In the isolated atom pair, spin flipping due to nuclear or spin-orbit coupling is an unlikely process in the flight time of these experiments. Thus the scattered waves from these two potentials do not mutually interfere and the observed scattering from unpolarized beams is the degeneracy weighted average of scattering from each potential and so the observed differential cross section, $\sigma(\theta)$, is given by

$$\sigma(\theta) = \tfrac{1}{4}{}^1\sigma(\theta) + \tfrac{3}{4}{}^3\sigma(\theta). \qquad (1)$$

For the alkalis these two potentials are very different, the singlet potential possessing a deep well while the triplet potential is mostly repulsive.

Measurement of the angular dependence of scattering over a range of impact energies provides inherently more information than total cross-section measurements over a similar energy range,[1] especially if angular structure can be resolved. In this work, intensity limitations confined the observations to angles within *ca.* 2° of the sodium beam. Angular structure can occur in this region for relative velocities such that $ka \gtrsim 50$, where a is a length parameter of the potential and $k[=(2\mu E/\hbar^2)^{\frac{1}{2}}]$ is the wave number of the colliding pair. The angular spacing of the undulations in $\sigma(\theta)$ yields information about the potential. In the present experiments up to four such small angle undulations in $\sigma(\theta)$ have been observed. Interpretation is complicated by the operation of two potential functions and while the present results alone do not permit both singlet and triplet potentials to be obtained unambiguously, a set of potential parameters can be found that is concordant with the observations and with other evidence.

EXPERIMENTAL

The apparatus consisted of a turntable on which both beam sources, of the usual thermal type, were mounted so that their well-collimated beams intersected at 90°. The sodium beam was velocity selected. The detector was in a separate u.h.v. chamber and consisted

*present address: Lash Miller Chemical Laboratories, University of Toronto, Toronto 5, Canada.

of a hot 0·030 in. wide Re ribbon on which ionization took place. The resulting ions were extracted into a quadrupole mass filter and finally struck an electron multiplier. Each ion arrival was counted by a fast scaler and the total arrivals per sec together with other experimental variables (such as scattering angle) were automatically punched on to paper tape for subsequent computer analysis. The computer analysis provided for cross correlation between the signal and the cross beam, burst noise rejection, deconvolution of the main beam width, time normalization (to correct for drifts in beam intensities) and averaging over several angular scans.

The apparatus and associated computer programs will be described in more detail elsewhere, but the critical dimensions were as follows: cross beam width, 16°; detector width, 0·15° (subtended at the scattering centre); main beam width, 0·12°; effective angular resolution after deconvolution, ~0·05°; distance of scattering centre to detector, 27·5 cm; velocity filter resolution = 15 % (FWHM); pressure in experimental chamber during operation $\sim 2 \times 10^{-7}$ torr.

RESULTS

Angular scattering measurements were made at six different impact velocities ranging from 936 to 1420 msec^{-1}. A typical result after computer analysis is shown in fig. 1 as a plot of the scattered intensity $I(\theta_{lab}) \cdot \theta_{lab}^{7/3}$ against θ_{lab}. Classically such a plot would be a straight line of zero slope. The undulatory quantum structure is clear. The observed peak positions for each observational energy are shown in fig. 3 and are the average of several angular scans.

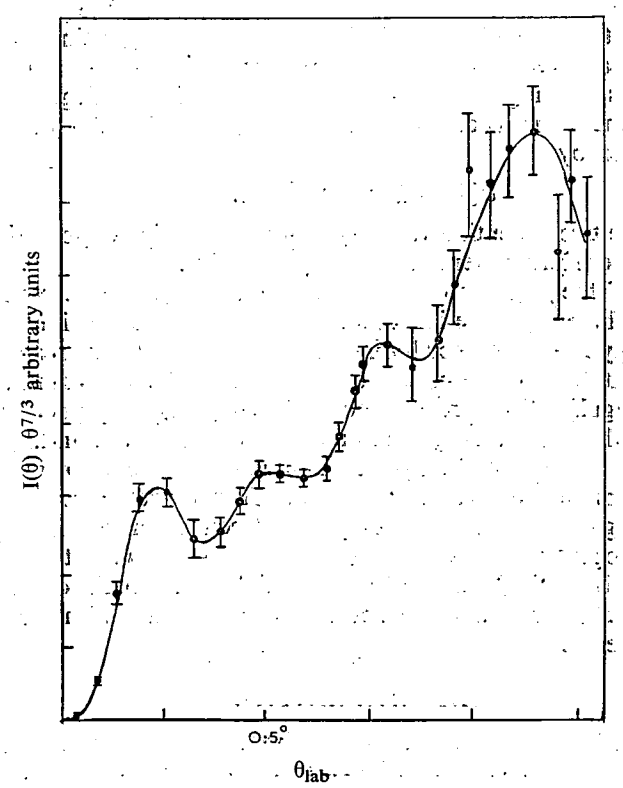

FIG. 1.—Retraced output from computer after analysis. The example is for a relative velocity 1420·0 m sec^{-1}. The scattering angle is in degrees (laboratory system). Error bars are two sample standard deviations in length.

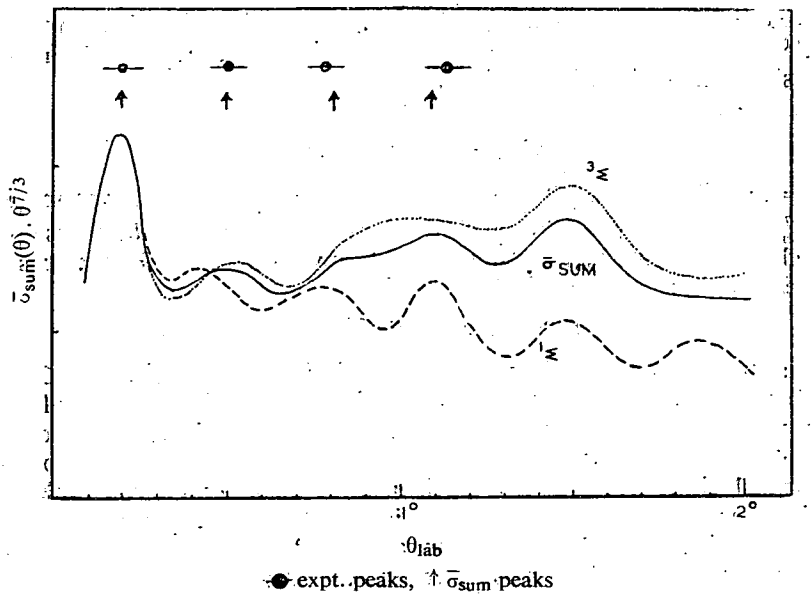

FIG. 2.—Forward calculation for the spectroscopic singlet potential, an assumed triplet potential and their weighted sum; relative velocity = 1420 m sec^{-1}.

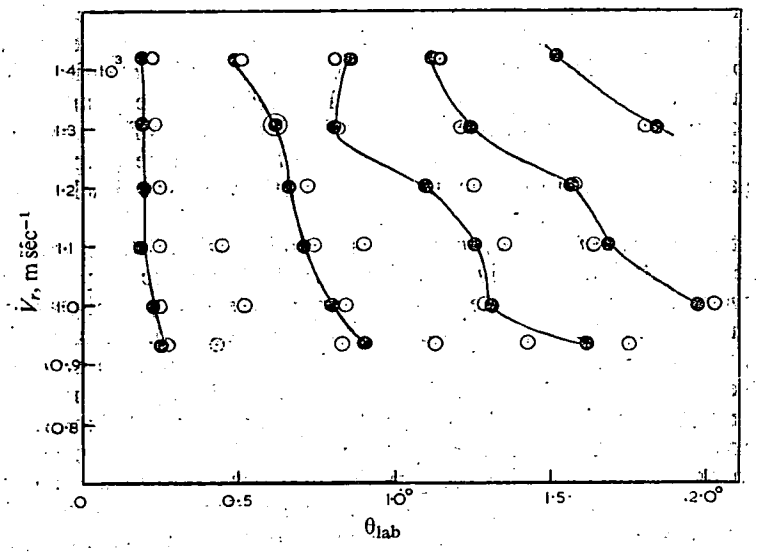

FIG. 3.—Comparison of observed peak position with those calculated from an apparatus averaged sum of singlet and triplet potentials. The triplet potential was a L.J. 8 : 6 with $\varepsilon = 2{\cdot}0 \times 10^{-14}$ ergs and $r_m = 5{\cdot}6$ Å. ○, expt.; ●, theory.

INTERPRETATION

The innermost peaks in fig. 3 arise from the finite total cross-section predicted by quantum mechanics.[2] At very small angles the classical $\theta_{cm}^{-7/3}$ dependence (for an inverse six power potential) changes to an exponential form that leads to a finite

value of the forward scattered intensity $I(0)$. The location of this peak is dependent to a good approximation only on the long-range attractive force, i.e., on the van der Waals $C^{(6)}$ parameter in the present case, which can be expected to be identical for both the singlet and triplet interactions.

Using the relation [3]

$$I(\theta_{cm}) = A \exp(-\alpha\theta_{cm}^2),$$

where $\alpha = 2{\cdot}08\, k^2 Q/8\pi$ and Q is the total cross section, we find the first maximum in $I(\theta_{cm}) \cdot \theta_{cm}^{7/3}$ to be at $\theta_m = \sqrt{7/(6\alpha)}$ (CM coordinates), (for the Na-K system at very small angles $\theta_{cm} = 1{\cdot}59\ \theta_{lab}$). Using the SLL approximation [2] for the cross section yields the relation:

$$C^{(6)} = 2{\cdot}668 \times 10^{-30}/k^4\theta_m^5\mu \qquad (3)$$

where μ is the reduced mass in a.m.u. Thus θ_m is very insensitive to $C^{(6)}$ so that even with good precision ($\sim 0{\cdot}05°$) in measuring θ_m, $C^{(6)}$ is not well defined. For example, with $k = 3 \times 10^9\ \text{cm}^{-1}$ an uncertainty of $\pm 0{\cdot}05°$ in θ_m leads to a tenfold change in $C^{(6)}$. The first peaks in the experimental plots (fig. 1 and 3) are consequently consistent with either Dalgarno and Davison's,[4] or Buck and Pauly's [5] value.

The information available on the K-Na interaction can be summarized as follows. (i) The calculation of $C^{(6)}$ by Dalgarno and Davison who give the value $2450 \times 10^{-60}\ \text{erg cm}^6$ with an error unlikely to exceed 10 %. (ii) A total cross-section measurement by Buck and Pauly [5] interpreted via the Massey–Mohr approximation to yield a value for $C^{(6)}$ of $1081 \times 10^{-60}\ \text{erg cm}^6$. (iii) The well depth [6] for singlet K-Na, $\varepsilon = 9{\cdot}9 \times 10^{-13}$ ergs. (iv) Spectroscopic (RKRV) data for the singlet states of Na_2 and K_2.[7] Using the potentials calculated from the spectroscopic data, it is possible with the help of combination rules to construct a singlet potential for KNa using an empirical potential function of the Morse type. This potential will be valid at intermediate separations and has a well depth of $9{\cdot}9 \times 10^{-13}$ ergs and $r_m = 3{\cdot}5$ Å. It was grafted on to a long range R^{-6} term and in view of the difference between the observed and calculated $C^{(6)}$ values, two such potentials were prepared, the first having Dalgarno and Davison's value and the other having Buck and Pauly's value.

A calculation of the apparatus averaged scattered intensity, ${}^1\sigma(\theta_{lab})$ was then made for the singlet potential at a relative velocity of $1{\cdot}42 \times 10^3\ \text{m sec}^{-1}$ by summation of the partial wave expansion for the scattered amplitude using semi-classical phase shifts. The results for the two values of $C^{(6)}$ were almost indistinguishable, except for $\theta_{lab} < 1°$, where the potential with Dalgarno's $C^{(6)}$ gave peak positions close to those observed experimentally. The forward calculation was then repeated for a number of triplet potentials of the Lennard-Jones 8 : 6 type all having Dalgarno and Davidson's value of $C^{(6)}$. The results for one pair of singlet and triplet potentials are shown in fig. 2, together with the experimental peak positions. The observed oscillations in $\sigma(\theta_{lab})$ at this energy correspond fairly closely to those arising from the singlet state and we are thus led to the conclusion that at this energy either the triplet cross section is almost structureless or it oscillates with nearly the same frequency and roughly in phase with the singlet. In the triplet case illustrated in fig. 2, ${}^3\sigma(\theta_{lab})$ is relatively structureless. No value of ε for the triplet potential was found that would reproduce the observed peak locations when used with potentials based on the Buck and Pauly value of $C^{(6)}$. The calculated Dalgarno and Davison value is thus preferred.

The observed peak positions over the whole energy range were then compared with calculations of $\sigma(\theta_{lab})$ for the singlet potential (with Dalgarno's $C^{(6)}$) and a

range of constrained triplet potentials with ε ranging from 0·01 to 0·4 picoergs and r_m constrained by the relationship

$$4\varepsilon r_m^6 = 2450 \times 10^{-60} \text{ erg cm}^{-6}. \quad (4)$$

The choice $\varepsilon = 2 \times 10^{-14}$ ergs, $r_m = 5{\cdot}6$ Å emerged as the best pair of values for the triplet parameters over a grid of 0·01 picoergs near the optimum value and 0·1 picoergs elsewhere. The full forward calculation for a single set of reduced potential parameters required 20 min on a KDF 9 computer, consequently fitting was limited to reproducing the observed peak locations. Calculated and observed peak positions for this " best fit " potential are given in fig. 3. The additional peaks observed at low energies may result from resonance phenomena, which would not appear in calculations based upon JWKB phase shifts; alternatively, they may be due to imperfect fitting by the potential chosen.

DISCUSSION

A pronounced oscillatory behaviour in ${}^1\sigma(\theta)$ has been observed and we seek its origin in the intermolecular potential. The usual cause of oscillation in the differential cross-section is interference between two or more branches of the classical deflection function. We therefore first look for the regions of stationary phase in the partial wave expansion, i.e., for values of the orbital angular momentum quantum number l at which the derivative of the phase shift, $\partial\eta_l/\partial l$, is $\sim\frac{1}{2}\,\theta_{cm}$. Choosing $0 \lesssim \theta_{cm} \lesssim 3°$, inspection of fig. 4 shows that four regions of l will contribute to ${}^1\sigma(\theta)$ in this angular range. Of these, the region around l_1 will dominate because of the slowly varying phase shift in the outermost branch and the region round l_4 (leading to an angle of deflection $\theta_{cm} \simeq 360 \pm 2°$) can be neglected because of the smallness of the region of stationary phase. The regions l_2 and l_3 either side of η_{max} will interfere to produce glory oscillations in the cross-section and will also interfere with the outermost branch around l_1 to produce undulations of higher frequency. The

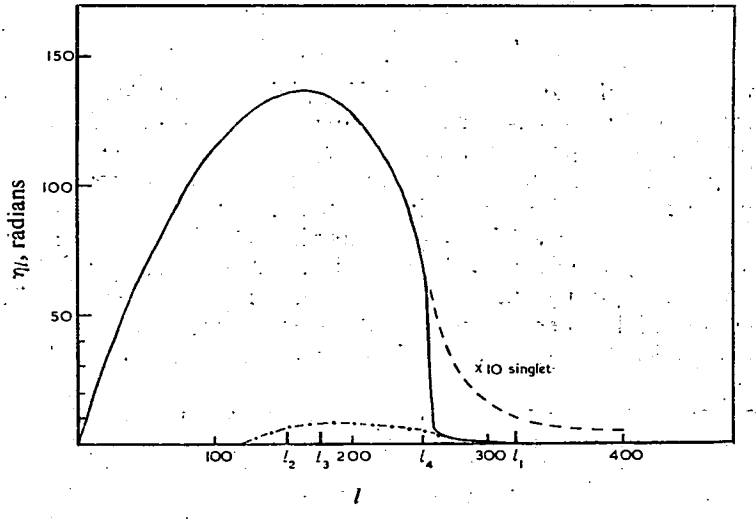

FIG. 4.—Phase shift against l for singlet and triplet potentials at 1420 m sec^{-1}. - - -, singlet; — · — triplet.

angular frequency of these interference effects can be estimated from the phase-shift curve using the semi-classical approximation of Ford and Wheeler.[8] At a relative velocity of 1420 msec^{-1} we obtain for the singlet potential:

$$\text{interference of } l_2 \text{ and } l_3 \; \Delta\theta_{23}(\text{cm}) = \pi/l_3, \text{ or } 0{\cdot}71°(\text{lab}), \tag{5}$$

interference of l_1 and l_2 (glory) $\Delta\theta_{13}(\text{cm}) = 2\pi/|l_1 - l_3|$ or 1·42° (lab). and for the triplet potential (assuming the regions of stationary phase to be separate, see below) $\Delta\theta_{23}(\text{lab}) = 0{\cdot}63°$ and $\Delta\theta_{13}(\text{lab}) = 1{\cdot}63$. Thus none of these effects although undoubtedly present, can be responsible for the observed periodicity of roughly 0·38° (lab) in both the forward calculation and in the experimental results. This structure is found to arise solely from the outermost branch l_1 and in fact appears in calculated differential cross sections for a range of potentials having the same value of $C^{(6)}$. In the integral approximation for the scattered amplitude[8] $f(\theta)$,

$$f(\theta) = \tfrac{1}{2}ik\int_0^\infty (2l+1)(\exp[2i\eta(l)] - 1)P_l(\cos\theta)\,\mathrm{d}l, \tag{6}$$

we can relate the undulations in the narrow angle scattering to the position of the outermost oscillation in $\exp[2i\eta(l)]$, centred at l^*, if a major contribution to the integral comes from values of l around l^*. For this to occur the phase shift function, $\eta(l)$, must rise rapidly near l^* so that $\exp(2i\eta(l))$ begins to oscillate more rapidly than the Legendre polynomial $P_l(\cos\theta)$. Making the random phase approximation there is then only the contribution $\int_0^{l^*}(2l+1)P_l(\cos\theta)\mathrm{d}l$ for $l<l^*$ (neglecting other branches of the deflection function) and this is to be combined with the contribution $\int_{l^*}^\infty (2l+1)2i\eta(l)P_l\mathrm{d}l$ to yield the scattered amplitude $f(\theta)$. Both contributions have a periodicity $2\pi/l^*$ and so $\sigma(\theta)(=|f(\theta)|^2)$ has a major component that oscillates with a frequency π/l^*, where l^* marks the onset of effectively random phase at lower values of l.

A similar situation has been discussed by Pauly and Toennies[9] for $\sin\theta < 1/l^*$, when $P_l(\cos\theta)$ can be replaced by $J_0(l\theta)$ but in the present work the periodicity of $P_l(\cos\theta)$ is well developed for $l \gtrsim l^*$. A rough value of l^* may be defined by $\eta_{l^*} = 1$ and so from the Jeffreys-Born approximation for the phase shift

$$l^* = [C^{(6)}\tfrac{3}{32}\pi k^6/E]^{1/5}. \tag{7}$$

At a relative velocity of 1420 m sec^{-1} $l^* = 320$, giving a predicted peak spacing for the singlet cross section of 0·36 (lab) compared with an observed value of 0·38°. Actual summation of the partial wave series for $f(\theta)$ shows that the above treatment can only be approximate because the effective value of l^* for the real and imaginary parts of the scattered amplitude are slightly different and so their contributions to $\sigma(\theta)$ are somewhat out of phase leading to irregular behaviour in the observed cross section. Eqn. (7) has been derived by assuming that the phase shift $\eta(l^*)$ is determined only by the long-range part of the potential. Direct calculation of the phase shifts for the potential chosen for the present system show that at the highest energy the singlet and triplet phase shifts at $l = l^*$ differ by ~20 % and at the lowest energy by 6 %.

The triplet phase shift function for a relative velocity of 1420 msec^{-1} and the best fit potential is also plotted in fig. 4. At the highest experimental energy the maximum positive phase shift, $\eta_{\max}$, is 6 radians and there should be a fairly well developed rainbow structure at ~15° (lab). As for small single undulations, the second derivative of the phase shift is smaller than in the singlet case and the forward glory scattering consequently interfere more importantly with the outer branch oscillations at l^*

leading to a confused structure. At still higher energies, when $\eta_{max} < \pi/2$, the forward glory region cannot be separated from the outer branch and a new oscillatory pattern with $\Delta\theta = \pi/l_0$ appears, where l_0 corresponds to the inner zero of the phase shift function which effectively marks the onset of random phase at lower values of l.

We thus conclude that the observed undulations in $\sigma(\theta)$ are primarily long range in origin. The angular spacing of these high-frequency oscillations is insensitive to $C^{(6)}$ as can be seen from eqn. (7). In the present system the small angle undulations are readily visible, partly because the effect is not a sensitive function of energy and so is not destroyed by energy averaging, and partly because of the 3 : 1 weighting of the triplet contribution which preserves some features that would otherwise be lost upon combining the singlet and triplet scattering patterns.

As a guide to future work, the phase shift plot for the singlet potential would predict that the oscillation in ${}^1\sigma(\theta)$ die out for $\theta \gtrsim 6°$(lab) when a region of true stationary phase develops. Furthermore, the triplet cross section should show the clear emergence of its high energy behaviour ($\Delta\theta = \pi/l_0$) at energies $\gtrsim 5 \times 10^{-13}$ ergs when the undulatory behaviour is determined by the repulsive branch of the potential. Much additional information could be obtained from measurements in the triplet rainbow though this will require improvement in the presently available signal-to-noise ratio. When these data become available a more complete potential fitting operation will become worth while.

Helbing and Rothe (private communication) have pointed out that the above values of ε and r_m lead to a value of η_{max} that is approximately one half the maximum phase shift for the Li-K system as deduced from total cross-section measurements [10] at the same energy. From a theoretical point of view the divergence between the two results is even more marked if the factor of $(2\mu)^{\frac{1}{2}}$ in the semi-classical expression for the phase shift is taken into account. If both results and their interpretation are correct, then the well depth in the Li-K case is ~ 3 times deeper than for Na-K. Alternatively, since the two types of measurement are sensitive to different parts of the potential, there may be a genuine discrepancy in any parameters deduced from them due to the inadequancy of the assumed potential.

One of the authors (L. T. C.) thanks the Science Research Council for a research studentship during the course of this work.

[1] R. B. Bernstein, *Science*, 1964, **144**, 141.
[2] R. B. Bernstein, *Adv. Chem. Phys.*, 1966, **10**, 75.
[3] H. Pauly, *Z. Phys.*, 1959, **157**, 54.
[4] A. Dalgarno and W. D. Davison, *Mol. Phys.*, 1967, **13**, 479.
[5] U. Buck and H. Pauly, *Z. Phys.*, 1965, **185**, 155.
[6] T. L. Cottrell, *Strengths of Chemical Bonds* (Butterworths, 1958).
[7] R. H. Davies, E. A. Mason and R. J. Munn, *Phys. Fluids*, 1965, **8**, 44.
[8] K. W. Ford and J. A. Wheeler, *Ann. Phys.*, 1959, **7**, 259.
[9] H. Pauly and J. P. Toennies, *Adv. Atomic Mol. Phys.*, 1965, **1**, 195.
[10] R. K. B. Helbing and E. W. Rothe, *J. Chem. Phys.*, 1968, **49**, 4750.

PRINTED IN GREAT BRITAIN AT
THE UNIVERSITY PRESS
ABERDEEN

Journal of Scientific Instruments (Journal of Physics E) 1969 Series 2 Volume 2

A crossed molecular beam apparatus and associated computer programs for the measurement of differential scattering cross sections

L T Cowley,† M A D Fluendy, D S Horne† and K P Lawley
Department of Chemistry, University of Edinburgh

MS *received 3 September 1969*

Abstract A crossed molecular beam apparatus for the measurement of differential scattering cross sections has been constructed. The effective angular resolution is better than 0·05° and permits the observation in the laboratory of quantum undulations with a period of the order of 0·2°. For sodium or potassium in a clean system the signal standard deviation is 3 counts per second permitting neutral fluxes of 1 atom per second into the detector to be estimated in a reasonable integrating time. The associated data capture and deconvolution procedures are also described.

1 Introduction

Molecular beam measurements of differential scattering cross sections can yield information on the intermolecular potentials operative between the collision partners, and in the case of reactive systems on the detailed dynamics of the chemical reaction.

In this paper an apparatus to measure these cross sections with high resolution is described, together with the associated computer programs for data capture and analysis. The scientific results are reported elsewhere (Cowley *et al.* 1969, Horne 1969 Thesis, University of Edinburgh). Observation of the gross angular features in scattering (e.g. rainbow and supernumaries) yield important information on the intermolecular potential. Complete information, however, can only be obtained if the high frequency quantum interference structure can also be resolved. In general the highest angular frequency that can be present is:

$$\Delta\theta_{CM} \sim \pi\hbar/\mu V a \qquad (1)$$

where μ is the reduced mass of the collision partners, V their relative velocity and a is the effective range of the potential. For typical atomic and molecular systems $\Delta\theta \sim 0{\cdot}2°$ in the laboratory system.

The differential cross sections and hence scattered fluxes may vary from a maximum of 10^6 Å^2 at interference peaks near 0° to less than 1 Å^2 at wide angles. The primary design criteria for the apparatus are thus: (i) an angular resolution of 0·05°; (ii) a dynamic range of greater than 10^6; (iii) velocity resolution adequate to prevent energy averaging washing out the angular structure.

2 Apparatus

The apparatus is shown in overall schematic in figure 1. It is divided into two differentially pumped chambers. The scattering chamber A contains the two beam sources B and C, the beam velocity selector D, beam flag E and cross beam modulator F. The two thermal beam sources have multichannel orifices; the main beam source is of the double chamber type and is mounted kinematically to the rear of a heated collimating slit. A horizontally rotating disk velocity selector (Cowley 1969 to be published) is mounted directly in front of these slits. Its rotation velocity is monitored by a lamp and fast response photodiode, the output from which is counted into a crystal controlled frequency meter. The main beam may finally be interrupted by an electromechanical beam flag. The cross beam is chopped at 33 Hz by a rotating disk driven from a synchronous hysteresis motor. (This disk also interrupts a light beam to provide a timing signal via a photodiode.)

Both sources and selectors are mounted on a turntable which can be positioned in increments of 0·05° from outside the vacuum system by a d.c. stepping motor K. The turntable position is monitored by an optical shaft encoder G. Gas and water cooling feeds are led to the oven mounts and velocity selector motor via a rotatable vacuum seal within the turntable bearing. The entire turntable–oven assembly can be readily lifted from the vacuum chamber for adjustment.

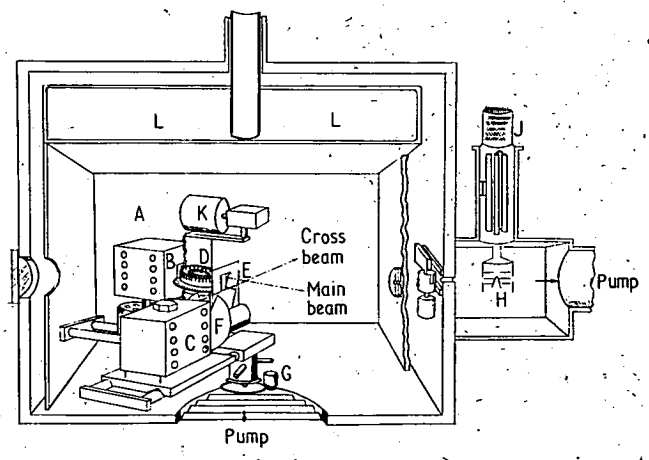

Figure 1 Apparatus layout

This chamber is pumped by a 12 in oil diffusion pump, while a liquid nitrogen cooled shroud L fixed to a reservoir in the removable lid extends to cover all but the floor of the chamber. The shroud carries additional baffling where the main and cross beams impinge to trap as much of the beam material as possible. During operation the pressure is typically 0·2 μtorr.

† Now at Lash Miller Chemical Laboratories, University of Toronto, Canada

The second chamber contains the detector. It communicates with the scattering chamber via slits 0·050 cm by 0·3 cm high and can be entirely isolated by a gate valve. The detector of the Langmuir–Taylor type is a heated 0·050 cm wide rhenium ribbon H located inside an ion lens system. The lens focuses the ions emitted from the surface of the hot ribbon into a quadrupole mass filter I. After mass selection the ions are accelerated at 5 kv into a seven-stage multiplier J (EMI 9643/2) where, after amplification and pulse height discrimination, the individual ion arrivals are recorded on fast scalers. The data are finally collected on eight-hole paper tape for computer analysis.

The detector and chamber are of all-bakeable construction and the chamber is pumped by an 80 l s^{-1} ion pump together with a titanium sublimation pump working on to a liquid-nitrogen cooled substrate. The pumping is arranged so that material entering the detector chamber and not striking the ribbon impinges directly on a cryobaffle. As a further precaution against contamination of the detector, a rotating cylinder attenuator M is moved across the detector chamber entrance when operating close to the main beam position. The pressure in this chamber during operation is typically less than 1 ntorr.

The most important apparatus dimensions and other characteristics are summarized in table 1.

Table 1 Dimensions

Main beam source to scattering centre	14·25 cm
Cross beam source to scattering centre	1·5 cm
Scattering centre to detector ribbon	29 cm
Main beam collimating slit to scattering centre	3·2 cm
Cross beam collimating slit to scattering centre	0·2 cm
Width of main beam source	0·02 cm
Width of cross beam source	0·075 cm
Width of main beam collimating slit	0·023 cm
Width of cross beam collimating slit	0·075 cm
Width of detector filament	0·075 cm
Height of beam at scattering centre	0·5 cm
Transmission from ribbon through quadrupole	15%
Counting efficiency (multiplier voltage 5 kv)	50%

3 Detection system

Since the scattered flux for typical atomic and molecular processes are small compared with the available beam intensities, the signal-to-noise ratio determines the possible resolution in angle and velocity, and indeed the feasibility of any experiment. For elastic processes we measure a quantity $\sigma_v(\theta)$, although ultimately, perhaps, we may wish to determine certain parameters in a model (e.g. in an intermolecular potential). Formally, therefore, we are measuring intensities with respect to variation in θ and V. In practice these observations must extend over a period of time, so that the time dependence of the signals must be considered. The extraction of the desired cross sections must therefore involve filtering in both time and angle sequences. We consider the time sequence first.

Measurement of a relative differential cross section requires at least four separate observations with the cross beam on and off at each of two angular locations. Thus at angle θ:
measurement of scattered flux + background from time 0 to τ_n

$$= \int_0^{\tau_n} \{g(t)\,\sigma(\theta) + n(t)\}\,\mathrm{d}t \tag{2a}$$

measurement of background from time τ_n to $2\tau_n$

$$= \int_0^{\tau_n} n(t+\tau_n)\,\mathrm{d}t. \tag{2b}$$

At a normalizing angle θ_m:
scattered flux + background from τ_θ to $\tau_\theta+\tau_n$

$$= \int_0^{\tau_n} \{g(t+\tau_\theta)\,\sigma(\theta_m) + n(t+\tau_\theta)\}\,\mathrm{d}t \tag{2c}$$

background from $\tau_\theta+\tau_n$ to $\tau_\theta+2\tau_n$

$$= \int_0^{\tau_n} n(t+\tau_\theta+\tau_n)\,\mathrm{d}t. \tag{2d}$$

$g(t)$ is the time dependence of the product of main and cross beam intensities and $n(t)$ is an additive noise in counts per second; τ_n is the duration of the sequential cross beam on and off conditions and τ_θ is the time from the start of observations at θ and their start at θ_m.

The relative differential cross section is then estimated as:

$$\widehat{(I_\theta - I_{\theta m})} = \int_0^{\tau_n} \{n(t) + g(t)\,\sigma(\theta) - n(t+\tau_n) - n(t+\tau_\theta) - g(t+\tau_\theta)\,\sigma(\theta_m) - n(t+\tau_\theta+\tau_n)\}\,\mathrm{d}t \quad \text{counts per second.} \tag{3}$$

The precision with which this estimation can be made will depend upon the variance of $\widehat{(I_\theta - I_{\theta m})}$, i.e.

$$\begin{aligned}\mathrm{Var}(I_\theta - I_{\theta_m}) = 4\{&\mathrm{Var}(n) - \phi_n(\tau_n) + \bar{n}^2\} \\ &+ 2\{\phi_n(\tau_n+\tau_\theta) + \phi_n(\tau_\theta-\tau_n) - 2\phi_n(\tau_\theta)\} \\ &+ 2(1+C)\{\phi_{ng}(0) - \phi_{ng}(\tau_n)\} \\ &+ 2\{\phi_{ng}(\tau_\theta+\tau_n) - \phi_{ng}(\tau_\theta)\} \\ &+ 2C\{\phi_{ng}(\tau_\theta-\tau_n) - \phi_{ng}(\tau_\theta)\} \\ &+ \{(1+C^2)\,\mathrm{Var}(g) - 2C(\phi_g(\tau_\theta) - \bar{g}^2)\}\end{aligned} \tag{4}$$

where

$$\mathrm{Var}(x) = \overline{x^2} - \bar{x}^2,\quad \phi_n(\tau) = \int n(t)\,n(t+\tau)\,\mathrm{d}t,$$

$$\phi_{ng} = \int n(t)\,g(t+\tau)\,\mathrm{d}t \text{ and } C = \sigma(\theta)/\sigma(\theta_m).$$

The objective in any detection system is the minimization of the variance, e.g. equation (4). In this work the optimal scheme in the Wiener (1942) sense was not possible owing to the limited sampling rate of a paper tape punch. Nevertheless the variance can be appreciably reduced by using available information about the statistics of the signal and noise counting rates. The scattered signal has a steady d.c. expectation value, but its fluctuations will not be truly Gaussian in distribution since excess low frequency components arise from slow drifts in oven temperatures and in lens focusing potentials. Typically these are 2–3% per hour.

The statistics of the noise are more complicated since there are three principal sources of noise: (i) that from main beam material scattered from background gas (and thus strongly correlated with main beam intensity and background pressure); (ii) that from residual main beam material in the detector chamber; (iii) that due to alkali metal impurities in the hot ribbon. The statistics for all these contributions are different. The first two have excess low frequency components arising from pressure fluctuations in the experimental and detector chambers, while the ribbon noise occurs predominantly as intense bursts of ions emitted in 1 ms or less (depending on ribbon temperature).

The variance (equation (4)) can be minimized by making τ_n sufficiently small that $\phi_n(\tau_n)$ and $\phi_{ng}(\tau_n)$ approach $\overline{n^2}$ and $\overline{ng}$ respectively and all but the final term in (4) are minimized. The contribution of the final term can be reduced by cross correlating all the measurements involving $g(t)$ with a function $f(t)=c/g(t)$. In practice τ_n cannot be made small enough to reject burst noise which has a very short correlation time; however a rejection technique in the computer analysis provides a partial removal of noise from this source. The net effect of all these measures is to whiten the time dependent noise.

Similar considerations apply to the angular dependence of the scattered intensity. The observed flux at θ is

$$I_{\text{obs}}(\theta)=\int f(\theta')\,\sigma(\theta-\theta')\,\mathrm{d}\theta'+n(\theta) \qquad (5)$$

where $f(\theta')$ is the apparatus filter function, i.e. approximately the observed main beam profile and $n(\theta)$ is an additive noise. Once again non-Gaussian noise can be removed by a suitable filtering process. In this case the filtering can be combined with deconvolution to obtain $\sigma(\theta)$, i.e. the delta function response (Robinson 1967). The procedure for filtering and deconvolution is similar to that used by Morrison (1962) and is described in §4.

4 Electronics and experimental procedure

The data capture and processing are carried out by a mixture of apparatus hard-ware and off-line computer calculation, using paper tape as an intermediate storage medium.

The detection schematic diagram is shown in figure 2. After amplification the signal pulses have an amplitude of the order

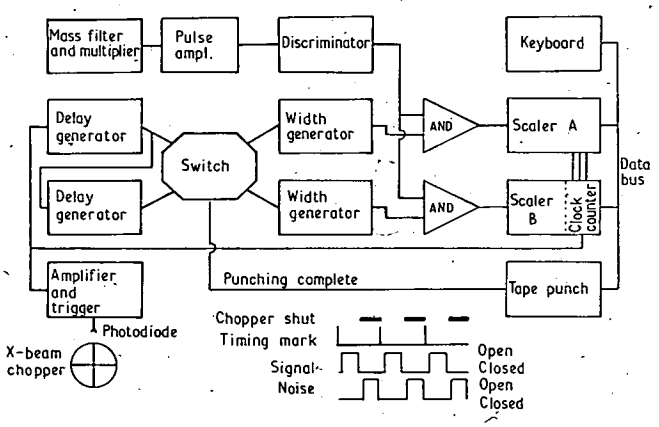

Figure 2 Detector schematic diagram

of 1 v and are 10 ns wide. The pulse discriminator threshold is set to maximize the ratio (counts per second beam on)/(counts per second main beam off)$^{1/2}$; a typical plot of threshold against $S/N^{1/2}$ is shown in figure 3. The discriminator also stretches the accepted pulses to 200 ns width as a partial means of rejecting burst noise from the ribbon. The overall pulse pair resolution of the system is then 240 ns and the maximum useful counting rate 0·5 MHz.

After discrimination the pulses are counted into two scalers gated via variable delay and width generators from the cross beam modulator. The delays are arranged so that scattered signal counts accumulate in one scaler and the background counts in the other. The respective gate open times relative to the cross beam condition are shown in figure 3. After a set number (usually 100) of these modulation cycles have been counted on an ancillary counter both gates are closed and the total in each scaler, together with other experimental data, are punched on to paper tape. After punching is complete the

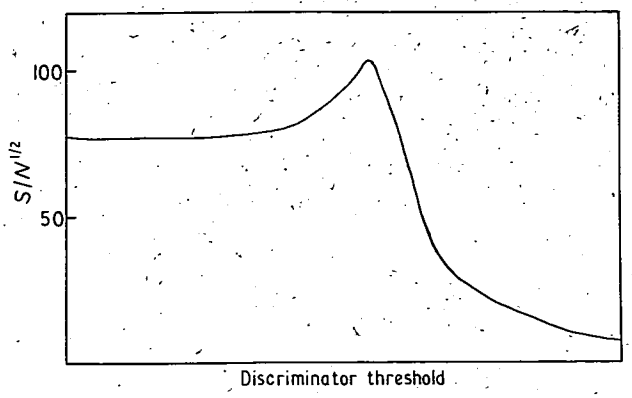

Figure 3 Signal-to-noise plotted against discriminator threshold

scalers are reset to zero and the delay chains to the scaler are interchanged. The scaler and its associated width generator, previously counting signal, now accumulate background and vice versa, this change in role being indicated by a code on the paper tape. The scattered signal can now be found by forming differences (scaler A − scaler B) and (scaler B − scaler A) alternately, thus averaging out any asymmetry in scaler response or in the width generators. When sufficient data at any angle have been accumulated the turntable is rotated, the new angular position entered on to the paper tape and the process continued. Each angular scan is initiated by setting up the velocity selector to the desired speed and punching an identification code on to the paper tape. The turntable is then rotated to one side of the main beam and a slow scan begun across it and out as far as desired. In this way the apparent main beam profile is recorded for each angular scan. This will be used later in the data analysis to deconvolute the observed scattering. At intervals of approximately 20–30 minutes the turntable is returned to a standard angle (where the scattered intensity is changing slowly) so that sequential observations here may be used to correct for drift in the parent beam intensities.

In a typical experiment lasting 20–40 hours some 3 miles of data on paper tape may be generated.

5 Computer programs

The large amounts of data that can be stored on paper tape together with the ease with which it can be interpreted by a computer bring important advantages. Firstly, more data can be collected and used to improve both the resolution and sensitivity of the experiment; secondly, the computer provides a more flexible processor than fixed program devices permitting filtering operations to approach the optimum. Finally the bulk storage of raw data allows the analysis programs to be re-run so that the effect of different filtering procedures on the same data may be compared.

In this work the data are analysed in two stages, the intermediate results being recorded on magnetic tape. This arrangement allows the intermediate data to be manually checked as to format and permits the second stage of processing which contains the more elaborate routines to be readily rerun without reading the bulky paper tape.

The flow diagram for the first program is shown in figure 4. This program carries out data validation, correction and organization. The binary tape is translated into decimal and the marker flags indicating beam condition used to separate the continuous data stream into individual 'sentences', each sentence containing the output from both scalers, etc., for one observation period. The individual 'words' in each

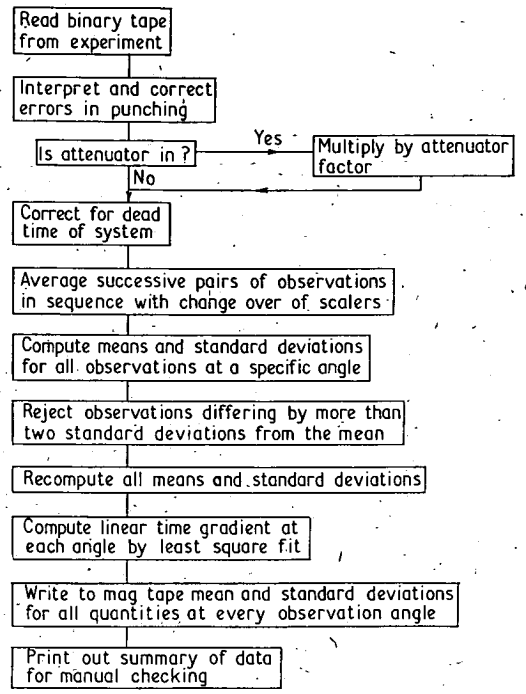

Figure 4 Preliminary data reduction and time averaging program

sentence are then checked for consistency, and if any discrepancy is discovered, e.g. flag out of permissible range, unallowed character, etc., the entire sentence is deleted. At this stage any operator codes introduced via the manual keyboard are recognized and appropriate action taken. Time filtering of the data also takes place in this program with a consequent great reduction in volume of data. This is essentially simple averaging, though a burst noise rejection procedure which removes data differing by more than two standard deviations from the mean is included. At this rejection level approximately 5–10% of the observations are rejected – approximately that expected from the observed mean interval between bursts of about 20 s. This filter is also useful in removing any punch corruptions which have escaped detection in the data validation phase. The least squares time gradient of the scattered signal is also computed at each angle for use in a later cross-correlation routine. If a faster recording medium or a direct on-line computer were available the sampling rate could be made comparable to the correlation time of the noise and greater sensitivity obtained. The real time processing of data would also be advantageous in allowing the experiment to be monitored during the actual data collection phase.

The output of this program, including the observation time, mean scattered signal, time gradient of signal and their standard deviations, is written to magnetic tape. At this stage in processing a potassium or sodium scattered signal may typically have a standard deviation of the order of 20 counts per second for an actual background count rate of 500 counts per second. For a freshly baked detector chamber and flashed filament the background rate may fall to about 15 counts per second (5 counts per second for rubidium or caesium). The standard deviation of the signal is then approximately 3 counts per second or less. Thus with observation times of the order of 1 minute, precisions of 4 or 0·4 counts per second respectively can be achieved with these background rates.

The second analysis program is shown in figure 5. This program initially carries out a time normalization procedure for all observations greater than 1°.

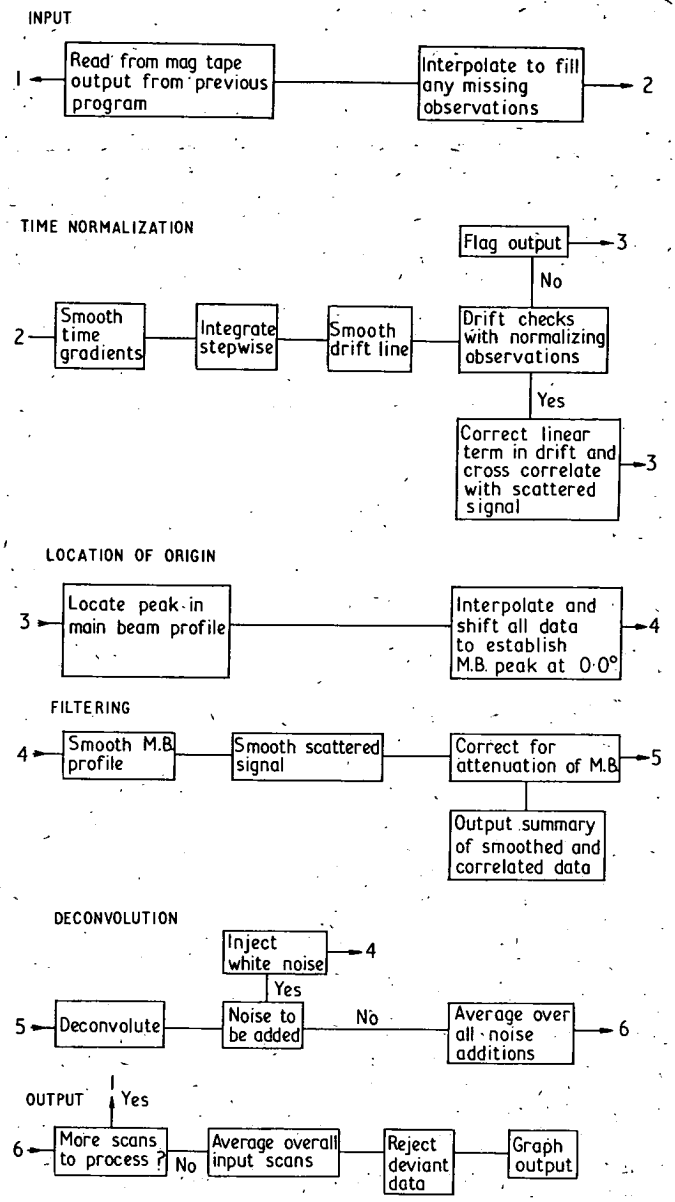

Figure 5 Angle filtering and deconvolution program

At smaller angles the signal changes so rapidly with angle that small changes in turntable position make the process unstable. In general this correction is only necessary for very wide angle scans taking more than an hour to complete. When required, both the time gradients and the repeated observations at normalizing angles are used. The gradients are first smoothed and then integrated stepwise, the resultant drift line being then further smoothed by fitting to a cubic polynomial. The predicted drift is compared with the observed change between repeated angles, and the linear term in the drift expression corrected to obtain concordance. If the required adjustment is too large the output is flagged for manual investigation. The drift line is then cross-correlated with the scattered signal.

The time-normalized main beam profile and scattered-signal data are then filtered using Morrison's iterative method in which a smoothing function f is applied, i.e.

$$I_{1(\theta)} = I_{(\theta)\text{obs}} * f$$
$$I_{i(\theta)} = I_{i-1(\theta)} + \{I_{(\theta)\text{obs}} - I_{i-1(\theta)}\} * f \qquad (6)$$

The process is iterated until all noise incompatible with the transform f is removed.

This technique is first applied to the main beam profile using a fixed trapezoidal filter function 0·4° full width. The iterated values are constrained to be within four standard deviations of the observed intensity. The resulting smoothed profile is then used in turn as the convolution function to filter the scattered signal. At this stage the cross beam attenuation of the main beam which results in apparently negative scattering at very small angles is removed; the scattering in and out of the detector cone at each angle being computed iteratively until convergence is obtained. The corrected and smoothed scattered signal is finally deconvoluted using the main beam profile and Van Citterts iterative method, i.e.

$$I_{1(\theta)} = I_{(\theta)\text{smoothed}} + (I_{(\theta)\text{smoothed}} - I_{(\theta)\text{smoothed}} * f)$$
$$I_{i(\theta)} = I_{i-1(\theta)} + (I_{(\theta)\text{smoothed}} - I_{i-1(\theta)} * f). \quad (7)$$

In both filtering and deconvolution processes any un-physical negative values which arise during the iteration are suppressed and replaced by zeros.

In figure 6 the results of applying this procedure to data from an angular scan are shown. The mean of several such statistically independent scans in the form output by the computer is shown in figure 7. The stability of both the filtering and deconvolution procedures can be checked for any data set by adding white noise with a standard deviation equal to that observed. In almost all cases little or no significant change in the output was produced. The loss of resolution apparent on averaging arises largely from errors in the angular measurement, the error bars being much larger in regions where the scattered intensity is changing rapidly with angle.

Several improvements to the apparatus described are already in hand, notably improvements in the ion injection efficiency into quadrupole and in more rapid data collection which will benefit the signal-to-noise ratio. In the experimental chamber differential pumping to permit the use of high flux nozzle beams is planned.

Finally the use of electron bombardment or field ionization devices in place of the l.t. hot wire will enable species other than alkalis to be detected.

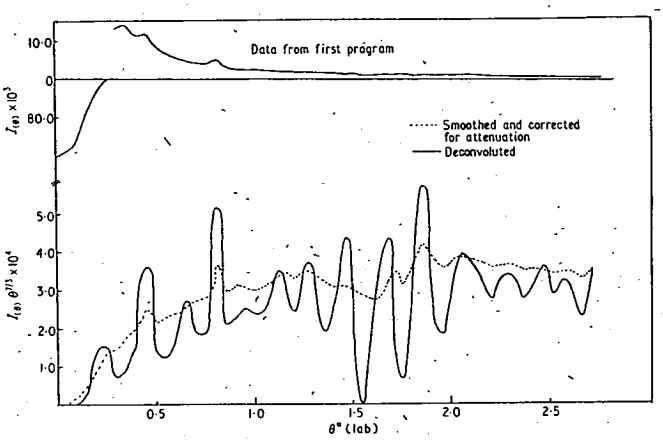

Figure 6 Angular scan for potassium scattering from atomic iodine. The upper curve is the data output from the first stage program; the lower curves show the same data after filtering and after deconvolution. The error bars calculated from the signal statistics are too small to show

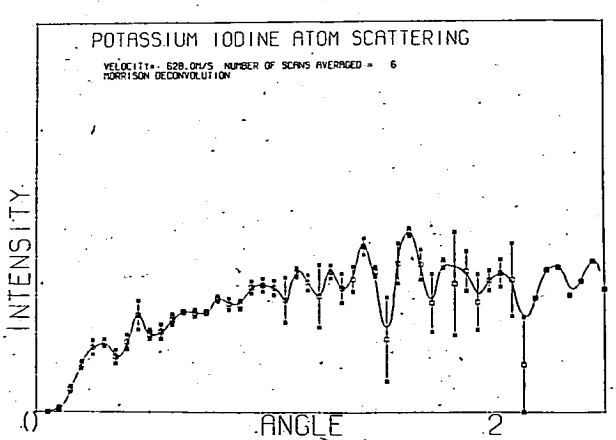

Figure 7 Computer output for the same system showing the mean of six independent experiments. The error bars are now calculated from the averaging of the scans and not from the signal statistics

References

Cowley L T Fluendy M A D and Lawley K P 1969 *Trans. Farad. Soc.* **65** 2027

Morrison J D 1962 *J. Chem. Phys.* **39** 200

Robinson E A 1967 *Statistical Communication and Detection* (London: Griffin)

Wiener N 1942 *The Interpolation, Extrapolation and Smoothing of Stationary Time Series* (Cambridge, Mass: MIT)

temperature measurements made use of the argon first ion lines of multiplet number six, of which 4806 Ar^{II} is a member, and the doubly ionized argon lines 3311.25 Ar^{III}, 3301.88 Ar^{III}, and 3285.88 Ar^{III}. Electron concentration measurements were made using the line profile of $H\beta$.[6] These data gave pressure changes consistent with the pressure transducer results.

ACKNOWLEDGMENTS

The authors express their appreciation to E. Soehngen and P. Schreiber of the Aerospace Research Laboratories for their interest and support which did much to further the progress of this work.

* Work supported by the Aerospace Research Laboratories, Office of Aerospace Research of the U. S. Air Force (Contract F33615-68-C-1081).

[1] J. C. Morris, R. U. Krey, and R. L. Garrison, Phys. Rev. 180, 167 (1969).
[2] W. Lochte-Holtgreven, Rep. Progr. Phys. 21, 312 (1958).
[3] J. C. Morris, J. Quant. Spectrosc. Radiat. Transfer 9, 1629 (1969).
[4] J. C. Morris, R. P. Rudis, and J. M. Yos, Phys. Fluids 13, 608 (1970).
[5] J. C. Morris and R. U. Krey, Phys. Rev. Lett. 21, 1043 (1968).

THE REVIEW OF SCIENTIFIC INSTRUMENTS VOLUME 41, NUMBER 5 MAY 1970

A Radial Disk Velocity Selector for Molecular Beams

L. T. Cowley,* M. A. D. Fluendy, and K. P. Lawley
Department of Chemistry, University of Edinburgh, Edinburgh EH9 3JJ, Scotland

(Received 10 September 1969)

A molecular beam velocity selector is reported in which the beam passes diametrically across a rotating slotted disk. Alignment is checked without reference to assumptions about the source velocity distribution. The selector is compact, easily constructed, and is mounted directly on the driving motor shaft.

INTRODUCTION

A NEW type of molecular beam velocity selector is described in which the beam passes across a slotted rotating disk. The selector has some advantages over conventional designs.[1–3] It has only two parts and can be aligned relative to the beam system without any knowledge of the beam velocity distribution, since when aligned, the transmission characteristics are independent of its direction of rotation. The selector is compact (6 cm diam) and is mounted on the driving motor shaft—the need for extra high speed bearings is eliminated, and, since the motor is beneath the disk, shorter source to scattering center distances are made possible with a resulting gain in scattered flux in a crossed beam experiment. With small modifications the selector could be suspended magnetically, permitting velocity selection of high energy beams.

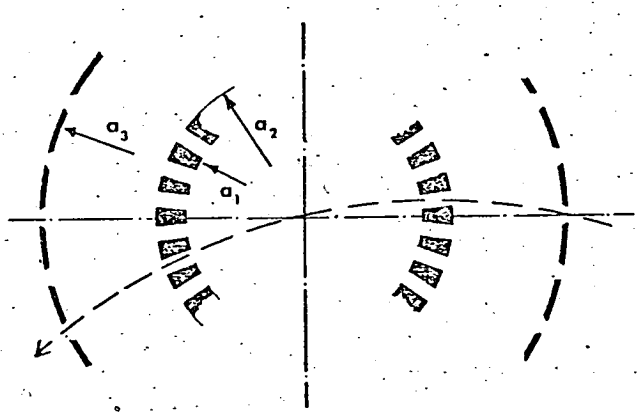

FIG. 1. Radial disk velocity selector. The dashed curve is the apparent path of a beam molecule. The mean radius of the inner disk is half that of the outer one. All slitwidths are equal.

SELECTOR DESIGN

A radial disk selector could be made by machining spiral grooves corresponding to the apparent trajectories of beam molecules crossing the disk. However, construction would be difficult for small selectors and there is the disadvantage that rejected molecules accumulate within the grooves. The actual design is shown in Fig. 1; the spiral grooves are replaced by two slotted rings. The outer ring effects the narrow band velocity selection, while the relatively thick inner ring eliminates sidebands.

The transmitted velocity is

$$u_0 = na_3\omega/2\pi,$$

where ω (rad·sec^{-1}) is the angular speed, and n is the number of slits in each ring. For a narrow beam, the resolution ($\Delta u/u_0$ where Δu is the half-intensity velocity spread) is

$$R = ln/4\pi a_3,$$

l being the width of the slits. The resolution and fractional transmission for a given velocity $T(u)$ depend on the beam width. Characteristics for wide beams were obtained by a Monte-Carlo computer simulation of the selector.[4] Similar calculations were also made to determine the minimum

TABLE I. Computed characteristics for radial velocity selector with 90 slits (all dimensions are in millimeters).

Slitwidths	Beamwidth	$T(u_0)\%$	Resolution
0.254	0.000	9.2	5.8%
	0.051	9.7	7.1
	0.102	8.0	8.0
	0.254	3.6	10.0
0.381	0.000	16.1	9.2
	0.051	15.8	10.0
	0.102	14.8	10.4
	0.254	10.2	13.6
	0.508	5.4	15.0
0.508	0.000	21.2	12.0
	0.051	21.5	12.4
	0.102	20.4	13.4
	0.254	17.1	15.4
	0.508	10.2	21.2

nickness of the inner ring that would eliminate velocity debands. Table I shows some computed transmission haracteristics for a selector having 90 slits.

The absolute intensity of molecules with a speed u_0 ansmitted is proportional to the product of $T(u_0)$ and ie beamwidth: This becomes constant beyond a certain eamwidth since molecules further off-axis are rejected. he resolution improves with decreasing beamwidth ecause the transmitted velocity is slightly different for I-axis molecules. This effect is important in that it nables the selector to be precisely aligned—only when lignment is good will the measured velocity distribution the beam be independent of the direction of rotation of ie selector.

Disks with the same relative dimensions have identical ansmission characteristics, though very small selectors e impracticable because of construction difficulties and ie beamwidth limitations that ensue.

CONSTRUCTION AND PERFORMANCE

A selector was made of aluminum alloy with 90 slits)558 cm wide and 0.6 cm high in each ring. The disk dii (see Fig. 1) were 1.35, 1.65, and 3.00 cm, respectively. ie selector was mounted directly on the shaft of a three ase synchronous hysteresis motor capable of rotating at 000 rpm (corresponding to $u_0 = 1.35 \times 10^5$ cm·sec^{-1}). A riable frequency supply powered the motor, and speed

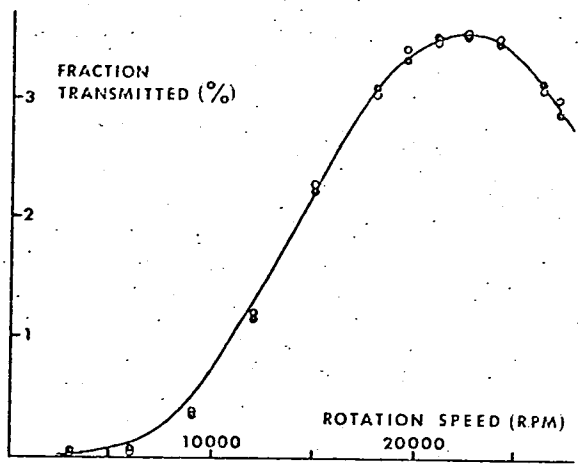

FIG. 2. Velocity analysis of an Na beam vs rotor speed. Open circles refer to the selector rotating clockwise, closed circles anticlockwise. The solid curve is a computer prediction for the selector assuming that the Na source was effusive.

was monitored by allowing the slits to modulate a light shining on a photodiode.

Performance tests were made using a sodium beam from an effusive source at 420°C (source pressure 0.16 Torr) collimated to a width of 0.015 cm. The computed resolution for this beamwidth was 15% and the transmission for u_0 was 21.5% (a higher resolution was not required for the intended measurements[5]). Results are shown in Fig. 2. There is very good agreement with the computed predictions except at low velocities where the measured intensity is smaller than expected. This effect is usually attributed to preferential scattering of low velocity atoms from the beam by the gas cloud in front of the source aperture.

Misalignment effects were also as expected. Alignment was checked by taking a velocity profile and then repeating the measurements with the disk rotating in the opposite direction. Adjustments were made until both profiles were identical. The test was sensitive, and an alignment error of 0.002 cm (which would have resulted in an error of 1% in the transmitted velocity) was readily detectable.

* Present address: Department of Chemistry, University of Toronto, Toronto 5, Canada.

[1] H. Hostettler and R. B. Bernstein, Rev. Sci. Instrum. 31, 872 (1960).
[2] J. L. Kinsey Rev. Sci. Instrum. 37, 61 (1966).
[3] A. E. Grosser, Rev. Sci. Instrum. 38, 257 (1967).
[4] L. T. Cowley, Ph.D. thesis, Edinburgh, 1968.
[5] L. T. Cowley *et al.*, Trans. Faraday Soc. 65, 2027 (1969).

MOLECULAR PHYSICS, 1970, VOL. 19, No. 5, 659–671

9

Elastic scattering of alkali atoms from iodine atoms and molecules at thermal energies

by M. A. D. FLUENDY, D. S. HORNE†, K. P. LAWLEY and A. W. MORRIS

Department of Chemistry, University of Edinburgh, West Mains Road, Edinburgh EH9 3JJ

(*Received* 9 *March* 1970)

High-resolution, small-angle measurements of the elastic differential cross sections have been made for the systems K/I and K/I_2. In all cases the structure at small angles is found to arise predominantly from collisions occurring along the adiabatic potential. The off-diagonal matrix element of the electronic hamiltonian between the covalent and ionic states in the K/I system is found to be $\sim 6 \times 10^{-15}$ ergs.

1. INTRODUCTION

The alkali atom/halogen atom or molecule collision system is a well-known example of avoided curve crossing. At short range alkali halides are almost entirely ionic in character. They dissociate adiabatically, however, to neutral atoms. The potentials for KI are shown in figure 1 [1]. Slow collisions between neutral atoms follow the adiabatic potential with what amounts to an electron transfer from the alkali to the halogen taking place at r_c. Fast collisions occur along the diabatic curve and there is no electron transfer. At intermediate

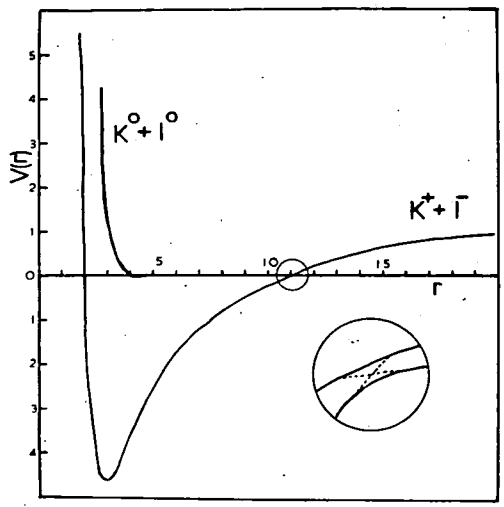

Figure 1. Diabatic and adiabatic potentials for K/I. The expanded portion shows the pure coulomb and van der Waals potentials dotted. (Distances in ångströms, energies in 10^{-19} J.)

† Present address: Lash Miller Chemical Laboratories, St George Street, Toronto, 5, Canada.

velocities both types of behaviour may occur with comparable probabilities and the different semi-classical trajectories resulting then interfere to produce structure in the differential cross section. This change in behaviour can be simply understood in terms of the atom and electron velocities. If electron relaxation and adiabatic behaviour is to occur the electron transit time from alkali to halogen at r_c must be short in comparison with the motion of the colliding atoms through a small region around r_c. The alkali/halogen family is especially convenient for studying this behaviour since the available range of ionization potentials and electron affinities which determine the crossing distance r_c, covers the band over which the transition between the two types of behaviour can be expected.

These systems have recently attracted considerable theoretical interest and offer prospects for rather detailed calculations [2, 3].

For the atom–atom systems [4, 5] colliding at thermal energies dissociation into ions is not energetically possible and only the elastic channel is open for exit to neutral atoms. In the case of alkali/halogen molecule collisions, chemical reaction is possible and is known from molecular scattering data to occur with high probability. In these collisions it is believed that electron transfer or 'harpooning' is the precursor to chemical reaction. The resulting alkali ion 'strips' a halogen ion from the molecule to yield the alkali halide molecule in a highly excited vibrational state [6–10]. There are thus two exit channels, elastic and reactive, available.

There are several potentials available to the two systems K/I and K/I_2 and any guidance that theory can give to the accessibility of these energy surfaces will be useful in interpreting the experimental results.

Dealing first with the systems K/I, the iodine atom is in a $^2P_{3/2}$ state and thus will be found in the four states $M_J = \pm\frac{3}{2}, \pm\frac{1}{2}$, with equal probability, while the alkali atom, $^2S_{1/2}$ is equally likely to be in one of the two states $M_J = \pm\frac{1}{2}$ before collision. The ionic molecular state is $^1\Sigma^+$ or more properly as $R\to\infty$, 0^+ and can only arise from a combination of the halogen states $M_S = \pm\frac{1}{2}$, $M_L = 0$ with the alkali states $M_S = \mp\frac{1}{2}$. Consideration of the parentage of these states shows that the chance of a random collision following the ionic potential adiabatically is $\frac{1}{8}$. Coupling of the nuclear spin of ^{127}I with the electronic angular momentum makes M_J no longer a good quantum number, but the two moments are readily uncoupled as the two atoms approach and the factor of $\frac{1}{8}$ holds.

Theory has less to say about the precise form of the interatomic potentials corresponding to the molecular states $^3\Sigma$, ^{3}, $^1\Pi$. The $^3\Sigma$ state may exhibit a minimum and all the potentials become repulsive at a separation

$$r \sim \langle r^2\rangle^{1/2}_{I(5p)} + \langle r^2\rangle^{1/2}_{K(4s)}$$

at which the overlap of the two outermost electron shells becomes appreciable (~ 4 Å).

The topology of scattering from normal potentials under semi-classical conditions (angle of scattering not too small) is well known. However, inspection of the very small angle scattering to be expected from potentials exhibiting rapidly varying behaviour at some value of the interparticle separation, a, shows the existence of diffraction peaks in $\sigma(\theta)$ arising from scattering at this 'edge' in the potential [11].

For a very sharply varying potential, such as the adiabatic, these diffraction peaks will be similar to the well-known Fraunhofer diffraction from a circular

plate with:

$$I(\theta) \sim I_0 \left[\frac{2J_1(\theta . a/\lambda)}{\theta . a/\lambda}\right]^2, \tag{1}$$

where a is the potential range and $\lambda = \hbar/\mu v$, i.e. the angular periodicity $\Delta\theta_{\text{c.m.}}$ of these oscillations is:

$$\Delta\theta_{\text{c.m.}} = \pi/l^* = \pi\hbar/\mu v a, \tag{2}$$

where $l^* = \mu v a/\hbar$ is the orbital momentum corresponding to impacts grazing the edge; μ is the reduced mass and v the relative velocity of the colliding atoms.

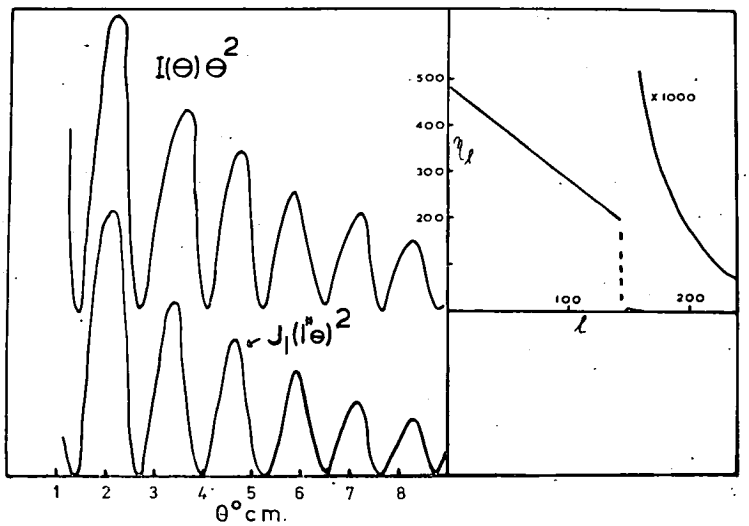

Figure 2. Edge diffraction structure and phase shift curve from which it was calculated $l^* = 145$. $J_1(l^*\theta)^2$ is shown for comparison.

In figure 2 we show an example of such a diffraction effect together with the corresponding phase shift behaviour. The rapid change in phase shift required to produce this effect can arise from either the repulsive and attractive branches of the potential or indeed from the steep edge in the imaginary component of an optical potential.

For the case illustrated in figure 2, as for the adiabatic K/I potential, the step in the phase shift curve occurs at such a large value of r that the van der Waals part of the potential is effectively zero. The small-angle scattering shows a very strong diffraction effect in this case which is diagnostic of electron transfer and the consequent abrupt change in potential.

2. Experimental

The experiments reported here were made with the modulated cross-beam apparatus already described [12]. The primary alkali beam was velocity selected [13]. The scattered alkali was detected using a hot wire ionizer, mass spectrometer and gated ion counting system. The data was recorded on a paper tape punch for computer filtering and deconvolution.

The iodine source was of the two chamber type constructed of monel metal and glass. The first stage operated between 25–40°c and served to maintain an I_2 pressure of $\sim 1{\cdot}0$ torr throughout the source. The second chamber, connected

to the I_2 vapour source by a thermally insulating glass stem and heat shunt, was operated at ~ 530°c. Under these conditions thermal dissociation to ground state atoms ($^2P_{3/2}$) is more than 90 per cent complete. The beam finally emerged through a gold micro mesh (EMI) aperture. The same source, with the second chamber operated at 100°c, was used for the I_2 beam.

A chlorine atom source using a capacitively coupled r.f. discharge was also developed to yield more than 90 per cent of atoms but was not used in the present series of experiments.

A major problem in this work was the corrosion produced by iodine and alkalis. Electrical wiring appeared to be particularly susceptible and because of the large number of such connections in the vacuum chamber this led to a short time between failures. It was largely for this reason that the measurements were not systematically extended to larger angles. Scans with a sample interval of 0·05° over a wider angle would typically take 5–6 hours.

3. Results

The potassium/iodine atom system was studied at three impact energies: 0·098, 0·188 and $0{\cdot}315 \times 10^{-19}$ J between 0 and 2·5°. The rapid oscillatory structure shown typically in figure 3 was found throughout these experiments.

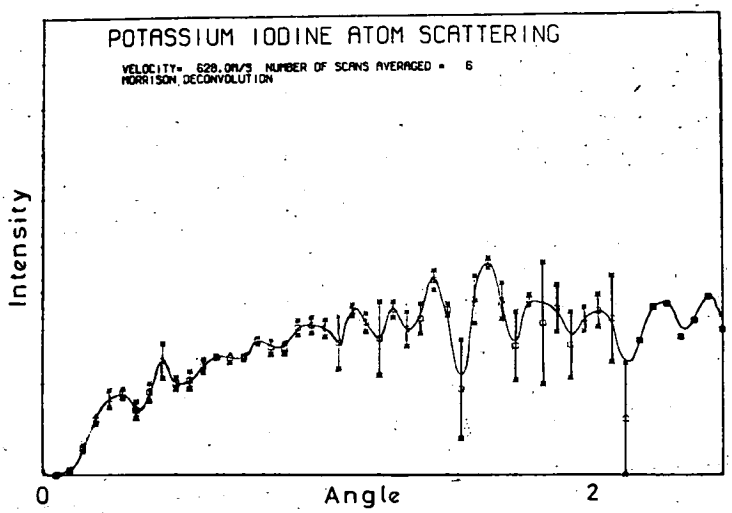

Figure 3. Typical experimental results after computer analysis for the K/I system.

The error bars shown are somewhat pessimistic—the peaks appear on each independent scan but are slightly shifted due to difficulties in reproducing angles of observation precisely and thus ' blur ' on averaging. The mean peak positions are shown in figure 4. The sodium/iodine atom results were limited in accuracy due to noise problems and this system was consequently not investigated closely. Nevertheless, the limited initial experiments revealed oscillating structure similar in character to that found in K/I. In the region between 0° and 0·3° the finite detector height produces a decrease in resolution which is not removed by deconvolution or averaged over in the theoretical calculation. This is the reason for the systematic discrepancy in peak heights between observation and calculation.

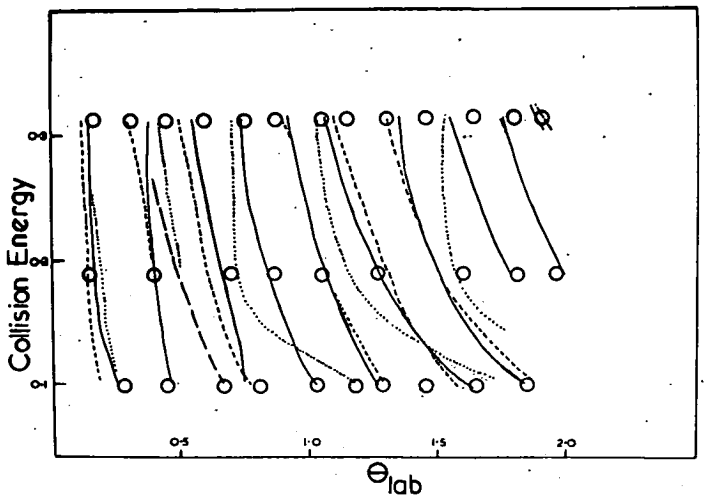

Figure 4. Experimental peak positions at three collision energies are shown as ○. The solid line is the calculated peak positions for the apparatus averaged scattering from $\frac{1}{8}$ adiabatic and $\frac{7}{8}$ van der Waals potential. The dashed and dotted line represent the peak positions for the adiabatic and van der Waals scattering taken separately. (Laboratory angle in degrees, energies in 10^{-19} J.) ($C^{(6)} = 1400 \times 10^{-60}$ ergs cm^6. $\sigma = 4.37$ Å.)

The potassium/iodine molecule system was investigated at four collision energies: 0·091, 0·135, 0·193 and $0{\cdot}331 \times 10^{-19}$ J. Once again an oscillating structure was observed as shown in figure 5. The K/I_2 data was taken at an early stage in the development of the experimental system and is noisier than the

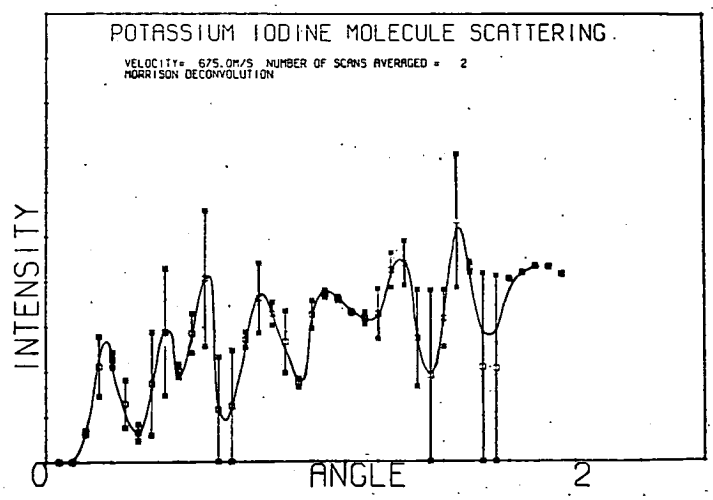

Figure 5. Typical experimental data for K/I_2 system.

subsequent K/I result. The peak positions at each energy are shown in figure 6. In this system the detector cannot distinguish between K and reactively scattered KI. However, since the KI has been observed to be peaked at 20° and the elastic differential cross sections are at least 10^3 larger than those possible for the product KI this structure can be attributed to K atoms.

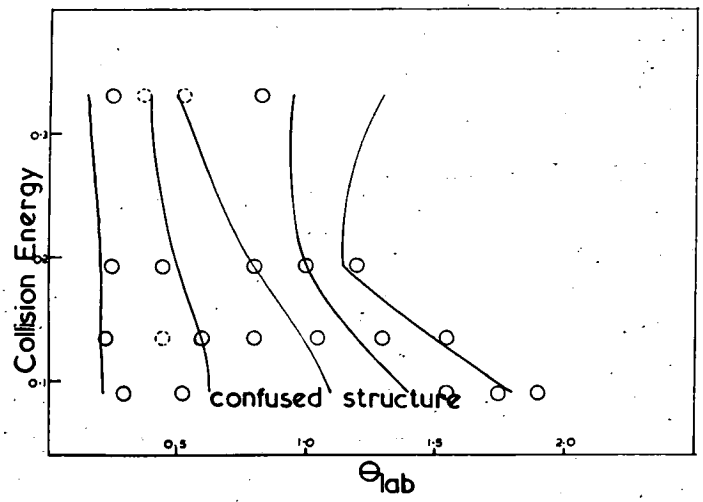

Figure 6. Experimental and calculated peak positions for K/I_2. The calculated positions are for scattering from the adiabatic potential.

4. Discussion

4.1. *K/I system*

As already discussed, at long ranges the K/I system interacts on three potentials with $\Lambda = 0, 1, 2$. The full analysis of scattering measurements must in principle therefore involve the interaction of all three states and the ionic adiabatic potential together with their consequent mutual interference effects. Neither present theory nor this experimental work can usefully tackle this complexity. We therefore make the following assumptions:

(i) That spin is conserved in the collisions contributing at small angles, i.e. that only the 0^+ state having $\frac{1}{8}$ total weight interacts with the ionic potential curve.

(ii) That in the large l range contributing to the observed scattering the probability of electron transfer is either large or small. We thus neglect mutual interference between diabatic and adiabatic trajectories.

While plausible the validity of these assumptions must rest upon their success in accounting for the present observations. From these assumptions the following extreme cases now emerge:

(1) *Crossing probability small—diabatic behaviour*

(*a*) The $\Lambda = 0$, 1 and 2 potentials are so similar at long ranges that they can be replaced by a single equivalent van der Waals potential. All the observed scattering arises from this single potential.

(*b*) The $\Lambda = 0, 1, 2$ potentials are very different at long ranges and contribute separately to the narrow angle scattering.

(2) *Crossing probability large—adiabatic behaviour*

In this case the O^+ state behaves adiabatically with electron transfer occurring at r_c.

(*a*) This contribution to $\sigma(\theta)$ may be superimposed on either case (1 *a*) a single van der Waals potential or

(*b*) on case (1 *b*) a family of van der Waals potentials.

Finally gross failure of our initial assumption could occur: for example, if only scattering from an adiabatic potential could be seen this would indicate that spin was not being conserved and a multi-state interpretation would be essential.

We now consider these possibilities systematically. The observed angular frequency $\sim 0{\cdot}23°$ in the systems leads to a single potential with a size parameter in the range ~ 20 Å, clearly unphysical. Thus at least two potentials must be operating and case (1 *a*) can be eliminated, and also purely adiabatic scattering from gross failure of spin conservation.

A family of up to three van der Waals potentials (in L.J. 12,6 form) was then sought which when appropriately weighted would yield the observed peak positions.

A value of $C^{(6)} \sim 1400 \times 10^{-60}$ erg cm^6 was estimated (using the London formula) as representing the long-range behaviour of all the potentials and a search in σ and well depth was made. The best fit found is shown in comparison with experiments in figure 7. The second peak from 0° was found particularly

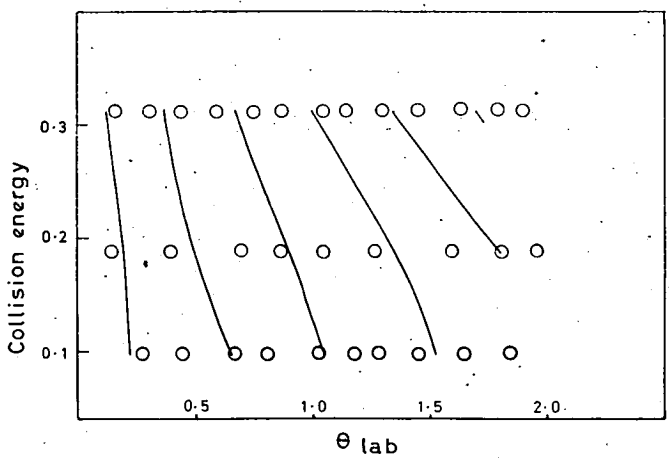

Figure 7. Best fit found for K/I system using three van der Waals type potentials weighted and averaged.

difficult to match and required a van der Waals potential with $\sigma = 8$ Å as one contribution! Considering the three variable parameters and the unphysical value of σ required for one potential this is not a satifactory fit. Case (1 *b*) is not therefore supported.

We now consider the adiabatic cases. An adiabatic potential was constructed using the Varshni–Shukla [1] form for KI out to the crossing distance r_c, and an inverse-six power potential with $C^{(6)} \sim 1400$ thereafter. The two potentials were joined smoothly over a distance of 0·1 Å around r_c using a switching function. This potential is shown in figure 1.

Scattering from this potential in the 0–4° laboratory region is insensitive to $C^{(6)}$ and the switching function, and is largely determined by r_c. This potential provides a clear case of the diffraction scattering already discussed. The phase shift falls very rapidly (by 10^2) as the impact parameters increase through r_c,

producing strong oscillations in the cross section with a periodicity of

$$\Delta\theta_{\text{c.m.}} = \pi\hbar/\mu v r_c.$$

Since r_c is determined by the ionization potential of potassium and the electron affinity of iodine the adiabatic scattering at narrow angles is independent of any variable parameter. Typical structure arising from this potential is shown in figure 8. A single van der Waals potential with $C^{(6)}$ constrained to 1400 was

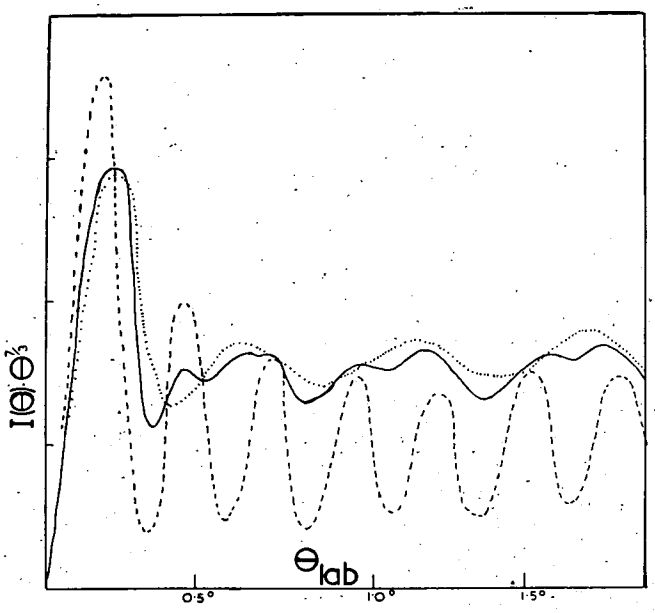

Figure 8. An example of the apparatus-averaged scattering expected for K/I on the adiabatic (dashed), diabatic (dotted) potentials and their appropriately averaged sum (solid line).

now sought, which, when apparatus averaged and appropriately statistically weighted, would yield the observed peak structure. The result of such a calculation is also shown in figure 4. The agreement is excellent considering the reasonable value of σ (4·37 Å) required for this van der Waals potential and that this is the only variable parameter. We conclude therefore that case (2 *a*) applies, that spin is conserved in these long range encounters, and that the 0^+ state behaves adiabatically with high probability.

If the simple Landau–Zener view of curve crossing, in which the electron transfer occurs overwhelmingly in a small region around r_c, is taken then this transfer must occur in a time short compared to 10^{-14} s, the transit time of the atoms through r_c at the experimental velocities.

For valence electrons, transfer times (over 11·3 Å) are of the order 10^{-15} s, so that these experiments are not inconsistent with theory.

The reverse conclusion was reached by Berry [14] from spectroscopic data for KI. He found that transition to the upper state produced diffuse spectra (in contrast to NaI) and concluded that the KI system behaved diabatically. His experiments are not, however, directly comparable to ours since:

(i) They were made for low l values $l \sim 50$, the most probable value in the thermodynamic equilibrium distribution under his conditions.

(ii) The effective velocity at r_c was much higher.

From inspection of figure 9, which compares the effective potentials for $l=50$ (spectroscopy) and $l=400$ (beam scattering), we can see that the radial velocity at r_c in the scattering case will be at the most one-quarter of that in the spectroscopic experiment. This change in behaviour is therefore to be expected on even the most naive grounds.

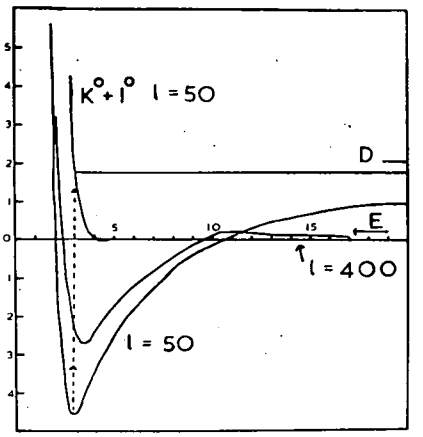

Figure 9. Comparison of the effective potentials for KI operating in the spectroscopy ($l=50$) and beam scattering experiments ($l=400$). The impact energy is shown at E.

The transition probability for an electron jumping in the Landau–Zener approximation [2] is:

$$P_l = \left| \exp\left(\frac{-2\pi A^2}{\hbar v_l |f_1 - f_2|} \right) - 1{\cdot}0 \right|, \tag{3}$$

where v_l is the radial velocity at r_c, f_1 and f_2 are the adiabatic and diabatic forces at r_c and A is the matrix coupling element.

From the scattering and spectroscopic evidence together it is possible to place bounds on the matrix element A, since under spectroscopic conditions P_l is small while the reverse is true in the scattering case.

We arbitrarily take the probability of electron transfer in the two cases to be:

$$P_l \text{ thermal energy scattering} \sim 0{\cdot}8,$$

$$P_l \text{ spectroscopic experiment} \sim 0{\cdot}2.$$

In the spectroscopic experiment a maximum in the continuum is observed at 3·83 ev (probably arising from Franck–Condon effects) [14], corresponding to transitions terminating in the upper state and 0·5 ev exothermic with respect to dissociation to ground state atoms. Observations further to the red also failed to show any structure, so that diabatic behaviour is well developed at these energies. Since the potential bowl in the upper state (figure 1) is close to the energy zero out to the crossing distance r_c this exothermicity will be present almost entirely as radial velocity. A radial velocity of $1{\cdot}5 \times 10^5$ cm s^{-1} is therefore an upper limit above which diabatic behaviour is certainly occurring with high probability.

For the scattering experiment relative velocities up to $\sim 10^5$ cm s^{-1} appeared to show adiabatic behaviour in the narrow angle region. The radial velocities at r_c for these collisions depend upon the range of l values contributing to this narrow-angle structure. From the amplitude of the structure observed a minimum estimate is that 10 per cent of partial waves around l_c behave adiabatically. Hence (since $\dot{r} \sim v[1-(b^2/r_c^2)]^{1/2}$) a minimum estimate for the radial velocity below which all collisions proceed adiabatically is 4×10^4 cm s^{-1}. Finally since the covalent curve is flat at r_c we take $|f_1 - f_2|$ as e^2/r_c^2.

Thus we have:

$$\exp\left(\frac{-2\pi A^2}{\hbar(e^2/r_c^2)4 \times 10^4}\right) \sim 0{\cdot}2$$

for thermal scattering and

$$\exp\left(\frac{-2\pi A^2}{\hbar(e^2/r_c^2)1{\cdot}5 \times 10^5}\right) \sim 0{\cdot}8$$

for the spectroscopic experiment.

The matrix element for the K/I system is thus bounded on fairly conservative estimates of probability and radial velocity by the values $3{\cdot}5 \times 10^{-15}$ ergs and 1×10^{-14} ergs with a value of $\sim 6 \times 10^{-15}$ ergs as the most likely estimate.

This estimate may be compared to a value for A of $\sim 8 \times 10^{-14}$ ergs found for K/Br_2 by Beade *et al.* [4].

The extension of these experiments both to wider angles and higher collision energies should yield a precise value for this matrix element. These experiments are in hand.

The high probability of crossing found at wide impact parameters (~ 12 Å) raises the possibility of chemical reaction occurring by the harpooning mechanism at similar ranges, i.e. that reaction cross sections may be limited by r_c or ionization potantial–electron affinity differences rather than considerations of adiabacity.

2.2. K/I_2

This system is basically similar to K/I in that transition may occur from a van der Waals form of potential to an ionic one, the crossing distance being estimated as 5·5 Å. If we ignore the rotational states of the I_2 there is only one van der Waals potential operating. At thermal energies two exit channels are open:

$$K + I_2 \rightarrow K + I_2 \quad \text{elastic},$$

$$K + I_2 \rightarrow KI + I \quad \text{reactive}.$$

The system has already been investigated both as regards the distribution of scattered product KI and the elastically scattered K. (Though not with the high angular resolution used in these experiments.) As a result of this work the mechanism appears to involve an electron transfer as a first stage to reaction. The reactive cross section estimated at > 100 Å^2 and neutral-coulombic crossing radius r_c then imply that a large fraction of the encounters in which electron transfer occurs proceeds to chemical reaction.

If we then represent the combined effects of elastic and reactive scattering by an optical potential [15] of the form:

$$V_{opt}(r) = V(r) + iW(r), \qquad (4)$$

at least four parameters are required: (i) the van der Waals $C^{(6)}$ common to both adiabatic and diabatic potentials, (ii) the value of r_c, the separation at which the potential changes to the coulombic form, (iii) a length parameter, r_a characterizing the range of the imaginary part of the potential, (iv) a steepness parameter for the onset of $W(r)$. Furthermore, if it is suspected that the upper (diabatic) potential surface is sampled at separations less than r_c, then a second Lennard–Jones parameter, ϵ or σ, will be needed for $V(r)$.

Instead of postulating an analytical form for $V_{opt}(r)$ and solving the resulting radial wave equations to obtain the S matrix, we proceed by postulating a form for the S_{ll} directly:

$$S_{ll}=\exp(-2\xi_l+2i\eta_l),$$

where

$$\xi_l=\left\{1+\exp\left(\frac{l-l_a}{\Delta l}\right)\right\}^{-1},$$

η_l = phase shift from $V(r)$ potential alone

and Δl is the range of l values over which the attenuation changes from, effectively, 0 to 1, l_a is related to r_a by $l_a=\mu v r_a/\hbar$ and r_a will be called the radius of the absorbing sphere. Δl is given the value 25 in all subsequent calculations and is not varied. The case of intermediate probability of electron transfer occurring at the crossing point must still be handled by solving the appropriate coupled radial wave equations that permit interference between the adiabatic and non-adiabatic trajectories. This situation cannot be represented by a simple optical potential.

Returning to the parameter list for the complete potential, $C^{(6)}$ and r_c are taken to have the values 2000×10^{-60} ergs cm^6 and 5·5 Å with the Shukla potential for the ionic part of the adiabatic potential. For the upper or diabatic curve, $\sigma=4\cdot75$ Å was used with a well depth of $0\cdot0242\times10^{-12}$ ergs.

Various extreme possibilities in the value of r_a or l_a can be distinguished:

(1) The bulk of small-angle scattering is determined by the diabatic potential and chemical reaction does not start until separations at the classical turning point reach a value of somewhat less than r_c: i.e. $r_a<r_c$, V diabatic. This would not correspond to the harpooning model for reaction.

As r_a exceeds r_c, the scattering pattern becomes dominated by the diffraction pattern of the black sphere, with angular periodicity $\Delta\theta=\pi/l_a$. For r_a appreciably less than r_c, various interfering branches of the classical deflection function emerge from collision and lower frequency interference effects are superimposed upon, and destroy, the simple black sphere structure.

(2) $V(r)$ is of the adiabatic form showing coulombic behaviour at separations less than r_c. One may then distinguish the cases:

(*a*) $r_a\gg r_c$: The diffraction structure of $\sigma(\theta)$ has an angular spacing π/l_a and the magnitude of $\sigma(\theta)$ rapidly falls off with angle.

(*b*) $r_a\lesssim r_c$: The coulomb potential dominates the elastic scattering. In the limit $r_a=0$ a small-angle edge diffraction structure is well developed with angular spacing π/l_c. Branch interference between trajectories may also be seen, introducing a lower frequency structure into $\sigma(\theta)$. At intermediate values of r_a, $\sigma(\theta)$ is complicated, exhibiting the effects of edge diffraction from both the imaginary (black sphere) and real parts of the potential (coulomb 'edge' and

different branches), the latter tending to dominate. Typical scattering to be anticipated from these cases is shown in figures 10 and 11. The effect of increasing the black sphere diameter is clearly seen.

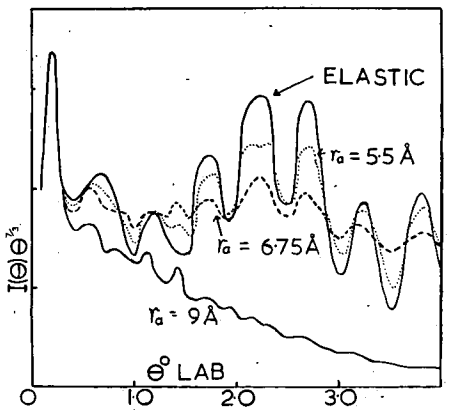

Figure 10. Elastic scattering from K/I_2 on the diabatic potential with several sizes of black sphere (r_a) representing chemical reaction.

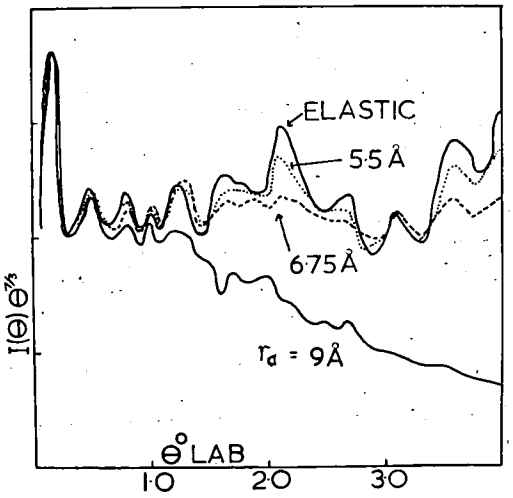

Figure 11. Elastic scattering from K/I_2 on the adiabatic potential with several sizes of black sphere (r_a) to represent chemical reaction.

The salient feature of these rather crude attempts at fitting is that in order to introduce the observed number of maxima in between 0° and 2° (laboratory), diffraction effects arising from the edge of the coulomb potential must be included. That is, models (1) and (2 *a*) are unacceptable. The peak structure arising from the adiabatic potential is shown in figure 6.

This conclusion is further supported by the sharp fall in elastically scattered K intensity observed at wide angles [10]. As suggested by Herschbach this behaviour is typical of orbiting at large impact parameters [16] and would be the expected behaviour or trajectories around the rim of a steeply falling adiabatic potential.

These experiments suggest that electron transfer is not inevitably followed by chemical reaction because elastically scattered (i.e. unreacted) potassium shows signs of having experienced a coulomb potential.

The cause of this might be sought either in angular momentum considerations, effect of the re-orientation of the I_2 in the time of approach of the alkali atom or, just possibly, in some more general angular momentum requirement related to the rotational state of the halogen molecule. All these questions can be illuminated by a study of the classical trajectories resulting from various assumed potentials.

D. S. Horne thanks the Carnegie Trust and A. W. Morris the Science Research Council for support. All the authors thank the Science Research Council for a grant for equipment.

References

[1] Varshni, Y. P., and Shukla, R. C., 1961, *J. chem. Phys.*, **35,** 582.
[2] Child, M. S., 1969, *Molec. Phys.*, **16,** 313.
[3] Bandrauk, A. D., 1969, *Molec. Phys.*, **17,** 523.
[4] Beade, A. P. M., Moutinho, A. M. C., de Vries, A. E., and Los, J., 1969, *6th International Conference on the Physics of Electronic and Atomic Collisions*, M.I.T., p. 592.
[5] Rothe, E. W., and Helbing, R. K. B., 1969, *J. chem. Phys.*, **51,** 1607.
[6] Grosser, A. E., and Bernstein, R. B., 1965, *J. chem. Phys.*, **43,** 1140.
[7] Minturn, R. E., Datz, S., and Becker, R. L., 1966, *J. chem. Phys.*, **44,** 1149.
[8] Birely, J. H., Herm, R. R., Wilson, K. R., and Herschbach, D. R., 1967, *J. chem. Phys.*, **47,** 993.
[9] Herschbach, D. R., and Moulton, M. C., 1966, *J. chem. Phys.*, **44,** 3010.
[10] Greene, E. F., Hoffman, L. F., Lee, M. W., Ross, J., and Young, C. E., 1969, *J. chem. Phys.*, **50,** 3450.
[11] Cowley, L. T., Fluendy, M. A. D., and Lawley, K. P., 1969, *Trans. Faraday Soc.*, **65,** 2027.
[12] Cowley, L. T., Fluendy, M. A. D., Horne, D. S., and Lawley, K. P., 1969, *J. scient. Instrum.*, **2,** 1021.
[13] Cowley, L. T., Fluendy, M. A. D., and Lawley, K. P., 1970, *Rev. scient. Instrum.*, **41,** 666.
[14] Berry, R. S., 1957, *J. chem. Phys.*, **27,** 1288.
[15] Nikitin, E. E., 1967, *Chem. Phys. Lett.*, **1,** 266.
[16] Herschbach, D. R., 1966, *Adv. chem. Phys.*, **10,** 336.

10

CHAPTER 3

MONTE CARLO METHODS

Malcolm Fluendy

DEPARTMENT OF CHEMISTRY
UNIVERSITY OF EDINBURGH
EDINBURGH, SCOTLAND

I. Philosophy of the Monte Carlo Method

Traditionally investigators have sought to reduce the complexities of experiment to concise mathematical statements or "models." These formulations have fulfilled two principal functions. First, and of immediate practical value, they enabled the results of an experiment to be predicted. Second, they frequently provided an insight into the mechanism of the process. The kinetic theory of gases is a classic example. Unfortunately, to obtain this concision idealizations and approximations are often required, and in many cases no useful analysis of anything approaching the real situation is possible.

The Monte Carlo method (*1–7*) is no less ambitious in function but replaces the mathematical analysis by a digital-computer algorithm in which the approximation due to the requirements of the mathematical analysis can be avoided. In its conceptually simplest form the method may be a direct mathematical simulation of the physical system. Thus Alder and Wainwright (*8*) have studied the dynamics of gases composed of hard spheres. The trajectories of molecules were followed by solving the simultaneous classical equations of motion numerically to predict the locations of the particles at successive short intervals of time. After each interval the system was examined to discover whether any collisions had occurred. After any collision suitable new velocities were given to the particle involved and the process continued. The changes in velocity distribution, for example, were then followed by recording the velocity of every particle through many cycles. This application is typical of many in the molecular sciences in that the individual processes (in this case the collisions) may be quite well understood, but the bulk or average properties can not be readily related to these events. These calculations are of special interest in illustrating the use of the method as a guide to intuition. For this purpose the numerical accuracy of the computed results may be of secondary importance to the design of output arrangements that enable a comprehensive picture of the process to be gained. As an example, Fig. 1 shows the trajectories of hard-sphere molecules in solid and liquid phases (*8*). The computed molecular paths are output directly to a cathode ray tube and photographed; the effect of changing the parameters in the model can then be quickly explored visually.

In other applications, e.g., to polymer properties, the Monte Carlo technique has used a more probabilistic formulation. Thus if we wished to calculate the time-independent properties of a freely jointed chain of non-overlapping particles, we could proceed in two ways. We might prefer to use a simulation and follow the time evolution of such a system (starting from an arbitrary state) by solving the equations of motion and so calculate a time

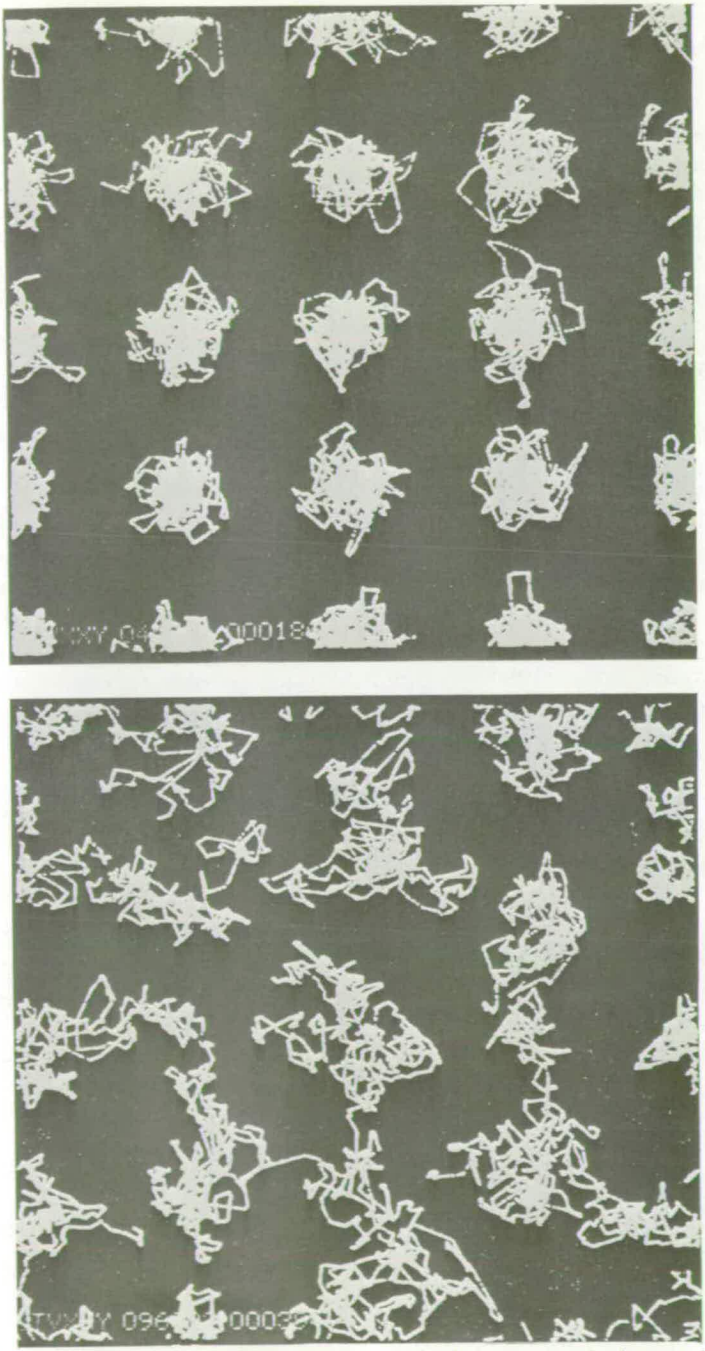

Fig. 1. Trajectories of hard-sphere particles are displayed on a cathode ray tube hooked directly to a computer. Top shows solid state, bottom liquid. Reprinted from Ref. (*8*), p. 124, by courtesy of Scientific American, Inc.

average of the property. Alternatively we could generate a series of specific configurations of the chain. If this series is chosen at random it will form an unbiased sample of the population of all possible configurations of the chain. The properties of the sample will then be an estimate of the properties of the population, i.e., of the chain. This estimate can be made as accurate as we wish by taking a large enough random sample (though in practice enough will often be inconveniently large).

To develop these ideas further it is useful to consider a trivial but analogous problem, the evaluation of an integral

$$I = \int_a^b f(x)\,dx \tag{1}$$

In practice if such an integral could not be evaluated analytically, a conventional numerical method would be used. Nevertheless, a Monte Carlo estimate of I, $\hat{I}$ can be made. The procedure is to draw a sequence of random numbers ϵ_i from a uniform distribution, i.e., a distribution in which any number in the range has an equal probability of being chosen. The random numbers ϵ_i so drawn are used to generate a series of $f(\epsilon_i)$'s that are a representative sample of the population of all possible $f(x)$'s. Intuition will then suggest and the Strong Law of Large Numbers confirm that our estimator $\hat{I}$ will be:

$$\hat{I} = \left[\frac{(b-a)}{N}\right] \sum_{i=1}^{N} f(\epsilon_i) \qquad a \leqslant \epsilon_i \leqslant b \tag{2}$$

and that in the limit,

$$I = \lim_{N \to \infty} \hat{I} \tag{3}$$

Somewhat different prospects appear when attempting to calculate properties that arise from nonuniform distributions. For example, integrals arising in statistical mechanics of the type

$$\bar{f} = \frac{\int_0^b f(q) \exp[-E(q)/kT]\,dq}{\int_0^b \exp[-E(q)/kT]\,dq} \tag{4}$$

where $\bar{f}$ is the average or expectation value of the property $f(q)$. Frequently a large region of q is of high energy (E) and contributes little to $\bar{f}$.

This type of problem could be tackled as before by sampling from a uniform distribution of q and evaluating the estimate as

$$\hat{f} = \frac{b}{N} \sum_{i=1}^{N} f(\epsilon_i) \exp\left(\frac{-E(\epsilon_i)}{kT}\right) \tag{5}$$

More usefully in this case we might draw random q's from a Boltzmann distribution, i.e., such that the probability of drawing a particular value of q was proportional to $\exp[-E(q)/kT]$. The estimate of $\bar{f}$ would then be

$$\hat{f} = \frac{b}{N} \sum_{i=1}^{N} f(\epsilon_i) \tag{6}$$

The latter method avoids the difficulties associated with the integral, since relatively few cases will be taken from the energetically unfavorable regions of q.

The simple examples given so far serve to illustrate the spirit of the method, which has been called experimental mathematics. In many applications the straightforward methods of simulation will require an impossibly large amount of work. More complicated but related procedures must then be employed in which all our available a priori knowledge of the problem is used to reduce the amount of work needed. To understand these procedures we must consider the method in more detail.

II. Statistical Introduction

It should already be clear that a knowledge of elementary statistics is basic to the understanding and successful employment of the Monte Carlo method. A brief outline of the more important statistical techniques or concepts is therefore given here. Undoubtedly, however, the intending practitioner will do well to broaden his knowledge by consulting some more extensive works (*9*, *10*) on the subject.

A. FUNDAMENTAL IDEAS—EVENTS, SAMPLES, AND PROBABILITY

As in many other fields, considerable use is made in statistics of the "ideal" or "conceptual" experiment so that we may ride roughshod over the mundane difficulties with which the real world would otherwise oppose us. For example, the primitive statistical experiment of coin tossing is idealized so that we may consider only two possible outcomes, heads or tails, and neglect other physically real, but for our purpose irrelevant, possibilities, such as the loss of the coin.

The outcome of any experiment or observation on an ideal system such as this can then be regarded as a point, a *sample point*, in a space described by all points corresponding to possible outcomes of the experiment. Such a space is, naturally enough, known as a sample space. Thus in a simple dietossing experiment the sample space will comprise the 6 sample points

corresponding to scores of 1 to 6. The result of any experiment can then be described in terms of sample points. For example, a result in which we score more than 3 is represented by the sample points 4, 5, and 6. Such an aggregate of sample points is known as an *event*. The event that we score more than 3 can be said to contain the sample points 4, 5, 6.

In this simple example the sample points are all discrete, but the sample-space description can equally well be applied to a system containing a continuous distribution of points, representing, for instance, the distance between the points of impact of shells and their target. The examples discussed so far have involved simple events. The term *compound events* can be applied to results comprising several simpler events. Thus the event that we score more than 3 in each of two throws of a die is decomposable to the two simple events of scoring more than 3 in each throw.

Having established our notions of sample points and sample space, we can now introduce the concept of *probability* by means of the following convention.

(1) For a discrete sample space containing the sample points E_1, E_2, $E_3, \ldots$, we assume that with each point E_j there is associated a number called the probability of E_j, denoted by $\mathscr{P}[E_j]$. It must be nonnegative and is normalized by the convention

$$\mathscr{P}[E_1] + \mathscr{P}[E_2] + \cdots = 1 \tag{7}$$

For simplicity we are considering discrete sample spaces, but by a fairly straightforward extension continuous spaces can be dealt with in a similar way.

(2) Further, we define the probability $\mathscr{P}[A]$ of an event A as the sum of the probability of the sample points in it.

Thus if $\mathscr{P}[A1]$ and $\mathscr{P}[A2]$ are the probabilities of a sample point lying in the circles $A1$ and $A2$ of Fig. 2, the event that a sample point lies in any

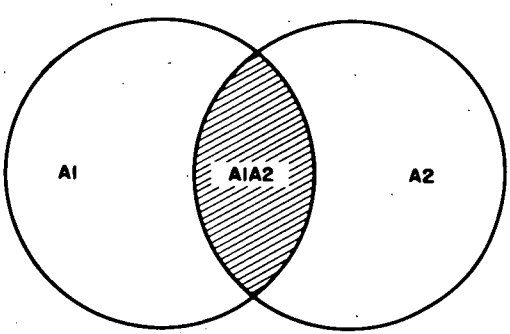

Fig. 2. Venn diagram of nonindependent events $A1$ and $A2$.

circle is

$$\mathscr{P}[A] = \mathscr{P}[A1] + \mathscr{P}[A2] - \mathscr{P}[A1A2] \tag{8}$$

where $\mathscr{P}[A1A2]$ is the probability of the sample point lying in the shaded region common to both circles. This probability must be subtracted on the right-hand side of Eq. (8), since it is included in both $\mathscr{P}[A1]$ and $\mathscr{P}[A2]$ and would otherwise be counted twice.

If $\mathscr{P}[A1A2] = 0$, i.e., if no sample points are common to $A1$ and $A2$, then

$$\mathscr{P}[A] = \mathscr{P}[A1] + \mathscr{P}[A2] \tag{9}$$

We are now in a position from which knowledge of the $\mathscr{P}[E_i]$ for each sample point enables us to calculate the probability of any event or combination of events occurring in that sample space. The simplest assumption of equal probabilities for each sample point is applicable to our ideal coin- or dice-tossing experiment.

In more complicated compound events it is useful to use the ideas of combination and permutation. For example, from a population of n discrete events we can choose r elements to form a sample of size r. Depending on whether or not we replace each event after sampling it (i.e., whether or not we allow each element to be sampled more than once), there will be

$$\begin{aligned}(n)_r &= n(n-1)(n-2)\cdots(n-r+1) \\ &= \frac{n!}{(r-1)!}\end{aligned} \tag{10}$$

different samples possible without replacement and n^r with replacement.

If samples are regarded as unique only if they differ in the elements they contain, i.e., if different orderings of the same elements do not form a distinguishable sample, then there will be

$$\frac{n(n-1)(n-2)\cdots(n-r+1)}{r!} = \frac{(n)r}{r!} \tag{11}$$

distinct samples (without replacement), since there are $r!$ ways of ordering r elements. The term $(n)r/r!$ is often written as $\binom{n}{r}$ and is a binomial coefficient. In such a situation the probability of drawing r specific elements in a sample of size n would be $r!/(n)r$.

A well-known example of the utility of these ideas is provided by Maxwell–Boltzmann statistics. This problem can be regarded as the allocation of r indistinguishable objects among boxes. There are n^r ways of distributing r objects among n boxes. But since the objects themselves are identical, only arrangements having a different number of objects in one or more cells will be distinguishable. If the limits of the boxes are represented by bars and the

objects by balls, a particular configuration might be drawn as $|000|\,|\,0|\cdots|$, i.e., 3, 0, 1, . . . , etc. objects in the first few boxes. Since $n+1$ partitions are required to form n boxes and the first and last items must necessarily be partitions, the number of distinguishable arrangements is equal to the number of ways of selecting r positions from the $n+r-1$ at our disposal. There are thus $\binom{n+r-1}{r}$ distinguishable arrangements. Such arrangements will not have equal probabilities, since each is compounded from many permutations. Individual permutations have equal probabilities by definition, but each distinguishable arrangement will have a probability in proportion to the number of permutations of objects and cells that achieve that particular arrangement.

B. PROBABILITY DISTRIBUTIONS

In the discussion so far we have considered the probability of discrete events only. In many cases a continuous range of distribution (as, for example, the end-to-end distance in a polymer molecule) is possible. It is convenient in this situation to define a function of x such that $f(x)\,dx$ is the probability that the value of the variable lies between x and $x+dx$. Such a function is known as the probability density function (pdf). In the same way $f(x, y)$ represents the probability of the event lying in the square bounded by x, $x+dx$, y, $y+dy$, and so on in higher dimensions.

In multidimensional distributions it is also useful to define functions $f(x \mid y)$ etc., which represents the *conditional* probability of an event lying between x and $x+dx$ if the other variable is known to have the specific value y. The function $f(x \mid y)$ is called a conditional probability density function. The joint pdf of the variables x and y is given by

$$f(y, x) = f_2(y) f_3(x \mid y) = f_4(x) f_5(y \mid x) \tag{12}$$

and the one-dimensional distribution by

$$f(x) = \int_{-\infty}^{\infty} f(x, y)\,dy \tag{13}$$

and so on. The variables x and y are said to be independent if

$$f(y, x) = f_2(y) f_4(x) \tag{14}$$

There is no correlation between y and x, and a knowledge of one is of no value in predicting the other.

In analogy with the compound events of discrete sample spaces, the

probability of the event lying in the range a to b will be

$$\mathscr{P}[a \leqslant x \leqslant b] = \int_a^b f(x)\,dx \tag{15}$$

and similarly in higher dimensions. It is sometimes convenient to use such integrated pdf's instead of the simple pdf's. A special case is the cumulative distribution function (cdf):

$$F(x) = \int_{-\infty}^{x} f(x)\,dx = \mathscr{P}[\text{event lies between } x \text{ and } -\infty] \tag{16}$$

There are an infinite number of distribution functions possible, but in practice it is found that only a few distributions occur very widely. The rectangular (uniform) distributions and the normal (Gaussian) distribution are examples.

1. Rectangular Distribution

The rectangular distribution has a pdf.

$$f(x) = \begin{cases} 1/(a-b) & a < x < b \\ 0 & \text{otherwise} \end{cases} \tag{17}$$

The probability density distribution and cumulative functions are shown in Fig. 3. The function meets the usual requirements for a pdf being positive

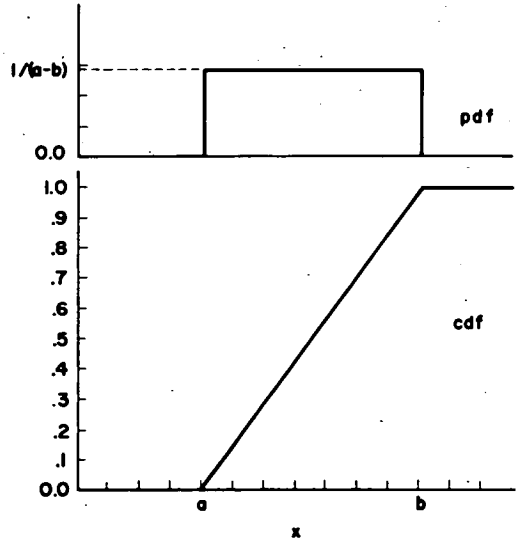

Fig. 3. A rectangular distribution between a and b showing the probability density and cumulative distribution functions.

throughout the range and having unit area under the curve. The limits of distribution are usually taken as 0 and 1 if not otherwise specified.

2. Normal Distribution

The normal distribution is perhaps the best-known, since it is found to describe the distribution of error in an observation where the measurement is subject to a large number of independent random additive errors (a result expressed more formally later as the central-limit theorem).

The normal-distribution function has a pdf

$$f(x) = \frac{1}{2\pi\sigma^2} \exp\left[\frac{-(x-\mu)^2}{2\sigma^2}\right] \qquad -\infty < x < \infty \tag{18}$$

and a cdf

$$F(x) = \frac{1}{2\pi\sigma^2} \int_{-\infty}^{x} \exp\left[\frac{-(y-\mu)^2}{2\sigma^2}\right] dy \tag{19}$$

as shown in Fig. 4. The parameters σ and μ describe the width and location of the distribution and will be discussed in more detail later.

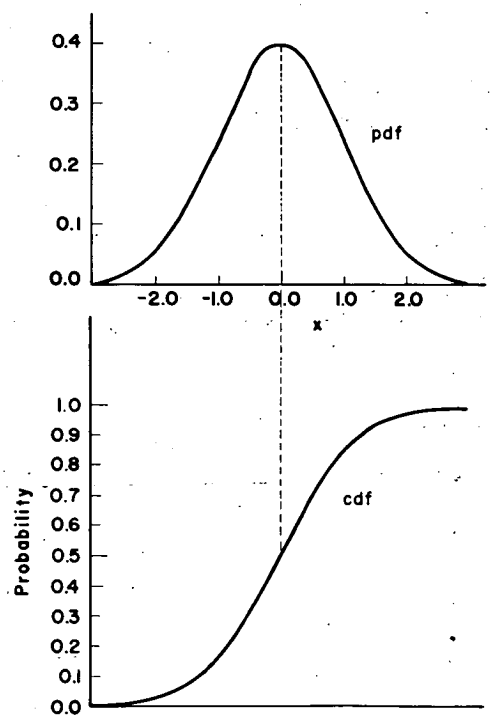

Fig. 4. The Normal or Gaussian distribution. Both pdf and cdf are shown ($\mu = 0.0$ $\sigma^2 = 1.0$).

The most probable event is at the peak in the pdf and the region of steepest gradient in the cdf, both at μ.

3. Poisson Distribution

The Poisson distribution is another important distribution. The number of radioactive disintegrations occurring in a time t is a well-known process following the Poisson distribution.

The distribution has a pdf

$$p(x) = [(\lambda t)^x/x!] \exp(-\lambda t) \qquad \text{for} \quad x = 0, 1, 2, \ldots \tag{20}$$

where $p(x)$ is the probability of exactly x events occurring in an interval t and λ is a parameter describing the distribution. $p(x)$ is, of course, a discrete distribution in x. Thus the normalization condition does not result from an integration but from the summation of $p(x)$ for all x, i.e.,

$$1.0 = \sum_{x=0}^{\infty} p(x)$$

The distribution shown in Fig. 5 shows the variation in $p(x)$ as a function of t, i.e., time.

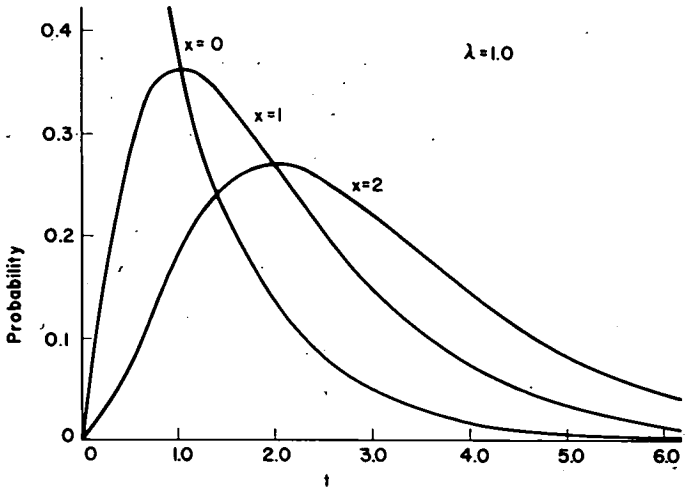

Fig. 5. The Poisson distribution. The probability of exactly 0, 1, and 2 events occurring in a time t are shown as a function of t.

4. Chi-Squared Distribution

The χ^2 distribution has a pdf

$$f(x) = \frac{[x^{\nu/2-1}\exp(-x/2)]}{2^{\nu/2}\Gamma(\nu/2)} \quad \text{where} \quad 0 < x < \infty \quad \text{and} \quad \nu = 1, 2, 3, \ldots \tag{21}$$

$\Gamma(y)$ denotes a gamma function of y, and ν is a parameter corresponding to the number of degrees of freedom. The distribution is plotted for several

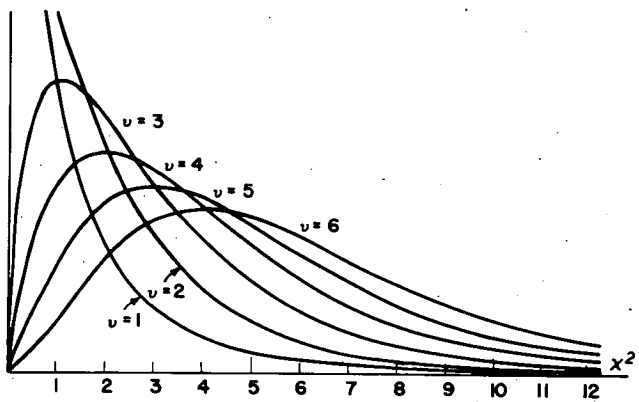

Fig. 6. The chi-square distribution. Reprinted from Ref. (*10*), p. 153, by courtesy of John Wiley and Sons, Inc.

degrees of freedom in Fig. 6. This distribution is sometimes used in testing the goodness of fit of data to hypotheses. It can be shown that if there are k possible outcomes to an experiment and if the hypothesis suggests that these have frequencies $\alpha_1, \ldots, \alpha_i, \ldots, \alpha_k$, while experimentally frequencies $\eta_1, \ldots, \eta_i, \ldots, \eta_k$ are observed, then the quantity

$$F = \operatorname*{Lim}_{M\to\infty} \sum_{i=1}^{k} \frac{(\eta_i - \alpha_i)^2}{\alpha_i} \tag{22}$$

will be distributed as a χ^2 variable with $k - 1$ degrees of freedom as the number of experiments (M) increases to infinity. Extensive tables of this function exist, so by evaluating F for a particular experiment we can check the probability of the hypothesis being well-founded.

C. MOMENTS AND EXPECTATIONS

For the distributions considered so far, at most two parameters were required to specify them completely. In general such parameters can be

related to the so-called moments of the distribution; for example, a pdf $f(x)$ will have its first moment about the origin

$$\mu_1' = \int_{-\infty}^{\infty} x f(x)\, dx \tag{23a}$$

and its nth moment about the origin

$$\mu_n' = \int_{-\infty}^{\infty} x^n f(x)\, dx \tag{23b}$$

(By definition $\mu_0' = 1.0$ for a normalized distribution.)

In the same way central moments, i.e., moments calculated about μ_1' or the mean value of the distribution, are defined as

$$n\text{th central moment} \quad \mu_n = \int_{-\infty}^{\infty} (x - \mu_1')^n f(x)\, dx \tag{24}$$

The most important are the first moment and the second central moment—the mean and variance, respectively. The mean is the measure of the location of the distribution, and the variance of its width or dispersion.

For the normal distribution the mean and variance will be

$$\mu_1' = \frac{1}{2\pi\sigma^2} \int_{-\infty}^{\infty} x \exp\left[\frac{-(x-\mu)^2}{2\sigma^2}\right] dx \tag{25}$$

$$= \mu$$

and

$$\mu_2 = \frac{1}{2\pi\sigma^2} \int_{-\infty}^{\infty} (x - \mu_1')^2 \exp\left[\frac{-(x-\mu)^2}{2\sigma^2}\right] dx$$

$$= \sigma^2 \tag{26}$$

The mean and variance are thus μ and σ^2 as expected.

The Poisson distribution

$$p(x) = \frac{(\lambda t)^x}{x!} \exp(-\lambda t) \tag{20}$$

is rather different. It has mean and variance both equal to λt. In addition the Poisson distribution has higher moments; e.g., $\mu_3 = (\lambda t)^{-1/2}$, which is a rough measure of its asymmetry or skewness.

For some distributions moments may not exist; thus the Cauchy distribution

$$f(x) = (\pi[1 + (x - \theta)^2])^{-1}$$

yields expressions for the moment, i.e., Eq. (23), that are not absolutely convergent.

Moments can also be defined for conditional and joint pdf's. For $f(x \mid y)$ the variance of x given a specific value for y is

$$\text{var}(x \mid y) = \int (x - \mu'_{x|y})^2 f(x \mid y)\, dx \tag{27}$$

where

$$\mu'_{x|y} = \int x f(x \mid y)\, dx$$

For joint pdf's $f(x, y)$ a covariance can be defined as

$$\text{covar}(x, y) = \iint (x - \mu'_x)(y - \mu'_y) f(x, y)\, dx\, dy \tag{28}$$

where μ'_x and μ'_y are the one-dimensional means, i.e.,

$$\mu'_y = \int x \left[\int f(x, y)\, dy \right] dx \tag{29}$$

The covariance is a rough measure of the independence of the two variables. If x and y are independent,

$$f(x, y) = f(x) f(y) \tag{30}$$

and then Eq. (29) is zero, i.e.,

$$\text{covar}\ (x, y) = 0 \tag{31}$$

Note that the reverse need not be true; a zero covariance is not proof of the independence of x and y. As an illustration we can consider two independent variables x and y with the same distribution $h(x)$ and $h(y)$. The composite variables

$$X = h(x) + h(y)$$
$$Y = h(x) - h(y)$$

are then clearly dependent; a knowledge of one contains much information about the other. Nevertheless, the covariance

$$\begin{aligned} \text{covar}\ (X, Y) &= (\overline{XY}) - \mu_X \mu_Y \\ &= \overline{x^2} - \overline{y^2} = 0 \end{aligned}$$

i.e., covar $(X, Y) = 0$.

The calculations of moments is a special case of the use of expectation values. In general the expectation value of a function h—in physical cases usually some property of the system—will be

$$E(h) = \int h(x) f(x)\, dx \tag{32}$$

where $f(x)$ is as usual the pdf describing the distribution in x. [For discrete distributions we replace $\int$ by $\sum$ and $f(x)$ by $p(x)$.] The variance in this formulation [writing σ^2 for $\text{var}(x)$] is

$$\begin{aligned}\sigma^2 &= E(x-\mu_1)^2 \\ &= E(x^2) - 2\mu_1 E(x) + \mu_1{}^2 \\ &= E(x^2) - \mu_1{}^2 = \int_{-\infty}^{\infty} x^2 f(x)\,dx - \left[\int_{-\infty}^{\infty} x f(x)\,dx\right]^2 \end{aligned} \tag{33}$$

a form that is often more convenient to use in computations. With these definitions it can be seen from the properties of integration that

$$E(ch) = c\,E(h) \tag{34}$$

$$E(h_1 + h_2) = E(h_1) + E(h_2) \tag{35}$$

But

$$E(h_1 h_2) \neq E(h_1)\,E(h_2) \tag{36}$$

unless h_1 and h_2 are independently distributed. Similarly it can be shown that

$$\text{var}(ax + b) = a^2\,\text{var}(x) \tag{37}$$

and that the total variance of a sum of many different sorts of observations x_1, each type of observation having a variance $\sigma_i{}^2$, is

$$\begin{aligned}\text{var}\left(\sum_{i=1}^{n} x_i\right) &= \sum_{i=1}^{n} \sigma_i{}^2 + 2\sum_{j=1}^{n}\sum_{k>j} \text{covar}(x_j, x_k) \\ &= \sum_{i=1}^{n} \sigma_i{}^2 + \sum_{j=1}^{n}\sum_{k\neq j}^{n} \text{covar}(x_j, x_k)\end{aligned} \tag{38}$$

or, if each observation is statistically independent,

$$\text{var}\left(\sum_{i=1}^{n} x_i\right) = \sum_{i=1}^{n} \sigma_i{}^2 \tag{39}$$

D. ESTIMATION AND THE CENTRAL-LIMIT THEOREM

As was seen in the introduction, the Monte Carlo method involves the estimation of the expectation value of some property of a system. We attempt to find $\hat{h}$, an estimate of $\bar{h}$, the expectation of h where

$$\bar{h} = \int_b^a h(x) f(x)\,dx \tag{40}$$

(Again this example is trivial, but sufficient to carry the argument.)

The method that we adopt to produce an estimate of $\bar{h}$ depends upon the statistical result known as the central-limit theorem (*9*, Chapter 10). If, as suggested, we estimate $\bar{h}$ by $\hat{h}$, then

$$\bar{h} = \lim_{N\to\infty} \hat{h} = \lim_{N\to\infty} \frac{(b-a)}{N} \sum h(\epsilon_i) f(\epsilon_i) \tag{41}$$

where the ϵ_i are independent random numbers (the definition of *random* we defer to the next section) distributed uniformly over the range of the functions h and f. The central-limit theorem then asserts (subject to certain conditions) that for large N, the variable $(\hat{h} - \bar{h})/(\sigma/N^{1/2})$ is approximately normally distributed with a mean of zero and a variance of one, where

$$\begin{aligned} \sigma^2 &= \int [h(x)]^2 f(x)\, dx - \left[\int h(x) f(x)\, dx\right]^2 \\ &= \overline{h^2} - \bar{h}^2 \end{aligned} \tag{42}$$

In other words the estimate $\hat{h}$ is normally distributed with mean $\bar{h}$ and variance σ^2/N. That is,

$$\mathscr{P}\left[\left|\frac{\hat{h} - \bar{h}}{\sigma/N^{1/2}}\right| < \beta\right] \simeq (2\pi)^{-1/2} \int_{-\beta}^{\beta} \exp\left(\frac{-x^2}{2}\right) dx \tag{43}$$

The central-limit theorem via Eq. (43) enables us to quote the probability of an error in an estimate of $\bar{h}$ exceeding the limit of $\pm\beta\sigma/N^{1/2}$, if we know σ^2, the variance, for the process—an unlikely event in a real problem in which we would attempt to evaluate the mean. Nevertheless, a reasonable guess at σ^2 may yield much information about the practicality of a particular problem. The probability that an estimate $\hat{h}$ is in error by more than $\pm\beta\sigma/N^{1/2}$ for various values of β is shown in Fig. 7. The 99% confidence limits can be set at $h \pm 2.58\sigma/N^{1/2}$ (σ is known as the standard deviation).

The central-limit result will hold provided the values of the function $h(x_i) f(x_i)$ are chosen randomly, are mutually independent and bounded. As it is a limiting law holding as $N \to \infty$, its practical value will depend upon how large N need be for the result to hold with useful accuracy. This value for N will depend upon the distribution being sampled. In practice for almost all distributions, $N = 50$ is effectively infinite. As an example, Fig. 8 shows the distribution of the random variable $x = \frac{1}{10} \sum_{i=1}^{10} \epsilon_i$ where the ϵ_i are random numbers rectangularly distributed between 0 and 1. They fit a normal distribution rather well. Most problems of physical interest will or can be made to satisfy these rather weak conditions. Thus for a particle executing a one-dimensional random walk, the expectation value for the number of steps N between successive returns to the origin does not exist. The number of such returns in N steps is in fact proportional to $N^{1/2}$, i.e., a return becomes

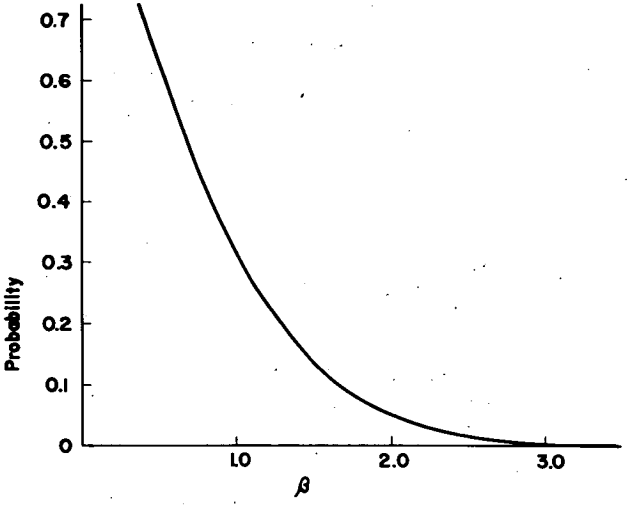

Fig. 7. Probability of an error exceeding $\beta\sigma/N^{1/2}$ for a range of β's.

progressively less likely as the walk proceeds. However, although the ratio of the number of returns to the number of steps does not converge, the expectation value for the ratio of the number of returns to the square of the number of steps does exist, and a limit theorem can be used.

If the mean exists but the variance does not, or is infinite, weaker limiting theorems known as the laws of large numbers will hold. Under slightly different conditions the strong and weak laws assert that the limit

$$\lim_{N\to\infty} \frac{1}{N} \sum h(x_i) f(x_i) = \bar{h} \tag{44}$$

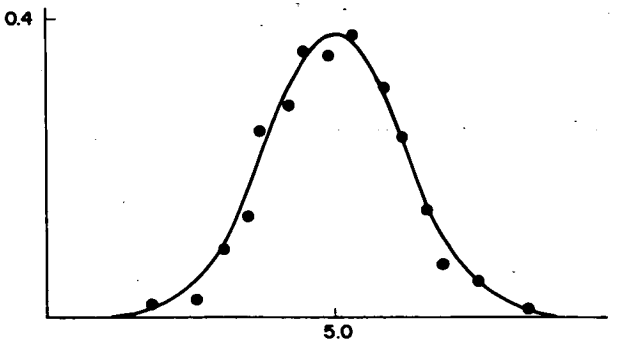

Fig. 8. Distribution of 100 sums of ten random numbers each. The random numbers were drawn from a rectangular distribution. Reprinted from Ref. (*10*), p. 145, by courtesy of John Wiley and Sons. Inc.

still holds, though they can provide no information about the precision of an estimate at a particular N. In practice such problems are unlikely to be profitable targets for the Monte Carlo method, and some transformation of the problems to a more amenable form will be necessary.

E. TIME AVERAGES

Thus far we have been concerned with estimations in which each sample is selected randomly and without memory of previous samples. If this is not the case and the samples are related, as would be in the case in any "time" averaging method where successive samples are snapshots of the system at short intervals of time, rather different problems arise. First, the expectation values we are attempting to compute may themselves be changing with time, i.e., they may be nonstationary. Even for a stationary system it may be found that the time average may not converge to the same value as would be obtained from a random sampling method. This is of course the familiar problem in statistical mechanics of relating time and space averages. Systems in which they may be equated are called *ergodic*, and any part of the system may be reached in a finite number of steps from any other part (*9*, Chapter 15). The requirements for this ergodic behavior are discussed in more detail in Chapter 2, Section III,F.

In real sampling experiments the conditions are more severe, since the number of steps required to pass between any two regions must be small compared to the total number of samples or steps made in the computation. These requirements are discussed in more detail by Wood and Parker (*11*), who describe systems in which time averages converge in the sampling context as quasiergodic. Frequently the practitioner will have to rely upon intuition in deciding whether a particular system and sampling procedure is quasiergodic. The use of a series of different starting configurations to generate (in analogy with the ideas of statistical mechanics) an ensemble of life histories for the model will be of value in deciding upon the ergodicity of a system.

If we confine our attention to *stationary* time averages, i.e., systems in which the expectation values are not themselves changing in time, the time-average properties of a system may be related to moments and distribution functions (*12*). Thus for ergodic systems the cdf $F(x)$ is

$$F(x) = \lim_{T\to\infty} \frac{1}{2T} \int_{-T}^{T} C_x[x(t)]\, dt \tag{45}$$

where

$$C_x[y] = \begin{cases} 1 & \text{if } y \leqslant x \\ 0 & \text{if } y > x \end{cases}$$

More generally, expectation values for a function $h(x)$ (e.g., x^2 for determination of variance) are

$$\bar{h} = \int_{-\infty}^{\infty} h(x) f(x)\, dx = \lim_{T\to\infty} \frac{1}{2T} \int_{-T}^{T} h[x(t)]\, dt \tag{46}$$

where $f(x)$ is the pdf describing the distribution of the time process $x(t)$. The central-limit theorem will also hold for these estimates, $\hat{h}$

$$\hat{h} = \frac{1}{N} \sum_{i=1}^{N} h(x_{t_i}) \tag{47}$$

provided that both the mean and variance of h are finite.

III. Random Numbers—Generation and Testing

The accuracy of sampling methods, whether applied to a real population as in a Gallup poll or to a population formed from a hypothetical model, as in a Monte Carlo calculation, depends upon the sample being typical of the population from which it is drawn. This is usually ensured by selecting cases for inclusion by a purely random process and by taking care to have a sample sufficiently large to represent the fluctuations in the population. The random selection is produced by generating cases from a series of random numbers. The first requirement for the method is thus a supply of "high quality" random numbers.

In a strict sense any noninfinite sequence of numbers cannot be random, since eventually we shall be able to discover a test of randomness that they will fail. It is more convenient to define them operationally. Thus random numbers will be of good quality if they produce an unbiased estimate in a particular problem. For other problems this sequence might be less successful. In practice it is found that sequences meeting a relatively few statistical criteria perform well in a large range of problems.

A. GENERATION OF RANDOM NUMBERS

Random numbers have been generated by a number of physical processes, usually involving the gating of an electronic noise generator to produce a series of pulses. A typical example is the technique used in the generation of RAND's 1,000,000 random digits (*13*). Unfortunately, physical methods of random-number generation are rather slow, and bias is likely to creep in as a result of physical deterioration in the equipment, as in fact happened in the RAND operation. Such a bias can be detected only retrospectively. Physical methods are therefore not suitable for direct coupling to a digital computer.

For such applications an alternative method might be to generate the random numbers off-line and after checking to ensure that they meet the desired statistical specifications store them in the fast-access memory of the computer. Since very large quantities of random numbers are involved, this method is expensive of computer storage and has so far not been widely used. However, machine capacity is increasing, and input devices operating simultaneously with the computation make it desirable to re-examine this approach. In some installations it may well be economic to keep a small store of immediate-access random numbers, "topped up" from a larger store such as a magnetic tape.

For computers in which storage is too "expensive" or scarce to allow for this type of table look-up operation, it is necessary to sacrifice speed to storage limitations and to "compute" the random numbers as required. Such numbers will not be genuinely random, since they are produced by some deterministic sequence of machine operations. They are normally described as pseudorandom numbers. It is difficult to improve the definition of such numbers given by Lehmer (*14*) as "a vague notion embodying the idea of a sequence in which each term is unpredictable to the uninitiated and whose digits pass a certain number of tests traditional with statisticians and depending somewhat upon the use to which the sequence is to be put"! It is worth considering the methods used to obtain such sequences of pseudo-random numbers, since besides their direct application they might conveniently be used to produce off-line stocks of random numbers for use with a table look-up procedure.

Attention will be confined to the generation of uniformly distributed random numbers in the range 0–1, a rectangular distribution. From a distribution of this type it is possible to produce any other distribution of random numbers, as will be described later.

Many methods have been used to generate such sequences of pseudo-random numbers, but multiplicative methods now seem to be in most general use (*15*). They depend upon recurrence relations of the type

$$r_i = (kr_{i-1} + C) \bmod N \qquad 0 \leqslant r_1 < N \tag{48}$$

where the instruction "mod N" means divide $(kr_{i-1} + C)$ by N and take the remainder as r_i; k and C are integers between 0 and $N - 1$.

Thus if $N = 8, k = 5, C = 3$, and $r_0 = 4$, the sequence of random numbers will run

$$4, 7, 6, 1, 0, 3, 2, 5, 4, 7, \ldots$$

The sequence repeats itself after 8 steps, and it can be shown that all such sequences repeat *at least* after N steps. Fortunately, by taking N very large and by choosing suitable values for k and C, the cycle length can be made

longer than the number of random numbers required in any conceivable Monte Carlo calculation (*2*). Most computer software packages now include pseudorandom number generating routines of this general type.

B. TEST FOR RANDOM-NUMBER SEQUENCES

The actual tests employed will depend upon the nature of the problem for which they are required. In general we shall wish the random numbers to be uniformly distributed and (particularly in polymer or other random-walk-type problems) uncorrelated along the sequence.

1. Tests for Uniformity

As a partial test for uniformity we may consider the moments of a sample of the pseudorandom numbers. For a completely uniform random distribution between 0 and 1 the moments must be

$$\text{1st moment} = \frac{1}{N}\sum_{i=1}^{N} x_i$$

$$= \int_0^1 x\,dx = 0.5 \qquad \text{as} \quad N \to \infty$$

$$\text{2nd moment} = \frac{1}{N}\sum_{i=1}^{N} x_i^2$$

$$= \int_0^1 x^2\,dx = 0.333 \qquad \text{as} \quad N \to \infty$$

$$\text{3rd moment} = \frac{1}{N}\sum_{i=1}^{N} x_i^3$$

$$= \int_0^1 x^3\,dx = 0.250 \qquad \text{as} \quad N \to \infty$$

and so on.

A particular sequence of 30,000 pseudorandom numbers generated by a multiplicative method with $r_0 = 0173161123$, $k = 2973357946$, and r_i taken as the least significant ten digits divided by 10^{10} gave the moments shown in Table 1. The central-limit theorem result may be used to examine these moments. It can be shown that estimates of each moment will be approximately normally distributed about the expectation value. Thus our estimate of the first moment $\hat{x}$ will have a variance

$$\frac{\text{var}(x)}{N} = \frac{\sigma^2}{N}$$

TABLE 1
MOMENTS OF A PARTICULAR SEQUENCE OF 30,000 PSEUDORANDOM NUMBERS

Moment	Found	Expected	Deviation
1st	0.49839	0.5000	−0.00161
2nd	0.33116	0.3333	−0.00217
3rd	0.247715	0.2500	−0.0023
4th	0.197763	0.2000	−0.002237

so that

$$\mathscr{P}[|[x - E(x)](\sigma/N^{1/2})| < \beta] = (2\pi)^{-1/2}\int_{-\beta}^{\beta} \exp\left(\frac{-y^2}{2}\right) dy$$

The value of β chosen provides confidence limits for the deviation $|\hat{x} - E(x)|$, for example 99% confidence limits are given by $\beta = 2.58$; i.e., in only one calculation of $\hat{x}$ in a hundred do we expect the deviation to exceed $2.58\ \sigma/N^{1/2}$. The exact confidence limit at which we choose to reject the hypothesis that our estimated moments are compatible with a uniform distribution of random numbers is a subjective matter. Nevertheless, a deviation greater than the 99% limits would be surprising enough to raise doubts about the uniformity of the distribution.

The variance of the population can be calculated as

$$\text{var}(x) = \int_0^1 x^2\, dx - \left(\int_0^1 x\, dx\right)^2$$

Using the central-limit theorem we find the 31.7% confidence limits on our estimate of the first moment are

$$\left(\frac{0.0833}{30{,}000}\right)^{1/2} = \pm 0.0017$$

i.e., 31.7% of first moments calculated from a sample of this size would be expected to differ from the exact mean for the population by more than 0.0017. The deviation actually found (0.0016) is thus in accord with our hypothesis that the random numbers are uniformily distributed. Similarly for the second moment:

$$\text{var}(x^2) = \int_0^1 (x^2)^2\, dx - \left(\int_0^1 x^2\, dx\right)^2$$
$$= 0.0889$$

The 31.7% limits are now

$$\left(\frac{0.0889}{30{,}000}\right)^{1/2} = \pm 0.0017$$

compared with an observed deviation of 0.00217, which is likely to be exceeded in about 12% of cases (see Fig. 7). The deviations of the moments are thus, with quite high probability, not different from those that might be observed in a sample drawn from a population with a truly rectangular distribution. On the basis of these tests we have no grounds for rejecting the hypothesis that the random numbers are rectangularly distributed.

The uniformity of the distribution can be further tested by dividing the range into a series of intervals. The frequency with which random numbers

TABLE 2
FREQUENCY OF PSEUDORANDOM NUMBERS IN TEN EQUAL INTERVALS

Interval	Observed frequency f_j	Expected frequency f_j
0–0.1	2,487	2,555
0.1–0.2	2,521	2,555
0.2–0.3	2,559	2,555
0.3–0.4	2,553	2,555
0.4–0.5	2,631	2,555
0.5–0.6	2,583	2,555
0.6–0.7	2,491	2,555
0.7–0.8	2,627	2,555
0.8–0.9	2,557	2,555
0.9–1.0	2,561	2,555
Total	25,550	

fall into each interval can then be compared with that predicted for a uniform distribution. Such a test was applied to a sample of 25,550 random numbers generated by the same multiplicative routine as before.

The random numbers (x_i) in the sequence were sorted into ten classes corresponding to ten equal intervals in x by applying the test

$$(j - 1)/10 \leqslant x_i \leqslant j/10$$

where j assumes integral values from 1 to 10. The total number of random numbers in each class was then recorded as f_j, The results of the tests are shown in Table 2. From the results of the table it can be seen straightaway that the distribution is at least resonably uniform. A more revealing test, however, can be made by making use of the properties of the χ^2 distribution (*10*, Chapter 10).

For Table 2, if the hypothesis of uniform distribution is correct, the

statistic:

$$\sum \frac{(f_j - \bar{f}_j)^2}{f_j} = 8.67 \tag{49}$$

must be distributed with a χ^2 distribution of nine degrees of freedom (10 − 1, since the total number of random numbers in the table is known in advance). By reference to tables of the χ^2 functions we find that 95% of statistics calculated from data for which the uniform hypothesis is correct will yield $\chi^2 < 16.919$, while only 5% will have $\chi^2 < 3.325$. The value 8.67 found here is thus in the center of the range expected and supports the hypothesis of randomness in the number sequence tested.

2. Tests for Serial Correlation

To test for serial correlations, i.e., any periodicity in the sequence, we may use a rather more elaborate version of Table 2 and the χ^2 test. In this test we compute the frequencies f_{jk} with which our random numbers x_i, x_{i+1}, . . . satisfy the conditions

$$\frac{j-1}{10} \leqslant x_i \leqslant \frac{j}{10} \quad \text{and} \quad \frac{k-1}{10} \leqslant x_{i+h} \leqslant \frac{k}{10}$$

where $h = 1, 2, 3$, etc. to test for various periods of correlation. The numbers x_i are thus divided into 100 classes and once again we may use the χ^2 test to compare the observed class frequencies with those predicted for a truly random distribution. As an example, Table 3 shows the result obtained

TABLE 3

CORRELATION BETWEEN ADJACENT NUMBERS f_{jk} IN SEQUENCE

j	k									
	0	1	2	3	4	5	6	7	8	9
0	245	270	257	231	242	263	245	270	232	231
1	257	214	237	248	257	256	270	271	250	261
2	262	256	266	280	272	247	255	233	250	234
3	272	249	278	269	233	249	232	267	259	225
4	291	267	237	273	258	264	245	262	246	278
5	260	274	251	262	273	281	275	227	243	237
6	251	230	238	256	258	237	241	250	266	264
7	227	256	248	270	300	277	282	260	239	267
8	258	257	231	243	247	250	251	280	247	265
9	254	247	254	227	261	261	250	285	271	244

Total = 25,500

from the same sample of 25,500 numbers with $h = 1$. The statistic is now

$$\chi^2 = \sum_{j=1}^{10} \sum_{k=1}^{10} \frac{(f_{jk} - \bar{f}_{jk})^2}{f_{jk}} \tag{50}$$

The expected value in each class ($\bar{f}_{jk}$) is 255. From Table 3, χ^2 is calculated as 107.4. In comparison, tabulated values for χ^2 for 99 degrees of freedom show the following limits:

$\chi^2 > 77$ for approx. 95% of samples
$\chi^2 < 124$ for approx. 5% of samples

Thus 90% of samples will lie in the range 77–124. A value of 107.4 is well within the likely range of distribution. The results in Table 3 thus show no evidence of adjacent-pair correlation. The test may be repeated for larger values of h to test for longer periods in the sequence.

This particular sequence seems to meet the most important criteria of randomness. Many other tests can be applied and may be important for particular applications. Nevertheless, the ultimate test for all number sequences will be their successful use in a specific problem. Sequences meeting the tests discussed here can be expected to perform well in most applications.

C. EFFICIENCY OF RANDOM-NUMBER GENERATION METHODS

The random-number routine will usually be required at every iteration in a Monte Carlo computation and will often appear in the innermost loop of the program. The time required for the generation of the random number can then be an appreciable fraction of the total computing time required for a problem.

Typical multiplicative sequences require on the order of 5 basic instructions equivalent to about 10 microseconds per random number at current machine speeds. Other methods of generation, e.g., by additive processes that require fewer instructions, have been suggested, though not widely adopted. A generator of this type is described by Taussky and Todd (*15*).

The efficiency of the alternative procedure in which a stock of random numbers is maintained on a tape or disc store depends critically on the reading speed, the rate at which random numbers are required, and the characteristics of the machine. A problem that required several random numbers in rapid succession followed by a longer pause would obviously be less demanding in read-in speed if a rapid-access buffer store were available. Magnetic-tape reading speeds are now in the range of 100,000 characters per second. Other large-capacity stores, such as discs or drums, have speeds on the order of 200,000 characters per second. Average demand rates up to

20,000 ten-digit random numbers per second can thus be met, with the possibility of higher peak rates if a rapid-access buffer store is used. For machines working in a time-sharing multiple-access mode (as is increasingly the case) other considerations arise. In such installations it is possible to arrange for machine time that would otherwise be wasted during the random-number read-in to be used for other purposes, the economic penalty so being avoided.

In all cases read-in rather than generation is likely to be much more useful if the random variables required are of a specialized nature, i.e., drawn from a particular frequency distribution. Alternatively, it is possible to input details of a particular random sample of case histories, e.g., of polymer configurations. Such samples could then be weighted approximately and used in normal Monte Carlo averaging. In such application the case histories might be the result of previous Monte Carlo calculations.

IV. Techniques for Transforming Random-Number Distributions

So far we have discussed the generation of rectangularly distributed random numbers only. Random numbers with other distributions will often be required and can usually best be obtained by transforming a series of rectangularly distributed numbers.

The procedure is particularly simple if we wish to choose between discrete events. Consider the events of E_i, E_j, E_k, which exhaust the sample space and have normalized probabilities $\mathscr{P}_i$, $\mathscr{P}_j$, $\mathscr{P}_k$ ($\mathscr{P}_j + \mathscr{P}_i + \mathscr{P}_k = 1.0$). If ϵ_i is a random number distributed uniformly between 0 and 1, the probabilities for choosing E_i, E_j, E_k can be realized by casting lots, i.e.,

$$\begin{aligned} &E_i \text{ to occur if} && 0 \leqslant \epsilon_i \leqslant \mathscr{P}_i \\ &E_j \text{ to occur if} && \mathscr{P}_i < \epsilon_i \leqslant \mathscr{P}_i + \mathscr{P}_j \\ &E_k \text{ to occur if} && \mathscr{P}_i + \mathscr{P}_j < \epsilon_i \end{aligned} \tag{51}$$

In a similar way, using the transition probabilities, a Markov chain can be realized Thus if the states $A_1, A_2, \ldots, A_n$ are the possible outcomes, and the matrix of transition probabilities is

$$\begin{pmatrix} P_{11} & P_{12} & \cdots & P_{1n} \\ P_{21} & P_{22} & \cdots & P_{2n} \\ \cdot & \cdot & \cdots & \cdot \\ \cdot & \cdot & \cdots & \cdot \\ \cdot & \cdot & \cdots & \cdot \\ P_{n1} & P_{n2} & \cdots & P_{nn} \end{pmatrix} \tag{52}$$

Then at each state A_i, lots will be cast to determine the succeeding state A_j, This realization with the appropriate probabilities can be effected by solving the following equation for j:

$$\sum_{k=1}^{j-1} \mathscr{P}_{ik} < \epsilon \leqslant \sum_{k=1}^{j} \mathscr{P}_{ik} \tag{53}$$

where ϵ is a uniformly distributed random number.

For more complicated transformations involving continuous distributions several general methods are available (*3*, *5*).

A. INVERSION OF THE CUMULATIVE DISTRIBUTION FUNCTION

Consider a normalized pdf, $f(x)$, and its cdf, $F(x)$. From the properties of a probability, $F(x)$ must be a monotonically increasing function of x (see Fig. 9) ranging between 0 and 1.

The probability of choosing a random number ϵ_i from a uniform distribution that corresponds to a value of $x = x_i$ in Fig. 8 is

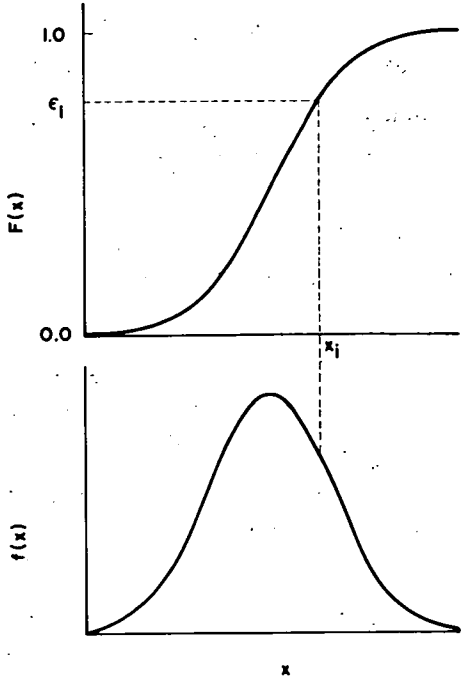

Fig. 9. Transforming from a uniform distribution by inverting the cdf. The uniform random number ϵ_i transforms to x_i with the desired distribution.

$dF/dx_i = f(x_i)$; but

$$\epsilon_i = F(x_i) = \int_{-\infty}^{x_i} f(x)\,dx \tag{54}$$

Thus the x_i corresponding to a sequence of ϵ_i are distributed according to the pdf $f(x)$. Inversion of Eq. (54) will therefore yield a relation for transforming a uniform distribution of random numbers into a distribution with pdf $f(x)$.

As an example the pdf e^{-ax} where x may run from 0 to ∞ can be sampled in this fashion. Relation (54) is now

$$\epsilon_i = \int_0^{x_i} \exp(-ax)\,dx$$

$$= \frac{[1 - \exp(-ax_i)]}{a}$$

so that

$$x_i = \frac{-\ln(1 - a\epsilon_i)}{a} \tag{55}$$

provides a source of random numbers x_i with an exponential distribution.

This method is of general use provided only that relation (54) can be inverted. In some cases the inversion, while possible, may lead to a complicated expression involving several exponentials, etc. In such cases alternative methods may be less expensive of computer time.

B. REJECTION TECHNIQUE

If the inversion method is inconvenient or impossible, the rejection technique may provide a suitable alternative. Once again uniformly distributed random numbers are used, but in this method they are subjected to a test, the outcome of which is determined by another random number. The test is so arranged that those numbers satisfying it have the desired distribution. The basis of the method can be understood from Fig. 10. M_x is the maximum value of the required pdf $f(x)$, which is zero outside a, b. The prescription for producing a sequence of random numbers with the desired distribution is to choose a pair of random numbers ϵ_i, η_i from a uniform distribution. They are then used to define a location in the rectangle (dashed in Fig. 10).

$$\begin{aligned} x_i &= \epsilon_i(b - a) + a \\ f_i &= M_x\eta_i \end{aligned} \tag{56}$$

These locations are uniformly distributed about the rectangle.

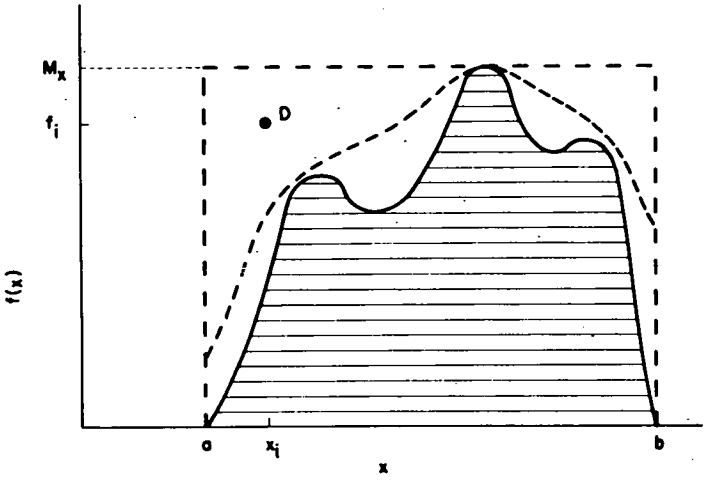

Fig. 10. Realization of a pdf by rejection. The desired pdf is represented by the shaded area. The point $D(f_i, x_i)$ would be rejected.

$$\begin{aligned} &\text{If } f_i \leqslant f(x_i) && x_i \text{ is accepted as a random number from the pdf } f(x). \\ &\text{If } f_i > f(x_i) && \text{a new pair of random numbers is generated and the process repeated.} \end{aligned} \tag{57}$$

For any x the probability of occurrence in the final sequence is

$$\mathscr{P}[x] = \mathscr{P}[\text{being chosen in step 1}]\mathscr{P}[\text{acceptance in step 2}]$$

In this example since the initial distribution of x_i is uniform:

$$\mathscr{P}[x] = f(x)$$

While this method may be used to generate a sequence of random numbers of any distribution that is bounded, it may be very inefficient if the number of x_i rejected at step 2 is high. In Fig. 10 the fraction of numbers accepted is represented by the ratio of the shaded area to that of the whole rectangle, i.e.,

$$\text{fraction accepted} = \frac{\int_a^b f(x)\,dx}{(b-a)M_x} = \frac{1}{(b-a)M_x} \tag{58}$$

If both the rejection and inversion methods are unsatisfactory alone, the two may be combined with advantage. Thus in Fig. 10 we could decrease the rejection rate by sampling locations not in the rectangle but in some figure that enclosed the desired $f(x)$ but was of smaller area than the rectangle.

To use this technique we factor the pdf we wish to realize, say $f(x)$, as

$$f(x) = h(x)\, G[k(x)] \tag{59}$$

where the distributions $h(x)$ and $G[y]$ (a cdf) are chosen so as to be conveniently realizable (e.g., by an inversion method), and $k(x)$ is a function at our disposal.

The prescription is then much as for the simple rejection method. We pick a location x_i, y_i; x_i is chosen from the pdf $h(x)$ and y_i from the distribution $g(y)$ (cumulative distribution $G[y]$).

$$\begin{aligned} &\text{if} \quad y_i \leqslant k(x_i) \qquad \text{then } x_i \text{ is accepted} \\ &\text{if} \quad y_i > k(x_i) \qquad \text{then the process is repeated} \end{aligned} \tag{60}$$

The probability of accepting x_i at the first step, i.e., of $y \leqslant k(x_i)$, is

$$G[k(x_i)]$$

The overall probability of x_i occurring in the final sequence is therefore

$$h(x_i)\, G[k(x_i)] = f(x_i)$$

as desired.

The probability of acceptance at each trial is

$$\int_{-\infty}^{\infty} h(x)\, g[k(x)]\, dx \tag{61}$$

For good efficiency this probability should be high. In general we shall want $h(x)$ to mimic $f(x)$ as closely as possible (cf. the broken curve on Fig. 10).

C. COMPOSITION METHODS

The composition method, like the rejection method, is also based upon compounding probabilities. If the pdf we wish to realize can be expressed in the form

$$f(x) = \int_{-\infty}^{\infty} h_z(y)\, dG(z) \tag{62}$$

where $h_z(y)$ represents a family of distribution functions related through the parameter z and $G(z)$ is a cumulative distribution function, then from Eq. (62) we see that $f(x)$ can be realized by a two-stage sampling process. The first random number is drawn from the distribution $G(z)$ and is used to select a particular $h_z(y)$ from its family of related pdf's. The second random number is then drawn from this distribution $[h_z(y)]$ and will have the desired pdf.

D. PIECEWISE FITTING

If no convenient or efficient generating method exists for a particular distribution, it may often be sufficiently accurate to use a piecewise approximation to the required distribution. Figure 11 shows the method. The distribution to be realized is the solid curve. It must be bounded or truncated and is then divided into a number of regions $(C_i - C_{i-1})$, $(C_{i+1} - C_i)$, etc. Each region is associated with a fixed probability k_i chosen as an approximation to the required probability $f(x)$ in that region. The probability of a sample drawn from $f(x)$ lying in the interval $(C_{i+1} - C_i)$ is

$$\int_{C_i}^{C_{i+1}} f(x)\,dx = k_i \tag{63}$$

But $\int_a^b f(x)\,dx = 1$, since $f(x)$ is a normalized pdf. Therefore, $\sum k_i = 1.0$. Thus if n intervals provide a sufficiently good approximation to $f(x)$, we may choose convenient C_i's and evaluate all the k_i's. A specific interval j can then be chosen in accordance with its probability by solving the relations for j:

$$\epsilon \leqslant \sum_{i=1}^{j} k_i, \qquad \epsilon > \sum_{i=1}^{j-1} k_i \tag{64}$$

A value for x_j is finally obtained by selecting another random number η (again from a uniform distribution) and using the relation

$$x_j = C_{j-1} + \eta(C_j - C_{j-1}) \tag{65}$$

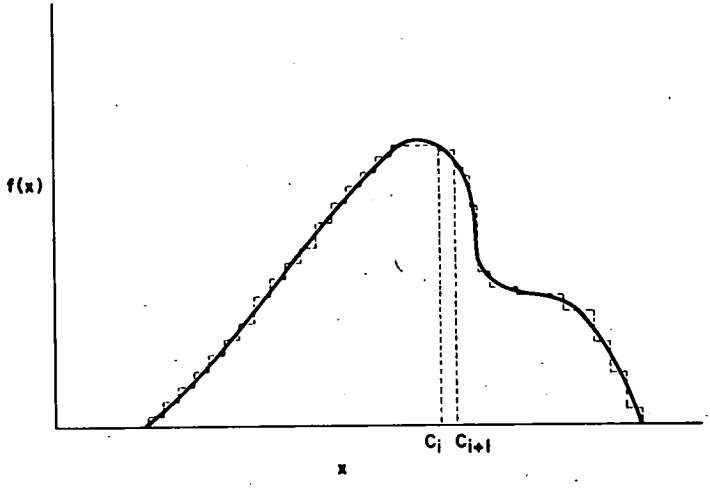

Fig. 11. Piecewise fitting. The pdf (solid curve) is approximated by the dotted line.

This method is often of special value when used in conjunction with a correction or weighting factor. The value of x_j found in Eq. (65) can then be awarded a weighting factor w_j so that the piecewise approximation to the probability combines with the weight to produce the exact probability. For example, if the value of x chosen, x_j, falls in the region $C_i - C_{i-1}$ then

$$w_j = f(x_j)/k_i$$

The use of these weights is discussed in more detail later.

E. EXAMPLES OF USEFUL TRANSFORMATIONS

For the more commonly used distributions rather efficient transformation methods have been developed, some of which are listed here. A more comprehensive account is given by Khan (*3*).

Once again ϵ_i, η_i, ρ_i represent random numbers from a uniform distribution between 0 and 1.

1. Normal Distribution

$$f(x) = \left(\frac{2}{\pi}\right)^{1/2} \exp\left(\frac{-x^2}{2}\right) \qquad -\infty \leqslant x \leqslant \infty \tag{66}$$

a. Central-Limit Theorem. One of the simplest methods relies upon the central-limit result that the sum of a large number of independent random variables is normally distributed.

The relation used is

$$x_i = 2\left(\sum_{i=1}^{N} \epsilon_i\right) - N \tag{67}$$

For applications in which the tails of the distribution are not of special

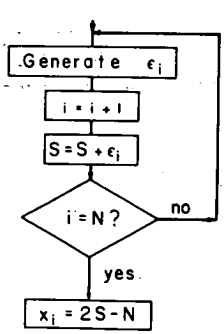

Fig. 12. Block diagram of generation of normally distributed random numbers x_i from uniformly distributed random numbers ϵ_i using the central-limit theorem.

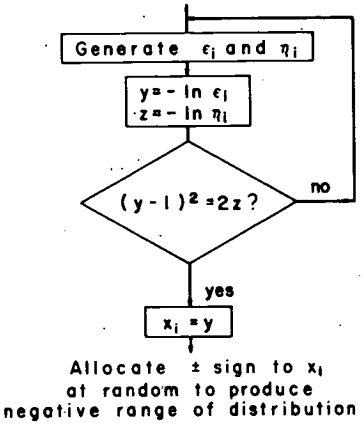

Fig. 13. Block diagram of generation of normally distributed random numbers x_i from uniformly distributed random numbers ϵ_i, η_i, and ρ_i using a rejection technique.

interest, N may be $\sim$10. The procedure is illustrated by the block diagram in Fig. 12. Faster convergence to the asymptotic behavior may be achieved by a further transformation (*16*).

b. Rejection Techniques. A straightforward application of the rejection method yields the prescription shown in Fig. 13. The probability of the acceptance at each trial is 0.76.

2. Sine and Cosine Distributions

The prescription shown in Fig. 14 generates the sine and cosine of a uniformly distributed angle by a rejection method. This procedure is considerably more efficient in machine time than the alternative of generating a random angle and then computing its cosine or sine.

3. Random Square Roots

The straightforward generation of a random square root by taking

$$x_i = \sqrt{\epsilon_i} \tag{68}$$

is a rather time consuming process because of the square-root extraction. The same distribution can be achieved more rapidly by a rejection method. By reversing the arguments used in discussing the inversion method, we can show that the x_i generated by Eq. (68) will have a pdf $= 2x$. Choosing a random number from this distribution will be equivalent to Eq. (68). An especially simple technique can be used for this pdf. Two random numbers are generated, ϵ_i, η_i, and the larger of the two is accepted. The probability

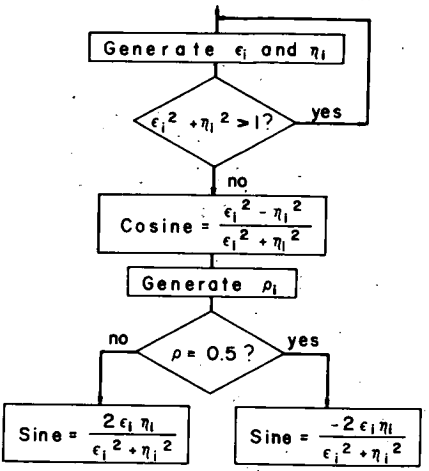

Fig. 14. Block diagram of generation of sine and cosine of uniformly distributed angles from uniformly distributed random numbers ϵ_i, η_i, and ρ_i.

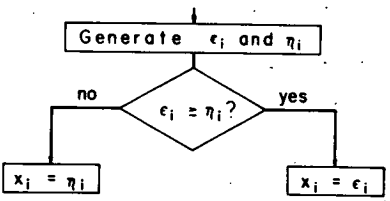

Fig. 15. Block diagram of generation of random square roots from uniformly distributed random numbers ϵ_i and η_i.

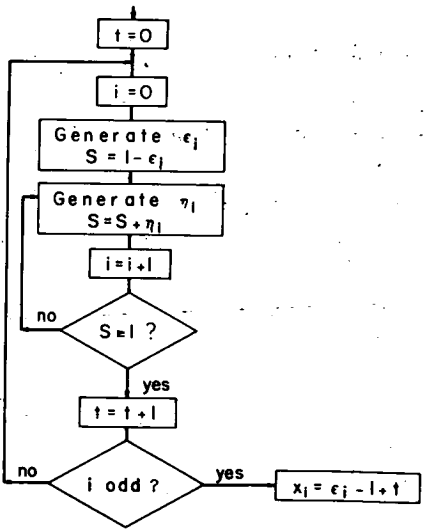

Fig. 16. Block diagram of generation of exponentially distributed random numbers x_i from uniformly distributed random numbers ϵ_i and η_i using a rejection technique.

of either being accepted is given by their cdf, i.e., x. The distribution generated is the sum, $2x$.

This is illustrated in Fig. 15 and is a special case of a more general method. The distribution nx^{n-1} can be realized by choosing the largest of n independent numbers.

4. Exponential Distribution

An exponential distribution can be achieved by an inversion method discussed in Section IV,A. Alternatively a rejection technique due to Von Neumann can be used (*3*, *17*) as shown in Fig. 16.

V. The Monte Carlo Method

As discussed in the beginning of this chapter, the term Monte Carlo has been employed to describe a wide range of procedures involving the notion of sampling. In a straightforward simulation the high speed of digital computers is used to explore the properties of a system not susceptible to conventional mathematical analysis. For example, much work has been carried out on war games in which the effect of different strategies can be rapidly examined. In other applications the mathematical model being sampled may bear little immediately apparent relation to the real situation; such transformations may often drastically reduce the amount of computation required to produce a satisfactory accuracy.

In many applications the Monte Carlo technique is essentially used to perform a multidimensional integration. As an example of special interest here we may consider the self-avoiding random walk on a lattice, which is the model for many treatments of the polymer molecule. This is closely related to a multidimensional integral over all the configurations of the molecular chain. For the purposes of discussing the Monte Carlo method in more detail it is therefore convenient to consider its application to integration.

A. PLAIN METHOD

Consider the trivial example used in Section I of the estimation of

$$I = \int_a^b f(x)\,dx \tag{1}$$

We have already seen from the central-limit theorem that the estimate

$$\hat{I} = \frac{b-a}{N}\sum_{i=1}^{N} f(\epsilon_i) \qquad a \leqslant \epsilon_i \leqslant b \tag{2}$$

is normally distributed about the true value $\hat{I}$. The 95% confidence limits on $\hat{I}$ are

$$\pm 2\sigma/N^{1/2} \tag{69}$$

where σ^2 is

$$\text{var}[f(x)] = \int_a^b [f(x) - I]^2 \, dx$$

$$\sigma^2 = \int_a^b [f(x)]^2 \, dx - \left(\int_a^b f(x) \, dx \right)^2 \tag{70}$$

For a precision in the estimate $\hat{I}$ of $\pm E$ (with, say, 95% confidence) the work needed will be

$$\text{work} = N\tau = (2\sigma/E)^2\tau \tag{71}$$

where τ is the time or cost per sample or iteration of the calculation. The efficiency is optimum when σ^2 is a minimum.

The Monte Carlo method will clearly not yield high accuracy, since the work increases very rapidly as E is decreased. Convergence is only proportional to $N^{-1/2}$; e.g., a tenfold improvement in precision requires a hundred fold increase in the number of samples.

In real applications it is very unlikely that we would have a priori knowledge of the variance of $f(x)$. It is more usual to calculate a *sample* variance as the computation proceeds. Simultaneous estimates of $\hat{I}$ and var$[f(x)]$ are thus obtained. For large N, var$[f(x)]$ can be estimated as

$$\text{var}[f(x)] = \frac{1}{N} \sum f(\epsilon_i)^2 - \frac{1}{N^2} [\sum f(\epsilon_i)]^2 \tag{72}$$

The accuracy of our estimate of the error thus increases as the calculation proceeds. Figure 17 shows typical behavior. The error bars represent 95% confidence limits calculated using the sample variance. Initially they are wildly optimistic, but as the calculation proceeds the estimates become more realistic. The separate curves represent repetition of identical calculations with different random-number sequences. It is interesting to note that as the calculation proceeds the estimates do not oscillate about the true value but rather converge slowly from one side or the other. This is characteristic of this type of calculation and can be understood in terms of the first arc sine law (*9*, Chapter 3).

It can be shown that the number of occasions on which the curve crosses the exact value is proportional to $N^{1/2}$. As N increases, such crossings become less and less frequent. More specifically the probability P of the curve spending less than a fraction a of the total number of iterations on one

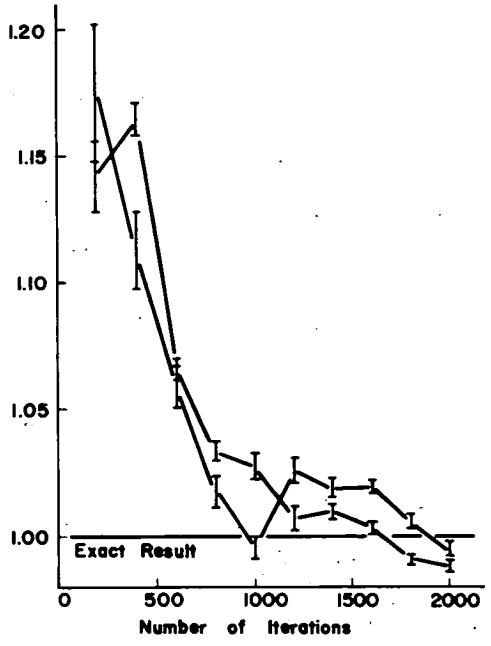

Fig. 17. Convergence of Monte Carlo estimate to the exact result. Two sets of results for different random number sequences are shown (*16*).

particular side of the exact value is

$$P = \frac{2}{\pi} \arcsin a \tag{73}$$

Thus with probability 0.287, the curve will spend 95% of the time on one side of the exact value.

The rate at which Monte Carlo calculations converge, given by Eq. (69), is very slow compared to that of a more conventional numerical integration. Thus in the well known Simpson Quadrature the integration is performed by a systematic advance across the region to be integrated. The function is evaluated at regular intervals h, N in number (N must be even). Then

$$I = \tfrac{1}{3}h(f_0 + 4f_1 + 2f_2 + 4f_3 + \cdots + 2f_{n-2} + 4f_{n-1} + f_n) \tag{74}$$

In this method the error decreases as N^{-4}. Other systematic methods can perform even better. Nevertheless, as the number of dimensions in the integral increases, the Monte Carlo method becomes advantageous.

In the systematic methods similar to Eq. (74) the number of intervals (or

samples using the Monte Carlo description) increases exponentially with the dimensionality of the problem. This is not the case with the Monte Carlo approach, where the efficiency depends upon the variance σ^2. It is of course true that σ^2 also tends to increase with the dimensionality of the integral. However, this is not a necessary situation, and by special sampling techniques it may be overcome. As a rule of thumb, integrations in six or more dimensions are usually better performed by Monte Carlo methods.

B. IMPROVING EFFICIENCY

From relation (69) we can see that the speed of the method might be improved in two ways: by increasing the convergence rate, i.e., the $N^{-1/2}$ dependence, or by decreasing the variance. The latter method has so far met with more success.

1. Quasirandom Sampling

The rate of convergence can be improved by the use of *quasi*random samplings. Such sampling is not truly random and is based upon a number sequence equidistributed in such a way as to produce an unbiased estimate but with a faster convergence. Such methods might be roughly described as following a self-avoiding trajectory through the sample space, in this way avoiding wasteful duplication due to several random-sample points falling in close proximity. Prescriptions for generating such sequences are described by Haselgrove (*18*). They are also discussed by Hammersley and Handscomb (*5*).

2. Variance Reduction

In most practical applications of the Monte Carlo method attention has been concentrated upon reducing the variance of the sampling process rather than the use of quasirandom number sequences. Essentially similar results can be achieved. Thus subdividing the region of integration into several smaller ones goes some way to ensuring the equidistribution of sampling produced by quasirandom sampling.

In all cases the variance reduction depends upon using information about the integral or process being studied to improve the sampling procedure. This information might be available before the computation or might be accumulated during the process of computation.

a. Correlated Sampling. It should already be clear that the Monte Carlo method is one of the last resort. If part of the problem can be handled analytically, it should be. Correlated sampling can be understood by

returning to the original example:

$$I = \int_a^b f(x)\,dx \tag{1}$$

and its variance

$$\sigma^2 = \int_a^b [f(x)]^2\,dx - \left[\int_a^b f(x)\,dx\right]^2 \tag{70}$$

If we can find a function $h(x)$ that can be integrated exactly over the range a to b, then the integral (1) can be written as

$$I = \int_a^b [f(x) - h(x)]\,dx + \int_a^b h(x)\,dx$$

and estimated as

$$\hat{I} = \frac{(b-a)}{N}\sum_{i=1}^{N}[f(\epsilon_i) - h(\epsilon_i)] + J \qquad a \leqslant \epsilon_i \leqslant b \tag{75}$$

where J is the exactly calculable integral of $h(x)$. The variance of the estimate of I using Eq. (75) is

$$\sigma_*^2 = \int_a^b [f(x) - h(x)]^2\,dx - (J - I)^2 \tag{76}$$

The virtue of this procedure is apparent if we choose $h(x)$ to mimic $f(x)$ as closely as possible. σ_*^2 will then be smaller than σ^2 and the labor required to estimate I to a given precision much reduced. Thus if an approximate solution [e.g., $h(x)$] exists, it may be advantageous to estimate the difference between the approximate and the exact results. The correlation between the solutions then serves to reduce the variance.

b. Stratified Sampling. Stratified sampling is a technique widely used in surveys, polls, etc. Samples are no longer picked at random from the whole range; instead, the sample space is broken into a number of regions. A specific number of samples is then drawn from each region. For example, integral (77) is equivalent to

$$I = \int_a^b f(x)\,dx = \int_{C_0}^{C_1} f(x)\,dx + \int_{C_1}^{C_2} f(x)\,dx + \cdots \int_{C_{n-1}}^{C_n} f(x)\,dx$$

where $C_0 = a$ and $C_n = b$.

If we take M_i samples from each region our estimate of I will be

$$\hat{I} = \sum_{i=1}^{n} \frac{C_i - C_{i-1}}{M_i} \sum_{j=1}^{M_i} f(\epsilon_j) \qquad C_{i-1} \leqslant \epsilon_j \leqslant C_i \tag{77}$$

The variance of this estimate is

$$\sigma_*^2 = \sum_{i=1}^{n} \frac{(C_i - C_{i-1})^2 \sigma_i^2}{M_i} \tag{78}$$

where

$$\sigma_i^2 = \frac{1}{C_i - C_{i-1}} \int_{C_{i-1}}^{C_i} [f(x)]^2 \, dx - \left(\frac{1}{C_i - C_{i-1}} \int_{C_{i-1}}^{C_i} f(x) \, dx \right)^2$$

The estimator in Eq. (77) has a number of variable parameters describing the division of the sample space into regions and the number of samples to be drawn from each region. By their proper selection the variance σ_*^2 can be reduced compared with that of the simple Monte Carlo estimate.

To achieve this improvement we must:

(1) Choose the individual regions so that the individual σ_i^2 of Eq. (78) are as small as possible. This is equivalent to choosing regions in which $f(x)$ fluctuates as little as possible.

(2) Allocate the number of samples to be drawn from each region. The optimum strategy for this can be found by minimizing Eq. (78) subject to the limitation $\sum M_i = M$.

The minimum occurs when

$$\frac{M_i}{M} = \frac{(C_i - C_{i-1})\sigma_i}{\sum_{i=1}^{n} (C_i - C_{i-1})\sigma_i} \tag{79}$$

M is the total number of samples taken in all regions. The strategy suggested thus allocates samples to each region in proportion to the product of its range and standard deviation. Where either or both of these are large, the error will also tend to be large and correspondingly more samples will be needed. To make this optimum allocation would require knowledge of the σ_i's, an unlikely situation. These will usually have to be estimated; in the absence of better information we might take all σ_i as equal. Even this very rough and ready approximation will lead to a decrease in variance.

c. Importance Sampling. An alternative procedure in which we replace our estimated σ_i's by similar values for I_i's is known as importance sampling, i.e., a strategy in which samples are allocated according to the size of the contribution a region makes to the overall result. This method however is usually applied in a rather more flexible form.

Using the sample of Eq. (1) again we can see that

$$I = \int_a^b f(x) \, dx = \int_a^b \frac{f(x)\, h(x)}{h(x)} \, dx \tag{80}$$

and equivalently the estimates of I are

$$\hat{I} = \frac{a-b}{N}\sum f(\epsilon_i) = \frac{a-b}{N}\sum \frac{f(\eta_i)}{h(\eta_i)} \tag{81}$$

where ϵ_i is drawn from a uniform distribution between a and b as usual. The other random numbers η_i however are drawn from the pdf $h(x)$. The function $h(x)$ must of course have the properties of a pdf in the range a to b, i.e., positive throughout and with

$$\int_a^b h(x)\,dx = 1$$

The new estimator in Eq. (81) will still yield an unbiased result for $\hat{I}$, but the variance of the two estimates will be different. For the straightforward sampling,

$$\sigma^2 = \int_a^b [f(x) - I]^2\,dx \tag{82}$$

For the new estimator,

$$\sigma_*^2 = \int_a^b \left(\frac{f(x)}{h(x) - I}\right)^2 h(x)\,dx \tag{83}$$

The advantages of this estimator lies in the choice of $h(x)$—our sampling pdf. By choosing more samples in the region of the integral that contributes most importantly to I, we can reduce the variance. More formally, from Eq. (83) we see that by choosing

$$h(x) = f(x)/I \tag{84}$$

we obtain a zero variance. Every sample of $f(x)$ chosen when multiplied by the *weighting function* $h(x)$ yields exactly the result I. Unfortunately, this optimum sampling scheme for I can only be achieved with a knowledge of I, and we have a circular situation. However, by good choice of a sampling function we can decrease the variance—in principle to zero. Conversely, a bad choice of sampling function can increase the variance. The method must therefore be applied with discretion.

d. Antithetic Variates. The antithetic-variates prescription depends upon choosing two or more samples simultaneously with a negative correlation. As an example consider Fig. 18. We may choose samples from this function with the required negative correlation by taking $f(\epsilon_i)$ and $f(b - \epsilon_i)$. (ϵ_i is as usual uniformly distributed.) The estimate of I will be

$$\hat{I} = \frac{b}{N}\sum \left[\frac{f(\epsilon_i)}{2} + \frac{f(b-\epsilon_i)}{2}\right] \tag{85}$$

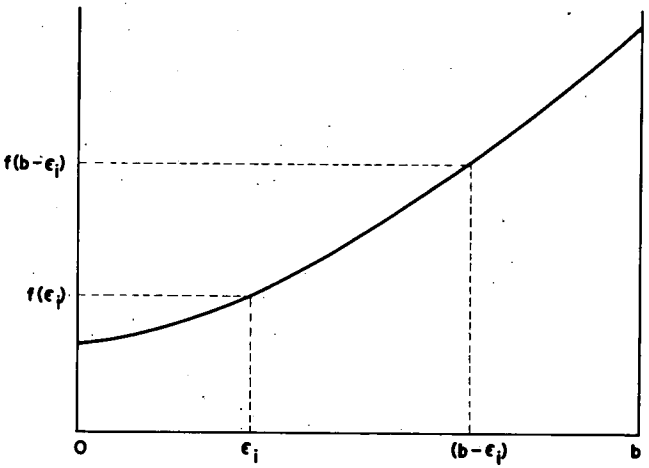

Fig. 18. Antithetic samplings.

The variance of this process is reduced compared to that of plain Monte Carlo sampling. For example, in Fig. 18 the lower-than-average value of $f(\epsilon_i)$ is partially compensated by the higher-than-average value $f(b - \epsilon_i)$. The variance of the estimate in Eq. (85) is correspondingly reduced. Obviously this compensation or negative correlation between the two samples arises from the monotonic character of the function.

More formally, the variance of estimate (85) is

$$\sigma_*^2 = \tfrac{1}{4}\sigma^2(I_1) + \tfrac{1}{4}\sigma^2(I_2) + \tfrac{1}{2}\,\mathrm{covar}(I_1, I_2) \tag{86}$$

where $\sigma^2(I_1)$ and $\sigma^2(I_2)$ are the separate variances of the two terms in the estimator (85). In this example $\sigma(I_1) = \sigma(I_2)$.

As would be expected in real problems, especially those involving many dimensions, rather complicated sampling schemes are needed to produce a negative correlation.

C. VARIANCE-REDUCTION METHODS IN POLYMER CALCULATIONS

The techniques of variance reduction described are by no means exhaustive of the methods that can be used. Each problem will require fresh thought. Nevertheless those described are likely to be of wide applicability.

The polymer problems with which we are primarily concerned here raise certain special difficulties. The configuration of a long-chain polymer

requires a large number of parameters to define it. The generation of a sample is thus expensive in random numbers and computing time. Even more serious is the large proportion of the configurations generated that have virtually zero probability of occurring because of intermolecular repulsions. It is consequently difficult to generate samples falling in a particular region of configuration (i.e., sample) space. Indeed, so serious is this limitation at long chain lengths that the mere production of a sample is a considerable feat. Special methods are therefore required to meet these difficulties. These are discussed in more detail in Chapter 5. Analogous problems (though possibly less severe) arise in Monte Carlo calculations of the equilibrium properties of gases and liquids. In this situation important configurations are precious and must be fully exploited. For this purpose a rather special sampling scheme is used. Samples are no longer independent. Instead, an initial configuration (which may be far from random) is prepared. This configuration is perturbed in a convenient fashion, and the new configuration produced is either accepted or rejected with a probability dependent upon the Boltzmann factors of both configurations. The successive configurations (A_i, A_k) form a Markov chain with transition probabilities P_{jk} depending only upon the states A_j, A_k. For ergodic systems the probabilities P_{jk} can be so arranged that configurations appear in the chain with a frequency proportional to their Boltzmann factors. Equation of state properties can then be calculated by averaging over a long sequence of these configurations. The advantage of this method is that the configurations are concentrated in the most important region of sample space. Similar methods may be of value in polymer calculations.

Another technique for achieving a measure of importance sampling in cases where the generation of a sample in a particular region of space is difficult has been used in diffusion problems. In criticality calculations, for example, neutrons diffusing near the surface of the material are more likely to escape than those in the center. Trajectories near the center thus contribute most importantly, and a method known rather colorfully as "Russian roulette and splitting" has been used to sample these trajectories more intensively. In this technique the sample region is subdivided. If the diffusing particle or random walk finds its way into a division that contributes importantly to the final result, it is "*split.*" The single walk or diffusion trajectory is branched, and N branches continue the diffusion. Each branch is associated with a statistical weight $1/N$; these weights are multiplied at any succeeding branch point. Conversely, if the trajectory enters an unimportant region, the sampling density may be reduced (and computing time saved) by discontinuing the diffusion. To avoid introducing bias, lots are cast so that the walk is terminated with a probability P. Walks that survive are then awarded a statistical weight $1/(1 - P)$.

VI. Formulation of a Monte Carlo Calculation

As indicated in the introduction to this chapter, the Monte Carlo method is likely to be useful in two distinct situations—the first in which numerical results of a specified accuracy are required, possibly for some utilitarian purpose; the second, perhaps more fundamental, in providing guidance to the theoretician's intuition, e.g., by comparing Monte Carlo results with those from approximate theories. In both cases it will be essential to decide exactly what information, with what precision, is required for the calculation to be of value. It will be important to estimate the labor needed to achieve this precision. Almost certainly no accurate value of the variance will be available. To some degree the variance may be guessed from experience with similar problems or by examining the possible range of values the function may assume. In situations where no clear guidance as to the probable labor required can be obtained, it may be necessary to proceed to the next stage, construction and programming of the model. Often very limited Monte Carlo calculations of the variance on a simplified model (e.g., short random walks) can be extrapolated to the real system and an indication of the likely computing time required reached.

A. THE MODEL, DEBUGGING, AND INITIAL CALCULATIONS

The physical content of the model will depend upon the purpose of the calculation and may therefore be more or less idealized. Alternatively, we may seek to find the minimum model capable of producing results of the required accuracy. In either case the success will depend upon our intuition, and a degree of trial-and-error progress may be needed. It will be important at this stage to decide whether correlated sampling, as described in the previous section, will be useful.

Initial calculations with the model should use specific rather than random numbers and may be confined to a very small system. In this way the result for particular cases can be checked against exact calculations, e.g., the end-to-end distance for a fully stretched polymer chain. Needless to say, this is an important stage: the discovery of an unsuspected bug in the model routine after much Monte Carlo calculation is an expensive experience.

In addition, calculations with specific rather than random numbers can be used to explore the sample space systematically and thus obtain guidance as to which regions are important and possibly a rough indication of the variance. Model testing may be finally completed by using a plain sampling method to estimate the quantities required. Initially this calculation could

be restricted to rather small or specialized cases where the computed estimate can be compared with the exact result. These preliminary calculations are often very informative in providing insight into the problem.

From this exploratory work improvement in efficiency may be sought in three ways: by using faster computing routines, especially in the innermost loops; by simplifying the model; or by using specially designed sampling schemes. The amount of effort expended on this stage will depend upon the number of calculations required and the relative cost of computing time compared with the cost of additional programming (and its debugging if complicated).

If much production time is likely to be required, it will be necessary to consider the computing arrangements carefully. In particular, the mean time between machine faults should be discovered. If this is at all comparable with the computing time, it will be important to provide a means of restarting the calculation. For example, during the machine computation it might be convenient to provide a periodic dump onto magnetic tape or drum of all the data required to restart the calculation. These data might consist of all the running totals being accumulated plus the current random number.

For very long calculations involving perhaps the systematic exploration of a problem by varying parameters it is often valuable to allow a great degree of operator intervention during the running of the program. In this way the operator can "drive" the calculation, adjusting parameters, etc., to scan the regions of interest and achieve a much greater degree of sophistication than could be achieved by programmed control. This type of intervention will be especially useful if machine input/output facilities such as visual displays, light pens, etc. are available.

The termination of a calculation when a specified precision in the result has been achieved is not easy, as will be seen from Fig. 17. The computed confidence limits are almost always optimistic. In this situation it is good policy to select a fraction of the cases for extensive computation. Two or three different random-number sequences should be used and the computation continued for three or four times longer than apparently required for convergence. In the case of time- or sequence-dependent calculations, several initial configurations should also be studied to ensure the quasi-ergodicity of the problem.

An ill-chosen sampling scheme can introduce seemingly rapid convergence initially, followed by occasional wild fluctuations. These fluctuations can arise when two or more separate regions of the sample space contribute importantly. A common example in molecular terms corresponds to fluid/solid phases. A sampling scheme approximate for the fluid state is likely to be wildly inefficient for the solid. Thus even if the solid phase were overwhelmingly stable, sampling might still be concentrated in the liquid phase

with only occasional samples being drawn from the solid. Such samples would then produce large fluctuations in the running estimates of partition functions, etc.

REFERENCES

The first seven items refer to general discussion of the Monte Carlo method.

1. H. A. Meyer (ed.), *Symposium on Monte Carlo Methods (1954)*, Wiley, New York, 1956.
2. J. Curtiss et al., *Monte Carlo Method, Natl. Bur. Std. (U.S.) Appl. Math. Ser.*, Vol. 12, 1951.
3. H. Kahn, *Applications of Monte Carlo*, RAND Corporation Research Report Rm-1237-AEC (1956).
4. M. A. D. Fluendy and E. B. Smith, *Quart. Rev. (London)*, **16**, 241 (1962).
5. J. M. Hammersley and D. C. Handscomb, *Monte Carlo Methods*, Methuen, London, 1964.
6. Yu. A. Shreider, *The Monte Carlo Method*, Pergamon, New York, 1966.
7. B. J. Alder, S. Fernbach, M. Rotenburg (eds.), *Methods in Computational Physics*, Vol. 1, Academic, New York, 1963.
8. B. J. Alder and T. E. Wainwright, *Scientific American*, **201** No. 4, 113 (October, 1959).
9. W. Feller, *Introduction to Probability Theory and Its Applications*, Vol. I, 2nd ed., Wiley, New York, 1957.
10. P. G. Hoel, *Introduction to Mathematical Statistics*, 3rd ed., Wiley, New York, 1964.
11. W. V. Wood and F. R. Parker, *J. Chem. Phys.*, **27**, 720 (1957).
12. E. M. Hofstetter, in *The Mathematics of Physics and Chemistry*, Vol. II (H. Margenau and G. M. Murphy, eds.), Van Nostrand, Princeton, N. J., 1964, Chap. 3.
13. The RAND Corp., *A Million Random Digits with 100,000 Normal Deviates*, The Free Press, Glencoe, Ill. 1955.
14. D. H. Lehmer, *Harvard Univ. Comp. Lab. Ann.*, **26**, 141 (1951).
15. O. Taussky and J. Todd, in *Symposium on Monte Carlo Methods (1954)* (H. A. Mayer, ed.), Wiley, New York, 1956.
16. D. S. Horne, private communication.
17. J. W. Butler, in *Symposium on Monte Carlo Method (1954)* (H. A. Meyer, ed.), Wiley, New York, 1956.
18. C. B. Haselgrove, *Math. Comp.*, **15**, 323 (1961).

11

MOLECULAR SCATTERING

BY

M. A. D. FLUENDY

Reprinted from Annual Reports
1970

London
The Chemical Society

7 Molecular Scattering

By M. A. D. FLUENDY
Department of Chemistry, University of Edinburgh

THE field of atomic and molecular beam scattering has been rather well served by reviewers, most recently by Toennies[1] on its application to chemically reactive systems, and by Pauly and Toennies[2] on experimental methods. The proceedings of a summer school held in 1968 have also been published[3] and provide a broad view of the field at that time. The explanation for this popularity probably lies in the conceptual simplicity of scattering observations coming as they do very close to the '*gedenken*' experiment for investigating collision phenomena. In principle, scattering methods permit the measurement of the elementary quantum channels by which microscopic change occurs. For example, collisions in which species in defined quantum states i and j collide with a translational energy E to yield new species in states k, l having a final translational energy E' and scattering into a region of solid angle at θ and φ with respect to the initial relative velocity, *i.e.*

$$A_i + B_j \longrightarrow C_k + D_l$$

have a probability expressed in terms of a differential cross-section $\sigma_{ij}^{kl}(E, \theta, \varphi)$.

In scattering experiments attention is therefore focussed on these channel cross-sections rather than the rate constants of classical chemical kinetics. The quantum mechanical problems of the collision are thus separated from the largely statistical ones associated with state and transport properties in bulk phase experiments. In particular, the disappointingly ubiquitous applicability of the Arrhenius relation is avoided, which, yielding only averaged energy and entropy values for the collision complex, provided small leverage for theoretical effort. There is no doubt that this shift of interest has provoked much new theoretical work on intermolecular forces as well as the processes of chemical reaction and energy transfer. Additional advantages in this approach stem from the fact that conservation laws and microscopic reversibility apply strictly to these cross-sections.

This stimulation has been provided by a rather small quantity of published data, much of it in some sense incomplete in respect of energy or angular range and

[1] J. P. Toennies, *Ber. Bunsengesellschaft Phys. Chem.*, 1968, **72**, 927.
[2] H. Pauly and J. P. Toennies, 'Methods of Experimental Physics', 7A, p. 227, Academic Press, London, 1968.
[3] Ch. Schlier, ed., 'Molecular Scattering and Chemical Kinetics', Academic Press, New York, 1970.

resolution. Experimentally the technique has enjoyed a long infancy[4–6] full of excitement but underdeveloped in achievement.

In the last two or three years the first signs of maturity have appeared and a more realistic appraisal of the scientific prospects for this class of experiment is now possible. In this review the author hopes to evaluate these prospects on the basis of recent achievements; necessarily this will be a personal view. The literature is drawn mainly from the past two years and while reasonably complete is not exhaustive (a function more nearly fulfilled by the Oak Ridge Data Centre Bibliography[7]).

Work in this area can be conveniently considered in three groups, depending upon whether the collisions involved are *elastic* in the sense that the incident and exit quantum states are unchanged, *inelastic* involving transfer of energy, or chemically *reactive*. Furthermore, in most experiments either the angular dependence [*i.e.* the differential cross-section $\sigma(\theta)$] is measured, or else a total cross-section, $\sigma(E)$, for the process integrated over all angles is determined. In total cross-section experiments, measurement of $\sigma(E)$ for a range of energies is desirable. In both types of experiment some degree of averaging or summing over quantum channels due to resolution limitations is usual.

1 Elastic Scattering

Formally the post- and pre-collision system wave functions Ψ_e, Ψ_i are connected by[8]

$$\mathscr{S}\Psi_i \rightarrow \Psi_e$$

where $\mathscr{S}$ the scattering matrix (in general, multidimensional and of infinite order) contains all the information about the collision. For systems interacting by an isotropic force and colliding at energies well below the threshold for excitation to any higher state, the $\mathscr{S}$ matrix has diagonal terms only. These then correspond to the phase shifts for particles colliding with different orbital angular momenta. For this situation the theory is well developed;[9] quantum effects are important and these, coupled with the bipolar nature of atomic potentials, give rise to striking interference oscillations in the scattering cross-sections as a function of angle and energy. Measurements of these quantities yield information on the intermolecular/atomic forces operating, an application reviewed recently by Schlier.[10] The inversion of this type of cross-section data to yield the potential is crucial to the usefulness of the technique and until recently has been one of its least satisfactory aspects. Scattering data yield information on the potential at around the same energy as the turning point for the motion, so that mapping the

[4] L. Dunoyer, *Compt. rend.*, 1911, **152**, 594.
[5] T. H. Bull and P. B. Moon, *Discuss. Faraday Soc.*, 1954, No. 17, p. 54.
[6] E. H. Taylor and S. Datz, *J. Chem. Phys.*, 1955, **23**, 1711.
[7] Bibliography of Atomic and Molecular Processes, Oak Ridge National Laboratory, Oak Ridge, Tennessee, U.S.A.
[8] N. F. Mott and H. S. W. Massey, 'Theory of Atomic Collisions', Clarendon, Oxford, 1965.
[9] R. B. Bernstein, *Adv. Chem. Phys.*, 1966, **10**, 75.
[10] Ch. Schlier, *Ann. Rev. Phys. Chem.*, 1969, **20**, 191.

potential over a wide range of energy requires an equally wide range in the reduced experimental variable $E\theta$.[11] (Collisons scattering at wide angles penetrate more deeply:) This has frequently not been available due to technical limitations and the experimental cross-sections have then been fitted to simple two or three parameter forms (*e.g.* LJ, 12 : 6). Since absolute measurements are difficult this has normally involved matching only the locations of the interference peaks in the cross-section. As is shown by Luoma[12] and Olson[13] such a procedure is unreliable. Theoretical calculations usually present potentials in the form of multipole coefficients which are not directly measurable. When such calculations are compared with data fitted by appropriate r-dependent terms, similar difficulties arise. Recently, much wider ranges of $E\theta$ have been covered with good resolution, and inversion techniques have been developed which yield numerical values for the potential in a pointwise form, or in which a very flexible functional form with a large number of variable parameters is used to fit the data.[14—16] In either case it is the numerical values of the potential obtained rather than any of the parameters which are significant. The comparison with theory must now be made against these numerical potentials. For this purpose much more effort will be needed in the calculation of the potential in the difficult region around the potential minimum[17,18] where experimental precision is greatest.

For precise determination of the potential it is necessary to have relative differential cross-sections with resolved rainbow and high-frequency structure over as wide an angular and energy range as possible. Additional precision can be obtained from total cross-section measurements, particularly if several glory undulations can be observed in its energy dependence. Data of this character are available for the alkali–rare-gas systems Li–Kr, Na–Kr, Na–Ar, Na–Xe, K–Ar, K–Kr and have been analysed by Schlier.[16] Total cross-section measurements at energies in the 6—1000 eV region have been used[19,20] to extend the energy range of the K–Kr potential. Buck and Pauly, using a pointwise inversion procedure,[21] have applied thermal energy differential cross-section measurements to yield a numerical Na–Hg potential.[22] These are the systems for which presently we have the most accurate intermolecular potentials, though further measurements of differential cross-sections at higher energies would be valuable in extending the potentials to smaller internuclear distances.

[11] F. T. Smith, R. P. Marchi, and K. G. Dedrick, *Phys. Rev.*, 1960, **150**, 79.
[12] J. R. Luoma, *J. Chem. Phys.*, 1970, **53**, 129.
[13] R. E. Olson, *J. Chem. Phys.*, 1968, **49**, 4499.
[14] G. Vollmer, *Z. Physik*, 1969, **226**, 423.
[15] W. H. Miller, *J. Chem. Phys.*, 1969, **51**, 3631.
[16] R. Düren, G. P. Raabe, and Ch. Schlier, *Z. Physik*, 1968, **214**, 410.
[17] J. O. Hirschfelder, *Adv. Chem. Phys.*, 1967, **12**, 3.
[18] H. Margenau and N. R. Kestner, 'Theory of Intermolecular Forces', Pergamon, Oxford, 1969.
[19] M. Hollstein and H. Pauly, *Z. Physik*, 1967, **201**, 10.
[20] C. J. Malerich and R. J. Cross, *J. Chem. Phys.*, 1970, **52**, 386.
[21] U. Buck and H. Pauly, Max Planck Institut für Strömungsforschung, report 109/1970 and 110/1970.
[22] U. Buck and H. Pauly, *J. Chem. Phys.*, 1969, **51**, 1662.

Thus, atoms or molecules interacting by a single central potential with alkali atoms can be investigated using existing techniques to yield very accurate potentials. The need here is for a steady development of these rather laborious experiments particularly in those systems of greatest theoretical interest. There seems little merit in this field for experiments confined to narrow velocity or angular ranges or in which the resolution is insufficient to resolve fine structure.

Alkali systems interacting by more than one potential are at a less advanced state, in that scattering measurements have so far only been fitted to simple potentials. Alkali–alkali interactions have been particularly studied, here the interaction is by $^1\Sigma^+$ and $^3\Sigma^+$ potentials and spin exchange may occur on collision.[23] Total cross-section measurements by Rothe and Helbing[24] at thermal energies interpreted by the well-established BOB plot[25] have yielded values for the product εr_m (in an LJ, 8 : 6 potential) for the $^3\Sigma$ states of Li with several other alkali metals. Similar measurements by Neumann and Pauly[26] at collision energies $\sim$100 eV for the Na–Cs system have led to similar values for the singlet potential—a nice illustration of the need to match the impact energy to the energy range of the potentials sought.

Differential cross-section measurements have also been made in these systems[27] most usefully with magnetic spin selectors and analysers so that the spin exchange cross-sections could also be studied.[28–31] The probability of spin exchange is a sensitive function of the difference between the two potentials and imposes tight constraints on them. Observations of the rainbow angle also yielded information on the triplet potential, primarily its well depth. It is clear that these measurements, sensitive to different regions of the potential, are not consistent with a simple LJ potential. High-resolution state-selected measurements would be valuable in permitting a precise inversion to obtain these potentials, which are of particular interest in that both the $C^{(8)}$ and $C^{(10)}$ terms in the potential may be unusually important.[32,33]

Total cross-section measurements for the interaction of alkalis with a wide range of other molecules have been made,[34,35] notably at thermal energies by Rothe and Helbing[36–39] and at super-thermal energies by Pauly.[26] Glory

[23] H. O. Dickinson and M. R. H. Rudge, *Atomic Molecular Phys.*, 1970, **3**, 1448.
[24] E. W. Rothe and R. K. B. Helbing, *J. Chem. Phys.*, 1968, **49**, 4750.
[25] R. B. Bernstein and T. J. P. O'Brien, *J. Chem. Phys.*, 1967, **46**, 1208.
[26] W. Neumann and H. Pauly, *J. Chem. Phys.*, 1970, **52**, 2548.
[27] L. T. Cowley, M. A. D. Fluendy, and K. P. Lawley, *Trans. Faraday Soc.*, 1969, **65**, 2027.
[28] D. Beck, U. Henkel, and A. Schultz, *Phys. Letters*, 1968, **27A**, 277.
[29] D. E. Pritchard, G. M. Carter, F. Y. Chu, and D. Kleppner, *Phys. Rev.*, 1970, **2**, 1922.
[30] D. E. Pritchard and F. Y. Chu, *Phys. Rev.*, 1970, **2**, 1932.
[31] D. E. Pritchard, D. C. Burnham, and D. Kleppner, *Phys. Rev. Letters*, 1967, **19**, 1363.
[32] W. D. Davison, *J. Phys. (B)*, 1968, **21**, 139.
[33] P. R. Fontana, *Phys. Rev.*, 1961, **123**, 1865.
[34] E. Richman and L. Wharton, *J. Chem. Phys.*, 1970, **53**, 945.
[35] S. O. Colgate and T. C. Imeson, *J. Chem. Phys.*, 1970, **53**, 1270.
[36] R. K. B. Helbing and E. W. Rothe, *J. Chem. Phys.*, 1968, **48**, 3948.
[37] R. K. B. Helbing and E. W. Rothe, *J. Chem. Phys.*, 1969, **50**, 3531.
[38] R. K. B. Helbing and E. W. Rothe, *J. Chem. Phys.*, 1970, **53**, 1555.
[39] R. K. B. Helbing and E. W. Rothe, *J. Chem. Phys.*, 1970, **53**, 2501.

undulations in the total cross-section have been resolved in most of this work so that values for εr_m or other constraints on the elastic potential are available. These data will be of greatest value when combined with other measurements *e.g.* of the rainbow scattering, so that individual potential parameters may be determined.

A feature of particular interest has been the quenching of the glory oscillations that occurs in some systems, a phenomenon first observed by Gislason and Kwei.[40]. This is seen as a decrease in their amplitude as compared to that predicted from their reduced mass and potential derived from the peak locations. Except for quenching by chemical reaction in systems with very large reactive cross-sections, the quenching seems closely connected with the anisotropy of the target molecule–atom potential and consequent rotational inelasticity. The process has attracted interest as a possible route to such anisotropic potentials.[41—45] Unfortunately, while the degree of quenching correlates sensibly with the anisotropy it seems unlikely to offer much precision. A similar conclusion was reached by Cross[46] in respect of differential cross-sections resulting from collisions averaged over all orientations of an anisotropic potential. Such anisotropy seems a rather elusive quantity more likely to be observed in total cross-section measurements from oriented targets[47,48] (J, M selected) or in rotationally inelastic collisions.[49]

The most exciting achievement in elastic scattering in the past two years has been the final breaching of the alkali barrier. The technical limitations have restricted almost all work until now to species containing alkalis which can readily be detected by surface ionisation. The technical factors contributing to this advance will be discussed later. In the elastic scattering field a number of experiments of this type have been reported by several laboratories. Particularly encouraging has been the rapid progress in the resolution and power of this work, the most recent data comparing favourably in resolution with present alkali work.

Total cross-section measurements resolving glory undulations have been reported by Baratz and Andres[50] for Ar–Ar and by Dondi *et al.*[51] for ^{4}He–^{4}He. The latter results were particularly interesting since the quantum structure arose from the indistinguishability of the particles and corresponded to a backward glory, *i.e.* the effect of direct backward scattering rather than the usual forward glory.

[40] E. A. Gislason and G. H. Kwei, *J. Chem. Phys.*, 1967, **46**, 2838.
[41] R. E. Olson and R. B. Bernstein, *J. Chem. Phys.*, 1968, **49**, 162.
[42] W. H. Miller, *J. Chem. Phys.*, 1969, **50**, 3124.
[43] P. R. Le Breton and H. L. Kromer, *J. Chem. Phys.*, 1969, **51**, 3627.
[44] R. K. B. Helbing, *J. Chem. Phys.*, 1970, **53**, 1547.
[45] R. K. B. Helbing, *J. Chem. Phys.*, 1969, **51**, 3628.
[46] R. J. Cross, jun., *J. Chem. Phys.*, 1970, **52**, 5703.
[47] W. H. Miller, *J. Chem. Phys.*, 1969, **50**, 3410.
[48] W. H. Miller, *J. Chem. Phys.*, 1969, **50**, 3868.
[49] H. G. Bennewitz, R. Gegenbach, R. Haerten, and G. Muller, *Z. Physik*, 1969, **226**, 279.
[50] B. Baratz and R. P. Andres, *J. Chem. Phys.*, 1970, **52**, 6145.
[51] M. G. Dondi, G. Scoles, F. Torello and H. Pauly, *J. Chem. Phys.*, 1970, **51**, 392.

Differential cross-section measurements on the same systems[52,53] have been made in which the rainbow angles were resolved. While these data have not been analysed in detail they seem to be consistent with the total cross-section work. For He–He, agreement with published potentials is only moderate while for Ar–Ar agreement with the Dymond–Alder[54] potential is reported in one case[53] and the reverse in another.[50] Further analysis and experiments can be expected in these systems and it should soon be possible to compare potentials obtained from bulk properties with accurate scattering data. Other rare-gas systems have been investigated by Mueller.[55,56]

Rainbow scattering has also been observed in the Ar–N_2 system by two different laboratories.[57,58] Reassuringly, the well depths deduced for a LJ 12 : 6 potential agree within the experimental errors. Potentials have also been obtained describing the short-range interaction of this system using high velocity argon beams.[59]

Experiments with higher effective resolution have been reported by Kuppermann[60] for the system D_2–N_2. High-frequency interference oscillations were observed and yielded estimates for the potential range.

Particularly striking results for Ne–rare-gas systems are described by Lee. Accurate potentials have not yet been obtained by inversion, though the data appear to warrant it. Initial fitting to LJ forms suggests the superiority of the LJ 20 : 6 to the 12 : 6.[61] In the case of Ne–Ne,[62] strong oscillations around 90° are seen due to the interference between atoms scattered at $90° - \theta$ and $90° + \theta$.

A further class of experiments involve the elastic scattering of excited state species (so far only metastable electronic states). The collision-free conditions pertaining in a beam experiment are ideally suited to the study of such systems, particularly since in many cases they may be efficiently detected by Auger electron ejection.[63] Surprisingly, there has been relatively little work in recent years, Rothe[64] reported a total collision cross-section for He(^3S) with several partners, while Grosser and Haberland have studied the differential cross-sections.[65]

[52] M. Cavallini, G. Gallinoro, L. Meneghetti, G. Scoles, and U. Valbusa, *Chem. Phys. Letters*, 1970, **7**, 303.

[53] M. Cavallini, L. Meneghetti, G. Scoles, and M. Yealland, *Phys. Rev. Letters*, 1970, **24**, 1469.

[54] J. H. Dymond and B. J. Alder, *J. Chem. Phys.*, 1969, **51**, 309.

[55] J. Penta, C. R. Mueller, W. Williams, R. Olson, and P. Chakraborti, *Phys. Letters*, 1967, **25A**, 658.

[56] W. Williams, C. R. Mueller, P. McGuire, and B. Smith, *Phys. Rev. Letters*, 1969, **22**, 121.

[57] R. W. Bickes and R. B. Bernstein, *Chem. Phys. Letters*, 1969, **4**, 111.

[58] F. Kalos and A. E. Grosser, *Chem. Phys. Letters*, 1970, **6**, 537.

[59] J. E. Jordan, S. O. Colgate, I. Amdur, and E. A. Mason, *J. Chem. Phys.*, 1970, **52**, 1143.

[60] D. H. Winicur, A. L. Moursund, W. R. Devereaux, L. R. Martin, and A. Kuppermann, *J. Chem. Phys.*, 1970, **52**, 3299.

[61] J. M. Parson, T. P. Schafer, F. P. Tully, P. E. Siska, Y. C. Wong, and Y. T. Lee, *J. Chem. Phys.*, 1970, **53**, 2123.

[62] P. E. Siska, J. M. Parson, T. P. Schafer, F. P. Tully, Y. C. Wong, and Y. T. Lee, *Phys. Rev. Letters*, 1970, **25**, 271.

[63] E. E. Muschlitz, *Adv. Chem. Phys.*, 1966, **10**, 171.

[64] E. W. Rothe, R. H. Neynaber, and S. M. Trujillo, *J. Chem. Phys.*, 1965, **42**, 3310.

[65] J. Grosser and H. Haberland, *Phys. Letters*, 1968, **27A**, 634.

In summary, we conclude that, for particles interacting by single potential beam scattering, techniques now have a demonstrated ability to produce accurate potentials without recourse to parametrised models. This technique of continuum spectroscopy appears to provide greater precision than is available from discrete state spectroscopy. Although, for deep potential wells supporting many bound states suitable for treatment by RKR methods[66] the reverse may be true. The direct scattering observation of the analogous quasi bound states as resonances will be very difficult.[67—69] A major need is for the co-ordinated study of a few systems in a number of laboratories, so that total and differential cross-sections may be measured over a wide energy range. In this way the rather large experimental effort involved will not be dissipated in providing incomplete data for a wider range of partners. As Herschbach has pointed out, accurate combining rules will rapidly extend the number of systems for which potentials are available.[70]

For simple atomic systems interacting by relatively few potentials the position is also bright (specially if one of these partners is an alkali). Accurate potential data can be expected in the near future. In more complex situations involving large numbers of potentials associated, for example, with the different rotational and vibrational states of molecules (large numbers of which may be populated) the situation is more gloomy. Not only are experimental difficulties likely to limit the resolution of experiments here but the theory required to interpret their scattering and yield a potential is not available. Potentials applicable to averages over ranges of states are the best likely to be obtainable in the next few years. It will be important to exploit the various distortions of phase space available experimentally and any additional information, *e.g.* from spectroscopic data for specific interactions, will be particularly valuable.

2 Inelastic Scattering

In contrast to elastic collisions where interest is centred almost entirely on the potential as revealed by the scattering pattern, in inelastic scattering the development and validation of the approximate theories required is equally important to elucidation of the coupling terms in the potential responsible for the inelasticity. Indeed, it is likely that until theory is secure in relating inelastic scattering to potentials we shall gain little information about these terms. These energy transfer processes do not manifest themselves only in scattering experiments of course, and a great deal of effort has been applied to their understanding in other fields as described by Gordon, Klemperer, and Steinfeld in a recent review.[71] A useful introduction to these problems in the scattering context is given by Cross.[72]

[66] E. A. Mason and L. Monchick, *Adv. Chem. Phys.*, 1967, **12**, 339.
[67] A. S. Dickinson, *Mol. Phys.*, 1969, **18**, 441.
[68] A. S. Dickinson, *Mol. Phys.*, 1969, **18**, 305.
[69] G. D. Mahan, *J. Chem. Phys.*, 1970, **52**, 258.
[70] H. L. Kramer and D. R. Herschbach, *J. Chem. Phys.*, 1970, **53**, 2792.
[71] R. G. Gordon, W. Klemperer, and J. I. Steinfeld, *Ann. Rev. Phys. Chem.*, 1968, **19**, 215.
[72] R. J. Cross, jun., in Ref. 3.

Although a complete formal solution for inelastic collisions is available in the $\mathscr{S}$ matrix in which the off-diagonal terms correspond to these transitions, this is of limited practical value. The cross-section for transition between two states or indeed for elastic scattering below the threshold energy for excitation involves contributions from many other states of the system. As a consequence the numerical problem presents itself as the solution of a large number of coupled equations, usually too numerous to be attractive as a computational solution. A feature of this field is thus the wide range of approximate methods in use *e.g.* Born or Distorted Wave variants applicable to weakly inelastic situations; semiclassical or classical approximations for systems with well-defined trajectories, and statistical models appropriate to strong coupling in systems with many levels. Unfortunately, the region in which these models are valid is often ill-defined, and experimental data are still too sparse to decide upon their usefulness. In this situation, comparison of approximate models with 'exact' but laborious numerical computations is useful.[73]

Scattering in atom–diatom systems, in which the diatom is regarded as a rigid rotor, has attracted particular attention in this respect. The formalism of Arthurs and Dalgarno[74] has provided the framework for 'close-coupled' calculations in which a small number of states are selected for inclusion in a rigorous numerical computation. When the number of states accessible during the collision is small this type of calculation can yield effectively exact results.[75—77] A novel method for solving this type of problem has been described by Gordon.[77a] Eu[78] has considered a similar process in the semiclassical approximation where, due to the resulting simplification, many more states can be included. The results of these 'exact' calculations have been compared to other methods by Bernstein,[79—82] Levine,[83] and Kinsey.[84]

The full problem of atom–diatom collisions involving simultaneous vibration and rotation transfer is much more difficult to treat since many more states are involved. Furthermore, since both small (rotational) and large energy changes (vibrational) are involved, approximation methods suitable for the first are often unsuitable for the second. To avoid this difficulty, calculations have frequently been restricted to collinear collisions in which only vibrational energy can be transferred. Classical trajectory calculations by Wolfsberg[85] in three dimensions

[73] R. W. Fenstermaker, C. F. Curtiss, and R. B. Bernstein, *J. Chem. Phys.*, 1969, **51**, 2439.
[74] A. M. Arthurs and A. Dalgarno, *Proc. Phys. Soc.*, 1960, **A25**, 540.
[75] W. A. Lester and R. B. Bernstein, *J. Chem. Phys.*, 1968, **48**, 4896.
[76] M. Von Seggern and J. P. Toennies, *Z. Physik.*, 1969, **218**, 341.
[77] B. R. Johnson and D. Secrest, *J. Chem. Phys.*, 1968, **48**, 4682.
[77a] R. G. Gordon, *J. Chem. Phys.*, 1969, **51**, 14.
[78] B. C. Eu, *J. Chem. Phys.*, 1970, **52**, 1882.
[79] R. D. Levine, B. R. Johnson, and R. B. Bernstein, *J. Chem. Phys.*, 1969, **50**, 1694.
[80] J. T. Muckerman and R. B. Bernstein, *J. Chem. Phys.*, 1970, **52**, 606.
[81] R. D. Levine, B. R. Johnson, J. T. Muckerman, and R. B. Bernstein, *J. Chem. Phys.*, 1968, **49**, 56.
[82] W. A. Lester and R. B. Bernstein, *J. Chem. Phys.*, 1970, **53**, 11.
[83] R. D. Levine, M. Shapiro, and B. R. Johnson, *J. Chem. Phys.*, 1970, **52**, 1755.
[84] J. L. Kinsey, J. W. Riehl, and J. S. Waugh, *J. Chem. Phys.*, 1968, **49**, 5269.
[85] J. D. Kelley and M. Wolfsberg, *J. Chem. Phys.*, 1970, **53**, 2967.

without this restriction have shown the danger in drawing conclusions from such simplified models.

Inelastic scattering experiments fall into three classes. In the first the change in quantum state resulting from collision is followed directly by the use of rotational state selectors and analysers. This type of experiment is in many ways comparable to the molecular beam resonance technique except that the transition-inducing '*C*' field is replaced by the collision process. The second class of experiment measures the velocity change on collision and so infers the internal state change. Finally, the more energetic inelastic processes may be monitored directly by observing photons, ions, *etc.* emitted from the collision zone. Broadly speaking, the first technique is appropriate to rotationally inelastic collisions and the second to those involving larger energy changes such as vibration. Bernstein[86] has used this technique to study $J = 0 \rightarrow J = 2$ transitions in ortho H_2 induced by collisions with K atoms.

In such experiments the beam technique is extended to its full and there seems no prospect of these methods being applicable to the generality of systems, as in the elastic scattering case. Rather peculiarly, favourable systems in which detectability and ease of selection make the experiment feasible must be sought.

Experiments of the first type in which specific $|JM\rangle$ states of TlF were selected by electrostatic four-pole fields and inelastic cross-sections for the transitions $|3, 0\rangle \rightarrow |2, 0\rangle$, $|2, 0\rangle \rightarrow |1, 0\rangle$, and $|1, 0\rangle \rightarrow |2, 0\rangle$ measured for a wide range of collision partners have been carried out by Toennies.[87] Similar experiments in which the ratio of the elastic total cross-sections for scattering of TlF in $|1, 0\rangle$ and $|1, 1\rangle$ and of CsF in $|2, 0\rangle$ and $|2, 2\rangle$ states have been described by Bennewitz.[88–90] From measurements of this type over a range of velocities it has been possible to determine anisotropy parameters characterising both the long- and short-range parts of the potential. Since this appears to be the only system for which such anisotropy data are combined with measurements of inelastic cross-sections it should be of considerable theoretical interest.

Velocity-change measurements for collisions of Li^+ with H_2 have been made by Toennies.[91,92] The flight times for Li^+ ions scattered directly backwards in the centre-of-mass co-ordinate system and thus appearing at 0° were measured in the laboratory. By using very short pulses ~ 50 ns wide with a careful peak-fitting data analysis it was possible to identify transitions from the ground state to the first nine vibrational levels. Collisions in which electronic excitation occurs have attracted increased interest recently. This appears to be for several reasons. Firstly, such processes may be the precursor to many types of chemical reaction *e.g.* harpooning.[93] Secondly, although the wave functions and coupling potentials

[86] A. R. Blythe, A. E. Grosser, and R. B. Bernstein, *J. Chem. Phys.*, 1964, **41**, 1917.
[87] J. P. Toennies, *Z. Physik.*, 1965, **182**, 257.
[88] H. G. Bennewitz, R. Haerten, and G. Müller, *Z. Physik.*, 1969, **226**, 139.
[89] H. G. Bennewitz, R. Genganbach, R. Haerten, and G. Müller, *Z. Physik.*, 1969, **226**, 279.
[90] H. G. Bennewitz and R. Haerten, *Z. Physik.*, 1969, **227**, 399.
[91] J. Schottler and J. P. Toennies, *Ber. Bunsengesellschaft Phys. Chem.*, 1968, **72**, 979.
[92] W. D. Held, J. Schottler, and J. P. Toennies, *Chem. Phys. Letters*, 1970, **4**, 304.
[93] D. R. Herschbach, *Adv. Chem. Phys.*, 1966, **10**, 319.

are only poorly known, the number of states involved is relatively few so that close-coupled calculations become possible. Finally, the larger energies and energy changes involved in these processes make the experiments somewhat easier.

Experiments of the velocity change type for H^+ and H_2^+ scattering from several target gases have been reported by Doering.[94] Electrostatic energy selection and analysis was used at collision energies between 150—500 eV. Quite large cross-sections (~ 1 Å^2) were observed and it was possible to resolve the vibrational fine structure on the electronic transitions.

Experiments involving photon emission have been reported by several workers. Herschbach[95,96] and Schlier[97] have studied the translational excitation of potassium to the 4^2P state by collisions in the energy range 1—600 eV with a variety of target molecules. The excitation was detected by the rapid fluorescence emission from the potassium. The cross-sections were large (~ 10 Å^2) and the thresholds for excitation could be correlated with potential curve crossings in the collision systems. In particular, interesting differences in threshold behaviour were observed between K–inert-gas collisions where crossing occurs high on the repulsive wall and systems such as K–Cl_2 in which the crossing takes place at large intermolecular distances.

Vibrational to electronic conversion has been examined using a beam technique in the system N_2–Na;[98] a vibrationally hot N_2 beam prepared in a high-temperature source was crossed with an Na beam and the resonance emission from the excited sodium measured. The reverse type of process has been described by Martin.[99] Here an electronically excited Hg beam prepared by electron bombardment collided with a range of target molecules. The cross-section for the process Hg $6^3P_2 \longrightarrow {}^3P_1$ was measured by observing the subsequent fluorescence of the $^3P_1$ state. The cross-section for CO was larger than that for N_2, which suggests that chemical interaction is more important than the close matching of vibrational state energies.

Collisions leading to ionisation have been considered theoretically by Bandrauk,[100] while Helbing[101] and Los[102,103] have both reported experiments with fast alkali beams in which the cross-section for ion production was measured. From the energy dependence of these cross-sections it was possible to estimate the electron affinities for the target molecules, while by use of the Landau–Zener theory a value for the interaction energy at the pseudo crossing point between the

[94] J. H. Moore, jun., and J. P. Doering, *J. Chem. Phys.*, 1970, **52**, 1692.
[95] R. W. Anderson, V. Aquilanti, and D. R. Herschbach, *Chem. Phys. Letters*, 1969, **4**, 5.
[96] K. Lacman and D. R. Herschbach, *Chem. Phys. Letters*, 1970, **6**, 106.
[97] V. Kempter, W. Mecklenbrauck, M. Menzinger, G. Schuller, D. R. Herschbach, and Ch. Schlier, *Chem. Phys. Letters*, 1970, **6**, 101.
[98] J. E. Mentall, H. F. Krause, and W. L. Fite, *Discuss. Faraday Soc.*, 1967, No. 44, p. 157.
[99] L. J. Doemeny, F. J. Van Itallie, and R. M. Martin, *Chem. Phys. Letters*, 1969, **4**, 302.
[100] A. D. Bandrauk, *Mol. Phys.*, 1969, **17**, 523.
[101] R. K. B. Helbing and E. W. Rothe, *J. Chem. Phys.*, 1969, **51**, 1007.
[102] A. P. M. Baede, A. M. C. Moutinho, A. E. de Kries, and J. Los, *Chem. Phys. Letters*, 1969, 3, 530.
[103] A. P. M. Baede and J. Los, preprint.

potentials corresponding to short- or long-range coulombic interactions was obtained. Similar information was reported for the system K–I by elastic scattering measurements below the threshold for excitation.[104]

In general, it seems unlikely that quantum channel cross-sections over wide angle and energy ranges will become available in the near future. Many of the experiments described are amongst the most difficult yet undertaken and in particular the state and velocity change type remain in the 'heroic age'. Nevertheless, the prospects of observing the many continuum resonance processes occurring in these systems,[76] which have formed such an interesting chapter in electron and neutron scattering, are so intriguing that one feels the requisite technique must eventually become available.

3 Reactive Scattering

It is in the study of collisions which lead to chemical reaction that the scattering technique has impinged most directly on a major area of chemistry. The effect has been to concentrate interest much more on the detailed trajectories of the particles when reacting, and away from statistical theories. This shift has been triggered by the realisation that quite primitive observations, particularly of the angular distribution of product, can be very informative as to the dynamics. This information from experiment has been used to obtain estimates of the potential surface involved in the reaction usually by comparison with Monte Carlo trajectory calculations.[105–107]

Although quantum theory methods for reactive scattering[108,109] have been used (for an introduction see J. Ross in ref. 3) these results from experiments and experimental mathematics have usually been interpreted on the basis of simplified models.[110–113]

The most important model classifications are between those involving direct processes and long-lived complexes. In the direct reactive encounter, reaction is complete and the products separate before half a revolution of the total system *i.e.* the collision lasts $< 10^{-13}$ s.

Extreme cases of the direct process include 'stripping dynamics' in which the incoming atom or group captures an atom from the target molecule and continues its motion with little interaction with the remaining target fragment which 'spectates'. In the 'recoil' encounter the opposite dynamic appears and the incoming atom recoils backward along its line of approach bearing the captured target fragment with it. These two mechanisms reveal themselves by forward or

[104] M. A. D. Fluendy, D. S. Horne, K. P. Lawley, and A. W. Morris, *Mol. Phys.*, 1970, **19**, 659.
[105] D. L. Bunker and M. D. Pattengill, *J. Chem. Phys.*, 1970, **53**, 3041.
[106] M. Karplus, R. N. Porter, and R. D. Sharma, *J. Chem. Phys.*, 1966, **45**, 3871.
[107] D. L. Bunker and C. A. Parr, *J. Chem. Phys.*, 1970, **52**, 5700.
[108] J. N. L. Connor and M. S. Child, *Mol. Phys.*, 1970, **18**, 653.
[109] J. N. L. Connor, *Mol. Phys.*, 1970, **19**, 65.
[110] E. E. Nikitin, *Ber. Bunsengesellschaft Phys. Chem.*, 1968, **72**, 949.
[111] R. Grice, *Mol. Phys.*, 1970, **19**, 501.
[112] D. J. Locker and D. J. Wilson, *J. Chem. Phys.*, 1970, **53**, 2858.
[113] D. D. Parrish and R. R. Herm, *J. Chem. Phys.*, 1970, **53**, 2431.

backward peaking in the product angular distribution and in the magnitude of the total reactive cross-section which is large (~ 100 Å^2) for the stripping dynamics and smaller (~ 10 Å^2) for the recoil case. These two mechanisms are exemplified by:

$$K + ICl \rightarrow KI + Cl \quad \text{stripping}^{114}$$

and

$$K + MeI \rightarrow KI + Me \quad \text{recoil}^{115}$$

Most of the exothermicity of these reactions appears as internal excitation of the products.

Long-lived complexes, in which the collision system rotates several times before decaying, result in loss of all memory of the initial velocities, without of course violating angular momentum conservation requirements. In particular, since the major contribution to the angular momentum of the complex comes from the relative motion of the two reactants, their motion is confined approximately to a phase. The random decomposition of the complex, which is uniform in the plane, then results in forward and backward peaking along the relative velocity vector. Laboratory distributions are thus bimodal. Typical of this class of reaction is:[116]

$$Cs + RbCl \rightarrow CsCl + Rb$$

The qualitative features of the potential surfaces which can lead to these extreme dynamics are now fairly well established.

Elastic scattering from reactive systems can also provide much information on the nature of the reactive encounter since experiments of this type not only map out the lower reaches of the potential between the reactants but can yield information on the type of collisions which lead to reaction.[117] This type of information is normally described with the aid of a complex optical potential in which the imaginary term represents the absorption in the elastic channel due to reaction.[118–122]

Recent work has taken place within this framework and can be summarised under the following heads.

(*a*) The discovery of a number of reactions with dynamics intermediate between the extreme cases described and the correlations of their dynamics with the electronic structure of the reactants.

(*b*) The detailed study of some of the typical alkali reactions using energy- and state-selection techniques.

(*c*) The investigation of reactions not involving alkalis.

[114] G. H. Kwei and D. R. Herschbach, *J. Chem. Phys.*, 1969, **51**, 1742.
[115] G. H. Kwei, J. A. Norris, and D. R. Herschbach, *J. Chem. Phys.*, 1970, **52**, 1317.
[116] W. B. Miller, S. A. Safron, and D. R. Herschbach, *Discuss. Faraday Soc.*, 1967, No. 44, p. 108.
[117] E. F. Greene, A. L. Moursund, and J. Ross, *Adv. Chem. Phys.*, 1966, **10**, 135.
[118] B. E. Eu, *J. Chem. Phys.*, 1970, **52**, 3021.
[119] C. Nyeland and J. Ross, *J. Chem. Phys.*, 1970, **49**, 843.
[120] R. B. Bernstein and R. D. Levine, *J. Chem. Phys.*, 1969, **49**, 3872.
[121] D. A. Micha, *J. Chem. Phys.*, 1969, **50**, 722.
[122] R. E. Roberts and J. Ross, *J. Chem. Phys.*, 1970, **52**, 1464.

The dynamical models described represent extremes of behaviour. Not surprisingly, these dynamics may be modified by changing the impact energy or the chemical species involved. Neutral–neutral scattering is difficult over a wide energy range but ion-molecule data can be revealing. For the system $C_2H_4^+ + C_2H_4 \longrightarrow C_3H_5^+$ transition from complex to stripping dynamics is observed as the collision energy varies from 1—5 eV.[123] How far this type of change is a general phenomenon is not yet clear.[124]

Alkali reactions with a range of different species have been widely investigated.[125–127] In general, the direction of recoil correlated with the potential crossing radius r_c given by

$$e^2/r_c = I_{P(M)} - E_{A(reactant)}$$

in accordance with the electron jump model for these reactions.[128,129] This type of model may also account for the vibrational excitation in the products. A mass-dependent effect in the dynamics of Li reaction has been suggested.[130,131] In the reaction of alkali atoms with NO_2 and CH_3NO_2 to yield NO and MNO_2[132] the picture is confused by the variety of potentials and reaction paths that are open and which may provide an alternative explanation for the complex distribution of product. Similar complex formation has been inferred by Kinsey[133] in systems such as K–SO_2 where the reactive channels are closed at thermal collision energies. Unchanged reactant scattering back out of the complex was observed to have the typical 'long-lived complex' symmetry. It was also concluded that considerable transfer of translational to vibrational excitation of the SO_2 took place in these collisions. Greene, Ross, and co-workers have made an extensive study of the direct elastic scattering from reactive systems.[134] Optical model analysis yielded results for the cross-section for reaction as a function of energy and distance of closest approach in the collision. Their data suggested that a more gradual change to an attractive potential occurred than that provided by an electron jump model. Experiments on the K–I_2 system,[104] where elastically scattered K was apparently experiencing the coulombic well, suggested that an electron transfer did not invariably lead to reaction. Detailed experiments by Bernstein[135] using a velocity-selected primary beam and energy analysis of the scattered product for the K–HBr and K–DBr systems found σ_R for HBr 40%

[123] Z. Hermann, A. Lee, and R. Wolfgang, *J. Chem. Phys.*, 1969, **51**, 452.
[124] A. Hengtein, *J. Chem. Phys.*, 1970, **53**, 458.
[125] K. R. Wilson and D. R. Herschbach, *J. Chem. Phys.*, 1968, **49**, 2676.
[126] R. J. Gordon, R. R. Herm, and D. R. Herschbach, *J. Chem. Phys.*, 1968, **49**, 2684.
[127] T. J. Odiorne and P. R. Brooks, *J. Chem. Phys.*, 1969, **51**, 4676.
[128] R. Grice, M. R. Cosandey, and D. R. Herschbach, *Ber. Bunsengesellschaft Phys. Chem.*, 1968, **72**, 975.
[129] M. Polanyi, *Endeavour*, 1949, **8**, 3.
[130] D. D. Parrish and R. R. Herm, *J. Chem. Phys.*, 1968, **49**, 5544.
[131] D. D. Parrish and R. R. Herm, *J. Chem. Phys.*, 1969, **51**, 5467.
[132] R. R. Herm and D. R. Herschbach, *J. Chem. Phys.*, 1970, **52**, 5783.
[133] D. O. Ham and J. L. Kinsey, *J. Chem. Phys.*, 1970, **53**, 285.
[134] E. F. Greene, L. F. Hoffmann, M. W. Lee, J. Ross, and C. E. Young, *J. Chem. Phys.*, 1969, **50**, 3450.
[135] K. T. Gillen, C. Riley, and R. B. Bernstein, *J. Chem. Phys.*, 1970, **50**, 4019.

larger than for DBr. In defiance of the simple model, however, HBr also gave more product scattering at wide angles.

Some refinement of the electron jump model thus appears necessary; in particular, charge migration in the target during the approach and departure phases of the collision (pre- and post-migration[114]) may have a critical effect on the trajectories. Migration seemingly occurs in the interhalogen systems, M–ICl, IBr where KCl/KBr is the dominant product. At present the Monte Carlo studies diverge, the calculations of Polanyi[136–138] and Karplus[139] indicating the need for such a process to account for the forward peaking in the product distribution, while Blais[140,141] reached the reverse conclusion. Such contradictions are not surprising and are best resolved by additional experimental constraints, particularly as to the internal excitation of the products. Information on this point has been provided recently by Toennies[142] for the system Rb–Br_2, using a quadrupole field to measure the rotational state distribution in the product RbBr. About 5 kcal mol^{-1} appeared in rotation leaving $\sim$37 kcal mol^{-1} in vibration a result in fair accord with Blais's calculation.

Experiments with beams of orientated molecules *e.g.* symmetric tops in selected *KMJ* states have been described in detail by Bernstein[143] for the system K–MeI. The iodine end was approximately four times more reactive than the methyl end of the molecule. The results are in rough agreement with a simple hard-sphere exclusion model. A recent experiment by Brooks[144] on the system

$$CF_3I + K \longrightarrow CF_3 + KI$$

yielded surprisingly the reverse conclusion. This may be a direct demonstration of charge migration with the initial electron capture occurring in the CF_3 group.

The further refinement of potential surfaces will require more of those detailed state-selection experiments. This is particularly true in those systems proceeding by complex dynamics in which the angular distributions are (apart from the characteristic symmetry) rather uninformative. A wide range of impact energies will also be useful, particularly if the dynamics are substantially modified at high energies *e.g.* by complex $\longrightarrow$ stripping transitions.

Thus, much still remains to be done in understanding alkali reactions. Although the initial electron transfer and downhill approach are qualitatively well established, a more quantitative description of this process is needed in terms of the potentials and coupling between them, while in the subsequent departure phase of the motion the role of charge migration or of further collisions between the atoms is unclear. In this respect experiments in the reverse direction *e.g.*

[136] P. J. Kuntz, M. H. Mok, E. M. Nemeth, and J. C. Polanyi, *Discuss. Faraday Soc.*, 1967, No. 44, p. 229.
[137] P. J. Kuntz, M. H. Mok, and J. C. Polanyi, *J. Chem. Phys.*, 1969, **50**, 4623.
[138] P. J. Kuntz, E. M. Nemeth, and J. C. Polanyi, *J. Chem. Phys.*, 1969, **50**, 4607.
[139] M. Godfrey and M. Karplus, *J. Chem. Phys.*, 1968, **49**, 3602.
[140] N. C. Blais, *J. Chem. Phys.*, 1968, **49**, 9.
[141] N. C. Blais, *J. Chem. Phys.*, 1969, **51**, 856.
[142] R. Grice, J. E. Marsh, S. A. Safron, and J. P. Toennies, *J. Chem. Phys.*, 1970, **53**, 3376.
[143] R. J. Beuhler jun. and R. B. Bernstein, *J. Chem. Phys.*, 1969, **50**, 5305.
[144] P. R. Brooks, *J. Chem. Phys.*, 1969, **50**, 5031.

$MX + R \rightarrow XR + M$ would be revealing, though the production of the intense vibrationally very hot MX beam required for reversibility will be difficult.

As in the elastic scattering field, the past two years have seen the extension in several laboratories of these reactive scattering experiments to non-alkali systems. This is of particular significance since alkali reactions are not likely to be characteristic of more general chemical processes.

The non-alkali reactions most intensively investigated so far are the interhalogen ones:

$Cl + Br_2 \rightarrow ClBr + Br$	(refs. 145—148)
$Cl + I_2 \rightarrow ClI + I$	(ref. 149)
$Br + I_2 \rightarrow BrI + I$	(ref. 145)
$Cl + IBr \rightarrow ClI + BrCl$	(ref. 149)

Surprisingly, the product scattering distribution observed in these reactions was similar to that found in the alkali–halogen reactions. Strong forward peaking of the product reminiscent of stripping dynamics is found, though reactions involving reaction with iodine yield a broader distribution. In contrast with the alkali reactions, the cross-sections are only of the order 5—20 Å^2, much smaller than for the $M–X_2$ systems. The detailed dynamics are not therefore likely to be too similar. Herschbach[149] has proposed an osculating complex model resulting from strong attractive forces operating at short ranges. The lifetime of the complex and consequent broadening of the product distribution then correlate with the stability of the halogen complex formed on collision *i.e.* the most stable complexes have I as the middle atom.

The reaction $D + H_2 \rightarrow HD + H$ has also been studied and may be of similar type since a rather symmetrical product distribution is observed.[150] In contrast, H or D atom reactions with halogen molecules appear to proceed by recoil dynamics.[151] Experiments on the reverse process $F + D_2 \rightarrow FD + D$ have been described by Lee[152] in which it was possible, due to kinematic restrictions, to observe the angular distribution of product in specific vibrational states. In view of the additional data available from chemiluminescence studies on this system[153,154] a rather precise picture of the dynamics for this reaction is likely to

[145] Y. T. Lee, J. D. McDonald, P. R. Le Breton, and D. R. Herschbach, *J. Chem. Phys.*, 1968, **49**, 2447.
[146] D. Beck, F. Engelke, and H. J. Loesch, *Ber. Bunsengesellschaft Phys. Chem.*, 1968, **72**, 1105.
[147] J. B. Cross and N. C. Blais, *J. Chem. Phys.*, 1969, **50**, 4108.
[148] N. C. Blais and J. B. Cross, *J. Chem. Phys.*, 1970, **52**, 3580.
[149] Y. T. Lee, P. R. Le Breton, J. D. McDonald, and D. R. Herschbach, *J. Chem. Phys.*, 1969, **51**, 455.
[150] J. Geddes, H. F. Krause, and W. L. Fite, *J. Chem. Phys.*, 1970, **52**, 3296.
[151] J. Grosser and H. Haberland, *Chem. Phys. Letters*, 1970, **7**, 422.
[152] T. P. Schafer, P. E. Siska, J. M. Parson, F. P. Tully, Y. C. Wong, and Y. T. Lee, *J. Chem. Phys.*, 1970, **53**, 3385.
[153] J. C. Polanyi and D. C. Tardy, *J. Chem. Phys.*, 1970, **51**, 5717.
[154] J. C. Polanyi *et al.*, *J. Chem. Phys.*, 1970, **53**, 4091.
[155] Ch. Ottinger and R. N. Zare, *Chem. Phys. Letters*, 1970, **5**, 243.

emerge soon. In many ways the kinetic spectroscopic techniques are complementary to beam methods. They provide more highly detailed rate data for reaction to specific levels than is possible in beam experiments, but yield less or no information on the incident collision conditions or on scattering angles. The combination of the two techniques as described recently by Zare in studying Ba and Ca reactions with NO_2 is therefore likely to be a powerful tool.[155]

Finally, as if to emphasise the growing fusion of molecular dynamics and chemical kinetics, the classic reaction investigated by Bodenstein, $HI + HI \rightarrow H_2 + I_2$ has been studied using beam methods.[156] Impact energies in the range 40—215 kcal mol^{-1} were achieved using an aerodynamically accelerated HI beam. Unfortunately no reaction was observed, setting an upper limit of 0·04 $Å^2$ on the reactive cross-section. It seems that vibrational excitation is required to activate this reaction. The experiment is nevertheless significant in being, apparently, the first neutral beam study of reactions requiring an appreciable activation energy, while the need for an intense beam source for vibrationally excited species emerges as perhaps the next bottle-neck in the technique.

It is concluded that the scattering approach to the study of chemical reaction has already yielded important information on these processes that could be obtained in no other way. The extension of this work to cover a more typical range of chemical reactions is successfully under way. The reviewer looks forward particularly to studies with short-lived, translationally or internally hot species which will permit wholly novel processes to be examined. Initially this may be by way of single-beam gas target experiments rather than of the more powerful but difficult cross beam type.

4 Technique

The power and range of beam methods are at present limited by technique rather than more fundamental causes. A recent review[2] has covered this field in detail. The most important recent developments have been those leading to the final breach in the alkali barrier. A number of machines for this purpose have been described.[157–159] The general prescription combines a high-efficiency mass spectrometer detector in a UHV environment with one or two intense nozzle beam sources each with several stages of differential pumping. A typical machine may thus have 9 or 10 separately pumped chambers. Detection systems commonly use ion counting into several phase-locked scalers.[160]

Other developments include a free-radical source based on thermal pyrolysis[161] and a detector preferentially sensitive to vibrationally excited alkali halide

[156] S. B. Jaffe and J. B. Anderson, *J. Chem. Phys.*, 1969, **51**, 1057.
[157] R. W. Bickes and R. B. Bernstein, *Rev. Sci. Instr.*, 1970, **41**, 759.
[158] Y. T. Lee, J. D. McDonald, P. R. Le Breton, and D. R. Herschbach, *Rev. Sci. Instr.*, 1969, **40**, 1402.
[159] G. E. Busch, J. F. Cornelius, R. T. Mahoney, R. I. Morse, D. W. Schlosser, and K. R. Wilson, *Rev. Sci. Instr.*, 1970, **41**, 1066.
[160] L. T. Cowley, M. A. D. Fluendy, D. S. Horne and K. P. Lawley, *J. Sci. Instr.*, 1970, **41**, 666.
[161] F. Kalos and A. E. Grosser, *Rev. Sci. Instr.*, 1969, **40**, 804.
[162] K. T. Gillen and R. B. Bernstein, *Chem. Phys. Letters*, 1970, **5**, 275.

molecules.[162] Sputtering sources have been developed to yield atomic beams in the awkward 1—40 eV range.[163] Bernstein[164] has produced beams of TlF in selected vibration–rotation states using an electric resonance method, while Brooks has used a hexapole field to focus asymmetric top molecules.[165] Time of flight techniques for velocity analysis have been discussed by Knuth.[166] Zare has reported an optical pumping method for producing polarised gas targets.[167]

[163] J. Politiek, P. K. Rol, J. Los, and P. G. Ikelaar, *Rev. Sci. Instr.*, 1968, **39**, 1147.
[164] T. G. Waech and R. B. Bernstein, *Chem. Phys. Letters*, 1968, **2**, 477.
[165] E. M. Jones and P. R. Brooks, *J. Chem. Phys.*, 1970, **53**, 55.
[166] J. A. Alcalay and E. C. Knuth, *Rev. Sci. Instr.*, 1969, **40**, 438.
[167] R. E. Drullinger and R. N. Zare, *J. Chem. Phys.*, 1969, **51**, 5532.

Volume 14, number 1 CHEMICAL PHYSICS LETTERS 1 May 1972

THE ANGULAR SCATTERING OF SUPERTHERMAL K BY I_2

B.S. DUCHART, M.A.D. FLUENDY and K.P. LAWLEY
Department of Chemistry, University of Edinburgh, Edinburgh EH9 3JJ, UK

Received 8 November 1971

The small angle scattering of 100 eV potassium atoms from a thermal cross beam of iodine molecules has been measured. There is considerable structure, which is interpreted as coming from the Coulomb potential. Some contribution from the upper diabatic state is also probably needed and there is evidence of attenuation of the elastic scattering beyond $\approx 0.9°$.

1. Introduction

Chemical reaction in the system $K + I_2$ has been thoroughly studied at thermal energies by crossed beam techniques [1, 2] and from the magnitude of the reaction cross section is deduced to proceed by a 'harpooning' mechanism. The elastic scattering at relative velocities below 10^5 cm sec^{-1} shows some high frequency structure [3] thought to be due to the Coulomb potential, but the situation is complicated by the dominant reactive process. At energies $\approx$ 100 eV, the reactive cross section is a much smaller fraction of the total cross section and elastic scattering can be used to probe more of the potential energy surface. This system has also been studied from the aspect of ion production by Los [4, 5, 7] and his co-workers in the energy range 1–40 eV.

2. Experimental

A 100 eV K atom beam was generated in a standard manner by surface ionisation through a porous tungsten plug, followed by acceleration and neutralisation by resonant charge transfer. Detection was on a warm Pt/W ribbon followed by an ion counting system similar to that described previously [3]. The nominal angular resolution was $\approx 0.02°$ and time of flight analysis of the main beam yielded a value for the velocity resolution $\Delta V/V \approx 0.2\%$.

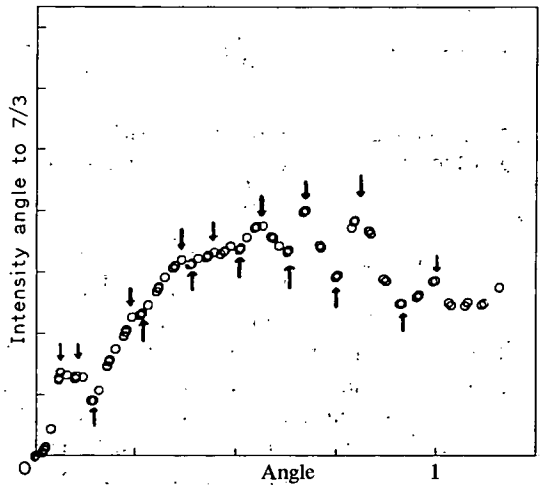

Fig. 1. Observed scattering of 100 eV K atoms from I_2 $I(\theta)\theta^{7/3}$ is plotted against laboratory angle θ. Data is the mean of five scans.

The results are shown in fig. 1. There is a pronounced peak at $\approx 0.07°$ (LAB) and regular structure beyond (periodicity $\approx 0.12°$ (LAB) though of low amplitude. The scattered intensity on a $\theta^{7/3}I(\theta)$ plot diminishes with angle beyond $\approx 0.9°$.

3. Interpretation

There are two electronic states of the system $K + I_2$

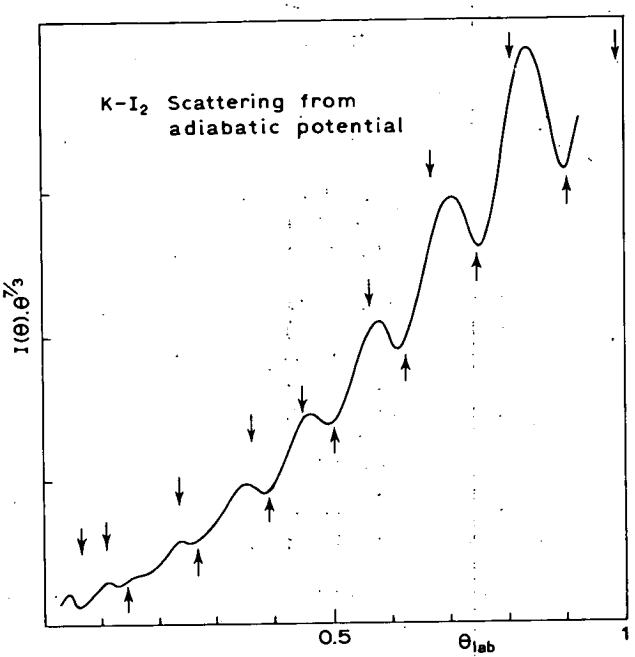

Fig. 2. Apparatus averaged scattering in the laboratory system computed for the adiabatic potential described. Collision energy 100 eV.

(see e.g., [3]) that are likely to operate, the familiar adiabatic (ionic) and diabatic (covalent) $^1\Sigma$ states with an avoided curve crossing at $r_c \approx 5.5$ Å. The scattering including the effect of averaging over the apparatus dimensions, calculated for the lower, adiabatic, potential is shown in fig. 2. The arrows indicate the location of the observed undulations. Although the envelope differs from that observed there is a striking agreement in the periodicity and positions of the peaks. In the computed $I(\theta)$ these undulations are the supernumaries of a rainbow appearing at $\approx 2°$ (LAB). This agreement is all the more striking because the ionic potential used has effectively no adjustable parameters. Apart from a narrow switching region ≈ 0.4 Å wide at the avoided crossing point, the adiabatic potential used was compounded from the Varshni–Shukla potential [6] for $r < r_c$ and a longer range inverse six power attractive potential for $r > r_c$. This latter term had little or no effect on the calculated scattering pattern. In other words the observed peak locations are given very well by a model which treated the K^+/I_2^- pair as point charges with masses appropriate to K and I_2 but with the equilibrium separation of KI. Several refinements are obvious but will not markedly alter the well depth and range of the ionic potential. We deduce from the agreement with experiment that we are observing some elastic scattering from the ionic potential and hence that electron transfer or harpooning is still occurring at 100 eV at least on some trajectories.

The upper $^1\Sigma$ state predicts relatively featureless scattering with a single maximum at somewhat $< 0.1°$ which contains the rainbow and the forward diffraction peak. The well depth and other key parameters of this state are not well characterised but ϵ is probably $\approx 5 \times 10^{-14}$ ergs and so the rainbow will occur at $\approx 0.1°$ at this energy, with the structureless dark side covering the region in which we observe structure in $I(\theta)$.

It is hard to tell from a comparison of the observed scattering and that computed from the adiabatic potential whether we have an excess of scattering at $\leqslant 0.2°$ or a diminution in scattering at angles greater than this angle. In the former case, some contribution from the upper, diabatic state would be necessary to enhance the very small angle scattering. Almost certainl there is attenuation of the elastic scattering at angles $> \approx 0.9°$, and measurements over a wide angular range will settle this point.

The relative importance of the two electronic states in determining the elastic scattering and ion productior depends, in the Landau–Zener approximation on $H_{12}(r_c)$ and the relative velocity. Although becoming increasingly inaccurate at higher energies, the Landau–Zener formula has been used exclusively in the interpretation of the ion production experiments [4] and [5]. Using Baede and Los's value [5] for $H_{12}(r_c)$ of 3.6×10^{-2} eV in the Landau–Zener formula predicts that on trajectories having their turning points in the region of steepest descent of the Coulomb potential, i.e., those contributing to the rainbow structure, the probability of adiabatic behaviour at the crossing is ≈ 0.7–0.8. In this type of situation it is not, of course correct to take the appropriate linear combination of $\sigma_{\text{adiabatic}}(\theta)$ and $\sigma_{\text{diabatic}}(\theta)$ but the close coupled 2-state problem must be solved and this is in progress. An alternative explanation of the apparently mixed scattering behaviour might come from assuming that $H_{12}(r_c)$ is strongly dependent on the orientation of the iodine molecule. The observed scattering would then be a weighted superposition of largely adiabatic

patterns.

The presumably analogous systems K + Cl_2 and K + Br_2 have been investigated by Schlier and co-workers [8] in the energy range 0.5–12 eV and rather similar behaviour was observed. Their interpretation differs however from that proposed here.

4. Conclusions

At 100 eV some elastic scattering in the K/I_2 system take place from the lower, adiabatic state and rainbow supernumaries from this potential have been observed. There is also evidence of extra scattering below $\approx 0.2^\circ$ and a fall off in intensity about $\approx 0.9^\circ$, the latter probably due to the opening up of non-elastic channels. Current values of $H_{12}(r_c)$ do permit mixed adiabatic/diabatic behaviour at 100 eV but the precise way in which these states are to be combined must await a solution of the close coupled problem. Ultimately, a unified explanation of both the ion production (total and differential) cross sections [4, 5, 7], and the elastic scattering must be found.

References

[1] J.H. Birely, R.R. Herm, K.R. Wilson and D.R. Herschbach, J. Chem. Phys. 47 (1967) 993.
[2] K.T. Gillen, A.M. Rulis and R.B. Bernstein, J. Chem. Phys. 54 (1971) 2831.
[3] M.A.D. Fluendy, D.S. Horne, K.P. Lawley and A.W. Morris, Mol. Phys. 19 (1970) 659.
[4] A.M.C. Moutinho, Chemi-ionisation in neutral–neutral systems, Thesis, University of Leiden (1971).
[5] A.P.M. Baede and J. Los, Report Amolf – 807 (1970), F.O.M. Institute, Amsterdam.
[6] V.P. Varshni and R.C. Shukla, J. Chem. Phys. 35 (1961) 582.
[7] G.L. Delvigne and J. Los, Proc. VIIth ICPEAC, eds. L.M. Branscomb et al. (North-Holland, Amsterdam, 1971) p. 277.
[8] V. Kempter, Th. Kneser and Ch. Schlier, J. Chem. Phys. 52 (1970) 5851.

The Angular Scattering of Superthermal Potassium by Hg and I_2

B.S.Duchart, M.A.D.Fluendy and K.P.Lawley

Dept. of Chemistry, University of Edinburgh, Edinburgh, Scotland.

The differential cross sections for scattering 100 eV K atoms from thermal cross beams of Hg and I_2 have been measured at small angles. Experiments on these systems, both well explored at thermal energies[1,2] are of interest in extending potential energy functions derived from thermal scattering into regions of positive potential energy (i.e. the repulsive branch). Furthermore, at these energies new inelastic channels open up and, in the case of K/I_2, the question of adiabatic versus non-adiabatic electronic behaviour arises.

The fast K beam was prepared by surface ionisation through a porous tungsten plug followed by acceleration of the ion beam and resonant charge transfer. Detection was on a 'warm' tungsten ribbon followed by an ion counting system similar to that described previously[3]. The angular resolution in these experiments was $\sim 0.02^{\circ}$; time of flight analysis of the beam velocity yielded $\Delta v/v \approx 0.2\%$.

The results for the K/Hg system are shown in fig 1, where the error bars are two standard deviations in length. The dashed line is an apparatus averaged calculation based upon the potential derived from thermal energy measurements[1] and matched to the observed scattering at 0.5°. The peak at 0.07° in the caculated curve contains the rainbow and other oscillatory structure which, under the resolution of the experiment is in broad agreement with the observed scattering, but cannot yield new information in this region. At angles greater than $\sim 0.3^{\circ}$ the scattering falls off more slowly than predicted from the thermal 8:6 potential, suggesting

Figure 1.

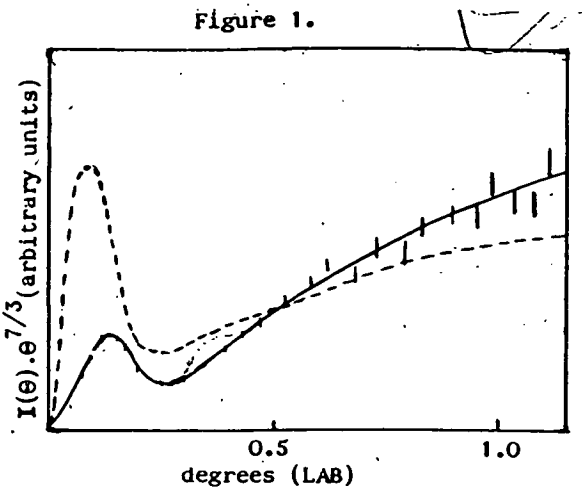

a harder repulsive wall. Inelastic processes are unlikely to be important at these small angles since the potential energy at the turning point of trajectories leading to scattering through $\sim 1^{o}$ is only ~ 0.3 eV.

Results for K/I_2 scattering are shown in fig. 2. In contrast to K/Hg scattering, these show a broad maximum at $\approx 0.7^{o}$, superimposed upon which is some oscillatory structure of higher frequency. A large number of inelastic channels are open in this system, though classical trajectory claculations indicate that at these energies reaction and energy transfer processes do not contribute much to the K scattering at small angles. The dominant process in this region may therefore be either scattering from the adiabatic (Coulomb) or diabatic potentials [4,5]. In the former case the deep well will produce a rainbow in the $0.8\text{–}1.5^{o}$ region while the diabatic case will lead to a very small θ_r as in K/Hg. The scattering expected from potentials of these general types is also shown in fig.2 (——,diabatic,-·-·- adiabatic). These preliminary results suggest that the observed scattering arises from both potentials. This explanation is supported by the recently estimated

matrix element[4] governing the separation of the ionic and covalent potentials at the crossing point, r_c, which if incorporated in the Landau-Zener formula predicts only partial electron transfer at these energies, depending on the impact parameter.

Figure 2.

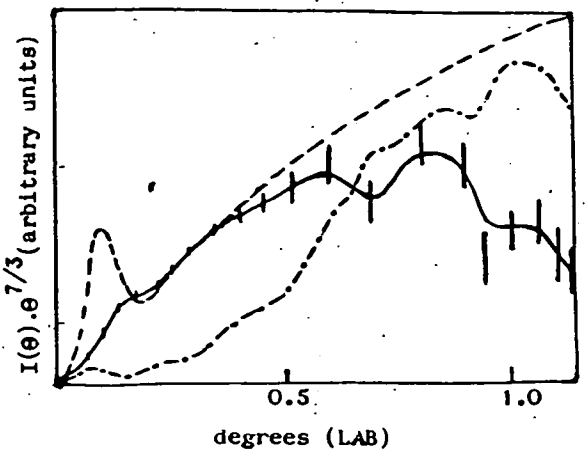

Collisions with impact parameters much less than r_c then scatter predominantly from the diabatic potential while those with larger impact parameters scatteradiabatically. The loss of intensity at angles greater than 1° might then be due to the onset of diabatic behaviour, though inelastic processes cannot be excluded.

References

(1) W.Neumann and H.Pauly, J.Chem.Phys. 52, 2548,(1970)

(2) J.P.Toennies, Ber. Bunsen. Phys. Chem., 72, 927 (1968)

(3) L.T.Cowley, M.A.D.Fluendy, D.S.Horne and K.P.Lawley, J.Sci.Instr., 2, 1021 (1969)

(4) A.P.M.Baede and J.Los, preprint, F.O.M. Institute, Amsterdam.

(5) M.A.D.Fluendy, D.S.Horne, K.P.Lawley and A.W.Morris, Mol. Phys., 19,659 (1970)

ACKNOWLEDGEMENTS

The authors wish to thank A. Milazzotto for help with some of the experiments. This work is supported in part by the Consiglio Nazionale delle Ricerche, and by the European Office of Aerospace Research, OAR, United States Air Forces, under contract F61052-68-C-0068.

REFERENCES

[1] J. Perel, H.L. Daley, J.M. Peek, and T.A. Green, Phys. Rev. Letters 23, 677 (1969) ; L.L. Marino, Phys. Rev. 152, 46 (1966).
[2] J.M. Peek, T.A. Green, J. Perel, and H.H. Michels, Phys. Rev. Letters 20, 1419 (1968) ; D.P. Dewangan and S.B. Karmohapatro, Phys. Rev. Letters 24, 1 (1970) ; D. Rapp and D. Storm, J. Chem. Phys. 53, 1333 (1970).
[3] C.R. Fischer and P.J. Kemmey, Phys. Rev. 186, 272 (1969).
[4] A.C. Roach and M.S. Child, Molecular Phys. 41, 1 (1968) ; A. Dalgarno, C. Botteher, and G.A. Victor, Chem. Phys. Letters 7, 265 (1970) ; D. Rapp and J.R. Ward, J. Chem. Phys. 54, 2766 (1971).
[5] See, e.g. A.C.G. Mitchell and M.W. Zemanski, *Resonance Radiation and Excited Atoms*, Cambridge (1961).
[6] R.W. Anderson, V. Aquilanti, and D.R. Herschbach, Chem. Phys. Letters 4, 5 (1969).
[7] R.E. Weber and L.F. Cordes, Rev. Sci. Instr. 37, 112 (1966).
[8] O. Heinz and R.T. Reaves, Rev. Sci. Instr. 39, 1229 (1968).
[9] G.A.W. Rutgers, in S. Flügge, *Handbuch der Physik*, 26, 129 (1958).
[10] F.J. de Heer, paper presented at the International Conference on Mass Spectrometry, Brussels (1970).
[11] W. Aberth, O. Bernardini, D. Coffey, Jr., D.C. Lorents, and R.E. Olson, Phys. Rev. Letters 24, 345 (1970).
[12] R.D. Hudson, J. Chem. Phys. 43, 1790 (1965).

Elastic differential scattering of metastable mercury 6^3P_2 from K and Hg

E.C. DARWALL, M.A.D. FLUENDY and K.P. LAWLEY,
Department of Chemistry, University of Edinburgh,
Edinburgh, EH9 3JJ, Scotland.

A report is made on the preliminary results of the differential elastic projection of electronically excited Hg, K and Hg. An intersecting beams technique is used, in which the metastable flow is produced by a bombardement of electrons. In the KHg system, at least two potentials are required to interpret the observations. With a K/Hg potential, primary and secondary halos are seen, which suggests the evaluations of* $\epsilon = 2.8 \times 10^{-14}$ *ergs and* $\sigma = 4.9$ *Å, and with another potential KHg*, the L.J. parameters 12:6 receive more tentatively the values* $\epsilon \sim 1 \times 10^{-14}$ *ergs and* $\sigma = 6$ *Å. In the Hg* Hg system, the halo does not appear, but the supernumerary structure suggests a rather deep trough with the approximate value of* $\epsilon \sim 5 \times 10^{-14}$ *ergs.*

On rapporte les résultats préliminaires de la projection élastique différentielle de Hg électroniquement excité, de K et Hg. Une technique de faisceaux entrecroisés est employée, dans laquelle le flux metastable est produit par un bombardement d'électrons. Dans le système KHg, il faut au moins deux potentials pour interpréter les observations. Avec l'un potential K/Hg, on voit des iris primaires et secondaires, ce qui suggère des évaluations de* $\epsilon = 2.8 \times 10^{-14}$ *ergs et* $\sigma = 4.9$ *Å, et avec un autre potential KHg*, les paramètres L.J. 12:6 reçoivent plus tentativement les valeurs* $\epsilon \sim 1 \times 10^{-14}$ *ergs et* $\sigma = 6$ *Å. Dans le système Hg* Hg, l'iris ne se montre pas, mais la structure surnuméraire suggère un creux un peu plus profond avec la valeur approximative de* $\epsilon \sim 5 \times 10^{-14}$ *ergs.*

1 INTRODUCTION

Energy transfer and chemical reaction processes in flames, shock waves, electrical discharges and photochemistry are all situations in which electronically excited atomic and molecular species are of importance. The understanding of these processes must be based upon the intermolecular potentials by which these excited species interact with ground state atoms and molecules. [1-2] Such potentials can in a principle be most accurately obtained from beam scattering experiments, [3] a technique which is perhaps peculiarly suitable for studying short lived species. Total cross section measurements have been made for He metastables by Muschlitz [4] and by Rothe [5] while Grosser [6] has examined their differential scattering with low angular resolution. It is perhaps surprising that more work has not been reported in this area in view of its importance in chemical problems. The reasons for this can probably be found in the fact that most metastable atomic species will not be in S states so that their interaction with other atoms will depend upon their orientation (M_j) and may thus not be describable by a single effective potential.

In this work experiments have been made with metastable Hg atoms since their chemistry is well developed with the object of discovering the importance of these individual potentials and then studying their quenching behaviour by an optical model analysis. [7]

2 EXPERIMENTAL

These experiments were performed in a modulated cross beam apparatus using gated dual channel scalers with paper tape output for data collection. All the beam sources are of the thermal effusion type. For this work the apparatus previously described [8] was modified by the introduction of a metastable atom source and detector.

The metastable beam was formed by crossing a ground state mercury atom beam with a flux of electrons of controlled energy. This device is similar to that described by Martin [9] except for the use of a standard oxide cathode in the present work and is shown schematically in figure 1. About 1 in 10^5 of the Hg atoms in the

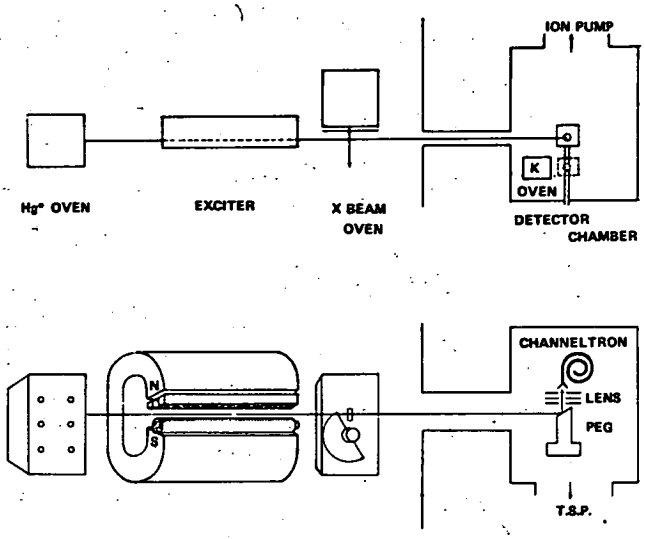

Fig. 1 Apparatus schematic showing electron gun for metastable excitation and Auger detector.

beam could be excited corresponding to a metastable flus of 10^{10}-10^{11} atoms steradian $^{-1}$ sec^{-1}. After collimation the metastable beam collided with a modulated cross beam of the target material (K or Hg in this work). The scattered atoms then entered a U.H.V. chamber (ca 10^{-9} torr) via a narrow channel. Here they struck a clean potassium surface plated from a beam. Electrons ejected from this surface were focussed into a Mullard channel multiplier and counted in the usual way. The maximum counting rate observed was ca 10^5 counts sec^{-1}, while the background count rate for the detector alone (valved off from the main chamber) was 0.1 count sec^{-1} ; more typically when measurements were in progress the background was 2-3 counts sec^{-1}. Once prepared this surface was stable in performance over several days of use.

The known states [10] of Hg with lifetimes sufficiently long to traverse the apparatus (ca 5×10^{-3} secs) are the $^3P_0$, $^3P_2$ and $^3D_3$ located 4.64, 5.43 and 9.05 eV above the ground level. Any of these states could therefore eject an electron from the K surface. A graph of the observed couting in the main beam direction (normalised by the exciter current) versus electron energy is shown in figure 2.

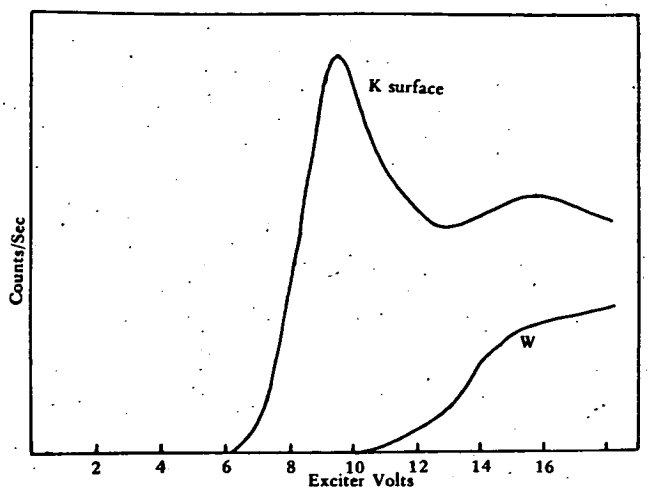

Fig. 2 Excitation function observed on K and W surfaces in the detector for Hg.*

Two maxima are observed at 9.5 eV and 15.5 eV on the potassium surface, the appearance potential for the first was ca 5.9 eV while experiments on a *W* surface yielded only the second maxima with an appearance potential of ca 10 eV.

The differential sensitivity of the K and W surfaces for the D state is not known so that it is impossible to estimate the importance of cascade transitions in producing ^3P at these higher energies. Such cascades were presumably responsible for the second maxima observed by Lichten. The maxima in the excitation function observed at 9.7 eV was in good agreement with measurements by Martin [11] using a different, surface ionisation, technique to detect the metastable flux. In contrast calculations of the electron excitation cross sections for the direct production of the $^3P_{0,1,2}$ states by McConnell and Moiseiwitsch [12] yield a peak in this function at ca 6.5 eV. Although no allowance for contact potentials has been made this difference seems significant and may reflect the inadequacy of coulomb wave functions in the case of the 6P state of Hg.

In the scattering experiments the electron energy was maintained at 10.0 eV so that only ^3P states could contribute. At this energy calculations [12] predict the cross sections for production of $^3P_2$ to be some five times larger than that for $^3P_0$. Since the P_2 would also be more efficiently detected by the K surface, the observed scattering in tentatively attributed solely to this state. Confirmation is currently being sought by magnetic analysis of the beam.

3 RESULTS AND DISCUSSION

The first results of these experiments are shown in figures 3 and 5. In the system K/Hg* the dark and bright sides of a rainbow located at ca 6° LAB (ca 26° CM)

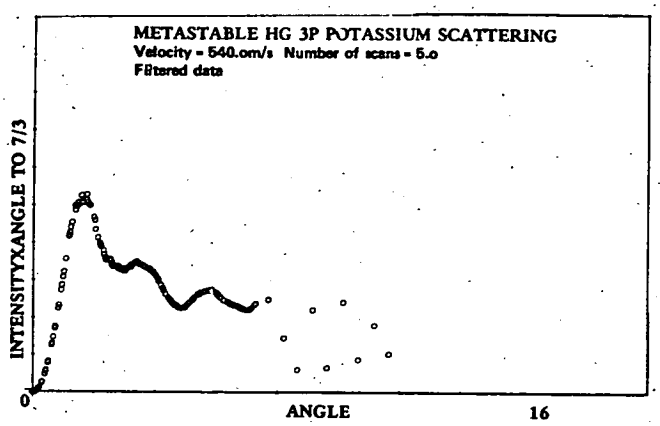

Fig. 3 K/Hg scattering observed in LAB system.*

are distinguishable together with a secondary bow at ca 3°. This pattern in terms of peak positions corresponds approximately to an L.J. 12:6 potential with $\sigma = 4.9$ A° and $\epsilon = 2.8 \times 10^{-14}$ ergs. Figure 4 shows a calculation for such potential. The amplitude of the

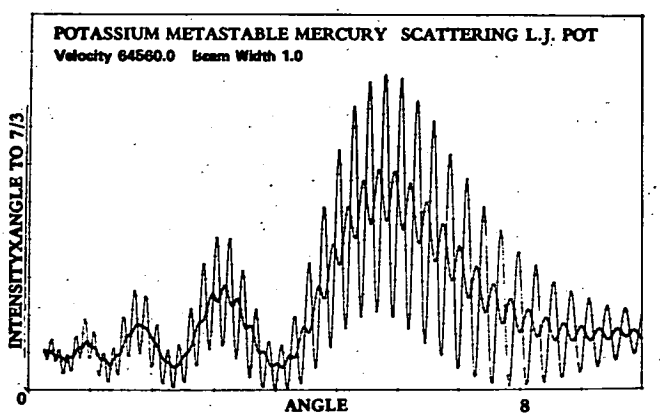

Fig. 4 Scattering calculated for K/Hg with an L.J. 12.6 potential $\sigma = 4.9\ A^{\circ}$, $\epsilon = 2.8 \times 10^{-14}$ ergs.*

innermost peak is clearly very badly reproduced and although accuracy is not high in this region due to the proximity of the main beam the discrepancy is significant. It has not been possible to find a potential with the usual r^{-6} long range form producing this ratio of amplitude in the peaks. Although all inelastic channels up to the free electron continuum are open it seems unlikely that inelastic processes can be responsible for attenuating the rainbow peak. This would require quenching cross sections of the order $\pi \beta^2_{\theta R}$ where $\beta_{\theta R}$ is the impact parameter leading to scattering at the rainbow angle, i.e. in this case to quenching cross sections ca 100 Å. A cross section of this magnitude is unlikely in view of the energy defects involved and the large transfer of energy to translation that must consequently occur in such inelastic collisions.

The coupling scheme for the molecule KHg* is not known but asymptotically a range of potentials must occurs corresponding to the different M_j states of the $^3P_2$ Hg. Due to the large spin orbit coupling it is not possible to describe all the states in terms of single valence bond structures but some can be expected to show substantial differences.

The innermost peak may therefore arise from the operation of a second potential with a shallower well (ca 1×10^{-14} ergs) which would yield a rainbow at this angle. If this potential is constrained to the same $C^{(6)}$ (15×10^{-58} ergs cms^6) as obtained for the other potential then σ must be ca 6Å. In comparison with the ground state interaction these potentials are much shallower and of longer range. Interestingly the Slater Kirkwood estimates for $C^{(6)}$ are in much closer agreement here than for the ground state potential where present experiments and theory differ by a factor of 5 [2].

In the Hg/Hg* system a number of potentials are again operating and in principle the possibility of interference effects arising from the exchange of the excitation also exists. However, symmetry oscillations due to identical particle collisions are not likely to be too important due to the wide range of isotopes present.

The measurements, figure 5, show quite clearly the $\theta^{-7/3}$ dependence expected for a long range r^{-6} potential

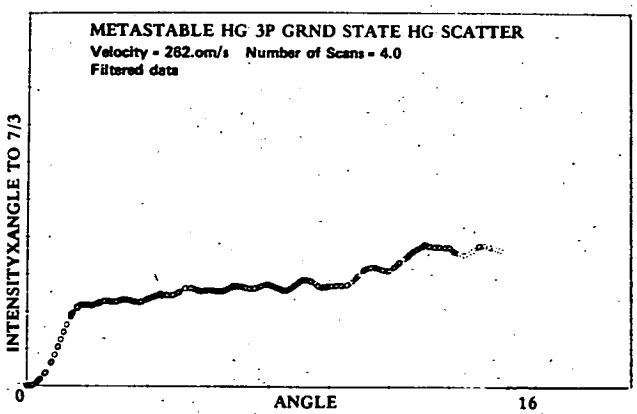

Fig. 5 Hg/Hg scattering observed in LAB system.*

form. Considerable structure is also visible though the measurements do not apparently extend as far as the rainbow. The lower limit of 48° CM thus established for this phenomena implies $\epsilon = 3 \times 10^{-14}$ ergs. For comparison in figure 6 a calculation for an L.J. 12.6 with $\epsilon = 3 \times 10^{-14}$ $\sigma = 4.3$ Å is shown ; quantitative fitting is not worthwhile in the absence of a rainbow but nevertheless an interpretation of the structure in terms of a single potential with σ ca 4.5-5.0 Å, ϵ ca 5×10^{-14}

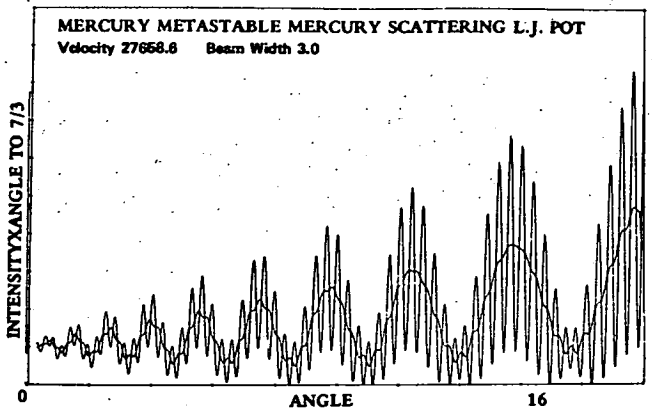

Fig. 6 Scattering calculated for Hg/Hg with an L.J. 12.6 po tential σ= 4.3 A°, ϵ= 3 x 10^{-14} ergs.*

ergs seems possible. Unfortunately such a potential yields $C^{(6)}$ ca 10^{-57} ergs, four or five times larger than Slater Kirkwood estimates, although this difference is no worse than that currently existing between theory and experiment for the ground state alkali/mercury interaction. It is thus possible that this anomaly, implying considerable departure from the L.J. form in the outer part of the potential bowl is associated with the S state of Hg and that Hg/Hg* collisions can be reasonably described by a single effective potential.

Support from the North Atlantic Treaty Organisation and from the U.K. Science Research Council is gratefully acknowledged.

REFERENCES

[1] H.J. Kolker and H.H. Michels, J. Chem. Phys., 50, 1762, (1969).
[2] E.C. Darwall, M.A.D. Fluendy and K.P. Lawley, Mol. Phys. 19, 673, (1970).
[3] R.B. Bernstein and J.T. Muckerman, Adv. Chem. Phys., 12, 389, (1967).
[4] H.L. Richards and E.E. Muschlitz Jr., J. Chem. Phys., 41, 559, (1964). and G.M. Smith and E.E. Muschlitz Jr., J. Chem. Phys., 33, 1819, (1966).
[5] E.W. Rothe, R.H. Neynaber and S.M. Trujillo, J. Chem. Phys., 46, 346, (1967).
[6] J. Grosser and H. Haberland, Phys. Letts. 27A, 634, (1968).
[7] R.M. Harris and J.F. Wilson, J. Chem. Phys., 54, 2088,(1971).
[8] L.T. Cowley, M.A.D. Fluendy, D.S. Horne and K.P. Lawley, J. Sci. Inst., 2, 1021, (1969).
[9] L.J. Doemeny, F.J. Van Itallie and R.M. Martin, Chem. Phys. Letters, 4, 302, (1969).
[10] M.N. McDermott and W.L. Lichten, Phys. Rev., 119, 134, (1960).
[11] R.M. Martin and J. Landenslager, Private communication (1970).
[12] J.C. McConnell and B.L. Moiseiwitsch, J. Phys. B., 1, 406, (1968).

Space focusing of molecules with a negative slope Stark interaction

D.C. LAINÉ and R.C. SWEETING
Physics Department, University of Keele,
Staffordshire, ST5 5BG, U.K.

Methods of space focusing of molecules that decrease in energy in an applied electric field are described. Experimental results are presented for coaxial, single-wire, Maltese-cross and crossed-wire electrode geometries. Of these methods, the crossed-wire focuser appears to possess superior focusing properties in practice. Applications of this type of molecular optical system are briefly discussed.

Les méthodes de focalisation spatiale de molécules qui décroissent en énergie dans un champ électrique se sont ici decrites. Les résultats expérimentaux sont présentés pour les géométries d'électrodes en forme de coaxial, de fil-simple, de croix-de-Malte et fils-croisés. De ces méthodes le focalisateur en forme de fils-croisés apparaît posséder des propriétés focalisantes pratiquement supérieures. L'application de ce type de système d'optique moléculaire sont discutées brièvement.

1 INTRODUCTION

Space focusing of molecules that increase in energy in an applied electric field is readily achieved by the use of multipole focusers of the type used in beam masers and other molecular beam systems. However, space focusing of molecules that decrease in energy in an applied electric field is more difficult, but is possible in principle using the following methods (i) coaxial, (ii) single-wire, (iii) Maltese-cross (iv) crossed-wire and (v) alternate-gradient focusing. Results for method (v) have been reported in some detail by Kakati and Lainé [1] and by Gunther and Schügerl [2]. Alternate-gradient focusing represents a special case, since molecules whose Stark energy either increases or decreases (positive or negative slope Stark interaction, respectively), may be simultaneously focused under favourable circumstances. A combination of alternate-gradient with a conventional multipole focuser can in principle, however, be used to selectively focus molecules whose Stark energy decreases in an applied field [3].

Potential energy surfaces and collision processes

M. A. D. FLUENDY and K. P. LAWLEY

Department of Chemistry, University of Edinburgh, Edinburgh, Scotland

1. Introduction

The forces exerted among a group of atoms are traditionally divided into two classes, those operating between molecules (intermolecular) and those arising intramolecularly and responsible for bonding. In this article we stress the essential unity of such forces, their common origin in quantum theory and their representation as the gradients of a multidimensional potential surface. From this foundation we trace the influence of these surfaces upon the properties of isolated molecules and of systems containing large numbers of interacting species. Such a programme embraces most of chemistry and a sizeable fraction of physics. This discussion will be confined to relatively simple systems where some degree of quantitative understanding is possible and will be strongly biased towards their time dependent behaviour.

The connection between potential surfaces and bulk behaviour is made in two stages. In Section 3 the interaction between pairs of atoms or small molecules is discussed in terms of collision cross sections for various processes. The Boltzmann equation, which relates these cross sections for pair interactions to the bulk behaviour of a large system, forms the core of Section 4. With these two steps it is possible to relate properties such as viscosity and thermal conductivity to the potential surface. Solid state properties are, of course, also governed by a many body potential surface but the cross section concept is less useful here and this phase is not discussed.

Many potential surfaces have a minimum and are capable of supporting bound states. This region of the potential is the domain of spectroscopy. If other atoms or molecules are introduced the contours of the surface are altered and can be explored through the pressure broadening of spectral lines or, if attention is shifted to the perturbing species, by scattering methods.

The use of such scattering methods is described in Section 5 which is especially concerned with the interaction of three particle systems and extends the more elementary results of previous sections to the problem of chemical reaction. This has been a particularly active area in the last decade and computer simulation of the reaction process using classical mechanics has been a valuable tool. Experimentally the new techniques of molecular beam scattering and the study of light emission from chemical reactions, 'chemiluminescence', have yielded much new information.

To say that any phenomenon is governed by a single intermolecular or atomic potential that does not contain the positions of all the electrons explicitly is an approximation since the possible coupling of the electronic and molecular motion has been discarded. Potentials of this type for adiabatic or 'relaxed' electronic motion are perfectly satisfactory for interpreting most vibrational spectra and collision processes occurring at thermal energies. However, in some phenomena such as electronic energy transfer or chemi-ionization this approximation fails. Such cases are then usually described by a family of potentials corresponding to the possible quantum states of the collision system and the non-adiabaticity introduced by allowing transitions from one potential surface to another. Systems of this type are discussed in Section 6.

2. The origin and mathematical description of the forces between atoms

An energy surface is a multi-dimensional plot of the electronic energy of a group of atoms such that all geometrical configurations are covered. We can use quantum mechanics in several ways in describing these surfaces. Firstly, we could attempt a complete calculation of the whole surface starting with the properties of the isolated atoms. Failing this, we can hope for guidance as to the mathematical form or parametrization of the potential energy and a classification of the various electronic states of the whole system. Finally, wave mechanics will help us pick out particular atomic arrangements that are unusually stable.

Calculating the electronic energy of a group of atoms in a sequence of arbitrary configurations is not an easy problem in wave mechanics. To obtain the various electronic properties of stable molecules, one starts with the nuclei fixed in their equilibrium positions and finds the electronic eigenenergy and eigenfunctions. In contrast, to map the potential energy function of even a three atom system—which may not give rise to a stable triatomic molecule—a grid of nuclear configurations must be covered over which the electronic energy is found, thus increasing the length of the calculation many times. For instance, if it is reckoned that ten points are sufficient to define a diatomic potential energy curve up to 1 eV, then somewhat in excess of 10^3 points will be needed to define a 3-atom potential function up to the same energy with the same precision.

Bond energies are normally calculated by a variational method, in which small changes in the electron distribution are made until a minimum in the electronic energy is found. This is a time consuming process and in calculating the potential energy function of aggregates of atoms the emphasis has been on semi-empirical methods. The crudest of these and one much used in the early days of transition state theory, is simply to assume that the energy of

a group of n atoms is the sum of the energies of the $n!/\{2!(n-2)!\}$ possible diatomics that can be picked out. However—and this is the root of the problem—interatomic potentials are not additive in this way and the method in general predicts potential minima on the surface that are far too deep and correspond to spuriously stable polyatomic molecules.

The systems of three hydrogen atoms and of two hydrogen atoms and a proton occupy a unique place in the absolute theory of reaction rates and the former especially forms a test case for all theories of bimolecular reactions ($H + H_2 \rightarrow H_2 + H$). Even here, however, the most commonly used three atom potential is a semi-empirical one based upon the division of the three atom configuration into the three possible atom pairs, (1,2), (2,3) and (1,3).

As for the general interaction of three or more atoms other than hydrogen the full machinery of quantum chemistry has yet to be employed. The present position in this important field is that purely empirical surfaces are constructed from experimental observations of the details of chemical reaction, molecular spectra and collisions.

The problem of calculating intermolecular forces simplifies considerably if the atomic configuration is such that various molecules with essentially non-overlapping electron distributions can be picked out. Perturbation methods can then be used to calculate the dispersion forces between these molecules and the moments of charge can be usefully defined (dipole, quadrupole etc.) together with their interaction energy. *Dispersion forces* arise from the fact that any instantaneous electron-nucleus configuration has a dipole moment. For two atoms there will be a pair of dipoles and consequently an energy of interaction between them which is a function of the co-ordinates of all the electrons. Upon weighting this interaction energy by the probability of the corresponding configuration of electrons in the isolated atoms and integrating over all electron co-ordinates—as we must to arrive at an observable property—we find that this contribution vanishes! However, their mutual interaction perturbs the electron distributions and upon averaging the instantaneous dipole-dipole energy over this perturbed electron distribution, a non-vanishing result is found. This may be viewed as a correlation of the electron motion in the two atoms and the limiting form of the potential for two S-state atoms or spherically polarisable molecules is:

$$V(r) \simeq -C^{(6)}/r^6 - C^{(8)}/r^8 \qquad (1)$$

Where the r^{-6} and r^{-8} terms correspond to second order dipole/dipole and dipole/quadrupole interactions respectively.

The calculation of the coefficient $C^{(6)}$ is reliable to a few percent if the electronic spectrum of the atom is dominated by a single very intense line, for then the mutual perturbation of the two atoms that results in the dispersion force effectively causes the mixing of only one excited electronic

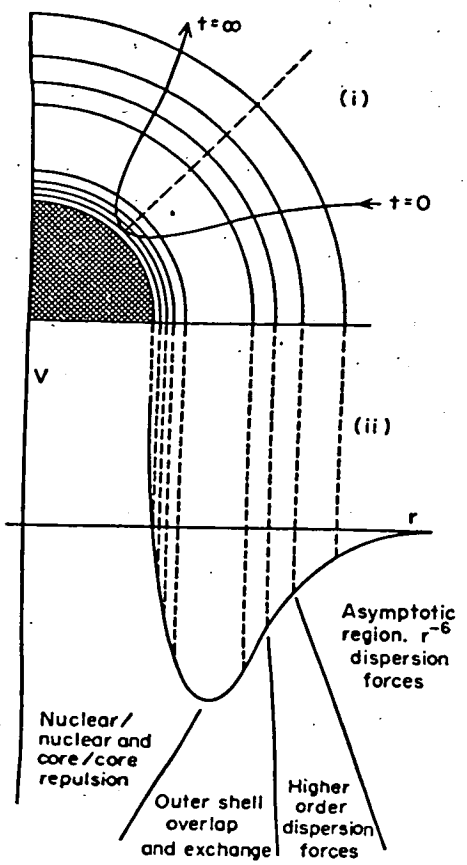

FIG. 1 A typical bipolar potential, shown in (i) as an equi-potential contour diagram (one quadrant only) and in (ii) as a plot of $V(r)$, which is also a radial section through the surface represented in (i). Superimposed on (i) is a typical trajectory $r(t)$. The major forces operating over different portions of the internuclear separations are also indicated. —

Clearly, a potential of the form (2) or (3) even if adequate for atomic collisions, omits some essential features of molecular interactions. Firstly, the potential will in general be angle dependent and there are sound reasons [illegible]

$$V(r, \theta) = -C^{(6)}r^{-6}\{1 + \gamma^{(6)} \cos^2 \theta\} + C^{(12)}r^{-12}\{1 + \gamma^{(12)} \cos^2 \theta\} \quad (5)$$

where $\gamma^{(n)}$ is an anisotropy parameter. For a heteronuclear pair symmetry arguments would require the inclusion of a term in $\cos \theta$ or some higher odd power.

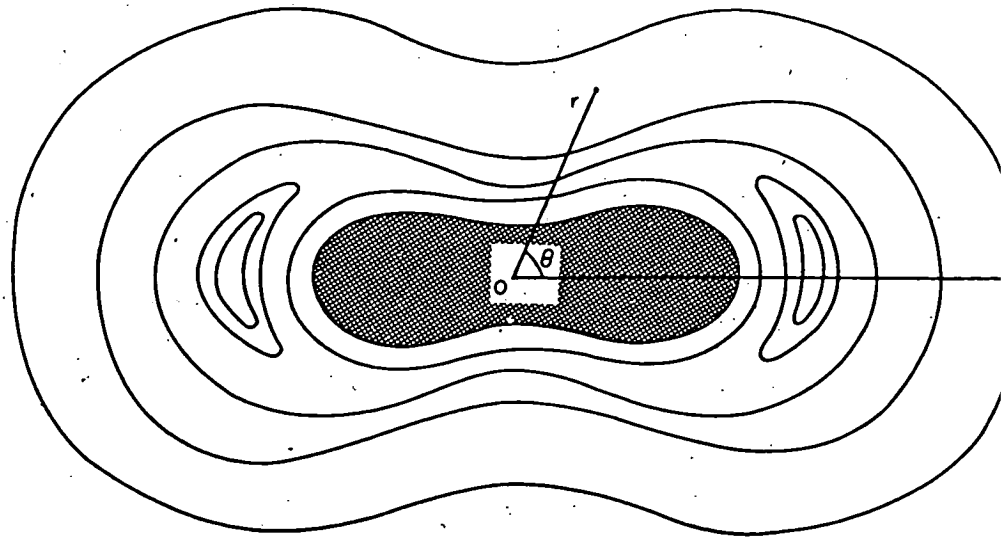

FIG. 2 A polar plot of an angle dependent potential. Compare Fig. 1(i).

A potential of the type (5) can be plotted on a polar diagram, Fig. 2. However, the equations of motion of the combined system are now much more difficult to solve because the angular motion of the interparticle vector **r** is coupled to the rotation of the molecule through the angle dependent terms in the potential. Both quantum mechanically and classically the possibility of rotational energy transfer exists. This will occur very readily even with light diatomics as can be seen from the rapid equilibration of the rotational energy with the translational energy in gases at thermal energies. It has, however, proved rather difficult to devise experiments to measure $\gamma^{(6)}$ and $\gamma^{(12)}$ directly. From a spectroscopic point of view the relevant phenomenon is the pressure broadening of rotational lines, but the analysis of the data in terms of potential anisotropy coefficients—except in cases where the long range part of the potential broadening is dominated by very long range dipole quadrupole effects (falling off as r^{-4})—has not been achieved. Perhaps the root of the trouble can be seen from quantum (or classical) calculations of rotational transition probabilities for single collisions. It is found that while the anisotropy in the attractive part of the potential exerts a couple on the molecule in one direction, the anisotropy in the repulsive branch (at least in the form (5)) exerts a couple in the opposite sense and in any collision leading to appreciable rotational interaction these effects partially cancel each other. Since collisions cannot be examined before completion, there is no direct way of assigning the resultant energy transfer between the two terms in the potential. Clearly, what is needed is an effect due to grazing collisions so that only the longest

range part potential is sampled and a special scattering experiment is indicated. A few such experiments have been performed but only on highly polar molecules and the method is not yet a general one. Another technique of some promise in the field of anisotropic potential measurement is the relaxation of nuclear spin polarization. Here, collision induced J or m_J transitions in a gas are transmitted to the nuclear alignment previously induced by a magnetic field and hence result in spin depolarization. So far, the method has only been applied quantitatively to H_2, where such collisions (mainly those changing m_J) are the result of long range quadrupole-quadrupole forces in which the coupling potential varies as the inverse fifth power of the molecular separation and does not probe very deeply into the potential. As far as bulk properties are concerned, some angle averaged value of the coefficient of the inverse sixth part of the potential is measured and the effect of γ and C cannot be separated.

We now tackle the problem of writing down a general intermolecular potential between an atom and a diatomic molecule. Equation (5) is clearly not sufficient in that it does not contain the separation of the two atoms comprising the diatomic. As far as the long range part of the potential is concerned this is of no consequence because although it might be argued that the polarisability of a molecule and hence the value of $C^{(6)}$ depends upon the interatomic distance, the potential given by (5) really refers to a particular vibrational state of the molecule. Gentle collisions cannot cause vibrational transitions and the quantum number dependence is suppressed. However, for harder collisions the possibility of vibrational energy transfer or even bond rupture exists and the A—B co-ordinate must be explicitly included in any expression for the potential. The minimum number of variables that must now appear in the potential $V(r_{AB}, r_{AC}, r_{BC})$ is three because, of the nine co-ordinates needed to specify the positions of the three atoms with respect to some fixed origin, three can be regarded as fixing the position of the centre of gravity and three as fixing the orientation of the triangle formed by ABC in space; to all of which the potential is invariant. The forces involved will now be of the long range attractive and short range repulsive types discussed together with 'chemical' forces, i.e. those depending on the interaction of electrons with antiparallel spins.

If we wish to represent a function of three variables, e.g. $V(r_{AB}, r_{AC}, r_{BC})$ or the electron density of a molecule, $P(x, y, z)$ we can plot its value on some chosen plane in the co-ordinate space which, in turn, imposes a relationship between the three variables thus reducing them to only two independent ones. The most common choice is to plot the potential of a linear configuration (imposing the restriction $r_{AC} = (r_{BC} + r_{AB})$. When this is done, three types of surface might be encountered, Fig. 3. All three are based upon the common feature that both AB and BC are stable molecules and the surfaces are thus

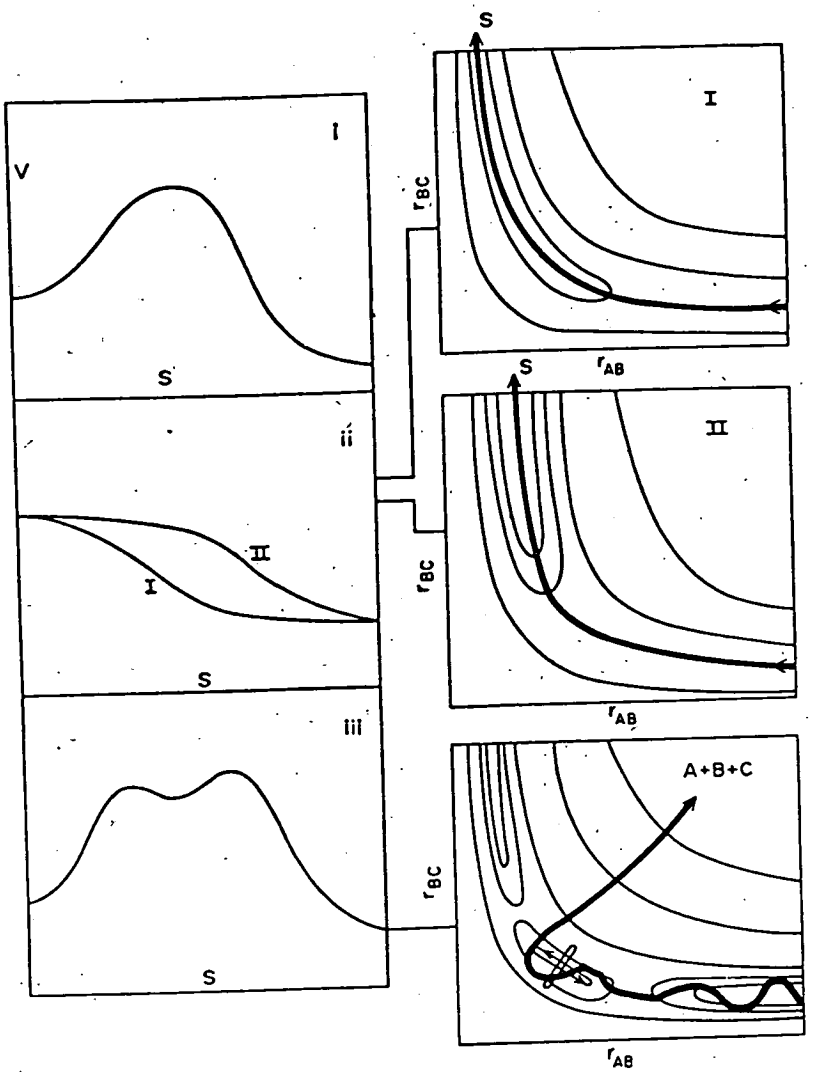

FIG. 3 Three typical 3-body potential surfaces. On the left the potential energy along the path of minimum potential is plotted. In (i) a potential barrier is encountered. The surfaces that give rise to monotonically falling (or rising) potential (ii) are of two kinds, illustrated on the right. (I) is of the early downhill kind and in (II) the exoergicity is released later in the collision.

In surface (iii), a potential well is enclosed by two potential barriers. The trajectories of the two normal stretching modes, 1 (asymmetric) and 2 (symmetric) are shown, together with that of a collision (3) leading to dissociation.

characterized by an entrance and an exit valley in which r_{AB} or r_{BC} becomes large. In passing from one of these valleys to the other, by the route of lowest potential, the first type of surface is characterized by a potential maximum (in fact a saddle point) somewhere along the path, the second type by a monotonically rising or falling potential along the path and the third by a potential minimum.

The third type of surface, exhibiting a potential minimum, is capable of supporting a stable triatomic molecule, which would be linear in the example illustrated. In principle, the vibrational levels of this molecule can be investigated by infra-red spectroscopy and in Fig. 3(iii) the part of the surface traversed during execution of two normal modes of vibration is sketched. We can display the course of a collision by plotting on the same surface the trajectory of the point $r_{AB}(t)$, $r_{BC}(t)$. Much more of the surface is explored on this path than by bound state spectroscopy.

The calculation of trajectories under the influence of these more complicated potentials must be by numerical integration (Section 4). For the linear configuration, the essential results can be visualized by the simple device of skewing the axes.

It is of considerable interest to know whether a given group of atoms can form a stable complex, i.e. if their lowest potential surface is of the type shown in Fig. 3(iii). Theory, based on simple molecular orbital arguments, gives some guidance for triatomic groups. The number of valence electrons in bonding, anti-bonding and non-bonding orbitals is counted and the balance determines whether the group will exhibit a potential minimum. Furthermore, the shape, whether bent or linear, can also be deduced from an inspection of the correlation diagrams connecting the linear molecular orbitals to those of the 90° configuration. These are familiar in spectroscopy as Walsh's rules and there is every reason to expect them to hold for metastable species as well.

3. Potential surfaces and collision cross sections

Collisions are fundamental to chemistry. Thus, chemical and thermal equilibrium are maintained by collision, while the rates of chemical change, mass and energy transfer are all controlled by the frequency and detailed dynamics of molecular collisions. In their turn these are a function of the potential surfaces over which the molecules interact. To understand these phenomena it is necessary to break the problem into two. In the first part the pairwise behaviour of two particles is described as a probability or *cross section* for some specific process. A statistical theory is then used to extrapolate these bimolecular properties to systems containing very many particles. It is with the first stage of this programme that we are concerned in this section.

Collisions can be divided into two types.

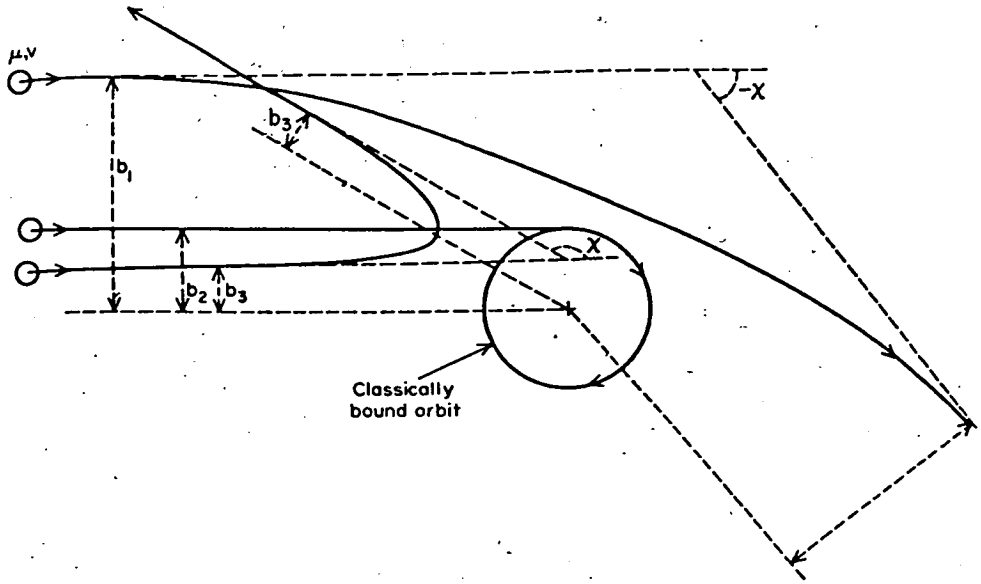

FIG. 4 Trajectories followed by particles with a reduced mass μ and velocity v moving in a Lennard Jones 12:6 potential (centre of mass, CM, co-ordinates). Collisions with large impact parameters, b_1, interact primarily with the attractive branch of the potential and result in negative deflection angles $-\chi$. Collisions with small impact parameters, b_3, are dominated by the repulsive part of the potential and exit with a positive deflection angle. A classically bound orbit is also shown; at higher collision energies this infinite deflection collision is replaced by one with the maximum negative deflection scattering at the rainbow angle.

spend the maximum time in close proximity and indeed, at the lowest positive energies, to atoms entering classically stable bound orbits about one another.

On the molecular scale it is not possible to select collisions with specific impact parameters, though other collisions properties such as the velocity may be more or less closely defined. Observation of the results of collision must therefore invariably be the result of averaging over many collisions in which the impact parameters are distributed randomly over a plane perpendicular to the impact velocity, Fig. 6. As a further consequence it is no longer possible to distinguish positive and negative deflections, all trajectories ultimatley exiting between 0 and π (CM angles). Thus scattering at b_1, b_2 and b_3, in Fig. 5, will all contribute at the same angle. This fact will have important results when we construct a quantum mechanical theory.

The angular intensity from the random flux of atoms as pictured in Fig. 6, is defined in terms of a *differential cross section*, $\sigma(\chi)$:

$$\sigma(\chi)\,d\omega = \frac{\text{Flux of atoms scattered into solid angle element } d\omega \text{ at angle } \chi \text{ (atom sec}^{-1}\text{)}}{\text{Incident flux (atoms sec}^{-1}\text{ metres}^{-2}\text{)}} \qquad (6)$$

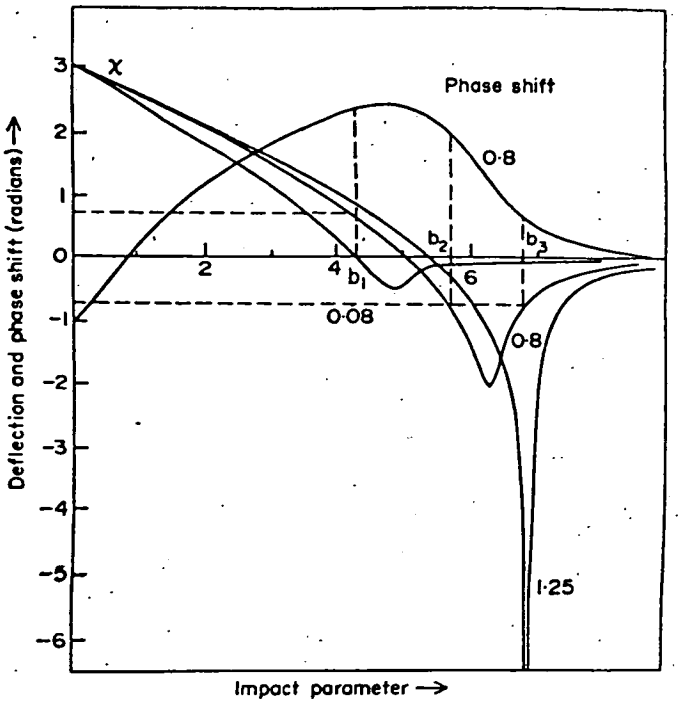

FIG. 5 The variation of phase shift and deflection angle with impact parameter is shown for several reduced energies (ε/E). Collisions with impact parameters at b_1, b_2 and b_3 all produce deflections through the same polar angle, $|\chi|$. The phase shifts experienced by these collisions are all different so that the trajectories will mutually interfere.

Thus $\sigma(\chi)$ has the dimensions of area; analogous laboratory differential cross sections can be obtained by a suitable transformation. The number of atoms entering the collision zone through the shaded ring b to $b + \mathrm{d}b$ if a uniform flux of I atom sec^{-1} metre^{-2} falls on the plane containing the ring is:

$$\mathrm{d}n = I\,2\pi b\,\mathrm{d}b \tag{7}$$

A similar number must exit through the shaded area on the sphere at the right which subtends a solid angle $\mathrm{d}\omega$. Since the potential is independent of angle the scattering is also independent of the azimuthal angle. Thus the solid angle element $\mathrm{d}\omega$ is 2π . $\sin\chi\,\mathrm{d}\chi$ and combining these results:

$$\sigma(\chi) = \frac{b}{\sin\chi\,|\mathrm{d}\chi/\mathrm{d}b|} \tag{8}$$

A classical calculation of $\mathrm{d}\chi/\mathrm{d}b$ from the impact velocity and interatomic potential will produce a result for $\sigma(\chi)$ valid in the classical limit.

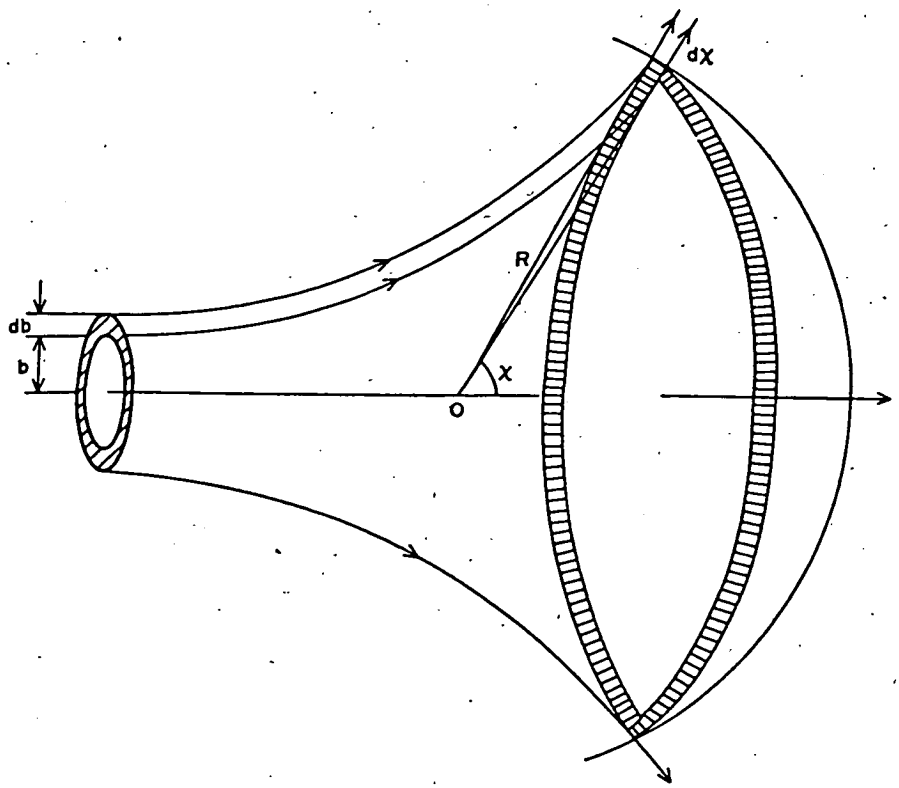

FIG. 6 Particles incident in the ring between b and $b + db$ exit through the shaded strip between an angle χ and $\chi + d\chi$. The target molecule is at 0 and the scattered flux is mapped over a large sphere radius R centred at 0.

Other types of cross section are also useful for example in the inelastic process:

$$A_i + B_j \rightarrow A_k + B_l \tag{9}$$

in which the quantum states of the atoms are changed we can define $\sigma_{kl}^{ij}(\chi, v)$ as the probability of a collision at velocity v between the species A_i and B_j resulting in A_k and B_l being scattered into unit solid angle at χ. More importantly we can define a total cross section representing the total probability for a process irrespective of the final scattering angle as:

$$\sigma_{\text{total}} = 2\pi \int_0^{\pi} \sigma(\chi) \sin \chi \, d\chi$$

where the sin χ factor allows for the increase in solid angle as $\chi \rightarrow \pi/2$.

At this point disaster strikes! In classical mechanics any force no matter how

small will produce a finite deflection so that for any unbounded potential we reach the unhappy conclusion that total crosss sections must always be infinite. This feature is resolved in a quantum mechanical theory which is also more elegant in providing a unified view of both bound and unbounded motion, as well as accounting for experimentally observed interference effects.

Once again the centre of mass and relative motions can be separated. The total wave function Ψ being the product of the wave function U describing the relative motion and G the function for the motion of the centre of mass. As before, the relative motion, $U(r, \theta, \phi)$ contains all the chemistry. In the usual fashion the function $U(r, \theta, \phi)$ is related to the Hamiltonian operator $\mathscr{H}$ by the eigen-value equation:

$$\mathscr{H}U = EU \tag{11}$$

or, writing this relation in full and with the Hamiltonian in polar co-ordinates:

$$\frac{h^2}{8\pi^2\mu}\left[\frac{1}{r^2}\frac{\partial}{\partial r}\left\{r^2\frac{\partial U}{\partial r}\right\} + \frac{1}{r^2\sin\theta}\frac{\partial}{\partial\theta}\left\{\sin\theta\frac{\partial U}{\partial\theta}\right\} + \frac{1}{r^2\sin^2\theta}\frac{\partial^2 U}{\partial\phi^2}\right] - V(r)U = EU \tag{12}$$

where $V(r)$ is the potential operating between the atoms. This relation exactly parallels that for the H atom which after all concerns the motion of two particles, a proton and an electron, in a spherically symmetric potential. Its solution correspondingly follows a similar course.

Since $V(r)$ depends only on r it is possible to separate the radial and angular parts of (12) by writing:

$$U(r, \theta, \phi) = R(r)\,Y(\theta, \phi) \tag{13}$$

The angular solutions are the *spherical harmonics* $Y_{lm}(\theta, \phi)$ with l and m as quantum numbers, and are the functions producing the usual hydrogen like orbital shapes. The energy due to rotation is, $E_{\text{rot}} = h^2l(l+1)/8\pi^2I$; for the equivalent centre of mass sytem of interest here the moment of inertia, I, is μb^2 and:

$$l = 2\pi\mu vb/h \tag{14}$$

where l is the angular momentum quantum number irrespective of whether the motion is bounded ($E < V(\infty)$) or not for the angular momentum is quantized in both regimes.

The radial wave equation is:

$$\frac{1}{r^2}\frac{\mathrm{d}}{\mathrm{d}r}\left\{r^2\frac{\mathrm{d}R}{\mathrm{d}r}\right\} + \left\{\frac{8\pi\mu}{h^2}(E - V(r)) - \frac{l(l+1)}{r^2}\right\} R = 0 \tag{15}$$

It is usual to combine this potential and the repulsive centrifugal contribution, the $l(l+1)/r^2$ term, together. The radial motion then takes place in an effective potential

$$W_l(r) = V(r) + \hbar^2 l(l+1)/2Ir^2, \quad \text{where} \quad \hbar = h/2\pi$$

shown in Fig. 7, different for each l value and for which, in the general case, solutions can only be obtained by numerical integration. Two types of solution are found corresponding to $E < V(\infty)$ bounded motion and $E > V(\infty)$ unbounded motion and are illustrated for a particular effective potential (l value) in the same figure. In the first case the spectrum of solutions is discrete with only specific eigen energies being permitted; these are solutions corresponding to a stable vibrating and rotating diatomic molecule. When the total energy of the system becomes positive there is no longer a restriction on the energies and a continuum of solutions corresponding to unbounded

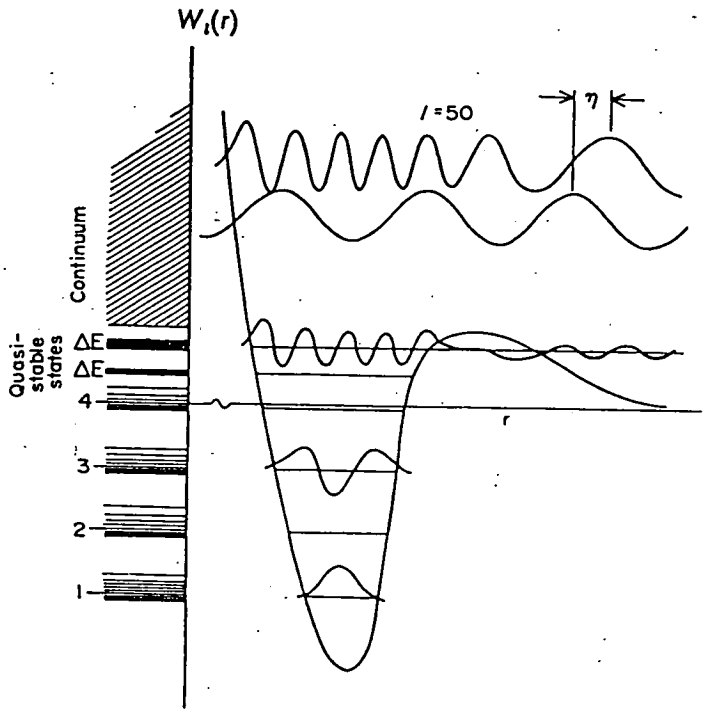

FIG. 7 Spectrum of continuum and bound state solutions for a particle moving through a potential well with a specific angular momentum, $l = 50$. The total manifold of solutions will be the sum over all such pictures, one for every l value; elements in such a spectrum are shown on the left. The phase shift η_l of the continuum solution relative to a free particle is also shown.

motion arise. A 'hangover' effect may be seen, however, the centrifugal potential can result in atoms being 'trapped' in close proximity to one another for quite long periods. These quasi-stable states are known as *resonances* and depending on their lifetime may have quite well defined energies ΔE. Some of the various possibilities are illustrated in Fig. 7.

The importance of these discrete states via statistical mechanics in determining thermodynamic properties is well known, while the combination of these same solutions and information about their coupling with electromagnetic radiation in the form of selection rules leads to a whole wealth of spectroscopic data. All this, however, is another story; here we are primarily concerned with continuum solutions which represent unbounded motion.

In these systems our interest lies not in the immediate region of the collision but in the ultimate change produced. At times long before the collision the system will behave as independent free particles and for a specific energy and angular momentum the wave function for their relative motion valid at $t \to -\infty$ will be of the form $\sin(\mu vr/\hbar - l\pi/2)$. Since there are no terms in the potential that can change the final translational velocity or angular momentum the collision is elastic. The only possible change in the wavefunction at $t \to +\infty$ is a phase shift, η_l, so that the wave function now becomes $\sin(\mu vr/\hbar - l\pi/2 + \eta_l)$. Such phase shifts are illustrated in Fig. 7. An atom entering the potential is first accelerated and then decelerated so that the de Broglie wave is correspondingly compressed and expanded relative to that of the freely moving atom. This phase shift is the only result of the encounter and is a measure of the strength of the potential.

Just as in the classical theory it was impossible to prepare collisions with a specified impact parameter it is not possible to observe the results of a collision made with a specified relative angular momentum. Classically we considered the results due to a uniform flux of particle distributed with impact parameters between 0 and ∞ in terms of a probability function, the differential cross section $\sigma(\chi)$. A similar prescription is suitable in the quantum theory. The uniform flux of particles is now represented by a plane wave, $e^{i\mu vz/\hbar}$ moving along the z axis. After collision the scattered material moves outwards in a spherical wave, $f(\theta)e^{i\mu vr/\hbar}/r$ with a $1/r^2$ fall off in intensity and a modulation in angular distribution given by $f(\theta)$. As would be expected from the connection between the classical impact parameter and the angular momentum quantum number l, (14), it is possible to construct the initial incident plane wave from a suitably weighted sum of individual *partial waves* each with a different l value.

After scattering each partial wave in the incident flux differs only in its phase shift. Physically the interesting part of the post scattered wave is its angular dependence $f(\theta)$ since $|f(\theta)|^2 = \sigma(\theta)$, the differential cross section expressing the relative probability of scattering into unit solid angle at θ. This

term can be extracted from the scattered wave and in terms of the phase shifted partial waves is found to be:

$$\sigma(\theta) = |f(\theta)|^2 = \left| \frac{\hbar}{2i\mu v} \sum_{l=0}^{l=\infty} (2l+1) P_l(\cos\theta)(e^{2i\eta_l} - 1) \right|^2 \qquad (16)$$

where $(2l + 1)P_l(\cos\theta)$ is the angular part of the lth wave and $P_l(\cos\theta)$ is a Legendre function of order l and argument $(\cos\theta)$ and is closely related to $Y_{lm}(\theta, \phi)$. The total cross section then follows by integration over θ as:

$$\sigma_{\text{total}} = \frac{4\pi\hbar^2}{\mu^2 v} \sum_{l=0}^{\infty} (2l+1) \sin^2\eta_l \qquad (17)$$

Cross sections calculated using these quantum relations show a great wealth of structure both in their angle and velocity dependence which is not found in the classical results. The origin of these effects, which can be confirmed experimentally, are seen on Fig. 6 where both phase shifts $\eta(b)$ and deflection angles $\chi(b)$ for $b = l\hbar/\mu v$ are plotted. Scattering occurring at angles where several branches of the deflection function may contribute have different phases. Consequently the scattered wave contribution from each b region will interfere to produce rapid oscillations in their angular dependence with a period of approximately $2\pi/(l_2 - l_1)$. A typical example of such interference can be seen in Fig. 8 where experimental results are compared with a quantum calculation. These observations were made using a crossed molecular beam technique. Two well collimated beams of molecules are formed in a high vacuum tank where the mean free path is very long and are made to intersect at right angles. Collisions between molecules in the beam occur in the intersection region and as a result are scattered out of the beam. The angular distribution of these scattered atoms is then measured by rotating a detector, possibly a mass spectrometer, about the collision zone so that the laboratory differential cross section is obtained. In more precise measurements one or more of the beams would be velocity selected by rotating chopper discs and in some cases a degree of quantum state selection might also be employed. The most interesting feature in this example, the oscillation of widest angle occurring here at 22°, is known as a *rainbow*. It has its origin in the extrema in the deflection angle, $\chi(b)$, versus impact parameter plot where $(d\chi/db) = 0$. Here trajectories with a range of impact parameters are focused into a narrow angular region about the rainbow. The low frequency oscillations in the cross section arise from interference between trajectories lying on either side of this bowl in the deflection angle plot and are known as supernumary bows. The high frequency oscillations are similarly due to interference between these trajectories and those with small impact parameters scattering from the

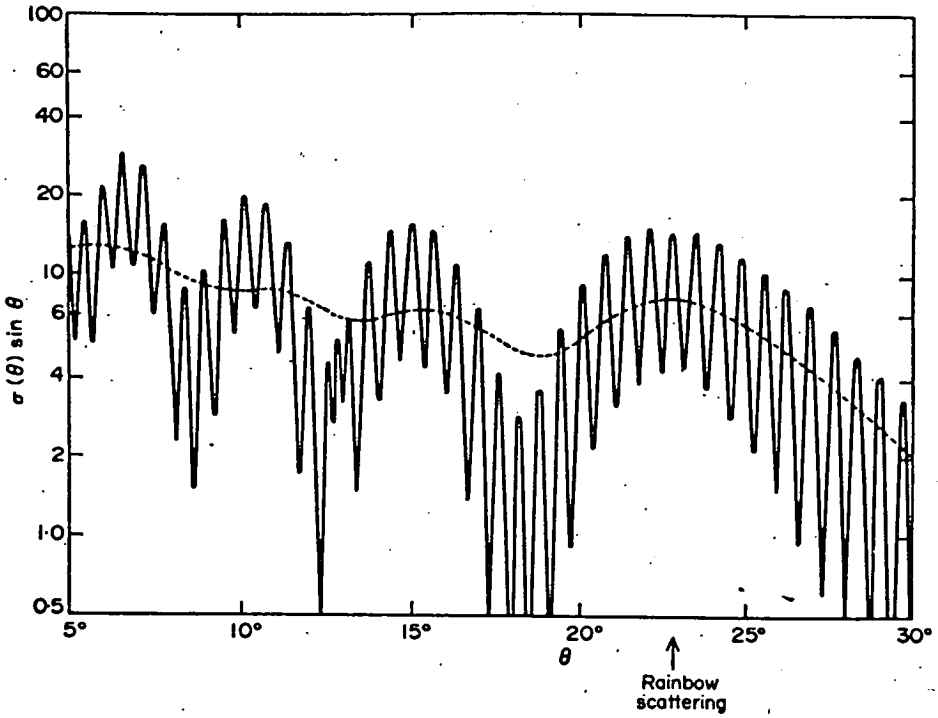

FIG. 8 Differential scattering cross section as calculated and measured for the system Na/Hg at a collision velocity of 1475 ms^{-1} (Reproduced from Hundhausen and Pauly, Zeit. f. Physik. **187**, 305 (1965)). A rainbow is seen at 22° with supernumerary bows at smaller angles.

repulsive part of the potential. Experimental observations of these interference structures and their variation with impact energy can provide detailed information about the potential, though this information is limited to the regions of potential sample by the trajectories, which is always less than or equal to the energy of the impacts. More importantly, cross sections of this type are the input to the theories describing the bulk properties of matter.

4. Relation of cross sections to bulk properties

The first steps in making the connection between the potentials operating at a molecular scale and the observed properties of large aggregates of matter were made in the previous section. There the differential cross section emerged as the natural description of results of binary particle interactions. This quantity is the interface between collision theories and the statistical treatments of an ensemble which will yield results for bulk properties such as viscosity, pressure or chemical reaction rate. As in the previous section the

discussion is largely limited to bimolecular systems in which only elastic collisions are important. The extension to include inelastic processes is straightforward, though tedious, and introduces no new concepts.

Total understanding of a bulk sample of matter would require momentum and position co-ordinates for all the particles in the system. Fortunately, in practice a much reduced scale of information provides an adequate description. This information is usually presented in the forms of a distribution function, $f(\mathbf{r}, \mathbf{p}, t)$, the probability of finding a molecule between $\mathbf{r}$ and $\mathbf{r} + d\mathbf{r}$ with momentum $\mathbf{p}$ to $\mathbf{p} + d\mathbf{p}$ relative to another molecule at time t to $t + dt$. These functions, their measurement and relation to bulk properties are discussed in detail by J. S. Rowlinson (Ref. 3); suffice it to say here that the bulk behaviour of a system can be calculated in a straightforward way from $f(\mathbf{r}, \mathbf{p}, t)$. The distribution functions required for this calculation can be observed experimentally in favourable cases by X-ray or neutron diffraction methods. The ultimate aim, however, must be to relate them to the potential surface between the molecules, the molecular density and the energy. Such a relation with at least approximate validity in the gas phase can be obtained in the following rather intuitive manner.

The number of molecules in an element of *phase space* (i.e. a hyperspace having position and momenta as dimensions) is $f(\mathbf{r}, \mathbf{p}, t)\, d\mathbf{r}\, d\mathbf{p}$. If *no* collisions occur the same number of molecules must arrive in a similar volume at $\mathbf{r} + \mathbf{p}/m\, dt$, $\mathbf{p} + \mathbf{X}\, dt$, $t + dt$ where m is the mass and $\mathbf{X}$ is any net external force acting on the molecules. Thus:

$$f(\mathbf{r} + \mathbf{p}/m\, dt, \mathbf{p} + \mathbf{X}\, dt, t + dt)\, d\mathbf{r}\, d\mathbf{p} = f(\mathbf{r}, \mathbf{p}, t)\, d\mathbf{r}\, d\mathbf{p} \qquad (18)$$

If we now allow collisions to occur a certain number of molecules $\Gamma^{(-)}\, d\mathbf{r}\, d\mathbf{p}\, dt$ will suffer collision removing them from the final volume element. Similarly a number $\Gamma^{(+)}\, d\mathbf{r}\, d\mathbf{p}\, dt$ will now arrive in the final volume from regions outside the original starting volume and the relation becomes:

$$f(\mathbf{r} + \mathbf{p}/m, \mathbf{p} + \mathbf{X}\, dt, t + dt)\, d\mathbf{r}\, d\mathbf{p} = f(\mathbf{r}, \mathbf{p}, t)\, d\mathbf{r}\, d\mathbf{p} + (\Gamma^{(+)} - \Gamma^{(-)})\, d\mathbf{r}\, d\mathbf{p}\, dt \qquad (19)$$

Expanding the L.H.S. in a Taylor series, rearranging and retaining linear terms only yields:

$$\frac{\partial f}{\partial t} + \frac{1}{m}\left(\mathbf{p} \cdot \frac{\partial f}{\partial \mathbf{r}}\right) + \left(\mathbf{X} \cdot \frac{\partial f}{\partial \mathbf{p}}\right) = \Gamma^{(+)} - \Gamma^{(-)} \qquad (20)$$

Since linear terms only are retained, this expression is not valid in systems where large gradients occur as in shock fronts. The quantities $\Gamma^{(+)}$, $\Gamma^{(-)}$ are known as *collision integrals*. Collisions which contribute to $\Gamma^{(-)}$ i.e. remove molecules from the region $\mathbf{r}$, $\mathbf{p}$ must occur with other molecules present in the same region of space at time t but which have a different momentum, $\mathbf{p}'$.

The number of such collisions which scatter molecules out of the volume element $d\mathbf{r}\, d\mathbf{p}$ in time dt is given by (number density at $\mathbf{r}, \mathbf{p}$)^2 × volume $d\mathbf{r}\, d\mathbf{p}$ × velocity × total cross section; integrating the differential cross section over θ to give the total cross section and using the distribution functions for the number density we obtain:

$$\Gamma^{(-)}\, d\mathbf{r}\, d\mathbf{p}\, dt = \iiint f(\mathbf{r}, \mathbf{p}, t) f(\mathbf{r}, \mathbf{p}', t) \sigma(\theta, \phi, v) v \sin\theta\, d\phi\, d\theta\, d\mathbf{p}'\, d\mathbf{r}\, d\mathbf{p}\, dt \tag{21}$$

$\sigma(\theta, \phi, v)$ is the differential cross section for scattering into solid angle at θ, ϕ for collisions with velocity $v = |(\mathbf{p} - \mathbf{p}')/m|$.

A number of assumptions are inherent in this expression. Firstly that only two body collisions are important and secondly that the probability of a molecule having a momentum $\mathbf{p}'$ is unaffected by the presence of another molecule with momentum $\mathbf{p}$ at a distance $\mathbf{r}$ i.e. that the momenta are not correlated. These relations will consequently only be satisfactory at low densities.

The collision integral $\Gamma^{(+)}$ results from collisions between molecules in the region $\mathbf{r}$ but with momenta $\mathbf{p}_0$ and $\mathbf{p}_0'$ such that after collision they yield one molecule with the desired momentum $\mathbf{p}$. These collisions are the inverse of those contributing to $\Gamma^{(-)}$ i.e. by running time backwards we convert a collision contributing to $\Gamma^{(-)}$ into one contributing to $\Gamma^{(+)}$. By *microscopic reversibility* arguments we can then show that:

$$\Gamma^{(+)}\, d\mathbf{r}\, d\mathbf{p}\, dt = \iiint f(\mathbf{r}, \mathbf{p}_0, t) f(\mathbf{r}, \mathbf{p}_0', t) \sigma(\theta, \phi, v) v \sin\theta\, d\phi\, d\theta\, d\mathbf{p}_0'\, d\mathbf{r}\, d\mathbf{p}_0\, dt \tag{22}$$

where $\mathbf{p}_0$ and $\mathbf{p}_0'$ can be calculated from $\mathbf{p}$, $\mathbf{p}'$ and $\sigma(\theta, \phi, v)$. Combining these results for the collision integrals with the expression (20) yields the Boltzmann equation:

$$\frac{\partial f}{\partial t} + \frac{1}{m}\left(\mathbf{p} \cdot \frac{\partial f}{\partial \mathbf{r}}\right) + \left(\mathbf{X} \cdot \frac{\partial f}{\partial \mathbf{p}}\right) = \iiint (f_0 f_0' - f f') \sigma(\theta, \phi, v) v \sin\theta\, d\theta\, d\phi\, d\mathbf{p}' \tag{23}$$

(where $f_0 = f(\mathbf{r}, \mathbf{p}_0, t)$ etc).

All the potential surface information is contained in $\sigma(\theta, \phi, v)$ and in the relation between f and f_0. Solution of integro-differential equations of this type is not easy and must usually be approximate. Nevertheless expressions for transport properties such as viscosity can be derived from (23).

A fairly recent development has been the use of computer simulation calculations in which the trajectories of large numbers of molecules interacting by some potential are followed by numerical integration of the equations

of motion. A complete history of the system can therefore be built up in the computer memory and averages corresponding to observable properties calculated directly. This technique is not limited in the same way by the approximation of small gradients and low densities as the Boltzmann Equation and if sufficient computer time is invested the precision is limited largely by the accuracy of the potential surfaces used.

In some cases the rates of change in a system are slow in comparison to the collision rate and the system does not deviate much from thermal equilibrium. As an example, many chemical reactions have a very small cross section and proceed at a rate slow with respect to the processes maintaining the vibrational, rotational and translational distributions. These distributions then remain close to the equilibrium Boltzmann predictions. In this very common situation the chemical rate constant $k(T)$ at temperature T can be related to σ_R, the velocity dependent total reaction cross section by:

$$k(T) = \int_0^\infty I(v,T) v \sigma_R(v)\, dv \tag{24}$$

where $I(v, T)$ is the usual Maxwellian distribution. As the reaction cross section increases the vibrational and then rotational distributions will progressively deviate from their equilibrium values.

5. Potential surfaces leading to chemical reaction

In a previous section we were able to arrive at a complete theory for the interaction and collision dynamics of two structureless particles and show how at modest gas densities such information could be translated into an understanding of bulk properties. While all this was perhaps intellectually satisfying a chemistry limited to such systems would be extremely sparse. The extension of these results to the full diversity of real systems is extremely difficult though some progress has been made. This deficiency in theoretical understanding is to some extent masked by a parallel lack of detailed experimental information. In the reaction

$$K + I_2(v, J) \xrightarrow{\text{impact energy} = E} KI(v', J') + I + \Delta E \tag{25}$$

complete information would be contained in the family of energy dependent cross sections $\sigma_{Rv'J'}^{vJ}(E, \theta, \phi)$ specifying the probability of reaction at collision energy E between specific quantum states to yield other specified states emerging at θ, ϕ, there being such a cross section for each specific quantum *channel*.

Information in this detail is not yet available for any system, though the above reaction is perhaps the closest approach at present to this ideal. Of course, this reaction is not the only possible outcome open to collisions between

K and I_2. If for example, the collision energy is high enough, electronic excitation of one or more of the product fragments is possible. Collision of this type where the atoms can no longer be regarded as structureless particles on a single potential surface will be discussed in the final section. Here we shall be concerned with the small but important class of three body collisions where the potential can be, at least approximately, regarded as a function of the three interatomic distances only.

We have already discussed the general shape of such surfaces. Their most important qualitative features are:

(a) The location of the exoergicity release, e.g. whether manifested as reactant attraction or product repulsion.

(b) The barrier height (if any) and the general shape of the potential at the saddle point,

(c) The width of the entrance and exit valleys.

In a similarly cavalier fashion we can group the collision dynamics leading to reaction into two classes. The first class in which the atoms follow fairly simple trajectories from reactant to product are known as *DIRECT*. The second class of trajectories are those that follow a tortuous path over the surface. These are of the *COMPLEX* type. This division is also reflected in the theoretical models used in their description. In reactions proceeding by direct dynamics the models involve the concept of trajectories linking the initial and final states of the collision directly. Treatments of collisions following complex dynamics use statistical descriptions of the collision complex and no longer trace trajectories across the surface. Finally, a third class of theories is concerned with penetrating collisions that do not lead to reaction. These are often as revealing about the reactive processes as those that actually result in reaction. Reactions with intermediate types of behaviour occur frequently but the simple division described remains a useful aid to intuition, particularly in correlating the dynamics with the shape of the potential surface. It is with this connection that we shall be mainly concerned.

DIRECT DYNAMICS

The clearest examples of reactions exhibiting this behaviour are provided by alkali metal/halogen reactions of the type:

$$M + XR \rightarrow MX + R$$

Where X and M are a halogen and an alkali metal and R be either another halogen or an alkyl group. In interactions of a very strong nucleophile (M) and an electrophile (XR) an electron transfer occurs from the alkali metal to the halogen at a distance r_c related to the ionisation potential I_p and electron affinity E_a by:

$$r_c = \frac{e^2}{I_{p(M)} - E_{a(XR)}} \tag{26}$$

A strong coulombic interaction then dominates their potential at distances less than r_c. The details of this electron transfer or '*harpooning*' are looked at more closely in the final section, here we simply consider its consequences.

Most of our information about this class of reaction comes from molecular beam experiments in which the angular distribution and final translational energies of both the product MX and the elastically scattered M are measured. These reactions are particularly suitable for this type of experiment since they involve an alkali atom which is especially easy to detect; the interpretation is aided by the existence of 20 different alkali/halogen pairs that can be studied, each with the same type of surface but with a systematically changed harpooning radius r_c and reduced mass.

The major observations can be summarized as follows:

(i) The total reaction cross section is only a little less than πr_c^2 so that most of the collisions in which harpooning occurs result in reaction.

(ii) The elastic or unreacted alkali metal scattering has a similar angular distribution to that found in non-reactive systems at narrow angles. At wide angles this scattering falls off more sharply and in the case of reactions with large r_c the usual elastic rainbow scattering may not appear at all.

(iii) The division of the exoergicity between translation and vibration of the products varies with r_c. Vibrational excitation is predominant in systems where r_c is large, translation becoming more important as r_c decreases. Rotational excitation is relatively unimportant in removing the exoergicity.

(iv) The relative distribution of the scattered product with angle changes with r_c. When it is large compared to the gas kinetic diameters the product is predominantly forward scattered along the relative velocity vector. Conversely in systems where r_c is small most of the product appears in the backward hemisphere.

(v) The reaction cross section is rather insensitive to the impact energy i.e. there is no barrier to reaction in these reactions, a result in accord with rate constant measurements in these systems which indicate a zero activation energy.

(vi) In the case of the reaction $CH_3I + K \rightarrow KI + CH_3$, at least, the reaction occurs at the I end of the CH_3I molecule. The effective area for reaction on the CH_3I molecule being comparable to that predicted by geometric arguments of accessibility. This last observation is the result of an ingenious experiment in which a target of oriented CH_3I is prepared by passing a beam of the molecules through a strong inhomogenous field. Polar molecules entering this field with a small transverse component of velocity experience a restoring force which depends upon their effective dipole moment in the direction of the field and execute sinusoidal oscillations about the axis. By a suitable arrangement of stops and orifices it is possible to arrange for only a narrow band of orientations to be transmitted. The potassium beam can

then be made to approach either predominantly the CH_3 or the I end of the molecule and the resulting changes in angular distribution of the product observed by scanning a detector about their mutual collision zone.

The major qualitative trends observed can be rationalized in terms of the potential surface which in reactions of this type correlates strongly with r_c. This correlation helps our interpretation considerably and in a rather intuitive spirit we might argue as indicated in Fig. 9. The model that emerges is one in which collisions where r_e is large are viewed as two body affairs; initially as M+ (RX) and then after harpooning as $M^+ + X^-$ with the R group simply spectating and playing no part in the dynamics. For systems where r_e is small all the particles are coupled strongly and product repulsion is more important.

OBSERVATION			
σ_R varies roughly with πr_e^2 (1)	Elastic scattering falls off at wider angles as r_e increases (2)	Vibrational excitation increases, translational excitation of product decreases as r_e increases (3)	Percentage of product forward scattered increases with r_e (4)
DEDUCTION			
After harpooning the strong interaction between the ions which form the final product result in most such collisions emerging as product.	Alkali atoms with turning points inside r_e react, consequently elastic scattering that would have been seen at wide angles (corresponding to the same small turning radius) hardly appears.	The bond between MX is formed abruptly at r_c. If $r_e \gg$ equilibrium bond distance the product will be vibrationally excited. Conversely if r_e is small all three atoms are close and will repel each other.	If the new bond is formed at large distances the interaction between the product molecule and the reactant fragment R will be small. The product MX will then continue along the incident M direction (broadened by any momentum brought to the product by X) Conversely product formed at small r_e will interact strongly with the R fragment and large deflections will occur.

FIG. 9 Correlation of experimental observations with the dynamics of motion over the potential surface in harpooning reactions.

Obviously special features are found in many reactions but there is a good element of truth in these simple ideas. Much more detailed models must be used, however, if a quantitative understanding of these results is required. The most successful of these models treat reactive collisions as a classical multi-body problem and use a computer simulation or Monte Carlo sampling technique for their solution. In these computer experiments a potential surface is constructed to represent the interaction of all the atoms. The history of a large number of trajectories is then followed by numerical integration of the classical equations of motion. If the starting points for these trajectories are drawn randomly from a population representative of that in the experiments being modelled we can compare the *average* results of these computations with experiment. We may also test the rather intuitive ideas in Fig. 9, against these calculations. A trajectory calculated for a model of the K/I_2 system is shown in Fig. 10 the large vibrational excitation in the product KI is clearly seen. In principle the use of classical mechanics in these calculations is a serious weakness. In most cases, however, the deviation between the QM and classical results is not large as for example in Fig. 11. The classical results are very close to an average of the quantal prediction and would be hard to distinguish experimentally. Indeed the relative paucity of experimental information is a serious limitation to further theoretical development. For

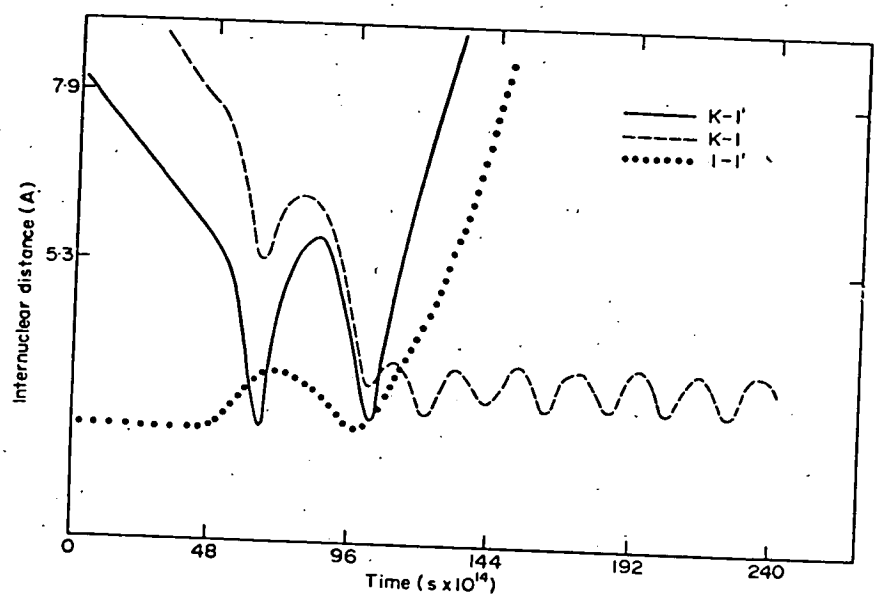

FIG. 10 Plot of the internuclear distance r_{K-I}, $r_{K-I'}$ and $r_{I-I'}$ as a function of time for collisions of K and I_2 at thermal energies. The high vibrational excitation of the product KI is easily seen.

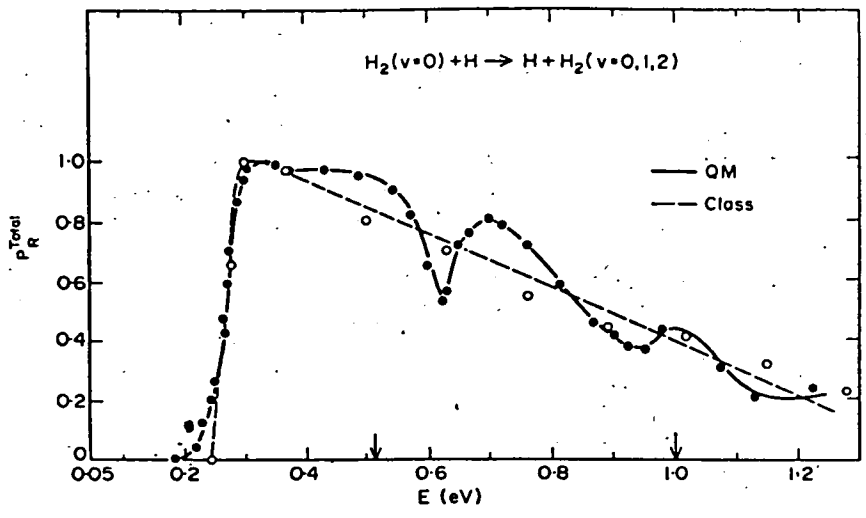

FIG. 11 Quantum and classical calculations for the probability of reaction in the hydrogen atom exchange reaction over a range of collision energies. (Reproduced from Bowman and Kuppermann VII ICPEAC, Amsterdam, 1971.)

example, in the case of the alkali/halogen reactions a number of potential surfaces can claim agreement with experiment. The initial abrupt change in the potential associated with electron transfer is a feature of all of them, but they differ markedly in their description of the potential in the region where the products are separating. Thus potentials with either:

(i) very weak exit interactions,

(ii) strong shortrange repulsive forces followed by long range attractive ones, or,

(iii) in which the charge in the halogen molecule may migrate from one halogen atom to the other during this phase of the motion, all fit the present data. Yet more information, possibly about the disposal of the angular momentum or about the inverse collisions $KI + I \rightarrow K + I_2$ will be required to resolve this ambiguity.

COMPLEX DYNAMICS

A very large number of reactions are thought to proceed via a collision complex with a lifetime greater or comparable to its rotational period. In gas phase experiments, information has been obtained from unimolecular reaction kinetics. In these reactions competition between the rates of reaction and deactivation of the activated complex yield information on its lifetime. The more detailed information provided by beam scattering experiments is

available for only a few systems, e.g.

$$\left.\begin{aligned} Cs + SF_6 &\rightarrow CsF + SF_5 \\ Cs + RbCl &\rightarrow CsCl + Rb \end{aligned}\right\} \quad (27)$$

The actual features in the potential surface which produce this longevity of the complex are not clear. The classical Monte Carlo type of calculation is not very useful because the large number of particles involved and the long period over which these trajectories must be followed make it difficult to maintain numerical precision. The important requirement appears to be the existence of a large number of accessible quasi-stable states of the complex in which the internal degrees of freedom of the target molecule are excited. Decaying states of this kind, sometimes also called *resonances* can leak away to form either the products or via the elastic channel to reform the reactants. Resonances arise for specific effective potentials i.e. orbital angular momenta and are characterized by both their energy and their life time for decay, t_R and t_E into the reactive and non-reactive channels respectively. This finite life in conjunction with the uncertainty relation $\Delta E\, \Delta t = \hbar$ requires the resonance to have a finite energy width Γ, collisions within this width excite the resonance and then decay partly into products and partly back into reactants.

This situation can be represented by using a complex phase shift, $\eta_l + i\varepsilon_l$, in which the imaginary part corresponds to the attenuation of the lth partial wave by reaction. The expression for $f(\theta)$ equation (16) using this complex phase shift then allows the elastic scattering in the presence of reaction to be calculated. Interpretation of experimental data in this fashion can yield both the potential $V(r)$ and the probability of complex formation as a function of r.

In the molecular systems the resonances are usually so numerous and so closely spaced that their effect can only be considered in some average way. In the Rice Ramsperger Kassel Marcus (RRKM) theory of unimolecular reactions these effects are considered purely statistically. In this model all the possible excited states of the complex at a specific energy E are divided into two classes. In the first group are all those states in which the excitation energy is largely present in internal modes of the complex not directly involved in the reaction so that insufficient energy remains in the *reaction co-ordinate* for dissociation to take place. The second class of states are conversely those in which at least E_0, the threshold or activation energy remains in the reaction co-ordinate so that decomposition can occur directly. This model can be applied to the complex formed by the collision of the two reactant species. If the lifetime of the complex is sufficiently long and all the states are well coupled to each other the collision energy will be rapidly distributed amongst them. Every state can then be assumed to be equally likely to be populated and the average lifetime is related to the ratio of the statistical weights of the two classes.

If $N(E)\,dE$ is the number of states in the first class between energy E and $E + dE$ and $P(E - E_0)$ is the number of states at the same total energy with at least E_0 in the reaction co-ordinate then the mean reactive lifetime of the complex is:

$$\langle t_R \rangle \sim hN(E)/P(E - E_0) \tag{28}$$

The energy dependence of this lifetime depends upon the relative rates at which $N(E)$ and $P(E)$ change with total energy. In almost all cases $N(E)$ increases more slowly than $P(E)$ so that the complex lifetime falls sharply with increasing energy. Typical behaviour for $\langle t_R \rangle$ as a function of energy

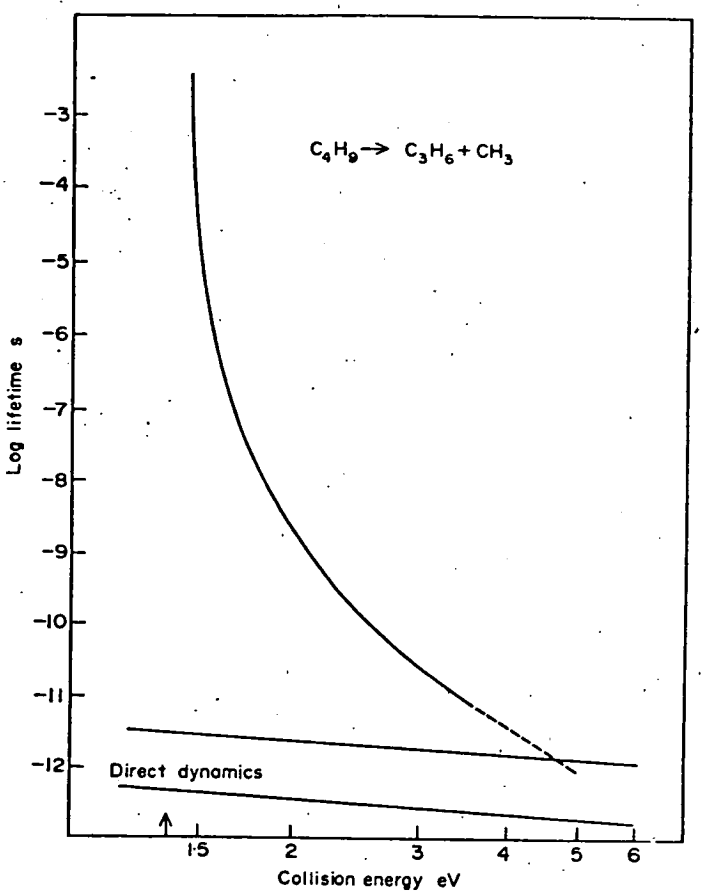

FIG. 12 Plot of lifetime for the radical decomposition of C_4H_9 versus total energy of the complex. The two lines at the bottom of the figure are upper and lower bounds on the lifetime for direct dynamics. The reaction is therefore expected to change from complex to direct dynamics at 5 eV collision energy.

calculated for the process $C_4H_9 \rightarrow C_3H_6 + CH_3$ is shown in Fig. 12. At higher energies the lifetime predicted becomes very short and comparable to that for processes with direct dynamics. It is not surprising therefore that in the ion molecule reaction $C_2H_4^+ + C_2H_4 \rightarrow C_3H_5^+$ with a C_4 transition state the dynamics change from complex to direct as the collision energy varies from 1 to 5 eV.

Although equipartition of energy will take place in the internal modes of the complex its total angular momentum J must be conserved both in magnitude and direction throughout the collision. This total angular momentum is initially comprised of two quantities, the relative orbital angular momentum $\mathbf{L}(=\mu \mathbf{v} \times \mathbf{b})$ brought to the complex by the relative motion of the two reactants and I the internal angular momentum of the reactants. If the cross section for complex formation is sizeable the impact parameters of collisions producing the complex must be large so that $\mathbf{I} \gg \mathbf{I}$ and $\mathbf{J} \simeq \mathbf{L}$. The total angular momentum will be approximately perpendicular to the direction of the incident relative velocity. This information is now frozen irrevocably into the complex. At first sight it would seem that the decay products from such a long lived complex would be released isotropically; that is a detector moving over the surface of a sphere centred on the complex would register a flux independent of angle. In general this is not so because the total angular momentum vector is not isotropically orientated but is uniform in a plane. The angular distribution of product now depends upon how much of this total angular momentum appears in the product. If the product is only weakly rotationally excited its angular distribution will be primarily forward and back (at 0 and π) in the centre of mass system. Conversely if almost all the angular momentum in the complex appears as rotation of the products then the distribution will be predominantly sideways. Only if the products are formed with a wide range of rotational energies will an isotropic centre of mass distribution be seen. In any of these cases however the product distribution is symmetrical about $\pi/2$; any asymmetry about this angle indicates a decay lifetime comparable to the rotational period for the complex so that some 'memory' of the initial orientation of the complex at formation remains. Measurement of this asymmetry would thus allow the lifetime to be estimated while the spread of the distribution provides information on the distribution of angular momentum in the complex and hence on the types of trajectories responsible for its formation.

Arguments of this type have been applied to the reaction:

$$Cs + SF_6 \rightarrow CsF + SF_5 \qquad (29)$$

for which rather detailed information is available from molecular beam electric resonance experiments. In these experiments product CsF, formed at the intersection of thermal energy beams of Cs and SF_6, is introduced into

the spectrometer. The MBER spectrometer consists of a series of static and RF electric fields with a geometry of slits and holes so arranged that only molecules undergoing particular transitions in the RF field can reach a detector; by choosing suitable RF frequencies it is possible to determine the population of the CsF molecules in particular vibrational states.

The results of this and related experiments were broadly in agreement in showing that:

(i) The velocity, rotational and vibrational distributions of the CsF product were roughly Boltzmann in distribution and corresponded to a temperature of 1200 °K.

(ii) The product angular distribution was symmetrical about $\pi/2$ with peaks in the forward and backward quadrants. These distributions are in good accord with estimates based on equilibrium conditions in the complex. The SF_5 radical which by difference must be formed with $\sim$1·6 out of the 2 eV exothermicity also corresponding to a temperature of 1200 °K.

6. Transitions between potential surfaces

So far in our discussion we have assumed that the course of a molecular collision is governed by a single potential surface. The collisional phenomena of the quenching of resonance radiation, intermultiplet transitions, transfer of electronic excitation and chemi-ionization are all examples of processes that cannot be described by a single potential energy function or quantum state. In vibrational spectroscopy, examples of the coupling of electronic states are provided by predissociation, the perturbation of line intensities and Λ doubling. In all cases, two electronic states of the same symmetry have nearly the same energy at some configuration. Nuclear motion taking the system through that configuration can then induce transitions between these states.

It is worth looking at the reason for this in more detail, with the electronic states of some diatomic molecules as examples. Consider the interaction of He with H^+. Some of the molecular potential energy curves arising from this separated ion atom pair are shown in Fig. 13 together with the excited He state to which they dissociate. In among these excited states is the state He^+/H, in which one electron is transferred to the proton. The states drawn as a first approximation are constructed solely from the atomic states of the dissociated atoms and there is no mixing of different states, or of states with the electrons differently partitioned between the two nuclei. The energy curve of the molecular state evolving from the $1s^12p_z^1$ configuration of He falls sharply with the approach of the two nuclei (because of the large polarizability of this excited state) and in fact crosses the $A\Sigma$ state evolving from He^+/H. The electron distribution in these crude states does not change much with the internuclear separation in that the initial atomic distributions

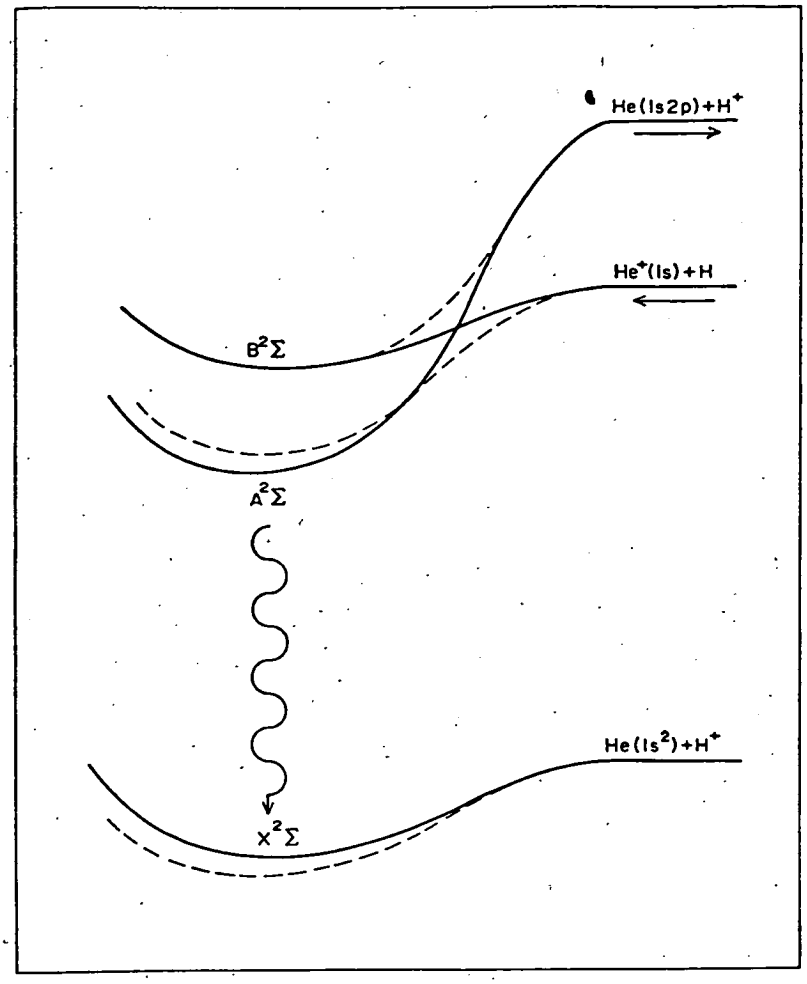

FIG. 13 Some of the molecular states of the HeH^+ system. The heavy lines are the potential energy curves in the 'diabatic' approximation, i.e. constructed solely from the atomic states to which they dissociate (indicated at the right). The dashed lines represent the shift in the electronic energy when configuration interaction is introduced. There is an avoided crossing between A and B states.

are largely undistributed. We feel intuitively that in the limit of very fast collisions, these curves must be approximately those producing the interatomic force, in that the electrons do not have time to adjust to the changing internuclear separation. These potential curves are called *diabatic*. If, on the contrary, the electron distribution adjusts to the changing separation (i.e. we trace out the true eigenfunctions of the static problem) the resulting potential curves are appropriate to infinitely slow nuclear motion and are

called *adiabatic*. We can now describe the resulting wave functions as superpositions of the simpler diabatic states; this mixing is illustrated in Fig. 13 by the shift to the dashed curves. Consider first the mixing of the He (1s2p) and ($1s^2$) states by the incoming proton: the change in character of the lower state is towards a gradual increase in p-character (sometimes described as hybridization), perhaps achieving 50% near the equilibrium separation. Now we follow the interaction of the two upper diabatic states (dissociating to He^*, H^+ and He^+, H respectively). The mixing is at first small because of the large energy separation but increases rapidly as the zeroth order or diabatic crossing is approached. At this point the two new adiabatic states are each a 50/50 mixture of the parent states and their difference in energy is H_{12}, the matrix element of the complete Hamiltonian between the two zeroth order states. Then, as r decreases further, the character of the lower states rapidly becomes that of $He(1s2p)/H^+$, so in the space of a few angstroms an electron has in effect been transferred from the hydrogen atom to the 2p orbital of He. The changeover is more rapid the greater the difference in gradients of the upper and lower zeroth order states at the crossing. This behaviour is to be contrasted with the more gradual change in bond character of the lowest (X) state which does not cross another state.

This arrangement of potential energy curves in the He^+/H system has important dynamical consequences; if collisions are sufficiently slow, their relative motion will be governed by the adiabatic potential of the $A(\Sigma)$ state and the electron will be transferred at the avoided crossing. However, as the speed of the relative motion increases the time spent in traversing the region rapidly changing electron density decreases. There is then a growing likelihood that the electron will fail to adjust to the new minimum energy configuration and will be caught in the upper $B\Sigma$ state. Inside the crossing, where the electron distribution is again slowly varying with R the motion is adiabatic. It is true that the system can leave this state by radiation to the ground state ($X^1\Sigma$) but the lifetime of excited electronic states (in the absence of any dynamic coupling) is typically $\sim 10^{-8}$ s, many times longer than the duration of the collision ($\lesssim 10^{-12}$ s, unless there is a resonance). The system thus emerges from the collision as either $He^* + H^+$ or $He^+ + H$ with a probability dependent on the adiabaticity.

To move towards a more quantitative picture of motion over an avoided crossing, we might guess that, if the energy separation of the two states at r_c is ΔE, then the perturbation caused by the relative motion can induce a transition between the two adiabatic states if its time dependence has a strong Fourier component of frequency $\Delta E/\hbar$. The effective duration of the collision is typically $\Delta r/v$, where Δr is the range of r over which most of the electronic rearrangement takes place and v is the relative velocity. Thus, a parameter to gauge the non-adiabaticity (or probability of transition

between adiabatic states) might be $\Delta E \Delta r/\hbar v$. To proceed further, time dependent perturbation theory must be invoked and the following famous result:

$$P \simeq \exp\left(-H_{12}^2/(2\,|F_1 - F_2|\,\hbar v)\right) \tag{30}$$

is obtained for P the probability of non-adiabatic behaviour after a single passage over the crossing of two potential curves with gradients F_1 and F_2 at the crossing. This, the Landau Zener formula, occupies a central place in non-adiabatic collision theory. It is an approximate formula, but a good one and the argument of the exponential in (30) is closely related to the non-adiabaticity parameter discussed above.

In order to obtain the overall probability of non-adiabatic or adiabatic behaviour as the result of a collision, equation (30) must be applied each time the crossing is traversed—one on the inward path and once on the outward. The final probabilities are then:

$$\begin{aligned}
\text{Probability of a non-adiabatic collision} &= \begin{pmatrix}\text{Prob. at 1st crossing of}\\ \text{non-adiabatic behaviour}\end{pmatrix} \times \begin{pmatrix}\text{Prob. at 2nd crossing of}\\ \text{adiabatic behaviour}\end{pmatrix} \\
&\quad + \\
&\quad \begin{pmatrix}\text{Prob. at 1st crossing of}\\ \text{adiabatic behaviour}\end{pmatrix} \times \begin{pmatrix}\text{Prob. at 2nd crossing of}\\ \text{non-adiabatic behaviour}\end{pmatrix} \\
&= 2P(1-P) \\
\text{Probability of an adiabatic collision} &= P^2 + (1-P)^2
\end{aligned} \tag{31}$$

The maximum value of the probability for non adiabatic collisions in this approximation is 1/2. If (30) is inserted for P in (31), the overall probability of non-adiabatic behaviour will be found to have an energy dependence such that $P(E)$ rises to a maximum and then falls off fairly sharply, tending to zero as E tends to infinity.

A qualitative analysis of a curve crossing situation thus consists of first identifying the various spectroscopic states that might cross the state under consideration and roughly locating the values of r_c. The maximum non-adiabatic cross section is then:

$$\sigma_{\substack{\text{total}\\ \text{non-ad}}}(E) = \pi b_c^2/2$$

where b_c is the impact parameter leading to a turning point at r_c when the relative kinetic energy is E. Under some conditions, enough is known about the potential curves to attempt an evaluation of $P(b)$ with the aid of (30).

The non-adiabatic cross section is then:

$$\sigma_{\substack{\text{total}\\\text{non-ad}}}(E) \simeq 2\pi \int_0^\infty P(b)_{\text{non-ad}}\, b\, db \tag{32}$$

Like P, $\sigma(E)$ would show threshold and peak dependence on E.

It should be emphasized that (30) and the equations derived from it presuppose that all the change in the population of the two states occurs around the crossing point. It may well be that in an actual system the difference in gradients, F_1 and F_2, of the two diabatic states is very small or that the states do not actually cross but merely come close in energy. The crossing point is then ill-defined and the population of the states will change slowly over much of the trajectory. In this case a more elaborate quantum theory must be used. Such a situation occurs in vibrational energy transfer where the incoming atom couples various vibrational states of the target molecule but a curve crossing is not necessarily involved and, partly because of this, transition probabilities (i.e. non-adiabatic effects) are small.

As examples of systems in which curve crossing effects have been observed we begin by discussing the interactions of two S-state atoms, K and Ar, Fig. 14; when the atoms are well separated the first excited state is the ^{2}P state of potassium with the argon excited states lying considerably higher in energy. At small separations ($\sim$1–2 Å) there is an avoided crossing between the ground $^2\Sigma$ state and the $A^2\Sigma$ state dissociating to a ^{2}P K atom. A mechanism for the quenching of the ^{2}P state, which is readily excited by electron bombardment or by the adsorption of resonance radiation, is then for the excited atom to suffer a collision with an argon atom such that the crossing point is reached and the system emerges in the $X^2\Sigma$ state which dissociates to ground state atoms.

One of the most studied examples of a curve crossing occurs in the system discussed in Section 5:

$$\left.\begin{aligned} M + X_2 &\rightarrow M^+ + X_2^- \quad \ldots \\ M + X &\rightarrow M^+ + X^- \quad \ldots \end{aligned}\right\} \tag{33}$$

where M is an alkali metal and X or X_2 a halogen atom or molecule. The non-adiabatic phenomenon here is chemi-ionization and the mechanism can be seen from Fig. 15. Regarding the X_2 molecule as an atom of appropriate electron affinity, the key feature of the first two $^1\Sigma$ diatomic states is that the upper, largely ionic one (dissociating to $M^+ + X^-$, or X_2^-) falls rapidly in energy due to the coulomb attraction between anion and cation and crosses the ground state curve at between 5 and 12 Å depending on M and X. At smaller separations the lower state takes an almost purely ionic character. Once again this is an avoided crossing, though the splitting is only $\sim$0·1 eV

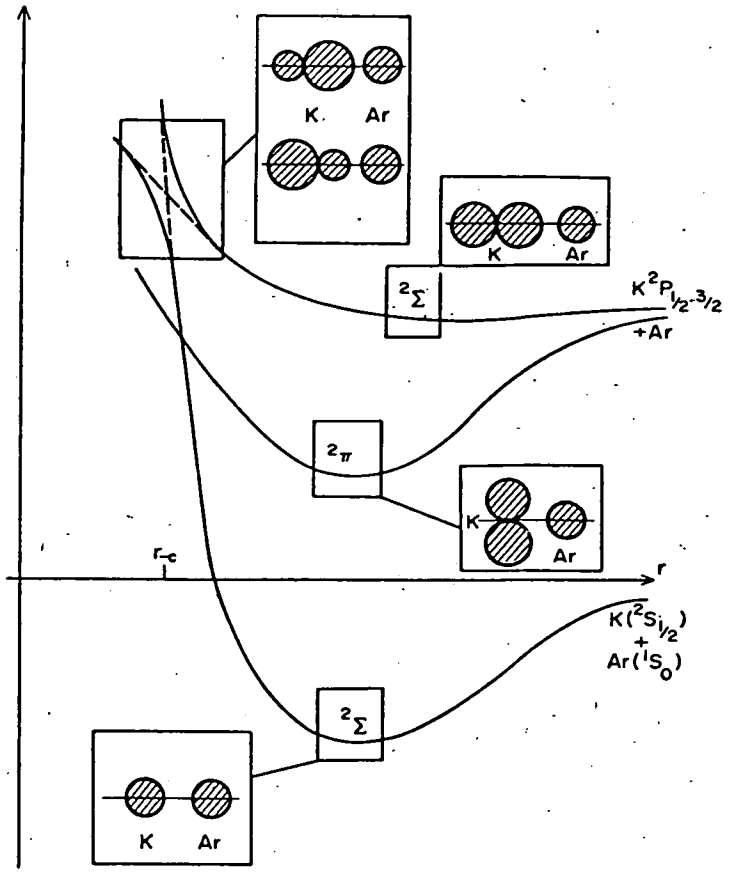

FIG. 14 Some of the molecular states of the KAr system. The changing hybridization of the atoms is schematically indicated in each state. At the avoided crossing, the two new states are different in the direction that the sp_z hybrid points. The Π state crosses the ground state, but in the absence of nuclear motion does not mix with it.

because of the large value of r_c. The mechanism for chemi-ionization is thus for the system to enter the first crossing as a neutral pair and though a non-adiabatic transition on either the inward or the outward path to emerge in the upper ionic state. Naturally, the relative kinetic energy must be greater than the energy required for ion production (~2 eV) but because of the very small energy gap at the crossing, ion production is seen at energies just above this threshold.

For clarity, examples have been drawn from diatomic systems and there the test for whether two diatomic states actually cross or avoid a crossing if they become degenerate is simply (i) whether they are of the same symmetry

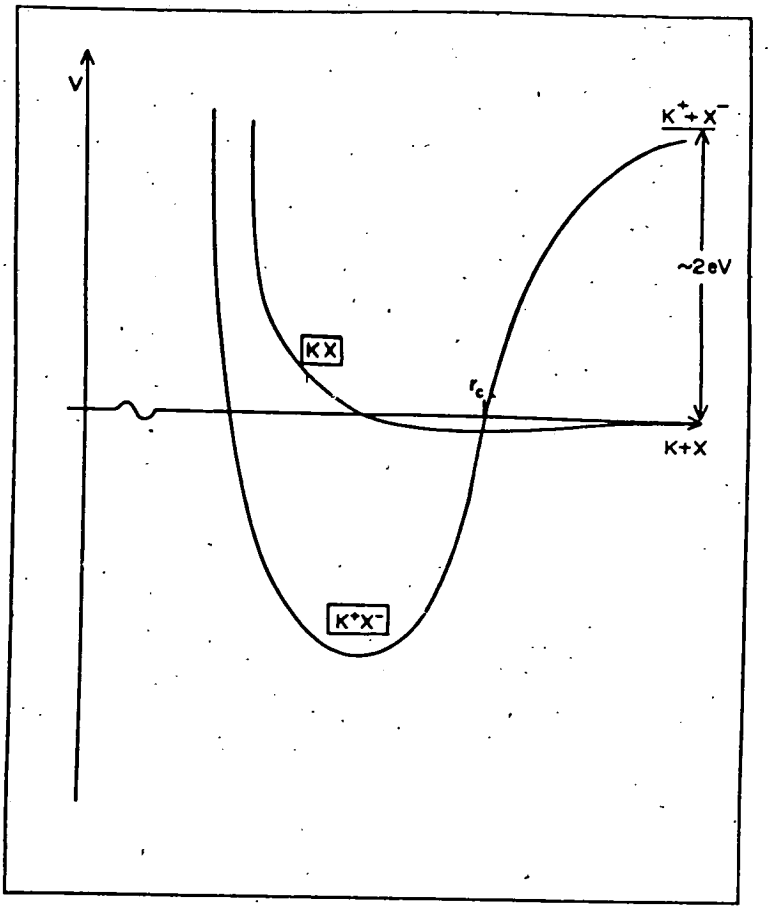

FIG. 15 The two lowest states of KX. There is an avoided crossing at r_c, to the left of which the lower state assumes almost complete ionic character. The energy splitting at r_e is too small to show.

(+, −, g, u); (ii) whether they have the same Λ value; (iii) whether they have the same spin multiplicity. If any of these conditions is not fulfilled the coupling matrix element H_{12} vanishes. It is then much more difficult to induce transitions.

On a polyatomic surface the same considerations apply, with all the symmetry operations appropriate to the geometrical configuration being applied. However, in molecular collisions all possible molecular geometries are sampled and one is effectively left with the rule that only states with the same multiplicity can avoid a crossing.

With more than two atoms, simple crossing at a point is replaced by a line along which the surfaces intersect and the subject is of considerable

complexity, although an important one in that such crossing especially between excited states of the system might be quite common.

FURTHER READING

1. Eyring, H., Walter, J. and Kimball, G. E. (1944), "Quantum Chemistry", Wiley, New York.
2. Pauly, H. and Toennies, J. P. (1968) in "Methods of Experimental Physics", (Ed. B. Bederson and W. L. Fite) Vol. 7A, 227, Academic Press, New York.
3. Rowlinson, J. S. (1970) in "Essays in Chemistry" (Ed. J. N. Bradley, R. D. Gillard and R. F. Hudson) Vol. 1, 1, Academic Press, London.
4. Herschbach, D. R. (1966) in Adv. Chem. Phys. (Ed. J. Ross) Vol. 10, 319, Interscience, New York.
5. Landau, L. D. and Lifshitz, E. M. (1958). "Quantum Mechanics", (English edition), Pergamon Press, Oxford.
6. Fluendy, M. A. D. and Lawley, K. P. (1972), "Chemical Applications of Molecular Beam Scattering", Chapman and Hall, London.

Offprinted from the *Faraday Discussions of The Chemical Society*, No. 55, 1973

SCATTERING OF METASTABLE MERCURY ATOMS.

Scattering of Metastable Mercury Atoms

By T. A. Davidson, M. A. D. Fluendy and K. P. Lawley

Dept. of Chemistry, University of Edinburgh, Edinburgh EH9 3JJ

Received 10*th January*, 1973

Differential elastic cross sections for the scattering of the metastable 6^3P_2 state of mercury from sodium, potassium and rubidium have been measured at thermal energies. Interference structure is resolved in all cases, suggesting that the atoms interact by a single effective potential in the attractive region probed at these energies. No attenuation of the interference structure is observed so that quenching of the metastable state is not an important process along trajectories sampling only the attractive part of the potential.

Collisions between ground state Hg atoms ($^1S_0$) and alkali metal atoms ($^2S_{\frac{1}{2}}$) at thermal energies are necessarily elastic and occur under the influence of a single potential. Scattering measurements on these systems have been made by several groups [1-7] and recently Buck and Pauly [8, 9] have reported accurate differential cross section measurements and their inversion to yield potentials. This inversion may be in some degree ambiguous as shown by Boyle [10]; nevertheless the potential between the alkali metals and ground state mercury is now comparatively well established.

The corresponding interaction between alkali atoms and the excited states of Hg [12] is much less well understood. The lowest of such states are the 6^3P_0, 6^3P_1 and 6^3P_2 at, respectively, 4.64, 4.89 and 5.43 eV above ground. The 6^3P_0 and 6^3P_2 states are metastable with a lifetime [11, 12] $\sim 10^{-3}$ s, comparable to the flight time in the crossed beam apparatus used for the present experiments. The $^3P_1$ state decays after $\sim 10^{-7}$ s. The thermal energy collision of these atoms with other species is now complicated not only by the possibility of electronic energy transfer but also by the fact that a manifold of potentials arises from the separated atoms due to the possible spin pairings (if the partner is not a singlet atom) and m_J states of the Hg atom.

Table 1.—ΔE for processes involving Hg ($^3P_2$) and alkali metals

process	Na	K	Rb
ionisation of M	−0.31	−1.11	−1.27
excitation transfer to 1st excited state of M	−3.33	−3.82	−3.87

The photochemistry [13] of these states and in particular of the $^3P_1$ atoms is of great importance and has been widely studied. However, the understanding of the fundamental processes of electronic energy transfer and their relation to curve crossing must begin with simple systems where a knowledge of the adiabatic potential curves can be obtained. The alkali metal + Hg* system is a useful case for this purpose since both theoretical studies and the unravelling of potential energy curves through magnetic state selection offer the hope of a complete picture.

The various processes that can occur are: (*a*) elastic scattering, (*b*) intermultiplet transitions ΔJ, which will be followed by quenching if the $^3P_1$ state is formed, (*c*)

Δm_J transitions within a given J state, (*d*) ionisation, (*e*) transfer of electronic excitation to the alkali metal.

For the $6\,^3P_2$ state, all these channels are open for the series Na to Cs, though with fairly considerable exoergicities except for cases (*a*) and (*c*); exoergicity values are given in table 1. In this paper we describe the results of differential cross section measurements on the process (*a*), elastic scattering accompanied by (*c*), m_J transitions, i.e., for scattering without change in J value.

EXPERIMENTAL

The apparatus is shown schematically in fig. 1. The two beam sources rotate on a turntable in front of the fixed detector which is located in a differentially pumped chamber.[14] The excited mercury beam is produced by bombarding a ground state Hg beam effusing from a glass capillary array with electrons of controlled energy. The electrons were collimated by a magnetic field and, with an excitation voltage of 10 eV, an electron current ~ 10 mA excited roughly 1 in 10^5 of the Hg atoms resulting in a metastable flux of 10^{10}-10^{11} atoms steradian^{-1} s^{-1}. Higher electron energies mainly resulted in increased production of photons as shown by time of flight experiments using a pulsed excitation voltage. After re-collimation (the electron bombardment can produce deflections $\sim 2°$ in the Hg* beam), the metastable atoms crossed a modulated target beam of alkali metal atoms. The scattered atoms entered a UHV chamber ($\sim 10^{-9}$ Torr) via a narrow channel to strike a clean potassium surface plated *in situ*. Electrons ejected from this surface were focused into a Mullard channel electron multiplier and counted on dual scalers gated in delayed synchronism with the target beam modulation. The maximum counting rate observed was $\sim 10^5$ Hz while the background count rate for the detector alone (valved off from the main chamber) was 1-0.1 Hz; more typically, when measurements were in progress, the background was 2-3 Hz. Once prepared, the K surface was stable in performance for periods of several months. All the experimental data were recorded on paper tape and processed off line by computer.[14]

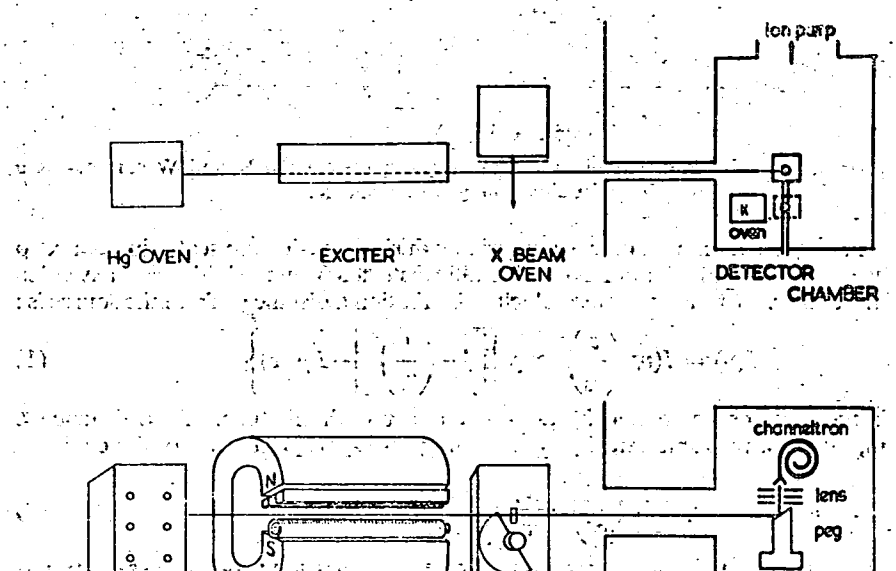

FIG. 1.—Apparatus schematic showing electron gun for metastable Hg production and the Auger detector.

The excitation function observed with this equipment is shown in fig. 2 as a plot of main beam signal (normalised by the excitation current) versus excitation voltage. The first maximum with a threshold at ~6.0 eV arises from the $6\,^3P_{0,1,2}$ states, the other maximum with a threshold at 10 eV observed on a tungsten surface results from photons plus possibly some long lived $^3D_3$ Hg atoms.[15] In the results to be described, 10 eV electrons were used so that only the $6\,^3P_{0,1,2}$ states need be considered. Of these three possibilities, time of flight experiments showed the photon contribution (from decay of $^3P_1$ Hg) to be only ~10 % of the total signal. Since the scattering cross section for 2537 Å photons with alkali metals is very much smaller than for atom–atom collisions, these photons will not be modulated by the cross beam and hence not registered as scattered signal. Calculations [16] for the $^3P_2$ and $^3P_0$ states suggest that the ratio of their cross sections for formation by electron bombardment is roughly 5 : 1 (i.e., the simple statistical ratio). Their lifetimes are probably similar and since the $^3P_2$ would be more efficiently detected by the K surface, the observed scattering is tentatively attributed solely to this state. Magnetic deflection analysis of the beam to confirm this is in progress.

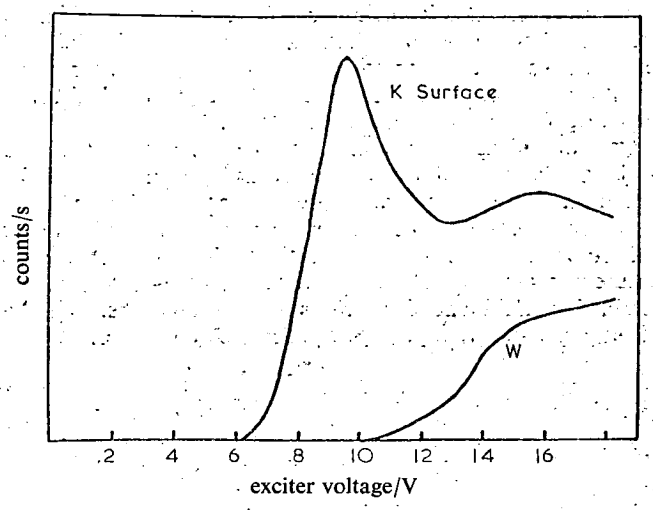

FIG. 2.—Apparent excitation function observed for Auger ejection from K and W surfaces as a function of exciter voltage in the source.

Because the $^3P_2$ Hg atom flux decays appreciably during transit from scattering centre to detector, the Hg* velocity distribution is considerably distorted from the initial v^2 Maxwellian one out of the exciter. The appropriate velocity distribution a distance L from the source is:

$$I(v) = I(v_0^*)\left(\frac{v}{v_0^*}\right)^2 \exp\left\{\left[1-\left(\frac{v}{v_0^*}\right)^2\right]-L/(\tau v)\right\} \qquad (1)$$

where v_0^* is the most probable velocity at source and τ is the lifetime. At a distance L downstream, the most probable velocity v_L^* is given by the appropriate root of the cubic

$$\left(\frac{v_L^*}{v_0^*}\right)^3 - \frac{v_L^*}{v_0^*} = \frac{L}{2\tau v_0^*}. \qquad (2)$$

From the dimensions of the apparatus (L = 61 cm), the most probable velocity of the Hg* is ~38 % greater than that for a stable species at the same temperature. The relative velocity distribution is not affected so much, the full width at half height being reduced by 10 %. The most probable relative velocity also changes slightly with angle of scattering. Finally, the relative masses and velocities are such that at a given laboratory angle of observation (θ) there are two centre of mass angles (χ) contributing, leading to fast and slow scattered

components. However, partly because of the ratio of Jacobians but also because of substantially greater decay, the slow component is <10 % of the fast component and may be neglected.

RESULTS AND DISCUSSION

Laboratory distribution for Hg* elastically scattered from the alkali metals Na, K and Rb are shown in fig. 3, 5 and 7. The corresponding centre of mass angles are also shown on the axes. The results for Rb are rather limited in precision pending further observations. Fig. 4 and 6 show the result of deconvoluting the curves shown in fig.

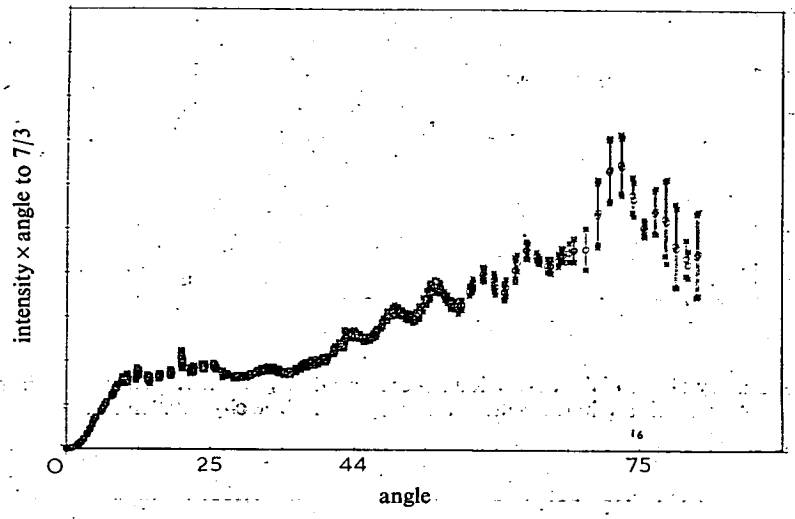

FIG. 3.—Laboratory differential cross section for Hg 6^3P_2 scattering from sodium. The angles shown below the axis are in the centre of mass system. Velocity 895.0 m s^{-1}.

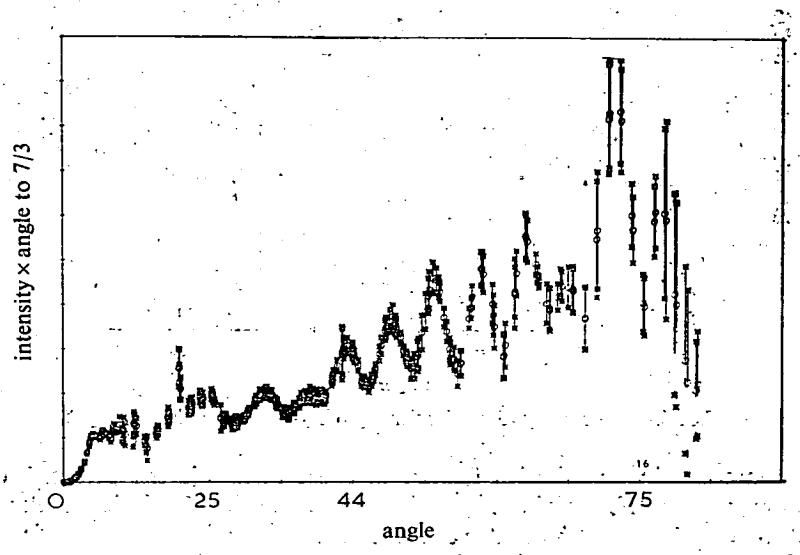

FIG. 4.—Laboratory differential cross section for Hg 6^3P_2 + Na deconvoluted using the main beam profile, data of fig. 3.

3 and 5 using the observed main beam profile as the filter function. The deconvoluted results are rather noisy, but structure partially resolved before deconvolution can now be clearly seen. The laboratory angles are shown above the axis.

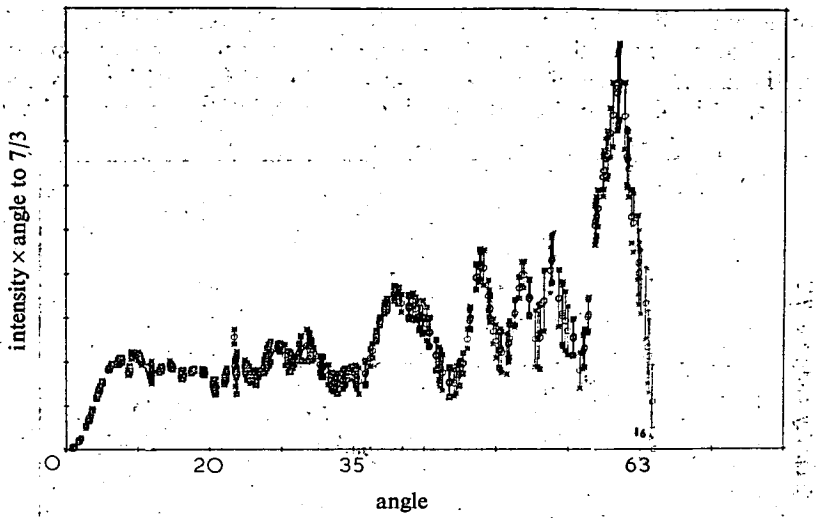

FIG. 5.—Laboratory differential cross section Hg 6^3P_2 scattering from K. The angles shown below the axis are in the centre of mass system. Velocity 660.0 m s^{-1}.

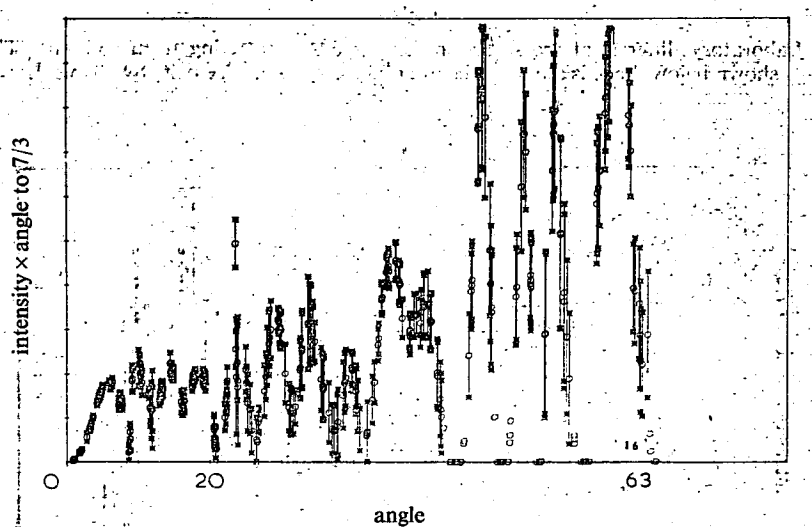

FIG. 6.—Deconvoluted results for Hg 6^3P_2+K, same data as fig. 5.

The most striking qualitative feature of these results is the presence of strong undulations in the differential cross sections which cover the whole angular range of observation (out to 85° in the centre of mass in some cases) with undiminished amplitude. This points to two quite separate conclusions. Firstly, we are seeing the operation of either a single potential or a group of potentials that are very similar in

the parts of them covered by the observations. For, if several rather different potentials with similar weights were operating, the net interference structure would be much weakened by superposition of the separate patterns. Furthermore, the presence of strong interference structure means that at least two branches of the deflection function are present. Thus, quenching cannot be removing the inner branch of the deflection function or, if several similar potentials are operating, only one or two at most can be affected in this way otherwise the amplitude of the interference structure would be diminished.

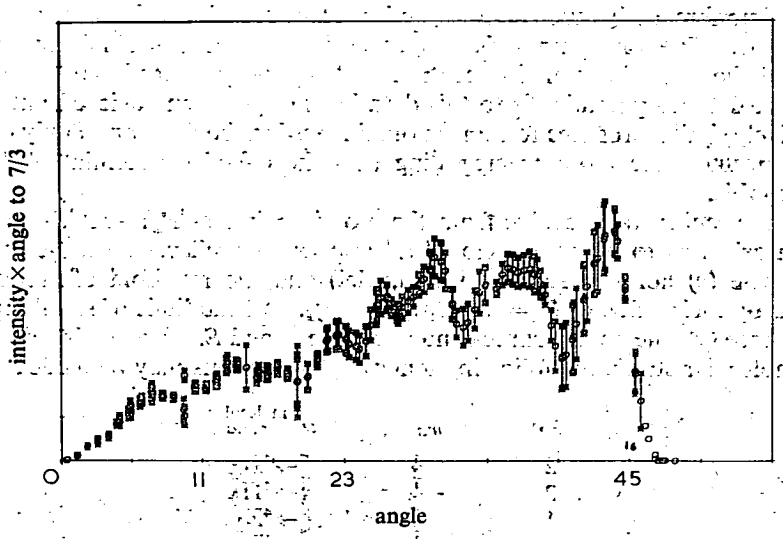

FIG. 7.—Laboratory differential cross section for Hg 6^3P_2 scattering from Rb. The angles shown below the axis are in the centre of mass system. Velocity 470.0 m s^{-1}.

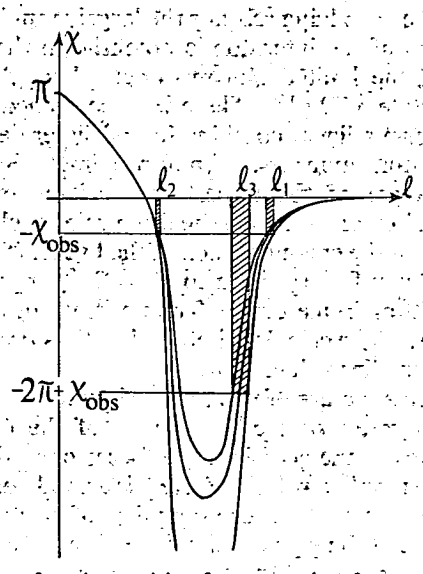

FIG. 8.—A family of deflection functions arising from a group of potentials having similar values of σ and C_6 but different values of ε. Also shown are the l values of some interfering branches.

Turning to the details of the scattering structure, there is a regular pattern in which two periods may be seen, a high frequency one with an average period of $\sim 5.8°$ (Na) and 3.7° (K) and a lower frequency one of smaller amplitude with a period of 24° and 13° respectively in Na and K. This rather simple structure is similar to that expected from a single potential at collision energies leading to orbiting or a rainbow well beyond the angular observation range. Referring to fig. 8, analysis of the angular periods in the interference structure can be made using the semi-classical relation $\Delta\chi = 2\pi/(l_1 - l_2)$ where l_1 and l_2 are the orbital momenta values for two interfering branches on the attractive side. The high frequency oscillations would then correspond to interference between two attractive branches with deflection χ and spaced 2-3 Å apart. The low amplitude longer period oscillations similarly arise from regions of the deflection function centred at $2\pi - \chi$ and χ, spaced ~ 0.8 Å apart, (see fig. 8). A detailed potential fit to this data has not yet been achieved but at least a qualitatively similar cross section can be obtained using the Buck and Pauly potential [9] for the ground state atoms; suggesting that the effective potential of Hg*/M is similar to this.

Five molecular states evolve from the atomic pair $Hg(^3P_2) + M(^2S_{\frac{1}{2}})$ and so the question arises as to why they should all appear so similar. At large separations Hund's case (*c*) holds (assuming fixed nuclei) and the manifold of states may be classified by their value of $\Omega (= m_J(\mathrm{Hg}) + m_s(\mathrm{M}))$. In the limit of small separations (Hund's case (*a*)) the good quantum numbers are Λ and S. Depending on the order of the molecular states, the following tentative correlations may be made;

m_J	m_S	Ω	molecular state
2	$\frac{1}{2}$	$\frac{5}{2}$	$\rightarrow {}^4\Pi_{\frac{5}{2}}$
2	$-\frac{1}{2}$	$\frac{3}{2}$	$\rightarrow {}^4\Pi_{\frac{3}{2}}$
1	$\frac{1}{2}$	$\frac{3}{2}$	$\rightarrow {}^4\Sigma_{\frac{3}{2}}$
1	$-\frac{1}{2}$	$\frac{1}{2}$	$\rightarrow {}^4\Pi_{\frac{1}{2}}$
0	$\frac{1}{2}$	$\frac{1}{2}$	$\rightarrow {}^4\Sigma_{\frac{1}{2}}$

It is clear that neither the deep lying $^2\Sigma_{\frac{1}{2}}$ nor the largely repulsive $^2\Sigma_{\frac{1}{2}}^*$ correlate with the $^3P_2$ state. Calculations of the interatomic potential in the m_J, m_S coupling scheme have been made using the limited Hartree–Fock–Slater 2-electron orbitals already calculated for the $^3P_2$ state of Hg.[17] These were combined with HFS valence orbital of the alkali metal to form a linear combination of Slater determinants that preserved J and m_J as good quantum numbers. An approximate Hamiltonian using the core potentials (with exchange) of the unperturbed atoms together with the specific electron–electron repulsion terms among the three valence electrons was then used in a first order computation of the energy of each of the five states listed above. Relatively shallow wells ranging from 8×10^{-14} erg to 13×10^{-14} erg were found, all much less than the spin-orbit splitting in mercury. The positions of the potential minima were roughly constant at 4 Å. The calculated potentials thus bracket the ground state well depth but have rather smaller values of σ.

So far, then, we have a picture of five rather similar potentials originating with the $^3P_2$ states, partly as a result of the restrictions of the correlation diagram itself. Turning to the dynamics of the collision, the forces operating depend upon whether m_J in a space fixed system or in a rotating system is a good quantum number. Thus for collisions of large impact parameter the coupling of electronic motion to the interatomic motion is weak and the phase shifts depend only slightly on m_J. That is, the adiabatic phase shifts (those calculated assuming m_J a good quantum number) are scrambled. As the impact parameter decreases strong coupling ensues, at first near

the turning point. Finally, for collisions of small impact parameter, m_J in a rotating frame is a good quantum number and the phase shift functions are well separated.

The impact parameter at which coupling becomes important is determined by the splitting of the adiabatic potentials. The dependence of the polarisability [17] of the $^3P_2$ state on m_J is less than 10 % of the mean value and this presumably means a similarly small range of C_6 values. Taking the range of C_6 values to be given effectively by

$$\Delta C_6 = 4\Delta\varepsilon\sigma^6 \tag{3}$$

where $\Delta\varepsilon$ is the range of well depths quoted above and applying [19]

$$b_c = \left(\frac{\frac{3}{8}\Delta c_6}{\hbar v}\right)^{1/5} \tag{4}$$

to determine the critical impact parameter for coupling, b_c, values ~ 6 Å are obtained with a relative velocity $v \sim 6.6 \times 10^2$ m s^{-1}.

We thus adopt the following tentative picture. At small angles of scattering, the lack of coupling between the Hg* m_J state and the passing atom results in a scrambling of the manifold of interatomic potentials to give one effective potential curve. As b decreases, coupling ensues but the potentials, all belonging to quartet states, remain inherently similar and the interference structure from them coincides. The observation of a weak structure of longer periodicity in $\sigma(\theta)$ shows that the deflection functions associated with the various adiabatic potentials can not diverge appreciably until near the minimum where the resulting interference structure from each state would be lost (see fig. 8) in the averaging over m_J.

The observation of quantum structure also sets an upper limit on the size of the quenching cross section since both branches of the deflection function must be present for this structure to be seen. In the absence of a detailed potential fit to the experimental data, it is not possible to give a precise value to this limit, but quenching is clearly not an important process for collisions with impact parameters $\geq \sigma$ and the total quenching cross section can hardly exceed gas kinetic values. No other data on the absolute magnitude of the quenching cross section for Hg $6\,^3P_2$ have been reported, though Martin [20] has measured relative total cross sections for the intermultiplet process (*d*) with a wide range of gases; preliminary results [21] for excitation of the alkali metals are not incompatible with a cross section of gas kinetic magnitude.

The authors thank the Science Research Council and N.A.T.O. for financial support and T. A. D. the Carnegie Trust for a scholarship.

[1] F. A. Morse and R. B. Bernstein, *J. Chem. Phys.*, 1962, **37**, 2019.
[2] F. A. Morse, R. B. Bernstein and H. U. Hostettler, *J. Chem. Phys.*, 1962, **36**, 1947.
[3] H. U. Hostettler and R. B. Bernstein, *Phys. Rev. Letters*, 1960, **5**, 318.
[4] E. Hundhausen and H. Pauly, *Z. Naturforsch.*, 1964, **19a**, 810.
[5] E. Hundhausen and H. Pauly, *Z. Phys.*, 1965, **187**, 305.
[6] P. Barwig, U. Buck, E. Hundhausen and H. Pauly, *Z. Phys.*, 1966, **196**, 343.
[7] U. Buck and H. Pauly, *J. Chem. Phys.*, 1969, **51**, 1662.
[8] U. Buck and H. Pauly, *J. Chem. Phys.*, 1971, **54**, 1929.
[9] U. Buck, M. Kick and H. Pauly, *Proc. VII Int. Conference on Physics of Electronic and Atomic Collisions* (North-Holland, Amsterdam, 1971), p. 543.
[10] J. F. Boyle, *Mol. Phys.*, 1971, **22**, 993.
[11] P. Baltayan and J. C. Pebey-Peyroula, *Compt. Rend.*, 1965, **260**, 6569.
[12] E. C. Darwall, M. A. D. Fluendy and K. P. Lawley, *Entropie*, 1971, **42**, 162.
[13] J. G. Calvert and J. N. Pitts, *Photochemistry* (Wiley, New York, 1966).

[14] L. T. Cowley, M. A. D. Fluendy, D. S. Horne and K. P. Lawley, *J. Phys. E*, (*Sci. Instr.*), 1969, **2**, 1021.
[15] M. N. McDermott and W. L. Lichten, *Phys. Rev.*, 1960, **119**, 134.
[16] J. C. McConnell and B. L. Moiseiwitsch, *J. Phys. B*, 1968, **1**, 406.
[17] E. C. Darwall, M. A. D. Fluendy and K. P. Lawley, *Mol. Phys.*, 1970, **19**, 673.
[18] J. Levine, R. J. Celotta and B. Bederson, *Phys. Rev.*, 1968, **171**, 31.
[19] M. A. D. Fluendy, I. H. Kerr and K. P. Lawley, to be published.
[20] F. J. Van Itallie, L. J. Doemeny and R. M. Martin, *J. Chem. Phys.*, 1972, **56**, 3689.
[21] R. M. Martin, private communication, 1972.

PRINTED IN GREAT BRITAIN AT
THE UNIVERSITY PRESS
ABERDEEN

Studies in Chemical Physics

Chemical Applications of Molecular Beam Scattering

M.A.D. Fluendy and K.P. Lawley

Science Paperbacks

Chemical Applications of Molecular Beam Scattering

Chemical Applications of Molecular Beam Scattering

M. A. D. FLUENDY *and* K. P. LAWLEY
Lecturers in Chemistry
University of Edinburgh

CHAPMAN AND HALL · LONDON

First published 1973
by Chapman and Hall Ltd
11 New Fetter Lane, London EC4P 4EE

Typeset by Santype Limited (Coldtype Division), Salisbury, Wiltshire, and printed in in Great Britain by Lowe and Brydone (Printers) Ltd., Thetford, Norfolk

ISBN 0 412 11810 6 (cased edition)
ISBN 0 412 15550 8 (Science Paperback edition)

Distributed in the U.S.A.
by Halsted Press, a Division
of John Wiley & Sons, Inc., New York

Library of Congress Catalog Card Number 73-6262

Preface

The ideas and methodology developed by nuclear physicists have recently had an important influence in chemistry. The use of a cross-section rather than a rate constant to characterize collision processes is now widespread and interest is increasingly directed to the detailed dynamics of molecular encounters rather than the overall kinetic mechanism. This change in emphasis is reflected not only experimentally in new techniques but also in theoretical developments where the adaptation of scattering theory to chemically reactive collisions is an active field.

The stimulus for this change in approach has been a surprisingly small amount of data obtained by the molecular beam technique. Progress has been limited both by experimental difficulties and the relative novelty to chemists of many of the techniques required. Although important experimental improvements are in prospect, these practical difficulties, rather than any lack of scientific interest, are likely to limit the application of molecular scattering methods. Nevertheless, where applicable, they provide a uniquely detailed insight into intermolecular forces and chemical reaction.

Because of the importance of technical problems, we have thought it worthwhile to discuss experimental matters in some detail. Thus, Chapters 3, 4 and 5 deal with molecular beam sources, selectors and detectors respectively.

This book does not aim at anything like a comprehensive treatment of scattering; rather we have tried to provide an account of those ideas and results which will be of immediate use in interpreting the results of scattering experiments and which will illustrate the beam approach to chemical kinetics. Thus Chapters 2 and 6 are concerned with the classical and quantum theories

of elastic scattering, while Chapter 9 indicates, very much in outline, the way in which these methods can be generalised to deal with more complex situations, such as energy transfer collisions. Finally in Chapters 7 and 8, the results of experimental work in elastic and reactive scattering, where the technique has made its greatest impact, are described.

In writing this book we have attempted to provide a link between the twin streams of chemical kinetics and collision physics and so demonstrate the latter's utility in the chemical field. The level throughout would be roughly described as 'graduate physical chemist' and should be readable by a beginning graduate student.

It is a pleasure to acknowledge the help of our colleague Dr Alastair Rae in reading the manuscript and making numerous helpful suggestions, also Dr Roger Grice for similarly helpful comments on Chapter 8. Finally we thank our research and undergraduate students for their lively and critical interest in the preparation of this manuscript.

Malcolm Fluendy
Kenneth Lawley

Edinburgh,
May 1972

Contents

CHAPTER ONE

Introduction

1.1 Molecular collisions in chemistry

Collisions are fundamental to chemistry. Thus, chemical and thermal equilibrium are maintained by collisions, while the rates of chemical change, mass and energy transfer are all controlled by the frequency and detailed dynamics of molecular collisions. Yet in spite of their central place in chemistry, it is only in the last twelve years that a really concerted beginning has been made in the direct study of inter-molecular dynamics. By comparison, in physics, the field of particle scattering has been of major importance since the days of Rutherford, particularly in the study of nuclear and elementary particles. The principal theme of this book is that the application of conceptually similar scattering methods to chemical problems gives an insight into intermolecular dynamics that could not be obtained in any other way.

A loose division between the interests of chemists and physicists in scattering can be made on energetic grounds. Most chemical processes such as bond rearrangement and ionization occur on impact with energies less than a few tens of electron volts. In distinction, the physics of fundamental particles extends through the GeV range. There has recently been a marked increase in interest in ion and electron scattering processes occurring between 1 and 100 eV and in this energy range the fields of chemistry and physics merge (J. B. Hasted, 1964; N. F. Mott and H. S. W. Massey 1965; H. S. W. Massey, 1971).

The objective of a large part of physical chemistry is the understanding of the macroscopic properties of matter in terms of the fundamental laws of

physics. Thus experiments are usually carried out on a bulk sample of matter which is in thermal equilibrium with its surroundings. The Boltzmann distribution of molecules among the available states is assumed not to be disturbed and if the measured property, for example reaction rate, is a function of the quantum state of the molecule, only an ensemble average value can be obtained. Full interpretation of such measurements involves a statistical theory of the state of the sample as well as of the quantum mechanics of the isolated processes, e.g., of binary collision leading to reaction.

By using molecular beam scattering techniques it is possible to select a single quantum state or range of states for measurement and to explore the dynamics of the molecular collision and the angular and energy dependence of the associated scattering. In this way direct molecular information can be obtained without recourse to rather inadequate theories relating molecular to non-equilibrium bulk properties. It will be worth outlining this technique now so that its application may be more clearly discussed.

1.2 The beam technique

Any molecular scattering experiment involves a molecular or atomic beam which is allowed to strike a target in such a way that the results of the beam-target collisions can be monitored. A molecular beam is a well collimated stream of molecules moving through a high vacuum while the target may consist of a small volume of gas, a solid surface or another molecular beam. The background pressure in the apparatus must be low enough so that molecular collisions with the beam are not so frequent as to destroy its collimation. The density of molecules in the beam or their velocity relative to each other must also be small enough to eliminate collisions between them and consequent broadening of the beam. Molecular collisions are now introduced in a controlled manner by inserting the target. For the moment we will consider the case of two crossed beams.

A typical cross-beam experiment is shown schematically in Fig. 1.1; in this example the detector is moved about a fixed scattering centre. The beams are generated by effusion or continuum expansion from two 'oven' sources and are directed at right angles to each other (orthogonality is not a necessary requirement, but simplifies analysis of the results). The beams are collimated by narrow knife-edge slits and may be velocity selected by mechanical or, in the case of paramagnetic species, magnetic devices so that only a narrow band of velocities is transmitted. These devices are described more fully in Chapter 4. The detector, the subject of Chapter 5, presents only a small

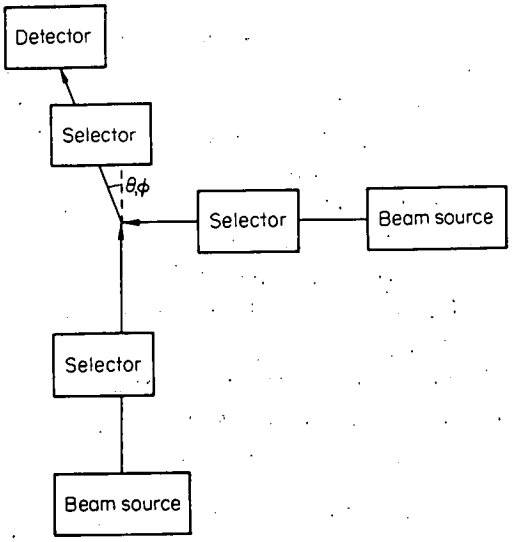

Fig. 1.1 Schematic of a basic beam experiment. According to the aims of any particular experiment, some or all of the quantum state or velocity selectors may be omitted.

effective area to the scattering centre and usually functions as an ionization device converting the molecular flux to an electric current.

As the detector is moved around the scattering centre the intensity of scattered particles is measured as a function of deflection angle, defined by reference to one of the beams. The scattering caused by the target or cross beam is differentiated from that due to the background pressure by comparing signals with the cross-beam alternately on and off. The measurement at each angle takes from a few seconds to many minutes depending upon the strength of the signal. This basic measurement of intensity versus angle is then repeated over a wide range of collision velocities and internal states of the collision partners.

It is important even at this early stage in the discussion to form some idea of the intensities and magnitudes of signal that can be expected since the technique is always likely to be limited by these experimental constraints. For an *effusive source** we might typically expect to form a beam 10 mm tall, 0.05 mm wide at a distance of 1 m from the source with a flux there of 5×10^{16} mol s^{-1} m^{-2}. This intensity falls off as the square of the distance from the source. Thus a detector with an effective area of 1 mm^2 would

* As will be seen in Chapter 3 more intense beams can be generated by working under conditions of hydrodynamic flow.

collect 5×10^{10} mol s^{-1} and if it ionized the beam with unit efficiency would yield a current of about 10^{-8} A. Such currents are readily measurable and with an ionization efficiency of 10^{-4}, as for example in a mass spectrometer detector, the resulting currents are still adequate. Even the additional introduction of a velocity selector which may reduce the beam intensity to 1 per cent or less of its original intensity, equivalent to a current of 10^{-14} A, presents no great problems. There is thus no difficulty in detecting a single molecular beam, even using a detector that registers only one ion for 10^4 neutral molecules. Unfortunately the detection of a scattered beam is much more difficult.

Consider an experiment in which two beams intersect. The number of collisions occurring in their intersection region of volume V is:

$$Z_{AB} = \frac{F_A F_B}{v_A v_B} V v_{AB} \sigma \tag{1.1}$$

where F_A and F_B are the fluxes of the two beams in mol s^{-1} m^{-2}, v_A and v_B are their velocities and v_{AB} the relative velocity ($v_{AB} = (v_A^2 + v_B^2)^{1/2}$ for beams meeting at right angles). σ is the cross-section representing in terms of an effective area the probability of collisions removing molecules from the beam. This quantity will be defined more closely later; suffice it to say that for typical molecular systems σ is of the order 500 Å^2 for the sum of all processes that can remove molecules from the beam, i.e., σ is the *total* cross-section. For specific results of a collision, e.g., chemical reaction, the effective cross-section will be much smaller, varying downwards without limit.

For two 'standard beams' colliding at a distance of 100 mm from their respective sources in a collision volume of $10 \times 0.05^2 = 2.5 \times 10^{-2}$ mm^3 and with velocities of 5×10^3 m s^{-1}, i.e., in the thermal energy range:

$$Z_{AB} = \frac{5 \times 10^{18}}{5 \times 10^3} \times \frac{5 \times 10^{18}}{5 \times 10^3} \times 2.5 \times 10^{-2} \times 10^{-9} \times 7 \times 10^3 \times 5 \times 10^{-18}.$$

$$\sim 9 \times 10^5 \text{ collisions } s^{-1}.$$

If the scattered molecules are evenly smeared out over all angles in the laboratory then the number of particles per second striking a detector subtending a solid angle θ_d to the scattering centre is:

$$N_{\text{detector}} = \frac{\theta_d}{4\pi} Z_{AB} \text{ s}^{-1}. \tag{1.2}$$

Thus a detector 5 mm tall and 0.2 mm wide located 100 mm from the scattering centre will receive about 7 particles per second – an ion current of 10^{-18} A even with unit ionization efficiency – a very low flux indeed that can only be measured by using particle counting methods and even then only if the noise or background is sufficiently small.

In practice the scattered material is not distributed evenly over 4π sr but is strongly peaked near the undeflected beam, i.e., small angles of deflection predominate. Scattering is more intense and so more easily measured in this region than our simple calculation would suggest, though correspondingly more difficult at wide angles.

It is also instructive to compare the number density in a 'standard beam' ($F/v \sim 10^{15}$ m^{-3} at 0.1 m from the beam source) with that due to the background gas or contamination in our apparatus. A typical 'good' laboratory vacuum of 10^{-7} Torr corresponds to 10^{15} mol m^{-3} so that the 'vacuum' is as dense as our primary beam and many times more so than the scattered material. As a consequence the number of particles scattered from the background molecules is much greater than that scattered from the target cross-beam, since the path length through the apparatus is many times the thickness of the target. It is clear then that scattering experiments present some considerable difficulties with respect to the intensity of the particle fluxes that must be detected, particularly since the background particle densities are so high.

Here is perhaps the reason that scattering methods are a relatively new development in the study of molecular collisions, since high pumping speeds permitting the attainment of pressure in the range 10^{-7} to 10^{-9} Torr have only recently become available.

1.3 The field of application for beam techniques

Beam methods in chemistry have so far been used to study intermolecular forces, bimolecular reactions and, by single beam techniques, some electric and magnetic properties of isolated molecules. A beginning has also been made in investigating internal energy transfer accompanying bimolecular collisions.

We first briefly compare the beam and conventional methods of measuring intermolecular forces, which has been one of the important fields of physical chemistry and chemical physics for several decades. Certain characteristic advantages and disadvantages of beam methods will emerge that recur wherever these techniques are used. Conventional and beam methods of measuring reaction cross-sections will then be outlined to illustrate the new approach of the beam method.

The measurement of the second virial coefficient can be taken as representative of conventional methods for determining intermolecular forces (Hirschfelder *et al.*, 1964). It is a bulk property, derived from the gas compressibility and is a function of temperature, $B(T)$. The relationship between $B(T)$ and the intermolecular potential $V(R)$ of spherical molecules is:

$$B(T) = 2\pi N \int_0^\infty (1 - \exp(-V(R)/kT)R^2 \, dR \qquad (1.3)$$

where N is Avogadro's number and k Boltzmann's constant. $B(T)$ is in general a smoothly varying function of T. It has not proved possible to obtain the functional form of $V(R)$ by an analysis of the temperature dependence of $B(T)$, the temperature range required for inversion of the data is so wide as to preclude experimental observations over the whole range (and in any case such inversions are unique only for monotonic potentials). If a particular functional form for $V(R)$ is assumed, with three or four adjustable parameters, then values for these parameters can be found which fit the observed values of B over a temperature range of perhaps 200°. The experimental method requires careful attention to technique, is subject to systematic errors and the results are generally only reliable for nearly perfect (i.e. nonpolar) gases.

The molecular beam approach makes use of the fact that collision dynamics are determined by the intermolecular potential. In particular, the angle of deflection in a binary collision is a function of the relative kinetic energy, the relative angular momentum and $V(R)$. In a typical beam experiment designed to investigate the intermolecular potential between two dissimilar molecules A and B, a beam of A molecules whose velocity has been selected to lie in a narrow range about v_A is crossed with a beam of B molecules moving with the velocity v_B. The beam intensities will be sufficiently low so that any beam molecule passing through the collision zone undergoes either no collision or collides only once with a molecule from the other beam. A detector is then scanned round the scattering centre and the intensity of scattered particles (it is probably necessary here to distinguish between species A and B) is recorded as a function of deflection angle measured from the direction of the parent beam. Surprisingly complicated scattering patterns are obtained in this way. Part of the structure is due to the fact that intermolecular potentials are not monotonic functions, additional peaks are interference effects resulting from the wave-like nature of the colliding particles and further complications are introduced by the fact that measurements are made in a laboratory system of co-ordinates rather than in a frame moving with the centre of mass of a particle pair.

In addition to this angular pattern the attenuation of either beam as a result of scattering by the other can be measured. As in the scattering or absorption of light, the logarithm of the attenuation of the beam intensity $\ln(I_0/I)$, is proportional to a quantity σ having the dimension of area and designated the total cross-section for photon/particle or particle/particle scattering i.e.:

$$\ln(I_0^{(A)}/I^{(A)}) = n_B \sigma l \tag{1.4}$$

where n_B is the number density of target molecules in the collision region of length l. This relationship is based upon the conservation of particles.

If this attenuation measurement is repeated over a range of velocities of beam A, $n_B\sigma$ as a function of v_A will be obtained and if n_B is held constant, or measured, the velocity dependence of σ itself is found. We will show in Chapter 7 that σ is given by the following expression for a monotonic potential, $V = C_s R^{-s}$ (N. F. Mott and H. S. W. Massey, 1965):

$$\sigma(v) \simeq f_s \left(\frac{C_s}{\hbar v}\right)^{2/(s-1)} \tag{1.5}$$

where f_s = 8.083 for s = 6 Thus, even if n_B is not known, a plot of ln σ vs. ln v yields s directly while if n_B and hence σ is known absolutely C_s can be found. If the potential is not monotonic the above result holds only at very low and very high energies where s is given a value appropriate to long and short range parts of the potential respectively.

An effect common in beam work is found in the relative velocity distribution if the velocity of the beam molecules is not selected, and they simply effuse from an oven at temperature T. The velocity distribution in either beam is now v^3 Maxwellian, i.e., the probability of finding a molecule, mass m, with speed between v and $v + dv$ is:

$$P(v, T)\,dv = \frac{1}{2}(m/kT)^2 v^3 \exp(-mv^2/2kT)\,dv \tag{1.6}$$

Taking the two beam particles and the oven temperature to be identical and using the result:

$$v_{AB}^2 = v_A^2 + v_B^2$$

for the relative velocity, v_{AB}, of two beam particles (A) and (B) moving at right angles, one obtains:

$$P(v_{AB}; T) = \frac{1}{48}(m/kT)^4 v_{AB}^7 \exp(-mv_{AB}^2/2kT) \quad (1.7)$$

A considerable sharpening of the relative velocity distribution is evident. The total cross-section deduced from the beam attenuation is then:

$$\sigma(T) = \int_0^\infty \sigma(v_{AB}) P(v_{AB}, T) dv_{AB}. \quad (1.8)$$

Since we cannot be sure that the potential is effectively monotonic over the whole range of v_{AB} in the integration, a much more complicated expression than (1.5) for $\sigma(v)$ as a function of the intermolecular potential parameters must in general be used. The important point is that the unfolding of $\sigma(T)$ to give $\sigma(v)$ by Equation 1.8 is then almost as difficult as unfolding $B(T)$ to give $V(R)$ directly and illustrates the general rule that beam methods only achieve their full power when some velocity selection is used. It might seem from Equation 1.7 that a v^7 Maxwellian distribution is near enough a delta function for velocity selection to be unnecessary. However, it will emerge on closer examination of the problem that not only the magnitude but also the direction of the relative velocity must be closely defined if meaningful differential and total cross-sections are to be measured, and this is only poorly defined in unselected crossed thermal beams.

If part of the angular scattering pattern is observed, although the relationship between this pattern and the intermolecular potential is far more complicated than Equation 1.5, the structure in favourable cases is sufficiently detailed for an unambiguous assignment of three parameters in $V(R)$ to be made directly without recourse to statistical methods of fitting. It will emerge that, at any one energy, various features of the scattering pattern can often be associated with different parts of the potential.

We now turn to the second major application of beam techniques, the investigation of bimolecular reactions. Apart from a few special techniques the kinetics of chemical reactions have hitherto been investigated by mixing the reactants in a time, short compared with some time constant of the reaction, and sampling the mixture of appropriate intervals thereafter. It often requires considerable ingenuity to separate the effects of various competing reactions, but having done this the bi- and uni-molecular rate constants of each elementary reaction can be obtained. The temperature dependence of the bimolecular rate constant, $k_{AB}(T)$, gives the activation energy and pre-exponential factor. This is generally the limit of the information that can be extracted from bulk kinetic data.

Rate constants are directly useful in that with their aid the most probable

path of a complicated many step reaction can be determined and interesting correlations made with other molecular properties. They are not, however, the most fundamental pieces of information about a reactive molecular encounter; more detailed questions can be asked such as, 'what is the probability of reaction when two reactant molecules collide with given relative angular momentum, kinetic energy and specified internal quantum states? Furthermore, how does this probability of reaction vary with the quantum states of the products and the angle through which they are scattered?' When such detailed questions are asked, either very fast spectroscopic methods of analysis have to be used, or the actual kinematics of reactive collisions investigated. In the former class are the methods of flash photolysis and the study of chemiluminescence but, important as these techniques are, neither provides a complete answer to the questions asked above, if only because the state of the reactants is not controlled. Difficult though these answers may be to obtain – and there are perhaps only two or three reactions for which nearly complete information is available – reaction probabilities between specified quantum states and into specified solid angles do provide the most detailed information possible about potential energy surfaces in reacting systems.

A somewhat idealized molecular beam experiment to investigate the reaction between species A and B would be along the following lines. Two beams, one of each kind of molecule, are prepared and allowed to intersect in a high vacuum. Ideally, both beams are velocity and state selected. A detector sensitive to the required product molecule C is then scanned round the point of intersection of the beams and in this rather painstaking way the intensity of scattered C molecules is mapped out. In the ultimate experiment the detector would be sensitive only to a particular quantum state of C. In order to interpret such data, it is useful to define the reaction cross-section for the process:

$$A(\nu_A) + B(\nu_B) \longrightarrow C(\nu_C) + D(\nu_D) \qquad (1.9)$$

at a relative velocity v of the reactants; the ν_i stand collectively for the set of quantum numbers needed to specify the state of the species present. The definition is best given in practical terms at this point:

=	total number of C molecules emerging per second in state ν_C $\sum_{\nu_D} \sigma(\nu_A, \nu_B, \nu_C, \nu_D; v)$ x number of A molecules in the scattering volume x mean density of B molecules in the scattering volume x relative molecular velocity.

The scattering volume is simply that volume defined by the intersection of the two beams, and the density of particles in a beam is the flux per unit velocity. It will be recognized that this definition parallels that of the gas kinetic cross-section in the elementary theory of hard sphere gases (R. D. Present, 1958); σ would then be the cross-section for collision. A very similar definition holds for the experimentally simpler case of a beam of A molecules passing through a static gas of B molecules. The reaction volume would then be the product of the beam cross-section area and the path length of the beam through the gas.

Returning to our hypothetical scattering experiment, the flux of C molecules integrated over all scattering angles yields $\sigma(v_A, v_B, v_C, v_D; v)$ after suitable normalization. The bimolecular rate constant is related to $\sigma(v)$ thus:

$$k(v_A, v_B, T) \propto \sum_{v_C, v_D} \int \sigma_{v_C v_D}^{v_A v_B}(v)\, v^3 \exp(-\mu_{AB} v^2/2kT)\, dv \qquad (1.10)$$

$$k(T) \propto \sum_{v_A v_B} k(v_A, v_B, T) \exp(-[E v_A) + E(v_B)]/kT)$$

where it has been assumed that a Maxwellian distribution of velocities holds in the reacting mixture (μ_{AB} is the reduced mass of the pair A..B, see Section 2.1 and the partition functions in the Boltzmann weighting of the initial states have been omitted for simplicity). Once again the energy dependence of the quantity measured in the beam experiment is replaced by the temperature dependence of a property, $k(T)$, measured in thermal equilibrium with a heat bath. In deciding which is the more useful quantity, $k(T)$ or $\sigma(v)$, from the point of view of the theorist, it should be remembered that transition state theory and allied phase space theories give $k(T)$ directly, whereas purely quantum or classical theories that consider one collision at a time give $\sigma(v)$ and its angular dependence. Reaction cross-sections do have other advantages in that they obey microscopic reversibility which sometimes enables rather inaccessible cross-sections to be deduced.

It has already been hinted that the full dependence of cross-sections on the quantum states of reactants and products has so far eluded measurement and that some averaging, especially over initial rotational states, is almost always present. However, it is important not to lose sight of the most important advantages of the beam method which are that a single step in a reaction is isolated and that the rapid separation of the products after collision freezes the population of the final states. A unique feature of the

beam method arising from this is that the angular distribution of products emerging from the collision can be measured. This information is a sensitive probe of the kinematics of the reaction. In fact, it will emerge that angular distributions are just as interesting as the energy dependence of reaction cross-sections.

Rate constants will not feature prominently in this book but before leaving them it is worth noting that although $k(T)$ can in principle be unfolded via Equation 1.10 to obtain $\sigma(v)$ if a sufficiently wide temperature range is available, it will in practice be almost impossible to achieve this range. The difficulties in extracting reaction probabilities as a function of the relative energy from $k(T)$ can be illustrated by the following simplified example. Suppose $\sigma(v)$ is a single step function of v, then suppressing the v_i,

$$\begin{aligned} \sigma(v) &= 0, \qquad 0 < v < v^* \\ \sigma(v) &= \sigma^*, \qquad v^* < v < \infty \end{aligned} \tag{1.11}$$

$(v^* = \sqrt{2E^*/\mu}$, where E^* is the activation energy)

then, $k(T)$ is readily found by integrating Equation 1.10 to be of the Arrhenius form when $kT \ll E^*$

$$k(T) \approx \sigma^* \left(\frac{\mu}{kT}\right)^{3/2} \left(\frac{2}{\pi}\right)^{1/2} \frac{2E^*}{\mu^2} kT \exp(-E^*/kT). \tag{1.12}$$

Now suppose that the single step function Equation 1.11 is replaced by a double step function, σ^* increasing by a factor f at E_2^*, i.e. in addition:

$$\sigma(v) = f\sigma^*, \qquad v > \sqrt{2E_2^*/\mu}. \tag{1.13}$$

Upon evaluating the integral in Equation 1.10 again, $k(T)$ is found to be:

$$\begin{aligned} k(T) \approx \sigma^* \left(\frac{\mu}{kT}\right)^{3/2} \left(\frac{2}{\pi}\right)^{1/2} \frac{2kT}{\mu^2} E_1^* \exp(-E_1^*/kT) \\ \times \left\{1 + \frac{E_2^*}{E_1^*}(f-1)\exp(-[E_2^* - E_1^*]/kT)\right\}. \end{aligned} \tag{1.14}$$

Unless measurements are carried out in the temperature range $kT \sim E_2^* - E_1^*$, it will be very difficult to detect the presence of the second step, and this

condition would clearly be very difficult to fulfil if $E_2^* \approx E_1^*$, since it is also necessary to maintain the ratio E_1^*/kT to a value at which reaction with a measurable rate actually occurs. Using beam techniques, on the other hand, it is only necessary to ensure that the energy resolution is smaller than $E_2^* - E_1^*$ and that beam energies can be obtained to scan across both E_1^* and E_2^*.

Perhaps a second example from reaction kinetics is not out of place. Suppose it is required to differentiate between the following two hypothetical energy dependences of the reaction cross-section, the distinction having important theoretical implications:

$$\begin{aligned} &\text{model (1)} && \sigma(E) = \sigma^* \\ &\text{model (2)} && \sigma(E) = \sigma^* E^*/E \end{aligned} \tag{1.15}$$

the cross-section being zero for $E < E^*$ in both cases. The bimolecular rate constant can readily be calculated for the two cases as:

$$\begin{aligned} &(1) \quad k_1 \propto \sigma^*(E^* + kT/2)(kT)^{-\frac{1}{2}} \exp(-E^*/kT) \\ &(2) \quad k_2 \propto \sigma^* E^* (kT)^{-\frac{1}{2}} \exp(-E^*/kT) \end{aligned} \tag{1.16}$$

This functional difference would be very difficult to detect unless the rate constant were measured over a wide range of temperature in the region $kT >> E^*$. To use the beam method to distinguish between the cases in Equation (1.15) a smaller energy range is necessary. The only requirement is that the relative energy of the beam particles must be greater than the activation energy and one of the beams can remain thermally cold. The great advantage of the beam technique in this type of measurement lies in its ability to achieve a comparatively narrow distribution of velocities about the high velocity of interest. In contrast, in the bulk experiment, the population at high velocities can only be increased by raising the temperature and hence at the same time broadening the velocity distribution.

The use of molecular beam methods to measure the magnetic or electric dipole moment of molecules or atoms has already been mentioned. In these experiments, the molecules isolated in the beam interact with laboratory magnetic or electric fields which serve to focus particles with a selected effective dipole moment on to a detector. In this way extremely accurate determinations of the dipole moment associated with particular quantum states may be made. Thus these measurements compare with bulk values for the dipole moment in the same way as reactive cross-sections for specific quantum states compare with bulk rate constants.

It is again characteristic of beam methods that the formulae for the deflection of a molecule in an applied field, or for the focal length of a beam focusing device involve the molecular parameters and the speed of the molecule. In contrast, the interpretation of bulk properties such as dielectric polarization involves the temperature of the sample.

In this book we are primarily concerned with collision processes and although much of the technique is common to both fields we will not discuss beam spectroscopic measurements further. A number of excellent works may be referred to for further details (N. F. Ramsey, 1956; K. F. Smith, 1955).

CHAPTER TWO

The Classical Mechanics of Molecular Scattering

2.1 Classical mechanics of two-body collisions

As is well known, the transport and equilibrium properties of gases can be treated successfully by classical mechanics, quantum effects appearing only in the properties of individual molecules. The quantum corrections to bulk behaviour are normally important only for light gases at very low temperatures. In contrast, scattering experiments are a much more delicate tool for observing two-body interactions and we will see later that quantum mechanics plays an essential part in many scattering effects. Nevertheless, classical mechanics is capable of illuminating the outline of the subject and provides a vital conceptual frame in which to introduce the underlying ideas and language. The elementary theory will now be summarized and further details can be found in H. Goldstein, 1964; L. D. Landau and E. M. Lifschitz, 1960.

It was found in Section 1.2. that the primary information to come from a crossed beam scattering experiment, is the fraction of the incident beam flux, N/N_0, that results in scattering into a specified solid angle. If we take this solid angle to be the infinitesimal $d\omega$, we are interested in the relationship between $d(N/N_0)/d\omega$ and the intermolecular potential. In this chapter we shall consider the simplest possible situation: that in which the particles are structureless and interact by a central conservative force. No energy can then be exchanged between the relative motion of the particles and any internal modes; collisions of this type are called *elastic*. In distinction, *inelastic* collisions involve the transfer of energy from or to internal modes while in *reactive* collisions chemical bonds are made or broken. This present

restriction to elastic collisions is less severe than might at first seem, because such collisions normally predominate in a scattering experiment.

The force between structureless particles interacting by a central potential (in the absence of any external field) depends only on their distance apart; it does not depend on their absolute position in space. We thus replace the vector positions of the two particles $\mathbf{R}_A$ and $\mathbf{R}_B$, defined with respect to a fixed origin in the laboratory, by their relative position vector $\mathbf{R}_{AB} = \mathbf{R}_{AC} - \mathbf{R}_{BC}$ and by $\mathbf{R}_{cm}$ the position of the centre of mass of the two particles (Fig. 2.1). Since the potential energy of the system depends only on $\mathbf{R}_{AB}$ and not at all on $\mathbf{R}_{cm}$ the motion of the centre of mass is unaccelerated and does not contribute to the chemistry. Thus we need only consider the particles' relative motion, though as we shall see later the motion of the centre of mass may profoundly affect the appearance of scattering in the laboratory.

Working in these relative or centre of mass co-ordinates reduces the problem to that of a single particle of mass μ moving about a fixed centre of force. We may write the energy as

$$E = \frac{1}{2}\mu \dot{R}_{AB}^2 + \frac{L^2}{2\mu R_{AB}^2} + V(R_{AB}) \tag{2.1}$$

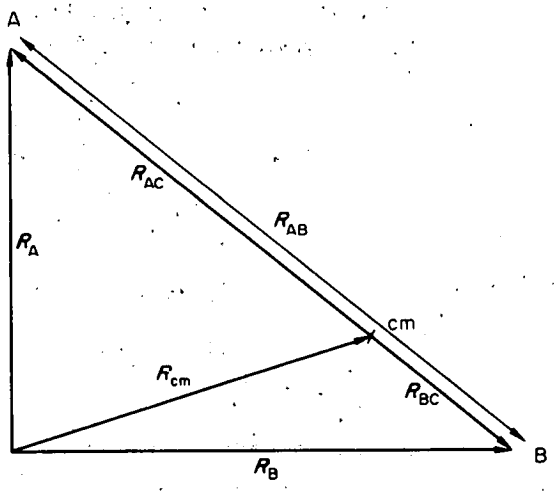

Fig. 2.1 Position vector diagram for two particles A and B colliding. The centre of mass position vector, $\mathbf{R}_{cm}$, divides the relative position vector $\mathbf{R}_{AB}$ in the inverse ratio of the masses of A and B and the centre of mass is at cm.

and the orbital angular momentum as:

$$L = \mu R_{AB}^2 \dot{\chi} \tag{2.2}$$

where μ is the reduced mass, $m_A m_B/(m_A + m_B)$, and χ is the angle between the relative velocity vector $\dot{\mathbf{R}}_{AB}$ and an initial beam direction $\mathbf{R}_A$ or $\mathbf{R}_B$.

Since there are no angle dependent terms in the potential, no couple can act on the system and the angular momentum in conserved. Thus the motion is confined to the plane defined by $\dot{\mathbf{R}}_A$ and $\dot{\mathbf{R}}_B$.

The radial velocity and hence $d\chi/dR_B$ follows from Equations 2.1 and 2.2:

$$\dot{R}_{AB} = \pm\left\{\frac{2}{\mu}\left(E - \frac{L^2}{2\mu R_{AB}^2} - V(R_{AB})\right)\right\}^{\frac{1}{2}} \tag{2.3}$$

$$\frac{d\chi}{dR_{AB}} = \pm\frac{L}{\mu R_{AB}^2}\left\{\frac{2}{\mu}\left(E - \frac{L^2}{2\mu R_{AB}^2} - V(R_{AB})\right)\right\}^{-\frac{1}{2}} \tag{2.4}$$

The sum of the true potential $V(R_{AB})$ and the centrifugal term $L^2/2\mu R_{AB}^2$ is known as the effective potential. Depending on the precise form of $V(R)$ there may be one or more classical turning points of the motion corresponding to the zeros of Equation 2.3 where the radial velocity is zero. If several turning points exist these will be separated by classically forbidden regions. Thus, classically, a pair of particles approaching from infinity can penetrate only as far as the outermost turning point (Figs. 2.2, 2.3).

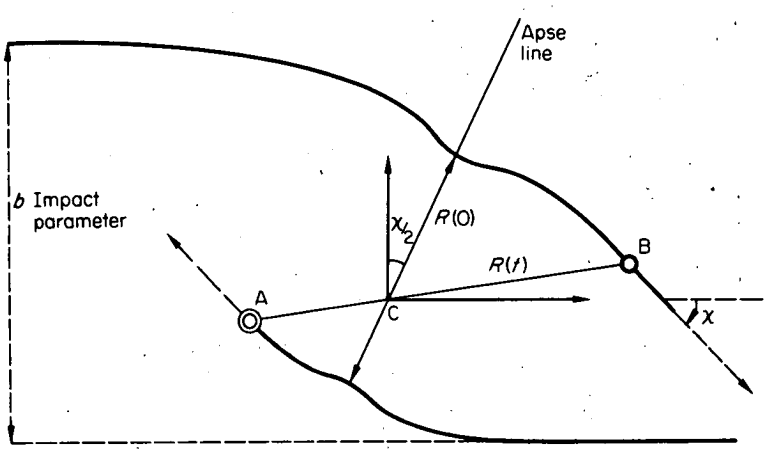

Fig. 2.2 The trajectories of two particles colliding under the influence of a central force, displayed with the centre of mass fixed at C. The angle of deflection is $\chi(b)$ and the distance of closest approach is $R(0)$. For the case illustrated, $m_A > m_B$.

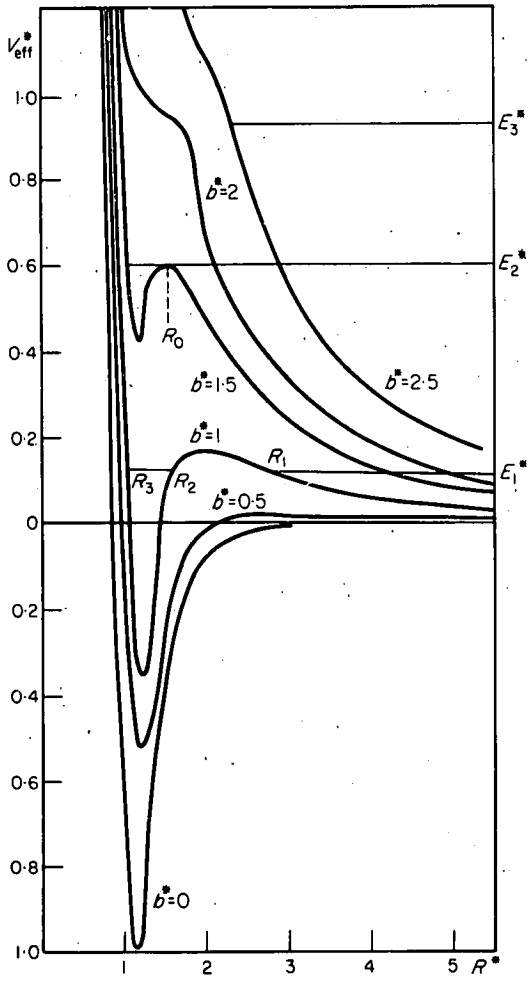

Fig. 2.3 A family of effective potential curves for the Lennard-Jones potential Equation (2.12). The reduced energy V_{eff}/ϵ is plotted against the reduced separation R/σ and the results for a range of reduced impact parameters b/σ are shown. A particle incident with reduced energy E_1^*, $b^* = 1$ will approach to a distance R_1^* and the classically allowed region between R_2^* and R_3^* will be inaccessible. At an incident energy E_2^*, the two particles go into orbit with radius R_0^* when the impact parameter is 1·5. At E_3^* no orbiting is possible at any impact parameter and the distance of closest approach decreases smoothly with b.

Equations 2.3 and 2.4 can be integrated to yield $R_{AB}(t)$ and $\chi(R_{AB})$. Before doing so we adopt the convention that the collision starts at $R_{AB} = \infty$, $t = -\infty$ and the turning point is reached at $t = 0$. $\dot{R}_{AB}$ is negative until the turning point ($R_c = R(0)$) and then positive, the two branches (the roots of Equations 2.3 or 2.4) joining smoothly at $t = 0$. We now change the representation of $\chi(t = \infty)$ to $\chi(b)$ in order to show the parametric dependence of the asymptotic angle of deflection on the impact parameter. The form of $\chi(b)$ can be seen in Fig. 2.5. The impact parameter b is defined as the perpendicular distance apart of the two asymptotic lines of approach and is related to the orbital angular momentum and the asymptotic velocity, $v = \sqrt{2E/\mu}$, by:

$$L = \mu v b \tag{2.5}$$

On integrating Equation 2.4 we can obtain $\chi(\infty)$, the total deflection, as:

$$\chi(E, L) = \pi - 2\int_{R_c}^{\infty} \frac{L\,dR}{R^2\left[2\mu\left(E - V(R) - \frac{L^2}{2\mu R^2}\right)\right]^{1/2}} \tag{2.6}$$

where the subscript AB on R_{AB} has been dropped and where a negative sign for $\chi(\infty)$ indicates an overall bending of the trajectory towards the target. The only result of these elastic encounters is thus to rotate $\mathbf{R}_{AB}$ and, as we shall see in Section 2.4, to transfer some kinetic energy between the two particles. Various qualitative conclusions and approximations will be extracted from Equation 2.6 but for most potentials the integration cannot be performed analytically. Tables of the deflection function, $\chi(b)$, will be found in J. O. Hirschfelder *et al.*, 1964 for the Lennard-Jones potential.

Although beams in the laboratory can be made extremely narrow, there will be no selection of impact parameters on a molecular scale. If we examine a large number of collisions we find that the impact parameters are randomly distributed over a plane normal to the relative velocity that is virtually infinite in extent compared with atomic dimensions. To compare our classical calculations with experiment we must therefore first calculate the deflection as a function of impact parameter, denoted by $\chi(b)$, and then weight each deflection or transition probability by the probability of finding that value of b for the impact parameter in our random distribution of collisions. From Fig. 2.4 bearing in mind that the trajectories are uniformly distributed across the incident plane on the left, the probability of a given collision occurring with an impact parameter between b and $b + db$ is proportional to the area of the first shaded ring, $2\pi b db$. The conservation of particles can be applied to

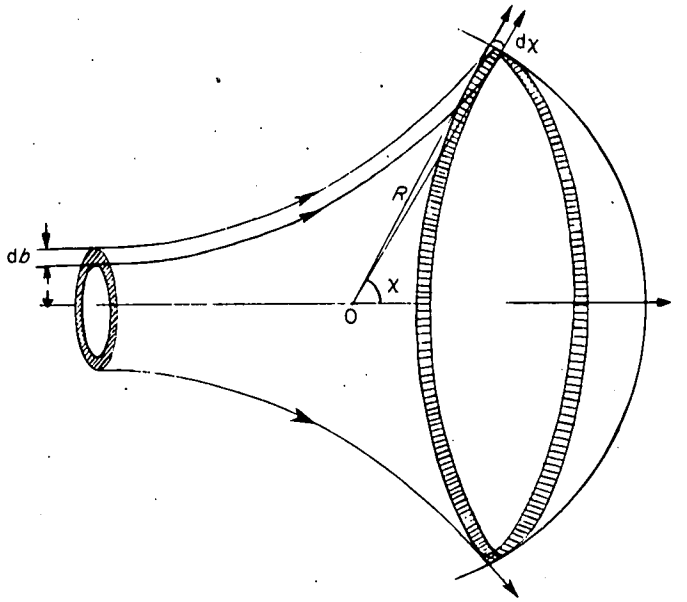

Fig. 2.4 Particles incident in the annular region between b and $b + db$ emerge through the shaded strip between an angle χ and $\chi + d\chi$. The target molecule is at O and the scattered flux is mapped over a large sphere radius R, centered at O.

the general collision with the aid of Fig. 2.4 to yield the result that all the particles which enter the collision zone with impact parameters between b and db must emerge into the solid angle $d\omega$ subtended by the shaded strip lying between χ and $\chi + d\chi$. The emerging particles are counted a distance R away from the scattering centre where R is sufficiently large for the intermolecular force to be negligible and the trajectories are again straight lines. The number of particles crossing the shaded strip at R per second is then:

$$dn = I_0 \times 2\pi b \mid db \mid \tag{2.7}$$

where I_0 is the incident flux and we assume a unique relationship between χ and b. We define the differential cross-section $\sigma(\chi)$ for elastic scattering from a single target molecule as:

$$\sigma(\chi)d\omega = \frac{\text{number of molecules scattered into solid angle } d\omega \text{ per second}}{\text{incident flux}} \tag{2.8}$$

$\sigma(\chi)$ has the dimensions of area and $\sigma(\chi)d\omega$ is the effective area presented by the target molecule for scattering through an angle between χ and $\chi + d\chi$. If the potential is independent of the azimuthal angle ϕ, molecules entering the collision with angles between ϕ and $\phi + d\phi$ leave with the same angle and so the flux is uniform around the 'exit' strip in Fig. 2.4 and we can proceed with considering the fate of the whole bundle of trajectories lying initially between b and $b + db$. Introducing the expression for the solid angle $d\omega$,

$$d\omega = 2\pi \sin\chi \mid d\chi \mid \tag{2.9}$$

and dn from Equation 2.7 into Equation 2.8 gives:

$$\sigma(\chi) = b/(\sin\chi \mid d\chi/db \mid). \tag{2.10}$$

Disregarding the possibility of divergence of this expression we can also define a total elastic cross-section by integrating $\sigma(\chi)$ over the surface of the macroscopic sphere traversed by the detector:

$$\sigma_{\text{total}} = \int_0^{2\pi}\int_0^{\pi} \sigma(\chi)\sin\chi d\chi d\phi = 2\pi\int_0^{\pi}\sigma(\chi)\sin\chi d\chi. \tag{2.11}$$

σ_{total} is now a measure of the probability of molecules being scattered from the beam, i.e., of its attenuation. Other more specialized cross-sections may be defined for particular processes; thus, for a change in quantum state of the system from v_i to v_j, the total cross section (referred, as always, to a single target molecule) is defined as:

$$\sigma_{v_i}^{v_j} = \frac{\text{number of collisions per second in which } v_i \rightarrow v_j}{\text{incident intensity in state i}}$$

We now look more closely at the elastic deflection function $\chi(b)$. Qualitatively, two very different cases can be distinguished according to whether the potential $V(R)$ is monotonic or whether it possesses extrema. The Coulomb potential is an important example of the former type, but intermolecular potential potentials generally exhibit one minimum. Intermolecular potentials are often parametrized in the Lennard-Jones (12:6) form:

$$V(R) = 4\epsilon\{(\sigma/R)^{12} - (\sigma/R)^{6}\} \tag{2.12}$$

where ϵ is the well depth and σ the position of the inner zero of the potential. Returning to the deflection function and noting that:

$$\int_b^\infty \frac{b\,dR}{R^2(1-b^2/R^2)^{1/2}} = \pi/2 \tag{2.13}$$

we can see from Equation 2.6 that positive monotonic potentials (purely repulsive), for which $R_c > b$, lead to positive angles of deflection while purely attractive potentials (for which $R_c < b$) lead to negative angles of deflection. For potentials with both attractive and repulsive regions the angle of deflection changes from negative to positive as the impact parameter decreases. The minimum value of the angle of deflection is called the rainbow angle, although the optical analogy is not perfect. A typical family of deflection curves for a bipolar potential is shown in Fig. 2.5 for a range of incident energies. An important qualitative feature emerges from an inspection of these curves. As the collision energy E decreases the rainbow angle moves to larger impact parameters and at the same time becomes more negative until at critical energy E_c the deflection angle reaches $-\infty$, this behaviour persisting at all lower energies. Physically the two colliding particles have gone into orbit about their (moving) centre of gravity and a classically bound state has been formed. For a simple bipolar potential orbiting and the rainbow effect cannot occur at the same energy. The relation of these types of motion to the impact energy and impact parameter (or angular momentum) is shown in Fig. 2.6. In this figure the behaviour at each combination of reduced energy and angular momentum is plotted. Thus the leftmost 'line of zero deflection' is the locus of those values of L^* and E^* which result in a net zero deflection after collision.

To proceed further with the evaluation of the deflection integral, Equation 2.6, it is convenient to cast the intermolecular potential function into a dimensionless form. The reduction parameters required are a length and an energy. We take the energy parameter to be the well depth ϵ and measure distances in terms of the radial distance to the inner zero of the potential, σ. The expression for the Lennard-Jones potential then becomes:

$$V^*(R^*) = 4\{R^{*-12} - R^{*-6}\} \tag{2.14}$$

where

$$R^* = R/\sigma$$

$$V^* = V/\epsilon$$

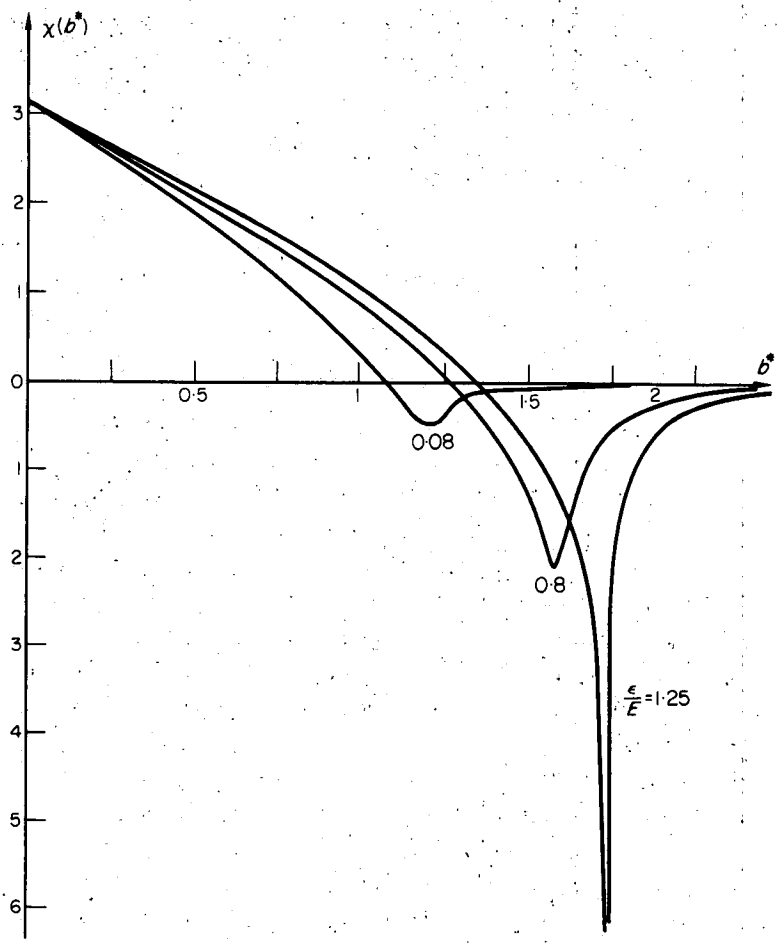

Fig. 2.5 The classical deflection function $\chi(b^*)$ vs. impact parameter b^* for a Lennard-Jones potential at various reduced well depths. The case $\epsilon/E = 1.25$ shows orbiting, the minima in the other cases are the rainbow angles.

and, below

$$E^* = E/\epsilon.$$

The deflection function expression is now:

$$\chi(b^*) = \pi - 2\int_{R_c^*}^{\infty} \frac{E^{*\frac{1}{2}} b^* \mathrm{d}R^*}{R^{*2}\left\{E^*\left(1 - \frac{b^{*2}}{R^{*2}}\right) - 4(R^{*-12} - R^{*-6})\right\}^{\frac{1}{2}}} \qquad (2.15)$$

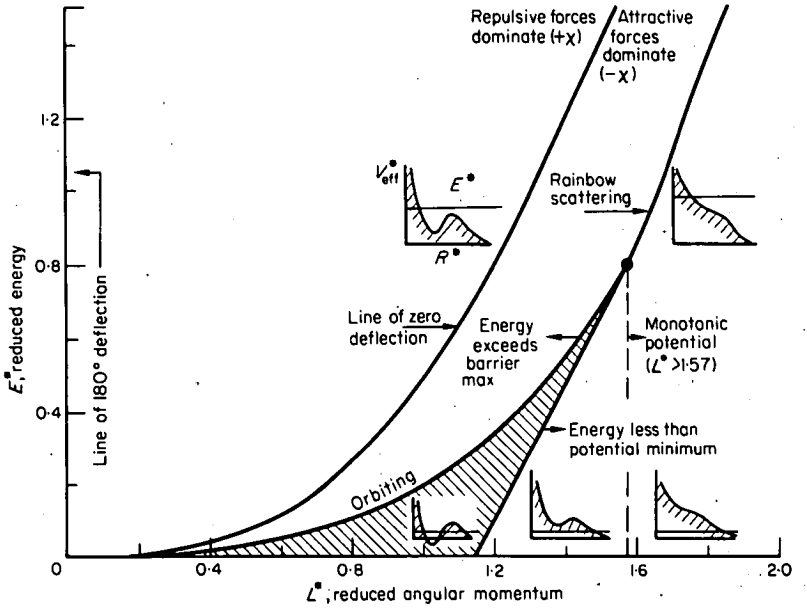

Fig. 2.6 Topology of classical scattering from a Lennard-Jones (12:6) potential. Tracing the deflection χ for a chosen value of E^* along the appropriate horizontal line; χ starts from the left with the value π at $L^* = 0$, and falls monotonically to zero at the line of zero deflection and is negative (net attraction) to the right of this line. χ approaches either $-\infty$ if the orbiting line is crossed or a finite minimum, the rainbow angle, if the rainbow line is crossed. Thereafter χ approaches zero as $L^* \to \infty$.

The changing form of V^*_{eff} is also conveyed pictorially on the diagram. In the shaded region there are three classical turning points.

(Reproduced from K. W. Ford and J. A. Wheeler, 1959).

The rainbow angle at a fixed energy with variable ϵ and σ depends only on ϵ as can be seen by the following argument; the rainbow angle is characterized by:

$$\partial\chi/\partial b^* = 0, \qquad \text{i.e.,} \qquad F(E^*, b_r^*) = 0. \tag{2.16}$$

where $F(E^*, b_r^*)$ is a cumbersome expression of the reduced energy and impact parameter not needed explicitly. If, now, E^* is assigned a value, b_r^* can be found from Equation 2.16 and this value substituted into Equation 2.15 to give the rainbow angle without a knowledge of σ being necessary.

It emerges from a detailed consideration of Equations 2.15 and 2.16 that the reduced distance of closest approach associated with the rainbow angle is largely independent of the energy until close to the onset of orbiting.

Table 2.1

ϵ/E	χ_r (radians)	$-\chi_r . E/\epsilon$	R_c/σ
0.02	-4.089×10^{-2}	2.044	1.20
0.05	-1.026×10^{-1}	2.052	1.20
0.10	-2.066×10^{-1}	2.066	1.21
0.20	-4.202×10^{-1}	2.101	1.21
0.50	−1.140	2.281	1.22
0.80	−2.129	2.661	1.24
1.00	−3.237	3.237	1.25

This is exemplified in Table 2.1 where χ_r, ϵ/E and R_c^* are listed. The latter is almost constant for small ϵ^* at a value of $R_c^* \approx 1.2$, which corresponds to a turning point in the region of maximum negative slope of the potential, and stated in this form the result holds for other potential forms than the Lennard-Jones (12:6).

The conditions for orbiting are that the radial acceleration and radial velocity must simultaneously be zero, i.e., from Equation 2.3:

$$E^*(1 - b^{*2}/R_0^{*2}) - V^*(R_0^*) = 0$$

and

$$2E^*b^{*2}/R^{*3} - \left(\frac{\partial V^*}{\partial R^*}\right)_{R^*=R_0^*} = 0. \tag{2.17}$$

For the Lennard-Jones potential it can be shown that the maximum value of E^* for which orbiting can occur is 0.8. At impact energies above this value rainbow scattering will replace orbiting. From the conditions in Equation 2.17, the orbiting radius under the influence of a Lennard-Jones potential (12:6) is:

$$R_0^* = 1.308(1 - \sqrt{1 - 5E^*/4})^{-1/6}. \tag{2.18}$$

Inspection of Equation 2.18 indicates that R_0^* is only a very insensitive function of the reduced energy E^* and for energies not too close to zero is given by $R_0^* \approx 1.3$, which merges into the value 1.2 as the rainbow phenomenon replaces orbiting.

2.2 Classical scattering cross-sections

Having examined the behaviour of $\chi(b)$ for a typical bipolar potential, we must now consider its relation to the classical differential cross-section $\sigma(\chi)$.

The general form of this relation has already been given in Equation 2.10. It is important to note that although the deflection function $\chi(b)$ can have values ranging from $+\pi$ (direct back scattering) to $-\infty$ (orbiting), $\sigma(\chi)$ is only defined for the range $0 \rightarrow \pi$. A moment's thought will show that positive and negative deflection are indistinguishable in the laboratory since on the molecular scale it is impossible to tell whether the trajectory passed to the left or right of the target molecule. Both positive and negative deflections as well as those with $\chi > \pi$ are therefore mapped on to the range $0 \rightarrow \pi$ in the differential cross-section.†

From Equation 2.10 it is apparent that a singularity will occur in $\sigma(\chi)$ when $|\,d\chi/db\,| = 0$, i.e., at the extremum in the deflection function or rainbow angle. $\sigma(\chi)$ can also rise to infinity if $\sin\chi$ in the denominator of Equation 2.10 passes through zero while b is non-zero. Such a peak in the cross-section is called a forward or backward glory depending upon whether the deflection function is an even or odd multiple of π. The product $\sin\chi\sigma(\chi)$ when $\chi \rightarrow 0$, $n\pi$ does not exhibit this effect, but still diverges at the rainbow angle.

The rainbow phenomenon is frequently observed in molecular scattering and is of key importance in extracting an intermolecular potential from the observed scattering pattern. However, the finite energy spread in the beams and, less trivially, quantum effects, remove the divergence in $\sigma(\chi)$. Nevertheless, a pronounced maximum in the scattered intensity can often be observed with modest velocity selection.

The classical behaviour of $\sigma(\chi)$ near χ_r can be investigated in more detail by approximating the $\chi(b)$ curve near $b = b_r$ by a parabola having the same curvature at the minimum:

$$\chi(b) = \chi_r + q(b - b_r)^2 \tag{2.19}$$

so that:

$$\frac{d\chi}{db} = 2q^{1/2}(|\chi - \chi_r|)^{1/2}. \tag{2.20}$$

Then, the differential cross-section becomes:

$$\sigma(\chi) \cong b_r/(2\sin\chi\, q^{1/2}\,|\chi - \chi_r|^{1/2}), \tag{2.21}$$

† We shall see later that for indistinguishable particles this range falls to $0 \rightarrow \pi/2$.

and the signal received by a detector at χ_r subtending an angle 2Δ in the centre of mass system is:

$$I_\Delta(\chi_r) \propto \frac{b_r}{2q^{1/2}} \int_{-\Delta}^{\Delta} d\chi \mid \chi - \chi_r \mid^{-1/2} = 2b_r\Delta^{1/2}/q^{1/2} \qquad (2.22)$$

which is finite, although the normalized intensity, $I_\Delta \div$ (area of detector), tends to infinity as $\Delta \to 0$.

The glory phenomenon has proved more elusive. The forward glory would lead to scattering in the direction of the incident beam and would be detectable only at very narrow angles where the noise from the main beam makes measurement difficult. The effect has only been detected in measurements of the total cross-section. Backward glories are presumably rendered insignificant by the large value of $d\chi/db$ near $\chi = \pi$ making $\sigma(\chi)$ small (see Equation 2.10).

Inspection of the plots of $\chi(b)$ versus b (Figs. 2.5 and 2.7) shows that for a bipolar potential a given value of $\mid \chi \mid$ may result from collisions at three different impact parameters. If we retain our picture of the incident molecules being spread uniformly over a plane normal to the initial relative velocity three annular zones at b_1, b_2 and b_3 lead to scattering into the solid angle at χ. *Classically* the cross-section will be:

$$\sigma(\chi) = \sigma_1(\chi) + \sigma_2(\chi) + \sigma_3(\chi) \qquad (2.23)$$

each term on the right-hand side being given by Equation 2.10 with the appropriate value of b. In general, the contribution of the outermost branch of $\chi(b)$, corresponding to the largest value of the impact parameter, will be the major term because of the presence of the b factor in the numerator of Equation 2.10.

We now proceed to use some of the foregoing results to derive the limiting form of the classical differential cross-section at small angles. Mathematically, the method is to expand the expression for $\chi(b)$, Equation 2.6, in inverse powers of E^* and then, retaining only the leading term, to substitute the derivative for $\mid d\chi/db \mid$ in Equation 2.10. We will deal first with the large impact parameter contribution in Equation 2.23 and this will be the only contribution for a monotonic potential.

Taking a potential of the more general form:

$$V(R) = \sum_s C_s R^{-s} \qquad (2.24)$$

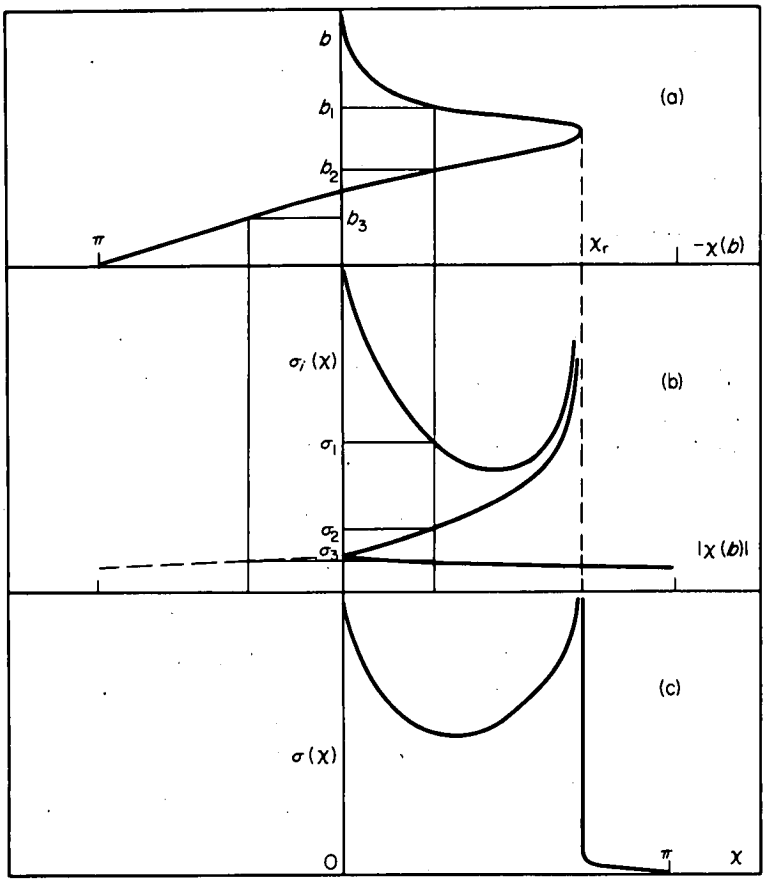

Fig. 2.7 The contributory branches of the differential cross-section.
(i) The deflection function $\chi(b)$ v b. χ_r is the rainbow angle.
(ii) The three contributions σ_i to the differential cross-section. The contribution to each σ_i comes from impact parameters around the corresponding b_i.
(iii) The net differential cross-section as a function of the true polar angle of deflection, χ.

and substituting into Equation 2.4 gives a rather intractable integral which in the general case must be evaluated by numerical quadrature, for example, the Gauss-Mehler method or by the solution of the coupled differential equations, an approach which avoids the singularity at the turning point of Equation 2.6;

$$\dot{R} = -\left\{\frac{2}{\mu}\left(E - \frac{L}{2\mu R^2} - V(R)\right)\right\}^{1/2} \tag{2.25}$$

and

$$\dot{\chi} = L/\mu R^2,$$

for which several efficient digital computer programs exist. The expansion of χ in powers of the reduced potential parameters $C_s^* = C_s/E$ is not straightforward and the result is quoted in Section 2.7. Here we confine ourselves to obtaining the first order approximation to χ by a physically more illuminating method involving Newton's second law explicitly in an approach that will also be found useful in the quantum treatment. The intermolecular force **F** is resolved into components parallel and perpendicular to the direction of relative motion and Newton's second law applied in the form of an action integral:

$$\Delta \mathbf{p} = \int_{-\infty}^{\infty} \mathbf{F}\, \mathrm{d}t \tag{2.26}$$

where $\Delta \mathbf{p} = \mathbf{p}_{\mathrm{final}} - \mathbf{p}_{\mathrm{initial}}$ is the vector change in relative momentum. If, as an approximation valid for small angles of deflection, we replace the trajectory by a straight line we can resolve $\Delta \mathbf{p}$ into two components:

$$\begin{aligned} \Delta p_z &= \int_{-\infty}^{\infty} F_z\, \mathrm{d}t \\ \Delta p_y &= \int_{-\infty}^{\infty} F_y\, \mathrm{d}t \end{aligned} \tag{2.27}$$

the motion being confined to the yz plane. The first integral vanishes ($F_z(-t) = -F_z(t)$) and the second yields:

$$\Delta p_y = 2b\left(\frac{\mu}{2E}\right)^{1/2} \int_b^{\infty} \left(\frac{\mathrm{d}V}{\mathrm{d}R}\right)(R^2 - b^2)^{-1/2}\, \mathrm{d}R \tag{2.28}$$

where the equations of the path:

$$v = \mathrm{d}z/\mathrm{d}t \quad \text{and} \quad z^2 = R^2 - b^2$$

have been used.

If the deflection angle is small:

$$\chi \simeq \Delta p_y / p_z \tag{2.29}$$

and so:

$$\chi \simeq \frac{b}{E} \int_b^\infty \left(\frac{dV}{dR}\right) (R^2 - b^2)^{-1/2}\, dR \tag{2.30}$$

whence, for any of the terms in Equation 2.23:

$$\chi_s \simeq sC_s \pi^{1/2} \left[\frac{\Gamma((s+1)/2)}{\Gamma\left(\frac{s}{2}+1\right)}\right] \Big/ (2Eb^s). \tag{2.31}$$

It can also be seen from Equation 2.30 that the deflection angle χ in the small angle region is the sum of the contributions χ_s from each term in the potential.

We now complete the evaluation of the differential cross-section by combining Equations 2.10 and 2.30. In the limiting case where the dominant contribution to χ comes from only one term in the potential, the differential cross-section is given by:

$$\sigma_s(\chi) = \frac{1}{s}\left(s\pi^{1/2} \frac{\Gamma((s+1)/2)\, C_s}{\Gamma\left(\frac{s}{2}+1\right) E}\right)^{2/s} \chi^{-(2+2/s)} \tag{2.32}$$

Defining a reduced potential parameter C_s^*, with the aid of any convenient length parameter, d

$$C_s^* = C_s/(Ed^s)$$

Equation 2.32 can be put in the reduced form:

$$\sigma_s(\chi)^* = \frac{\sigma^{(s)}}{d^2} = \frac{1}{s}\left(s\pi^{1/2} \frac{\Gamma((s+1)/2)\, C_s^*}{\left(\Gamma\, \frac{s}{2}+1\right)}\right)^{2/s} \chi^{-(2+2/s)} \tag{2.33}$$

The contribution of the inner branches of the deflection function, if there were any, to the small angle cross-section would not be susceptible to simple approximation because the forces acting during the collision are not necessarily small, but a typical order of magnitude may be obtained from a

rough value of $(d\chi/db)_{b=b_2}$ estimated from tables of angles of deflection for the Lennard-Jones potential. We suppose that three branches contribute to the scattering at some value of χ close to zero. Inspection of a typical deflection plot shows that as $\chi \to 0$ at b_0, the two inner branches (labelled (2) and (3) in Fig. 2.7) merge and that the deflection function in the region of b_2 and b_3 can be approximated by the linear term:

$$\chi = (b_0 - b)(d\chi/db)_{b=b_2,b_3}.$$

The contribution of these two inner branches to $\sigma(\chi)$ is thus:

$$\sigma(\chi) = \frac{b_2}{\sin\chi \left|\frac{d\chi}{db}\right|_{b=b_2}}$$

Both b_2 and $d\chi/db$ are relatively insensitive functions of energy (near $\chi = 0$) and one finds over the energy range $E/\epsilon = 1 - 10$:

$$\sigma_{\substack{\text{inner}\\\text{branch}}}(\chi) \sim 0.4\,\chi^{-1}\,\sigma_{LJ}^2 \qquad (2.34)$$

where σ_{LJ} is the Lennard-Jones length parameter

To summarize, in a system in which a bipolar potential is operating, $\sigma(\chi)$ at angles appreciably less than the rainbow value (perhaps $\lesssim 0.1$ rad) is dominated by the outermost branch of the deflection function and hence the radial dependence of the longest range part of the deflection function can be found. At angles well beyond the rainbow and at reduced energies $E^* \gg 1$, the scattering becomes dominated by the shortest range part of the potential, but this region, even for 'normal' potentials, may well lie outside the range of thermal energy scattering.

It is not worthwhile identifying these regions more closely because small angle scattering is subject to important quantum effects which are discussed in Chapter 6. Nevertheless, Equation 2.32 retains a region of validity under low angular resolution even in a full quantum treatment.

Before leaving the subject of the differential cross-section, an important consequence of Equation 2.33 must be mentioned. We will suppose that Equation 2.33 gives the differential cross-section for all values of χ, not just in the small angle region – and for monotonic potentials for which there cannot be a rainbow region Equation 2.33 has qualitatively the right appearance of a rapid fall off in intensity at large angles. Integrating over χ

with Equation 2.33 substituted in Equation 2.11 gives the total cross-section

$$\sigma_{tot} = f(s) \int_0^{\pi} \chi^{-(1+2/s)} d\chi \tag{2.35}$$

This integral is clearly divergent for all positive values of s and so we conclude that classical mechanics generally predicts infinite total cross-sections for potentials of infinite range. In fact, total cross-sections are finite and the experimental basis for this very important result is discussed in Chapter 7. The discrepancy is resolved by the wave mechanical treatment of scattering (Chapter 6), but the prediction of infinite cross-sections (whether total or differential) remains one of the more striking failures of classical mechanics. From an experimental point of view, the situation is less dramatic. Equation 2.35 predicts that if the attenuation, $(I_0 - I)/I_0$, of a beam by a cross beam or any sort of target is measured with a progressively narrower detector, a constant value is not achieved, but instead the attenuation tends to unity in some fashion with the detector width (assuming also that the beam width is kept narrower than the detector!) In practice, a limiting attenuation less than unity is readily observed with detectors of finite resolution.

We now introduce two further quantities which, like the angle of deflection, can serve to characterize a collision. These are the phase shift and the time delay. Both can be given a classical definition, but they achieve their full significance in the quantum theory of scattering. A particle moving through field free space has associated with it a wave motion of wavelength given by the de Broglie relationship:

$$\lambda\!\!\!^{-} = \hbar/mv = \hbar/\sqrt{2mE} = \frac{1}{k}. \tag{2.36}$$

In the presence of a force field the wavelength depends on the position of the particle and a phase shift relative to an identical particle moving through a field-free region is introduced (see Fig. 2.8). It is only of interest to compare the motions of a particle along trajectories that have the same angular momentum and in regions sufficiently remote from the scattering centre for the phase shift to have become independent of position. We are thus led to a definition of the form:

$$\eta(b) = \lim_{R \to \infty} \left\{ \underbrace{\int_{R_c}^{R} \frac{dR}{\lambda}}_{\text{real path}} - \underbrace{\int_{b}^{R} \frac{dR}{\lambda}}_{\text{zero potential path}} \right\} \tag{2.37}$$

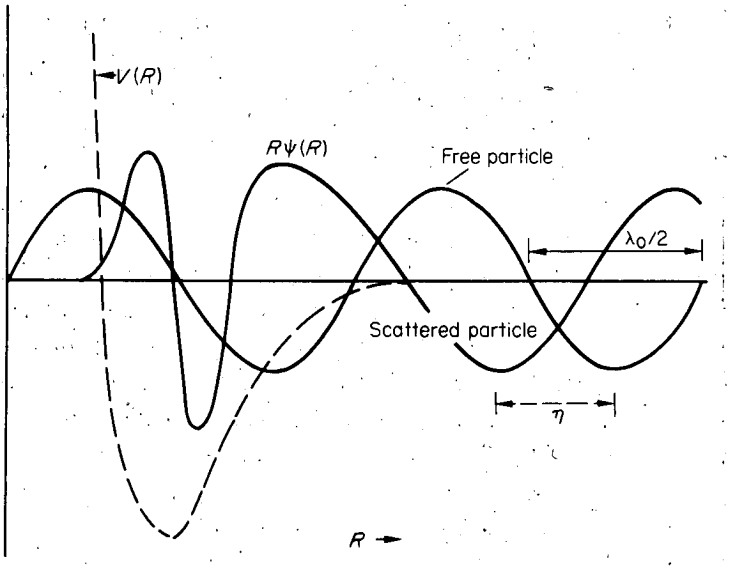

Fig. 2.8 The radial wave function $\psi(R)$ for a free particle and a particle of positive total energy moving in the potential $V(R)$.

where, classically, the field-free path is a straight line trajectory that passes within a distance b of the origin of the polar co-ordinate R and the integration in both cases extends from the appropriate turning point to R. We have defined the phase shift to apply to the radial motion and so the radial velocity is inserted into the de Broglie relationship giving:

$$\eta(b) = k\left\{\int_{R_c}^{\infty}\left(1-\frac{V(R)}{E}-\frac{b^2}{R^2}\right)^{\frac{1}{2}}\mathrm{d}R-\int_{b}^{\infty}\left(1-\frac{b^2}{R^2}\right)^{\frac{1}{2}}\mathrm{d}R\right\}. \qquad (2.38)$$

Because of the combined presence of the wave number and the classical turning point this is called the semi-classical expression for the phase shift. Differentiation of Equation 2.38 with respect to the angular momentum quantum number $l = \mu v b/\hbar$ leads immediately to the result:

$$\frac{\partial\eta(l)}{\partial l} = -\int_{R_c}^{\infty}\frac{b\mathrm{d}R}{R^2\left(1-\frac{V}{E}-\frac{b^2}{R^2}\right)^{\frac{1}{2}}}+\int_{b}^{\infty}\frac{b\mathrm{d}R}{R^2\left(1-\frac{b^2}{R^2}\right)^{\frac{1}{2}}}=\frac{\chi}{2} \qquad (2.39)$$

(note that the lower limits of integration do not have to be differentiated because the integrand is zero at the turning point).

Fig. 2.9 shows the relationship of phase shifts and deflection angles to the

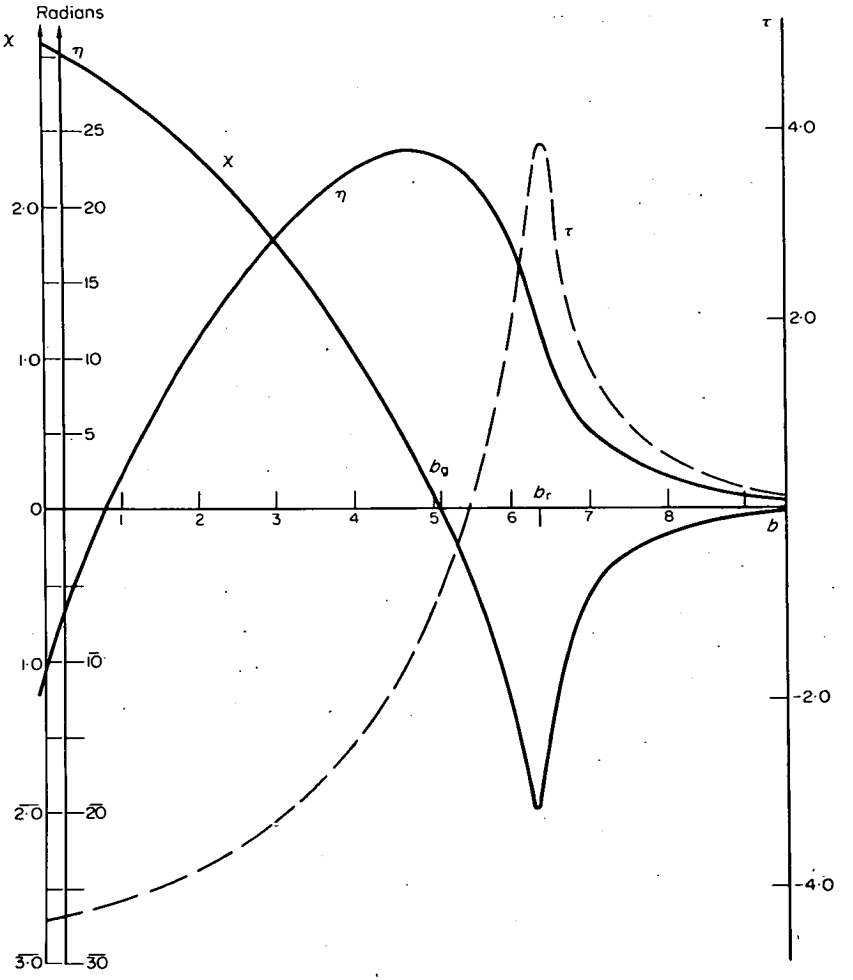

Fig. 2.9 The angle of deflection χ, phase shift η and time delay τ as a function of impact parameter for a Lennard-Jones potential with $\epsilon/E = 0.8$. The units of τ are 10^{-12} s and b is in Å.

impact parameters for a typical bipolar potential. Their mutual relationship exemplified in this figure will be of great importance throughout this book, and a great deal of the difficulty in analyzing scattering patterns comes from the fact that there is no simple relationship between $\chi(b)$ and $\eta(b)$ for a bipolar potential. Various perturbation approximations are available for the phase shift, but these will be discussed later when we return to consideration of the phase shift in the quantum treatment of scattering.

The time delay τ is defined in a similar way to the phase shift as the

difference in time required for a particle to pass through a sphere of radius R about the scattering centre in the presence and absence of the force field. Again we compare only trajectories having the same angular momentum and let $R \to \infty$,

$$\tau(b) = 2 \operatorname*{Lim}_{R \to \infty} \left\{ \int_{R_c}^{R} \frac{dR}{v} - \int_{b}^{R} \frac{dR}{v} \right\}$$

$$= \frac{2}{v} \left\{ \int_{R_c}^{\infty} \left(1 - \frac{V(R)}{E} - \frac{b^2}{R^2}\right)^{-\frac{1}{2}} dR - \int_{b}^{\infty} \left(1 - \frac{b^2}{R^2}\right)^{-\frac{1}{2}} dR \right\} \quad (2.40)$$

It can readily be verified that:

$$\partial\eta(l, E)/\partial E = \tau/2\hbar. \quad (2.41)$$

Delay times may be positive or negative depending on whether attractive or repulsive forces dominate in the collision. For a normal intermolecular potential with values of the parameters that do not lead to orbiting, delay times $<10^{-12}$ s are predicted by Equation 2.40. From a computational point of view, the time derivative of $\eta(R)$ can be integrated simultaneously with Equation 2.3 and 2.4 (with time as the independent variable) to obtain complete information about a classical collision.

2.3 The Coulomb potential

Although $\chi(b)$ can be obtained analytically for a number of inverse power potentials (H. Goldstein, 1964) of these only the Coulomb potential is of importance in atomic or molecular systems. The effective potential in this case is (in e.s.u.)*

$$V_{\text{eff}} = Z_A Z_B e^2/R + Eb^2/R^2. \quad (2.42)$$

For like charges the potential is monotonically repulsive and for unlike charges the effective potential shows only one extremum in contrast to

* In S.I. Equation 2.42 becomes:

$$V_{\text{eff}} = (4\pi\epsilon_0)^{-1} Z_A Z_B e^2/R + Eb^2/R^2$$

where lengths are in metres, charges in coulombs, energy in joules and ϵ_0, the permittivity of free space, is 8.85415×10^{-12} C^2 N^{-1} m^{-2}. In this book e.s.u. are used throughout.

attractive potentials with a steeper R dependence than R^{-2} for which V_{eff} has both a maximum and a minimum. The deflection function, from Equation 2.6, is:

$$\chi(b) = \pi - 2b \int_{R_c}^{\infty} R^{-2} \left(1 - \frac{b^2}{R^2} - \frac{Z_A Z_B e^2}{ER^2}\right)^{-\frac{1}{2}} dR \qquad (2.43)$$

Changing to the dimensionless variable $u = b/R$ yields the standard form:

$$\chi(b) = \pi + 2 \int_{u_0}^{\infty} \frac{du}{\left(1 - u^2 - \frac{Z_A Z_B e^2}{be} u\right)^{\frac{1}{2}}} \qquad (2.44)$$

so that:

$$\chi = 2 \sin^{-1} \left\{1 + 4 \left(\frac{bE}{Z_A Z_B e^2}\right)^2\right\}^{-\frac{1}{2}} \qquad (2.45)$$

inverting and differentiating gives:

$$\frac{db}{d\chi} = \frac{Z_A Z_B e^2}{4E \sin^2(\chi/2)} \qquad (2.46)$$

Thus from Equation 2.10:

$$\sigma(\chi) = \frac{1}{4} \left(\frac{Z_A Z_B e^2}{2E}\right)^2 \frac{1}{\sin^4(\chi/2)}, \qquad (2.47)$$

which is the Rutherford result originally derived for the scattering of α-particles by nuclei.

From Equation 2.46 it can be seen that no extremum in the deflection function exists so that in the Coulomb potential neither rainbow scattering nor orbiting can occur. The total cross is again infinite, while the phase shifts calculated from Equation 2.38 diverge logarithmically and only become finite for potentials falling off more rapidly than R^{-1}.

The potential between an ion and a dipole varies as R^{-2}, but contains a strongly angle dependent factor.

$$V = Ze\mu \cos\theta / R^2 \qquad (2.48)$$

where θ is the angle between **R** (the vector from the dipole to the ion) and the

dipole axis. The dynamics of collisions involving non-central forces are intimately bound up with the transfer of energy between rotation and translation and none of the formulae for $\chi(b)$ in this chapter are applicable, although the impulse formulae Equation 2.26 can be adapted if the target is assumed stationary throughout the collision.

The long range potential between an ion and an isotropically polarizable molecule, with polarizability α, is:

$$V = -\frac{1}{2}\alpha Z^2 e^2 R^{-4} \tag{2.49}$$

the basis of the Langevin potential and of some models for ion-molecule reactions. Substituting this potential into the deflection function formula Equation 2.6 yields, after rearrangement, a standard elliptic integral of the first kind. The equation for the orbiting radius is readily found from Equation 2.17 to be:

$$R_0 = \left(\frac{\alpha Z^2 e^2}{2E}\right)^{1/4} \tag{2.50}$$

and the critical impact parameter for orbiting is $b_0 = \sqrt{2}R_0$.

We conclude this section by noting an important though approximate scaling rule of great use in the qualitative interpretation of scattering patterns. Inspection of Equation 2.31 shows that for small angle scattering $E\chi$ is a function only of the strength of the potential and the impact parameter. Thus, if we compare the scattering in a system at different energies but at angles that lead to the same value of $E\chi$, we can be sure that we are comparing events that occurred at the same impact parameter. Similarly, expansion of Equation 2.45 shows that $E\chi$ for Coulomb scattering with given values of Z_A and Z_B is a function only of b at small angles. A brief inspection of the deflection function expression Equation 2.15 shows that for the general potential, $E\chi$ is not solely a function of ϵ and b^*. However, the deflection can be developed as an expansion in the reduced potential parameters and the distance of closest approach. For the bipolar potential:

$$V = C_n R^{-n} + C_m R^{-m} \tag{2.51}$$

the form of the expansion is:

$$\chi = a_1 C_n/(ER_c^n) + b_1 C_m/(ER_c^m) + a_2 (Cn/ER_c^n)^2 + \ldots \tag{2.52}$$

If the linear term in E^{-1} is dominant, as it will be at high energies, a constant value of $E\chi$ implies a constant value of R_c. By comparing scattering at different energies but at a constant value of $E\chi$, we are examining trajectories with roughly the same value of the distance of closest approach. It is now customary in plotting scattering data to use $E\chi$ rather than χ as the abscissa and it is found that a variety of features in the differential cross-section, including some occurring on the dark side of the rainbow, are superimposable by this means. Amongst these is the rainbow itself which is characterized by a nearly constant value of R_c and in table 1 $E\chi_r$ is also listed and exhibits near constancy especially at $E^* > 2$. This property of $E\chi_r$ also enables tables of the deflection function to be extrapolated much more accurately by interpolating in $E^*\chi_r$ rather than χ_r itself.

2.4 The conversion from centre of mass to laboratory co-ordinates

So far, we have derived formulae for the angle of deflection of the inter-particle vector **R** and hence $\sigma(\chi)$ in terms of the intermolecular potential. We now seek a method of passing from $\sigma(\chi)$ to $\sigma(\theta)$ the differential cross-section in laboratory (lab) co-ordinates that would be measured in an actual experiment. With this transformation the path is then complete, in either direction, between the potential and the observed scattering pattern resulting from it. The transformation lab $\leftrightarrow$ cm is based on the triangle rule for the addition of vectors and deals only with quantities observed after the collision is over and so it holds for the transformation of both classical and quantum differential cross-sections. We recall that the angle of deflection, χ, in cm co-ordinates is the angle between the initial and final relative velocity vectors of the partners in a collision and that the angle of deflection θ in lab co-ordinates is the angle between the initial and final laboratory velocity vectors. It is then clear that central to the transformation is the 'Newton diagram' of the process, which is the vector diagram of the velocities of all the particles present before and after collision. A Newton diagram can be drawn for every type of molecular encounter, reactive or non-reactive and they are invaluable even at the preliminary stages of planning a beam experiment.

The simplest of all Newton diagrams (Fig. 2.10) results from the following process: a photon hits a molecule AB which then dissociates into two fragments A and B. In Fig. 2.10(a) the initial lab molecular velocity is $\mathbf{v}_{AB}$, and those of the fragments $\mathbf{v}_A$ and $\mathbf{v}_B$. The centre of mass initially coincides with that of the AB molecule and since the photon has a negligible momentum, the velocity of the centre of mass, $\mathbf{v}_{cm}$, is equal to $\mathbf{v}_{AB}$. After collision, the centre of mass continues with unchanged velocity and the two fragments emerge in opposite directions in the cm frame.

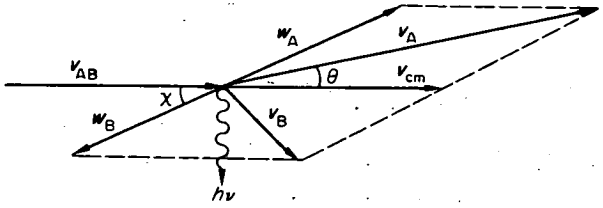

Fig. 2.10 (a) Velocity vector diagram for the process $AB + h\nu \rightarrow A + B$. The momentum of the photon is ignored. v_{AB} is the velocity of the molecule prior to dissociation in laboratory coordinates. w_A, w_B are the post-collision velocities of the fragments relative to the cm.

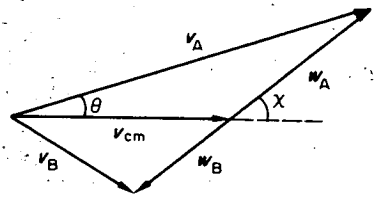

(b) The essential construction of (a) in condensed form, making up the Newton diagram. θ is the angle of scattering in the laboratory. v_{cm} now coincides with v_{AB}.

The direction in which the fragment A emerges is that of v_A, given by the vector addition of v_{cm} and w_A:

$$\mathbf{v}_A = \mathbf{v}_{cm} + \mathbf{w}_A, \quad \mathbf{v}_B = \mathbf{v}_{cm} + \mathbf{w}_B \tag{2.53}$$

where

$$m_A w_A = m_B w_B .$$

The application of elementary geometry to Fig. 2.10 gives:

$$\cos\chi = -p\sin^2\theta \pm \sqrt{p^2\sin^4\theta - p^2\sin^2\theta + \cos^2\theta}$$

$$w_A = \sqrt{v_A^2 + v_{cm}^2 - 2v_A v_{cm}\cos\theta} \tag{2.54}$$

where $p = v_{cm}/w_A$ the magnitude of $\mathbf{w}_A$ may be known in advance from the conservation of energy:

$$\frac{1}{2}m_A w_A^2 \left(1 + \frac{m_A}{m_B}\right) = h\nu - \Delta E \tag{2.55}$$

where ΔE is the energy required for the process $AB \rightarrow A + B$. The ideal beam

experiment would measure the final laboratory velocity v_A in order to find ΔE and hence to identify the spectroscopic state of the products.

We next turn to two qualitative features of this scattering process that emerge from an inspection of Figs. 2.11 and 2.13. Firstly, if w_B is less than v_{cm}, then at any given angle of observation θ, A or B particles will emerge with two different velocities, v_f and v_s. That is, although two particles may emerge from a collision at the same lab angle, they have not necessarily undergone the same deflection in the cm system. The importance of this is that any theory of the scattering process will lead to a prediction of $\sigma(\chi)$ first, and the lab cross-section is then calculated from the sum of $\sigma(\chi_f)$ and $\sigma(\chi_s)$. If the fast and slow components of the scattered flux are not measured separately, there is no reliable way of deducing $\sigma(\chi_f)$ and $\sigma(\chi_s)$ separately although in practice χ_f is usually very different from χ_s and observations are conveniently restricted to angular regions in which $\sigma(\chi_f) \gg \sigma(\chi_s)$.

The second general use of the Newton diagram is in deducing the Jacobian for the transformation between lab and cm co-ordinates. Jacobians will be familiar to the reader in their purely mathematical role as the ratio of the infinitesimal volume in one co-ordinate system to the corresponding volume in another co-ordinate system of the same dimensionality:

$$dx_1 dx_2 \ldots dx_n = J\left(\frac{x_1 x_2 \ldots x_n}{\xi_1 \xi_2 \ldots \xi_n}\right) d\xi_1 d\xi_2 \ldots d\xi_n. \qquad (2.56)$$

Thus, in transforming from Cartesian to polar co-ordinates in ordinary

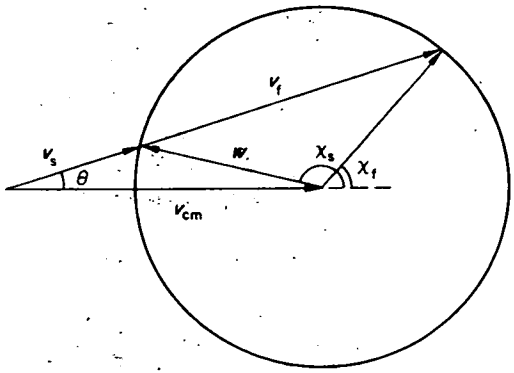

Fig. 2.11 The fast and slow collision products. Scattering of B at χ_f and χ_s in the cm system leads to particles emerging at the angle of observation θ with velocities v_f and v_s.

three-dimensional space we have:

$$dx\, dy\, dz = r^2 \sin\theta\, dr\, d\theta\, d\phi$$

so:

$$J\left(\frac{x, y, z}{r, \theta, \phi}\right) = r^2 \sin\theta.$$

In scattering problems the Jacobian of the cm to lab transformation has a simple physical significance. If we place a detector that subtends a solid angle $d\Omega$ at the scattering centre in lab co-ordinates, then from Fig. 2.12, all the particles that reach the detector must have emerged through the shaded area, i.e., into a solid angle $d\omega$ in the cm system, where:

$$\frac{d\Omega}{d\omega} = \frac{\sin\theta\, d\theta\, d\Phi}{\sin\chi\, d\chi\, d\phi} = \frac{(dA/v_A^2)\cos\alpha}{(dA/w_A^2)} \tag{2.57}$$

and so:

$$d\Omega = \cos\alpha\,(w_A/v_A)^2\, d\omega$$

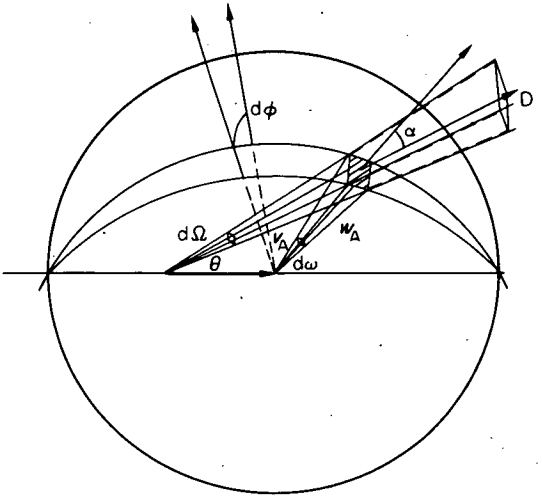

Fig. 2.12 Particles scattered into solid angle $d\omega$ in the cm system arrive in $d\Omega$ in the lab system. The detector D subtends an area dA (shaded) on the surface of the sphere on which the tip of w_A lies.

while from the definition of the differential cross-section:

$$\sigma(\omega)\mathrm{d}\omega = \sigma(\Omega)\mathrm{d}\Omega$$

so that

$$\sigma(\omega) = J\left(\frac{\cos\theta, \Phi}{\cos\chi, \phi}\right)\sigma(\Omega) \tag{2.58}$$

where

$$J\left(\frac{\cos\theta, \Phi}{\cos\chi, \phi}\right) = \cos\alpha\left(\frac{w_A}{v_A}\right)^2 = J\left(\frac{\cos\chi, \phi}{\cos\theta, \Phi}\right)^{-1} \tag{2.59}$$

The Jacobian for the fast and slow scattered particles at any angle of observation will be different and the observed differential cross-section measured without velocity analysis will be

$$\sigma(\theta, \Phi) = J_f\left(\frac{\cos\chi_f, \phi}{\cos\theta, \Phi}\right)\sigma(\chi_f) + J_s\left(\frac{\cos\chi_s, \phi}{\cos\theta, \Phi}\right)\sigma(\chi_s). \tag{2.60}$$

This result is quite general.

Returning to the photodissociation process, the polar direction is taken to be that of v_{AB} and clearly the azimuthal angles ϕ and Φ are identical. Application of the cosine rule to Fig. 2.10 yields the following result for the Jacobian $\mathrm{d}\Omega/\mathrm{d}\omega$ in terms of the observables θ and v_A:

$$J\left(\frac{\cos\theta, \Phi}{\cos\chi, \phi}\right) = \left[1 + \left(\frac{v_{AB}}{v_A}\right)^2 - 2\frac{v_{AB}}{v_A}\cos\theta\right]^{1/2}\left(1 - \frac{v_{AB}}{v_A}\cos\theta\right) \tag{2.61}$$

If v_A is not measured, but w_A is deduced from Equation 2.55 then we eliminate v_A from Equation 2.60 with the aid of:

$$\frac{v_A}{v_{AB}} = \cos\theta \pm \left[\cos^2\theta - 1 + \left(\frac{w_A}{v_{AB}}\right)^2\right]^{1/2} \tag{2.62}$$

The importance of the Jacobian can be illustrated by the edge effect,

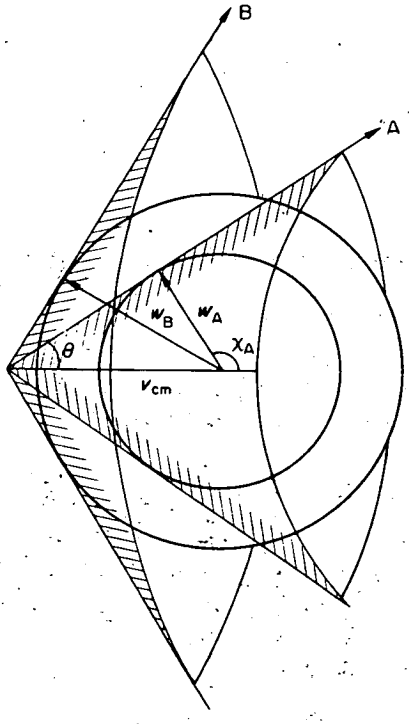

Fig. 2.13 The edge effect. Scattered A and B particles are restricted in the laboratory to emerge within cones generated by the rotation of w_A and w_B about v_{cm}.

which arises if w_A or w_B is less than v_{cm}. Reference to Fig. 2.13 shows that in this case the scattered intensity is zero at laboratory angles greater than $\theta_e = \sin^{-1}(w_A/v_{cm})$ and that, classically, the laboratory differential cross-section must rise to infinity at θ_e since here $\cos\alpha$ is zero. This conclusion is not altered by the application of wave mechanics since the trajectories at the edge are not coherent (they have emerged at slightly different values of χ). But, as in the discussion of the rainbow, the intensity at the edge measured by a real detector subtending an angle Δ remains finite. In Fig. 2.14 the effect of the operation of the Jacobian at the edge is illustrated for the case $w_A = v_{cm}/2$ in a reaction in which the products are scattered isotropically in the cm system, i.e., $\sigma(\chi) = \sigma_0$. The contributions of the slow and fast product molecules are shown separately, 90 per cent of the observed intensity coming

from the fast component at low angles. The effect of scanning this scattering pattern with a detector of finite width ($\Delta = 0.01$ rad) is also shown.

A Newton diagram and Jacobian identical to those for the photodissociation process will apply to dissociation following the collision of an electron with a molecule if the momentum of the electron can be neglected in comparison with the molecule.

We now turn to the co-ordinate transformation for the elastic and reactive scattering of two particles for the important case in which the number of particles is conserved, i.e.

$$A + B \longrightarrow C + D$$

($A \equiv C$, $B \equiv D$ for elastic scattering).

Before the collision $\mathbf{R}_{cm}$ and $\mathbf{R}_{AB}$ are given by the vector diagram Fig. 2.1, whence, by differentiation with respect to time the velocity diagram is obtained (Fig. 2.15): after collision the particles C and D emerge with velocities w_C, w_D relative to the centre of mass and hence the emergent laboratory velocities v_C or v_D can be obtained by vector addition of w_C or

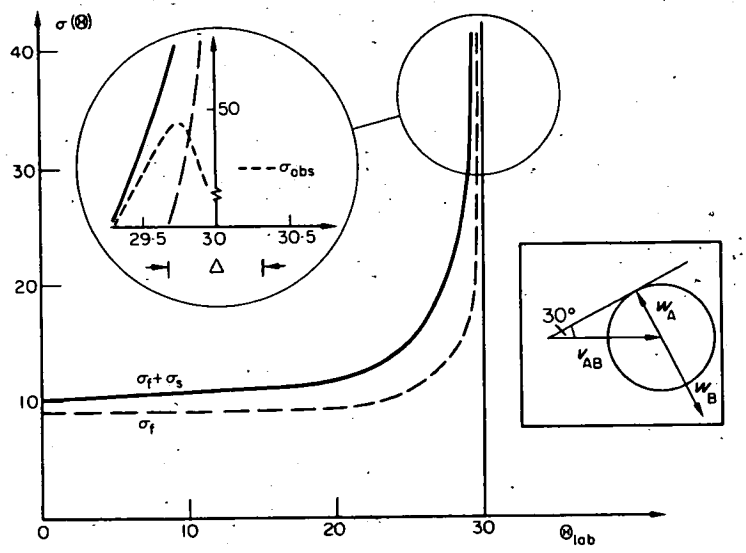

Fig. 2.14 The laboratory cross-section for scattering exhibiting the edge effect. σ_f and $\sigma_f + \sigma_s$ are shown, together with the effect of finite apparatus resolution Δ on the observed cross-section near the edge angle. Also shown is the Newton diagram.

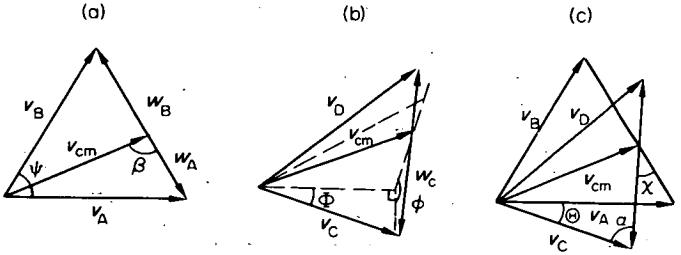

Fig. 2.15 The velocity vector diagrams before (a) and after (b) scattering and superimposed with v_{cm} in common (c). (a) lies in the plane of the paper; v_C, v_D and v_{cm} lie in a plane tilted with respect to (a).

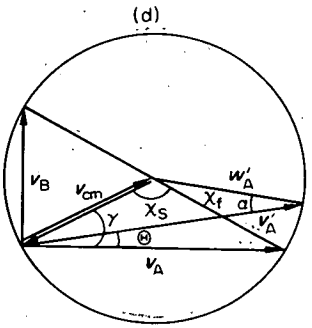

(d) The Newton diagram for the elastic scattering of two particles of equal mass.

w_D and v_{cm}. v_{cm} is thus common to both the pre- and post-collision velocity vector diagrams and the two v_{cm}'s can be superimposed by a simple translation to give Fig. 2.15(d), the Newton diagram.

From an experimental point of view, it is convenient to define angles of deflection with respect to one of the beam directions which can be measured and is independent of energy, rather than with respect to the direction of v_{cm}. The Jacobian for the general case has been given by F. A. Morse and R. B. Bernstein (1962) among others, and the derivation follows similar lines to the photodissociation case. The details of this transformation are given in appendix B. As in the photodissociation case if the final velocity of the product from a reactive collision is not measured there is considerable uncertainty as to the Jacobian for this transformation. Since, in general, the disposition of exothermicity between translational and internal modes of the products is not known this can lead to problems in interpretation. In principle measurements of the laboratory out of plane scattering can reduce this uncertainty but in practice experimental difficulties in providing out of plane motions are formidable.

2.5 The hard sphere potential

We will illustrate the foregoing results by deriving the differential cross-section expression in cm and lab co-ordinates for the hard sphere potential. It must be said at the outset that the hard sphere potential is never a good approximation for the small angle scattering of real molecules because of its finite range, but it has been used extensively in the kinetic theory of gases and is the limiting form of progressively steeper repulsive potentials. The potential is:

$$V = 0 \quad R \geqslant d$$

$$V = \infty \quad R < d$$

The mechanics of the collision are that, at the moment of impact, the component, w_n, of the relative velocity w_{AB} along the line of centres is reversed and the final vector, w', is obtained by adding $-w_n$ to the unchanged tangential component w_t of w_{AB} (Fig. 2.16) whence:

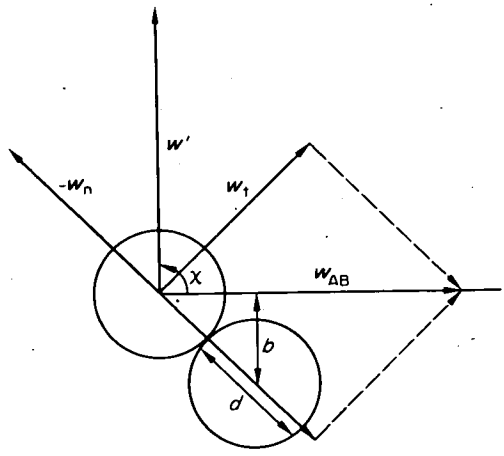

Fig. 2.16 The collision of two hard spheres in the cm system. The relative initial velocity is w_{AB}. After collision the component of $\overline{w}$ along the line of centres is reversed to give $-w_n$. The final relative velocity w' is then the sum of $-w_n$ and the unchanged tangential velocity w_t. χ is the deflection angle and the impact parameter is b.

$$\cos(\pi - \chi) = 1 - 2(b/d)^2 \tag{2.63}$$

Substituting in Equation 2.10 gives the differential cross-section,

$$\sigma(\chi) = \frac{1}{4} d^2 \tag{2.64}$$

which is independent of χ.

The Jacobian for transforming from cm to lab is:

$$J\left(\frac{\cos\chi, \phi}{\cos\theta, \Phi}\right) = \frac{v'_A}{w_A} \frac{2v'^2_A}{w_A^2 + v_A^2 - v_{cm}^2} \tag{2.65}$$

where the necessary relationships for measurement in the plane of the two beams are Fig. 2.15(d):

$$\begin{aligned} v'_A &= v_{cm} \cos(\gamma - \theta) + w_A \cos\alpha \\ \alpha &= \sin^{-1}\left[(v_{cm}/w_A)\sin(\gamma - \theta)\right] \\ \gamma &= \sin^{-1}\left[m_B v_B/(2(m_A + m_B)v_{cm})\right] \\ w_A &= (m_B/(m_A + m_B))/(v_A^2 + v_B^2)^{1/2} \end{aligned} \tag{2.66}$$

In the case $m_A = m_B$, $w_A = w_B$, the lab cross-section is found to be from Equations 2.65 and 2.66,

$$\sigma(\theta, \Phi = 0) = d^2 \left|\cos\left(\frac{\pi}{4} - \theta\right)\right| \tag{2.67}$$

and is plotted in Fig. 2.17. The zero intensity at $\theta = -\pi/4$ and $3\pi/4$ is due to the zero velocity of the molecules emerging in the laboratory at these angles. Defining a more symmetrical lab angle, $\beta = \pi/4 - \theta$, the reader can verify directly that:

$$2\pi \int_{-\pi/2}^{\pi/2} \sigma(\beta) \sin\beta \, d\beta = 2\pi \int_0^{\pi} \sigma(\chi) \sin\chi \, d\chi,$$

so that the total cross-section remains unchanged under the cm $\leftrightarrow$ lab transformation. Note that implicit in this verification is the knowledge that the differential cross-section in either co-ordinate system is independnet of the azimuthal angles associated with χ or β; whilst the former symmetry is quite general, the laboratory azimuthal symmetry is peculiar to this problem.

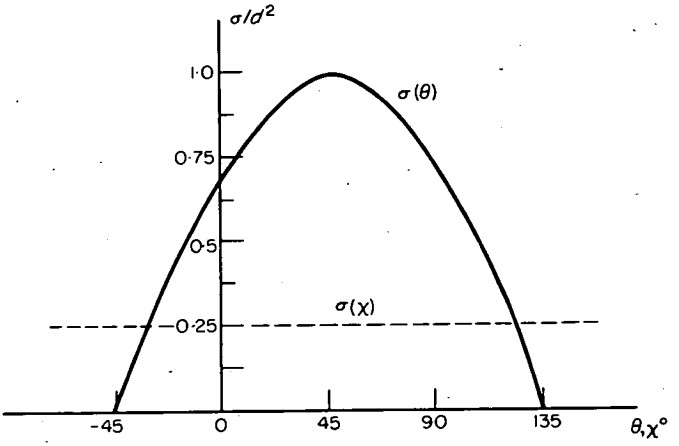

Fig. 2.17 The differential cross-section for the scattering of like hard spheres in lab (θ) and cm (χ) co-ordinates. The increase in intensity in the lab in the direction of motion of the centre of mass is apparent. Both the cross-sections are reduced by d^2, where d is the hard sphere diameter.

2.6 High energy collisions

Scattering phenomena investigated at energies large on the chemical scale ($\gtrsim 5$ eV) are generally performed with one beam thermal and the other at the required energy. The target or slow beam molecules can then be regarded as stationary before impact. The wider range of processes that are available with superthermal collisions compared with thermal energy bombardment is indicated in the following scheme:

$A + B_2$	$\xrightarrow{I}$	$A + B_2$	(elastic)
	$\xrightarrow{II}$	$A + B_2^*$	(inelastic/internal excitation)
	$\xrightarrow{III}$	$AB + B$	(reaction)
	$\xrightarrow{IV}$	$A + B + B$	(dissociation)
	$\xrightarrow{V}$	$A + B_2^+ + e$	(ionization into a variety of channels)

The last two possibilities become more probable with increasing energy at the expense of reaction. At high energies the Newton diagram takes on a simplified form, and those for processes I, II, IV and V (if the momentum of the ejected electron is neglected) are summarized in Fig. 2.18.

If the lab velocity v_A and angle of scattering θ of the emergent A atoms is

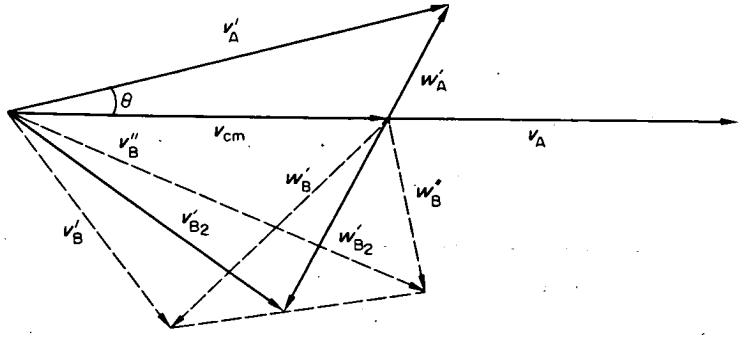

Fig. 2.18 Newton diagram for the collision of fast A with stationary B_2. Two possibilities are shown; (1) $A + B_2 \rightarrow A + B_2$ (full lines), characterized by $v'_A < v_A$ (2) $A + B_2 \rightarrow A + B + B$ (dotted lines) in which the two B particles emerge with different lab velocities v'_B and v''_B.

measured, then the energy transferred to internal motion, ΔE, (resulting in excitation, dissociation or ionization) is given by:

$$\frac{v'_A}{v_A} = \frac{m_A}{m_A + m_{B_2}} \left[\cos\theta \pm \left\{\left(\frac{m_{B_2}}{m_A}\right)^2 \left(1 - \frac{\Delta E}{E_{cm}}\right) - \sin^2\theta\right\}^{\frac{1}{2}}\right] \qquad (2.68)$$

where E_{cm} is the initial relative kinetic energy, $\frac{1}{2}\mu w_A^2$. It is important to measure the magnitude of v_A so that the predominant collision process at various angles of scattering can be inferred from ΔE.

2.7 Summary of useful formulae

The more important classical formulae connected with scattering are summarized here; they are numbered according to their position in the text.

The deflection function is defined by:

$$\chi(b) = \pi - 2\int_{R_c}^{\infty} \frac{b\,dR}{R^2(1 - V(R)/E - b^2/R^2)^{\frac{1}{2}}} \qquad (2.6)$$

and an approximation for small deflections is:

$$\chi(b) \approx \frac{b}{E}\int_b^{\infty} \frac{dV}{dR}(R^2 - b^2)^{-\frac{1}{2}}dR \qquad (2.30)$$

For the (12.6) L.J. potential a useful approximation is:

$$\chi(R_c) = -\frac{15}{16}\pi\frac{4\epsilon}{E}\left(\frac{\sigma}{R_c}\right)^6 + \frac{693}{512}\pi\frac{4\epsilon}{E}\left(\frac{\sigma}{R_c}\right)^{12} + 0\left[\frac{\epsilon}{E}\left(\frac{\sigma}{R_c}\right)^6\right]^2$$

which is good to ± 10 per cent for deflection less than, roughly, 0.3 rad. Another formula for the deflection function sometimes more convenient for approximation (F. T. Smith *et al.*, 1966), e.g., in deriving Equation 2.30, is:

$$\chi(b) = -b\int_{R_c}^{\infty}\left(\frac{R}{E}\frac{\mathrm{d}V(R)}{\mathrm{d}R}\right)\left(1-\frac{V(R)}{E}\right)^{-1}\left(1-\frac{V(R)}{E}-\frac{b^2}{R^2}\right)^{-\frac{1}{2}}\frac{\mathrm{d}R}{R^2}.$$

The classical differential cross-section is:

$$\sigma_{cl}(\chi) = b\Big/\left\{\left|\frac{\mathrm{d}\chi}{\mathrm{d}b}\right|\sin\chi\right\}. \tag{2.10}$$

For a potential of the form $V = C_s R^{-s}$ ($s \geqslant 3$):

$$\sigma_{cl}(\chi) = s^{-1}\left(s\pi^{\frac{1}{2}}\frac{\Gamma([s+1]/2)\,C_s}{\Gamma\left(\frac{s}{2}+1\right)E}\right)^{2/s}\chi^{-(2+2/s)}. \tag{2.32}$$

The semi-classical phase shift is given by:

$$\eta_{sc}(b) = k\left\{\int_{R_c}^{\infty}\left(1-\frac{V(R)}{E}-\frac{b^2}{R^2}\right)^{\frac{1}{2}}\mathrm{d}R - \int_{b}^{\infty}\left(1-\frac{b^2}{R^2}\right)^{\frac{1}{2}}\mathrm{d}R\right\} \tag{2.38}$$

which satisfies the relationship:

$$\frac{2}{k}\frac{\partial\eta}{\partial b} = \chi(b). \tag{2.39}$$

An approximation for small phase shifts is:

$$\eta(b) \approx \frac{k}{E}\int_{b}^{\infty}\frac{\mathrm{d}V}{\mathrm{d}R}(R^2-b^2)^{\frac{1}{2}}\mathrm{d}R. \tag{2.69}$$

The rainbow angle is given approximately by:

$$\chi_r \approx 2\epsilon/E$$

for a range of $(n, 6)$ potentials and is useful for $\epsilon/E < 0.4$ (see also Table 2.1). Finally the relationship between the phase shift function and the differential cross-section is:

$$\sigma_{sc}(\chi) = \left(2\left|\frac{\partial^2\eta}{\partial b^2}\right|\sin\chi\right)(kb)^{-1} \tag{2.70}$$

Appendix A The transformation between lab and cm co-ordinates for reactive scattering

For a reaction of the type A + B = C + D, useful relationships are (Morse and Bernstein, 1962)

$$J_c\left(\frac{\cos\theta, \Phi}{\cos\chi, \phi}\right) = \left(\frac{w_c}{v_c}\right)^2 |\cos\alpha| \tag{2.A1}$$

$$\chi = \cos^{-1}\left\{\frac{w_A^2 + w_C^2 - (v_A^2 + v_C^2) + 2v_A v_C \cos\theta \cos\Phi}{2w_A w_C}\right\} \tag{2.A2}$$

and

$$w_C = w_A\left\{\frac{m_A m_D}{m_B m_C}\left(1 - \frac{\Delta E}{E_i}\right)\right\}^{1/2} \tag{2.A3}$$

where ΔE is the difference between the final (E_f) and initial (E_i) relative kinetic energies, Fig. 2.19.

To pass from cm to lab, use:

$$v_C = \{v_{cm}^2 + w_C^2 - 2v_{cm} w_C(\cos\chi\cos\beta - \sin\chi\sin\beta\cos\phi)\}^{1/2} \tag{2.A4}$$

where the quantities appearing on the right hand side are most conveniently written in terms of the Cartesian components the of the particle velocities:

$$v_{cm} = (m_A v_{Ax} + m_B v_{Bx})^2 + m_B^2 v_{By}^2\ {}^{1/2}/(m_A + m_B)^2 \tag{2.A5}$$

$$\cos\beta = \frac{v_{Cx}(v_{Ax} - v_{cmx}) - v_{Cy}^2}{v_A[(v_{Ax} - v_{Cx})^2 + v_{Cy}^2]} \tag{2.A6}$$

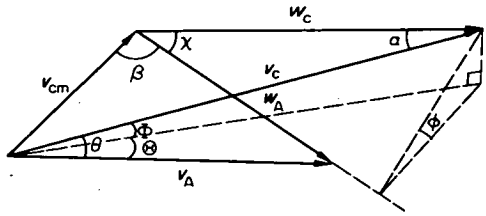

Fig. 2.19 Part of the Newton diagram for A + B → C + D. Only the velocities of A and C are shown. Φ and θ are the polar angles of v_C with respect to v_A, so $\cos\theta = \cos\theta\cos\Phi$. ϕ is the azimuthal angle of w_C with respect to the plane containing v_A and w_A, with w_A as the polar direction.

$$\cos\alpha = \frac{v_{Cx}(v_{Cx} - v_{cm\,x}) + v_{Cy}(v_{Cy} - v_{cm\,y}) + v_{Cz}^2}{|\,v_C\,|\,[(v_{Cx} - v_{cm\,x})^2 + (v_{Cy} - v_{cm\,y})^2 + v_{Cz}^2]^{1/2}} \qquad (2.A7)$$

and so forth, where the x/y plane is defined by the two incident beams. In transforming from lab to cm, ΔE will in general not be known. If the magnitude as well as the direction of v_C is measured, a possible recipe for effecting the transformation is:

(1) compute $\cos\alpha$ from Equation 2.A7

(2) compute w_C from

$$w_C = v_C\left[\cos\alpha \pm \sqrt{\frac{v_{cm}^2}{v_C^2} - \sin^2\alpha}\;\right] \qquad (2.A8)$$

(the sign is chosen by inspection of the Newton diagram). The cm angle of deflection is then obtained from 2.A2 and the Jacobian from 2.A1 with or without the cosine factor as appropriate.

In elastic scattering, the final lab velocity is usually not measured. A useful set of equations for in-plane scattering is then:

$$|\,w_A\,| = \sqrt{v_{cm\,y}^2 + (v_A - v_{cm\,x})^2} \qquad (2.A9)$$

The presence of the $\cos\alpha$ factor in the Jacobian for *reactive* scattering has been the subject of some debate. If the product differential cross-section is measured with velocity analysis the Jacobian required is $J(\cos\theta, \Phi, v_C/\cos X, \phi, w_C)$ and this, after some rather heavy trigonometry is found to be simply $(w_C/v_C)^2$ (K. T. Gillen *et al.*, 1971 and references therein). The reader can more readily verify this for the simpler case of photodissociation with the aid of the relevant Newton diagram, Fig. 2.10. If the quantum state of the product is measured, then Equation A1 is the appropriate Jacobian.

$$v_{Ax} = v_{cmx} + v_{cmy} \tan\theta$$

$$\frac{\pm\sqrt{(v_{cmx} + v_{cmy}\tan\theta)^2 - (1+\tan^2\theta)(v_{cm}^2 - w_A^2)}}{1+\tan^2\theta} \qquad (2.A10)$$

where the positive sign gives the fast scattered component and the negative sign the slow component.

$$v_{Ax} = v_A x \tan\theta \qquad (2.A11)$$

The two cm scattering angles contributing at an angle of observation θ are:

$$\chi = \cos^{-1}\left\{\frac{(v'_{Ax} - v_{cmx})(v_{Ax} - v_{cmx}) - (v'_{Ay} - v_{cmy})v_{cmy}}{w_A^2}\right\}$$

where the fast or slow value of v'_A is used as appropriate.

CHAPTER THREE

Molecular Beam Sources

3.1 General design considerations – signal/noise

Some hint of the experimental difficulties inherent to the scattering technique has already been given. Before proceeding to discuss in detail the particular aspects of generation, state selection and detection of molecular beams we propose to consider the experiment as a system. In this way the relative contributions of these parts to the overall performance can be better estimated.

In Fig. 3.1 we show a rather generalised experimental configuration incorporating two sources S_1, S_2, three filters F_1, F_2, F_3 and a detector D. In any real experiment it is unlikely that all the selectors shown would be a feasible proposition; nevertheless we include them here for completeness; it is then a simple matter to drop any unwanted terms from the results. We define the following quantities: I_1 and I_2, the beam fluxes of molecules with velocities v_1 and v_2 in molecules s^{-1} sr^{-1}; the transmission of the filters T_1, T_2 T_3 defined as the ratio of molecules (with specified velocities v_1, etc.) incident to that transmitted, the respective beam widths W_1, W_2, and height h define the scattering volume $W_2 W_2 h$. The distances l_1, l_2 and l_3 are from the sources and detector to the scattering centre. The laboratory differential cross-section is σ_j (E, θ) for in-plane scattering by the process labelled j e.g. elastic scattering at angle θ. The effective area of the detector is A_d and it has an efficiency of q counts per incident molecule of species i.

We further assume that the number density of background molecules of all types present in the apparatus is n_b cm^{-3} and that they have a mean velocity

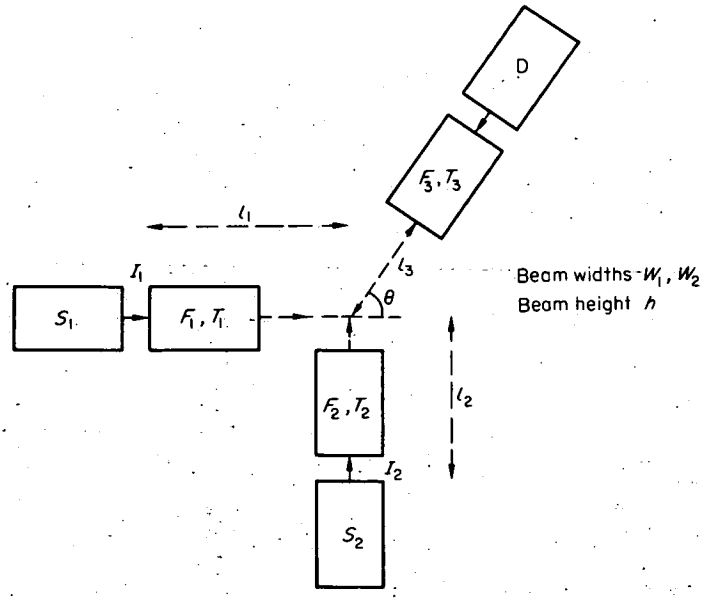

Fig. 3.1 Generalized scattering experiment.

v_b cm s^{-1}. The number density of the molecules to which the detector is sensitive is n_i cm^{-3} (also with mean velocity v_b).

The density of species 1 at the scattering centre is:

$$\frac{I_1 T_1}{l_1^2 v_1} \text{ cm}^{-3} \tag{3.1}$$

The number of collisions Z_{12} leading to scattering by process j into unit solid angle at θ in the laboratory is:

$$Z_{12} = \frac{I_1 T_1 I_2 T_2 W_1 W_2 h \sigma_j(E,\theta)(\mathbf{v}_1 - \mathbf{v}_2)}{v_1 v_2 l_1^2 l_2^2} \text{ s}^{-1} \tag{3.2}$$

where $E = \frac{1}{2}\mu(v_1 + v_2)^2$ = the impact energy and $W_1 W_2 h$ is the scattering volume. The number of counts recorded by the detector will be:

$$Z_{12} T_3 A_d q / l_3^2 \text{ s}^{-1}. \tag{3.3}$$

Thus the detected signal is:

$$S = \frac{I_1 T_1 I_2 T_2 W_1 W_2 h \sigma_j(E,\theta)(\mathbf{v}_1 - \mathbf{v}_2) T_3 A_d q}{v_1 v_2 l_1^2 l_2^2 l_3^2} \text{ s}^{-1} \tag{3.4}$$

The feasibility of the experiment will depend upon the count rate S. Clearly if S becomes very small e.g. less than 0.001 counts s^{-1} the experiments will be exceptionally tedious and perhaps even impractical. However, before this stage is reached it is normally found that the noise count limits the sensitivity attainable. It is the signal to noise ratio which is crucial.

The noise counting rate is difficult to estimate, unlike Equation 3.4 for the signal for which all the parameters can be fairly well guessed. It arises from two principal sources:

(a) From the partial pressure of the species being detected inevitably present in the detector region and (b) from scattering of the beams by background gas.

For the first contribution the noise counting rate will be:

$$N_n = n_i q A_d v_b / 3 \quad s^{-1} \tag{3.5}$$

representing the flux of molecules on to the detector surface. The difficulty is in estimating n_i. Even a partial pressure of $10^{-1.6}$ torr corresponds to 3 atoms per cm^3 or at thermal energies some 10^5 collisions cm^{-2} s^{-1} on the detector!

In the second contribution we are concerned with the densities of the target beam and the background gas (of all species). The count rate arising from this source will be:

$$N_n \simeq \frac{n_b T_1 I_1 W_1 W_2 h T_3 A_d q \sigma_b(\theta)}{l_1^2 l_3^2} \quad s^{-1} \tag{3.6}$$

(We assume that the detector views only the scattering volume).

Noise from this source will be much more severe in the case of elastic scattering for which $\sigma_b(\theta)$, the differential cross-section for scattering from background gas into angle θ, will be of the same magnitude as the cross-section being studied.

In general it will be an objective of design to achieve a target gas density greater than 100 times that of the background i.e.

$$n_b \simeq 0.01\, T_2 I_2 / v_2 l_2^2. \tag{3.7}$$

The noise count rate we have calculated represents the mean counting rate; as we shall discuss later in Chapter 5 it is the fluctuations in this rate that play the crucial part in an experiment. By making successive observations with one

or other beam switched off we can estimate the signal plus noise and the noise alone, hence by subtraction estimating the signal with an uncertainty which depends upon the standard deviation of the noise. If we assume that all the noise processes contributing are 'white' (i.e. purely random) we can estimate their standard deviation as the square root of their mean.

The signal noise ratio is thus:

$$S/N = \text{Signal count rate}/(\text{noise count rate})^{1/2} \tag{3.8}$$

or combining Equations 3.4, 3.5 and 3.6:

$$S/N = \left[\frac{I_1 T_1 I_2 T_2 W_1 W_2 h \sigma_j(E,\theta)(v_1 - v_2)(T_3 A_d q)^{1/2}}{v_1 v_2 l_1^2 l_2^2 l_3^2} \right] \times \left[\frac{3}{n_i v_b} + \frac{l_1^2 l_3^2}{n_b T_1 I_1 W_1 W_2 h \sigma_b(\theta)} \right]^{1/2} \tag{3.9}$$

This relation provides the kernel of the molecular scattering design problem. Note in particular that the signal/noise varies as the inverse squares of the distances in the apparatus, linearly with the beam intensities but only as the square root of the detection efficiency.

Unfortunately it is not sufficient simply to choose values for the dimensions so as to provide an adequate signal/noise ratio. Our choice is limited not only by practical considerations of machinability and strength of materials but more fundamentally by considerations of resolution. In any experiment we are concerned with measuring some parameter of the molecular behaviour rather than of the apparatus. This implies that the angular and energy resolutions of the apparatus must all be adequate to observe the effect of this parameter. In this chapter we shall not be concerned with the question of the resolution required to determine some specific molecular parameter, a topic reserved for discussion in Chapter 7. Rather, given a required resolution in the laboratory system, we will examine the resulting apparatus constraints.

3.2 Resolution

The resolution of velocity and state filters will be discussed later (in Chapter 4). Here we are concerned with the effect of apparatus dimensions on the measurement of the angular dependence of scattered intensity i.e. on total and differential cross-sections. We shall assume for the sake of simplicity

that the velocities and states of our colliding particles are already completely defined. The extension of these arguments to cover beams with a distribution of velocities or states being straightforward though tedious. With this simplification the resolution of our apparatus will depend solely upon the geometric aperture of the detector and shapes and divergences of the beams.

Different techniques of beam generation (as discussed later in this chapter) will yield their own characteristic distribution of intensity with respect to angle in the forward direction. In general this distribution is too broad for direct application and a system of collimating orifices is used to further define the beam. Such a system consisting of a source of uniform brightness at O of width W_s and a collimation slit C of width W_c will yield a trapezoidal beam intensity distribution as shown in Fig. 2, of size

$$\begin{aligned} A &= W_c + (W_c - W_s)\,a \\ B &= W_c + (W_c + W_s)\,a \\ a &= l_{cd}/l_{sc} \end{aligned} \tag{3.10}$$

The dimensions are normally chosen with $W_c >> W_s$ so as to yield a reasonably steep sided beam of the required width W_c. All the other dimensions being kept as small as is compatible with other apparatus constraints.

When measured by a detector with a finite angular width M the trapezoidal distribution will be broadened. The apparent profile as measured by the detector now being:

$$I(\theta)_{\text{apparent}} = \int_{-M/2}^{M/2} I(\theta + \theta')\mathrm{d}\theta'. \tag{3.11}$$

It might be thought that this apparent width represented the resolution of the whole beam detector system. Unfortunately the beam height, which has not yet been explicitly considered, complicates this simple picture. The angular resolution of a system is normally described in terms of the 'Kusch' angle. That is the angle of deflection suffered by molecules in the beam at which the beam intensity registered by the detector, is reduced to 50% of that at zero degrees. The change in intensity with angle for tall beams can only be calculated if we allow for scattering occurring out of the plane defined by AC and O in Fig. 3.2 and 3.3. Here we see that molecules in each element ds in the beam are scattered both in and out of this plane. If the beam or target molecules producing this scattering are polarized (i.e. have aligned angular momenta) this scattering may depend on the polar angle ϕ as well as

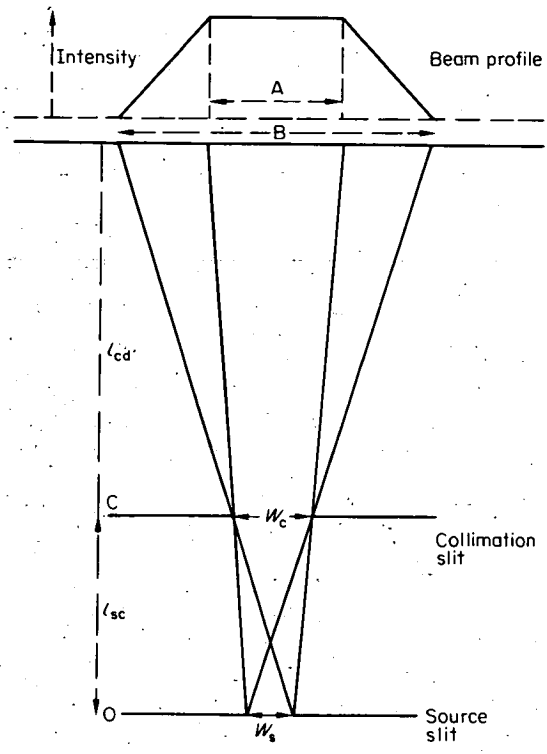

Fig. 3.2 Relation of source and collimation apertures to the beam profile.

on θ. For the usual case of unpolarized beams, however, the scattering intensity is independent of the angle ϕ. The fall in intensity registered by a detector placed in line with the beam as the deflection of the beam particles increases can be calculated and is a useful function to describe the overall angular resolution of the experiment. When scattered through an angle θ at a random azimuthal angle, particles originally travelling in a small section of the beam will arrive in an annular area in the detector plane. Part of this flux may miss the detector, resulting in a decrease in the recorded intensity $I(\theta)$. By integrating over the area of the beam, the total change in intensity at the detector can be calculated as a function of θ and an efficiency function $\mathcal{J}(\theta)$ for detecting molecular deflections can be computed. For tall rectangular beams and detector, R. J. Cross and C. J. Malerich, (1970) have shown that if:

$$\mathcal{J}(\theta) = (I(0) - I(\theta))/I(0)$$

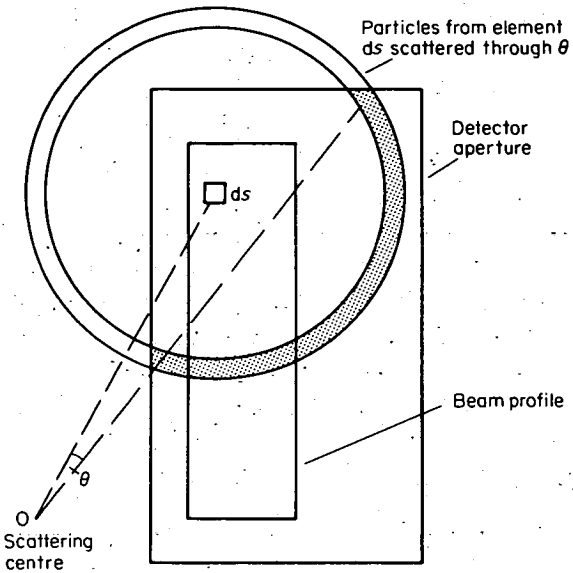

Fig. 3.3 Effect of out-of-plane scattering on resolution. Effective response for scattering through θ is obtained by integrating over all elements ds in the beam.

then:

$$\mathscr{I}(p) = 0, \quad p \leqslant 1 - \alpha$$

$$\mathscr{I}(p) = (\pi\alpha)^{-1} \{[p^2 - (1-\alpha)^2]^{1/2} - (1-\alpha)\cos^{-1}[(1-\alpha)/p]\}, \quad (1-\alpha) \leqslant p \leqslant (1+\alpha)$$

$$\mathscr{I}(p) = (\pi\alpha)^{-1} \{[p^2 - (1-\alpha)^2]^{1/2} - [p^2 - (1+\alpha)^2] - (1-\alpha) \times \cos^{-1}[(1-\alpha)/p] + (1+\alpha)\cos^{-1}[(1+\alpha)/p]\}, \quad (1+\alpha) < p \quad (3.12)$$

where $p = l_{ds}\theta/b$ and $\alpha = a/b$, l_{ds} being the detector-scattering centre distance, a the half width of the detector and b the beam half width. The Kusch angle, θ_K, of course corresponds to $\mathscr{I}(\theta) = 0.5$. Unfortunately we are still not out of the wood. As a simple example we will consider the single beam + gas target experiment to measure the total collision cross-section. Here we observe the attenuation of a beam passing through a collision chamber (or possibly a cross beam) containing a known pressure of the target.

The total cross section is $\sigma = 2\pi\int_0^\pi \sigma(\theta)\sin\theta d\,\theta$, where $\sigma(\theta)$ is the differential cross-section describing the angular dependence of the scattering.

We have already seen that the narrow angle contribution to this integral predominates.

In the laboratory the observed angular dependence for an apparatus with perfect resolution would be:

$$\sigma(\theta) = \int_0^{2\pi} \sigma(\theta, \Phi)\mathrm{d}\Phi = \int J\left(\frac{\cos\theta, \Phi}{\cos\chi, \phi}\right) \sigma(\chi, \phi)\mathrm{d}\phi$$

(since the random velocities of the target molecules makes the scattering symmetric about the main beam), where, as already discussed in Chapter 2 $J(\cos\theta, \Phi/\cos\chi, \phi)$ is the Jacobian describing the CM → LAB transformation.

If the total cross-section is to be measured to an accuracy ϵ then the apparatus efficiency function $\mathcal{J}(\theta)$ must be such that:

$$\epsilon = 2\pi \int_0^{\pi} \sigma_{\mathrm{lab}}(\theta_{\mathrm{lab}}) \sin(\theta_{\mathrm{lab}}) \mathcal{J}(\theta_{\mathrm{lab}})\, \mathrm{d}\theta_{\mathrm{lab}} - 2\pi \int_0^{\pi} \sigma_{\mathrm{lab}}(\theta_{\mathrm{lab}}) \sin(\theta_{\mathrm{lab}})\, \mathrm{d}\theta_{\mathrm{lab}} \tag{3.13}$$

or more approximately the Kusch angle must be small compared to the angle η for which:

$$\epsilon \sim \int_0^{\eta} \sigma_{\mathrm{lab}}(\theta_{\mathrm{lab}}) \sin(\theta_{\mathrm{lab}})\, \mathrm{d}\theta_{\mathrm{lab}}.$$

For elastic scattering the CM value of η can be estimated rather approximately using the uncertainty relation as:

$$\eta_{\mathrm{CM}} < \frac{\hbar}{\mu v}\left(\frac{\pi}{\sigma_{\mathrm{tot}}}\right)^{1/2} \tag{3.14}$$

where σ_{tot} is an approximate cross section for the potential and μ and v are the reduced mass and relative velocity of the collision partners. For molecular systems η will typically be less than a few minutes of arc at thermal speeds.

Since mechanical alignment considerations make slits with a width of less than 0.03 mm difficult to work with, this resolution requirement generally predicates a beam length of some 0.1 – 1 m, thus introducing a considerable intensity loss. It should also be noted from Equation 3.13 that the resolution required will be a function of the Jacobian. If this is unfavourable in the sense of compressing a large CM range of angle into a narrow laboratory one then the experimental resolution will be corre-

spondingly worse. In general one tries to operate with this factor in one's favour by scattering and detecting the lighter of the two particles.

Further problems arise from the motion of the target gas in the scattering chamber. Firstly this random target motion with respect to the laboratory frame will broaden the relative velocity distribution and may if severe wash out any energy dependent structure in the total cross section. This topic and the appropriate correction factor are discussed in more detail in Chapter 7 also (K. Berkling et al., 1962). A second effect more relevant to this discussion arises from the spread of Jacobians arising from the target velocity distribution. Thus some collisions which for a stationary target would have fallen outside the detector will now be detected and will thus reduce the apparent total cross section. In some cases further corrections may be necessary to allow for the finite width of the target zone.

It will be easily appreciated that the apparatus resolution depends upon many factors including the nature of the beam and target materials and their temperature as well as the apparatus geometry. The Kusch criterion coupled with Equation 3.14 enables a first estimate of the required geometry to be made. However, for the accurate interpretation of measured attenuations in terms of total collision cross-sections very careful analysis of the whole range of factors contributing to the resolution is required.

In a cross beam experiment the resolution problem is yet more complex. Once again the experimental design must proceed via some approximate forward calculation using guessed potential parameters. The effect of various apparatus geometries can then be explored in a laborious but straightforward way using numerical integration techniques to produce an apparatus-averaged cross section in either the CM or LAB systems. In many cases it will be found that the particular purposes of an experiment do not require a very close approach to the apparatus with perfect resolution. Indeed at this stage some trade between resolution and signal/noise ratios as calculated by Equation 3.9 is almost inevitable.

3.3 Vacuum considerations

The most important component in any molecular beam experiment is quite simply the vacuum in which the beams are formed and their collisions studied. As a consequence the development of beam experiments has been closely linked to improvements in vacuum technology. It is not the purpose of this book to discuss vacuum technique; however, a few specialised topics arising in beam experiments are worth considering.

In any beam experiment there are three major requirements of the vacuum technique.

(i) To provide mean free paths very long in comparison with beam path lengths, thus avoiding significant attenuation and broadening of the beams.
(ii) To maintain the density of background material at a much lower figure than the density in the collision target or cross beam.
(iii) To minimise background densities in the beam detector chamber, particularly of species that are indistinguishable by the detector from the beam species.

The mean free path requirement is not normally difficult to achieve. The mean free path for a molecule with total cross section σ_{tot} is:

$$\lambda_f \sim (4\sqrt{2}\ \sigma_{tot} n)^{-1}. \tag{3.15}$$

Thus for a typical molecular cross section on adequate λ_f may be achieved with pressures of the order $10^{-5} - 10^{-6}$ torr. An exception to this rule may arise in the case of very slow atoms or molecules when the cross section may become very large indeed compared to that obtaining at normal thermal velocities.

The background density requirement is more severe. As we will see later in this chapter a typical effusive source may yield a flux of 10^{13} molecules sr^{-1} s^{-1}. For thermal velocities this corresponds to a static pressure of $< 10^{-7}$ torr in a target zone 1 m from the source. Considering the much larger path though the background pressure in the chamber as compared to the target zone itself we can see that ideally we should need to achieve pressures below 10^{-9} torr if background scattering is to be reduced to 10% of that for the target. In practice by keeping all beam paths as short as possible and by ensuring that the detector 'sees' only a narrow volume around the scattering centre this limit can be relaxed. A pressure of $10^{-7} - 10^{-8}$ torr in this region is quite commonly accepted at present.

The final requirement for low background densities in the detector region is very severe, particularly in the case of universal detectors such as mass spectrometers. This problem is discussed in more detail in the chapter dealing with detectors and its magnitude can be appreciated from the static partial pressure equivalent to a flux of 1 molecule s^{-1} cm^{-2} at thermal speeds, namely $\sim 10^{-21}$ torr. In vacuum terms we shall normally be reduced to simply doing as well as possible in this region, perhaps 10^{-10} torr total pressure.

In the design of systems to provide the required environment the beam fluxes themselves provide the major gas load, other contributions from wall and component outgassing being small in comparison. In this situation, differential pumping, in which the system is divided into a series of separately pumped chambers communicating only by narrow orifices through which the beam passes, offers important advantages. In Fig. 3.4a and 3.4b a 'nozzle source' with an aperture $\sim 5 \times 10^{-3}$ cm^2 and a driving pressure of 10^3 torr provides the beam, typically of intensity 10^{19} molecules sr^{-1} s^{-1} in the forward beam direction.

The gas load will obviously depend upon the temperature and molecular weight of the gas in the source.

The number passing through orifice $\approx$

$$\left(\frac{\text{Area of orifice x molecular velocity x n. density}}{4}\right) \text{ s}^{-1} \qquad (3.16)$$

For the conditions given here the gas load will be ~ 20 cm^3 at N.T.P. To achieve a pressure of 10^{-8} torr in this chamber (requirement ii) a pumping speed of $\sim 10^9$ litres s^{-1} is needed – a speed that could be achieved by a

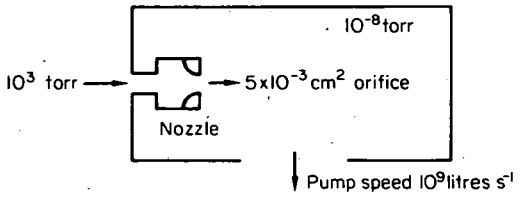

(a)

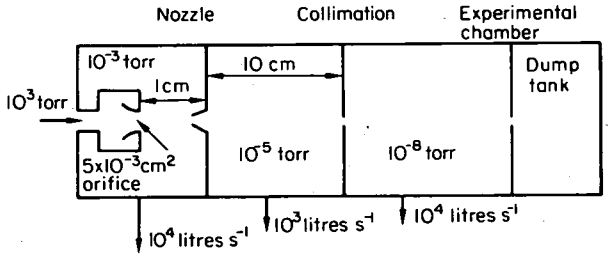

(b)

Fig. 3.4(a) and (b) showing the advantages of differential pumping in reducing the pump speed required to obtain the desired ultimate pressure in the experimental chamber.

pump with a completely effective area (in the sense that all molecules that cross it are pumped) of > 100 square metres!

In a system employing differential pumping the speed requirements are very much reduced. The total gas load is balanced between several chambers the maximum possible amount being pumped at the higher pressures. In this arrangement the source operates in a separate chamber (Fig. 3(b) since the beam path in this chamber is short (~ 1 cm) the comparatively high pressure of 10^{-3} torr will suffice. The pumping speed required in this chamber is now only $\sim 10^4$ litres s^{-1}. The second collimating chamber serves as a buffer between this chamber and the experimental one. The pumping load in this chamber based on the beam intensity and the entrance aperture to it is:

Beam Intensity x solid angle of entrance

$$= 10^{17} \text{ molecules } s^{-1} \sim 2 \times 10^{-2} \text{ cm}^3 \text{ s}^{-1} \text{ at N.T.P.} \qquad (3.17)$$

so that a pumping speed of 1,000 litres s^{-1} would maintain a pressure of 10^{-5} torr. In the final experimental chamber the gas load will consist of all the gas scattered from the beam (say 10% of the beam flux) plus that which enters from the buffer chamber via its exit aperture. Thus for the dimensions in the figure a pumping speed of 10^4 litres s^{-1} is required, a speed readily obtained at these pressures by cryo panels or titanium getter pumps.

The great savings in pump speeds and hence in cost by the use of this staged pumping is very clear. These pumping speeds are obtainable by a combination of diffusion and liquid nitrogen cooled cryo-traps. For the higher vacuum chambers where the actual N.T.P. gas load is small, Ti getter pumps, preferably working on a liquid nitrogen cooled substrate provide great pumping speeds at relatively low cost for most chemical species, Table 3.1. This type of pump has now made the attainment of pressures of the order $10^{-8} - 10^{-9}$ torr a simple operation not requiring baking or other elaborate techniques necessary when only the slower ion pumps were available (which are now only required to handle the inert gases).

The major difficulty in constructing vacuum systems of the staged type, particularly for cross beam experiments, lies in the geometry, the requirements of short path lengths to the scattering centre and detector conflicting directly with the need for differential pumping stages and the actual size of the pumping equipment required to handle the gas load. When these problems are combined with the need to vary the detector angle, possibly both in and out of the plane, and to preserve some flexibility in the insertion of velocity filters etc. then considerable ingenuity is required to realise an effective system.

Table 3.1 Ti getter pump speeds litres s^{-1} cm^{-2}

Ti film temperature	Gas					
	H_2	N_2	O_2	CO_2	CO	H_2O
300 K	20	15	11	30	66	20
77 K	40	40		60	70	90

3.4 Beam sources – thermal energy

In Section 3.1 of this chapter we have shown how the overall signal/noise ratio depends upon the various apparatus parameters. In practice once having decided on the resolution required in an experiment our only remaining variables will be the beam intensities and detector sensitivity. Although in principle shrinking the distances which the beam must traverse is possible, machining and alignment considerations make it difficult to use beams less than a few tens of microns wide. The angular resolution required then dictates the minimum beam distances possible. Since the signal/noise ratio depends linearly upon the beam intensities but only as the square root of the detector sensitivity, the beam intensity available is usually the key factor in determining the feasibility of an experiment.

In recent years a wide range of techniques have been used to produce molecular beams. These methods have been discussed in a number of general reviews (H. Pauly and J. P. Toennies, 1965, 1968; N. F. Ramsey, 1956) as well as some more specialised reports (J. B. Fenn and J. Deckers, 1968; J. B. Anderson, et al., 1968). In general these techniques may be grouped into two main classes. Those covering the approximately thermal collision energy range extending at most up to 1 eV (3000 K hydrogen) and those operating at energies above this limit and thus not available from an equilibrium source. We shall see later that the intermediate region of beam energy, say from 1 to 20 eV, is an especially difficult one in which to work. The production of very slow beams is similarly difficult.

A further class of sources is designed to produce beams of free radicals, metastable species, dissociated atoms etc. These sources are normally adapted versions of the more usual types using electron or photon fluxes to produce the required excitation. In all these devices their efficiency as sources will depend most importantly on the following factors.

(i) The forward intensity in molecules sr^{-1} s^{-1} along the beam axis. Clearly the greater this intensity the better.

(ii) The ratio of forward intensity to the total gas load. In other words the directivity of the beam as it emerges from the source. A beam having most of its intensity in the useful forward direction will be more economic in its pumping requirements for a given beam intensity.

(iii) The range of velocities which the source will produce. Ideally we should like to vary the beam energy smoothly and continuously over a wide range from a few milli electron volts to several thousand eV. In practice sources are much less versatile.

(iv) The velocity dispersion in the beam Δv(*width at half height*)/v. If the beam energy is readily variable then a very narrow spread in the velocities of the molecules emerging from the source is desirable. Alternatively a suitable velocity selector can be used with a source producing a range of velocities so as to obtain the benefit of both a wide energy range and a narrow dispersion in velocity (though at some cost in intensity).

(v) The atomic and molecular state of the particles in the beam. In some cases we may wish to produce beams of dissociated atoms or other excited species. We shall almost always require to operate with beams in a well characterized internal state.

(vi) The stability of the source both as regards short term changes in intensity or in alignment and in the longer term due to corrosion etc.

Most thermal energy beam sources utilise a flow system in which the beam material flows as a vapour from an oven into a chamber of lower pressure. Here collimation and differential pumping stages are used to produce a final well defined beam in the experimental or collision chamber. This type of system can operate under two different regimes – *molecular effusion* or *'hydrodynamic flow'*. In the molecular flow condition the molecules move through the slit and beam without undergoing collisions. Their motion is thus mutually independent. Under these conditions the 'Knudsen number' K_n where

$$K_n = \frac{\text{Mean free path in source}}{\text{smallest dimension of orifice e.g. slit width}}$$

is greater than 1. For the reverse condition $K_n < 1$ hydrodynamic or bulk flow occurs through the orifice and for some distance down stream. Collisions are frequent and a degree of energy transfer from the internal modes of the molecules to beam translational energy occurs.

(i) Effusive sources $K_n > 1$

Historically the earliest (L. Dunoyer, 1911) and still the best characterized, in that the beam properties can be fairly accurately predicted, is the effusion source or 'oven'. This consists of a small chamber containing the beam material as a vapour at a pressure of a few torr. The beam leaves the chamber via a narrow slit ~0.02 mm across and perhaps 10 mm tall. The gas pressure in the source is adjusted so as to produce molecular effusion rather than bulk flow through the slit. This condition is fulfilled by making the mean free path in the source greater than the slit width ($K_n > 1$). The slit height is not critical in this respect.

Under these conditions simple kinetic theory considerations predict that the number of molecules, N, leaving the source per second is:

$$N = \frac{1}{4} n \bar{v} A_s \quad \text{for } n \ll 1/W\sigma \tag{3.18}$$

where A_s is the area of the slit, n is the number density and $\bar{v}$ the mean velocity of the molecules in the source. The slit width is W and the molecular cross section σ.

Since the flux is equal into every solid angle element the angular distribution of the molecules emerging from the slit follows a cosine law. The flux at θ from the forward direction and at a distance r is:

$$I(\theta, r) = \frac{1}{4} n\bar{v} A_s \cos\theta/\pi r^2 . \tag{3.19}$$

In terms of source pressure p, temperature and molecular weight:

$$I(\theta, r) = 1.11 \times 10^{20} A_s\, p \cos\theta/r^2\,(MT)^{1/2} \text{ mol mm}^{-2}\text{s}^{-1}, \tag{3.20}$$

or:

$$I(\theta, r) = 1.11 \times 10^{20}\, A_s p \cos\theta/(MT)^{1/2} \text{ mol sr}^{-1}\text{ s}^{-1} . \tag{3.21}$$

At a distance of 1 m from the source the intensity for any gas will be of the order 5×10^{10} mol mm^{-2} s^{-1}. Thus for a typical detector with an angular resolution of 0.1° a flux of $10^{10} - 10^{11}$ molecules per second will fall on the detector.

The cosine law flux distribution from an effusive source, Fig. 3.5 is very

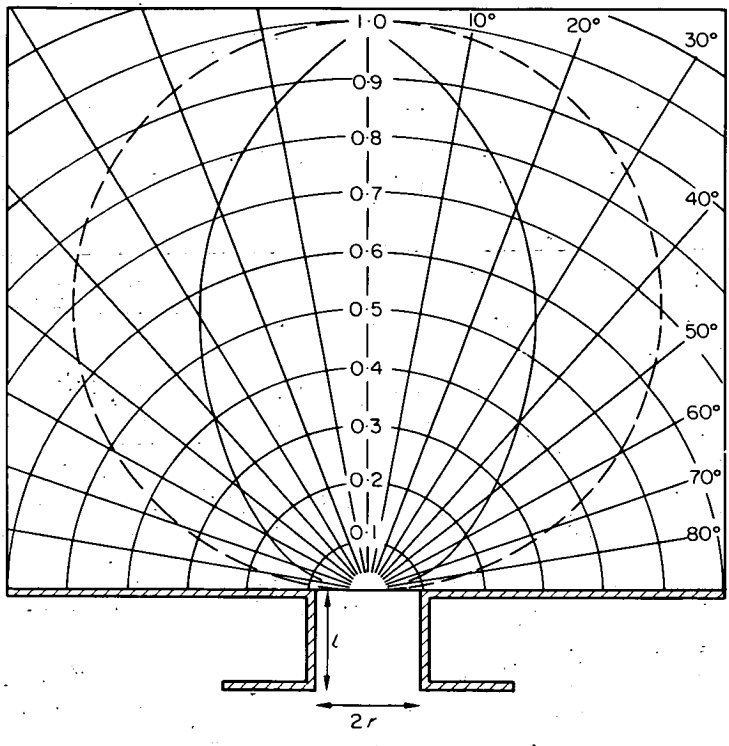

Fig. 3.5 Cosine distribution of flux from an effusion source (dashed line). The solid curve shows the distribution for a short canal (length = diameter). Reproduced from N. F. Ramsey, 1956.

broad and considerable collimation is required to produce a well defined beam. The directivity in respect of our standard beam (0.1°), that is the ratio of useful molecules in the beam to the total number emitted from the source is only $\sim 10^{-10}$. Simple effusion sources are thus relatively uneconomic in their pumping requirements.

The velocity distribution in the emergent beam is readily calculable. Since the slit is narrow compared to the dimensions of the source the gas inside is in thermal equilibrium with a Maxwellian velocity distribution:

$$N(v)\mathrm{d}v = C\frac{v^2}{\alpha^3}\exp(-v^2/\alpha^2)\mathrm{d}v \qquad (3.22)$$

where α is the most probable velocity $(2RT/M)^{1/2}$ and C is a constant.
The number of these molecules which escape per second depends upon their

velocity. The distribution of velocity in the beam is therefore:

$$vN(v) \text{ i.e.}$$

$$I(v)\mathrm{d}v = C\left(\frac{v}{\alpha}\right)^3 \exp(-v^2/\alpha^2)\,\frac{\mathrm{d}v}{\alpha}. \tag{3.23}$$

For many purposes this distribution is too wide to yield the required energy resolution and some form of velocity selection might then be used. The velocity distribution calculated is found to hold well in experiments except at the lowest velocities in the tail of the distribution. Here slightly lower intensities than predicted are observed, probably due to collisions scattering out the slow molecules from the beam.

The energy range over which useful beam intensities can be obtained is about a factor of 5 centred on kT for the source temperature. The maximum energy available even with high temperature operation of the source thus lies in the region below 1 eV.

Since the source operates at thermal equilibrium and very few collisions occur in the beam itself the effusion technique produces an equilibrium mixture of internal states and molecular species. This can be an important advantage. We shall see later that many of the other types of beam source are much less well defined in this respect. Furthermore by heating the source the internal distribution can be changed in a controlled fashion.

The effusion source is very simple in construction. For condensable materials such as alkali metals, single or double chamber ovens may be used in which the source both contains the charge of beam material and maintains thermally the required operating vapour pressure. The second chamber can then be used to vary the vapour temperature without altering the vapour pressure, in this way varying the velocity distribution in the emergent beam.

The heaters for effusion sources of this general type are normally made from Nichrome or tantalum wire. They are arranged so as to raise the orifice or slit temperature somewhat above that of the bulk of the oven; thus preventing condensation and blockage of the slits. Other problems arise from corrosion, particularly around the defining slits. Monel is the usual material for these ovens but for some very corrosive species such as the halogens it may be necessary to construct the source from graphite or to use gold slits.

Some materials, e.g. NaOH, are especially prone to bumping or 'spritzing' in the ovens producing unstable intensities in the beam. This difficulty may be minimized by careful control of the temperature when initially heating the charge and by the use of baffles inside the source itself.

Some typical designs of effusion source are shown in Fig. 3.6

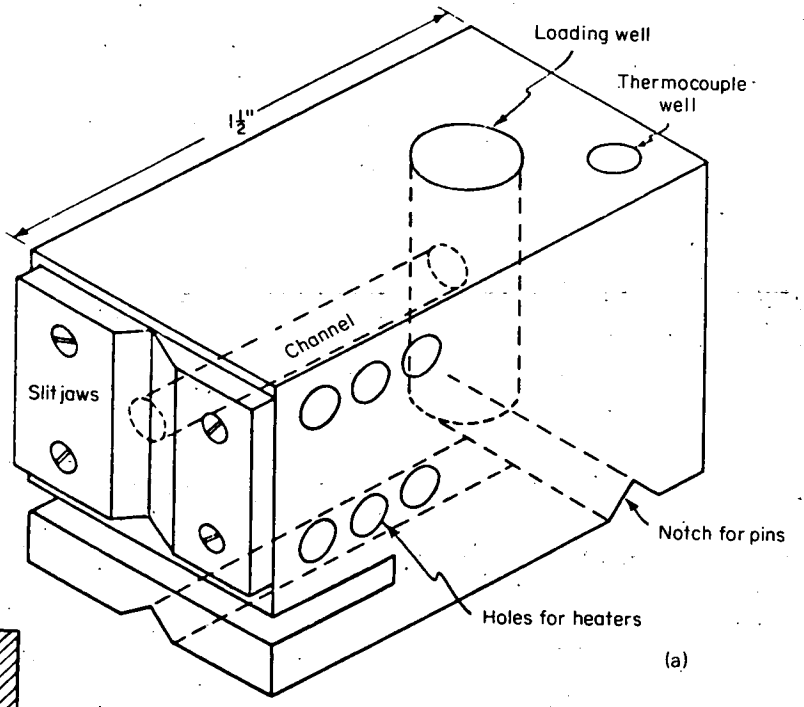

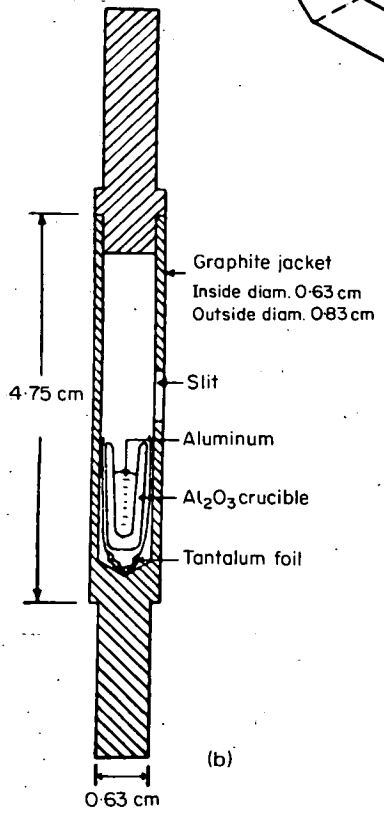

Fig. 3.6 Effusion molecular beam sources
(a) single chamber source
(b) directly heated source for high temperatures (H. Lew, 1949).

In practice these sources are usually operated at somewhat higher pressures than those yielding strictly effusive flow. The intensities obtained are then somewhat higher and rather more material is concentrated in the forward direction.

A much greater improvement in directivity while still maintaining the effusion condition can be achieved by the use of long canals or arrays of such canals in place of the thin defining slits at the orifice of these sources. For a single long canal the directivity is improved by a factor $3l/8r$. The critical distance for the mean free path now being the canal length l rather than the aperture radius r. This longer mean free path and the consequent lower operating pressure in the source means that the forward intensity in the beam is less than that from a thin slit. The advantage lies in the greater directivity, the gas load for a given intensity falling by the factor $3l/8r$.

Much more useful are arrays of such canals. In particular glass plates containing multiple parallel capillary tubes with radii down to $3\,\mu$ and an overall transparency of 75 percent can be obtained commercially. For a given total gas load a higher forward flux can be obtained from these arrays than from a thin slit (provided that the mean free path in the source is comparable to the tube length).

The improvement in forward intensity compared to that produced by a thin slit orifice operated at the *same pressure* has been calculated by J. A. Giordmaine and T. C. Wang (1960) to be:

$$\frac{I(0)\text{ array}}{I(0)\text{ thin orifice}} = \frac{0.32}{\pi^{1/4}} \left(\frac{\bar{v}}{N}\right)^{1/2} \frac{1}{d} (A\tau m)^{1/4} \qquad (3.24)$$

where A is the total source area, τ is the transparency of the array, m the number of holes in the array, N the total flow rate in molecules s^{-1}, d the collision diameter and $\bar{v}$ the mean velocity of the molecules in the source. The half intensity width of the array and the thin orifice beams are approximately in the inverse ratio of their forward intensities as given by Equation 3.24 above. The actual experimental performance of these arrays is a little worse than that predicted, presumably due to collisions between molecules emerging from different channels (J. C. Johnson, et al., 1966).

As the pressure inside any of these array sources is raised, the effective channel length decreases until eventually the array behaves like a thin orifice of equal effective area. This behaviour is nicely illustrated in Fig. 3.7. The maximum forward intensity obtainable from these arrays is thus no better than from an orifice. The improvement in directivity obtained, however, is considerable, Fig. 3.8.

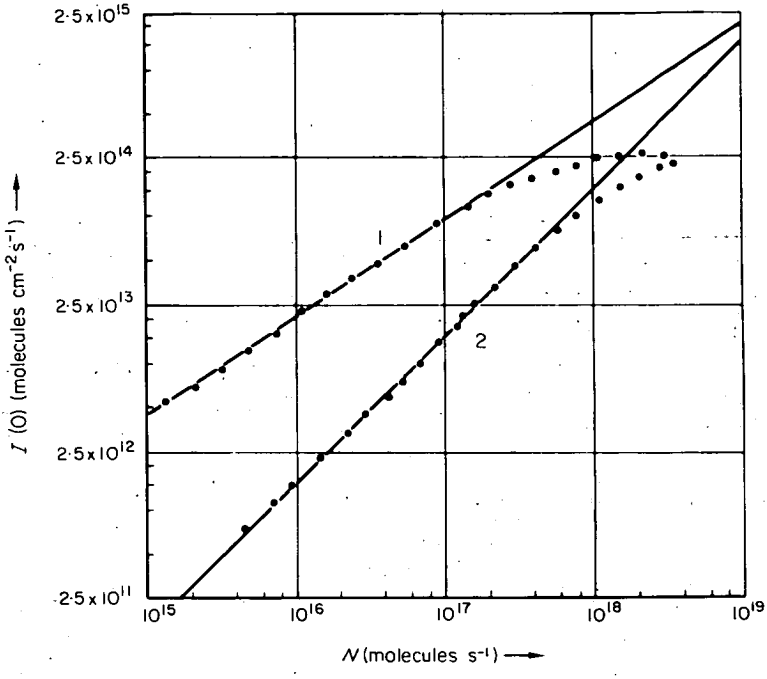

Fig. 3.7 Comparison of forward intensities at 1m versus total flow (i.e. gas load) for a channel array (1) and an orifice source (2). Reproduced from H. Pauly and J. P. Toennies, 1965.

The most important application of these devices is in the cross or target beam source where a relatively extended target region is permissible and the minimum gas load is desirable. Glass arrays are now available in quite large sheets ~5 cm and in a variety of geometries. Some workers have recently described shaped arrays in which the channels are not parallel but are angled so as to bring the beam material to a fairly well defined focus. Clearly collisions within the converging beam must limit the densities achievable and it is not yet clear how useful this technique will prove.

The velocity distribution from an array source has been reported to be slightly deficient in slow velocities as compared to the effusive v^3 distribution.

(ii) Hydrodynamic flow sources, $K_n < 1$

The hydrodynamic source is gaining very rapidly in importance, since intensities up to 10^3 greater than those from effusive orifices can be obtained. There seems little doubt that in cases where the intensity limits experimental performance hydrodynamic sources will be the normal choice.

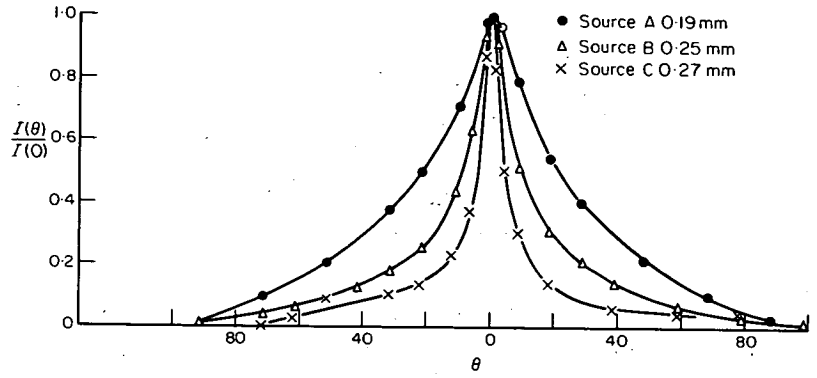

Source	Tube length cm	Effective radius of single tube cm	No. of tubes	Overall source diameter cm	Approximate shape of tube cross section
A	0.66	1.65×10^{-2}	224	0.51	Hexagonal
B	0.31	2.35×10^{-3}	1.28×10^{1}	1.3	Circular
C	0.95	2.69×10^{-3}	1.80×10^{4}	1.1	Triangular

Fig. 3.8 Ratio of intensity at θ to forward intensity for several sources and pressures. (Reproduced from J. A. Giordmaine and T. C. Wang, 1960).

This type of source originated with a suggestion by A. Kantrowitz and J. Grey, 1951, that the Maxwellian gas inside an effusive source be replaced by a supersonic jet of gas already moving in the beam direction. An arrangement to exploit this idea is shown schematically in Fig. 3.9. The beam material emerges through a nozzle from a chamber in which the pressure is of the order 10^2–10^3 torr. The flow is hydrodynamic through this nozzle and a large jet of gas expands into the nozzle chamber. This jet strikes a truncated hollow cone known as the skimmer. In this way a sample of the rapidly translating gas is obtained and the remaining gas in the jet deflected away for pumping. In the region of the skimmer the flow changes from continuum to molecular, i.e. the collision rate drops very sharply. The post skimmer chambers serve to collimate the beam and to provide the differential pumping necessary. (See Section 3.3).

Since the operation of this source includes the transition from continuum to molecular flow the actual conditions present in these gas jets has been of considerable interest (J. B. Anderson et al., 1965, 1966; E. L. Knuth, 1964). Although much progress has been made in their understanding a complete

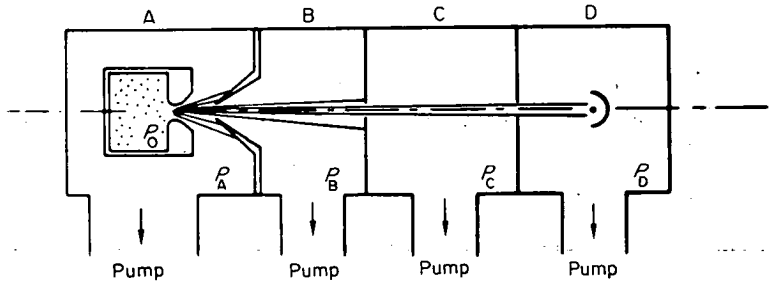

Fig. 3.9 Schematic of a nozzle beam source. A, B, C, and D are the nozzle, collimation, experimental and detection chambers respectively. The separate differential pumping stages are a crucial feature.

theory is still not available. However, from a users viewpoint a simple theory combined with some pragmatism in design and operation is usually adequate.

The simple theory of the action of nozzle beams is based upon the assumption that the expansion is isentropic. The increase in forward velocity of the beam then comes from a reduction in the local enthalpy of the gas. The lowering in temperature, from T_i to T_f, accompanying the expansion is given by:

$$T_f/T_i = \left[1 + \frac{\gamma - 1}{2} M^2\right]^{-1} \tag{3.25}$$

where $\gamma = C_p/C_v$ and M is the Mach number in the collision free zone downstream from the jet. The Mach number is defined as:

$$M = V/C \tag{3.26}$$

where V is the bulk velocity and C the local velocity of sound. Typically $M \sim 10$ and so with $\gamma = 5/3$, T_f/T_i may approach 3×10^{-2}, a very considerable degree of cooling. In a beam of molecules having internal energy, some of the energy for the increase in forward translational energy can come from vibration and rotation and it is hard to predict in practice whether relaxation among all the degrees of freedom is complete (this would be reflected in the value of γ used above). The marked lowering of the relative as opposed to the bulk kinetic energy of the beam molecules can result in dimerisation or clustering in certain cases, there being enough collisions to stabilise thesynew species (R. J. Gordon et al., 1970).

The increase in forward velocity after expansion can be calculated in the ideal case to be:

$$v_f/v_i \simeq M\left(\frac{\gamma}{3}\frac{T_f}{T_i}\right)^{1/2}. \tag{3.27}$$

Again taking a Mach number of 10, but with a beam of diatomic molecules in which rotational relaxation is complete ($\gamma = 7/5$), we find that the increase in translational energy compared to an effusive source of the same temperature is twofold. From the decrease in the internal temperature of the beam we can also calculate the width of the velocity distribution after expansion:—

$$\frac{\Delta v}{v} \sim \left(\frac{2}{\gamma}\right)^{1/2} \Big/ M. \tag{3.28}$$

Finally the actual forward intensity of a nozzle beam $I(o, v)$ as a function of velocity can also be calculated from simple kinetic theory. If n_0 and α_0 are the number density and velocity in the source, A_s the area of the skimmer and M is the Mach number at the skimmer. Then Anderson and Fenn have shown that:

$$I(o, v) = \frac{n_o A_s}{\pi^{3/2}}\left(\frac{v}{\alpha_o}\right)^3 \left[1 + \frac{\gamma^{-1}}{2}M^2\right]^{3/2-(1/\gamma-1)} \cdot \exp\left\{-\left(\frac{v}{\alpha_o}\left[1 + \frac{\gamma-1}{2}M^2\right]^{1/2} - \frac{\gamma^{1/2}M}{\sqrt{2}}\right)^2\right\}. \tag{3.29}$$

In comparison with an effusive source the ratio of forward intensities at the most probable velocity is approximately

$$\frac{I_{\text{nozzle}}(v)}{I_{\text{effusion}}(v_{\text{most prob.}})} = \frac{n_{o\ \text{nozzle}}}{n_{o\ \text{effusion}}} f(M, \gamma) \tag{3.30}$$

For Mach number >5 (the interesting range) $f(M, \gamma) \simeq 9$ for monatomic gas and $80/M^2$ for diatomics. The improved intensity provided by a nozzle source thus originates very largely in the greater source densities that can be used. The vital advantage lies in the removal of the effusion constraint on the mean free path in the source.

The elementary calculations presented so far have all been in terms of the Mach number. The actual development of this ratio as the expansion proceeds has been calculated by P. L. Owen and C. K. Thornhill, (1948). With the important proviso that the expansion was free and without shock waves their calculation yielded the prediction illustrated in Fig. 3.10. Here the Mach number in a free jet is shown as a function of the ratio of distance

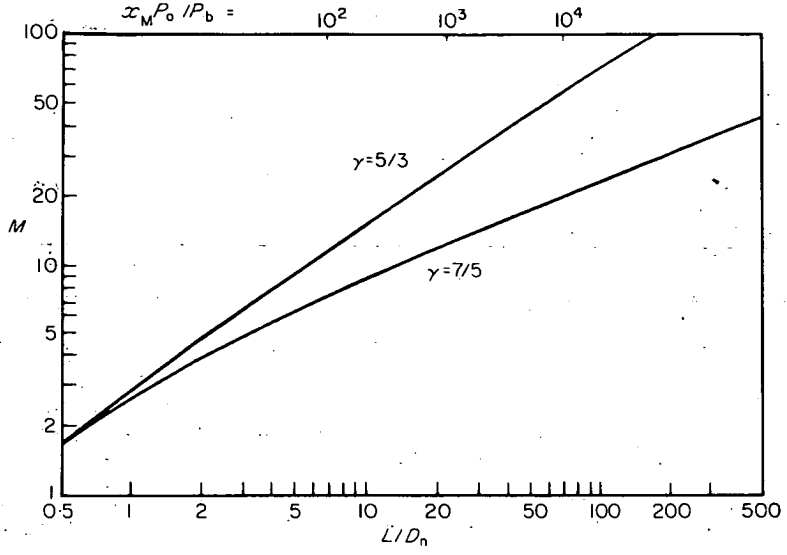

Fig. 3.10 Calculated values of Mach number at distance L downstream from nozzle of diameter D_n. Location of Mach disc x_M for various pressure ratios is shown on top. Reproduced from H. Pauly and J. P. Toennies, 1968.

downstream from nozzle to the nozzle diameter. Thus naively by selecting a suitable skimmer nozzle distance we might expect to produce a beam of any desired Mach number and hence be able to predict the other characteristics of the beam. Unfortunately while it is true that the nozzle skimmer distance is of prime importance a number of other factors, complicate the picture. Firstly J. B. Fenn and J. Deckers, 1963, have found that in contrast to the Owen-Thornhill calculations in which Mach number increased monotonically a definite maximum or Terminal Mach number is reached. Here the collision rate becomes so low that free molecular flow occurs and no further expansion takes place. They find the Terminal Mach number M_T to be given by:

$$M_T \triangleq 1.2 \left(\frac{\lambda_0}{D_n} \right)^{-0.4} \tag{3.31}$$

where λ_0 is the mean free path in the source and D_n is the nozzle throat diameter.

A second complication arises from the presence of shock waves in the expanding jet. From Schlieren photographs these shocks are known to have

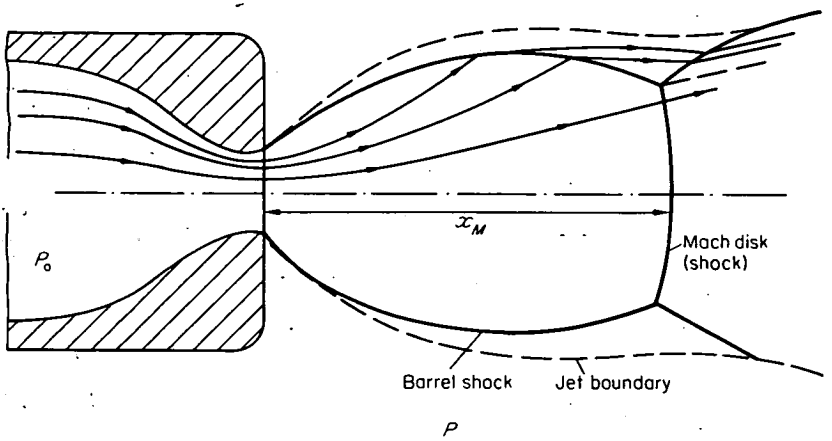

Fig. 3.11 Flow lines and shock fronts in an expanding gas jet. Reproduced from H. Pauly and J. P. Toennies, 1968.

broadly the configuration shown in Fig. 3.11. Particularly important is the shock front perpendicular to the flow direction known as the Mach disc. This shock is believed to originate in collisions of the beam molecules with the background gas. Its position varies roughly as [nozzle pressure/background pressure] $^{1/2}$ and its location is shown in Fig. 3.10.

Forward of the Mach disc the expansion is approximately free and the ideal Owen-Thornhill calculations are reasonably valid. Aft of the disc recompression of the gas occurs and the beam is attenuated. In practice many workers have found an optimum nozzle – skimmer distance to exist. At short distances nozzle-skimmer interference appears while at large distances the Mach disc degrades the beam.

Fenn and Deckers have found experimentally that the intensity actually observed compared to that predicted by calculations is decreased approximately in the ratio Knudsen No. at skimmer $\div M$. In practical operation the nozzle skimmer distance is adjusted to yield the optimum beam flux. Under these conditions the mean free path at the skimmer is several times the skimmer aperture and the exact shape of the nozzle and skimmer are relatively unimportant (K. Bier and O. Hagenna, 1963).

The relative performance of the nozzle and effusion sources have been compared by H. Pauly and J. P. Toennies, 1968, Fig. 3.12. It is clear that nozzle sources offer very much higher beam intensities and are much more economical in terms of forward intensity per given gas load than is the effusion source. However, the useful energy range is still rather limited. The

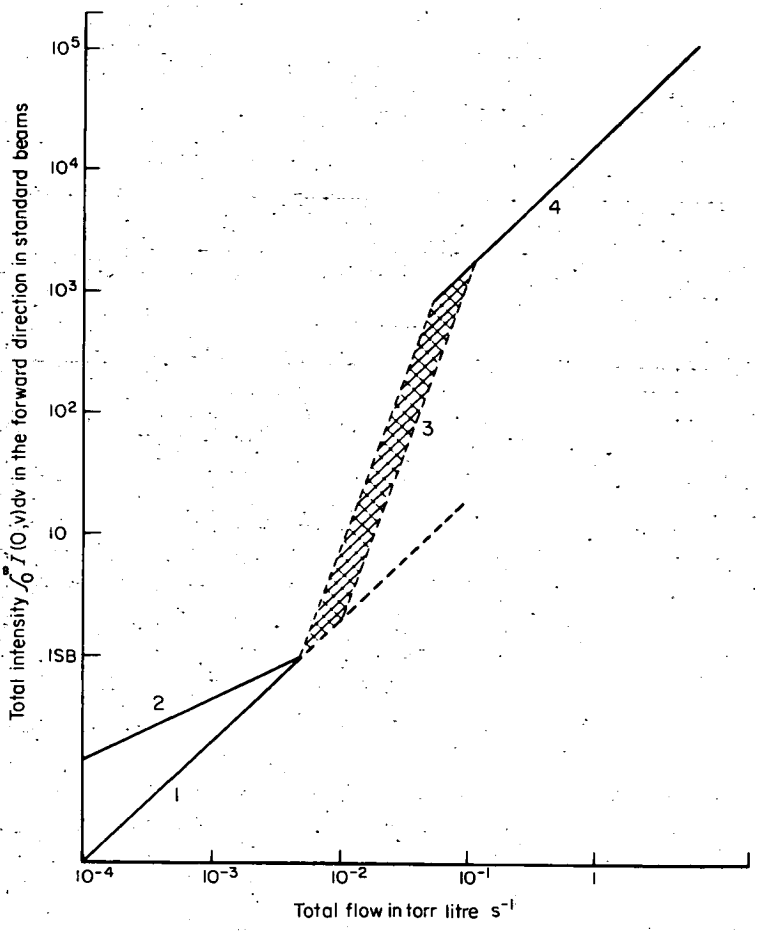

Fig. 3.12 Calculated comparison between
(1) Slit effusion source
(2) Multi channel effusion source
(3) Nozzle source (transition region)
(4) Nozzle source (hydrodynamic flow) $M = 10$
Aperture area same for all sources. Reproduced from H. Pauly and J. P. Toennies, 1968.

beam energy available being roughly:

$$E = \int_0^{T_{nozzle}} C_p dT \qquad (3.32)$$

i.e. a few tenths of an eV at normal operating temperatures.

(iii) Constructional details

In a nozzle source the major design consideration will be the provision of sufficient pumping speed to handle the large gas flows produced by this type of source. As already discussed (Section 3.3) this will inevitably involve several stages of differential pumping. Much of the design effort will be expended in securing a compact design, minimising the beam path length but at the same time providing sufficient pumping speed along the beam. If the beam materials are condensible the pumping requirement is considerably eased since cryogenic pumping can be used. Other considerations will be the operating temperature of the nozzle and any corrosion problems.

A typical nozzle source (J. G. Skofronik, 1967) developed for beam experiments is shown in Fig. 3.13. The nozzle, skimmer and collimator were accurately machined from brass and precisely aligned in an aluminium mount. The nozzle is arranged to slide in this mount so that the nozzle skimmer distance can be varied during operation. The external angle of the skimmer was 86° and its internal angle 70°. The nozzle chamber was pumped by a 40 cm oil diffusion pump and the collimation chamber by a 10 cm one. The operating pressures were 200 torr stagnation pressure in the nozzle, 5×10^{-5} torr in the skimmer chamber and 10^{-6} torr in the collimator. With this system the observed intensity shows a maximum as the skimmer nozzle distance is varied. For N_2, H_2 and He beams intensities of 4×10^{18}, 3×10^{19} and 1.5×10^{19} molecules sr^{-1} s^{-1} were achieved.

A rather simpler design for alkali metals has been described by E. Hundhausen and H. Pauly, 1965. In essentials their source is simply an effusive oven fitted with a narrow convergent divergent slit. It is operated at much higher pressures than appropriate for an effusion source and is provided with sufficient pumping in the form of cryo panels to handle the vapour load. In another series of experiments using an inhomogenous magnetic field to separate the paramagnetic K atoms from K_2 it was shown that the dimer concentration was not markedly different from that obtaining at equilibrium in the nozzle chamber provided that the expansion was not taken beyond Mach 10. At higher expansions the fraction of dimers rose rapidly (D. Morgenstern and D. Beck, 1967).

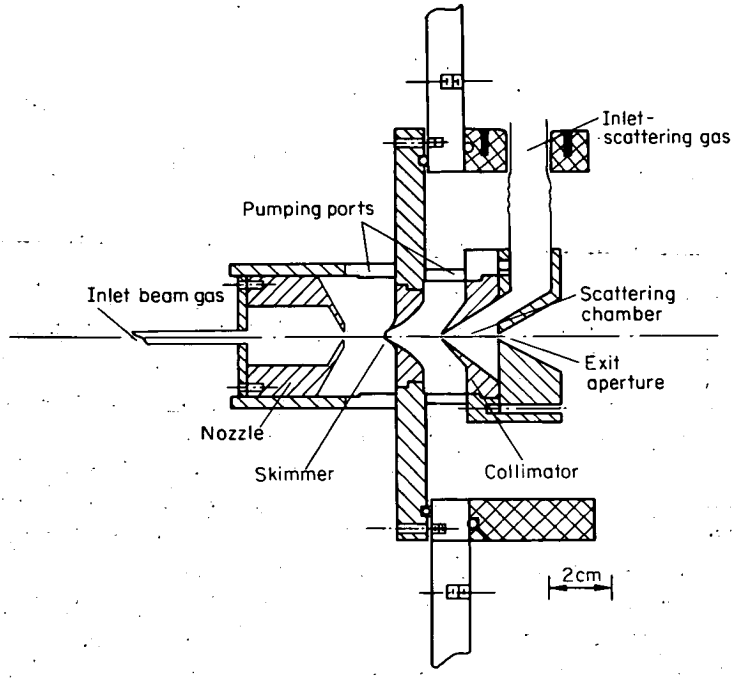

Fig. 3.13 Nozzle source for non-condensibles (J. G. Skofronik, 1967). The figure also shows the scattering chamber used with this source.

A design using liquid He pumps is shown in Figs. 3.14 and 3.15. Intensities for Argon of 4×10^{18} molecules $sr^{-1}\ s^{-1}$ were obtained.

Nozzle sources have also been used to produce beams of dissociated atoms by combining the nozzle source with an R.F. discharge. In Fig. 3.16 a source developed to produce O atoms is shown. Here the nozzle chamber incorporates an R.F. loop so that a discharge may be maintained in the range 15–70 torr. The gas feed to the nozzle was a mixture of 95 percent He and 5 percent O_2. With this gas mixture the O_2 is approximately 30 percent dissociated by the discharge.

Since the helium is present in large excess the bulk flow velocity through the nozzle and into the skimmer is governed by the helium. The oxygen atoms and molecules ride with the jet as passengers at almost the same bulk speed as the predominant helium. The heavier O and O_2 are thus accelerated into the beam with velocities equal to the helium atoms, corresponding at their heavier mass, to energies much above thermal. For the system described an O atom flux of 10^{17} atoms $sr^{-1}\ s^{-1}$ with translational energies up to 0.33 eV was obtained.

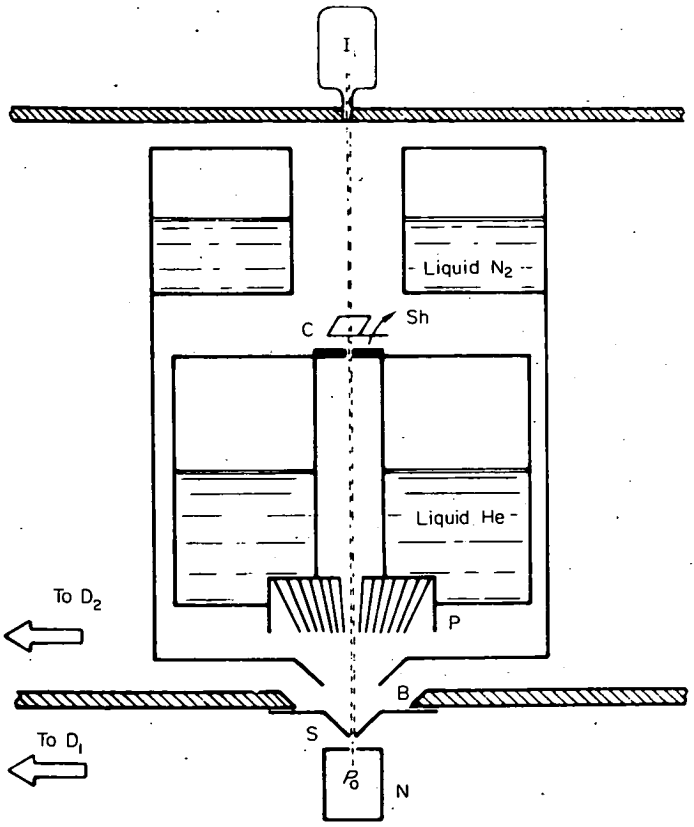

I = Ionization gauge detector
Sh = Shutter
C = Collimator
P = Cryopump
B = Shield opening
S = Skimmer
N = Nozzle
D_1 = 10 000 l s^{-1} booster diffusion pump
D_2 = 10 l s^{-1} diffusion pump

Fig. 3.14 Nozzle source using liquid He cryopumps (G. Scoles and F. Torello, 1967).

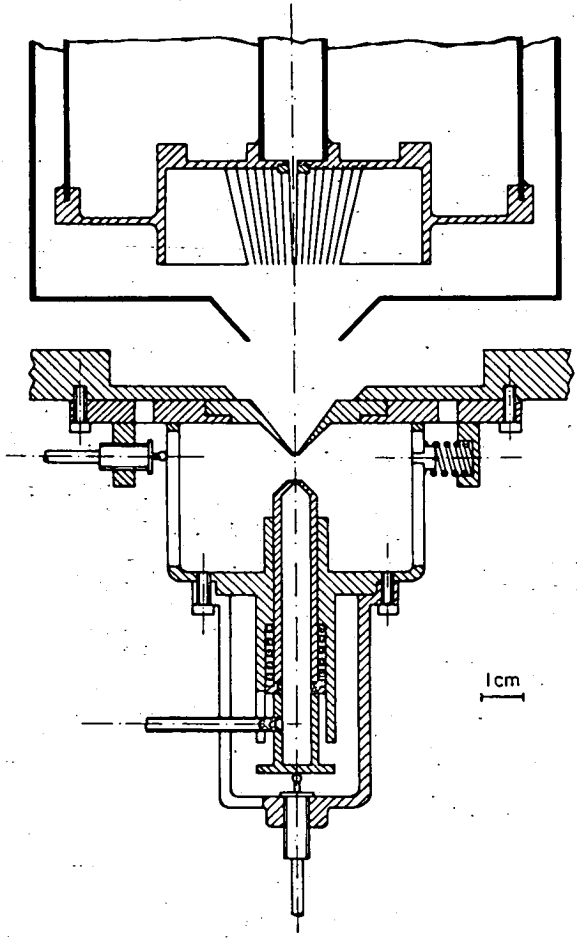

Fig. 3.15 Scale plan of nozzle source shown in Fig. 14 (G. Scoles and F. Torello, 1967).

3.5 Beam sources – superthermal energy

A wide range of techniques has been used to produce beams with energies above those obtainable thermally. The lower end of this energy range 1–20 eV has proved the most difficult one in which to work. This is particularly disappointing since this region is the most interesting of all to chemists embracing as it does the dissociation energies of all chemical bonds and the activation energies for most chemical reactions. In this region nozzle sources have been pressed into service either by running them at elevated

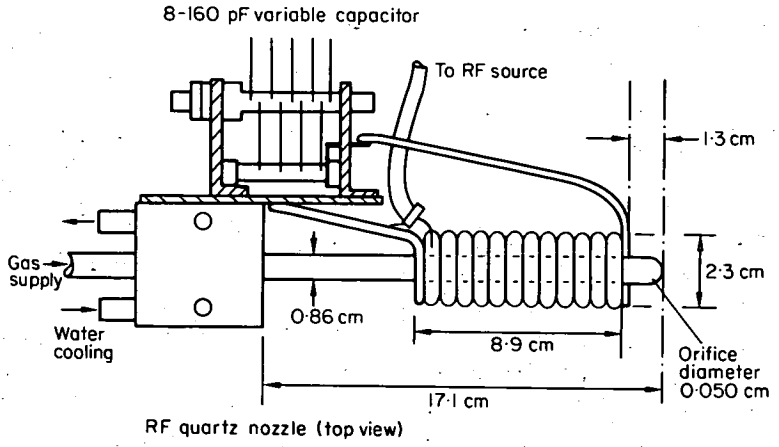

Fig. 3.16 Nozzle source with R.F. discharge to produce O atoms in mixed O_2/He 95% gas (D. R. Miller and D. F. Patch, 1969).

temperatures or by using the 'seeded beam' technique mentioned in the previous section. Recently a sputtering technique has also been used in which a solid target of the beam material is bombarded by high energy ions and the sputtered material collimated and velocity selected to form a beam.

In the energy range above 20 eV the charge exchange source is paramount. Here the beam material is first ionized and focused into a well defined and reasonably monoenergetic ion beam. This ion beam is then neutralized, usually by running it through a thin gas target of the beam material itself so that resonant charge exchange occurs. This technique is extremely convenient but limited in intensity at low beam energies by space charge effects.

(i) Nozzle sources for energies above 1 eV

The seeded beam method of aerodynamic acceleration can be applied to any heavy species. In this method a small percentage, e.g. 1–5 percent of the heavy beam molecule is mixed with a light inert carrier gas, usually helium, and expanded through a nozzle. The bulk flow rate is determined by the helium mass, the beam molecules riding along at this velocity. The final beam produced by skimming and collimation in the usual way thus consists of low energy helium atoms plus the high energy beam species. The technique is especially useful since it can be applied to fragile molecules that would not withstand acceleration by more violent means such as high temperatures. The energy, E, available with this method assuming that the heavy particles are

accelerated to the same velocity as the light carrier gas, is:

$$E = \frac{M_{\text{beam}}}{M_{\text{carrier}}} \int_0^{T_{\text{nozzle}}} C_p dT \qquad (3.33)$$

where M_{beam} and M_{carrier} are the molecular weights of the beam and carrier molecules.

In practice some degree of 'slip' occurs between the velocities of the two species. For small mole fractions the slip is quite small. This technique has been applied to a wide range of species, Fig. 3.17. Intensities are typically 10^{16} molecules sr^{-1} s^{-1}. For experiments in which the presence of the carrier gas in the beam is no disadvantage this technique is likely to be most valuable.

Another approach to producing fast beams from nozzle sources has used a plasma jet technique (R. W. Kessler and B. Koglin, 1966). Here the nozzle is arranged so that an arc can be burnt in the nozzle itself, thus raising the effective stagnation temperature to several thousand degrees. A device of this type, Fig. 3.18 has produced Ar beams of 3 eV energy and an intensity of the order 10^{19} atoms sr^{-1} s^{-1}. The further combination of this type of very high temperature source with the seeded beam method could lead to even higher energies, e.g. 20 eV for Ar in Ar/He mixtures.

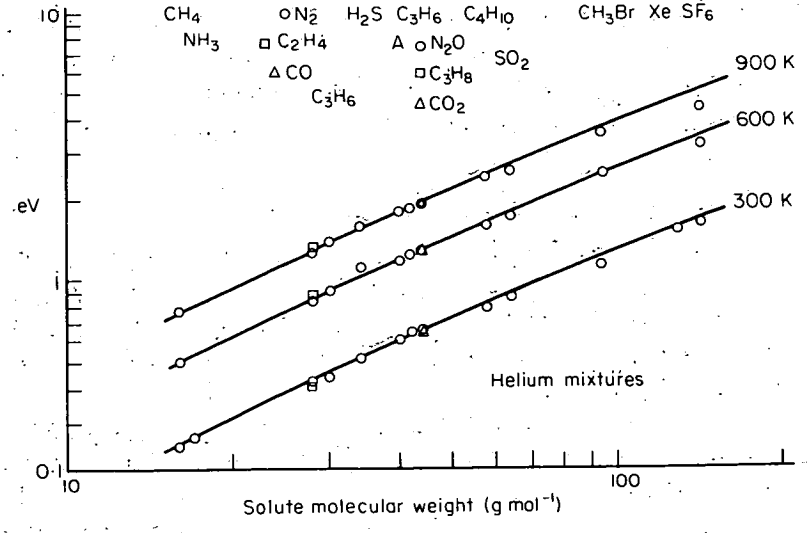

Fig. 3.17 Examples of molecules accelerated aerodynamically in Helium mixtures. (Reproduced from N. Abuaf, 1966). Molecular species are shown above their respective data points.

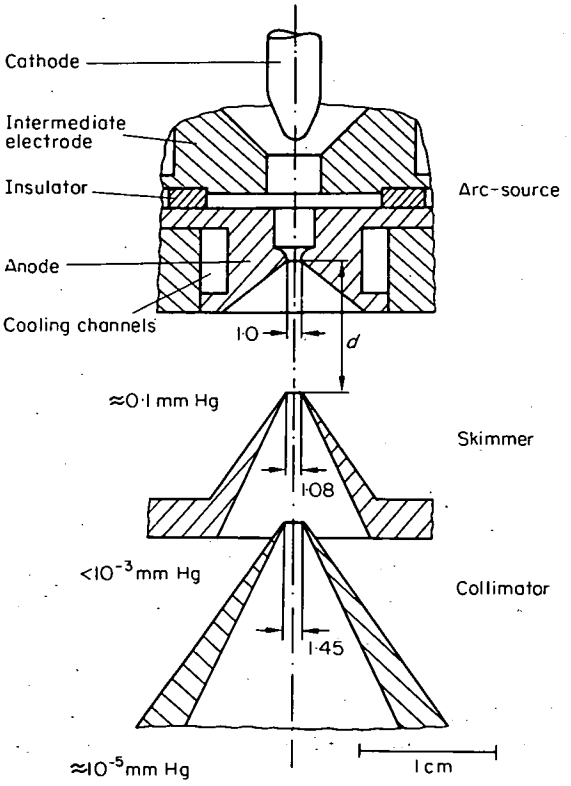

Fig. 3.18 Arc nozzle source (R. W. Kessler and B. Koglin, 1966).

Heating the gas in the nozzle chamber by a shock source can yield even higher intensities (G. T. Skinner, 1966). A system for beam production using this technique is shown in Fig. 3.19. Very high intensities of the order 10^{21} molecules $sr^{-1}\,s^{-1}$ at 2 eV can be obtained. Unfortunately the source is of necessity intermittent providing a beam pulse of only a few miliseconds duration and of poor duty factor. Correspondingly the pumping requirements are modest since the experiment is complete before the base gas pressure has risen. A disadvantage is the rather ill characterized nature of the particles in the beam, e.g. metastables may be present.

(ii) Sputtering sources

The sputtering of a solid target by energetic ion beams has been developed by the Amsterdam group to yield a very useful beam (J. Politiek et al., 1968). The device is shown in Fig. 3.20. The distribution of velocities in the ejected

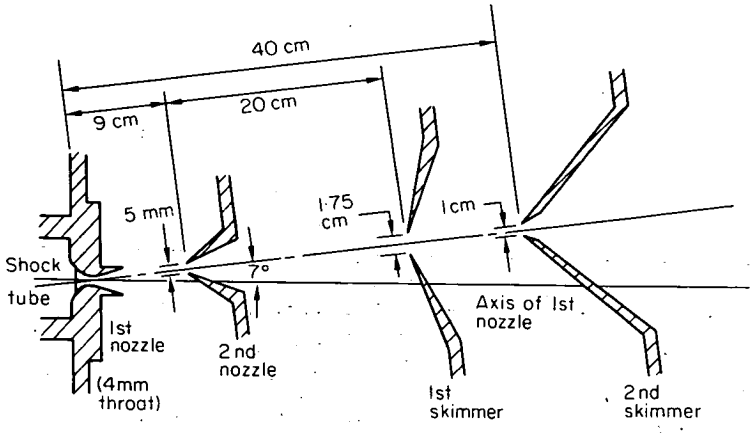

Fig. 3.19 Nozzle beam source with shock tube driver (J. B. Fenn, 1968).

atoms is relatively broad ranging from 0.2–45 eV for K, so that a velocity selector is essential. The intensity distribution for a K beam (though the device is not limited to alkalies) is shown in Fig. 3.21. Intensities appear to be $\sim 10^{13}$ atoms sr^{-1} s^{-1}, rather low.

(iii) Charge exchange beam sources

Sources of this type depend upon the fact that the cross-section for the resonant charge transfer process, i.e.

$$X^{+}_{\text{fast}\rightarrow} + X \rightarrow X + X^{+}_{\text{fast}\rightarrow}$$

is very much larger than the momentum transfer cross-section. If a well focused ion beam with a narrow energy distribution is passed through a thin gas target of the parent species charge transfer occurs with high probability. Furthermore the neutral species so provided retain most of their original directivity and energy distribution. The unexchanged ions can finally be swept out of the beam by a deflection field to leave the fast neutral beam. The technique is illustrated schematically in Fig. 3.22.

This ion technique is extremely convenient since while still ionized the beam may be mass analysed, deflected, modulated, etc., in a straightforward manner. The major drawback is that only relatively low intensities can be obtained, particularly at the lower beam energies, i.e. $\lesssim$20 eV.

This difficulty is a fundamental one due to the mutual repulsion or space

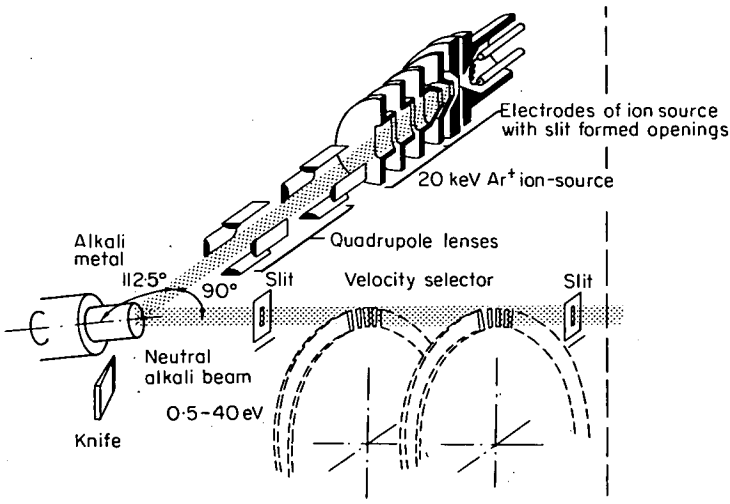

Fig. 3.20 Sputtering source for neutral beams (J. Politiek et al, 1968).

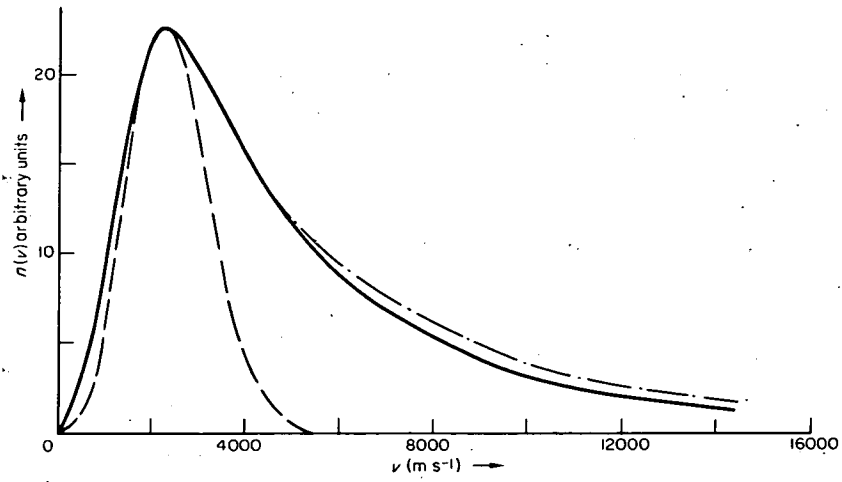

Fig. 3.21 Velocity distribution from a sputtering source. Dotted line ---- is flux calculated for an effusion source at same temperature. The other two lines represent measurements with a single and multi bounce surface ionizing detector. (J. Politiek et al., 1968).

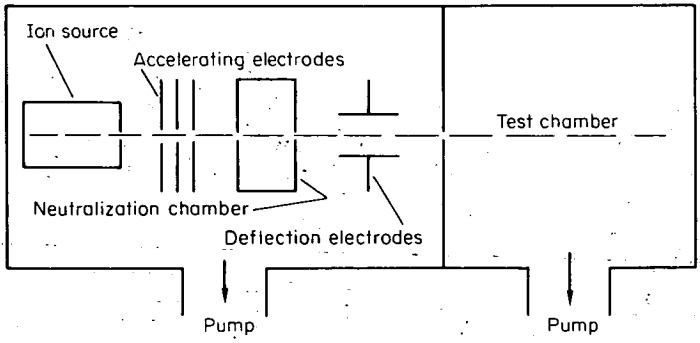

Fig. 3.22 Schematic arrangement of a charge neutralization beam source.

charge effects which limit the density that can be obtained in an ion beam. Very careful work indeed is needed to produce ion beams with energies below 5–10 eV.

The maximum ion current that can be focussed into a beam of divergence γ with energy V eV is:

$$I_{max} = 4.67\,\pi\epsilon_0 \left(\frac{e}{2M}\right)^{1/2} \times V^{3/2} \tan^2 \gamma \qquad (3.34)$$

where e is the electronic charge and M the mass of the ion.

Beam fluxes after neutralization are necessarily less than this. In practice neutral fluxes of the order 10^{12} atoms sr^{-1} s^{-1} at 5 eV rising to 10^{16} at 100 eV have been obtained. At the lower energies this is many orders of magnitude less than that obtainable by seeded nozzle beam methods.

The actual production of these ions may be via electron bombardment as in the Nier source or by plasma discharges as in the duoplasmatron source. Alternatively some use has been made of surface ionization techniques since these may yield more monochromatic ion beams. The detailed design of these sources and their attendant lens and mass focussing systems has been discussed widely by other authors and is a major field in itself. We confine ourselves here to referring readers to these other texts (J. B. Hasted, 1964; J. R. Pierce, 1954).

A particularly simple and attractive surface ionising device described by R. K. B. Helbing and E. W. Rothe, 1968, is shown in Fig.3.23. The ionization, acceleration and neutralization all take place in a single chamber filled with alkali metal vapour, resulting in a particularly simple design. The ions are formed by ionization on a tungsten wire and are then accelerated by a potential towards a mesh screen. Some of the accelerated ions are then

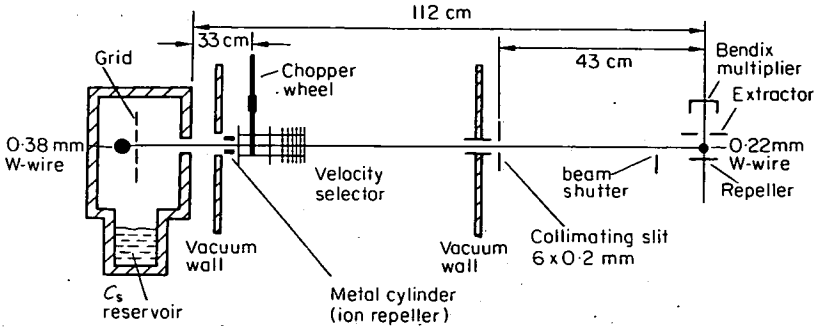

Fig. 3.23 Fast neutral alkali source. Exit slit on source box is 1.6 x 6 mm, a baffle (not shown) is installed above the Cs reservoir to prevent splashing on the electrodes (R. K. B. Helbing and E. W. Rothe, 1968).

neutralized by collision with the neutral alkali vapour and exit via the slits. The velocity distribution produced by this source was narrower than the resolution of the selector (6 percent) used to investigate it. This source seems particularly attractive at the lowest beam energies ~6 eV.

A more conventional exchange source is shown in Fig. 3.24 (B. S. Duchart, 1971). Here ionization of alkali metals is brought about by surface ionization on a porous tungsten disc, the alkali diffusing through from a chamber to the rear. The disc is heated to 1500°C by a radiation heater so that ionization is more than 90 percent complete for potassium. The resulting ions are extracted at a few hundred volts, accelerated in a second lens stage, steered by a series of X, Y deflection plates (which may also be used to pulse the

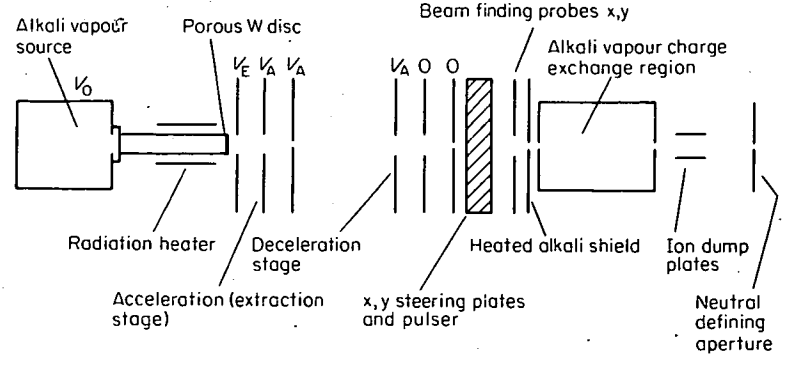

Fig. 3.24 Charge neutralization neutral beam source using surface ionization (B. S. Duchart, 1971)

beam for time of flight measurements) and finally enters the charge exchange chamber. This chamber is filled with alkali metal vapour by careful temperature regulation of a reservoir contained in the same chamber.

This system produced a neutral flux of $\sim 10^{14}$ atoms sr^{-1} s^{-1} at 100 eV. The energy spead in the neutral beam as measured by time of flight methods was ~0.1 eV.

3.6 Sources for Excited Species

The production of beams of excited species is an important requirement since the scattering technique is uniquely suitable for studying the collision properties of such short lived species. The production of translationally hot atoms has already been discussed, here we consider species with internal excitation. The lifetimes of these species in the absence of collisions may be $>10^{-3}$ s for some metastable atoms down to 10^{-8} s for species with an optically allowed electronic transition to the ground state. Depending upon the species required the state may either be generated specifically or selected from a much larger mixed population (e.g. from a thermal equilibrium distribution). The selection devices are described in Chapter 4.

In general these techniques are simply a combination of the methods used to produce excitation in bulk experiments with the beam production methods already described. The most important are thermal, electron impact, optical pumping and chemical reaction.

(i) Thermal dissociation sources

This is perhaps the simplest technique and is suitable for exciting states with an energy comparable to kT for the oven or arc source used. It is thus suitable for producing most dissociated atomic species (except N) and the ground state fine structure levels of B, Al, Ga, In, Tl, Cl, Br, etc. The major problem with these sources are corrosion and in the dimensional instabilities which can occur at high operating temperatures.

A typical design for a dissociated atom source is shown in Fig. 3.25 (M. A. D. Fluendy et al., 1967). It consists of a hollow cylinder of tungsten (or graphite if for use with halogens) fed with gas at one end and heated electrically by a current ~600A. A slit of width 25μ is machined in its side through which the atoms emerge. Two water cooled copper or nickel clamps provide electrical connections and secure the cylinder, which it clamped tightly at one end. At the other end expansion can occur between spring loaded jaws. With this source, intensities for H atoms of $\sim 10^{18}$ atoms sr^{-1} s^{-1} were obtained. A similar device with a graphite tube has been used for Br and I

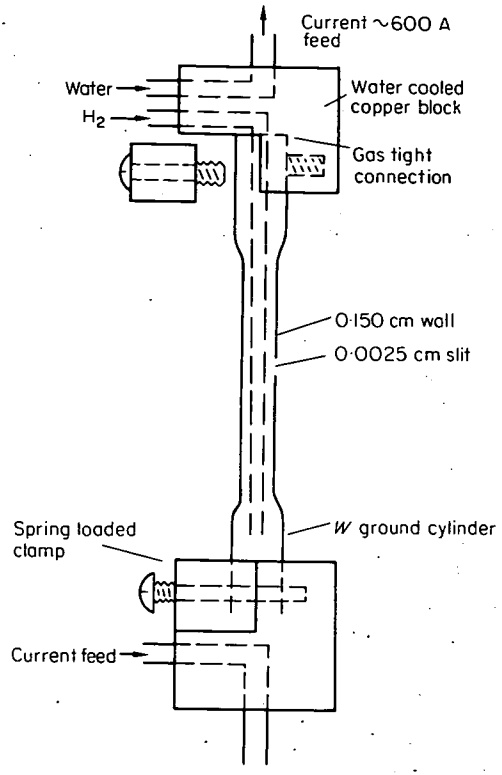

Fig. 3.25 Thermal dissociation source for atomic hydrogen. The tungsten tube is heated by a 600A a.c. supply coupled via the water cooling pipes. The tungsten tube is free to expand longitudinally between the lower spring loaded copper jaws. The whole copper block and tube assumbly is mounted rigidly on a carriage adjustable from outside the vacuum (M. A. D. Fluendy et al., 1967).

atoms (Y. T. Lee et al., 1969). Iodine can also be dissociated in a monel oven if gold slits are used (M. A. D. Fluendy et al., 1970).

Arc nozzle sources have also been used to produce atom beams of high intensity. If problems of stability and corrosion can be overcome this is likely to be an important technique.

(ii) Electron bombardment sources

This technique is a useful one for states with a lifetime of 10^{-3} s or longer, i.e. metastable states. The first and most famous example is its use in the Lamb-Retherford experiment. Here an atomic H beam produced by thermal

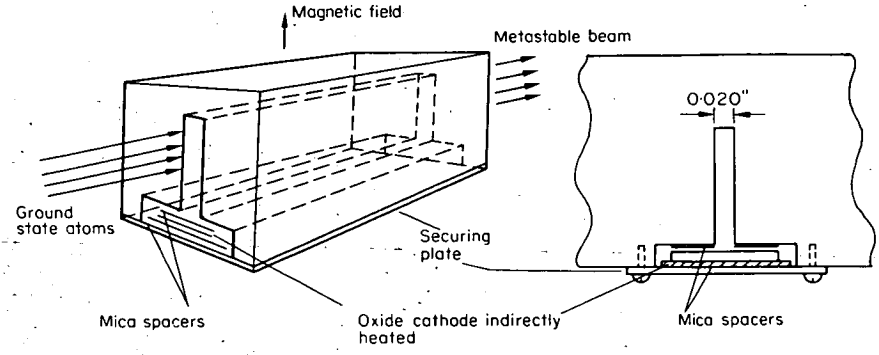

Fig. 3.26 Electron bombardment metastable source. A standard oxide cathode is used spaced ~0.008 cm from the stainless (nonmagnetic) steel anode by a mica sheet.

dissociation in a tungsten oven was crossed by an electron beam of controlled energy to excite the metastable state $H(2^2S)$.

A more recent source designed to produce metastables for scattering work is shown in Fig. 3.26. A standard oxide cathode provides a source of electrons which are accelerated into the slit in the anode through which a beam of Hg atoms in the ground state is passing. The electrons are collimated by a magnetic field. A typical excitation curve is shown in Fig. 3.27, peaks due to the $6^3P_{0,2}$ and ^3D states can be seen.

The use of an electron source with a reasonably narrow energy spread thus permits the selective generation of these species. Intensities of the order 10^{10} atoms sr^{-1} s^{-1} were obtained (E. C. Darwall, 1972).

The extension of the electron excitation method to molecular species such as metastable CO and N_2 also appears possible (R. S. Freund and W. Klemperer, 1967; R. Clampitt and R. S. Newton, 1969). Another possibility is the use of certain negative ion resonances which decay to specific vibrational states.

(iii) Discharge sources

R.F. and microwave discharges have been used for the production of dissociated atoms either in an inert gas carrier (Figure 3.16) or as a pure beam. The mechanism is presumably again electron bombardment dissociation. A microwave source for atomic chlorine is shown in Fig. 3.28 (L. Davis et al. 1949). The source was mounted inside a microwave resonant cavity and fed with 50 watts of power; between 30 and 60% dissociation was achieved. An

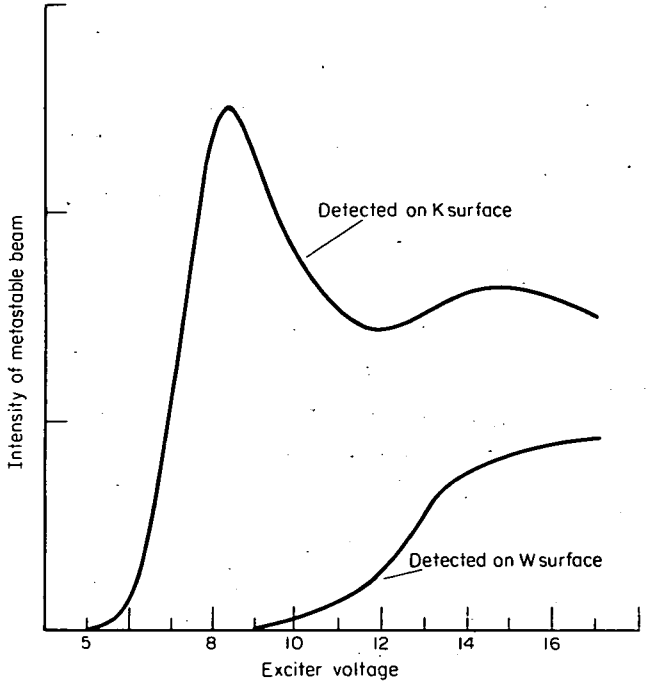

Fig. 3.27 Excitation curves observed for Hg using an electron bombardment source for metastable production (E. C. Darwall, 1972).

alternative source (D. S. Horne, 1969) is shown in Fig. 3.29 and uses an r.f. generator capacitively coupled to a quartz tube. Coating the inside of the tube according to the recipe of Ogryzlo (E. A. Ogryzlo, 1961) raised the Cl_2 dissociation from 36% at 0.8 torr to $>$ 90% at 0.5 torr. A disadvantage with these non equilibrium non specific excitation sources is the possible presence of metastable states in the beam.

(iv) Optical pumping

A technique similar to that described for electrons but using a photon flux as the exciting agent may be applied. The usefulness of this method depends very much upon the conjunction of a suitable absorption line and an intense light source. Even at saturation no more than 50% of the beam will be in the excited state. Depending upon the lifetime of the excited state the excitation may be applied either at the beam source or at the actual collision zone. If

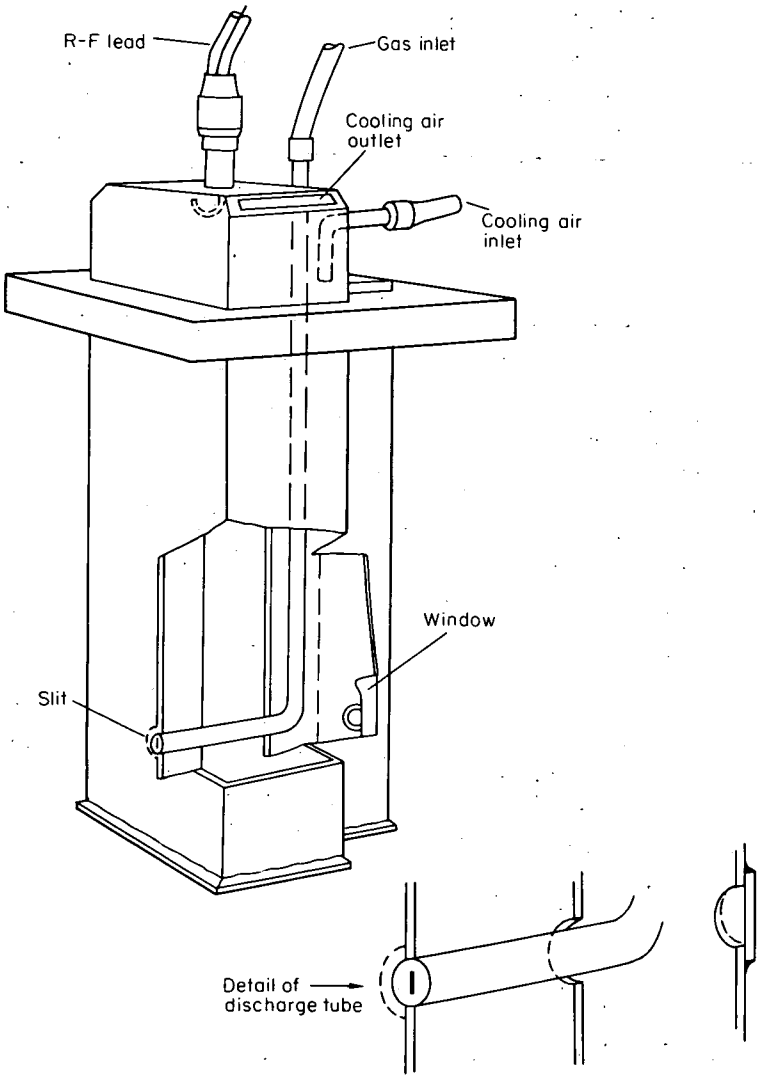

Fig. 3.28 Microwave discharge source for Cl atoms (L. Davis et al., 1949)

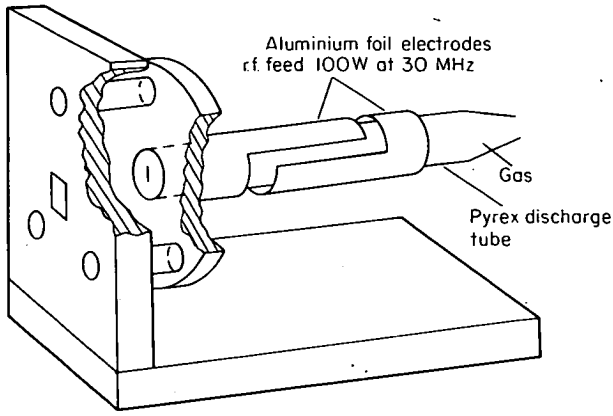

Fig. 3.29 r.f. discharge source for atomic chlorine (D. S. Horne, 1969).

applied at the collision zone states with lifetimes as short as 10^{-8} s will undergo collisions.

Microwave pumping of a vibration rotation line has also been used in conjunction with selecting fields to produce beams in a specified vibration-rotation state (T. G. Waech and R. B. Bernstein, 1968) and Chapter 4.

CHAPTER FOUR

Energy and State Selection

In a thermal beam source a wide range of rotational and translational states are populated. This population, with some modification if there is hydrodynamic flow at the orifice, will persist in the emerging beam. The ideal beam experiment requires complete selection of the quantum states of both collision partners, but we will find that this ideal is only partially achieved. Translational energy selection, through velocity selection, is always possible. Spin, rotational and even vibrational states can be selected but these cases are not yet numerous, comprising perhaps a dozen atoms and molecules.

State selection and focusing are often achieved simultaneously. If a molecule passing through the selecting device executes simple harmonic motion in its lateral movement then the possibility exists for focusing and the focal length will, in general, depend on the quantum state of the molecule. In designing a scattering experiment incorporating some state selection, the loss in intensity that results from using only a small fraction of the parent beams might seem to be crippling. In general, if more than one property is being selected in a beam (e.g. velocity + orientation) or if both beams are being selected (e.g. for velocity) then one of the selectors must have a focusing capability to recoup intensity.

The performance of these devices is ultimately limited by the constraint provided by the Liouville equation in that the density in phase space of the parent beam cannot be increased. Selectors may therefore isolate small volumes from this population, may accelerate them to other regions of phase space or distort them in other ways. They can never increase the density of molecules within a specified range of state parameters so that sources with a low characteristic temperature are desirable.

In some cases it is possible to alter the population of quantum states by optical pumping. The limit to the population change comes when the temperature (electronic, rotational etc., as appropriate) of the sample reaches that of the source of radiation. The effect of such population changes in a beam on scattering from the beam depends upon the lifetime of the excited state and is an interesting but, as yet, little used tool and will not be discussed further here (R. E. Drullinger and R. N. Zare, 1969).

4.1 Velocity selection

Almost every scattering phenomenon is velocity or energy dependent. In Chapter 2 it was found that the classical differential and total cross-sections for scattering under the influence of any potential, other than the hard sphere, were velocity dependent. In Chapter 6 it will be shown that the new effects that arise when quantum mechanics is applied to scattering, which may be generally classed as interference effects, are also velocity dependent. Furthermore, it is commonly found in chemical kinetics that reaction rates are an exponential function of temperature and this implies that the reaction cross section is energy dependent. Finally, it has been seen that the apparatus resolution depends upon the beam velocities, as does the Jacobian for transforming between laboratory and centre of mass co-ordinates.

Much information will thus be lost, together with one of the unique capabilities of beam experiments, unless scattering patterns are measured as a function of the relative velocity of the beam particles. Velocity filters select molecules whose velocity falls within a segment of the parent velocity distribution and we define the velocity resolution as the width Δv of this truncated distribution at half intensity divided by the median velocity transmitted. An important question in the design of the beam experiment is the amount of velocity resolution that is required and the amount that is practicable, having regard to the available beam intensity.

The usual requirement in the total cross-section experiment is that sufficient velocity resolution be available to identify the quantum 'glory' oscillations in the cross-section. The origin of these interference effects is discussed in detail in Chapters 6 and 7; suffice it at this point that these undulations are located at velocities v_n such that:

$$v_n \sim \epsilon\sigma/\hbar N \tag{4.1}$$

where ϵ,σ are the potential parameters and $N = 1, 2, 3$ indicates the first, second, third etc., oscillations in the cross section (counting from high

velocity downwards). Thus to resolve these oscillations up to M, we need a resolution:

$$\frac{\Delta v}{v} \ll \frac{v_M - v_{M-1}}{v_M} \sim \frac{1}{M-1} \tag{4.2}$$

and generally $M \lesssim 5$.

As already seen in Chapter 2 the gross features of $\sigma(\theta)$ versus θ plots at different energies are superimposed to a good approximation by plotting $\sigma(\theta)$ against $E\theta$. The resulting spread in $\sigma(\theta)$ due to simultaneous uncertainties in v and θ is then:

$$\frac{\Delta\sigma(\theta)}{\sigma(\theta)} \propto 2\,\frac{\Delta v}{v} + \frac{\Delta\theta}{\theta}\,. \tag{4.3}$$

Thus if the angular resolution $\Delta\theta/\theta$ required to resolve a given feature in the differential cross-section is known the velocity resolution $\Delta v/v$, required will be approximately half this. The question of angular resolution has already been discussed in Chapter 3 and will be considered further in Chapter 7.

The price paid in intensity for this level of resolution depends upon the velocity distribution in the parent beam. For a v^3 Maxwellian distribution, the fraction of molecules with velocities within $\pm\,\Delta v/2$ of the most probable velocity v^* is

$$f_{\Delta v} \approx 1.00\Delta v/v^* \tag{4.4}$$

Velocity resolution 1–10 per cent is commonly aimed at.

In an orthogonal crossed beam experiment, the relative velocity v_r is given by

$$v_r = \sqrt{v_A^2 + v_B^2} \tag{4.5}$$

and if $v_A \gg v_B$, $\Delta v_r/v_r \approx \Delta v_A/v_A$ and the faster beam only is velocity selected. If the unselected beam has a v^3 Maxwellian distribution, the full width at half intensity $\Delta v_B/v_B^*$ is ≈ 0.95. Substituting this into the expression for the overall spread in the relative velocity:

$$\Delta v_r/v_r \approx \Delta v_A/v_A \left(\frac{v_A}{v_r}\right)^2 + \Delta v_B/v_B \left(\frac{v_B}{v_r}\right)^2 \tag{4.6}$$

sets a lower limit on $\Delta v_r/v_r$ of $\approx (v_B/v_r)^2$, though it must not be forgotten that the spread in cross beam velocity also introduces a spread in the direction as well as the magnitude of v_r.

Velocity selection of neutral particles is usually performed mechanically by passing the beam through a series of phased choppers so that only those molecules moving in a narrow velocity band arrive at each chopper as it opens and so are transmitted (Fig. 4.1). The actual form of the device varies but is typically a series of thin slotted discs locked together and rotating about an axis parallel to the beam direction. The principle is an old one (J. A. Eldridge 1927), has been improved in the last two decades (R. C. Miller, and P. Kusch, 1955; H. U. Hostettler and R. B. Bernstein, 1960; J. Wykes, 1969) and the size has progressively decreased, the slots now being cut by photo-etching. Occasionally space can be saved by adopting a slightly different geometry (L. T. Cowley et al., 1970; A. E. Grosser et al., 1963; S. O. Colgate and T. C. Imeson, 1955) in which the beam passes across the surface of toothed concentric cups, Fig. 4.2.

For discs of negligible thickness, design is simple with the aid of a diagram of the type shown in Fig. 4.3. The motion of a molecule is displayed relative to the discs as stationary so that a tangential component v_c is added to the forward molecular velocity v_m, where v_c is the peripheral speed of rotation of the discs. The trajectory of the molecule then makes an angle α with the axis of the rotor, where

$$\tan \alpha = v_c/v_m$$

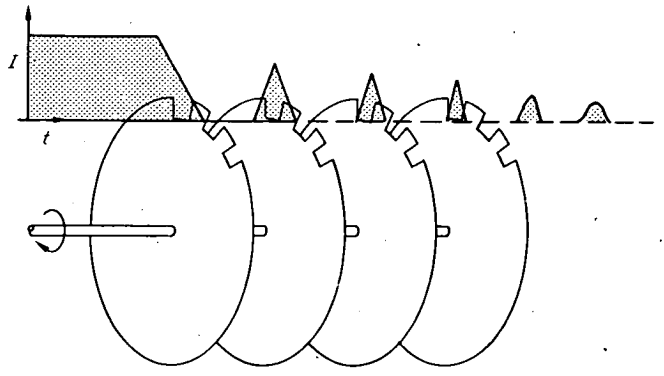

Fig. 4.1 A multi-disc velocity selector. Some of the particles in each pulse arrive at the next disc in time to pass through a slot.

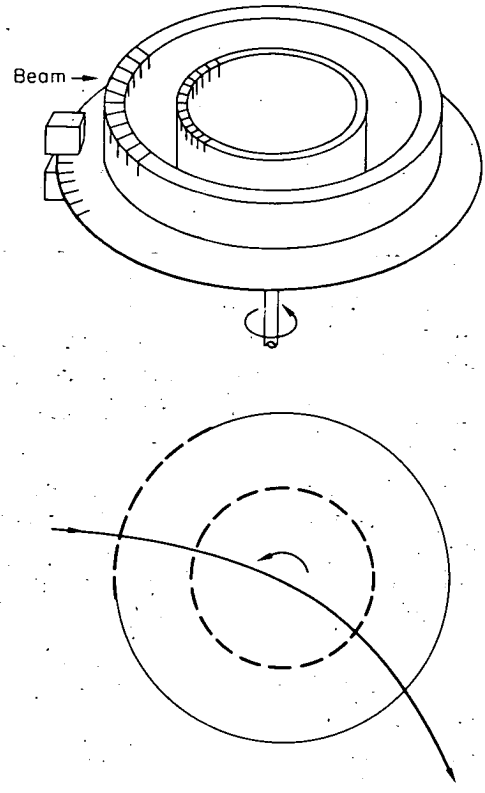

Fig. 4.2 Alternative design of velocity selector using only the motor bearings.

Molecules will be transmitted when:

$$\tan \alpha = \Delta/L$$

where Δ is the offset of the exit slit from the entrance slit (see Fig. 4.3) and L is the distance between first and last discs. The median velocity transmitted is

$$v_m = 2\pi R\omega L/\Delta = v_c L/\Delta \qquad (4.7)$$

where $2\pi R\omega$ is the peripheral speed of the selector disc, v_c. Typical speeds of rotation are 10,000 – 20,000 r.p.m., leading to values for $v_c \sim 5 - 10 \times 10^3$ cm s^{-1} for discs ~5 cm radius – approaching molecular velocities and strength of materials limitations.

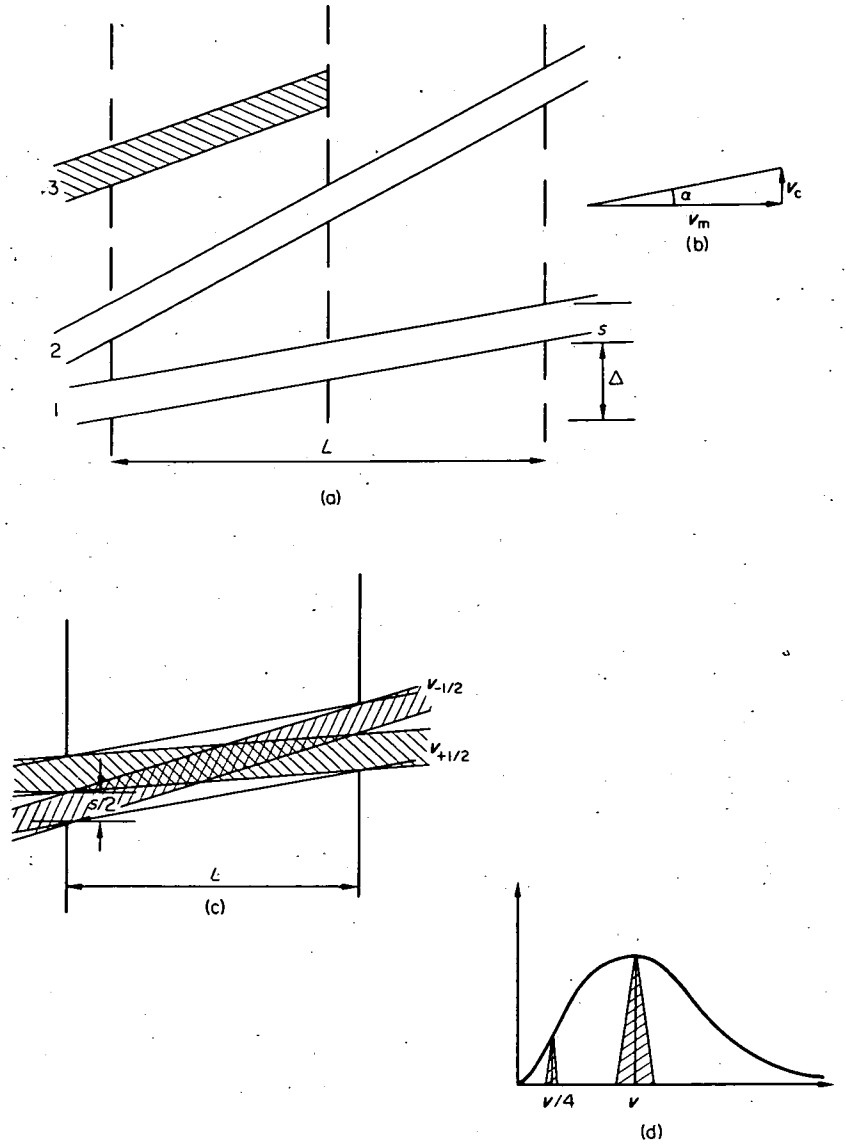

Fig. 4.3 The design of a slotted disc selector. (a) Molecules with the design velocity (1) are transmitted, but so are those (2) with ¼ of this speed. Those moving with ½ the design speed are stopped on the face of the second disc. The offset of each disc is determined from the vector diagram (see Equation 4.7), (b). The half width of the velocity bands transmitted is calculated from (c) in which only half those molecules with speeds $v_{\pm ½}$ (shaded) are transmitted. (d) is the resulting velocity distribution (shaded), in which the outer envelope is the parent distribution.

The resolution of a mechanical selector of the parallel disc type is determined solely by the slit width S and the separation L. If the velocity distribution in the incident beam is effectively constant over a range of velocities transmitted (as would be the case for a high resolution selector working at the most probable speed in a Maxwellian distribution) the velocity distribution of the transmitted particles is triangular. The velocities at half intensity of this distribution, $v_{\pm\frac{1}{2}}$, are found from the condition that molecules travelling with these speeds are only transmitted if they enter the first slit before it is half open for $v_{-\frac{1}{2}}$ or when it is between half and fully closed for $v_{\frac{1}{2}}$. From Fig. 4.3(c),

$$\tan \alpha_{\pm\frac{1}{2}} = (\Delta \pm S/2)/L$$

so the velocity resolution for a particular band (full width at half height) when $v_c \ll v_m$ is:

$$\mathcal{R}_{\frac{1}{2}} = \frac{\Delta v}{v_m} \simeq S/\Delta \tag{4.8}$$

Thus once the working velocity and resolution required have been decided substitution into Equations 4.7 and 4.8 will yield simple relations for the selection of rotation speed, selector length and slit width.

It is usually desirable to keep the selector length as short as possible to minimise $1/L^2$ losses in intensity. The design then reduces to determining the maximum tip speed that can be produced and the smallest slit width practicable. A typical set of dimensions is:

Speed of rotation ω	10 000 rpm
Radius of disc R	5 cm
peak transmitted speed v_m	5×10^4 cm/s.
Slit width S	1 mm
Length L	10 cm
Overall offset $\Sigma\Delta_i$	1 cm
Resolution $\mathcal{R}_{\frac{1}{2}}$	± 5%

Mechanical velocity selectors become rapidly less useful at molecular speeds above 10^5 cm s^{-1}. From Equation 4.7 it is seen that as v_m increases, either (i) ω must increase in proportion or (ii) L must increase in proportion or (iii) Δ must decrease in proportion to v_m. If solution (i) is adopted, an upper limit is set by the mechanical strength of the discs; (ii) results in

increasing loss of intensity ($\alpha\ 1/L^2$); (iii) has the disadvantage that in order to maintain the same resolution with increasing v_m, the slit width S must be decreased in proportion to Δ (from Equation 4.8). If slits are to be made narrower than $\sim 0.002''$ machining and especially alignment problems arise. With $S = 0.002''$, and $\omega = 10\,000$ rpm $L = 10$ cm, the maximum speed transmitted with a resolution of 5 per cent is 10^5 cm s^{-1} and this perhaps can be doubled by changing some of the other design parameters. At higher velocities time of flight or methods depending upon magnetic deflection of the beam are more useful.

The overall transmission of the slotted disc selector can be defined for a *parallel incident beam* as

$$T = \left(\frac{nS}{2\pi R}\right) \mathcal{R}_{1/2} \tag{4.9}$$

so for $\mathcal{R}_{1/2} = 10$ per cent, $T \sim 5$ per cent when the tooth: slit width ratio is 1:1.

A two disc selector has the disadvantage of transmitting sidebands, that is, molecules whose speeds are certain rational fractions of the design speed v_m. How this arises can be seen from Fig. 4.3. In the design shown the exit channel for the design speed is indexed as $n + 1$, where the entrance slit is the nth. Inspection of the figure shows that, with only two discs, slower molecules can exit through slots $n + 2$, $n + 3$, etc., if they have speeds $v_m/2$, $v_m/3$ etc., and molecules having speeds $>2v_m$ (for equal tooth and slit widths) are transmitted through slit n. The fast molecules and those having $v = v_m/2$ are eliminated by inserting a third disc as shown; a fourth disc eliminates yet more sidebands and with five discs the elimination is virtually complete.

If the original beam is generated by flow through relatively long channels, there is a deficiency of slow molecules in the beam, and complete elimination of the slowest sidebands is not a pressing problem. A selector with fewer, thicker discs might be appropriate here, unless designed for very high speeds when a low moment of inertia is essential.

In an actual experiment, the incident beam is not parallel and the discs may have a thickness comparable to the slit width. Under these conditions, the transmission is best calculated by a computer sampling of trajectories through the device.

These selectors are normally driven by synchronous hystersis motors, ball bearings of the dry self-lubricating type being used throughout the selector and motor. Careful attention to the dynamic balance of the rotor as well as accurate alignment of the discs is required. It is usually essential to provide water cooling for the bearings and drive motor. Further constructional details

may be found in (J. L. Kinsey, 1966). In a crossed beam experiment, the full analysis requires that the velocity of the product as well as that of the incident particles be measured. Unless many inelastic channels are open, the velocity analyser need not have good sideband suppression and merely serves to pinpoint a particular process. In an experiment designed (K. T. Gillen et al., 1969) to find the correlation between the angle of inelastic scattering and the degree of internal excitation of the KI from the reaction $K + I_2$, a four disc selector was chosen for the incident K beam ($\mathcal{R}_{½}$ = 14.4 per cent), the I_2 beam was unselected and a six disc selector was placed in front of the detector ($\mathcal{R}_{½}$ = 4.7 per cent). A relatively coarse primary beam selector was appropriate because under the experimental conditions the velocity of the cross beam molecules was roughly one quarter that of the potassium.

4.2 Time of flight methods (T.O.F.)

There are at least two situations in which mechanical velocity selection is unsuitable. The first is when one of the beams is of unavoidably low intensity, e.g. a beam of metastable atoms. To insert a mechanical velocity selector would reduce the density of molecules at the scattering centre at least tenfold, in addition to the loss arising from the transmission factor, simply because of the increased source/scattering centre distance. This might well make the time taken to accumulate a statistically significant signal, impracticably long. Time of flight methods help here by simply not taking up any space – a single disc or deflecting plate is sufficient to chop a beam. Secondly, at energies above a few eV the length/speed of a mechanical velocity selector becomes inconveniently high, but T.O.F. techniques have an almost unlimited energy range.

The essence of the T.O.F. method is to chop one of the incident beams into a sequence of short pulses and to gate the detector in synchronism but with a measured phase and hence time lag. By scanning a range of time delays, a time of arrival spectrum (T.O.A.) of the scattered particles is built up. In its crudest form, the technique becomes identical with phase sensitive detection (see Chapter 5) in which relatively low chopping frequencies are used and the phase is not varied.

One of the earliest applications of the technique in beam work was that of S. N. Foner, 1966, who produced a chopped free radical beam of $\sim 50\mu$ sec. pulse width and gated a mass spectrometer detector over 20μ sec. periods. By this means, molecules reaching the detector directly were distinguished from those bouncing from the walls.

T.O.F. methods have been applied to pulsed supersonic beams, (energy ~ 1eV), in particular to the determination of the velocity distribution of molecules scattered from solid surfaces, e.g. (P. B. Scott, 1965), and to the determination of the velocity distribution in nozzle beams themselves (W. E. Amend, 1968). This technique is only possible if a detector of sufficiently fast response time is available (see Chapter 5) and will be most valuable in systems where rapid gating of the beam is also possible. Thus, beams of metastable species excited by electron bombardment may be gated for periods $\sim 10^{-8}$ s by pulsing the electron beam and an Auger detector for these species has a comparable response time. The technique is particularly fruitful in ion-molecule scattering where the highest energy resolution can be achieved (J. Schottler and J. P. Toennies, 1968).

There are not many general formulae that can be used in planning time of flight experiments. The key to the design is the calculation of the spreading of the initial pulse by the time it reaches the detector. This, in turn, determines the pulse repetition rate if undue overlapping of the pulses is to be avoided. The potentialities of the method can be illustrated by the process

$$K + I_2 \longrightarrow KI^{\dagger} + I, \quad \Delta E \sim 1.9\,\text{eV}$$

investigated between 5 eV and 100 eV. The purpose of the experiment is to map the angular distribution of the product KI and to measure its velocity in order to deduce its internal energy. We would like to measure the translational energy to ±10 per cent and hence the velocity must be known to ±5 per cent. The KI, whatever its internal state, is considerably delayed with respect to the elastically scattered K because of conservation of momentum requirements and so is easily distinguished by crude T.O.F. analysis.

The optimum set of values has to be found for the following parameters:

(1) The initial pulse width at source τ_s.
(2) The path length from source to scattering centre, L_s and from scattering centre to detector, L_d.
(3) The gate time for the detector, τ_d.
(4) The repetition rate, τ_R, which determines the duty cycle.

In deciding τ_s, the key factors are the extent of spreading of the pulse at the scattering centre and of the product pulse at the detector, due in both cases to the velocity distribution of the molecules leaving the source which would typically have a temperature of 1100°C – 1200°C. The order of magnitude of this spreading can be found by following the motion of a pulse that begins as a delta function in time. If the velocity distribution within this

pulse is initially v_i^2 Maxwellian (appropriate for ions emitted from a surface), electrostatic acceleration imparts a new velocity v_f to each molecule which is related to the initial velocity by:

$$\tfrac{1}{2}mv_f^2 = \tfrac{1}{2}mv_i^2 + eV_0 \tag{4.10}$$

where V_0 is the accelerating voltage. Substituting this into the original velocity distribution and re-arranging to give the number of molecules between v_f and $v_f + dv_f$, then introducing the time of arrival through $v_f = L/t$, we find the distribution of arrival times is given by:

$$n(t) \approx n^* \left(\frac{u}{u^*}\right)^{\frac{1}{2}} e^{\frac{1}{2}} e^{-u/2u^*} \tag{4.11}$$

where $\begin{cases} u = \dfrac{L}{t} - v_0, \quad v_0^2 = 2eV_0/m \\ u^* = \dfrac{L}{t^*} - v_0 \approx kT/2mv_0 \end{cases}$

and n^* is the peak arrival rate, $n(t^*)$, at t^*. The full width at half maximum (FWHM), i.e. $n(t_{\frac{1}{2}}) = n^*/2$, is found to be

$$\Delta\tau_\delta \approx 1.8 \frac{L}{v_0^3} \frac{kT}{m} \tag{4-12}$$

If the original pulse has a FWHM equal to $\Delta\tau_s$, this has increased on arrival at the detector to a value given by

$$\Delta\tau \approx \Delta\tau_s + \Delta\tau_\delta \tag{4.13}$$

for a δ-function pulse of potassium accelerated to 100 eV ($v_0 \approx 2 \times 10^6$ cm s^{-1}, $v_i^* \approx 8 \times 10^4$ cm s^{-1}) $\Delta\tau$ is approximately 5×10^{-8} s at 60 cm from the source; under these conditions initial pulse widths, τ_s, less than 10^{-7} s are unnecessary. The upper limit to τ_s, and hence the duty cycle, is determined by the velocity resolution required as we will see below.

More generally, if the initial pulse is not a Δ-function, the distribution in time of the intensity at time t is given by

$$I(L;t) = \int G(t') I_\delta (L; t - t')\, dt, \tag{4.14}$$

where $G(t)$ is the initial distribution in time. The spread in arrival of the product KI pulse can be calculated from Equations 4.12 or 4.14 (with $L = L_d$) if the new mean pulse velocity, v'. is known from the exothermicity. This contribution to the spreading can be added to the value of $\Delta\tau$ in Equation 4.13 if the latter is small.

Finally, the effect of the gate width of the detector, τ_d, on the apparent shape of the pulse must be computed. With an electron bombardment detector or gated counter, the detector function is essentially rectangular with a width typically $\sim 1\mu$ s in the present example. More generally, the measured pulse shape is given by

$$I_{obs}(L; t) = \int_{t'-\tau_d/2}^{t'+\tau_d/2} I(L; t - t')S(t')\,dt', \tag{4.15}$$

where $S(t)$ is the detector function, the open time being between the limits of integration.

Returning to our model calculations, the parent potassium pulse has now reached the cross beam where it generated a pulse of KI which then travels to the detector, spreading as it does so. We can form a picture of both the elastically and reactively scattered particles by integrating Equations 4.11 and 4.15 numerically. The results at 1 eV are displayed in Fig. 4.4, calculated with the assumption of an initial δ-function pulse and that all the exothermicity goes into relative motion. Using momentum and energy conservation conditions, the reaction exothermicity, ΔE, can be calculated from the time of arrival of the K and KI pulses, τ_K and τ_{KI}. For small angle scattering of the product the result is:

$$\Delta E = \frac{(L_s + L_d)^2}{2\tau_K^2}\left[\frac{m_{KI}M}{m_I}\left(\frac{L_d/L_s}{(1 + L_d/L_s)\tau_{KI}/\tau_K - 1} + \frac{m_K}{M}\right)^2 - \frac{m_K m_L}{M}\right] \tag{4.16}$$

where M is the total mass of the two molecules. The experimental uncertainty in ΔE can then be estimated from the uncertainty in the times of arrival of the pulses, $\Delta\tau_K$ and $\Delta\tau_{KI}$. The duty cycle can be decided from the criterion adopted for the resolvability of adjacent pulses. If a 50 per cent valley: peak ratio is demanded, then in the 1 eV example it is seen from Fig. 4.4 that the minimum delay time between K pulses is approximately 140 microseconds. The initial K pulse width (τ_s) can be made as long as 5 microseconds without sacrificing too much energy resolution so the duty cycle is 5 : 140, a rather poor figure. At 100 eV a duty cycle equivalent to an overall transmission of 30 per cent can be achieved. In contrast to mechanical

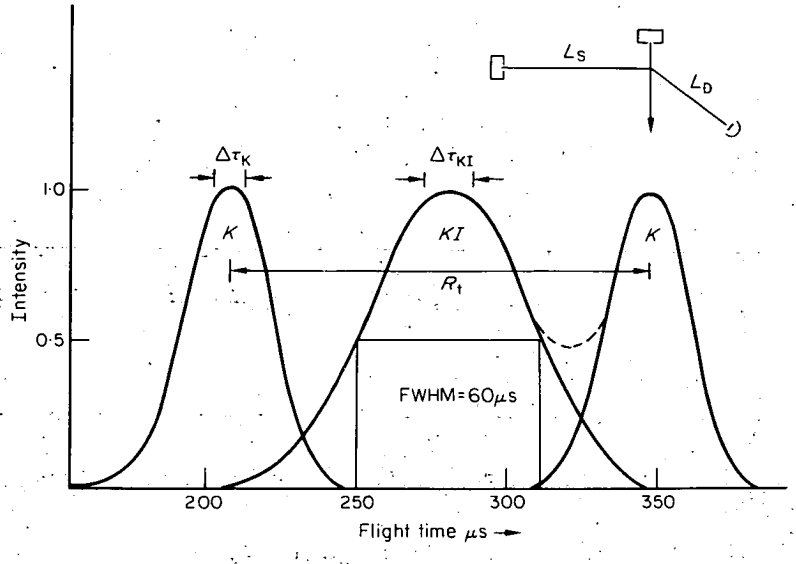

Fig. 4.4 TOA spectrum for K/I_2 scattering.

selectors transmitting a single velocity, the T.O.F. method, in conjunction with a multi-channel scaler at the detector, can record the whole velocity spectrum of the product at once and the technique therefore makes more effective use of the signal despite the lower transmission at lower energies.

Time of flight techniques may also be used in the measurement of total cross-sections (J. F. Wilson and G. D. Lempert, 1970). The T.O.A. spectrum of main beam pulses is measured with and without a target gas and the resulting distortion of the pulses through the velocity dependence of the beam attenuation can be interpreted in terms of the velocity dependence of the total cross-section. In the field of ion-molecule scattering, the vibrational energy transfer in the system

$$Li^+(10-50\text{ eV}) + H_2\ (n=0) \longrightarrow Ii^+ + H_2\ (n=0,1,2)$$

has been partially resolved (J. Schottler and J. P. Toennies, 1968) with a detector gate width (in the form of a multi-channel scaler) of 300 nanoseconds. This experiment is only made possible by starting with a nearly monoenergetic ion beam formed by magnetic velocity analysis. The interpretation of the results and an improved signal to noise factor comes from the knowledge that the energy loss must be in discrete vibrational quanta (see also below).

More efficient use still can be made of the available flux by using a cross correlation technique originally evolved for electrical wave filter analysis. In this, the delta function response, $I_\delta(L; t - t')$ in Equation 4.14 is obtained as the cross correlation ϕ_{GI} between a random modulation of the parent beam and the consequent detector response, i.e.

$$\phi_{GI}(\tau) = \int G(t - \tau) I(L; t) dt \tag{4.17}$$

Multiplying Equation 4.14 by the parent pulse time distribution $G(t - \tau)$ and taking the time average (in theory over an infinite time interval) yields:

$$\int I(L, t) G(t - \tau) dt = \int G(t - \tau) \int G(t') I_\delta(L; t - t') dt' dt$$

but, making use of the random nature of $G(t)$,

$$\int G(t - \tau) G(t - t') dt = \delta(t' - \tau)$$

so

$$\phi_{GI}(\tau) = \int \delta(t' - \tau) I_\delta(L, t') \, dt' = I_\delta(L, \tau) \tag{4.18}$$

and the measured correlation is identical with the delta function response of the apparatus. Inelastic collisions result in a further spreading of the arrival pulse in addition to that due to the spread of velocities present in the parent beam. The first step in analysis is then to cross correlate the signal with the initial random word pulse as in Equation 4.17 to obtain the scattered signal in response to a delta function in time at the source. A particular process resulting in an energy loss ΔE will give rise to a pulse at the detector whose shape $I_{\Delta E_n}(t)$ can be predicted by arguments similar to those leading to Equation 4.14 from a knowledge of the shape of the elastically scattered pulse. A fitting is then carried out in which $\phi_{GI}(t)$ is analysed in terms of a linear combination of the $I_{\Delta E_n}(t)$, the unknowns ΔE_n and C_n being found by a least squares procedure

$$\phi_{GI}(t) = \Sigma \, C_n \, I_{\Delta E_n}(t).$$

The chief advantage of the random word modulation lies in the greater spectral density that can be achieved in comparison with any approach to delta function modulation. Since the probability of the beam being on is equal to it being off, the spectral density or transmission is 50 per cent.

Furthermore, since the resolution depends only on the bandwidth of the noise modulation, this high transmission can be obtained without any loss of resolution inherent in the delta function approach.

The application of these techniques in an atomic scattering experiment is described by C. A. Visser et al., 1970. In this experiment the random modulation was pulse coded, the beam being either fully on or off for random periods thus avoiding problems of non-linearity that could arise with amplitude modulation.

The great advantage of all time of flight techniques lies in the ease with which the resolution and hence the transmission may be varied during the course of an experiment without recourse to moving parts inside the vacuum chamber.

4.3 Magnetic state selection

Unlike ions, neutral species are comparatively difficult to deflect by external fields. The 'handle' by which such a field interacts with the molecule is either its electric or magnetic moment and the deflection in an inhomogeneous field is then a function of the field gradient, the molecular moment and kinetic energy together with the distance traversed through the field. By choosing a field gradient of the right radial dependence and having axial symmetry, a bundle of paraxial molecular trajectories can be brought to a focus and the focal length is a function of the parameters just listed. The device can be regarded either as a velocity selector, a rotational state selector or a molecular orientation selector according to the requirements of the experiment. Rather than pursue a unified treatment, we begin by distinguishing the three important types of behaviour, according to whether the particle is an atom possessing a magnetic moment, a linear molecule with an electric dipole moment or a symmetric top.

We deal first with the focusing of atoms that have a permanent magnetic moment, μ. The energy of such an atom in a magnetic field B is

$$W_{mJ} = -\mu . B = m_J g \mu_B |B|, \tag{4.20}$$

where m_J is the component of the total angular momentum in the direction of the field and μ_B the Bohr magneton. The force acting on the atom is

$$F_r = -m_J g \mu_B \, \partial B/\partial r. \tag{4.21}$$

In order for the atom to execute transverse simple harmonic motion in the

field, the magnitude of B must be quadratic in the displacement r and this is achieved with a hexapole field, Fig. 4.5. In the magnetic case, the field can be generated by permanent magnets or electromagnetically. In the latter case, if a current i is passed through a hexagonal array of conductors, each a distance R from the axis, the field is given by

$$B = \frac{3ir^2}{10\pi R^3} = B_0(r/R)^2 . \tag{4.22}$$

The direction of B picks out the direction of quantisation and the force acting on an atom distance r from the centre is $F = -2m_J g\mu_B B_0 r/R^2$ and this force is everywhere radial. The focal length is then readily found to be

$$f = \pi v R \sqrt{M/(2m_J g\mu_B B_0)} \tag{4.23}$$

where B_0 is the field strength at the pole tips in gauss and the atom is of mass M. A hexapole array of conducting loops gives rather too weak a field for ordinary applications (although B_0 is precisely calculable in this configuration), but an array of permanent magnets can easily produce 0.5 T at the pole tips, giving a focal length of roughly 12 cm for potassium at thermal speeds with a pole gap of 0.5 cm. The detailed design and use of a hexapole spin filter has most recently been described by H. M. Brash et al., 1969. Only

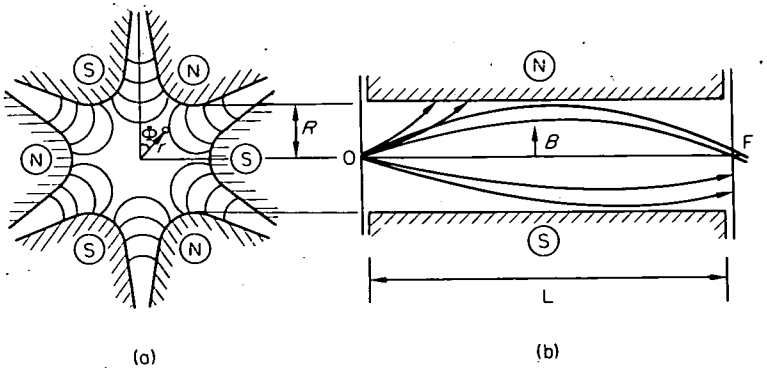

Fig. 4.5 The hexapole focusing field.
(a) End on view showing arrangement of pole tips and lines of force.
(b) Longitudinal view. The entrance slit is at O and the exit slit at F. Trajectories corresponding to two different velocities are shown, one of which is brought to a focus at the exit slit F. A third pair of trajectories is shown for atoms with moments parallel to the field, which leads to de-focusing.

atoms with $m_J > 0$ are focused, but a wide range of velocities come to a focus beyond the exit from the field. If the device is to be used as a velocity selector, entrance and exit slits must be positioned to reject all molecules except those whose focal plane lies at the exit slit.

The key quantity in hexapole lens design is a 'phase angle', ϕ

$$\phi = \frac{L}{R}\left(\frac{2m_J g\mu_B B_0}{M}\right)^{1/2}\frac{1}{v} \tag{4.24}$$

where L is the length of the magnetic field and R the radius of the circle on which the pole tips lie. Then, if a point source is located at distance 'a' from the entrance aperture, the image will be formed at distance 'b' beyond the end of the field where 'd' and 'b' are related by Fig. 4.6.

$$\phi_n = \arctan(L/a\phi_n) + \arctan(L/b\phi_n) + n\pi \tag{4.25}$$
$$(n = 0, 1, \ldots)$$

a, b and L are generally dictated by other experimental requirements, e.g. resolution and so the value of the field strength B_0 for the required velocity v_0 is found from Equation 4.24 with ϕ assigned from Equation 4.25. 'Harmonics' will still be passed by the filter that arise from values of n in Equation 4.25 other than the chosen one (generally zero). However, the ratio v_n/v_0 will not be a rational one and so the addition of a simple two disc mechanical velocity selector will eliminate these velocity sidebands. The resolution of the filter regarded as a velocity selector is a function of the ratio of the radius W of the exit aperture to R, as well as of $A = a/L$ and $B = b/L$;

$$\frac{\Delta v}{v_0} = \frac{2\sqrt{2}\,\frac{W}{R}\,(A+B)(A^2 + 1/\phi_0^2)^{1/2}}{\phi_0 \sin\phi_0\{A^2B^2\phi_0^2 + A^2 + B^2 + AB(A+B) + (A+B+1)/\phi_0^2\}} \tag{4.26}$$

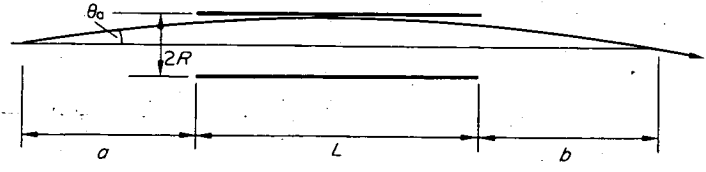

Fig. 4.6 The critical dimensions of the general hexapole filter. The magnetic field occupies a length L, the source is a distance a in front of the entrance and the focal plane is a distance b beyond the end of the field.

Tall beams, with slit rather than circular geometry can also be focused, but the velocity resolution will be poorer.

A typical hexapole lens, discussed in (H. M. Brash et al., 1969) had the following values of the parameters.

	L	=	0.12 m
	L/R	=	48
A =	a/L	=	1.8
B =	b/L	=	4.0
	W	=	0.1 mm
	v	=	390 m s^{-1}
	B_0	=	0.118 T (permanent magnet)
	$\Delta v/v_0$	=	11% (FWHM)

Fields up to 2 T may be obtained with an electromagnet allowing L $\approx$ 0.03 m to maintain the same value of ϕ. The gain in intensity as a result of the focusing action may be calculated from the angle of acceptance θ_a of the device for those particles that are brought to a focus. Referring to Fig. 4.6 and assuming that the effect of the central stop is negligible, θ_a is given by

$$\theta_a = R/L\,(A^2 + 1/\phi^2)^{-\frac{1}{2}}. \tag{4.27}$$

The number of particles N_f passing through the focus is thus:

$$N_f = \frac{1}{4} F_n F_{\Delta v} I_0 \theta_a^2 \tag{4.28}$$

where I_0 is the number of particles per second per steradian emerging from the source, F_n is the fraction of molecules in the selected band of quantum states and $F_{\Delta v}$ is the fraction in the transmitted velocity range. For mechanical selection, if the scattering volume subtends an angle θ'_a at the source, the corresponding expression for the number of particles passing through the scattering volume is $\frac{1}{4}F_{\Delta v} T I_0 \theta'^2_a$, where T is the mechanical transmission factor. In general, $\theta_a/\theta'_a \sim 2 - 10$ and a gain in scattered signal of at least an order of magnitude can be expected.

It is worth remembering that although many atomic states possess unpaired electrons, not all are suitable for magnetic focusing. Firstly, for the atom which has zero nuclear moment only those states with $m_J > 0$ can be focused and since the focal length depends upon $v/m_J^{\frac{1}{2}}$, sidebands will appear in the transmitted beam due to different combinations of m_J and v if $J > \frac{1}{2}$.

Secondly, if the nuclear spin is non-zero, the effective magnetic moment of the atom is, for weak field coupling:

$$\mu_{\text{eff}} = \left[\frac{\mu_J}{J}\left\{\frac{F(F+1)+J(J+1)-I(I+1)}{2F(F+1)}\right\} + \frac{\mu_I}{I}\left\{\frac{F(F+1)+I(I+1)-J(J+1)}{2F(F+1)}\right\}\right] m_F \quad (4.29)$$

where **F(=I + J)** is the total angular momentum, m_F its projection quantum number and $\mu_I = g_I \mu_{NI}$ where g_I is the nuclear g factor and μ_N the nuclear magneton. Since $\mu_N \approx \mu_e/2000$, the dominant contribution to μ_{eff} comes from the first term in Equation 4.29, but the range of m_F values renders a weak field magnet useless as a velocity selector. In the strong field case (in which the nuclear and electronic angular momenta are decoupled) the effective moment is given by:

$$\mu_{\text{eff}} = \mu_J \frac{m_J}{J} + \mu_I \frac{m_I}{I} \quad (4.30)$$

The field strength needed to achieve this depends upon the isotope and for the alkali metals working values might be (in MHz)

K	Na	Rb	Cs	
450	1800	3000	9000	most abundant isotope
250		7000		less abundant isotope

Hexapole filters are very convenient for potassium and are just possible for Na and Rb. In the case of Cs, however, it is necessary to use a Stern Gerlach magnetic with yields more intense fields (I. I. Rabi, et al., 1934) but which is only a partially focusing device (see below). The states $m_J = 3/2$ and $1/2$ of gallium ($J = 3/2$) have also been selected with a hexapole lens (K. Berkling et al., 1962). Although this atom has a relatively large nuclear moment, the coupling of I and J is small because the unpaired electron is not in an s-orbital and hence has zero density at the nucleus. Halogen atoms and some of the metastable inert gas atoms might prove good candidates for magnetic focusing.

If the experiment requires that both μ_{eff} and $-\mu_{\text{eff}}$ can be selected, then the older type of deflection field with two-wire geometry is used (N. F.

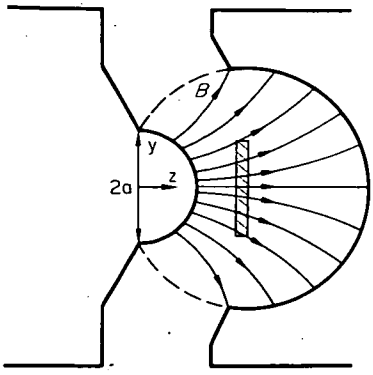

Fig. 4.7 A modern beam deflecting magnet, based on the two wire field. The magnetic field lines are shown and a tall beam (shaded) in roughly the position shown will experience a nearly constant field gradient over its height for values of $y \leqslant a$. (N. F. Ramsey, 1956).

Ramsey, 1956). The inhomogeneous field is produced between two pole faces shaped such that $\partial B/\partial z \propto z$ and both B and $\partial B/\partial z$ remain nearly uniform over the height of the beam, Fig. 4.7. Since the restoring force in the z direction is again proportional to z,, there is focusing in this direction but not in the y direction. Particles with effective moment μ_{eff} suffer a deflection δ in traversing a field length L where:

$$\delta = L^2 \mu_{\text{eff}} \partial B/\partial z \; (2Mv^2)^{-1} \qquad (4.31)$$

and by placing the exit slit appropriately, states with positive or negative moments can be selected. This is put to practical use in spin exchange experiments (D. E. Pritchard et al., 1970) and the device has also been used as a velocity selector for H atoms (M. A. D. Fluendy, 1965) but the lack of whole field focusing is a disadvantage here.

4.4 Electrostatic state selection

The electrostatic analogue of the 1st order Zeeman effect, by which magnetic sub-states are separated in a magnetic field, is the 1st order Stark effect exhibited by symmetric top molecules. The discussion of this effect exactly parallels that of spin focusing, except for two factors. Firstly, there are no complications due to the nuclear dipole moments which are zero in the electrostatic case. Secondly, the rotational state of a symmetric top molecule is specified by three quantum numbers j, m and K. The non-vanishing component of the permanent dipole moment μ in the direction of the applied field **E** (which defines the axis of quantization) is given by:

$$\mu_E = \mu \langle \cos\theta \rangle = \mu m K/[j(j+1)] \qquad (4.32)$$

where θ is the angle of precession of the figure axis around the direction o the applied field. The induced energy is linearly dependent on E:

$$W^{(1)}_{jmK} = -\mu \cdot \mathbf{E} = -\mu EmK/j(j+1)$$

and the force is

$$\mathbf{F} = \mu \text{ grad } | \mathbf{E} | mK/j(j+1) \tag{4.33}$$

Thus, if both m and K are non-zero and either of them is negative, the mean dipole component is antiparallel to the field and focusing can be achieved if grad $|\mathbf{E}|$ is positive. If either m or K is zero then the molecule behaves as a linear one and the energy dependence on the field is quadratic (see below).

Focusing will be obtained with an electrostatic hexapole array, for which the potential is given by

$$V = V_0 \left(\frac{r}{R}\right)^3 \cos 3\Phi \tag{4.34}$$

where R is the radius of the electrode tips from the axis Φ the azimuthal angle defined in Fig. 4.5 and V_0 the electrode potential. Then,

$$| \mathbf{E} | = 3V_0 r^2/R^3 \tag{4.35}$$

The focal length is then readily found for the state (j, m, K)

$$f_{jmK} = \pi v \left\{ \frac{R^3}{6V_0} \left[\frac{M}{\mu} \frac{j(j+1)}{mK} \right] \right\}^{1/2} \tag{4.36}$$

For a representative molecule having $\mu = 1.5$D, $M = .5 \times 10^{-23}$ g and moving at a speed of 3×10^2 m s^{-1}, a focal length of at least 0.15 m for an applied potential (V_0) of 2 KV is calculated. Although very polar ($\mu \geqslant 2$D) symmetric top molecules are rare, convenient focal lengths can be obtained for some compounds of the type CYX_3 or for ammonia. For the rather heavy molecule CH_3I, a focal length of ~1 m has been attained.

With three quantum numbers as well as the velocity determining the focal length, the electrostatic hexapole analyser is better regarded as selecting molecules with a given value of $\langle \cos\theta \rangle$ rather than in a particular rotational state. In this mode of operation a mechanical velocity selector is inserted between the exit of the hexapole array and the scattering centre, so that the range of values of $\langle \cos\theta \rangle$ transmitted is considerably narrowed.

The method has been used particularly by Bernstein and his co-workers (R. J. Beuhler and R. B. Bernstein, 1969) for CH_3I and CHI_3 and by P. R. Brooks et al. (1969) for a wider group of CX_3Y molecules. The degree of the selection of $\langle\cos\theta\rangle$ is largely determined by the resolution of the velocity selector. Thus, the geometrical arrangement of slits and stops essentially selects a range of values of ϕ, defined analogously to the magnetic case (Equation 4.24) as

$$\phi = \frac{L}{Rv}\left(\frac{2\mu\langle\cos\theta\rangle V_0}{MR}\right)^{\frac{1}{2}}, \tag{4.37}$$

so

$$\left|\frac{\Delta\langle\cos\theta\rangle}{\langle\cos\theta\rangle}\right| \simeq 2\left\{\left|\frac{\Delta\phi}{\phi}\right| + \left|\frac{\Delta v}{v}\right|\right\}, \tag{4.38}$$

and if $\Delta\phi/\phi$ is typically 10 per cent, the resolution in $\langle\cos\theta\rangle$ will be 30 per cent with a good velocity selector.

The presence of the velocity selector with its poor transmission and spatial demands, together with the fact that such a small volume of the phase space of the molecules is being selected means that intensities will be small, perhaps 10^5–10^6 particles arriving per second at the focus. Whether the molecules are oblate or prolate tops there is a statistical deficiency of those with values of $\langle\cos\theta\rangle$ close to unity and the most probable value of $\langle\cos\theta\rangle$ is in both cases zero, a non focusable orientation. With the angular resolution quoted above, the fraction of molecules having the required orientation will be $\leqslant 10$ per cent. The beam intensity (for $\langle\cos\theta\rangle \sim 1/2$) at the exit of a combined hexapole/mechanical selector might be 10^{-1}–10^{-2} times that at the exit of a conventional mechanical selector, still sufficient for total cross section work.

Linear molecules possessing a permanent dipole moment exhibit a quadratic Stark effect in the presence of an electric field E and for a non-polarizable linear molecule the second order perturbation energy, $W_{jm}^{(2)}$ is given by

$$W_{jm}^{(2)} = \frac{\frac{1}{2}(\mu E)^2}{\hbar^2/2I}\left\{\frac{j(j+1) - 3m^2}{j(j+1)(2j-1)(2j+3)}\right\} \tag{4.39}$$

so the radial restoring force becomes

$$F_r = -\frac{\mu^2 E \partial E/\partial r}{\hbar^2/2I}\mathscr{F}(j, m)$$

where

$$\mathscr{F}(j, m) = [j(j+1) - 3m^2] / [j(j+1)(2j-1)(2j+3)] \tag{4.40}$$

If E can be made to vary in a linear fashion with r, the motion in the field is simple harmonic if both $\partial E/\partial r$ and the quantum number factor in Equation 4.40, $\mathscr{F}(j, m)$, are positive. For a quadrupole array of conductors the potential is given by

$$V = V_0 (r/R)^2 \cos 2\Phi \tag{4.41}$$

(where R is the distance of an electrode tip from the axis) and so the magnitude of the field at (r, Φ) is

$$|\mathbf{E}| = 2V_0 r/R^2 \tag{4.42}$$

which has the required r dependence.

The focal length (for the case a = b = 0, Fig. 4.6) is given by

$$f = \frac{\pi \hbar v R^2}{\mu V_0} \sqrt{\frac{M}{8I\mathscr{F}(j, m)}} \tag{4.43}$$

where M is the molecular mass. All rotational states for which $\mathscr{F}(j, m) > 0$ can be focused (note that for $j = 0$, $\mathscr{F}(j, m) = -1/3$ and so this state cannot be focused). As with the hexapole field, there will in general be several combinations of v, j and m that lead to the same focal length and a velocity selector is always incorporated to narrow the range of j and m.

The question of what is being selected in classical terms is perhaps less clear than in the hexapole case. If the source temperature is high enough for the molecular rotation to be treated classically and very low values of j are not being selected, the mean dipole moment in the direction of the field is

$$\mu_E = \frac{\mu^2 E}{4W_{\text{rot}}} (3\cos^2 \alpha - 1) \tag{4.44}$$

where α is the angle between $\mathbf{J}$ and $\mathbf{E}$ and W_{rot} is the rotational energy appropriate to the source temperature. For a molecule with $\mu \sim 5$D and with $E \sim 10^6$ volts m^{-1}, $\mu_E/\mu \leqslant 10^{-3}$ at thermal energies and so there is little net alignment of the dipole and even this asymmetry virtually disappears when the molecule leaves the quadrupole and enters the region of weaker uniform

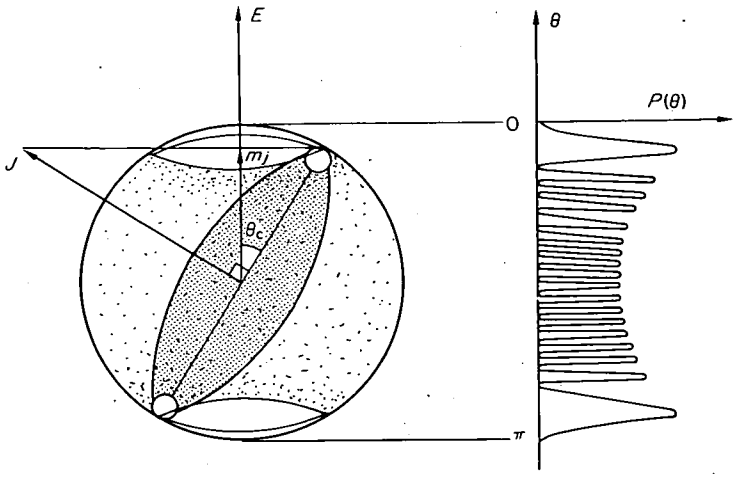

Fig. 4.8 The classical representation of the quantum motion of a linear dipolar molecule in a weak field E. A region near the poles, defined by the cone of semi-angle θ_c is forbidden to the classical motion. The quantum mechanical probability distribution of the axis orientation is shown on the right for the case $j \sim 20$, $m_j \sim 10$. As j increases, the quantum motion is more sharply centered at $\pm\theta_c$, where $\sin\theta_c = m_j/j$.

field. In this latter region the classical motion for fixed values of j and m is displayed in Fig. 4.8. In the absence of an applied field, the rotation is confined to a plane; when a field is applied, precession of **J** about **E** begins. Writing

$$\cos\theta_c = \sqrt{1 - m^2/(j(j+1))} \tag{4.45}$$

where θ_c is the minimum angle between the dipole axis and **E**, it can be said that motion of a monoenergetic beam through a quadrupole lens selects the range of values of $\cos\theta_c$ and W_{rot} that together satisfy Equation 4.43 for the chosen value of the focal length. θ_c is found to range from 0° to roughly 35° (Equation 4.45) with $m^2 = 1/3j(j+1)$) for states which can be focused and each value of θ_c is weighted by the population of the corresponding rotational state in the beam. That is, a limited range of (j, m) states is selected and these have the molecular axis pointing more in a polar than an equatorial direction with respect to the axis of quantisation. Unlike the symmetric top case, this will not lead to marked anisotropy in the chemical cross-section for a reaction in which one end of the molecule is preferentially attacked.

However, anisotropy terms of even symmetry in the intermolecular potential can be investigated by altering the focusing conditions.

The device is most useful when designed to transmit only the lowest rotational states, (1, 0) or (2, 0), for then $\mathscr{F}(j, m)$ is a rapidly varying function of j and m and with mechanical velocity selection different rotational states are readily resolved. For the state (1, 0) the focal length is given by:

$$f_{10} = 7.854 \frac{\bar{v}R^2}{\mu V_0 r_{AB}} \frac{m_A + m_B}{(m_A m_B)^{1/2}} \times 10^5 \text{ m} \qquad (4.46)$$

where v is in m s^{-1}, R is in m, μ is in Debyes, V_0 is in volts and r_{AB}, the bond length, is in Angstroms. The focal length is clearly shortest for slow (heavy) molecules with large dipole moments. Thus J. P. Toennies (1965) has focused the (1, 0); (2, 0) and (3, 0) states of TlF and used them to investigate rotational transitions in a crossed beam experiment Fig. 4.9. For this particularly favourable molecule ($\mu = 4.4$D) focal lengths of 0.15–0.2 m are achievable.

For highly polar molecules, the possibility arises of selecting rotation-vibrational states through the rather large change of dipole moment with vibrational quantum number. Thus, $(\mu(n = 0) - \mu(n = 1))/\mu_0$ is ½ per cent for CsCl (from the beam resonance method) and 1 per cent for CsF. However, the focal length is essentially determined from Equation 4.43 by $(\mu^2 I)^{1/2}$ and this quantity may be expected to change by 2–3 per cent upon going from the n^{th} to the $(n + 1)^{\text{th}}$ vibrational state. Thus, groups of perhaps two or three vibrational levels might be separated. The fraction of molecules

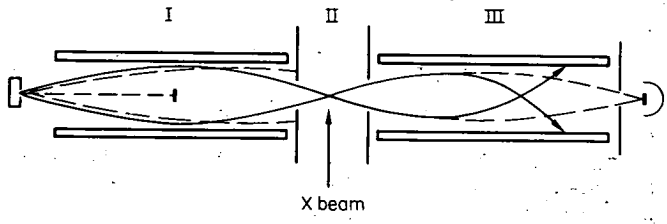

Fig. 4.9 A quadrupole system for detecting rotational transitions. The selecting field I focuses molecules in the (1,0) state (trajectory ——) and molecules in the (2,0) (– – – –) and higher states either miss the exit aperture or hit the axial stop for molecules entering on the axis. In region II a uniform field establishes the axis of quantisation and a cross-beam intersects the focused beam, inducing rotational transitions. The analysing quadrupole, III, is set for the (2,0) state, which is focused onto the detector.

in these low rotational states at the high oven temperatures is very small; for CsF .03 per cent of the molecules are in the (1, 0) state.

More promising for the selection of vibrational states is a technique adapted from single beam resonance experiments (L. Wharton et al., 1963). A highly polar linear molecule is prepared in, say, the (1, 0) state by passage through a quadrupole lens and led adiabatically into a uniform field region where it is pumped by microwave radiation at the resonant frequency for the $(n, j, m) = (0, 1, 0) \rightarrow (1, 2, 1)$ transition. A second quadrupole lens is then set to pass the (2, 1) rotational state, thereby also selecting the $n = 1$ vibrational state. The experimental arrangement would be that of Fig. 4.9 with the cross-beam replaced by a microwave cavity. Nearly equal populations of the two levels can be obtained in the C-field region and sufficient intensity of vibrationally excited molecules for scattering experiments seems obtainable (T. G. Waech et al., 1968).

Single beam deflection experiments have been performed with non-polar molecules using the force arising from the interaction of the induced electric moment with the external field. The induction energy is quadratic in the field strength (2^{nd} order Stark effect) and so the focusing conditions are analogous to those for linear molecules discussed above. For an isotropically polarisable molecule, polarisability α, the interaction energy is

$$W^{(2)} = -\tfrac{1}{2}\alpha E^2 \qquad (4.47)$$

However, molecular polarisabilities are roughly 10^{-28}–10^{-29} m^3 and so $W^{(2)}$ in the non-polar case is $10^{-3} - 10^{-4}$ less than that arising from the permanent moment. Although the absence of a rotational state factor from Equation 4.47 increases the fraction of the parent population that can be focused, the focal length of a quadrupole lens operating on non-polar molecules will be approximately ten times greater than that designed for polar molecules and scattering experiments have not yet been carried out with beams selected by this means.

CHAPTER FIVE

Detection and Measurement

As in nuclear scattering the final link in any beam experiment is the detection of the particles after scattering. Unfortunately at the low energies appropriate to molecular scattering, the detection methods are severely handicapped. The fundamental problem is in distinguishing the molecules of the beam from the overwhelming background (pressure) inevitably present in our detectors. For the nuclear or elementary particle physicist the very high energy of the particles of interest serve to distinguish them from the background and efficient devices such as scintillation counters responding to this energy can be used. In contrast at thermal energies no such simple differentiation is possible and the beam properties of direction of motion and chemical species provide a much inferior distinction between beam and background.

Since Dunoyer's first experiments (L. Dunoyer, 1911) when he detected a sodium beam by condensing it upon a cooled surface, a wide range of devices has been used to detect molecular beams. In general these devices measure either the molecular beam flux as in Dunoyer's experiment or the molecular density. Most detectors currently in use convert the molecular current into an electric current, though for some applications condensation targets are still useful. Thus, Kinsey used a condensation target followed by radioactive counting to detect scattered tritium (L. R. Martin, J. L. Kinsey, 1967).

In general the most successful detectors have been those providing a high degree of differentiation between beam and background molecules. Unfortunately such selectivity is usually bought at the price of severe limitations on the range of materials that can be detected.

The overall performance of a detector is a function not only of the actual

beam sensor itself but also of the whole experimental configuration including any filtering or correlation processes that may be used. Nevertheless it is convenient to divide the discussion into two parts and consider first the beam detectors proper.

5.1 Beam detectors – Introduction

The most important parameters characterizing beam detectors are sensitivity, noise and response time.

Sensitivity is the output current or number of events per sec (in the case of ion counting systems) in response to a unit incident flux. The range of materials detectable, and their relative sensitivities must also be considered.

Noise is the random electrical output of the device, it can be conveniently measured in terms of the resulting uncertainty in beam flux: this uncertainty will depend not only upon the actual amplitude of the noise current but also upon the statistics of its time variation. Thus, if σ_N is the standard deviation of the noise measured with unit bandwidth then with 95 per cent confidence the uncertainty in a measurement will not exceed:

$$\pm 2\sigma_N / t^{1/2}\ \mathrm{s}^{-1},\ t > \frac{1}{\Delta\nu} \quad \text{or} \quad \pm 2\sigma_N \Delta\nu^{1/2}\ \mathrm{s}^{-1},\ t < 1/\Delta\nu \tag{5.1}$$

where $\Delta\nu$ is the bandwidth of the detector and t is the observation time. Contributions to σ_N arise from many sources, if the standard deviations for these processes are known the total will be

$$\sigma_N{}^2 = \sum_i \sigma_i{}^2 + \sum_j \sum_i \mathrm{cov}_{ij} \tag{5.2}$$

or if these different sources are uncorrelated $\mathrm{cov}_{ij} = 0$ and

$$\sigma_N{}^2 = \sum_i \sigma_i{}^2 \tag{5.3}$$

In almost all detectors one component of the noise output arises from the random motion of background gas molecules. If the motion of these molecules is entirely uncorrelated we may use the de Moivre Laplace limit theorem to estimate their contribution to the standard deviation of the noise. Thus if the noise current, I_N, from the background gas pressure (assuming a flux dependent detector) is:

$$I_N = \sum_i n_i q_i \sqrt{\frac{RT}{2\pi M}} \tag{5.4}$$

where n_i is the background gas number density of species i and q_i is their detection efficiency, then the theorem leads to the result that:

$$\sigma_N \longrightarrow \left(\sum_i n_i q_i \sqrt{\frac{RT}{2\pi M}}\right)^{1/2} \tag{5.5}$$

In practice the background atom motion is not entirely uncorrelated and macro pressure fluctuations in the detector due to pumping irregularities etc., can occur. Such fluctuations will depend upon the size of the vacuum chamber and its pumping speed. The contribution from this source has been discussed by S. N. Foner, (1966) in terms of an electrical analogue (Fig. 5.1).

The following identifications are made, where S is the pumping speed and V the chamber volume

$$\text{Beam flux} = I, \qquad R = 1/S, \qquad C = V.$$

E_s is then the signal output from the detector and E_b the noise output (due to pressure fluctuations). The noise output can clearly be minimized by decreasing the impedance of the RC circuit across which E_b is developed.

The impedance of this RC circuit is:

$$|Z| = R/[1 + \nu^2 C^2 R^2]^{1/2} = 1/S[1 + \nu^2 V^2/S^2]^{1/2} \tag{5.6}$$

where ν is the frequency of the signal current I.

Thus the impedance and hence the noise output E_b can be decreased by moving the signal frequency ν to a suitably high value. In practice this corresponds to modulating the molecular beam at a frequency such that $\nu V \gg S$. The noise output is then reduced to about $S^2/\nu V$ times the zero

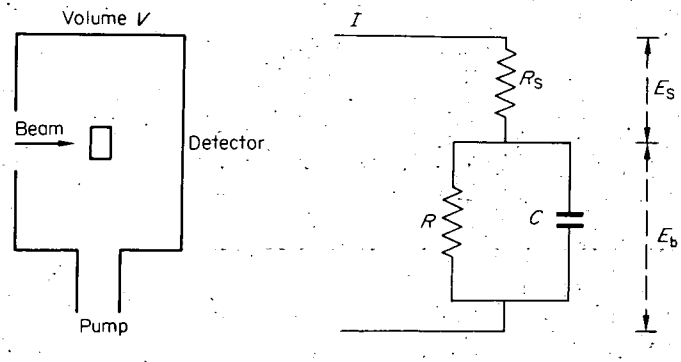

Fig. 5.1 Electrical analog for noise arising from background pressure fluctuations.

frequency level. Noise from this source is thus far from Gaussian and is concentrated primarily at low frequencies.

Noise due to both effects is best combated by lowering the partial pressure of the background material to which the detector responds (typically by installing additional liquid N_2 shielding). Beam modulation methods will also be useful in dealing with other sources of fluctuation noise and will be discussed in more detail later.

Response time τ is defined as the time taken for the output of the detector to rise to 63 per cent, $(1 - e^{-t/\tau})$, of its final value in response to a step change in input. This time will limit the rate at which the incident beam can be varied, e.g. by modulation or velocity scans.

Types of Detectors

5.2 Ionization detectors

The most widely used class of detectors operate by ionizing the molecule and then measuring the resultant ion current. Several techniques may be used to accomplish the initial ionization.

(i) Hot wire detectors

In this type of detector beam molecules with a low ionization potential are ionized by collision with a hot wire of high work function such as tungsten. The operation of this device can be understood in terms of the Saha-Langmuir equation (E. Ya Zandberg, N. I. Ionov, 1959) which relates the temperature T, the ionization potential E_b of the beam material and the work function of the hot wire surface ϕ_w to the proportion of molecules ionized by the collisions as:

$$\frac{\text{number of ions emitted}}{\text{number of neutrals}} = \frac{(1-\gamma_+)}{(1-\gamma_n)}\frac{j_+}{j_n}\exp -\left(\frac{E_b - \phi_w}{kT}\right) \qquad (5.7)$$

where j_+, j_- are the reflection coefficients and γ_+, γ_n the degeneracies of the ion and neutral particle states respectively. Equation 5.7 is, of course, an equilibrium relation and its useful temperature range in this connection is limited to that over which the neutral atoms do not permanently condense on the surface.

Values for $(E_b - \phi_w)$ for various combinations of wire and beam material are given in Table 5.1.

Table 5.1

Wire Material	ϕ_w eV	Beam Material $(E_b - \phi_w)$ eV							
–	–	Li	Na	K	Rb	Cs	Ga	In	Tl
W clean	4.58	+0.81	+0.56	−0.24	−0.40	−0.71	1.42	1.21	1.5
W oxygenated	5.9	−0.51	−0.76	−1.56	−1.72	−2.03	0.1	−0.11	0.2
Re	5.17	+0.22	−0.03	−0.83	−0.99	−1.30	0.83	0.62	0.9
Ionization Potential E_b	–	5.39	5.14	4.34	4.18	3.87	6.00	5.79	6.1

The agreement between the predicted and observed behaviour is illustrated by Figs. 5.2 and 5.3 (S. Datz and E. H. Taylor, 1956) which show the percentage ionization found for alkali metals on tungsten and on platinum. Alkali metal compounds such as halides can also be ionized by suitable hot wires. In this case the molecule is dissociated and the alkali metal emitted as an ion. The mechanism for this process is rather less clear. Figs. 5.4 and 5.5 show the ionization of some alkali halides on tungsten and on platinum. It is apparent that the W surface is a fairly efficient ionizer, the platinum much less so. An especially valuable fact becomes apparent if we compare Figs. 5.2 and 5.4 and Figs. 5.3 and 5.5. The tungsten surface is approximately equally effective at ionizing both alkali metals and their halides whereas the platinum surface at temperatures in the 1200°K region ionizes the metals almost exclusively (with the exception of KF). Thus in a mixed alkali/metal halide flux the difference in signals recorded from tungsten and the platinum wires is a measure of the alkali halide flux. This differential hot wire detector has played a most important role in the study of chemical reaction by molecular beam methods. Recently, however, K. T. Gillen and R. B. Bernstein (1970) have found that highly vibrationally excited alkali halides are also quite readily ionized on a platinum filament, the ionization efficiency varying exponentially with excitation energy and approaching 20 per cent for highest states.

This observation has important implications in the original interpretation of the wide angle elastic scattering from reactive systems. In experiments, using alloy filaments the K flux was considerably overestimated.

Surface ionization detection has also been used in the reverse sense. Thus the collision of an atom or molecule having a large electron affinity with a hot wire of low work function can lead to electron transfer from the metal and the formation of a negative ion. Such negative surface ionization is a much less efficient process than the formation of positive ions. For ionization

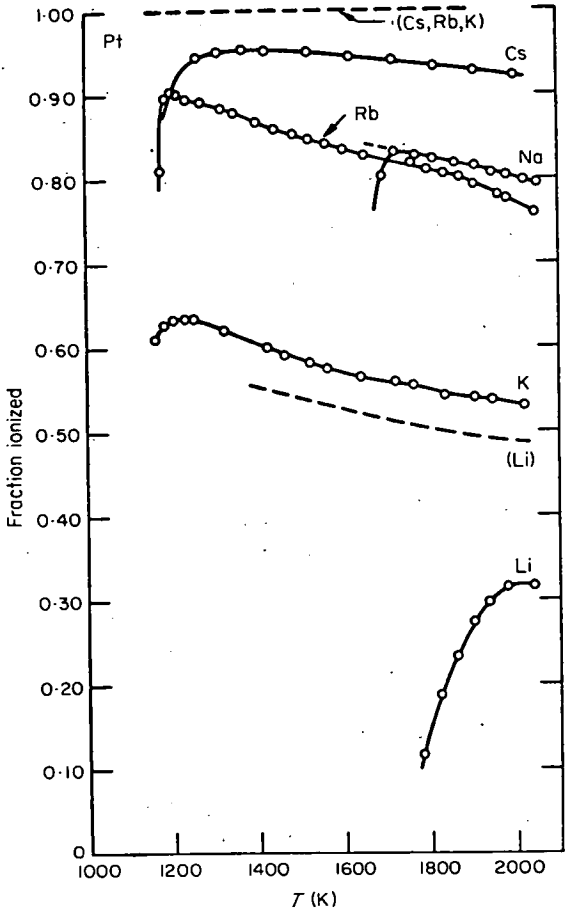

Fig. 5.2 Ionization of alkali metals on platinum. Dotted lines are the calculated behaviour (S. Datz and E. H. Taylor, 1956).

on a carburretted thoriated tungsten wire efficiencies of 1–2 per cent for CBr_4 ranging downwards for other electronegative species were found by E. F. Greene et al., 1968. Apart from the rather low efficiency this method also suffers from the drawback that some form of mass spectrometer is required to distinguish negative ions from the otherwise overwhelming thermionic electron current. Greene found a simple magnetic field configuration highly effective for this purpose at low background pressures. Some typical sensitivities found in his work are listed in Table 5.2.

Table 5.2 Relative negative ionization efficiencies on thoriated tungsten wire (K on Re at 1200 K ≡ unit efficiency)

KI	1.8×10^{-3}	CBr_4	1.9×10^{-2}
CCl_4	1.5×10^{-2}	I_2	6.3×10^{-8}
C_2Cl_6	1.4×10^{-3}	HI	1.8×10^{-4}
C_6H_5Cl	2.6×10^{-3}	C_2H_5I	7.7×10^{-4}
Br_2	4.5×10^{-3}	C_6H_5I	1.5×10^{-3}

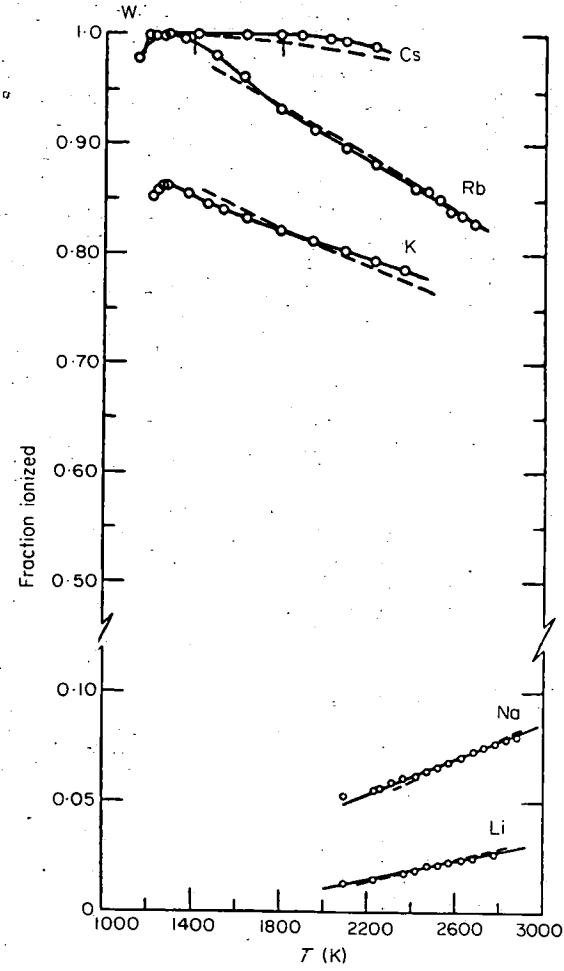

Fig. 5.3 Ionization of alkali metals on tungsten. Dotted lines are the calculated behaviour (S. Datz and E. H. Taylor, 1956).

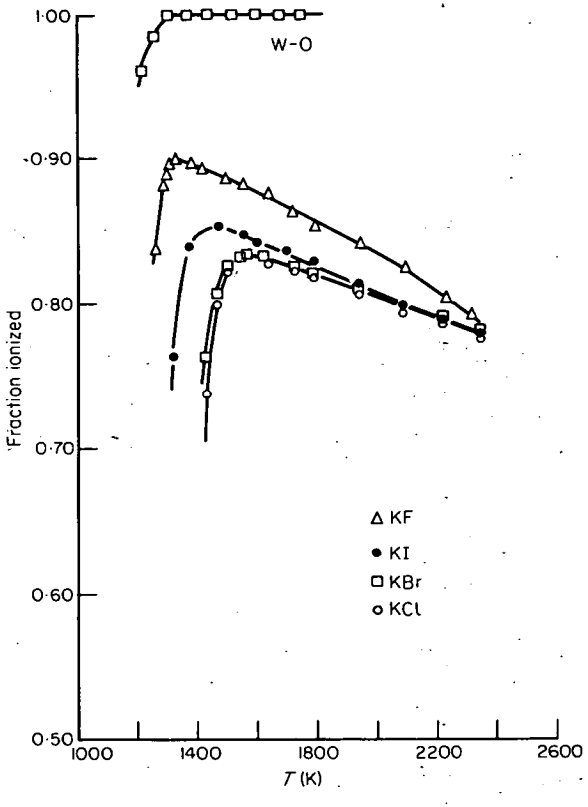

Fig. 5.4 Ionization of alkali halides on tungsten (S. Datz and E. H. Taylor, 1956).

Construction

The most usual form of hot wire detector is shown in Fig. 5.6. The hot wire is suspended under spring tension between two insulating mounts which also provide the feed for the d.c. heating current. The two ends of the wire are screened by small earthed cylinders to prevent the cooler end regions of the wire being exposed to the beam flux. A cylindrical collector slotted in two places to allow the beam to enter and leave is mounted on alumina insulators and biased about 40 volts negative with respect to the filament. The ions formed on the wire surface are thus attracted to the collector and the resulting current measured on an electrometer. A metal screen finally surrounds the whole assembly to form an electric shield.

The normal operating temperatures for tungsten and platinum filaments are 1870 K and 1290 K respectively. For 0.003″ wires these correspond to

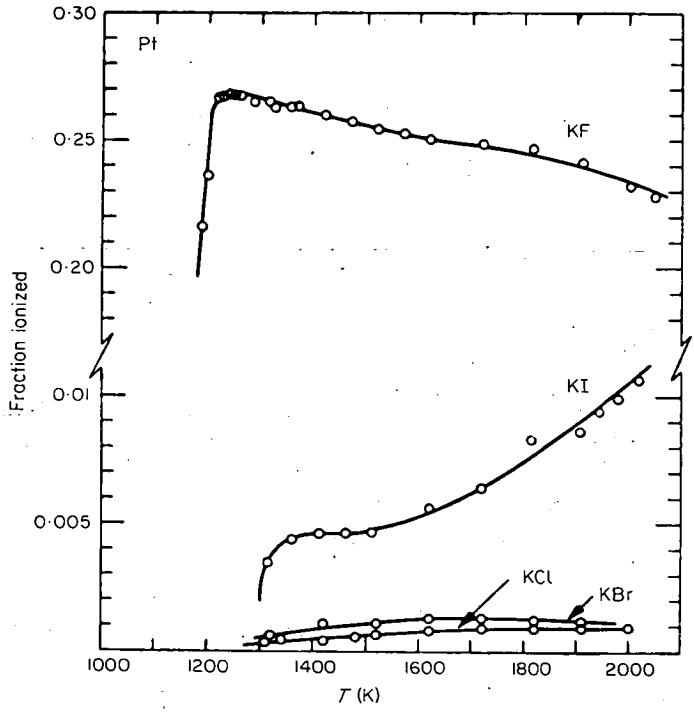

Fig. 5.5 Ionization of alkali halides on platinum. Slow response noted at temperatures below vertical dashed lines. (S. Datz and E. H. Taylor, 1956).

0.600A and 0.200A currents. Oxygenated filaments of tungsten are prepared either by running the filament at 1500 K in a slight pressure of oxygen or alternatively by allowing a capillary jet of oxygen from a reservoir at about 5×10^{-3} torr to play upon the filament during use.

Filaments with a high platinum content have two different surface states. In one with a high work function they can ionize alkali halides, in the other known as mode N (T. R. Trouw and J. W. Trischka, 1963) the work function is lower and the filaments ionize essentially only the alkali metals or highly excited species, e.g. KI. Mode N can be prepared by ageing the Pt wire at 1520 K for several hours and then running it at 1600 K for a few minutes in methane at a partial pressure of $\sim 5 \times 10^{-4}$ torr.

Several variations of the basic device described have been used. Thus the collector can be replaced by the first dynode of an electron multiplier and the bias increased to 2–3 kV. In this way advantage can be taken of the low noise amplification provided by such devices. In other cases (Fig. 5.7) the hot wire

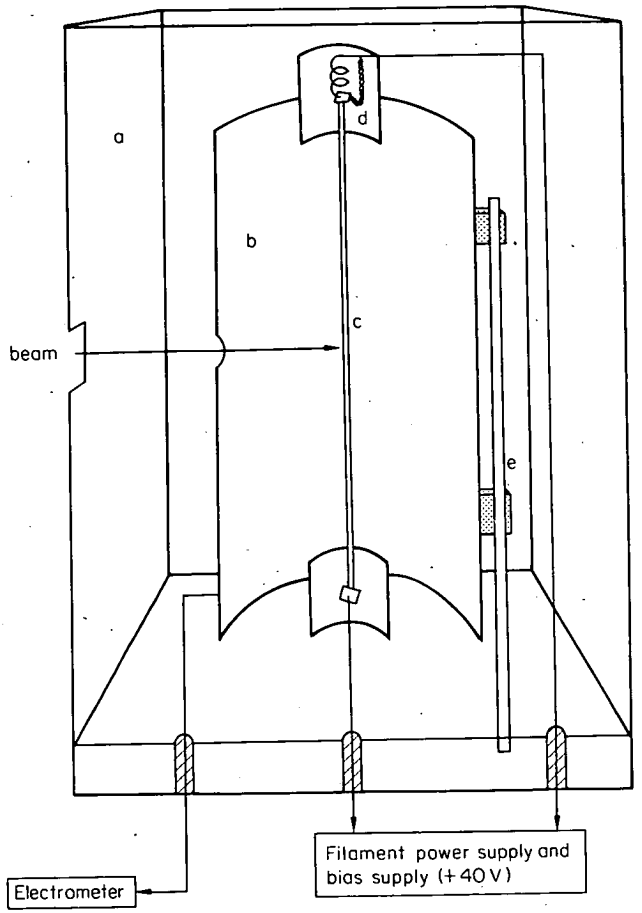

a electrostatic shield c filament e alumina rod
b collector d spring and current by-pass

Fig. 5.6 Hot wire beam detector with electrometer to measure a positive ion current.

is mounted at the entrance to a mass spectrometer so that the various alkali ions etc. can be distinguished. Careful design of the focusing and extraction lenses is required if the ion collection efficiency is to approach 10–50 per cent.

Sensitivity

Positive surface ionization detectors perform with good efficiency when the work function is greater than the ionization potential. They are thus

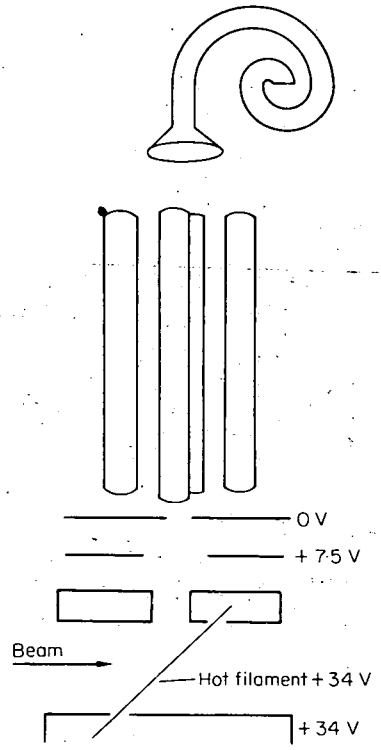

Fig. 5.7 Hot wire detector and quadrupole to detect alkalis selectively. A lens focuses the positive ions from the ribbons into the quadrupole. Total detection efficiencies of the order ~50% can be achieved.

primarily limited to the alkali metals and their compounds together with In, Ga, Tl, Pr, Al and Ba. For the alkali metals the detection efficiency is 80–100 per cent, i.e. $\sim 1.6 \times 10^{-19}$ A per unit incident flux per m^2 of detector surface. Our 'standard beam' of 5×10^{10} molecules sec^{-1} mm^{-2} at one metre from the source would thus produce a current of 8×10^{-9} A mm^{-2} or for a 1 cm tall beam on a 0.003″ wire a current of $\sim 6 \times 10^{-10}$ A.

Linearity

The detector is linear over a wide range. At the highest beam fluxes ($\sim 10^{-8}$ A) where surface coverage by the alkalis is significant some decrease in efficiency has been observed (K. Wilson, 1964).

Noise

There are two principal sources of noise in the hot wire detector. The first, common to all detectors, is due to those background gas molecules that are ionizable on a hot wire and has already been discussed. The noise from this source can be estimated from kinetic theory considerations. The number of ions produced will be approximately the number of collisions of ionizable material with the hot wire (of the appropriate mass if a mass spectrometer is used), i.e. number of ions $s^{-1} = I = 1/3\, n_b \bar{v}$ cm^{-2} of detector surface, where n_b is the number density and $\bar{v}$ the average molecular velocity.

Then as before:

$$\sigma(I) = (\tfrac{1}{3}\, n_b \bar{v})^{\frac{1}{2}} \tag{5.8}$$

Thus a background partial pressure of 10^{-15} torr on the surface of a typical detector (5×10^{-3} cm^2) will produce an average ion current of

$$I = 10^{-15}\,A$$

and the standard deviation of the noise rate from this source would be:

$$\sigma(I) \sim (2 \times 10^4)^{\frac{1}{2}} \cong 140 \text{ counts } s^{-\frac{1}{2}}$$

The second noise source is specific to this class of detector and arises from alkali metal impurities in the wire. These diffuse to the surface during operation and are ionized. Tungsten wires are especially prone to this since some KCl is incorporated during manufacture. Fortunately pure tungsten wires drawn from a single crystal of the metal are now available and are much less noisy. In all cases it is standard practice to 'age' wires by running them at an elevated temperature for a few hours. Typically tungsten is aged at 2030 K and platinum alloy at 1520 K; the noise decreases very markedly during this procedure.

The statistics of diffusion noise are very far from Gaussian; the emission of impurities from the interior of the wire appears as sharp pulses of current in which up to 10^8 ions may be released in less than 100 μs (i.e. a current peak of $\sim 10^{-9}$A). (The time width of the pulses is related to the wire temperature – at the lowest operating temperatures they may spread over ~50ms). (R. E. Minturn, et al., 1960). In the case of tungsten wires the impurities are very largely potassium so that if the beam material is different a considerable noise reduction can be achieved by using a mass spectrometer. Clipping or limiting circuits have also been used to reduce this form of noise.

Table 5.3 Noise count s^{-1} arising from impurities in tungsten ribbon*

	Operating current	
	1A	1.4A
Na	434	17,942
K	121,332	137,889
Rb	437	1,148
Cs	122	264

* Ribbon was 0.020" x 0.001" 92% W/8% Pt alloy

Table 5.3 shows a typical distribution of noise from a Tungsten alloy filament. The much lower noise level obtained for Rb is clearly seen. Platinum or single crystal purity W filaments are much less noisy and will normally be used whenever possible.

Response time

The response time of hot wire detectors varies roughly inversely with the wire temperature and ionization efficiency (F. Knauer, 1949; H. Lew, 1953; H. L. Daley et al., 1969). At the very lowest temperatures at which ionization can be observed the emission of an ion may follow in the order of seconds after the neutral atom collision with the surface. For the usual operating temperatures alkali metals are ionized with delays ranging from 10^{-2} seconds for Platinum at 1200 K to 10^{-5} seconds on tungsten wires at high temperatures. Unfortunately the noise pulses from wire impurities decrease in time width in rather a similar way; modulation at a sufficiently high frequency to deal with diffusion noise is therefore difficult. For d.c. experiments, i.e. without modulation the build up of beam material in the detector chamber will also contribute to the response time. Using the electrical analogue again we see that the pumping time constant is RC or chamber volume/pumping speed.

(ii) Surface ionization of fast alkali beams

For very fast alkali beams of >3 eV collision energy the efficiency of the hot wire detector begins to drop off; probably due to reflexion effects.

Fortunately it has been found that ionization of these energetic alkalis can be accomplished on a cold filament of high work function. (E. Hulpke and C. Schlier, 1967.) This process has two important advantages in comparison with a hot wire ionizer. Firstly there is virtually no noise from the ribbon or from the thermalized alkali background, i.e. the detector is highly specific for the

beam. Secondly the response time is very small < 0.1 μs so that a detector using this process can be used in time of flight experiments. The disadvantage of this detector is the rapid change in ionization efficiency which occurs between threshold at about 7 eV and 50 eV above which the efficiency becomes relatively constant (Fig. 5.8). This loss of sensitivity arising from an increased reflection of neutral particles at energies between 3 eV–50 eV both on hot and cold surfaces has been circumvented in a detector described by Politiek. In this detector (J. Politiek and J. Los, 1969) the fast atoms enter a heated tungsten cylinder via a narrow slit and hence suffer multiple collisions with the surface during which ionization can be achieved.

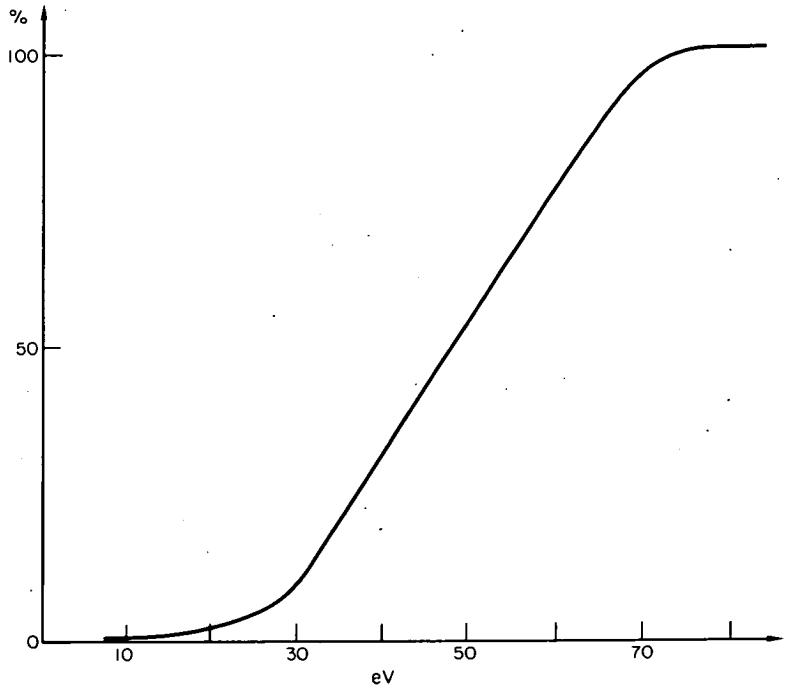

Fig. 5.8 Efficiency of ionization for fast neutrals striking a cold tungsten wire (data from R. K. B. Helbing and E. W. Rothe, 1969).

In practice the ribbon is normally operated 'warm', i.e. just below the threshold for thermal ionization in order to prevent contamination of the ribbon surface. The construction of detectors using this approach is similar to the hot wire pattern; an electron multiplier would normally be incorporated, e.g. Fig. 5.7, take advantage of the fast response time.

(iii) Electron bombardment detectors

This type of detector in its essentials is the same as the sources used in conventional mass spectrometers. A high density of electrons with sufficient kinetic energy to ionize the beam molecules is arranged to intersect the molecular beam. The resulting ions are extracted from the ionizing region – usually via a mass spectrometer and the ion current measured. Since the partial pressure of beam material in the device will be very low, careful attention must be paid to the efficiency of the source.

The number of ions produced from a beam flux of $F(v)$ molecules $cm^{-2}\ s^{-1}$ with a velocity v is related to the detector parameters by:

$$N_j = \frac{i}{e} \frac{Q_j(E)B}{\bar{v}} k_j F(v)\ \ s^{-1} \tag{5.9}$$

where i is the electron current in amps, e the electronic charge (1.6×10^{-19} coloumbs), and $Q_j(E)$ the ionization cross-section for molecules of species j at a collision energy E. A and l are the width and length of the high electron density region and B is the height of the beam lying in the area Al. Finally k_j is the mass spectrometer transmission for species j.

The number of ions from the background will similarly be:

$$N_n = \frac{i}{e} B \sum_h n_h Q_h(E) k_{(j-h)}\ \ s^{-1} \tag{5.10}$$

Where n_h is the number density of molecules h and $k_{(j-h)}$ is their transmission through the mass spectrometer (tuned to mass j).

The signal to noise ratio after 1 second (neglecting pressure fluctuation contributions) will thus be:

$$S/N = N_j/(N_n)^{1/2}$$

$$= \left(\frac{i}{e}B\right)^{1/2} Q_j k_j F(v)/\bar{v} \left(\sum_h n_h Q_h(E) k_{(j-h)}\right)^{1/2} \tag{5.11}$$

The primary design considerations may be summarized as:

(1) To match the beam and ionizing volume cross-sections i.e. A = beam width.
(2) To achieve the highest electron density in the beam path.
(3) To reduce the background gas pressure (especially that appearing at the same mass number as the beam material).

(4) To obtain high extraction into and transmission through the mass spectrometer.
(5) To minimize fluctuation noise by modulation methods.

Further problems can also arise from fragmentation of the parent molecule in the ionizer. In some cases only a small fraction may appear as the parent ion.

Construction

Several designs for beam detectors using electron bombardment have appeared in the literature, e.g. (R. Weiss, 1961). A design due to G. O. Brink (1966) is shown in Fig. 5.9. The electrons produced by the filament oscillate through the molecular beam region several times before ultimate collection on the grid. To improve the stability of the device the d.c. filament heating current is controlled by an emission regulator which samples the grid current and varies the heating current through the filament to maintain constant emission.

The detailed design of sources such as these is a difficult problem in ion and electron optics especially since space charge effects are large because of the high electron density required. The reader is referred to more specialized texts.

Sensitivity

The detector is number density dependent with a sensitivity inversely proportional to velocity as seen from Equation 5.11; and is therefore not very suitable for detecting fast (super thermal) beams.

Inserting typical values into Equation 5.10 we see that we can expect to ionize between 1 in 10^2 and 1 in 10^3 of the molecules in a beam at thermal velocities. In comparison Weiss reported 1 in 40 for argon and Brink 1 in 600 for argon and 1 in 800 for krypton. Ionization cross-sections do not vary very widely from molecule to molecule and electron bombardment ionizers are

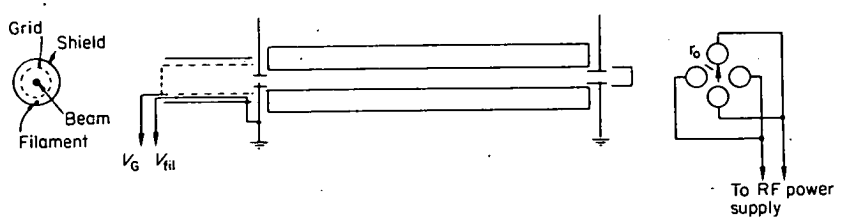

Fig. 5.9 Typical high efficiency electron bombardment ionizer (reproduced from G. O. Brink, 1966).

therefore of universal application; though particular mass numbers may be virtually impossible to detect if coincident with persistent background gases.

Linearity

The device is likely to be linear over the usual range of beam fluxes though non-linearities due to space charge effects can occur if operated in a high background pressure.

Noise

The noise in bombardment detectors is due almost entirely to background gas, both low frequency fluctuations (which have already been dealt with) and random 'white' contributions being important. The number of ions from the background is N_n:

$$N_n = \frac{i}{e} B \sum_h n_h Q_h(E) k_{(j-h)} \ s^{-1} \tag{5.12}$$

and the standard deviation of the noise $(N_n)^{1/2}$.

Noise reduction thus depends principally upon vacuum technique and in particular the partial pressure of background gas falling in the mass spectrometer transmission band. U.H.V. techniques, using oil free bakeable equipment, and possibly including liquid He cryogenic pumping are therefore mandatory. Chemical getter pumps to handle particular contaminants or beam material may also be useful. Typical background pressures as a function of mass numbers are shown in Fig. 5.10.

Response time

At thermal beam speeds the most important factor in determining the response time is the length of the region over which ionization can occur. Thus a rectangular step in beam flux will produce a ramp output of duration:

$$\tau = \frac{l}{v_b} - \frac{l}{v_i} \tag{5.13}$$

where v_b is the beam velocity, v_i is the average velocity of the ion and l the length of the ionizer. If $v_i \gg v_b$ then $\tau \approx l/v_b$. Response times are thus typically 10^{-5} seconds, by making $v_i \approx v_b$ the dispersion of the pulse can be minimized, a result which is often more important than reduction of the actual delay between the arrival of a beam pulse and the output of the signal. In some ionizers in which the high electron density is achieved by trapping

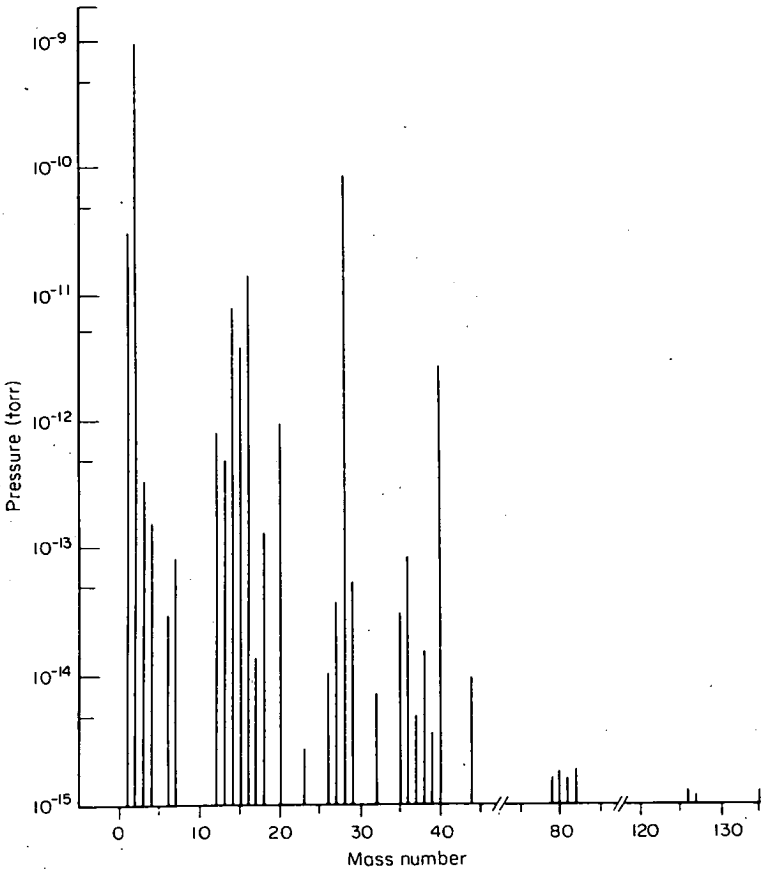

Fig. 5.10 Background partial pressures in an electron bombardment detector (reproduced from Y. T. Lee et al, 1969).

the electrons in a potential well, the net field in the ion may be very small. The response time can then rise to $\sim 10^{-2}$ s.

(iv) Field ionization detector

The use of the field ionization sources in conventional mass spectrometry is a comparatively recent innovation and as yet this technique has not been much used in molecular beam work. Nevertheless field ionization seems likely to offer important advantages over electron bombardment sources and, when certain problems are overcome, may find very wide use in beam detectors.

The actual process of field ionization has been the subject of several reviews (e.g. E. W. Muller, 1960; H. D. Beckey, et al., 1963). Ionization is

brought about by quantum mechanical tunnelling of an electron through a distorted atomic or molecular potential, this distortion being brought about by a very intense electric field (of the order 10^7–10^9 Vm^{-1}). This intense field may be generated around a needle point (as in the original experiments) 5000°A in radius or by a thin wire 2×10^{-4} cm in diameter biased 3–20 kV positively. The actual collecting area is considerably larger than the surface of the point or wire since molecules in a region round about are polarised by the field and attracted inwards. The size of this collection region can be estimated as the distance r_c at which the polarization due to the field balances the centrifugal motion of the molecules about the wire. (R. Gomer and M. G. Ingram, 1955.)

Thus for a needle point radius r_0:

$$\frac{1}{2} Mv^2 = \frac{1}{2} \alpha F_0^2 \left(\frac{r_0^2}{r_c^2}\right)^2 \tag{5.14}$$

Where M is the mass and α the polarizability of a molecule moving with velocity v and F_0 is the field strength at the tip. The number of ions N_s produced by a needle point exposed to a unit incident flux of molecules is thus:

$$N_s = \pi r_c^2 = \pi \left(\frac{\alpha}{Mv^2}\right)^{1/2} F_0 r_0^2 \ s^{-1} \tag{5.15}$$

The ions formed by field emission are usually predominantly the parent ion; much less fragmentation occurring than is common with electron bombardment ionizers. The chief difficulties with this type of ionizer arise from instabilities in the ionization efficiency due either to erosion of the surface or condensation of polar molecules upon it. The wide angle over which the ions are emitted from the edge or point also makes their extraction into a mass spectrometer difficult. Elaborate lens system compensated for spherical aberration are required to achieve a high efficiency (H. D. Beckey, 1961).

Construction

The construction of a beam detector using this principle has been described by W. D. Johnston and J. G. King (1966). Their device is shown in Fig. 5.11. The ions emitted from the needle point follow field lines and strike a phosphor screen. The screen is viewed by a photomultiplier, scaling circuits are then used to count the ions arriving at the screen. Low frequency noise in the phosphor was reduced by beam modulation.

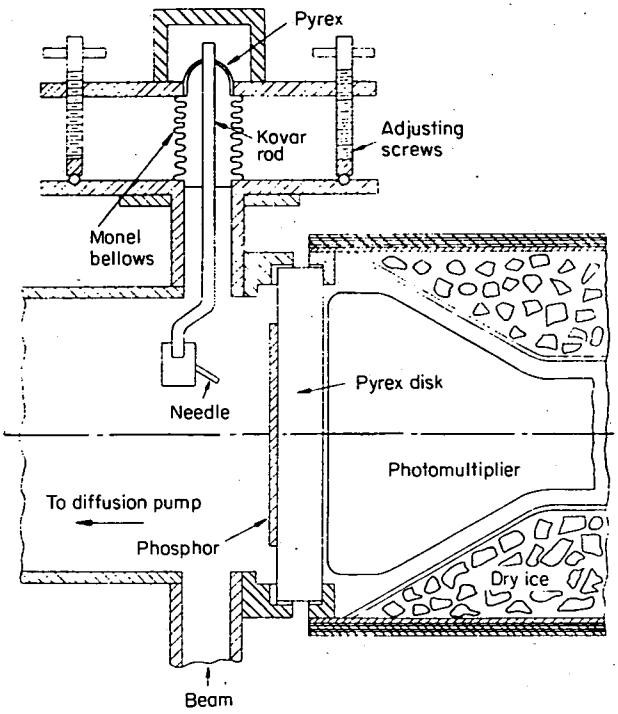

Fig. 5.11 Universal detector using field emission ionization and scintillation counting (reproduced from W. D. Johnston and J. G. King, 1966).

Another source consisting of a series of thin wires approximately 2μ in diameter has been described by H. D. Beckey et al, (1963), to replace a conventional mass spectrometer source.

Sensitivity

The principal factors governing the sensitivity are the matching of the ionizing region bounded by r_c with the beam cross-section and the extraction of the ions into the mass spectrometer.

Noise

For the background gas the number of ions formed will be just the number of molecules crossing a sphere of surface area $4\pi r_c^2$ centred on the point, i.e.

$$N_n = 2\pi r_c^2 \, \bar{v} n_b \qquad (5.16)$$

where n_b is the number density of the background gas and $\bar{v}$ its average velocity.

The signal to noise ratio for a single needle point detector from background contributions of this type after mass selection is thus:

$$S/N = \frac{N_j k_j F(v)}{(\Sigma k_{(j-h)} N_h)^{1/2}} = \frac{\pi r_c^2 k_j F(v)}{(\Sigma 2\pi r_{c(h)}^2 \bar{v} n_h k_{(j-h)})^{1/2}} \qquad (5.17)$$

where k_j is the mass spectrometer transmission and $r_c^{2}{}_{(h)}$ is the critical distance for species h.

Response time

The actual period required for ionization is short of the order 10^{-11} s and the ionization region is relatively small so that response times in the range of 10^{-7} s might be expected.

5.3 Other types of detector

(i) Bolometer detectors

Thus far we have considered only detectors in which the beam molecules are ionized and differentiated from the background either by a mass spectrometer or by selective ionization. Other properties of the beam molecules however can be used. Thus detectors sensitive to the energy of the beam particles have been successful. The bolometers used for this purpose respond either to the kinetic energy of the beam or to some exothermic reaction of the material catalyzed by the bolometer surface, e.g. $2H \rightarrow H_2$ on a platinum surface (M. A. D. Fluendy, 1964). Bolometer detectors are likely to be of especial value in detecting super thermal beams for which electron bombardment ionization is inefficient. However, a superconducting bolometer operating at liquid He temperatures and capable of detecting thermal energy beams of 2×10^{14} molecules m^{-2} s^{-1} has been described (M. Cavallini, et al., 1967).

Construction

Bolometers used for molecular beam detection have usually been commercial devices designed for IR radiation detection. Both semiconductor and metal strip bolometers have been used. Their detailed construction will not be discussed further.

Sensitivity

The device is flux dependent – an important advantage.

A flux $F(v)$ of molecules mass M will yield a power to the bolometer of:

$$N_s = \tfrac{1}{2}Mv^2 F(v)\alpha\,(\tfrac{1}{2}Mv^2 - kT) \tag{5.18}$$

where T is the temperature of the bolometer and α is the accommodation coefficient of the beam material on the bolometer surface. If a reaction occurs between the beam molecules on the bolometer surface a power

$$W = \Delta H\beta F(v) + N_s \tag{5.19}$$

will be available. Where ΔH is the exothermicity and β is the sticking coefficient. (It is assumed that the whole of ΔH is available to the surface, i.e. the reaction products leave the surface completely accommodated.) In the case of H atoms, a detection limit of 5×10^{14} atoms m^{-2} s^{-1}, using their heat of recombination, was achieved.

Noise

Noise in bolometer detectors arises in several ways. Low frequency flicker noise is as usual minimized by modulating the beam and using a lock in amplifier. Other noise is due to collisions of the background gas with the bolometer and to Johnson noise in the bolometer itself. Ultra high vacuum technique using liquid helium will be especially valuable, since the low temperature will not only lower the background pressure but will also decrease the energy carried by the individual molecules to the bolometer. The lower operating temperature will also decrease the Johnson noise of the bolometer itself. Unhappily very low temperatures may inhibit surface diffusion and reaction so that detectors responding to an exothermic surface reaction may not be operable at these low temperatures.

Response time

Response times are typically 1–20 ms.

Stability

Instabilities in detector performance due to surface contamination can occur (especially in catalytic detectors). Improved vacuum technique is the usual solution.

5.4 Detection of excited atoms and molecules

Experiments with excited atoms or molecules have been rather popular since the problem of generating a beam of excited species are more than offset by

the relative ease of detection. This ready detectability is due to two factors. Firstly the excited species commonly possess sufficient internal energy to differentiate them from the background gas by the ease with which they are ionized or bring about electron ejection from surfaces. Secondly their efficient de-excitation on collision with surfaces means that a 'background' of excited molecules does not develop in the apparatus.

The detection of excited atoms has been reviewed by J. B. Hasted, 1965, and also by E. E. Muschlitz, Jun., 1966. The most frequent method of detection is via electron ejection from a metal surface and measurement of the resulting current.

If E_a is the excitation energy of the species, ϕ the work function of the metal and D_q the depth of the lowest electron level, ejection will occur if:

$$E_a > \phi < D_q - \phi \tag{5.20}$$

For 2^3S He atoms Stebbings found an ejection efficiency of 0.29 from a gold surface. Lichten has used a surface plated with sodium (by evaporation) to detect mercury metastables (M. N. McDermott and W. C. Lichten, 1960). The sensitivity of these devices can be increased by incorporating an electron multiplier. Thus E. W. Rothe et al. (1965) has used a resistive strip multiplier to detect He 2^3S, the excited atom ejecting electrons from the multiplier strip itself. Metastables have also been detected by quenching the excited state in an electric field and detecting the photon liberated, e.g. W. L. Fite et al. (1959) quenched $2^2S_{½}$ hydrogen atoms to the radiating state $2^2P_{½}$. The detection of highly vibrationally excited alkali halides (where the radiative lifetime is long enough to enable beam formation) also appears possible. K. T. Gillen and R. B. Bernstein (1970) found that on a Pt/W (92.8 per cent) alloy filament, the fractional increase in KI ionized, was approximately exp ($E_{ex}/4\ kT$), where E_{ex} is the excitation energy carried by the KI. There would thus seem to be a possibility of a sensitive, though not highly selective detector for these states.

(i) Construction

Fig. 5.12 shows a detector for low energy metastables, e.g. Hg 6^3P_2. A low work function surface is prepared by plating a surface with alkali metal. Electrons ejected from this surface are focused into a channel electron multiplier. The tungsten peg shown in the figure may be withdrawn a few cms to be plated with potassium from a small effusive source A located close by. In an alternative pattern the peg is replaced by a rotating drum so that plating may proceed simultaneously with detection, this procedure being more successful in systems where contamination occurs rapidly.

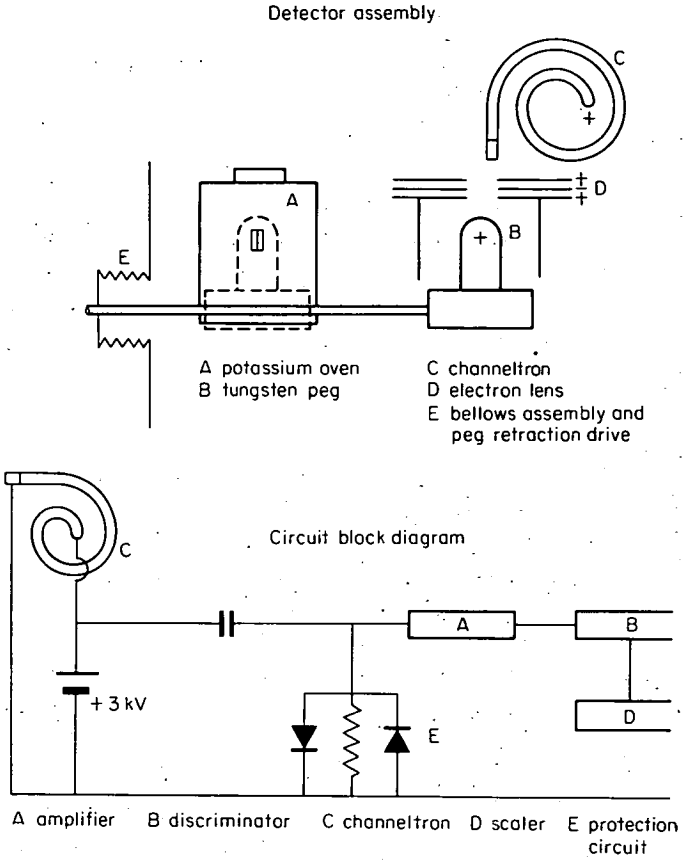

Fig. 5.12 Detector for metastable species using Auger electron ejection and particle counting

(ii) Sensitivity

Sensitivities in the range 0.5 electrons ejected per incident excited atom have been reported.

(iii) Noise

The noise is usually very small and may be largely electronic in origin, e.g. multiplier dark currents or response to photons.

(iv) Response time

For a detector using a multiplier the response time is largely a function of the multiplier construction and may be as short as a few nanoseconds. These detectors are thus the fastest available.

(v) Stability

Electron multipliers are rather sensitive to contamination by hydrocarbon or mercury vapour. As a result their initial gain may drop rapidly from say 10^7 to 10^5 or less, the final value being moderately stable. The resistive strip or channel multipliers are less sensitive to contamination than BeCuO types and are to be preferred in most applications. The stability problem can also be overcome by isolating the multiplier vacuum from the experimental system. Thus in Fig. 5.13 the electrons ejected from the surface by ion impact are accelerated through 40 kV to strike a phosphor surface. The resulting light pulses enter a sealed photo multiplier tube and are detected in the usual way.

5.5 The theory of detection systems

So far in this chapter we have discussed only the detectors themselves. In practice the actual sensors form only one element in the experiment and any meaningful analysis of their performance and capability must consider the system as a whole. To do so, we must digress briefly to consider the rate at which information can be obtained from experiments.

In principle we can achieve any desired precision provided we are prepared to observe our experiment for long enough. Unfortunately there is quite a restrictive practical limit to this procedure and we cannot normally extend our observation time by very many orders of magnitude. The *rate* at which we can acquire information from an experiment is therefore crucial. For a particular experimental configuration there will be a maximum possible rate at which information can be collected. This rate will depend upon the bandwidth (or response time) of the detector, the ratio of signal to noise powers and the statistics or frequency spectrum of the signal and noise. This result is due to Shannon who showed that if both signal and noise were Gaussian in distribution the maximum information rate was:

$$I = \Delta\nu \lg_2(1 + S^2/N^2)$$

where ν is the bandwidth and S^2 and N^2 are the signal and noise powers. In contrast to the maximum rate, the useful rate at which information can be accumulated will depend upon the rate at which the experimental variables are changed, e.g. the rate at which velocity or angle scans are made. If these are made too rapidly, the signal will vary faster than the detector response producing distortion and attenuation. On the other hand, scanning too slowly will not utilize the full bandwidth of the detector and the noise power will be

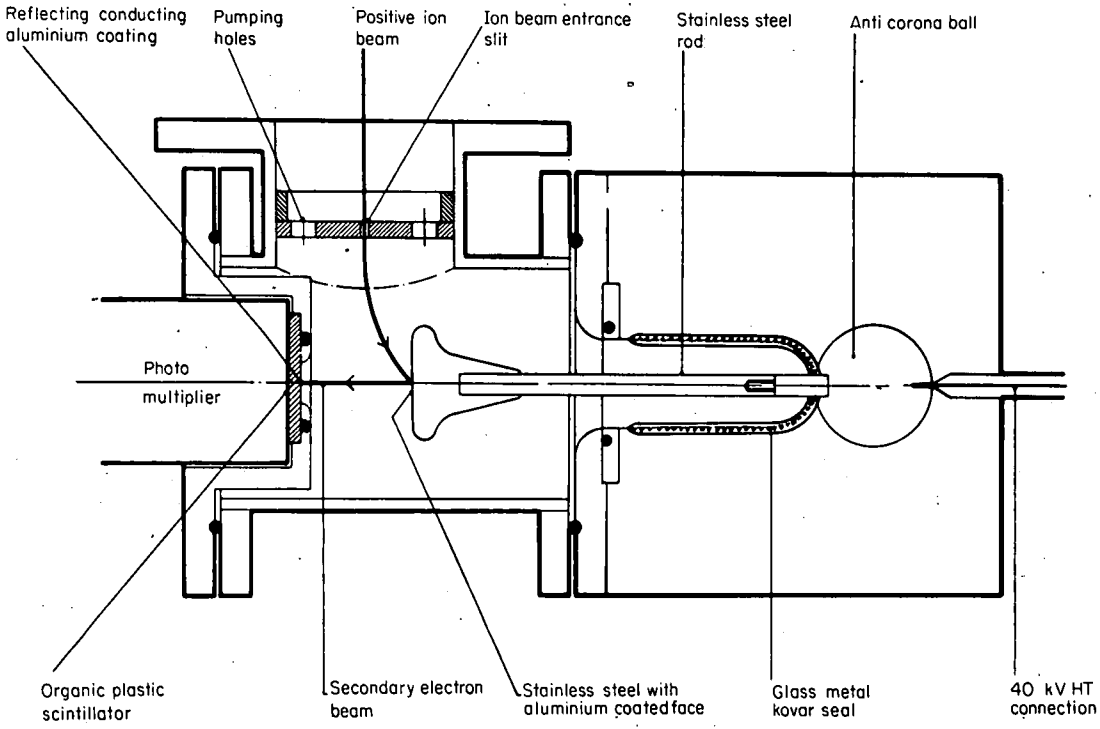

Fig. 5.13 Particle counting using an external photomultiplier to prevent dynode contamination (reproduced from N. R. Daley, 1960).

higher than necessary (as we shall see, white noise increases linearly with bandwidth). The detector bandwidth should therefore be matched to the rate of scanning, the limit to Fourier terms in the expression of the signal output being set by the bandwidth.

Unfortunately a calculation of the maximum information rate possible in an experiment does not provide a prescription for achieving this efficiency. It does, however, provide a yardstick against which we can compare any filtering or analysis process we care to contrive.

(i) Frequency and time domains

Before we can go on to discuss methods of filtering etc., which may improve the rate at which information can be acquired we must discuss the representation of the signal and the noise.

For periodic signals it is possible to use a Fourier transform between frequency and time. Thus a wave-form having a time dependence $I(t)$ (in the time domain) may be equivalently written as a sum of harmonic sine waves:

$$I(t) = \frac{a_0}{2} + \sum_{n=1}^{\infty} \left(a_n \cos\left(\frac{2\pi nt}{\tau}\right) + b_n \sin\left(\frac{2\pi nt}{\tau}\right)\right. \tag{5.21}$$

where τ is the period of $I_{(t)}$ and:

$$\left.\begin{aligned} a_n &= \frac{2}{\tau}\int_{-T/2}^{T/2} I(t) \cos\left(\frac{2\pi nt}{\tau}\right) \mathrm{d}t \\ b_n &= \frac{2}{\tau}\int_{-T/2}^{T/2} I(t) \sin\left(\frac{2\pi nt}{\tau}\right) \mathrm{d}t \end{aligned}\right\} \tag{5.22}$$

Thus for periodic $I(t)$ we can work either in a time or frequency domain with complete equivalence and we are able to consider filtering analysis techniques in either domain. This technique is powerful enough when dealing with signals which are periodic but is clearly inadequate to deal with signals and noise with random periods.

The Wiener Khintchine theorem generalizes these transformations to handle random signals and relates two functions, the auto correlation function:

$$F(\tau) = \int I(t)\, I(t+\tau) \mathrm{d}t \tag{5.23}$$

and the power density spectrum:

$$W(f) = 4\int_0^{\infty} F(\tau) \cos(2\pi f\tau)\, \mathrm{d}\tau \tag{5.24}$$

The auto correlation function is a measure of the 'memory' or correlation of the signal $I(t)$ over the time τ. It varies from the mean square value of the signal $\overline{I^2}(t)$ at $\tau = 0$ to $\bar{I}(t)^2$ (or zero if the signal is pure a.c.) at $\tau = +\infty$ and contains all the information about the distribution of amplitudes in $I(t)$. Thus Gaussian white noise containing an infinite range of frequencies, is entirely uncorrelated so that the signal at time t has no predictive value for the signal at t + dt and the auto correlation function is zero except at $\tau = 0$. Conversely an entirely non-random periodic signal produces an $F(\tau)$ with a similar period extending over all τ for an infinite wave train.

The power density spectrum $W(f)$, in contrast to the representation of periodic signals in Equation 5.21, where only discrete harmonic frequencies appeared, represents a continuous distribution of frequencies with an energy $W(f)$ in the range f to $f + df$. This power density spectrum will not in general be a unique representation of $I(t)$, many $I(t)$s will exist which yield the same $W(f)$.

The bandwidth and response time of the detector can be related by these methods. Thus if the detector output is a time function $S(t)$ it can be shown that $S(t)$ can be uniquely determined by a sequence of only $2\Delta\nu$ points per second where $\Delta\nu$ is the bandwidth. In other words the change in S over an interval $1/2\Delta\nu$ is determined completely by the speed of response limitations and not at all by changes in the 'message'. This result is known as the *Sampling Theorem*, i.e., we only need the input S at a discrete series of $2\Delta\nu$ points per second to generate the continuous output $S(t)$.

(ii) Noise

The noise forms ($n(t)$) we can expect to confront can be divided into two classes. The first comprises the 'highly organized' man made forms coming perhaps from adjacent experiments. Such interference is normally dealt with by shielding, turning off equipment etc., and need not concern us further.

The second class of noise is more fundamental in origin and as already discussed arises from the statistics of the devices used in the experiment and the random thermal motion of the electrons, atoms, etc., in the experimental arrangement. At absolute zero this noise will reach a minimum. There will also be a contribution to the noise due to the movement of electrodes, mechanical vibrations etc., this is often known as flicker noise.

Nyquist was able to show on thermodynamic grounds that the correlation of the thermal noise was zero except for extremely short times, i.e. the auto-correlation function = 0 except for $\tau = 0$ since positive and negative

deviations cancel. For such noise we can see from Equation 5.24 that the power density is independent of frequency. The noise is 'white'.

The noise voltage developed across a resistor, R, in a band of $\Delta\nu$ at frequency ν is:

$$S(\nu) = \left(4kTR\,\Delta\nu\right)^{\frac{1}{2}} \tag{5.25}$$

For other types (e.g. flicker) $n(t)$ may be correlated for much longer periods and such noise will be far from white. In general we shall need to investigate the statistics or power density spectrum of both signal and noise before desiging an analysis or filtering method that will improve the information acquisition rate.

(iii) Beam detection

To proceed further let us consider a specific experiment in which we are concerned to distinguish between the signal due to a molecular beam which itself has short term fluctuations and contributions arising from background noise etc. At least two sorts of measurement are required. One with the beam running (beam flag open) the other with the beam off (flag closed). If we represent the signal due to the beam as a time function $s(t)$ and the background noise as $n(t)$ the two measurements will be:

$$\begin{aligned} I_1 &= \frac{1}{T_3 - T_2}\int_{T_2}^{T_3} (s(t) + n(t))\,\mathrm{d}t \\ I_2 &= \frac{1}{T_2 - T_1}\int_{T_1}^{T_2} n(t)\,\mathrm{d}t \end{aligned} \tag{5.26}$$

Where the flag is open during $T_3 - T_2$ and closed during $T_2 - T_1$ the times being long in comparison to the response time of the detector. The estimate* of the steady beam signal where:

$$\bar{S} = \lim_{T\to\infty} \frac{1}{2T}\int_{-T}^{T} s(t)\,\mathrm{d}t \tag{5.27}$$

will be:

$$\hat{S} = I_1 - I_2 \tag{5.28}$$

* We make the assumption that both the signal and the noise are stationary distributions, i.e. their average properties are time independent. This is likely to be a good approximation in most steady state experiments.

If the bandwidth of the detectors is $\Delta\nu$ we may use the central limit theorem to estimate the accuracy of this estimate $\hat{S}$. Ninety-five per cent confidence limits for $\hat{S}$ after N cycles of observation of I_2 and I_1 will be:

$$\pm 2\left(\frac{\mathrm{Var}(\hat{S})}{N}\right)^{\frac{1}{2}} s^{-1} \tag{5.29}$$

and the figure of merit for this detection system defined as the minimum particle current that can be measured with 95 per cent confidence to ±20 per cent in an integration time of 100 seconds will be:

$$D = (\mathrm{Var}(\hat{S}))^{\frac{1}{2}}/C \quad s^{-1} \tag{5.30}$$

where C is the sensitivity of the sensor. More usefully we can express $\mathrm{Var}(\hat{S})$ in terms of the functions $s(t)$ and $n(t)$†

Thus

$$\begin{aligned}\mathrm{Var}(\hat{S}) &= \mathrm{Var}(I_1 - I_2) \\ &= \mathrm{Var}(I_1) + \mathrm{Var}(I_2) - 2\,\mathrm{Covar}(I_1 I_2)\end{aligned} \tag{5.31}$$

But

$$\mathrm{Var}(I_2) = \frac{\mathrm{Var}(n)}{t_c} = \mathrm{Var}(\hat{n}) \text{ if } \Delta\nu > 1/t_c$$

where $\mathrm{Var}(\hat{n})$ is the variance or square of the standard deviation of the population of samples t_c long viewed through a bandwidth window $\Delta\nu$ wide – t_c and t_o being the flag closed and open times respectively.

Similarly

$$\mathrm{Var}(I_1) = \mathrm{Var}(\hat{s}) + \mathrm{Var}(\hat{n}) - 2\,\mathrm{Covar}(\hat{n}, \hat{s}) \tag{5.32}$$

and

$$\begin{aligned}\mathrm{Var}(\hat{S}) &= \mathrm{Var}(\hat{s}) + 2\,\mathrm{Var}(\hat{n}) - 2\,\mathrm{Covar}(\hat{n}, \hat{n}(t + t_0)) \\ &\quad + 2\,\mathrm{Covar}(\hat{n}, \hat{s}) - 2\,\mathrm{Covar}(\hat{s}, \hat{n}(t + t_0))\end{aligned}$$

If the signal and noise are uncorrelated

$$\mathrm{Var}(\hat{S}) = \mathrm{Var}(\hat{s}) + 2\,\mathrm{Var}(\hat{n}) - 2\,\mathrm{Covar}(\hat{n}, \hat{n}(t + t_0)) \tag{5.33}$$

† $(\mathrm{Covar}\,(x, y) = \overline{xy} - \bar{x}\,\bar{y})$.

In this equation the final term represents the correlation between the noise during t_c and during t_o when the beam is on. It is thus a measure of the noise memory. For purely white or Gaussian noise covar $(\hat{n}(t)\,\hat{n}(t+\tau)) = 0$. In most experiments however, this is not true, though if the alternation between beam on and off is made slowly enough there will be zero correlation between the noise in the two intervals. Thus for these dc experiments the Equation 5.33 becomes:

$$\mathrm{Var}(\hat{S}) = \mathrm{Var}(\hat{s}) + 2\,\mathrm{Var}(\hat{n}) \tag{5.34}$$

The optimum strategy for the ratio between beam on and off conditions is clearly that which will yield equal absolute precision in the two sub estimates I_2 and I_1. The best ratio of times t_o and t_c for beam on and beam off will be

$$\frac{t_o}{t_c} = \frac{\mathrm{Var}(\hat{s}) + \mathrm{Var}(\hat{n})}{\mathrm{Var}(\hat{n})} \tag{5.35}$$

The dc experiment is far from optimum if the noise is correlated, i.e. its auto-correlation function is non zero for a range of τ.

Considerable improvement can be effected in this event. Looking again at Equation 5.28 we can rewrite the estimate of S as:

$$\hat{S} = \int_{T_o}^{T_1} \Big\{ s(t) + n(t) - n(t+\tau) \Big\} \mathrm{d}t \tag{5.36}$$

where $\tau = T_1 - T_0$; here we have combined the two equations (5.26) assuming equal on-off times. The variance for this estimate can be written with the covar $(n, n',)$ term replaced by:

$$\mathrm{Covar}\ (n, n') = F_n(T_1 - T_0) - \bar{n}^2 \tag{5.37}$$

where $F_n(\tau)$ is the auto correlation function.

$$F_n(\tau) = \underset{T\to\infty}{Lim}\ \frac{1}{2I} \int_{-T}^{T} n(t)\,n(t+\tau)\,\mathrm{d}t, \tag{5.38}$$

or in the case of successive measurements occupying a finite time as here

$$F_{\hat{n}}(j) = \sum_{i=0}^{i=\infty} \hat{n}_i \hat{n}_{i+j}$$

Depending upon the behaviour of $F_{\hat{n}}(\tau)$ and the period $(T_1 - T_0)$ the covar term Equation 5.37, will vary from covar $(\hat{n}, \hat{n}') = \text{Var}(\hat{n})$ at $(T_1 - T_0) = 0$, to zero when $(T_1 - T_0)$ is large. Thus if the period $(T_1 - T_0)$ can be made sufficiently short the Var $(\hat{n})$ and Covar (n, n') terms can be made to cancel, and a considerable reduction in variance is obtained.

$$\text{Var}(S) \rightarrow \text{Var}(\hat{s}) \tag{5.39}$$

The particular period chosen for $(T_1 - T_0)$ will depend upon the auto-correlation function of the noise. This modulation frequency* is usually picked by using the Wiener-Khintchine theorem to find the power density spectrum of the noise. The frequency at which minimum noise power is found is then the optimum modulation frequency (subject of course to detector response time limitations). In practice, the covariance term will not completely counterbalance the variance due to the noise. Nevertheless, the modulation process is almost always advantageous. Fig. 5.14 shows a typical arrangement.

In many applications the noise and signal can be quite highly correlated. It is then important to modulate that feature of the experiment which has the

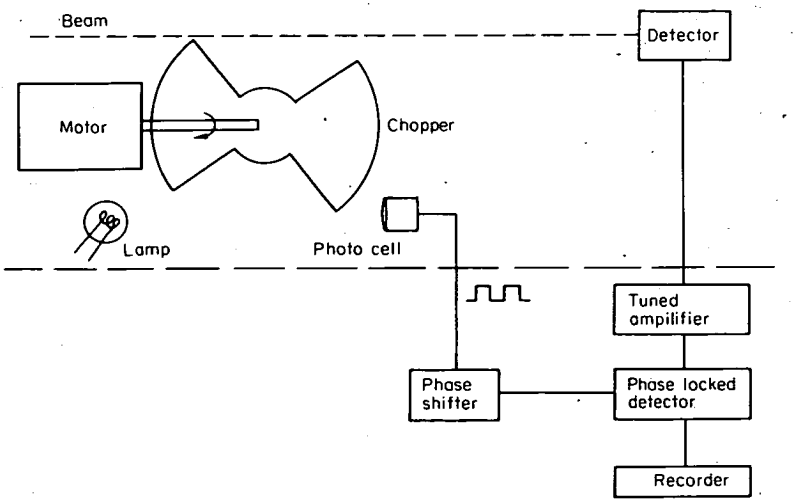

Fig. 5.14 Modulated beam system with a phase locked amplifier in the detection chain.

* Normally the open and closed periods are taken equal in the modulation process for electronic convenience and the beam is interrupted by a rotating disc driven by a synchronous electric motor.

minimum correlation with the additive noise. Thus if we are detecting K scattered from a cross beam of another species we should modulate the cross beam. Only in this way can we distinguish the K scattered from the cross beam from that scattered into the detector by collisions with the background gas.

Still further improvements to the filtering of the detector output are possible. Consider the two estimates I_1 and I_2 again, but now suppose that we continuously divide the detected signal by some time dependent quantity f(t).

$$I_1 = \frac{1}{T_3 - T_2} \int_{T_2}^{T_3} \left(\frac{s(t)}{f(t)} + \frac{n(t)}{f(t)} \right) \mathrm{d}t$$
$$I_2 = \frac{1}{T_2 - T_1} \int_{T_1}^{T_2} \frac{n(t)}{f(t)} \, \mathrm{d}t \qquad (5.40)$$

If $f(t)$ is strongly correlated with $s(t)$, for example if $f(t)$ was the main beam signal and s(t) the signal scattered at some angle (θ). Then the differential cross-section $\sigma(\theta)$ is given by:

$$\sigma(\theta) \propto \frac{s(t)}{f(t)}$$

so that

$$\sigma(\theta) \propto \mathrm{Lim}\,(I_1 - I_2) \qquad (5.41)$$

and the relative cross-section can be estimated directly. The variance of this estimate will be:

$$\mathrm{Var}\,(\sigma(\theta)) = 2\,\mathrm{Var}\left(\frac{\hat{n}(t)}{f(t)}\right) - 2\,\mathrm{Covar}\left(\frac{\hat{n}(t)}{f(t)}, \frac{\hat{n}(t+\tau)}{f(t+\tau)}\right) \qquad (5.42)$$

We have removed the variance introduced by changes in the beam intensity of Equation 5.34. Experimentally this involves recording the output from two detectors simultaneously. One detector recording the main beam and the other s(t). This system of analysis is known as cross correlation. Since the main beam signal will be large we can neglect the additive noise and treat the recorded signal from this detector as being purely due to beam fluctuations.

As before, beam modulation can be used to reduce the noise arising from

the background. The appropriate auto-correlation function will be:

$$F(\tau) = \int \left(\frac{n(t+\tau)}{f(t+\tau)} \right) \left(\frac{n(t)}{f(t)} \right) \mathrm{d}t \tag{5.43}$$

An alternative procedure might rely upon the signal statistics. For normal beam sources the signal auto-correlation is appreciable for quite large τ. Consequently we could use a modulation technique in which a single detector measures the signal intensity sequentially under two different conditions. Thus if these different observations are:

$$I_1 = \int_{T_0}^{T_1} (s(t) + n(t))\, \mathrm{d}t$$

$$I_2 = \int_{T_0}^{T_1} n(t+\tau)\, \mathrm{d}t$$

$$I_3 = c \int_{T_0}^{T_1} s(t+2\tau)\, \mathrm{d}t \tag{5.44}$$

where $cs(t)$ is the 'normalising' signal condition and $\tau = T_1 - T_0$. The estimate of σ relative to the normalising condition is:

$$\bar{\sigma} = (I_1 - I_2)/I_3$$

averaged over many periods.

The variance of this estimate is:

$$\mathrm{Var}\,(\sigma) = \frac{1}{c^2}\,\mathrm{Var}\left(\frac{I_1 - I_2}{I_3}\right) = \frac{1}{c^2}\left[\int \left(\frac{s(t)}{s(t+2\tau)}\right)^2 \mathrm{d}t - \left(\int \frac{s(t)}{s(t+\tau)}\,\mathrm{d}t\right)^2 \right.$$

$$\left. + \frac{2}{\bar{S}^2}(\bar{n}^2 - \phi_n(\tau)) + 2\frac{\bar{n}}{\bar{S}} \int \frac{s(t)}{s(t+2\tau)}\,\mathrm{d}t \right. \tag{5.45}$$

The variance due to beam fluctuations has thus been replaced by a measure of its auto-correlation so that if τ can be made short enough the variance from this source will be reduced.

Filtering

The techniques for signal analysis discussed are examples of auto and cross correlation. The procedures described are by no means exhaustive. A more

comprehensive theory has been developed by N. Wiener (1949). We shall see that it is in principle possible to design an optimum filter for any application for which the statistics of the signal and noise are known.

In any experiment we are in general concerned to measure the scattered intensity as a function of one or more experimental variables such as collision energy or scattering angle. The problem is to determine the optimum filtering operation which when applied to the primary measurements will yield the closest approach to the correct result.

Consider a set of $m + 1$ observations:

$$b_0, b_1, \ldots b_k, \ldots b_m$$

representing a series of intensity measurements at values of the variable $0, 1, \ldots k, m$. Further let us suppose that the exact values that we should have observed if our measurements had been made under noiseless conditions are:

$$M_0, M_1, \ldots M_k, \ldots M_m$$

We perform a linear filtering operation with a lag s on the observed values to yield an output.

$$a_{k-s} = \sum_{n=0}^{n=h \leqslant m} A_n \, b_{k-n} \tag{5.46}$$

Where the coefficients A_n represent our filter function of h elements.

The error between the exact value and the output filtered results is therefore:

$$I_{k-s} = M_{k-s} - a_{k-s}$$

$$I_{k-s} = M_{k-s} - \sum_{0}^{h} A_n \, b_{k-n}$$

The mean square error over the whole series will thus be:

$$I = \frac{1}{m + h} \sum_{k=0}^{m+h} \left(M_{k-s} - \sum_{n=0}^{n-h} A_n b_{k-n} \right)^2 \tag{5.47}$$

The filter can be optimized in the sense of providing an output with the least mean square error by differentiating Equation 5.47 with respect to each filte

coefficient and equating each differential coefficient to zero:

$$\frac{\partial I}{\partial A_1} = \sum_{k=0}^{m+h} (m_{k-s} - \sum_{n=0}^{h} A_n b_{k-n})(-b_{k-j}) = 0$$

so

$$\sum_n A_n \sum_k b_{k-n} b_{k-j} = \sum_k M_{k-s} b_{k-j} \tag{5.48}$$

But $(m+h)^{-1} \sum_k b_{k-j} b_{k-n}$ is the discrete signal form, $F_b(n-j)$, of the auto-correlation function Equation 5.25 for a lag of $(n-j)$. Similarly, $(m+h)^{-1} \Sigma M_{k-s} b_{k-j}$ is the cross-correlation function (defined as $\int M(t) b(t+\tau) \mathrm{d}t$), $X_{Mb}(s-j)$. Thus we obtain:

$$\sum_{n=0}^{h} A_n F_b(n-j) = X_{Mb}(s-j) \tag{5.49}$$

as our optimising equation from which the optimum set of filtering coefficients can be obtained. For an additive noise N_i:

$$b_i = M_i + N_i \tag{5.50}$$

we can write the auto- and cross-correlation functions in Equation 5.49 as the sum of the individual functions for the noise and 'message':

$$F_b(n-j) = F_M(n-j) + F_N(n-j) + 2X_{MN}(n-j)$$

and

$$X_{Mb}(s-j) = F_M(s-j) + X_{MN}(s-j) \tag{5.51}$$

Thus information on the message (M) and noise statistics can be applied directly to the calculation of an optimum filter. The best lag and length for the filter are usually determined by letting s and m increase until the mean square error shows little further decrease.

In the event that the filtering scheme is required not to produce as closely as possible the noiseless 'message' but merely to yield some parameter of it such as its arrival time similar techniques can be used but will yield smaller mean square errors. For a more detailed discussion the reader is referred to C. A. Robinson (1967).

5.6 Ion counting systems

The foregoing analysis has been made for continuous or analog signals but can be extended to include the output of particle counters. The primary signal in such counting systems however is still in analog form, e.g. the output of an electron multiplier. This signal is digitized by a discriminating circuit which has an output only when the input signal exceeds a certain level. The signal can thereafter be handled digitally and without fear of adding any electronic noise. The optimum threshold for the discrimination depends upon the amplitude and statistics of the noise and signal. The larger the difference in amplitude between noise and signal pulses the less important the setting of the discriminator threshold (Fig. 5.15).

To extend our analysis to deal with this type of pulse output we must interpret the signal and noise time dependent functions used in interpreting analog signals as probability density functions. These describe the probability of a pulse occurring in a period t to $t + dt$, i.e. as instantaneous count rates. Thus for the simple experiment already discussed in which the beam flag is alternately opened and closed at near zero frequency we have

N_n = average number of noise counts sec^{-1}

S = average number of signal counts sec^{-1}

C = neutral particle counting efficiency (counts $molecule^{-1}$)

σ_n = standard deviation of the noise count rate.

The figure of merit* for the detector (minimum particle current measurable to ±20 per cent in 100 secs with 95 per cent confidence) will be:

$$D = \sigma_n / C$$

For white noise, i.e. uncorrelated arrivals of the noise pulses the de Moivre

* The *maximum* rate at which counts may be accumulated depends upon the 'resolving time' or time after counting one pulse during which the system will not respond to another. Due to the random arrival of the pulses some counts will inevitably be lost due to overlap. For uncorrelated pulses, if S is the observed count rate, t the resolving time, the true count rate n will be

$$n = \frac{S}{1 - St} \tag{5.52}$$

The counting loss should not be allowed to exceed a few per cent or the accuracy of the measurements will be badly affected. Particular care is needed if the pulse statistics are not Gaussian, thus emission of ions from a hot filament occurs in 'bursts' during which the instantaneous count rate may be very large. The counting loss may then greatly exceed that calculated from Equation 5.52.

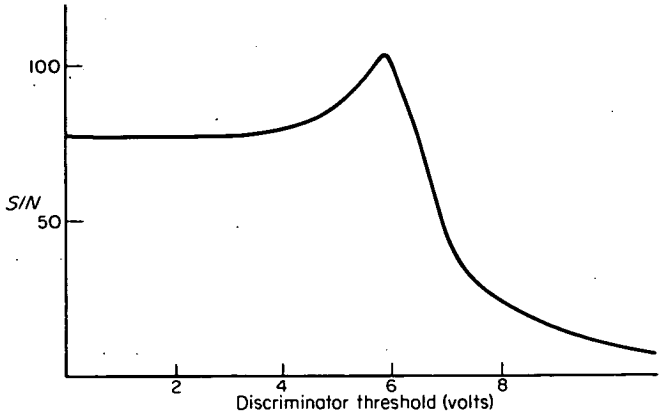

Fig. 5.15 Plot of signal/noise ratio versus pulse height transmitted showing the optimum discriminator setting. A sizeable fraction of the noise has a lower peak height than the average signal pulse.

Laplace theorem asserts that $\sigma_n \approx \bar{N}_n^{1/2}$, i.e. for white noise the figure of merit is:

$$D = \bar{N}_n^{1/2}/C \tag{5.53}$$

The optimum threshold for the discriminator can thus be determined by optimizing D above. Improvement in the sensitivity can be achieved either by increasing C or by decreasing the noise background. In both cases however, the overall improvement in sensitivity will only vary as the square root since the noise count is also proportional to C.

The counting efficiency depends upon the detector (the average number of ions or electrons ejected per incident molecule), the transmission to the multiplier and the multiplier gain. Conventional multipliers using BeCuO plates are sensitive to contamination (particularly by reactive chemical species) and are best avoided. Resistive strip or channel multipliers are much less sensitive and very much more suitable.

If the rate of arrival of the noise pulses is non Gaussian, and in particular, if low frequency noise components are present, modulation methods similar in principle to those already described may be used. In these systems the phase sensitive detector is replaced by two or more pulse counters. Each counter is then opened for a different phase of the modulation. This type of system can be fairly readily extended to encompass quite complicated modulation schemes. As an example Fig. 5.16 (L. T. Cowley et al., 1969)

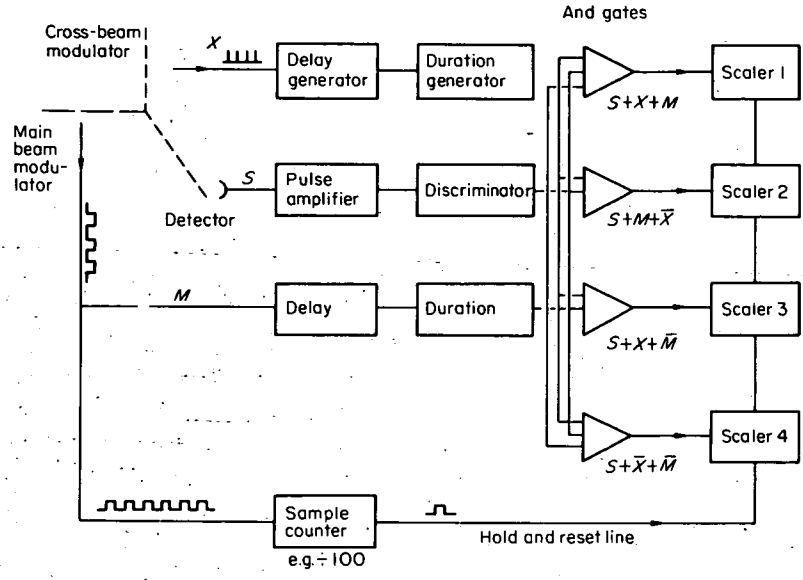

Fig. 5.16. Counting analog of a 'lock in' detector scheme. Both cross and main beams are modulated at different frequencies.

shows a cross-beam experiment in which both beams are modulated, one at a convenient multiple of the frequency of the other.

If $m(t)$ and $x(t)$ are functions representing the main and cross-beam signals, $n(t)$ is the background signal from the species being detected and $V(t)$ is linearly related to the pressure in the scattering chamber. Then the detector output Si(t) will be given approximately by the following table:

Cross beam	Main beam	
on	on	$S_1(t) = Km(t)\,x(t) + n(t) + V(t)m(t) + V(t)x(t)$
off	on	$S_2(t) = n(t) + m(t)V(t)$
on	off	$S_3(t) = n(t) + x(t)V(t)$
off	off	$S_4(t) = n(t)$

Where $m(t)V(t)$ and $x(t)V(t)$ represent the noise contribution produced by scattering the main and cross-beam respectively from the background gas. The scattered signal $Km(t)x(t)$ containing the differential cross-section information will thus be $I = S_1 - S_2 - S_3 + S_4$. Arguing as before we can see Var(I) will include a number of terms describing the co-variation of $x(t)$, $m(t)V(t)$ and $n(t)$ during the observation periods of $S_1 S_2 S_3 S_4$. Thus if the time spent in observing S_1 to S_4 can be made short compared to the time over which the

functions $x(t)$, $m(t)$, $V(t)$, $n(t)$ are appreciably auto-correlated then the variance of I will be reduced. In the figure each of the four scalers is driven via a coincidence, anti-coincidence gate so that counts corresponding to the four possible beam flag conditions can be accumulated.

(i) Coincidence and time of flight systems

The use of coincidence gates can be extended to obtain much more detailed information. For two body collisions the centre of mass motion is conserved and two particles of mass M_1 and M_2 emitted from such a collision and scattered through angles θ_1 and θ_2 to the incident beam direction must have specific velocities v_1 and v_2. Thus if two detectors are sited on a radius of l at θ_1 and θ_2 the two emitted particles will produce signal pulses at times $l\,v_1$ and $l\,v_2$ one from each detector. In general, pulse pairs will arrive with time delays determined by the energy transferred in the collision. A system which responds to pulses from different detectors spaced in time by an appropriate amount will thus yield information on the exothermicity of the collisions. A further advantage is the large reduction in signal variance that can be achieved.

Let the number of collisions of the specified sort (i.e. given exothermicity channel and differential cross-section) be N per second and the number of background particles striking at detectors A and B be M_A and M_B. If ϵ_A and ϵ_B are the efficiencies with which the detectors convert particles incident upon them to pulses then the number of signal and noise pulses will be:

At Detector A

Noise $= M_A \epsilon_A$ Signal $= N\epsilon_A$

At Detector B

Noise $= M_B \epsilon_B$ Signal $= N\epsilon_B$

Thus for random arrival of noise pulses the figure of merit for each detector will be:

$$\sqrt{M_A/\epsilon_A} \quad \text{and} \quad \sqrt{M_B/\epsilon_B}$$

and the minimum number of potentially detectable events that could be measured with the specified precision would be:

$$N = \sqrt{\frac{M_A}{\epsilon_A}} \quad \text{and} \quad \sqrt{\frac{M_B}{\epsilon_B}}$$

at each detector.

If we now use a coincidence detection system such that an output is only taken if detector B has a pulse present in a period τ some specified time after a pulse has occurred in detector A. Then the noise and signal will be:

$$\text{Noise} = \epsilon_A M_A \tau M_B \epsilon_B$$

$$\text{Signal} = N \epsilon_A \epsilon_B$$

(Assuming $N \ll M_A$ and M_B which is the interesting case.)

The minimum number of potentially detectable collisions that must occur to be measured with our standard precision is:

$$N = \sqrt{\frac{M_A M_B \tau}{\epsilon_A \epsilon_B}} \tag{5.56}$$

Thus if τ can be made sufficiently short and ϵ_A and ϵ_B are not too different from unity a large improvement in sensitivity can be achieved. As an example let

$$\epsilon_A \sim \epsilon_B \sim 0{\cdot}5, M_A \sim M_B \sim 10^4 \text{ and } \tau = 10^{-7} \text{ s}$$

The individual detectors would have a figure of merit of:

$$\sqrt{\frac{M_A}{\epsilon_A}} \sim 140 \text{ counts s}^{-1}$$

As a coincidence system the minimum count rate would be:

$$\sqrt{\frac{M_A M_B \tau}{\epsilon_A \epsilon_B}} = 6.3 \text{ counts s}^{-1}$$

For the coincidence system additional information as to the exothermicity of the collision would also be available. Unfortunately the detector requirements of high efficiency and very fast response time are met by few detectors, essentially only those involving direct excitation of the multiplier, either by the collision of an energetic particle or by a photon being suitable. Relatively low backgrounds are also required if the gated detector is not to be permanently open, i.e. $M_A \tau$ must be small compared to 1 s.

Fig.5.17 shows a suitable arrangement for coincident detection. By using beam choppers and suitable additional logic units modulation could be superimposed on the coincidence detector.

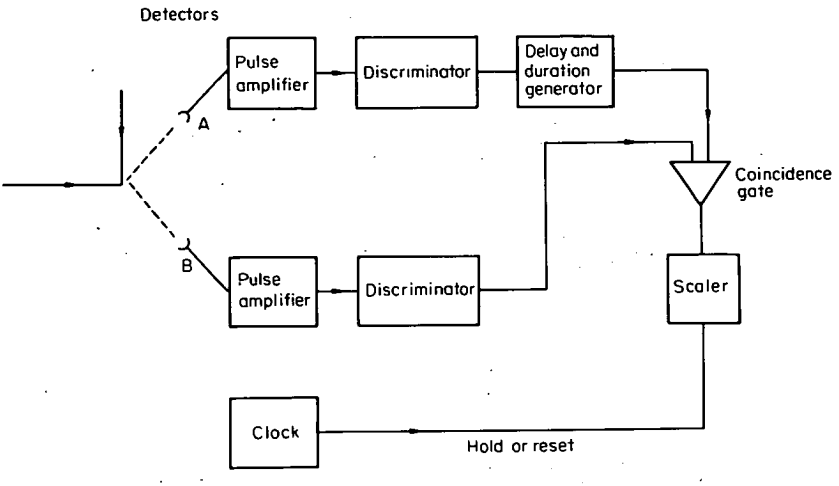

Fig. 5.17 Coincident detection scheme.

The delayed coincident detection system suffers from the drawback that only one particular exothermicity is accepted for each setting of the delay. In some experiments a range of post collision velocities are present and it may be desired to examine their distribution experimentally. The simplest but slowest procedure would be to use the coincident system and take a range of measurements for different delay times. Another alternative would be to use additional delay generators, coincidence gates and scalers, each chain corresponding to a different delay time. Unfortunately if many observation points are required this arrangement becomes very expensive. In these circumstances the arrangement shown in Fig. 5.18 may be used. This system employs a pulse height analyzer which is capable of sorting input pulses into a large number of separate scalers according to the pulse amplitude. The pulses

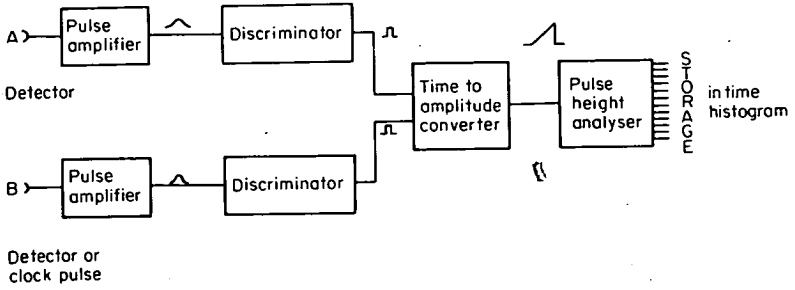

Fig. 5.18 Time of flight analysis using a time to amplitude converter followed by pulse height analysis.

are amplified and discriminated in the usual way and then both detector pulses pass to a time to amplitude convector which produces pulses whose amplitude is proportional to the time difference between successive pulses in channels A and B. The PHA then accumulates the output pulses in accordance with their amplitude (i.e. time difference in this case). The random noise pulses in both detectors are uncorrelated and produce a flat distribution. A disadvantage of this system is the relatively slow speed of the PHA so that counts and hence data can only be accumulated fairly slowly. Of course, if the available signal count rates are already low, this is no additional disadvantage.

As an alternative to coincident detection a single detector may be employed. One of the beams is then pulsed to provide a time reference and the received signal gated after a suitable delay. This technique of 'time of flight' is discussed in more detail in Chapter 4.

CHAPTER SIX

Quantum Mechanics of Scattering

6.1 Introduction

This chapter is largely devoted to deriving the more commonly used formulae that relate elastic scattering to intermolecular potentials and to indicating how the forward calculation, from assumed potential to scattering pattern, can be made. At the outset the notation has been made formal enough to allow the framework to cover inelastic collisions, though in practice the analysis of such events is much more subject to approximation than is elastic scattering. Elementary scattering theory is nowadays treated in all textbooks of wave mechanics for physicists and notable among these are those by E. Merzbacher (1961) and L. D. Landau and E. M. Lifshitz (1958), for their treatment of scattering; a fuller development can be found in L. S. Rodberg and R. M. Thaler (1967), T. Y. Wu and T. Ohmura (1962) or R. Newton (1966).

The evidence for the breakdown of classical mechanics in calculating the details of elastic molecular collisions can be summarized as follows:

(1) The existence of finite rather than infinite total cross-sections. Experimentally (Chapter 7), the differential cross-section $\sigma(\chi)$ reaches a finite limiting value as the scattering angle tends to zero and so the measured total cross-section also tends to a finite value as the angular resolution is improved.

(2) The observation that rainbow structures have a finite amplitude that becomes independent of the resolution as the resolution is improved. Classical mechanics (Chapter 2) predicts a divergence in $\sigma(\chi)$ at the rainbow.

(3) The observation of undulations in $\sigma(\chi)$, especially at small angles, where classical mechanics predicts monotonic behaviour.
(4) The existence of undulations in the energy dependence of the total cross-section, when classical mechanics predicts a monotonic dependence (this point will turn out to be closely related to (3)).

Finally when a cross-section is measured for scattering accompanied by a specific change in internal quantum state, then wave mechanics will have to be used, if only to treat the internal motion.

In general, the differences in behaviour predicted by classical and quantum mechanics for the details of thermal collisions are very pronounced – unlike, say, the quantum corrections to gas compressibilities or transport properties at room temperature. The essential factor here is resolution; under conditions of poor angular or energy resolution, quantum molecular scattering patterns will be close to those predicted by classical mechanics if both results are averaged over the appropriate apparatus functions. However, partly because absolute cross-sections are difficult to measure, the usefulness of elastic scattering data lies in resolving and interpreting the angular or energy structure. Here wave mechanics is essential, although low resolution experiments can yield a great deal of information when applied to gross effects such as chemical reaction.

With the insight given by wave mechanics we can see two reasons why classical mechanics might break down when applied to an actual molecular scattering experiment. The first is that the best wave packet we might construct to represent the classical particle by a wave function, does not move along a well defined trajectory in the presence of the intermolecular field. The second difficulty is that classically a particle reaching the detector might have followed one of several paths resulting in the same angle of deflection. This is a similar situation to the hypothetical interfering slit experiment discussed in wave mechanics and the absence of any information as to the actual path leads to mutual interference.

Treating first the approximation of replacing a wave packet by a classical particle, there are two aspects of the problem. If we are to use classical mechanics for the radial motion associated with any particular trajectory, we require that the equivalent wave packet does not spread appreciably during the collision, either in the forward or transverse direction. Such a wave packet is constructed from a range of momentum states and if the classical property, such as deflection angle or time delay, varies appreciably among the constituent waves of the packet, classical mechanics cannot give a reliable picture of the behaviour of the whole wave packet, merely of its centroid.

If the change in time delay induced by the collision in constituent plane waves of slightly differing velocity is too large, the wave packet will begin to spread rapidly after the collision. Under these conditions both the classical approximation and the concept of interference between different parts of the scattered wave front, frequently used in this chapter, breaks down (T. Y. Wu and T. Ohmura, 1962). We saw in Chapter 2 that the classical time delay is related to the phase shifts by

$$\tau_l = \frac{1}{\hbar}\frac{\partial \eta_l}{\partial E} = \frac{2\mu}{\hbar k}\frac{\partial \eta_l}{\partial k}$$

The spread in time delay across a wave packet constructed from a range of wave numbers thus depends upon $[\partial^2 \eta_l/\partial k^2]\,\Delta k$. If this quantity becomes too large, the 'resonance' must be considered separately (L. D. Landau and E. M. Lifschitz, 1958). Fortunately, the maximum time delay normally associated with molecular scattering at thermal speeds is $\lesssim 10^{-12}$ s, which is much shorter than the time taken for the whole wave packet to pass the target. Long delay times, associated with classical orbiting, do occur but affect only a small part of the incident wave front.

A wave packet also ceases to behave like a classical particle if the predominant wavelength λ (= $1/k$) becomes comparable to the range of the scattering potential. Under these conditions reflection occurs from the regions of more rapidly changing potential – an entirely non-classical phenomenon. At thermal energies $\lambda/\sigma_{LJ} \lesssim 0.2$ and so such reflections (and associated tunneling phenomena) should not cause a widespread breakdown of classical mechanics.

A rather different reason why we might not be able to construct a wave packet that moves along the expected classical trajectory, lies in the precision with which we must specify the impact parameter and the effect this has on the uncertainty in the transverse momentum of the wave packet, p_x. Let the angle of deflection in CM coordinates be χ; the transverse momentum transferred from projectile to target is

$$\Delta p_x \approx \mu v_z \sin\chi \approx \mu v_z \chi \tag{6.1}$$

where the initial velocity is in the z-direction. In theory we can construct a wave packet with as precise a transverse velocity as we wish, but the price is paid in the growing uncertainty of the lateral displacement, b. Like all relationships based upon wave packet considerations, the result is given by

the appropriate uncertainty principle,

$$\delta b \delta p_x \sim \hbar \tag{6.2}$$

For the classical trajectory to be well defined, we require $\delta b \ll b$ and so the wave packet must be constructed from a range of momentum states of width $\delta p_x \gg \hbar/b$. This uncertainty δp_x implies, from Equation 6.1, an uncertainty in the angle of deflection $\delta\chi$ given by

$$\delta\chi \approx \delta p_x/\mu v_z. \tag{6.3}$$

From Equation 2.31, χ is related to b at small deflections by

$$\chi \approx sC_s/(Eb^s) \sim V(b)/E, \tag{6.4}$$

the first relationship holding for a potential of the form $V = C_s R^{-s}$. If the fractional uncertainty in the angle of deflection is to be small, $\delta\chi/\chi \ll 1$, combining the above relationships gives

$$\lambda/b \ll \chi \tag{6.5}$$

But, from Equation 6.4, $\chi \propto b^{-s}$ and so whatever the value of λ, Equation 6.5 imposes a lower limit on χ beyond which the scattering cannot be classical. At thermal energies $\lambda \sim 10^{-8}$ mm and so the breakdown of classical scattering can be expected for angles less than $\sim 1°$. When the partial wave analysis of scattering is discussed, it will emerge that at very small angles, in contrast to larger angle scattering, the scattered intensity cannot be attributed to a narrow range of impact parameters centred around the value corresponding classically to the angle of observation.

For molecular scattering, a much more important deficiency of classical mechanics is its failure to take into account interfering trajectories. These arise when two or more impact parameters lead to the same angle of deflection. In an actual scattering experiment the target is bombarded by a beam of macroscopic dimensions that, however well collimated, contains a virtually infinite number of angular momentum states. Even if the beams are stopped down to 0.1 mm (which would be very good collimation) the range of possible impact parameters would extend to $\sim 10^6$ molecular diameters. If the beam were made so narrow that it extended over only the dimensions of a molecule, diffraction effects at the slit (themselves a scattering phenomenon) would be so pronounced that the measured differential cross-section could not be defined with respect to a parallel incident beam.

No measurement is made of the impact parameter during the collision and we must make any wave function of the system reflect this virtually complete uncertainty. Adopting the terminology of optics for a moment, a detector in a beam experiment receives contributions from all the secondary scattered waves originating across a virtually infinite wave front. The amplitudes of each partial wave must be added before squaring to calculate the resulting intensity. If we choose to analyze the problem in terms of angular momentum states, the scattered amplitude resulting from each state must be added to calculate the final scattered amplitude. It will emerge that in molecular scattering there are, over a wide angular range, frequently two or three groups of angular momentum states with almost stationary phase and these correspond to classical interfering paths in R. P. Feynmann's and A. R. Hibbs' (1965) sense.

6.2 Boundary conditions for solutions of the wave equations

The wave mechanical problem is discussed in the relative co-ordinate system that was used for the classical treatment, augmented by whatever internal co-ordinates are necessary to cover inelastic events. The motion of the centre of mass of the whole system is factored out of the wave function, leaving the wave function for relative motion $\psi(\mathbf{R})$ to satisfy

$$\{-\hbar^2/2\mu\nabla^2 + V(R)\}\,\Psi(\mathbf{R}) = E\Psi(\mathbf{R}) \tag{6.6}$$

where, as for most of this chapter, the colliding particles are assumed to be structureless. $\psi(\mathbf{R})$ must have the following asymptotic form outside the range of the potential $V(R)$;

$$\Psi(\mathbf{R}) \xrightarrow[R\to\infty]{} \frac{1}{\mathcal{N}^{1/2}} \left\{ e^{ikz} + \frac{1}{R} f(\chi) e^{ikR} \right\} \tag{6.7}$$

and also satisfy

$$\Psi(\mathbf{R}) \xrightarrow[R\to 0]{} 0 \tag{6.8}$$

This type of wave function can be interpreted with the aid of the momentum operator,

$$\mu v = -i\hbar\partial/\partial\mathbf{R} \tag{6.9}$$

and the derived flux Equation 6.10 below. The gradient in Equation 6.9 is taken in the direction in which the component of the velocity of the equivalent classical particle mass μ is required.

The first term in Equation 6.7 represents a plane wave travelling with velocity $v = \hbar k/\mu$ in the z-direction and the second term is an outgoing spherical wave with an angle dependent amplitude $f(\chi)$. The function $f(\chi)$ contains all the information about the scattering process and it is central to the discussion of all scattering processes. The plane wave function $\exp(ikz)$ represents a uniform density of particles extending from $z = -\infty$ to ∞; Equation 6.7 thus represents a steady state solution with a continuous input of particles. The plane wave in Equation 6.7 also has an infinitely broad front, unlike the well collimated beams of actual experiments, but no error will result if interference terms between the incoming and outgoing waves are neglected except in the region where they do in fact overlap along the positive z-axis.

Before the calculation of $f(\chi)$ is discussed, the use of Equation 6.7 is illustrated by deriving the formula for the elastic differential cross-section $\sigma(\chi)$ in terms of $f(\chi)$. The asymptotic flux at a point (R, χ, ϕ) other than on the z-axis is given solely by the second term in Equation 6.10 as $R \to \infty$, provided that the incident beam is of finite width. Applying the standard formula for the flux,

$$\mathbf{j} = -\frac{\hbar}{2i\mu}\left\{\Psi \nabla \Psi^* - \Psi^* \nabla \Psi\right\} \tag{6.10}$$

(Note that the normalization factor $\mathcal{N}$ in Equation 6.7 must have the dimensions of volume in order to give j the dimensions of flux and it is conveniently assigned the value 1 cm^3), the plane wave gives a flux of v particles cm^{-2} in the z direction and the spherical wave in Equation 6.7 yields

$$j_R = |f(\chi)|^2 v/R^2 \tag{6.11}$$

Only the radial component of j is non-zero (as can be verified later) after the scattering is over. From the definition (see Section 2.1) of the differential cross-section $\sigma(\chi)$ in terms of the number of particles dn scattered into a solid angle $d\omega$ per second per unit incident flux, Equation 6.11 gives

$$dn = |f(\chi)|^2 \, d\omega$$

and so

$$\sigma(\chi, \phi) = dn/d\omega = |f(\chi)|^2 \tag{6.12}$$

The total cross-section follows from the integration of $\sigma(\chi)$ over a sphere centred on the scattering centre:

$$\sigma_{tot} = \int_0^{2\pi}\int_0^{\pi} |f(\chi)|^2 \sin\chi \, d\chi \, d\phi \tag{6.13}$$

We can discuss some aspects of the conservation of matter during collision. In order to generalize the discussion a little, we will suppose that the target has internal states $\Phi_n(\mathbf{r})$ and that these can be excited during collision. Equation 6.7 is then readily generalized to

$$\Psi \xrightarrow[R\to\infty]{} e^{ikz}\Phi_0(\mathbf{r}) + \frac{1}{R}\sum_{n=0} f_n(\chi)\, e^{ik_n R}\Phi_n(\mathbf{r}) = \sum_n \Psi_n(\mathbf{R})\Phi_n(\mathbf{r}) \tag{6.14}$$

where the normalization factor has been dropped and the wave number k_n is given by

$$k_n = \sqrt{2\mu E_n}/\hbar \tag{6.15}$$

where $E_n = E_0 - \epsilon_n$ is the relative kinetic energy after exciting the n^{th} state. The conservation of energy is thus built into the wave function. To ensure the conservation of particles, the total current across a closed surface s surrounding the scattering centre must vanish:

$$\sum_n \int_S \mathbf{j}_n \cdot d\mathbf{s} = 0 \tag{6.16}$$

where $\mathbf{j}_n$ is the flux of particles scattered with excitation of the n^{th} state and the integration is conveniently over the surface of an infinitely large sphere. In principle, we can measure separately the fluxes associated with exciting different internal states by placing a velocity or state selector in front of the detector. If this is not done, the total signal i received by the detector is the sum of the contributions from the different states:

$$i(\chi) = \sum_n i_n(\chi), \tag{6.17}$$

since there is no interference between the signals, just as the total cross-section is the sum of the cross-sections contributed by different exit channels rather than the square of the sum of the scattered amplitudes. We

thus extend the flux formula slightly to the inelastic case by writing

$$\mathbf{j}_n = -\frac{\hbar}{2i\mu}\left\{\Psi_n \nabla \Psi_n^* - \Psi_n^* \nabla \Psi_n\right\} \tag{6.18}$$

where the orthogonality of the internal states Φ_n ensures that there is no asymptotic interference between different exit channels.

The expression 6.18 is most conveniently evaluated by changing completely to spherical polar co-ordinates, and so the plane wave component is written $e^{ikR\cos\chi}$. The number of particles scattered per second that leave the target in its original state, i_0, is then

$$\begin{aligned} i_0 = \int_s \mathbf{j}_0 \, dS = \frac{\pi\hbar}{i\mathcal{N}\mu}\int R^2 \sin\chi d\chi \Big\{ & e^{+ik_0 R\cos\chi} \nabla_R e^{-ik_0 R\cos\chi} \\ & + R^{-1} e^{ik_0 R\cos\chi} \nabla_R f_0(\chi) e^{-ik_0 R} + R^{-1} e^{ik_0 R} f_0(\chi) \nabla_R e^{-ik_0 R\cos\chi} \\ & + R^{-2} |f_0(\chi)|^2 e^{ik_0 R} \nabla_R e^{-ik_0 R} - \text{complex conjugate} \Big\} \end{aligned} \tag{6.19}$$

The reader should follow through each term in Equation 6.19. Thus, the first term reduces to $(\pi\hbar R^2/\mathcal{N}\mu)\int_0^{2\pi} k_0 \cos\chi \sin\chi \, d\chi$, which vanishes by symmetry. The second and third terms together with their complex conjugates represent interference between the plane and spherical waves. Upon repeated integration by parts, an expansion in $1/R$ is developed. Retaining only the leading term as $R \to \infty$, the result is

$$i_0 = \frac{4\pi v_0}{k\mathcal{N}} \operatorname{Im} f_0(0) + \frac{2\pi v_0}{\mathcal{N}} \int_0^{\pi} |f_0(\chi)|^2 \sin\chi d\chi \quad (v_i = \hbar k_i/\mu) \tag{6.20}$$

where the first term comes from the second and third terms in Equation 6.19 and the second term from the fourth and fifth terms in Equation 6.19. We note that, in accord with experimental conditions, the interference term (the first one in Equation 6.20) between the plane wave and the spherical scattered wave depends only on the forward scattered amplitude, $f(0)$. For particles scattered inelastically, the interference term is absent and

$$i_n = 2\pi v_n \mathcal{N}^{-1} \int_0^{\pi} |f_n(\chi)|^2 \sin\chi d\chi \tag{6.21}$$

Then, the inelastic differential cross-section is

$$\sigma_n(\chi) = i_n(\chi) \cdot \mathcal{N}/v_0 = v_n/v_0 \, |f_n(\chi)|^2 \tag{6.22}$$

and the total cross-section, obtained by generalising Equation 6.13, is

$$\sigma_{tot} = 2\pi \sum_n \frac{v_n}{v_0} \int_0^\pi \sigma_n(\chi) \sin \chi d\chi \tag{6.23}$$

The conservation of particles results in

$$\sum_{n=0} i_n = 0 \tag{6.24}$$

and so

$$\sigma_{tot} = \frac{4\pi}{k_0} \text{Im} f_0(0) \tag{6.25}$$

which shows that the conservation requirement is fulfilled by the interference between the incoming and outgoing elastic channels in the forward direction. The result Equation 6.25 is known as the optical theorem and also holds in the presence of reactive scattering, which simply adds other exit channels.

6.3 The formal solution of the wave equation

We now come to the problem of solving the wave equation itself, subject to the boundary condition of Equation 6.7, so that the scattered amplitude can be extracted. The wave equation can either be solved as a differential equation or converted to an integral equation. The former turns out to be the more convenient path for molecular scattering problems, but the integral equation approach leads directly to Born's approximation which occupies an honoured place in scattering theory – though in its full form it has little application to molecular as opposed to electron scattering. The wave equation for elastic scattering, Equation 6.6 can be re-arranged in the form

$$(E - H_0)\,\Psi(\mathbf{R}) = V(\mathbf{R})\,\Psi(\mathbf{R}) \tag{6.26}$$

where H_0 is the kinetic operator for relative motion,

$$H_0 = -\frac{\hbar^2}{2\mu}\left\{\frac{1}{R^2}\frac{\partial}{\partial R}R^2\frac{\partial}{\partial R} + \frac{1}{R^2 \sin\chi}\frac{\partial}{\partial\chi}\sin\chi\frac{\partial}{\partial\chi} + \frac{1}{R^2\sin^2\chi}\frac{\partial^2}{\partial\phi^2}\right\} \tag{6.27}$$

and $V(\mathbf{R})$ is the potential energy of interaction. If the terms on the r.h.s. of

Equation 6.26 are for the moment regarded as known functions of the co-ordinates, $\rho(\mathbf{R})$, the whole equation assumes the form of an inhomogeneous second order differential equation but with a particularly simple differential operator on the l.h.s.

$$(E - H_0)\,\Psi(\mathbf{R}) = \rho(\mathbf{R}) \tag{6.28}$$

Now a general solution of such an equation having any required asymptotic form can be constructed from the appropriate Green's function, $G(\mathbf{R}, \mathbf{R}')$, which in turn is a solution of the inhomogeneous equation

$$(E - H_0)\,G(\mathbf{R}, \mathbf{R}') = \delta(\mathbf{R} - \mathbf{R}') \tag{6.29}$$

Direct substitution into Equation 6.28 shows that

$$\Psi(\mathbf{R}) = \int G(\mathbf{R}, \mathbf{R}')\,\rho(\mathbf{R}')\,d\mathbf{R} \tag{6.30}$$

is a particular solution of Equation 6.28 when the following property of the delta function is used:

$$\rho(\mathbf{R}) = \int \delta(\mathbf{R} - \mathbf{R}')\,\rho(\mathbf{R}')\,d\mathbf{R}' \tag{6.31}$$

A complete solution of Equation 6.28 is then the sum of the particular integral, Equation 6.30 and the solution of the homogeneous equation

$$(H_0 - E)\,\chi_0(\mathbf{R}) = 0 \tag{6.32}$$

giving

$$\Psi(\mathbf{R}) = \chi_0(\mathbf{R}) + \int G(\mathbf{R}, \mathbf{R}')\,\rho(\mathbf{R}')\,d\mathbf{R}' \tag{6.33}$$

We choose $\chi_0(\mathbf{R})$ to be $e^{i\mathbf{k}_0\cdot\mathbf{R}}$ and so a Green's function having the asymptotic R dependence e^{ik_0R}/R is needed. The required result is:

$$G(\mathbf{R}, \mathbf{R}') = -\frac{\mu}{2\pi\hbar^2}\,\frac{e^{ik_0|\mathbf{R}-\mathbf{R}'|}}{|\mathbf{R}-\mathbf{R}'|} \tag{6.34}$$

Then, letting $\mathbf{R} \to \infty$ so that over effectively the whole field of integration in Equation 6.33 $R \gg R'$, the following result for $f(\chi)$ (the coefficient of

e^{ik_0R}/R in Equation 6.33) is obtained:

$$f(\chi) = -\frac{\mu}{2\pi\hbar^2}\int e^{i\mathbf{k}\cdot\mathbf{R}'}\, V(\mathbf{R}')\,\Psi(\mathbf{R}')\,d\mathbf{R}' \tag{6.35}$$

where $k_0|\mathbf{R}-\mathbf{R}'| \approx k_0(R - \mathbf{R}'\cdot\mathbf{R}/R) = k_0R - \mathbf{k}\cdot\mathbf{R}'$ has been used and k s the wave number vector in the direction of observation R. The angle of scattering, χ, is the angle between k and $\mathbf{k}_0$. It may not seem that much progress has been made in Equation 6.35 because the exact wave function still appears in the expression. However, the way is now open for the development of a series expansion of the scattered amplitude in terms of $V(\mathbf{R})$ – the Born expansion. The first Born approximation gives $f(\chi)$ to $0(V)$ and is obtained by substituting the undistorted plane wave function for the exact wave function $\Psi(R')$ in Equation 6.35. In general the n^{th} order approximation to $f(\chi)$ is obtained by substituting the $(n-1)^{th}$ approximation to the wave function into Equation 6.35 but only the first and second order approximations are at all used. Pursuing the 1st order approximation we have

$$f(\chi) = -\frac{\mu}{2\pi\hbar^2}\int e^{-i(\mathbf{k}-\mathbf{k}_0)\cdot\mathbf{R}'}\, V(\mathbf{R}')\,d\mathbf{R}' \tag{6.36}$$

Then with

$$|\mathbf{k}-\mathbf{k}_0| = 2k\sin\chi/2 = q \tag{6.37}$$

we may take the direction of the vector q as a new polar axis to replace the z-axis and carry out the angular integration in Equation 6.36 with respect to this new axis with α as the new polar angle. The volume elements of integration transform as

$$R^2\sin\chi\, d\chi d\phi dR = R^2\sin\alpha\, d\alpha d\phi' dR$$

and the scattered amplitude becomes for a central potential

$$f(q) = -\frac{2\mu}{\hbar^2 q}\int_0^\infty \sin(qR)\, V(R)R\, dR \tag{6.38}$$

This is the first Born approximation. It suffers from one formal fault and one

practical disadvantage. Firstly, it gives a scattered amplitude that is wholly real and so cannot satisfy the optical theorem; this is the result of using an undistorted plane wave in the source function $\rho(\mathbf{R})$ without taking into account the attenuation of the incident wave. The second difficulty is that the integral in Equation 6.38 diverges for all commonly used molecular potentials (more precisely, for all functions $V(R)$ that vanish more rapidly than R^{-1}). From a physical point of view, all molecular potentials have a hard core extending out to several times λ at thermal energies which causes a major distortion of a considerable part of the wave front and which cannot be conveniently treated by perturbation methods. It is indeed a pity that the first Born approximation for $f(\chi)$ is not applicable to molecular scattering because if the phase as well as the magnitude of $f(q)$ can be obtained experimentally over the complete angular range, the inversion of Equation 6.38 to yield the potential directly is possible, but this route to $V(R)$ is only open for electron scattering, since the potential is then a shielded Coulomb one. To proceed further we must make a partial wave analysis of the problem.

6.4 The partial wave expansion

The standard procedure for separating the variables in a wave equation governing the relative motion in polar co-ordinates is to write

$$\Psi(\mathbf{R}) = g(R)\,\Theta(\chi)\Phi(\phi) \tag{6.39}$$

For the central potential problem, the wave equation 6.26 then separates into three equations familiar from bound state problems (e.g. the hydrogen atom), the only difference being in the functional form of the potential and the fact that the total energy is positive. The separated equations for radial and angular motion are:

$$-\frac{\hbar^2}{2\mu}\frac{1}{R^2}\frac{\mathrm{d}}{\mathrm{d}R}R^2\frac{\mathrm{d}g_l}{\mathrm{d}R} + V(R)\,g_l + \frac{\hbar^2}{2\mu}l(l+1)\,g_l = Eg_l \tag{6.40}$$

$$\begin{cases} \sin\chi^{-1}\ \dfrac{\mathrm{d}}{\mathrm{d}\chi}\sin\chi\ \dfrac{\mathrm{d}\Theta_{lm}}{\mathrm{d}\chi} - m^2\sin^{-2}\chi\,\Theta_{lm} = l(l+1)\Theta_{lm} \\ \mathrm{d}^2\Phi_m/\mathrm{d}\phi^2 = m^2\Phi_m \end{cases} \tag{6.41}$$

The last two equations have as solutions the spherical harmonics, $Y_{lm}(\chi, \phi)$

closely related to the Legendre polynomials, P_{lm} (cos χ);

$$\Theta_{lm}(\chi)\Phi_m(\phi) = Y_{lm}(\chi, \phi) = (-1)^m [(2l+1)/4\pi]^{1/2} \left(\frac{l-m}{l+m}\right)^{1/2} P_{lm}(\cos\chi)e^{im\phi} \tag{6.42}$$

We now see if a solution of the form

$$\Psi(\mathbf{R}) = g_l(R)\, Y_{lm}(\chi, \phi) \tag{6.43}$$

where g_l is the radial wave function of the l^{th} angular momentum state, can be made an acceptable solution of the scattering problem. In comparing Equations 6.43 and 6.7 a difficulty at once emerges in that the asymptotic form of Equation 6.7 does not refer to a particular angular momentum state but to the totality of all such states that make up an infinite plane wave, i.e. the angular momentum quantum numbers must be introduced into Equation 6.7. Clearly, in order to arrive at Equation 6.7, a linear combination of degenerate terms of the type Equation 6.43 will have to be taken

$$\Psi(\mathbf{R}) = \sum_{l,\, m} A_{lm}\, g_{lm}\, (R)\, Y_{lm}\, (\chi, \phi) \tag{6.44}$$

The weighting A_{lm} that is given to each state must be such that asymptotically, the wave function ψ contains only an incoming plane wave and an outgoing spherical wave without an incoming spherical wave. Once the coefficients A_{lm} have been found, then the scattered amplitude is determined. To find these coefficients we need the expansion of a plane wave in terms of the spherical harmonics

$$e^{ikz} = (4\pi)^{1/2} \sum_{l=0}^{\infty} (2l+1)^{1/2}\, i^l j_l\, (kR)\, Y_{l0}\, (\chi, \phi) \tag{6.45}$$

where the polar axis has been taken to be the z-axis and the spherical Bessel functions $j_l(kr)$ are one class of the solutions, f_l, of the radial wave equation with zero potential:

$$\frac{1}{\rho^2}\frac{\mathrm{d}}{\mathrm{d}\rho}\rho^2\frac{\mathrm{d}}{\mathrm{d}\rho}f_l(\rho) - \frac{l(l+1)}{\rho^2} f_l(\rho) + f_l(\rho) = 0 \tag{6.46}$$

where $\rho = kR$ and $k\hbar = \mu v$.

The solutions of Equation 6.46 can be made the building blocks of th solution of any problem in the continuum, just as bound state problems ar conveniently expanded in terms of the more familiar Laguerre or Hermit polynomials. Two different types of solution can be distinguished by thei behaviour at $\rho = 0$, the regular (i.e. tending to zero) solution j_l behaving as ρ and the irregular or Neumann functions n_l behaving as $\rho^{-(l+1)}$; a few of thei properties are listed in Appendix 1. The functions j_l and n_l, being entirely real, do not represent any net flow of particles. Their asymptotic form o large ρ, however, suggests that they can be decomposed in the manner o ordinary trigonometric functions to give two complex functions whic represent incoming and outgoing waves respectively. These are the Hanke functions of the first and second kind

$$h_l^{(1)}(\rho) = j_l(\rho) + in_l(\rho) \xrightarrow[\rho \to \infty]{} \frac{1}{\rho} e^{i(\rho - (l+1)\pi/2)} \tag{6.47}$$

$$h_l^{(2)}(\rho) = j_l(\rho) - in_l(\rho) \xrightarrow[\rho \to \infty]{} \frac{1}{\rho} e^{-i(\rho - (l+1)\pi/2)}$$

The two Hankel functions are complex conjugates, separately satisfying th wave equation 6.46 and the recurrence relationship (A2); $h_l^{(1)}$ and $h_l^{(2)}$ represent a flux that falls off uniformly as R^{-2} – as may be verified by substituting Equation 6.47 into Equation 6.10, the results for $h_l^{(1)}$ and $h_l^{(2)}$ being

$$j_R^{(1),(2)} = \pm \frac{v}{\mathcal{N}} \Big/ (kR)^2. \tag{6.48}$$

Returning to the plane wave expansion of Equation 6.45, we can ask fo the probability of finding a particle with angular momentum $l\hbar$ in a plane wave. This is a familiar type of problem in wave mechanics and in Equation 6.45 we have the required expansion in terms of the eigenfunctions of the angular momentum operator. Noting from Equation 6.48 that the flux o particle density represented by the radial part of every angular momentum state is independent of l, inspection of Equation 6.45 shows that the squares of the coefficient of the product eigenfunctions $j_l Y_{l0}$ are proportional to $2l + 1$. This result is often given a simple geometrical interpretation. The classical impact parameter is redefined as being related to l by

$$kb_l = l \tag{6.49}$$

which at first sight seems to imply that b is quantized through the quantisation of l. The interpretation is that all impact parameters lying between $b_l = l\lambda$ and $(l+1)\lambda$ correspond to a single quantum state with angular momentum $l\hbar$. Thus, if the wave front is pictured divided by concentric circles into annular zones, the radius of the l^{th} circle being b_{l+1}, the area of the l^{th} zone is, from Equation 6.49 $(2l+1)\,\pi/k^2$. If the intensity across the wave front is uniform, the number of trajectories passing through the l^{th} zone is proportional to its area and thus the probability of picking at random a trajectory with angular momentum $l\hbar$ is proportional to $2l+1$ as in the quantum treatment.

In our analysis of scattering in terms of partial waves, we now have the asymptotic form

$$\Psi(\mathbf{R}) \xrightarrow[\rho\to\infty]{} \sum_l \left\{(2l+1)i^l j_l(\rho) + c_l h_l^{(1)}(\rho)\right\} P_l(\cos\chi) \qquad (6.50)$$

where the scattered spherical wave has also been subject to a partial wave analysis,

$$\rho^{-1} f(\chi) e^{i\rho} = \sum_l c_l h_l^{(1)}(\rho) P_l(\cos\chi) \qquad (6.51)$$

The program now is to solve the radial wave equation 6.40 for the functions $g_l(\rho)$ and then to compare expressions 6.44 and 6.50 so that the $c_l(\rho)$ can be identified.

The precise asymptotic form of the function $g_l(R)$ can only be found by integration of the differential Equation 6.40 but its general form can be readily found by the following argument. If the potential term in Equation 6.40 has a range that is shorter than the centrifugal term, that is, it falls off more rapidly than R^{-2}, then as $R \to \infty$ the centrifugal term $l^2\hbar^2/2\mu R^2$ alone need be retained. The wave equation then becomes identical with the radial equation 6.46, the relevant solutions of which have already been identified as the spherical Bessel functions; we thus conclude that the asymptotic solution of the complete radial wave equation must be a linear combination of j_l and n_l,

$$g_l(\rho) \xrightarrow[\rho\to\infty]{} a_l j_l(\rho) + b_l n_l(\rho) \qquad (6.52)$$

As the potential term in Equation 6.40 tends to zero, only the regular solution remains and one can say that the effect of introducing the potential term is to mix some of the irregular solution $n_l(\rho)$ with the regular solution.

The fuller significance of this can be seen by writing without loss of generality

$$\left.\begin{aligned} a_l &= d\cos\eta_l \\ b_l &= -d\sin\eta_l \end{aligned}\right\} \tag{6.53}$$

so that

$$g_l \longrightarrow \frac{1}{\rho}\sin(\rho - l\pi/2 + \eta_l), \tag{6.54}$$

where

$$\tan\eta_l = b_l/a_l. \tag{6.55}$$

Thus, the only effect of the potential is to introduce a phase shift η_l into the elastically scattered wave.

Before discussing the solution of the radial wave equation subject to the limiting form Equations 6.52 or 6.54, the relationship must be found between the phase shift η_l, or the coefficients a_l and b_l and the differential cross-section, which is the actual measured quantity. To do this, we return to the complete partial wave expansion 6.50 which we write in limit of large R as

$$\Psi(\mathbf{R}) \longrightarrow \sum_l (\mathscr{A}_l h_l^{(1)} + \mathscr{B}_l h_l^{(2)}) P_l(\cos\chi) \tag{6.56}$$

where

$$\left.\begin{aligned} a_l &= \tfrac{1}{2}(\mathscr{A}_l + \mathscr{B}_l) \\ b_l &= \tfrac{1}{2}i(\mathscr{A}_l - \mathscr{B}_l) \end{aligned}\right\} \tag{6.57}$$

Upon subtracting a plane wave from Equation 6.56 only an outgoing spherical wave must remain if the solution is to correspond to scattering; to facilitate this operation we write Equation 6.50 as

$$\Psi(\mathbf{R}) \longrightarrow \sum_l \tfrac{1}{2}(2l+1)i^l(h_l^{(1)} + h_l^{(2)})P_l(\cos\chi) + \sum_l c_l h_l^{(1)} P_l(\cos\chi) \tag{6.58}$$

In general, the Legendre polynomials are not all zero for any value of χ, so that to match Equations 6.56 and 6.58 we equate coefficients of the $P_l(\chi)$

$$\mathscr{A}_l h_l^{(1)} + \mathscr{B}_l h_l^{(2)} - (2l+1)\, i^l\, \tfrac{1}{2}\{h_l^{(1)} + h_l^{(2)}\} = c_l h_l^{(1)} \tag{6.59}$$

and so

$$\mathscr{B}_l = \tfrac{1}{2}i^l(2l+1), \quad c_l = \mathscr{A}_l - (2l+1)i^l/2 \tag{6.60}$$

Restoring the phase shifts η_l from Equations 6.57, 6.55 and 6.60

$$\mathscr{A}_l = \tfrac{1}{2}(2l+1)i^l\, e^{2i\eta_l} \tag{6.61}$$

so that the coefficient of e^{ikR} in Equation 6.7 becomes

$$f(\chi) = \frac{1}{2ik}\sum_l (2l+1)\{e^{2i\eta_l} - 1\}P_l(\cos\chi) \tag{6.62}$$

Instead of writing the important result, Equation 6.62, in terms of the phase shifts, greater symmetry and a more flexible notation results if a new set of quantities is defined that make up the scattering matrix $\{S\}$. The diagonal elements of this matrix $\{S\}$ are the ratios of the amplitudes of the outgoing and incoming spherical waves in l^{th} channel in the limit of large R. In the elastic case the complete wave function can be written

$$\Psi \longrightarrow \sum_l \mathscr{B}_l \rho^{-1}\{e^{-i(\rho - l\pi/2)} - S_{ll}\, e^{i(\rho - l\pi/2)}\}P_l(\cos\chi) \tag{6.63}$$

where, from Equation 6.56

$$S_{ll} = \mathscr{A}_l/\mathscr{B}_l = e^{2i\eta_l} \tag{6.64}$$

The complex elements S_{ll}, form a square array and in the central forces elastic scattering case the conservation of relative angular momentum ensures that only the diagonal elements S_{ll} are non-zero and that the wave equations for different angular momentum states are uncoupled (as in Equation 6.41). The components of the S matrix can be regarded as transforming an incident spherical wave in a particular channel into an outgoing wave in the same or another channel. The S matrix elements thus conveniently store all our knowledge of the scattering effect of any potential and they replace phase shifts and transition probabilities.

We can immediately derive a formula for the scattered amplitude in terms of S_{ll} by substituting Equations 6.61 and 6.64 into 6.62:

$$f(\chi) = \frac{1}{2ik}\sum_l (2l+1)\{S_{ll} - 1\}P_l(\cos\chi) \tag{6.65}$$

If inelastic exit channels open up (those in which the final values of the internal quantum numbers differ from the initial values) then Equation 6.65 still holds if the summation is carried out over only the diagonal elements, $S_{nl:nl}$ where n labels the initial state. The phase shift notation does not adapt quite so readily. To anticipate the results of Chapter 8, the simple factor $e^{2i\eta_l}$ in Equation 6.62 must be replaced by $e^{2i\eta_l}e^{-\xi_{l,n}}$ in the presence of inelastic events, where $\xi_{l,n}$ is a measure of the attenuation of the l^{th} partial wave.

The total cross-section in terms of the S matrix elements is found by forming $|f(\chi)|^2$ from Equation 6.65 and integrating over all scattering angles:

$$\sigma_{total} = \frac{\pi}{k^2}\sum_l (2l+1)\{|S_{ll}|^2 + 1 - 2\mathrm{Re}(S_{ll})\} \tag{6.66}$$

where the orthogonality of the Legendre polynomials, has been used.

In writing down the asymptotic form Equations 6.56 or 6.58 we have not made use of our knowledge that elastic scattering cannot lead to net adsorbtion or emission of particles, whereas Equation 6.54 does contain this information. To apply this conservation condition to Equation 6.63 and hence to the S matrix, we substitute Equation 6.63 into the expression for the flux Equation 6.3 and integrate the result over the surface of a sphere at infinity; the resulting current is then placed equal to zero,

$$j_l = 4\pi\frac{\hbar k}{\mu}\left\{|\mathscr{B}_l|^2 - |\mathscr{B}_l S_{ll}|^2\right\} = 0 \tag{6.67}$$

leading to

$$|S_{ll}|^2 = 1 \tag{6.68}$$

whence Equation 6.66 becomes

$$\sigma_{total} = \frac{2\pi}{k^2}\sum_l (2l+1)\{1 - \mathrm{Re}(S_{ll})\} \tag{6.69}$$

Applying the optical theorem to Equation 6.65 also yields Equation 6.69 which thus also applies in the presence of inelastic or reactive scattering, provided that the summation is carried out only over the relevant diagonal elements of the scattering matrix, $S_{nl:nl}$, where n agains labels the initial quantum state.

Although it is not of direct use in computing individual elements of the large scattering matrices met with in molecular scattering, the formal description of the S matrix cannot be left without mentioning that it is a *unitary* matrix. For elastic scattering the required result follows immediately from Equation 6.64 that

$$\{S\}\{\tilde{S}^*\} = 1 \tag{6.70}$$

More generally (see also Sections 6.14 and 6.15) if the colliding molecules can exist in a variety of internal states with wave functions $\phi_a\phi_b \ldots$ then the asymptotic form of Equation 6.63 becomes

$$\Psi_a \longrightarrow \Phi_a \sum_l \mathscr{B}_l \rho^{-1}\{e^{-i(k_aR - l\pi/2)} - S_{al:al}e^{i(k_aR - l\pi/2)}\}P_l(\cos\chi) + \phi_b \sum_{l,l'} \mathscr{B}_l \rho^{-1} S_{al:bl'}e^{i(k_bR - l\pi/2)}P_{l'}(\cos\chi) + \ldots \tag{6.71}$$

for a collision which began in internal state a, where al, bl', are said to label the entrance and exit channels. If the system had begun in state b, the formal description of the asymptotic wave function would be similar to Equation 6.71 with the S matrix elements replaced by $S_{bl:al'}$, $S_{bl:bl'}$ etc. Note that in every case the incoming wave e^{-ikR} would be associated only with the entrance channel.

A colliding system starting in state 'a' is, through the orthogonality of the ϕ_a, $\phi_b \ldots$ orthogonal to a system starting in any other state. Furthermore, although the system may emerge in a mixture of states a, b . . ., it must remain orthogonal throughout the collision to a system originating in any other entrance channel because the colliding system *as a whole* is not acted upon by external forces and so must remain in the same quantum state until perturbed by the act of observation. At the end the act of observation will force the system to be registered in *one* of the states a, b . . . and for any partial wave the probability of emerging in a particular exit channel b from an entrance channel a is

$$\sum_{l'} P_{al \to bl'} = \sum_{l'} |S_{al:bl'}|^2 \tag{6.72}$$

The orthogonality of states is simply expressed for any pair of entrance and exit channels al and bl'

$$\sum_n \sum_{l''} S_{al:nl''} S^*_{bl':nl''} = 0, \quad \text{unless } b = a, l' = l \tag{6.73}$$

Similarly, in order to conserve flux, the complete wave function Ψ_a must remain normalised throughout the collision, i.e.

$$\sum_{n} \sum_{l''} |S_{al:nl''}|^2 = 1 \tag{6.74}$$

These conditions are automatically fulfilled when the S matrix is accurately calculated (a very difficult matter for complex systems) and together they result in the unitarity of the complete S matrix.

With the aid of Equation 6.62 the problem of calculating $f(\chi)$ for elastic collisions has been converted to one of finding the phase shifts η_l or, equivalently through Equation 6.56 of finding the relative asymptotic contributions of the spherical Bessel and Neumann functions to the solution of the radial wave equation 6.40.

Defining a slightly modified radial function $G(\rho)$

$$G_l(\rho) = \rho g_l(\rho) \tag{6.75}$$

so that first derivatives are eliminated in the wave equation,

$$-\frac{d^2G}{d\rho^2} + \mathscr{V}G_l + \frac{l(l+1)}{\rho^2}G_l = G_l$$

where

$$\mathscr{V}(\rho) = 2\mu\, V(\rho)/(\hbar k)^2 \tag{6.76}$$

the problem is reduced to solving the second order linear differential Equation 6.76 subject to 6.54. For the general potential there are no analytical solutions to Equation 6.76. For some specially constructed potentials, solutions can be found for $l = 0$ and for the Coulomb, square well, hard sphere and delta function potentials there are solutions for $l > 0$ in terms of known functions. Unfortunately, none of these is a good enough potential form to fit the high resolution data now available. Numerical methods of solving Equation 6.76 are discussed in Section 6.8, but first we pursue a little analysis in order to arrive at some approximations.

6.5 The Born approximation for the phase shifts

It is instructive to convert Equation 6.76 into an integral equation and to do so the inhomogeneous form is again adopted:

$$-\frac{d^2G_l}{d\rho^2} + \left\{\frac{l(l+1)}{\rho^2} - 1\right\} G_l = -\mathscr{V}(\rho)G_l \tag{6.77}$$

If two linearly independent solutions of Equation 6.77 with $V = 0$ (i.e. two complementary functions) are known, $v_l(\rho)$ and $w_l(\rho)$, then a general solution is

$$G_l(\rho) = W^{-1}\left\{v_l\int_a^\rho w_l \mathscr{V} G_l d\rho' + w_l\int_\rho^b v_l \mathscr{V} G_l d\rho'\right\} + Nf_l(\rho);\ f_l = v_l \text{ or } w_l \tag{6.78}$$

where W is the Wronskian $(v_l w_l' - w_l v_l')$ of v_l and w_l and the constants N, a and b are as yet undetermined. That this is a solution of Equation 6.77 can be verified by direct substitution and it contains the two adjustable constants a and b needed to fit the boundary conditions of a second order differential equation. As $\rho \to 0$, we require that only the regular solution remains so clearly a must be put equal to zero and w_l identified with $\rho j_l(\rho)$. As $\rho \to \infty$ the solution must become a linear combination of the functions j_l and n_l; furthermore, in the absence of a perturbing potential the solution must be everywhere $\rho j_l(\rho)$. Dealing with this latter condition first, it is apparent that whatever values are assigned to a and b, $G_l(\rho)$ will tend to Nf_l as V tends to zero; clearly $\rho j_l(\rho)$ must be inserted for $Nf_l(\rho)$, (N is not an adjustable constant but a scaling or normalising factor which does not affect the following argument). If, now, b is put equal to ∞, Equation 6.78 becomes

$$G_l(\rho) = \rho\left\{n_l(\rho)\int_0^\rho \rho' j_l(\rho')\mathscr{V} G_l(\rho')d\rho' + j_l(\rho)\int_\rho^\infty n_l(\rho')\rho'\mathscr{V} G_l(\rho')d\rho'\right\} + \rho j_l(\rho) \tag{6.79}$$

and so from Equation 6.55, in the limit $\rho \to \infty$

$$\tan\eta_l = \int_0^\infty \rho j_l(\rho)\mathscr{V} G_l(\rho)d\rho \tag{6.80}$$

where, it is worth emphasising again, $\rho G_l(\rho)$ must be asymptotically of the form Equation 6.52. If, now, $V(\rho)$ is everywhere small, the dominant term on the R.H.S. of Equation 6.79 is ρj_l, provided that integrals of the type Equation 6.81 below converge and ρ is not too small. Substituting ρj_l for $G_l(\rho)$ in Equation 6.80 gives

$$\tan\eta_l \approx \eta_l \approx \int_0^\infty \rho^2 j_l(\rho)^2 \mathscr{V}(\rho)d\rho \quad (\text{to } 0(V)) \tag{6.81}$$

which is the first Born approximation for the phase shift. Although the Born approximation to the scattered amplitude, Equation 6.38, diverges for all

potentials of the type R^{-s} with $s > 1$, the limiting behaviour of the spherical Bessel functions as $\rho \to 0$ (appendix A) shows that the Born phase shift expression 6.81 is integrable for $l > \frac{1}{2}(s-2, s-1)$, ($s$ even, odd). Whether the resulting value of η_l is reliable depends upon the extent of the distortion of the incident plane wave by the intermolecular field and a measure of this is the actual phase shift calculated. Equation 6.81 is commonly held to be unreliable for phase shifts greater than half a radian. For these larger phase shifts the second Born approximation (obtained by including terms $O(V^2)$ in $G_l(\rho)$ is rarely used and instead a semi-classical approximation (Section 6.7) is adopted or the wave equation is solved numerically (Section 6.8).

6.6 Small angle scattering; the random phase approximation

We recall that elastic is always strongly forward peaked and that most of the particles are scattered out of the beam by less than a degree. Thus, regarding the total cross-section as the integral of the differential cross-section, we can hope to get a good approximation for the former if we calculate only the small angle behaviour of $\sigma(\chi)$ accurately and this suggests the use of the Born approximation. Because of the factor $(2l+1)$ in Equation 6.62 we concentrate on the outermost branch of the deflection function and calculate the contribution to $\sigma(\chi)$ from a potential of the form

$$V(R) = -C_s R^{-s} \tag{6.82}$$

Substituting Equation 6.82 into Equation 6.81 gives a standard integral and yields

$$\eta_l^B = -\frac{\mu C_s}{\hbar^2}\left(\frac{k}{2}\right)^{s-2} \pi \frac{\Gamma(s-1)\,\Gamma\left(l-\frac{s}{2}+\frac{3}{2}\right)}{\left(\Gamma\left(\frac{s}{2}\right)\right)^2 \Gamma\left(l+\frac{s}{2}+\frac{1}{2}\right)} \tag{6.83}$$

For some value L of the angular momentum quantum number, η_l^B will reach $\pi/2$ where the Born approximation is unreliable. At smaller values of l, $e^{2i\eta_l}$ oscillates with increasing rapidity. The approximation sometimes called the random phase approximation is now introduced that both the real and imaginary parts of $e^{2i\eta_l}$ are effectively zero for $l < L$. The partial wave summation for the forward scattered amplitude is now

$$f(0) = \frac{i}{2k}\sum_0^L (2l+1) - \frac{i}{2k}\sum_L^\infty (2l+1)\,\{\cos 2\eta_l + i \sin 2\eta_l - 1\} \tag{6.84}$$

and so

$$\sigma_{\text{total}} = \frac{4\pi}{k} \operatorname{Im} f(0) = \frac{2\pi}{k^2}\left[\sum_{l=0}^{L} (2l+1) + \sum_{l=L}^{\infty} (2l+1)^2 \eta_l^2\right] \quad (6.85)$$

where in Equation 6.87 the approximation

$$\cos 2\eta_l \approx 1 - 2\eta_l^2, \ \eta_l \ll \pi/2$$

has been introduced. Then, with the knowledge that for molecular scattering $L \gg 1$, we obtain

$$\sigma_{\text{total}} \approx \frac{2\pi L^2}{k^2} + \frac{8\pi}{k^2} \int_L^{\infty} l\eta_l^2 \, dl \quad (6.86)$$

Substituting Equation 6.83 into Equation 6.86 gives the Massey-Mohr formula (H. S. W. Massey and C. Mohr, 1933)

$$\sigma_{\text{tot}}^{\text{MM}} \cong \pi\left(2 + \frac{\pi^2}{s-2}\right)\left(\frac{f_s C_s}{\hbar v}\right)^{2/(s-1)}, \quad (6.87)$$

where

$$f_s = \frac{1}{2^{s-3}} \frac{\Gamma(s-1)}{(\Gamma(s/2))^2} \quad (6.88)$$

The accumulated effect of the approximations, including the ambiguity in the choice of η_L, is to make the Massey-Mohr formula reliable only to ~±30 per cent. It is perhaps worth noting that the problem of assigning a value to η_L can be overcome by evaluating the integral form of Equation 6.69 analytically,

$$\sigma_{\text{tot}} \cong \frac{8\pi}{k^2} \int_0^{\infty} l \sin^2 \eta_l \, dl \quad (6.89)$$

with η_l given by Equation 6.83 over the whole range of l. The result, due to Landau and Lifshitz (LL), is

$$\sigma_{\text{tot}}^{\text{LL}} \cong 2\pi^{s/(s-1)} \sin\left[\frac{\pi}{2}\frac{s-3}{s-1}\right] \Gamma\left(\frac{s-3}{s-1}\right)\left[\frac{\Gamma\left(\frac{s}{2} - \frac{1}{2}\right)}{\Gamma\left(\frac{s}{2}\right)}\right]^{2/(s-1)} \left(\frac{C_s}{\hbar v}\right)^{2/(s-1)} \quad (6.90)$$

and is generally preferred to Equation 6.87. It is to be noted that Equations 6.90 and 6.87 predict a monotonic energy dependence of the total cross-section, $\sigma_{tot}(E) \propto E^{-1/(s-1)}$

If a bipolar potential of the form

$$V(R) = -C_s R^{-s} + C_t R^{-t} \tag{6.91}$$

is used, the Born phase shift is the sum of the contributions from the two parts of the potential, and the scattered amplitude is the sum of long and short range contributions. However, if these phase shifts were used to evaluate the total cross-section in Equation 6.89, we will see in Section 6.10 that important interference effects are neglected and the MM approximation gives only the average behaviour of $\sigma_{tot}(E)$.

Small angle scattering is also dominated by collisions of large impact parameter and there should be a small angle approximation to $\sigma(\chi)$ analogous to the MM and LL formulae for the total cross-section. This hope is only realised after some drastic approximations as we will now see.

The contribution from partial waves inside the random phase region ($l < L$) to the scattered amplitude is

$$f_<(\chi) = (2ik)^{-1} \sum_{l=0}^{L} (2l+1)\, P_l(\cos\chi)$$

$$\cong (ik)^{-1} \left(\frac{\chi}{\sin\chi}\right)^{1/2} \int_0^L (l+\tfrac{1}{2})\, J_0[(l+\tfrac{1}{2})\chi]\, \mathrm{d}l$$

$$\cong -i\left(\frac{\chi}{\sin\chi}\right)^{1/2} \frac{L}{k\chi} J_1(L\chi) \tag{6.92}$$

where the approximation, useful over the whole range of $l\chi$,

$$P_l(\chi) \cong \left(\frac{\chi}{\sin\chi}\right)^{1/2} J_0[(l+\tfrac{1}{2})\chi] \tag{6.93}$$

has been used. The contribution to $f(\chi)$ from partial waves with $l > L$ is found using the Born approximation to be

$$f_>(\chi) \cong (ik)^{-1} \int_L^\infty (2l+1)\, \eta_l^B\, P_l(\cos\chi)\, \mathrm{d}l \tag{6.94}$$

Taking $\eta = \pi/2$ to mark the onset of random phase (which gives close agreement with the LL result for the total cross-section) and writing

$$\eta_l^B = \frac{\pi}{2}\left(\frac{l}{L}\right)^{-s+1}, \quad l \geqslant L \tag{6.95}$$

gives

$$f_> \cong \frac{\pi}{ik}\frac{L^2}{s-3}\left\{1-\left(\frac{s-3}{s-5}\right)\frac{L^2\chi^2}{4}+\cdots\right\}, s>5 \tag{6.96}$$

Expanding $J_1(L\chi)$ in Equation 6.92 and combining $f_>$ and $f_<$ gives

$$J_1(L\chi) = \frac{L\chi}{2} - \frac{(L\chi)^3}{16} + \cdots \tag{6.97}$$

$$\sigma(\chi) \cong \frac{L^4}{4k^2}\left\{\frac{2\pi+s-3}{s-3}\right\}^2\left[1-(L\chi)^2\frac{(s-3)(4\pi+s-5)}{4(s-5)(2\pi+s-3)}+\cdots\right] \tag{6.98}$$

From Equation 6.96, as $s \to \infty$ the contribution from $l > L$ goes to zero and the cross-section can then be assigned the hard sphere (HS) value; for $\chi = 0$,

$$\sigma_{HS}(0) = L^4/4k^2 \tag{6.99}$$

Thus, the small angle differential cross-section is

$$\sigma(\chi) \cong \sigma_{HS}(0)\left\{\frac{2\pi+s-3}{s-3}\right\}^2\left[1-k\sigma_{HS}(0)^{1/2}\chi^2\frac{(s-3)(4\pi+s-5)}{2(s-5)(2\pi+s-3)}+\cdots\right] \tag{6.100}$$

Writing the coefficient of χ^2 in Equation 6.100 as C, the foregoing result is sometimes summarised by saying that the differential cross-section falls off as $\exp(-C\chi^2)$, but this is only accurate to $0(\chi)^2$.

From Equation 6.100, a plot of $\chi^2\sigma(\chi)$ vs. χ will reach a maximum at $\chi = 1/\sqrt{C}$. Such a plot is illustrated in Fig. 6.1. However, this route to L and hence to C_s is not particularly useful because, for thermal scattering, L is greater than 100 and the extremum in the $\chi^2\sigma(\chi)$ plot occurs at very small angles where the precision in angular measurement is poor. Other authors (E. A. Mason et al., 1964; R. J. Munn et al., 1964) have produced alternative formulae to Equation 6.100.

The full form of $f_<(\chi)$, Equation 6.93 and of $f_>(\chi)$ (when evaluated more accurately) exhibit very pronounced oscillations from the presence of the term $J_1(L\chi)$. However, when $f(\chi)$ is evaluated by exact summation without breaking the partial wave summation these oscillations are much less in evidence (see Fig. 6.1). The exponential form at very small angles is found to join onto the classical envelope with its $\chi^{-(s-2)/(s-3)}$ dependence after only a few oscillations, of which the first two might be detectable for heavy atoms at thermal speeds. The oscillations in $f_{<,>}(\chi)$ and the residual structure in the exactly computed $f(\chi)$ are really a diffraction effect resulting from the rapidly changing gradient of the potential and are discussed more fully in

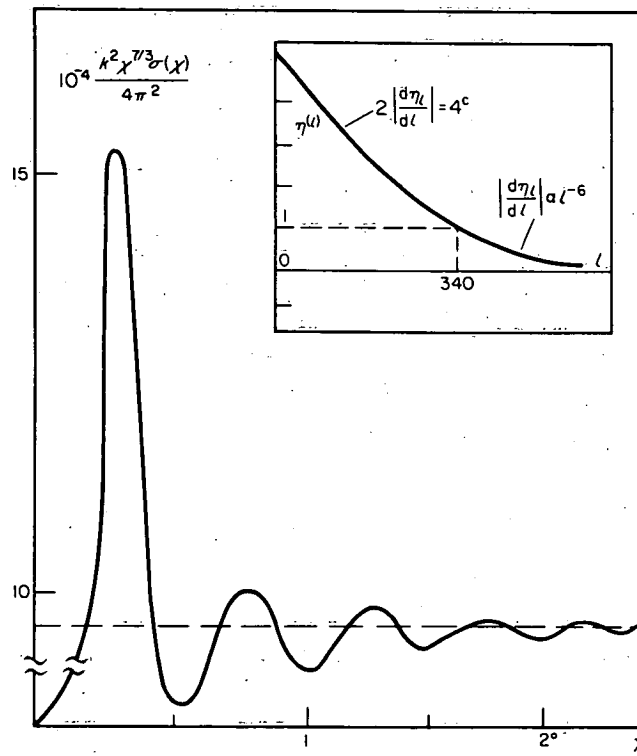

Fig. 6.1 The computed differential cross-section resulting from a monotonic phase shift function (inset), for which the maximum angle of deflection is 4 radians and only one classical branch is present. The very pronounced first maximum is a property of the function $\chi^{7/3}\exp(-C\chi^2)$ and effectively classical scattering sets in soon afterwards. In this particular model calculation roughly 900 partial waves were used.

Section 6.13. Pronounced undulations are indeed observed in $\sigma(\chi)$ but they arise from a different cause and occur outside the very small angle region; they are discussed in Section 6.10.

6.7 Semi-classical phase shifts

If we wish to extend our calculations of $\sigma(\chi)$ to larger angles of scattering via the partial wave summation, a means must be found of evaluating phase shifts that are greater than $\pi/2$. The radial Schrodinger equation 6.40 must be solved subject to the boundary condition of Equation 6.54

$$G_l(\rho) \longrightarrow \sin(\rho - l\pi/2 + \eta_l) \tag{6.101}$$

There are two methods of solution in use, the exact numerical integration of the wave equation and the semi-classical solution, which leads to a simple quadrature for the phase shift.

The use of semi-classical methods is suggested by the fact that for molecular collisions at thermal energies and higher, the wavelength of relative motion ($<5 \times 10^{-10}$ cm) is comfortably less than the range of the potential ($>10^{-8}$ cm). The Wentzel-Kramers-Brillouin (WKB) continuum solutions are introduced through the classical action integral $S(\rho)$;

$$S(\rho) = \int_{\rho_c}^{\rho} \xi(\rho)\, d\rho \tag{6.102}$$

where

$$\xi(\rho) = \sqrt{1 - V(\rho) - (l + \tfrac{1}{2})^2/\rho^2} = v(\rho)/v(\infty) \tag{6.103}$$

and ρ_c is the classical turning point such that $\xi(\rho_c) = 0$.

Taking as a trial wave function

$$G_l^{\pm}(\rho) = \xi^{-\frac{1}{2}}\, e^{\pm iS(\rho)} \tag{6.104}$$

The conditions under which Equation 6.104 is a solution of Equation 6.40 are well known (L. D. Landau and E. M. Lifshitz, 1958) and may be summarized as:

$$\frac{\partial \xi}{\partial \rho} \ll 1 \quad \text{and} \quad \xi(\rho) \sim 1 \tag{6.105}$$

over the range of ρ leading to the major contribution to the action integral. The region close to the classical turning point is excluded from this test. For a bipolar potential range σ and well depth ϵ, these two tests are roughly equivalent to

$$\frac{\lambda}{\sigma} \ll 1 \quad \text{and} \quad \frac{\epsilon}{E} \lesssim 1 \tag{6.106}$$

The latter condition is related to the existence of bound states within the potential well and is the subject of Section 6.11.

The next step is to find the linear combination of incoming and outgoing spherical waves G_l^+ that joins smoothly onto an exponential decaying function at the classical turning point. We may replace this by a simpler requirement that the wave function vanishes at the turning point, which is satisfied by

$$G_l = \xi(\rho)^{-\frac{1}{2}} \{ e^{iS(\rho)} - e^{-iS(\rho)} \} \tag{6.107}$$

In order to compare with the asymptotic form of Equation 6.101, the action integral is written as

$$S(\rho) = \rho + l\pi/2 + \left[\int_{\rho_c}^{\rho} \left\{ 1 - \mathscr{V}(\rho) - \frac{(l+\frac{1}{2})^2}{\rho^2} \right\}^{\frac{1}{2}} d\rho - \int_{l+\frac{1}{2}}^{\rho} \left\{ 1 - \frac{(l+\frac{1}{2})^2}{\rho^2} \right\}^{\frac{1}{2}} \right] d\rho \tag{6.108}$$

The second term in Equation 6.108 converges to a finite limit as $\rho \to \infty$ and in writing down the whole expression we have used

$$\int_{l+\frac{1}{2}}^{\rho} d\rho \left\{ 1 - \frac{(l+\frac{1}{2})^2}{\rho^2} \right\}^{\frac{1}{2}} = \rho + l\pi/2 \tag{6.109}$$

So

$$\eta_l = \int_{\rho_c}^{\infty} \left\{ 1 - \mathscr{V}(\rho) - \frac{(l+\frac{1}{2})^2}{\rho^2} \right\}^{\frac{1}{2}} d\rho - \int_{l+\frac{1}{2}}^{\infty} \left\{ 1 - \frac{(l+\frac{1}{2})^2}{\rho^2} \right\}^{\frac{1}{2}} d\rho \tag{6.110}$$

which is the semi-classical expression for the phase shift, derived from plausibility arguments in Chapter 2. The expression 6.110 can be evaluated for any strength of potential and an approximation to the complete phase shift function built up. This absence of any warning signals might lead us to use Equation 6.110 as an approximation for all circumstances, but there is a

major deficiency to the semi-classical phase shifts in the presence of orbiting, or when there are three classical turning points. These cases are illustrated in Figs. 6.2 and 6.10. Four types of behaviour are found at energies less than the critical value for orbiting. In the large impact parameter region (III) of Fig. 6.10, the effective potential is monotonic, there is only one classical turning point and the quantum and WKB phase shifts agree to, typically, better than 1 per cent. In region II there are three classical turning points and, although the inner region between R_3 and R_2 is classically inaccessible in a bimolecular collision, its presence has the effect, to a first approximation, of adding π^c, to

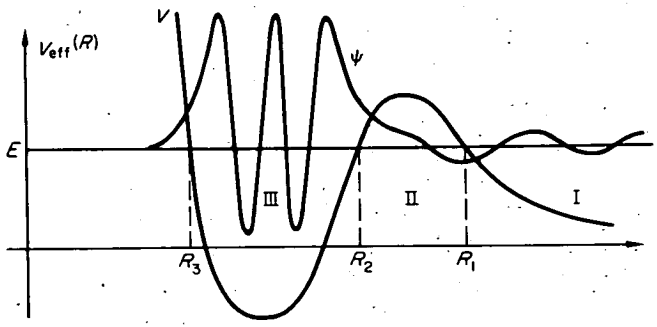

Fig. 6.2(i) A resonant case. The effective potential well, V_{eff}, has a bound state of energy E in resonance with the incident kinetic energy. The resulting wave function ψ has a large amplitude inside the well (region III), leaks through the potential barrier (II) to become the wave function of relative motion of two free particles in region I. The classical turning points are at R_1, R_2 and R_3.

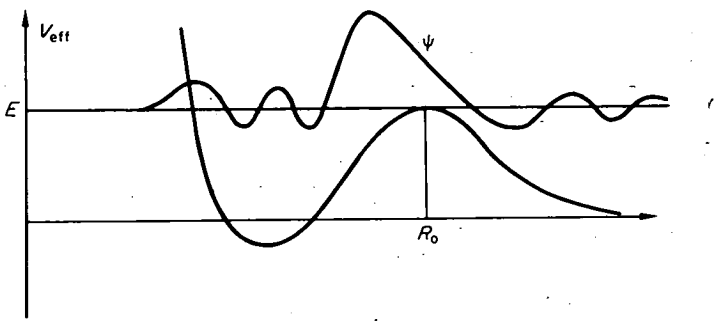

Fig. 6.2(ii) The orbiting case. At the outermost classical turning point R_0, the effective radial force is zero and the classical particle cannot pass this point. The quantum wave function ψ, however, shows that there is a finite possibility of finding the particle inside R_0.

the JWKB phase shift each time a resonance is passed through. This result can be found from a more complete WKB solution of the problem in which the oscillatory solution between R_2 and R_3 is joined smoothly onto the exponentially decaying solutions for $R < R_3, R_2 \leqslant R \leqslant R_1$ and thence onto the oscillatory solution for $R > R_1$. As the impact parameter passes through the critical value for orbiting the crude semi-classical phase shifts (from Equation 6.110) jump by several radians due to the sudden change in the turning point from R_1 to R_3. The quantum or exact semi-classical value will change rapidly in this region but, as in passing through the resonances, there will be no discontinuity in the gradient (with l regarded as a continuous variable). For impact parameters less than the orbiting value the crude and exact JWKB phase shifts again nearly coincide.

For any particular bipolar potential, orbiting will only occur at reduced energies E/ϵ below a certain critical value. At energies somewhat above this value e.g. $E/\epsilon > 0.8$ for the Lennard-Jones potential, we may be reasonably confident that the semi-classical phase shifts for all partial waves are reliable, provided that there are no near discontinuities in the potential.

The numerical evaluation of the integrals of Equation 6.110 presents no problems. If the turning point is located sufficiently accurately, any stepwise integration routine may be used. Gauss-Mehler quadrature has been suggested (F. J. Smith and R. J. Munn, 1964) as a quicker method, though convergence at low values of the reduced energy must be carefully tested.

A useful approximation for small phase shifts can be obtained by substituting the JWKB radial wave function for zero intermolecular potential into the quantum Born expression 6.83 where it replaces $j_l(\rho)$ when both incoming and outgoing waves are combined. Thus,

$$j_l(\rho) \approx \frac{1}{2}\frac{1}{\xi^{1/2}\rho}\left\{e^{iS_0(\rho)} - e^{-iS_0(\rho)}\right\}, \tag{6.111}$$

and so

$$\eta_l \approx \int_{\rho_c}^{\infty} \frac{\mathscr{V}(\rho)\,d\rho}{(1-(l+\frac{1}{2})^2/\rho^2)^2} \tag{6.112}$$

where terms containing the phase factor $\cos S(\rho)$ that results from squaring Equation 6.111 have been averaged to zero. The numerical results from this approximation differ slightly from those of the quantum Born approximation (they become identical in the limit $l \to \infty$) but, inasmuch as the Born contribution to the scattered amplitude is small, Equation 6.112 is an

adequate approximation. Integrating Equation 6.112 by parts results in the 'classical' small phase shift approximation Section 2.2.

6.8 Numerical methods

In the following sections various approximate methods of summing the partial wave expansion will be presented and these yield useful formulae for extracting crude potential parameters from the observed structure in $\sigma(\chi)$. However, when confronted with high resolution plots of $\sigma(\chi)$ over a range of angles and energy, the final fitting must be done by a forward calculation from an assumed potential containing several adjustable parameters. The core of this calculation is that of phase shifts.

The methods available are:–

(1) Numerical solution of the Schrödinger Equation.
(2) Evaluation of the semi-classical phase shifts. (F. J. Smith and R. J. Munn, 1964).
(3) Evaluation of the Born phase shifts, or the contribution of these to $f(\chi)$ directly via Equations 6.95 or 6.97.

The strategy adopted depends upon the particular circumstances and the ingenuity of the programmer, guided by the general consideration that quantum phase shifts will be necessary when there are two or three classical turning points and that Born phase shifts only become reliable at values of $\eta_l < 0.1^c$. The use of semi-classical phases throughout the whole range of l will probably not lead to gross error in $\sigma(\chi)$ except at very low values of E/ϵ and the dominant interference patterns present will be reproduced.

Even without resorting to quantum phase shifts, the time taken to calculate a differential cross-section over a fine enough angular mesh to capture all the structure in the angular range of a typical experiment may well take 5–30 minutes of computer time (IBM 360/50) and the additional calculations required to incorporate any averaging due to apparatus resolution effects will increase this time by a factor of two to five.

If the quantal behaviour is highly developed and the perturbation of the incident wave is large, neither the semi-classical nor the Born approximation will be useful and the wave equation must be evaluated numerically for each partial wave as required. In an elastic scattering problem where strong quasi-chemical forces are involved up to ~50 phase shifts may lie in the quantal regions and a fast numerical technique is therefore essential.

All such methods depends upon replacing the differential in Equation 6.40

by the finite difference formula (using the notation $G_i \equiv G(\rho_i)$

$$\frac{d^2G}{d\rho^2} \xrightarrow[h \to 0]{} \left\{ G_i - 2G_{i-1} + G_{i-2} \right\} h^{-2} \tag{6.113}$$

and the wave equation itself is more concisely written as

$$G'' = D(\rho)\, G. \tag{6.114}$$

In Equation 6.113 the G_i are discrete values of the wave function tabulated at equal intervals, h, of ρ. The subsequent stage in the calculation then depends upon the nature of the boundary conditions. In the case of bounded motion, negative total energy, the asymptotic value is known at both ends of the range of the function. The finite difference form of Equation 6.114 can then be cast into matrix form describing the conditions which must be fulfilled at each interval and the solution is by normal matrix methods. In the scattering case, however, the situation is very different. The motion is unbounded and though the asymptotic form of G is known boundary conditions can only be placed on $G(\rho)$ at $\rho = 0$. The solution to this type of initial value problem must be obtained by a stepwise integration procedure, until the asymptotic behaviour (Equation 6.101) of the function is achieved.

Since the precision of each step depend upon that of all previous ones accurate finite difference formulae are required. A wide range of such formulae have been suggested and a suitable one is the Numerov,

$$G_i = \frac{2G_{i-1} - G_{i-2} + \dfrac{h^2}{12}\left[G_{i-2}\, D_{i-2} + 10G_{i-1}\, D_{i-1}\right]}{1 - \dfrac{h^2}{12} D_i}. \tag{6.115}$$

In the scattering problem $G(\rho)$ is an oscillating function and the integration must be carried over a considerable range before asymptotic behaviour is established and the phase shift can be established. Errors can arise from two sources, firstly from the inevitable truncation errors associated with the finite word length in the computer and secondly from the approximation inherent in the finite difference formula. In some cases the second difficulty can lead to the build-up of an exponentially increasing solution. There is thus an optimum step length for these calculations; if h is too large the finite difference approximation is poor; while if h is too small the build-up in truncation errors can be disastrous.

Fortunately there is often a considerable intermediate range of h where solutions can be obtained without difficulty. In some cases, however, these problems of instability may be severe and special methods are then required (L. Fox, 1962). The obvious solution to these problems, that of using great precision in the numerical calculation, is only of limited value since this ultimately results in a much longer computing time and the calculation becomes impracticable. For atomic or molecular systems these instabilities are not severe except possibly in those cases where integration through a wide potential barrier is involved or if the initial values for starting are not well chosen.

Outside the classical turning point of the motion the wave function is oscillatory. Inside these points, in the classically forbidden region, the wave function decays exponentially. Since we are not interested in the final amplitude of the wave, but only its relative phase, it is sufficient to choose the two starting values inside the classically forbidden region at a point where the wave function is small, the two points being related exponentially as:

$$G_i = \exp(-D_i/(\rho_c - \rho_i) \tag{6.116}$$

where ρ_c is the classical turning point. The stepwise numerical integration can then be carried out with arbitrary amplitude from this point. The phase shift could be calculated by continuing the outward integration until the wave function becomes sinusoidal, the phase then being obtained by comparison with the zero potential asymptotic form:

$$G_l \sim \frac{1}{k} \sin(\rho - l\pi/2).$$

It is more expeditious, however, to use the exact free particle wave function:

$$F_l(\rho) = j_l(\rho) + n_l(\rho) \tag{6.117}$$

and to compare the two solutions before the fully asymptotic form is established. Thus, if R_n is one of the zeros of the calculated wave function $G(\rho)$,

$$\eta_l = \tan^{-1}\left(\frac{j_l(\rho_n)}{n_l(\rho_n)}\right) \tag{6.118}$$

and estimates of η_l can be made for successive values of n until convergence is obtained.

Instead of finding a polynomial approximation to the wave function over successive intervals (which is the basis of the Numerov method), we can make a polynomial approximation to the *potential* over appropriate intervals such that the simplified wave equation can be solved in terms of known functions. This approach is attractive in that the potential is a smoothly varying function of the interparticle separation whereas the wave function is highly oscillatory. The details will be found in R. G. Gordon 1969.

6.9 Semi-classical scattering

We have seen how the phase shift function η_l can be constructed either from the WKB or exact solutions of the radial wave equation. The effect of actual or near discontinuities in the phase shift function on $\sigma(\chi)$ can be investigated by the method of random phase and the contribution to $\sigma(\chi)$ and σ_{tot} from partial waves of small phase shift has also been discussed. However, most phase shift functions are smooth functions of l and, for thermal scattering, are greater than $\pi/2$ over most of their range so that $e^{2i\eta_l}$ is oscillatory. To handle this situation we introduce the very important technique of stationary phase for approximating the partial wave summation. (K. W. Ford and J. A. Wheeler, 1954.)

The partial wave summation for $f(\chi)$ is first replaced by an integration (permissible when η_l varies little from one l value to the next) and the integral split into two parts;

$$f(\chi) = -\frac{1}{2ik}\left\{\int_0^\infty (2l+1)\,e^{2i\eta(l)}P_l(\cos\chi)\,dl - \int_0^\infty (2l+1)\,P_l(\cos\chi)\,dl\right\} \tag{6.119}$$

The second integral is a delta function, $\delta(\chi)$, and so vanishes for $\chi \neq 0$. Next, an approximation for the Legendre polynomials in the first integral of Equation 6.119 is introduced that displays their asymptotic behaviour in the region $l\chi \gg 1$:

$$P_l(\cos\chi) \cong \left[\frac{1}{2}(l+\tfrac{1}{2})\pi\sin\chi\right]^{-\frac{1}{2}} \sin\left[(l+\tfrac{1}{2})\chi + \frac{\pi}{4}\right] + O\left(\frac{1}{l}\right) \tag{6.120}$$

Inserting this into Equation 6.119 gives

$$f(\chi) \cong -\frac{1}{k(2\pi\sin\chi)^{\frac{1}{2}}}\int_0^\infty (l+\tfrac{1}{2})^{\frac{1}{2}}\left\{e^{i\phi_+(l)} - e^{-i\phi_-(l)}\right\}dl, \tag{6.121}$$

where

$$\phi_{\pm}(l) = 2\eta(l) \pm (l + \tfrac{1}{2})\chi \pm \pi/4. \tag{6.122}$$

The contribution of a range of l values width Δl around some value l_i to $f(\chi)$ can be examined by expanding $\eta(l)$ in a Taylor series about l_i so that the phase ϕ becomes:

$$\phi_{\pm}(l) = 2\eta(l_i) + 2\left(\frac{\partial\eta}{\partial l}\right)_{l=l_i}(l - l_i) + \left(\frac{\partial^2\eta}{\partial l^2}\right)_{l=l_i}(l - l_i)^2 \pm (l + \tfrac{1}{2})\chi \pm \pi/4. \tag{6.123}$$

We now introduce the important result for semi-classical phase shifts derived in Chapter 2:

$$2\mathrm{d}\eta/\mathrm{d}l = \chi, \tag{6.124}$$

and neglect higher terms than the quadratic as in Equation 6.123 to find that there is a region of stationary phase in $\phi(l)$ centered about l_χ, where l_χ satisfies

$$2(\mathrm{d}\eta/\mathrm{d}l)_{l=l_\chi} = \pm\chi_{\mathrm{obs}} \tag{6.125}$$

The width Δl of the stationary phase region in which $\phi_\pm$ changes by less than $\sim\pi$ is seen from

$$\phi_{\pm}(l) \approx 2\eta(l_\chi) - 2(l_\chi \pm \tfrac{1}{2})\eta'(l_\chi) + \eta''(l_\chi)(l - l_\chi)^2 \pm \pi/4, \tag{6.126}$$

to be proportional to $\eta''(l_\chi)^{-\frac{1}{2}}$, but need not be specified if we use the following standard integral to evaluate Equation 6.121 when Equation 6.126 is substituted;

$$\int_{-\infty}^{\infty} \mathrm{e}^{\pm iax^2}\,\mathrm{d}x = \left(\frac{\pi}{a}\right)^{\frac{1}{2}} \mathrm{e}^{\pm i\pi/4}, \tag{6.127}$$

so that

$$f(\chi) = -k^{-1}\left(\frac{l_\chi}{2\,|\,\eta''(l_\chi)\,|\,\sin\chi}\right)^{\frac{1}{2}} \mathrm{e}^{i\alpha_{\pm}(\chi)} \tag{6.128}$$

where

$$\alpha_{\pm}(\chi) = 2\eta(l_\chi) - 2(l_\chi \pm \tfrac{1}{2})\eta'(l_\chi) + \frac{\eta''(l_\chi)}{|\,\eta''(l_\chi)\,|}\frac{\pi}{4}, \tag{6.129}$$

in which the term $\eta''/|\eta''|$ takes care of a change in sign of $a(=\eta'')$ in Equation 6.127. In arriving at Equation 6.128, the factor $(l+\frac{1}{2})$ in the integrand has been taken out and replaced by l_χ. The leading semi-classical approximation to $\sigma(\chi)$ is then:

$$\sigma(\chi) = |f(\chi)|^2 = l_\chi \Big/ \left[2k^2 \left|\frac{d^2\eta}{dl^2}\right|_{l=l_\chi} \sin\chi\right], \tag{6.130}$$

and is identical with Equation 2.10. Upon substituting the large l result for the phase shifts resulting from a potential $V = -C_s R^{-s}$, namely

$$\eta(l) = f_s \left(\frac{C_s}{E}\right) l^{-s+1} k^s \tag{6.131}$$

where

$$f_s = \frac{\pi^{1/2}}{2} \Gamma\left(\frac{1}{2}[s-1]\right) \Big/ \Gamma\left(\frac{s}{2}\right),$$

(a simplified version of Equation 6.83), the following expression is obtained for the small angle semi-classical differential cross-section:

$$\sigma(\chi) \approx \frac{1}{s}\left(2[s-1]\,\frac{f_s C_s}{E}\right)^{2/s} \chi^{-(2+2/s)}. \tag{6.132}$$

This result merges with the quantum $\exp(-C\chi^2)$ form at very small angles with some diffraction structure in between, as illustrated in Fig. 1. Thus, to calculate the differential cross-section at some angle χ, it must first be found whether the corresponding phase shift $\eta(l_\chi)$ is appreciably greater or less than 1 radian. In the former case a region of stationary phase will be well developed in the partial wave summation and Equation 6.130 may be used (subject to the reservations in Section 6.10). If the phase shift is $< 1^c$, the parabolic approximation to $\eta(l)$ gives increasingly too large a width Δl to the region of stationary phase, and $\sigma(\chi)$ is best evaluated by direct summation of the partial wave expansion.

For an R^{-s} potential, the angle at which the classical result merges into the quantum form (roughly the position of the first maximum in the function $\chi^{2+2/s}\,\sigma(\chi)$) can be calculated from Equation 6.131 together with the condition that the critical phase shift is $\eta^* \sim 1$ radian, with the result

$$\chi^* \approx 2(s-1)\left(\frac{E}{f_s C_s k^s}\right)^{1/(s-1)} \tag{6.133}$$

Typically, at thermal energies $\chi^* \sim 1.5^\circ$ in agreement with deductions from the uncertainty principle (Section 6.1).

6.10 Interfering branches of the deflection function

There is one important respect in which Equation 6.130 may be in error and this arises from the possible presence of more than one region of stationary phase in $\phi_\pm$. The condition for stationary phase is that l satisfies Equation 6.125, and this may well be fulfilled by more than one value of l. In particular, for values of χ less than the rainbow value, there will always be three solutions of Equation 6.125, two corresponding to stationary phase in ϕ_+ and one in ϕ_-, as can be seen from an inspection of Fig. 6.3. It must be remembered that the angle χ that appears in the partial wave summation is the true polar angle of observation (in the CM system) and so must be positive. The deflection function $\chi(l)$, however, can be positive or negative but these alternatives or *branches* cannot be separated experimentally and so both must be included in computing the scattered amplitude at a given angle of observation. If the energy is such that the rainbow angle is greater than 2π, the situation is even more complicated because trajectories that suffer a deflection of $\chi + 2n\pi$ are experimentally indistinguishable from those deflected through χ, and so each contributes a region of stationary phase and is a separate branch of the deflection function. Since the maximum deflection in the orbiting case is ∞ there can be an infinite number of such branches (Fig. 6.4). In order to obtain the correct phase to $|2\pi|$ between all these branches, a new phase β is defined that replaces α in Equation 6.129:

$$\beta = 2\eta(l_\chi) - 2(l_\chi + \tfrac{1}{2})\eta'(l_\chi) - \left(2 - \frac{\eta'}{|\eta'|} - \frac{\eta''}{|\eta''|}\right)_{l=l_\chi} \frac{\pi}{4} \qquad (6.134)$$

where the term $\eta'/|\eta'| \pi/4$ provides the relative phase change of $\pi/2$ in passing from the positive to the negative branch of the deflection function, i.e. from ϕ_+ to ϕ_-. Let the three regions of stationary phase be centered on l_1, l_2 and l_3. Each such region gives a contribution to $f(\chi)$ of the form of Equation 6.128 and their sum is the resultant amplitude. The semi-classical differential cross-section then becomes

$$\sigma(\chi) \approx \left|\sum_n f_n(\chi)\right|^2 \qquad (6.135)$$

$$= \sum_n |f_n(\chi)|^2 + \sum_{\substack{n \\ n \neq m}} \sum_m |f_n(\chi)|\,|f_m(\chi)| \cos(\beta_n - \beta_m), \qquad (6.136)$$

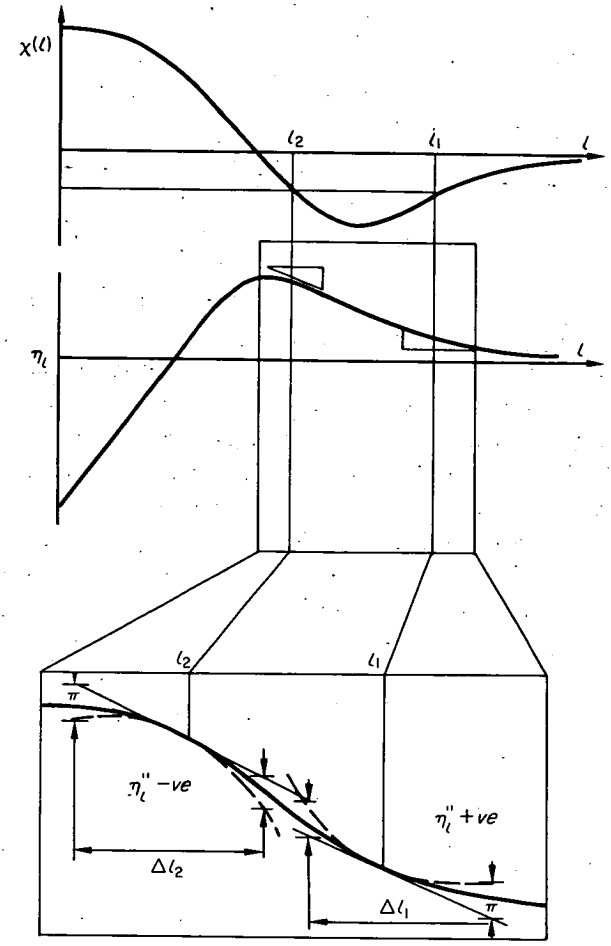

Fig. 6.3 The method of stationary phase applied to two interfering branches of the deflection function $\chi(l)$ at l_1 and l_2. The osculating parabolas are shown as dashed curves and the ranges of l values that lead to coherent scattering, Δl_1 and Δl_2, are determined by the range over which the parabolic approximation departs by less than π from the linear approximation, which is also the phase of the function $P_l(\cos\chi)$.

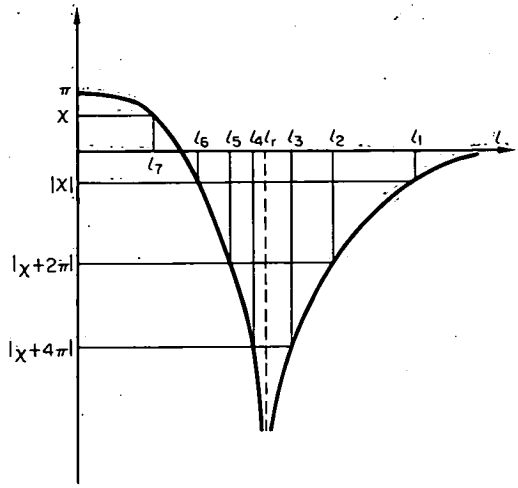

Fig. 6.4 A deflection function exhibiting orbiting. Each of the indicated l values is the centre of a region of stationary phase (for the given value of χ), of which there are an infinite number.

where the second term in Equation 6.136 represents an oscillatory contribution (see Equation 6.138) in the presence of the dominant first term. In fact, we can introduce the classical value of $\sigma(\chi)$ for the non-oscillatory part to get

$$\sigma_{cl}^{(n)}(\chi) = |f_n(\chi)|^2, \tag{6.137}$$

and so

$$\sigma_{sc}(\chi) = \sum_{\text{all branches}} \sigma_{cl}^{(n)}(\chi) + \text{interference terms between all branches}$$

For heavy particle scattering, the second term in Equation 6.134 is dominant and so, remembering that $\eta'(l_\chi)$ changes sign in passing from ϕ_+ to ϕ_-;

$$\beta_n - \beta_m \approx (l_n \mp l_m)\chi, \tag{6.138}$$

the upper sign referring to the case in which both branches come from ϕ_+,

and the lower sign to one branch from ϕ_+ and the other from ϕ_-. Defining the periodicity Δ of the undulations as

$$\cos(\beta_n - \beta_m) = \cos 2\pi\chi/\Delta \qquad (6.139)$$

one obtains

$$\Delta \approx 2\pi/|\, l_n \mp l_m \,|$$

There is a simple picture of the choice of sign in Equations 6.138 and 6.139; from Fig. 6.5 it is seen that the effective grating spacing for trajectories originating on opposite sides of the scattering centre is $b_n + b_m$, whereas for those originating on the same side and experiencing the same deflection the grating spacing is $b_n - b_m$.

If only two branches contribute, the amplitude of $\sigma(\chi)$ oscillates between

$$\sigma_{max} = \{|f_1(\chi)| + |f_2(\chi)|\}^2$$

and (6.140)

$$\sigma_{min} = \{|f_1(\chi)| - |f_2(\chi)|\}^2$$

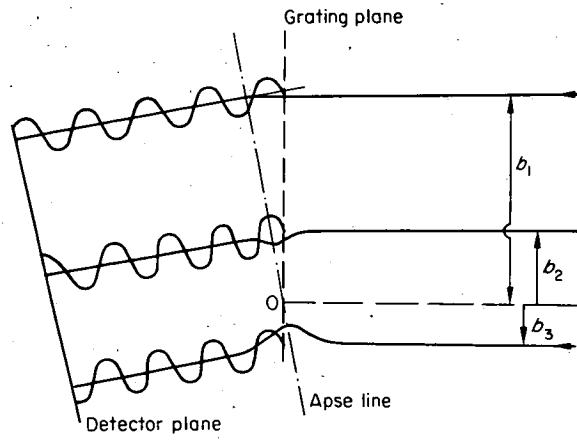

Fig. 6.5 Three trajectories with different impact parameters are shown that emerge at the same angle of scattering. In the simplest approximation they may be regarded as scattered from centres at b_1 and b_2 above the origin O and b_3 below. The effective grating spacings are then $b_1 - b_2$, $b_2 + b_3$ and $b_1 + b_3$. Zero potential wave trains scattered from these points on a hypothetical grating are shown.

In the course of fitting experimental results, the elastic scattering pattern that would be seen under low or intermediate angular resolution is often required. If the complete partial wave summation is evaluated and the resulting differential cross-section averaged over the apparatus angular resolution, the high frequency from the interference of branch 3 with branches 1 and 2 is wiped out. This is a rather clumsy procedure and the following expedient is sometimes adopted to remove the high frequency contribution from the partial wave sum from the outset. In Equation 6.121, the term ϕ_+ contributes the interference terms having $d\eta_l/dl = -\chi/2$ and ϕ_- those regions of stationary phase around $d\eta_l/dl = \chi/2$, i.e. the high frequency ones. Thus, evaluating

$$\sigma(\chi) = (2\pi k^2 \sin\chi)^{-1} \left| \int_0^\infty (l+\tfrac{1}{2})^{\frac{1}{2}} e^{i\phi_+(l)}\, dl \right|^2 \qquad (6.141)$$

will give the appearance of $\sigma(\chi)$ under intermediate angular resolution.

6.11 Glory undulations in $\sigma(\chi)$ and σ_{tot}.

As a first example of the application of the idea of interfering branches, we consider the structure in the differential cross-section at small angles and the related energy dependence of the total cross-section. Referring to Fig. 6.6, strong interference between branches 2 and 3 will arise near $\chi = 0$ because of their almost equal amplitude. This structure will be superimposed on the much stronger scattering from the branch at l_1. Since the two inner branches lead to deflections of opposite sense, the periodicity of their interference pattern is given, from Equation 6.139, by

$$\Delta_{23} \approx 2\pi/(l_2 + l_3) \approx \pi/l_0, \qquad (6.142)$$

and the latter approximation is appropriate to the high frequency structure near $\chi = 0$ (see Fig. 6.8).

Of particular experimental interest is the contribution of the forward glory (i.e. the inner zero deflection branch of $\chi(l)$) to the total cross-section. To tackle this we apply the optical theorem to the semi-quantal forward scattered amplitude $f(0)$:

$$f(0) \cong \frac{1}{2ik} \int_0^\infty (2l+1)[e^{2i\eta(l)} - 1]\, dl. \qquad (6.143)$$

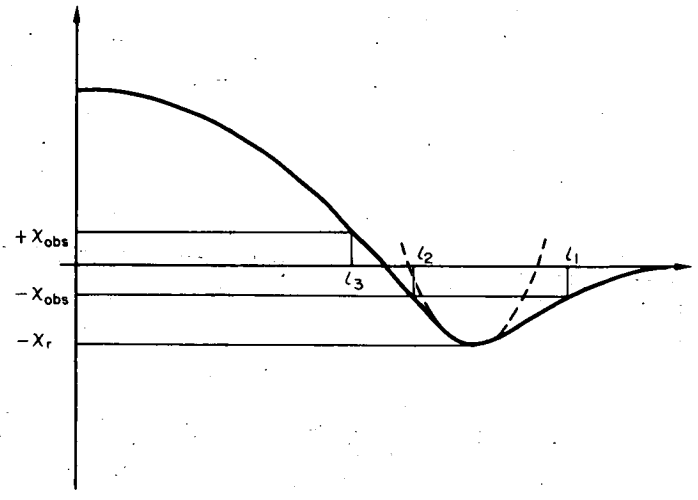

Fig. 6.6 A typical deflection function exhibiting the rainbow phenomenon at $\chi = \chi_r$. Interference effects will be observed near an angle of observation χ_{obs} between the branches at l_1, l_2, and l_3. The osculating parabola at the rainbow angle is shown as a dashed curve.

There are two regions of stationary phase which we subscript (1) and (2,3 the latter two branches having merged at $\chi = 0$ where they are exactly in phase. We require the imaginary part of $f_1(0)$ and so from

$$f_1(0) \cong k^{-1} \int_L^\infty (2l+1)(\eta^B(l) + i\eta^B(l)^2)\, dl$$

we use

$$f_1(0) \cong e^{i\pi/2} k\sigma_{tot}^B/4\pi \qquad (6.144$$

where the Born phase shifts η^B are adequate and σ_{tot}^B is the contribution o the large impact parameter region to the total cross-section. The contributio of the inner branches is obtained from a parabolic fit to the phase shif function around $l = l_0$:

$$\eta(l) \approx \eta(l_0) + \frac{1}{2}\eta''(l - l_0)^2 \qquad (6.145$$

to give a contribution of the form of Equation 6.128 to the scattere

mplitude:

$$f_{2,3}(0) \approx \frac{l_0}{k}\left(\frac{\pi}{\eta''(l_0)}\right)^{1/2} e^{2i\eta(l_0)-i\pi/4} \tag{6.146}$$

Noting that their relative phase is energy is dependent, the two amplitudes are ow combined:

$$\sigma_{tot} = \frac{4\pi}{k}\,\mathrm{Im}\{f_1(0)+f_{2,3}(0)\} \approx \frac{4\pi}{k^2} l_0\left(\frac{\pi}{\eta''(l_0)}\right)^{1/2} \sin(2\eta(l_0) - 3\pi/4) + \sigma_{tot}^{B} \tag{6.147}$$

Thus, the forward glory gives an oscillatory contribution to the energy ependence of the total cross-section as it passes in and out of phase with the ulk of the forward scattered wave front. The condition for an extremum in ne velocity dependence of σ_{tot} is that the wave number k satisfies:

$$\eta_{l_0}(k) = \left(N - \frac{3}{8}\right)\pi$$

where the integer N, running to N_{max}, can be used to index successive naxima. The amplitude of these undulations is ~10 per cent σ_{tot} and xamples are given in Chapter 7. N_{max} is of interest in itself in that it is the umber of bound states that can be contained in the potential well formed by $V(R)$. The proof of this involves Levinson's theorem, an account of which can e found in M. Wellner, 1964. From a practical point of view, however, it is ifficult to extend total cross-section measurements to a low enough energy or N_{max} to be measured and the counting is further complicated by the ppearance of resonance spikes at low energies in the structure of σ_{tot} Appendix B).

The spacing of the structure in the spectrum of σ_{tot} is, of course, a unction of the intermolecular potential. The turning point of trajectories nat lead to zero deflection lies close to R_m over a range of values of E^* and nus the phenomenon of glory interference probes further into the repulsive art of the potential than the rainbow effect (see Section 6.11). This can be een in a more quantitative fashion from the limiting high energy expression or η_0. If the Born approximation is applied to both the attractive and epulsive parts of a bipolar potential the high energy expression for the

overall phase shift is obtained. For the Lennard-Jones potential the result is

$$\eta(l_0) \cong \frac{240\pi}{847}\left(\frac{231}{160}\right)^{1/6} \epsilon\sigma/\hbar w, \tag{6.148}$$

and so the location of maxima is given by values of v that satisfy

$$N - \frac{3}{8} \cong 0.3012\, \epsilon\sigma/\hbar v_N. \tag{6.149}$$

Although these expressions only apply for $E^* >> 1$, they do illustrate the much greater sensitivity of the phenomenon to σ than, say, the magnitude of the envelope or low resolution value of the total cross-section. A fuller analysis of the problem by Bernstein can be found in J. Ross, 1966.

6.12 Rainbow scattering

As the angle of observation approaches the rainbow angle, branches (1) and (2) merge (see Fig. 6.6) and can no longer be considered as separate regions of stationary phase. In order to extend the region of stationary phase over both branches, the deflection function near the rainbow is approximated by an oscillating parabola such that at $\chi = \chi_r$ its curvature and that of $\chi(l)$ are matched,

$$\chi(l) = \chi_r + \frac{1}{2}\left(\frac{d^2\chi}{dl^2}\right)_{l=l_r}(l - l_r)^2, \tag{6.150}$$

or equivalently

$$\eta(l) = \eta(l_r) + \frac{\chi_r}{2}(l - l_r) + \frac{1}{12}\left(\frac{d^2\chi}{dl^2}\right)_{l=l_r}(l - l_r)^3 \tag{6.151}$$

From Equation 2.10 the classical differential cross-section is readily found to be

$$\sigma_{cl}(\chi) = \frac{b_r}{k \sin\chi}\left|2\left(\frac{d^2\chi}{dl^2}\right)_{l=l_r}(\chi - \chi_r)\right|^{-1/2} \tag{6.152}$$

as derived in Chapter 2. However, upon going to the semi-classical formula for

he scattered amplitude,

$$f_{sc}(\chi) \cong \left(\frac{l_r + \tfrac{1}{2}}{2\pi \sin\chi}\right)^{\tfrac{1}{2}} \frac{e^{i(2\eta_r - l_r\chi)}}{k} \int_{-\infty}^{\infty} \exp\left[i(\chi_r - \chi)(l - l_r) + \frac{i}{6}\left(\frac{d^2\chi}{dl^2}\right)_{l=l_r}(l-l_r)^3\right] d(l - l_r), \quad (6.153)$$

where only ϕ_- has been included, an inessential phase factor has been omitted and the factor $l + \tfrac{1}{2}$ again taken outside the integration in order to cast the integral into a standard form, the Airy integral,

$$\mathrm{Ai}(\chi) = \frac{1}{2\pi} \int_{-\infty}^{\infty} \exp\left[i\chi u + \frac{1}{3} iu^3\right] du. \quad (6.154)$$

The Airy function is purely real and so the phase of $f(\chi)$ near the rainbow region is, from Equation 6.153, $2\eta_r + l_r\chi$. The lower limit of integration in Equation 6.154 is extended to $-\infty$ in a completely unphysical fashion, but this has little effect on the value of the integral, to which the major contribution comes from $|u| < \pi$. Finally, then,

$$\sigma_{sc}(\chi) = \frac{b_r}{k \sin\chi} 2\pi |\chi''(l_r)/2|^{-2/3} \mathrm{Ai}(\chi)^2 \quad (6.155)$$

where

$$x = |\chi''(l_r)/2|^{-1/3} (\chi_r - \chi)$$

The Airy function is purely real and so the phase of $f(\chi)$ near the rainbow rapid than exponential decay on the dark side ($\chi > \chi_r$) and an oscillatory behaviour on the bright side. Useful approximations are

$$\text{(i)}\ \mathrm{Ai}(x) \approx 2^{-1}\pi^{-\frac{1}{2}}x^{-\frac{1}{4}} \exp\{-(\tfrac{2}{3})x^{3}_{2}\} \quad x \to \infty \quad (6.156)$$

$$\text{(ii)}\ \mathrm{Ai}(x) \approx \pi^{-\frac{1}{2}}|x|^{-\frac{1}{4}} \cos\{\tfrac{2}{3}|x|^{\frac{3}{2}} - \pi/4\} \quad x \to -\infty.$$

Substituting Equation 6.156 ii into Equation 6.155, replacing the $\cos^2$ factor by $\tfrac{1}{2}$, yields twice the classical value for $\sigma(\chi)$ given by Equation 6.152. This is because the semi-classical result (for $\chi < \chi_r$) includes both branches of the deflection function on either side of the rainbow. The classical rainbow (at

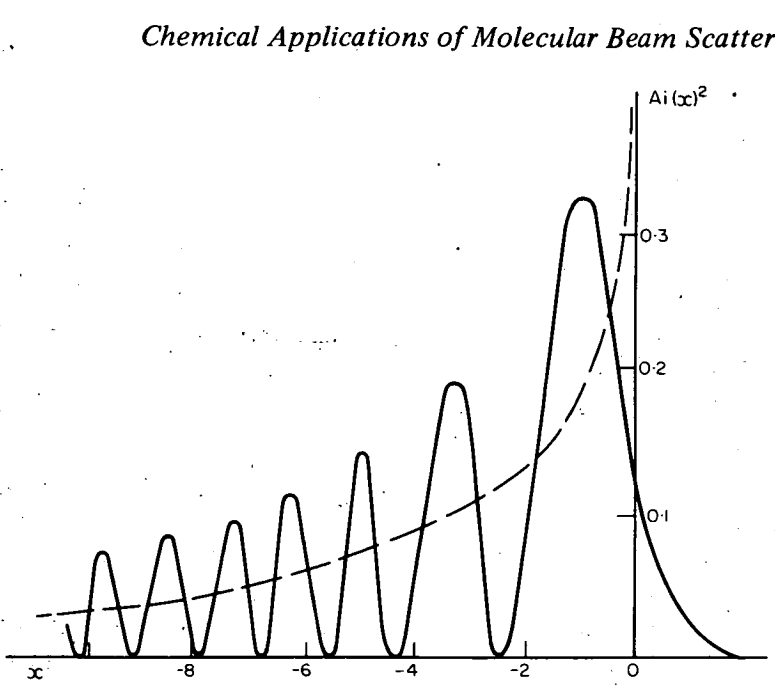

Fig. 6.7 The function $\mathrm{Ai}(x)^2$.

x = 0) coincides with the point of maximum gradient on the dark side of th semi-classical differential cross-section, not with the maximum of the Air function. The supernumerary structure arises from the interference of partia waves scattered from either side of minimum of the deflection function, l and l_2 in Fig. 6.6.

In this discussion of the rainbow phenomenon, the third interfering branc coming from positive angles of deflection has so far been neglected. Referrin to Fig. 6.6, this contribution comes from impact parameters centered aroun b_3 and we may use the result of Equation 6.139 to deduce that a hig frequency structure will be superimposed upon the rainbow oscillations. I the rainbow contribution is regarded as a single branch (i.e. with branches (1 and (2) merged) and written in the form,

$$f_r(\chi) = |f_r(\chi)|\, e^{i[2\eta_r + l_r|\chi| - 3\pi/4]} \qquad (6.157$$

then combining with the third branch

$$f_3(\chi) = k^{-1}\left(\frac{l_3}{2\,|\eta_3''|\,\sin\chi}\right)^{1/2} e^{i(2\eta_3 - l_3\chi)}. \qquad (6.158$$

gives a scattered amplitude

$$|f(\chi)|^2 = |f_r|^2 + |f_3|^2 + 2|f_r||f_3|\cos[(l_r + l_3)\chi + \delta] \quad (6.159)$$

which oscillates with approximately the frequency $\Delta = 2\pi/(l_3 + l_r)$. This type of structure is illustrated in Fig. 6.8. As χ approaches zero, the two rainbow branches separate and the inner one merges with the glory branch.

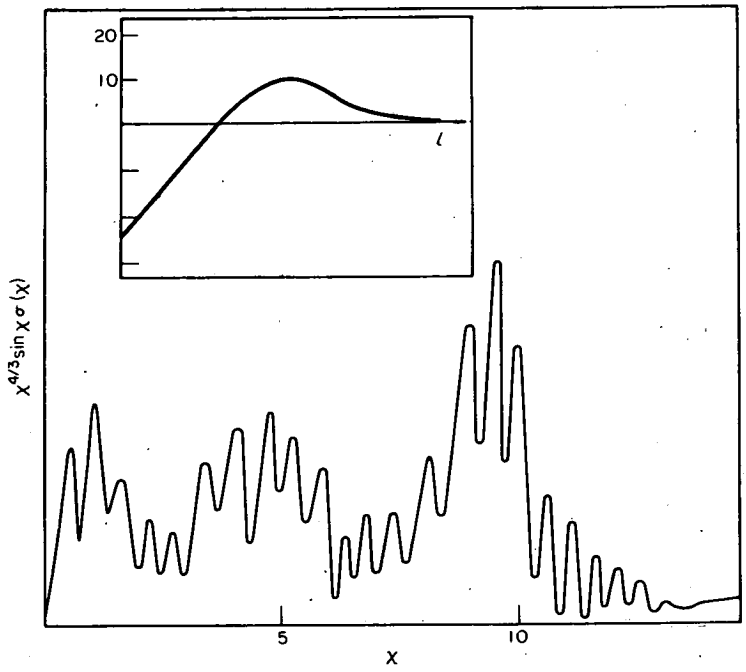

Fig. 6.8 A typical high resolution differential cross-section plot exhibiting the rainbow effect. Both high and low frequency interference effects are evident. The form of the phase shift function is inset. The classical rainbow angle is at 10°.

The above simple treatment of the rainbow and its supernumerary structure is not valid far from χ_r. For this, a uniform approximation to the integral of Equation 6.121, i.e. one valid with specified precision over the whole angular range in which $P_l(\cos\chi)$ is oscillating, has been given by M. V. Berry (1966) but is inevitably less convenient than Equation 6.153.

6.13 Hard sphere scattering and Fraunhofer diffraction

The phase shifts for the scattering of impenetrable spheres radii a_1 and a_2 are sometimes approximated by (N. F. Mott and H. S. W. Massey, 1965).

$$\begin{aligned} \eta(l) &= -kd + l\pi/2 \quad l \leqslant kd \\ \eta(l) &= 0(ka/l)^l \quad l > kd \end{aligned} \tag{6.160}$$

where the distance of closest approach $d = a_1 + a_2$. The semi-classical value for $l > kd$ are zero, but the quantum value is of the order shown and arise from the fact that the Bessel function decays as ρ^l inside the classical turning point.

Neglecting the phase shifts for $l > kd$, and replacing the partial wave summation, Equation 6.65, by integration over l we have

$$\sigma_{\text{tot}} \cong 2\pi d^2, \tag{6.161}$$

a result twice the classical value. This effect was first noticed by H. S. W. Massey and C. Mohr, 1933, and is essentially the result of constructive interference in the forward direction as can be seen by the following analysis. The scattered amplitude can be broken up into two contributions after substituting Equation 6.160 into the partial wave summation with $L = kd$

$$f_c = -\frac{i}{2k} e^{-2ikd} \sum_0^L (-1)^l (2l+1) P_l(\cos\chi) \tag{6.162}$$

$$f_d = \frac{i}{2k} \sum_0^L (2l+1) P_l(\cos\chi) \tag{6.163}$$

These contribute equally to the total cross-section and the reader can readily verify that

$$2\pi \int_0^\pi |f_c(\chi)|^2 \sin\chi d\chi = 2\pi \int_0^\pi |f_d(\chi)|^2 \sin\chi \, d\chi = \pi d^2 \tag{6.164}$$

(the cross term $|f_c \| f_d|$ vanishes through the operation of the $(-1)^l$ factor in f_c). However, their contribution to the differential cross-section is very different as can be seen from the two forward scattered amplitudes $f_c(0)$ and $f_d(0)$;–

$$|f_c(0)| = \frac{1}{2} d(-1)^{kd}$$

$$|f_d(0)| = \frac{1}{2} kd^2,$$

i.e. the contribution from f_d is $0(kd)$ greater than that from f_c. $|f_d(\chi)|^2$ is, in fact, a very sharply peaked function near $\chi = 0$ and contains the interference cone of angular width $1/kd$ described above. f_c is called the classical amplitude because it gives the whole of the classical contribution outside the diffraction cone (assuming the exact $\eta(l)$ to be used).

Using the approximation of Equation 6.94 for the Legendre polynomials, the following approximation for the small angle scattering is derived from f_d with the aid of Equation 6.163:

$$\sigma(\chi) \approx [d^2/\chi \sin \chi] J_1^2(kd\chi). \tag{6.165}$$

The first minimum occurs at $\chi \approx 3.8/kd$ and the complete function is displayed in Fig. 6.9. The undulations in $\sigma(\chi)$ are the result of interference between waves trains scattered from either side of the sphere from (A5) the periodicity is

$$\Delta\chi = \pi/kd \tag{6.166}$$

since the hard sphere diameter is effectively half the spacing of the diffraction grating.

Making use of the asymptotic form of $J_1(x)$ for $x \gg 1$ (Appendix A) shows further that with the phase shifts used above:

$$\sigma(\chi) \xrightarrow{\chi \to \pi} 0(d/k) \tag{6.167}$$

while the correct classical limit is $0(d^2)$. In order to obtain the quantum equivalent of this result, a more accurate phase shift function must replace Equation 6.160. Starting from the classical deflection function in Equation 6.63 and using

$$\eta(l) = \eta(0) + \frac{1}{2}\int_0^l \chi(l')\, dl' \tag{6.168}$$

where $\eta(0) = -kd + \pi/4$ for the hard sphere case, we obtain:

$$\eta(l) = l\chi/2 - kd \sin(\chi/2) + \frac{\pi}{4} \tag{6.169}$$

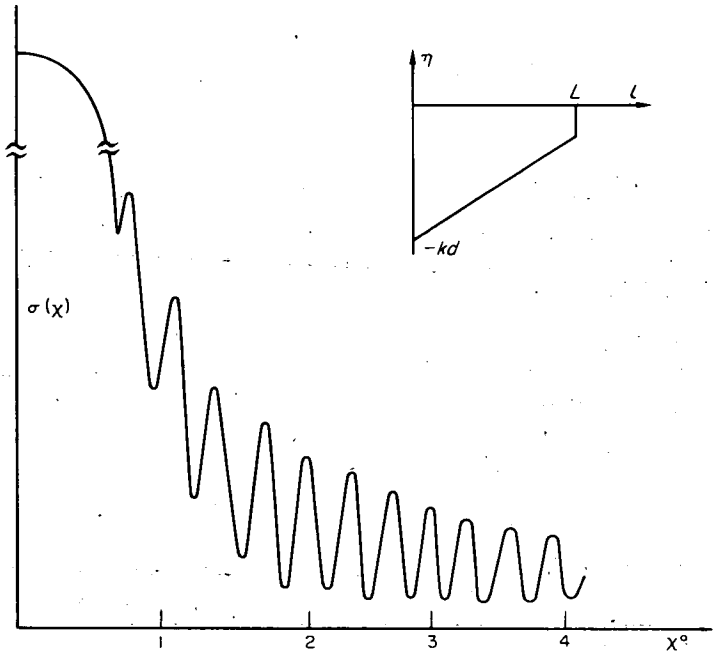

Fig. 6.9 The small angle scattering resulting from a step in the phase shift function (inset), of the type represented by (6.160). The exponential decay of $\sigma(\chi)$ at very small angles is shown, with the quadratic decay of the envelope at larger angles. The function displayed is essentially $J_1(L\chi)$.

where $\chi(l)$ is the classical deflection function. There is a discontinuity in the gradient of this phase shift function at $l = kd$. Once again $f(0)$ is split up into a diffraction term f_d identical to Equation 6.163 and a potential scattering term,

$$f_c(\chi) = \frac{i}{2k} \sum_{l=0}^{\infty} (2l+1)\, e^{2i\eta_l} P_l(\cos\chi) \tag{6.170}$$

with η_l given by Equation 6.169; $f_c(\chi)$ can be evaluated by the usual semi-classical method (Section 6.9) and the classical result

$$\sigma_c(\chi) = |f_c(\chi)|^2 = \frac{\pi}{2} \frac{d^2}{\sin\chi} \qquad \chi > \frac{1}{kd} \tag{6.171}$$

obtained. However, the diffraction contribution $f_d(\chi)$ is still present and

makes a small oscillatory contribution at large angles, with the envelope determined by Equation 6.171.

In optics this type of interference is familiar as Fraunhofer diffraction. Its molecular manifestation is not limited to the artificial hard sphere potential but may arise from any potential yielding a region in which the phase shift varies discontinuously with l. Thus, scattering from a deep 'chemical' potential well supporting many quasi-bound states will show this effect; in Fig. 6.10 the discontinuities produced by these resonances would merge into a single large step in region II. This edge in the phase shift function at $l = L$ leads to oscillations in the differential cross-section of a frequency from Equation 6.139 of π/L. To a crude approximation $\sigma(\chi)$ can be estimated by assuming random phases for $l < L$ and zero phase shifts for $l > L$, whence

$$\sigma(\chi) = |f_d(\chi)|^2 \tag{6.172}$$

with $f_d(\chi)$ given by Equation 6.163. In practice the phase shifts will not be

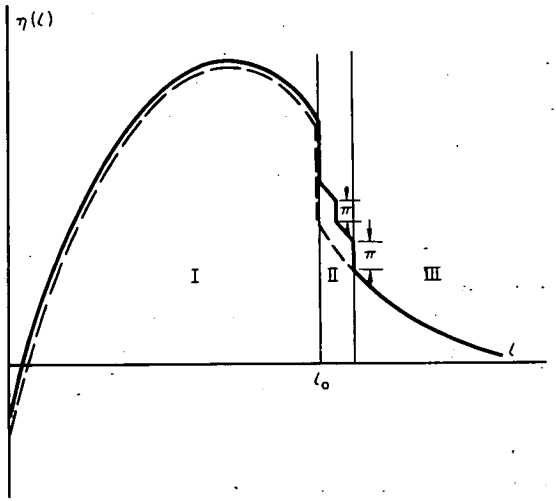

Fig. 6.10 The phase shift function in the presence of orbiting. The orbiting value of l is l_0; for $l < l_0$, region I, there is only one classical turning point and the quantum (full line) & semi-classical (dashed line) phase shifts nearly coincide. In region II there are either two ($l = l_0$) or three classical turning points and resonances occur in the quantum phase shift. In region III the effective potential energy curve is monotonic and the quantum and semi-classical values coincide.

random and interfering branches may exist either side of the 'edge' leading to lower frequency oscillations superimposed upon the Fraunhofer pattern (L. T. Cowley et al. 1969. M. A. D. Fluendy, 1970).

6.14 Resonances

Resonances play an important part in electron and nuclear scattering, but their role so far in molecular scattering has been negligible. One reason for this is that a single resonance affects only a few partial waves, whereas the width of a semi-classical branch of the scattered amplitude in heavy particle scattering typically exceeds 100 partial waves. In contrast, in low energy nuclear and electron scattering, the s-wave contribution to the differential cross-section is usually dominant and a resonance can become of paramount importance. Nevertheless, the theory of resonances and especially their effect on the total cross-section follows identical lines in all cases to yield one of the best known formulae of nuclear scattering, the Breit-Wigner formula (appendix B), thus reminding chemists that their interests are but part of a larger story.

The key to the interpretation of resonances is the relationship between the lifetime Γ of a compound state formed as the result of a collision and the range of energy ΔE over which the total cross-section is perturbed:

$$\Gamma.\Delta E \sim h \tag{6.173}$$

The most promising area to search for resonances in molecular scattering is in the energy dependence of the total cross-section where the basic structure is simple and slowly varying. Two requirements are then that the potential should be deep enough to support at least one bound state, and that the lifetime of a state (essentially trapped behind the centrifugal barrier) should be sufficiently short for the corresponding energy width, ΔE, to be large, as indicated by Equation 6.173. For the lifetime to be short, the centrifugal barrier must not be too high or too wide, and the frequency of the classical motion inside the barrier must be high. These condition are fulfilled by a pair of particles of small reduced mass near orbiting. Stwalley (W. C. Stwalley, 1969) has thus suggested that the scattering of hydrogen atoms from a variety of species should yield relatively pronounced resonances in $\sigma_{tot}(E)$. In the most favourable case, that with the shortest Γ, we can set an upper limit on ΔE by assuming that the lifetime in the well is equal to the classical periodicity and that the system passes back through the barrier on the first

attempt. From Equation 6.173, ΔE is then $\sim 10^{-14}$ ergs; this is to be compared with the typical energy resolution in a total cross-section experiment at thermal energies, which is also $\sim 10^{-14}$ ergs so detection even in the most favourable case is still difficult.

6.15 The scattering of identical particles.

Since Equation 6.7 is the wave function for the relative motion of two particles, it must have a definite parity with respect to the interchange of the two colliding particles if these are indistinguishable. The correct wave functions for fermions will be anti-symmetric and for bosons symmetric with respect to this permutation. For the purposes of elastic scattering, the pair wave function is the product of the nuclear spin function and the overall rotational wave function, just as it would be for a Σ state diatomic molecule. Depending on the nuclear spin, a variety of spin wave functions can be constructed that are either symmetric or anti-symmetric with respect to the interchange of nuclear labels. This interchange also results in the inter-nuclear vector, **R** being reversed in sign, which is a symmetry operation on the rotational wave function. Thus, the inversion of the coordinates of particle (1) through the origin results in the change of its polar co-ordinates from (χ, ϕ) to $(\pi - \chi, \pi + \phi)$. Under this transformation, the Legendre polynomials behave as follows:

$$P_l(\cos\chi) \xrightarrow{\chi \to \pi - \chi} (-1)^l P_l(\cos(\pi - \chi))$$

and, from Equation 6.45,

$$e^{ikz} \longrightarrow e^{-ikz}$$

(the purely radial functions e^{ikR} or $j_l(kR)$ are unchanged). The operation of an exclusion principle ensures that for bosons nuclear and rotational states of like symmetry are combined and for fermions only those of unlike symmetry combine. This situation is familiar in spectroscopy where for half integral spin particles the even rotational levels are called para states and the odd levels ortho states.

In the scattering problem we must impose odd or even symmetry on the spatial wave function if the nuclei are identical. For a given pair of atoms in a definite nuclear spin state (which is not necessarily known but which does not change during the collision) only odd or even partial waves can be

included in any part of Equation 6.7. The initial plane wave thus becomes

$$e^{ikz} \longrightarrow e^{ikz} \pm e^{-ikz} = 2\sum_{l \text{ even, odd}} i^l(2l+1)j_l(kr)P_l(\cos\chi), \tag{6.174}$$

which represents the approach of identical particles from both left and right with equal flux, which is what is occurring physically (Fig. 6.11). The partial wave expansion of the scattered amplitude now reads

$$f_\pm(\chi) = 2\frac{1}{2ik}\sum_{l \text{ even, odd}}(2l+1)(e^{2i\eta_l}-1)P_l(\cos\chi), \tag{6.175}$$

(where the factor 2 has come from the doubling of the intensity of each allowed value that results from using Equation 6.174).

To restore the complete summation over l we introduce $P_l(\cos(\pi-\chi))$,

$$2\sum_{l \text{ even, odd}}(2l+1)(e^{2i\eta_l}-1)P_l(\cos\chi) = \sum_{\text{all } l}(2l+1)(e^{2i\eta_l}-1)\Big\{P_l(\cos\chi) \pm P_l(\cos(\pi-\chi))\Big\}. \tag{6.176}$$

Then,

$$f_\pm(\chi) = f(\chi) \pm f(\pi-\chi), \tag{6.177}$$

and so

$$\sigma(\chi) = |f(\chi)|^2 + |f(\pi-\chi)|^2 \pm 2|f(\chi)||f(\pi-\chi)|. \tag{6.178}$$

Finally, we must include the weighting of the ortho (+) and para (−) states w_+ and w_- to give

$$\sigma(\chi) = |f(\chi)|^2 + |f(\pi-\chi)|^2 + 2(w_+ - w_-)|f(\chi)||f(\pi-\chi)|. \tag{6.179}$$

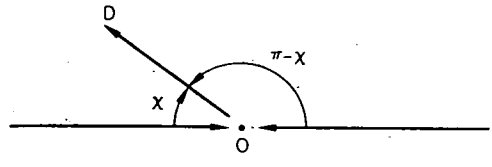

Fig. 6.11 Identical particles approaching from left and right in the cm must be scattered through $(\pi-\chi)$ and χ respectively to reach the detector D.

The partial wave summations for $f(\chi)$ and $f(\pi - \chi)$ can be evaluated in the semi-classical fashion as described in Section 6.9 and the molecular symmetry of the problem has no effect on this stage of the calculation. However, the overall differential cross-section $\sigma(\chi)$ is rendered symmetrical about $\chi = \pi/2$ (CM). Classically, this is because we cannot tell whether a particle reaching the detector has come from the main beam or the cross-beam. Besides this entirely new symmetry in the scattering pattern, novel interference effects have appeared from the cross-term $2f(\chi)f(\pi - \chi)$ in Equation 6.178, but for this term to be important $f(\chi)$ and $f(\pi - \chi)$ must have similar amplitudes and this will only occur near $\chi = \pi/2$.

If the two beams are differently isotopically labelled, we can perform two experiments;

I Detector cannot discriminate between the isotopes, in which case

$$\sigma(\chi) = |f(\chi)|^2 + |f(\pi - \chi)|^2 . \tag{6.180}$$

II Detector is mass sensitive, in which case

$$\sigma(\chi) = |f(\chi)|^2 . \tag{6.181}$$

In either case the special interference effects are destroyed. The total cross-section for the scattering of spinless bosons (I = 0) is readily obtained by applying the optical theorem to Equation 6.176

$$\begin{aligned}\sigma_{tot} &= \frac{2\pi}{k^2}\sum_l (2l+1)(1-\cos 2\eta_l)(P_l(1)+P_l(-1)) \\ &= \frac{2\pi}{k^2}\left\{\sum_l (2l+1)(1-\cos 2\eta_l) + \sum_l (2l+1)(1-\cos 2\eta_l)\cos \pi l\right\} \\ &= \frac{2\pi}{k^2}\left\{\sum_l (2l+1)(1-\cos 2\eta_l) + \sum_l (2l+1)(-1)^l \right. \\ &\qquad \left. - \sum_l (2l+1)\cos 2\eta_l \cos \pi l\right\} \end{aligned} \tag{6.182}$$

where the equivalent forms $P_l(-1) = \cos \pi l = (-1)^l$ have been used as needed.

The first term in 6.182 represents the normal contribution that would be obtained for unlike particles without any symmetry requirements. The second term has been seen (Section 6.13) to be negligible. The third term can

exhibit a region of stationary phase if the deflection function passes through $\pm\pi$, so that $2\eta_l - \pi = 0,\ 2\pi$ at $l = l_{\pm\pi}$. The region of stationary phase at $\chi(l) = \pi$, which occurs at $l = 0$, is always present; the occurrence of the other branch depends upon the attractive part of the potential being sufficiently strong. Making a parabolic fit to the phase shift function near $l = 0$ and $l = l_{-\pi}$ results in

$$2\eta(l) - l\pi = \begin{cases} 2\eta(l_\pi) + 2l^2\eta''(l_\pi) \\ 2\eta(l_{-\pi}) + (l - l_{-\pi})^2\eta''(l_{-\pi}) - 2\pi l. \end{cases} \tag{6.183}$$

The range of integration in the Fresnel integral that is obtained when Equation 6.183 is substituted into Equation 6.182 is now $0 \to \infty$ in the first case and $-\infty \to \infty$ in the second (which is similar in all quantitative respects to a forward glory). The scattered amplitude in the forward direction due to these inner branches is now given by

$$f(0) = \frac{l_\pi}{4ik}\left\{\cos 2\eta(l_\pi) + \sin 2\eta(l_\pi)\right\}\left(\frac{\pi}{2\eta''(l_\pi)}\right)^{1/2} + \frac{l_{-\pi}}{2ik}\left\{\cos 2\eta(l_{-\pi}) + \sin 2\eta(l_{-\pi})\right\}\left(\frac{\pi}{2\eta''(l_{-\pi})}\right)^{1/2} \tag{6.184}$$

Then, neglecting the possible presence of a forward glory, the total cross-section is given by:

$$\sigma_{\text{tot}} = \sigma_{\text{tot}}^{\text{cl}} + \frac{\pi l_\pi}{2k^2}\sin\left[2\eta(l_\pi) + \pi/4\right]\left(\frac{\pi}{\eta''(l_\pi)}\right)^{1/2} + \frac{\pi l_{-\pi}}{k^2}\sin\left[2\eta(l_{-\pi}) + \pi/4\right]\left(\frac{\pi}{\eta''(l_{-\pi})}\right)^{1/2} \tag{6.185}$$

The physical interpretation of this result is that a cross-beam particle deflected through $\pm\pi$ into the direction of the main beam, will reach the detector in a total cross-section experiment and cannot be distinguished from a particle originating in the main beam. The two wave trains thus interfere, and a maximum in the total cross-section occurs every time η_π or $\eta_{-\pi}$ passes through $(\pi/4 + 2\pi n)$.

For very low energy scattering of light particles in which only a few partial waves participate, only the S-wave contribution at $\chi = \pi$ is important and the semi-classical nature of Equation 6.185 would be inappropriate. Such a situation arises in the scattering of He^4 from He^4 (Section 7.4) at very low temperatures. In this case the interatomic potential is essentially

purely repulsive and the $\chi = -\pi$ branch is absent. For Ne or Ar, also spinless bosons, the presence of a minimum in the intermolecular potential means that a forward glory must be present and this contributes yet another interfering branch which must be included in Equation 6.185.

In the treatment of identical particle scattering so far it has been assumed that only one intermolecular potential is operating, irrespective of the nuclear spin state. This is a valid assumption for atoms in S states. However, when the scattering of like particles that possess non-zero electronic spin is considered, new phenomena appear which are discussed in Section 6.17.

6.16 Scattering from mixed electronic states; exchange scattering

We now discuss the scattering of excited atoms or ions (M^*, M^+) from the corresponding ground state species (M). The need for a separate treatment of this problem arises from the fact that the electronic energy levels of the two particle system that dissociate to $M^* + M$ are of two kinds and hence two potential energy functions can govern the relative motion of the pair. These electronic states are classifiable with respect to inversion of the electrons in the centre of symmetry of the nuclear charges (i.e. the centre of mass in the present problem). The scattering of a metastable molecule from a ground state partner is a much more complicated situation; the symmetry of the problem depends upon the orientation of the two molecules and there is considerable coupling between molecular rotation and electronic motion.

In a crossed-beam experiment (M^*/M), a diatomic system is in effect prepared in which it is known which of the two atoms is excited initially by the position they occupy in the laboratory. We must first describe this unusual situation in terms of eigenfunctions having the full symmetry of this molecule which are the gerade and ungerade states, ψ_g and ψ_u. For slow collisions we will need only the lowest members of these two classes (the others lying too high in energy to be accessible) and so

$$\psi_{g,u} = \frac{1}{\sqrt{2}} \left\{ \phi_A \phi_B^* \pm \phi_A^* \phi_B \right\} \tag{6.186}$$

where A and B label the two identical atoms, one from each beam, and ϕ_A, ϕ_B are the ground state atomic eigenfunctions. The electronic wave functions in the actual entrance channels of the experiment are

$$\left.\begin{matrix} \phi_A \phi_B^* \\ \text{or} \\ \phi_A^* \phi_B \end{matrix}\right\} = \frac{1}{\sqrt{2}} \left\{ \psi_g \pm \psi_\mu \right\} \tag{6.187}$$

Our first approach might be that, equipped with wave function 6.187 we calculate an interatomic potential from 1st order perturbation theory

$$V_{AB^*}(R) = V_{A^*B}(R) = \frac{1}{2}\left\{\langle\psi_g \mid H \mid \psi_g\rangle + \langle\psi_u \mid H \mid \psi_u\rangle - (E_0 + E_0^*)\right\} \tag{6.188}$$

where H is the complete electronic Hamiltonian and E_0, $E_0{}^*$ are the energies of the isolated ground and excited atoms. In arriving at Equation 6.188, use has been made of the fact that, by symmetry, $\langle\psi_g \mid H \mid \psi_u\rangle = 0$. The scattering, we might think, would then be confined to the AB* or A*B channel and in either case proceed under the influence of the potential in Equation 6.188.

The difficulty is that the interaction potential in H, by which an electron on one atom experiences a field due to the neighbouring atom, connects the state AB* and A*B in the sense that the matrix element

$$\langle\psi_A\psi_{B^*} \mid H \mid \phi_{A^*}\phi_B\rangle = \langle\psi_g \mid H \mid \psi_g\rangle - \langle\psi_u \mid H \mid \psi_u\rangle \tag{6.189}$$

is not zero. The result of this is that if we were to start the collision in the state AB*, then time dependent perturbation theory (or the method of analysis to follow) tell us that the 'exciton' (labelled*) oscillates between the two atoms during the collision. This problem seems to require the solution of two simultaneous wave equations to replace the single one (Equation 6.6) with which this chapter began, but fortunately there is an equivalent route that decouples the states.

The interatomic potentials for the states described by ψ_g and ψ_u are also well defined

$$V_{g,u}(R) = \langle\psi_{g,u} \mid H \mid \psi_{g,u}\rangle - \frac{1}{2}\ (E_0 + E_0^*), \tag{6.190}$$

and the Hamiltonian is diagonal in this representation:

$$\langle\psi_g \mid H \mid \psi_u\rangle = 0.$$

Thus, regardless of whether in practice we can prepare the u and g states, we can define a scattering matrix for the collision of the two atoms with entrance and exit channels formally labelled g and u. The advantage of this is that the complete S matrix is now factored into two sub-matrices, one for

scattering between (g, l) channels and the other between (u, l) channels. Physically, if we prepare a gerade state, then however violent the collision we cannot possibly end up in an ungerade state because there is no term in the Hamiltonian that couples terms of different symmetry. For the scattering of ground state S atoms, the scattering matrix is completely diagonalised because states of different relative angular momentum (l – value) are not coupled by the Hamiltonian. This remains true to a good approximation for the scattering of excited or ionised $2S$ or $3S$ states, and somewhat less true of P states, where electronic orbital angular momentum is more readily coupled to translational angular momentum, especially with regard to changes in the projection quantum number m_L.

Assuming that the relative angular momentum is separately conserved, we deduce that the S matrix in the g, u description is completely diagonalised, and the lth sub-matrix down the diagonal is of the form

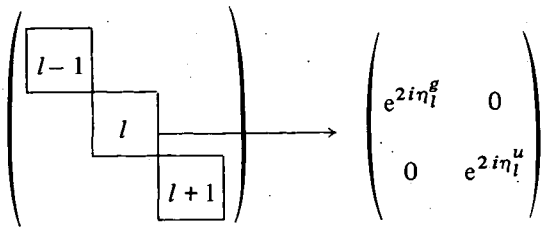

(6.191)

The phase shifts $\eta^{g,u}$ can be calculated by any of the methods outlined in Sections 6.5, 6.7 or 6.8 using $V_{g,u}(R)$ as appropriate.

From our knowledge of the S matrix in one basis, (Equation 6.191) we can readily find it in any other orthonormal basis by the appropriate unitary transformation (Section 6.4). In the present case the matrix $\{T\}$ that converts the $\{\psi_u, \psi_g\}$ basis into the $\{\phi_A, \phi_B\}$ basis is, from Equation 6.187.

$$\{T\} = \begin{pmatrix} \frac{1}{\sqrt{2}} & \frac{1}{\sqrt{2}} \\ \frac{1}{\sqrt{2}} & -\frac{1}{\sqrt{2}} \end{pmatrix} = \{T\}^{-1}, \tag{6.192}$$

and so the l^{th} factor of the scattering matrix in the $\{\phi_A \phi_B\}$ basis is given by the similarity transformation

$$\{S_l\}_{A,B} = \{T\}^{-1} \{S_l\}_{g,u} \{T\}$$

where the first transformation deals with the exit channels and the second with the entrance channels. The result is

$$\begin{pmatrix} S_{AB^*l:AB^*l} & S_{AB^*l:A^*Bl} \\ S_{A^*Bl:AB^*l} & S_{A^*Bl:A^*Bl} \end{pmatrix} = \begin{pmatrix} \frac{1}{2}\left\{e^{2i\eta_l^g} + e^{2i\eta_l^u}\right\} & \frac{1}{2}\left\{e^{2i\eta_l^g} - e^{2i\eta_l^u}\right\} \\ \frac{1}{2}\left\{e^{2i\eta_l^g} - e^{2i\eta_l^u}\right\} & \frac{1}{2}\left\{e^{2i\eta_l^g} + e^{2i\eta_l^u}\right\} \end{pmatrix}$$

The new S matrix is, of course, unitary but is no longer diagonal. The probability of transition from the entrance channel $(AB^*;l)$ to the exit channel $(A^*B;l)$, i.e. for the transfer of excitation from one atom to the other is

$$P_{AB^*l:A^*Bl} = |S_{AB^*l:A^*Bl}|^2 = \tfrac{1}{2}\left[1 - \cos 2(\eta_l^g - \eta_l^u)\right]. \qquad (6.193)$$

The differential cross-section for elastic scattering of either the excited or the ground state is given by

$$\begin{aligned} f_{AB^*:AB^*}(\chi) &= \frac{1}{2ik}\sum_l (2l+1)\left\{\frac{1}{2}(e^{2i\eta_l^g} + e^{2i\eta_l^u}) - 1\right\} P_l(\cos\chi) \\ &= \frac{1}{4ik}\left\{\sum_l (2l+1)(e^{2i\eta_l^g} - 1)\, P_l(\cos\chi)\right. \\ &\quad \left. + \sum_l (2l+1)(e^{2i\eta_l^u} - 1)\, P_l(\cos\chi)\right\} \\ &= \frac{1}{2}\left\{f_g(\chi) + f_u(\chi)\right\} \end{aligned} \qquad (6.194)$$

The gerade and ungerade scattered amplitudes can be summed separately by any of the methods previously outlined. In particular, if the semi-classical method is used and the regions of stationary phase for a given value of χ located in both $f_g(\chi)$ and $f_u(\chi)$, we can write

$$\sigma_{AB^*:AB^*}(\chi) = \frac{1}{4}\left\{\sigma_g(\chi) + \sigma_u(\chi) + 2\left[\sigma_g(\chi)\sigma_u(\chi)\right]^{1/2}\cos(\beta_g - \beta_u)\right\} \qquad (6.195)$$

where it is assumed that there is only one region of stationary phase in each of the $f_g(\chi)$ and $f_u(\chi)$; β_g, β_u are defined analogously to Equation 6.134. A new interference structure has thus emerged, with a frequency

$$\Delta\chi \approx 2\pi/(l_\chi^g - l_\chi^u), \qquad (6.196)$$

where the difference between η_l^g and η_l^u in $\beta_g - \beta_u$ has been neglected. This structure will only be pronounced if the amplitudes of $f_g(\theta)$ and $f_u(\theta)$ are similar.

The exchange differential cross-section is similarly found to be given by

$$\sigma_{AB^*:A^*B}(\chi) = \frac{1}{4} |f_g(\chi) - f_u(\chi)|^2, \tag{6.197}$$

and so also exhibits interference structure of the same frequency as the direct scattering but 180° out of phase. At large separations of the particles, the g and u potentials differ only slightly, as do the associated phase shifts. Re-arranging Equation 6.197 to introduce an average phase shift,

$$\frac{1}{2}(\eta_l^g + \eta_l^u) = \eta_l^{av}$$

gives

$$f_{AB^*:A^*B}(\chi) = \frac{1}{2k} \sum_l (2l+1)\, e^{2i\eta_l^{av}} \sin(\eta_l^g - \eta_l^u) P_l(\cos\chi) \tag{6.198}$$

For small angle scattering, then, the term $\sin(\eta_l^g - \eta_l^u)$ in Equation 6.198 is but slowly varying and we need only look for stationary phase in η^{av}. The treatment of Section 6.9 will then give an average scattered amplitude $f_{av}(\chi)$ and the exchange cross-section expression becomes

$$\sigma_{AB^*:A^*B}(\chi) \approx |f^{av}(\chi)|^2 \sin^2(\eta_\chi^g - \eta_\chi^u) \tag{6.199}$$

a formula valid for $\eta_\chi^g - \eta_\chi^u \ll \pi/2$. Thus it can be said that exchange scattering is directly dependent on the difference in gerade and ungerade potentials. In particular, at small angles, when the Born approximation for the phase shifts is applicable, the exchange cross-section is quadratically dependent on the difference in strengths of the two potentials.

Exchange scattering of the type described in this section has been most thoroughly studied in ion/neutral systems, notably He^+/He from 15 eV to 300 eV. In this case it is not an exciton that is exchanged but an electron, but the foregoing treatment remains unchanged, except for the complication of identical nuclei for which the treatment of Section 6.15 can be incorporated as follows. The entire atomic pair wave function

$$\psi = \left(\psi_{\substack{\text{nuclear}\\\text{spin}}}\right)\left(\psi_{\substack{\text{electronic}\\\text{co-ordinate}}}\right)\left(\psi_{\substack{\text{molecular}\\\text{rotation}}}\right)\left(\psi_{\substack{\text{electron}\\\text{spin}}}\right), \tag{6.200}$$

must be either symmetric (bosons) or anti-symmetric (fermions) with respect to interchange of identical particles. The He^+/He system can be treated as a 1-electron one and only the first three factors in Equation 6.200 are relevant (i.e. only doublet molecular states considered). For He^4 ($I = 0$), gerade electronic states are associated with even rotational states and ungerade with odd states. Then,

$$f_g(\chi) = f_g(\chi) + f_g(\pi - \chi) = \frac{1}{ik} \sum_{l\,\text{even}} (2l+1)[e^{2i\eta_l^g} - 1]\, P_l(\cos\chi),$$
$$f_u(\chi) = f_u(\chi) + f_u(\pi - \chi) = \frac{1}{ik} \sum_{l\,\text{odd}} (2l+1)[e^{2i\eta_l^u} - 1]\, P_l(\cos\chi) \qquad (6.201)$$

replace f_g and f_u in Equation 6.194. The number of possible interfering branches of the deflection function has now increased to four or more and the simplicity of the earlier pattern is marred. However, we have seen (Section 6.15) that if the scattering can be described in a semi-classical fashion, nuclear symmetry effects only become apparent at angles somewhat greater than the rainbow value. For the case of He^+/He in the low eV region, many partial waves contribute and a semi-classical treatment is appropriate. In this system it is the ungerade state that possesses a deep potential minimum and the gerade state is effectively everywhere repulsive. There are thus three branches contributing to $f_u(\chi)$ at angles less than the rainbow and only one branch to $f_g(\chi)$.

All these interference effects can be found in the experimental results for the $^4He/^4He^+$ system. The potentials and deflection functions are sketched in Fig. 6.12 together with the calculated (semiquantal) differential cross-section at 15 eV (Fig. 6.13). The observed scattering (D. C. Lorents and W. Aberth, 1965) follows the calculated curve quite closely, although the highest frequency oscillations on the bright side of the rainbow (arising from f_u) have not been resolved.

The radial separation at which gerade and ungerade potentials begin to diverge depends upon the electronic states of the two atoms. Thus, in the case of the He/He^+ system, a typical matrix element that governs the gerade/ungerade splitting is a 1-electron integral;

$$H_{AB} = \int \phi_A(r_A) \left\{ \frac{1}{r_A} + \frac{1}{r_B} - \tfrac{1}{2}\nabla^2 \right\} \phi_B(r_B)\, dr \qquad (6.202)$$

However, for the system $H(1s)/H(2s)$ or $He(1s^2\,;\,^1S)/He(1s^1\,2s^1\,;\,^3S)$ a two electron exchange integral is involved, which is a roughly quadratic function of the overlap of the two atomic orbitals. The splitting of the gerade and

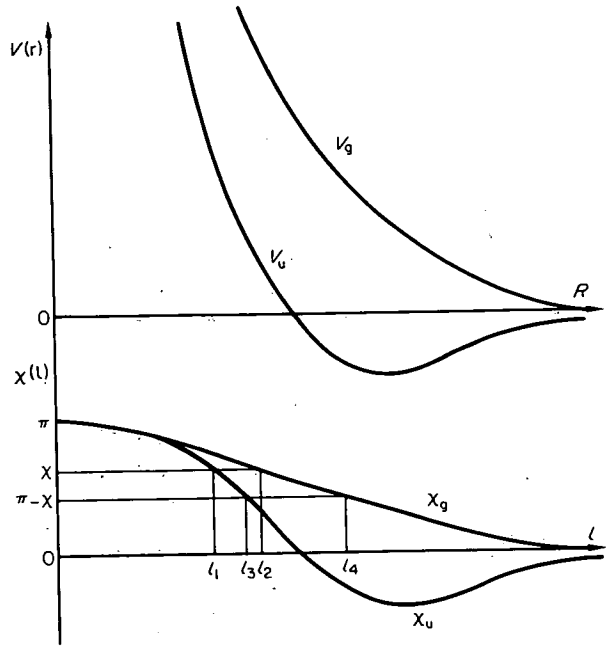

Fig. 6.12 Potentials and deflection functions for ^4He, $^4He^+$ scattering. For the angle of deflection, χ, illustrated ($\chi > \chi_r$), there are four interfering branches of the deflection function centered at $l_1 \ldots l_4$. The gerade potential will have a shallow minimum at a fairly large value of R that arises from the charge-induced dipole interaction and is not shown.

ungerade states thus begins at much closer separations in the latter cases and so the associated interference effects (e.g. from Equation 6.199) appear at larger angles of deflection and are less accessible to observation.

6.17 Scattering from mixed spin states

We now turn to the problem of the mutual scattering of ^2S atoms, i.e. of atoms with one unpaired electron. Two types of experiment have been performed, in the first case one of the beams is spin state selected ($M_S = \pm 1/2$) while the detector has an analyser also tuned to one of the spin states. The other configuration is one in which no spin selection at all is used.

Concentrating on the case of unlike nuclei (labelled A and B) the various atom pair wave functions that fulfill the anti-symmetric rule for the

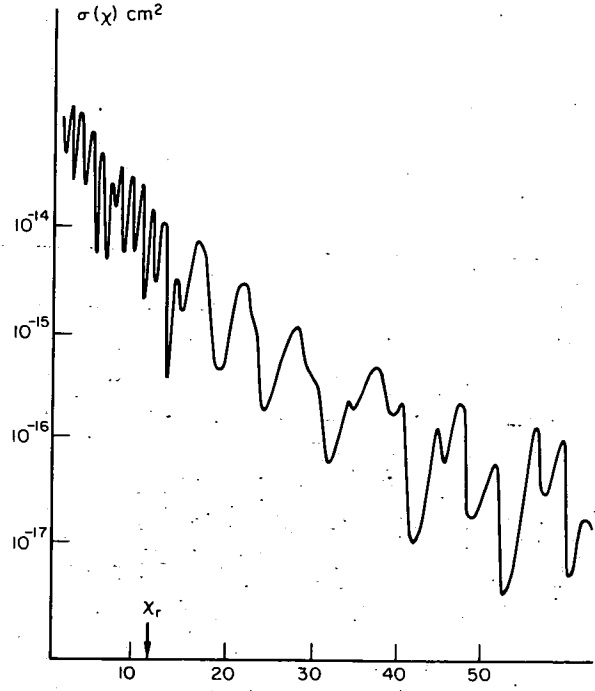

Fig. 6.13 The differential cross-section for $He^+ - He$ scattering at 15 eV, identical nuclei. The high frequency structure at $\chi < \chi_r$ is apparent, giving way to a simpler low frequency structure beyond the rainbow. This, in turn, shows the increasing interference from the exchange scattering ($|f(\chi)| \, |f(\pi - \chi)|$) at larger angles. The pure exchange scattering, $|f(\pi - \chi)|^2$ is negligible throughout this angular range. (Adapted from R. P. Marchi and F. T. Smith, 1965.)

electronic wave function are the familiar singlet and triplet states;

$$\psi_{00} = \{\phi_A(r_1)\phi_B(r_2) + \phi_B(r_1)\phi_A(r_2)\}\{\alpha(1)\beta(2) - \alpha(2)\beta(1)\}$$

$$\psi_1 \begin{Bmatrix} 1 \\ 0 \\ -1 \end{Bmatrix} = \{\phi_A(r_1)\phi_B(r_2) - \phi_B(r_1)\phi_A(r_2)\} \begin{Bmatrix} \alpha(1)\alpha(2) \\ \alpha(1)\beta(2) + \alpha(2)\beta(1) \\ \beta(1)\beta(2) \end{Bmatrix} \tag{6.203}$$

The potentials associated with these two states are very different, the triplet potential generally exhibiting only a very shallow minimum and the singlet state leading to a deep 'chemical' well. However, with no spin selection at all,

or even with the spin of only one atomic partner known, we have no a priori means of knowing whether the colliding pair is in the singlet or triplet state. However, if the spin is not coupled strongly to the relative angular momentum, transitions between singlet and triplet states are unlikely and we can expect the S matrix to be diagonal in the true singlet/triplet representation. The situation is thus very similar to the gerade/ungerade scattering of excited atoms or of ions treated in Section 6.14 and the formalism can be largely carried over.

From an experimental point of view, we need to describe the various atom pair wave functions according to the spin of each atom. Thus, if both atoms have $M_s = +\frac{1}{2}(\equiv \alpha)$,

$$\phi_{\alpha\alpha} = \| \phi_A \alpha \, \phi_B \alpha \|.$$

If atom A has spin α and atom B spin β,

$$\phi_{\alpha\beta} = \| \phi_A \alpha \, \phi_B \beta \|.$$

and so forth. Expanding these wave functions in terms of the singlet and triplet eigenfunctions ψ_{SM_s} gives:—

$$\begin{aligned} \phi_{\alpha\alpha} &= \psi_{1\,1} \\ \phi_{\alpha\beta} &= 2^{-\frac{1}{2}} (\psi_{0\,0} + \psi_{1\,0}) \\ \phi_{\beta\alpha} &= 2^{-\frac{1}{2}} (\psi_{0\,0} - \psi_{1\,0}) \\ \phi_{\beta\beta} &= \psi_{1\,-1} \end{aligned} \tag{6.204}$$

Clearly, although the singlet and triplet eigenfunctions diagonalize the total energy operator, the basis $(\alpha\beta)$ does not and in particular the matrix element

$$\int \phi_{\alpha\beta} \, V \phi_{\beta\alpha} \, d\tau = \int \psi_{0\,0} V \psi_{0\,0} \, d\tau - \int \psi_{1\,0} V \psi_{1\,0} \, d\tau \tag{6.205}$$

is not zero. In this situation it is more convenient to evaluate the S matrix elements in the (SM_s) basis and to subsequently transform to the $(\alpha\beta)$ basis. The observed scattering pattern will then be the superposition of the scattering resulting from the $(\alpha\alpha)$ $(\beta\beta)$, $(\alpha\beta)$ and $(\beta\alpha)$ entrance channels

weighted according to the spin selection used in the experiment. Thus, if $\sigma_{\alpha\beta:\gamma\delta}$ denotes the cross-section for scattering from the entrance channel $(\alpha\beta)$ to the exit channel $(\gamma\delta)$ we have, using the fact that either spin state is equally likely in an unselected beam (the cross-beam in cases I, II and IV below)

Case I. Atom A in state α, analyzer for atom A set for state β;

$$\sigma_{\mathrm{I}}(\chi) = \frac{1}{2}\,\sigma_{\alpha\beta:\beta\alpha}(\chi). \tag{6.206}$$

Case II. Atom A in state α, analyzer for atom A set for state α;

$$\sigma_{\mathrm{II}}(\chi) = \frac{1}{2}\left[\sigma_{\alpha\alpha:\alpha\alpha}(\chi) + \sigma_{\alpha\beta:\alpha\beta}(\chi)\right]. \tag{6.207}$$

Case III. Atom A in state α, atom B in state β, no spin analysis at the detector;

$$\sigma_{\mathrm{III}}(\chi) = \sigma_{\alpha\beta:\alpha\beta}(\chi) + \sigma_{\alpha\beta:\beta\alpha}(\chi). \tag{6.208}$$

Case IV. No spin selection or analysis;

$$\sigma_{\mathrm{IV}}(\chi) = \frac{1}{4}\left[\sigma_{\alpha\alpha:\alpha\alpha}(\chi) + \sigma_{\beta\beta:\beta\beta}(\chi) + \sigma_{\alpha\beta:\alpha\beta}(\chi) + \sigma_{\beta\alpha:\beta\alpha}(\chi) + \sigma_{\beta\alpha:\alpha\beta}(\chi) + \sigma_{\alpha\beta:\beta\alpha}(\chi)\right] \tag{6.209}$$

In cases III and IV the spin exchange cross-sections must be included because the detector cannot discriminate between direct and exchange scattering.

Relying upon the fact that the interaction potential is diagonal in the (SM_s) representation, we know that the S matrix for scattering from these states will be diagonal.

The l^{th} sub-matrix reads

$$\begin{pmatrix} e^{2i\eta_l^{1\,1}} & 0 & 0 & 0 \\ 0 & e^{2i\eta_l^{1\,0}} & 0 & 0 \\ 0 & 0 & e^{2i\eta_l^{1\,-1}} & 0 \\ 0 & 0 & 0 & e^{2i\eta_l^{0\,0}} \end{pmatrix}, \tag{6.210}$$

CHAPTER SEVEN

Elastic Scattering

7.1 Introduction

In the preceding chapters we have discussed mainly the results of collisions between particles without internal structure and interacting via a single potential. These collisions were of necessity elastic in the sense that there was no change in the internal states of the particles after collision. In the real world of atoms and molecules internal states are legion and collisions often result in transitions between them. Furthermore, scattering may not take place under the influence of a single intermolecular potential if the Born-Oppenheimer approximation breaks down. In this situation even collisions which are formally elastic in that the incident and final states are identical, may not be two body collisions in the sense of the theory presented in Chapter 6. Potentials that are apparently velocity dependent would be one indication of behaviour of this sort. Fortunately for the evolution of the field it appears that at thermal energies most atomic and molecular systems can be thought of to a good approximation as interacting according to well defined potentials, i.e. the electronic motion is adiabatic.

Elastic scattering experiments are primarily aimed at extracting intermolecular potentials and, less directly, with any concurrent inelastic or reactive processes. A full discussion of the other experimental techniques and their theory that are relevant to the topic of intermolecular forces would occupy several volumes. Fortunately, a number of recent books have treated this subject in depth (J. O. Hirschfelder, 1967; H. Margenau and N. R. Kestner, 1969; C. Schlier, 1969) and here we shall be concerned only with the scattering aspects of the problem.

The intermolecular potential is usually given a bipolar analytical form, with a long range attractive part and a short range repulsion term. We have seen that the operation of both attraction and repulsion in a molecular collision is responsible for much of the structure in molecular scattering patterns. A purely repulsive potential would be much less rich in quantum interference structure. A very wide range of analytical forms have been proposed for these potentials, the best known being the Lennard-Jones 12-6 potential:

$$V(R) = -C_6 R^{-6} + C_{12} R^{-12} \tag{7.1}$$

$$= 4\epsilon\left\{\left(\frac{\sigma}{R}\right)^{12} - \left(\frac{\sigma}{R}\right)^{6}\right\} \tag{7.2}$$

The advantage of using such a universal formulation lies in the readiness with which comparison between different molecular systems may be made in terms of only two parameters. In addition, the measurement of intermolecular forces reduces to the determination of the coefficients in the potential if a simple parametrised form is adopted. This approach, although widespread, suffers from a number of disadvantages.

Firstly, it is already clear that these forms are over-simplifications. The parameters in the potential, when they do have a clear physical meaning such as a well depth, can only yield the best approximation to the actual value that the form of the potential allows. For instance, in a truncated multipole expansion of the potential the various coefficients C_6, C_8 etc. although having a precise physical meaning alter their apparent value as more terms are included in the potential used to fit the data. A second difficulty with these forms is that they seem to apply to an infinite range of intermolecular separations and energies even though the experiments to which they are fitted have only sampled a very limited range of these variables. Thus, a measurement of the differential cross-section, even over 180 degrees, will only yield information on the potential over the range of R actually sampled by the classical trajectories, and most accurately on values of R near the classical turning points. The cautious experimenter should thus perhaps present his data as a table of values of the potential, defined with varying precision, to which spline functions can be fitted for analytical purposes.

Data on intermolecular potentials has been obtained by a number of techniques other than by scattering methods. The most important of these are (i) bulk measurements of state and transport properties and (ii) spectroscopic methods. Typical bulk data are second virial coefficients and viscosities of gases over a range of temperatures. Unfortunately, the

where $\eta_l^{SM_s}$ is the l^{th} phase shift derived from the potential

$$V^{SM_s}(R) = \langle \mathrm{SM}_s \mid H(r, R) \mid SM_s \rangle - (E_0^{\mathrm{A}} + E_0^{\mathrm{B}}) \tag{6.211}$$

and V is independent of M_s. Then, to convert from the (SM_s) to the $(M_{s_1} \mathrm{M}_{s_2})$ basis:

$$\begin{pmatrix} \alpha\alpha \\ \alpha\beta \\ \beta\alpha \\ \beta\beta \end{pmatrix} = \begin{pmatrix} 1 & 0 & 0 & 0 \\ 0 & 2^{-\frac{1}{2}} & 0 & 2^{-\frac{1}{2}} \\ 0 & -2^{-\frac{1}{2}} & 0 & 2^{-\frac{1}{2}} \\ 0 & 0 & 1 & 0 \end{pmatrix} \begin{pmatrix} 1, & 1 \\ 1, & 0 \\ 1, & -1 \\ 0, & 0 \end{pmatrix} \tag{6.212}$$

The S matrix in the $(\alpha\beta)$ representation then becomes: (l^{th} factor only shown)

$$\begin{pmatrix} e^{2i\eta_l^1} & 0 & 0 & 0 \\ 0 & 2^{-1}(e^{2i\eta_l^{1\,0}} + e^{2i\eta_l^{0\,0}}) & 2^{-1}(e^{2i\eta_l^{1\,0}} - e^{2i\eta_l^{0\,0}}) & 0 \\ 0 & 2^{-1}(e^{2i\eta_l^{1\,0}} - e^{2i\eta_l^{0\,0}}) & 2^{-1}(e^{2i\eta_l^{1\,0}} + e^{2i\eta_l^{0\,0}}) & 0 \\ 0 & 0 & 0 & e^{2i\eta_l^{1}} \end{pmatrix} \tag{6.213}$$

The differential cross-section for case I (pure exchange scattering) is found from

$$f_{\alpha\beta:\beta\alpha}(\chi) = \frac{1}{4ik} \sum (2l+1) \left\{ e^{2i\eta_l^{1\,0}} - e^{2i\eta_l^{0\,0}} \right\} P_l(\cos\chi) \tag{6.214}$$

to be (with the notation $1 \equiv$ singlet, $3 \equiv$ triplet)

$$\sigma_{\alpha\beta:\beta\alpha}(\chi) = \frac{1}{4} \mid f_1(\chi) - f_3(\chi) \mid^2 \tag{6.215}$$

$$= \frac{1}{4} \left\{ \mid f_1(\chi) \mid^2 + \mid f_3(\chi) \mid^2 - 2\cos(\alpha_1 - \alpha_3) \mid f_1(\chi) \mid \cdot \mid f_3(\chi) \mid \right\}$$

where (see Equation 6.129)

$$f_{1,3}(\chi) = \frac{1}{2ik} \sum (2l+1) \begin{Bmatrix} e^{2i\eta_l^{0\,0}} \\ e^{2i\eta_l^{1\,0}} \end{Bmatrix} P_l(\cos\chi) = \mid f_{1,3}(\chi) \mid e^{i\alpha_{1,3}} \tag{6.216}$$

and we have used the off-diagonal element $S_{\alpha\beta:\beta\alpha}$ in Equation 6.213. Equation 6.214 shows that the exchange scattering is determined by the difference between the singlet and triplet potentials.

The scattering in case II is given by:

$$\sigma_{II}(\chi) = \frac{5}{8} |f_3(\chi)|^2 + \frac{1}{8} |f_1(\chi)|^2 + \frac{1}{4} \cos(\alpha_1 - \alpha_3) |f_1(\chi)| \cdot |f_3(\chi)| . \tag{6.217}$$

This experiment, without a spin selected cross-beam, is much simpler than the direct observation of spin exchange scattering (case I) and the interference oscillations arising from the last term in Equation 6.217 have been observed by D. E. Pritchard and F. Y. Chu, 1970. It is clear that little is gained by spin selecting the cross-beam; the weighting of the interesting cross-term would increase but no new effects would emerge.

The cross-section in case III is given by:

$$\sigma_{III}(\chi) = \frac{1}{2} \left\{ |f_3(\chi)|^2 + |f_1(\chi)|^2 \right\} \tag{6.218}$$

The cross-section for scattering from unselected beams, case IV, is given by:

$$\sigma_{IV}(\chi) = \frac{3}{4} |f_3(\chi)|^2 + \frac{1}{4} |f_1(\chi)|^2 \tag{6.219}$$

The interference terms have disappeared, the oscillations in $\sigma(\chi)$ from the direct and exchange scattering (contributed by $\sigma_{a\beta:a\beta} + \sigma_{\beta a:\beta a}$ and $\sigma_{a\beta:\beta a} + \sigma_{\beta a:a\beta}$ respectively) being 180° out of phase. The weighting 3:1 of the triplet and singlet cross-sections is simply the relative probability of finding these states in a random mixture of spins drawn from the two beams. The unselected spin experiment has been performed with sodium scattered from potassium and although it is difficult to deduce both singlet and triplet potential parameters from this sort of experiment alone, they can be extracted when the results are considered in conjunction with the spin selected experiments.

Experiments can also be devised to measure the total cross-section in cases II-IV. In cases III and IV, those without spin analysis at the detector, the measured intensity in the forward direction, besides giving the attenuation of the main beam, also contains a contribution from the exchange scattering, $\sigma_{a\beta:\beta a}(0)$ and $\sigma_{\beta a:a\beta}(0)$ which reduces the apparent total cross-section from the true value given by the optical theorem. The outer branch contributions to the singlet and triplet scattered amplitudes are in phase at $\chi = 0$ (for large impact parameters the difference between the singlet and triplet potentials

disappears) and so give no contribution to $\sigma_{exch}(0)$, leaving only the small inner branch contributions of which there may be several. Experimentally, see Fig. 7.20, it is observed that $\sigma_{exch}(0)$ is indeed very small, being less than 1 per cent of σ_{tot} (D. E. Pritchard, et al., 1970).

Calculating σ_{tot} in cases III and IV presents no problems, we can simply integrate expressions Equation 6.218 or 6.219 over χ and add the forward exchange contribution to obtain for the apparent total cross-section Q:

$$Q^{IV} = \frac{3}{4}\sigma_{tot}^{(3)} + \frac{1}{4}\sigma_{tot}^{(1)} - \frac{1}{2}\sigma_{exch}(0). \tag{6.220}$$

However, when we come to integrate $\sigma_{II}(\chi)$,

$$\int_0^{\pi} \cos(\alpha_1 - \alpha_3)\,|f_3(\chi)|\cdot|f_1(\chi)|\sin\chi d\chi$$

has to be evaluated. We by-pass this by applying the optical theorem to the relevant scattered amplitude to obtain:

$$\sigma_{tot}^{II} = \frac{3}{4}\sigma_{tot}^{(3)} + \frac{1}{4}\sigma_{tot}^{(1)}, \tag{6.221}$$

since the forward exchange contribution is clearly zero under the experimental conditions.

Appendix A Some properties of Bessel functions

Useful limiting forms of spherical Bessel functions are:

$$\left.\begin{aligned} j_l(\rho) &\longrightarrow \rho^l/1.3.5\ldots(2l+1) \\ n_l(\rho) &\longrightarrow -1.3.5\ldots(2l+1)/\rho^{l+1} \end{aligned}\right\} \rho \ll l$$

$$\left.\begin{aligned} j_l(\rho) &\longrightarrow \frac{1}{\rho}\sin(\rho - l\pi/2) \\ n_l(\rho) &\longrightarrow -\frac{1}{\rho}\cos(\rho - l\pi/2) \end{aligned}\right\} \rho \gg l \tag{6.A1}$$

The Wronskian is

$$j_l \frac{d}{d\rho} n_l - n_l \frac{d}{d\rho} j_l = \frac{1}{\rho^2}. \tag{6.A2}$$

In generating these functions in the region $\rho \gg l$ on a digital computer (for calculating quantum phase shifts) an upward recursion formula is sufficient:

$$\begin{gathered} j_{\pm l}(z) = f_{\pm l}(z) \sin z + (-1)^{l+1} f_{\mp l-1}(z) \cos z \qquad (j_{-l} \equiv n_l) \\ f_0(z) = z^{-1} \qquad f_1(z) = z^{-2} \\ f_{l+1}(z) = (2l+1) z^{-1} f_l(z) - f_{l-1}(z) \end{gathered} \tag{6.A3}$$

If the argument is appreciably greater than the order, the magnitude of successive j_l and n_l is similar (from A.1) and upward recursion may be used without cumulative error.

The first two Bessel functions of integral order, $J_l(\rho)$, encountered in Section 6.6 are expanded thus as $\rho \to 0$;

$$\begin{aligned} J_0(\rho) &\approx 1 - \rho^2/4 + \rho^4/64 + \cdots \\ J_1(\rho) &\approx \rho/2 - \rho^3/16 + \rho^5/384 + \ldots \end{aligned} \tag{6.A4}$$

and for $\rho \to \infty$ the asymptotic behaviour is

$$\begin{aligned} J_0(\rho) &\approx (2/\pi\rho)^{1/2} \cos(\rho - \pi/4) \\ J_1(\rho) &\approx (2/\pi\rho)^{1/2} \sin(\rho - \pi/4) \end{aligned} \tag{6.A5}$$

Appendix B Resonances

Analytically, the simplest way in which resonances arise is by reflection at an abrupt change in the potential, even though classically there is no barrier to the motion. Thus, a commonly used model of the nuclear potential, the square well, permits the continuum S-wave functions to penetrate the well for some energies but completely reflects the incoming wave at other energies. (Fig. B1). In molecular scattering, potentials that change abruptly over a wavelength of the relative motion are rare and resonances generally arise by reflection and transmission at a centrifugal barrier, Fig. B1(2). In the latter case there are classically bound states of positive energy that are absent from the S-states of the square well. There are, nevertheless very close formal

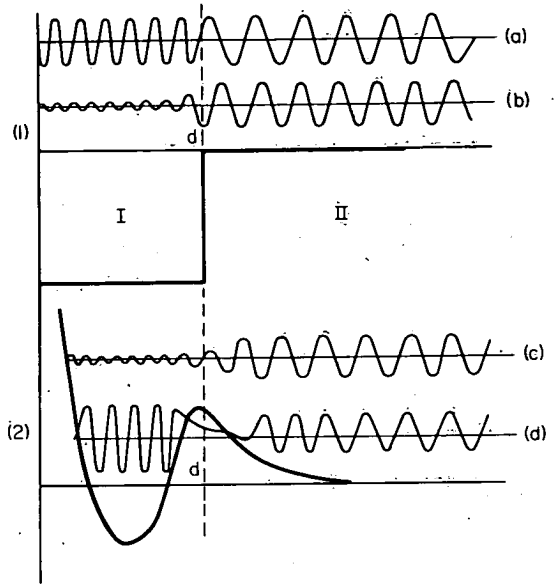

Fig. B1. Resonances arising from (1) a square well potential, (2) a centrifugal barrier. In case (a) the particle passes into the well and experiences a large positive phase shift. In (b), reflection at d prevents the incident particle from passing over the step and the phase shift is that of hard sphere scattering.

In (c), the energy is above the critical value for orbiting, but slight reflection can occur near the potential maximum (vestigial behaviour of type (b)) leading to small perturbations of the quantum cross section. In (d) there is a resonance with a quasi-bound state in the well, where the amplitude exceeds that of the exterior wave function. The phase shift will rapidly increase by π radians at this energy.

similarities between the two cases and we develop in very simple terms the potential step case up to the Breit-Wigner formula and then state the parallel results for the centrifugal barrier case. The first part of the path is a well trodden one and clear treatments are in T. Y. Wu and T. Ohmura, 1962, and E. Merzbacher, 1961.

For the square well potential,

$$\begin{aligned} V &= -V_0, \quad R \leqslant d \\ V &= 0, \qquad R > d \end{aligned} \tag{6.B1}$$

wave functions of the standing wave type inside and outside the well are, for the case of zero angular momentum,

$$\begin{aligned} \psi_{\mathrm{I}} &= \mathrm{C} \sin [KR] \\ \psi_{\mathrm{II}} &= \mathrm{D} \sin [kR + \eta_0(E)], \end{aligned} \tag{6.B2}$$

where the asymptotic forms appropriate to regions where the oscillatory behaviour is well developed ($kR \gg 1$) are used. The wave number inside the well, K, is given by

$$K = \frac{1}{\hbar}\sqrt{2\mu(E + V_0)}. \tag{6.B3}$$

The two solutions for Equation B2 are joined at $R = d$ by matching their gradients and amplitude, generally telescoped into the logarithmic derivative,

$$f = \left(\frac{1}{4}\frac{\mathrm{d}\psi}{\mathrm{d}R}\right)_{R=d} \tag{6.B4}$$

In order to make use of standard results, the S matrix elements (of which there is only one for $l = 0$) is found in terms of f. From Equation 6.63,

$$\psi_{\mathrm{II}} = \mathscr{B}\{\mathrm{e}^{ikr} - S_{00}\mathrm{e}^{-ikr}\} \tag{6.B5}$$

and from Equation 6.B4 applied to the exterior wave function,

$$S_{00} = \frac{f + ikd}{f - ikd}\,\mathrm{e}^{-2ikd} \tag{6.B6}$$

and so the total cross-section is, from Equation 6.65

$$\sigma_{\mathrm{tot}} = \frac{\pi}{k^2}\left|(1 - \mathrm{e}^{2ikd}) + \frac{2ikd}{f - ikd}\right|^2, \tag{6.B7}$$

where the scattered amplitude has been broken up into a hard sphere contribution (phase shift $\eta = -kd$ from Equation 6.160) and a resonance part.

Incorporating the actual wave functions ψ_{I} and ψ_{II} gives the matching condition

$$f = kd \operatorname{cotan} [kd + \eta_0] = Kd \operatorname{cotan} Kd \tag{6.B8}$$

which determines η_0. Referring to Equation B7, the resonance contribution to the total cross-section passes through a maximum every time f passes through zero. $\eta_0(E)$ can be found from Equation B8 to have the following form: in the region $K \gg k$ $(E \ll V)$ $\eta_0 = -kd + n\pi$ except when Kd passes through an odd multiple of $\pi/2$, when η_0 rapidly increases by π to sweep $\cot(kd + \eta)$ through zero. In the limit $E \gg V$, $K \approx k$, η_0 tends smoothly to zero, finally to be given by the Born approximation (e.g. from Equation 6.81 with $(kR)^2 j_0(kR)^2$ replaced by 1/2 in the integral)

$$\eta_0 \approx \frac{V_0}{E} kd. \tag{6.B9}$$

Thus, building up the phase shift function from the high energy end, there is a smooth rise from zero until K/k is appreciably greater than unity when a step-like structure appears in $\eta_0(E)$, the points of maximum gradient occurring at the resonant energies E^* at which

$$\frac{1}{\hbar}\sqrt{2\mu(E^* + V_0)} = (n + \tfrac{1}{2})\pi. \tag{6.B10}$$

We now need an approximation to f in the region of a resonance and take a linear approximation,

$$f \approx (E - E^*) \mid df/dE \mid_{E=E^*} \tag{6.B11}$$

Introducing Equation 6.B8,

$$df/dE \approx \frac{kd\, \partial\eta/\partial E}{\sin^2[kR + \eta_0]} \quad \therefore \quad \mid df/dE \mid_{E=E^*} = kd(\partial\eta/\partial E)_{E=E^*}, \tag{6.B12}$$

where we have used the knowledge that η is much more rapidly varying than k near a resonance. Defining a quantity Γ with the dimensions of energy,

$$\Gamma = 2 \mid (\partial\eta/\partial E) \mid^{-1}_{E=E^*} \tag{6.B13}$$

we have

$$\eta_0 = \eta_0^0 - \tan^{-1} \Gamma/2(E - E^*) \tag{6.B14}$$

where $\eta_0^0 = -kd$ is the phase shift induced by scattering at the boundary d; and so Γ is the range of E over which the phase shift effectively changes by π.

Then, substituting Equations B11 and B12 into Equation B7 gives

$$\sigma_{tot} = \frac{\pi}{k^2}\left|\frac{i\Gamma}{(E-E^*)+i\Gamma/2} + (1-e^{2i\eta_0^0})\right|^2 \qquad (6.B15)$$

and if the resonant contribution is dominant near E^*,

$$\sigma_{tot} \approx \frac{\pi}{k^2}\frac{\Gamma^2}{(E-E^*)^2+\Gamma^2/4} \qquad (6.B16)$$

This has the form of the Breit-Wigner formula. Γ has added significance through its connection with the delay time of the scattering. From Equation 2.41,

$$\tau = 2\hbar\,\partial\eta/\partial E$$

and so

$$\Gamma = 4\hbar/\tau. \qquad (6.B17)$$

Thus, the shorter the delay time, i.e. the shorter the lifetime of the system within a radius d, the broader the resonance. This is the basis of the argument used in Section 6.14. In deciding the best experimental conditions for observing resonances.

We now turn to a qualitative discussion of the changes in the above results when the resonances are associated with states trapped behind a centrifugal barrier, so called shape resonances. There are strong formal similarities between the two cases and these are emphasised in Fig. B1, where the matching boundary at $r = d$ is extended into the potential with a centrifugal term and forms a notional boundary at which interior and exterior solutions are matched in the latter case. A phase sensitive detector situated at $r \gg d$ would see only the step-like behaviour of the phase shift which can always be fitted by the form of Equation B14, with the aid of only two parameters and without a detailed knowledge of the nature of the potential.

Important differences between the two cases are that the amplitude inside the well can now exceed that of the exterior wave and very long lifetimes are encountered. Secondly, at a given energy there may be several partial waves in or near resonance, but generally these will be sparsely scattered and we will continue to assume that only one is present.

The semi-classical approach is to match the three WKB solutions in regions I, II and III of Fig. 2.1, and after some manipulation the form of Equation

B12 is regained for the phase shift, but with two changes (J. N. L. Connor, 1968). For the n^{th} resonance of the l^{th} angular momentum state,

$$\Gamma_{nl} = \frac{h\nu_{nl}}{2\pi} \ln \left[1 + \exp\left(2\hbar^{-1} \int_{R_1}^{R_2} |\, p(R)\, | \, dR\right)\right] \qquad (6.B18)$$

where ν_{nl} is the classical frequency of oscillation in the well of the effective potential. The logarithmic factor in Equation B18 represents the effect of the centrifugal barrier and ranges between zero for very thick barriers to ln2 for a barrier of zero width. Equation B18 is derived for the case of a parabolic barrier, but the dependence on the action integral through the barrier will not be a sensitive function of the barrier shape. The phase shift, far away from resonance, η_0, is now given by the usual semi-classical value, in Equation 6.110.

Finally, the contribution of an isolated resonance at $l = l^*$ to the observed total cross-section can be found by integrating Equation B15 over the energy resolution δE of the experiment to give (for $\delta E \gg \Gamma_{nl}$)

$$\delta\sigma_{l^*} = \frac{1}{\delta E} \int_{E-\delta E/2}^{E+\delta E/2} \sigma_{tot}^{res}\, dE \cong \frac{4\pi}{k^2} (2l^* + 1) \left\{ \sin^2 \eta_l^0 + \pi \frac{\Gamma_{nl}}{\delta E} \cos 2\eta_l \right\}. \qquad (6.B19)$$

The most favourable conditions for observing a resonance are thus for Γ_{nl} and l^* to be large. This points to a level near the top of the centrifugal barrier, but even so the measure of the resonance is small. Thus, the maximum value for l^* will be that for orbiting and if the orbiting radius is d, $l^* = kd$ and so

$$\frac{\delta\sigma_{tot}^{res}}{\sigma_{tot}} \leqslant \frac{1}{kd} \frac{\Gamma_{nl}}{\delta E}, \qquad (6.B20)$$

generally a small fraction for even the lightest atoms ($1/kd \leqslant 0.01$).

Appendix C Summary of useful formulae

In the partial wave summation the scattered amplitude is

$$f(\chi) = \frac{1}{2ik} \sum (2l + 1)[S_{ll} - 1] P_l(\cos\chi) \qquad (6.C1)$$

and the differential cross-section

$$\sigma(\chi) = |f(\chi)|^2 .$$

The total cross-section is

$$\sigma_{\text{tot}} = \frac{2\pi}{k^2}\sum(2l+1)[1 - \text{Re}\, S_{ll}] \qquad (6.C2)$$

$$= \frac{4\pi}{k^2}\sum(2l+1)\sin^2\eta_l , \qquad (6.C3)$$

where S_{ll} is the diagonal scattering matrix element $e^{2i\eta_l}$ and η_l is the phase shift of the l^{th} partial wave.

The optical theorem connects the imaginary part of the forward scattered amplitude, Im $f(0)$, with the total cross-section,

$$\sigma_{\text{tot}} = \frac{4\pi}{k}\,\text{Im}\, f(0) \qquad (6.C4)$$

In the semi-classical approximation the phase shift is given by

$$\eta_l = \int_{\rho_c}^{\infty}\left[1 - \frac{2\mu V(\rho)}{\hbar^2 k^2} - \frac{(l+\tfrac{1}{2})^2}{\rho^2}\right]^{\frac{1}{2}} d\rho - \int_{l+\frac{1}{2}}^{\infty}\left[1 - \frac{(l+\tfrac{1}{2})^2}{\rho^2}\right]^{\frac{1}{2}} d\rho \qquad (6.C5)$$

The condition of validity of Equation C5 is sometimes expressed in terms of the de Boer parameter Λ^*

$$\Lambda^* = h/[\sigma(2\mu\epsilon)^{\frac{1}{2}}] , \qquad (6.C6)$$

(closely related to the condition of Equation 6.106 with $E = \epsilon$) and is $\Lambda^* \lesssim 1$.

In the Born approximation the phase shift is given by

$$\eta_l^{\text{B}} = \frac{2\mu}{(\hbar k)^2}\int_0^{\infty} j_l(\rho)^2\, V(\rho)\rho^2\, d\rho \qquad (6.C7)$$

$$\rho = kR$$

and is valid for $\eta \lesssim 0.5$ or $\Lambda^* \ll 1$.

For a potential of the form $V = -C_s R^{-s}$ the Born result reduces to

$$\eta_l^B = \frac{\mu C_s}{2\hbar^2} \left(\frac{k}{2}\right)^{s-2} \pi \frac{\Gamma(s-1)\Gamma\left(l - \frac{s}{2} + \frac{3}{2}\right)}{\left(\Gamma\left(\frac{s}{2}\right)\right)^2 \Gamma\left(1 + \frac{s}{2} + \frac{1}{2}\right)} \tag{6.C8}$$

and for the total cross-section:

$$\sigma_{\text{tot}}(v) = 2\pi^{s/(s-1)} \sin\left[\frac{\pi}{2}\frac{s-3}{s-1}\right] \Gamma\left(\frac{s-3}{s-1}\right) \left[\frac{\left(\Gamma\frac{s}{2} - \frac{1}{2}\right)}{\Gamma\frac{s}{2}}\right]^{2/(s-1)} \left(\frac{C_s}{\hbar v}\right)^{2/s-1} \tag{6.C9}$$

For a potential with $s = 6$, this reduces to:

$$\sigma_{\text{tot}}(v) \approx 8.083 \left[\frac{C_6}{\hbar v}\right]^{2/5} \tag{6.C10}$$

At not too small angles of observation, the semi-classical or classical outer branch contribution to $\sigma(\chi)$ is:

$$\sigma(\chi) \approx \frac{1}{s} \left([s-1] \frac{C_s}{E}\right)^{2/s} \chi^{-2+2/s} \tag{6.C11}$$

If the Born approximation is valid for *all* phase shifts,

$$f(q) = -\frac{2\mu}{\hbar^2} \int_0^\infty q^{-1} \sin(qR)\, R\, V(R)\, dR, \tag{6.C12}$$

where

$$q = 2k \sin(\chi/2)$$

so that in this case inversion to yield the potential is possible,

$$RV(R) = -\pi \int_0^\infty q \frac{\hbar^2}{\mu} f(q) \sin(qR)\, dq. \tag{6.C13}$$

The extrema in the total cross-section for a Lennard-Jones potential occur at velocities v_N given by:

$$N - 3/8 = 0.3012\,(\epsilon\sigma/(\hbar v_N)) \tag{6.C14}$$

where N is an integer for maxima and half integral for minima. The transition between attractive and repulsive behaviour in the total cross section energy dependence occurs at:

$$v \approx 2.5\,\epsilon\sigma\hbar^{-1}\,. \tag{6.C15}$$

The total cross-section is approximately related to the differential cross-section at zero degrees by

$$\sigma_{tot} \approx \frac{4\pi}{k}\,[\sigma(0)]^{1/2} \tag{6.C16}$$

temperature range over which such data can be obtained is limited and the results are relatively structureless, Fig. 7.1. The information about potentials that can be extracted is therefore limited and these methods are perhaps of most value in testing potentials devised by other means.

Spectroscopic methods have been applied in various ways, perhaps most important is the Rydberg-Klein-Rees (RKR) method (J. T. Vanderslice et al., 1959). In this technique vibration-rotation bands are analyzed to yield values of the potential at the classical turning points of the internal motion and no prior assumptions about the potential form are involved. Unfortunately, this

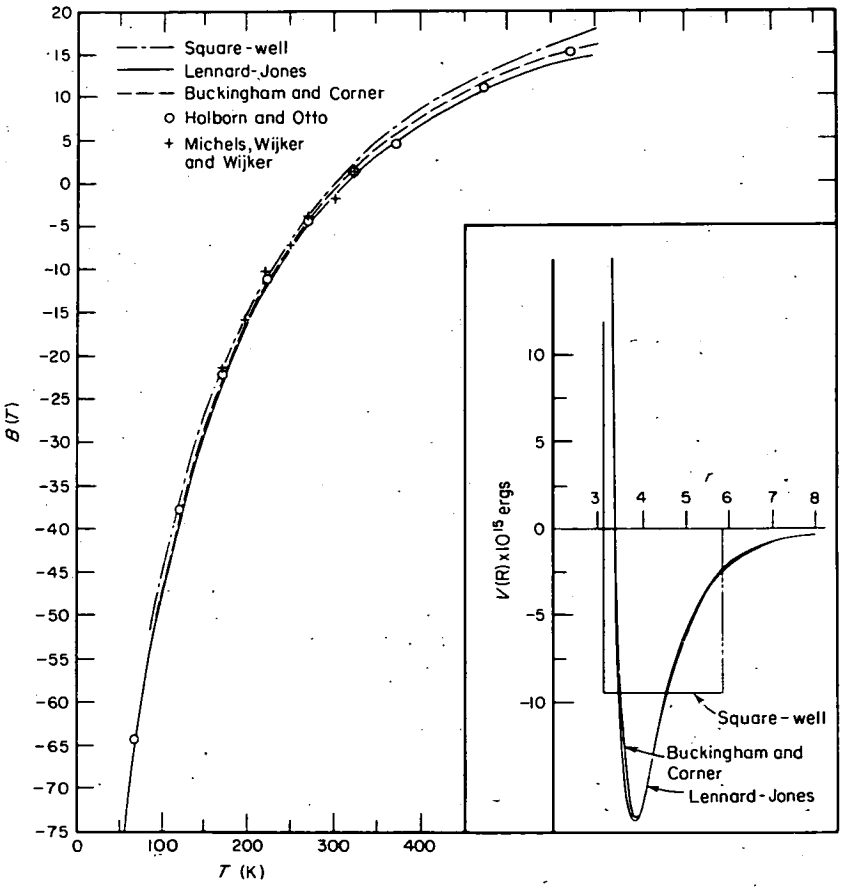

Fig. 7.1 Second virial coefficients for argon calculated for several molecular models. The potential functions obtained from the experimental $B(T)$ data are also shown. The experimental data are those of L. Holborn and J. Otto, *Z. Physik*, 33, 1 (1925), and A. Michels, Hub. Wijker, and Hk. Wijker, *Physica*, 15, 627 (1949). (Reproduced from J. O. Hirschfelder et al., 1964).

method is only suitable for relatively deep potentials which can support many vibrational states. The broadening of atomic spectral lines as a function of pressure also yields information on the difference between ground and excited electronic state potentials.

Scattering methods, on the other hand, can readily explore a wide range of relative energies and potential depths. Also, if high resolution experiments are possible, very detailed quantum structure can be observed, e.g. as in Fig. 7.2. The information content is large, and tight constraints can be placed on the form of the potential over the range of separations effectively explored. The major limitations of the method are mundane experimental ones and also that, for atoms not in ^1S states, separation of the various possible molecular states of the colliding system depends upon selecting the (J,m_J) state of the incident atoms, sometimes a difficult task. The extent of this problem is shown in Table 7.1, where the various electronic states arising from different atomic states are shown; each such molecular state will be associated with a rather different intermolecular potential.

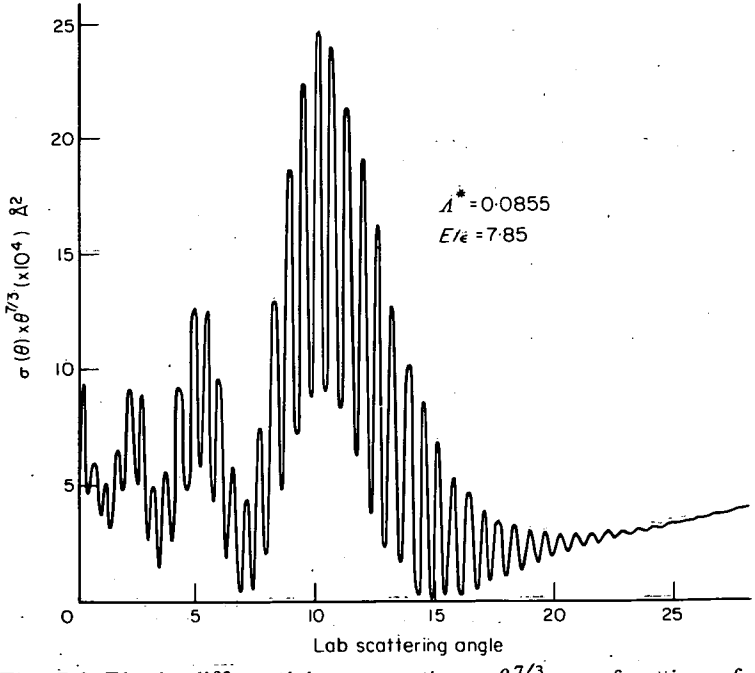

Fig. 7.2 Elastic differential cross-section x $\theta^{7/3}$ as a function of laboratory scattering angle, calculated for a LJ potential with parameters $E/\epsilon = 7.85$, $\sigma_{LJ} = 4.25$ A; $\Lambda^* = \hbar/[\sigma_{LJ}(2\mu\epsilon)^{1/2}] = 0.0855$ and $\chi_{CM} \approx 1.17\,\theta_{lab}$. The rainbow angle is 12.5° (lab) and two supernumerary bows are visible.

To date, atomic scattering measurements have been largely confined to atoms in Groups I and VIII, mercury and the halogen atoms. For collisions involving molecules, the problem is formally much worse both because of the intrusion of inelastic events and because even if the motion is adiabatic with respect to the rotational and vibrational motion, different potentials might be associated with different internal states. However, these potentials may not be very different and especially in the case of a nearly spherical molecules an average potential is often adequate. In any case, this simplification is normally imposed by experimental considerations.

7.2 Extraction of potential data from scattering measurements

The formal inversion of a differential cross-section to yield a potential is a difficult problem. For cases in which a very few partial waves are involved, e.g. nuclear scattering, rather sophisticated procedures have been evolved (T. Y. Wu and T. Ohmura, 1962). These have not, however, been extended to thermal molecular scattering where the effective range of the potentials is much greater and thousands of partial waves are required. If either classical mechanics or the Born approximation is valid then inversion processes can be formulated directly. The Born approximation gives for the scattered amplitude

$$f(q) = -\int_0^\infty q^{-1} \sin(qR)\mu R V(R) \mathrm{d}R/(2\pi\hbar^2) \tag{7.3}$$

where $q = 2k \sin(\chi/2)$

and so $RV(R)$ is the Fourier transform of $f(q)$:

$$RV(R) = -\frac{2}{\pi}\int_0^\infty q f(q) \sin(qR)\left(\frac{2\pi\hbar^2}{\mu}\right)\mathrm{d}q \tag{7.4}$$

Thus the potential can be determined by observation of the complete energy dependence of $f(q)$ ($= \sigma(\chi)^{1/2}$) in the Born approximation) at a fixed angle of scattering. Unfortunately (see Chapter 6), Equation 7.3 is not valid for potentials that become comparable to the relative kinetic energy over any part of their range, as intermolecular potentials always do because of their hard core. The Born approximation finds its greatest use in electron and X-ray diffraction work where the inversion property Equation 7.4 is the key to its structural exploitation.

If classical mechanics is valid at the energy of observation and the potential is monotonically repulsive, there is a 1:1 correspondence between impact parameter and angle of deflection. The differential cross-section can

Table 7.1 Diatom electronic states: unlike atoms.
Reproduced from R. B. Bernstein and T. J. P. O'Brien, 1963.

		Atom 2		
Atom 1		Group: I	II, VIII	III A
Group	State	State: $^2S_{1/2}$	$^1S_0$	$^2P_{1/2u}$
I	$^2S_{1/2}$	$^1\Sigma^+, ^3\Sigma^+$.		
II, VIII	$^1S_0$	$^2\Sigma^+$.	$^1\Sigma^+$.	
III A	$^2P_{1/2u}$	$^1\Sigma^+, ^1\Pi, ^3\Sigma^+, ^3\Pi$.	$^2\Sigma^+, ^2\Pi$	$^1\Sigma^+(2), ^1\Sigma^-, ^1\Pi(2), ^1\Delta,$ $^3\Sigma^+(2), ^3\Sigma^-, ^3\Pi(2),$
IV A	$^3P_0$	$^2\Sigma^-, ^2\Pi, ^4\Sigma^-, ^4\Pi$.	$^3\Sigma^-, ^3\Pi$	$^2\Sigma^+, ^3\Sigma^-(2), ^2\Pi(2), ^2\Delta,$ $^4\Sigma^+, ^4\Sigma^-(2), ^4\Pi(2),$
VA	$^4S_{1/2u}$	$^3\Sigma^-, ^5\Sigma^-$.	$^4\Sigma^-$.	$^3\Sigma^-, ^3\Pi, ^5\Sigma^-, ^5\Pi$.
VI A	$^3P_2$	$^2\Sigma^-, ^2\Pi, ^4\Sigma^-, ^4\Pi$.	$^3\Sigma^-, ^3\Pi$.	$^2\Sigma^+, ^2\Sigma^-(2), ^2\Pi(2), ^2\Delta,$ $^4\Sigma^+, ^4\Sigma^-(2), ^4\Pi(2),$
VII A	$^2P_{1/2u}$	$^1\Sigma^+, ^1\Pi, ^3\Sigma^+, ^3\Pi$.	$^2\Sigma^+, ^2\Pi$.	$^1\Sigma^+(2), ^1\Sigma^-, ^1\Pi(2), ^1\Delta,$ $^3\Sigma^+(2), ^3\Sigma^-, ^3\Pi(2),$

then be inverted to yield the potential (I. Amdur, 1968). This approach will clearly be most useful at high energies.

Unfortunately, even this technique is of very limited applicability in molecular scattering. Experimental observations will be limited in angular and energy range, be of less than perfect resolution and will include some noise. Under these conditions any formal inversion procedure is unreliable and what is required is an algorithm for making the connection between an assumed potential and the scattering pattern associated with it. The details will vary, but the components of this algorithm will be:

(1) Apply all available information from other sources to estimate the potential and choose an analytical form for it.
(2) Identify and use any key features in the scattering observations, e.g. rainbows or glories, to refine the original estimates of the potential parameters.

	V A	IV A	VIII A
	$^4S_{½u}$	$^3P_0$	$^2P_{½u}$
(2), $^1\Sigma^-$, $^1\Pi(2)$, $^1\Delta$, so triplets and uintets of above.			
, $^2\Pi$, $^4\Sigma^+$, $^4\Pi$, Σ^+, $^6\Pi$.	$^1\Sigma^+$, $^3\Sigma^+$, $^5\Sigma^+$, $^7\Sigma^+$.		
(2), $^1\Sigma^-$, $^1\Pi(2)$, $^1\Delta$, lso triplets and uintets of above.	$^2\Sigma^+$, $^2\Pi$, also $^4(\ )$ and $^6(\ )$.	$^1\Sigma^+(2)$, $^1\Sigma^-$, $^1\Pi(2)$, $^1\Delta$, also $^3(\ )$ and $^5(\ )$ of above.	
, $^2\Sigma^-(2)$, $^2\Pi(2)$, $^2\Delta$, Σ^+, $^4\Sigma^-(2)$, $^4\Pi(2)$, $^4\Delta$.	$^3\Sigma^-$, $^3\Pi$, $^5\Sigma^-$, $^5\Pi$.	$^2\Sigma^+(2)$, $^2\Sigma^-$, $^2\Pi(2)$, $^2\Delta$, $^4\Sigma^+$, $^4\Sigma^-(2)$, $^4\Pi(2)$, $^4\Delta$.	$^1\Sigma^+(2)$, $^1\Sigma^-$, $^1\Pi(2)$, $^1\Delta$, also $^3(\ )$ and $^5(\ )$ of above.

(3) If the data is of high enough resolution, carry out some fitting between a forward calculation of the expected scattering pattern (with appropriate averaging to allow for apparatus resolution) and the observed pattern.

In many cases interpretation has stopped at stage (2). However, as better data becomes available the full statistical treatment implied in (3) will become more usual.

Recently an inversion based on classical mechanics and due to Firsov has appeared (V. G. Firsov, 1953) which relates the classical deflection function and the potential†. This has been extended by U. Buck, 1971, who allows the deflection function to have both positive and negative branches, as

†

$$R_c(b) = b \exp\left\{\frac{1}{\pi}\int_b^\infty \frac{\chi(b')\mathrm{d}b'}{(b'^2 - b^2)^{½}}\right\}$$

$$V(R_c) = E(1 - b^2/R_c(b)^2);\ (2R)^{-1}\mathrm{d}(R^2V)/\mathrm{d}R < E$$

it should. The deflection function has to be obtained by a fitting process based on a semi-classical approximation to $\chi(b)$ in terms of b. The advantage of this process is that the potential is obtained pointwise rather than as a constrained function.

Elastic scattering measurements fall into two classes, those of the total cross-section $\sigma_{tot}(v)$ by primary beam attenuation, and those of the differential cross-section $\sigma(\chi)$. The latter measurement always involves two beams so that the angular scattering can be measured as a function of collision energy from an accurately defined collision volume. Although $\sigma(\chi)$ in principle contain more information than total cross-section measurements, experimental considerations frequently make the single beam σ_{tot} measurement the most fruitful in practice, but in either case the effect of imperfect angular and energy resolution must be carefully allowed for in any interpretation.

7.3 Total cross-sections

(i) Interpretation

The key features in the dependence of total cross-sections on collision velocity have already been discussed in Chapter 6 and in Fig. 7.3 we show the major features in a plot of σ_{tot} *vs.* velocity. At high energies the major

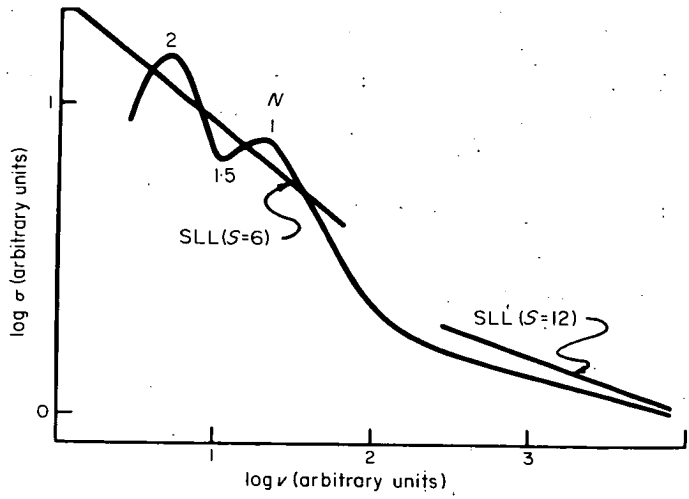

Fig. 7.3 Plot of log total cross-section versus log impact velocity (LJ potential (12:6), $2\mu\epsilon\sigma^2/\hbar = 125$). (Reproduced from R. B. Bernstein, 1966.)

contribution to the cross-section comes from scattering by the repulsive core; this is followed by a transition region where both attractive and repulsive forces are important and then a low energy region where attractive forces dominate. In this region, oscillations in the amplitude of the cross-section arise from the maximum in the phase shift curve passing alternately through odd and even multiples of $\pi/2$. Finally at reduced energies $E/\epsilon < 0.8$ sharp resonance spikes due to quasi bound states may be seen. In the case of angle dependent potentials the situation is more complex. However, if the molecule is rotating either very slowly or very rapidly with respect to the motion of the incident atom, some averaged potential may operate. In the first case the sudden approximation can be used (R. B. Bernstein and K. H. Kramer, 1964), and in the latter case the angular dependence is effectively wiped out by the rotation so that broadly similar features to those of Fig. 7.3 can be expected.

The preliminary interpretation of data such as is shown in Fig. 7.3 will concentrate on the mean slope of the velocity plot and proceed via the Massey-Mohr approximation. We recall that the exact result for σ_{tot}:

$$\sigma_{tot} = \frac{4\pi}{k^2} \sum_l (2l+1) \sin^2 \eta_l \tag{7.5}$$

becomes:

$$\sigma_{tot}^{MM} \approx f_s \, [C_s/(\hbar v)]^{2/(s-1)} \tag{7.6}$$

where f_s has been given in Equation 6.C9. Using this approximation,

(i) The gradient of $\ln \sigma_{tot}$ versus $\ln v$ plots will be $-2/(s-1)$ if the observations are made either in the low or high velocity regions. As can be seen from Fig. 7.3 (R. B. Bernstein, 1966), precision is limited by the existence of undulations in the attractive region and by the slow convergence of the gradient to its limiting value at high energies.

(ii) The transition region cannot be accurately located, but for a 12:6 potential:

$$v_{trans} \approx 2.5 \, \epsilon \sigma_{LJ}/\hbar \tag{7.7}$$

so that $\epsilon\sigma_{LJ}$ can be estimated rather crudely.

(iii) An absolute measurement of the total cross-section will yield C_6 since in the MM approximation (with v in cm s^{-1}, σ in cm^2):

$$C_6 \approx 5.76 \times 10^{-30} \, v \sigma_{tot}^{5/2} \text{ erg cm}^6 \tag{7.8}$$

This approximation is not too accurate, but is probably adequate for the experimental precision (±15 per cent) in the measurement of absolute total cross-sections.

The glory undulations which provide much more precise constraints on the intermolecular potential are not predicted by the MM approximation and it is necessary to go to the semi-classical treatment. We recall from Chapter 6 that these undulations have their origin in the joint operation of the attractive and repulsive parts of the potential, the turning points of the trajectories responsible lying close to R_m, the position of the potential minimum.

Taking the particular case of the 12:6 potential, the relevant Equation 6.147 becomes:

$$\sigma_{tot} = 8.083\,[C_6/\hbar\sigma_{LJ}]^{2/5} + \frac{4\pi l_0}{k^2}\,[\pi/\eta''(l_0)]^{1/2}\sin(2\eta(l_0) - 3\pi/4) \quad (7.9)$$

where maxima in σ_{tot} occur when the wavenumber k satisfies

$$\eta_{l_0}(k_N) = \pi(N - 3/8) \quad (7.10)$$

where N is an integer. The amplitude of the undulations described by Equation 7.9 is determined by $[l_0/\eta_0'']^{1/2}$, but from an experimental point of view the most reliably measured quantities are the extrema wave numbers k_N since the amplitude of oscillation depends very strongly on the apparatus resolution.

In the normal method of analysis, the various extrema are indexed with integers for the maxima, and half integers for the minima, the numbering starting from the high velocity end. The relative velocities v_N corresponding to these extrema constitute an atom impact spectrum and the experimental results are plotted as $\sigma_{tot}(v).v^{2/5}$ versus v. An example of this plot is shown in Fig. 7.4. The indexing may be checked by plotting the index number N against $1/v_N$; the plot should be linear at high velocities and yield an intercept of $N = 3/8$ at $v = \infty$ and if this is not the case, the indexing is probably incorrect. The limiting gradient at high v_N of this latter plot can be calculated using Born phase shifts for $\eta(l_0)$; for the Lennard-Jones (12:6) potential the result is:

$$N - 3/8 = 0.3012\,\frac{\epsilon\sigma_{LJ}}{\hbar v_N} \quad (7.11)$$

enabling an initial estimate of the product $\epsilon\sigma$ to be made before more detailed fitting is begun.

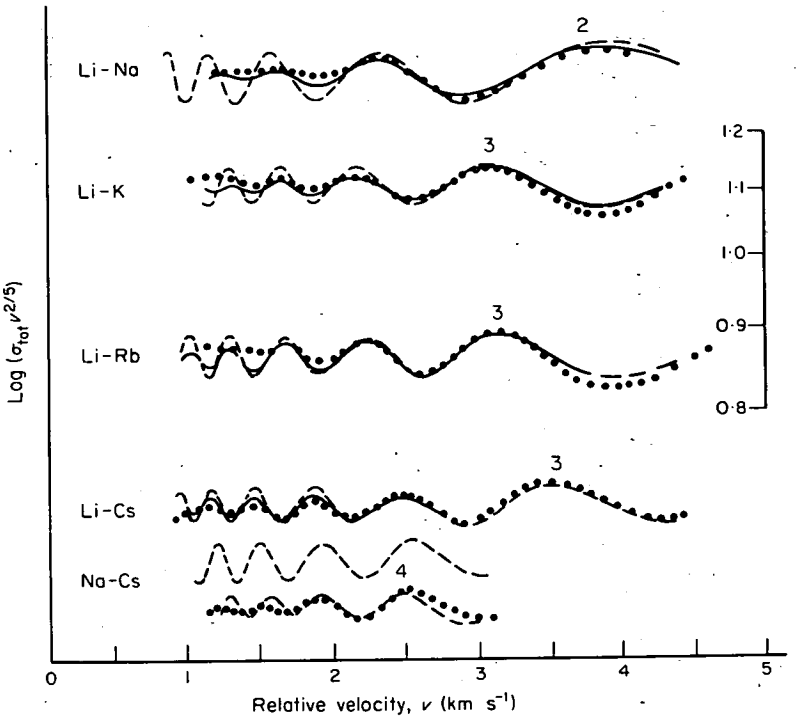

Fig. 7.4 Atom impact spectra for the alkali systems. Reproduced from E. W. Rothe and R. K. B. Helbing, 1968. Integers are the index numbers of the extrema. Dots are experimental values, dashed lines are forward calculations with no allowance for apparatus resolution. The full lines are apparatus averaged calculations.

More detailed analysis is normally based on the Bernstein-O'Brien (BOB) plot in which $(N-3/8)v_N$ is plotted against E_N^{-1} (collision energy) (R. B. Bernstein and T. J. P. O'Brien, 1965, 1967; Fig. 7.5). The data is then fitted numerically to a quadratic form:

$$(N-3/8)v_N = I - S_1\bar{E_N^1} + S_2\bar{E_N^2} \tag{7.12}$$

to yield values for I and S_1 with good precision and for S_2 with rather poorer accuracy. For any assumed potential form I, S_1 and S_2 can then be interpreted in terms of particular potential parameters. In the Bernstein-O'Brien treatment Equation (7.12) is shown to be equivalent to:

$$(N-3/8)v_N = \frac{2\epsilon R_m a_1}{\pi\hbar}\left(1 - \frac{A_1\epsilon}{a_1 E_N} + \frac{A_2\epsilon^2}{a_1 E_N^2}\right), \tag{7.13}$$

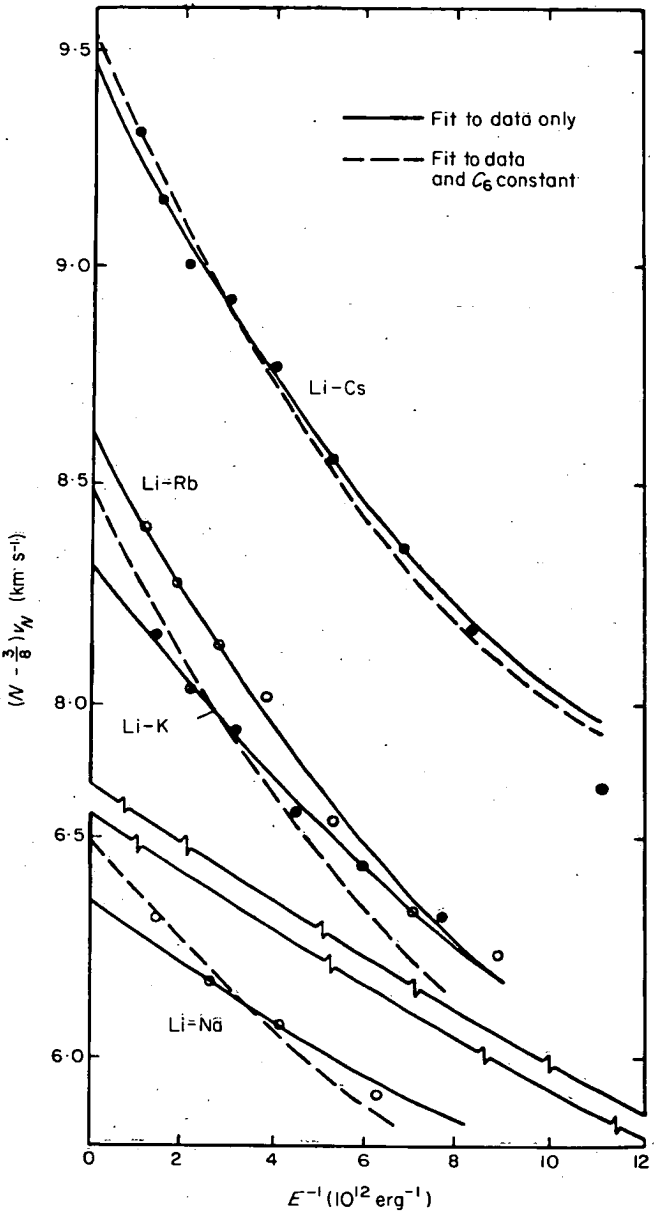

Fig. 7.5 BOB plot for data of Fig. 7.4. Reproduced from E. W. Rothe and R. K. B. Helbing, 1968. The dashed curves are the best fit to the data with values of ϵ and σ that are related by $4\epsilon\sigma_{LJ}^6 = C_6^{\text{calc}}$. The fact that rather different values for ϵ and σ are obtained with constrained and unconstrained fits means either that the theoretical C_6 value is wrong or that the potential is not of the Lennard-Jones form.

where

$$\begin{aligned} \epsilon R_m a_1 &= (\pi\hbar/2)\, I \qquad \text{(A)} \\ \epsilon/a_1 &= S_1/(A_1 I) \qquad \text{(B)} \\ \epsilon^2/a_1 &= S_2/(I A_2) \qquad \text{(C)} \end{aligned} \tag{7.14}$$

so $$a_1 = S_2 A_1^2/S_1^2 A_2 I^2 \qquad \text{(D)}$$

and A_1, A_2 are almost independent of the potential form, having the values $A_1 = 0.1625$ and $A_2 = 0.0801$. On the other hand, the parameter a_1 depends primarily, but still rather weakly upon the curvature of the potential at the minima and only to a much less extent on the actual potential form chosen. The curvature κ at the potential minima is defined as

$$\kappa = \left[\frac{\partial^2 (V/\epsilon)}{\partial (R/R_m)^2}\right]_{R=R_m} = f^{(2)}, \tag{7.15}$$

i.e. it is the second term in an expansion of the potential about the minimum of the form:

$$V(\gamma)/\epsilon = -1 + \tfrac{1}{2}\kappa\gamma^2 + \sum_{n=3}^{N} \frac{\gamma^n}{n!} f^{(n)}, \tag{7.16}$$

where $\gamma = R/R_m - 1$ (the reduced displacement). The variation of the parameter a_1 with κ is shown in Fig. 7.6. It can be seen that the curvature can be reasonably well determined without recourse to a specific potential form. Alternatively an assumed potential form can be used to calculate a_1 for a range of curvatures and differing potentials. The data may then be used to determine the other parameters in the potential. A table due to Bernstein for three potentials of the forms:

(1) L.J. n, 6; $$V/\epsilon = \left(\frac{6}{n-6}\right)\left(\frac{R_m}{R}\right)^n - \left(\frac{n}{n-6}\right)\left(\frac{R_m}{R}\right)^6 \tag{7.17}$$

(2) Kihara: $$V/\epsilon = \left(\frac{1-\alpha}{R/R_m - \alpha}\right)^{12} - 2\left(\frac{1-\alpha}{R/R_m - \alpha}\right)^6 \tag{7.18}$$

(3) Exponential:

$$V/\epsilon = \left(\frac{6}{\alpha - 6}\right)\exp\left[-\alpha\left(\frac{R}{R_m} - 1\right)\right] - \left(\frac{\alpha}{\alpha - 6}\right)\left(\frac{R_m}{R}\right)^6 \tag{7.19}$$

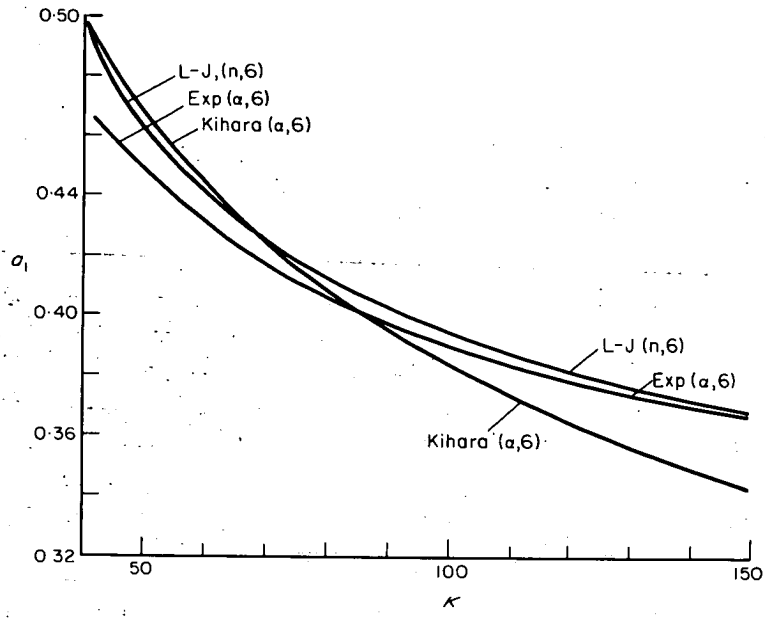

Fig. 7.6 Variation of a_1 parameter with κ, reduced curvature for three potentials; (i) Lennard-Jones (n:6) (ii) Kihara (Equation 7.18) (iii) exp-6 (Equation 7.19).

is shown in Table 7.2. For the L.J. potential the curvature is given by $\kappa = 6n$. For the other potentials the nomogram given by R. B. Bernstein and T. J. P. O'Brien, (1967) may be used. Thus, if a particular potential form is selected, and a_1 estimated, a measurement of I and S_1 enables both ϵ and R_m to be obtained from Equation 7.14A or B and if both S_1 and S_2 can be measured then a_1 can be found from Equation 7.14D and the form of the potential thereby subjected to a test. The product $\epsilon^2 R_m$ is obtained with greater accuracy than ϵ or R_m individually and can provide a very useful constraint in analysing other data (e.g. differential cross-section).

It should be noted that the above interpretation of glory oscillations has not required absolute measurements of the total cross-section – a considerable advantage in view of the experimental difficulties in obtaining absolute scattering data.

A typical BOB plot from Rothe's work (E. W. Rothe and R. K. B. Helbing, 1968) is shown in Fig. 7.5, where some data from alkali systems are plotted. The final confirmatory stage of the analysis is shown back in Fig. 7.4 where the observed data is compared with the results of a forward calculation using the derived potential parameters and the effect of the thermal motion of the target molecules on the total cross-section measurements is illustrated.

Table 7.2 a_1 parameter for various curvatures κ and potentials. The three potentials are defined in Equations 7.17, 7.18, and 7.19. (Reproduced from R. B. Bernstein and T. J. P. O'Brien, 1965).

	a_1		
κ	potential 1	potential 2	potential 3
48	0.47000	0.47421	0.45209
60	0.44113	0.44432	0.43063
72	0.42156	0.42156	0.41462
84	0.40727	0.40338	0.40232
96	0.39630	0.38838	0.39257
108	0.38757	0.37568	0.38465
120	0.38043	0.36474	0.37808
132	0.37446	0.35515	0.37253
144	0.36938	0.34666	0.36776

The interpretation of the velocity dependence of σ_{tot} for the scattering of atoms is now quite well understood.

(ii) Measurement of the total cross-section

The technique for determining total cross-sections by measuring the attenuation of a narrow primary beam by a target gas has already been described. The expression:

$$I/I_0 = e^{-n\sigma tot(v)l} \tag{7.20}$$

(where I is the attenuated beam flux, I_0 the primary beam flux, nl the number density times path length of the target gas) defines the observed total cross-section. If the velocity is low enough, or if by other arguments we know that inelastic or reactive processes make a relatively small contribution, σ_{tot} can be equated to the total elastic cross-section. If non-elastic channels are important, total cross-section measurements are still informative, but their analysis is reserved until Chapter 8.

Difficulties arise with the measurement of all the observables in Equation 7.20. Firstly, the angular resolution must be sufficient to distinguish between scattered and unscattered material at angles outside the forward diffraction cone. Secondly, the spread of relative velocity between the primary and target molecules must be small enough to avoid blurring any of the structure in the velocity dependence of $\sigma_{tot}(v)$. Finally, if absolute total cross-sections are to be measured, the target density and length must be known.

Angular resolution

If the true quantum total cross-section is to be measured, the angular resolution of the apparatus must be sufficient for the error $\delta\sigma$ (calculated from Equation 3.14) to be small. Since this error estimation involves an integration over $\sigma(\chi)$, information which is unlikely to be available in advance, some approximate treatment is needed. Fortunately, $\sigma(\chi)$ is a steeply falling function of θ so that a small angle approximation to $\sigma(\chi)$ is sufficient. Thus, substitution of Equation 6.100 into Equation 3.14 will enable the apparatus resolution to be determined.

To proceed further, we define an apparatus dependent angle β such that all deflections greater than β in the CM system miss the detector, while all those with $\chi < \beta$ are collected with unit efficiency. Using Equation 6.100 in its exponential form, the fractional error in the total cross-section is:

$$\delta\sigma/\sigma_{\text{tot}} \approx \int_0^{\beta} e^{-\alpha\chi^2} \chi \, d\chi \Big/ \int_0^{\infty} e^{-\alpha\chi^2} \chi \, d\chi$$

where

$$\alpha \approx k^2 \sigma_{\text{tot}}/(8\pi) \approx k\sigma(0)^{1/2}/2$$

Integrating we find:

$$\delta\sigma/\sigma_{\text{tot}} \approx \alpha\beta^2,$$

so, for good precision in the total cross-section measurement,

$$\beta_{\text{CM}} < \frac{1}{k} (\pi/\sigma_{\text{tot}})^{1/2} \sim \frac{\lambda}{a} \tag{7.21}$$

For light atoms at thermal speeds β_{CM} is $\leqslant 0.5°$.

The methods of Chapter 2 can now be used to transform β into the LAB system for particular cases.

Calculations of the resolution required with a more realistic apparatus function have been made (R. K. B. Helbing, 1966; F. von Busch, 1966). For an apparatus with a beam and detector of circular cross-section, Helbing found:

$$\theta_a \approx \beta_{\text{LAB}}, \tag{7.22}$$

while for tall narrow beams von Busch calculated:

$$\theta_a \approx 0.1\beta_{\text{LAB}}, \tag{7.23}$$

where in both cases θ_a is the angular half width of the apparent beam profile. The improvement in resolution between tall rectangular and circular beam geometry is due to out-of-plane scattering. In the case of circular geometry, a much narrower angular range can enter the detector via out-of-plane deflections (see Fig. 3.3 of Chapter 3). The resolution required at thermal energies is therefore typically between 1 and 10 minutes of arc.

Velocity resolution

The velocity resolution required to resolve specific structure in $\sigma(v)$ can be estimated by a forward calculation using guesses of the potential parameters, e.g. Equation 7.13 can be used for the resolution needed for glory undulations.

In general, the attainable resolution is not limited by that of the primary beam and its velocity selector, but by the motion of the target molecules. Averaging arising from this motion not only limits the velocity resolution, obscuring, for example, features with a very narrow energy width such as resonances, but also produces a systematic deviation between the measured and true total cross-section.

There are two configurations of the total cross-section experiment of interest. In the first, target molecules are contained in a scattering chamber and have a Maxwellian distribution of velocities in random directions. The velocity averaging can only be minimized by operating the chamber at as low a temperature as condensation will permit. In the second configuration the target is a cross-beam. If this is well collimated, the velocity averaging introduced can be very small. The use of nozzle cross-beams of high Mach number is particularly attractive here.

For a relative velocity $w(=|\mathbf{v}_1 - \mathbf{v}_2|)$, the probability of a collision in a length l in passing through the target is $n_2\sigma_{tot}(w)wl/v_1$ and the attenuation of the primary beam from its initial value I_0 is:

$$\frac{I(w)}{I_0(w)} = e^{-n_2\sigma_{tot}(w)wl/v_1}. \tag{7.24}$$

The measured attenuation is the average of $I(w)/I_0(w)$ over the relative velocity distribution $f(w)$. If a mean total cross-section for a given incident velocity v_1 is defined:

$$\bar{\sigma}_{tot}(v_1) = \int_0^\infty \sigma_{tot}(w) f(w) \frac{w}{v_1} \, dw, \tag{7.25}$$

then the measured attenuation is given to a good approximation ($\Delta I/I_0 < 0.1$) by:

$$\frac{I(v_1)}{I_0(v_1)} \approx e^{-n_2 \bar{\sigma}_{tot}(v_1) l} \tag{7.26}$$

Appropriate distributions $f(w)$ are readily worked out for the important case of two crossed effusive beams, when the distribution is quite sharp (see Equation 1.7) and for a monoenergetic beam passing through a thermal scattering gas, when the distribution in w is somewhat sharper than the Maxwellian distribution appropriate to the temperature of the scattering gas.

The correction arising from Equation 7.25 is fairly small if the most probable velocity in the chamber is less than a third that of the primary beam. An approximate relation for $\sigma(v)$ can then be used, the Mott and Massey based result:

$$\sigma(w)/\sigma(v_1) \approx (v_1/w)^{2/(s-1)} \tag{7.27}$$

usually being adequate. The correction factors calculated from Equations 7.25 and 7.27 for an unselected secondary beam and for a scattering chamber have been tabulated for a range of s values and target temperatures by K. Berkling et al., 1962.

Measurement of path length and target density

If the absolute total cross-section is to be measured, the number of scattering molecules in the target must be known. Absolute cross-sections are of particular value in determining C_6 coefficients but these depend on a high power of σ_{tot} so that accurate cross-section measurements are required. If a crossed-beam configuration is used, the absolute density cannot at present be obtained with sufficient accuracy because the absolute efficiency of beam detectors is not reliably known. Absolute cross-section measurements have therefore been made with the scattering chamber configuration despite the lower velocity resolution that results. The pressure in the target gas chamber is adjusted to yield about 10–20 per cent attenuation, a level at which multiple collisions are rare. Errors arising from molecules deflected by a small angle at their first collision but arriving at the detector by a second bounce are thus minimized. Unfortunately, pressure measurements in the necessary range ($\sim 10^{-4}$ Torr) are difficult. Indeed, in much of the early work total cross-sections ~30 per cent too high were reported due to a systematic error in measurements with McLeod gauges (E. W. Rothe, 1964, and with

R. H. Neynaber, 1965). More recently, diaphragm manometers have been used and appear to yield good accuracy.

In an alternative approach (R. J. Cross et al., 1966) a monitor molecular beam passing orthogonally through the scattering chamber has been used to measure the pressure. In this way a series of cross-sections can be measured relative to the monitor/target particle cross-section. Errors can also arise in measuring the path length through the target. Since target gas will flow out of the scattering chamber through the entrance and exit slots, the effective path length will be larger than the chamber dimension. These end effects can be compensated for by a series of measurements with differing chamber lengths.

7.4 Apparatus and results – total cross-sections

We now consider a few experiments which will exemplify the technique and the results obtainable. The apparatus used by E. W. Rothe and R. K. B. Helbing (1968) is shown in Fig. 7.7. This was designed to measure cross-sections as a function of velocity of alkali atoms scattered from a variety of partners. Since absolute cross-sections were not measured a crossed beam configuration was used to minimize the relative velocity spread. The apparatus used fairly conventional beam sources and a hot wire detector. The modulation and data collection was particularly interesting in the efforts made to minimize noise arising from fluctuations in the beam intensities. The primary velocity selected alkali beam was modulated at 10 Hz while the cross-beam was modulated at 17 Hz. Two lock-in amplifiers, one tuned to each frequency, then process the signal from the hot wire detector. The

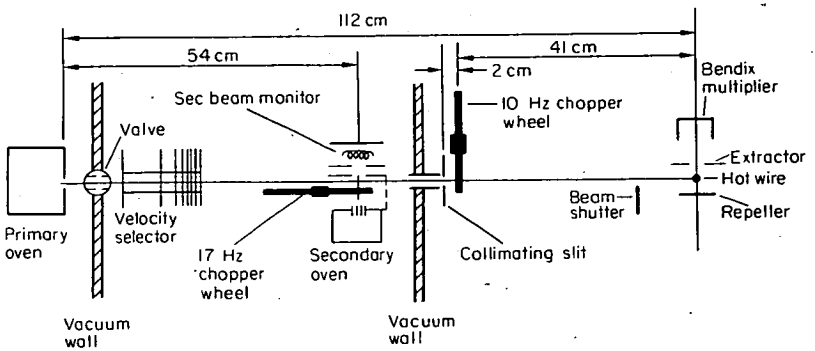

Fig. 7.7 Apparatus for total cross-section measurements with a primary alkali beam. Reproduced from E. W. Rothe and R. K. B. Helbing, 1968.

10 Hz signal I_{10} is proportional to the unattenuated primary beam and the 17 Hz signal (I_{17}) to the attenuated signal. Thus for small attenuations:

$$\frac{I}{I_0} = \frac{I_{17}}{I_{10}} \propto n_2 \sigma_{\text{tot}} l. \tag{7.28}$$

The ratio of the output of the two detectors is proportional to the cross-section. Fluctuations in the density of the target molecules were eliminated by cross-correlation using an ion gauge as a density detector to monitor the cross-beam. Potential parameters were obtained for a wide range of diatomics and hydro- and fluorocarbons. Typical atom impact spectra are shown in Fig. 7.8. (E. W. Rothe and R. K. B. Helbing, 1969). Particularly interesting was the apparent quenching of the glory undulations (a topic also investigated by P. R. LeBreton and H. L. Kramer (1967)). The explanation of these unexpectedly small (when compared with atom-atom impact spectra) oscillations in the cross-section has been sought in four directions; the shape of the potential, the effect of vibrational motion on the elastic scattering, the effect of angle dependent intermolecular forces on the elastic scattering or the effect of rotationally inelastic collisions. For most of the systems studied, a possible fifth cause – chemical reaction (see Section 8.4) – can be excluded.

In purely elastic scattering, the amplitude of the glory oscillations depends inversely on the curvature of the phase shift function ($\partial^2\eta(l)/\partial l^2$) at its maximum. This, in turn, is loosely related to the width of the potential bowl; potentials with broad minima give rise to large amplitude oscillations in the total cross-section. Weak oscillations may therefore arise directly from rather narrow potential wells. However, the data obtained by Rothe for a wide range of fluorocarbons (Fig. 7.9) that might be expected to have rather similar potentials suggests that in this case this is not the origin of the effect. Weak oscillations were found to correlate with anistropic targets. The explanation then, is that scattering takes place from a range of potentials, each with a slightly different glory spacing, which results in a blurring of the overall pattern. This hypothesis requires that the molecule remains essentially stationary during the collision. The third possible explanation is that low frequency vibration of the target (in particular the breathing modes of the more nearly spherical molecules) can lead to a change in polarisability and hence in C_6 during the collision. This, in turn, leads to a range of phase shifts of the forward scattered amplitude (if the vibrational period is appreciably longer than the lifetime of the collision) and hence to a partial quenching of the glory pattern. This process is now thought to be less important (P. R.

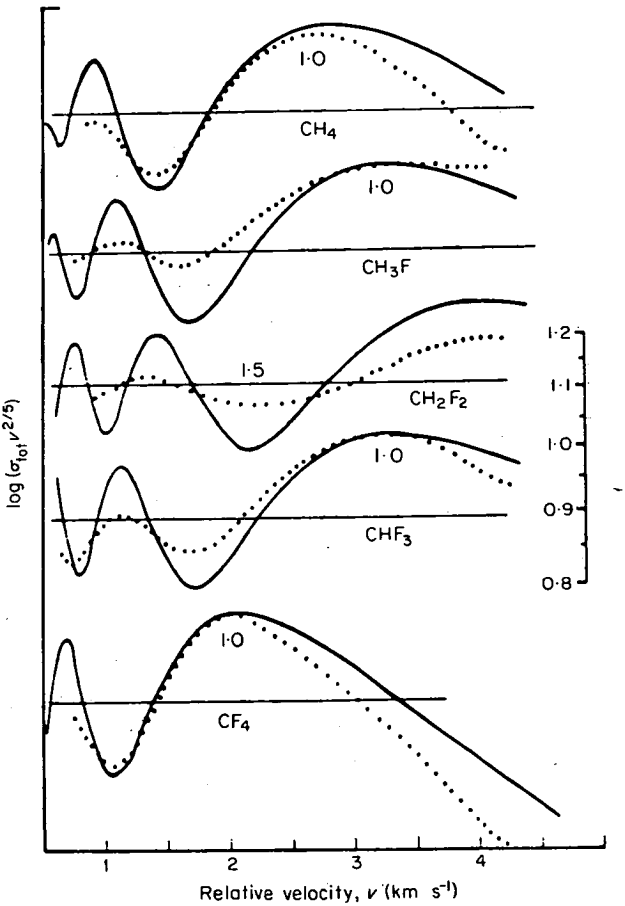

Fig. 7.8 Atom impact spectra for Li scattered from fluorinated methanes. The dotted lines represent mean experimental results, the solid curves are calculations based on a fitted LJ (12:6) potential. The apparent quenching at low velocities seems to increase with the dipole moment of the target; the molecular shape (i.e. the angular dependent part of the repulsive branch of the potential) remains almost unchanged in the series (E. W. Rothe and R. K. B. Helbing 1969.)

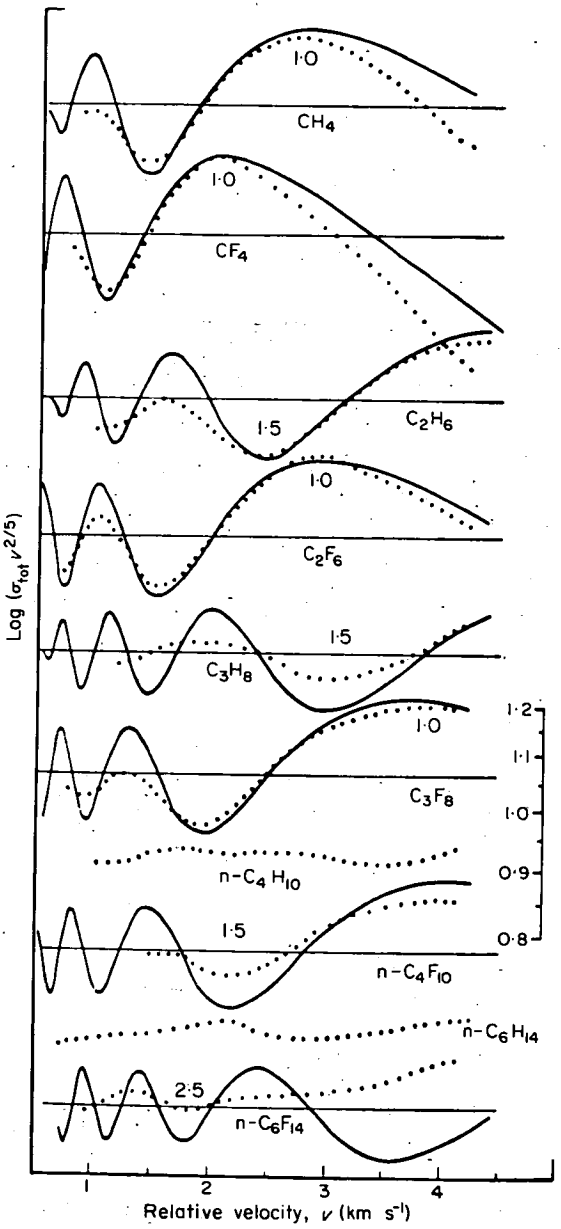

Fig. 7.9 Atom impact spectra for Li colliding with a series of hydro- and fluorocarbons. There is a correlation between the extent of damping of the glory undulations and the target asymmetry. Solid curves are predictions from a simple LJ (12:6) potential. The dipole moments of these molecules, in contrast to some of those in Fig. 7.8, are relatively small (E. W. Rothe and R. K. B. Helbing, 1969.)

LeBreton and H. L. Kramer, 1969 and R. K. B. Helbing, 1969) than the potential anisotropy. Rotationally inelastic collisions on the forward glory trajectory can also reduce the amplitude of $f(0)$ and hence damp its interference structure with the outer (entirely elastic) branch. This last effect is undoubtedly operating in some systems, but is difficult to disentangle from the effect of the anisotropy in the potential because the larger the anisotropy the more likely is rotational energy transfer.

Calculations by R. B. Bernstein and R. E. Olsen (1968) on the degree of damping of the glory structure to be expected from anisotropic potentials (target stationary during the collision) show that the observations in some cases can be completely accounted for. Thus, starting with a potential of the form

$$V(R,\theta) = C_{12}R^{-12}[1 + b_1P_1(\cos\theta) + b_2P_2(\cos\theta)] - C_6R^{-6}[1 + a_2P_2(\cos\theta)], \quad (7.29)$$

and defining the anisotropy parameter a as:

$$a = 2a_2 - b_2, \quad (7.30)$$

they obtain as a first approximation (for $E^* > 1$)

$$1 - \frac{u}{u_0} \approx 4.45 \times 10^{-3}\left(\frac{2\mu\epsilon R_m}{\hbar^2 E^*}\right)a^2\left[1 - \frac{1.54}{E^*}\right]f(j) \quad (7.31)$$

where u_0 is the amplitude of the undamped glory oscillations (i.e. calculated for the potential with a_2, b_1 and b_2 zero), u is the observed amplitude, $E^* = E/\epsilon$ and $f(j)$ depends on the rotational state of the target and approaches 1 rapidly as j increases. Applying Equation 7.31 to Rothe and Helbing's data on Li scattered from the hydrogen halides, values of $|a| \approx 1.1$ were found. This analysis is, of course, sensitive not only to the resolution of the experiment (and poor resolution can easily produce apparent quenching) but also to the values of ϵ and R_m used in calculating the unperturbed amplitude u_0. The quenching of total cross-section undulations is thus not a very reliable way of measuring anisotropy in the intermolecular potential.

Another apparatus for total cross-section measurement, this time for non-alkali species, is shown in Fig. 7.10 (M. G. Dondi, 1969) and has been used to measure the velocity dependence of σ_{tot} for He^4/He^4 scattering. The primary beam source is a nozzle operating at 77 K and a stagnation pressure of 3 torr. The primary beam is velocity selected with resolution $\Delta v/v = 5$ per

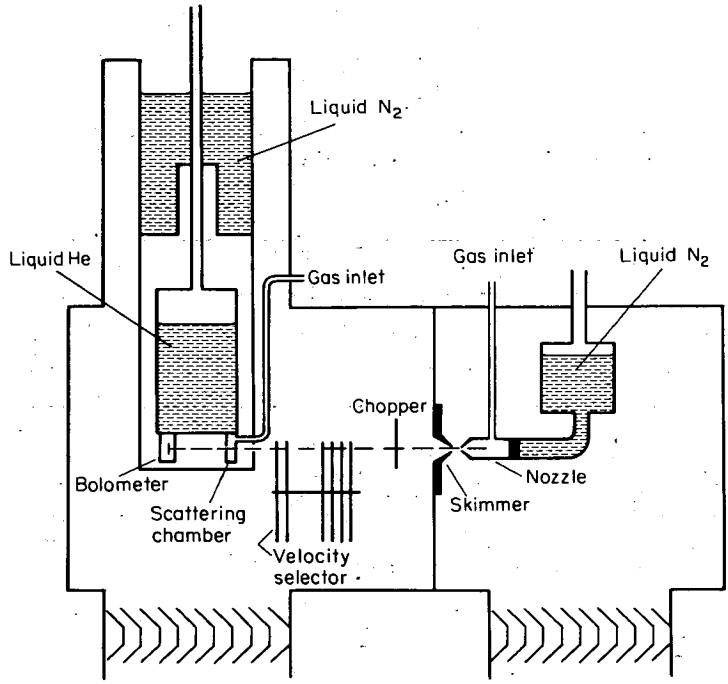

Fig. 7.10 Apparatus for total cross-section measurements used for He + He. Reproduced from M. G. Dondi, 1969.

cent. The scattering chamber is maintained at 2 K to minimize velocity averaging. The importance of this low ambient temperature can be seen from Fig. 7.11 where the effect of different scattering chamber temperatures on the resolution in σ_{tot} is shown; above 10 K the undulations are not resolved. The detector is a sensitive bolometer which responds to the kinetic energy of impinging beam molecules (M. Cavallini, 1967) and detects a minimum flux of 2×10^8 molecules s^{-1}. The results of this experiment are shown in Fig. 7.12.

The structure observed in $\sigma(v)$ is of particular interest since it does not arise from the normal glory region of stationary phase, but from the identical nature of the particles. Particles scattered through χ will be indistinguishable from those scattered through $(\pi-\chi)$ from the other beam and will therefore mutually interfere. The total cross-section has been found in Section 6.15 to be:

$$\sigma_{tot} = \frac{4\pi}{k^2}\left\{\sum_l (2l+1)(1-\cos 2\eta(l)) + \sum_l (2l+1)(-1)^l(1-\cos 2\eta(l))\right\}, \quad (7.3$$

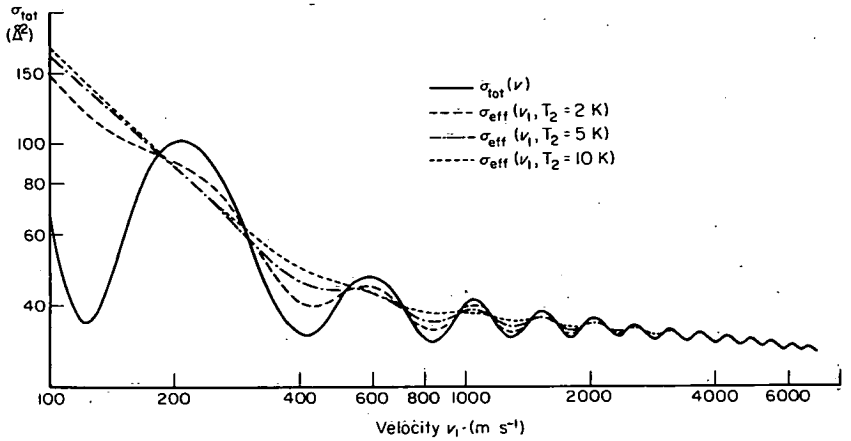

Fig. 7.11 Effect of scattering chamber temperature on observed total cross-section for $He^4 + He^4$ (calculated for LJ (12:6) potential $R_m = 3.0$ Å, $\epsilon = 1.4 \times 10^{-15}$ erg). Reproduced from M. G. Dondi, 1969.

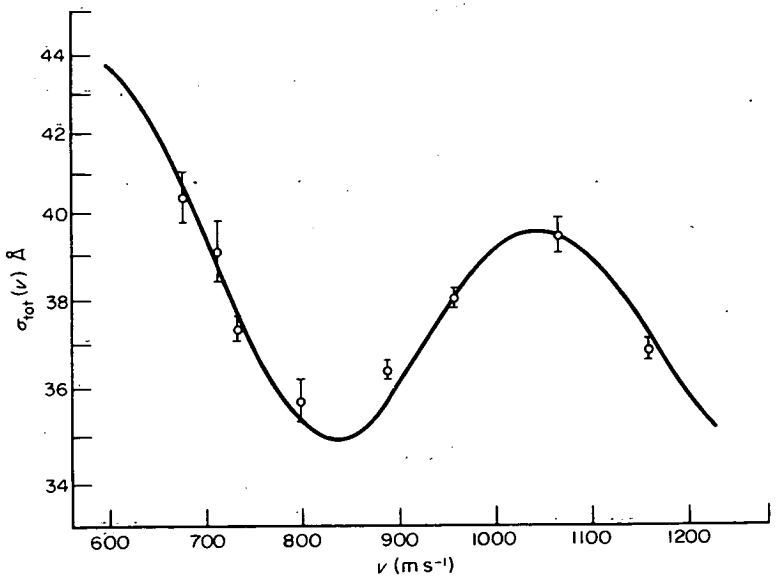

Fig. 7.12 $\sigma_{tot}(v)$ for $He^4 + He^4$. The very large amplitude glory oscillation is characteristic of identical boson scattering when only the S wave contributes. The full curve is calculated from a LJ (12:6) potential that gives the best fit. (M. G. Dondi, 1969.)

putting $(-1)^l = \cos l\pi$ yields:

$$\sigma_{\text{tot}} = \frac{4\pi}{k^2}\left\{\sum_l (2l+1)(1-\cos 2\eta(l)) + \sum_l (2l+1)\cos l\pi - \sum_l (2l+1)\cos(2\eta(l) - l\pi)\right\} \quad (7.33)$$

Using the semi-classical approximation we may expect extrema in the total cross-section whenever any of the terms in Equation 7.33 are stationary. This occurs when

$$\text{(I)}\ \frac{\partial\eta(l)}{\partial l} = 0; \quad \text{(II)}\ \frac{\partial\eta(l)}{\partial l} = l\pi/2. \quad (7.34)$$

Of these, (I) arises from the first term in Equation 7.33 and gives rise to the normal glory oscillations in σ_{tot}; (II) arises from the third term in Equation 7.33 and represents back scattering of the main beam particle through π, and hence forward scattering of the second particle. If the negative deflection due to the attractive branch of the potential does not exceed $-\pi$, contribution (II) comes solely from the *S*-wave scattering (i.e. $b = 0$). The oscillations in σ_{tot} arising from this term thus correspond to η_0 passing through $\pi/2$, π etc. From this structure we thus obtain additional information compared with that from the normal glories in that not only is the velocity at which the phase of the forward scattered amplitude passes through multiples of $\pi/2$ known, but also that this refers to the $l = 0$ partial wave contribution. The authors also show that the *S*-wave phase shift is almost entirely dependent on the potential range parameter. Thus, for a L-J potential they determine R_m directly.

It is one of the advantages of the crossed beam technique that a very wide 'temperature' range is experimentally accessible. Measurements of total cross-sections at superthermal energies in excess of 10^4 K have been made by several groups. Both M. Hollstein and H. Pauly (1967) and R. J. Cross and C. J. Malerich (1968) have used charge exchange alkali atom sources to measure σ_{tot} for alkali atom/rare gas systems. In their energy range of 6 eV–1000 eV the transition occurs between attractive behaviour ($\sigma(v) \propto v^{-2/5}$) and the slower dependence characteristic of the repulsive potential. In the apparatus by Pauly, both the generation of the parent ion beam and the neutral alkali atom detection are by surface ionization on tungsten. The detector is run 'cold' to reduce noise without impairing efficiency at these high energies. Some typical results for K, Na/gas systems are shown in Fig. 7.13.

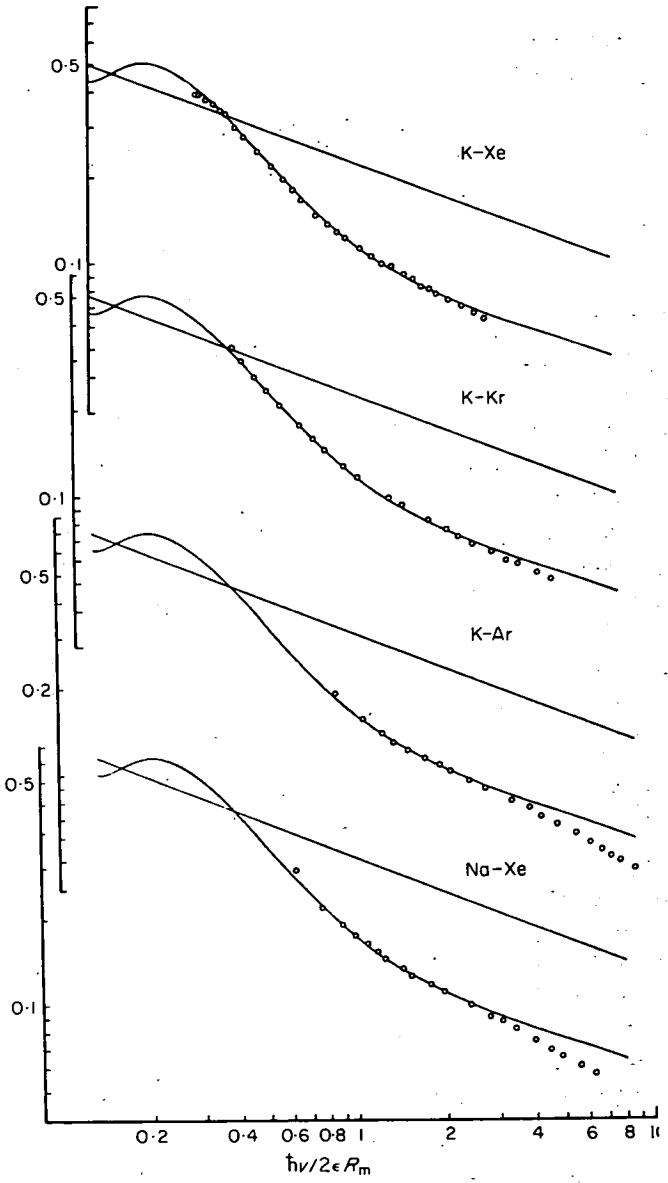

Fig. 7.13 Total cross-sections for alkali metals + rare gases in the superthermal collision range (M. Hollstein and H. Pauly, 1967). The transition between a total cross-section dominated by the attractive part of the potential and the repulsive part is seen at $\hbar v/2\epsilon R_m \sim 2$ (see Equation 7.7) and the first glory maximum ($N = 1$) is also visible.

By grafting results of experiments at this energy onto the thermal data, a potential valid over a much larger energy range can be established. It has become clear that the two parameter L-J form is not adequate to cover this energy range and that potentials with more parameters are required (C. Schlier et al., 1968).

7.5 Elastic differential cross-sections

(*i*) *Interpretation*

Fig. 7.2 gave some idea of the structure available in measurements of the differential cross-section. The calculation was, in fact, for potassium scattered from a heavy partner (I_2). The results were given in the laboratory reference system and ideal resolution was assumed. Clearly, considerable information about the intermolecular potential can be obtained from data with this amount of structure provided that the angular resolution is good enough – 0.2° (LAB) would be adequate for most potentials at thermal energies.

Once again interpretation follows the algorithm already suggested, namely estimation of parameters, identification and interpretation of key features, statistical fitting between observations and forward apparatus averaged calculations from a trial potential. These key features are, in order of increasing resolution necessary for their observation,

(i) The low resolution envelope of log $\sigma(\chi)$ versus χ plots, yielding some indication of the power law of the potential.
(ii) The location of the rainbow maximum, providing a good measure of the potential well depth.
(iii) Location and spacing of supernumerary rainbow maxima. The first of these yields information on the potential range and subsequent peaks give some evidence as to the curvature of the potential near its minimum.
(iv) The spacing of the high frequency interference oscillations, from which σ_{LJ} can be extracted with only an approximate knowledge of ϵ.

It has already been shown that, under classical (Equation 2.32) or semi-classical (Equation 6.132) conditions the major contribution to $\sigma(\chi)$ is given by:

$$\sigma(\chi) = s^{-1} \left(\frac{(s-1)}{E} C_s\right)^{2/s} \chi^{-(2s+2)/s}. \tag{7.35}$$

By grafting results of experiments at this energy onto the thermal data, a potential valid over a much larger energy range can be established. It has become clear that the two parameter L-J form is not adequate to cover this energy range and that potentials with more parameters are required (C. Schlier et al., 1968).

7.5 Elastic differential cross-sections

(*i*) *Interpretation*

Fig. 7.2 gave some idea of the structure available in measurements of the differential cross-section. The calculation was, in fact, for potassium scattered from a heavy partner (I_2). The results were given in the laboratory reference system and ideal resolution was assumed. Clearly, considerable information about the intermolecular potential can be obtained from data with this amount of structure provided that the angular resolution is good enough $\pm$ 0.2° (LAB) would be adequate for most potentials at thermal energies.

Once again interpretation follows the algorithm already suggested, namely estimation of parameters, identification and interpretation of key features, statistical fitting between observations and forward apparatus averaged calculations from a trial potential. These key features are, in order of increasing resolution necessary for their observation,

(i) The low resolution envelope of log $\sigma(\chi)$ versus χ plots, yielding some indication of the power law of the potential.
(ii) The location of the rainbow maximum, providing a good measure of the potential well depth.
(iii) Location and spacing of supernumerary rainbow maxima. The first of these yields information on the potential range and subsequent peaks give some evidence as to the curvature of the potential near its minimum.
(iv) The spacing of the high frequency interference oscillations, from which σ_{LJ} can be extracted with only an approximate knowledge of ϵ.

It has already been shown that, under classical (Equation 2.32) or semi-classical (Equation 6.132) conditions the major contribution to $\sigma(\chi)$ is given by:

$$\sigma(\chi) = s^{-1} \left(\frac{(s-1)}{E} C_s\right)^{2/s} \chi^{-(2s+2)/s}. \tag{7.35}$$

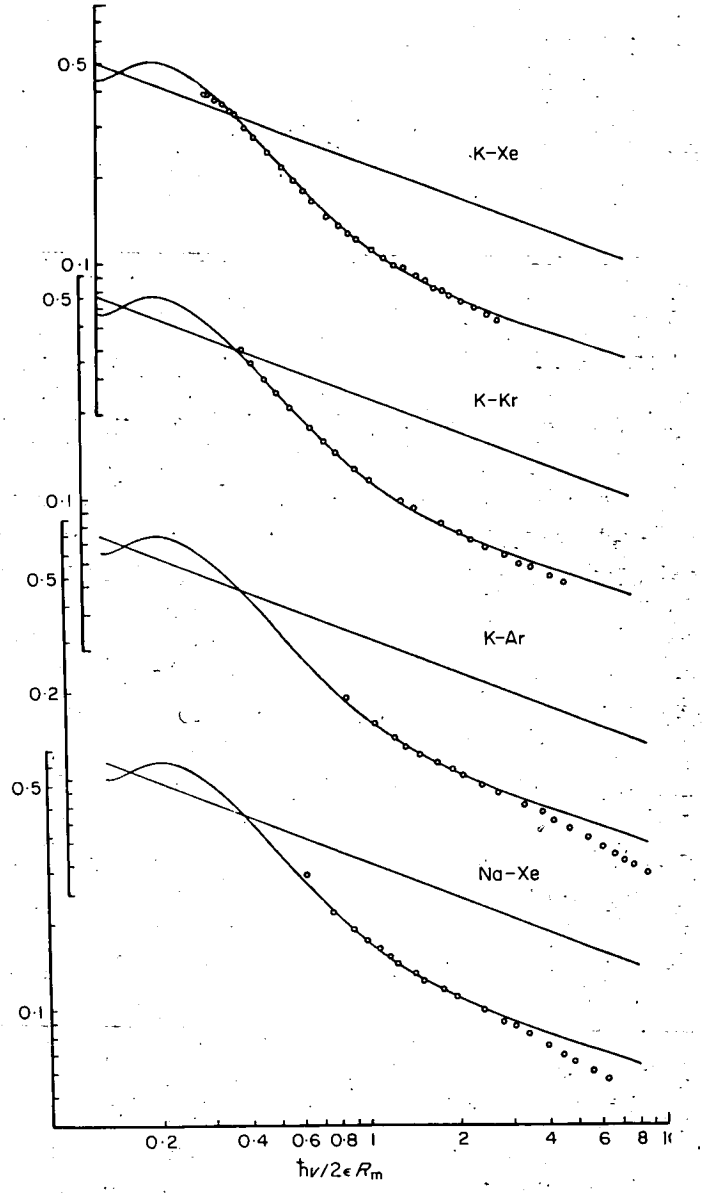

Fig. 7.13 Total cross-sections for alkali metals + rare gases in the superthermal collision range (M. Hollstein and H. Pauly, 1967). The transition between a total cross-section dominated by the attractive part of the potential and the repulsive part is seen at $\hbar w/2\epsilon R_m \sim 2$ (see Equation 7.7) and the first glory maximum ($N = 1$) is also visible.

Thus a log plot of low resolution differential cross-section (in which the quantum interference structure is not resolved) against angle will yield a line with gradient $-(2s + 2)/s$ at angles smaller than the rainbow. In Fig. 7.2 a line drawn through the mean of the oscillations in the region 1°–8° of the plot $\sigma(\theta)$. $\theta^{7/3}$ versus θ is approximately horizontal in accord with these calculations and so verifies the 6 power attractive term used in the forward computations.

Quantum mechanically the maxim in the differential cross-section occurs at slightly narrower angles than the classical rainbow. To a good approximation

$$\chi \text{ rainbow} = \chi_{max} + 0.772\,(\chi_{max} - \chi_{\text{first min}}), \tag{7.36}$$

where χ_{max} is the rainbow maximum in the differential cross-section and χ_{min} is the minimum between χ_{max} and the first supernumerary bow.

The semi-classical interpretation of the rainbow and of the supernumerary bows has already been discussed in Chapter 6. Their most important feature in determining elastic potentials is that the rainbow location is largely dependent only on the reduced energy and but weakly on the length parameter in the potential. This can be seen in Fig. 7.14 where the location of the rainbow maximum is plotted against the reduced collision energy. With no knowledge at all of Λ^* (which contains the length parameter σ) ϵ can be determined to ±10 per cent. Calculations for a range of different potentials forms have shown that this is true for a wide range of potentials so that a measurement of χ_{max} yields a value of the well depth to 10 per cent or 15 per cent directly irrespective of potential form or other parameters. If a supernumerary bow can be observed as well, information as to the potential range can be obtained. Similarly, additional bows can be interpreted to yield potential curvatures etc. With additional information of this kind an iterative process can be used to refine the initial estimate of ϵ. As an example consider the scattering in Fig. 7.2.

θ max:	$= 10.2°$ lab $= 11.9°$ centre of mass
θ 1st supernumerary bow	$= 5.2°$ lab $= 6.04°$ centre of mass
Collision energy	$= 1.9 \times 10^{-13}$ ergs.

From Fig. 7.14, $\chi_{max} = 11.9°$ yields a first estimate for E/ϵ of 7.2–9.2. From Fig. 7.15 we can relate the angular spacing Δ_χ between the two bows to Λ^* thus finding for $E/\epsilon = 8$ and $\Delta\chi = 5.9°$ that $\Lambda^* \approx 0.078$. Returning to

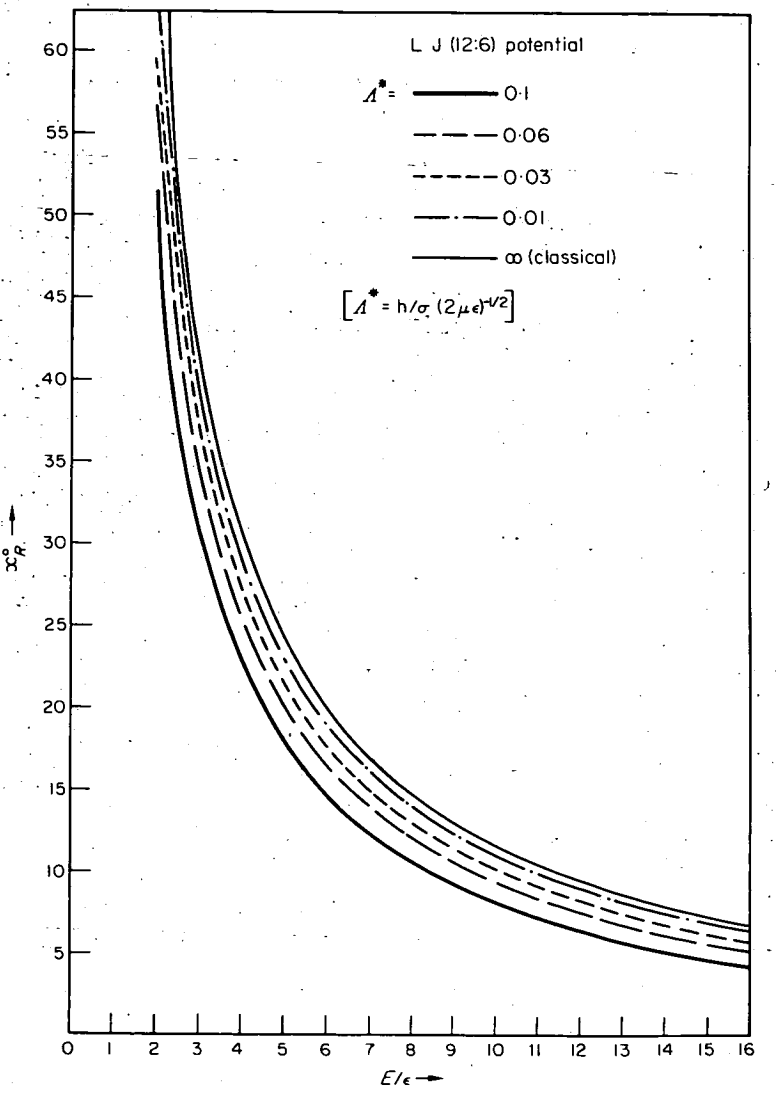

Fig. 7.14 Angle of rainbow maximum versus reduced impact energy for LJ (12:6) potential (R. J. Munn and F. J. Smith, 1966).

Fig. 7.14 with this value of Λ^* gives a revised value for E/ϵ of 7.8. Finally, Λ^* may be corrected using Fig. 7.16 where Λ^* and E/ϵ are related for various values of $\Delta\chi$. We finally obtain estimates for the potential parameters of $E/\epsilon = 7.8$ and $\Lambda^* = 0.083$, compared with the values 7.85 and 0.0855 used in the calculation of Fig. 7.2. Similar schemes can be set up to produce estimates of the potential function curvature from observations of additional

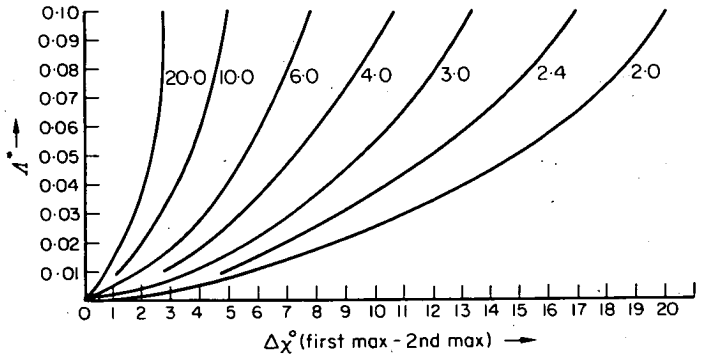

Fig. 7.15 Angle between rainbow maximum and secondary rainbow maximum versus Λ^*, Bohr parameter, for several reduced impact energies (LJ (12:6) potential). (R. J. Munn and F. J. Smith, 1966).

supernumerary bows. However, it is probably preferable to begin more detailed fitting computations at this stage together with the exploration of different potential forms.

The importance of operating in the optimum energy range can be appreciated from Fig. 7.14 or from the underlying relationship $\chi_r E^* = \text{const}$. If there is an error $\Delta\chi$ in measuring the position of the rainbow and ΔE in the relative energy, there will be an error

$$\Delta\epsilon/\epsilon = \Delta\chi/\chi + \Delta E/E$$

in the derived well depth. For an apparatus of normal resolution, a rainbow in the region 15°–60° is perhaps optimum.

The spacing of the highest frequency structure is primarily dependent on the range a of the potential. If this can be precisely located, e.g. by a marked change in gradient of $V(R)$ at $R = a$, we can define a partial wave l^* such that

$$l^*\hbar = \mu v a$$

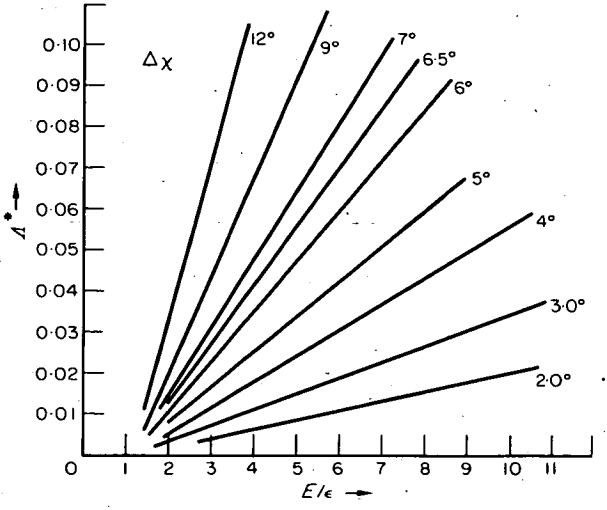

Fig. 7.16 Relation between Λ^* (and hence σ) and the reduced energy for several rainbow maxima to 1st supernumerary angular spacings.

The angular frequency for scattering from this edge (see Section 6.13) will then be:

$$\Delta\chi = \pi/l^*, \tag{7.37}$$

so that a can be determined directly. For smoothly varying potentials, e.g. of the L-J form, the parameter a is less easily defined, but will clearly be not too different from σ. For these potentials the high frequency structure arises from the interference between the inner two branches of $\chi(b)$ that lead to deflections of opposite sign. The interference spacing is given by (see Section 6.10)

$$\Delta\chi \approx 2\pi/[l_2 + l_3], \tag{7.38}$$

where l_2 and l_3 satisfy $|\chi(l_2)| \mu |\chi(l_3)| = \chi_{obs}$. l_2 and l_3 converge at $\chi = 0$ and for small angles

$$\Delta\chi \approx 2\pi/[k\sigma(b_2^* + b_3^*)] \approx \frac{\pi}{kb_0}, \tag{7.39}$$

where $b_0^*(= b_0/\sigma)$ is the reduced impact parameter leading to the forward

glory. Then, using the fact that R_g^*, the reduced distance of closest approach on the forward glory trajectory is only a slowly varying function of E^* and also that $V(R_0) \approx 0.6\epsilon$ for an R^{-6} potential, we obtain:

$$\Delta\chi \approx \frac{\Lambda^*}{2.2}\left(\frac{1}{0.6+E^*}\right)^{1/2}, \tag{7.40}$$

where Λ^* is the de Boer parameter. The basic dependence of $\Delta\chi$ on σ_{LJ} for $E^* > 1$ is apparent and Equation 7.40 enables a preliminary estimate of σ to be made.

A more rigorous analysis using the peak locations has been made by R. E. Olsen, 1968. Bernstein has shown that for $\chi < 30°$ and inside the rainbow the scattered intensity $I(\chi)$ can be written:

$$I(\chi) = I_1(\chi)\{1 + y(\chi)^2 + 2y(\chi)\cos\gamma(\chi)\}, \tag{7.41}$$

where I_1 is the scattered intensity contributed by the outermost branch of the deflection function. The peaks in $I(\chi)$ are then determined by the periodicities of $y(\chi)$ and $\cos\gamma(\chi)$:

$$y(\chi) = 2\left[\frac{I_{2\,3}(\chi)}{I_1(\chi)}\right]^{1/2}\cos(l_{2\,3}\chi - \pi/4) \tag{7.42}$$

and

$$\gamma(\chi) = 2\eta(l_1) + l_1\chi - \pi/2 \tag{7.43}$$

$y(\chi)^2$ is associated with the forward glory contibution and the second term in Equation 7.41, $y(\chi).\cos\gamma(\chi)$, arises from the interference between the forward glory and the outermost branch centered at l_1. There are thus three wavelengths of oscillation possible in the combined scattered amplitude,

$$\Delta\chi_{1:2\,3} = 2\pi/|l_{2\,3} \pm l_1| \tag{7.44}$$

resulting from the third term in Equation 7.41 and a structure of smaller amplitude having $\Delta\chi_{2\,3} = \pi/l_{2\,3}$ resulting from the second term in Equation 7.41 and already discussed in Equations 7.38–7.40. Olson (1968) and Bernstein have suggested that the finite apparatus resolution will erase the highest frequency structure, leaving the highest observed perioditicy to be $\Delta\chi_{2\,3}$. For a typical potential and angles of deflection at thermal energies

$\leqslant 10°$, l_1 and $l_{2\,3}$ might be ~600 and 200 respectively so that $\Delta\chi_{1:2\,3}/\Delta\chi_{2\,3} \leqslant \frac{1}{2}$. These authors found that for the Li-Hg system a plot of χ_N^{-1} versus $(N + \frac{1}{4})^{-1}$, where N labels successive maxima and minima, gave a good linear plot and the slope was equated to $l_{2\,3}$. Hence from scans at several energies, a plot of $(l_{2\,3} + \frac{1}{2})/k$ versus E^{-1} can be constructed, in the same way that the BOB plots of $\eta_{2\,3}/k$ versus E^{-1} were used.

The curvature of these lines again analogously, can be written as:

$$(l_{2\,3} + \tfrac{1}{2})/kR_m = B_0(E^*) + B_1E^{*-1} - B_2E^{*-2} \qquad (7.45)$$

where B_0 depends upon the curvature of the potential and $B_1 = 0.3530$ and $B_2 = 0.1488$. Tables of B_0 for the Buckingham Corner potential have been given by R. E. Olsen, 1968, so that these oscillations may be interpreted directly in terms of this potential.

(ii) Measurement of differential cross-sections

The number of particles per second reaching a small detector a distance R away from the scattering centre in a direction (θ, ϕ) is (see Equation 3.4)

$$S(\theta,\Phi) = \frac{A_d}{R^2} J\begin{pmatrix}\chi, \phi\\ \theta, \Phi\end{pmatrix} \frac{I_1 I_2}{v_1 v_2} \times \begin{pmatrix}\text{scattering}\\ \text{volume}\end{pmatrix} |\mathbf{v}_1 - \mathbf{v}_2|\, \sigma(\chi, \phi), \qquad (7.46)$$

where I_1 and I_2 are the fluxes of beam particles with velocities v_1 and v_2, $\sigma(\chi, \phi)$ is the CM differential cross-section and $J(\chi, \phi/\theta, \Phi)$ the Jacobian for the CM → LAB transformation.

In general, to make the transition $S(\theta, \Phi) \leftrightarrow \sigma(\chi, \phi)$ it is necessary to either average or unfold the results with respect to the distribution in magnitude and direction of the relative velocity $v_1 + v_2$, which is mainly felt through its influence on the co-ordinate transformation and on the Jacobian. The spread in velocity of the unselected cross-beam is usually the most important agent in blurring the scattering pattern, though the angular spread of v_2 can be important for slow heavy target molecules.

Some design criteria associated with apparatus resolution have already been discussed in Chapter 3. The ideal design procedure is to make a forward calculation from an assumed potential of roughly the right form through full apparatus averaging to $S(\theta, \Phi)$ via Equation 7.46 and to adjust the operating conditions so that enough structure is preserved in $S(\theta, \Phi)$ to allow a good fit to be made to the potential.

In practice, an experiment in which the supernumerary oscillations are resolved is always worthwhile and we can estimate the relative velocity

resolution Δv needed to preserve this structure. In the CM system, if we require that Δv must be sufficiently small for the rainbow peak position to shift by less than one half the supernumerary spacing, we find from Fig. 7.14 that the reduced energy must range between 6.4 and 9.4, i.e. a 15 per cent spread in the relative velocity would just permit the resolution of the rainbow and first supernumerary.

The resolution of the higher frequency oscillations sets a much more severe limit on the velocity spread permissible. From Equation 7.39 we see that their period is inversely proportional to k and hence to the relative velocity. Thus the acceptable spread in velocity Δv if successive maxima and minima are not to overlap is:

$$\Delta v/v \sim (k\sigma\chi)^{-1}. \qquad (7.47)$$

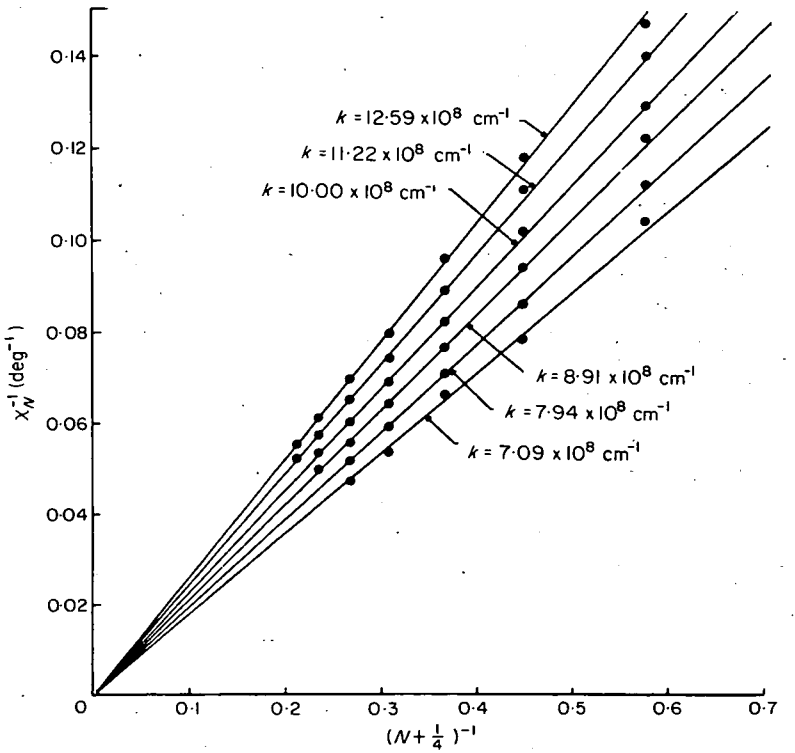

Fig. 7.17 Plot of reciprocal of interference extrema locations versus $(N+\frac{1}{4})^{-1}$ where N is the index number of extrema. The slope of the plot at each energy is αl_0 where l_0 is the l value of the forward glory. The example illustrated is for Li–Hg and for such a system with small reduced mass l_0 is typically ~50, making the high frequency structure easy to resolve. (From R. E. Olson, 1968.)

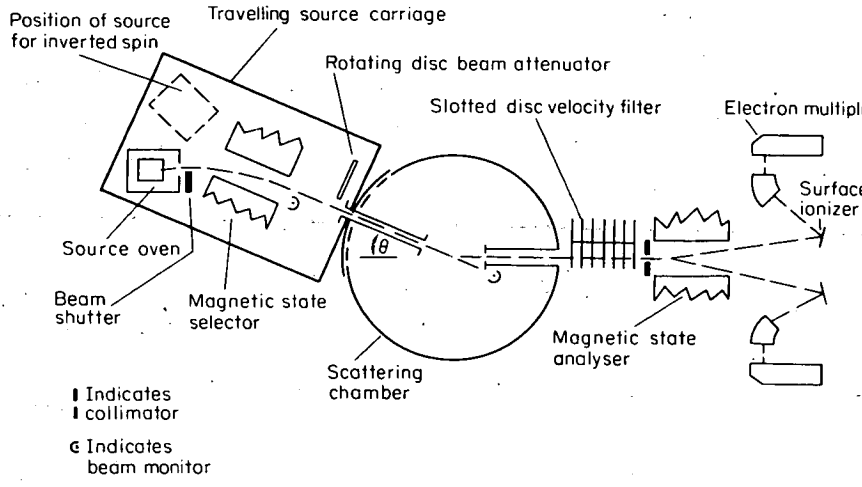

Fig. 7.18 Apparatus for studying spin dependence of alkali alkali collisions. (D. E. Pritchard et al., 1969.)

Typically a velocity resolution $\lesssim$10 per cent is required, together with an angular resolution $\sim\Delta\chi/2$, i.e. $\sim$0.2°. The resolution of this structure becomes easier at small angles.

Because of the important contribution to the resolution made by the cross-beam velocity spread, it is normal to use the heavier species in this beam and to operate the source at the lowest temperature possible. Besides minimising the velocity spread, the loss of angular resolution associated with the LAB → CM transformation (which generally results in χ being greater than θ) is also reduced. Even with the optimum configuration of masses, using a thermal effusive cross-beam can frequently result in an uncertainty of 0.5° in the CM angle of deflection. A further reduction in the effect of the cross-beam velocity spread especially at small angles of scattering can be achieved by firing the cross-beam in a plane perpendicular to the plane of the primary beam and detector motion (E. F. Greene et al., 1969).

7.6 Apparatus and results – differential cross-sections

Once again we propose to discuss only a few experiments to illustrate the technique and its present capabilities.

Because of the alleviated detection problem, alkali scattering experiments have seen the most ambitious applications of state and velocity filters to define the quantum channel of the collision. In the experiments of D. E. Pritchard and F. Y. Chu, 1970, the scattering of unlike alkali atoms was

studied. Alkali atoms interact by two potentials depending upon their overall spin state, triplet or singlet, the two potentials being very different. In unpolarized beams, particles are incident in each pair state with a statistical weight of 3:1 ($^3\Sigma$:$^1\Sigma$). The particles may then scatter with or without an exchange of spin (see Section 6.17). To isolate the singlet and triplet potentials and to study the spin flipping process itself, two spin state selectors are required. The configuration used by Pritchard and Chu is shown in Fig. 7.18. The primary beam is spin selected by a two wire field magnet and then crosses a chopped unpolarized Na beam. The scattered K is velocity selected and finally spin selected again. The source and detector can be arranged to transmit and receive either spin state. The subsequent detection is of the modulated ion counting type. Differential cross-sections for spin exchange, $\sigma_{exch}(\chi)$ and for non-exchange (i.e. direct scattering), $\sigma_{direct}(\chi)$, were measured. These cross-sections are related to the scattered amplitudes due to the singlet, $f_1(\chi)$, and triplet, $f_3(\chi)$, potentials by

$$\sigma_{exch}(\chi) = \tfrac{1}{4} \mid f_1(\chi) - f_3(\chi) \mid^2, \tag{7.48}$$

and

$$\sigma_{exch}(\chi) + \sigma_{direct}(\chi) = \sigma_{sum}(\chi) = \tfrac{1}{4} \mid f_1(\chi) \mid^2 + \tfrac{3}{4} \mid f_3(\chi) \mid^2. \tag{7.49}$$

The two potentials can thus be determined from observations of $\sigma_{exch}(\chi)$ and $\sigma_{sum}(\chi)$ and in particular their difference can be found with good precision. Typical results obtained are shown in Figs. 7.19 and 7.20.

The alkali metals interact with the rare gases by only one potential in each case, and if the collision energy is below the threshold for any electronic excitation no state selectors are needed to specify the exit channel. The greater beam intensity then available permits much higher angular and velocity resolution to be used. The Bonn Group (P. Barwig et al., 1966) have studied these systems and have resolved the quantum interference structure out to wide angles. A typical example is the Na/Xe measurements shown in Fig. 7.21, in which the location of all the quantum peaks can easily be seen. With data of this quality, the functional dependence of $V(R)$ in the experimental energy range can be unambiguously determined. The usual forms of the Lennard-Jones potential (n, ϵ and σ as adjustable parameters) have proved inadequate under this searching examination and a series of potentials with five parameters have been fitted to the data (C. Schlier et al; U. Buck and H. Pauly, 1968). The apparatus used is shown in Figure 7.22. Data with the resolution of that shown in Fig. 7.21 can now be

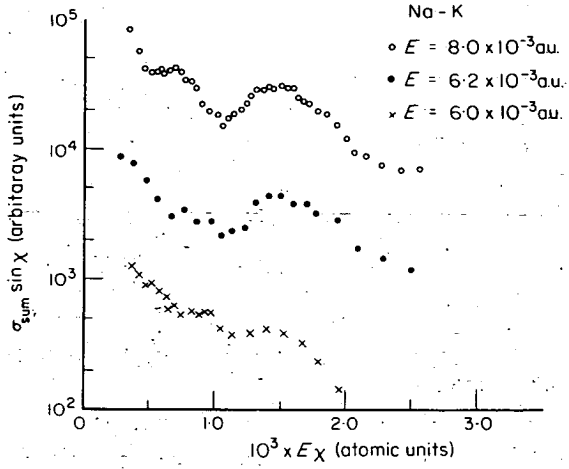

Fig. 7.19 $\sigma_{sum}(\chi)$ for Na–K scattering. Note the good scaling with respect to $E\chi$. The overall appearance is that of typical elastic scattering. (D. E. Pritchard et al., 1970a.)

subject to a two stage inversion procedure. The deflection function is first constructed, using any auxiliary information on R_m, χ_r and the phase shift of the forward glory branch; its functional form at this stage can still contain adjustable parameters equal in number to the number of resolved rainbow extrema and these are fixed by fitting the observed differential cross-section, a much speedier process than working with adjustable parameters in the potential. The deflection function is then inverted by Firsov's procedure to yield $V(R)$ pointwise, i.e. without making any assumptions about its analytical form. The potential for Na/Hg in Fig. 7.23 was obtained in this way and clearly illustrates the inadequacy of the Lennard-Jones potential in analyzing high resolution scattering. It is also observed in Li/Cs singlet state scattering (H. Kanes et al., 1971) that the actual potential minimum is broader than the Lennard-Jones form, but this may not turn out to be true of interatomic potentials in general (P. E. Siska, et al., 1971, or J. M. Parson et al., 1971, for the inert gases). If alkali atom scattering data is to be fitted with only a two parameter potential, then the (8:6) form rather than the (12:6) can be tried with its much smaller curvature ($\kappa = 20.2$) at the potential minimum.

Experiments with non-alkali partners are at a slightly less advanced stage due to the difficulties of detection. Advances in nozzle sources and vacuum

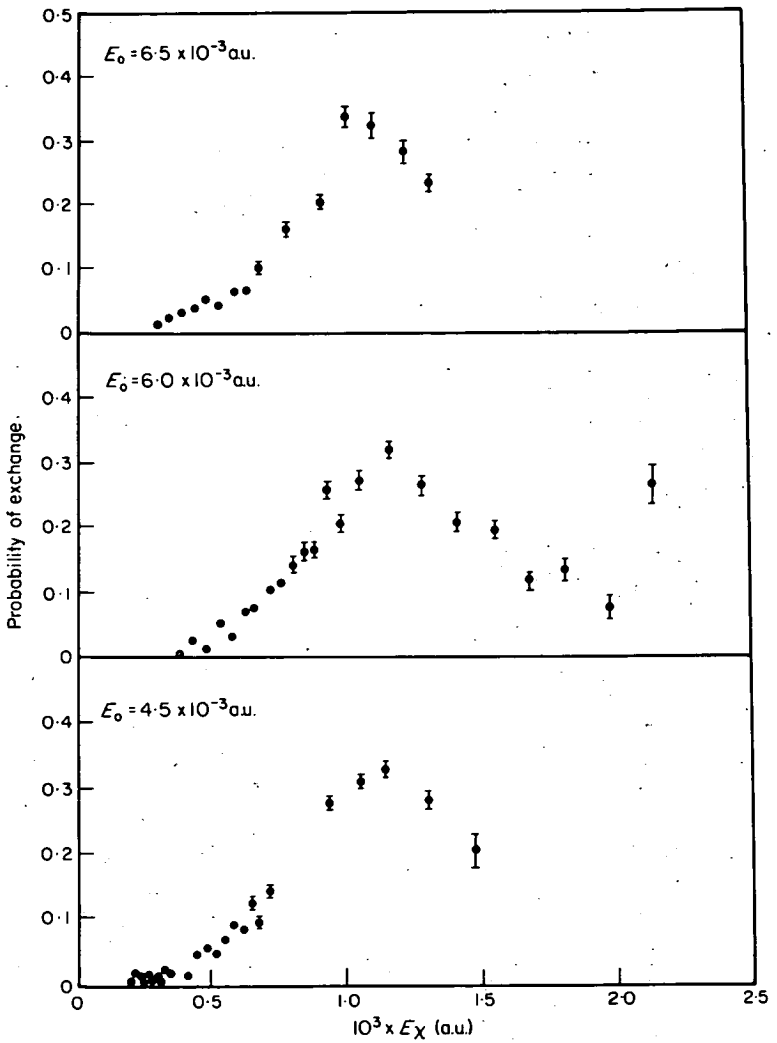

Fig. 7.20 The exchange scattering of Na from K at three energies. A maximum in $P_{ex}(\chi)$ is observed and occurs when the phase difference between the singlet and triplet scattered amplitudes at χ, $\arg(f_1(\chi)) - \arg(f_3(\chi))$, reaches an odd multiple of π. The first of these extrema is visible, with the suggestion of a higher order one in the run at $E_0 = 6 \times 10^{-3}$. The very good scaling of $P_{ex}(\chi)$ at different energies with respect to $E\chi$ indicates that the outermost branches of the triplet and singlet deflection functions are dominant. (D. E. Pritchard et al., 1970.)

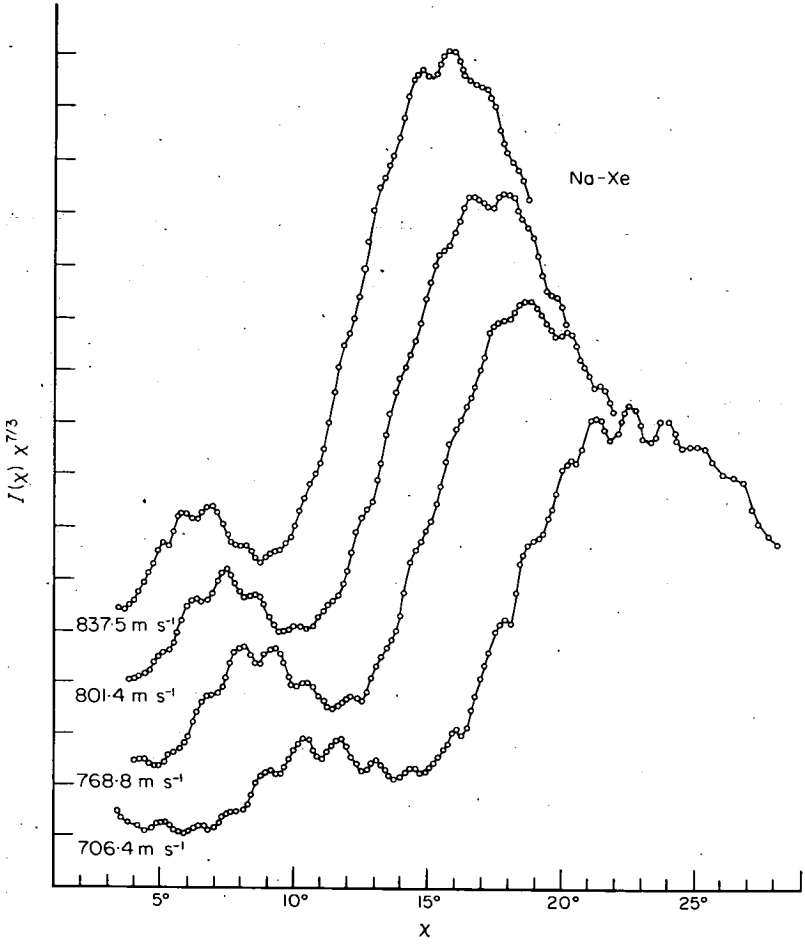

Fig. 7.21 Na–Xe scattering. The rainbow and one supernumerary bow are visible, together with high frequency structure of the type indexed in Fig. 7.17. (Taken from P. Barwig et al., 1966.)

techniques have, however, brought rapid progress. Recently the systems:

Ne + Ne, Ar, Kr, Xe	(J. M. Parson et al., 1970; P. E. Siska et al., 1970).
Ne + Ar	(W. Williams et al., 1969; M. Cavallini et al., 1970).
He + He	(M. Cavallini et al., 1970; P. E. Siska et al., 1970; P. Cantini et al., 1972; H. G. Bennewitz et al., 1971).
$D_2 + N_2$	(D. H. Winicur et al., 1970; V. Aquilanti et al., 1971).
$Ar + N_2$	(R. W. Bickes and R. B. Bernstein, 1970; K. G. Anlauf et al., 1971; p. Cantini et al., 1972).

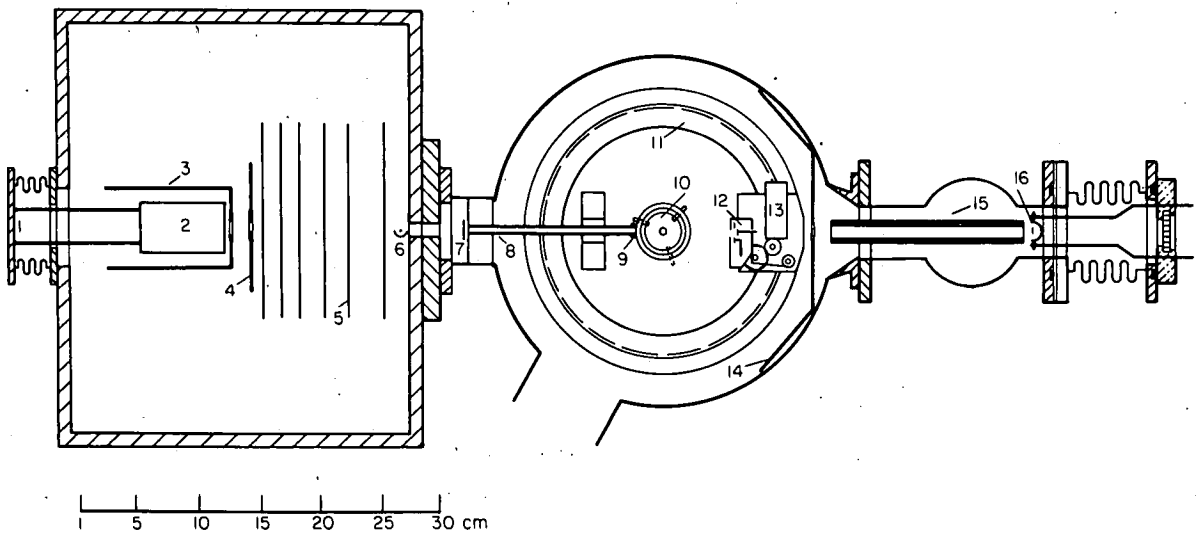

Fig. 7.22 Scale drawing of a cross-section through a molecular beam apparatus for measuring differential scattering cross-sections. The important parts of the apparatus are **2** oven, **5** velocity selector, **6** monitor detector, **10** secondary beam oven, **12** movable detector on the rotating platform **11**, **13** motor for raising and lowering the detector, **16** monitor detector, **4**, **8**, **14**, and **15** are liquid nitrogen cooled surfaces. (H. Pauly and J. P. Toennies, 1968.)

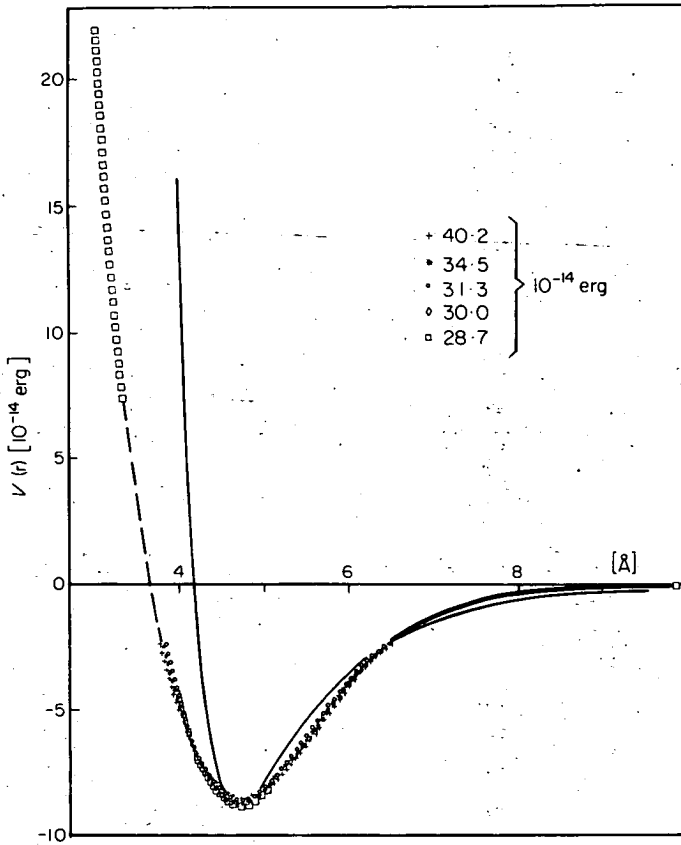

Fig. 7.23 Potential for the Na–Hg system determined by a two stage inversion of the differential cross-section. The various sets of points refer to $\sigma(\theta)$ data at different energies; the insensitivity of the derived potential to the energy of the scattering experiment is an important check of the validity of the procedure. The full line is the Lennard-Jones potential having the same value of ϵ and R_m. (U. Buck, 1971.)

CCl_4 + iso-octane	(M. J. Cardillo et al., 1971).
Ar + Ar	(J. M. Parson et al., 1972).
He + Ar, Ne, Kr	
Ne + Kr	(G. D. Lempert et al., 1971).
Ar + Kr	(J. W. Bredewout et al., 1971).
He + Ne	(F. G. Collins and F. C. Hurlburt, 1972).

have been the subject of initial reports. Rainbow angles and quantum interference structure have been observed and initial estimates of potential

parameters have been made. The apparatus used by Y. T. Lee et al., 1969, employed two nozzle beams and an electron bombardment mass filter in a UHV chamber at $< 10^{-10}$ Torr which was separated by three stages of differential pumping from the scattering chamber. A modulated ion counting scheme was employed. The apparatus is shown in Figs. 7.24 and 7.25 and some data for inert gas scattering obtained with a similar machine is shown in Fig. 7.26. Clearly several research groups now have the capability of producing high resolution differential cross-section data for non alkali systems and continuing progress can be expected. Scattering measurements of this kind, extended over an even wider energy range, must now be our best source of intermolecular potentials.

Progress has also been made in determining potentials for excited species. The beam technique, in contrast to pressure broadening, is most suited to investigating metastable species rather than the short lived states that can decay by dipole radiation to the ground state. The crossed beam scattering of ^3S He (Grosser and H. Haberland, 1968) and of the $^3P_2$ and $^3P_0$ states of Hg (E. C. D. Darwall et al., 1971) have been reported. This, too, can be expected to be an area of growing interest.

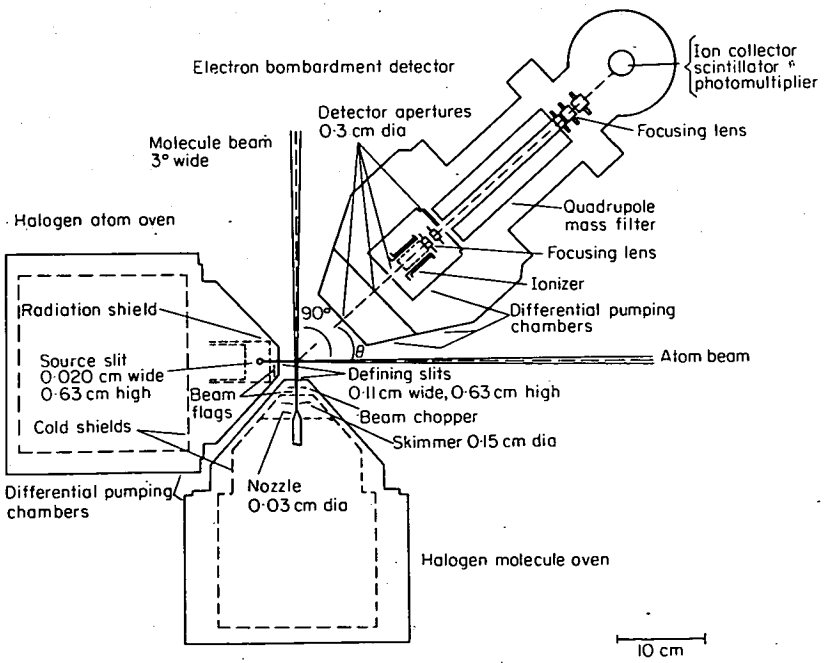

Fig. 7.24 Schematic of apparatus (top view). (Y. T. Lee et al., 1970.)

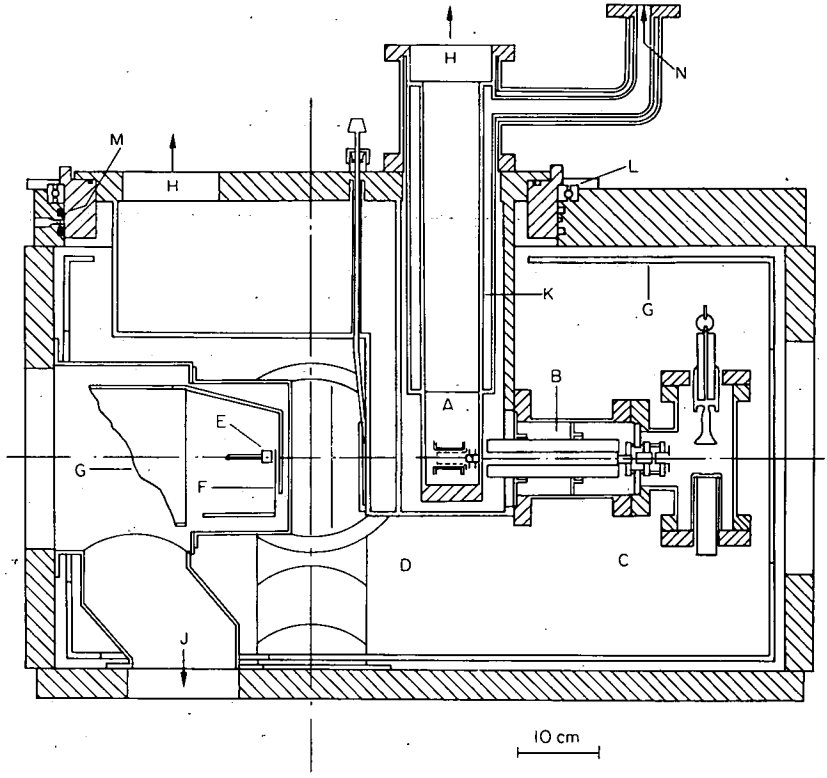

Fig. 7.25 Side view of apparatus. (**A**)–electron bombardment ionizer; (**B**)–quadrupole mass filter; (**C**)–ion counter; (**D**)–isolation valve; (**E**)–molecular beam source; (**F**)–beam flag; (**G**)–cold shields; (**H**)–to ion pumps; (**J**)–to oil diffusion pump; (**K**)–liquid nitrogen trap; (**L**)–ball bearing support of rotatable lid; (**M**)–rotatable vacuum seal; and (**N**)–to liquid nitrogen reservoir. (Y. T. Lee et al., 1970.)

7.7 Prospects

In this chapter we have only been able to discuss the results of a very few experiments. It is useful to close, therefore, with a rather broader view of the prospects in this field.

It now seems that beam production and detection techniques are sufficiently powerful to make experiments with almost any atomic or molecular system feasible. Limitations to further development now arise from the complexity of these systems when more than one potential operates and the inadequacy of current state selection methods that can resolve some of these cases. For the interaction of polyatomic molecules, the scattering without state or molecular orientation selection will tend to be rather

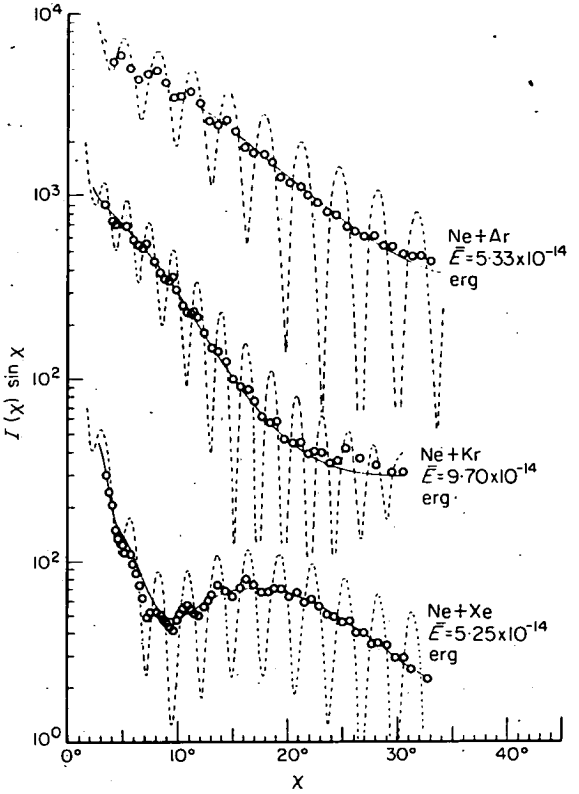

Fig. 7.26 Differential cross-sections for scattering of Ne from the heavier rare gases. Two lines are drawn through the experimental points; the full curve is the low resolution cross-section calculated from a LJ (20:6) potential and the dashed curves the high resolution cross-sections from the same potentials. The high frequency structure is just resolved experimentally. (J. M. Parson et al., 1970.)

structureless and at best only average potentials will be obtainable. In addition, in the case of non-central forces inelastic processes become important and again the state analysis methods are not sufficiently developed to explore these.

In contrast, for single central potential systems very accurate data should now be obtainable, although the experimental effort required to collect this information over a wide energy range will continue to be very great. Direct unfolding procedures will be improved and the development of accurate combining rules (H. L. Kramer and D. R. Herschbach, 1970) will be of especial value in extending this information to a wider range of systems.

CHAPTER EIGHT

Reactive Scattering

8.1 Scope of beam techniques in investigating chemical reaction

As already suggested in Chapter 1, the unique advantages of the scattering approach to studying chemical reaction arise from the ability to control the impact velocity (and, less easily the incident quantum state) and to measure the post-collision velocities, as well as the angular scattering pattern. Technical difficulties have limited the information obtainable about the internal state of the products, but this important information is in principle also accessible. The leverage that this very detailed information about reactive collisions brings to the understanding of chemical reaction is increased by the fact that the principle of microscopic reversibility can be applied to detailed cross-sections, thus extending the range of usefulness of the data into experimentally inaccessible regions.

Reactive scattering experiments have as their ultimate aim the mapping of the potential surfaces on which reaction occurs, but preliminary analysis and experiments of low resolution have the more modest aims of:

(1) Classifying the type of reactive encounter, largely from the angular scattering pattern.
(2) Estimating the reaction cross-section, sometimes as a function of incident energy.
(3) Estimating the partitioning of any energy released between relative translational energy of the products and their internal motion.

Current beam techniques are most powerful when applied to simple reactions in which only a few reactive channels are open. In these cases, if sufficiently intense beams are available, something approaching a complete kinematic analysis can be performed. Even relatively primitive observations of the angular dependence of the product flux, the minimal experiment, afford considerable chemical insight and permit correlation of properties (1–3) above with other properties of the reactants. In collisions where many reactive channels are open, such as those at high energies, the elementary

beam technique is less useful. Some spectroscopic information of the products is then required and might be obtained in a separate bulb experiment, or perhaps eventually in a combined beam/spectroscopic system. These kinetic spectroscopy experiments are thus complementary to, rather than competitive with, scattering experiments; the interrelation of some of these techniques and their relations to current theoretical models is summarised in Fig. 8.1.

There are three main types of scattering measurement possible with reactive systems. The elastic differential cross-section, $\sigma(\theta, E)$ in which the distribution of unchanged reactant is measured; the reactive differential cross-section, $\sigma_R(\theta, E, \Delta E)$ in which some kinetic energy analysis of the scattered product is carried out and the total cross-section, $\sigma_{tot}(E)$ can also be measured. All of these can be accompanied by some internal state selection of reactant or product as appropriate.

The present state of the experimental front can be judged from Table 1, in which is listed the more definitive beam experiments performed since 1956. Not all of the work of the larger groups is included, but this can be traced from the references given. The evolution of the field is apparent; starting with alkali metal reactions at thermal energies without velocity selection, the techniques now in use cover universal detectors, velocity selection of reactants and products, beams of metastable species and beam energies that are limited only by the chemical interest of the results. The present limitations of the technique must not be disguised, however. Intensity problems are much more severe than in elastic scattering and have so far limited the applications of universal detectors to unselected beams. Until very recently velocity selectors have only been used on either reactant or product beams, not on both simultaneously. The range of materials that can be formed into a sufficiently intense beam for differential scattering is still small, though most organic compounds are suitable. In particular, it has proved difficult to build up sufficient densities of short lived ($< 10^{-6}$ s) excited species to carry out scattering experiments, although the high photon flux from lasers will doubtless provide a solution. There is still something of a gap in the beam energy available between 0.5 eV and 5 eV that is slowly being bridged by seeded beams. Finally, although vibrational excitation seems to be generally an important means of providing any activation energy necessary for reaction, very few scattering experiments have been carried out with vibrationally excited molecules. There is no reason to doubt, however, that all of these difficulties will be overcome, principally through the use of nozzle beams to increase source intensity and computerized data handling techniques at very low signal levels. The whole field of reactive scattering has most recently been surveyed by J. L. Kinsey (1972).

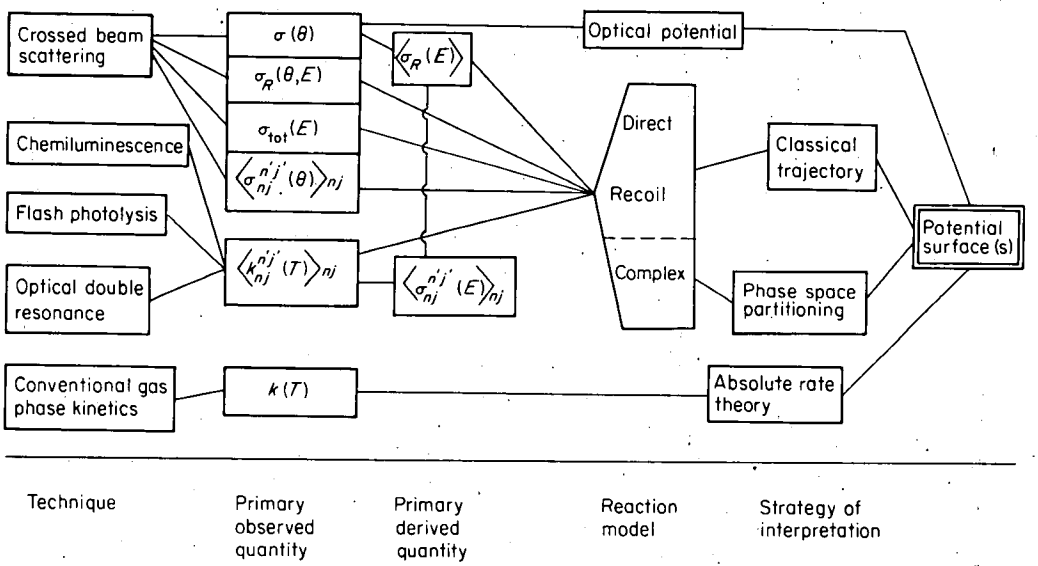
Crossed beam scattering
Chemiluminescence
Flash photolysis
Optical double resonance
Conventional gas phase kinetics
$\sigma(\theta)$
$\sigma_R(\theta,E)$
$\sigma_{tot}(E)$
$\langle \sigma^{n'j'}_{nj}(\theta) \rangle_{nj}$
$\langle k^{n'j'}_{nj}(T) \rangle_{nj}$
$k(T)$
$\langle \sigma_R(E) \rangle$
$\langle \sigma^{n'j'}_{nj}(E) \rangle_{nj}$
Optical potential
Direct
Recoil
Complex
Classical trajectory
Phase space partitioning
Absolute rate theory
Potential surface (s)
Technique
Primary observed quantity
Primary derived quantity
Reaction model
Strategy of interpretation

Fig. 8.1

(1) In the second column, the basic beam technique is taken to consist of two fixed effusive sources (or one replaced by a Laval nozzle), a movable hot wire detector (usually tungsten or Pt/W alloy) and no velocity selection or analysis. Only variants on this design are noted.
(2) In the second column, $\sigma_R(\theta,v')$ indicates that the angle of scattering and the product velocity have been measured. The velocity analysed elastic differential cross-section, $\sigma(\theta,v')$ in the presence of reaction has received very little attention so far.
(3) The angular resolution is rarely given in the earlier papers. Most of the experiments are of intermediate to poor angular resolution, with the detector subtending 0.5–1° (LAB) at the scattering centre.
(4) Some of the measurements of $\sigma_R(\theta)$ were obtained with a Pt–8%W alloy filament operated in a bimodal fashion. There is now considerable doubt (see Chapter 5) whether good discrimination is obtained in this way between highly vibrationally excited alkali halide molecules and alkali atoms, and also whether the presence of unreacted halogens can alter this relative sensitivity.
(5) An increasing number of ion/molecule beam experiments have been carried out in which $\sigma_R(\theta,E)$ is measured for the ionic product. In this way, the same detailed information is obtained as in neutral particle scattering, but with less severe intensity problems because of the higher detection efficiency. Some of these results are included in table 2.

System	Technique/measurements		Reference
K + HBr	$\sigma_R(\theta)$		E. H. Taylor and S. Datz, 1955
K + CH_3I, C_2H_5I	$\sigma_R(\theta)$	Vel. selected K beam	D. R. Herschbach et al., 1961
K + HBr	$\sigma(\theta)$ $\sigma_R(\theta)$	Pt. detector for K	D. Beck, E. F. Greene, and J. Ross, 1962
D + H_2	$\sigma_R(\theta)$	HD velocity estimated by time of flight. Electron bombardment det.	S. Datz and E. H. Taylor, 1963
K + HCl, HI	$\sigma(\theta)$	Vel. selected K. Optical potential analysis.	M. Ackerman et al., 1964

System	Technique/measurements		Reference
$Cs + Br_2$	$\sigma_R(\theta)$	Vel. selected Cs.	S. Datz and E. E. Minturn, 1964
$K + HBr$	$\sigma(\theta)$	Vel. analysis of KBr	A. E. Grosser et al., 1965
$K + \begin{cases} CH_3I \\ Br_2 \\ ICl \end{cases}$	$\sigma_R(\theta)$	Magnetic deflection analysis of KX	R. R. Herm, R. G. Gordon and D. R. Herschbach, 1964
$\left.\begin{matrix} K \\ Rb \\ Cs \end{matrix}\right\} + \begin{cases} Br_2 \\ I_2 \end{cases}$	$\sigma_R(\theta)$	Vel. analysis of KBr	J. H. Birely and D. R. Herschbach, 1965; A. E. Grosser and R. B. Bernstein, 1964
$K + Br_2$ $Cs + HBr$	$\sigma_R(\theta)$	Electric deflection analysis of KBr, CsBr $T_{rot} \sim 1300$ K (see also C. Maltz and D. R. Herschbach, 1967)	R. R. Herm and D. R. Herschbach, 1965
$K + Br_2$	$\sigma_R(\theta)$	Vel. analysis KBr. Differential surface det.	J. H. Birely and D. R. Herschbach, 1965
$K + CH_3I$	$\sigma_R(\theta)$	CH_3I orientated by 6-pole field	P. R. Brooks and E. M. Jones, 1966
$KBr\dagger + Na \rightarrow K^* + NaBr$	$\sigma_R(\theta)$	Chemiluminescence of K* product. A triple beam experiment. Angular distribution of resonance radiation measured	M. C. Moulton and D. R. Herschbach, 1966

$\left.\begin{matrix}Cs\\K\end{matrix}\right\} + RbCl$	$\sigma_R(\theta,v')$	Bimodal surface det. + Mass spec. Velocity anal. products.	W. B. Miller et al., 1967
$\left.\begin{matrix}K\\Rb\\Cs\end{matrix}\right\} + \left\{\begin{matrix}Br_2\\I_2\end{matrix}\right.$	$\sigma_R(\theta)$	Thermal energy range	J. H. Birely et al., 1967
Na + polyhalides	$\sigma_{R_{tot}}(E)$	Quenching of glory undulations	E. A. Gislason and G. H. Kwei, 1967
$\left.\begin{matrix}K\\Cs\end{matrix}\right\} + TBr$	$\sigma_R(\theta)$	Radiosotope detection	L. R. Martin and J. L. Kinsey, 1967
CsCl + KI	$\sigma_R(\theta) + \sigma(\theta)$	Preliminary results. Velocity anal. products.	W. B. Miller et al., 1967
$Cs + \left\{\begin{matrix}TlCl\\TlI\end{matrix}\right.$	$\sigma_R(\theta)$	Preliminary results.	G. A. Fisk et al., 1967
$\left.\begin{matrix}K\\Rb\\Cs\end{matrix}\right\} + Cl_2$	$\sigma_R(\theta)$	Thermal energy range	R. Grice and P. B. Empedocles, 1968
$Li + \left\{\begin{matrix}HHal\\MHal_2\end{matrix}\right.$	$\sigma_{R_{tot}}(E)$	Thermal energy range	R. K. B. Helbing and E. W. Rothe, 1968
$K + CH_3I$	$\sigma_{R_{tot}}$	6–1,000 eV, static gas target	R. J. Cross and C. J. Malerich, 1968
$N_2^{\dagger} + Na$		$N_2^{\dagger}$ vibrationally excited, $n \approx 8$. Total cross-section for energy transfer $\rightarrow N_2 + Na$ from emission of resonance radiation.	J. E. Mentall et al., 1967

System	Technique/measurements		Reference
Cs, K, Na + various halides	$\sigma_R(\theta)$, $\sigma(\theta)$	Inhomogeneous magnetic field in front of detector	R. J. Gordon et al., 1968
K, Rb, Cs + various organic and inorganic halides	$\sigma_R(\theta)$	Thermal energy range	K. R. Wilson and D. R. Herschbach, 1968
K, Rb + CH_3I	$\sigma_R(\theta)$	At fixed θ. CH_3I velocity and orientation selected with 6-pole field	R. J. Beuhler and R. B. Bernstein, 1969
$Cl + Br_2$ etc.	$\sigma_R(\theta)$	Mass spec./electron bombardment detector	D. Beck et al., 1968; Y. T. Lee et al., 1968
K + Me_3CBr, $SiCl_4$, Hal_2, ICl	$\sigma(\theta)$	Pt. detector. Out of plane configuration. Velocity sel. K beam.	E. F. Greene et al., 1969
$Cs + Br_2$	$\sigma_{ionsn}(E)$	Velocity dependence of total ionisation cross-section in energy range 1.5–16.5 eV	R. K. Helbing and E. W. Rothe, 1969
K, Rb, Cs + ICl, IBr	$\sigma_R(\theta)$	Thermal energy range	G. H. Kwei and D. R. Herschbach, 1969
$Na + O_2$	$\sigma_{ionsn}(\theta)$	Merging beams. Energy range 5–25 eV. Retarding potential curves of Na^+ current	R. H. Neynaber et al., 1969

$Li + \begin{cases} Cl \\ ICl \\ Br_2 \\ SnCl_4 \\ PCl_3 \end{cases}$	$\sigma_R(\theta)$	Inhomogeneous magnetic field in front of detector. Oxygenated W detector.	D. D. Parrish and R. R. Herm, 1969
$\left.\begin{matrix} H_2^* \\ D_2^* \end{matrix}\right\}$ + M, RH_2		Relative product ion abundancies. Low angular resolution. Electron bombardment source	H. Hotop, et al., 1969
$Na + \begin{cases} CH_3I \\ Br_2 \\ ICl \end{cases}$	$\sigma_R(\theta)$	Thermal energy range.	J. H. Birely et al., 1969
$\left.\begin{matrix} K \\ Na \\ Li \end{matrix}\right\} + Br_2$	$\sigma_{R\,tot}(\theta)$	Static gas target. Sputter source of fast alkali.	A. P. M. Baede et al, 1969
$K + CF_3I$	$\sigma_R(\theta)$	Parallel and anti-parallel molecular alignment. KI product?	P. R. Brooks, 1969
$K + I_2$	$\sigma(\theta)$	Small angle scattering, high resolution. Velocity sel. K.	M. A. D. Fluendy et al., 1970
$Cl + Br_2$	$\sigma_R(\theta)$	Low resolution. Velocity analysis of product. Unselected beams. Mass spec. analysis.	N. C. Blais and J. B. Cross, 1970
$K + RI$	$\sigma_R(\theta)$	In and out-of-plane measurements. Bimodal surface detection.	G. H. Kwei et al., 1970
$D + H_2$	$\sigma_R(\theta)$	Product velocity anal. by time of flight. Mass. spec. det.	J. Geddes et al., 1970

System	Technique/measurements		Reference
$K + \begin{cases} C_6H_{12} \\ CCl_4 \\ SiCl_4 \\ SnCl_4 \\ Cl_2 \\ Br_2 \end{cases}$	$\sigma_R(\theta)$	Sputter source, 0.5–12 eV. Cool ribbon det. Pulsed K beam. Time of flight anal.	V. Kempter et al., 1970
$F + D_2 \rightarrow FD + D$	$\sigma_R(\theta)$	Angular distribution of product in specific vibrational states.	T. P. Schafer et al., 1970
$Rb + Br_2$	$\sigma_R(\theta)$	Rotational state distribution of RbBr product by quadrupole analyser.	R. Grice et al., 1970
$K + \begin{cases} HBr \\ DBr \end{cases}$	$\sigma_R(\theta)$	Velocity analysis of scattered product.	K. T. Gillen et al., 1969
$K + \begin{cases} NO_2 \\ CH_3NO_2 \end{cases}$	$\sigma_R(\theta)$	Magnetic and electric deflection analysis of product in order to elucidate structure.	R. R. Herm and D. R. Herschbach, 1970
$K + \begin{cases} HCl \\ Cl_2 \\ N_2 \\ CO \\ NO \\ O_2 \end{cases}$	σ_{ionsn}	Cross sections for ionisation of K and excitation to 4^2P state. Charge transfer beam source	K. Lacmann and D. R. Herschbach, 1970
$K + I_2$	$\sigma_R(\theta, v')$ $\sigma(\theta, v')$	Thermal energy range. Differential surface detection of KI and K, coupled with velocity selection and analysis	K. T. Gillen et al., 1971

$\left.\begin{matrix}H\\D\end{matrix}\right\}+\begin{cases}K_2\\Rb_2\\Cs_2\end{cases}$	$\sigma_R(\theta)$	M, M_2 and MH signals separated by kinematic arguments M_2 from nozzle source.	Y. T. Lee et al., 1971
$Cs + SF_6$		Vibrational temperature of CsF measured from vibrational fine structure of flop-in resonance spectrum. A fixed angle expt.	S. M. Freund et al., 1971
$Cl + \begin{cases}Na_2\\K_2\end{cases}$		Fixed angle observation of Na and K resonance radiation. Estimation of total reaction cross-section.	W. S. Struve et al., 1971
$Li + \begin{cases}NO_2\\CH_3NO_2\\SF_6\\CCl_4\\CH_3I\end{cases}$	$\sigma_R(\theta)$	Magnetic state deflection as in Parrish 1969	D. D. Parrish and R. R. Herm, 1971
$Cs + \begin{cases}SF_6\\SF_4\end{cases}$		As in Freeman 1971. Vibrational temp. of CsF product.	H. G. Bennewitz et al., 1971
$K + HCl$	$\sigma_R(\theta)$	HCl vibrationally pumped with resonant laser radiation. Enhancement of reaction cross-section	T. J. Odirone et al., 1971
$\left.\begin{matrix}Na\\Na^+\\K\\K^+\end{matrix}\right\} + H_2$		Inelastic back scattering, $\theta > 175°$ TOF analysis.	P. F. Dittner and S. Datz, 1971
$K + CH_3I$	$\sigma_R(E)$	Integration of $\sigma_R(\theta)$ in energy range 0.1–1 eV.	M. E. Gersh and R. B. Bernstein, 1971, 1972

System	Technique/measurements		Reference
K, Cs + {RHal, $RHal_2$}	$\sigma_R(\theta)$	As in Kwei, 1969. Unsaturated and aromatic halides	E. A. Entemann and G. H. Kwei, 1971
K, Rb, Cs + {CCl_4, CH_3I, $SnCl_4$}	$\sigma(\theta)$	Optical potential analysis	R. M. Harris and J. F. Wilson, 1971
Na + {SO_2, NO_2}	$\sigma_{excitn}(E)$	In 1–30 eV energy range for emission of the Na D-line. App. as in Kempter, 1970	P. R. LeBreton et al., 1971
Cl + I_2	$\sigma_R(\theta)$	Velocity selector in front of detector, keeps reactants from detector surface. Corrects Lee, 1968.	J. B. Cross and N. C. Blais, 1971
D + {Cl_2, Br_2, I_2, ICl, IBr}	$\sigma_R(\theta,v)$	Thermal dissociation and discharge source.	J. D. McDonald et al., 1972
Ba, Sr + NO_2		Polarization of visible emission from electronically excited MO. Single beam/scattering gas confign, fixed energy.	C. D. Jonah et al., 1972
K_2 + {Br_2, ICl, IBr, BrCN}	$\sigma_R(\theta)$	Dimer source as in Lee, 1971. Differential detection of both K and KX products.	P. B. Foreman et al., 1972; J. C. Whitehead et al., 1972

8.2 Reactive differential cross-sections and the LAB→CM transformation

The procedure adopted in interpreting reactive scattering data depends upon the type of information e.g. $\sigma(\theta)$ $\sigma_R(\theta,E)$ etc. As in elastic scattering, the detail available in respect to resolution and range of experimental parameters explored will determine whether deductive argument based on gross features of the scattering is used or some more quantitative but laborious fitting process undertaken. In the latter case there is an important distinction between the reactive and elastic fields. In the latter it is now possible, in favourable circumstances, to deduce the potential by directly unfolding the data. No model potential is required. In interpreting reactive data, whether detailed rate constants or beam results, one must decide at the outset if detailed trajectory calculations with an assumed potential are appropriate, or whether a statistical approach is adopted. Ultimately, both approaches are governed by the same multi-dimensional potential surface, but at least in the present stage of development a model is needed, not only of the potential but of the type of collision. This preliminary classification into direct and complex collisions is of interest in itself. In one sense there is an analogy here with elastic scattering; if the reduced energy in an elastic scattering experiment is so low that orbiting and quasi-bound states are encountered, it is not yet possible to unfold the potential directly, however good the experimental information and in some energy domains the interpretation would be in terms of energy levels and widths (see Section 6.14) rather than the detailed shape of the potential.

The first step in interpreting $\sigma_R(\theta)$ is the transformation of the LAB scattering pattern into the CM system of co-ordinates. By so doing, the trivial dependence of the LAB results on the motion of the centre of mass of the colliding pair is removed and results obtained with different beam geometries (e.g. out of plane measurements or angles of intersection other than 90°) should reduce to the same CM pattern (Fig. 8.2). The transformation depends upon the product velocity which, unlike the elastic case, cannot be deduced from the angle of scattering and the incident velocity. Ideally, a simultaneous measurement of either the product velocity or its internal energy together with the scattered intensity is needed. Until recently, beam intensities were not high enough to permit the product flux to be velocity analysed and two procedures were adopted to fix w'. In earlier work (G. H. Kwei and D. R. Herschbach, 1970) the extent of out of plane scattering was used in a rough estimate of w' (see Fig. 8.3); if w' is small the scattering is largely confined to the plane of the two incident beams. When possible, it is now customary to use an iterative procedure to build up an acceptable centre of mass

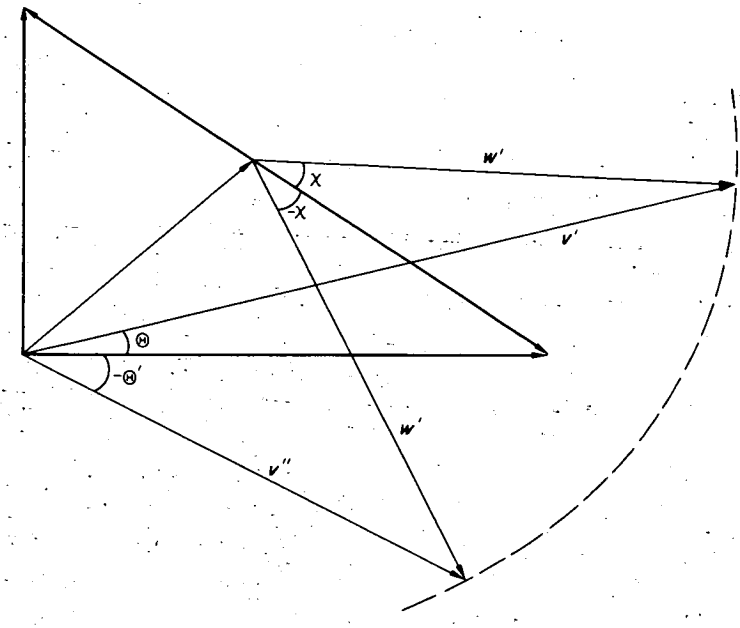

Fig. 8.2 Laboratory observations either side of the main beam must transform into a CM differential cross-section that is symmetrical about $\chi = 0$, even though $\sigma(\theta) \neq \sigma(-\theta)$. This serves to fix w', provided the scattered intensity at negative laboratory angles is not too small.

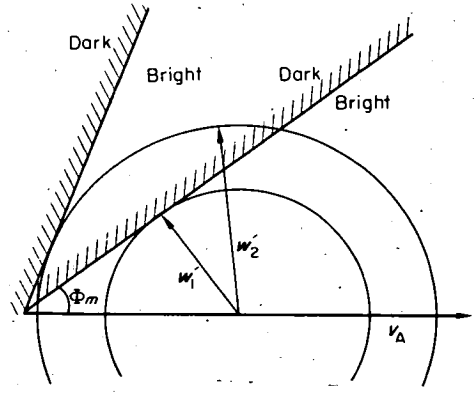

Fig. 8.3 Observation of out-of-plane scattering allows w' to be assigned once Φ_m is located. The larger w', the more extensive the out-of-plane scattering. The Newton diagram is viewed along v_B, with v_A forming the horizon.

distribution that is uniquely consistent with all the observed scattering. The reasoning behind the method is as follows; in favourable circumstances the laboratory angles corresponding to CM scattering through χ and $-\chi$ are well separated and w' can be adjusted until the scattering from one laboratory branch gives an identical CM differential cross-section to that deduced from the other branch, which is the required conclusion because we know that $\sigma_R(-\chi) = \sigma_R(\chi)$. Thus, in the case illustrated by Fig. 8.2, $w' > w$, scattering on either side of the main beam corresponds to scattering through positive and negative values of χ respectively. In the case $w' < v_{CM}$ a slow component in the scattered LAB signal is present due to scattering through some quite different CM angle, but it is usually found that $\sigma_R(\chi)$ is a fairly sharply peaked function and the slow component is much attenuated by the smallness of the associated differential cross-section. However, in Fig. 8.4, where $w' < w$, the two LAB angles corresponding to scattering through χ and $-\chi$ nearly overlap and laboratory measurements at any particular value of θ contain important contributions from both positive and negative values of χ. It would then be difficult to obtain an unambiguous choice of w'.

In principle, the observation of the angle of the edge effect can decide w'. However, in the cases most suited for observing this phenomenon ($w' << w$),

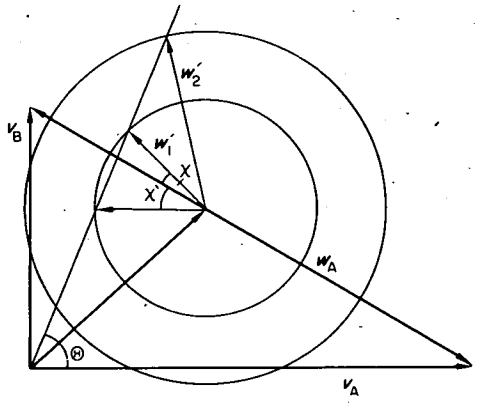

Fig. 8.4 Observation of scattering at θ does not allow w' or χ to be deduced. Two possible choices are shown. The observed scattering contains important contributions from particles scattered through the CM angles χ and χ' (assuming w_1' to be the true CM final velocity). Contrast this with the situation in Fig. 8.2 where only one value of χ contributes at a given angle of observation.

one edge occurs near the cross-beam position. Furthermore, the strong angular dependence of $\sigma_R(\chi)$ can mask the effect by causing a rapid fall-off in intensity before the edge is reached.

For any guessed value of w', the LAB→CM transformation can be performed either on the scattered signal or on the differential cross-section; in the latter case,

$$\sigma_R(\chi, w') = \sigma_R(\theta, v') \, J\left(\frac{\theta, \Phi}{\chi, \phi}\right) \tag{8.1}$$

where a primed velocity is that of a product. As for elastic scattering (Section 2.4), the Jacobian for a particular exit channel can be written* (K. T. Gillen et al, 1971)

$$J\left(\frac{\theta, \Phi}{\chi, \phi}\right) = \left(\frac{v'}{w'}\right)^2 \cos\alpha \tag{8.2}$$

where α is the angle between v' and w'. For strongly exothermic reactions w', $v' > v_{CM}$ and α remains close to unity for a large range of scattering angles. v'/w' then tends to increase with increasing CM angle of scattering and the general effect of the Jacobian in Equation 8.1 is to enhance the ratio $\sigma(\chi)/\sigma(\theta)$ at larger CM scattering angles.

After the transformation (Equation 8.1) to CM co-ordinates, the results are best displayed in a polar diagram where $I(\chi)$ or $\sigma(\chi)$ is represented by the point (R,χ) and the radius R is proportional to the observed quantity. Ideally, a contour map can be built up, each contour corresponding to a quantum state of the product.

An important bonus from making the LAB→CM transformation is that the total reaction cross-section can then be estimated in favourable circumstances from laboratory observations confined to the plane of the two beams. The key step is recognizing that in the CM frame the scattered intensity has axial symmetry about the relative velocity vector w_{AB} (this is only true with unorientated target molecules). Exactly the same symmetry obtains in elastic scattering, with the difference that in reactive scattering the motion in individual collisions is not confined to a plane. This cylindrical symmetry of $\sigma(\chi,\phi)$ is in strong contrast to the asymmetry of $\sigma(\theta,\Phi)$ with respect to the plane defined by the two incident beams; the only symmetry possessed by

* See appendix A, Chapter 2, for situations in which the cos α factor is not appropriate

the scattering in the laboratory is that $\sigma(\theta,\Phi) = \sigma(\theta,-\Phi)$. Using the CM symmetry we can obtain the total cross-section from $\sigma_R(\chi,\ \phi = 0)$ by integrating immediately over ϕ and then over χ so that

$$\sigma_{R\,\mathrm{tot}} = 2\pi \int_0^{\pi} \sigma_R(\chi) \sin \chi \, d\chi \tag{8.3}$$

in which the scattered flux is integrated over the surface of a sphere surrounding the centre of mass of the colliding pair. Thus, we do not need to make any out-of-plane measurements in the laboratory if the transformation to CM is performed. As with elastic scattering, absolute measurements are difficult – even more so in view of the fact that the scattered product has to be detected with the same efficiency as the main beam reactant. However, the energy dependence of the total reaction cross-section can be obtained quite reliably from Equation 8.3 while the uncertainty in the absolute value may amount to a factor of 2. There are, unfortunately, few other methods of measuring absolute reaction cross-sections (but see Section 8.3), although methods for absolute rate constants abound.

It was found that when the limited data on reactive scattering of alkali metals available in the mid 1960's was examined in this way that two types of behaviour could be distinguished. In those designated class I, the product was predominantly back scattered in the centre of mass and in class II forward scattered (i.e. the MX emerged in the same general laboratory direction as the incident alkali metal, the Newton diagram being roughly that of Fig. 8.5). A somewhat idealized version of these cases is illustrated in Fig. 8.6. Work in

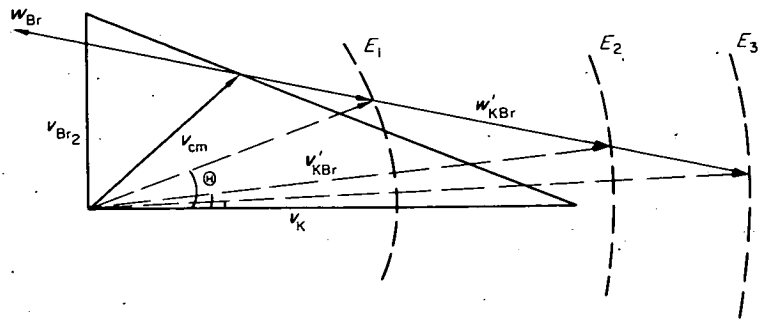

Fig. 8.5 Newton diagram for a stripping reaction, $K + Br_2 \rightarrow KBr + Br$. The product KBr appears at an angle Θ in the LAB which depends upon the energy partitioning, ΔE, the amount of energy transferred to translation of the products from the energy liberated. Three cases of increasing final relative kinetic energy are shown, leading to increased forward scattering.

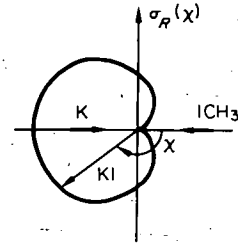

Fig. 8.6(i) Typical CM polar diagram of the reactive differential cross-section of a class I reaction. The KI vector is drawn proportional to the KI signal at χ.

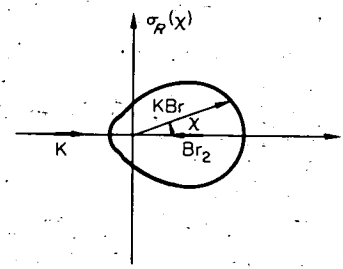

Fig. 8.6(ii) Typical CM polar diagram of the reactive differential cross-section of a type II reaction.

the last few years on a greater range of halogen containing compounds has produced evidence of a gradation in behaviour between these two classes even in the limited field of an alkali metal partner and in a sequence of reactions such as (R. J. Gordon et al, 1968)

$$Cs/Br_2 \ldots /CCl_4 \ldots /CHCl_3 \ldots /CH_3I$$

the peak in the scattered product intensity moves from $\sim 0°$ to $\sim 180°$ (CM).

A third and much less common type of scattering pattern (class III) has emerged from the work of Herschbach and his co-workers (W. B. Miller et al, 1967; G. A. Fisk et al, 1967; S. M. Freund et al, 1971) and is characterized by a CM product distribution symmetrical about 90°, often with strong peaking at 0° and 180°. This behaviour has been observed in the systems $Cs + SF_6$, $Cs + SF_4$ Cs + RbCl, Rb + CsCl, K + RbCl, Rb + KCl and Cs + TlCl (Fig. 8.7), though the LAB → CM transformation is not completely unambiguous yet. Inspite of the discovery of an increasing number of transitional cases that blurr this classification by means of the predominant angle of product scattering, the divisions remain useful ones because they have given rise to three important models of chemical reaction which would seem to have real validity as limiting cases. These are the recoil model associated with class I behaviour, stripping associated with class II and complex formation in class III. Estimates of total reaction cross-sections reinforce the division between class I and II behaviour in that, broadly, two

groups of values are found coinciding with these classes. The reactions of class I have small reaction cross-sections, barely larger than the gas kinetic cross-section i.e. $\lesssim 30$ Å^2, while reactions of class II exhibit large cross-sections, $\gtrsim 80$ Å^2. Further work has produced a range of $\sigma_{R\,tot}$ values from 300 Å^2 downwards and a good correlation has emerged in alkali metal reactions between the magnitude of $\sigma_{R\,tot}$ and the shift from forward to backward product scattering.

As we have already seen, total reaction cross-sections are difficult to estimate accurately, but in the field of alkali metal reactions additional support at least for the relative reaction cross-sections in a series of reactions comes from the sodium flame experiments of M. Polanyi (1932) which indicated reaction cross-sections considerably larger than the gas kinetic diameter for the reaction Na/Hal_2 and of the order of the gas kinetic diameter for the reaction Na/CH_3I. By following spectroscopically the decay of flash generated caesium atoms in I_2 vapour Davidovits and his co-workers (C. C. Brodhead, et al., 1969) have found the reaction cross-section to be $195 \pm 40°$ Å^2, a value close to that estimated from beam studies. The attenuation of elastic scattering, to be discussed in Section 8.3, confirms that the total reaction cross-section for these reactions of the alkyl halides is $\lesssim 40$ Å^2.

Some simple deductions follow from the facts so far presented. The reactions of class I, characterized by back-scattering of the alkali halide product largely along the relative velocity vector of the incoming alkali atom

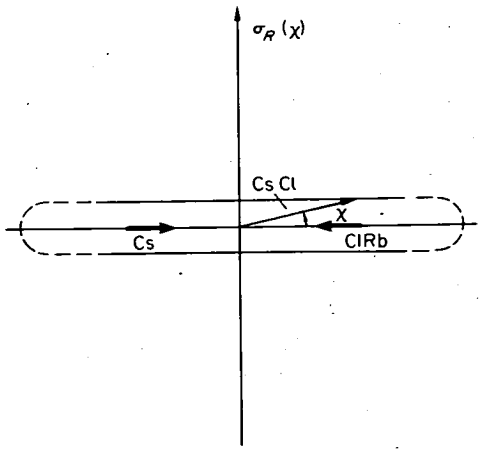

Fig. 8.7 Typical CM polar diagram of the reactive differential cross-section for a type III reaction. Note the symmetry about $\chi = 90°$ and compare with Fig. 8.6.

are of the simple recoil type. The alkali atom collides with the target in a nearly head-on fashion (hence the back-scattering) with an impact parameter not much greater than the equilibrium bond length of the K-X bond to be formed, the X-Y bond then breaks and the K-X bond forms as the products separate rapidly. The product back scattering is possibly accentuated by the mutual repulsion of the products.

The large cross-sections of class II reactions must be the result of the operation of either unusually strong intermolecular forces or of long range chemical forces. While the distinction is not a completely clear cut one, the two explanations might be as follows; in the first case the dispersion forces or other electrostatic forces draw in the approaching particles from large impact parameters to distances of closest approach comparable with equilibrium bond lengths, whereupon reaction follows. Alternatively, the intermolecular forces are of normal strength, but electron re-arrangement begins at distances much greater than normal bond lengths and so a larger bundle of trajectories than in class I lead to reaction. When the electron rearrangement begins, the inter-particle forces are no doubt much increased and the reaction proceeds to completion under their influence. For neutral-neutral reactions the second mechanism seems to be the more realistic for the simple reason that neither calculation nor total cross-section measurements indicate that C_6 values in class II reactants are uniformly greater than those in class I, or that the probable order of C_6 values (as estimated, for instance, from the molecular polarisability) parallels the order of reactivity within the class. For ion/molecule reactions, however, there is every indication that at low energies the dipole-induced dipole forces determine the often large reaction cross-sections which then approach the total cross-section in magnitude.

The picture that has emerged of class II reactions is based upon two simple models, the harpooning mechanism of J. L. Magee (1940), and the stripping model of nuclear reactions. As the two reactants approach, an electron is transferred from the alkali atom to the target molecule at distances R_c up to $\sim 9°$ A. Two ions are created by this harpooning and at thermal energies reaction follows with high probability, leading to a reaction cross-section equal to πR_c^2. At R_c the ionic potential surface crosses the atomic or covalent one, and the condition for this is to a first approximation given by

$$I - E_a - e^2/R_c = 0 \qquad (8.4)$$

where I is the ionization energy of the metal M, E_a is the electron affinity of the target molecule and e^2/R_c is the potential energy of the newly created dipole. In writing down this energy balance it is assumed that R_c is

sufficiently large for dispersion and polarizability terms to be negligible (i.e. $R_c \gtrsim 5$ A). The target molecules of class II reactions are characterized by consistently larger electron affinities than those of class I and which are of the right order of magnitude to account for the large reaction cross-sections. A more detailed evaluation of Equation 8.4 is made difficult by the following uncertainty in the model. If the electron transfer is rapid compared with the target vibrational motion, E_a must be interpreted as the vertical electron affinity; if, however, the electron transfer is gradual and the target atoms have time to adjust their positions to the changing electronic environment, then something like the adiabatic (e.g. equilibrium) electron affinity is required, which is the energy liberated when a molecule is converted into the anion in its equilibrium configuration – assuming a stable anion exists. The difference is appreciable numerically, and is illustrated schematically in Fig. 8.8. There has been found to be a good correlation between the electron capture coefficient and the magnitude of the total reaction cross-section in a whole sequence of Na flame reactions Na/I_2 ... Na/CH_3Cl. It is not certain that all these species have stable anions and the electron capture coefficient is then a complicated ratio of rate constants, but one may assume that the larger the electron

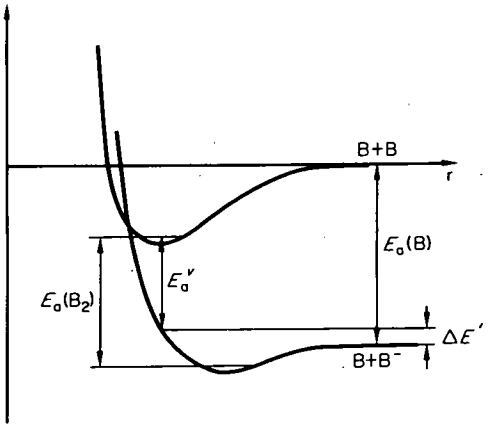

Fig. 8.8 The energetics of electron transfer. The equilibrium electron affinity of B_2 is $E_a(B_2)$ and that of B atom $E_a(B)$. The vertical electron affinity is E_a^v and if this value is used to determine the critical radius for harpooning, then an amount of energy $\Delta E'$ is released subsequent to electron transfer and can appear as either relative kinetic energy of the products or as internal excitation.

capture coefficient, the larger the cross-section for the process $e + AB \rightarrow A + B^-$, although no simple formula akin to Equation 8.4 can be written for R_c.

The harpooning model was originally developed to explain the larger cross-sections observed in the sodium flame experiments and without further elaboration it does not lead to the strong forward scattering revealed by beam experiments. The spectator stripping model was first applied to this phenomenon by Herschbach and, with some important modifications, still offers as good an interpretation as can be expected from a simple model. In essence, upon transferring the electron to the target molecule, the bond joining the reacting halogen atom to the rest of the molecule is severed and there is no further force acting between the detached halogen ion and the other fragment which looks on while the halogen atom is carried off. Although a strong Coulomb force operates between the newly formed anion and cation, the centre of mass of the MX product continues to move in the forward direction since the molecule experiences no repulsion by the spectator and predominantly forward scattering results. The model will be discussed in more detail when the experimental results on energy partitioning are discussed. At small impact parameters ($b \lesssim \sigma_{LJ}$) a collision between the newly formed products is unavoidable and will introduce some backscattering but the measure of these trajectories is small.

Type III reactions, in which $\sigma_R(\chi)$ is bipolar and symmetrically distributed about $\chi = \pi/2$ are thought to be due to the formation of a collision complex whose lifetime is greater than its rotational period ($\gtrsim 5 \times 10^{-12}$ s). That this will lead in some circumstances to strong peaking of the scattered intensity at $\chi = 0$ and 180° can be seen as follows. Suppose that the reaction is the transfer of excitation or charge between two structureless particles that do not possess intrinsic angular momentum. The conservation of angular momentum, in this case solely that arising from the relative motion, confines the motion to a plane (Fig. 8.9). The direction in which the products emerge is determined, at least classically, by the impact parameter and the relative kinetic energy. According to our definition of a long lived complex, at least one complete revolution has been performed and χ is greater than 360°. The complete scattering pattern is built up by superimposing many trajectories covering the range of b and E represented in the beam; if, now, χ is a sensitive function of these parameters as it generally will be when large forces are involved the particles are released in effectively random directions even in a classically deterministic situation. Furthermore, if the completely random distribution of the plane of motion of successive collisions is taken into account by superimposing a number of circularly symmetrical distributions

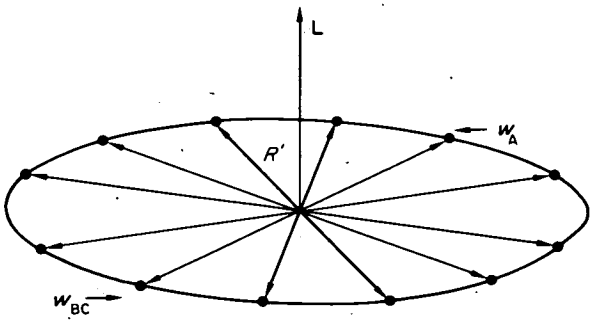

Fig. 8.9 A single long-lived collision. The reactants approach from left and right, form a collision complex from which the products are released in a direction indicated by the final relative position vector R'. The direction of R' is effectively random in the plane defined by constant relative angular momentum L.

about a common diameter that coincides with the initial relative velocity vector, we see a concentration of products emerging at the poles of the sphere generated by this rotation (Fig. 8.10). This uniform emission of product in the plane of motion has the results that the number of particles emerging between $\chi, \chi + d\chi$ and $\phi, \phi + d\phi$ per second is

$$dn = \frac{1}{2\pi^2} I_0 \sigma_{R\,tot}\, d\chi\, d\phi \tag{8.5}$$

where I_0 is the incident intensity. The differential cross-section is then found from

$$dn = I_0 \sigma_R(\chi,\phi) \sin\chi\, d\chi\, d\phi \tag{8.6}$$

to be

$$\sigma_R(\chi,\phi) = \sigma_{R\,tot}/(2\pi^2 \sin\chi) \tag{8.7}$$

If, now, the particles have an initial internal angular momentum j_i and a final j_f, the conservation of angular momentum **J** results in the asymptotic conditions (i.e. after the internal angular momentum has become frozen and is no longer coupled to L)

$$J = j_i + L_i = j_f + L_f, \tag{8.8}$$

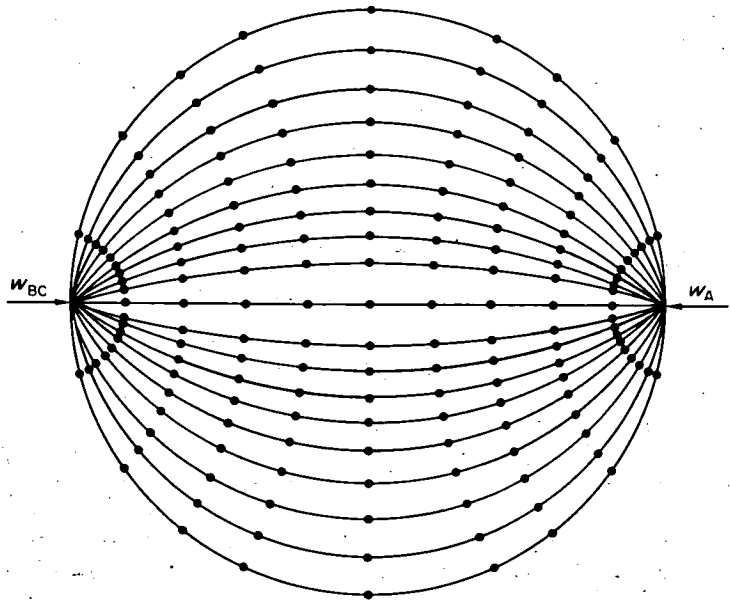

Fig. 8.10 The cumulative result of many collisions of the type shown in (i) is to superimpose all possible planes of motion of the complex consistent with L perpendicular to w. The product flux is thereby concentrated at the poles defined by the initial direction of approach.

so that $L_i \neq L_f$ and the exit plane of motion no longer co-incides with the incident plane. In processes with fairly large cross-sections at thermal energies and above, J_i is generally small compared with L_i so that

$$J \approx L_i = L_f + j_f$$

a range of j_f values in the product will thus produce a related distribution of L_f (Fig. 8.11). Superimposed upon this is the additional distribution arising from the undefined plane of the motion so that all orientations of the vector J in a plane perpendicular to the relative motion are equally probable in the sample. We might try to approximate the system at the point of break-up as either a diatomic molecule, the interparticle axis of which gives the direction of departure of the products (w'), or as a symmetric top in which w' lies along the principal axis. From either model, we can ask for the probability distribution of the orientation of the molecular axis and hence, if the disintegration rate is constant, of the angular distribution of the scattered products. Quantum mechanically, the diatomic system is characterized by a

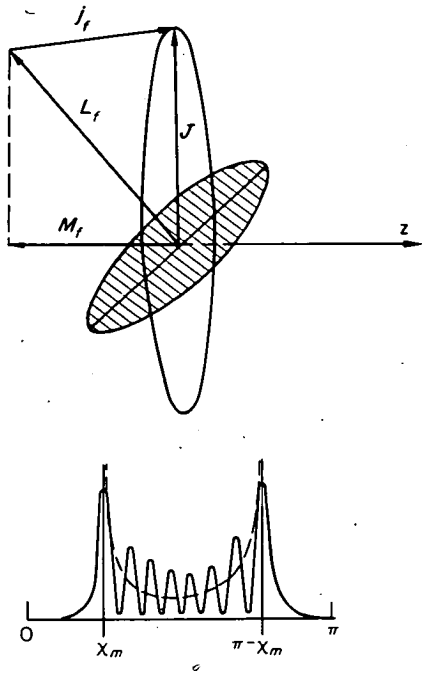

Fig. 8.11 (1) The final orbital angular momentum, L_f is the resultant of j_f and J. The plane of motion (shaded) of the two departing fragments is $\perp$ to L_f and χ is the polar angle between the axis of the diatomic and the initial direction of approach which defines the z-axis. In a sequence of collisions all directions of J in a plane perpendicular to z are equally likely and so the resultant L_f lie on the surface of a cone with constant z–component M_f.

(2) Quantum mechanically, this distribution of the plane of motion with constant M_f of the relative motion results in an angular distribution described by the spherical harmonic $Y_{L_fM_f}$, the envelope of which (dashed line) approximates the classical distribution, with χ ranging between χ_m and $\pi - \chi_m$.

total angular momentum quantum number L_f with a range of projection quantum numbers ranging from $-M_f$ to M_f as discussed above. The diatomic complex wave functions will be spherical harmonics so that the probability of product scattering at angle χ from a diatomic complex with quantum number L_f and M_f is $\mathscr{P}(\chi) = |\, Y_{L_fM_f}(\chi, \phi)\,|^2$. More usefully, this probability can be expressed in terms of the state of the scattered product j_f and m_j. From Fig. 11 it is clear that $M_f = m_j$, while if $j_f \ll L_f$ then $L_f \sim L_i$ (or more generally $L_f = (J^2 + j_f^2 - 2Jj_f \cos\beta)^{1/2}$). The distribution of product in this state is thus $|\, Y_{L_f,\, m_j}(\chi\, \phi)\,|^2$. A typical distribution is sketched in Fig. 8.11. In general the transition state is formed in a range of angular momentum and orientation states. The observed intensity (without state analysis) will then be the superposition of many such distributions, those with low m_j values peaking at angles near 0 and π while product with high m_j scatters near the equator, $\chi \sim \pi/2$. The net effect of such averaging is, in the limit of $j_f \sim L_f$, to wash out the bipolar form and produce a spherically isotropic distribution of product. A possible ansatz to describe this range of possibilities might be:

$$\mathscr{P}(\chi) = \sum_{L_f} \sum_{m_f} \mathscr{W}(L_f, M_f)\, |\, Y_{L_fM_f}(\chi, \phi)\,|^2 \qquad (8.9)$$

where $\mathscr{W}(L_f, M_f)$ is the probability of finding the state $(L_f M_f)$ in the ensemble. This formulation does not give us $\mathscr{W}(L_f M_f)$, which must come from some further assumption about the distribution of j_f. If, for instance, in the rather artificial case that j_f is isotropically distributed in direction and all values of M_f from $-j_f$ to j_f are equally probable, then if j_f is appreciably less than L_i we may neglect the correlation between L_f and M_f and write

$$\mathscr{W}(L_f M_f) = \frac{1}{2j_f + 1}; \quad L_f \sim L_i. \tag{8.10}$$

Taking these equations to define the model, and regarding M_f as continuously distributed and replacing $Y_{L_f M_f}$ by its asymptotic approximation (from Equation 8.18) with $K = 0$)

$$\begin{aligned} \mathscr{P}(\chi) &= \frac{1}{4\pi^2} \int_{-L_i \sin\chi}^{L_i \sin\chi} (L_i^2 \sin^2\chi - M_f^2)^{-\frac{1}{2}} \mathrm{d}M_f \\ &= \frac{1}{4\pi^2}; \quad L_i \sin\chi < j_f \\ &= \frac{1}{4\pi^2} \int_{-j_f}^{j_f} (L_i^2 \sin^2\chi - M_f^2)^{-\frac{1}{2}} \mathrm{d}M_f \\ &= \frac{1}{2\pi^2} \sin^{-1}(j_f / L_i \sin\chi); \quad L_i \sin\chi > j_f \end{aligned} \tag{8.11}$$

where the two ranges of the integral are caused by the restriction $M_f \leqslant j_f$. The result (Equation 8.11) is plotted in Fig. 8.12. The object of this simple model is to illustrate the smoothing out of the poles at $\chi = 0$ and π that occurs when product angular momentum is introduced. In the limit $j_f \gg L_i$ $(L_f \approx j_f)$ and again with all values of M_f equally likely, we can use the completeness relationship

$$\sum_{M_f=-L_f}^{L_f} |Y_{L_f M_f}(\chi, \phi)|^2 = (2L_f + 1)/4\pi \tag{8.12}$$

to show from Equation 8.9 that the distribution $\mathscr{P}(\chi)$ becomes independent of χ (i.e. the contribution of the second integral in Equation 8.11 vanishes).

A more realistic model would allow us to include some correlation between the direction of j_f and L_f, and more progress can be made if the

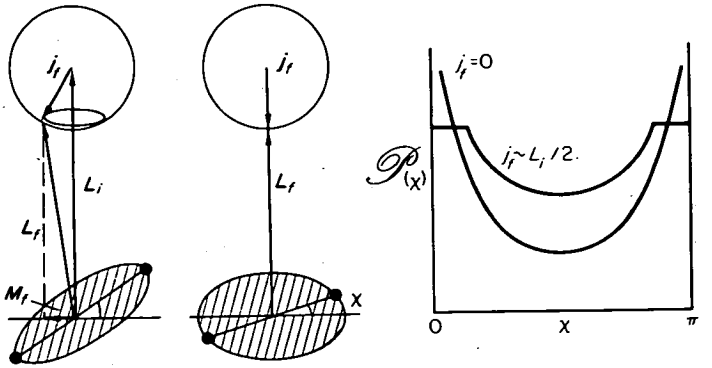

Fig. 8.12 The effect of various orientations of j_f with respect to L_i is to introduce a spread of M_f values. The superposition of the angular distribution $Y_{L_f M_f}(\chi)$ with a range of M_f values then destroys the poles in the probability distribution $\mathscr{P}(\chi)$.

complex on the point of break-up is regarded as a symmetric top. Quantum mechanically, a symmetric top is characterized by its total angular momentum J and the components of J on a space fixed axis, M and on the body fixed symmetry axis, K (see Fig. 8.13). If we know the distribution of J, of M and of K, the probability distribution of the symmetry axis orientation can be found from:

$$\mathscr{P}(\chi) = \sum_J \sum_{|M} \sum_K \mathscr{W}(J, M, K) \frac{(2J+1)}{8\pi^2} |\mathscr{D}^J_{MK}(\phi, \chi, \alpha)|^2 \qquad (8.13)$$

where the $\mathscr{D}^J_{MK}$ are the Wigner functions.

Once again, if the weights $\mathscr{W}(J_f M_f K)$ are independent of either M or K we can use the sum rule

$$\sum_{m \text{ or } m'=-j}^{j} |\mathscr{D}^j_{mm'}|^2 = 1 \qquad (8.14)$$

to show that the distribution of χ is isotropic, provided that $j_f \gg L_f$ so that a sufficient range of M_f states are available to complete the summation.

In the case $j_i = 0$ (and hence $J = L_i, M = 0$) the result:

$$\mathscr{D}^J_{OK}(\chi, \alpha) = \frac{4\pi}{2J+1} e^{-iK\alpha} Y_{LK}(\chi) \qquad (8.15)$$

yields

$$\mathscr{P}(\chi) = \sum_L \sum_K \mathscr{W}(L, K) |Y_{LK}(\chi)|^2. \qquad (8.16)$$

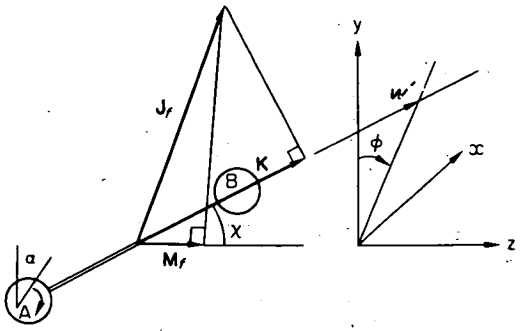

Fig. 8.13 The two product fragments, A and B, of a collision complex regarded as a symmetric top. The projection, K, of J_f on the symmetry axis AB is a constant of the motion and the orientation of AB is described by three angles (α, χ, ϕ). The direction of the symmetry axis at break-up (when K is frozen) coincides with the final relative velocity vector, w'.

A typical simple model of complex formation that would then enable $\mathscr{W}(L,K)$ to be extracted consists of two parts;

(i) All impact parameters up to b^* lead to complex formation and hence to a reactive channel. The upper limit to L in Equation 8.16 is thus given by $L^* = \mu v b^*$.

(ii) The distribution of K values for a given value of J is of the form

$$\mathscr{W}(K) = e^{-K^2/2K^{*2}}, \quad K \leqslant J \sin\chi. \tag{8.17}$$

($J \sin\chi$ being the maximum value of the component of J on w'). There are thus two parameters in the model, L^* and K^*. These may be fitted empirically to the observed $I(\chi)$, or deduced from a statistical mechanical analysis of the collision complex in its 'saddle point' configuration i.e. in the transition state of absolute reaction rate theory. The analysis is completed by substituting integration for the summations in Equations 8.16, with the asymptotic replacement for the smoothed $\mathscr{D}$ functions

$$|\mathscr{D}^J_{MK}(\phi,\chi,\alpha)|^2 \xrightarrow[J \gg 1]{} \pi^{-1}\,[J^2\sin^2\chi - M^2 - K^2 + 2MK\cos\chi]^{-\frac{1}{2}} \tag{8.18}$$

to yield the scattered intensity distribution

$$I(\chi) = 2\pi \int_0^{L^*} \mathscr{P}(\chi, L)\, L\, \mathrm{d}\, L. \tag{8.19}$$

The broad features of the model are summarized in Fig. 8.14 where $\sigma(\chi)$ is plotted for various values of the parameter $(L^*/2K^*)^2$. For $K^* = 0$, the problem reduces to that of the reaction of two point masses and Equation 8.7 holds; for $K^* \to \infty$ (i.e. all allowed values of K equally probable) the scattering is isotropic as required by Equation 8.14. Essentially the same angular plots are obtained from this crude statistical model when it is applied to rotationally inelastic scattering of atoms from diatomics (W. H. Miller, 1970).

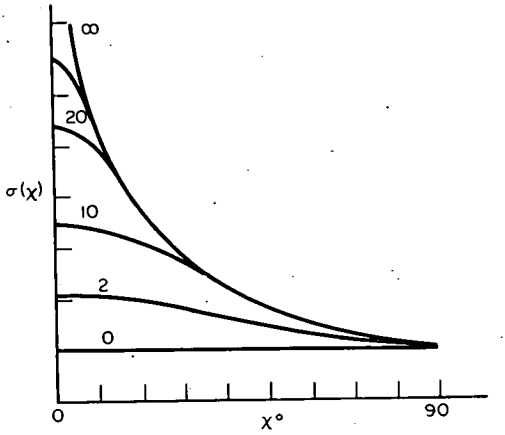

Fig. 8.14 The progressive disappearance of the poles in the product scattered intensity with increasing angular momentum of the products about the final interparticle vector. The various $\sigma(\chi)$ are scaled to unity at 90°, and are labelled with the value of $L^{*2}/2K^{*2}$. (From I. Halpern and V. M. Strutunskii, 1958.)

Besides the final partitioning of the angular momentum between internal and relative motion, another basic parameter of the problem of complex formation is the lifetime τ_c of the complex. So far, we have assumed that τ_c comfortably exceeds a rotational period of the complex, τ_r; but as τ_c diminishes, the symmetry between forward ($\chi = 0$) and back ($\chi = \pi$) scattering is destroyed. The attenuation of the back scattering is already pronounced for $\tau_c = \tau_r$ and finally when $\tau_c \ll \tau_r$, the very anisotropic distributions characteristic of direct reactions are obtained. This effect has probably been observed in the scattering of Cs from thallium halides where the results can be interpreted by $\tau_c/\tau_r \sim 0.8$ (G. A. Fisk et al., 1967).

The whole subject of the angular distribution of products from the breakup of complexes is of interest in nuclear fission theory and a development of some of the ideas of this section can be found in L. Wilets, 1964.

8.3 Elastic scattering in the presence of reaction

Because of the strength of the elastically scattered signal compared with that of the reaction products, measurement of the elastic differential cross-section in the presence of reaction is an attractive, if indirect method of investigating some parts of the potential surface governing reaction. The basic limitation of the technique is, of course, that it cannot probe the interaction of the products in the reactive exit channels; a separate elastic scattering experiment starting with the products would be necessary for this.

Even in the presence of reaction, elastic scattering is determined solely by the diagonal S-matrix elements. In the absence of inelastic or reactive exit channels, we found in Chapter 6 that, for the l^{th} partial wave associated with the n^{th} internal state of the system, the diagonal elements were:

$$S_{nl:nl} = e^{2\,i\eta_l} \tag{8.20}$$

and so the probability of emerging after the collision in the (n,l) exit channel is unity:

$$\mathscr{P}_{nl:nl} = |S_{nl:nl}|^2 = 1. \tag{8.21}$$

In the presence of new exit channels, the $\mathscr{P}_{nl:nl}$ will be less than unity so that probability can be conserved and in general we can write for the elastic channel

$$S_{nl:nl} = e^{-2\epsilon_l} e^{2i\eta_l}$$

so

$$\mathscr{P}_{nl:nl} = e^{-4\epsilon_l}. \tag{8.22}$$

From $\epsilon(l)$ and $\eta(l)$, the elastic scattered amplitude can be constructed:

$$f_n(\chi) = \frac{1}{2ik}\sum(2l+1)\,(S_{nl:nl} - 1)\,P_l(\cos\chi). \tag{8.23}$$

Just as a knowledge of the potential energy function in the elastic case enables the phase shift function to be calculated, so a complex or *optical* potential,

$$V_{\text{opt}}(R) = V(R) + iW(R) \tag{8.24}$$

yields a complex phase shift function and hence S matrix elements of the type (Equation 8.22). The solution of the radial wave equation with a complex potential splits it into coupled real and imaginary parts and is not straightforward; however, as might be hoped, it can be shown that the attenuation factor $\epsilon(l)$ is given to a good approximation by a Born type expression (R. E. Roberts and J. Ross, 1970):

$$\epsilon(l) = \left(\frac{\mu}{2}\right)^{\frac{1}{2}} \hbar^{-1} \int_R^{\infty} \frac{W(R)\mathrm{d}R}{\{E - V(R) - \hbar^2(l+\frac{1}{2})^2/2\mu R^2\}^{\frac{1}{2}}}. \qquad (8.25)$$

Although a knowledge of the optical potential that reproduces the observed elastic scattering could conveniently summarize a large body of scattering data and enable some of the transport properties in the presence of reaction to be calculated, it is hard to ascribe any physical reality to the details of $W(R)$. Instead, interest has so far centered on the absorption function $\epsilon(l)$ and this is extracted from the scattering data and interpreted in a semi-classical fashion parallel to that of $\eta(l)$. Thus, if the concept of a classical path is valid in the presence of reaction, i.e. if Equation 8.23 can be evaluated by the method of stationary phase in which $\epsilon(l)$ plays no part, then Equation 8.21 means that along the classical path with angular momentum l^{th} the probability of reaction is, from Equation 8.22, $\exp(-4\epsilon(l))$. The interpretation of $\sigma(\chi)$ is now as follows; the potential parameters of $V(R)$ are deduced from $\sigma(\chi)$ in the angular regions assumed to be unaffected by inelastic events. The unattenuated differential cross-section over the whole angular range is then deduced from this potential, and deviations from the observed scattering at any angle are ascribed to reaction on the classical trajectory leading to the observed deflection. More precisely, defining $\mathscr{P}(b)$ as the reaction probability on a trajectory with impact parameter b, we have

$$\mathscr{P}(b) = \frac{\sigma_{\text{calc}}(\chi(b)) - \sigma_{\text{obs}}(\chi(b))}{\sigma_{\text{calc}}(\chi(b))} \qquad (8.26)$$

The reactions that respond well to this analysis are those of small reaction cross-section in which the rainbow structure is intact (class I) and where $\mathscr{P}(b)$ is appreciable only where $\chi(b)$ is single valued. The observed $\sigma(\theta)$ for the K/HX reactions are of the form sketched in Fig. 8.15 and are characterized by a rainbow structure of apparently normal amplitude and a fairly pronounced step in the scattered intensity beyond the rainbow. It is typical of these reactions that $\sigma(\chi)$ *vs.* $E\chi$ plots at different energies are nearly superimposable, indicating that the step in $\sigma(\chi)$ at χ_c occurs on trajectories with

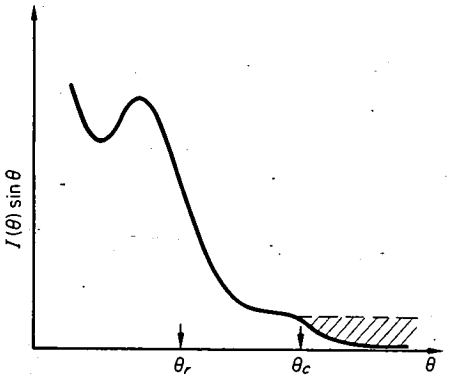

Fig. 8.15 Typical elastic scattering pattern in the presence of reaction confined to small impact parameters (Class I). The dashed line is the predicted behaviour from the rainbow structure and there is evidence for the onset of reaction at θ_c. The shaded area represents the number of particles lost per second by reaction.

the same value of the turning point R_c. Using Equation 8.22 and the deflection function $\chi(b)$ deduced from the Lennard-Jones parameters obtained from the rainbow angle, the reaction probability function, either $\mathscr{P}(b)$ or $\mathscr{P}(b/\sigma)$ if the estimation of σ is felt to be unreliable, is deduced. The general form is given in Figs. 8.16 and 8.17. Although the experimental and deductive uncertainty in $\mathscr{P}(b)$ is high, it seems clear that the reaction probability does not rise to unity even for head-on collisions, probably showing that the reaction cross-section has some orientation dependence, a conclusion in keeping with the classical trajectory calculations described in Section 8.7. Some additional weight is given to this method of interpretation of the elastic scattering from the observation that the potential energy at the distance of closest approach at the reaction threshold, $V(R_c)$, deduced from runs at different energies, is approximately constant. Similarly, the $\mathscr{P}(b)$ curves are nearly independent of the initial energy, at least over the rather limited velocity range so far explored.

There are at least two weaknesses in this analysis. The first is the uncertainty in the extrapolation of the hypothetical elastic scattering curve into regions of large deflections. The simple rainbow phenomenon is a poor guide to σ_{LJ} or any length parameter of the potential and extrapolation of

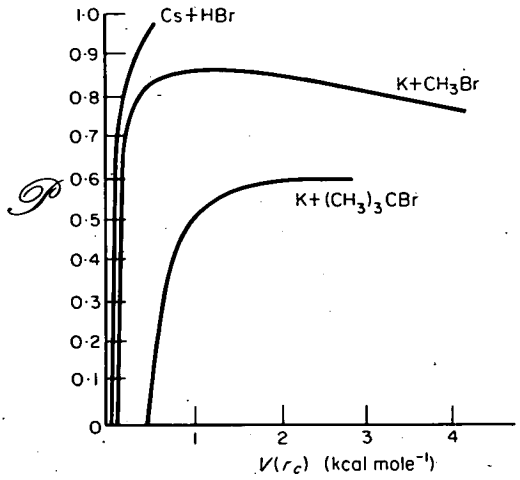

Fig. 8.16 The probability of reaction $\mathscr{P}$ vs potential energy at the distance of closest approach for various reactive systems. The relative initial kinetic energy in all cases is ~6 Kcal mole^{-1}. (Taken from E. F. Greene et al., 1969.)

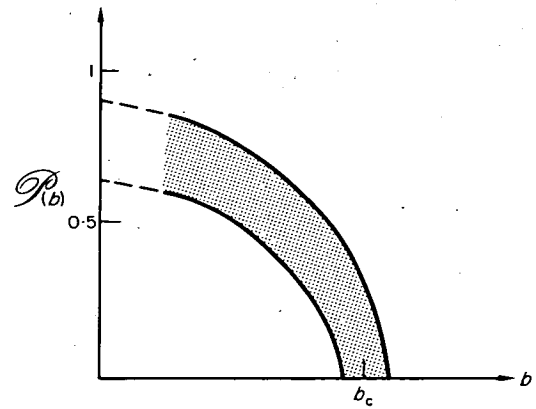

Fig. 8.17 The probability of reaction as a function of impact parameter for K + HX. The uncertainty in $\mathscr{P}(b)$ is indicated and the function has to be extrapolated to zero impact parameter because of the difficulty of measurement near $\chi = \pi$. The area under the curve, weighted by b is the total reaction cross-section (Equation 8.23).

$\sigma(\chi)$ beyond the rainbow is increasingly sensitive to the short range part of the potential. If the absolute total cross-section can be measured, $V(R)$ can be extrapolated more accurately (though only for some assumed form of the potential) but possibly the best procedure is to measure the supernumerary rainbow spacing from which the range of the potential can be deduced more accurately, (see Chapter 7 and below). A second objection to the above analysis is that inelastic events, mainly vibrational/rotational energy transfer near the reaction threshold, might smooth or distort the shape of the threshold step in $\sigma(\chi)$. This effect is probably present, but the range of trajectories affected, or the measure of the effect in influencing deduced values of $\sigma_{R\,\mathrm{tot}}$ is likely to be small unless the reaction cross-section itself becomes small, e.g. at higher energies.

When the elastic scattering in the presence of type II reactions is investigated, an entirely different pattern emerges. The rainbow is no longer seen and the scattered alkali atom intensity falls monotonically with increasing angle. The significance of this can best be appreciated by following the effect on the observed scattering pattern of an increasing value of the critical impact parameter for reaction, b_c. A typical deflection plot is shown in Fig. 8.18 and the 'black sphere' model assumes that all partial waves with an impact parameter less than b_c are absent from the scattered wave and so any interference structure in $\sigma(\chi)$ involving branches of the deflection function with $b \leqslant b_c$ will also be absent. Thus, for $b_c = b_1$ (case I, Fig. 8.18) the corresponding angle of deflection lies on the dark side of the rainbow and there are no semi-classical interfering branches at that angle; a simple step in $\sigma(\chi)$ is thus observed. As b_c increases such that, on the positive branch of the deflection function, $\chi_c < \chi_r$, the high frequency interference structure in $\sigma(\chi)$ is progressively attenuated until, when $b_c \approx b_0$, the forward glory is destroyed and with it the interference structure in the total cross-section. At this stage, (I), the supernumerary structure to the rainbow is still intact but as b_c increases still further this structure is damped out until, when $b_c \approx b_r$, it has disappeared (case II). Superimposed on all these cases is the small amplitude diffraction structure (not shown in Fig. 8.18) due to diffraction at the surface of the black sphere and thus of periodicity π/l_c (see Equation 6.13). This latter structure has not, so far, been observed and is easily suppressed by substituting a more gradual absorption function for the step function characteristic of the black sphere model. The relation between the absorption as a function of χ, $\mathscr{P}(\chi)$ and the probability of reaction as a function of distance of closest approach can be computed with the aid of Fig. 8.19 where $\chi(R^*)$ is plotted for several values of the reduced energy. It is generally at this point that the analysis stops.

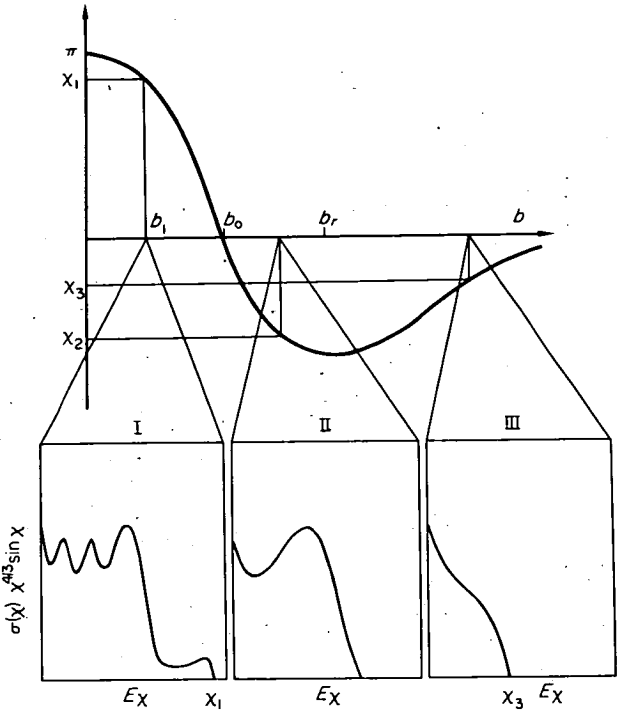

Fig. 8.18 The effect of a 'black sphere' type of optical potential on the elastic scattering pattern arising from a typical molecular deflection function. In case I, the rainbow and supernumerary structure is intact; in case II the rainbow only is present; in III ($b_c > b_r$) the scattered intensity falls monotonically to zero.

Since the total reaction cross-section is approximately πb_c^2, we expect reactions of large cross-section (class II) to exhibit a weakened or absent rainbow structure. This is borne out in practice by such systems as K/Br_2, K/CBr_4, K/Cl_2, $K/SnCl_4$ in which the rainbow is absent. Also in contrast to class I reactions, it has been observed (V. Kempter et al, 1970) that for systems K/Br_2, K/Cl_2 and $K/SnCl_4$ the $I(\chi)$-sin χ *vs* $E\chi$ plots at different energies are not superimposable but show a definite trend towards increased elastic scattering with energy in the range 1.5 – 6 eV (Fig. 8.20). This interesting behaviour, which is not observed for K/CCl_4 or $K/SiCl_4$, is tentatively ascribed to non-adiabatic electron behaviour. Thus, at the lowest energies, less than ~ 1.5 eV, the lower or ionic potential surface is exclusively followed. As the energy increases, the electron fails to jump on trajectories that take the system over the crossing point with sufficient speed – i.e. those

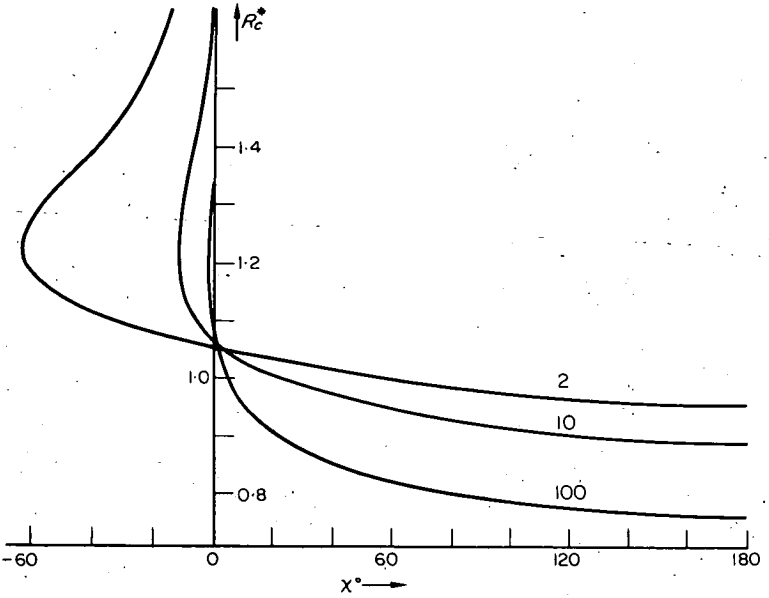

Fig. 8.19 Plot of reduced turning point versus deflection angle for a LJ (12:6) potential at various values of the reduced kinetic energy, E/ϵ.

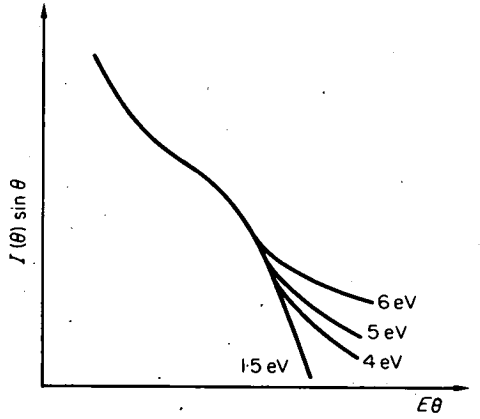

Fig. 8.20 Possible non-adiabatic behaviour in the scattering of superthermal potassium from a variety of halogen containing compounds in class II. The plots would be expected to be superimposable if only one potential (real or complex) were operating. Each curve is labelled with the energy of the alkali atom. (Adapted from V. Kempter et al., 1970.)

of smallest impact parameter – and elastic or possibly inelastic scattering from the upper potential surface is substituted for some of the reactive scattering. This new motion is sometimes described as *diabatic* and has been invoked to explain some of the small angle scattering of potassium from I_2 at 100 eV (B. Duchart et al, 1971) where it is probably quite widespread. At these high energies elastic scattering can also take place from the Coulomb potential because the relative velocity of the incoming K atom is now so high that, even though the electron may jump, the K atom may fail to pull away an I atom before the second crossing is reached. The electron will then return to the K atom and elastic scattering results. The probability of this happening is largely dependent on the mass ratio of M and X, the lighter X the more chemical reaction persists at high energies.

The whole question of non-adiabatic effects in reactive scattering has hardly been investigated. One of the most direct examples of the operation of the effect is in the phenomenon of auto-ionization. When a beam of alkali atoms collides with a halogen molecule or atom target, a considerable ionic flux is observed when the collision energy rises above the threshold for the process:

$$M + X_2 \longrightarrow M^+ + X_2^- \qquad + \Delta E_1$$

or

$$MX + A \longrightarrow M^+ + X^- + A + \Delta E_2 .$$

We will not discuss these experiments (see, for example A. P. M. Baede et al 1969, and F. P. Tully et al, 1971) except to remark that, ultimately, a unified description of high energy elastic scattering, reactive scattering and collisional ionization must be found, probably in terms of two potentials.

A useful bonus from the optical model of elastic scattering is that the total reaction cross-section can, in some cases, be obtained without recourse to absolute measurements. Thus, in terms of the reaction probability function $\mathscr{P}(b)$, the total reaction cross-section is given by

$$\sigma_R = 2\pi \int \mathscr{P}(b) b \, db. \tag{8.27}$$

Once again, if the estimate of σ_{LJ} is felt to be unreliable, Equation 8.23 can be expressed in the reduced form

$$\sigma_R / \sigma_{LJ}^2 = 2\pi \int \mathscr{P}(b^*) b^* \, db^*. \tag{8.28}$$

Values obtained in this way agree to within at least an order of magnitude with the directly integrated product flux (Section 8.2) and relative values in a sequence e.g. K/HCl, K/HBr, K/HI are sensible. Furthermore, in this route to σ_R the relative sensitivity of the detector to the product and to one of the reactants does not appear as a factor. Altogether, this is the most satisfactory route at present to σ_R for reactions of small-cross-section.

8.4 Energy dependence of the total cross-section

As we have seen, elastic scattering in the presence of reaction can be described by an optical potential which results in S-matrix elements of the form $S = e^{2i\eta_l} e^{-2\epsilon_l}$. The imaginary part of the phase shift, ϵ_l, represents the absorption of flux from the l^{th} incident channel. The total cross-section, as measured in the standard experiment described in Chapter 7, is found to be:

$$\sigma_{\text{tot}}(E) = \frac{2\pi}{k^2} \sum_l (1 - e^{-2\epsilon_l})(2l+1) + \frac{4\pi}{k^2} \sum_l (2l+1)\, e^{-2\epsilon_l} \sin^2 \eta_l \tag{8.29}$$

by applying the optical theorem to Equation 8.23. An elastic total cross-section can be defined in operational terms as the integrated elastic differential cross-section and so, integrating Equation 8.23,

$$\sigma_{el}(E) = \frac{4\pi}{k^2} \sum_l (2l+1)\, e^{-2\epsilon_l} \sin^2 \eta_l + \frac{\pi}{k^2} \sum_l (2l+1)(1 - e^{-2\epsilon_l})^2. \tag{8.30}$$

The total reaction cross-section is the difference between Equations 8.29 and 8.30:

$$\sigma_R(E) = \frac{\pi}{k^2} \sum_l (2l+1)(1 - e^{-4\epsilon_l}) \tag{8.31}$$

and so the largest possible ratio of σ_R to σ_{tot} is ½. Note that Equation 8.31 does not contain an l-dependent phase factor in the summation which is not, therefore, susceptible to the normal methods of stationary phase evaluation and the concept of interfering branches does not apply. For most functional forms of $\epsilon_l(E)$, then, $\sigma_R(E)$ will be a smooth function of E, perhaps exhibiting a single maximum, rather than an oscillatory function – in contrast to the behaviour of $\sigma_{\text{tot}}(E)$ and $\sigma_{el}(E)$. This does not, of course,

mean that the *differential* reaction cross-section is structureless; angular structure has, for instance, been observed in the ion production from $K + Hal_2$.

The l dependence of ϵ_l cannot at present be deduced from measurements of $\sigma(\chi)$ or $\sigma_{tot}(E)$ and is usually obtained from an assumed model of reaction in which an adjustable parameter is retained. The simplest such model, the black sphere, can readily be recast in terms of an optical potential or an absorption function. Thus, ϵ_l for a black sphere radius R_d is:

$$\begin{aligned} \epsilon_l &= \infty, \quad l \leqslant l_d \\ \epsilon_l &= 0, \quad l > l_d \end{aligned}; \quad l_d = \mu v R_d/\hbar \tag{8.32}$$

which represents the situation in which all particles approaching with an impact parameter R_d or less are absorbed. Referring to Equation 8.29, there are two types of behaviour that can arise according to whether l_d is greater or less than the value for the onset of random phase, l^*. We identify l^* by a Massey-Mohr criterion and so, if

$$l_d \leqslant l^* = k\left(\frac{2C_s f(s)}{\hbar w}\right)^{1/(s-1)}, \tag{8.33}$$

the random phase region encompasses the whole range of the partial wave summation in which ϵ_l is non-zero. In this random phase region, the $\sin^2\eta_l$ factor in Equation 8.29 averages to ½ and the contribution of partial waves with $l < l^*$ to $\sigma_{tot}(E)$ is independent of ϵ_l. $\sigma_{tot}(E)$ is therefore unchanged from the elastic case. However, the energy dependence of the two critical l values is different in the presence of intermolecular forces and they become equal at a velocity v_t given by:

$$v_t \approx 2C_s f(s)/(\hbar R_d^{s-1}). \tag{8.34}$$

At velocities higher than this value, reactive processes begin to increase the total cross-section above the purely elastic value. Finally, when $v \gg v_t$ and $e^{-2\epsilon_l}$ is still ~ 0, each partial wave contributes $2\pi\lambda^2(2l+1)$ to the total cross-section – the maximum possible value. The velocity dependence of σ_{tot} changes from the Massey-Mohr value of $-2/(s-1)$ for the energy exponent at low energies to become independent of velocity in the high energy limit.

The fate of the fine structure in $\sigma_{tot}(E)$ as the reactive part of the potential energy surface changes is more difficult to trace analytically since all regions of stationary phase must be included in the partial wave

summation. Qualitatively, the main features are as follows. For normal potentials we have seen that there are at least two contributions to the forward scattered amplitude in the incident channel, $f_i(0)$ and under semi-classical conditions we write

$$f_i(0) = f_i^{(1)}(0) + \sum_{\substack{\text{inner} \\ \text{branches}}} f_i^{(n)}(0). \qquad (8.35)$$

The first and largest contribution comes from those partial waves of large l value associated with phase shifts $\lesssim \pi/2$. The inner branch contributions come from those trajectories of smaller impact parameter with nearly zero deflection or multiples of 2π. In the elastic case these additional branches are responsible for the undulations in the energy dependence of the total cross-section. Reverting to classical language, molecules that contribute to the forward glory can be said to have penetrated to a distance of closest approach $R_0 \approx 1.05\sigma$ and constitute the leading inner branch, $f^{(2)}$. As we have seen, just as the rainbow is associated with a distance of closest approach that is almost independent of energy, so also is the inner trajectory of zero deflection (see Figs. 18.19 and 18.21). If any reactive or inelastic channels are open to these more penetrating collisions, the magnitude of the scattered elastic amplitude $f^{(2)}$ will be diminished and with it the amplitude of the undulations it causes in the total cross-section. This amplitude ranges between

$$\{|f^{(1)}| + |f^{(2)}|\}^2 \quad \text{and} \quad \{|f^{(1)}| - |f^{(2)}|\}^2.$$

Finally, when $f^{(2)}$ vanishes, the undulations disappear. If throughout the energy range only two branches contribute, the effect of a slowly increasing black sphere radius R_d can be followed from Fig. 8.21; note that we have slightly modified the primitive black sphere model from the discussion above to one in which the criterion for reaction depends upon the distance of closest approach rather than the impact parameter. The values of the reduced turning point on the zero deflection trajectory, R_0^*, slowly increase from 1 to 1.07 as the relative kinetic energy rises from 0 to ∞. Thus, a value of R_d^* less than unity will leave the undulatory structure of $\sigma_{tot}(E)$ intact. As R_d^* increases beyond unity, the undulations at low energies are first suppressed until with R_d^* somewhat less than 1.07 (the precise value depends upon the parameters) the highest energy undulation disappears, leaving $\sigma_{tot}(E)$ structureless across the whole energy range. In terms of the classification of the previous section (e.g. Fig. 8.18), the structure disappears across the whole energy range at the borderline between classes I and II of reactive systems.

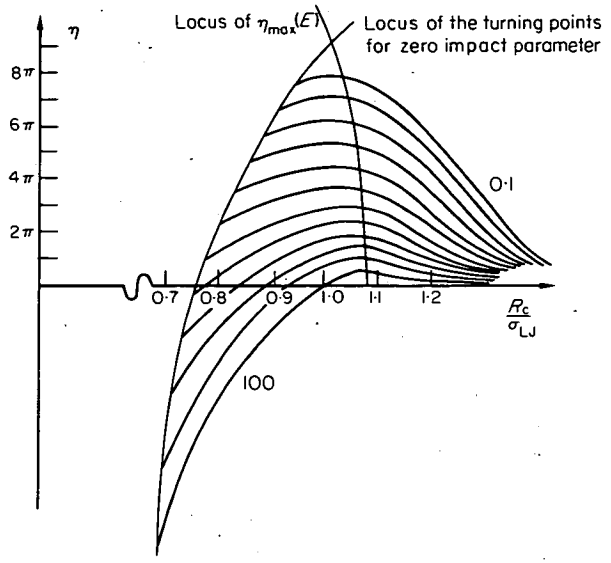

Fig. 8.21 A family of phase shift curves plotted against the reduced distance of closest approach and labelled with the reduced energy E/ϵ. The maximum in $\eta(R_c^*)$ for a given value of E^*, η_{max}, occurs on the forward glory trajectory. A maximum in the total cross-section occurs at the energies for which $\eta_{max}(E)$ passes through a multiple of π.

Because the range of R_d^* that separates the onset from the completion of quenching is so small it is likely in practice that cases of partial quenching due to reaction will be very rare.

There are several weaknesses in this primitive model, the major one being the neglect of inelastic events. We return to this later and discuss briefly the less important question of whether the introduction of a sharp cut-off in the partial wave summation, as in the black sphere model, will itself induce observable structure in the total cross-section of an interference nature. From Equation 8.29, the diffraction oscillatory structure can only come from the second term; as l_d changes, the magnitude of this term passes through a maximum every time $\eta(l_d)$ is equal to a multiple of $\pi/2$. Assuming for the purposes of an order of magnitude calculation that the phase shift varies linearly with l near $l = l_d$, we readily find that the difference between the maximum and minimum contributions of the $\sin^2\eta_l$ term in Equation 8.29 is given by

$$\Delta\sigma_{tot} \approx \frac{4\pi^2}{\eta'(l_d)} \frac{l_d}{k^2} \tag{8.36}$$

where $\eta'(l)$ is the gradient of the phase shift function. The ratio $\sigma_{tot}/\Delta\sigma_{tot}$ is thus of order $(1/\eta'(l)$ and is small unless $\eta'(l)$ is nearly zero, i.e. unless the critical impact parameter b_d is close to the glory value. This type of structure has not yet been observed.

Both chemical reaction and inelastic events can remove terms from the partial wave summation and the latter, especially rotational energy transfer, will probably have a rather less step-like dependence on the impact parameter than chemical reaction (a 'grey sphere' model) and could lead to a dampening of the structure of σ_{tot} across the complete energy range. The experimental $\mathscr{P}(b)$ functions, available from an optical analysis of the elastic scattering in the presence of reaction (Section 8.3), are found to be somewhat rounded by the imperfect angular resolution of the apparatus, but for some systems this function does approach step-like behaviour (e.g. for K + HX, Fig. 8.17, see also K/CCl_4, R. M. Harris and J. F. Wilson, 1971). In these systems, consistent application of the optical model would lead to almost complete or zero quenching respectively. However, partial quenching of the glory structure, especially at the low velocity end of the spectrum, is a common feature of molecular scattering, even in non-reactive systems. The favoured explanation here (W. D. Held et al., 1970 and Section 7.3) is an orientation dependent potential that effectively introduces a range of ϵ values into the collision dynamics. Experimentally, a small amount of quenching might well escape detection since the amplitude of the undulations in $\sigma_{tot}(E)$ depends upon the shape of the potential (in particular on the curvature of the potential near the minimum) and on the velocity and angular resolution.

Against this background, we now review the experimental data on $\sigma_{tot}(E)$ for reactive systems and this is summarized in Table 8.2 in which two relatively unreactive systems, Na/SF_6 and Li/SO_2, have also been included.

Total cross-section measurements are carried out with the lighter atoms Na and Li in order to improve resolution and the 'rainbow observed?' entry usually refers to the corresponding K/X system. There is a fairly clear cut division between complete and partial quenching that follows the division between class I and II reactions. Thus, for collisions involving the halogens, the Lennard-Jones parameter σ_{LJ} is estimated to be 4–5 Å, which is considerably smaller than the harpooning radius that is deduced from the magnitude of σ_R. It is thus entirely to be expected that the forward glory should be suppressed by reaction in class II. None of the molecules listed departs very much from spherical symmetry and thus should show only partial quenching of the glory structure due to shape effects, although the case of $Na/C(CH_3)_4$ (H. L. Kramer and P. R. Le Breton, 1967) which exhibits complete quenching may not be the sole exception to this rule. This partial

Table 8.2

System	Rainbow Observed?	Quenching	Reference
Na/CBr_4	no	complete	E. A. Gislason and G. H. Kwei, 1967
$/Br_2$	no	complete	
$/CCl_4$	yes	complete	
$/CH_3I$	yes	complete	
$/SiCl_4$	(yes)	complete	
$/SF_6$	yes	none	
Li/Br_2	no	complete	R. K. B. Helbing and E. W. Rothe, 1968
$/Cl_2$	no	complete	
/ICl	no	complete	
/HI,HBr	yes	partial	
/DCl,HF	yes	partial	
$/CH_3I$	yes	complete	E. W. Rothe et al., 1970
$/CH_3Br$	yes	complete	
$/SO_2$		complete	
$/CCl_4$	yes	almost none	

quenching is probably exhibited by the hydrogen halide reactions in class I where, because of the angular term of P_2 symmetry in the atom/molecule potential, rotational transitions may be responsible for the quenching. In the system Na/CCl_4, the critical distance of closest approach is estimated to be $\sim 0.90\sigma_{LJ}$ and thus no quenching through reaction or through asymmetry in the potential would be expected. The pairs methyl iodide/Li and methyl bromide/Li are borderline cases. The opacity function $\mathscr{P}(b)$ (R. M. Harris and J. F. Wilson, 1971) for the methyl halides are 'greyer' than for the hydrogen halides in the sense that some elastic scattering occurs at all impact parameters (probably due to steric factors). The transition region of the grey sphere extends from values of the reduced distance of closest approach of ~ 0.8 to ~ 1.2. Energy analysis of the elastic scattering in the presence of reaction is just beginning to reveal the importance of inelastic events in fairly hard collisions with $R_c^* \sim 1$ and it is probable that the virtually complete quenching of the structure in $\sigma_{tot}(E)$ that is observed for the alkali halide systems is due to both reactive and inelastic events. The case of Li/SO_2 is interesting in relation to the role of complex formation as a quenching mechanism. Release from a complex takes place through many inelastic channels and as far as elastic scattering is concerned, the target is essentially a black sphere with a cross-section equal to that for complex formation. For K/SO_2 this cross-section is estimated to be $\sim 350\,A^2$ and although the potential parameters are uncertain, 'normal' values would lead to a glory

impact parameter of between 3 and 5 Å – well below the radius for complex formation and so leading to the suppression of the glory undulations.

It follows from the above interpretation of the results for the hydrogen and methyl halides that inelastic events can quench the glory branch of the deflection function and yet have died out at larger impact parameters associated with the rainbow angle, for this feature is observed to be intact in all these systems.

The fairly common observation that the highest energy undulations in $\sigma_{tot}(E)$ for both reactive and non-reactive systems are the least quenched is possibly indicative of an orientation dependent well depth of the potential. Thus, for a given change in σ_{LJ}, the lower velocity peaks in $\sigma_{tot}(E)$ are more displaced relative to the local spacing than the higher energy ones, essentially through the operation of Equation 7.11. In a standard scattering experiment the observed beam attenuation is the average over all molecular orientations and so there is a progressive destruction of the lower energy peaks. Total cross-section measurements from orientated target molecules might be helpful here.

To summarise, the observation of glory quenching in the total cross-section only indicates that those particles that would have been elastically scattered in the forward direction on the inner branch of the deflection function have been removed by some process or that a rather anisotropic potential is operating. Since an anisotropic potential implies rotational energy transfer, the two effects are linked. The operation of chemical reaction is only unambiguous in reactions of type II where both the glory structure and the rainbow are absent.

8.5 Energy partitioning among reaction products

In direct reactions, i.e. those not proceeding through a long-lived complex, the energy and angular momentum partitioning between relative and internal motion of the products is very sensitive to the nature of the potential energy surface. In contrast, reactions involving an intermediate complex tend to conform, subject to angular momentum constraints, to the equipartition rule with the exoergicity shared equally among all the active degrees of freedom of the complex.

Experimentally, the program is a formidable one. For the simplest class of reaction, $A + BC \rightarrow AB + C$, a velocity analysis of one of the products together with a vibrational or rotational analysis of the diatomic product is required for a complete assignment of the energy liberated. In practice there

are three levels of sophistication in beam experiments:

(I) *'Kinematic' analysis*: no velocity or state analysis of the products is carried out, but a final CM velocity and angular distribution of assumed analytical form is derived that fits the observed LAB scattering.

(II) *Product velocity analysis only.* $\sigma_R(\theta, v)$ is measured over as wide an angular range as possible, generally $\lesssim 120°$ in the LAB. Sometimes, for reasons of intensity, the velocity profile at a fixed angle of observation is scanned and this velocity distribution assumed to hold at all angles. That is, recalling the definition in the CM co-ordinate system:

$\sigma_R^{(i)}(\chi, v_i)$ = number of product particles i scattered between χ, $\chi + d\chi$ and with velocity between w, $w + dw$ per second per unit reactant flux

the reaction cross-section is assumed to be factorisable thus:

$$\sigma_R^{(i)}(\chi, v_i) = \sigma_R^{(i)}(\chi) f^{(i)}(v). \tag{8.37}$$

The number of particles transported in to $d\chi$ with energy between E and $E + dE$ is related to the above cross-section by:

$$\sigma_R^{(i)}(\chi, E_i)dE_i = \sigma_R^{(i)}(\chi, v_i)dv_i$$

and so

$$\sigma_R^{(i)}(\chi, E_i) = \frac{1}{mv_i} \sigma_R^{(i)}(\chi, v_i). \tag{8.38}$$

This latter formula transforms between the differential cross-sections measured by energy analysis and those obtained by velocity analysis. The transformation is also a useful one when comparing beam measurements with the results of chemiluminescence studies which yield information about the distribution of products among energy levels.

(III) *Complete energy analysis.* In thermal energy scattering, the electronic state of the products is generally certain, leaving the translation and vibration/rotation energy assignment to be made. If the product is highly polar, inhomogeneous electric fields (see Chapter 4) can be used to focus or deflect low rotational states so that the relative population of specific rotational states can be obtained; more usually, for highly rotationally excited states, a rotational temperature can be obtained.

The vibrational-rotation distribution of the CsF formed in the reaction

$$Cs + SF_6 \longrightarrow CsF + SF_5$$

has also been measured (S. M. Freund et al., 1971). The CsF was analysed by a flop-in molecular beam resonance technique in which transitions of the type $njm \rightarrow njm'$ (Stark splitting) were observed. Since the moment of inertia and hence the resonant frequency for the transition varies with the vibrational quantum number n, the relative population of several vibrational states could be measured. The method is so far only applicable to highly polar diatomic products.

Beam data with state analysis of a product is still so meagre that it is best augmented for interpretative purposes by results on energy partitioning obtained by other techniques. These are basically spectroscopic and comprise:

(i) *Flash photolysis*, yielding the vibration rotation distribution of the molecular product but no angular information. A very versatile technique with regard to the number of reactions that can be studied, especially those involving very short lived species.

(ii) *Infra-red chemiluminescence*, again yielding the vibration-rotation state distribution of the product without angular information.

In neither of these methods is there selection of the initial translational or internal energy. With care, an average of absolute rate constants for the processes

$$AB(n,j) + C \longrightarrow A + BC(n',j')$$

can be obtained in which the true detailed rate constants $k_{nj}^{n'j'}(T)$ are appropriately weighted by the initial distribution of n and j. Then, if the functional form of $k(T)$ can be measured or assumed (S. H. Lin and H. Eyring, 1971), absolute reaction cross-sections with the same initial state averaging can in principle be obtained from the Laplace transform of $k(T)$:

$$E\langle \sigma_{nj}^{n'j'}(E)\rangle_j = \frac{1}{2\pi i}\int_{\gamma-i\infty}^{\gamma+i\infty} \langle k_{nj}^{n'j'}(\beta)\rangle_j \, e^{\beta E}\sqrt{\pi\mu/8}\,\beta^{-3/2}\,d\beta$$

where $\beta = 1/kT$ and Maxwell-Boltzmann translational energy distribution is assumed to hold during the measurement of $k(T)$. The integration of reactive

differential cross-sections with energy analysis yields a total cross-section for scattering into a final relative kinetic energy range dE. If both the energy density of final internal states and the partitioning of the energy between n and j is known, $\sigma_R(E)$ can be transformed into the total cross-section for scattering into a range $dndj$ of internal states (see Fig. 8.1). As yet, this complete tie up between the results of kinetic spectroscopy and reactive scattering with translational energy analysis remains to be made.

Rather than review the results from neutral beam work in isolation, the energy partitioning for a sample of reactions of the type A + BC → AB + C, A + BCD → AB + CD and A + BCD → ABC + D, whether or not investigated by beam techniques, will be discussed together. Collisionally induced dissociation reactions, A + BC → A + B + C are not included, though they have been observed in ion/neutral beam work. The results to be discussed are summarized in Table 8.3, which includes all the neutral beam work utilizing energy analysis of the scattered products up till 1972.

In all cases at least 25 per cent of the total available energy (exoergicity + collision energy) is converted into internal energy of the products. In stripping reactions involving the alkali metals and the halogens most of the available energy appears as vibrational excitation of the product, their effective rotational and translational temperatures being relatively cool. In contrast, reactions with recoil dynamics, e.g. K + CH_3I, appear to display the reverse behaviour with a large fraction of the available energy appearing in the final translational energy. Whether these two types of behaviour are characteristic of these two classes of reaction in general, or peculiar to alkali atom reactions is not yet clear.

Continuing our survey of direct reactions, the ion/molecule reactions in which $\sigma_R(\theta, E)$ has been measured are all characterised by strong forward scattering, i.e. on this basis alone they would be characterized as stripping reactions. They differ from the alkali reactions with regard to reaction parameters only in that the collision energy is greater than the exoergicity and that some of the reactions are endothermic.

The spectator stripping model allows the energy partitioning between reaction products to be calculated easily. In a collision in which the target molecule BC is at rest and A approaches in the z-direction, the initial and final momenta are related by the conservation of momentum thus;

$$\begin{aligned} P_z^A &= P_z^{AB'} + P_z^{C'} \\ P_y^{AB'} &= -P_y^{C'} \qquad P_x^{AB'} = -P_x^{C'} \end{aligned} \quad ; \qquad (8.39)$$

Table 8.3

System	Technique and energy partitioning	Model and reference
$N_2^+ + D_2 \rightarrow N_2D^+ + D$ $Ar^+ + D_2 \rightarrow ArD^+ + D$	Between 55 per cent and 90 per cent into internal energy, depending on E_t' in the range 0.1–3 eV Strong forward scattering.	Direct, (Z. Herman et al., 1967). Modified spectator stripping, Some recoil above 40 eV.
$H + Hal_2 \rightarrow HHal + Hal$ $H + HHal \rightarrow HHal^* + H$ $Hal + HHal \rightarrow HHal^* + Hal$	I. R. chemiluminescence. Between 45 per cent and 65 per cent into internal energy, rising to 80 per cent for Cl + HI.	Direct. Repulsive energy surface. (K. G. Anlauf et al., 1967; M. J. Mok and J. C. Polanyi, 1969).
$O(^3P) + CS_2 \rightarrow SO + CS$	Flash photolysis. 8 per cent to internal motion of CS 18 per cent to internal motion of SO	Direct. Linear encounters on a repulsive P.E. surface. (I. W. M. Smith, 1967).
$K + CH_3I \rightarrow KI + CH_3$	Thermal X-beam. Early results gave too high a value for product excitation. Direct energy analysis gives ~60 per cent to internal motion.	Direct, recoil. (R. B. Bernstein, M. E. Gersh and A. M. Rulis, 1971).
$K + Br_2 \rightarrow KBr + Br$	Thermal X-beam. Correlation of product velocity with angle of scattering. 90 per cent available energy to internal motion depending on angle.	Spectator stripping. (T. T. Warnock et al., 1967). Trajectory calculations (P. J. Kuntz et al., 1969).
$H + Hal_2, SCl_2 \rightarrow HHal + Hal, SCl$	I. R. chemiluminescence. > 37 per cent to internal motion of HCl.	(R. L. Johnson et al., 1970)
$N_2^+ + CH_4 \rightarrow N_2H^+ + CH_3$	Ion energy analysis at 25 eV. All the exoergicity into internal motion for forward scattered products.	Ideal stripping (E. A. Gislason et al., 1969).
$N_2^+ + H_2 \rightarrow N_2H^+ + H$	Ion energy analysis, 3–11 eV	Stripping, changing to knockout. (W. R. Gentry et al., 1968).

$CO^+ + H_2 \rightarrow HCO^+ + H$	Ion energy analysis	Stripping. (K. Lacmann and A. Henglein, 1965).
$CH_3^+ + CH_4 \rightarrow C_2H_5^+ + H_2$	Ion energy analysis, differential scattering	Pure stripping above 3 eV. (R. R. Herm and D. R. Herschbach, 1969).
$C_2H_4^+ + C_2H_4 \rightarrow CH_3 + C_3H_5^+$ $\searrow CH_3 + C_3H_3^+ + H_2$		Complex formation. RRK theory for lifetime.
$K + I_2 \rightarrow KI + I$	Thermal X-beam. ~ 97 per cent transfer to internal motion. Coupling between angular and recoil energy distributions.	Stripping (K. T. Gillen et al., 1971). Trajectory calculations, (P. J. Kuntz et al., 1969).
$Cs + SF_6 \rightarrow CsF + SF_5$	Thermal X-beam. Results correspond to equipartition.	Complex formation (S. M. Freund et al., 1971). (H. G. Bennewitz et al., 1971).
$Rb + Br_2 \rightarrow RbBr + Br$	Thermal X-beam Velocity and rotational analysis. ~ 5 Kcal $mole^{-1}$ into rotation and ~ 37 Kcal $mole^{-1}$ into vibration	Stripping (R. Grice et al., 1970).
$F + D_2 \rightarrow FD + D$	Thermal X-beam, Newton diagram analysis under favourable conditions.	(T. P. Schafer et al., 1970).
$D + \begin{cases} Cl_2 \\ \vdots \\ ICl \end{cases}$	Thermal X-beam, velocity analysis of DX. Between 55 per cent and 76 per cent of total available energy into internal motion.	Direct (recoil) Comparison of energy release with photo-dissociation spectra (J. D. McDonald et al., 1972)
K + HBr, DBr	Kinematics unfavourable for detailed analyses. Broad product velocity distribution peaked near 100 per cent transfer of available energy to internal motion	(K. T. Gillen et al., 1969).

where post-collision values are primed. In a pure stripping reaction the velocity of the spectator atom C is unchanged and so

$$P^{C'} = 0, \quad P_z^{A,B'} = P_z^A; \quad P_y^{A,B'} = 0, \quad P_x^{A,B'} = 0 \tag{8.40}$$

The amount of energy transferred to internal motion of AB is thus

$$E_{int} = \frac{m_B}{m_A + m_B} \times (\text{collision energy}) \tag{8.41}$$

but how this energy is partitioned between rotation and vibration depends upon the impact parameter. In Fig. 8.22 both the detailed post collision relative velocity vector diagram and the Newton diagram are given, the former constructed on the principle that immediately after reaction all particles continue to move with the same velocities that they had before the collision. From the Newton diagram for the more general case in which v_{BC} is non-zero it follows that the centre of mass velocity of the new diatomic AB is

$$w_{AB} = \frac{m_A m_C}{M(m_A + m_B)} w \tag{8.42}$$

where $w_r = w_A - w_{BC}$ is the relative velocity of the reactants and M is the mass of the whole system. In terms of LAB velocities with a stationary target, the final product velocity is given simply by

$$v_{AB} = \frac{m_A}{(m_A + m_B)} v_A. \tag{8.43}$$

These results are independent of the orientation of the target molecule at the moment of collision, of the force acting between the newly paired atoms and of the impact parameter. However, if C is to continue to move with unchanged velocity it is necessary that AB and C do not collide.

The partitioning of internal energy of the product diatomic is found by first calculating the angular momentum of AB with the aid of Fig. 8.22;

$$J_{AB} = \mu_{AB} w (b - [m_C/(m_B + m_C)] r_{BC} \sin\theta) \tag{8.44}$$

where θ is the orientation of BC with respect to the z-axis. If $b \gg r_{BC}$ (as is

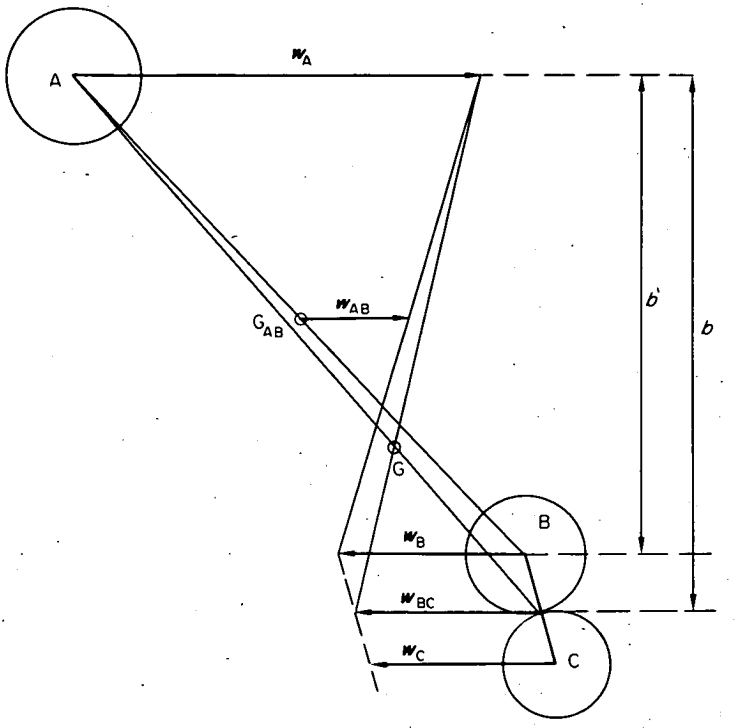

Fig. 8.22 A stripping collision between an atom A and a diatomic BC. The relative velocities, w_i, are drawn assuming a non-rotating target and are unchanged when the bond BC is broken. The atoms continue to move in their pre-collision directions until the force between A and B begins to take effect. The initial angular momentum (which is also the final value) can be calculated from this diagram (Equation 8.44). G is the centre of mass of the three particles and G_{AB} that of A and B.

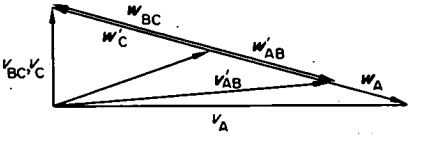

Fig. 8.22a Newton diagram for stripping, constructed on the basis that $v_c = v_{BC}$.

the case for thermal energy class II reactions) the rotational energy of AB is

$$E_{\text{rot}}^{\text{AB}} \cong \frac{1}{2}\mu_{\text{AB}} w_r^2 \, b^2/r_{\text{AB}}^2. \tag{8.45}$$

This leaves, by difference,

$$E_{\text{vib}}^{\text{AB}} \cong \frac{1}{2}\mu_{\text{AB}} w_{\text{A}}^2 \, (1 - b^2/r_{\text{AB}}^2) \tag{8.46}$$

as the final vibration energy of AB in the limit $w_{\text{A}} \gg w_{\text{BC}}$ appropriate to laboratory ion/molecule reactions.

These relations for the internal energy of the product in the stripping model impose constraints on the magnitude of the reaction cross-section which reduce the value πb_s^2 expected from the stripping impact parameter b_s. Thus, if the product is to survive, the vibrational energy $E_{\text{vib}}^{\text{AB}}$ must be less than the bond dissociation energy; this imposes a lower limit on b. In the limit of large impact parameters, $b \approx r_{\text{AB}}$, the rotational energy $E_{\text{rot}}^{\text{AB}}$ may be sufficient to dissociate the molecule if the relative velocity is large enough. Hence, from Equation 8.45, we see that at high energies both these constraints lead to a $1/E$ dependence of the stripping cross-section.

In the above discussion of stripping we have made three assumptions (1) the target BC has no internal energy, (2) there is no interaction between B and C after stripping and (3) all three atoms lie in a plane. If BC is not at rest but possesses internal momentum due to rotation or vibration, the product AB will no longer appear solely along the relative velocity vector but will be smeared out over a cone of half angle $\tan^{-1}(P^{\text{A}}/P^{\text{B}})$. All three limitations are unimportant at high energies but distort the model for thermal scattering.

We now turn to the experimental results for stripping reactions to see how closely the ideal case is obeyed in practice. Results of velocity or energy analysed reactive scattering are best displayed as a polar contour map (Figs. 8.23, 8.24) in which the distance R from the origin is proportional to the velocity of the scattered particle and θ the angle of observation. Contours are then drawn through observational points (R, θ) of the same signal strength. From the reactions in Table 8.3 we consider first a thoroughly investigated group that illustrate the operation of a predominantly stripping mechanism:

$$N_2^+ + CH_4 \longrightarrow N_2H^+ + CH_3 \quad \text{(at 25 eV)}$$
$$CH_3^+ + CH_4 \longrightarrow C_2H_5^+ + H_2 \quad \text{(at 3 eV)}$$
$$K + I_2 \longrightarrow KI + I \quad \text{(thermal)}$$

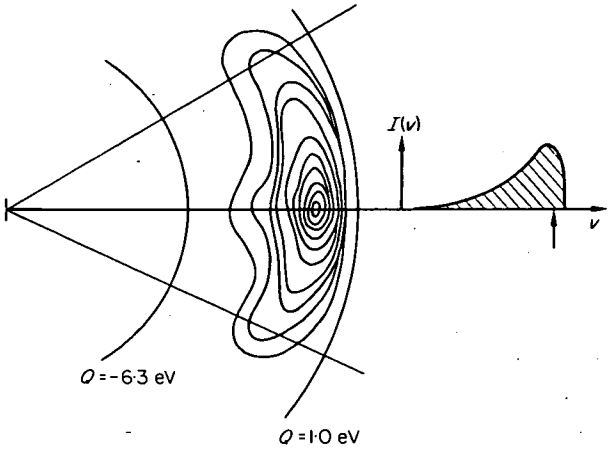

Fig. 8.23 A velocity contour map of the intensity of N_2H^+ from 25 eV N_2^+ colliding with CH_4. The beam velocity profile at $\theta = 0$ is shown on the right, in which the value of the stripping velocity is arrowed. Velocities for two values of Q, the energy transferred from the collision energy to internal motion of the products are shown and a 30° cone, into which almost all the reactive scattering is directed, is superimposed. (Taken from E. A. Gislason, et al., 1969.)

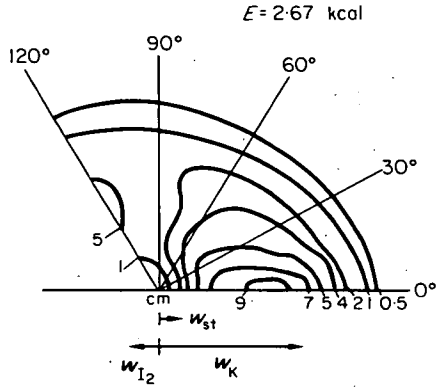

Fig. 8.24 Polar CM contour map of KI scattered in the reaction $K + I_2$. The relative velocities of the two reagents are shown beneath. The intensities labelling the contours are arbitrarily scaled with 10 as the maximum.

Also shown is the CM product velocity for pure stripping, w_{st}. (K. T. Gillen et al., 1971.)

All three of these reactions are characterized by strong forward peaking of the product intensity in the CM. For $N_2^+ + CH_4$ and $CH_3^+ + CH_3$, the peak product velocity corresponds closely to the stripping value of Equation 8.42, although as the impact energy falls below 1 eV the product velocity distribution shows increasing back scattering and the peak forward velocity is several times the stripping value.

The system $K + I_2$ shows evidence of fairly strong interaction between the newly formed products as they separate. Thus, the KI, although largely forward scattered, appears with a most probable velocity at least six times the stripping value and, although the experiments do not extend into the backward hemisphere, there is a hint of a second peak in the scattered intensity at $\chi \sim \pi$. In each case there is considerable sideways scattering, even after allowing for the angular and velocity distribution of the parent beams. In this system, there is no reason to doubt that a harpooning mechanism operates (Section 8.2), but in the two ion/molecule reactions electronic re-arrangement probably does not begin until separations only slightly greater than ordinary bond distances. Departure from the stripping predictions have perhaps rather different causes in the K/I_2 case and in the two ion/molecule reactions. Early energy release, before stripping, is unlikely in the K/I_2 reaction because the critical radius for stripping is so large, and post-stripping interactions are probably important. They can operate to transfer energy to either the internal modes of the newly formed product or to the relative kinetic energy of the departing fragments. A detailed analysis of these effects is best done by trajectory calculations (Section 8.7), but qualitatively the key factor is the nature of the interaction between the fragments of the ruptured bond in the target. This is most clearly illustrated in the case of harpooning by electron transfer. There are two possibilities in general

$$A + BC \longrightarrow A^+ + BC^-$$
$$A + BC \longrightarrow A^- + BC^+$$

with the former illustrated by $K + I_2$ and the latter by $H + K_2$. The potenti energy curves of I_2^- and I_2 were given in Fig. 8.8 and should be contraste with Fig. 8.25 for K_2^+ and K_2. Electron transfer is rapid compared with th motion of the target atoms and the transition will therefore be vertical. I the case of I_2 this transition is to a repulsive part of the negative ion potenti and the two fragments are initially forced apart but at larger separatior experience an attractive force. There is a net energy release and, according t the various reduced masses, this is partitioned between translation an internal motion of the products; in the case of $K + I_2$ it appears mainly

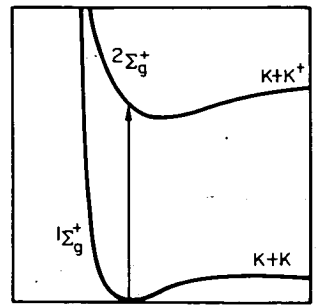

Fig. 8.25 The potential energy curves for the lowest Σ states of K_2 and K_2^+. Adiabatic ionisation would result in the transition shown.

enhanced kinetic energy. In contrast, the process $K_2 \rightarrow K_2^+ + e$ is followed by a slight repulsion of K^+ and K, but the K_2^+ cannot dissociate without further energy being supplied. This must come from the relative kinetic energy of the K_2^+ and H^- ions. Partly because of the increased bond strength of K_2^+ compared with K_2, the triatomic molecule K_2H is thought to have considerable stability (Y. T. Lee et al., 1971) and this leads to quasi-complex formation (as seen in the bimodal product distribution, Y. T. Lee et al., 1972) in contrast to the modified stripping behaviour of $K + I_2$. At higher energies this reaction might well move towards the stripping mechanism, except that the light mass of the hydrogen atom means that the duration of the collision is short compared to the time required to separate the two target K atoms. This is a point that has not been stressed in the discussion of stripping so far. If the atom A is very light, most of the motion in the newly formed AB molecule is the drawing in of A with relatively little motion of B. Under these conditions A may well begin to recede again before B and C have separated and the electron can then be transferred back from BC to A at the crossing point of the ionic and covalent surfaces appropriate to the current value of the BC separation leaving BC vibrationally excited. There is now direct evidence that this happens in K/I_2 scattering (see Section 8.3). Alternatively, the electron may fail to return and ionisation occurs.

The two ion/molecule examples in this section, involving the removal of an H atom from methane correspond to almost pure stripping over a range of a few eV. This is in part due to the fact that, compared with the K/I_2 thermal reaction, the exothermicity is now a much smaller fraction of the collision energy so its disposal is only a small perturbation on the initial motion. On these grounds we can expect $K + I_2$ to assume more stripping character as the energy increases above ~1 eV, with the same proviso about reverse electron transfer at high relative velocities.

The energy range in which the stripping model is adequate is bounded at the lower end by orbiting and complex formation and at the higher energy

limit by the increasing importance of recoil or knock-on reactions, in which the particles behave as almost elastic billiard balls. Furthermore, as the energy increases beyond ~10 eV, the direct dissociation channel ($A + BC \rightarrow A + B + C$) assumes greater importance. Finally, at still higher energies the electronic motion may cease to be adiabatic and more than one potential surface is needed.

In the case of the reaction $Cl + Br_2 \rightarrow BrCl + Br$, although the product is strongly forward scattered, the velocity analysis results indicate extensive sideways scattering and very little change in the peak LAB product velocity with angle. An important difference between this reaction and $K + I_2$ is that the total reaction cross-section is much smaller, suggesting the greater importance of small impact parameter collisions and hence to secondary encounters between the newly formed products. Thus, despite the forward scattering, this reaction may be much more comparable to the recoil type involving strong impulsive coupling of all three particles. Considerable energy transfer to the third particle is now possible and the division between stripping and recoil reactions is no longer useful. Recoil reactions do not produce any distinctive partitioning of the available energy into product excitation and translation in contrast to the high internal excitation characteristic of stripping. Experimentally it now seems that at least in some cases (e.g. $K + CH_3I$) a considerable fraction can appear as translation energy.

In the long lived complex type of reaction, class III, in which electron rearrangement results in a relatively stable transition state, the scattering is almost symmetrical in the forward and backward hemispheres and this is illustrated by the reactions

$$C_2H_4^+ + C_2H_4 \longrightarrow C_3H_5^+ + CH_3$$
$$Cs + SF_6 \longrightarrow CsF + SF_5 .$$

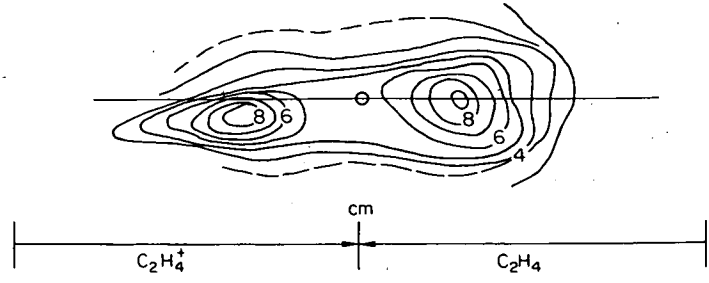

Fig. 8.26. The polar flux map of the $C_3H_5^+$ product of the reaction $C_2H_4 + C_2H_4^+$. The contours are arbitrarily scaled to 10 at the peak intensity. $E_r = 3.25$ eV. (From Z. Herman et al., 1969.)

In comparing the very different behaviour of $C_2H_4^+ + C_2H_4^+$ with $CH_3^+ + CH_4$, Wolfgang (Z. Herman et al., 1969) has used an RRKM model to account for the differences in lifetime of the respective molecular complexes resulting in the two systems. The fact that there is no evidence of complex formation in $CH_3^+ + CH_4$ is at first sight surprising in view of the stability of the well known molecular ion $C_2H_7^+$, but the essential result of the RRKM theory of unimolecular decay is that

$$\tau \approx 10^{-13}\left(\frac{E-E^*}{E}\right)^{1-s} \text{ s}, \tag{8.47}$$

where τ is the lifetime of the transition state, s the number of active modes and E^* the dissociation energy of the complex. In going from $(C_2H_7^+)^*$ to $(C_4H_8^+)^*$, the increase in the number of vibrational modes increases τ beyond $\sim 10^{-12}$ s and forward/backward symmetry in all the exit channels is found. More generally, there is a tendency in many ion/molecule reactions for stripping behaviour to emerge from complex formation as the relative energy increases, a direct result of the operation of Equation 8.47.

The neutral/neutral reaction $Cs + SF_6$ (S. M. Freund et al., 1971) also exhibits symmetrical scattering in the CM and here added evidence for complex formation comes from the observation that the rotational temperature and the vibrational temperature of the CsF product are almost equal and correspond to sharing of the total energy available by all the degrees of freedom except one – identified by the authors as the rotation needed to fulfill angular momentum conservation requirements. This equipartition result is for a fixed angle of scattering (near the forward peak) and deviations might be expected if a direct mechanism is superimposed upon that of complex formation.

Further analysis of the polar flux/velocity plots illustrated in this section must await trajectory calculations over various trial potential surfaces, but it is worth emphasising again that, experimentally, we have probed only a relatively narrow energy region and relatively few types of potential energy surface. The beam studies described in this section, particularly the ion/molecule ones, also underline how rapidly the nature of a reactive collision can change with energy – the sequence of complex formation → stripping → recoil can be passed through in a few eV.

8.6 Steric factors in reactive-scattering

A cross-section diminishing in a series of chemically related reactions all without energy of activation might be due either to a decreasing distance of approach necessary for reaction or to an increasingly stringent orientation requirement for reaction (an 'entropy of activation'). Orientation factors are certainly present and operate in a rather predictable fashion. There are two direct experiments that are relevant. In the first, the total cross-section for a series of reactions K + RI(R=CH_3 . . . C_7H_{15}) (G. H. Kwei et al., 1970) was measured and relatively little variation was found with the size of the alkyl group σ_R varying by less than a factor of 2 down the group. In the second type of experiment, a beam of CH_3I was prepared in either parallel or antiparallel alignment to the direction of approach of the potassium in the CM frame (i.e. $\cos\phi = \pm 1$) by passing through a hexapole filter (see Chapter 4) into a uniform electric field in the required direction (R. J. Beuhler and R. B. Bernstein, 1969) (Fig. 8.27). By this means either the halogen or the methyl end of the molecule was brought into the path of alkali atom. Even with the imperfect orientation of the molecule due to its residual precession ($\theta \approx 133°$ rather than 180°) it was deduced that the reactive cross-section in the favourable orientation exceeded that in the reverse orientation by at least 3:1. Expressed somewhat differently, if the CH_3I is regarded as a spherical target with its surface divided into reactive and non-reactive portions, then

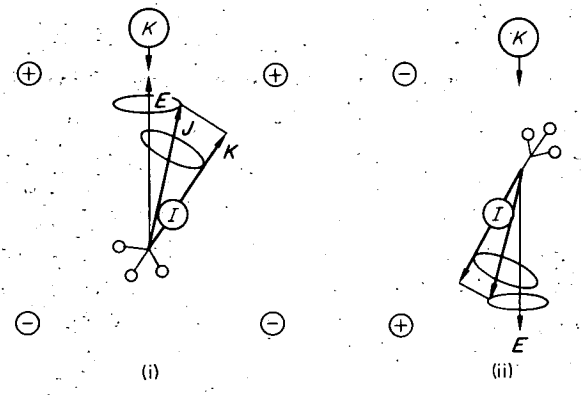

Fig. 8.27 Methyl iodide molecules with a selected range of orientations precess around the direction of E, which is reversed by reversing the polarity of the electrodes (*i*) → (*ii*). If E is aligned along the relative velocity vector, the two ends of the molecule are then presented in turn to the incoming potassium atom.

the reactive surface comprises ~70 per cent of the total (this is probably somewhat less than the admittedly imprecise fractional solid angle subtended by the iodine atom at the centre of the mass of the molecule). Another simple model has also been used to interpret these orientation experiments (P. R. Brooks and E. M. Jones, 1966). If the methyl iodide is pictured as two spheres of equal radius, then the fraction of the total hard sphere cross-section due to the iodine atom, averaged over the rotational motion of the molecule appropriate to the (jm) state, is readily calculated. From this may be directly calculated the experimental quantity

$$F = \frac{\text{signal in favourable orientation} - \text{signal in reverse orientation}}{\text{signal in favourable orientation}}$$

In this way a value $F = 0.4$ is calculated compared with an observed value of 0.6.

In a similar experiment in which methyl iodide was replaced by CF_3I, P. R. Brooks and E. M. Jones (1969) found, unexpectedly, that a larger reaction cross-section was obtained with the CF_3 group pointing towards the potassium atom than with the reverse orientation (the orientations are based on the assumption that the CF_3 group forms the negative end of the molecular dipole) but that the product was probably KI rather than KCF_3. The anisotropy factor **F** was again 0.6. It is very hard to account for this result if the mechanism is a recoil one (the total reaction cross-section is not known), but if a harpooning mechanism is invoked, it is possible that the critical radius for electron transfer, R_c, may be considerably larger if the CF_3 group points towards the incoming alkali atom. The simple formula for R_c (Equation 8.4) does not show any dependence of R_c on the target orientation, but as R_c decreases the location of the excess charge on the target becomes important in that the anion can no longer be regarded as a point charge but higher moments must be taken into account in evaluating R_c. The asymmetry of the charge distribution is then determined by the polarizability of the anion and the relative electronegativity of the two ends. A larger value of R_c is obtained when the more electronegative end (CF_3) is in the region of higher field strength, i.e. pointing towards the K^+ ion; subsequent reaction is accompanied by charge migration.

Also relevant to the question of steric factors are the elastic scattering experiments described in Section 8.3. In the sequence of recoil reactions (E. F. Greene et al., 1969) K + HBr, CH_3Br, $(CH_3)_3CBr$, σ_R/R_m^2 is found to be 1.75, 1.7 and 0.95, in approximate agreement with the changes in the again rather imprecise angle subtended by the bromine atom at the centre of mass.

One further deduction that can be made from all these experiments is that re-orientation of the target molecule as the alkali atom approaches is not pronounced. That is, both the conservation of angular momentum and the shortness of the collision lifetime make any large alteration in j difficult and the target axis does not readily follow the direction of the incoming atom.

8.7 Classical trajectory calculations

We have seen that reactive collisions can be characterized by the predominant directions of scattering of the products, by the total reaction cross-section and by the partitioning of the energy released between internal and translational modes of the products. All these, together with the notion of a critical distance of approach for reaction are classical concepts. So far, the only observations with a uniquely quantum origin are the relative probability of scattering into different vibrational channels (even these results are sometimes best reported as a vibrational or rotational temperature) and perhaps some undulations in the differential cross-section for ion production. Doubtless both elastic and reactive scattering experiments with better resolution will reveal quantum effects and systems will no doubt be discovered in which two electronic states of the molecular pair play an important part, with consequent interference between them. It is likely, though, that a model based on classical mechanics and a single potential surface will be successful in interpreting low resolution data over a significant energy range. The reactive scattering situation is similar to, and perhaps more favourable than, that of vibrational energy transfer where at least for collinear collisions there is good agreement (10–20 per cent), even quite close to threshold, between quantum and classical calculations (D. Secrest and B. R. Johnson, 1966). Classical calculations have also been surprisingly successful in treating charge transfer and ionization problems involving highly excited atoms where the electronic motion is almost classical (A. Norcliffe and I. C. Percival, 1968). It seems likely that for some time to come uncertainties in the potential surface will outweigh the errors arising from a classical approximation.

Classical models have ranged in complexity from very approximate two body models that can yield analytical results, three body systems constrained in some way (e.g. to collinear collisions) to be mathematically tractable, to the full complexity of many body (usually no larger than four) simulation models. The impetus to work with detailed models has largely come from beam work. The use of simplified three body potentials in which the potential energy is constrained to be a function of only two relative co-ordinates (i.e. fixed symmetry during collision) has a relatively long

history in chemical kinetics in the form of London-Eyring-Polanyi surfaces. Through the well known device of skewing the axes, the effect of changing the reduced masses of the particles on the amount of reflection back into the incident channel was convincingly demonstrated, together with the coupling of this mass effect with the effectiveness of initial vibrational energy in promoting chemical reaction. The same effects are discernible in the more sophisticated modern calculations to be described (D. L. Bunker, 1970).

Typical of the simplest models is that of R. D. Present (1958). Here the prescription is that reaction occurs in all collisions whenever potential energy at the distance of closest approach reaches a critical value E_c. The total reaction cross-section is then readily found, in the absence of intermolecular forces, to be:

$$\begin{aligned} \sigma(E) &= \sigma(E=\infty)\ (1 - E_c/E);\quad E > E_c \\ \sigma(E) &= 0; \qquad\qquad\qquad E \leqslant E_c. \end{aligned} \tag{8.48}$$

Recently, modifications to include additional steric and energy dependent factors have been made to improve agreement with more detailed calculations (R. Grice et al., 1970).

A more specialised model has been developed for stripping reactions. In this *spectator* model, discussed in Section 8.6, simplicity is bought at the price of entirely neglecting the motion of the spectator group after stripping and the effect of intermolecular forces beforehand. Models of this type are important because they represent limiting cases to which a variety of reactions tend, if only over a limited energy range. Models in which angular momentum effects are neglected would also fall into this class. Thus, it has been pointed out (J. D. McDonald et al., 1972) that in the series of reactions H, $D + X_2$, the very light mass of the hydrogen isotopes considerably simplifies the inter-relation of the potential surface and angular scattering pattern of the products. Both the linear and angular momentum of the initial motion provide severe kinematic restraints on the scattering pattern, but in this series of reactions (X = Cl . . . I) the reduced mass of the reactants is almost constant and the relative initial momentum very small; changes in reactive scattering among the systems are thus largely due to changes in the potential surface. Particularly in the case of reactions with late energy release, we can picture the following sequence of events; the H atom reaches the transition state by a virtually straight line trajectory and the X_2 bond then breaks with repulsion of the products which move away along the line of centres of the two heavy X atoms. This mechanism focuses attention on the

geometry of the transition state, for which one can picture two extreme models:

(i) The three atoms, H–X–X must be collinear to within some specified small solid angle $\Delta\Omega$ for reaction to occur.
(ii) There is no restriction on the geometry of the transition state.

It is now a simple exercise to calculate the two product scattering patterns, $\sigma_R(\chi)$. From (i) we calculate the deflection function of the product, $\chi_{pr}(b)$ (where b is the impact parameter of the *reactants*) to be (see Fig. 8.28)

$$\chi_{pr}(b) = \sin^{-1} b/R_c \tag{8.49}$$

where R_c is the critical distance of approach for reaction. The differential cross-section for reaction is then:

$$\sigma_R(\chi) = \frac{b\mathscr{P}(b)}{\sin\chi \left|\frac{d\chi}{db}\right|} = R_C^2 \cos\chi \frac{\Delta\Omega}{4\pi} \tag{8.50}$$

where $P(b)$ is the probability that, when the H atom strikes the sphere radius R_c it finds the X_2 molecule in a suitable orientation for reaction. The total cross-section is clearly $\Delta\Omega R_c^2/4$. Alternatively (see again Fig. 8.28 where this is emphasized), we can regard the $\cos\chi$ factor as coming from the angle dependent illumination of the reactant sphere by the incident H beam.

The consequences of model (ii) are very simple; since the X–X axis is isotropically distributed at the time of impact, the product departs isotropically.

In practice, the observed pattern is peaked at between 35° and 90° from the direction of approach of the H atom. We will not pursue the implications of this, but merely remark that some other ingredient, perhaps depending on the relative velocity at the turning point, must be put into the model.

There is no doubt that in the description of reaction by classical models the most important developments have been provided by the computer simulation method for studying many body collisions. A Monte Carlo algorithm is used to choose the starting configurations and the coupled equations of motion are integrated by any one of several stepwise procedures. Properties such as $\sigma_R(\chi)$ and energy partitioning are then determined as an average over an ensemble of trajectories. Consideration of these methods falls naturally into three parts; the choice of the initial conditions, the solution of the equations of motion and the adjustment of the potential hypersurface

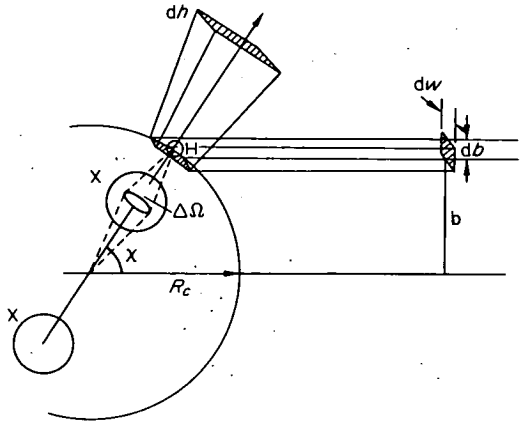

Fig. 8.28 A simple model for impulsive reactive scattering. H atoms incident in a plane wave from the right illuminate the reactant sphere with an intensity proportional to cos χ. If an X_2 molecule is encountered in the solid angle $d\Omega$ about χ, reaction ensues and the HX product departs along the line of centres of X_2. The detector, width dh, subtends an area $R_c d\chi dW$ on the reactant sphere. Thus, for an H atom to reach the detector as HX, it must be incident through an area dwdb, where $db = R_c d\chi \cos\chi$. Hence the differential cross-section is proportional to cos χ, Equation 8.50.

over which the reaction proceeds. The starting values that must be specified in a classical calculation are quite different from those of a quantum calculation. In the former, position, velocity and phase of motion replace the quantum state of the wave mechanical prescription. Luckily, the phase factors usually have little effect on final outcome so that a fairly coarse scan can be used for this parameter. The initial impact parameters must, however, be chosen from a uniform distribution between 0 and b^2_{max}, where b_{max} is taken as the limiting value of b above which the trajectories cannot influence the reactive scattering. Selection of the velocities of the particles (which determine the initial rotational and vibrational energy) will depend on the purposes of the calculation, which may either be to mimic a particular incident quantum channel or to represent the conditions in an experiment with less perfect resolution. In the latter case the velocities must be drawn from the correct Boltzmann distribution. The orientation angles of the

colliding molecules (the phase of the rotation) are then selected (in the ensemble average case) to provide a uniform probability for collision with respect to orientation.

The most convenient formulation of the classical equations of motion is Hamilton's which, for an N-particle system, takes the form of 6N-6 coupled first order differential equations for the relative motion of the particles:

$$\frac{\partial H}{\partial p_i} = \dot{q}_i; \quad \frac{\partial H}{\partial q_i} = -\dot{p}_i \tag{8.51}$$

where the p_i's and q_i's are the conjugate momenta and displacements. The Hamiltonian is of the usual form,

$$H = \frac{1}{2}\sum_{i=1}^{N-1} m_i(\dot{q}_{ix}^2 + \dot{q}_{zy}^2 + \dot{q}_{iy}^2 + \dot{q}_{iz}^2) + \sum_{i \neq j}^{N-1}\sum^{N-1} V(R_{ij}). \tag{8.52}$$

For a potential $V(R_{ij})$ defined in terms of all the interparticle distances (Equation 8.51) is solved by stepwise integration, such as the method of Runge and Kutta or by a predictor-corrector routine. The procedure is quite standard, though since a trajectory may take a second or more to compute, an efficient process is required. The stability of the calculation with regard to round-off error etc., is usually monitored by observing the conservation of energy (in the form of the Hamiltonian) and angular momentum during the collision.

In analysing the results of these computed trajectories, the final angle emergence (irrespective of the out-of-plane angle) from the collision together with the final relative velocity are noted. A histogram is then built up of the number of trajectories emerging in equal angular intervals $\Delta\chi$. This histogram is the classical numerical approximation to the differential cross-section and approaches statistically a smooth function as the number of trajectories is increased. With so many parameters to scan, the convergence is slow; Fig. 8.29 illustrates a typical histogram after 400 trajectories have been run and although the distribution clearly denotes strong back scattering of atom C (i.e. the diatomic product is forward scattered and the mechanism is a stripping one), it is far from smooth.

The relationship between the differential cross-section as computed, $q(\chi)$ and the true cross-section $\sigma_R(\chi)$, is simply

$$q(\chi)\Delta\chi = 2\pi\int_{\chi}^{\chi+\Delta\chi} \sigma_R(\chi)\sin\chi d\chi \tag{8.53}$$

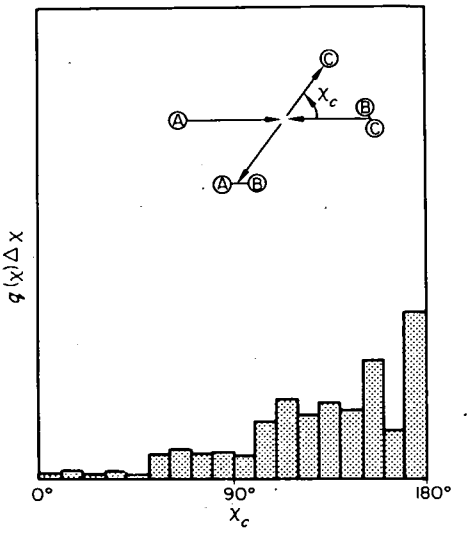

Fig. 8.29 A typical histogram after 400 trajectories compiled from ten initial values of χ_{BC}, ten of ϕ_{BC} and four values of the impact parameter. The reaction is a typical recoil one.

and so the total reaction cross-section is:

$$\sigma_{R\,\mathrm{tot}} \simeq \int_0^{\pi} q(\chi)\mathrm{d}\chi. \tag{8.54}$$

From a physical point of view, the most interesting feature of these model calculations is in the effect of the form of the potential on the type of scattering pattern. Before any detailed comparisons are made, a body of such calculations serves to 'educate' the intuition in this field. For this purpose we need an analytic form for the many body potential that is flexible enough to describe the variety of interactions encountered in reactive scattering and in which each adjustable parameter is as nearly as possible uniquely related to a key topographical feature of the surface.

Taking an example from elastic scattering, we might wish to test if a certain scattering phenomenon is a sensitive function of the well depth; for this purpose it would be unsuitable to take an intermolecular potential of the form:

$$V(R) = C_n R^{-n} - C_6 R^{-6} \tag{8.55}$$

because varying either C_n or C_6 alters the well depth. The natural choice in this case is:

$$V(R) = \frac{6\epsilon}{n-6}\left\{\left(\frac{R^0_{AB}}{R}\right)^n - \frac{n}{6}\left(\frac{R^0_{AB}}{R}\right)^6\right\} \tag{8.56}$$

where altering R°_{AB} does not influence the well depth ϵ. If, however, the effect to be investigated were changes in the long range part of the potential, the form (Equation 8.55) would be adopted. When we come to consider the potential energy of a group of three atoms A, B and C, of which A and B and B and C are known to form stable diatomic molecules, the simplest analytical expression for the potential would seem to be the sum of the two separate diatomic potentials. If we represent these by Morse functions (thereby introducing the approximation that will be implicit throughout this section that the long range part of the potential plays no part in the reactive scattering) the result is:

$$V = D_{AB}\{1 - e^{-\beta_{AB}(R_{AB} - R^0_{AB})}\}^2 + D_{BC}\{1 - e^{-\beta_{BC}(R_{BC} - R^0_{BC})}\}^2 \tag{8.57}$$

where D_{AB} and D_{BC} are the dissociation energies of Ab and BC respectively and R° is the relevant equilibrium diatomic separation. This potential is mapped in Fig. 8.30 for a collinear configuration in the familiar form of a contour diagram. Inspection of the surface shows that it is characterized by a deep potential minimum corresponding to a stable triatomic molecule ABC without preference for a bent or linear configuration. Although a potential of this form would be a possible choice for a system such as $O(^1S)$ + CO, there is no reason to suppose that it is suitable for the systems so far examined by beam methods that fall into class I or II. This is confirmed by trajectory calculations using potentials of the form Equation 8.57 from which it is found that for those impact parameters that permit the system to enter the well, a long lived complex is almost invariably formed and the atoms execute several vibrations before dissociating. This, in turn, leads to an almost isotropic distribution of products in the centre of mass frame (see the more detailed discussion in Section 8.2).

Two improvements suggest themselves; the introduction of repulsion between non-bonded atoms and the progressive attenuation of existing bonds as another atom approaches. These changes are incorporated in the N. C. Blais

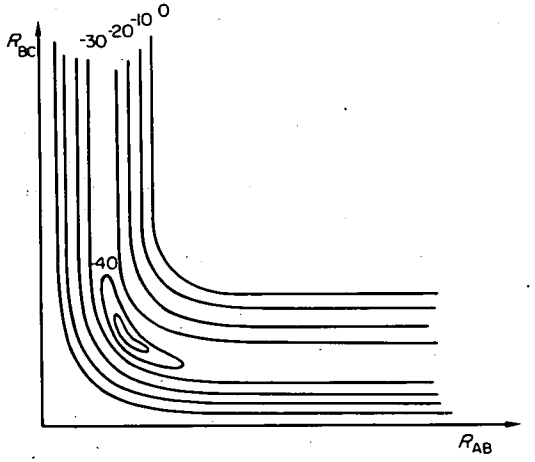

Fig. 8.30 Contour diagram of the potential $V = D_{AB}\ \{1 - \exp\ (-\beta(R_{AB} - R^{\circ}_{AB}))\}^2 + D_{BC}\ \{1 - \exp\ (-\beta(R_{BC} - R^{\circ}_{BC}))\}^2$ for a collinear configuration. Arbitrary energy units.

and D. L. Bunker (1962) potential:

$$\begin{aligned} V = {} & D_{AB}\{1 - e^{-\beta_{AB}(R_{AB} - R^{\circ}_{AB})}\}2 \\ & + D_{BC}\{1 - e^{-\beta_{BC}(R_{BC} - R^{\circ}_{BC})}\}2 \\ & + D_{BC}\{1 - \tanh(aR_{AB} + c)\, e^{-\beta_{BC}(R_{BC} - R^{\circ}_{BC})}\} \\ & + D_{AC}\, e^{-\beta_{AC}(R_{AC} - R^{\circ}_{AC})} \end{aligned} \tag{8.58}$$

where the third term introduces a tanh cut-off in the attractive part of the AB potential and the fourth term is an exponential repulsion between the non-bonded atoms. The adjustable parameters are now four — a, c, β and R°_{AC}. The tanh attenuation factor reaches a value of 0.5 at a value of the argument roughly equal to 0.55 and the steepness of the cut-off is determined by a. According to the value of c, such a potential can either be of the early or the late downhill type, illustrated in Fig. 8.31. In the former, the major energy release (potential drop) occurs when R_{AB} is still appreciably greater than its equilibrium value and in the latter case the energy release accompanies the repulsion of C which does not begin until the A–B bond is nearly complete. These two types of surface differ sharply in the distribution of the reaction exoergicity that they yield in the products. The early downhill type produces much more internal excitation than the late downhill surface.

The results from this surface with the parameters set to model the K + CH_3I reaction were not in accord with experiment. The computed differential cross-section for CH_3 scattering peaked at somewhat less than 90° and the total reaction cross-section was ~400 Å^2.

In the failure of potential (Equation 8.58), one weakness is clear. The force between the approaching A and B atoms is that of the full bonding force of the AB molecule, even though atom C is still present. The introduction of a second tanh function to switch between a bonded and a non-bonded force between A and B is clearly necessary:

$$\begin{aligned} V = & D_{AB}\{1 - \exp(-\beta_1(R_{AB} - R^0_{AB}))\}^2 \\ & + D_{BC}\{1 - \exp(-\beta_2(R_{BC} - R^0_{BC}))\}^2 \\ & + D_{BC}\{1 - \tanh(a_1 R_{AB} + c_1)\}\exp(-\beta_2(R_{BC} - R^0_{BC})) \\ & + D_{AB}\{1 - \tanh(a_2 R_{BC} + c_2)\}\exp(-\beta_1(R_{AB} - R^0_{AB})) \\ & + D_{AC}\exp(-\beta_3(R_{AC} - R^0_{AC})) \end{aligned} \tag{8.59}$$

With this type of surface, Fig. 8.32, the total reaction cross-section for CH_3I/K was ≈ 25 Å^2 with strong backward peaking of the KI in good agreement with experiment (L. M. Raff and M. Karplus, 1966). In a further application of this surface, Raff has investigated the effect of replacing the methyl group in CH_3I by an ethyl group, treating C_2H_5 as a diatomic group held together throughout the reaction by an unattenuated Morse function. In order that both the CH_3 and CH_2 groups participate in the reaction, a repulsion term between the K atom and the CH_3 centre of mass was introduced. In spite of the omission of several terms from this potential that a chemist would intuitively consider important, such as the changing properties of the C–C bond in passing from C_2H_5I to the ethyl radical, the conclusion that the ethyl radical carries away between 10 per cent and 20 per cent of the energy released as internal motion is probably qualitatively correct. This type of calculation should stimulate the study of such reactions by I. R. chemiluminescence and by crossed-beam product velocity analysis so the energy partitioning can be pinned down.

In a series of calculations using idealised surfaces, Polanyi and his co-workers (M. H. Mok and J. C. Polanyi, 1969) have explored the effect of early and late energy release on the energy partitioning and the effectiveness of vibrational compared with translational energy in providing the energy of activation.

These simulation calculations have now been made for quite a range of molecular systems including those of the stripping and recoil types. In all

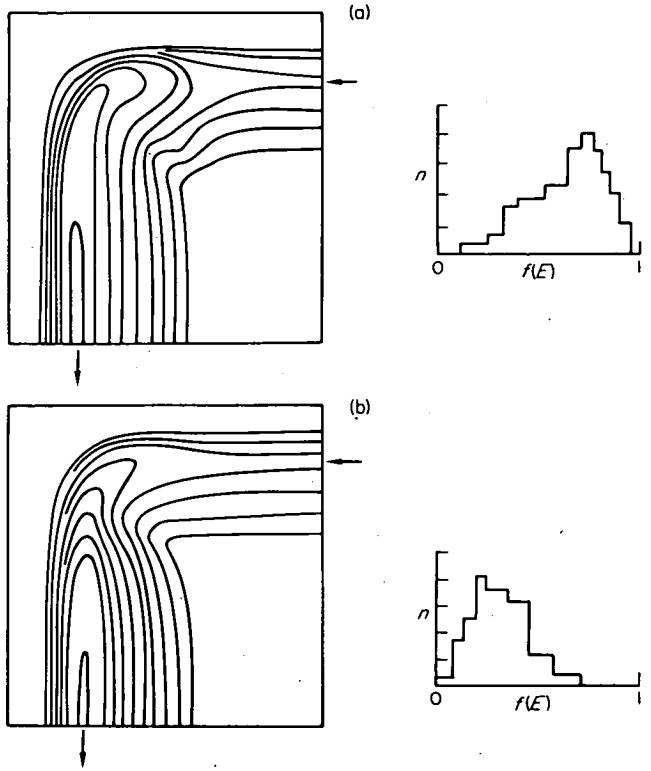

Fig. 8.31 Two surfaces illustrating early (i) and late (ii) release of the energy of reaction. The particles enter in the top valley and exit at the bottom. The corresponding fraction of the total available energy $f(E)$ that appears as internal motion of the products is plotted on the left, where n is the number of trajectories. (D. L. Bunker and N. C. Blais, 1964)

cases potentials capable of reproducing the angular scattering have been found, though the uniqueness of such surfaces is doubtful. An example of two rather different potentials that can give a similar scattering pattern introduces the concept of charge migration. In the reactions of the alkalis with the halogens, the electron transferred must take up a final position on one or other of the two halogen atoms as the products depart, but whether this electron can migrate from one halogen atom to the other during the collision according to the prevailing electric field arising from the cation is a question that, although not susceptible to direct experiment, must be settled before the potential can be written down. The work of Polanyi's school (P. J. Kuntz et al., 1969; M. Godfrey and M. Karplus, 1968) showed that, with only

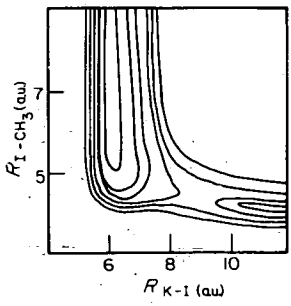

Fig. 8.32 The co-linear potential energy surface for $K + CH_3I$, with the CH_3 group treated as a point mass. (From L. M. Raff and M. Karplus, 1966), surface (8.59).

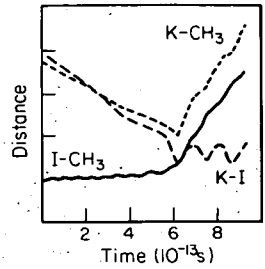

Typical trajectories over the modified Bunker and Blais surface used by Raff and Karplus for the $K + CH_3I$ reaction. A direct reactive collision is shown, for which the time while all the particle separations are small is 5×10^{-13}s.

a weakly repulsive potential between the atom and ion of the newly formed X_2^- charge migration, if allowed, frequently occurred and was found necessary to achieve the forward scattering found in practice. However, if an X_2^- potential is adopted that is strongly repulsive (see Fig. 8.8), then the required forward scattering can be obtained without invoking charge migration, (N. C. Blaise, 1968). This sort of question is best settled by a direct investigation of the kinematics of electron/halogen dissociative attachment collisions.

The broader question of the uniqueness of the potential surfaces that fit reactive scattering data turns on the amount of experimental detail available and the energy range over which $\sigma_R(\theta), v)$ is measured. At the present time, the spread in initial energy and angular momentum, together with the operation of simple reduced mass effects, often obscures the changes in the potential energy surface in a related series of reactions. There is currently a need for a parallel development in ab initio calculations of these surfaces; with increasing refinement of the scattering data they will both hopefully converge on the 'true' many body potential.

8.8 Summary of observations and reaction models

Most of the reactions so far investigated by crossed-beam techniques are of the direct type in which the product is scattered into a relatively narrow angular range. These reactions comprise the thermal energy reactions of the

alkali metals with halogen containing compounds and some reactions of halogen atoms and of hydrogen atoms. A much smaller class of reactions, notably those of the alkali metals with their halides, exhibit a symmetrical bipolar CM distribution. These reactions are thought to proceed through the formation of a complex that survives for several rotational periods, i.e. that has a lifetime τ greater than $\sim 10^{-13}$ sec. All bimolecular collisions can be assigned a place on the lifetime scale but, even for a given pair of molecules, τ is a function of the relative angular momentum and energy. It so happens that under current experimental conditions the reactions so far investigated fall into the short and long-lived groups with respect to τ, but examples will undoubtedly be found of an intermediate character. Furthermore, as the colliding energy increases it is probable that the lifetime of collisions that lead to reaction decreases and those proceeding via complex formation become direct, though probably with a change in the nature of the reaction products.

In the field of direct reactions, a fairly good correlation is observed in the following properties; dominant CM scattering angle, magnitude of the total reaction cross-section and the angular position of the onset of attenuation in the elastic scattering. The ranges of behaviour in these observables can be displayed in the following table in which the correlations are vertical:

Property	Trend				
$\sigma_R(\chi)$	forward peaked	⟶	sideways	⟶	backward peaked
σ_R	large ($\gtrsim$100 Å^2)	⟶	medium	⟶	small ($\lesssim$30 Å^2)
$\sigma_{el}(\chi)$	Monotonic fall in intensity with angle	⟶	rainbow appears	⟶	full rainbow and supernumerary structure
$\sigma_{tot}(E)$	Monotonic energy dependence	⟶	undulations appear	⟶	full undulatory behaviour
$\sigma_R(\chi, v)$	Very high product excitation	⟶	lower product excitation		

The behaviour of a reaction with respect to the last two properties, energy dependence of the total cross-section and energy partitioning in the products, is less predictable from the position of the reaction with respect to the first three properties.

The existence of these correlations points to the operation of a single potential energy surface (i.e. to the absence of non-adiabatic effects) in each reaction and these surfaces, though differing widely in chemical nature, are all characterized by a potential that falls monotonically along the reaction path

(i.e. zero activation energy). If a reaction fails to conform to the above trends, strong inelastic scattering may be the cause which can destroy the structure in $\sigma(E)$ and $\sigma(\chi)$, or a complex may be formed. In the latter case, with τ approximately equal to the rotational period of the complex, the product could still be thrown forwards or sideways but the total reaction cross-section need not be large.

The bunching of examples at either end of the various scales listed above suggests the use of simple models, two of which have achieved considerable importance – spectator stripping for reactions of large cross-section and recoil for those of small cross-section. Of these the stripping mechanism is capable of simple quantitative development and deviations from it serve as a measure of spectator participation both in neutral/neutral and ion/neutral reactions. Deficiencies in the model are numerous at thermal energies and the spectator generally plays a part in carrying off some of the energy liberated. Peculiar to reactions involving atoms of low ionization potential is the harpooning mechanism which leads to reactions of large cross-section and also suggests a convenient form for the initial part of the potential energy surface. Some of these surfaces have been described in Section 8.7 and have been quite successful in accounting for our knowledge of stripping reactions at thermal energies. The recoil mechanism is not so precise in its predictions or in formulating the nature of the potential surface and simply states that the pronounced back scattering found in these reactions is due (i) to the predominance of small impact parameter collisions in causing reaction and (ii) to the essentially binary rather than multiple nature of the reactive collision. Product back scattering, as in elastic scattering, is due to repulsion in this case of the newly formed products. Qualitative factors of interest are firstly the early or late release of the energy of reaction and secondly the directionality of the incident channel. The latter factor is related to the degree of linearity of the transition state and affects both orientation dependence of the reaction cross-section and the extent of sideways scattering.

Reactions proceeding via long lived complexes (lifetimes greater than their rotational period) are comparatively poorly represented in the beam literature in contrast to their important role in very low energy ion/molecule reactions and in unimolecular reactions. The reasons for this are probably (i) that neutral aggregates of a few atoms of which one is an alkali metal do not usually exhibit a pronounced potential minimum in the transition state configuration, (ii) most of the vibrational modes of the reactant molecules are inactive during the collision, (iii) the reactions studied are all exothermic. The only examples of the alkali metals participating in these reactions so far

encountered are their reactions with the alkali halides, SF_6 and, possibly, $H + K_2$, $H + Na_2$. As non-alkali systems become increasingly explored, especially those involving free radicals, this type of mechanism will no doubt become more common.

Theory is well prepared to deal with them through conventional transition state methods for the lifetime and energy partitioning, by angular momentum analysis for the angular scattering and perhaps by the prediction and observation of resonances.

The energy partitioning between translational and internal motion is an important additional observable that helps to define the potential energy surface. In neutral beam experiments to date, this has been achieved most usually by velocity analysis of one of the scattered products. These results, taken in conjunction with the mean energy partitioning from infra-red chemiluminescence and flash photolysis studies, show that a wide range of the total available energy may be found in the rotation and vibration of the products, from $\lesssim 25$ per cent to virtually 100 per cent. The most detailed results in this area promise to come from a marriage of I.R. luminescence or fluorescence and crossed-beam techniques by which the angular distribution of product excitation can be measured.

In almost all the reactions so far studied in beams, there has only been a single reactive exit channel open. As the relative kinetic energy or the complexity of the molecules increases, new reactive channels open up and the dimensionality of the potential energy surface increases. The amount of data needed to make a choice between various many-body potentials then escalates so that detailed analysis of only one of the scattered products becomes rapidly less useful. The exploration of these more complicated reactions has in the past been confined to bulb kinetic measurements of the reaction rates into the various product channels. There is now the possibility with existing beam techniques of measuring the relative cross-sections for the formation of the various products as a function of the angle and energy of scattering. Even under these more complicated conditions, an optical analysis of the true elastic scattering remains a simple way of summarizing the effects that remove incident particles from the beam. Some of the most exciting prospects in beam work are in the field of chemical reaction between simple molecules under unfamiliar conditions. New correlations and new models will surely be needed as an increasing range of reaction parameters such as activation energy and initial electronic state are explored.

CHAPTER NINE

Inelastic Scattering

Although the molecular beam technique has illuminated a whole area of chemical reaction and revolutionized the determination of intermolecular forces, its impact in understanding inelastic collisions has been much less dramatic. There are two reasons for this. The more important is that detection of single quantum state changes or the transfer of small amounts of internal energy is much more difficult than the detection of the gross effects of chemical change. This has the secondary effect that the theory needed to interpret such results must be correspondingly detailed. Although for a given system both reaction and inelastic processes may occur on the same potential surface, it is not yet clear how far the methods of classical mechanics that were central to the interpretation of reactive scattering can take us in discussing quantum changes. Nevertheless, although not ideally suited to the task, it is probable that classical mechanics will not be grossly in error when applied to vibrational and rotational energy transfer.

In this section the reader will not find tables of potential anisotropies or coefficients giving the dependence of the intermolecular potential on the internal co-ordinates of the system. As with relating chemical reaction to a potential surface, one is up against the problem of uniqueness. The terms in an intermolecular potential responsible for inelastic effects can rarely be reduced to a single parameter and in order to unravel a multiparameter situation detailed cross-sections (i.e. those between single quantum channels) over a wide angular or energy range are needed. These are not yet available. It is only in curve crossing problems – which result in electronic excitation – that one is possibly dealing with an effect governed by two quite different parameters (Section 9.4.iii) whose effects can be separated.

The extension of the quantum theory of scattering to more complicated systems in which chemical reaction and energy transfer can take place is possible in a formal sense and is currently the subject of investigation (R. D. Levine, 1969). The required formalism based on the S matrix has already been developed in the elementary particle and nuclear physics fields (T. Y. Wu and T. Ohmura, 1962). However, methods useful at high energies or where only a very few partial waves are involved are less useful in molecular systems and there is a great need for approximate methods. In this book we discuss these approximations in relation to energy transfer processes since theory and experiment can march more closely here and some systems may be sufficiently simple to permit comparison of theory and experiment at several levels of sophistication. The discussion of the theory given here is very much in outline and is intended to illuminate general principles and to show what is needed from experiment rather than to provide a working knowledge for the theorist. Excellent and more detailed accounts for the latter purpose can be found in R. D. Levine, 1969; N. F. Mott and H. S. W. Massey, 1965; D. R. Bates, 1961; M. L. Goldberger and K. Watson, 1964.

Experimental information on these processes is available from a number of sources including spectral line broadening, relaxation measurements of various types and shock tube data (R. G. Gordon et al., 1968) but we restrict the present discussion to scattering methods. Once again we shall see that the beam technique promises unique detail in providing not only probability but also phase information.

Beam measurements on inelastic processes can be divided into three classes according to the exact technique employed. There is the 'velocity change' method in which the pre and post collisions velocities are measured and the corresponding translational to internal energy change inferred. The 'state change' method in which state filters (usually operating on rotation or spin state properties) are used to select the incident beam and then to analyze the scattered particles. Finally, photon, ion or excited atom emission from the collision zone may be monitored.

9.1 The S matrix

The elements comprising the S matrix have already been defined in Chapter 6 as the ratio of the amplitude of the outgoing partial wave in one channel to the incident amplitude in some other channel. For the central force elastic problem only the diagonal elements were non-zero; in inelastic collisions the off-diagonal terms will play an essential role. Of course, as shown in the discussion on singlet-triplet scattering, Section 6.16, transformation of the S matrix

to a new description based on a more convenient set of quantum states may diagonalize a matrix that would otherwise appear to involve inelastic effects. In this section we assume that such simplifying transformations as are possible have already been made. (See also Section 9.3iii.)

Consider collisions of the type:

$$A_i + B_j \longrightarrow A_k + B_l \tag{9.1}$$

where particles in specific states i and j collide with a velocity corresponding to a wave number k_α. The wave function for a particular partial wave, relative angular momentum l, in the entrance channel $A_i + B_j$, which we label α, is:

$$\psi_{\alpha l0} = R^{-1}\, Y_{l0}\,(\chi, \phi)\, u_{\alpha l0}(R)\phi_\alpha \tag{9.2}$$

where ϕ_α is the total wave function of the two isolated species A_i and B_j appropriately symmetrised. $U_{\alpha lm}(r)$ is the translational wave function and Y_{lm} is a spherical harmonic. As usual only the asymptotic behaviour of $u_{\alpha lm}(r)$ is of importance and we can write:

$$\begin{aligned} u_{\alpha l0} &\xrightarrow[R\to\infty]{} k_\alpha^{-\frac{1}{2}} \left[\mathscr{B}_{\alpha l0}\, e^{-i(k_\alpha R - l\pi/2)} - \mathscr{A}_{\alpha l0}\, e^{i(k_\alpha R - l\pi/2)}\right] \quad \text{(a)} \\ u_{\alpha' l' m'} &\xrightarrow[R\to\infty]{} k_{\alpha'}^{-\frac{1}{2}}\, \mathscr{A}_{\alpha' l' m'}\, e^{i(k'_\alpha R - l\pi/2)} \quad \text{(b)} \end{aligned} \tag{9.3}$$

where in distinction to the case of purely elastic scattering, Equation 6.56, the ingoing and outgoing amplitudes are no longer equal and the inelastic channels α' have only outgoing waves. The amplitudes of the outgoing partial waves follow from the definition of the S matrix as:

$$\mathscr{A}_{\alpha' l' m'} = S_{\alpha l0 : \alpha' l' m'}\ \mathscr{B}_{\alpha l0} \tag{9.4}$$

for transitions between the entrance partial wave $\alpha l0$ and the exit channel $\alpha' l' m'$. The range of states available is of course limited by the requirement that the total angular momentum and energy be conserved during the collision.

The boundary conditions of interest in the calculation of cross-sections, i.e. an incident plane wave associated only with state α, can be achieved by correct choice of the incident amplitudes $\mathscr{B}_{\alpha l0}$, so that (comparing Equation 6.61):

$$2i\,\mathscr{B}_{\alpha l0} = -i^l(4\pi)^{1/2}\,k_\alpha^{-1/2}\,(2l+1)^{1/2} \tag{9.5}$$

and

$$2i\,\mathscr{A}_{\alpha' l' m'} = -S_{\alpha l0:\alpha' l' m'}\,i^l\left(\frac{4\pi}{k_{\alpha'}}\right)^{1/2}(2l+1)^{1/2}. \tag{9.6}$$

Since all partial waves are populated in the incident wave the amplitude in any exit channel α' must sum all their different contributions, i.e. the matrix relation

$$\mathscr{A} = \mathbf{S}\mathscr{B} \tag{9.7}$$

must be used so that the differential cross-section for scattering in the inelastic channel α' from an incident plane wave in the channel α is:

$$|f_\alpha^{\alpha'}(\chi,\phi)|^2 = \frac{4\pi}{k_\alpha k_{\alpha'}}\left|\frac{1}{2i}\sum_l i^l(2l+1)^{1/2}\sum_{l'm'} i^{-l'}\,S_{\alpha l0:\alpha' l' m'}\,Y_{l'm'}(\chi,\phi)\right|^2. \tag{9.8}$$

The summation over $l'm'$ calculates the scattering resulting from a single incident partial wave, l, and the first summation over l, accounts for all the partial waves in the incident flux.

In the usual way the total cross-section for the processes $\alpha \to \alpha'$ is:

$$\sigma_\alpha^{\alpha'} = \frac{\pi}{k_\alpha^2}\sum_{l'm'}\left|\sum_l (2l+1)^{1/2}\,i^l\,S_{\alpha l0:\alpha' l' m'}\right|^2. \tag{9.9}$$

The summation over l' and m' is formally over all the accessible states satisfying the energy and angular momentum constraints.

As already discussed in Section 6.16 the S matrix calculated in one representation may be transformed to alternative descriptions if required.

9.2 Wave equation for inelastic scattering

The formalism of the S matrix just described is a convenient 'store' for all possible experimental information about the molecular collision. The calculation of the elements in the matrix, however, must involve the solution of the total wave function for the system. As an example of the formulation of the required wave equation and to provide a basis for discussion of the several approximate methods useful in its solution, we consider (as a special

case of Equation 9.1):

$$A + B_i \longrightarrow A + B_n \tag{9.10}$$

where A is a structureless particle and B has a Hamiltonian $H_B(r_B)$ for its internal motion (the coordinate $\mathbf{r}_B$ represents all the internal coordinates of B). After an encounter at a relative wave number k_i the particle B may be excited to any of its states which are accessible. The exit wave number k_n will then be:

$$k_n^2 = \frac{2\mu}{\hbar^2}\Delta E + k_i^2 . \tag{9.11}$$

Energetically closed channels will have an imaginary wave number since they cannot result in unbounded solutions, but only in exponentially decaying ones.

The unperturbed states of the target B are given in the usual way by:

$$H_B(\mathbf{r}_B)|\phi_n = E_n\phi_n, \tag{9.12}$$

where E_n and ϕ_n are the eigen-values and functions appropriate to B. The Hamiltonian for the complete collision system will be:

$$H = -\frac{\hbar^2}{2\mu}\nabla_R^2 + H_B(\mathbf{r}_B) + V(\mathbf{R}, \mathbf{r}_B) \tag{9.13}$$

and $V(R,r_B)$ is the interaction potential between A and B. This must be a function of the internal coordinates of B if inelastic effects are to occur. The system wave function ϕ can be expanded in terms of the complete set ϕ_n as:

$$\Psi(\mathbf{R}, \mathbf{r}_B) = \left(\sum_n + \int\right) \phi_n(\mathbf{r}_B) F_n(\mathbf{R}) \tag{9.14}$$

where both the continuum and discrete states of ϕ are included. $F_n(\mathbf{R})$ is the translational wave function in the exit channel n and asymptotically at large $\mathbf{R}$ will have the form:

$$F_i(\mathbf{R}) = e^{ik_i z} + R^{-1}\, e^{ik_i R} f_i(\chi, \phi) \tag{9.15}$$

$$F_n(\mathbf{R}) = R^{-1}\, e^{ik_n R} f_n(\chi, \phi) \tag{9.16}$$

for the elastic and inelastic channels respectively. With the expansion

(Equation 9.14) and the Hamiltonian (Equation 9.13) the total system wave equation is:

$$(\sum_n + \int)\phi_n(\mathbf{r}_B)\left[\frac{\hbar^2}{2\mu}\nabla^2_{\mathbf{R}} + E + \frac{k_i^2\hbar^2}{2\mu} - E_n\right]F_n(\mathbf{R}) = V(\mathbf{R},\mathbf{r}_B)\Psi(\mathbf{R},\mathbf{r}_B) \quad (9.17)$$

where the result $H_B(\mathbf{r}_B)\,\phi_n = \phi_n E_n$ has been used. To proceed further we multiply Equation 9.17 by $\phi_n^*(\mathbf{r}_B)$ and integrate over $\mathbf{r}_B$, i.e. all the internal coordinates of B, to obtain:

$$\left\{\frac{\hbar^2}{2\mu}\nabla^2_{\mathbf{R}} + E - E_n\right\}F_n(\mathbf{R}) = \sum_m F_m(\mathbf{R})\int \phi_n^*(\mathbf{r}_B)V(\mathbf{R},\mathbf{r}_B)\phi_m(\mathbf{r}_B)d\mathbf{r}_B. \quad (9.18)$$

where there is a term on the R.H.S. for each state of the target. This still exact result can be written more succinctly by defining a matrix element $\mathscr{V}_{nm}$ of the intermolecular potential:

$$\mathscr{V}_{nm}(\mathbf{R}) = \frac{2\mu}{\hbar^2}\int \phi_n^*(\mathbf{r}_B)\,V(\mathbf{R},\mathbf{r}_B)\phi_m(\mathbf{r}_B)d\mathbf{r}_B \quad (9.19)$$

so producing the set:

$$[\nabla^2_{\mathbf{R}} + k_0^2]F_0(\mathbf{R}) = \sum_m F_m(\mathbf{R})\mathscr{V}_{0m}(\mathbf{R}),$$

$$\cdots\cdots\cdots$$

$$[\nabla^2_{\mathbf{R}} + k_n^2]F_n(\mathbf{R}) = \sum_m F_m(\mathbf{R})\mathscr{V}_{nm}(\mathbf{R}) \quad (9.20)$$

We can see from Equation 9.19 that the perturbation must be of the correct symmetry with respect to $\mathbf{r}_B$ if $\mathscr{V}_{mn}$ is to be non-zero. In practice this does not yield any useful collisional selection rules except in the limit of weak coupling.

The Equations 9.20 are hardly directly useful as they stand since not only is there an infinite number of them but also most computational schemes would be carried out after a partial wave expansion thus multiplying the number of equations still further. After applying the partial wave expansion to the $F_n(\mathbf{R})$ and solving the set of Equations 9.20, the S matrix elements $S_{nlo:n'l'm'}$ would in principle be obtained from the l^{th} translational wave function once it had settled down to its asymptotic form:

$$F_{n'l'm'}(R) \longrightarrow |F_{n'l'm'}|\,e^{i(k_{n'}R - l\pi/2 - \eta_{n'l'm'})}. \quad (9.21)$$

If the calculation were started with a wave of unit amplitude in the incident channel (*nlo*) we obtain from Equation 9.4:

$$S_{nl0:n'l'm'} = \left(\frac{k_{n'}}{k_n}\right)^{\frac{1}{2}} \left| F_{n'l'm'} \right| e^{i\eta_{n'l'm'}} \tag{9.22}$$

These S matrix elements may then be used in Equations 9.8 and 9.9 to compute differential cross-sections. Note that while there will be interference between partial waves of different l' values in a given inelastic exit channel, this will not occur between different exit channels since $k_n \neq k_{n'}$, i.e. the wavelengths are different.

9.3 Approximation methods

Further simplifications must be made if anything but a formal solution to the basic Equations 9.20 is required. A large number of different schemes have been proposed. Almost inevitably it is necessary to close the infinite set of coupled equations by selecting only a few channels for calculation, equivalent to representing ϕ by a limited number of terms in the expansion of Equation 9.14. In electronic excitation problems this is not a high price to pay because the conservation of energy severely limits the number of open exit channels and at most one or two virtual states might be required; but for rotational energy transfer where a quantum of energy is a small fraction of the incident kinetic energy at least ten rotational states might have to be included and classical mechanics is strongly indicated. Approximate quantum methods can be broadly classified into those that treat both the internal and relative motion quantum mechanically and those that introduce the concept of a classical path for the relative motion. Each of these classes can then be subdivided by the number of internal states that is included in the quantum description of the target (D. R. Bates, 1961).

(i) The close coupling approximation

In this, the most rigorous method, a limited number of channels are selected and the resulting set of coupled equations of the form of Equation 9.20 solved numerically. The effect of including additional channels can only be explored by repeating the calculations with an expanded basis set. In this method the prime requirement is for a fast and accurate numerical technique and a use of a polynomial approximation to the potential (rather than to the wave function) as discussed in Section 6.8 is particularly attractive. The incorporation of the special boundary conditions into the numerical problem

has been discussed by W. A. Lester and R. B. Bernstien (1968) for the particular case of the rotational excitation of a diatomic molecule by an atom.

(ii) The Born approximation

If the coupling and spherically symmetric part of the intermolecular potential are weak enough to produce only small changes in the incident wave, i.e. both small momentum changes and small transition probabilities, the inelastic Born approximation is appropriate. In the spirit of its application to elastic scattering, Section 6.5, we retain only a single term on the right hand side of the leading equation in Equation 9.20 and replace $F_m(\mathbf{R})$ by the incident plane wave. The amplitude in any channel is then considered separately as arising directly from the incident channel and we obtain the completely uncoupled equations

$$\{\nabla_{\mathbf{R}}^2 + k_n^2\}\, F_n(\mathbf{R}) = \mathscr{V}_{ni}(\mathbf{R})\, e^{i\mathbf{k}_i \cdot \mathbf{R}} \tag{9.23}$$

which clearly give the *first order* contribution of the coupling potential to the scattered amplitudes. In the case of the interaction of a homonuclear diatomic molecule with an S state atom, for which the coupling potential would contain the factor $P_2(\cos\beta)$ where β is the angle between $\mathbf{r}$ and $\mathbf{R}$, Equation 9.23 indicates that only $\Delta j = \pm 2$ transitions are allowed (even assuming both odd and even j states to be populated). As in elastic scattering, however, the Born approximation in this form is not really applicable to molecular problems because of the distortion of the plane wave by the diagonal term $\{\mathscr{V}_{ii}\}$. It is, however, an important method for transitions induced by electron/molecule collisions.

Proceeding in the same way as in the elastic case we can go on to obtain the scattering amplitude in the n^{th} channel (using vector notation again) as:

$$f_n(\chi, \phi) = -\frac{\mu}{2\pi\hbar^2} \int e^{i(\mathbf{k}_i - \mathbf{k}_n)\cdot \mathbf{R}}\, \mathscr{V}_{ni}(\mathbf{R})\, d\mathbf{R}. \tag{9.24}$$

(iii) Distorted wave approximation

The D.W.A. is a natural development of the Born method in which we use a better approximation to the wave function in the incident channel. In place of the incident plane wave we now use the wave function calculated assuming that $F_i(\mathbf{R})$ is governed solely by the potential $\mathscr{V}_{ii}(\mathbf{R})$, i.e. solving the equation

$$\{\nabla_{\mathbf{R}}^2 + \mathscr{V}_{ii}(\mathbf{R}) + k_i^2\}\, F_i^{(0)}(\mathbf{R}) = F_i^{(0)}(\mathbf{R}). \tag{9.25}$$

As in the Born approximation the excitation is assumed to be direct from the elastic channel and as an improvement on Equation 9.23 we have:

$$\{\nabla_{\mathbf{R}}^2 + k_n^2\}\, F_n(\mathbf{R}) = V_{in}(\mathbf{R}) F_i^{(0)}(\mathbf{R}) \tag{9.26}$$

where $F_i^{(0)}(\mathbf{R})$ is the unperturbed elastic function from Equation 9.25.

The advantage of this method is that the potential need no longer be weak. All that is required is that the coupling between states should be small, so that while the diagonal terms in the S matrix may be large the off diagonal ones remain small, a fairly common situation. A typical application of this approximation is to vibrational transitions in the system He/H_2 (F. H. Mies, 1965).

(iv) Time dependent perturbation methods

These methods are semi-classical in nature, using classical mechanics to describe the nuclear motion and reserving quantum theory for the internal behaviour. A number of different prescriptions have been used. Their common feature is the calculation of an average classical trajectory and the conversion of the R dependent matrix elements to an equivalent time dependent form. At high velocities, for example, the trajectory might be approximated by a straight line with the appropriate impact parameter b so that:

$$t = (R^2 - b^2)^{1/2}/v. \tag{9.27}$$

The standard results of time dependent perturbation theory then yield:

$$\begin{aligned} \dot{a}_1 &= (i\hbar)^{-1} \sum_n V_{1n}(t)\, a_n\, e^{i(E_1 - E_n)t/\hbar} \\ &\vdots \\ \dot{a}_m &= (i\hbar)^{-1} \sum_n V_{mn}(t)\, a_n\, e^{i(E_m - E_n)t/\hbar}. \end{aligned} \tag{9.28}$$

The matrix elements are those defined previously but with the R dependence replaced by the approximate t dependence and the $|a_n|^2$ are the probabilities of excitation to the state n.

This approximation is useful under the usual requirements for a semi-classical theory – that the trajectory be well defined so that $\lambda \ll$ the potential range. An additional constraint is that the energy change be small with respect to the incident energy so that the trajectories associated with the inelastic process approximate to the elastic path used in calculating the time dependent perturbation.

If the internal motion of the target is also slow in comparison with the relative velocity a further simplification, the 'Sudden' approximation can be obtained and at $t = \infty$ the final amplitudes are:

$$a_n^{\infty} = \int \phi_n^* \, e^{i\int_{-\infty}^{\infty} V(r_B, t)\,dt/\hbar} \, \phi_i \, d\mathbf{r}_B. \tag{9.29}$$

For small transition probabilities a first order approximation to the solution of Equation 9.28 is useful:

$$a_n^{\infty}(b) = (i\hbar)^{-1} \int_{-\infty}^{\infty} V_{ni}(t) \, e^{i(E_n - E_i)t/\hbar} \, dt \tag{9.30}$$

and the transition probability $i \to n$ for a trajectory following the path of integration in Equation 9.30 is:

$$\mathcal{P}_{in}(b) = |\, a_n^{\infty}(b) \,|^2.$$

The total cross-section for the transition is:

$$\sigma_{\text{tot}}^{i \to n} = 2\pi \int_0^{\infty} b \mathcal{P}(b) \, db. \tag{9.31}$$

Expression 9.30 serves to define the regions of strong $a_n^{\infty} \geqslant 1$, and weak $a_n \ll 1$, coupling and it may also be noted that Equation 9.29 reduces to Equation 9.30 upon expanding the exponential in Equation 9.29 and retaining only the leading term in V. Equation 9.30, if valid for all impact parameters, is essentially equivalent to Equation 9.24. Inspection of Equation 9.30 shows that the integrand is composed of a function $V_{ni}(t)$ that rises to a maximum near the turning point and decays again, while the second factor, $e^{i\Delta E t/\hbar}$, is a rapidly oscillating one. In general, therefore, appreciable transition probabilities will only be obtained in either near resonant cases (ΔE small) or when $V_{ni}(t)$ contains a Fourier component of frequency $\Delta E/\hbar$, which will lead to a region of stationary phase in the integration of Equation 9.30.

(v) Perturbed Stationary State method (PSS)

In the PSS approximation a different expansion for the total system wave function is used. The expression 9.17 in terms of the eigenfunctions of the isolated species is replaced by an expansion in the eigenstates of the *whole* system A + B (D. R. Bates, 1961). The aim of this transformation is to

diagonalize the matrix $\{V_{ij}\}$ so that transitions, now due to the *dynamic* coupling of states, are minimized and attention is focused on the non-adiabatic aspects of the problem rather than coupling through the potential energy. The requirement for adiabaticity is that $\Delta Ea/\hbar v \gg 1$, where ΔE and a are, respectively, the separation between the compound states (a function of R) and a is the range over which the new states are a rapidly varying function of R. The dynamic coupling can either be due to the rotation of the AB system or to the relative radial (R) motion. In atomic collision processes in which electronic levels are excited – for which the method was originally devised – this rotational coupling is a troublesome complication. Furthermore, collisions of small impact parameters which are usually the most important in producing inelastic effects, unfortunately have the largest radial velocity so that the approximation can become least useful in the most important region. It is at its most powerful in discussing spin exchange scattering (Section 6.17 or 6.16) where the new molecular states (defined by their total electron spin) can be regarded as completely uncoupled, at least for collisions at thermal speeds and non-adiabatic effects (spin decoupling in this case) only become apparent well above these relative energies.

(vi) Classical mechanics

Treatments based purely on classical arguments will be valid under the same conditions as described for elastic scattering, well defined trajectories that result in momentum changes that are not too small, but with the added requirement that quantization of the internal motion must be reliably modelled by simple box partitioning of the classical energy and momentum transfer. Techniques based on classical trajectories, as is the Monte Carlo approach to chemical reaction, Section 8.7, are useful in dealing with rotational and vibrational excitation.

9.4 Experimental methods

(i) State change technique

This technique is reminiscent of beam resonance spectroscopy in that both selection 'A' and analysis fields 'B' are employed. The RF 'C' field which produces transitions in the spectrometer is, however, replaced by a collision region; either a cross-beam or target chamber may serve this purpose. The resulting transitions are detected by the analyzer field.

Most experiments of this type have used TlF of CsF in the primary beam, molecules with a very large dipole moment which can also be detected by

surface ionization methods. As described in Chapter 4, a four pole electric field can focus such diatomic polar molecules at a point dependent upon their effective dipole moment or (jm_j) state and their velocity. The combination of such a field fitted with suitable stops and orifices to define molecular trajectories and a velocity selector can therefore be made to transmit only specified (jm_j) states.

In the experiments of Bennewitz and co-workers (H. G. Bennewitz; K. H. Kramer; W. Paul and J. P. Toennies 1964) total collision cross-sections for TlF in the (1,0) and (1,1) states and CsF (2,0) and (2,2) were measured for a range of atomic and molecular targets. In this work only a single selecting field on the primary beam was used so that the observed total collision cross-sections included contributions from transitions to all the accessible states. A uniform steady electric field was applied throughout the collision zone to maintain the polarization of the beam as prepared by the selector. By applying this field either perpendicular or parallel to the relative velocity the (1,0) or (1,1) polarization of the beam with respect to the collision could be achieved. It was thus possible to make accurate comparisons of the ratio $\sigma_{tot}(1,0)/\sigma_{tot}(1,1)$ over a range of velocities and by a classical impact approximation of the type discussed in Section 9.3 (*iv*) to obtain estimates for the long and short range potential anisotropies q_6 and q_{12} in a potential of the form:

$$V = \epsilon\left\{\left(\frac{R_m}{R}\right)^{12}(1 + q_{12}P_2(\cos\beta)) - 2\left(\frac{R_m}{R}\right)^{6}(1 + q_6 P_2(\cos\theta))\right\} . \tag{9.32}$$

Both selection and analyzing fields were used in the experiments of J. P. Toennies (1965; 1966), shown schematically in Fig. 9.1. The second, analyzer, field had an acceptance angle of $\sim\frac{1}{2}°$ so that either partial elastic or inelastic cross-sections, $\sigma_{jm_jj'm_{j'}}(\theta \sim 0)$ for forward scattering into the acceptance cone could be measured.

The rotation period of the TlF molecule is long compared to the interaction time of the collision, while the energy change (and change in k) associated with a rotational transition is only a small fraction of the translational energy. This situation is a favourable one for the application of time dependent perturbations methods. We may also regard the polar molecule as stationary in orientation during the interaction so that the anistropy in the potential can be treated by post-averaging the results of these computations over all orientations. In this 'sudden' approximation the rotor experiences a brief time dependent electric field in which the appropriate

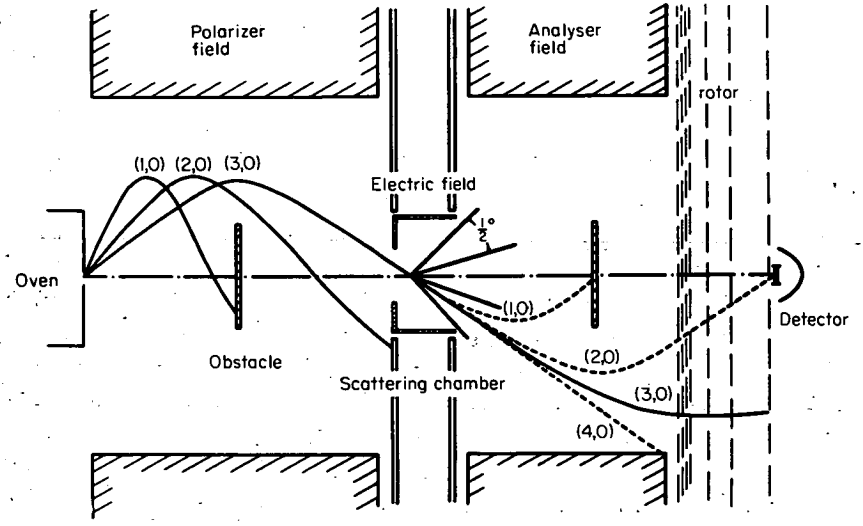

Fig. 9.1 Apparatus used by Toennies to study rotational transitions in TlF produced by collisions. The TlF rotational states are selected in the four pole electric field on the left and are analysed after collision by an identical analyser field. The velocity selector is required to define the velocities through the electric fields and thus to ensure that only the specified states are transmitted. (H. Pauly et al., 1964).

Fourier components can induce transitions $\Delta j = \pm 1$ for dipole interactions, ± 2 for quadrupole ones etc.

Experiments of this type in which interference effects e.g. glories, may in principle be observed make it possible to determine phase relations as well as amplitudes (probabilities) in the exit channels. In comparison most bulk experiments yield only the rate constants for processes and hence no phase information.

(ii) Velocity change method

Measurement of the pre- and post- collisions velocities is frequently sufficient to identify the scattering into specific quantum states if these are well spaced in energy. The ratio of incident and final relative velocities is given by:

$$v_{\text{final}}/v_{\text{initial}} = \left(\frac{E \mp \Delta E}{E}\right)^{\frac{1}{2}} \tag{9.33}$$

where $E = \frac{1}{2}\mu v^2_{\text{initial}}$ and ΔE is the exoergicity. The technique becomes less

useful at high collision energies or as ΔE decreases since the resolution in E is limited by the spread of incident relative velocities present in the apparatus. In the most favourable case a light test particle in the primary beam interacts with a heavy slow target molecule. An additional reduction in the contribution of the target velocity can be made by moving the detector in a plane perpendicular to the main and cross-beams since in this configuration the target velocity contributes only in the second order.

The velocity change technique was first used by A. R. Blythe (1964) to study the de-excitation process:

$$K + o - D_2\ (j = 2) \longrightarrow K + o - D_2\ (j = 0)$$

Velocity selectors with a resolution (half intensity full width) of 4.7 per cent were used on both the primary and scattered K beams and the ortho D_2 source was operated at 200K so to obtain the optimum concentration of the $j = 2$ state (55 per cent). Observations were made at a laboratory angle of 3° at which two centre of mass angles can contribute, as shown in Fig. 9.2. The narrow CM angle one at 29° associated with a fast velocity in the laboratory

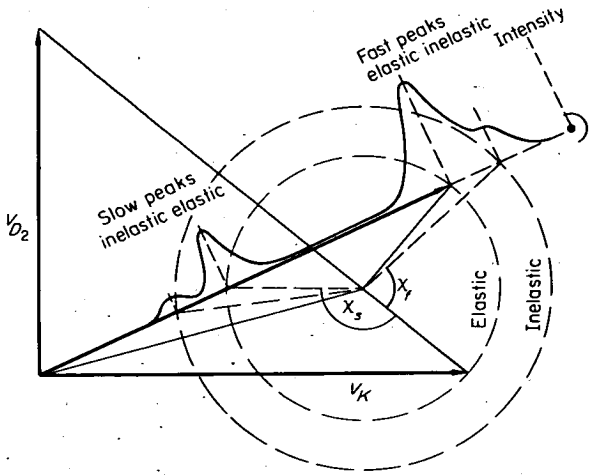

Fig. 9.2. Newton diagram for velocity change experiment used to study the process:

$$K + D_2(j = 2) \rightarrow K + D_2(j = 0)$$

A monenergetic K beam is prepared by the first velocity selector and the change in velocity after collision with the cross-beam of D_2 is measured by a second selector. (A. R. Blythe et al, 1964).

and the wide angle scattering at 108° with a slow laboratory velocity. Since $\sigma(29°) >> \sigma(108°)$ for atomic and molecular potentials, the fast component is the dominant contribution to the total signal observed. This narrow angle scattering arises from large impact parameters collisions which are unlikely to produce inelastic effects so that the more favourable final velocity range for observing these effects is that of the slow component corresponding to wide angle (CM), small impact parameter scattering. The D_2 excitation process $j = 0 \rightarrow j = 2$ is unlikely to be seen, since a velocity decrease in the backward (CM) direction results in an increase in laboratory velocity, and consequently to overlap with the spread of velocities in the particles in the fast elastic peck (Fig. 9.3). On the other hand the D_2 de-excitation process, rotational → translational energy transfer, moves the elastic peck into a velocity region where there is only a small elastic contribution so that this is a favourable situation for measurement. These experiments nevertheless were still very limited in signal/noise and the cross-section for $\sigma_{j=2}^{j=0}(108°)$ was estimated as 0.05 $A^{°2}$. As a relatively early experiment (published 1964) it would seem worth repeating these measurements with the more intense beams now available.

The velocity change method has also been applied (J. P. Toennies and J. Schottler, 1968; W. D. Held et al, 1970; R. David et al, 1971; P. K. Dittner and S. Datz, 1971.) to systems such as:

$$\begin{aligned} Li^+ + H_2\ (v = 0) &\longrightarrow Li^+ + H_2\ (v = 1, 2, 3 \ldots) \\ &\longrightarrow Li^+ + H + H \\ K^+ + H_2\ (v = 0) &\longrightarrow K^+ + H_2\ (v = 1, 2 \ldots) \end{aligned} \qquad (9.34)$$

where the light mass of the Li^+ ion and the wide spacing of the H_2 vibrational levels assist the resolution of the individual state transitions. The apparatus used by Toennies in these investigations is shown in Fig. 9.4. The Li^+ beam is formed by surface ionization, energy analyzed electrostatically to a spread $\Delta E/E \sim 0.4$ per cent and pulse modulated with a 50 ns width at a 10 kHz repetition rate. The beam then intersected the H_2 target formed by expansion to high Mach number through a nozzle, fluxes of the order 5×10^{20} molecules steradian^{-1} s^{-1} being achieved in the target. The ion arrivals at the electron multiplier detector were recorded in a 400 channel multi scaler synchronized to the beam pulse rate. A flight time spectrum recorded in this fashion is shown in Fig. 9.5. The peak labelled $0 \rightarrow 0$ is the elastic backward scattered contribution, the forward elastic peak is off the figure to the right at zero time. These experiments are capable of considerable development and

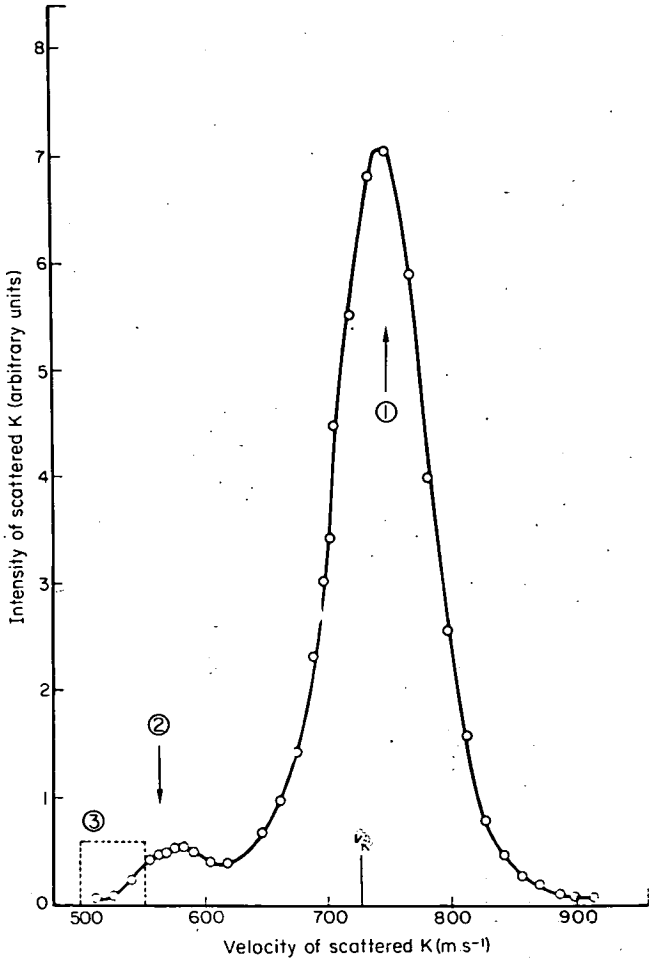

Fig. 9.3 Plot of the K intensity transmitted through the second selector as a function of velocity. The fast (1) and slow (2) elastic peaks together with the inelastic de-excitation contribution (3) are shown. (A. R. Blythe et al, 1964).

are likely to be an important source of information on translational energy transfer processes.

(iii) Techniques involving ion or photon emission

In some collisions the transitions may be either directiy to ions or to short lived electronically excited states. In either case the process can be studied since the product ions or photons (formed by decay of the excited species)

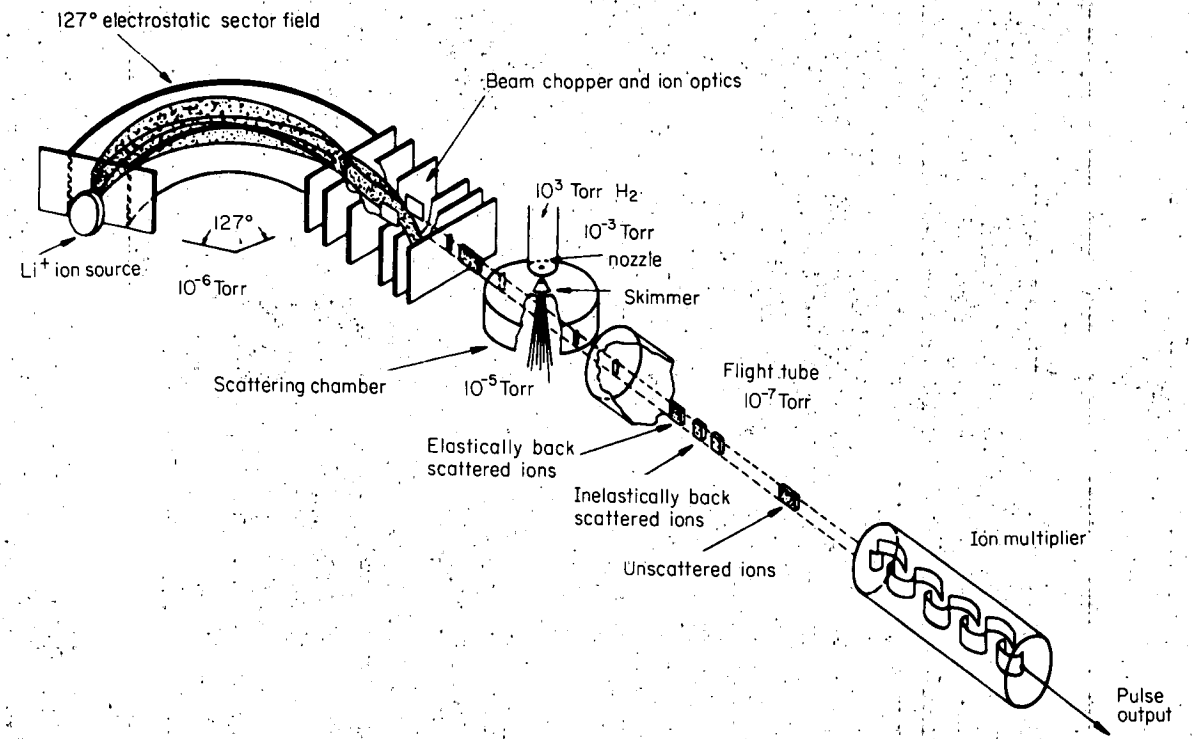

Fig. 9.4 Time of flight experiment to study processes such as

$$L_i^+ + H_2(v = 0) \rightarrow L_i^+ + H_2(v)$$

The almost monoenergetic Li^+ ion beam is pulse modulated and the scattered ion arrivals at the detector are recorded in a multichannel scaler as a function of their flight time. (R. David et al, 1971).

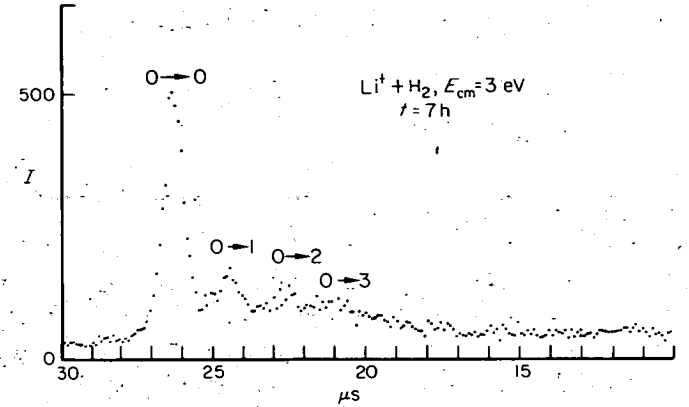

Fig. 9.5 Time of arrival spectrum for Li^+ ions inelastically scattered from H_2. Only ions backward scattered in the CM are observed, those forward scattered arriving before the time covered by this trace begins. The peaks are labelled with the relevant vibrational transition. (R. David et al, 1971).

are both fairly readily detectable and also serve to identify the inelastic transition.

This class of experiment is usually directed at measurement of a total cross-section for some process, but the work of G. A. L. Delvigne and J. Los (1971) on chemi-ionization yielded relative differential cross-sections for processes of the type:

$$K + Br_2 \longrightarrow \begin{cases} K^+ + Br_2^- \\ K^+ + Br^- + Br. \end{cases} \qquad (9.35)$$

In these experiments a fast neutral beam of potassium was produced by a sputtering technique and after velocity selection collided with Br_2 molecules in a target chamber. The product ions were scattered through a field free region into a detector for K^+ ions. The results of some of this work shown in Fig. 9.6, are interesting both in their apparent scaling by $E\theta$ (which would be expected only for elastic collisions) and in the considerable structure observed. Similar experiments in which total cross-sections for ion production from a range of target molecules are measured have been reported by other workers (R. K. B. Helbing and E. W. Rothe, 1969; A. P. M. Baede et al, 1969; K. Lacmann and D. R. Herschbach, 1970; R. H. Hammond et al, 1971).

In an alternative technique an aerodynamically accelerated beam of Xe in a He carrier has been used to study the dissociative ionization processes (F. P.

Tully et al., 1971; E. K. Parks and S. Wexler, 1971)

$$\begin{aligned} Xe + KBr &\longrightarrow K^+ + Br^- + Xe \\ Xe + TlBr &\longrightarrow Tl^+ + Br^- + Xe \end{aligned} \qquad (9.36)$$

at translational energies between 8 and 15 eV.

Experiments in which excitation to levels below the ionization limit was observed have been made by using a photomultiplier and interference filter to view the collision zone where beams of translationally (R. W. Anderson et al, 1969; V. Kempter et al, 1970; K. Lacmann and D. R. Herschbach, 1970) vibrationally (J. E. Mentall et al, 1967; M. C. Moulton and D. R. Herschbach, 1966) or electronically (L. J. Doemeny et al, 1969) hot species intersected. The theoretical interpretation of collisions producing electronic excitation is not too well developed. In general the results of these experiments have supported the importance of curve crossing situations in producing electronic

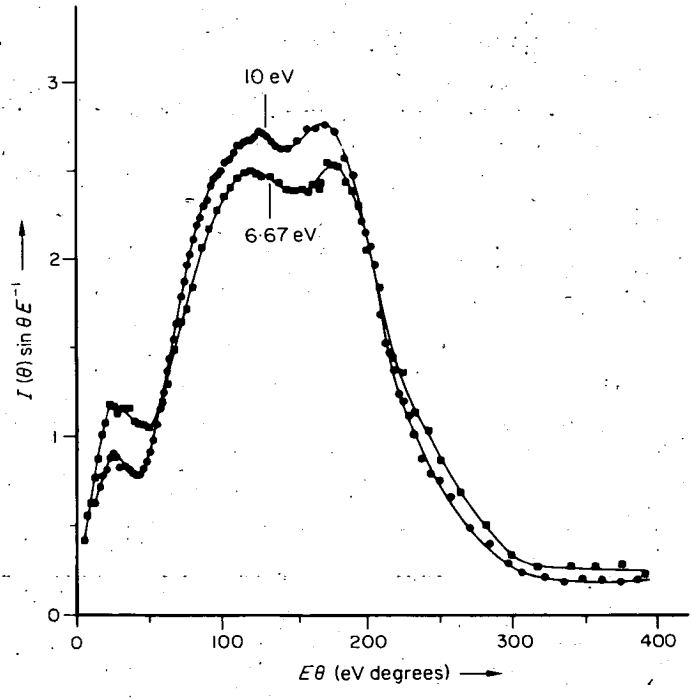

Fig. 9.6 Differential cross-sections for ionization in collisions of K and Br_2. The fast K beam was formed by a sputtering technique (G. A. L. Delvigne and J. Los, 1971).

excitation and in particular the importance of the ionic surface in alkali/halogen systems in coupling the various excited states.

This 'curve crossing' situation is usually treated by the Landau-Zener approximation (D. R. Bates, 1961) in which the transitions between states occur exclusively at their crossing points and motion outside this region is treated as purely elastic on the appropriate potential surface. In this approximation the crossing probability at each intersection is given by:

$$P_{12}(b) = 2\pi\, V_{12}(R_c)^2 / [\hbar w_r(b)\, |(S_1 - S_2)|] \tag{9.37}$$

where V_{12} is the matrix element connecting the two electronic states evaluated at the crossing point, S_1 and S_2 are the gradients of the two surfaces at this point and v_r is the radial velocity at the crossing. Since collisions must traverse the crossing region twice, the total probability of transition is:

(i) Probability of remaining in state 1,

$$\mathscr{P}_{11} = P_{12}^2 + (1 - P_{12})^2 \tag{9.38}$$

(ii) Probability of emerging in state 2,

$$\mathscr{P}_{12} = 2P_{12}(1 - P_{12})$$

The P_{12} in Equations 9.37 and 9.38 are impact parameter dependent through $v_r(b)$. Substituting Equation 9.38ii into Equation 9.31 we obtain the total cross-section for ion production or electronic excitation as a function of V_{12} and R_c (there is a weaker dependence on the intermolecular force operating at R_c). If R_c can be located on spectroscopic or other grounds, the energy dependence of $\sigma_{tot}^{1\,2}(E)$ gives V_{12} directly. It must be remembered, though, that Equation 9.37 is only an approximate solution of the Equations 9.28 for two states and one that becomes less valid the higher v_r. Its validity in any particular situation must be checked. Experiments in this area are particularly interesting since electronic rearrangement is the immediate precursor of most chemical reaction and some vibrational energy transfer.

Much remains to be done in the field of collisions in which the electronic motion is non-adiabatic and their elucidation will remain a challenge to the theorist and experimentalist for a considerable time to come.

References

Abauf, N. (1966), Ph.D. Thesis, Princeton University.

Ackerman, M., Greene, E. F., Moursund, A. L. and Ross, J. (1964), *J. Chem. Phys.*, **41**, 1183.

Airey, J. R., Greene, E. F., Reck, G. P., and Ross, J. (1967), *J. Chem. Phys.*, **46**, 3295.

Airey, J. R., Greene, E. F., Kodera, G. P., Reck, G. P., Ross, J. (1967), *J. Chem. Phys.*, **46**, 3287.

Amdur, I., (1968), *Methods of Experimental Physics*, **7A**, 341. Academic Press, New York.

Amend, W. E. (1968), U. California, Berkeley, Rept. No AS-68-4.

Anderson, J. B., (1968), *Intermediate Energy Molecular Beams from Free Jets of Mixed Gases*, Project Squid O.N.R. Tech. Rept. PR166P.

Anderson, J. B., Andres, R. P., and Fenn, J. B. (1965), *Adv. Mol. Phys.*, **1**, 345.

Anderson, J. B., Andres, R. P. and Fenn, J. B. (1966), *Adv. Chem. Phys.*, **10**, 275.

Anderson, R. W., Aquilanti, V. and Herschbach, D. R. (1969), *Chem. Phys. Lett.*, **4**, 5.

Anlauf, K. G., Bickes, R. W. and Bernstein, R. B. (1971), *J. Chem. Phys.*, **54**, 3647.

Anlauf, K. G., Kuntz, P. J., Maybotte, D. H., Pacey, P. D. and Polanyi, D. C. (1967), *Disc. Faraday Soc.*, **44**, 183.

Aquilanti, V., Luiti, G., Vecchio-Cattive, F. and Volpi, G. G. (1971), *Mol. Phys.*, **21**, 1149.

Baede, A. P. M., Moutinho, A. M. C., de Vries, A. E. and Los, J. (1969), *Chem. Phys. Lett.*, **3**, 530.

Barwig, P., Buck, U., Hundhausen, E. and Pauly, H. (1966), *Z. Physik*, **196**, 343.

Bates, D. R., Ed. (1961), *Quantum Theory, I, Elements*, Academic Press, London.

Beck, D. *Proc. Int. Sch. Phys. "Enrico Fermi." Course XLIV (Varenna)* (Ed. Ch. Schlier) (1970) Academic Press, New York.

Beck, D., Dummel, H. and Henkel, U. (1965), *Z. Physik*, **185**, 19.
Beck, D., Engelke, F. and Loesch, H. J. (1968), *Ber. Bunsen. Physik. Chem.*, **72**, 1105.
Beckey, H. D. (1961), *Advances in Mass Spectrometry*, **2**, 1.
Beckey, H. D., Knöppel, H., Metzinger, G. and Schulze, P. (1963), *Advances in Mass Spectrometry*, **3**, 35.
Bennewitz, H. G., Busse, H. and Dohman, H. D. (1971), *Chem. Phys. Lett.*, **8**, 253.
Bennewitz, H. G., Gegenbach, R., Haerten, R. and Müller, G. (1969), *Z. Physik*, **226**, 279.
Bennewitz, H. G. and Haerten, R. (1969), *Z. Physik*, **227**, 399.
Bennewitz, H. G., Haerten, R. and Müller, G. (1969), *Z. Physik.*, **266**, 139.
Bennewitz, H. G., Haerten, R and Müller, G. (1971), *Chem. Phys. Lett.*, **12**, 335.
Berkling, K. Helbing, R. Kramer, K. H., Pauly, H., Schlier, C. and Toschek, P. (1962), *Z. Physik*, **166**, 405.
Berkling, K., Helbing, R., Kramer, K. H., Pauly, H., Schlier, C. and Toschek, P. (1962), *Z. Physik*, **166**, 406.
Berkling, K., Schlier, C. and Toschek, P. (1962), *Z. Physik*, **168**, 81.
Bernstein, R. B. (1963), *J. Chem. Phys.*, **38**, 2599.
Bernstein, R. B. (Ed. J. Ross) (1966), *Adv. Chem. Phys.*, **10**, 75.
Bernstein, R. B. and Kramer, K. H. (1964), *J. Chem. Phys.*, **40**, 200.
Bernstein, R. B. and O'Brien, T. J. P. (1965), *Disc. Faraday Soc.*, **40**, 35.
Bernstein, R. B. and O'Brien, T. J. P. (1967), *J. Chem. Phys.*, **46**, 1208.
Berry, M. V. (1966), *Proc. Phys. Soc.*, **88**, 285.
Beuhler, R. J. and Bernstein, R. B. (1968), *Chem. Phys. Lett.*, **2**, 166.
Beuhler, R. J. and Bernstein, R. B. (1969), *J. Chem. Phys.*, **51**, 5305.
Bickes, R. W. and Bernstein, R. B. (1970), *Chem. Phys. Lett.*, **4**, 111.
Bier, K. and Hagena, O. (1963), *Rarefied Gas Dynamics*, **1**, 478, Academic Press, New York.
Birely, J. H. and Herschbach, D. R. (1965), *Bull. Ames. Phys. Soc.*, **10**, 634.
Birely, J. H. and Herschbach, D. R. (1966), *J. Chem. Phys.*, **44**, 1690.
Birely, J. H., Herm, R. R., Wilson, K. R., and Herschbach, D. R. (1967), *J. Chem. Phys.*, **51**, 5461.
Birely, J. H., Entemann, E. A., Herm, R. R., and Wilson, K. R. (1969), *J. Chem. Phys.*, **51**, 5461.
Blais, N. C., (1968), *J. Chem. Phys.*, **49**, 9.
Blais, N. C. and Bunker, D. L. (1962), *J. Chem. Phys.*, **37**, 2713.
Blais, N. C. and Cross, J. B. (1970), *J. Chem. Phys.*, **52**, 3580.
Blythe, A. R., Grosser, A. E. and Bernstein, R. B. (1964), *J. Chem. Phys.*, **41**, 1917.
Brash, H. M., Campbell, D. M., Farago, P. S., Rae, A. G. A., Siegmann, H. C. and Wykes, J. S. (1969), *Proc. Roy. Soc. Edin.*, **A68**, 158.
Bredewout, J. W., Bosman, N. J., Vissen, A. G., Kerving, J. and van den Meijdenberg, C. J. N. (1971), *Chem. Phys. Lett.*, **11**, 127.
Brink, G. O. (1966), *Rev. Sci. Instn.*, **37**, 857.
Brodhead, C. C., Davidovits, P. and Edelstein, S. A. (1969), *J. Chem. Phys.*, **51**, 3601.
Brooks, P. R. (1969), *J. Chem. Phys.*, **50**, 5031.
Brooks, P. R. and Jones, E. M. (1966), *J. Chem. Phys.*, **45**, 3449.
Brooks, P. R., Jones, E. M. and Smith, K. (1969), *J. Chem. Phys.*, **51**, 3073.
Buck, U. (1971), *J. Chem. Phys.*, **54**, 1923, and 1929.

Buck, U. and Pauly, H. (1968), *Z. Physik*, **208**, 390.
Buck, U. and Pauly, H. (1969), *J. Chem. Phys.*, **51**, 1663.
Bunker, D. L., *Proc. Int. Sch. Phys., 'Enrico Fermi', Course XLIV (Varenna)* (Editor, Ch. Schlier) (1970), Academic Press, New York.
Bunker, D. L. and Blais, N. C. (1964), *J. Chem. Phys.*, **41**, 2377.
von Busch, F. (1966), *Z. Physik*, **193**, 412.

Cantini, P., Dondi, M. G., Scoles, G. and Torello, F. (1972), *J. Chem. Phys.*, **56**, 1946.
Cardillo, M. J., Chou, M. S., Greene, E. F. and Sheen, D. R. (1971), *J. Chem. Phys.*, **54**, 3054.
Cavallini, M., Dondi, M. G., Scoles, G. and Valbusa, U. (1972), *Chem. Phys. Lett.*, **10**, 22.
Cavallini, M., Gallinaro, G. and Scoles, G. (1967), *Z. Naturforsch*, 22, 415.
Cavallini, M., Gallinaro, G. and Scoles, G. (1967), *Z. Naturforsch*, 22a, 413.
Cavallini, M., Gallinaro, G., Manghetti, L., Scoles, G. and Valbusa, U. (1970), *Chem. Phys. Lett.*, **7**, 303.
Cavallini, M., Meneghetti, L., Scoles, G. and Yealland, M. (1970), *Phys. Rev. Letters*, **29**, 1469.
Clampitt, R. and Newton, A. S. (1969), *J. Chem. Phys.*, **50**, 1997.
Clough, P. N. and Thrush, B. A. (1967), *Disc. Faraday Soc.*, **44**, 205.
Colgate, S. O. and Imeson, T. C. (1965), *Rev. Sci. Instr.*, **36**, 932.
Collins, F. G. and Hurlburt, F. C. (1972), *J. Chem. Phys.*, **56**, 2609.
Connor, J. N. L. (1968), *Mol. Phys.*, **15**, 621.
Cowley, L. T., Fluendy, M. A. D., Horne, D. S. and Lawley, K. P. (1969), *J. Sci. Instr.*, 2, 1021.
Cowley, L. T., Fluendy, M. A. D. and Lawley, K. P. (1970), *Rev. Sci. Instr.*, **41**, 666.
Cross, J. B. and Blais, N. C. (1971), *J. Chem. Phys.*, **55**, 3970.
Cross, R. J., Gislason, E. A. and Herschbach, D. R. (1966), *J. Chem. Phys.*, **45**, 3582.
Cross, R. J. and Malerich, C. J. (1968), *Chem. Phys. Lett.*, 2, 481.
Cross, R. J. and Malerich, C. J. (1970), *J. Chem. Phys.*, **52**, 386.

Daley, H. L., Yahiku, A. Y. and Perel, J. (1970), *J. Chem. Phys.*, **52**, 3577.
Daley, N. R. (1960), *Rev. Sci. Inst.*, **31**, 264.
Darwall, E. C. (1972), Ph.D. Thesis, University of Edinburgh.
Datz, S. and Taylor, E. H. (1956), *J. Chem. Phys.*, **25**, 389, 395.
Datz, S. and Taylor, E. H. (1963), *J. Chem. Phys.*, **39**, 1896.
David, R., Faubel, M., Marchand, P. and Toennies, J. P. (1971), *Proceedings VII ICPEAC*, 252, Amsterdam, North-Holland.
Davis, L., Field, B. T., Zabel, C. W. and Zacharias, J. R. (1949), *Phys. Rev.*, **76**, 1076.
Delvigne, G. A. L. and Los, J., *Proc. VII ICPEAC*, 277, Amsterdam, North Holland.
Delvigne, P. F., and Datz, S. (1971), *J. Chem. Phys.*, **54**, 4228.
Dittner, P. F. and Datz, S. (1971), *J. Chem. Phys.*, **54**, 4228.
Doemeny, L. J., van Itallie, F. J. and Martin, R. M. (1969), *Chem. Phys. Letts*, **4**, 302.
Dondi, M. G., Scoles, G., Torello, F. and Pauly, H. (1969), *J. Chem. Phys.*, **51**, 392.
Doverspike, L. D., Champion, R. L. and Bailey, T. L. (1966), *J. Chem. Phys.*, **45**, 4385.

Drullinger, R. E. and Zare, R. N. (1969), *J. Chem. Phys.*, **51**, 5532.
Duchart, B. S. (1971), Ph.D. Thesis, University of Edinburgh.
Duchart, B., Fluendy, M. A. D. and Lawley, K. P. (1971), *Chem. Phys. Letts.*, **14**, 129.
Dunoyer, L. (1911), *Computes Rend*, **152**, 594.

Eldridge, J. A. (1927), *Phys. Rev.*, **30**, 931.
Entemann, E. A. and Kwei, G. H. (1971), *J. Chem. Phys.*, **55**, 4879.

Fenn, J. B. (1968), *Molecular Beam Engineering at Intermediate Energies*, Project Squid, O.N.R. Tech. Rept. 115P.
Fenn, J. B. and Deckers, J. (1963), *Rarefied Gas Dynamics*, **1**, 516, Academic Press, New York.
Feynmann, R. P. and Hibbs, A. R. (1965), *Quantum Mechanics and Path Integrals*, McGraw-Hill, New York.
Firsov, V. G. (1953), *Zh. Eksp. Teor. Fiz.*, **24**, 279.
Fisk, G. A., McDonald, J. D. and Herschbach, D. R. (1967), *Disc. Faraday Soc.*, **44**, 228.
Fite, W. L., Brackmann, D. S., Hummer, D. G. and Stebbings, R. F. (1959), *Phys. Rev.*, **116**, 363.
Fluendy, M. A. D. (1964), *Rev. Sci. Inst.*, **35**, 1606.
Fluendy, M. A. D. (1965), *J. Sci. Instr.*, **42**, 489.
Fluendy, M. A. D., Horne, D. S., Lawley, K. P. and Morris, A. W. (1970), *Mol. Phys*, **19**, 659.
Fluendy, M. A. D., Martin, R. M., Muschlitz, E. E. Jun. and Herschbach, D. R. (1967), *J. Chem. Phys.*, **46**, 2172.
Foner, S. N. (1966), *Adv. At. Mol. Phys.*, **2**, 385, Academic Press, New York.
Ford, K. W. and Wheeler, J. A. (1959), *Ann. Phys.*, **7**, 259.
Foreman, P. B., Kendall, G. M. and Grice, R. (1972), *Mol. Phys.*, **23**, 127.
Fox L. (1962), *Numerical Solution of Ordinary and Partial Differential Equations*, Pergamon Press, Oxford.
Freund, R. and Klemperer, W. (1967), *J. Chem. Phys.*, **47**, 2897.
Freund, S. M., Fisk, G. A., Herschbach, D. R. and Klemperer, W. (1971), *J. Chem. Phys.*, **54**, 2510.

Geddes, J., Krause, H. F. and Fite, W. L. (1970), *J. Chem. Phys.*, **52**, 3296.
Gentry, W. R., Gislason, E. A., Mahan, B. H. and Tsao, C-W. (1968), *J. Chem. Phys.*, **49**, 3058.
Gersh, M. E. and Bernstein, R. B. (1971), *J. Chem. Phys.*, **55**, 4661.
Gersh, M. E. and Bernstein, R. B. (1972), *J. Chem. Phys.*, **56**, 6131.
Gillen, K. T. and Bernstein, R. B. (1970), *Rept. Theoretical Chemistry*, Institute Wisconsin, WIS-TCI-377X.
Gillen, K. T., Riley, C. and Bernstein, R. B. (1969), *J. Chem. Phys.*, **50**, 4019.
Gillen, K. T., Rulis, A. M. and Bernstein, R. B. (1971), *J. Chem. Phys.*, **54**, 2831.
Giordmaine, J. A. and Wang, T. C. (1960), *J. Appl. Phys.*, **31**, 463.
Gislason, E. A. and Kwei, G. H. (1967), *J. Chem. Phys.*, **46**, 2838.
Gislason, E. A., Mahan, B. H., Tsao, C-W and Werner, A. S. (1969), *J. Chem. Phys.*, **50**, 142.
Goldberger, M. L. and Watson, K. M. (1964), *Collision Theory*, Wiley, New York.
Goldstein, H. (1964), *Classical Mechanics*, Addison-Wesley, Reading, Mass.

Gomer, R. (1961), *Field Emission and Field Ionization*, Harvard University Press, Cambridge, Mass.
Gomer, R. and Inghram, M. G. (1955), *J. Chem. Phys.*, 22, 1279; (1955), *J.A.C.S.*, 77, 500.
Gordon, R. G. (1969), *J. Chem. Phys.*, 51, 14.
Gordon, R. J., Herm, R. R. and Herschbach, D. R. (1968), *J. Chem. Phys.*, 49, 2684.
Gordon, R. G., Klemperer, W. and Steinfeld, J. I. (1968), *Ann. Rev. Phys. Chem.*, 19, 215.
Gordon, R. J., Lee, Y. T. and Herschbach, D. R. (1970), *J. Chem. Phys.*, 54, 2393.
Greene, E. F., Hoffman, L. F., Lee, M. W., Ross, J. and Young, C. E. (1969), *J. Chem. Phys.*, 50, 3450.
Greene, E. F., Lau, M. H. and Ross, J. (1969), *J. Chem. Phys.*, 50, 3122.
Greene, E. F., Persky, A. and Kupperman, A. (1968), *J. Chem. Phys.*, 49, 2347.
Grice, R. and Empedocles, P. B. (1968), *J. Chem. Phys.*, 48, 5352.
Grice, R., Mosch, J. E., Safron, S. A. and Toennies, J. P. (1970), *J. Chem. Phys.*, 53, 3376.
Grosser, A. E. and Bernstein, R. B. (1965), *J. Chem. Phys.*, 43, 1140.
Grosser, A. E., Blythe, A. R. and Bernstein, R. B. (1965), *J. Chem. Phys.*, 42, 1268.
Grosser, J. and Haberland, H. (1968), *Phys. Rev. Letts.*, 27A, 634.
Grosser, A. E., Iczkowski, R. P. and Margrave, J. L. (1963), *Rev. Sci. Instr.*, 34, 116.

Ham, D. O. and Kinsey, J. L. (1970), *J. Chem. Phys.*, 53, 285.
Hammond, R. H., Henis, J. M. S., Greene, E. F. and Ross, J. (1971), *J. Chem. Phys.*, 55, 3506.
Halpern, I. and Strutunskii, V. M., *'Proceedings of the Second International Conference on the Peaceful Uses of Atomic Energy'*, Geneva (1958), United Nations, New York, 1958 paper P/1513.
Harris, R. M. and Wilson, J. F. (1971), *J. Chem. Phys.*, 54, 2088.
Hasted, J. B. (1964), *Physics of Atomic Collisions*, Butterworths, London.
Helbing, R. K. B. (1966) Thesis, University of Bonne.
Helbing, R. K. B. (1969), *J. Chem. Phys.*, 51, 3628.
Helbing, R. K. B. and Rothe, E. W. (1968), *J. Chem. Phys.*, 48, 3945.
Helbing, R. K. B. and Rothe, E. W. (1968), *Rev. Sc. Instr.*, 39, 1948.
Helbing, R. K. B. and Rothe, E. W. (1969), *J. Chem. Phys.*, 51, 1607.
Held, W. D., Schottler, J. and Toennies, J. P. (1970), *Chem. Phys. Letts.*, 4, 304.
Herm, R. R. and Herschbach, D. R. (1965), *J. Chem. Phys.*, 43, 2139.
Herm, R. R. and Herschbach, D. R. (1970), *J. Chem. Phys.*, 53, 285.
Herman, Z., Kerstetter, J., Rose, T. and Wolfgang, R. (1967), *Disc. Faraday Soc.*, 44, 123.
Herman, Z., Lee, A. and Wolfgang, R. (1969), *J. Chem. Phys.*, 51, 452, 454.
Herschbach, D. R., Kwei, G. H. and Norris, J. A. (1961), *J. Chem. Phys.*, 34, 1842.
Hirschfelder, J. O. (ed) (1967), *Adv. in Chem. Phys.*, 12, Wiley, New York.
Hirschfelder, J. O., Curtiss, C. F. and Bird, R. B. (1964), *Molecular Theory of Gases and Liquids* (2nd edition), Wiley, New York.
Hollstein, M. and Pauly, H. (1967), *Z. Physik*, 201, 10.
Hollstein, M. and Pauly, H. (1966), *Z. Physik*, 196, 353.

Horne, D. S. (1969), Ph.D. Thesis, University of Edinburgh.
Hostettler, H. U. and Bernstein, R. B. (1960), *Rev. Sci. Instr.*, **31**, 872.
Hotop, H., Lampe, F. W. and Niehaus, A. (1969), *J. Chem. Phys.*, **51**, 593.
Hulpke, E. and Schlier, C. (1967), *Z. Physik*, **207**, 294.
Hundhausen, E. and Pauly, H. (1965), *z.f. Naturforschung*, **20a**, 625.

Ioup, G. E. and Thomas, B. S. (1966), *J. Chem. Phys.*, **50**, 5009.

Johnson, J. C., Stair, A. T. and Pritchard, J. L. (1966), *J. Appl. Phys.*, **37**, 155.
Johnson, R. L., Perona, M. J. and Setser, D. W. (1970), *J. Chem. Phys.*, **52**, 6372.
Johnston, W. D. and King, J. G. (1966), *Rev. Sci. Inst.*, **37**, 375.
Jonah, C. D., Zare, R. N. and Ottinger, Ch. (1972), *J. Chem. Phys.*, **56**, 263.

Kalos, F. and Grosser, A. E. (1970), *Chem. Phys. Letts.*, **6**, 537.
Kanes, H., Pauly, H. and Vietzke, E. (1971), Max-Planck-Inst. f. Stromungsforschung, Ber. 102.
Kantrowitz, A. and Grey, J. (1951), *Rev. Sci. Instr.*, **22**, 328.
Kempter, V., Kneser Th. and Schlier, Ch. (1970), *J. Chem. Phys.*, **52**, 5851.
Kempter, V., Mecklenbrauck, W., Menzinger, M., Schuler, G., Herschbach, D. R. and Schlier, Ch. (1970), *Chem. Phys. Letts.*, **6**, 97.
Kessler, R. W. and Koglin, B. (1966), *Rev. Sci. Instr.*, **37**, 682.
Kinsey, J. L. (1966), *Rev. Sci. Instr.*, **37**, 61.
Kinsey, J. L. (1972), *M.T.P. Int. Rev. Sci*, London, Vol 9. (Ed. J. C. Polanyi)
Knauer, F. (1949), *Z. Physik*, **125**, 279.
Knuth, E. L. (1964), *Appl. Mech. Rev.*, **17**, 751.
Kramer, H. L. and Herschbach, D. R. (1970), *J. Chem. Phys.*, **53**, 2792.
Kramer, H. L. and Le Breton, P. R. (1967), *J. Chem. Phys.*, **47**, 3367.
Kuntz, P. J., Mok, M. H. and Polanyi, J. C. (1969), *J. Chem. Phys.*, **50**, 4607, 4623.
Kwei, G. H. and Herschbach, D. R. (1969), *J. Chem. Phys.*, **51**, 1742.
Kwei, G. H., Norris, J. A. and Herschbach, D. R. (1970), *J. Chem. Phys.*, **52**, 1317.

Lacmann, K. and Henglein, A. (1965), *Ber. d. Bunsens*δ, **69**, 292.
Lacmann, K. and Herschbach, D. R. (1970), *Chem. Phys. Letts.*, **6**, 106.
Landau, L. D. and Lifshitz, E. M. (1960), *Mechanics*, Addison-Wesley, Reading, Mass.
Landau, L. D. and Lifshitz, E. M. (1958), *Quantum Mechanics*, Pergamon Press, Oxford.
Le Breton, P. R. and Kramer, H. L. (1969), *J. Chem. Phys.*, **51**, 3627.
Le Breton, P. R., Mecklenbrauck, W., Schultz, A. and Schlier, Ch. (1971), *J. Chem. Phys.*, **55**, 2940.
Lee, Y. T., Le Breton, P. R., McDonald, J. D. and Herschbach, D. R. (1969), *J. Chem. Phys.*, **51**, 455.
Lee, Y. T., McDonald, J. D., Le Breton, P. R. and Herschbach, D. R. (1968), *J. Chem. Phys.*, **49**, 2447.
Lee, Y. T., McDonald, J. D., Le Breton, P. R. and Herschbach, D. R. (1969), *Rev. Sci. Instr.*, **40**, 1402.
Lee, Y. T., Gordon, R. J. and Herschbach, D. R. (1971), *J. Chem. Phys.*, **54**, 2410.

Lempert, G. D., Corrigan, S. J. B. and Wilson, J. F. (1971), *Chem. Phys. Letts.*, 8, 67.
Lester, W. A. and Bernstein, R. B. (1968), *J. Chem. Phys.*, **48**, 4896.
Levine, R. D. (1969), *Quantum Mechanics of Molecular Rate Processes*, Clarendon Press, Oxford.
Lew, H. (1949), *Phys. Rev.*, **76**, 1086.
Lew, H. (1953), *Phys. Rev.*, **91**, 619.
Lin, S. H. and Eyring, H. (1971), *Proc. Natl. Acad. Sci.*, **68**, 402.
Lorents, D. C. and Aberth, W. (1965), *Phys. Rev.*, **139A**, 1017.

Magee, J. L. (1940), *J. Chem. Phys.*, **8**, 687.
Maltz, C. and Herschbach, D. R. (1967), *Disc. Faraday Soc.*, **44**, 176.
Marchi, R. P. and Smith, F. T. (1965), *Phys. Rev.*, **139A**, 1025.
Margenau, H. and Kestner, N. R. (1969), *Theory of Intermolecular Forces*, Pergamon Press, Oxford.
Martin, L. R. and Kinsey, J. L. (1967), *J. Chem. Phys.*, **46**, 4834.
Mason, E. A. (1952), *J. Chem. Phys.*, **26**, 667.
Massey, H. S. W. (1971), *Electronic and Ionic Impact Phenomena, Vol. III – Slow Collisions of Heavy Particles* (2nd edition), Clarendon Press, Oxford.
Massey, H. S. W. and Mohr, C. B. O. (1933), *Proc. Roy. Soc.*, **A141**, 434.
Mason, E. A., Vanderslice, J. T. and Raw, C. J. G. (1964), *J. Chem. Phys.*, **40**, 2153.
McDermott, M. N. and Lichten, W. C. (1960), *Phys. Rev.*, **119**, 134.
McDonald, J. D., Le Breton, P. R., Lee, Y. T. and Herschbach, D. R. (1972), *J. Chem. Phys.*, **56**, 769.
Mentall, J. E., Krause, H. F. and Fite, W. L. (1967), *Disc. Faraday Soc.*, **44**, 157.
Merzbacher, E. (1961), *Quantum Mechanics*, Wiley, New York.
Mies, F. H. (1970), *J. Chem. Phys.*, **42**, 2709.
Miller, D. R. and Patch, D. F. (1969), *Rev. Sci. Instr.*, **40**, 1566.
Miller, R. C. and Kusch, P. (1955), *Phys. Rev.*, **99**, 1314.
Miller, W. B., Safron, B. A. and Herschbach, D. R. (1967), *Disc. Faraday Soc.*, **44**, 108, 292.
Miller, W. H. (1970), *J. Chem. Phys.*, **52**, 543.
Miller, W. H. (1970), *J. Chem. Phys.*, **53**, 1949.
Minturn, R. E., Datz, S. and Taylor, E. H. (1960), *J. Appl. Phys.*, **31**, 876.
Mok, M. H. and Polanyi, J. C. (1969), *J. Chem. Phys.*, **51**, 1451.
Morgenstern, D. and Beck, D. See reference to Pauly H. and Toennies, J. P. (1968).
Morse, F. A. and Bernstein, R. B. (1962), *J. Chem. Phys.*, **37**, 2019.
Mott, N. F. and Massey, H. S. W. (1965), *Theory of Atomic Collisions*, (3rd edition) Oxford University Press, London.
Moulton, M. C. and Herschbach, D. R. (1966), *J. Chem. Phys.*, **44**, 3010.
Munn, R. J., Mason, E. A. and Smith, F. J. (1964), *J. Chem. Phys.*, **41**, 3978.
Munn, R. J. and Smith, F. J. (1966), *Mol. Phys.*, **10**, 163.
Muller, E. W. (1960), *Adv. Electronics and Electron Physics*, **13**, 87.
Muschlitz, E. E. Jun. (1966), *Adv. Chem. Phys.*, **10**, 174.

Newton, R. (1966), *Scattering Theory of Waves and Particles*, McGraw-Hill.
Neumann, W. and Pauly, H. (1970), *J. Chem. Phys.*, **52**, 2548.

Neynaber, R. H., Myers, B. F. and Trujillo, S. M. (1969), *Phys. Rev.*, **180**, 139.
Norcliffe, A. and Percival, I. C. (1968), *J. Phys. B.*, **1**, 784.

Odirone, T. J., Brooks, P. R. and Kasper, J. V. V. (1971), *J. Chem. Phys.*, **55**, 1980.
Ogryzlo, E. A. (1961), *Can. J. Chem.*, **39**, 2556.
Olson, R. E. and Bernstein, R. B. (1968), *J. Chem. Phys.*, **49**, 162 and 4499.
Olson, R. E. (1968), Theoretical Chemistry Institute, U. Wisconsin, Report WISTC 1, 310.
Olson, R. E. and Bernstein, R. B. (1968), *J. Chem. Phys.*, **49**, 162 and 4499.
Owen, P. L. and Thornhill, C. K. (1948), Aeronautical Research Council (U.K.)., R & M No. 2616.

Parks, E. K. and Wexler, S. (1971), *Chem. Phys. Letts.*, **10**, 245.
Parrish, D. D. and Herm, R. R. (1969), *J. Chem. Phys.*, **51**, 5467.
Parrish, D. D. and Herm, R. R. (1971), *J. Chem. Phys.*, **54**, 2518.
Parson, J. M., Schafer, T. P., Tully, F. P., Siska, P. E., Wong, Y. C. and Lee, Y. T. (1970), *J. Chem. Phys.*, **53**, 2123.
Parson, J. M., Siska, P. E. and Lee, Y. T. (1972), *J. Chem. Phys.*, **56**, 1511.
Pauly, H. and Toennies, J. P. (1965), *Adv. At. Mol. Phys.*, **1**, 195.
Pauly, H. and Toennies, J. P. (1965), *Adv. At. Mol. Phys.*, **1**, 201.
Pauly, H. and Toennies, J. P. (1968), *Methods of Experimental Physics*, **7A**, 227, Academic Press, New York (Ed. Bederson, B. and Fife, W.).
Persky, A., Greene, E. F. and Kuppermann, A. (1968), *J. Chem. Phys.*, **49**, 2347.
Petty, F. and Moran, T. F. (1972), *Phys. Rev. A.*, **5**, 266.
Pierce, J. R. (1954), *Theory and Design of Electron Beams*, Van Nostrand, New York.
Polanyi, M. (1932), *Atomic Reactions*, Williams and Norgate, London.
Politiek, J., Kol, P. K., Los, J. and Ikelaar, P. G. (1968), *Rev. Sci. Instr.*, **39**, 1147.
Politiek, J. and Los, J. (1969), *Rev. Sci. Instr.*, **40**, 1576.
Present, R. D. (1958), *Kinetic Theory of Gases*, McGraw-Hill, New York.
Pritchard, D. E., Carter, G. M., Chu, F. Y. and Kleppner, D. (1970), *Phys. Rev. A.*, **2**, 1922.
Pritchard, D. E. and Chu, F. Y. (1970), *Phys. Rev. A.*, **2**, 1932.

Rabi, I. I., Kellog, J. M. B. and Zacharias, J. R. (1934), *Phys. Rev.*, **46**, 157.
Raff, L. M. and Karplus, M. (1966), *J. Chem. Phys.*, **44**, 1212.
Ramsey, N. F. (1956), *Molecular Beams*, Oxford University Press, London.
Roberts, R. E. and Ross, J. (1970), *J. Chem. Phys.*, **52**, 1464.
Robinson, C. A. (1967), *Statistical Communication and Detection.*
Rodberg, L. S. and Thaler, R. M. (1967), *Introduction to the Quantum Theory of Scattering*, Academic Press, New York.
Ross, J. (Ed.) (1966), *Adv. Chem. Phys.*, **10**, article by R. B. Bernstein.
Ross, J. and Greene, E. F. in *Proc. Int. Sch. Phys. 'Enrico Fermi' Course XLIV (Varenna)* (Editor, Ch. Schlier) (1970), Academic Press, New York.
Rothe, E. W. (1964), *J. Vac. Sci. Tech.*, **1**, 66.
Rothe, E. W., Neynaber, R. H. and Trujillo, S. M. (1965), *J. Chem. Phys.*, **42**, 3310.

Rothe, E. W. and Neynaber, R. H. (1965), *J. Chem. Phys.*, 42, 3306 and 43, 4177.
Rothe, E. W. and Helbing, R. K. B. (1968), *J. Chem. Phys.*, 49, 4750.
Rothe, E. W. Reinhard, K. and Helbing, B. (1970), *J. Chem. Phys.*, 53, 1555, 2501.

Schafer, T. P., Siska, P. E., Parson, J. M., Tully, F. P., Wong, F. C. and Lee, Y. T. (1970), *J. Chem. Phys.*, 53, 3376.
Schlier, C. (1969), *Ann. Rev. Phys. Chem.*, 20, 191.
Schlier, C., Duren, R. and Raabe, C. P. (1968), *Z. Physik*, 214, 410.
Schottler, J. and Toennies, J. P. (1968), *Ber. Bunsengesellschaft*, 72, 979.
Scoles, G. and Torello, F., 'Production of Molecular Beams from Free Expanding Jets, part 1', Report of the Gruppo di Strutture Della Materia del C.N.R., August 1967.
Scott, P. B. (1965), M.I.T. Fluid Dynamics Lab. Rept. No. 65 – 1.
Secrest, D. and Johnson, B. R. (1966), *J. Chem. Phys.*, 45, 4556.
Siska, P. E., Parson, J. M., Schafer, T. P., Wong, Y. C. and Lee, Y. T., *Phys. Rev. Letts.*, 25, 271.
Siska, P. E., Parson, J. M., Schafer, T. P. and Lee, Y. T. (1971), *J. Chem. Phys.*, 55, 5762.
Skinner, G. T. (1966), *Proc. 7th Agard Colloquium on Advances in Aerothermochemistry*, Oslo.
Skofronik, J. G. (1967), *Rev. Sci. Instr.*, 38, 1628.
Smith, F. J. and Munn, R. J. (1964), *J. Chem. Phys.*, 41, 3560.
Smith, F. T., Marchi, R. P. and Dedrick, K. G. (1966), *Phys. Rev.*, 150, 79.
Smith, I. W. M. (1967), *Disc. Faraday Soc.*, 44, 194.
Smith, K. F. (1955), *Molecular Beams*, Methuen, London.
Struve, W. S., Kitagawa, T. and Herschbach, D. R. (1971), *J. Chem. Phys.*, 54, 2759.

Taylor, E. H. and Datz, S. (1955), *J. Chem. Phys.*, 23, 1711.
Toennies, J. P. (1965), *Z. Physik*, 182, 257.
Toennies, J. P. (1965), *Z. Physik*, 193, 76.
Treanor, C. E. (1965), *J. Chem. Phys.*, 43, 532.
Trouw, T. R. and Trischka, J. W. (1963), *J. Appl. Phys.*, 34, 3635.
Tully, F. P., Lee, Y. T. and Berry, R. S. (1971), *Chem. Phys. Letts.*, 9, 80.

Vanderslice, J. T., Mason, E. A., Maisch, W. G. and Lippincott, E. R. (1959), *J. Mol. Spectr.*, 3, 17 and 5, 83.
Visser, C. A., Wolleswinkel, J. and Los, J. (1970), *J. Sci. Instr.*, 3, 483.

Waech, T. G. and Bernstein, R. B. (1968), *Chem. Phys. Letts.*, 2, 477.
Warnock, T. T., Bernstein, R. B. and Grosser, A. E. (1967), *J. Chem. Phys.*, 46, 1685.
Weiss, R. (1961), *Rev. Sci. Instr.*, 32, 397.
Wellner, M. (1964), *Amer. J. Phys.*, 32, 787.
Wharton, L., Berg, R. A. and Klemperer, W. (1963), *J. Chem. Phys.*, 39, 2033.
Wharton, L., Klemperer, W., Gold, L. P., Strauch, R., Gallagher, J. J. and Derr, V. E. (1963), *J. Chem. Phys.*, 38, 1203.
Whitehead, J. C., Hardin, D. R. and Grice, R. (1972), *Chem. Phys. Letts.*, 13, 319.

Wiener, N. (1949), *Extrapolation, Interpolation and Smoothing of Stationary Time Series*, John Wiley, New York.
Wilets, L. (1964), *Theories of Nuclear Fission*, Clarendon Press, Oxford.
Williams, W., Mueller, C. R., McGuire, P. and Smith, B. (1969), *Phys. Rev. Letts.*, **22**, 121.
Willner, M. (1964), *Amer. J. Phys.*, **32**, 787.
Wilson, J. F. and Lempert, G. D., Private Communication (1970).
Wilson, K. (1964), Ph.D. Thesis, Harvard University.
Wilson, K. R. and Herschbach, D. R. (1968), *J. Chem. Phys.*, **49**, 2676.
Winicur, D. H., Moursund, A. L., Devereaux, W. R., Martin, L. R. and Kuppermann, A. (1970), *J. Chem. Phys.*, **52**, 3299.
Wu, T. Y. and Ohmura, T. (1962), *Quantum Theory of Scattering*, Prentice Hall, New York.
Wykes, J. (1960), *J. Sci., Instr.* (J. Physics E), **2**, 899.

Zandberg, E. Ya and Ianov, N. I. (1959), *Usp. Fig. Nauk.*, **67**, 581.

Author Index

Subject Index

Science Paperbacks 140

Chemical Applications of Molecular Beam Scattering

M. A. D. Fluendy and K. P. Lawley

This book provides a unified and reasonably complete account of those techniques of molecular beam scattering which have contributed so much to chemical kinetics and the determination of intermolecular forces. The book introduces the classical and quantum theory of collisions – relatively unfamiliar to chemists – before going on to analyse the results. The emphasis throughout is on the beam approach to molecular dynamics and the contrast with conventional methods. The level of the book makes it primarily suitable for graduate students and research workers.

In the same series

Spectroscopy

Edited by B. P. Straughan and S. Walker

The three volumes on Spectroscopy constitute the one comprehensive text available on the principles, practice and applications of spectroscopy. By giving full accounts of those spectroscopic techniques only recently introduced into student courses – such as Mössbauer spectroscopy and photoelectron spectroscopy – in addition to those techniques long recognised as being essential in chemistry teaching – such as e.s.r. and infrared spectroscopy – the book caters for the complete requirements of undergraduate students and at the same time provides a sound introduction to special topics for graduate students.

Volume 1

Atomic spectra; Nuclear magnetic resonance spectroscopy; Nuclear quadrupole resonance spectroscopy; Electron spin resonance spectroscopy; Mössbauer spectroscopy.
1976, 304 pages

Volume 2

Molecular spectra; Symmetry and group theory; Microwave spectroscopy; Infrared and Raman spectroscopy; Far-infrared spectroscopy; Force constants; Thermodynamic functions.
1976, 362 pages

Volume 3

Molecular quantum numbers; Electronic spectra of diatomic molecules; Dissociation of diatomic molecules; Electronic spectra of polyatomic molecules; Fluorescence and phosphorescence spectroscopy; Astrochemistry; Photoelectron spectroscopy.
1976 324 pages

Science Paperbacks are published by
Chapman and Hall
11 New Fetter Lane London EC4P 4EE

MONTE CARLO SIMULATION OF K+I_2 COLLISIONS AT SUPERTHERMAL ENERGIES

D.R. McDONALD, M.A.D. FLUENDY, K.P. LAWLEY
Department of Chemistry, University of Edinburgh, Edinburgh, EH9 3JJ, Scotland

The study of alkali-halogen molecule collisions has recently been extended to much higher energies (1) (2). At these energies many exit channels including chemi-ionization and electronic excitation are open, so that there is interest in the 'electron dynamics' of these encounters. In the limit of strong coupling, however, the motion occurs only over the adiabatic potential surface. For the system K+I_2 the Landau-Zener result suggests that 80% of trajectories scattering in the Eθ range below 400 electron volt degrees move on the adiabatic surface. In this region, which includes the classical rainbow for the coulombic well, the motion is thus dominantly on a single surface so that the nuclear dynamics may be explored by classical Monte Carlo trajectory computations. This paper describes the results of such calculations.

The potential surface used in this work is based upon those employed by Blais (3) and Godfrey (4); while the initial starting conditions were averaged over in the usual way. At the energies of interest and assuming motion on a single surface, the processes:

K+I_2	→	K+I_2	elastic
	→	K+$I_2^\dagger$	vib. rot. excitation
	→	KI+I	reaction
	→	K+I+I	dissociation

can all occur. Fig. 1 shows the total cross sections for these channels as a function of collision energy. The reactive cross section falls very sharply from its value at thermal energies and the channel is effectively closed above 5 eV. This change results from momentum constrainst which make it increasingly difficult to accelerate an iodine ion away from its neutral partner during the collision time. Similar factors account for the behaviour of the dissociation cross section. This differs at high energies, however, where a residual small impact parameter 'knockout' process is still seen. This mechanism depends upon the repulsive potential between the atoms and is thus insensitive to the impact energy.

In Fig. 2 the differential cross section for K atom scattering with an energy loss, ΔE, <0.05 eV is shown, this is an approximation to pure elastic scattering. At the higher energies the classical rainbow is seen and the average energy loss for trajectories in this Eθ region is very small. The average energy loss is much larger at 10 eV ($\Delta E \sim 1$ eV) and the additional

scattering seen at angles beyond the rainbow probably arises from inelastic effects suggesting that the criterion $\Delta E < 0.05$ eV is now inadequate. At 1.0 eV the elastic scattering is strongly attenuated by reaction before the rainbow region is reached and it was impossible to generate sufficient trajectories to determine the cross section here; it is clearly very small.

The calculations suggest that at energies >30 eV collisions yielding scattering in the rainbow region are predominantly elastic. This region may thus provide a convenient window for studying the electron dynamics without the more complex reactive or energy transfer processes complicating the picture.

1. G.A.L. Delvigne and J. Los, Physica, 59, 61, (1972).
2. B.S. Duchart, M.A.D. Fluendy and K.P. Lawley, Chem. Phys. Letters, 14, 129, (1972).
3. N.C. Blais, J. Chem. Phys., 49, 9, (1968).
4. M. Godfrey and M. Karplus, J. Chem. Phys., 49, 3602, (1968).

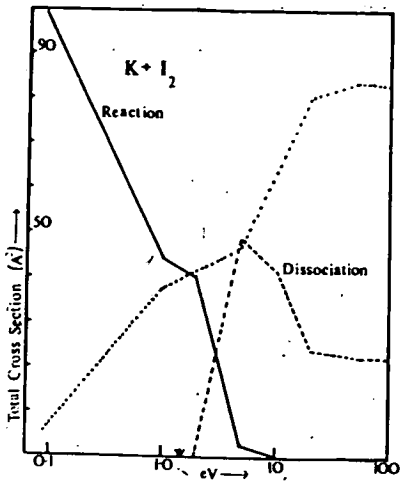

Fig. 1 Total cross sections for reaction and dissociation versus impact energy eV.

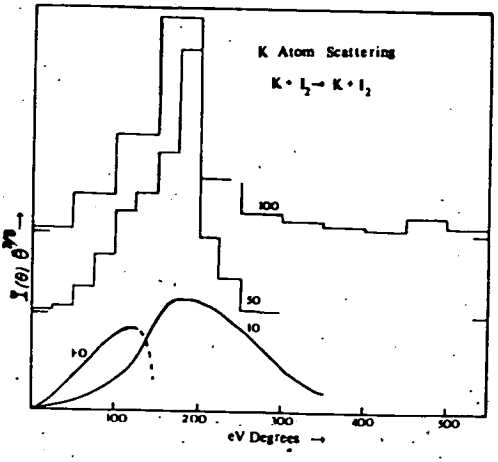

Fig. 2 $I(\theta)\theta^{7/3}$ for elastic K atom scattering versus $E\theta$ (eV degrees)

Two State Calculations on the Collisions of Alkali Metal and Halogen Atoms at Superthermal Energies

J. F. Reddington, M. A. D. Fluendy and K. P. Lawley,
Dept. of Chemistry, University of Edinburgh, Scotland.

The harpooning model of chemical reaction[1] in the alkali metal (M) + halogen (X_2) systems has served well to describe the observed elastic and reactive scattering at thermal energies. At higher energies a new exit channel opens to give $M^+ + X_2^-$ (or $X + X^-$). This ion production process can be investigated directly by beam scattering with ion detection in the low eV region[2], by elastic scattering in the same energy region[3] or by u.v. spectroscopy[4] in which an upper electronic state of MX is reached and predissociation observed.

The underlying phenomenon is that of non-adiabatic behaviour at an avoided curve crossing. Two 'diabatic' states of the MX molecule (or MX_2) cross at relatively large interatomic separations and, under the right symmetry conditions, a marked redistribution of the electron density in the true eigenstates of the system takes place around the crossing. The Landau-Zener-Stueckelberg (LZS) formula has been used almost exclusively to interpret the spectroscopic and ion production results. These formulae can be summarised as follows; at a single passage of an avoided crossing, the probability of adiabatic behaviour is given by

$$P_\ell = 1 - e^{-\{2\pi H_{12}/(\hbar v_\ell |F_1 - F_2|)\}} \qquad (1)$$

where v_ℓ is the radial relative velocity at the crossing and

where

$$F_i = \left| \partial H_{ii} / \partial R \right|_{R = R_x} \qquad (2)$$

The overall probability of non-adiabatic behaviour after two crossings is

$$P_\ell = 4 P_\ell (1 - P_\ell) \sin^2 \omega \qquad (3)$$

where ω is the difference in phase developed between the two crossings according to whether the motion takes place in the presence of the upper or the lower state potential. Although these three formulae have long been recognised to be possibly seriously in error in particular circumstances, they do enable the two state problem to be thought of in classical terms and they form a convenient point of departure in analysing results. Thus, the combination[5] of the oscillatory term in (3), written in the form $e^{i\omega} - e^{-i\omega}$, with the phase shifts developed along the two classical trajectories, that lead to the exit channel under discussion, results in S-matrix elements of the following form;

$$S_{1\ell} = P_\ell e^{2i\eta_1(\ell)} + (1 - P_\ell) e^{2i\eta_2(\ell)} \qquad (4)$$

$$S_{2\ell} = P_\ell^{1/2} (1 - P_\ell)^{1/2} \left(e^{2i\eta_3(\ell)} + e^{2i\eta_4(\ell)} \right) \qquad (5)$$

where the asymptotic form of the wave function in the ℓ^{th} angular momentum channel is

$$\Psi_\ell \xrightarrow[t \to \infty]{} S_{1\ell} \phi_1 e^{iE_1 t/\hbar} + \sum_{2\ell} \phi_2 e^{iE_2 t/\hbar} \qquad (6)$$

In (4) and (5), the phase shift η_1 refers to the trajectory that switches between diabatic states at both crossings, η_2 to no switching, η_3 to switching at the first crossing only and η_4 to switching at the second crossing; the latter two possibilities lead to exit in channel 2, the ionic channel. All these formulae neglect the possibility of specific phase changes occuring due to the switching process and they also depend upon ω being greater than $2\bar{\pi}$ otherwise the crossings can no longer be thought of as separate.

Inspection of (4) and (5) indicates two limiting cases. In the weak coupling case, P_ℓ is small and the S matrix elements for the elastic channel are essentially determined by η_2. In the strong coupling case, $P_\ell \sim 0.5$, $S_{1\ell}$ contains important contributions from both potentials. The scattered amplitude is given by

$$f_i(\theta) = \frac{1}{2ik}\sum_\ell (2\ell+1)(S_{i\ell} - \delta_{i1})P_\ell(\cos\theta) \qquad (7)$$

and so in the weak coupling case the elastic differential cross section, $\sigma_1 = |f_1(\theta)|^2$ is essentially that for scattering from the upper diabatic state, whereas in the strong coupling case it will contain interference terms between wave trains scattered from the upper and lower diabatic states.

In this paper we explore the validity of equations (1) - (5) for the system K + I in the energy range 20 - 100 eV by solving the coupled 2-state problem numerically within the framework of time dependent perturbation theory. The coupled equations are

$$i\hbar \frac{da_1}{dt} = H_{11}a_1 + H_{12}a\cdot e^{i(E_1 - E_2)t/\hbar} \qquad (8)$$

$$i\hbar \frac{da_2}{dt} = H_{22}a_2 + H_{12}a_1 e^{-i(E_1-E_2)t/\hbar} \quad (9)$$

where the coefficients a_i are those of the linear combination of diabatic states (taken to be the Heitler London covalent and ionic form)

$$\Psi = a_1\phi_1 e^{iE_1t/\hbar} + a_2\phi_1 e^{iE_2t/\hbar} \quad (10)$$

The following analytical potentials were used;

$$\begin{aligned} H_{11} &= Ae^{-BR} - CR^{-8} \\ H_{22} &= A'e^{-B'R} - 1/R \\ E_1 - E_2 &= IP - E_a \end{aligned} \quad (11)$$

and are displayed in figure 1.

Typical behaviour of the computed amplitude in the ionic channel, $|a_2(t)|^2$, is shown in figure 2 and is characteristic of weak coupling. The overall transition probability as a function of impact parameter oscillates about the LZ value (figure 3), and can be fitted by a formula such as (3). At energies above a few hundred eV the phase difference ω falls below 2π and the semi-classical treatment becomes invalid. The envelope of the elastic differential cross section at 20 eV and 100 eV scales well with $E\theta$ (figure 5). Distinctive features are the rainbow at 13 eV degrees and the slow undulations in the cross section on the dark side of the rainbow. Superimposed on these is a high frequency structure. The rainbows are at the position expected for the shallow diabatic potential that is given by $H_{11}(R)$. The low frequency undulations beyond the rainbow can best be understood from figure 6 in which the two deflection functions arising from $H_{11}(R)$ and $H_{22}(R)$ are plotted. The thickness of the curves is proportional to the factors P_ℓ and $(1-P_\ell)$ which are not, of course, the complete weighting factor for a semi-classical branch;

the classical factor $b/|d\chi/db|$ must also be included.

There are four branches of the deflection functions that can lead to scattering beyond the rainbow. The interference structure of longest angular period will come from branches A and B, one of which is weak and the other strong. The periodicity of the structure in $\sigma_1(\theta)$ is predicted to be $2\pi/|\ell_A - \ell_B|$, close to the observed value. Higher frequency structure comes from the interference of branches C and D (single or merged) with branch B.

The ionic differential cross section is shown in figure 7 . The semiclassical scattering is governed by a second pair of deflection functions similar to those in figure 6 but deeper because of the Coulomb potential operating after the second crossing. Two rainbows of equal strength are predicted and are also discernable in the exact calculations. The structure is, however, confused by the multiple possibilities of interference between branches of similar strength.

We conclude firstly that the simple LZ formula (1) accounts well for the computed ionic transition probabilities. Secondly, that studies of the elastic scattering in the system K/I in the energy range 20–100 eV will yield some information about the ionic potential and the magnitude of the coupling matrix element. Scattering on the dark side of the rainbow is particularly relevant in this respect and the information gained refers mainly to the repulsive branches of the two diabatic defelction functions. Elastic scattering in the halogen molecular system, K/I_2, would be more dependent on the ionic potential because of the stronger coupling at the avoided crossing and experimental studies of both systems in the superthermal energy range are in progress in this laboratory.

References

1. D.R.Herschbach, Adv. Chem. Phys., 10, 319, (1966)

2. G.A.L.Delvigne and J.Los, Physica, 59, 61, (1972)

3. B.S.Duchart, M.A.D.Fluendy and K.P.Lawley, Chem. Phys. Lett., 14, 129, (1971)

4. R.S.Berry, J. Chem. Phys., 27, 1288, (1957)

5. T.A.Green and R.E.Johnson, Phys. Rev., 152, 9, (1966)

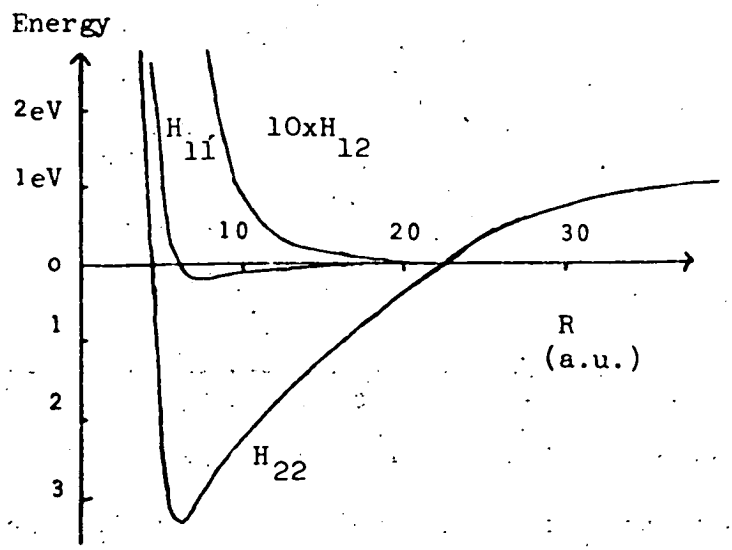

Figure 1: The matrix elements H_{11} H_{12} H_{22} versus the interatomic distance.

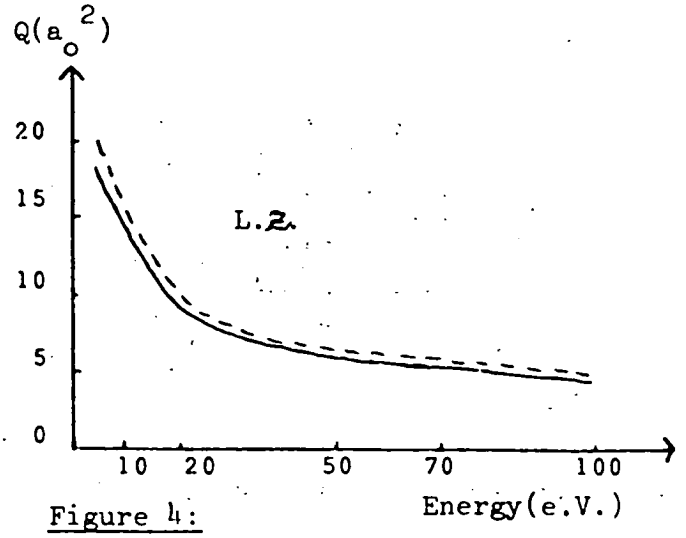

Figure 4:
Total cross section for ionization as a function of energy, this calculation -, L.Z. ....

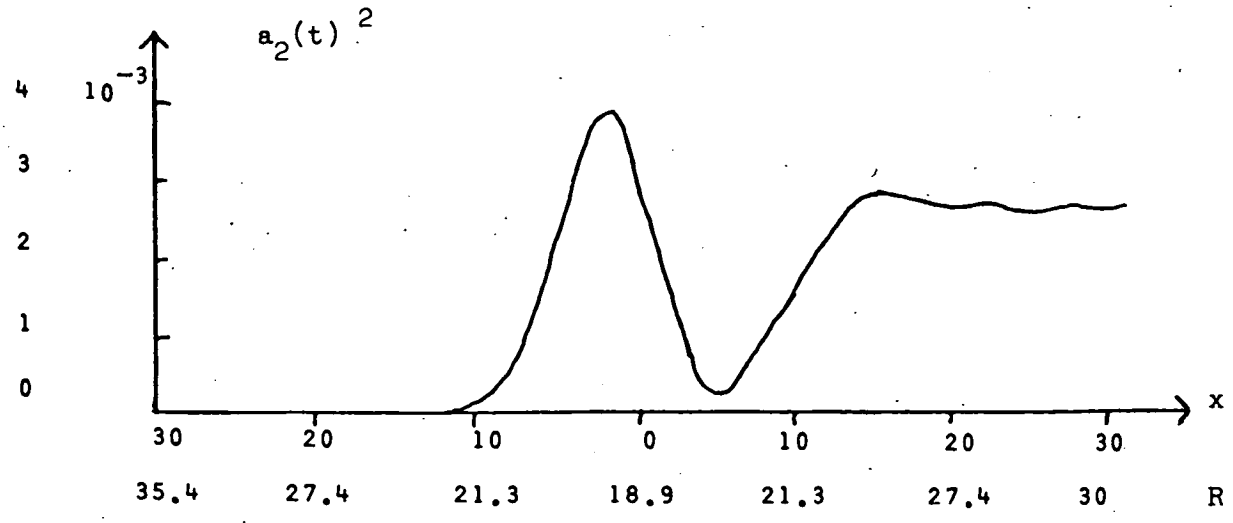

Figure 2a Plot of probability of ionisation as a function of distance, x, along the trajectory (b = 18.9 a.u., Energy = 100 eV).

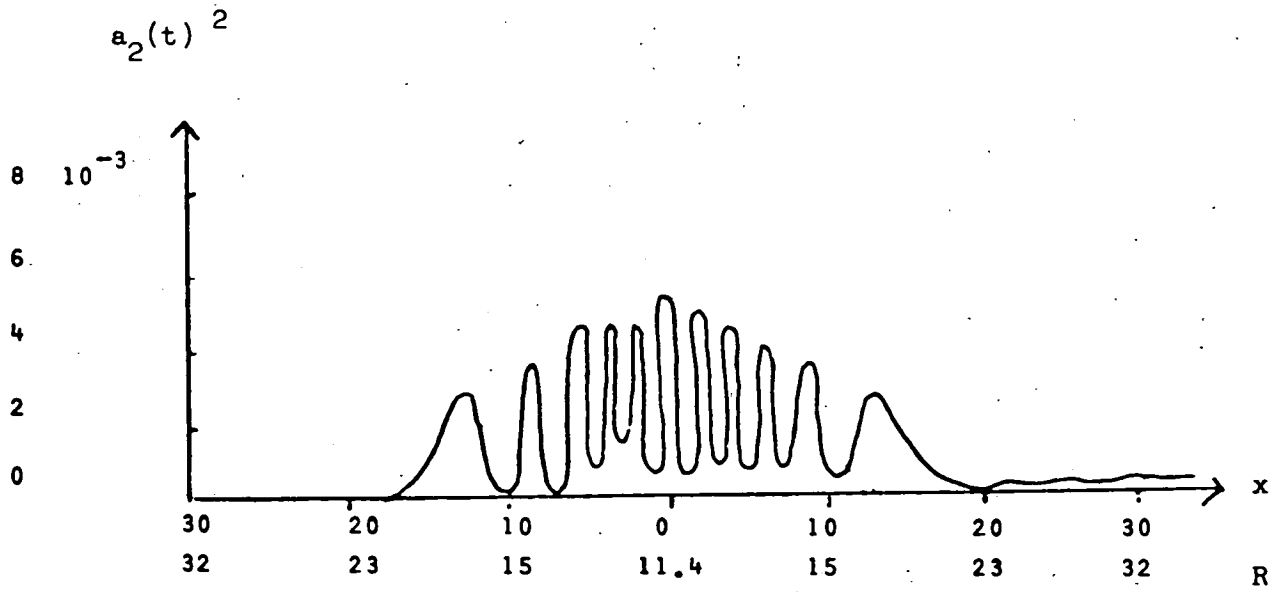

Figure 2b Plot of probability of ionisation as a function of distance, x, along the trajectory (b = 11.4 a.u., Energy = 100 eV).

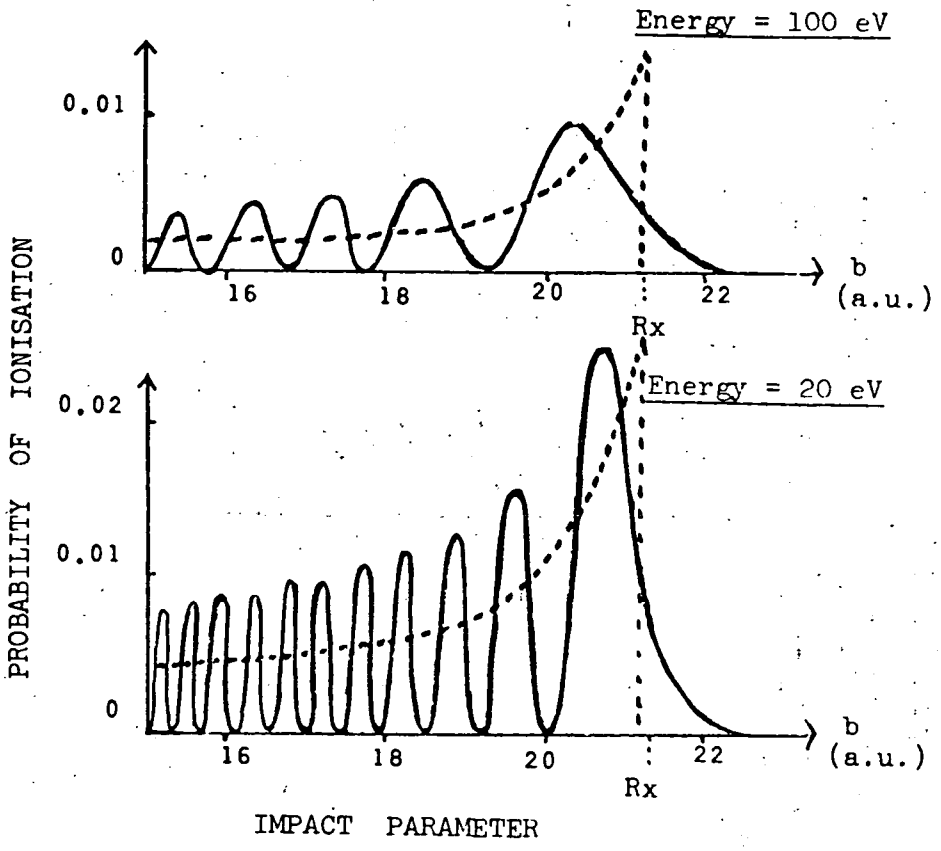

Figure 3: Probability of ionization versus impact parameter.

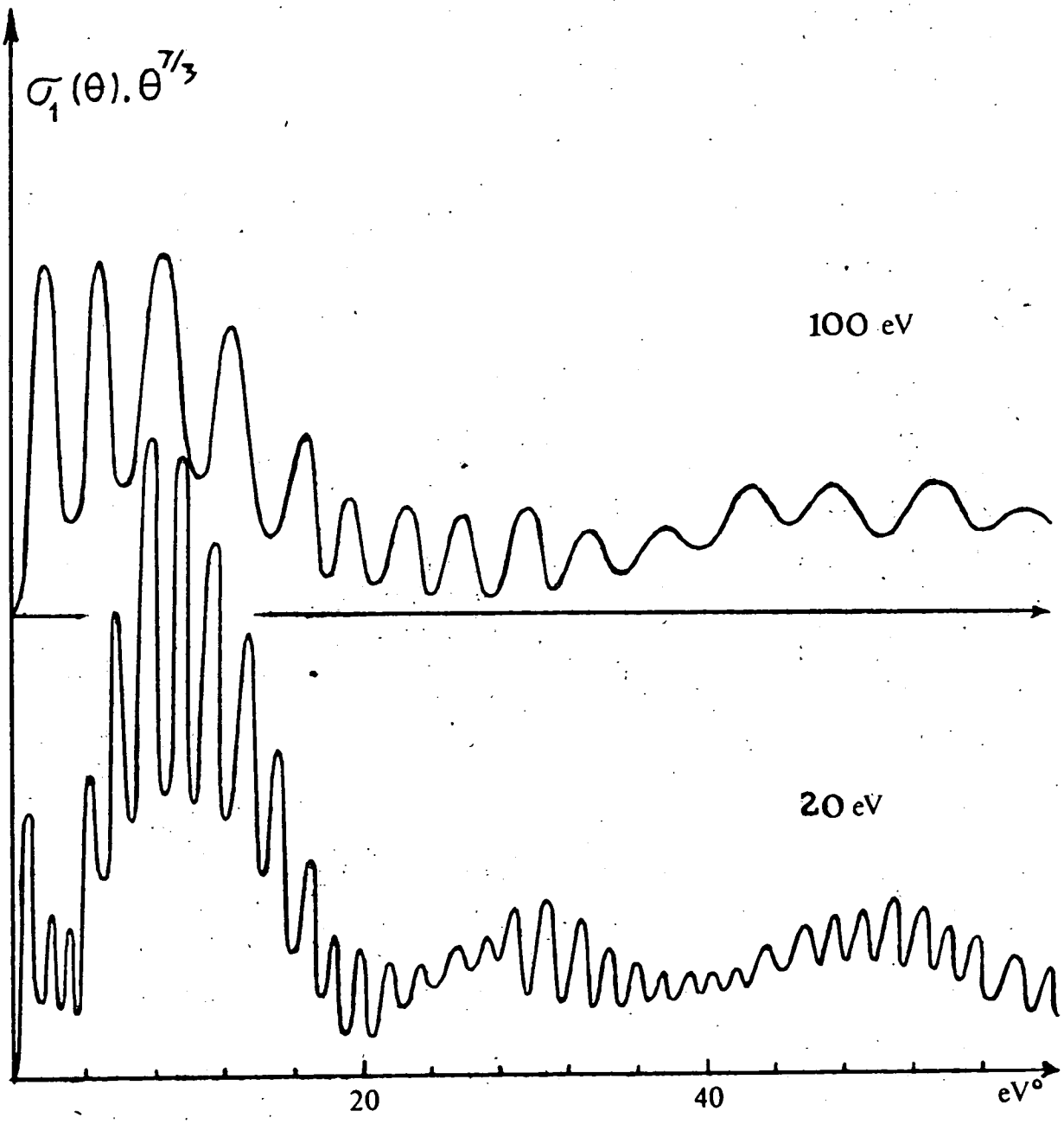

Figure 5 Differential cross section for elastic scattering (E = 100 and 20 eV).

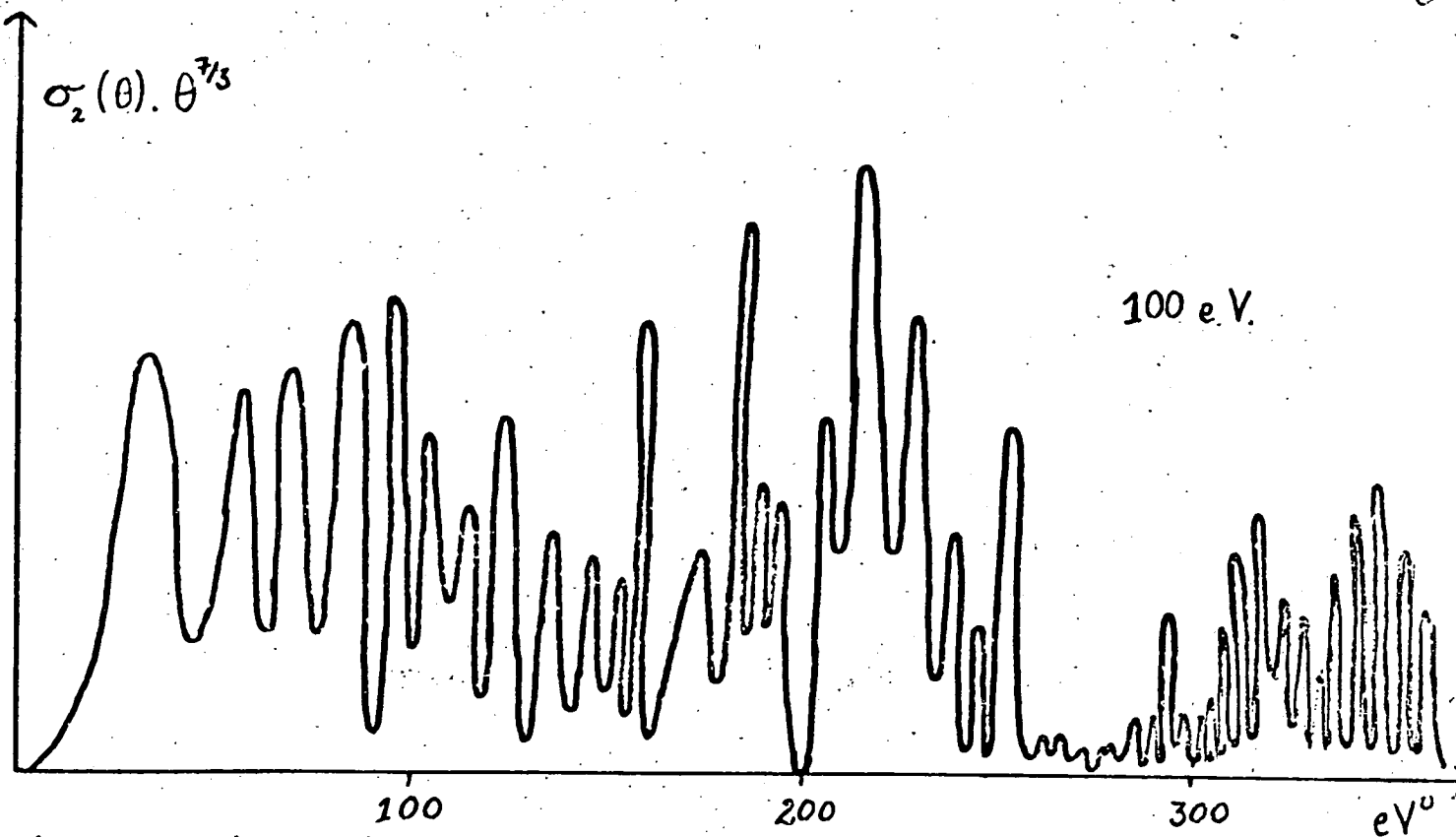

Figure 7 Differential cross sections for scattering as ions (E = 100 eV). The structure between 0 and 260 eV degrees is smoothed to remove the very high frequency oscillations, $\Delta\theta \simeq 2.0$ eV°.

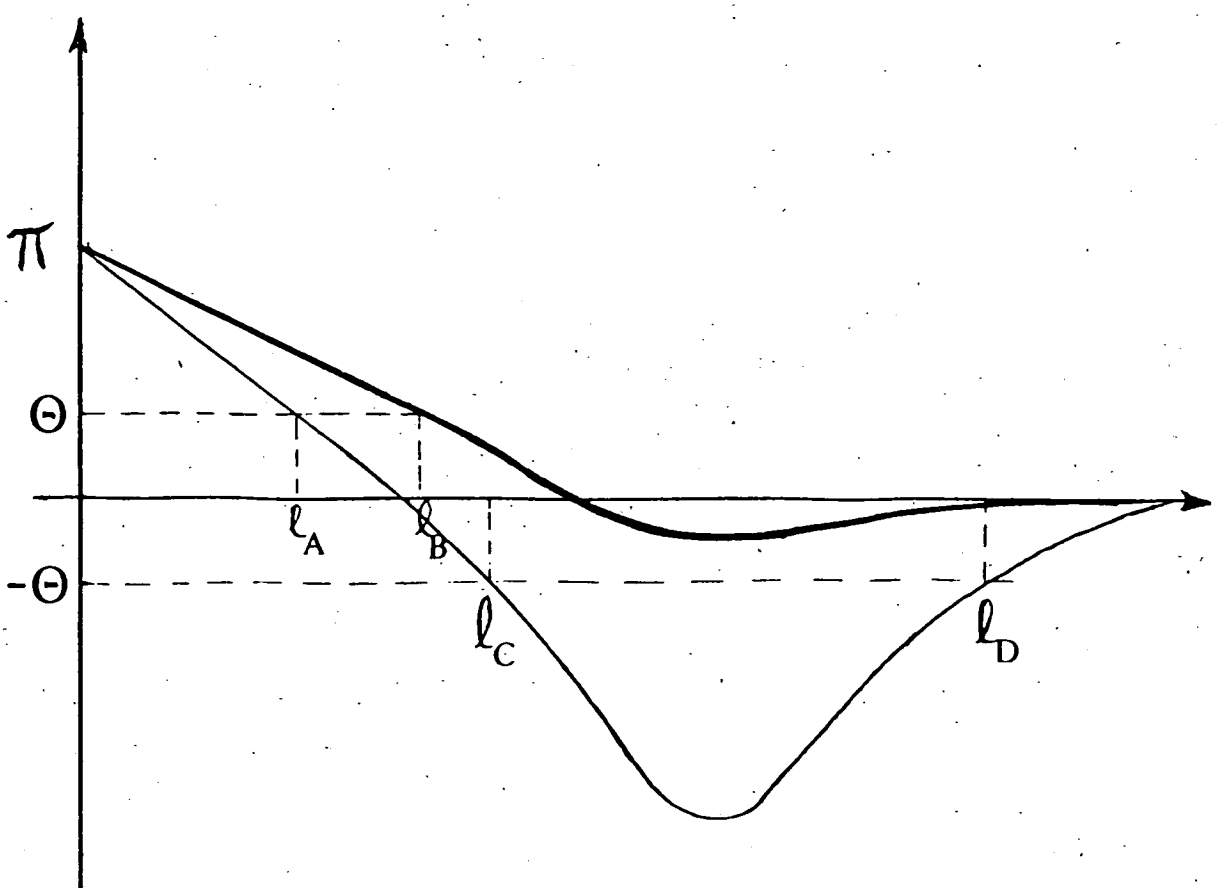

Figure 6 Deflection functions arising from $H_{11}(R)$ and $H_{22}(R)$.

MOLECULAR PHYSICS, 1974, VOL. 28, NO. 1, 69–80

26

Atomic scattering from heavy P-state atoms : role of depolarization

by M. A. D. FLUENDY, I. H. KERR and K. P. LAWLEY
Department of Chemistry, University of Edinburgh

(*Received* 1 *November* 1973 ; *revision received* 2 *January* 1974)

The anisotropy of the potential between two atoms, one at least of which has $J > \frac{1}{2}$, can cause partial re-alignment of the electronic angular momentum vector (i.e. M_J transitions) during collision. Within the framework of the semi-classical approximation, a single parameter akin to the Massey parameter is found to determine whether a given system will exhibit strong or weak coupling of the electronic to the relative atomic angular momentum. The consequence of these two coupling schemes for the position of the rainbow, the quenching of glory undulations and the magnitude of the total cross section are discussed. Particular reference is made to the metastable $^3P_2$ state of Hg and the inert gases where the fine structure splitting is much larger than the relevant part of the interatomic potential. In the case of Kr* and Xe* the rainbow and glory features are strongly dependent on the initial M_J state of the atom and the glory structure should be suppressed. In contrast, scattering from systems such as Hg*/Na or Hg*/Hg should take place under weak coupling conditions.

1. INTRODUCTION

Atomic scattering experiments, originally confined to the ground states of the alkali metals and inert gases, are being extended to an increasing range of atoms in many electronic angular momentum states [1–3]. The interpretation of the elastic scattering pattern is then complicated by the fact that the potential between two atoms, one or both of which are in a $J > \frac{1}{2}$ state, depends on Ω the magnitude of the component of the total electronic angular momentum **J** along the interparticle vector **R**. At long range, this effect can be regarded as due to the anisotropy of the atomic polarizability which for $J > \frac{1}{2}$ is itself M dependent ; this, in turn, gives rise to an $\Omega(=M_A+M_B)$ dependence of the dispersion force. At shorter range, specific electronic interactions are important and the potential becomes even more strongly dependent on Ω. In the presence of this manifold of potentials evolving from two separated atoms, the Coriolis force arising from their relative angular momentum in a collision can cause transitions in both M and J. If the Massey parameter $([E_J - E_{J'}]\sigma/\hbar v)$ for the atomic spin–orbit coupling is $\gg 1$, the only transitions induced will be in M, together with exciton exchange in resonant cases. In contrast, for the case of small spin–orbit coupling (e.g. in the ^2P states of the alkali metals) J transitions are readily induced by collision [4–6] and so quenching and mixing are both important processes. In the following sections we consider only the first case, i.e. fine structure splitting large compared with the relative kinetic energy.

There are various experimental consequences of these M transitions, notably in molecular scattering, the depolarization of atomic fluorescence [7, 8] and the pressure broadening of spectral lines [9]. In this paper we dwell mainly on the elastic scattering aspects of the problem, although all three phenomena are intimately linked to the relevant elements of the scattering matrix $S_{JMLO,\,JM'L'N'}$. For the purposes of illustration, discussion is mainly limited to the case of a $^3P_2$ atom interacting with a ^1S or ^2S atom.

The distinction has been drawn (e.g. [10]) between strong and weak collisions involving linear molecules. In strong collisions the axis of quantization for the projection quantum number (whether of electronic or molecular angular momentum) follows the rotating interparticle vector during most of the collision and so such a quantum number is useful in describing the collision ; in weak collisions a space-fixed axis of quantization is appropriate. Throughout this paper projection quantum numbers with respect to a rotating axis will be printed in upper case letters and space-fixed ones in lower case letters. In the collision of two atoms the two types of coupling would be labelled in spectroscopic terms as either Hund's case *a*, *b* or *c* (strong coupling) and case *d* (weak coupling). For the purposes of spin-alignment experiments, a rate constant is usefully defined, but from a scattering point of view we wish to know if scattering at a particular angle (and hence the relevant portions of the potential) can be labelled with the initial M or m state of the target, i.e. whether the contributions of the magnetic sub-levels can be unscrambled in one or other of the quantization schemes. We will find that different portions of the same trajectory may take place under different coupling conditions and the scattering phenomenon being analysed has to be specified more precisely. Experimentally, some of the more important features are (1) the position of the rainbow, (2) the spacing of the glory undulations and (3) the total cross section.

The effect of an M-dependent potential on elastic scattering is two-fold, in that both the phases and amplitudes of the diagonal S matrix elements become m or M dependent. This can be illustrated by applying the Born approximation for the phase shift η_{JM} or η_{Jm} to the two cases of strong and weak coupling in the limit of large impact parameters. For a $J=2$ atom interacting with an S-state atom under strong coupling (with M and M' labelling the initial M states being compared) :

$$(\eta_{2M}-\eta_{2M'})/\bar{\eta}=[C_6(2,\,M')-C_6(2,\,M)]/\bar{C}_6 \tag{1}$$

and in the weak coupling case

$$\left.\begin{aligned}(\eta_{22}-\eta_{21})/\bar{\eta}&=\frac{12}{128}\left\{\frac{C_6(2,\,2)-C_6(2,\,1)}{\bar{C}_6}\right\}+\frac{15}{128}\left\{\frac{C_6(2,\,2)-C_6(2,\,0)}{\bar{C}_6}\right\},\\(\eta_{21}-\eta_{20})/\bar{\eta}&=\frac{8}{128}\left\{\frac{C_6(2,\,2)-C_6(2,\,1)}{\bar{C}_6}\right\}+\frac{2}{128}\left\{\frac{C_6(2,\,2)-C_6(2,\,0)}{\bar{C}_6}\right\}.\end{aligned}\right\} \tag{2}$$

$C_6(JM)$ is the van der Waals coefficient for an atomic (JM) state defined in the same way as the polarizability tensor. The dependence of the phase shift on the initial orientation of the atom in the weak coupling case is thus only ~ 20 per cent that in the strongly coupled case and in this limit scattering will be insensitive to the initial M state. Conversely, collision cross sections in the strong coupling regime will reveal the operation of the anisotropy of the potential through their M dependence.

We now set up the problem of determining the S matrix semi-classically and describe the qualitative features of the solutions so that the boundaries of strong and weak coupling can be estimated. These estimates are compared with exact numerical solutions of the time dependent perturbation problem and some specific problems in the scattering of $^3P_2$ atoms are then discussed in detail.

2. Formulation of the problem

Let the initial axis of quantization be the direction of approach, $\mathbf{R}(t=-\infty)$, which also defines the z-axis. To describe the target atom (i.e. the partner not in an S state) we adopt a rotating frame of quantization, which is appropriate to a molecular description of the atom pair and leads to an angle-independent potential. Collisions in which M is effectively conserved will be called adiabatic.

The atomic wave functions at time t are expanded in terms of the stationary states $|\xi\Omega\rangle$ that evolve from the $|JM\rangle$ of the separated atoms at $t=\pm\infty$:

$$\left.\begin{aligned}\Psi(t)&=\sum_{\xi,\Omega} a_{\xi\Omega}(t)|\xi\Omega\rangle,\\ |\xi\Omega\rangle&\xrightarrow[R\to\infty]{}|J_\mathrm{A}M_\mathrm{A}\rangle|J_\mathrm{B}M_\mathrm{B}\rangle.\end{aligned}\right\} \tag{3}$$

The $|\xi\Omega\rangle$ are eigenfunctions of the complete clamped electronic hamiltonian

$$\mathscr{H}=\mathscr{H}_\mathrm{A}{}^{(0)}+\mathscr{H}_\mathrm{B}{}^{(0)}+\mathscr{H}_\mathrm{int}(\mathbf{r}_\mathrm{A},\mathbf{r}_\mathrm{B}:\ \mathbf{R}). \tag{4}$$

They are thus parametrically a function of $\mathbf{R}$ and while we need not specify them exactly, their behaviour at large R is given by the standard perturbation expressions:

$$|\xi\Omega\rangle\approx|J_\mathrm{A}M_\mathrm{A}\rangle|J_\mathrm{B}M_\mathrm{B}\rangle+\frac{e^2}{R^3}\sum_{J_\mathrm{A}'\ldots}\frac{\langle J_\mathrm{A}M_\mathrm{A}|\langle J_\mathrm{B}M_\mathrm{B}|\mathbf{r}_\mathrm{A}\cdot\mathbf{r}_\mathrm{B}-3(\mathbf{r}_\mathrm{A}\cdot\mathbf{R})R^{-2}(\mathbf{r}_\mathrm{B}\cdot\mathbf{R})|J_\mathrm{A}'M_\mathrm{A}'\rangle|J_\mathrm{B}'M_\mathrm{B}'\rangle\times|J_\mathrm{A}'M_\mathrm{A}'\rangle|J_\mathrm{B}'M_\mathrm{B}\rangle}{E_\mathrm{A}-E_\mathrm{A}'+E_\mathrm{B}-E_\mathrm{B}'} \tag{5}$$

$$E_{\xi\Omega}\approx E_{J_\mathrm{A}}+E_{J_\mathrm{B}}-\frac{e^4}{R^6}\sum_{J_\mathrm{A}'\ldots}\times\frac{\langle J_\mathrm{A}\ldots|\mathbf{r}_\mathrm{A}\cdot\mathbf{r}_\mathrm{B}-3(\mathbf{r}_\mathrm{A}\cdot\mathbf{R})(\mathbf{r}_\mathrm{B}\cdot\mathbf{R})R^{-2}|J_\mathrm{A}'\ldots\rangle^2}{E_\mathrm{A}-E_\mathrm{A}'+E_\mathrm{B}-E_\mathrm{B}'}. \tag{6}$$

The space-fixed and rotating bases are related by

$$|JM\rangle=\sum_m d_{Mm}{}^J(\theta)|Jm\rangle. \tag{7}$$

where the rotation of the inter-particle vector, making an angle θ with the z-axis, is assumed to be confined to a plane $\Phi=0$; the $d_{Mm}{}^J(\theta)$ are the rotation matrices of order J. On substituting (3) into the time-dependent Schrödinger equation and proceeding in the usual fashion to project into each of the $(\xi\Omega)$ states in turn, the following coupled equations for the coefficients $a_{\xi\Omega}(t)$ are obtained:

$$-i\hbar\dot{a}_{\xi\Omega}=i\hbar\sum_{\xi'\Omega'}\langle\xi\Omega|\frac{\partial}{\partial t}|\xi'\Omega'\rangle a_{\xi'\Omega'}+E_{\xi\Omega}a_{\xi\Omega}. \tag{8}$$

Introducing the classical path allows the substitution

$$\frac{\partial}{\partial t} \to \dot{\theta} \frac{\partial}{\partial \theta} + \dot{R} \frac{\partial}{\partial R}, \tag{9}$$

where $\partial/\partial\theta$ operates on the basis $|JM\rangle$ through (7) and $\partial/\partial R$ operates on the second term in (5). The contribution of terms involving $\partial/\partial R$ is of the form

$$\dot{R}\langle \xi\Omega| \frac{\partial}{\partial R} |\xi'\Omega'\rangle \approx \dot{R} \frac{\langle \xi\Omega| \frac{\partial \mathscr{H}_{\text{int}}}{\partial R} |\xi'\Omega'\rangle \, \delta_{\Omega\Omega'}}{E_{\xi\Omega} - E_{\xi'\Omega'}} \tag{10}$$

and so, if the states coupled by the dipole–dipole interaction are well separated in energy—as would be true if one of the partners was a ground-state atom—the effect of the $\partial/\partial R$ operator can be neglected in comparison with that of $\partial/\partial\theta$ which couples asymptotically degenerate states. This neglect of radial coupling remains sound as long as the splitting between ξ states remains large compared with the splitting between states of different Ω. The coupling between magnetic sub-states is of the form

$$\dot{\theta}\langle \xi\Omega| \frac{\partial}{\partial \theta} |\xi\Omega'\rangle \approx \langle J_A M_A J_B M_B| \frac{\partial}{\partial \theta} |J_A M_A' J_B M_B'\rangle \frac{L}{\mu R^2}, \tag{11}$$

where terms $0(R^{-6})$ and smaller have been neglected and $\theta = L/\mu R^2$ used, appropriate when no exchange of angular momentum between electronic and relative motion occurs. States with different ξ are now no longer coupled with the neglect of $\partial/\partial R$ and so J_A and J_B reappear as good quantum numbers.

The problem is now restricted to the case $J_A \neq 0$, $J_B = 0$. The coupling term (11) then becomes (dropping the suffix A)

$$\langle JM| \frac{\partial}{\partial \theta} |JM'\rangle = \sum_{N=-J}^{J} d_{M\pm 1N}^{J}(\theta) \frac{d}{d\theta} d_{MN}^{J}(\theta) = \mp \tfrac{1}{2}(J \pm M + 1)^{1/2}(J \mp M)^{1/2}$$
$$= \Delta_{MM\pm 1}^{J} \tag{12}$$

and the set of coupled equations reduces to

$$-i\hbar \dot{a}_{JM} = i\hbar \sum_{N} \Delta_{MN}^{J} \dot{\theta} a_{JN} + E_{JM}(R) a_{JM} \tag{13}$$

to which can be added the two classical equations for the motion of R and θ along a path under the influence of some mean central potential $\bar{E}(R)$. The diagonal terms in (13) can be written in terms of the C_6 coefficients if, as discussed above, the interaction is not too strong. The nature of the equation (13) is such that the amplitudes $a_{JM}(t)$ do not depend on the absolute values of the diagonal elements on the right-hand side of (13), but only on the differences between them. If all the $E_{JM}(R)$ are equal, the solutions $a_{JM}(\infty)$ are simply, apart from a constant phase factor, the rotation matrices $d_{MN}^{J}(\theta)$ (where θ is the angle of rotation of **R**), a useful check on the numerical integration. The onset of strong coupling is thus governed by the differences in the E_{JM} and the larger the splitting the more nearly adiabatic the motion in that region. At sufficiently large separations the diagonal terms become degenerate and so in

the initial and final stages of any collision ($R \to \infty$) the space-fixed quantization system is good.

The diagonal terms can be estimated most readily in the limit of large R when, as we have seen, the individual atomic quantum numbers are good. The second-order perturbation expression for C_6 in the Kirkwood–Slater form is

$$C_6(J_A M_A J_B M_B) \approx \{\tfrac{1}{2}\alpha_{xx}^{A}(J_A M_A)\alpha_{xx}^{B}(J_B M_B) + \alpha_{zz}^{A}(J_A M_A)\alpha_{zz}^{B}(J_B M_B)\} \times \frac{E_A E_B}{E_A + E_B}. \quad (14)$$

The anisotropy in C_6 is thus essentially that of the polarizability α and this can only be appreciable if the outermost shell is an incomplete P or D one (besides, of course, $J > \frac{1}{2}$) i.e. if, in the Russell–Saunders coupling scheme, $L \geqslant 1$. Thus for a $^3P_2$ atom with one electron in a P shell the *maximum* possible anisotropy (assuming zero core contribution and equal contribution of $P \to D$ and $P \to S$ terms) is

$$[C_6(2, 2) - C_6(2, 1)]/\bar{C}_6 = \tfrac{3}{10}\,; \quad [C_6(2, 1) - C_6(2, 0)]/\bar{C}_6 = \tfrac{1}{10}.$$

For a $^3P_1$ atom with the same configuration (i.e. a ^2S core),

$$[C_6(1, 1) - C_6(1, 0)]/\bar{C}_6 = \tfrac{3}{10},$$

while for a $^2P_{3/2}$ atom (^1S core)

$$[C_6(\tfrac{3}{2}, \tfrac{3}{2}) - C_6(\tfrac{3}{2}, \tfrac{1}{2})]/\bar{C}_6 = \tfrac{2}{5}.$$

Anisotropies of up to 40 per cent are thus possible, but in the case of the $^3P_2$ state of Hg and the inert gases, the measured M dependence of the polarizability leads to an anisotropy in C_6 of no more than 10 per cent [11–13].

The magnitude of all the diagonal elements in (13) is reduced by defining

$$c_{JM}(t) = a_{JM}(t) \exp\left(i \int_{-\infty}^{t} \bar{E}(R)\, dt/\hbar\right)$$

to give

$$-i\hbar\dot{c}_{JM} = i\hbar\Delta_{MM-1}{}^{J}\dot{\theta}c_{JM-1} + i\hbar\Delta_{MM+1}{}^{J}\dot{\theta}c_{JM+1} + (E_{JM}(R) - \bar{E}(R))c_{JM}, \quad (15)$$

where $\bar{E}(R)$ is the average interatomic potential function with respect to all the M states. The long-range form of the diagonal terms is now $\{C_6(JM) - \bar{C}_6\}R^{-6}$, but in order to integrate equation (14) over all paths some assumption must be made about the repulsive branch of the potential and its anisotropy. The familiar Lennard-Jones form is adequate for $\bar{E}(R)$, but we can only guess at the M dependence of the repulsive branch of $E_{JM}(R)$. In the scattering phenomena to be discussed, the turning points of the classical motion lie outside the repulsive branch of the potential and the results are not sensitive to assumptions about the short-range behaviour of $E_{JM}(R)$; the following form has been taken:

$$E_{JM}(R) = -\frac{C_6(JM)}{\sigma^6}\left\{\left(\frac{\sigma}{R}\right)^6 - \left(\frac{\sigma}{R}\right)^{12}\right\}. \quad (16)$$

3. Solutions of the coupling problem

In order to display the numerical solutions of the coupled equation (13) for a curvilinear trajectory more compactly, reduced quantities are defined as follows; time is reduced by σ/v, length by σ and energy by $\frac{1}{2}\mu v^2$ (E_0), where v is the initial relative velocity, σ the length parameter of the potential and μ the reduced mass of the system. If $E(R)$ can be characterized by two parameters σ and an energy ϵ, there are then three reduced parameters for the coupling problem, b/σ, ϵ/E_0 and the anisotropy parameters $p_M=(C_6(2, M)-\bar{C}_6)/(\hbar v\sigma^5)$. In these terms the coupled equations of motion assume the form

$$-i\frac{dc_M}{dt^*}=i\frac{b^*}{R^{*2}}\Delta_{MM\pm1}{}^J c_{M\pm1}+p_M(R^{*-12}-R^{*-6})c_M. \tag{17}$$

The parameter p_M plays the role of the Massey parameter, $(E_J-E_{J'})\sigma/\hbar v$ in fine-structure transitions [14].

The elasticity of a collision can be described by the modulus of the corresponding diagonal S-matrix element. If the equation (17) has been solved in a rotating basis, the amplitude of the scattered wave in the original m channel (remembering that at the start of the collision $m=M$) is

$$|S_{Jm:\,Jm}(b)|=|\sum_{M'}c_{mM'}(\infty)d_{M'm}{}^J(\theta(b))|, \tag{18}$$

where the rotation matrices $d_{MM'}{}^J(\theta)$ transform the exit channel amplitudes $c_{MM'}(\infty)$ computed in the rotating system back to the space-fixed system. For zero splitting of the Zeeman levels, all off-diagonal elements of **S** will be zero and we adopt for the definition of b_c a critical impact parameter for coupling, b_c,

$$|S_{Jm:\,Jm}(b_c^*)|=0{\cdot}9. \tag{19}$$

This coupling impact parameter is displayed as a function of the parameter p, figure 1. The onset of coupling is rapid and suggests that the concept of a coupling radius is a useful one. In figure 2 $|S_{22:\,22}(b)|$ is plotted as a function of b^* with the other parameters held constant. The intermediate region of b^*, in which the space-fixed system breaks down, is clearly visible. The oscillations in $|S_{JM:\,JM}(b^*)|$ or $|S_{Jm:\,Jm}(b^*)|$ in the close-coupled region are quantum in origin but are partly at least due to restricting the basis set to only five states. Their presence in principle affects computed cross sections but in practice any effect will be blurred by energy and initial-state averaging.

In order to discuss the effects of coupling on atomic scattering the centre of mass angle of deflection, θ, is a more useful variable than b. The dependence of S_{JmJm} on θ is displayed in figure 3. A family of curves is shown for a constant value of the reduced potential energy parameter ϵ^* and various values of p; the qualitative behaviour is independent of ϵ^*. The distinctive shape of the curves is a result of two factors. On the large impact parameter branch extending from $\theta=0$ to the rainbow angle θ_r, the increasing splitting of the degeneracy of the Zeeman levels near the turning point causes the rotating axis description to improve with a corresponding fall in the overlap $|S|$ from unity at $b=\infty$, $\theta=0$. Beyond the rainbow, the decreasing angle of deflection makes the two descriptions increasingly similar until at $b=0$, $\theta=\pi$ they coincide and $|S|=1$ again.

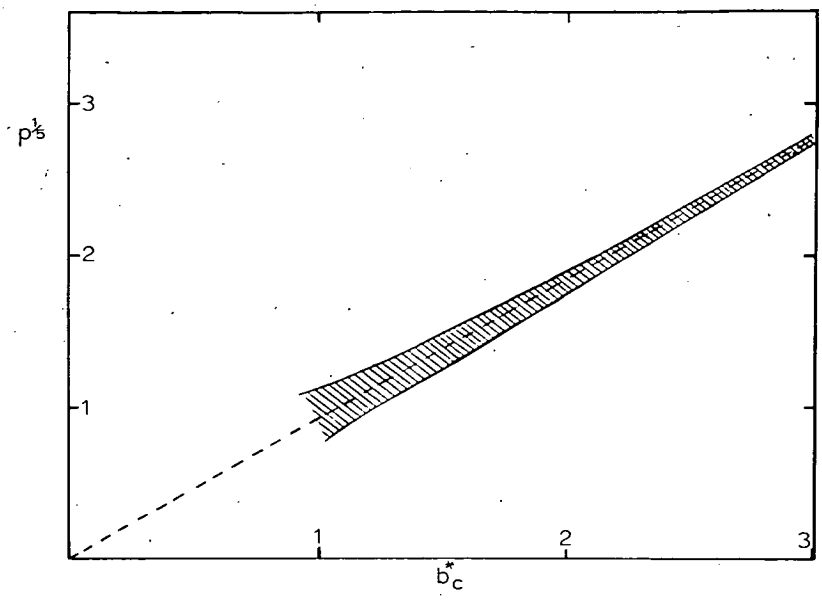

Figure 1. Plot of the reduced critical impact parameter for coupling ($S=0{\cdot}9$), b_c^*, versus p. The dashed line is that of the relationship (24) and the shaded area indicates the range of values of b_c^* obtained when ϵ^* varies between 1 and 100. Values obtained by numerical integration of the coupled equations (17).

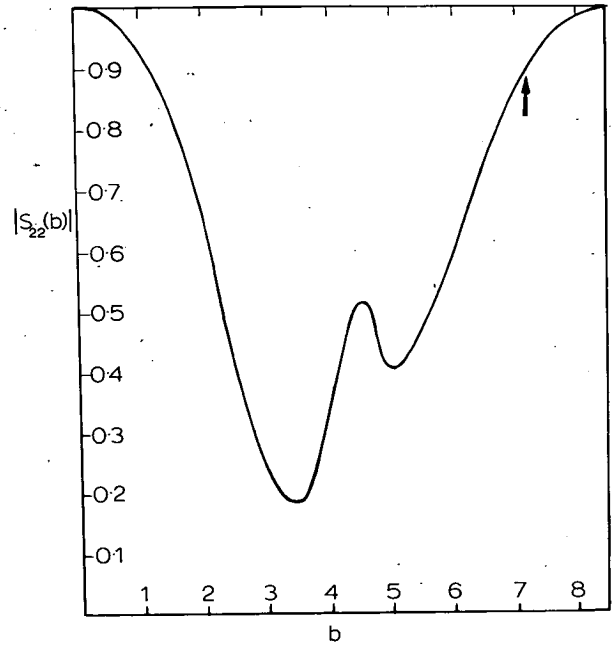

Figure 2. Plot of the diagonal S-matrix element for the $j=2$, $m=2$ channel as a function of the impact parameter b with p fixed at 40, $\sigma=4$ Å. Values obtained by numerical integration of equation (17). The arrow indicates the onset of strong coupling given by equation (24).

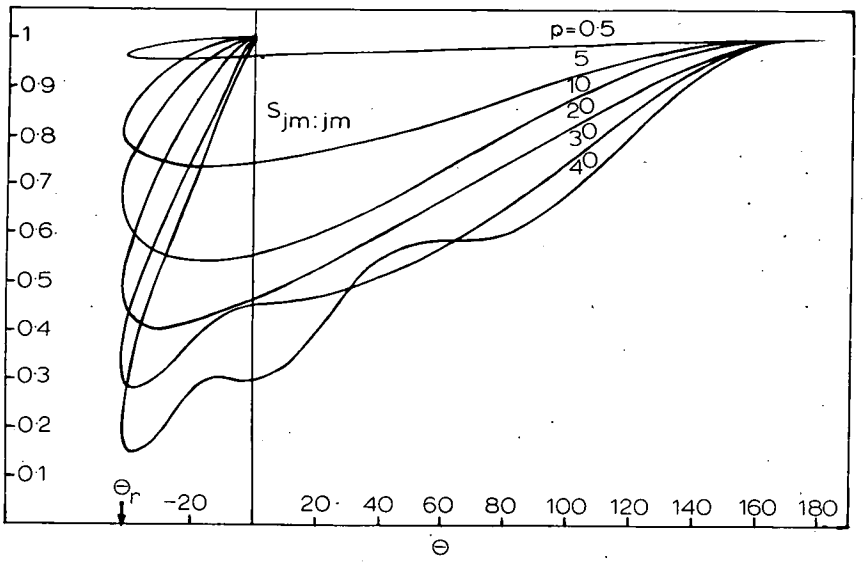

Figure 3. Plot of the diagonal S-matrix element ($j=2$, $m=2$ channel) versus angle of deflection Θ for a range of p values. ϵ^* is fixed at 0·33. Values of S obtained by numerical integration of equation (17). The rainbow angle Θ_r is indicated.

We can define a critical radius R_c for the onset of coupling as the separation at which the centrifugal and distortion (diagonal) terms in (17) become equal. This yields

$$R_c = \left\{ \frac{\Delta_{MM\pm1}{}^J p_M \sigma^5}{b} \right\}^{1/4} \tag{20}$$

in which the dependence on M is very slight and will subsequently be neglected. Alternatively, we may take the ' sudden ' solution of the coupled equations ;

$$\mathscr{C}(\infty) = \exp\left(-i \int_{-\infty}^{\infty} \mathscr{A}\, dt/\hbar \right) \mathscr{C}(-\infty), \tag{21}$$

where $\mathscr{A}$ is the transition matrix on the right-hand side of (17) and the common suffix J has been dropped. This type of solution has been used by Callaway and Bauer [15] in a discussion of the $^2P_{1/2} \rightarrow {}^2P_{3/2}$ cross section of the alkali metals. The diagonal terms in $\int \mathscr{A}\, dt$ are a semi-classical approximation to the differences from the central value in the adiabatic phase shifts for the various M channels ;

$$\hbar^{-1} \int_{-\infty}^{\infty} \mathscr{A}_{MM}\, dt = \hbar^{-1} \int_{-\infty}^{\infty} (E_{JM}(t) - \bar{E}(t))\, dt \approx \eta_{JM}(b) - \bar{\eta}_J(b) \tag{22}$$

while the off-diagonal terms are proportional to the angle of deflection,

$$\hbar^{-1} \int_{-\infty}^{\infty} \mathscr{A}_{MM\pm1}\, dt = \Delta_{MM\pm1}{}^J \theta. \tag{23}$$

There is complete scrambling among the exit channels when the off-diagonal elements (23) become comparable in magnitude to the diagonal elements (22).

We thus define a critical impact parameter b_c for strong coupling by equating (22) and (23). If both integrals are evaluated assuming a straight-line path so that θ in (23) equals π, we obtain

$$b_c^* \approx \{\tfrac{3}{8}\Delta_{MM\pm1}{}^J p\}^{1/5}, \tag{24}$$

where, once again, only the long-range part of $E_{JM}(R)-\bar{E}(R)$ has been retained. Equation (24) sets essentially the same limits to the region of strong coupling as (20). Referring to figure 1, the relationship (24) is followed rather well for a large range of values of p, but the underlying assumption, that of a straight-line trajectory, naturally breaks down for small values of b_c^*.

4. Application to scattering phenomena

We now analyse some specific scattering phenomena using the concept of the critical radius for coupling, R_c, and the general topology of coupling illustrated by the diagrams of $|S(\theta)|$. In discussing scattering phenomena semi-classically or classically (i.e. under conditions of a well-defined trajectory), it is useful to have a formula for the deflection and phase shift developed at any point along the trajectory. The following approximations, valid in the limit $R \ll b$, are useful ;

$$\theta(R^*) \approx -\tfrac{6}{7}\left(\frac{bC_6}{E\sigma^7}\right) R^{*-7} \tag{25}$$

$$\eta(R^*) \approx \tfrac{1}{5}\left(\frac{C_6}{\hbar v\sigma^5}\right) R^{*-5} \tag{26}$$

where the long-range part of the central potential is assumed to be $-C_6R^{-6}$.

Turning first to the rainbow phenomenon, the angle of deflection θ_r can be ascribed to a single M state if close coupling holds over a substantial portion of the rainbow trajectory. More specifically, a test can be made for adiabatic rainbow scattering by requiring that the portions of the trajectory with $R > R_c$ contribute less than 10 per cent to the overall deflection. The rainbow angle is given approximately (for $\epsilon^* \lesssim 1$) by

$$\theta_r \sim -2\epsilon^*. \tag{27}$$

Combining (24) and (25) gives an approximate lower limit for p if the strong-coupling condition is to be fulfilled in the rainbow region of

$$p \gtrsim 7{\cdot}5 b_r{}^{*11/7}. \tag{28}$$

b_r^* varies only slowly with ϵ^* and so the limiting value for p varies between 9 at $\epsilon^* \to 0$ and 17 at orbiting energies. We can compare this result with the $|S|$ versus p diagram for the rainbow impact parameter with a range of ϵ^* values shown in figure 4. The onset of coupling is marked by the sudden fall in $|S|$ at $p \approx 7$, largely independent of ϵ^*. This is compatible with essentially completely adiabatic behaviour as far as the rainbow deflection is concerned at $p = 9$ (except for reduced energies close to unity) and is in good agreement with the approximate relationship (28). Alternatively, we may say that motion along the rainbow trajectory is adiabatic when b_c, given by equation (24), is equal to the rainbow impact parameter. Once again this leads to a range of p values for the onset of coupling from 6·6 as $\epsilon^* \to 0$ to 20 as $\epsilon^* \to 1$.

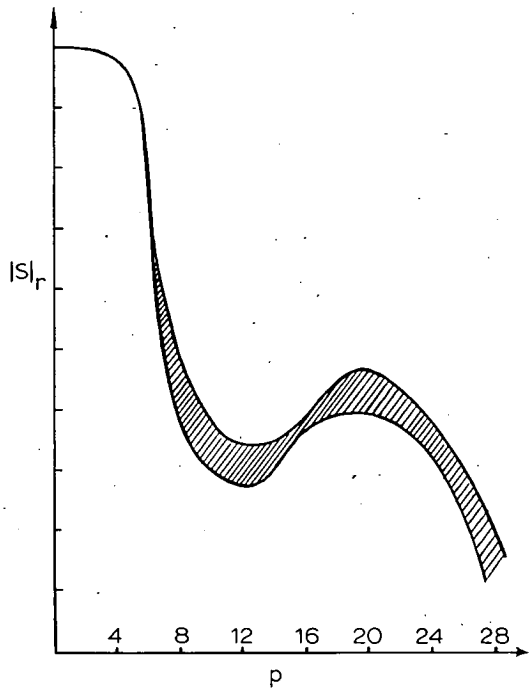

Figure 4. Plot of the diagonal S matrix element ($J=2$, $m=2$ channel) evaluated along the rainbow trajectory versus p. The shaded area indicates the range of values of $|S|_r$ obtained when ϵ^* is varied between 2 and 100.

Considering next the glory structure, the essential condition for the appearance of undulations is that there is appreciable amplitude in the elastic exit channel for impact parameters around the glory value. The outer branch contribution at small angles is always in the weak-coupling region and hence is necessarily elastic (see below for a discussion of the total cross section). As a condition for the survival of the glory structure we thus take $|S|_g = 0{\cdot}5$.

Inspection of a typical $|S|_g$ versus θ plot shows that the coupling does not change markedly between the rainbow and the forward glory trajectories and that a value $p \approx 8$ marks the rapid onset of coupling on the forward glory path. Again this is largely independent of ϵ^*. Thus for values of $p > 8$ we expect the undulations in the energy dependence of the total cross section almost to disappear. An inspection of $\sigma_{tot}(E)$ plots covering a sufficient energy range might well reveal the velocity region (around v^*) in which the oscillations die out, thus enabling ΔC_6 to be estimated from the relationship $p(v)^* = 8$.

Conclusions about the survival of the glory structure in particular are somewhat dependent on the assumption made about the anisotropy of the repulsive branch of the potential. If the scattered wave amplitude in the glory region, $|S(b_g)|$ is re-calculated for a coupling potential of the form $-C_6(JM)R^{-6}$, the critical value of p for the onset of coupling is reduced by about 15 per cent.

Finally, we discuss the M dependence of the total cross section itself within the framework of the Massey–Mohr approximation in which

$$\sigma^{tot} = 2\pi b_0^2 + 8\pi \int_{b_0}^{\infty} \sin^2 \eta(b) b \, db, \tag{29}$$

where b_0 is the impact parameter for random phase, typically given by $\eta(b_0)=\pi/2$. If a substantial portion of the integral of the phase shift function in (29) is determined under strong-coupling conditions (the ' rotating atom ' limit), then σ^{tot} is properly labelled with the initial (JM) state of the atom. Under these conditions the anisotropy in the total cross section is given by

$$(\sigma_{JM}{}^{\text{tot}}-\sigma_{JM'}{}^{\text{tot}})/\bar{\sigma}^{\text{tot}}=[C_6(JM)^{2/5}-C_6(JM')^{2/5}]/\bar{C}_6{}^{2/5}. \tag{30}$$

In contrast, if strong coupling does not begin until separations less than b_0 (i.e. $R_c<b_0$) the total cross section is that of the initial (Jm) state (' fixed atom ' limit) and the possible onset of strong coupling in the random phase region does not affect the total cross section. Under weak coupling conditions the anisotropy in σ^{tot} is only ~ 20 per cent that given by (30). The anisotropy in the potential, $\Delta C_6/\bar{C}_6$ necessary for σ^{tot} to be determined under strong-coupling conditions can be conservatively estimated by requiring that R_c be greater than the impact parameter for a phase shift of 0·1 radian. Using the standard expression

$$\eta=\tfrac{9}{16}\frac{C_6}{\hbar v b^5} \tag{31}$$

for the Born approximation to the phase shift resulting from the R^{-6} part of the potential and with R_c given by equation (20), one finds

I : Strong coupling for σ^{tot}, $\Delta C_6/\bar{C}_6>1$,

II : Weak coupling for σ^{tot}, $\Delta C_6/\bar{C}_6<0{\cdot}4$,

with an intermediate region in which detailed calculation is necessary.

5. Conclusions

Applying the above results to the systems Hg*/Hg, Hg*/M and Ne* . . . Xe*/Ne . . . Xe, where M is an alkali metal, leads to the conclusion that in all these systems and probably in every atom/atom system at thermal energies the total cross section is determined exclusively under weak coupling conditions. The atoms are almost spherically symmetric from the point of view of total cross section measurements and so these are not a useful route to the anisotropy in C_6. Thus, for the similar case of a $^2P_{3/2}$ atom, Ga, the anisotropy in the total cross section, $(\sigma_{3/2\,3/2}{}^{\text{tot}}-\sigma_{3/2\,1/2}{}^{\text{tot}})/\bar{\sigma}^{\text{tot}}$ was found [16] to be between 1 per cent and 2 per cent with the inert gases He, Ar and Xe as partners. The authors rightly interpreted their results in terms of a fixed atom (i.e. angle dependent) potential.

For Hg*/Hg, the Slater Kirkwood value of C_6 lies between 80 and 100×10^{-60} erg cm^6; the coupling parameter p then lies in the range 0·8–1·2 at thermal speeds ($\sigma\approx 4$ Å). The glory structure should thus be intact and the rainbow deflection almost independent of the initial magnetic substate; once again the Hg* atom is apparently spherically symmetric as far as scattering experiments are concerned. For the pairs Hg*/inert gas, C_6 is estimated to lie in the range $500–800\times 10^{-60}$ erg cm^6 and p between 4 and 7 at thermal speeds (σ in the range 4–4·5 Å). These are intermediate coupling cases; for the lighter alkali metals the rainbow will be almost independent of the initial M state of Hg* but, depending on the precise nature of the repulsive term in the coupling

potential, strong coupling might ensue for the heavier partners. The glory structure should still be visible for the lighter partners. For the M*/M inert gas pairs, p probably ranges between 20 and 70 (the size parameter is hard to estimate here and is given a value in the range 3·8–4·2 Å). Almost complete quenching of the glory structure is thus predicted and the rainbow angle is that of the initial (JM) state and is essentially determined by an angle independent potential. In these cases ($p \gtrsim 10$) elastic scattering measurements made with metastable atoms in random m_J states (' unselected ' beams) would show only the superimposed differential cross sections from different M_J states and the interference structure from each sub-state would be lost.

References

[1] Sheppard, A., Schmelling, S. G., and Brink, G. O., 1973, *Proc. VIII I.C.P.E.A.C.*, Belgrade, p. 852.
[2] Davidson, T. A., Fluendy, M. A. D., and Lawley, K. P., 1973, *Discuss. Faraday Soc.*, **55,** 158.
[3] Lee, Y. T., 1972, *Invited Talks and Progress Reports, VII I.C.P.E.A.C.*, Amsterdam, p. 357.
[4] Masnou-Seeuws, F., and Roueff, E., 1972, *Chem. Phys. Lett.*, **16,** 592.
[5] Dashevskya, E. I., and Mokhova, N. A., 1973, *Chem. Phys. Lett.*, **20,** 454.
[6] Nikitin, E. E., 1965, *Optics Spectrosc.*, **19,** 91.
[7] Barrat, J. P., Casalta, D., Cojan, J. L., and Hamel, J., 1966, *J. Phys., Paris*, **27,** 608.
[8] Omont, A., 1965, *J. Phys., Paris*, **26,** 26.
[9] Byron, F. W., and Foley, J. M., 1964, *Phys. Rev.*, **134,** A625.
[10] Ben Reuven, A., 1965, *J. chem. Phys.*, **42,** 2037.
[11] Darwall, E. C., Fluendy, M. A. D., and Lawley, K. P., 1970, *Molec. Phys.*, **19,** 673.
[12] Robinson, E. J., Levine, J., and Bederson, B., 1966, *Phys. Rev.*, **146,** 95.
[13] Levine, J., Celotta, R. J., and Bederson, B., 1968, *Phys. Rev.*, **171,** 31.
[14] Gordeev, E. P., Nikitin, E. E., and Ovchinnikova, M. Ya., 1971, *Optics Spectrosc.*, **30,** 101.
[15] Callaway, J., and Bauer, E., 1965, *Phys. Rev.*, **140,** A1072.
[16] Berkling, K., Schlier, Ch., and Toschek, P., 1962, *Z. Phys.*, **168,** 81.

J. Phys. B: Atom. Molec. Phys., Vol. 8, No. 10, 1975. Printed in Great Britain.

LETTER TO THE EDITOR

Differential scattering cross sections in the eV region: the K/Ar ground state potential

M A D Fluendy, I H Kerr, K P Lawley and J M McCall

Department of Chemistry, University of Edinburgh, West Mains Road, Edinburgh EH9 3JJ, Scotland

Received 23 May 1975

Abstract. Differential cross sections for the scattering of fast K atoms from Ar have been measured for CM collision energies between 50 and 200 eV in the angular range 0–9°. Pointwise inversion of this data yielded a potential for the ground state of this system between 0·2 and 5·3 eV.

These measurements were made using a crossed atomic beam apparatus in which a fast K atom beam, prepared by resonant charge transfer, scattered from a thermal energy target beam of Ar. Potassium ions were produced by surface ionization on a porous tungsten disc heated to 1500 K by radiation, the potassium being supplied to the ionizing surface by diffusion from the rear of the disc which was bathed with potassium vapour at a pressure of about 1 N m^{-2}. After ionization the K^+ ions were accelerated to the required laboratory collision energy and focused into the charge exchanging chamber. Here a pressure of 7×10^{-2} N m^{-2} was very steadily maintained so that about 50% of the ions were neutralized in this region. On exit from this chamber the ions were deflected and monitored via an electrometer; the fast neutral flux of K atoms remaining was collimated to form a well defined beam and finally entered a differentially pumped collision zone. In this region the argon target beam produced by effusion through a capillary array intersected the K beam at right angles in a well defined volume 4 mm long by 2 mm deep by 0·4 mm wide. The Ar beam was modulated by a chopper wheel and its intensity continuously monitored by a differential ion gauge and lock-in amplifier system which distinguished between changes in beam and background density. An electric field located just down stream of the collision zone removed any ions formed in the collision. The neutral scattered K atoms were detected on a cold tungsten ribbon 0·020 inches wide and the resulting K^+ ions counted via a channeltron and discriminator into a scaler system, gated in synchronism with the target modulation so that scattering from the target could be distinguished from noise. The detection assembly was rotated with high precision, $\pm 0{\cdot}002°$, in a plane normal to that of the two beams so that the angular dependence of the scattering could be measured.

Experimental data such as scaler readings, angular location of the detector, Ar target density, time etc were collected and processed on-line by a PDP 11/45 computer which was also controlled the angular scanning sequence for the detector. This was arranged so as to sample the angles in a random fashion and to return to the 0° (K beam) position at intervals of six minutes so that changes in the K beam intensity could be corrected. The computer also monitored pressures and beam fluxes as well as providing

feed-back to the operator as to the progress of the experiment. A typical series of measurements at a single collision energy took about $1\frac{1}{2}$ hours and involved measurements at 400 different angles.

The energy spread in the collisions as measured by a time-of-flight method was 0·3 eV and arose predominantly from the temperature of the porous disc. The angular resolution using the Kusch criterion was 0·1° in the laboratory frame. At small angles the apparatus resolution is a function of observation angle and alters the observed envelope of cross section as well as diminishing the amplitude of any oscillatory structure. A correction for this effect was computed by numerical integration over the beam and detector geometries. At the smallest angles used in the analysis (0·1° lab) the correction was 50% but fell off rapidly and was unimportant at 0·5°. Since the apparatus geometry can be precisely measured this correction is known to $\pm 5\%$ and introduces proportionately smaller errors into the corrected data.

Measurements of scattered intensity against laboratory angle were made at 100, 200, 300 and 400 eV potassium beam energies between 0–5°. The data were corrected for resolution effects and transformed to centre-of-mass coordinates. In this analysis attention is focused on the ground state $^2\Sigma^+$ potential and a smooth curve was drawn through the angular dependence (some weak oscillatory structure was barely resolved at narrow angles and will be discussed in a subsequent paper). Since only relative intensities were measured the observed cross sections were normalized at an angle χ_N to those calculated at the appropriate energy from the K/Ar potential of Buck and Pauly (1968). This potential is based upon a considerable amount of thermal energy data and is likely to be accurate below 0·5 eV, corresponding to scattering in the range $E\chi < 100$ eV deg overlapping substantially with the present observations, so that χ_N may be chosen in this range.

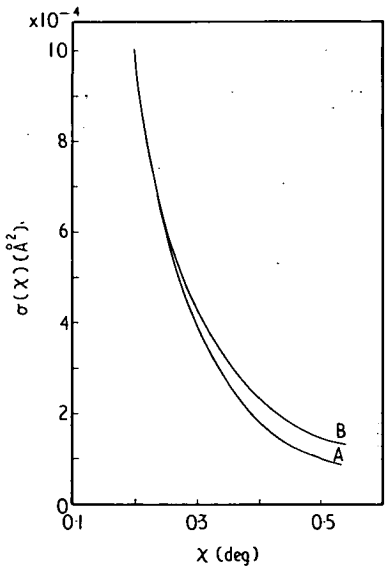

Figure 1. Comparison of cross sections measured at 200 eV (lab), curve A, and calculated from the potential of Buck and Pauly, curve B. The curves are normalized at $\chi = 0{\cdot}2°$. At all energies the observed $\sigma(\chi)$ falls off more steeply than calculations from the Buck and Pauly potential.

Each scan of $\sigma(\chi)$ at a given collision energy was inverted in the region corresponding to monotonic scattering from the repulsive potential to yield the classical deflection functions using the relation:

$$b(\chi) = \left(b^2(\chi_N) - 2\int_{\chi_N}^{\chi} \sigma(\chi')\sin\chi'\,d\chi'\right)^{1/2}$$

where $b(\chi_N)$ is the impact parameter corresponding to scattering at the normalization angle computed from the Buck and Pauly potential. The results of this inversion are plotted as $E\chi$ against b in figure 2. Data from cross section scans repeated under the same

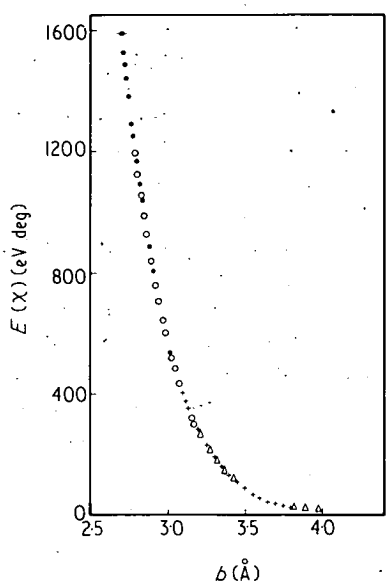

Figure 2. Reduced deflection function plot from measurements at laboratory collision energies of ● 400 eV, ○ 300 eV, + 200 eV and △ 100 eV. Only a 2·5% random sample of the data points are shown.

experimental conditions agree well and fall within the size of the symbols shown in the figure except at the ends of the accessible range where error bars are drawn. Since all these observations were made at small angles this plot is independent of collision energy to a very good approximation and the excellent agreement between the regions of $E\chi$ which could be explored at several different collision energies and laboratory angles confirms the precision of the resolution correction and normalization procedure. Changes in normalization produce deflection functions that diverge from each other so that any significant errors in this respect would be revealed in this plot.

A potential was calculated from these deflection functions on a pointwise basis by numerically evaluating the relations (Firsov 1953):

$$V(R) = E\left(1 - \frac{b^2}{R^2}\right) \qquad R = b\exp\left(\frac{1}{\pi}\int_b^{\infty} \frac{\chi(b')\,db'}{(b'^2 - b^2)^{1/2}}\right).$$

The mean potential, tabulated at intervals of 0·05 Å, evaluated from two independent sequences of measurements between 100 and 400 eV (lab) is given in table 1. The difference between these two independent sets of data is too small to be seen in figure 3, but

Table 1.

R(Å)	2·80	2·85	2·90	2·95	3·00	3·05	3·10	3·15	3·20	3·25	
V(eV)	5·68	4·61	3·74	3·04	2·46	1·99	1·61	1·29	1·03	0·82	
R(Å)	3·30	3·35	3·40	3·45	3·50	3·55	3·60	3·65	3·70	3·75	3·80
V(eV)	0·65	0·52	0·41	0·33	0·28	0·23	0·20	0·17	0·14	0·12	0·10

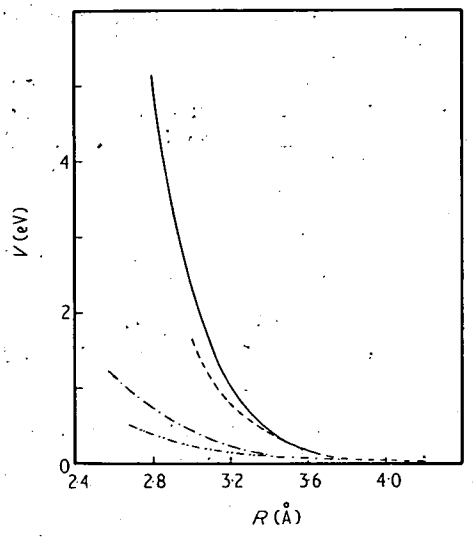

Figure 3. Potentials for K/Ar $^2\Sigma^+$. —— this work, – – – Buck and Pauly (1968), —·—· Malerich and Cross (1970), —·— calculation of Pascale and Vandeplanque (1974).

is within 1% except at the ends of the range where it is about 3·5%. The mean potential should thus be good to be better than 1% in the region covered by the table. At distances larger than 3·7 Å the potential of Buck and Pauly should, of course, be preferred. In the range covered by these experiments the potential can be approximately represented by:

$$V(R) = \alpha \exp(-\beta R) \qquad 2{\cdot}8 \leqslant R \leqslant 3{\cdot}8 \text{ Å}$$

where

$$\alpha = 6 \pm 1 \times 10^5 \text{ eV}, \qquad \beta = 4{\cdot}13 \pm 0{\cdot}07 \text{ Å}^{-1},$$

though no attempt has been made to join this form smoothly to the thermal potential at their intersection.

The potential derived in this work is considerably harder than that found by Malerich and Cross (1970) who fitted their total cross section data to an inverse power potential $V(R) = 618/R^{7{\cdot}25}$ eV, cf the $R^{-13{\cdot}6 \pm 0{\cdot}1}$ form, which is a reasonable fit to the present work, both results differing very sharply from the potential calculated by Pascale and Vandeplanque (1974) and illustrated in figure 3. However, the model Hamiltonian used in the calculated potential involves a crude approximation to the electrostatic (polarization) contribution when the K valence electron penetrates the argon atom; the sum of the radii of the outermost maximum in the K(4s) and in the Ar (3p) electron distributions is 2·84 Å and imperfections in the model Hamiltonian could well be very important even

before this separation is reached. The discrepancy between the present results and those of Malerich and Cross (1970) may arise from resolution effects in the total cross section measurements which are primarily functions of the very small angle scattering. The resolution angle quoted in the total cross section work is some five to ten times greater than that required to resolve the quantum cross section, so that very substantial corrections are necessary and will be energy dependent. In comparison, differential measurements only require correction at small angles and so substantially avoid this problem. In particular, it seems very unlikely that the $R^{-7.25}$ dependence reported by Cross could be compatible with the present measurements which furthermore at low energies agree very well with the potential of Buck and Pauly.

These results will be of interest not only as an ingredient in the analysis of excitation processes occurring in this system (Alber *et al* 1975) but also as a standard system with which to normalize differential cross section measurements that are difficult to make on an absolute basis.

References

Alber H, Kempter V and Mecklenbrauck W 1975 *J. Phys.* B: *Atom. Molec. Phys.* **8** 913
Buck U and Pauly H 1968 *Z. Phys.* **208** 390 (also Düren R, Raabe G P and Schlier Ch 1968 *Z. Phys.* **214** 410)
Firsov V G 1953 *Zh. Eksp. Teor. Fiz.* **24** 279
Malerich C J and Cross R J 1970 *J. Chem. Phys.* **52** 386
Pascale J and Vandeplanque J 1974 *J. Chem. Phys.* **60** 2278 (also 1974 *Molecular Terms of the Alkali–Rare Gas Atom Pairs* vol 3, Service de Physique Atomique, Centre d'Etudes Nucléaires de Saclay)

22

Chemical Physics 13 (1976) 425–432

CLASSICAL TRAJECTORY STUDIES OF THE COLLISION SYSTEM $K+I_2$ IN THE eV REGION

M.A.D. FLUENDY, I.H. KERR, K.P. LAWLEY and D.R. MACDONALD
Department of Chemistry, University of Edinburgh, West Mains Road, Edinburgh, EH9 3JJ, UK

Received 8 October 1975

Trajectory calculations on the lowest adiabatic surface for $K+I_2$ have been used to explore reactive and inelastic scattering in the eV region. These processes are found to proceed by two contrasting mechanisms, one using the attractive parts of the potential and the other the repulsive wall. The probability of processes occurring through attractive forces decreases with increasing collision energy while the short range mechanism is essentially a two body one with three body effects only making a contribution in a limited impact parameter range. A hard sphere spectator model is explored, but found to be quite inadequate for energy loss calculations. A spectator model with realistic interatomic forces is, in contrast, successful in interpreting the whole range of numerical results above about 20 eV. It is suggested that a two body potential will be useful in interpreting even very inelastic high energy scattering provided that the mass ratio is favourable.

1. Introduction

The collision properties of the alkali metal/halogen molecule systems have been very extensively studied both experimentally (e.g., refs. [1–3]) and by trajectory methods in the thermal energy range [4–7]. These systems are interesting in that curve crossing effects between covalent and ionic surfaces are intimately involved in the dynamics of the collision, at least at low energies. For this reason it is important to extend this work to collisions at high energies so that the role of these velocity dependent effects can be explored. Another area of interest is the mapping of the actual potential surface or surfaces and it is the purpose of the present paper to illustrate the changing nature of scattering dynamics on a single surface as the kinetic energy increases and to explore the validity of various simple models. Non-adiabatic effects will then show up as departures from this behaviour. Recent work in the relevant energy range (1–1000 eV) has explored the differential cross section for alkali ion production [8–10], for elastic scattering [11,12] and, at somewhat lower energies, reactive scattering [13]. Measurements of the total cross section for the production of various ions are also available [14–17].

Trajectory calculations in this energy region have also been reported. Havemann et al. [18], investigated the exit channels KBr+Br, $K^+ + Br_2^-$ and $K^+ + Br^- + Br$ using exclusively the ionic surface. Van der Meulen et al. [19] studied the KBr product distribution using an adiabatic surface (covalent at long rnage, coulombic at short range).

In this work we have adopted a similar approach to that of Van der Meulen, using exclusively an adiabatic surface to examine scattering in the elastic, vibrationally and rotationally inelastic, and the dissociation channels for $K+I_2$ collisions.

The use of a single adiabatic surface for this work means that ionisation and in particular interference effects between trajectories scattering on different surfaces will not be seen. The results are thus strictly valid only in the limit of $V_{12}(R_c)$, twice the splitting between the adiabatic states, being large. This matrix element has been calculated to be ~ 0.5 eV for the collinear configuration (Grice and Herschbach [20]) and has been estimated from experimental data on charge production [14] as 0.04 eV, the difference in these values being at least partly due to orientation averaging. Using a mean value of $V_{12}(R_c)$ of 0.2 eV, the probability of leaving the lowest adiabatic surface even at 100 eV is less than 0.3 (based on the Landau–Zener formula) so that the lowest surface can be expected to yield the major features of the dynamics. At collision energies > 10 eV both the upper and lower adiabatic surfaces are effectively repulsive and

the qualitative conclusions we draw below will not be affected by using one surface or the other.

2. The model surface

The coordinate system and equations of motion are described by Bunker and Blais [21]. The quasi-classical assumption is used to obtain the initial rotational and vibrational energies of the I_2 molecule from the most probable quantum states at room temperature. The initial and final separations are chosen so that the potential is virtually zero and the remaining parameters are taken at random from their statistical distributions by established Monte Carlo procedures. The equations of motion are solved by stepwise numerical integration and conservation of energy and backwards integration to yield the starting values are used as checks on accuracy. Energy is conserved in the longest trajectories studied to better than one part in 1000. 600 trajectories were calculated for each of the 8 collision energies and the initial and final values of the dynamical variables were stored for subsequent analysis.

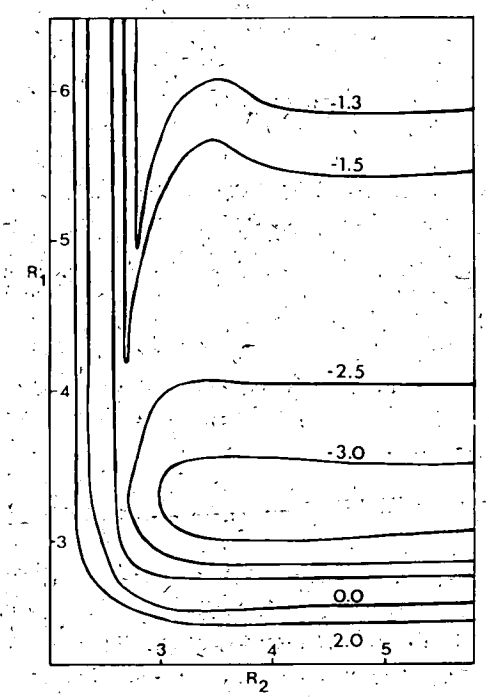

Fig. 1. Potential surface in the collinear configuration relative to an energy zero of the separated atoms, contours in eV. The K atom enters the collision from the top left hand corner of the figure.

The potential surface used is shown for a collinear configuration of the atoms in fig. 1. It is similar in shape to those used by Blais [4] and Godfrey and Karplus [5].

$$V_{cov} = D_{I_2}[(1 - \exp(-\beta(R_2 - R_{20}))^2 - 1] + A\exp(-R_1/\rho) + A\exp(-R_3/\rho)$$

where the first term describes the I_2 bond and the two final terms are K·I repulsions.

$$V_{ion} = [-e^2/R_1 - (\alpha_1+\alpha_2)e^2/2R_1^4 + A\exp(-R_1/\rho)+\delta] - [\tfrac{1}{2}\alpha_3 e^2\{1/R_2^4 + 1/R_3^4 - (R_2^2+R_3^2-R_1^2)/(R_2R_3)^3\}] + D_2(R_{02}/R_2)^{12} + D_3(R_{03}/R_3)^{12}.$$

The first bracketed term represents the K^+I^- interaction, the second term is an ion induced dipole form describing the interaction of the ions with the departing neutral iodine atom and the final two terms provide repulsive potentials between the neutral I atom and the K^+ and the I^-.

The parameters used are as follows:

D_{I_2} = 1.5417 eV
β = 0.642 Å^{-1} Spectroscopic values for I_2 [24]
R_{20} = 2.66 Å

A = 20700 eV
ρ = 0.311 Å
α_1 = 0.84 Å^3
α_2 = 7.16 Å^3
} Rittner [22]

α_3 = 5.0 Å^3
δ = 1.345 eV
} [23]

D_2 = 0.82 eV
D_3 = 1.084 eV
} Blais [4]

R_{02} = 2.84 Å
R_{03} = 2.00 Å
} adjusted Blais [4]

Crossing from the initial covalent surface to the ionic one was arranged so that the motion always took place on the surface of lowest energy. Thus recrossings were permitted (in contrast with the surface used by Blais) although these were not frequent at higher energies. Charge migration from one iodine atom to the

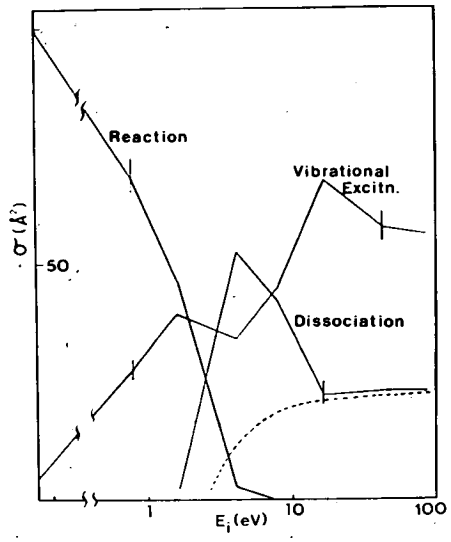

Fig. 2. Total cross sections for reaction, dissociation and vibrational excitation of I_2 (internal energy increased by more than one vibrational quantum). (– – –) Hard sphere spectator model for dissociation.

other was also permitted, the criterion once again being that the motion should always be on the lowest energy surface. (Godfrey and Karplus [5].)

3. Results

The total cross sections for the various processes possible on the single adiabatic surface used in this calculation are shown in fig. 2 as a function of the initial relative kinetic energy. The most significant feature is the closure of the reactive channel between 4.3 and 8.6 eV. The cross sections for dissociation and vibrational excitation reach a steady value with increasing energy after rising from threshold to a pronounced maximum at around 10 eV in the case of dissociation.

These trends in the various cross sections are primarily a result of the decreasing duration of the collision which makes it more and more difficult to accelerate the I atom during the collision, e.g., in the case of the reaction process, sufficiently for it to catch up with the departing K atom so that chemical reaction does not proceed for this mass ratio above 10 eV. At higher collision energies processes occur

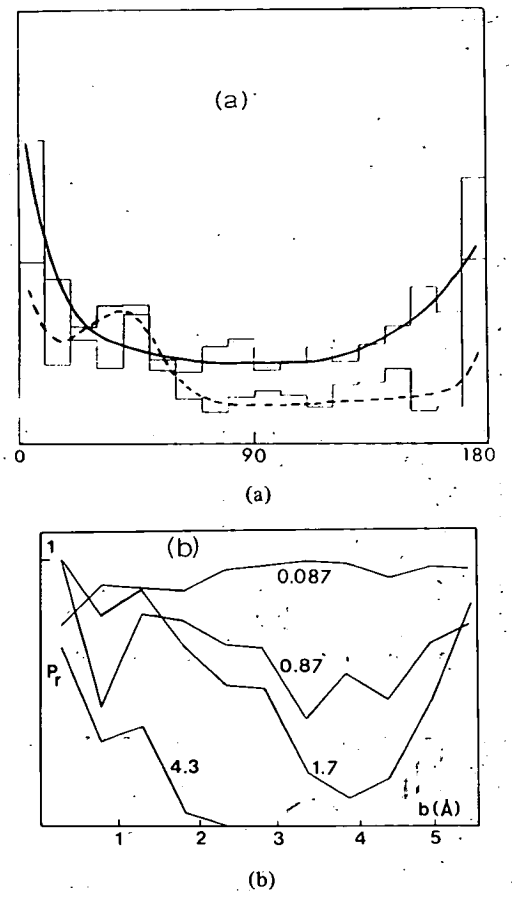

Fig. 3. (a) Angular distribution in 10° segments of reactively scattered KI. The smooth lines are drawn simply to aid the eye. (——) 0.087 eV, (– – –) 0.87 eV.

(b) Probability of reaction as a function of impact parameter at several collision energies (eV).

almost exclusively on the repulsive wall of the potential surface and the dynamics change from the attractive to repulsive type.

3.1. Reaction

The distribution of the product KI from reactive collisions is shown in fig. 3a. At thermal energies the product is forward scattered in accord with experiment and previous trajectory calculations on this type of surface. At higher energies the distribution becomes more symmetrical, as would be expected from the increasing importance of small impact parameters for reaction (fig. 3b), which result in enhanced scattering at larger angles.

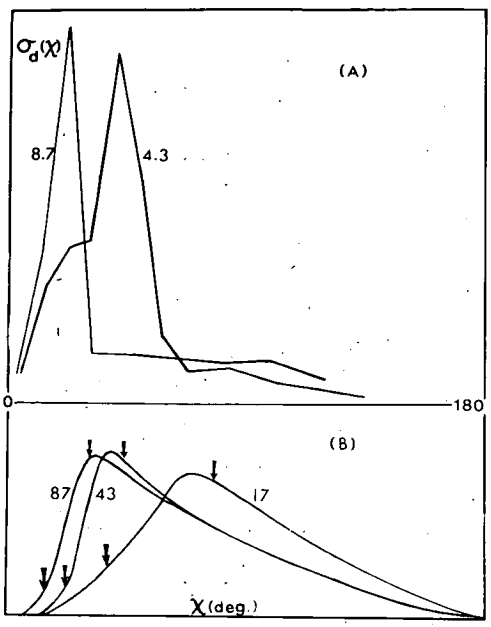

Fig. 4. (A) Angular distribution (arbitrary units) of K atoms after dissociative collision with I_2, collision energy 4.3 and 8.7 eV.

(B) As in (A) for collision energies of 87, 43 and 17 eV, the arrows show the threshold angle for dissociation through broadside and end on collisions. (Smoothed histogram.)

Simple dynamical models using only the attractive Coulomb part of the potential suggest a rather abrupt cut-off for reaction near 2.5 eV a result nicely confirmed by the present results summarised in fig. 3b and in accord with measurements on the K/Br_2 sys-

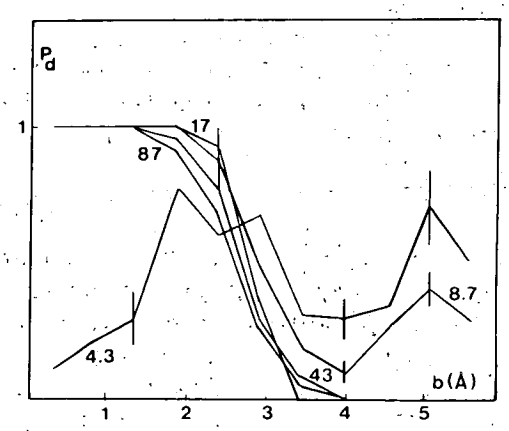

Fig. 5. Probability of dissociation as a function of impact parameter, energies in eV.

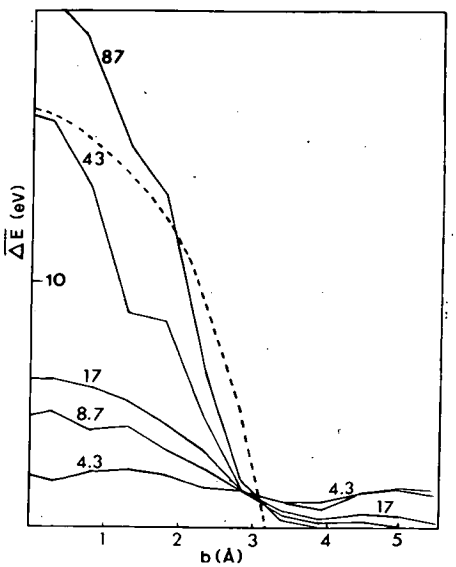

Fig. 6. Mean energy loss on collision as a function of impact parameter (——) M.C., (– – –) hard sphere spectator model at 43 eV.

tem [13]. Reactive collisions above this limit involve hard encounters and use the repulsive part of the potential until momentum constraints close this channel also.

3.2. Dissociation

The dissociation of the target I_2, like reaction, also proceeds by two different types of dynamics. Low values of $E\chi$ (where χ is the CM angle of deflection) correspond to motion in the attractive part of the potential and the departing K atom pulls an I atom in its wake. Trajectories of this type produce a "rainbow" at $E\chi = 215$ eV° at collision energies between threshold and 10 eV, fig. 4A. Only small energy losses above that required for dissociation are seen and inspection of fig. 6 shows that the mean energy loss accompanying dissociation at first decreases with increasing collision energy. The long range nature of these dynamics is shown by the impact parameter dependence of the probability for dissociation fig. 5. Trajectories of this type sample the potential surface around the attractive bowl and involve the joint motion of all three particles.

In contrast, at collision energies above 10 eV and

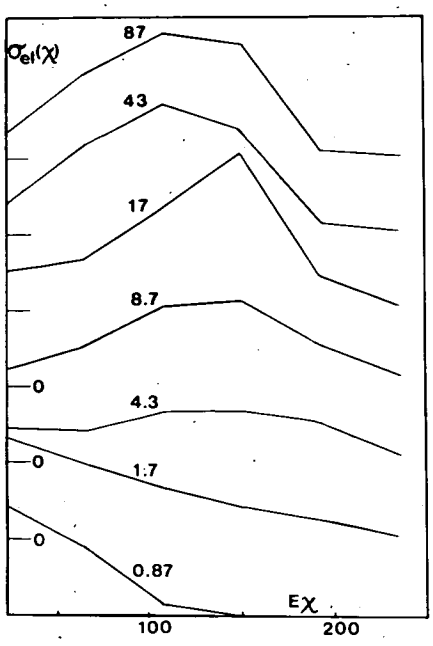

Fig. 7. Angular dependence of K atoms scattered after elastic collision ($\Delta E < 0.05$ eV).

$E\chi \gtrsim 250$ eV° a short range repulsive mechanism is responsible for dissociative K atom scattering. Collisions of this type have a mean energy loss that increases rapidly with collision energy. Inspection of typical trajectories of this type show that duration of the collision is short in comparison with the time required for the separation of the iodine atoms and their relative motion is predominantly monotonically extensive, suggesting that a simple two body impulsive model might be applicable.

3.3. Elastic scattering

The angular distribution of elastically scattered K atoms (defined as those in which the K atom energy loss < 0.05 eV) is shown in fig. 7. At energies below 3 eV a rapid fall off at large $E\chi$ is seen due to chemical reaction (cf. fig. 3b). Collisions in the range 5–10 eV show considerable inelasticity but a rather broad peak begins to emerge at ~ 150 eV°. At energies above 20 eV where the inelastic and dissociative processes using the attractive part of the potential have shut down this becomes a much more clearly developed peak at $E\chi = 125$ eV°. This rainbow arises from almost rectlinear trajectories in which the I··I distance is not changed from its initial value and provides a measure of the well depth (averaged over orientation) in this region of the potential; in this case ~ 1 eV in accord with estimates from the surface (fig. 1). As can be seen this well depth is very sensitive to the location of the valley head in a cut through the potential along R_2 and different regions of the surface in the neighbourhood could be explored by trajectories using vibrationally hot I_2 targets. The existence of this *elastic window* is valuable since this region is of especial importance in determining the nature of the reaction dynamics at thermal energies. The approximately rectilinear nature of these trajectories makes inversion of scattering data to yield potential information rather straight forward.

4. Discussion

4.1. Impulsive models

Two very simple models have for some years been applied to atom/diatomic collisions. In the more primitive of the two, the diatomic partner is regarded as spherically symmetric and the energy transferred from relative to internal motion is proportional to the "energy along the line of centres" at impact, i.e.,

$$\Delta E(\chi) \propto E_i \sin^2\chi/2, \qquad (1)$$

where χ is the CM angle of deflection and E_i the relative collision energy. In the second model, one of the target atoms is regarded as a spectator so that the first stage of the collision is an elastic atom/atom encounter involving the nearer of the two target atoms. The energy transferred to the relative motion of the two target atoms is, for the present example of a homonuclear diatomic,

$$\Delta E(\Theta) = \tfrac{1}{2}(M_K + M_{X_2})/(M_K + M_X)^2 M_K (1-\cos\Theta)E_i, \qquad (2)$$

where Θ is the angle of deflection in the CM system of the K/I pair (see fig. 9). Schottler and Toennies [25] have explored both models in connection with time of flight spectra obtained for the Na^+/D_2 system at energies upto 40 eV and they conclude that for this system the primitive hard sphere model and eq. (1) in particular represent the data well. This con-

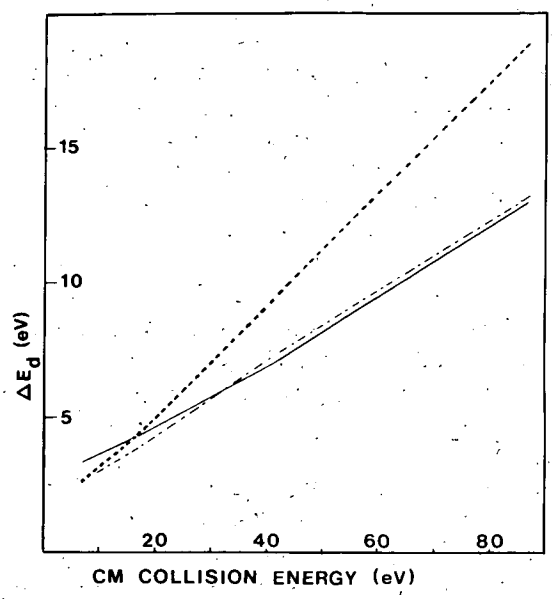

Fig. 8. Mean energy loss on collision; (——) M.C., (– – –) hard sphere spectator model, (–.–.) spectator model.

clusion does not necessarily hold for other systems or at other energies. More specifically, for the mass combination in which the projectile is much lighter than the target atoms (the reverse of the Na^+/D_2 case), the duration of the collision can become very short compared with the period of vibration of the target ($\sim 1.5 \times 10^{-13}$ s for I_2) and there is also less "persistence of velocity" in which the projectile continues to move in nearly the same direction after the first encounter thus increasing the chance of a multiple collision. As a result of both these effects, the second target atom does not experience any perturbation until the projectile has departed – i.e., the spectator model can be expected to become valid for the light projectile/heavy target combination at sufficiently high energies.

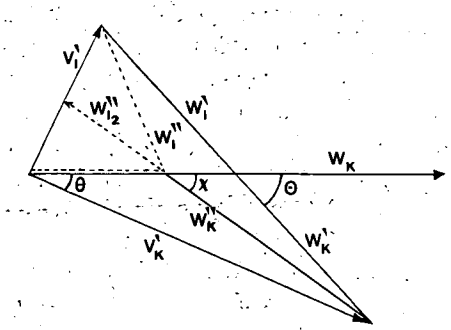

Fig. 9. Newton diagram for K/I_2 system showing effective CM angle, Θ for spectator model, together with the actual CM deflection χ for the molecular collision. W_I' is the CM velocity of an I atom elastically scattered in a K/I encounter and measured with respect to the K···I CM. W_I'' is the post collision I velocity with respect to the K···I_2 CM.

The spectator model can be developed further by defining a "local" differential cross section, $\sigma(\Theta)$ for the elastic scattering of the projectile at one of the target atoms. The overall energy loss per second is then

$$\overline{\Delta E} = \mathcal{I} f E_i \int_0^{\pi} (1 - \cos\Theta)\, \sigma(\Theta) \sin\Theta \, d\Theta, \qquad (3)$$

where $\mathcal{I}$ is the incident flux and f is the mass factor in eq. (2). This result is exact within the frame-work of the spectator model and further averaging over the orientation of the target molecule does not alter the result since in this approximation both target atoms are regarded as independent. Departures from eq. (3) may occur in real systems due to (i) distant collisions in which both target atoms experience a similar perturbation and energy is thus transferred mainly to the centre of mass of the target, (ii) multiple collisions in which both I atoms are struck, (iii) anisotropy in $\sigma(\Theta)$, since a bonded atom is not spherically symmetric, and (iv) non-adiabatic effects. The importance of these effects may be judged by comparison of this model with the Monte Carlo results.

At the outset, it is clear that neither eq. (1) nor (2) can apply at small values of E_i where elastic scattering is found to predominate – the pure spectator model would predict some energy loss at any angle of deflection. These models must thus be tested on smaller impact parameter phenomena. It will be difficult to distinguish between the two energy loss equations (1) and (2) for the light/heavy mass combination because, as can be seen from the Newton diagram (fig. 9), the centre of mass of the K/I_2 system almost coincides with that of the K/I system so that $\chi \approx \Theta$. More precisely,

$$\cos\chi = (W_K \cos\Theta + s)/[W_K^2 - 3s^2 - 2sW_K(1+\cos\Theta)]^{1/2},$$

$$s = [M_K M_I/(M_K+M_I)(M_K+2M_I)]\, V_K. \qquad (4)$$

The spectator model, however, when used in conjunction with a known atom–atom potential, has no adjustable parameters and we can compare its predictions

against the whole range of Monte Carlo results to form a good estimate of its validity.

The simplest model of this type is one in which all the atoms are taken to be hard spheres. The differential cross section in (3) is then simply $\frac{1}{2}\pi r_c^2$ where r_c is the hard sphere diameter, and eq. (3) becomes:

$$\Delta E(b) = 2f(1 - b^2/r_c^2)E_i, \tag{5}$$

where b is the "local" impact parameter for the K/I encounter. An inspection of figs. 5 and 6 in particular shows that at the higher energies (17–87 eV), the system is apparently exhibiting hard sphere behaviour, of which the step-like $\sigma_d(b)$ and a sharp cut-off in $\Delta E(b)$ are characteristic.

There is, however, an important correction that must be included if the hard sphere model is to give any better than qualitative agreement. Fig. 6 shows that, contrary to eq. (5), $\Delta E(b = 0)$ varies in a less than linear fashion with E_i, especially at the highest energy. In order to account for this an energy dependent collision radius, $r_c(E)$ can be introduced which replaces the hard sphere value r_c in eqs. (3)–(5). If the model is to retain any physical significance, $r_c(E)$ must be similar to the locus of turning points on the actual surface for small impact parameters. The K–I model repulsion is exponential and for a head-on collision the turning point is given by

$$r_0 = \rho \ln(A/E), \tag{6}$$

where ρ and A are already given. Thus r_0 values range from 1.7 to 2.4 Å and give a high energy limiting cross section that is ~ 10% too small. A slightly expanded set of hard sphere radii (ranging from 2 Å to 2.75 Å) can be devised that accounts well for the magnitude of the dissociation cross section down to ~ 12 eV if a small eclipse factor is introduced (fig. 2) which allows for the orientation averaged overlap of one target atom by the other, treating each as a sphere.

The effect of long range forces becomes particularly clear in the deviations of σ_{diss} from the modified hard sphere values (fig. 2) below 12 eV and in the $\Delta E(b)$ plots at 8.7 eV and 4.3 eV where the hard sphere model underestimates ΔE by almost one half (fig. 6).

Discrepancies remain, however, between the Monte Carlo results and the energy dependent hard sphere model and in some cases become *more* marked at higher energies. This is particularly evident in the mean energy transferred to the relative motion of the I atom as a result of a dissociative collision, ΔE_{diss}. This quantity should be rather insensitive to the hard sphere model parameters and geometrical factors, such as the eclipse effect, largely cancel (to within 5%)

$$\Delta E_d = fE_i[1 - \tfrac{1}{2}(1 - E_d/fE_i)]. \tag{7}$$

Fig. 8 shows quite good agreement between the exact and the hard sphere results almost from threshold until 20 eV, but at 87 eV the model predicts 40% too much energy loss.

These differences between the Monte Carlo and the spectator model results can arise either from three body effects or the non step-like nature of real interatomic potentials. Three body effects in the hard sphere case reduce to a succession of two body collisions in which first one then the other target atom is struck. The number of such double collisions in a random sample of trajectories is small and decreases with increasing energy; furthermore, each such collision may either add or subtract energy from the internal motion of the I_2. As a consequence three body effects are not likely to be responsible for the series failure of the hard sphere model at high energies.

The over-estimation of the energy loss by the hard sphere model even when total cross sections can be reproduced by judicious scaling, arises from the fact that real differential cross sections fall off with increasing angle of deflection in contrast to the angle independent hard sphere cross section. The real angular dependence of $\sigma(\Theta)$ is clearly visible in fig. 4B where the very similar $\sigma_d(\chi)$ falls slowly to zero after rising fairly rapidly from threshold to a maximum. $\sigma_d(\Theta)$ can be used in (3) to replace $\sigma(\Theta)$ by making a simple polynomial fit to the rather noisy $\sigma_d(\chi)$ functions in fig. 4B and evaluating the energy transfer integral (3). Very good agreement with the Monte Carlo results is then obtained at 87 eV and 43 eV but with some divergence already visible at 17 eV (see fig. 8).

The last topic to be discussed is the angular dependence of the differential cross section for dissociation (fig. 4B) just beyond the angular threshold. At the highest energy, $\sigma_d(\chi)$ approaches the form predicted by the spectator model, with an abrupt

cut-off at some threshold angle corresponding to the transfer of sufficient energy to produce dissociation. As the relative energy decreases however the rise from this threshold becomes more gradual. The clue to this behaviour is the assumption that if sufficient energy for dissociation is supplied to one of the atoms, the molecule will subsequently fall apart. This assumption ignores the centrifugal barrier that is set up if the velocity imparted to the I atom initially struck has a component perpendicular to the I–I bond vector. The barrier is at a maximum for collisions in which the apse line for the local K/I encounter is perpendicular to the bond and is zero when the apse line lies along the bond. From the conservation of momentum within the excited target molecule, and a knowledge of the attractive branch of the I–I potential, the height of this barrier can be calculated for any orientation at impact. The threshold angles for dissociative scattering in the "end-on" (χ_{min}) and "broadside-on" (χ_{max}) configurations can be calculated and are included in fig. 4B. The maximum in the dissociative cross section should be reached at the angle of scattering for which the target can be dissociated in any orientation and is in good agreement with the Monte Carlo results.

5. Conclusions

In the energy range between 0.1 eV and 100 eV, the K/I_2 collision system shows the expected change from three body dynamics in which attractive forces play a predominant part to the high energy region in which the scattering is essentially a two body process dominated by the repulsive wall of the potential. Above about 20 eV the spectator model accounts well for the dissociative process.

From an experimental point of view, spectator-like behaviour can be established as the dominant mechanism for energy loss by first transforming differential time-of-flight measurements from LAB angles to the CM angle (Θ) defined with respect to *one* of the target halogen atoms rather than the whole molecule. If the simple $1-\cos\Theta$ dependence of the energy loss is then found to be substantially obeyed, an elastic cross section for K/I scattering can be usefully defined and measured at high energies.

At collision energies above 20 eV observations of the narrow angle elastic scattering provide a window through which the potential surface in the entrance valley can be explored without the difficulty of interpretation inherent in reactive scattering measurements.

References

[1] K.T. Gillen, A.M. Rulis and R.B. Bernstein, J. Chem. Phys. 54 (1971) 2831.
[2] J.L. Kinsey, M.T.P. Int. Rev. Sci., Vol. 9 (1972).
[3] J.P. Toennies, Physical Chemistry – An Advanced Treatise, Vol. 4, eds. H. Eyring, W. Jost and D. Henderson (Academic Press, New York, 1973).
[4] N. Blais, J. Chem. Phys. 49 (1968) 9.
[5] M. Godfrey and M. Karplus, J. Chem. Phys. 49 (1968) 3602.
[6] P.J. Kuntz, E.M. Nemeth and J.C. Polanyi, J. Chem. Phys. 50 (1969) 4607 and 4623.
[7] N. Blais, J. Chem. Phys. 51 (1969) 856.
[8] G.A.L. Delvigne and J. Los, Physica 59 (1972) 61.
[9] G.A.L. Delvigne and J. Los, Physica 67 (1973) 166.
[10] C.E. Young, R.J. Beuhler and S. Wexler, J. Chem. Phys. 61 (1974) 174.
[11] B.S. Duchart, M.A.D. Fluendy and K.P. Lawley, Chem. Phys. Letters 14 (1972) 129.
[12] V. Kempter, Th. Kneser and Ch. Schlier, J. Chem. Phys. 52 (1970) 5851.
[13] A. van der Meulen, A.M. Rulis and A.E. de Vries, Chem. Phys. 7 (1975) 1.
[14] A.P.M. Baede and J. Los, Physica 52 (1971) 422.
[15] A.P.M. Baede, Physica 59 (1972) 541.
[16] A.M.C. Moutinho, J.A. Aten and J. Los, Physica 53 (1971) 471.
[17] A.P.M. Baede, D.J. Auerbach and J. Los, Physica 64 (1973) 134.
[18] U. Havemann, L. Zulicke, E.E. Nikitin and A.A. Zembekov, Chem. Phys. Letters 25 (1974) 487.
[19] A. van der Meulen and A.E. de Vries, to be published.
[20] R. Grice and D.R. Herschbach, Mol. Phys. 27 (1974) 159.
[21] D.L. Bunker and N.C. Blais, J. Chem. Phys. 41 (1964) 2377.
[22] E.S. Rittner, J. Chem. Phys. 19 (1951) 1030.
[23] K.S. Pitzer, Advan. Chem. Phys. 2 (1954) 78.
[24] G. Herzberg, Spectra of Diatomic Molecules (Van Nostrand, Princeton, N.Y., 1950).
[25] J. Schottler and J.P. Toennies, Chem. Phys. 2 (1973) 137.

ATOMIC AND MOLECULAR BEAM COLLISION MEASUREMENTS USING AN ON-LINE COMPUTER

M.A.D. Fluendy, J.H. Kerr, J.M. McCall, & D. Munro
University of Edinburgh

(Presented by J.M. McCall)

1 Objectives and experimental hardware

Atomic and molecular collision processes are normally described in terms of interaction potentials between the colliding atoms together with coupling terms which induce transitions between the accessible quantum states of the colliding species. Except in very favourable situations, these potentials and coupling coefficients are not available from theory with any accuracy. Measurements of the elastic and inelastic differential scattering cross-sections can, however, be interpreted to yield interaction potential and coupling coefficient data for comparison with theory (Smith, 1969).

If the atomic states excited during the collision involve exchange of energy between the relative motion of the atoms and their internal modes, measurement of the velocity change produced by a collision is sufficient to specify the excitation process. Measurements of the inelastic differential cross-section at a specified initial relative kinetic energy thus requires the scattered atomic flux to be determined as a function of the velocity change and deflection angle produced by the atomic collision. Furthermore, if absolute differential cross-sections are to be measured, the incident flux of both species involved in the collision must be known.

Fig.1 shows a crossed atomic beam apparatus designed to make measurements of this type for collisions of alkali metal atoms with

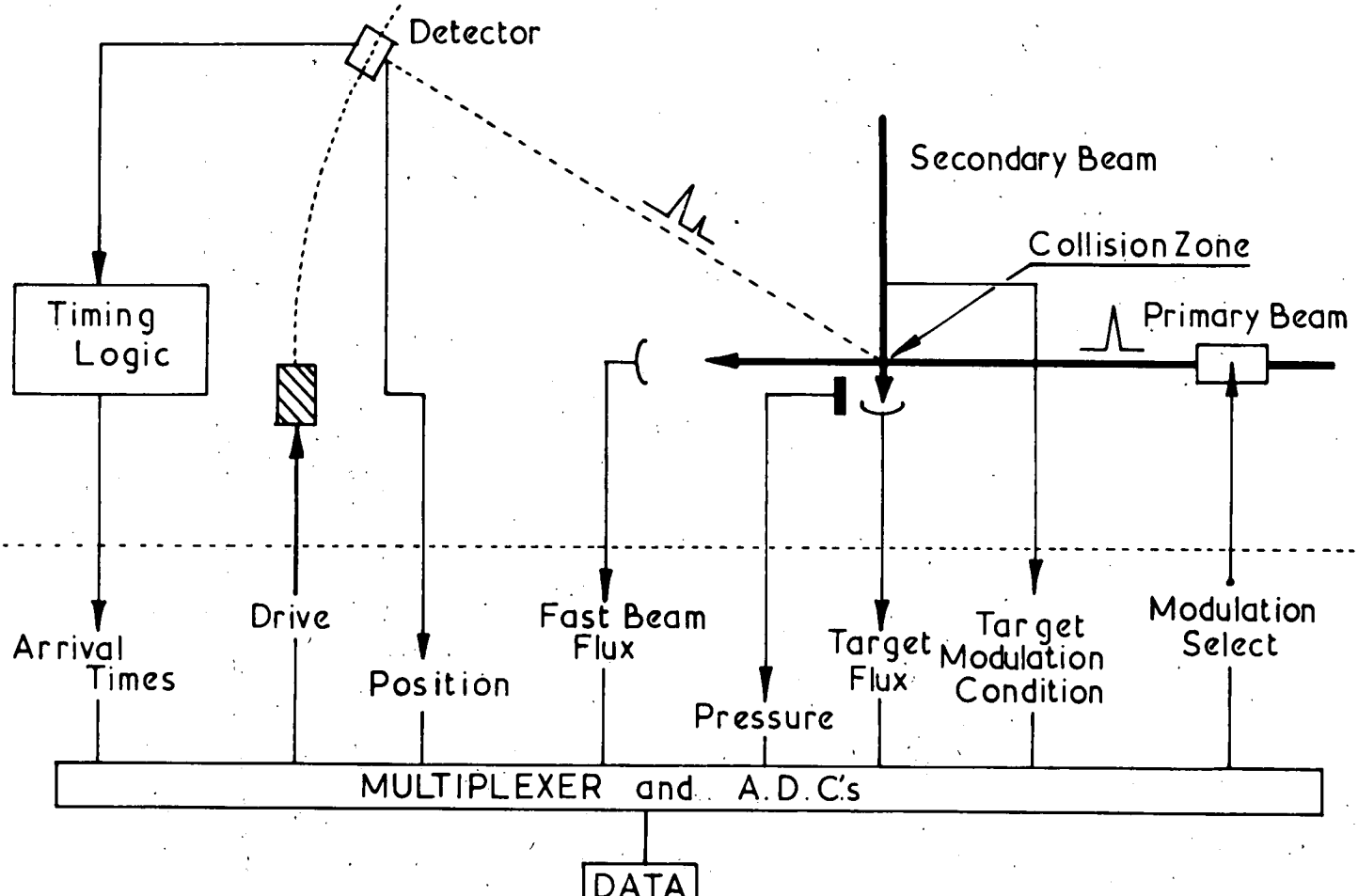

Fig.1 Schematic diagram of a crossed atomic beam experiment showing control and data ports.

various atomic and molecular targets. The main features are:

(i) There are two beam sources; the primary alkali metal beam is well-defined both in direction and in velocity and the target atoms form a secondary beam which intersects the primary beam orthogonally in a small collision zone.

(ii) A detector, sensitive to the alkali metal atoms, may be rotated precisely about the collision zone by a stepping motor. It provides a signal pulse whenever an alkali metal atom is incident in a small solid angle region about the detector position. The angular position of the detector relative to the primary beam is measured by a Moiré fringe device.

(iii) The primary beam is modulated so as to produce narrow pulses of atoms at the detector, 100-200 ns in duration, and in a regular sequence. Inelastic collisions which transfer energy from the relative motion of the atoms will result in atoms arriving with a delay relative to the unscattered species. This delay is recorded by arranging for each detected atom to stop the 50 MHz counts from a crystal clock into one of the 10-bit scalers in Fig.2. Since the primary beam modulation is synchronised with this same clock, the contents of the stopped scalers yield the flight time to a precision of 20 ns.

The secondary beam is modulated on and off at 47 Hz so that collisions between the primary and secondary beams may be distinguished from those occurring between the primary beam and the background gas in the apparatus. (Fluendy and Lawley, 1973).

(iv) Gauges to monitor the fluxes of the primary and secondary beams are provided so that observations of scattered flux at different angles and times may be compared. The experiment is carried out in a vacuum of 10^{-6}–10^{-7} torr.

Beam intensities are limited by space charge and similar considerations while the cross-sections of interest may be very small. Consequently, very long counting times may be required and the experiment has been designed to run continuously for periods of 100 hours.

The implications for the data capture and experimental control system are:

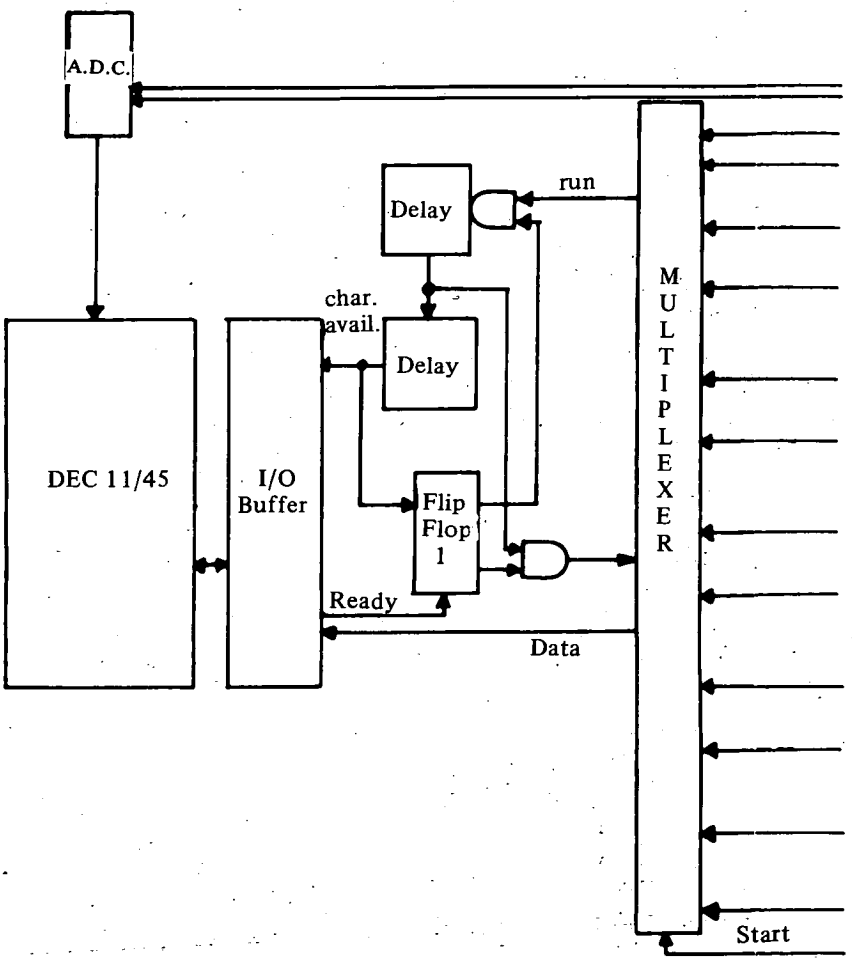

Fig.2 Data collection and control hardware.

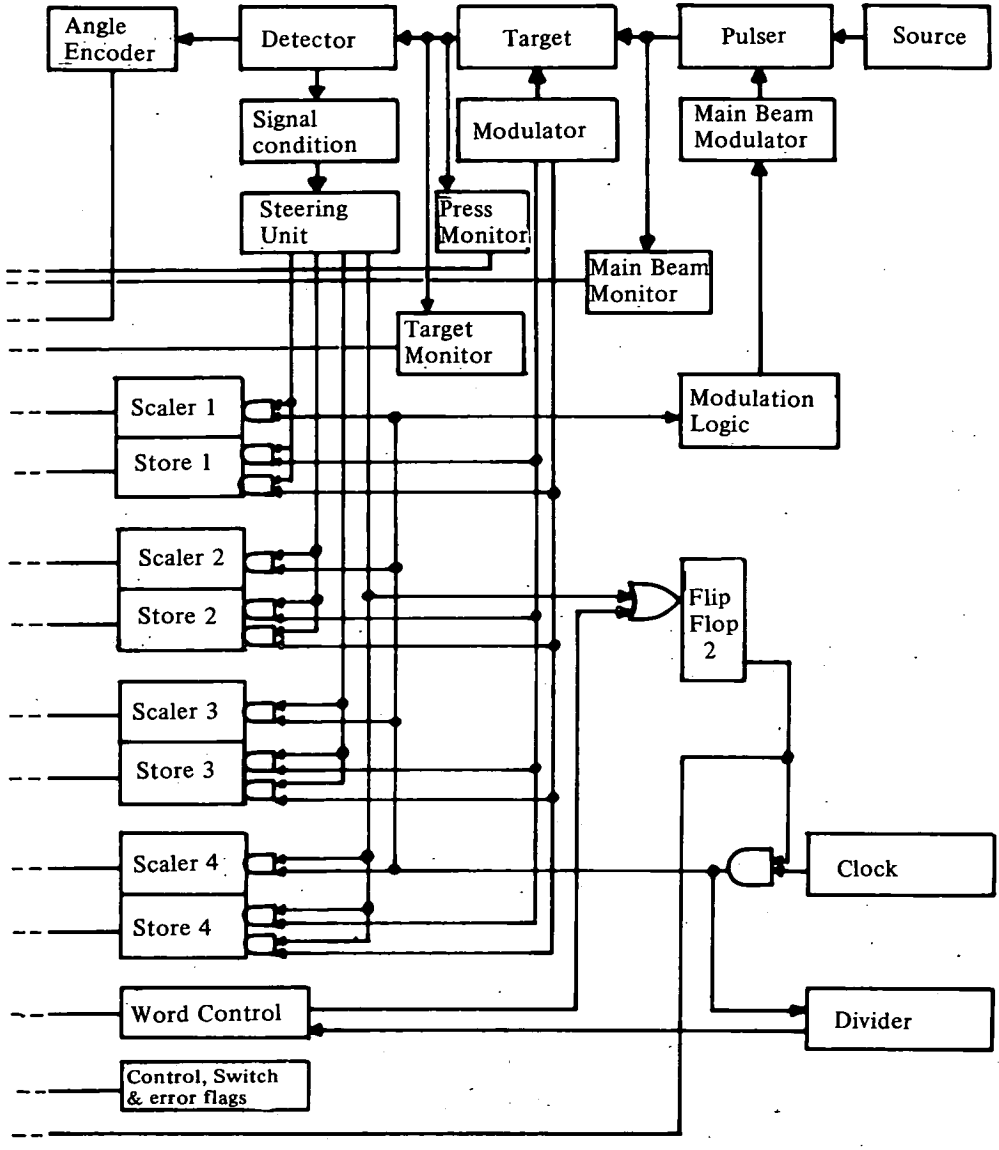
Angle Encoder
Detector
Target
Pulser
Source
Signal condition
Modulator
Main Beam Modulator
Steering Unit
Press Monitor
Main Beam Monitor
Target Monitor
Scaler 1
Store 1
Modulation Logic
Scaler 2
Store 2
Flip Flop 2
Scaler 3
Store 3
Scaler 4
Store 4
Clock
Word Control
Divider
Control, Switch & error flags

(i) Once the apparatus hardware has been optimised, the data rate is a function only of the size of cross-section under investigation. Data rates may therefore vary from 10^6 bytes s^{-1} downwards. A large volume of data is generated and some reduction in real time is essential.

(ii) The data is organisationally complex, the scattered atom flux being a function of arrival time, incident energy, primary beam flux, secondary beam flux, scattering angle, primary and secondary beam modulation phase, etc.

(iii) The apparatus must be held stable over a long period of time and a complex sequence of operations carried out.

(iv) It is necessary to provide some immediate analysis of the data so that the experiment may be operated optimally.

These considerations point to the use of a real time computer for data capture, preliminary analysis and control.

2 Implementation

Fig.1 shows the control and data ports. The information flow may be summarised as follows:

(i) **Control**
The primary beam modulation and the detector position may be altered by software instructions.

(ii) **Data**
Information from the apparatus falls into three overlapping categories:

(a) information on scattering processes, i.e. arrival times and secondary beam modulation condition;

(b) data to allow construction of differential cross-sections at a later stage, i.e. detector position and beam fluxes;

(c) data to allow assessment of the quality of the experiment in real time, i.e. beam fluxes, etc.

Fig.2 shows the data collection and control hardware in detail.

Since the computer is a time-shared system, the guaranteed interrupt service time is significantly longer than that of a dedicated system. For this reason some data buffering is provided in the interface. This is particularly necessary at small scattering angles when differential cross-sections become large and high data rates occur. At such rates the prime requirement is not to capture

all the arrivals but to ensure that a representative sample is recorded. If the arrival rate exceeds the service rate, a bias towards arrivals early in the modulation sequence is produced. To avoid this, it is necessary to capture all the arrivals associated with a specific modulation pulse of the primary beam; it is not, however, necessary to do so for every primary beam pulse. In other words, short periods of short service time with sufficient capacity to record all the atoms scattered from a single modulation pulse are required. The average service rate, however, can be quite low since it limits only the final rate of data collection. This is not an important constraint at high arrival rates since the observation times required to obtain the desired precision are in any case very short. In this system the average data transfer rate is 2000 bytes s^{-1} but can be considerably lower if many other users are operating. Buffering four arrivals is sufficient to cope with scattered fluxes up to 8×10^5 s^{-1}.

At the other end of the dynamic range, when the count rate is low, interrupts are generated at fixed time intervals by the modulation word counter to ensure regular sampling of the other experimental variables.

3 Software

Fig.3 illustrates the software organisation. The design principles followed in its construction may be summarised as follows:

(i) Data once validated are protected against accidental loss or corruption.

(ii) The system is robust and, as far as possible, self-checking so that operator or hardware errors are detected and damage to hardware or corruption of data are prevented.

(iii) Detected errors (requiring repositioning of the detector, the rejection of corrupt data, etc.) are either rectified under program control or reported to the operator and data collection is suspended.

(iv) Operator intervention is kept to a minimum and is required only in the initial setting up and in the event of a major failure. When the operator has to be involved, the programs are designed to be highly conversational and self-instructive.

(v) The system is flexible so that minor failures in equipment can be circumvented.

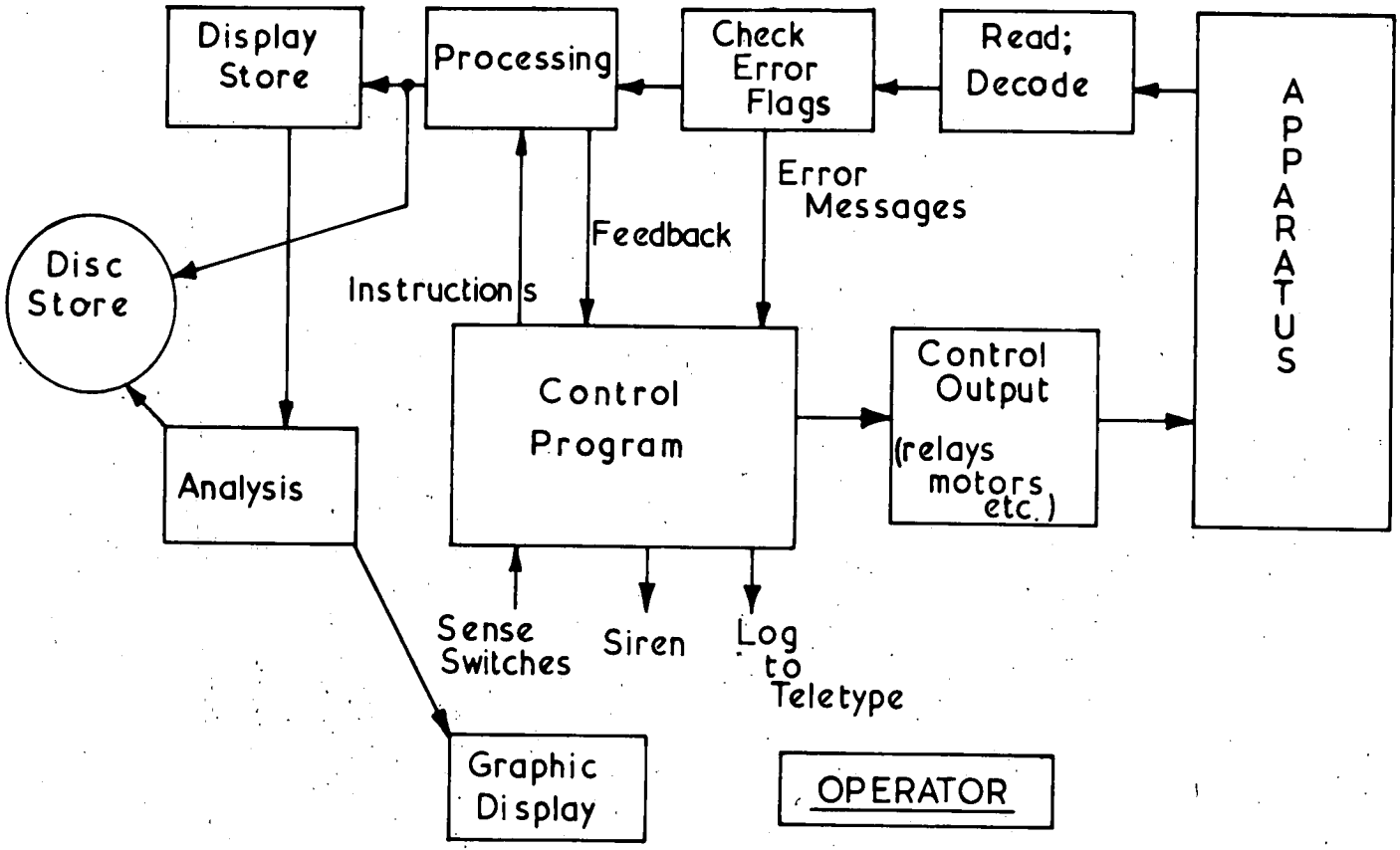

Fig.3 Organisation of the experimenter's software.

(vi) Control functions are initially validated by manually stepping through the instructions using program listings.

After initialisation by the experimenter the system collects data at a pseudo-random series of observation angles in a fully automatic fashion. Information is printed on the console at regular intervals or on demand so that the experimenter may assess the quality and progress of the experiment. If there are serious errors in the data or if the performance of the apparatus drifts outside specified limits, data collection is suspended and the experimenter alerted.

The experimenter may interact with the system in two ways, either via sense switches to override or alter the data collection procedures, or via the teletype/graphics terminal to examine and partially analyse the collected data. In the latter case data collection proceeds normally.

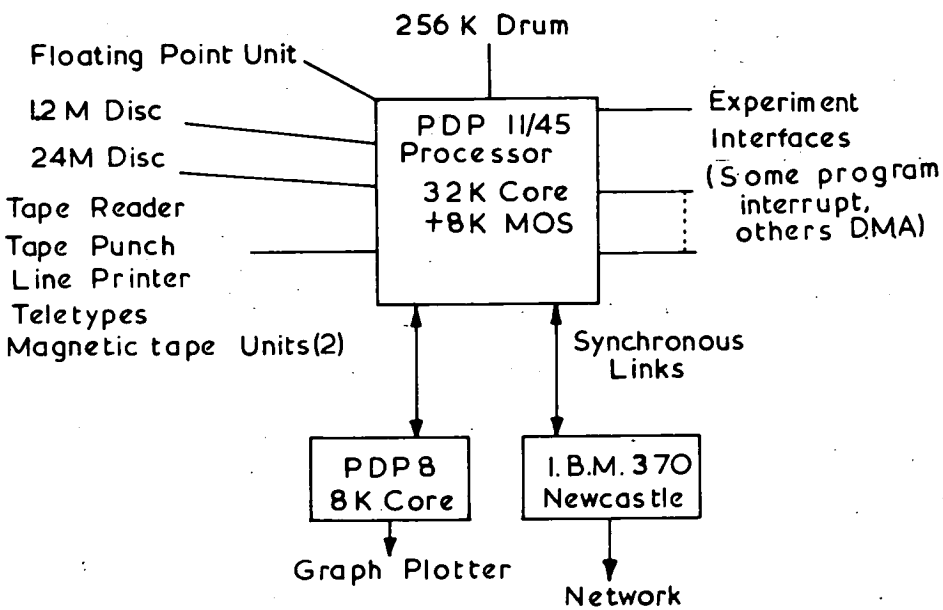

Fig.4 Schematic diagram of the on-line computer hardware.

4 Computer hardware and software

The present hardware configuration is shown in Fig.4. The heart of the system is a PDP11/45 central processor with a number of peripheral devices. It acts as a shared, real-time data collection system rather than as a batch processing system or a remote job entry terminal. For large-scale analysis, data may be transmitted via the synchronous link either to the IBM 370 at Newcastle or to the ICL System 4 in the Edinburgh Regional Computing Centre (ERCC).

The system software on the PDP 11/45 was written by the ERCC (Hayes, 1975). Each user program has a separate virtual address space maintained by the memory management unit. The supervisor dynamically allocates the space required and will swap programs using the drum if necessary. A clock is used to time-slice running programs, all of which have the same priority. Input/output is performed using 'EMT' instructions which are interpreted by the supervisor; where necessary a buffer is provided between the user program and the device.

In addition, a number of general utility programs are available. These include

(a) Text editor;
(b) PAL 11R assembler;
(c) File manipulation program;
(d) Archiving program to copy files to magnetic tape;
(e) 'BASIC' interpreter.

Large programs are usually written in 'IMP', a high-level language of the 'ALGOL' type, much used in Edinburgh. A cross-compiler and assembler have been written by the ERCC (Yarwood, 1975). A cross-loader is not available, so the binary code is punched on paper tape and loaded into the PDP 11/45 at a later stage. Small test programs may conveniently be written in assembler language and assembled on the PDP 11/45.

5 Summary and future developments

The concept of the multi-access system has been found to be sound both in satisfying the requirements of the users and from an economic point of view since users can pool their resources.

As far as the experimental system is concerned, future develop-

ments will be concentrated on providing more computer control of apparatus functions. This will be implemented using our own interface hardware rather than commercially available equipment such as CAMAC. The advantages of the latter, including versatility and saving in development, are severely outweighed by the cost element especially in a small installation such as ours.

Much work remains to be done on the software especially on the on-line analysis of raw data.

References

Fluendy, M.A.D., Lawley, K.P., *Chemical Applications of Molecular Beam Scattering*, 1973, Chapman and Hall, London.

Hayes, S.T., 1975, private communication.

Smith, K. in *Scattering Theory*, ed. A.O. Barut, 1969, Gordon and Breach, New York.

Yarwood, K., 1975, private communication.

Discussion

Pyle (York): Can you estimate the cost of designing, constructing and commissioning the interface between your apparatus and the PDP 11?

McCall: We have one electronics engineer who has spent one year designing, testing and building the coupler. Research students have contributed as well but they cost nothing. The electronics components cost about £500. The total cost was one year's salary plus £500.

Pyle: Do you know how much it would have cost to do it in CAMAC?

McCall: I do not know as the system was designed before I came so it was not my decision. As far as I can see, CAMAC would have cost us quite a bit more.

Rosner (Rutherford): Why did you not use the manufacturer's operating system?

McCall: That was not my decision either but the decision of the Physics Department who had the services of the computing centre consultant free of charge. He was able to do this sort of thing in his spare time so we do not have to buy DEC software which is quite expensive.

Rosner: Why did you not use an existing high-level language for the PDP 11, such as PL 11?

McCall: There are moves to start using it. The reason for using an IMP compiler at the moment is that the language is supported by the computer centre.

24

The Scattering of $Hg(6^3P_2)$ by CO, N_2 and CO_2

BY JOHN COSTELLO, MALCOLM A. D. FLUENDY AND KENNETH P. LAWLEY*

Department of Chemistry, University of Edinburgh,
West Mains Road, Edinburgh EH9 3JJ

Reprinted from

FARADAY DISCUSSIONS
OF
THE CHEMICAL SOCIETY

No. 62
POTENTIAL ENERGY SURFACES

1977

The Scattering of $Hg(6^3P_2)$ by CO, N_2 and CO_2

By John Costello, Malcolm A. D. Fluendy and Kenneth P. Lawley*

Department of Chemistry, University of Edinburgh,
West Mains Road, Edinburgh EH9 3JJ

Received 3rd May, 1976

The differential scattering pattern of a thermal beam of $Hg(6^3P_2)$ from CO, N_2 and CO_2 has been measured from 10° to 160° (CM). Pronounced and regular oscillations are observed over the whole angular range in each system. However, the envelope is not that of purely elastic scattering, the $\chi^{4/3} \sin \chi I(\chi)$ plot showing an almost monotonic decrease over the whole angular range. The spacing of the oscillations indicates a deflection function with an unusually broad bowl, interfering branches being 3 Å apart. Two models are put forward; both include partial adsorption of the wave front and the operation of two potentials. Detailed fitting of one model shows that a highly attractive long range potential (well depth $\approx 10\ kT$) is needed, but although the interference structure is well reproduced, the necessary range of the optical potential is not consistent with known quenching cross sections. A second model is given in outline and involves an avoided crossing around 8 Å producing a rapid steepening of the potential gradient at that point. Quenching begins at impact parameters ~7 Å thus indicating a very large quenching cross section unless a rather sharply peaked adsorption function is postulated with a width of only ~1 Å to give the known values of σ_{qu}.

The scattering of many ground electronic state species has now been thoroughly explored over a wide energy range by crossed beam techniques. The scattering of low lying excited electronic species remains largely unexplored and is, in a sense, complementary to ground state scattering in the 10–100 eV range in that there electronic excitation is frequently observed in the products. By starting with an excited state (of necessity a metastable one for beam work), curve crossings and diabatic state mixing become accessible at thermal kinetic energies, and may be expected to lead to marked inelastic scattering. So far, excited state phenomena have largely been studied through kinetic spectroscopic observation of quenching or collision induced fluorescence[1,2] though the more energetic metastable species (those of the inert gases) have been used in elastic[3] and Penning ionization studies.[4] Only relative quenching cross sections for $Hg(^3P_{2\rightarrow 1})$ have been measured in a beam experiment.[5]

$Hg(6^3P_2)$ is an attractive candidate for beam studies in that the nearest electronic state (the $^3P_1$) is only 0.57 eV away and provides a route for quenching. The $J = 2$ state is not sufficiently energetic (5.4 eV above the ground state) to ionize most small molecules. The following studies of the thermal elastic scattering (or, rather, scattering without change of electronic state) of Hg^* by CO, N_2 and CO_2 were undertaken to see if more light could be cast on the known quenching processes in these systems by examining the perturbation of the elastic scattering differential cross section.

EXPERIMENTAL

The crossed beam apparatus has been described before.[6] $Hg^*(^3P_2$ with less than 15% of the $^3P_0$ state[7]) is generated by electron bombardment (at 10 eV) of an effusive beam of Hg and crosses a thermal effusive beam of the target gas. The angular resolution is 0.5° LAB.

The detector, a fresh K surface, responds to the $^3P_2$ state, to the $^3P_0$ state with probably lower efficiency but not to the ground state. The $^3P_1$ state decays in flight between scattering centre and detector (transit time 5×10^{-3} s) and so is not detected. Typical main beam signals were 10^5 c.p.s. and counting techniques were used.

The CM scattering patterns, averaged over the stated number of scans, are reproduced as the lowest curve in fig. 1, 2 and 3. The factor $\chi^{4/3} \sin \chi$ multiplying the scattered intensity conveniently places all the observations within the compass of a linear scale and renders the envelope of scattering from an R^{-6} potential horizontal. The location of the major maxima and minima is reproduced in independent sets of four or five scans, though the peak-to-valley amplitude ratio varies. The envelope is unchanged by selecting different scans for averaging. The sudden fall-off in intensity at less than 16° is due to imperfect unfolding of the main beam coupled with the attenuating effect of the $\chi^{4/3} \sin \chi$ term at small angles. In the case of CO, closer examination of the data shows a barely visible high frequency structure in the 16–20° CM region with a period $\approx 1.25°$.

INTERPRETATION AND FITTING

The three scattering patterns are broadly similar (CO and N_2 being very similar) in the following respects: (i) the envelope is basically monotonically decreasing across the whole angular range, though in each case there is a maximum around 90–100° (arrowed as χ_2) and there is a pronounced perturbation of the envelope at 20° in the case of CO and N_2 and at $\approx 80°$ for CO_2, labelled as χ_1, (ii) oscillatory structure with an only slowly increasing period extends across the whole angular range, but the amplitude is not regular and is clearly perturbed by another frequency.

The envelope must be compared with that expected from purely elastic scattering. For a potential with an R^{-s} attractive branch a horizontal ($s = 6$) or slowly rising ($s < 6$) envelope with increasing χ is found. The absence of a well defined rainbow (the features at χ_2 do not fall away quickly enough on the dark side to be typical rainbows) may either mean orbiting, the superposition of scattering from several rather different potentials with an overlapping rainbow structure or extensive adsorption of the incident wave front beginning at impact parameters somewhat greater than the rainbow value.

The fact that interference structure is visible at all makes it unlikely that several rather different potentials are operating, for then the supernumerary spacing would be confused by the multiplicity of interfering branches. Although orbiting cannot be ruled out, it would upset the regularity of the supernumerary spacing by introducing further interfering branches (albeit of small amplitude). The same considerations apply to rainbow angles greater than 180°.

The near regularity of the interference structure across such a wide angular range (especially noticeable in the case of N_2) is unusual because supernumerary rainbow spacing (or inter-branch interference in general when both branches correspond to deflections in the same sense) usually decrease markedly with falling angle of observation as the two branches diverge in impact parameter. The present structure seems to indicate a dominant deflection function with nearly parallel sides, *i.e.*, that the rainbow angle is very large. The fact that the period of oscillation of $\sigma(\chi)$ nevertheless slowly increases with angle indicates that we are not observing interference structure arising between the positive and negative branches of a deflection function.

Putting the remaining experimental observations and the above deductions together, we arrive at the simplest model (I) for a trial fitting:

(i) The scattering is predominantly from a single deep potential that gives rise to a rainbow $\gtrsim 180°$.

(ii) The dominant potential must lead to a deflection function in which the separation of the two attractive branches is ≈ 3 Å at small angles (from $\Delta\chi = 2\pi/k\Delta b$).

(iii) Scattering from a second, shallower potential is needed to account for the maxima in the envelopes of the CO and N_2 date around χ_2 and the change of gradient of the CO_2 scattering in this region. These rainbow positions serve to fix the well depths of the shallow potentials.

(iv) Adsorption sets in early on both surfaces and is responsible for the falling envelope of $\sigma(\chi)$.

(v) The very high frequency structure with poorly resolved periodicity of $\sim 1.25°$ is interpreted as glory oscillations (interference between the positive and negative branches of the deflection function around $\chi = 0°$) and serves to assign the impact parameter b_0 for the inner zero of the deflection function at 5.3 Å in all cases. In fact, there is not too much latitude in this value if a sensible length parameter (position of the inner zero, σ) is to be obtained for the potential especially when very highly attractive potentials are operating.

With two potentials the possibility of mutual interference arises. Two different fits were obtained, with and without inter-state interference. Such structure, being predominantly between the outer attractive branches of two deflection functions, is inevitably of much lower angular frequency than that originating across a single deflection function unless the two deflection functions are considerably displaced from each other—in this case by ~ 3 Å. In the present model the dominant source of interference structure is between the two negative branches of the deep deflection function; inter-state interference produces only a small change in the scattering pattern, but agreement with experiment is marginally improved.

In order to fit the scattering pattern, a flexible deflection function divided into 7 sections was employed. In each section a simple functional form was adopted subject only to the constraint of a smooth join to the neighbouring sections. In order to complete the partial wave summation, the deflection function was smoothly joined to a tail resulting from the following $C^{(6)}$ values; Hg*/CO, 0.83×10^{-77} J m^6; Hg*/N_2 0.77×10^{-77} J m^6 and Hg*/CO_2, 1.12×10^{-77} J m^6. It was found in all three systems that an R^{-6} potential could not be used for impact parameters less than ~ 10 Å since it gave too slowly varying a deflection function for $\chi > 15°$, but $C^{(6)}$ is not well determined by the present experiments.

The best fits are shown as the upper curves in fig. 1, 2 and 3, the associated deflection functions in fig. 4, 5 and 6. The potentials derived by Firsov inversion of these deflection functions are plotted in fig. 7, 8 and 9.

DISCUSSION

The overall fits are good. Both the dominant angular structure and the envelope are well reproduced, with only isolated features such as the dips in $I(\chi)$ at χ_1 unaccounted for. However, this agreement is achieved only with the aid of a pair of unusually long range potentials and an equally long range adsorption function.

In fig. 7 the Hg*/CO potential is contrasted with a Lennard-Jones potential with the same well depth and R_m value. The much greater width of the potential bowl is apparent. The range of the outer branch of $V(R)$ comes directly from the range of the outer branch of $\chi(l)$ and this, in turn, comes inescapably from adding the glory l_0 value to the width Δl across the bowl dictated by the dominant interference structure. Thus, at $\chi = 40°$ a Δl value of 90–100 is required, giving an impact parameter for this deflection of ~ 7 Å.

The adsorption function $P(b)$ has to be similarly long range, rising to 0.9 at 9–10 Å,

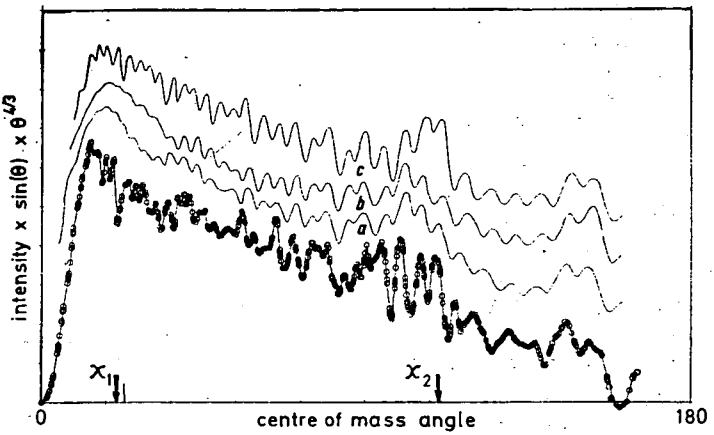

FIG. 1.—Observed angular scattering plot for Hg*/CO (lowest trace), velocity = 680 m s^{-1}, number of scans = 9. Calculated curves (*a*) and (*b*) differ only in the upper state deflection function while (*c*) incorporates interference between upper and lower states (see fig. 4). A displacement of the upper state clearly has little effect on the calculated scattering pattern.

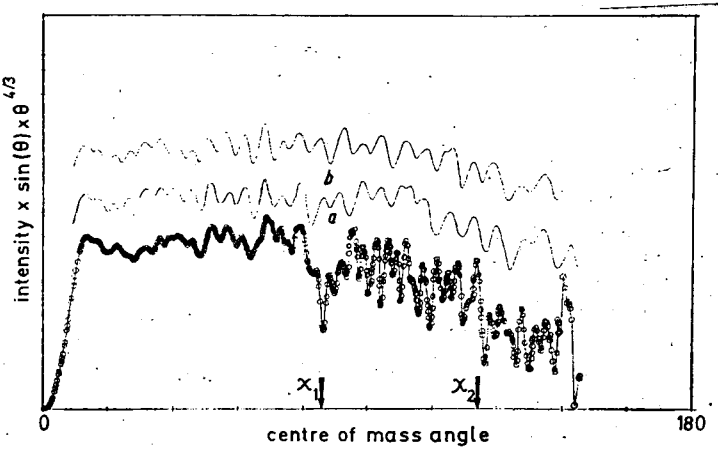

FIG. 2.—Scattering in the Hg*/N_2 system. Experimental, lowest trace velocity = 614 m s^{-1}, number of scans = 4. (*a*) is calculated from the sum of scattering from a deep and shallow potential (see fig. 5), (*b*) includes interference between them.

so that the scattering down to ~20° is affected. The behaviour of $P(b)$ for $b < b_0$ is not really probed by the present experiments. The maximum adsorption cross section implied by the above adsorption function is ≈350 Å^2 and the minimum 270 Å^2 in the case of N_2, where the two possible shapes of $P(b)$ are sketched in fig. 5. Implied quenching cross sections are slightly larger in the other two systems. Other quenching and depolarization cross section measurements on Hg($^3P_2$) are few and may be summarized by saying that with N_2 as partner the total quenching cross section (*i.e.*, to all possible final states) is [8,9,5] 11–19 Å^2; with CO_2 as partner the cross section for $^3P_2 \rightarrow {}^3P_1$ is ≈0.4 Å^2 and with CO as partner the cross section for the $J = 2 \rightarrow 1$ transition is similar to that with N_2. The depolarization cross sections are all much larger[8] (up to ~600 Å^2) but they seem to be due to a long range angle dependent term in the potential, probably a quadrupole-quadrupole term not connected with electronic state quenching.

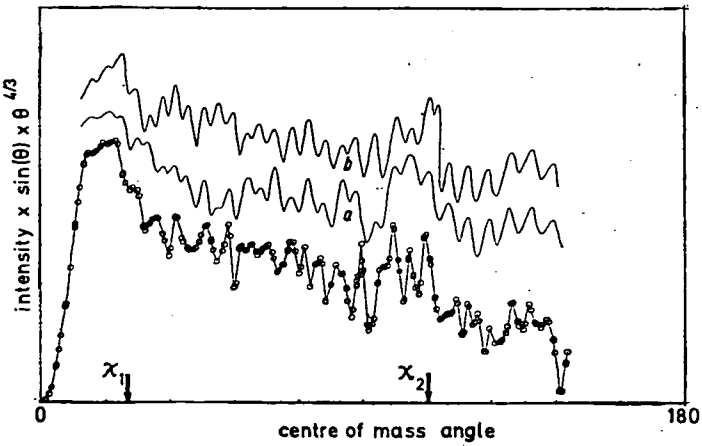

FIG. 3.—Scattering in the Hg^*/CO_2 system. Experimental, lowest trace velocity = 466 m s^{-1}, number of scans = 6. (*a*) Is calculated from the sum of scattering from a deep and shallow potential (see fig. 6), (*b*) includes interference between them.

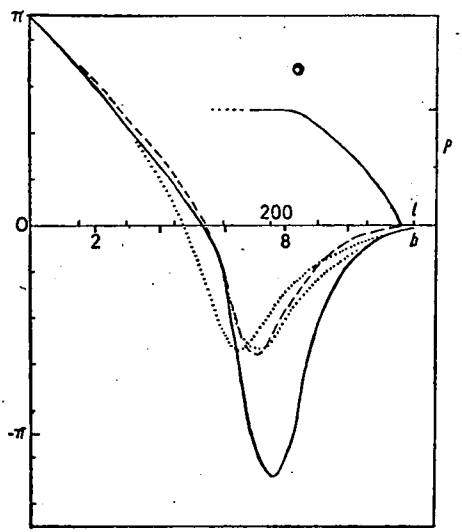

FIG. 4.—Deflection and adsorption functions for fig. 1 (Hg^*/CO). The two functions ··· give rise to the plots (*a*) and (*b*) in fig. 1, – – – to plot (*c*), both taken in connection with the lower state ——; *b*-scale in Å.

An observed quenching cross section of ~20 Å^2 implies a maximum impact parameter for quenching rather less than 3 Å. This range of attentuation function would, however, produce no detectable effect on the elastic scattering in the angular range of the present experiments unless the intermolecular potential were of rather short range. However, the interference structure points to an unusually long range potential.

In interpreting an elastic scattering envelope, there is a direct relationship between $V(R)$ and the adsorption function necessary for a fit. Classically, the differential cross section is proportional to $|d\chi/db|^{-1}P(b)$ and without an independent knowledge of $P(b)$ one cannot unambiguously separate the two terms. In the present case, if a

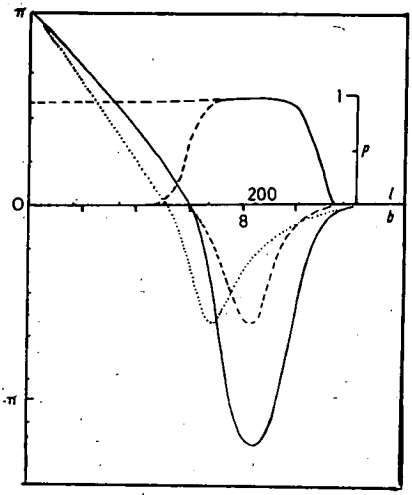

FIG. 5.—Deflection and adsorption functions for fig. 2 (Hg^*/N_2). The function ··· gives rise to the best fit including interference, – – – to the best fit without interference with the lower state ——. Two possible continuations of $P(b)$ are shown leading, respectively, to the maximum and minimum quenching cross sections compatible with the postulated deflection function.

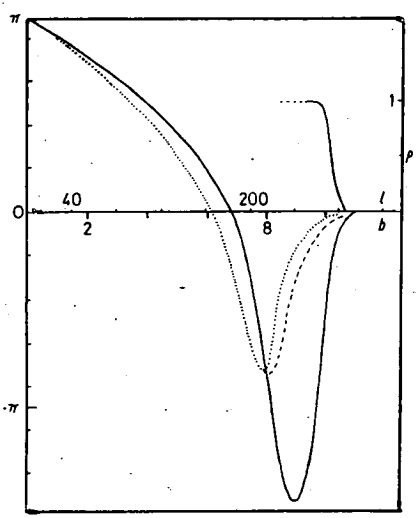

FIG. 6.—Deflection and adsorption functions for fig. 3 (Hg^*/CO_2). The ··· function gives the best fit without interference with the lower state ——, – – – optimises the fit with interference.

less steeply rising $P(b)$ is required, a more steeply falling deflection function must be employed. In order to preserve the periodicity of the observed interference structure the inner negative branch of the deflection function must be softened as the outer branch is hardened.

A rapidly varying potential at 8 Å (close to the smallest angle of observation) suggests an avoided crossing in which the diabatic Hg($^3P_2$) — AB($^1\Sigma$) pair state is depressed by interaction with another close lying state. A rather sudden change in gradient of the potential would produce a dip in $\sigma(\chi)$ and tentatively we assign the perturbations at χ_1 in each of the systems to this cause.

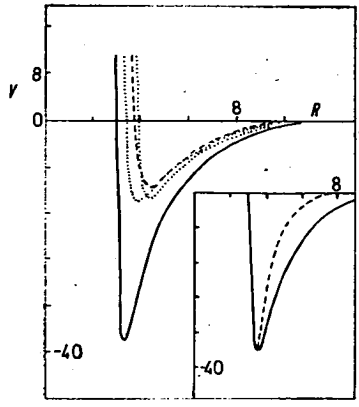

FIG. 7.—Potentials for Hg*/CO. The two upper state potentials ··· and --- are derived from the corresponding deflection functions in fig. 4. Inset is the Lennard Jones function having the same ε and R_m values; R scale in Å.

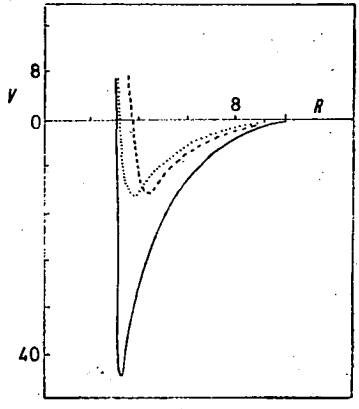

FIG. 8.—Potentials for Hg^*/N_2. The upper state potentials ··· and --- are derived from the corresponding deflection functions in fig. 6.

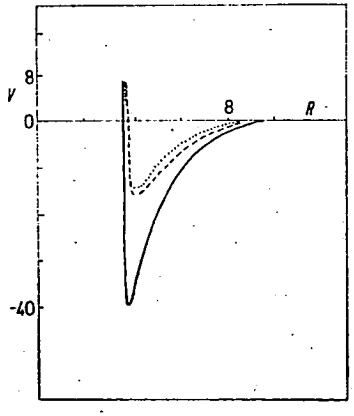

FIG. 9.—Potentials for Hg^*/CO_2. The upper state potentials ··· and --- are derived from the corresponding deflection functions in fig. 7.

Trying to accommodate the quenching data within the limits set by the scattering results, we construct model II:

(i) The small angle scattering ($\chi < \chi_1$) is from a single potential identified with the shallow state of model I.

(ii) This state is perturbed by a second state at a separation $R_c \approx 8$—8.5 Å. The crossing is sufficiently avoided for the motion to be almost adiabatic and most of the trajectories follow the lower surface. Nevertheless, sufficient amplitude (~10%) is found in the upper state for the shallow rainbow at χ_2 to be observed, though with low amplitude. At some impact parameter less than b_c, adsorption ensues on the lower surface and reaches 90% by the time the forward glory on the lower surface is reached.

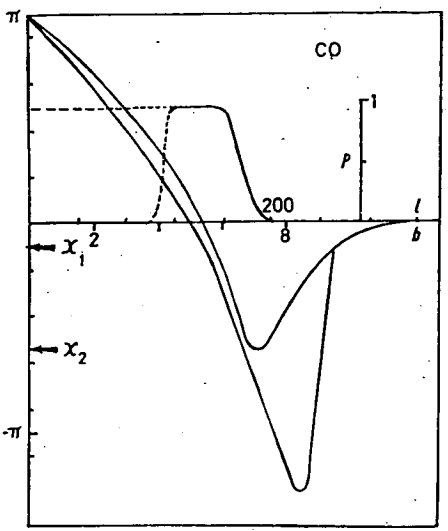

FIG. 10.—The type of deflection functions needed to minimise the opacity function. The upper state $\chi(b)$ is taken unchanged from fig. 4. The lower state function is sufficiently steep to produce the observed envelope of $\sigma(\chi)$. Two possible extrapolations of $P(b)$ are shown, the lower one leading to $\sigma_{qu} \sim 30$ Å^2.

(iii) The steepness of the attractive branch of the lower surface is at least three times greater than in model I in order to permit a much reduced $P(b)$ function at large b. The broad features of the deflection function and $P(b)$ function indicated by this model are given in fig. 10. The softening of the inner attractive branch is apparent, though it must be remembered that phase shifts in the presence of an optical potential do contain a contribution from the imaginary part of the potential and it is by no means clear that the ordinary semi-classical analysis holds. The inner branch to the potential must thus be regarded as conjectural. Even with an almost vertical outer branch to $\chi(b)$ adsorption must set in rapidly at $b \approx b_r$ (the rainbow value) and unless the $P(b)$ function is restricted to a band of b values between 5 and 6 Å the implied value of the quenching cross section is still ≈150 Å in each system.

The configuration interaction responsible for the perturbation of the outer branch of the potential energy function is still a matter of conjecture. A steeply plunging ionic state (Hg^+AB^- seems the more likely charge distribution[10,11] in view of the high I.P. of the molecular partners) has been postulated in the quenching of $Hg(^3P_2)$ by Na, but none of the present molecular partners has a positive electron affinity[13]

and a crossing of the $^3P_2$ state at $\approx$8 Å hardly seems feasible. More likely as the source of the perturbation is the interaction of the $Hg(^3P) - AB(^1\Sigma)$ pair state with the state dissociating to $Hg(^1S_0) - AB(^{1,3}\Pi_g)$. All three molecular partners have excited states close to 6 eV in which the $1\pi_g$ orbital is occupied and this level is nearly resonant with the Hg $^3P_2$ level at 5.4 eV. Although the overlap of the relevant orbitals would be small at 8 Å (neither the $6p$ nor 1π orbitals are grossly different from highest occupied orbitals in the ground electronic states)[13] the interaction energy need only be lowered by 4×10^{-14} erg from the normal dispersion energy at this separation to give the observed potential.

CONCLUSIONS

The thermal scattering of $Hg(^3P_2)$ from CO, N_2 and CO_2 exhibits a fairly simple interference structure that persists out to the largest angle of observation, nearly 180° (CM). Each system also shows evidence of quenching or an attenuation of the elastic scattering compared with that expected from a normal R^{-6} potential which begins at quite small angles of scattering. The very fact that structure is observed at all points to the conclusion that either the three molecular states evolving from the separated species ($\Omega = 0^-$, 1 and 2 in the linear configuration) have very similar potentials or that selective quenching on some branches simplifies the scattering pattern.

The spacing of the interference oscillations leads almost inescapably to a deflection function and hence to a potential that is very broad compared with the Lennard-Jones form. The simplest detailed model that fits most of the scattering data is a two state one correlating with degenerate levels at infinite separation. Adsorption is needed on both surfaces from ~10 Å inwards. Suitably broad potentials give a good fit to the observed angular structure which is interpreted as supernumerary bows in a deep well. The model, however, leads to unacceptably large values of the quenching cross section (~300 Å^2) and a second model is therefore proposed in which the outer branch of the deflection function is considerably steepened at separations $\approx$8–8.5 Å to account for some of the fall-off of the elastic scattering with increasing angle. A second, shallow potential is still needed to account for some of the features of the scattering. Even with an outer branch of almost infinite gradient [vanishing contribution to $\sigma(\chi)$], an adsorption function has to be applied to the inner attractive branch which now becomes the dominant one. Quenching cross sections $\approx$150 Å^2 would thus follow unless the adorption function was rather sharply peaked around 6 Å.

[1] *The Excited State in Chemical Physics*, ed. J. W. McGowan, *Adv. Chem. Phys.* (Wiley, New York, 1975), vol. 28.
[2] M. Bourene, O. Dutuit and J. Le Calve, *J. Chem. Phys.*, 1975, **63**, 1668.
[3] H. Haberland, C. H. Chen and Y. T. Lee, *Atom Physics*, ed. S. J. Smith and G. K. Walters (Plenum, New York, 1973), vol. 3.
[4] D. A. Micha, S. Y. Tang and E. E. Muschlitz, *Chem. Phys. Letters*, 1971, **8**, 587.
[5] F. J. Van Itallie, L. J. Doemeny and R. M. Martin, *J. Chem. Phys.*, 1972, **56**, 3689.
[6] T. A. Davidson, M. A. D. Fluendy and K. P. Lawley, *Faraday Disc. Chem. Soc.*, 1973, **55**, 158.
[7] H. F. Krause, S. Datz and S. G. Johnson, *J. Chem. Phys.*, 1973, **58**, 367.
[8] M. Baumann, E. Jacobson and W. Koch, *Z. Naturforsch.*, 1974, **29a**, 661.
[9] H. F. Krause, S. G. Johnson, S. Datz and F. K. Schmidt-Bleek, *Chem. Phys. Letters*, 1975, **31**, 577.
[10] E. R. Fisher and G. K. Smith, *Appl. Optics*, 1971, **10**, 1803.
[11] L. C.-H. Loh, C. M. Sholeen, R. R. Herm and D. D. Parrish, *J. Chem. Phys.*, 1975, **63**, 1980.
[12] M. Krauss and D. Neumann, *Chem. Phys. Letters*, 1972, **14**, 26.
[13] M. Krauss and F. H. Mies, *Phys. Rev.*, 1970, *A1*, 1592.

J. Phys. B: Atom. Molec. Phys., Vol. 10, No. 8, 1977. Printed in Great Britain. © 1977

25

Elastic scattering of slow electronically excited mercury atoms from neon and alkali-metal atoms: the interatomic potentials

J Costello, T A Davidson, M A D Fluendy and K P Lawley
Department of Chemistry, University of Edinburgh, West Mains Road, Edinburgh EH9 3JJ, Scotland

Received 6 October 1976, in final form 8 December 1976

Abstract. A modulated crossed-beam technique has been used to study the thermal-energy elastic scattering of electronically excited mercury in the 6^3P_2 state from Ne, Na, K and Rb. Relative differential elastic cross sections have been measured and interpreted to yield interatomic potentials. In the alkali-metal/Hg* systems, two models based on spherical potentials were in excellent agreement with observation. In both models, a potential (tentatively ascribed to an $\Omega = \frac{5}{2}$ or $\frac{3}{2}$ state) with $\epsilon = 30 \pm 2 \times 10^{-14}$ erg and $R_m \simeq 4{\cdot}0$ Å (Na/Hg*), $R_m \simeq 4{\cdot}6$ Å (K/Hg*) was responsible for the major features in the observed cross sections. Small-angle structure, however, could be interpreted in two ways, either as arising from a soft region at large R in the single potential or due to the operation of two additional rather shallow potentials ($\epsilon = 2{\cdot}7 \pm 0{\cdot}5$ and $1{\cdot}5 \pm 0{\cdot}5 \times 10^{-14}$ erg) ($\Omega = \frac{3}{2}$ and $\frac{1}{2}$ states).

In contrast, the Ne/Hg* system could not be fitted by any plausible single potential and three potentials having $\epsilon = 8 \pm 4$, 14 ± 4 and $22 \pm 2 \times 10^{-14}$ erg tentatively identified as $\Omega = 0$, 1 and 2 states, respectively, were required.

In neither case was there any evidence for quenching (J transitions) of the metastable atom on the attractive branch of the potential.

1. Introduction

In Davidson *et al* (1973) we reported the first results of differential elastic scattering experiments in the study of the interaction of electronically excited mercury atoms with other species. In this paper these results are extended to include a closed-shell atom (neon) and are interpreted to yield interatomic potentials.

There are two low-lying states of mercury with sufficiently long lifetimes to travel through a scattering apparatus, the 6^3P_0 and 6^3P_2 states with energies of 4·64 and 5·46 eV respectively. The 6^3P_1 at 4·89 eV radiates in 10^{-7} s, which is too short for detection. Magnetic analysis of the beam gives a lower bound on the fraction of $^3P_2$ atoms of 85% but, since no state selection is used in the scattering experiments, all the M_J states of the $^3P_2$ atom are represented in the beam. As the collision proceeds M_J, in a space-fixed frame of reference, ceases to be a good quantum number but, replaced by Ω (the total electronic angular momentum about the interatomic axis), may conveniently be used to label the different adiabatic potentials which evolve from each atomic M_J state as they interact with the target atom. The collisions

thus take place over a manifold of surfaces. In this situation, the Coriolis force arising from the relative motion of the atoms can induce transitions between these M_J states. Transitions between J states, which can then lead to quenching of the metastable, are also possible but, because of the large spin–orbit splitting, are relatively less frequent. Collisions with the alkali metals can also result in their ionization or electronic excitation.

In contrast, collisions between ground-state $Hg(^1S_0)$ and these target atoms are necessarily elastic at thermal energies and involve a single potential surface, so that scattering measurements may be inverted to yield an accurate potential. However, even in these systems, restrictions on the range of data or lack of an absolute calibration may result in ambiguities in the derived potential (Buck 1975).

The systems studied here are, in comparison, very complex with a large number of exit channels open, as well as possible interference effects between trajectories which sample two or more of the asymptotically degenerate potentials. The interpretation must correspondingly be more model-dependent, and indeed an important objective of this work is to discover whether a simple potential model corresponding to some dominant process is a useful approximation in describing these collisions (Fluendy *et al* 1974).

2. Experimental

2.1. Crossed-beam apparatus

The crossed-beam apparatus used has already been described (Cowley *et al* 1969) and only the essential features need be discussed here. The excited Hg atom beam was produced by bombarding a ground-state Hg beam effusing from a glass capillary array with a magnetically collimated electron beam of controlled energy. After recollimation, the excited Hg atoms entered the collision zone where they intersected the modulated target beam from a multichannel array. The target beam produced typically 10–15% attenuation of the Hg* flux, except in the case of Ne where pumping constraints limited the attenuation to 3%—the data for this system being consequently rather more noisy. The scattered excited Hg atoms were detected by Auger ejection of electrons from a clean potassium surface (coated *in situ*) located in a differentially pumped UHV chamber. Ejected electrons were detected by a channeltron and thence counted into a gated dual scaler system. The experiment was conducted by recording the scattered signal as a function of angle at intervals of about 0·3°, a single sweep over the range of angles explored taking approximately 3 h. Individual scans of this type were repeated until sufficient precision had been achieved. The angular resolution of the apparatus was 0·5°. Since both beams were from effusive sources and not velocity-selected, there was broadening in the relative velocity distribution in addition to that arising from the angular divergence of the incident beams. Forward calculations, in which a model centre-of-mass (CM) differential cross section function was convoluted with the appropriate distribution of centre-of-mass vectors, showed that structure with a CM period of 1° would just be observable in the laboratory.

2.2. Hg beam composition*

The excitation function for Auger ejection from the potassium surface in the detector was measured over a range of electron energies in the Hg atom exciter. A threshold

at around 6 eV rising to a maximum at around 10 eV was observed, in agreement with previous work. Time-of-flight measurements showed that higher excitation energies produced large quantities of photons without improving substantially the yield of metastables. In these experiments the exciter was operated at energies less than 9 eV, the electron energy scale being calibrated by extrapolating the excitation function to 5·46 eV. At about 9 eV, $^3P_0$ and $^3P_2$ are the only long-lived states accessible, the $^3D_3$ (also long-lived) being at threshold (about 8·7 eV) (Borst 1976).

Theory (McConnell and Moiseiwitsch 1968) suggests that the ratio of cross sections for the direct production of $^3P_0$ and $^3P_2$ by electron impact is close to statistical (i.e. 1:5) though, at the excitation energies used, cascade from higher levels may also be important. Measurements to investigate this point were made using a two-wire configuration inhomogeneous magnetic field between the metastable source and the detector. Calculation (Davidson 1973) and saturation experiments showed that this field could be operated as a shutter for $\mu = 0$ states so that the ratio [($\mu = 0$) states/all states] could be determined for the metastable atoms at various excitation voltages. Contributions from photons produced in the source were eliminated by using the flight time of the metastable, so that counting was only permitted during periods when the exciter voltage was off. The results of experiments of this type are shown in table 1; more detailed flight-time measurements showed that this ratio was independent of metastable-atom velocity.

This data, without further knowledge of the relative population of magnetic substates in the $^3P_2$ level, does not allow the J-state composition of the scan to be determined. If the magnetic substates of $^3P_2$ are equally populated—a reasonable approximation for (i) direct excitation with a very poorly collimated electron beam having a relatively high (approximately 0·3 V) energy spread (Ottley and Kleinpoppen 1975) *or* (ii) for population by cascade from a range of higher states produced at higher voltages—the $^3P_2$ composition shown in the table can be computed. If cascade from the 7^3S is important, enhanced populations in the $M_J = 0$ state will be produced and lead to even larger estimates for the $^3P_2$ fraction. It should be noted that the observed composition agrees closely with that expected for purely statistical excitation and detection of these states (83% $^3P_2$), further supporting this analysis and confirming the predominant $^3P_2$ composition of the beam.

Partly for simplicity and also in view of the lower detection efficiency for the $^3P_0$ state, the scattering data are attributed solely to the $^3P_2$ level. Where appropriate the M_J states are assumed to be populated equally (Krause *et al* 1975).

2.3. *Velocity distribution*

Flight-time measurements on the metastable-atom beam were made to distinguish photon production from genuine metastable atoms (§2.2) and also to determine their

Table 1.

Excitation voltage	Signal $\frac{\text{magnet on}}{\text{magnet off}}$	Percentage $^3P_2$ assuming all M_J equi-populated
8	0·43	71
9	0·31	86
11	0·32	85
14	0·31	86

most probable velocity. The measurements were made by pulsing the electron excitation current to produce pulses of metastable atoms approximately 100 μs long (a period determined by the length of the excitation region). The channel advance of a multiscaler was triggered simultaneously with the exciter pulse and the channel address incremented every 20 μs by a crystal clock. Metastable arrivals incremented the appropriate channel, so that by repetition of this sequence an arrival-time spectrum was constructed. The most probable flight time was found to be about 1·5 ms.

In comparison with the expected v^2 Maxwellian distribution (the exciter has an efficiency $\propto 1/v$) a substantial deficit of slow atoms was seen, possibly due to recollimation losses of the slower atoms following excitation. As a result of this loss, the velocity distribution is substantially narrower and the most probable velocity was 38% greater than that expected for an effusive beam at a similar temperature. The measured most probable velocity of $2{\cdot}48 \times 10^2$ m s^{-1} was used in subsequent calculations of the relative velocity of collision with the target atoms studied.

2.4. Treatment of data

The data reported, relative differential elastic cross sections, are the result of averaging six or more individual angle scans of the type described. The scans were first approximately normalized to each other and then merged by summing in successive small-angle increments (approximately half the angular resolution in width) to yield a mean value for the cross section in the angle increment. The mean laboratory cross sections computed in this way were then transformed into the centre-of-mass frame, using the Jacobian appropriate to the most probable relative velocity.

As can be seen from the Newton diagram, two centre-of-mass (CM) angles χ contribute to the scattering $I(\theta)$ at every laboratory angle θ, so that

$$I(\theta_1) = J(\theta_1, \chi_F)I(\chi_F) + J(\theta_1, \chi_B)I(\chi_B) \tag{1}$$

where $J(\theta, \chi)$ is the Jacobian transforming between laboratory angle θ and CM angle χ. $I(\chi_F)$ and $I(\chi_B)$ are the forward and back CM scattering intensities which contribute at θ_1. For the systems studied here, every angle χ_B also appears at some other laboratory angle θ_2 as a forward-scattered component. Now $J(\theta, \chi_F) > J(\theta, \chi_B)$, while $I(\chi_F) \gg I(\chi_B)$ since $\chi_F < \chi_B$, so that the backward contribution in equation (1) is small. An iterative scheme can therefore be used to extract the separate forward and back contributions.

A first estimate

$$I'(\chi_F) = J(\theta_1, \chi_F)^{-1} I(\theta_1) \tag{2}$$

is made for all laboratory angles. This estimate is then corrected by

$$I''(\chi_F) = I'(\chi_F) - J(\theta_1, \chi_F)^{-1} J(\theta_1, \chi_B) I'(\chi_B) \tag{3}$$

where $I'(\chi_B)$ is found via (2) at the appropriate laboratory angle θ_2. Equation (3) is then iterated until convergence is complete; typically only three iterations are required. The results of this analysis are finally plotted as relative differential elastic cross sections in the CM frame in the various figures.

3. Results and discussion

As already indicated, interpretation of elastic scattering in the present systems is subject not only to the usual difficulties associated with inverting limited data to yield a unique potential, but also to uncertainty as to the appropriate model for the process.

The data for the alkali-metal systems are presented in figures 1, 2 and 3. It supercedes the data presented, but not analysed, in Davidson (1973), in that a number of angle calibration errors affecting the superposition of different scans has been corrected. A striking feature of the scattering pattern is the wide-ranging and rather regular oscillatory pattern. This pattern is very reminiscent of the supernumerary

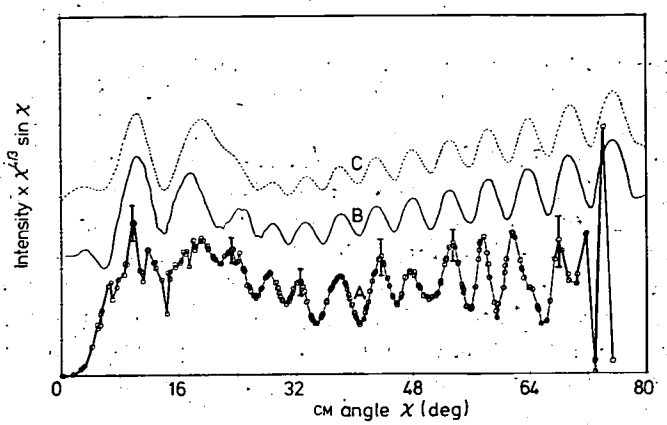

Figure 1. Relative differential elastic cross section for $Hg(^3P_2)/Na$. Curve A, experimental; curve B, single-potential fit; curve C, three-potential fit. Fitted curves are shifted on arbitrary amount upwards. Data is deconvoluted with the main beam profile and the representative error bars are twice the standard deviation of the signal based on the counting statistics. Velocity = 895 m s^{-1}; number of scans = 6.

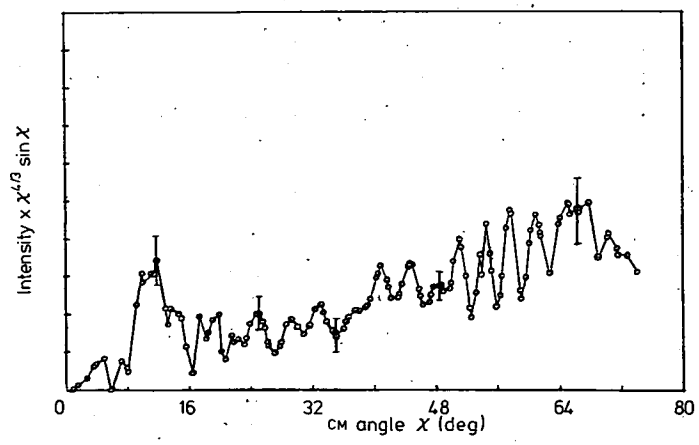

Figure 2. Relative differential elastic cross section for Hg $6^3P_2/K$ (experimental). Velocity = 660 m s^{-1}; number of scans = 3; filtered and deconvoluted data.

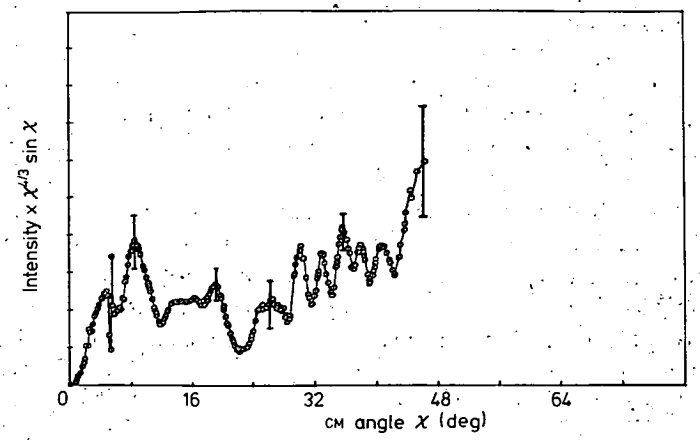

Figure 3. Relative differential elastic cross section for Hg 6^3P_2/Rb (experimental). Velocity = 470 m s^{-1}; number of scans = 6; filtered and deconvoluted data.

bows seen in simple elastic scattering inside the rainbow. Although individual oscillations are distorted by noise, the sequence and approximate location of peaks are reasonably secure. In contrast, the rather noisy Ne/Hg* data (figure 4), which might naively be expected to be less complex, show a much less regular and also a less pronounced structure although the smaller amplitude of the oscillations makes it difficult to identify specific features. The sharp fall-off in the cross section at small angles seen in all the systems is simply due to over-compensation for the attenuation of the main beams. This angular region is not used in subsequent fitting operations.

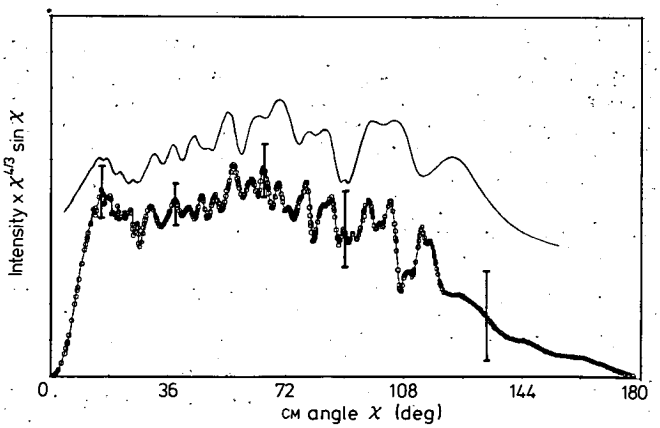

Figure 4. Relative differential elastic cross section for Hg 6^3P_2/Ne (full curve is three-potential fit). Velocity = 723 m s^{-1}; number of scans = 6.

3.1. Potential fitting

A number of techniques have been used to tackle the 'practical' inversion problem—the extraction of a potential in accord with limited experimental scattering data. The uniqueness of this potential depends upon the quantity and quality of data available. Inversion methods have recently been reviewed by Buck (1975) and in

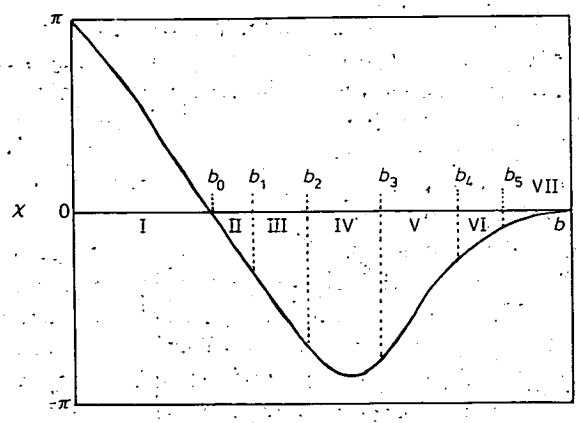

Figure 5. Schematic deflection function showing parametrization regions.

this work we use a version previously exploited by him in which a parametrized form for a deflection function is adjusted to produce agreement with the scattering data. The deflection function can then be inverted using the Firsov technique to yield the fitted potential. Buck has shown that the location of supernumerary rainbows and high-frequency glory oscillations is not affected significantly by apparatus averaging so that these features are particularly useful for fitting. In the Na, K and Rb data there are 21, 37 and 10 extrema, respectively, available for fitting; Buck's technique was therefore extended to allow a more flexible parametrization of the deflection function. The parametrization regions are shown in figure 5 and correspond to the following functions:

Region	Form	Adjustable parameters
I	$\pi - a_4 b - a_5 b^4$	
II	$a_2(b - b_0) - a_3(b - b_0)^2$	b_0, a_2
III	$-\chi_b - a_1(b - b_1)$	a_1, χ_b
IV	$-\chi_R + q(b - b_R)^2$	b_R, χ_R
V	$-C_1 b - C_2$	C_2
VI	$-\chi_C + C_3(b - b_4) - C_4(b - b_4)^2$	χ_C
VII	$\frac{15}{56}\pi(C_{(6)}/E)b^{-6}$	

The phase at b_0 (i.e. η_{max}) is also a variable. The value of $C_{(6)}$ calculated by Darwall *et al* (1970) was used to constrain the function at large b. The other parameters were determined to join smoothly the different regions of parametrization.

The information used from the cross section was:

(i) locations χ_N of supernumerary bows,

(ii) smoothed cross section at χ_N, $\bar{\sigma}_N$, and

(iii) high-frequency oscillation period $\Delta\chi_{HF}$ in the small-angle region.

The extrema locations provide rather precise information on the area enclosed in the deflection-function bowl while $\bar{\sigma}_N$ corresponds to the classical cross section and is primarily sensitive to the shape of the outer branch of $\chi(b)$; as with the extrema locations this property is not affected significantly by apparatus resolution. The glory oscillations $\Delta\chi_{HF}$ provide an initial estimate of the parameter $b_0 = (k\Delta\chi_{HF})^{-1}$.

Fitting is carried out using a uniform approximation to calculate the quantities (i)–(iii) from the parametrized deflection function which is then adjusted to produce the best fit. The $\chi(b)$ function is considerably over-determined since seven parameters are constrained by 40 or more input values.

3.1.1. The Hg–alkali-metal system.* The degeneracy of the Hg* M_J states is removed by the collision partner and five different molecular states evolve from the separated atoms (figure 6). Previous calculations (Fluendy *et al* 1974) have suggested that, in the limit of strong coupling between the different potential surfaces evolving from the mixture of M_J states in the incident beam, a single spherical effective potential can describe the scattering. In other cases interference effects between the different surfaces will be seen, but it is likely that the separate scattering features of each surface, e.g. rainbows, will remain important features in the total scattering. A model based on summing one or more single-surface elastic scattering cross sections is thus a natural starting point.

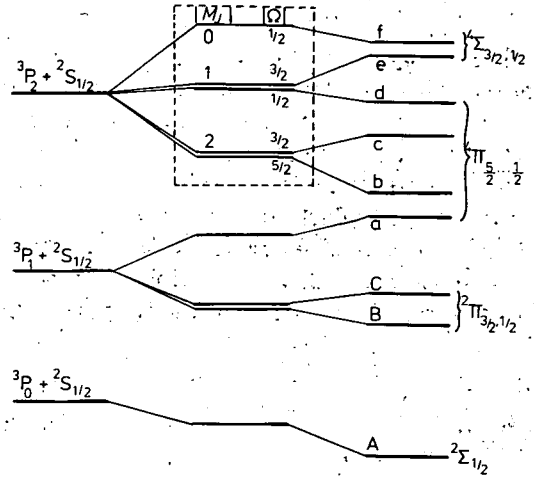

Figure 6. Suggested correlation diagram for Hg*/alkali atoms. The ordering of the levels at the right-hand side is appropriate for small separations and the framed portion is suggested for intermediate values of R where Hund's case (c) is appropriate, i.e. $V(R) \ll$ spin–orbit coupling energy. States dissociating to M*/Hg are omitted and all the levels shown are embedded in a continuum of states dissociating to $M^+ + \epsilon + Hg(^1S)$.

The alkali-metal cross sections show an unusual hump near 16° which, at least in the case of Na, seems to be resolved into two peaks. This feature can be reproduced in two principal ways, using either a single-potential model with a small maximum in its deflection function at large impact parameters (full curve in figure 7), *or* a three-potential model in which this feature is constructed by the addition of two primary bows (dotted curve in figure 7). It was not found possible to reproduce the small-angle scattering pattern by a combination of two normal (i.e. with only one rainbow) deflection functions, or by a single such function. The fits obtained with the inflected single-potential and the three-potential models are compared with the experimental data in figure 1; some deviation at wide angles is seen due to the restrictions of the parametrization, but both are in excellent agreement with the envelope and oscillation structure.

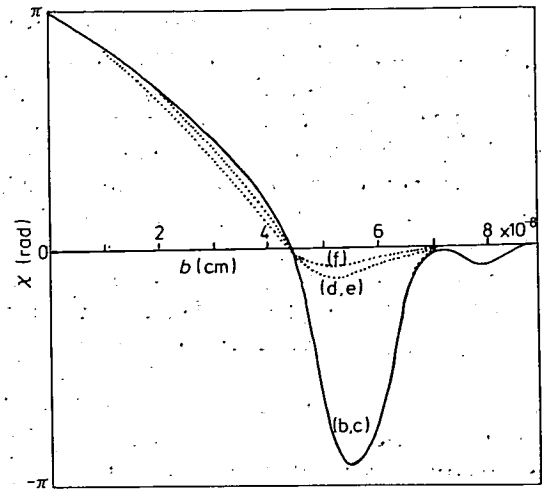

Figure 7. Fitted deflection functions for Hg*/Na scattering (full curve is single deflection function fit with small maximum; dotted curves are deflection functions for the three-potential model). The deepest function is common to both fits except where shown at the largest ranges. The labelling of states corresponds to the correlation diagram (figure 6).

The potentials calculated by Firsov inversion of these deflection functions are seen in figure 8. The deeper potential is very similar in both models, differing only in the softening seen at large separations in the single-potential fit.

The K/Hg* cross section had been analysed in a similar way, though in this case no small-angle high-frequency oscillations could be seen. The extrema spacing

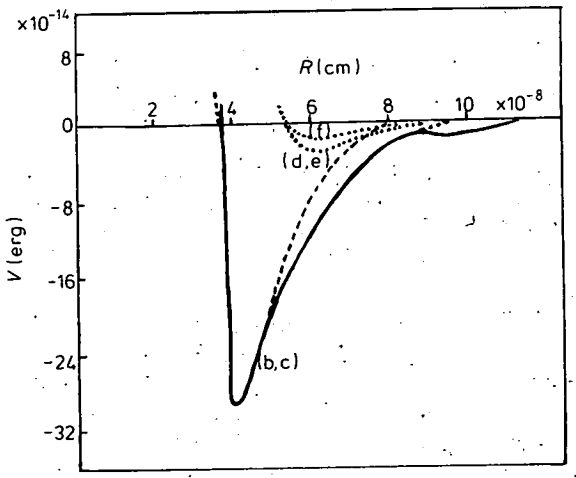

Figure 8. Potentials calculated from the fitted deflection functions for the Hg*/sodium system. The full curve is the single-potential model; the dotted curves are the three-potential fit, note that the deepest potential for each of these models only differ at very large R; the broken curve is the ground-state Hg/M potential reduced to the same ϵ and R_m (Buck 1975). The labelling of the states corresponds to that in the correlation diagram (figure 6). For Na/Hg*, $\epsilon = 3 \times 10^{-13}$ erg, $R_m = 4{\cdot}0$ Å; for Na/Hg $\epsilon = 8{\cdot}8 \times 10^{-14}$ erg, $R_m = 4{\cdot}72$ Å. The potentials are shown over the range determined by the data.

in the Na and K data, which relate to the phaseshift difference across the deflection bowl, can be reduced to a common plot if $R_m(K) = 1{\cdot}17\, R_m(Na)$. The potential in this region is correspondingly likely to be reducible, though the large number of extrema in the K data make it difficult to obtain a precise fit with the parametrized deflection function used. The Rb/Hg* data is rather poor and quantitative interpretation is difficult, the same general features—small-angle hump and supernumerary bows—as for the other alkali metals can, however, be seen.

The data available from experiment is primarily sensitive to the potential bowl, though the failure to observe primary bows in the angular range accessible means that the bottom of the bowl is rather poorly probed. The absolute location of the zero crossing to the potential is also only weakly determined by the data.

3.1.2. The Hg–inert-gas systems.* The correlation diagram for inert-gas/Hg* is shown in figure 9. Three potential states evolve from the Hg $J = 2$ state. In contrast to the alkali metals, the states correlating with excited Ne lie at much higher energies than the states of interest here and the collisions can be expected to be almost entirely elastic.

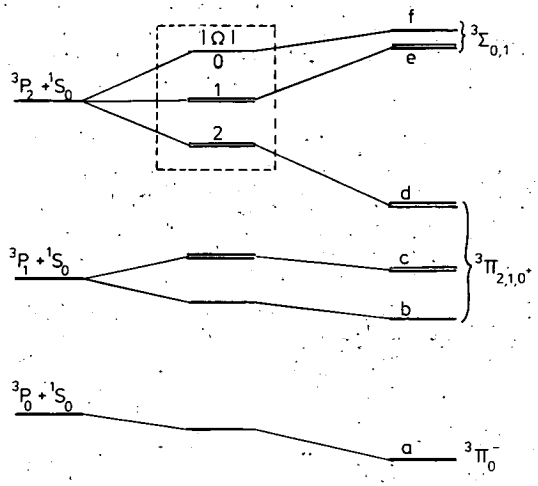

Figure 9. Correlation diagram for Hg*/Ne. The ordering of the levels at the right (small separations) is assumed to be dominated by electron/electron repulsion and the classification there corresponds to Hund's case (a).

The Ne/Hg* cross sections shown in figure 4 are noisy due to difficulties in pumping the inert gases and it proved impossible to obtain satisfactory data for the heavier members of this series. A clear division is seen between an angular region in which the cross section is oscillating strongly and a wide-angle zone where it decays smoothly. Since quenching cross sections for inert-gas collisions are small, this large-angle zone is almost certainly the dark side of a rainbow. A sequence of high-frequency oscillations is just visible at small angles from which a sensible b_0 value can be deduced. In contrast with the alkali metals, the extrema positions in the oscillating part do not fit a simple supernumerary bow sequence while the low-resolution envelope is also unlike that normally seen in atom/atom elastic scattering. No reasonable shape of deflection function capable of reproducing the overall behaviour could be found.

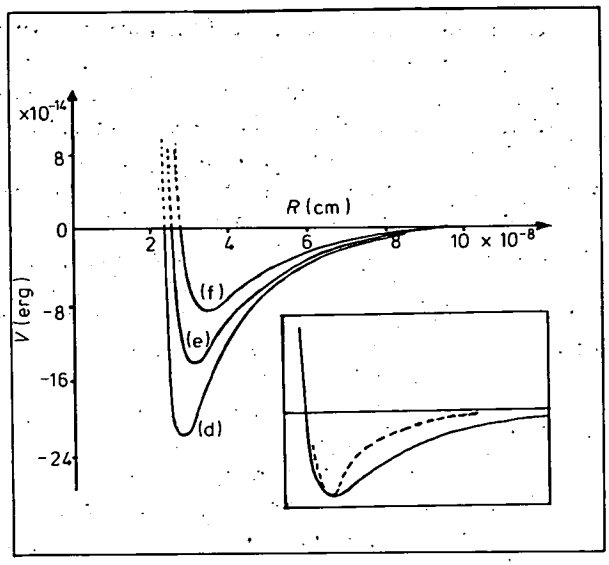

Figure 10. Three potentials fitted to Hg*/Ne scattering data. Inset is a Lennard-Jones potential (broken curve) with the same ϵ and R_m as the shallowest fitted potential (full curve). The labelling of the states corresponds to that in the correlation diagram (figure 9).

A three-potential model was therefore sought, using the techniques already described. The complexity of the data as well as the presence of some noise make it unrewarding to search for a perfect fit. The agreement obtained in figure 4, which reproduced the main features including the overall shape quite well, is therefore satisfactory. This was computed as the sum of three cross sections weighted 2:2:1 calculated from the potentials plotted in figure 10, the two deepest potentials each being awarded a weight of 2.

4. Discussion

4.1. Hg–alkali-metal pairs*

The most striking feature of the experimental results is the comparative simplicity of the scattering patterns. In §3, two models were shown to lead to a good fit of $\sigma(\chi)$, one involving a single potential with an unusual softening of the outer attractive branch and the other a three-potential model. The depth and location of the well of the single potential was very similar to the deepest potential of the second model. In neither case was it necessary to invoke quenching.

A possible correlation diagram is given in figure 6. In the case of weak interactions (large R), the electron spin of the alkali atom is only weakly coupled with that of Hg* and only three different potential energy states evolve from the separated atoms. As R decreases, Hund's case (c) is replaced by case (a) and at intermediate separations the five-fold degeneracy of the parent $^3P_2$ level is completely removed, to be replaced by a simpler splitting at small R where the $^4\Sigma_{1/2}$ and $^4\Sigma_{3/2}$ states become very nearly degenerate. No information is available on the ordering of the

$^4\Sigma$ and $^4\Pi$ levels and it is assumed that the lower electron–electron repulsion in the Π states (i.e. between $Hg(p_{\pm 1})$ orbitals and the M(s) orbital) places them below the Σ states (where the $Hg(p_0)$ orbital is occupied) in the limit of Hund's case (a).

At very large separations, where the interaction energy is entirely determined by dispersion forces, the greater polarizability in the bond direction, α_{zz}, of the $M_J = 0$ state may result in the $|\Omega| = \frac{1}{2}$ levels initially lying lowest and the $(\frac{3}{2}, \frac{5}{2})$ pair highest. However the anisotropy in the polarizability is small ($\lesssim 10\%$, Levine *et al* 1968) and this order would be easily reversed as the overlap between the two atoms increased, to give the order shown in figure 6.

Of the two models used in fitting the data, a single potential implies that the splitting in the manifold of levels remains small down to R_m ($\simeq 4$ Å in the case of Hg*–Ne) even though the interaction is strong ($\sim 0{\cdot}2$ eV). Outer maxima in the potential energy curves of excited diatomics have been reported (e.g. Cohen and Schneider 1974, Mulliken 1970) but in association with the penetration of a diffuse orbital occupied by a promoted electron (e.g. in the ^3P states of an inert-gas atom). The effect would not be expected at long ranges in the much more compact 6s6p configuration of ^3P Hg. Also, there seems no obvious state, e.g. a charge-transfer one, that could cross the states (b)–(f) (figure 6) at a separation of about $2R_m$ and hence perturb them in that region. The possible re-ordering of some of the $^3P_2$ manifold due to the onset of overlap referred to above would be expected around R_m, when repulsion forces begin to dominate.

The three-potential model is thus to be preferred on theoretical grounds and is in accord with the correlation diagram for Hund's case (c) and with relatively little contribution to the spin–orbit coupling energy from the electron in the still largely unperturbed valence shell of the alkali metal. The spectroscopic designation of the three groups of states is not settled by these scattering experiments since the fitting is not sufficiently sensitive to the weighting of each state, but on experimental grounds we favour the higher weight for the deeper states.

On either model a deep potential is required, possibly accompanied by shallower ones, having a well depth approximately 30×10^{-14} erg. This value is considerably greater than that of the ground state ($x\,^2\Sigma$) where $\epsilon = 9 \times 10^{-14}$ erg (Buck and Pauly 1971) and points to a specific interaction in this excited state.

4.2. Hg–Ne*

The probable correlation diagram for Hg* interacting with a ^1S atom is given in figure 9. At large separations M_J ($\equiv \Omega$ for a ^1S partner with the quantization axis along the interparticle vector) is a good quantum number. At large separations the state of maximum M_J lies lowest if, as discussed in §4.1, electron–electron repulsion dominates over dispersion forces. As R decreases and the coupling passes to Hund's case (a), the $^3\Sigma_0$ and $^3\Sigma_1$ states become degenerate, the e state being forced up in energy in energy by interaction with the c state (both $\Omega = 1$).

The observation that the scattering data are best fitted by three potentials is thus entirely consistent with the correlation diagrams and indicates that, at the range of separations scanned experimentally (essentially down to the inner zero of the potential), Hund's case (c) is appropriate because pure case (a) would predict only two potentials. Once again the spectroscopic labelling of the three states cannot be decided unambiguously from these scattering experiments, but we favour giving a weight of 2 to the two deeper states, indicating that the lowest state has $|\Omega| = 2$.

The Ne–Hg* and Na–Hg* potentials exhibit a much wider bowl than a Lennard-Jones potential having the same ϵ, R_m values (figures 8 and 10). This behaviour has been noted by Buck (1975) for ground-state Hg/alkali-metal potentials; it is not found in the ground/metastable state pairs of the inert gases (Winicur *et al* 1976).

5. Conclusions

The elastic scattering of Hg* in all the systems studied can, on a combination of theoretical and experimental evidence, best be interpreted in every case as the scattering from three distinct potential energy states. This is consistent with the partial removal of the degeneracy of the $^3P_2$ state at separations around 4 Å. The potential minima are sufficiently separated for it to be meaningful to assign separate deflection functions to each state, i.e. Hund's case (c) rather than case (e) applies when molecular rotation is taken into account.

In the case of the alkali metals, the absence of any marked attenuation due to ionization, which is energetically allowed in each system, is noteworthy. Coupling to the continuum is evidently small and one can continue to use the concept of a deflection function even when the classical path is embedded in a continuum.

References

Borst W L 1976 *Proc. 5th Int. Conf. on Atomic Physics, Berkeley* p 388
Buck U 1975 *Advances in Chemical Physics* vol 30, ed K P Lawley pp 313–88
Buck U and Pauly H 1971 *J. Chem. Phys.* **51** 1929
Cohen J S and Schneider B 1974 *J. Chem. Phys.* **61** 3230
Cowley L T, Fluendy M A D, Horne D S and Lawley K P 1969 *J. Phys. E: Sci. Instrum.* **2** 1021
Darwall E C, Fluendy M A D and Lawley K P 1970 *Molec. Phys.* **19** 673
Davidson T A 1973 *PhD Thesis* Edinburgh University
Davidson T A, Fluendy M A D and Lawley K P 1973 *Faraday Disc. Chem. Soc.* **55** 158–66
Fluendy M A D, Kerr I H and Lawley K P 1974 *Molec. Phys.* **28** 69–80
Krause H F, Johnson S G, Datz S and Schmidt-Bleek F K 1975 *Chem. Phys. Lett.* **31** 577–81
Levine J, Celotta R J and Bederson B 1968 *Phys. Rev.* **171** 31
McConnell J C and Moiseiwitsch B L 1968 *J. Phys. B: Atom. Molec. Phys.* **1** 406
Mulliken R S 1970 *J. Chem. Phys.* **52** 5170
Ottley T W and Kleinpoppen H 1975 *J. Phys. B: Atom. Molec. Phys.* **8** 621
Winicur D H, Fraites J L and Bentley J 1976 *J. Chem. Phys.* **64** 1757

Volume 42, number 1 CHEMICAL PHYSICS LETTERS 15 August 1976

VELOCITY DEPENDENCE OF VIBRATIONAL BRANCHING RATIOS IN ELECTRONIC ENERGY TRANSFER. COLLISIONS OF METASTABLE ARGON ATOMS WITH NITROGEN†

A.N. SCHWEID‡, M.A.D. FLUENDY‡‡ and E.E. MUSCHLITZ Jr.
Department of Chemistry, University of Florida, Gainesville, Florida 32611, USA

Received 2 April 1976

Measurements have been made of the vibrational branching ratio $(v' = 0)/(v' = 1)$ in N_2^* $(C\,^3\Pi_u)$ formed in electronic energy transfer collisions between argon metastable atoms and ground state nitrogen molecules, using crossed molecular beams. In the relative collision energy range, 0.08–0.20 eV, this ratio is 3.5 ± 0.2.

1. Introduction

Electronic energy transfer processes play an important role in a number of phenomena; for example, electrical discharges, combustion, high temperature shocks, secondary processes in radiation chemistry, and laser action [1]. Electronically excited atoms and molecules are produced in every case and their subsequent reactions must be taken into account in determining the ultimate disposal of energy. Molecular beam techniques make possible the measurement, for specific excited states, of the velocity dependence of reaction cross sections and the angular distribution of reaction products as well as their internal and kinetic energy distributions. In addition, the use of supersonic beams makes available a wide range of relative velocities.

Since the pioneering work of Robertson [2], the electronic energy transfer process:

$$Ar^*(^3P_{2,0}) + N_2(X\,^1\Sigma_g^+, v = 0) \rightarrow Ar(^1S_0) + N_2^*(C\,^3\Pi_u, v' = 0\text{–}3) \quad (1)$$

has been extensively studied in flowing afterglow experiments by Setser and co-workers [3]. In particular, they have investigated the rotational and vibrational population distributions in the product molecules at 298 K (0.039 eV) and 77 K (0.010 eV) by spectroscopic observation of the light emitted as N_2^* fluoresces from C → B.

This transfer process has also been studied using molecular beam techniques. Winicur and Fraites have determined the total cross section for quenching of Ar^* in N_2 by the optical model analysis of their differential elastic cross section measurements [4]. Lee and Martin [5] and Sanders et al. [6] have studied the velocity dependence of the formation of N_2^* (C) by measuring the total C → B emission. In the crossed molecular beam experiments reported here, a monochromator is used to analyze the C → B emission and the ratio $(v' = 0)/(v' = 1)$ determined in the relative energy range, 0.08–0.20 eV.

2. Experimental

The apparatus used in these experiments may be briefly described as follows (for details see ref. [7]). A thermal beam of metastable argon atoms originating from a low voltage dc discharge [8] is crossed by a supersonic nozzle beam of N_2 molecules produced in the standard fashion [9]. The metastable beam intensity is continuously monitored by meas-

† Supported by the U.S. National Science Foundation.
‡ Present address: Fakultät für Physik, Universität Freiburg, Freiburg i. Br., Germany.
‡‡ Present address: Department of Chemistry, Edinburgh University, Edinburgh, UK.

urement of the electron current ejected from the gold surface of a Faraday cup detector. The nozzle beam is monitored by a molecular beam detector consisting of an electron beam ionizer followed by a quadrupole mass spectrometer set at mass 28. To obtain a range of N_2 velocities, the nozzle beam was seeded with various amounts of He. Light from the ionizer filament precluded continuous monitoring of the N_2 beam; however, both the N_2 and He flow rates were continuously monitored during each run by electronic flowmeters equipped with digital readouts, and were found to be constant.

The light issuing from the region of intersection of the two beams (7.7×10^{-3} cm^3) is collected by means of an f/4 quartz lens system located above the intersection volume and a spherical mirror located below. The light is focussed onto the entrance slit of an f/4 monochromator with a dispersion of 40 Å/mm. Light exiting the monochromator is focussed onto the cooled cathode of an EMI 9558 photomultiplier tube.

The nozzle beam is collimated by a circular aperture then chopped by a two-bladed mechanical chopper rotated at 50 Hz. In the center of each sector-shaped blade, a 10 mil slit is cut. The purpose of these slits is to provide short beam pulses for TOF analysis of the N_2 beam. The chopper also interrupts a light beam generated by an LED and detected by a photodiode. A train of long and short triggering pulses is thereby produced which are first shaped then separated electronically.

In the TOF analysis the onset of the narrow triggering pulse defines time $t = 0$ and is used to trigger a PAR TDH-8 waveform eductor. The narrow beam pulses from the quadrupole mass spectrometer electron multiplier are converted to voltage pulses, amplified, then averaged by the waveform eductor. Flight times were determined by comparing the output of the eductor on an oscilloscope with timing pulses from a crystal clock actuated by the $t = 0$ triggering signal.

The photon pulses from the photomultiplier tube are amplified then counted by a dual channel counter. The onsets of the long triggering pulses, after being delayed sufficiently to allow for the N_2 transit time (from the chopper to the interaction region), are used to gate the counter. Counts are accumulated in one channel corresponding to a fixed interval during time the chopper is open and in the other channel for exactly the same interval while the chopper is closed. The instrument employed (SSR 1110 digital synchronous computer) provides the count rate for each channel as well as the difference between the two corresponding to the signal. Counts were accumulated until satisfactory statistics were obtained – up to 24 hours in some cases. The background count rates are determined almost entirely by the dark noise of the photomultiplier since the other contributors to the background are highly discriminated against by the severe focussing requirements of the light collection system and efficient shielding against stray light.

3. Treatment of experimental data

The velocity of the N_2 beam was taken at the maximum of the TOF distribution. The velocity resolution, Δv(fwhm)/v for this beam varied from 0.16 to 0.19 depending upon the seeding conditions. The Ar* beam had a Maxwell–Boltzmann distribution corresponding to a temperature of 650 K, as determined by a TOF analysis of this beam, and the most probable velocity was used. The square of the relative velocity was obtained by adding the squares of the two beam velocities and the relative energy determined by multiplying this sum by one-half the reduced mass.

The most intense bands in the N_2 ($C \rightarrow B$) system are well separated so that the signal could be significantly increased by using the monochromator with a wide band pass. Measurements were therefore made by setting the monochromator at the band head of each transition using 100 Å bandpass. The ratio of the count for the 0–0 transition to that for the other transitions was determined. The entire system was checked by comparing the ratio of the 0–0 to 0–1 intensities for N_2 ($C \rightarrow B$) with the ratio of the tabulated Franck–Condon factors [10]. The agreement was within the experimental error of the measurements.

In order to determine the relative population of the $v' = 0$ and $v' = 1$ states of N_2 (C), the ratio of the 0–0 to the 1–0 intensities was first obtained. This was then corrected to give the ratio $(v' = 0)/(v' = 1)$ by using the appropriate Franck–Condon factors [10]. In order to ensure that a bandwidth sufficient to include the entire band was employed, measurements of this ratio were repeated with the monochromator settings decreased by 25 Å. Within experimental error, the

ratio was the same. Within the range of the measurements (3000–4000 Å) no corrections were necessary for the detection efficiency of the optical system.

4. Results and discussion

A potential energy diagram showing the molecular states of nitrogen involved in this work is shown in fig. 1. In flowing afterglow experiments, Setser et al. [3] have observed emission corresponding to the transitions C → B, B → A, and A → X in N_2 following energy transfer from metastable argon atoms. They found that both the C and B states are directly populated, that the ratio of $v' = 0$ to $v' = 1$ in the C → B system is much larger than the Franck–Condon principle would predict for direct excitation of X → C, and that the bands in this system are strongly shaded toward the violet because of high rotation excitation in the C state. Their high resolution spectra show rotational quantum members as high as 54 for $v' = 0$ as well as other unusual features.

A discharge source similar to that used in this work produces metastable argon atoms with a ratio $^3P_2/^3P_0$ of about 7 under similar operating conditions [11]. Both the $^3P_2$ (11.55 eV) and the $^3P_0$ (11.72 eV) states have sufficient internal energy to excite N_2 up to $v' = 2$ of the C state. We were unable to obtain sufficient intensity to make measurements on $v' = 2$ and we saw no evidence of $v' = 3$ even at the highest relative energy used in these experiments.

In fig. 2 the branching ratio $(v' = 0)/(v' = 1)$ for reaction (1) is plotted against the relative collision energy. The flowing afterglow measurements of Robertson [2] and Stedman and Setser [3] are shown for comparison. Robertson's measurements were made by comparing intensities at the band heads. Because of the strong shading of the 0–0 band toward the violet, this result is probably too low [3]. Stedman and Setser do not estimate the error in their measurements, but from the number of significant figures reported, it appears to be no better than ±5%. For this reason, we have drawn a line through the data which decreases monotonically with increasing relative energy. Within the experimental error of the data reported here, however, the ratio is constant at 3.5 ± 0.2 in the range 0.08–0.20 eV.

Additional data are necessary to show conclusively whether or not the branching ratio falls with increasing relative collision energy approaching the Franck–Condon prediction for excitation of N_2 (X → C) at high energies. The range of the present results could be extended by heating the nozzle beam or by using crossed nozzle beams with electron impact to excite the Ar beam. We plan to modify the apparatus for

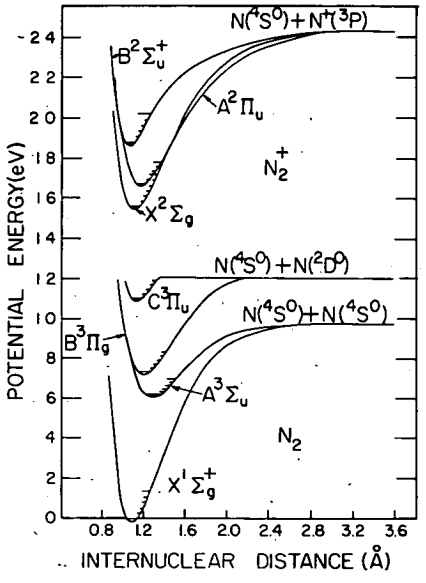

Fig. 1. Potential energy diagram for nitrogen. (Taken from F.R. Gilmore, J. Quant. Spectry. Radiative Transfer 5 (1965) 369.)

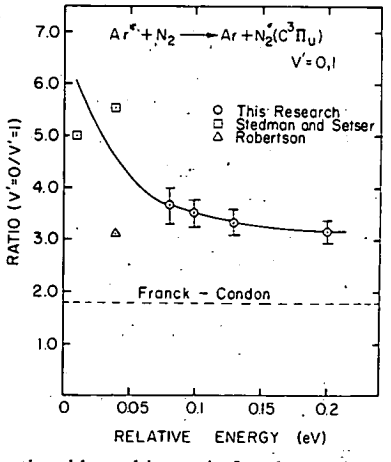

Fig. 2. Vibrational branching ratio for electronic energy transfer in collisions of metastable argon atoms with nitrogen as a function of relative collision energy. The dashed line represents the ratio for a vertical (Franck–Condon) transition from N_2 (X) → N_2 (C)

this purpose. The crossed nozzle-beam configuration should also provide a larger signal and better definition of relative velocity.

Acknowledgement

We wish to express our appreciation for the invaluable help of Mr. R.J. Dugan, Electronics engineer, and Mr. E.C. Whitehead, instrument maker, in the design and construction of the apparatus.

References

[1] D.H. Stedman and D.W. Setser, Progr. Reaction Kinetics 6 (1971) 193.
[2] W.W. Robertson, J. Chem. Phys. 44 (1966) 2456.
[3] D.W. Setser, D.H. Stedman and J.A. Coxon, J. Chem. Phys. 53 (1970) 1004;
D.H. Stedman and D.W. Setser, J. Chem. Phys. 52 (1970) 3957.
[4] D.H. Winicur and J.L. Fraites, J. Chem. Phys. 61 (1974) 1548.
[5] W. Lee and R.M. Martin, J. Chem. Phys. 63 (1975) 962.
[6] R.A. Sanders, A.N. Schweid and E.E. Muschlitz Jr., in: Electronic and atomic collisions, eds. J. Risley and R. Geballe (University of Washington Press, Seattle, 1975) p. 241, 242.
[7] R.A. Sanders, Ph.D. Dissertation, University of Florida (1975).
[8] S.Y. Tang, A.B. Marcus and E.E. Muschlitz Jr., J. Chem. Phys. 56 (1972) 566;
M.E. Gersh, G.D. Sides, S.Y. Tang and E.E. Muschlitz Jr., J. Appl. Phys. 44 (1973) 5356.
[9] J.B. Anderson, R.P. Andres and J.B. Fenn, Advan. Chem. Phys. 10 (1966) 275.
[10] W. Benesch, J.T. Vanderslice, S.G. Tilford and P.G. Wilkinson, Astrophys. J. 143 (1966) 236; 144 (1966) 408.
[11] S.Y. Tang, Ph.D. Dissertation, University of Florida (1970).

Reprinted from
CONTEMPORARY PHYSICS, Vol. 16, No. 2, March 1975

REACTIVE SCATTERING OF MOLECULAR BEAMS

BY

MALCOLM A. D. FLUENDY

Department of Chemistry, University of Edinburgh,
Edinburgh, EH9 3JJ, Scotland

CONTEMP. PHYS , 1975, VOL. 16, NO. 2, 147–172

Reactive Scattering of Molecular Beams

MALCOLM A. D. FLUENDY

Department of Chemistry, University of Edinburgh,
Edinburgh, EH9 3JJ, Scotland

SUMMARY. The rate and mechanism of chemical change has been studied for many years but until recently experimental work has been concerned with bulk systems so that the microscopic level of action was manifest only in some average way. In contrast, methods such as X-ray scattering yield direct information on molecular structure. The technique of molecular beam scattering is now a similar tool, capable of probing the dynamics of chemical reaction at the molecular level and leading to an understanding of the process in terms of the trajectories of the atoms participating. Discussion of the reaction is thus naturally in quantum channel cross-section terms; a change in emphasis, from conditions in the bulk sample to the collision proper, which has stimulated theoretical work. In particular, concepts and techniques developed for use in the atomic and nuclear collision field have been extended into this area. These rather rigorous calculations will be limited to the very simplest systems but, nevertheless, will form an important proving ground for more approximate models.

1. Introduction and theory

The range of processes that can occur when atoms or molecules collide is very large, ranging from slow collisions between spherically symmetric atoms that may be closely elastic, i.e. billiards ball in character, to the complexities of the chemical reactions that are important in biochemistry. Of the latter, most occur in solution, or at interfaces, where the properties of the liquid/surface play as important a part as the reactive encounter itself in determining the result.

In previous articles (Massey 1971, 1972, 1973) the phenomena associated with atomic collisions including diffraction effects and energy transfer have been discussed. In this article we attempt to extend this series by considering simple chemical reactions which occur in the gas phase so that the primary chemical change results from a single two-body collision. Even with this restriction a wide variety of reactions are found, many of great technical or natural significance. For example:

$$\begin{aligned} O + CH_4 &\rightarrow OH + CH_3 \\ H + O_2 &\rightarrow OH + H \end{aligned} \qquad (1)$$

are important in combustion, still the chemical process of most commercial significance. While the reaction

$$O_3 + NO \rightarrow NO_2 + O_2 \qquad (2)$$

is an important sink for atmospheric ozone and has been the centre of some controversy concerning the possible depletion of the ozone layer and consequent deleterious change in the solar radiation reaching the earth's surface. Turning even further afield:

$$O + H_2 \rightarrow OH + H \qquad (3)$$

has been suggested as a source of interstellar hydroxyl radicals.

In these examples, and indeed generally, it is the behaviour of a bulk mixture of the reactants which is of interest. The ultimate condition reached is determined by thermodynamics and an equilibrium mixture of products and reactants evolves in which the product/reactant ratio is determined by the properties of the isolated molecules. This rather well-understood long time limit provides no information as to the rate at which a reaction proceeds, which is often the practically important quantity. In a bulk system this rate is expressed as a rate constant, k, where using reaction (2) as an example:

$$\frac{\mathrm{d}[NO_2]}{\mathrm{d}t} = k[O_3][NO] \tag{4}$$

and where the square brackets denote concentrations of a species. Measurement of the time dependent reactant or product concentrations has been the classic tool of chemical kinetics and permits the elementary steps (commonly several reaction paths proceed competitively and consecutively in a bulk sample) to be identified and the associated rate constant determined. Historically the practical importance of bulk systems in chemistry concentrated interest on rate constants and their measurement, in contrast to the situation in nuclear or elementary particle physics where the microscopic collision process itself was of central interest and the description was naturally in terms of cross-sections for a specific channel.

Unfortunately the rate constant depends very strongly on the distribution of velocities and internal molecular states (vibration, rotation and electronic) in the molecules of bulk sample. Thus:

$$k(T) = \sum_j \sum_i f(i,T) \int_0^\infty \int_0^{2\pi} \int_0^\pi \sigma_{ij}(E,\theta,\phi) \sin\theta \, I(E,T) \left(\frac{2E}{\mu}\right)^{1/2} \mathrm{d}\theta \, \mathrm{d}\phi \, \mathrm{d}E \tag{5}$$

where $k(T)$ is the rate for production of product, all states, $\sum_j$ the sum over exit states j, $\sum_i$ the sum over incident states i, and where $\sigma_{ij}(E,\theta)$ is the differential cross-section in the channel $i \rightarrow j$ (the subscripts stand for all the quantum numbers required to label the reactants and products completely) and represents the probability of reaction in that channel between reactants with reduced mass μ and translational energy E scattering the product in state j at θ,ϕ. $I(E,T)$ and $f(i,T)$ are the distributions in translational energy and internal state i at the temperature T.

The rate constant is clearly a quantity in which the dynamic behaviour, contained in the cross-section, is very highly averaged by the distribution functions appropriate to the bulk mixture. Although formally eqn. (5) might be unfolded to yield the microscopic cross-section the measured temperature dependence of $k(T)$ normally only allows a threshold energy for an averaged total reaction cross-section for the state distribution in the mixture to be estimated. Rate constant data thus yields only rather weak constraints on any model of the collision itself so that it is difficult, for example, to determine whether models based on statistical assumptions owe their validity to the collision mechanics or to the averaging over collisions in different incident states, etc., in the bulk sample.

In contrast the differential reaction cross-section has a much greater dynamical content and poses a severe challenge to theory. In particular, cross-sections provide direct information as to the range and energy dependence of reaction, data that enables an understanding of the encounter in terms of the trajectories (dynamics) of the nuclei to be reached. (The simplistic classical picture is respectable since atomic masses are large enough for the path to be well defined in most circumstances). The new interest in chemical kinetics is thus in the detailed *dynamics* of reaction. Experimentally two techniques have been important in meeting this challenge: kinetic spectroscopy and molecular scattering. The latter class of experiments attempts to measure the cross-sections directly by measuring the angular distribution of product resulting from collisions between well defined beams of reactant molecules and in principal provides complete channel differential cross-section data though some degree of averaging (e.g. over rotational states) is usual. The various techniques of kinetic spectroscopy on the other hand yield only rate constants but these may now be for specific quantum channels, i.e. the summations in eqn. (5) are at least partially removed. In these experiments the reaction is initiated either by mixing the reagents or by generating them *in situ*, for example, by photodissociation so that short-lived states may also be studied. The concentration of various reactant or product states is then followed either by absorption or by observing the emission from excited electronic or vibrational product at very low densities (chemiluminescence). The two techniques are somewhat complementary since beam scattering is most effective in examining the angular and energy dependence of the process while spectroscopic methods attack eqn. (5) from the other end, yielding information primarily about state distributions. The recent combination of the two methods in laser induced fluorescence analysis of the scattered product flux in beam experiments is thus a most promising development.

The complexity of chemically reactive processes suggests that the rigorous methods of quantum scattering theory that have been so successful in understanding atomic collisions, as discussed for example in the general references cited will have a much more limited role to play. Nevertheless, attempts to stitch this seam between physics and chemistry, at least for the simplest processes of this type, have been in progress for the past forty years. Unfortunately, quantitative agreement between rigorous theoretical results and experiment is still some distance away, not least because adequate experimental data on quantum cross-sections is still lacking. These computations are thus of most interest at present in providing a yardstick against which other, more approximate, but perhaps more widely applicable methods may be compared. There is some hope also that studies of this kind may lead to symmetry related or other propensity rules which may be useful in more complex systems.

The simplest example of a chemical reaction is the exchange process:

$$\underset{\text{(para)}}{H+H_2} \rightarrow \underset{\text{(ortho)}}{H_2+H} \qquad (6)$$

which may be monitored, for example, via the heat capacity change involved in the ortho–para conversion. Alternatively cross-sections for inelastic processes such as rotational excitation which involves both a direct and a

contribution due to exchange of two atoms may be studied. This system is also that in which the largest quantum effects can be expected so that comparison of exact results with results from classical or semi-classical theories will be especially interesting. The non-relativistic Hamiltonian for the complete system is:

$$H=\sum_i T_{e_i}-\sum_i\sum_\alpha V_{e_iN_\alpha}+\sum_i\sum_j V_{e_ie_j}+\sum_\alpha\sum_\beta V_{N_\alpha N_\beta}+\sum_\alpha T_{N_\alpha} \tag{7}$$

where the terms are respectively the sum over the three electrons of their kinetic energy operators, the coulombic electron-nucleus potential, the coulombic electron–electron potential and the inter nuclear coulombic repulsion. The final term is the kinetic operator for the motion of the three nuclei.

The Hamiltonian of eqn. (7) can conveniently be written as the sum of an electronic part, H_e, and a nuclear part H_n, the final term in eqn. (7). The total system wave function can likewise be factored into electronic and nuclear parts using an orthonormal basis set of functions $\psi_e^{(i)}(\boldsymbol{R},\boldsymbol{r})$ which depend only parametrically on $\boldsymbol{R}$, the relative nuclear coordinates. The Schroedinger equation describing the motion of the system is then:

$$(H_n+H_e)\sum_i\psi_e^{(i)}(\boldsymbol{R},\boldsymbol{r})\chi_n^{(i)}(\boldsymbol{R})=E\sum_i\psi_e^{(i)}(\boldsymbol{R},\boldsymbol{r})\chi_n^{(i)}(\boldsymbol{R})$$

where $\chi_n^{(i)}(\boldsymbol{R})$ is the nuclear wave function and $\boldsymbol{r}$ represents the electron coordinates. Multiplying from the left by the functions $\psi_e^{(i)}$ in turn and integrating over the electron coordinates yields a series of equations

$$\sum_j\int\psi_e^{(i)}H_n\psi_e^{(j)}\chi_n^{(j)}d\boldsymbol{r}+\sum_j\chi_n^{(j)}\int\psi_e^{(i)}H_e\psi_e^{(j)}d\boldsymbol{r}=E\chi_n^{(i)}.$$

Since the electron velocity is very large in comparison with the velocity of the nuclei in low energy collisions, the electronic wave functions $\psi_e^{(i)}$ do not normally vary rapidly with R. Thus $H_n\psi_e\chi_n\simeq\psi_eH_n\chi_n$ and we obtain in this approximation (the well-known Born-Oppenheimer one) a coupled set of relations

$$(H_n+V_{ii}-E)\chi_n^{(i)}=-\sum_{j\neq i}V_{ij}\chi^{(j)} \tag{8}$$

where

$$V_{ij}(\boldsymbol{R})=\int\psi_e^{(i)}(\boldsymbol{R},\boldsymbol{r})H_e\psi_e^{(j)}(\boldsymbol{R},\boldsymbol{r})d\boldsymbol{r}$$

to describe the motion of the nuclei in the collision. If the functions $\psi_e^{(i)}(\boldsymbol{R},\boldsymbol{r})$ are chosen to be the eigenstates of H_e the off diagonal terms V_{ij} vanish. The nuclear motion now takes place over a single potential surface $V_{ii}(\boldsymbol{R})$ generated point by point from the solution of the electronic or 'clamped nuclei' Schroedinger equation.

$$H_e\psi_e^{(i)}(\boldsymbol{R},\boldsymbol{r})=V_{ii}(\boldsymbol{R})\psi_e^{(i)}(\boldsymbol{R},\boldsymbol{r}) \tag{9}$$

in which all effects due to the relative motion of the two nuclei are omitted. Of course, this choice of ψ_e would be unfortunate if ψ_e varied rapidly with R. In this event the diagonal representation is inadequate and a different basis set for the expansion must be chosen. The nuclear motion is then no longer confined to a single potential surface but may cross from one surface to another under the influence of the off diagonal V_{ij} terms.

Most theoretical work involving reactive collisions, however, has been confined to situations involving only a single potential surface. The problem then falls into two parts—the calculation of the potential surface and the scattering properties of the particles on this surface. At the present time the potential surface even for the H_3 system is not known with very great accuracy. The difficulties include the sheer numerical effort involved in computing multicentre integrals as well as covering the hyper-surface with a sufficiently dense mesh of points to permit interpolation. Furthermore, since thermal energy collisions may be sensitive to changes in the potential surface of less than 0·02 eV it is clear that a very considerable effort will be needed to obtain useful results. The problem is particularly urgent since experimental data cannot yet yield much direct information in these matters. In this situation semi-empirical hyper-surfaces involving a judicious blend of theory but adjusted to conform with available experimental data are useful. For H_3 such a surface is the ' Porter-Karplus ' shown in fig. 1 as an energy contour plot. Owing to the high dimensionality of the surface only a specific cut can be shown in this manner. That chosen corresponds to a collinear approach of the attacking atom to the molecule. The reactant entrance valley is at the lower right of the figure and a saddle point corresponding to a barrier height of 0·396 eV separates the reactants from the products, top left. For the $H-H_2$ system the surface is, of course, symmetric with respect to products and reactants. Bent configurations are considerably more energetic as can be seen from fig. 2, so that near threshold the reaction will pass close to this region of space.

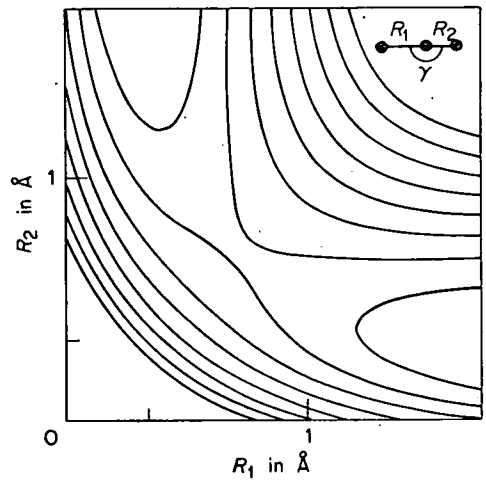

Fig. 1. Potential surface for the system $H+H_2$ in the collinear configuration, energy zero relative to separate H and H_2. (Porter 1964.)

The dynamics of the motion over the potential hyper-surface in the B.O. approximation follow from the nuclear Schroedinger eqn. (8). The difficulty of this full three-dimensional three body problem have led to many calculations in one or two dimensions or along specific paths, such as that along the line of lowest energy, through the potential. An instructive calculation of this type (McCullough 1971) confined to collinear collisions of the atoms, i.e. that part of the potential surface shown in fig. 1 used a time-dependent quantum method

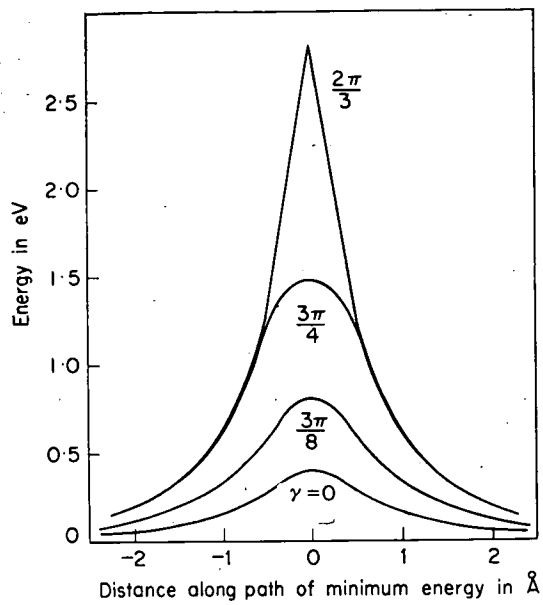

Fig. 2. Cut along the path of minimum energy in fig. 1 for various angles of bend γ, $\gamma=0$ is the collinear arrangement of the three atoms. (Porter 1964.)

to follow the evolution of a series of wave packets moving on the surface and compared their behaviour with that computed for a purely classical particle. The classical and q.m. probability distributions snapped at the same time instant are very similar (fig. 3) though plots at later time reveal an increasing probability for the quantum particles to cut the corner. Plots of the quantum flux revealed rather striking vortex behaviour with some flux actually moving in a backward direction, towards reactants. This sort of turbulent flow was found to depend strongly upon the curvature in the surface near the saddle

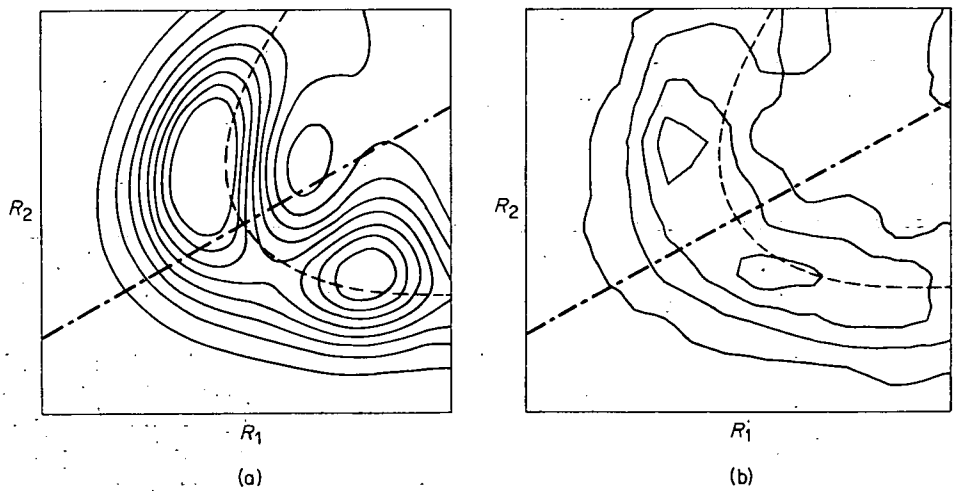

Fig. 3. Quantum (*a*) and classical (*b*) probability densities in the $H+H_2$ collision calculated at the same time instant $\sim 10^{-14}$ s after start of the collision. Collision energy = 0·38 eV. (McCullough 1971.)

point. The reaction probability, defined as probability of configurations on the product side of the symmetric position line, reached its asymptotic value after $\sim 2 \times 10^{-14}$ s (slightly earlier in the case of classical particles) a time comparable to that required for an interactionless fly by, indicating a direct type of collision not involving quasi bound states.

More usually a time independent steady-state formalism is used in which the relative translational motion of the reactants is represented as a continuous flux across a plane front. This viewpoint is most easily introduced by considering the simplest case: the motion of two particles over a single potential surface, $V(R)$, which depends only on their relative distance and not upon their orientation. The problem is thus formally identical with that of the hydrogen atom (with a suitable change in the potential) and the solution is correspondingly similar. The total wave function (in centre of mass coordinates) depends only upon the relative position of the two particles and can be factored into radial, $f_{lm}(R)$, and angular, $Y(\theta,\phi)$, parts. The radial wave functions are the solutions of:

$$\frac{1}{R^2}\frac{\mathrm{d}}{\mathrm{d}R}\left(R^2\frac{\mathrm{d}f_{lm}}{\mathrm{d}R}\right)+\left\{\frac{8\pi^2\mu}{h^2}(\mu v^2/2-V(R))-\frac{l(l+1)}{R^2}\right\}f_{lm}=0$$

where μ and v are the reduced mass and initial relative velocity. While the angular solutions are the spherical harmonics $Y_{lm}(\theta,\phi)$. In the scattering problem the orbital angular momentum number l is related to the impact parameter b characteristic of each collision trajectory (b is the closest distance to which the particles would approach along a specific trajectory if there were no potential operating) and $l \simeq (\mu v b/\hbar)$. Since all values of l are represented in the incident plane wave (reflecting the experimental fact that it is not possible to prepare collisions with specific b s) a solution for $f_{lm}(R)$ must be found for every l or ' partial wave '. The incident wave $\psi(\boldsymbol{R})$ can thus be written:

$$\psi(\boldsymbol{R})=\sum_{l=0}^{\infty} a_{lm} f_{lm}(R) Y_{lm}(\theta,\phi)$$

where the coefficients a_{lm} are chosen to satisfy the initial condition of an incident plane wave. In the collision problem it is only the asymptotic large R behaviour which is of interest and in this special case since there are no processes which can remove flux from an incident partial wave the only result of collision is a change in the phase of $f_{lm}(R)$. The post scattering wave function is thus as above but with appropriately modified coefficients and the intensity as a function of angle (the differential cross-section) can be computed from a knowledge of the phase shifts in $f_{lm}(R)$.

In the more general case in which energy transfer or chemical reaction may occur on collision there are many channels by which incident flux in a partial wave can be transferred to other final states and the asymptotic amplitude as well as the phase in every accessible final state is of interest. The wave function for the system must now include the internal coordinates $\boldsymbol{r}$, so that

$$\psi(\boldsymbol{R},\boldsymbol{r})=\sum_{lml'm'\nu} a_{lml'm'\nu} f_{lml'm'\nu}(R) Y_{lm}(\theta,\phi) U_{\nu}(\boldsymbol{r}) \qquad (10)$$

where U_{ν} is the wave function for the *internal* motion of the two particles in the state ν and the summation extends over all incident and exit states

since neither l, m or ν are conserved during the collision. If the motion is electronically adiabatic only a single potential surface, calculable from eqn. (9) in the clamped nuclei approximation is used. The nuclear Hamiltonian for the collision system can be written down and substitution of the expression (10) in the wave equation followed by some manipulation then leads to an infinite set of coupled differential equations, exactly analogous to those in eqn. (8) describing the motion and the coupling between the incident and various exit states. Truncation to include only the physically important states reduces the set to finite size so that numerical solution to find the asymptotic behaviour, amplitude and phase, is possible though difficult.

Calculations of this type have recently been made for $H+H_2$ using the full three-dimensional Porter–Karplus surface and rotational states up to $j=6$ in the ground vibrational state. Since each rotational state is $2j+1$ degenerate, many channels are involved and this currently limits the size of these computations. A comparison of classical and quantum results from this work for the differential cross-section for scattering from the $j=0$ to $j=1$ state (exchange (reaction) and direct contributions combined) is shown in fig. 4.

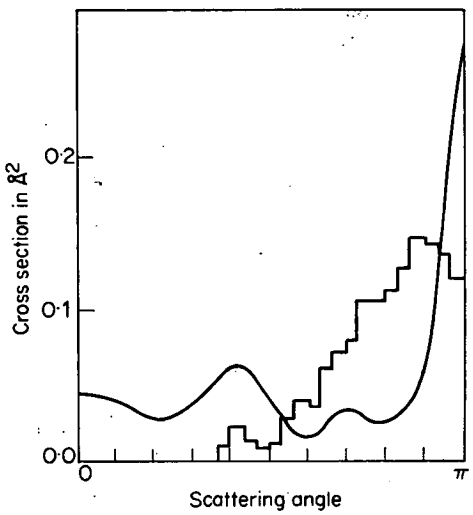

Fig. 4. Differential cross-section for scattering from the $j=0$ to $j=1$ rotational state in $H+H_2$ collisions. The histogram is the result of classical trajectory calculations for the process $j=0\rightarrow$all other states. Collision energy = 0·5 eV.

Results using larger basis sets and in particular including additional vibrational channels will be available in due course so that a rather precise understanding of the quantum dynamics over this surface should be possible. This degree of rigour will only be obtainable in a few systems, such as for hydrides which have a wide rotational level spacing, and for the overwhelming majority of reactions a much more approximate method that will nevertheless allow the important features of the potential surface to be correlated with the reaction dynamics is needed.

Models of this type fall into three classes shown schematically in the table. The phenomenological models have as their goal the representation of the

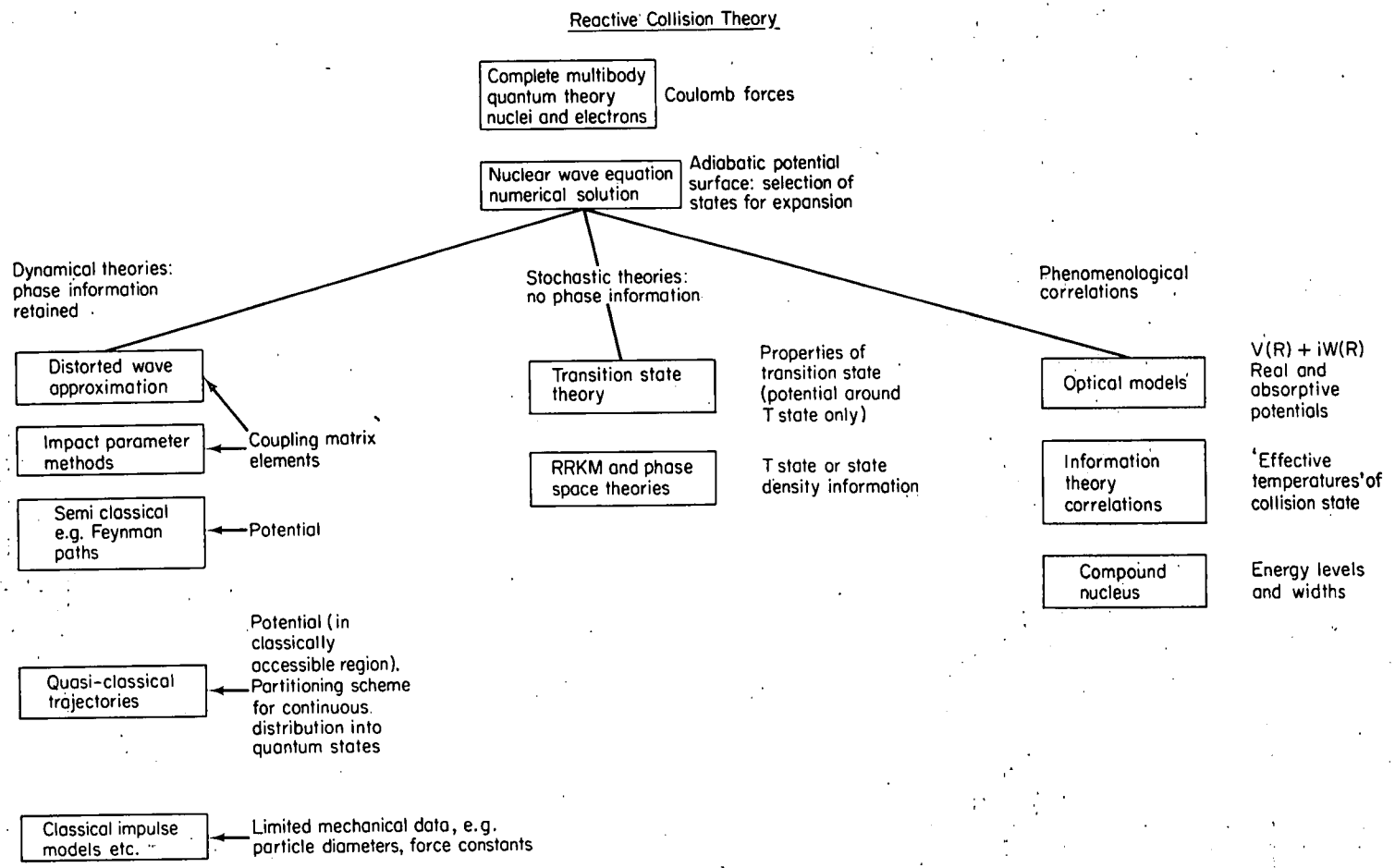
Reactive Collision Theory
Complete multibody quantum theory nuclei and electrons
Coulomb forces
Nuclear wave equation numerical solution
Adiabatic potential surface: selection of states for expansion
Dynamical theories: phase information retained
Stochastic theories: no phase information
Phenomenological correlations
Distorted wave approximation
Impact parameter methods
Coupling matrix elements
Semi classical e.g. Feynman paths
Potential
Quasi-classical trajectories
Potential (in classically accessible region). Partitioning scheme for continuous distribution into quantum states
Classical impulse models etc.
Limited mechanical data, e.g. particle diameters, force constants
Transition state theory
Properties of transition state (potential around T state only)
RRKM and phase space theories
T state or state density information
Optical models
V(R) + iW(R) Real and absorptive potentials
Information theory correlations
'Effective temperatures' of collision state
Compound nucleus
Energy levels and widths

results of reactive collisions in terms of a relatively few parameters in the same way that thermodynamic quantities correlate equilibrium properties. Thus product energy distributions may be characterized in some cases by an 'effective temperature' parameter.

Dynamical models yield the most detailed predictions since the complete potential surface is required as input data and phase information can be retained if required. The most useful model of this type is that of trajectory simulation. For a system of N atoms there are $6N-6$ coupled Hamiltonian equations which describe the relative classical motion:

$$\frac{\partial H}{\partial p_i} = \dot{q}_i; \frac{\partial H}{\partial q_i} = -\dot{p}_i \qquad (11)$$

so that if a potential surface describing the interaction of all the atoms is constructed the equations of motion can be solved numerically in a stepwise fashion using a large computer to yield the trajectories of the atoms. By choosing starting points for these trajectories from a population representing the initial state of the system being modelled the average results of a large number of such trials form estimates for the dynamical properties of the system. For example, the location of the energy release in a reaction (i.e. as reactant attraction or product repulsion) can be seen to correlate with the distribution of this energy between internal excitation of the products and their relative translational energy, fig. 5. Late energy release leads to translationally 'hot' products.

Inspection of the trajectories themselves may reveal the role of specific features in the potential surfaces. A trajectory calculated for the $H+H_2$ collision on the surface of fig. 1 shows (fig. 6) a collision of short duration, the three atoms approaching and receding quite smoothly. Collisions of this kind are known as *direct*. In contrast, the potential surface for the reaction $NaCl+KBr \rightarrow NaBr+KCl$ has a number of minima at close configurations, the deepest corresponding to a rhombhedral arrangement of the four atoms while shallow minima are found for linear arrangements. Trajectories such as that shown, fig. 7, following complicated paths and having lifetimes of up to 2500×10^{-14} sec are now seen and may decay either to reactants or products. Collisions of the direct type are also possible and contribute increasingly at higher energies, so that both *direct* and *complex* dynamics occur on this surface.

These calculations are based on classical mechanics, though extensions to this method incorporating at least approximately the effects of quantum mechanics have been made. In these developments the phase shifts in the relative translational wave function, $f(R)$ in eqn. (10), produced by the collision are calculated along classical trajectories. Differential cross-sections for scattering, for example, are then calculated by summing the results of individual trajectories but with the appropriate phase factor. In contrast with the purely classical calculations this approximation reveals the interference effects that occur when scattering through the same angle arises from several different paths through the collision.

In the absence of complete quantal calculations it is impossible to make a detailed comparison of the two types of calculation. Nevertheless, except near threshold energies or when only a few quantum states are accessible, so that the problem of allocating the continuous classical distribution from

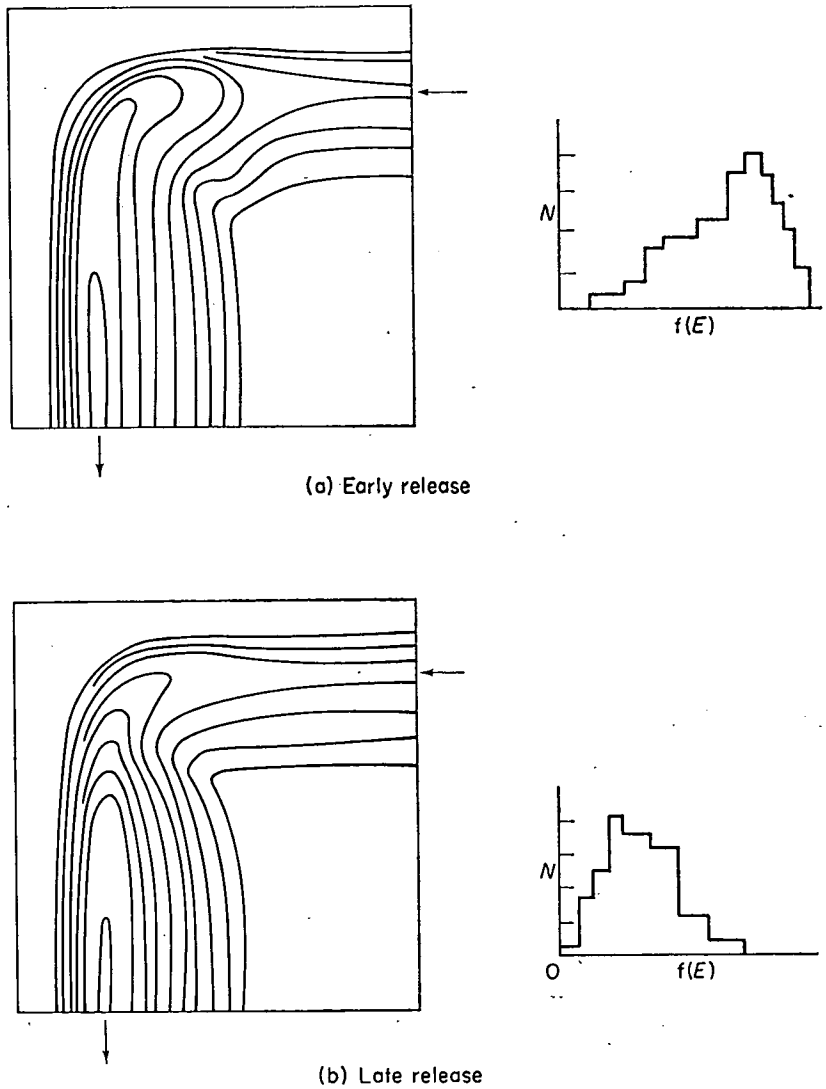

Fig. 5. The effect of early (*a*) and late (*b*) release of reaction exothermicity on the fraction of available energy, $f(E)$, that appears in internal modes of the product. (Bunker 1964.)

this type of calculation into quantum boxes becomes severe, the methods appear to yield results in good agreement with quantum calculations. It has certainly become one of the most useful tools in the interpretation of experimental data.

The third class of theories view the transient collision system as a distinct species with a known structure and consider some critical configuration. The assumption is then made that all quantum states in this region of phase space that are accessible given the energy and angular momentum constraints that are built in at the birth of the ' complex ' are equally populated. This may be true either for collisions averaged over impact parameters or perhaps more

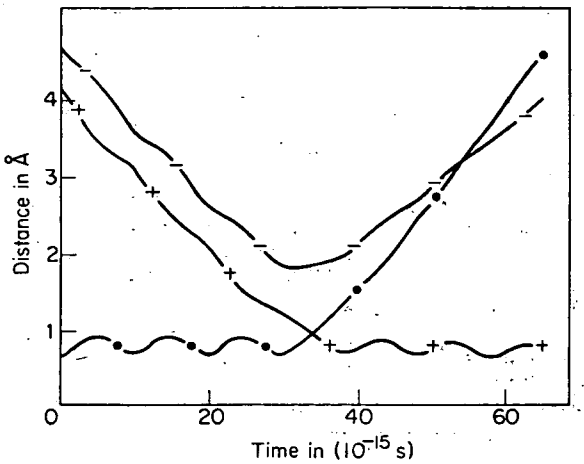

Fig. 6. Classical trajectory for the $H+H_2$ collision at 1·2 eV on the Porter Karplus surface. The interatomic distance for each atom pair is plotted as a function of time. The collision results in reaction. (Karplus 1970.)

generally over a small range, e.g. of collision energy. Once in this critical configuration some probability is associated with decomposition of the complex to products or back to reactants. This type of theory is applicable to systems in which all the modes are strongly coupled; collisions with long lifetimes generally fall into this class though formation of such a complex is neither a necessary nor a sufficient condition for validity.

In the phase space formulation strong coupling is assumed for collisions having impact parameters less than some value b_{max} and the critical configuration is taken at the well separated products. The probability of product formation from this configuration is thus unity and the cross-section for the reaction is:

$$\sigma_R = \pi b^2_{max} \frac{\text{number of accessible states in products}}{\text{total number of states accessible from complex}}. \quad (12)$$

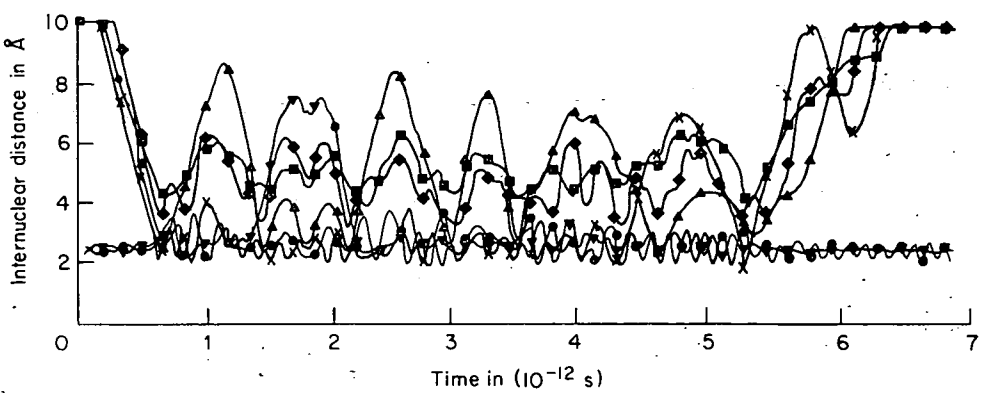

Fig. 7. Trajectory for a NaBr+KCl collision showing each interatomic distance. (Brumer 1973.)

The RRKM theory is similar but now identifies the critical configuration for a reaction channel as occurring when an energy E_c is exceeded in a specified degree of freedom, a vibration along the dissociation axis of the complex. The lifetime of a complex of energy E in this model is given by:

$$\tau = \frac{1}{\nu}\left(\frac{E}{E-E_c}\right)^{(s-1)} \tag{13}$$

where s is the effective number of oscillators and $\bar{\nu}$ is the average vibrational frequency in the complex. In theories of this type there is no potential information input, except that inherent in the structure assumed for the complex, once the original statistical assumption is made so that the quantities b_{max}'s, etc., are essentially parameters available for fitting data and from which rather intuitive conclusions may be drawn. On some surfaces the statistical approach may be valid in some regions but not others, while on surfaces containing wells at close configurations of all the atoms (which are conducive to complex formation) but which also have sizeable product interactions on the exit side of the potential, dynamical effects, such as excess translation energy in the products, may be superimposed on an otherwise statistical distribution. Finally the transition state theory which is widely used in interpreting thermal rate date considers a critical region, length δ, near the saddle point of the surface. If reaction can be associated with a free translation at this point along a single dimension the concentration of 'activated complexes' with this configuration can be calculated using equilibrium statistical mechanics:

$$N^+ = \frac{Q^+}{Q_A Q_B}(2\pi m^+ kT)^{1/2}(\delta/h)[A][B]\exp(-E_c/kT) \tag{14}$$

where Q^+ is the partition function for the activated complex less one degree of freedom which is approximated as a free translation $(2\pi m^+ kT)^{1/2}(\delta/h)$ and Q_A, Q_B, [A][B] are the partition functions and concentrations of the reactant species. The rate of the reaction is now taken as:

$$\text{rate} = N^+(kT/2\pi m^+)^{1/2}/\delta \tag{15}$$

where $(kT/2\pi m^+)^{1/2}/\delta$ is the average time for a system to pass through the activated complex configuration and the rate constant for the reaction is:

$$\text{rate constant} = (kT/h)\frac{Q^+}{Q_A Q_B}\exp(-E_c/kT). \tag{16}$$

The input to the theory is thus Q^+ and E_c, i.e. limited potential information around the transition state region only. The validity of the assumptions in this model which does not depend upon the existence of a long-lived complex but upon the use of equilibrium arguments to calculate the concentration of the transition state are not clear. Trajectory calculations to check this point suggest that its success or otherwise may depend upon the nature of the potential surface.

2. Experimental

We have already seen that measurements of a cross-section for a reaction provide a much more stringent test of the theory for such collisions than a rate constant. This is true not only because much of the averaging, which makes a rate constant primarily sensitive to the Boltzmann distribution, is not present, but also because properties such as the differential cross-section can be related by quite straightforward mechanical arguments to the impact parameter or range dependence of processes. Measurements of this sort open the way to a dynamical understanding in terms of the trajectories followed by the individual atoms during the collision.

Measurements of these properties have most significantly been made by crossed molecular beam techniques; though other approaches using spectroscopic methods have also provided important information. In the cross beam technique two well collimated and approximately translationally monoenergetic molecular beams are allowed to intersect in a small volume of space under high vacuum conditions. Molecules in a beam passing through this volume make at most one collision with a molecule from the other beam: those that do collide are detected, e.g. by a mass spectrometer which rotates about the scattering centre, so that the collision rate can be measured as a function of angle. Some form of velocity analysis, for example by rotating a chopper wheel in one of the primary beams and observing the flight time of the product to the detector is also usual. A fairly typical apparatus for this class of experiment is shown in fig. 8. The apparent complexity of the equipment arises from the need to maintain good vacuum under conditions of large leakage (i.e. beam flow) so that many stages of differential pumping are required. The beam sources work under hydrodynamic flow conditions so that supersonic jets of the reagent gas expand from nozzles into the first vacuum chamber. This adiabatic expansion produces a large amount of cooling both in the *relative* translational velocities in the jet and in the internal degrees of freedom in the reagent. At the skimmer the continuum flow changes to isolated molecular streaming so this situation is frozen in and a beam with very low internal energy spread results. The detector, a mass spectrometer with an electron bombardment ionizer is located in a U.H.V. chamber, often with liquid He cryo-pumping, and is buffered from the beam intersection region by several stages of differential pumping. These precautions are required to separate the directly scattered product from the otherwise overwhelming signal coming from reaction of the background pressures of the reagents. After ionization and mass selection the ions are counted into a multichannel scaler or mini computer as a function of flight time from the chopper so that the product flux as a function of angle and velocity can be recorded. Specific experiments may differ from the configuration described but will usually retain most of the features mentioned. Thus state selectors or analysers using the rotational and orientation dependence of the electric dipole moment of a molecule have been used to examine the dependence of reaction upon these properties.

Tunable lasers have been used to pump reagent beams to specific vibrational states but more significantly as a product analysis tool. In this application a narrow band tunable laser beam irradiates the product flux and is swept in frequency through its characteristic spectrum. When the laser frequency coincides with a molecular absorption line the products make a transition to an

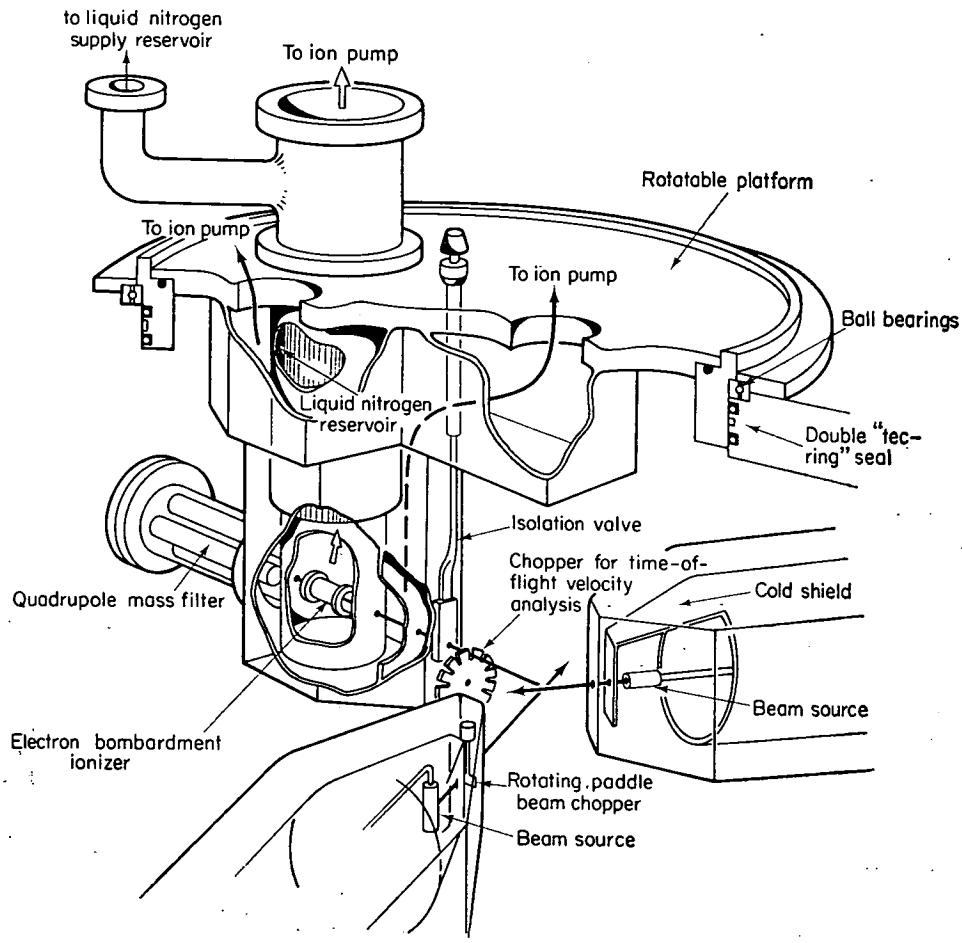

Fig. 8. View of a molecular beam scattering apparatus showing two beam sources in differentially pumped chambers, the scattering centre and a mass spectrometric detector which is swung about it. (McDonald 1972.)

excited electronic state and then reradiate (fluoresce). This radiation is detected and provides a signature for each particular product state. This system forms a sensitive and highly state selective detector, in which the dynamical and reagent state selection advantages offered by the molecular beam method are combined with the precision and selectivity in product analysis offered by spectroscopy. The technique is illustrated in fig. 9.

The very richness of chemistry in the number of reactions possible means that even though several hundreds have been investigated this represents only an infinitesimal sample. Nevertheless some general features have emerged and suggest, for example, that the distinction between direct and complex types of dynamics suggested as limiting behaviour by theory is a useful one. In this article no attempt will be made to provide an exhaustive catalogue of the systems studied, rather a few cases will be selected as examples, often of the extreme ranges of behaviour.

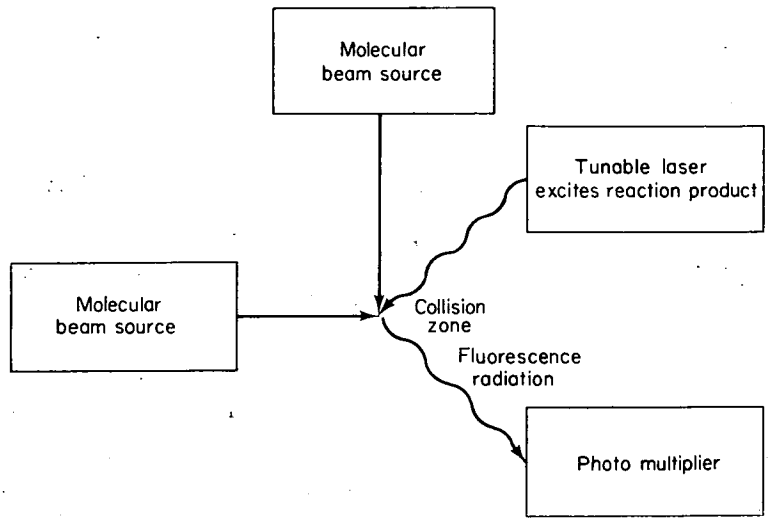

Fig. 9. Laser induced fluorescence technique for product state analysis.

(*a*) *Reactions on ionic potential surfaces*

Historically the earliest reactions studied by the molecular beam method were those involving alkali metals and halogen containing molecules such as:

$$\begin{aligned} K + CH_3I &\rightarrow KI + CH_3 \\ K + I_2 &\rightarrow KI + I. \end{aligned} \tag{17}$$

These reactions were attractive experimentally because the cross-sections were known to be very large (most chemists would describe them as explosions) and particularly since a sensitive detector, the differential hot wire, was available that could distinguish between alkali metal and alkali halide, the reactant and product in the examples. (A hot tungsten wire ionizes both species, a hot ' dirty ' platinum wire only the alkali metal.)

Although no *ab initio* computations are available for the potential surface in these systems it is clear (from spectroscopic evidence and semi-empirical calculations) that their adiabatic potential is dominated by the transfer of an electron from the alkali metal (with a low ionization potential, Ip) to the halogen containing molecule, which may have a substantial electron affinity Ea. The transfer occurs (adiabatically) at a distance:

$$R_c = e^2/(Ip - Ea) \tag{18}$$

where R_c may vary from several tens of angstroms downwards! (Clearly when R_c is large there must be a considerable probability of non-adiabatic effects even at thermal velocities.) At distances closer than R_c but outside the repulsive core where significant charge overlap occurs the interaction between the two molecules is coulombic. Since the alkali halide product is also ionic in structure the trajectories that lead to reaction do so under ionic forces that are strong and very long range in comparison with the dispersion forces operating between the neutral species and are also almost non-directional in

character. Once the electron transfer has occurred these processes could be described as ' no electron ' reactions. There are a large number of possible alkali/halogen, halide systems with different *Ip* s and *Ea* s so that the effect of varying the potential parameter R_c and the mass ratio of the species can be explored.

The collision dynamics of two reagents in a crossed beam can be represented in a Newton diagram, fig. 10. The two vectors $\boldsymbol{v}_K$, $\boldsymbol{v}_{I_2}$ are the initial laboratory velocities of the two beams intersecting at 90°, while $\boldsymbol{v}'_{KI}$, $\boldsymbol{v}'_I$ are the post collision velocities of the product. The process is most easily discussed in a coordinate system travelling with the centre of mass of the system, $\boldsymbol{c}$, so that the initial relative velocity is $\boldsymbol{w}_K + \boldsymbol{w}_{I_2}$. A series of final (post collision) relative velocities vectors $\boldsymbol{w}'_K$ for the production are also shown. The maximum final velocity corresponds to the formation of product KI in its ground vibrational state so that the whole exothermicity of the reaction plus the initial relative kinetic energy, E, all appear in the translational velocity of the product. Product formed in higher states appears at correspondingly slower CM velocities. In the laboratory the scattered flux along the vector $\boldsymbol{v}'_{KI}$ is measured: since a range of CM scattering angles χ can all appear at the same laboratory angle it is necessary to measure the laboratory velocity to obtain the CM angular distribution.

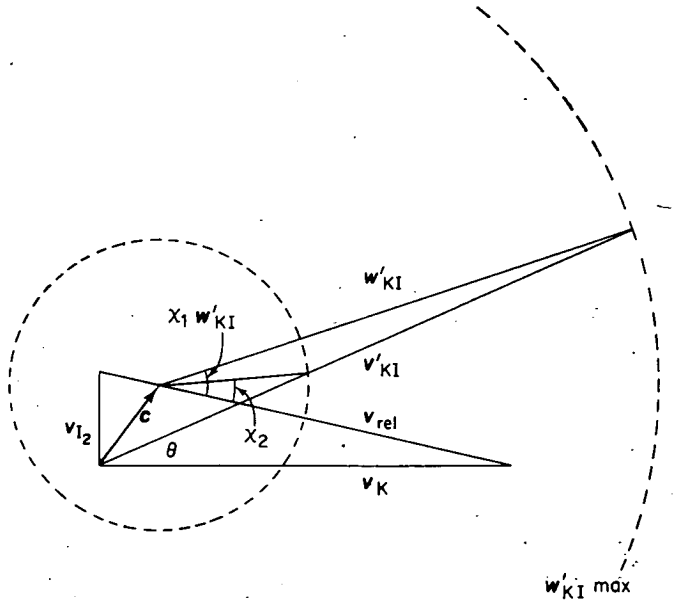

Fig. 10. Newton diagram representing collisions in the system $K+I_2 \rightarrow KI+I$.

Results of measurements of this type are normally plotted in centre of mass coordinates in a ' velocity contour map ' in which the vector distance from the origin represents the exit velocity of the product. Such a contour map for the process $K+I_2 \rightarrow KI+I$ is shown in fig. 11. The product KI is predominantly scattered in the forward direction, i.e. the same direction as the incident K atom and has a rather low most probable final velocity in comparison

with that permitted by exothermicity considerations. The product KI must therefore be formed in high vibration and/or rotation states. Integration of the reactive scattering over angle and velocity enables the total reactive cross-section to be measured; in agreement with other estimates a value of 127 A^2, a very large cross-section, is found.

In contrast the velocity contour map for the $K+CH_3I$ reaction, fig. 12, shows almost the reverse behaviour with backward or recoil scattering and most of the reaction exothermicity appearing in product translation, i.e. the product KI is internally cold. The total reaction cross-section at the collision energy of 0·15 eV for this process is ~ 35 Å^2 m^2.

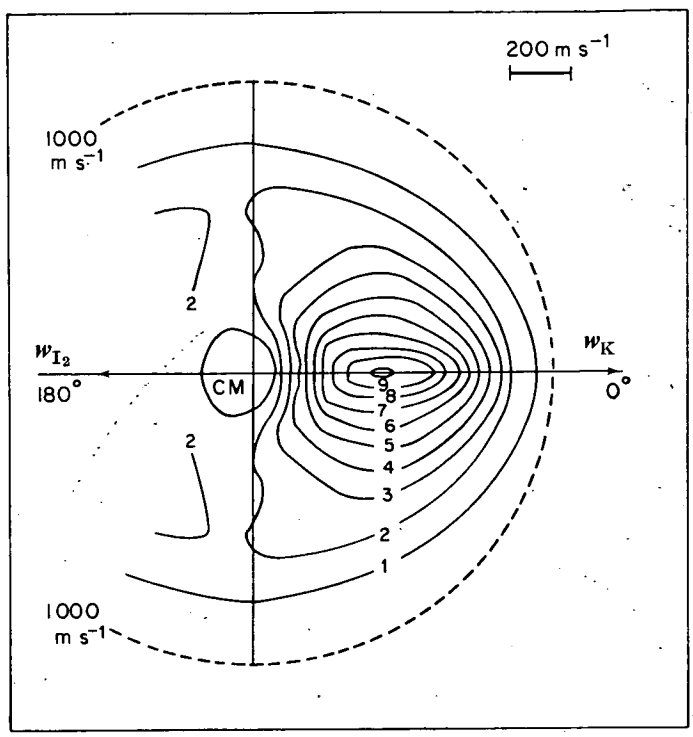

Fig. 11. Map of KI flux showing the distribution in angle and velocity in the CM frame of the product from the $K+I_2$ reaction. (Rulis 1972.)

Very detailed trajectory calculations have been performed on both these systems which are now perhaps the best characterized of any chemical reaction and judicious adjustment of the potential surface has permitted most of the observed behaviour to be reproduced. However, the most important features can be understood by considering the changes in the potential surface as R_c alters. In the K/I_2 reaction $R_c \sim 6$ Å, a distance at which the dispersion forces are still small and the potential is of the early downhill type with most of the reaction exothermicity being released as attraction between K^+ and I_2^- before the nonreacting I has moved an appreciable distance. The dynamics are like those in fig. 5 (*a*) and result in considerable vibrational excitation as the motion ' overshoots ' the exit valley and bounces out. Furthermore, the

I_2^- ion is only weakly bound and at the I_2 equilibrium distance at which it is presumably formed there is only a very weak force between the two iodine atoms. Thus the iodine atom remote from the attacking K is hardly coupled to the dynamics after electron transfer and 'spectates'. Conservation of momentum then requires the product to exit in the forward direction with an angular distribution governed by the momentum brought to the KI by the captured iodine. (The so-called stripping dynamics of nuclear physics.) Of course, small impact parameter collisions or those in which the spectating iodine atom undergoes a second collision with the nascent KI will occur and can be expected to have rather different dynamics; it is collisions of this type that may account for the small amount of transitionally hot product that is seen. However, these small impact parameter collisions contribute only 10–20 per cent to the overall product yield.

In the CHI_3/K reaction the methyliodide is only weakly electron negative and R_c is much smaller $\sim 3{\cdot}5$ Å. The captured electron presumably enters the lowest unoccupied orbital, 2σ, in the CH_3I which is dominantly located on the iodine atom. This is an antibonding orbital and at neutral CH_3I equilibrium carbon iodine distance produces a very strongly repulsive potential. Electron transfer thus switches on a repulsive force between the two products. The potential surface is of the late release or product repulsion type and we expect dynamics like these of fig. 5 (*b*) leading to low product internal excitation. Furthermore, since only small impact parameters, or almost head on collisions can reach R_c and so stand a chance of reacting we expect the product to recoil rapidly backwards as is observed.

Interestingly, the translational energy release in this reaction is very similar to that found in the photodissociation of CH_3I which involves excitation of an electron from a non-bonding to the same 2σ antibonding orbital, though in the reaction the presence of the K^+ ion must perturb the bonding scheme somewhat. The roughly Gaussian shape of the energy distribution seen in fig. 12 follows from Franck–Condon effects for transitions from the ground vibrational to the repulsive state of the CH_3I' as is also illustrated in the figure. These two reactions are both good examples of direct dynamics showing very non statistical energy distribution between product degrees of freedom and an angular distribution which is unsymmetric between forward and back directions. Of course, they represent rather extreme types of behaviour, but many other systems of this general ionic type fall between these examples depending upon R_c and the nature of the reactant negative ion.

The four centre ionic exchanges such as

$$Na + RbCl \rightarrow NaCl + Rb$$

and

$$NaCl + KBr \rightarrow NaBr + KCl$$

which have already been mentioned in the discussion of trajectory calculations illustrate a different type of dynamics: those involving the formation of a complex with a long life (in comparison with vibrational motion $\sim 10^{-13}$ s). If the assumptions of the RRKM model are valid the requirement for statistical behaviour is

$$\left(\frac{(E)}{(E-E_c)}\right)^{(s-1)} \gg 1$$

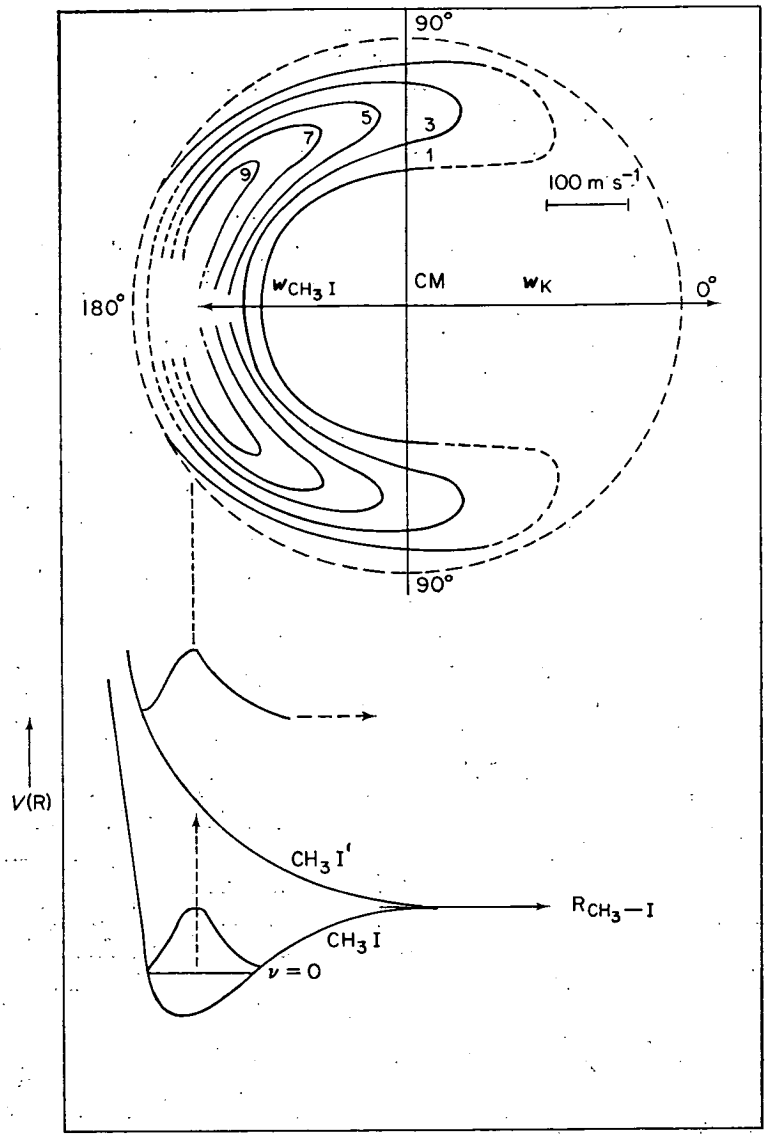

Fig. 12. Flux of KI product from $K+CH_3I$ reaction and illustration of a vertical transition from CH_3I to an antibonding state of CH_3I' on electron transfer. (Data from Gillen 1970.)

for the decay of the complex via any channel, differing channels possibly having different energy barriers. The most striking feature of the product distribution in this case is the forward back symmetry about $\pi/2$ which is characteristic of all collisions in which a complex living longer than its rotation period is formed. At first sight it would seem that the decay products from such a complex would be scattered isotropically. This is not the case, since the specified initial relative velocity in the collision produces a polarized complex even though the initial beams were unpolarized. The total angular momentum of the complex, J, is the sum of the internal angular momentum of the molecules forming the

complex, j_i, and their relative initial orbital angular momentum L_i. If the complex formation occurs with a large cross-section $L_i \gg j_i$ so that $J \simeq L_i$ and the total angular momentum of the complex (like L_i) will be distributed uniformly in a plane perpendicular to the initial relative velocity v. J is a constant of the motion so that on break up of the complex it must be partitioned again between the products' internal angular momentum, j_f, and their relative motion L_f. The angular momentum in the internal motion of the products is constrained only by conservation requirements but once fixed the angular distribution of product follows from geometry. The situation is illustrated in fig. 13. In fig. 13 (*a*) no angular momentum appears in the product and the exit relative velocities are distributed isotropically in a plane. Since J is also distributed in a plane about v the scattered product distribution results from compounding the two distributions to obtain the forward and backward peaked distribution shown. In the cases in (*b*) the product angular momentum is j_f so

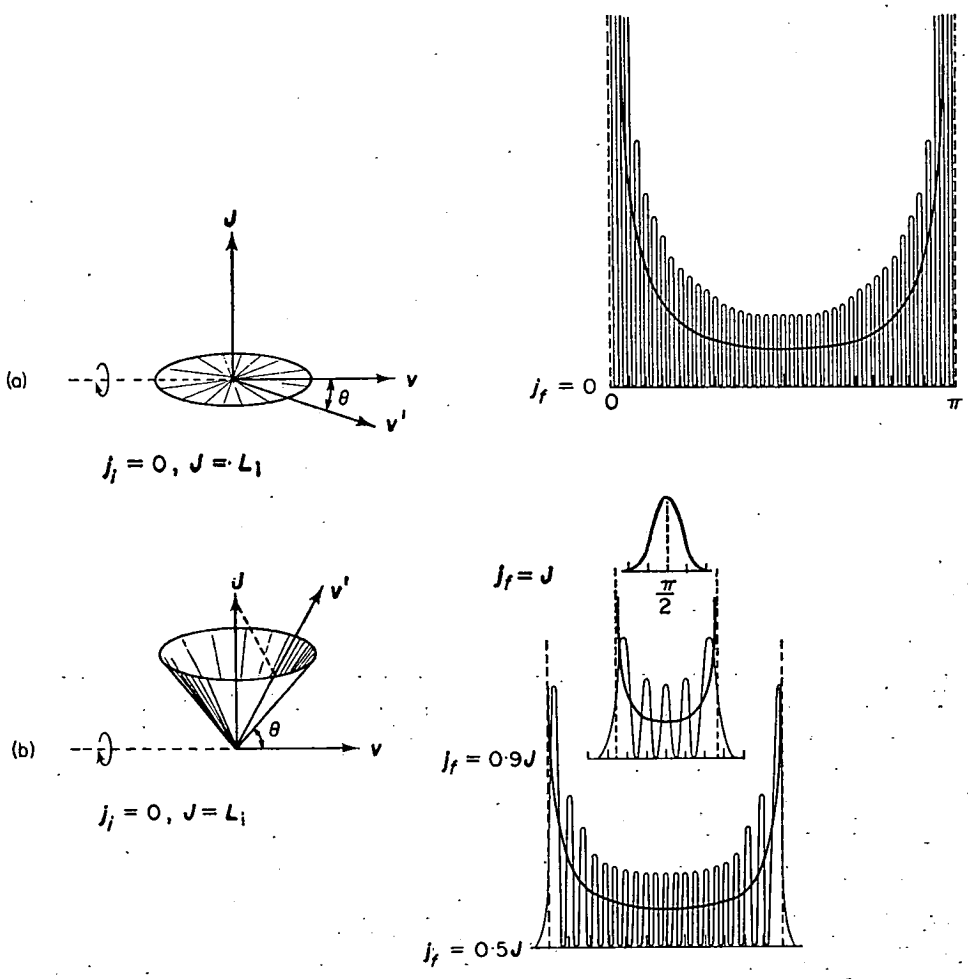

Fig. 13. Product angular distribution from a long lived complex showing the effect of different partitioning of the total angular momentum J in the complex between internal angular momentum of the products and orbital angular momentum at exit.

that L_f is tipped out of the incident plane and the scattering is restricted to a smaller angular range in the centre of mass and in the limit the scattering peaks at $\pi/2$.

In the reactions mentioned the scattering in the CM is symmetrically peaked at 0 and π indicating only weak rotational excitation of the product, a result which could be anticipated from the small exothermicity in these reactions which limits the possible rotational excitation, j_f. The distribution of energy between translation of the products and internal modes with 15–20 per cent appearing in translation is also in good agreement with a statistical model. The ratio of the two possible decay modes for the complex back to reactants or forward to products was, in contrast, markedly non statistical in the case of the four centre reaction. Instead of the almost equal decay rate expected in each direction (since the surface is almost symmetrical) only about half the expected product was found. From the trajectory calculation it appears that this deviation is due to two possible structures for the complex. The first in the region of the deepest well in the potential surface with a rather compact trapezoidal structure, the other structure is approximately linear and again corresponds to a minimum in the potential; in this case the exchange which must involve the interaction of the two ends of the chain is rather unfavourable since centrifugal forces operate to keep the chain extended, though not to limit energy flow.

(*b*) *Reactions on a covalent surface*

The potential surface between species in which no substantial charge polarization occurs are described as of covalent character. In direct contrast to ionic surfaces these tend to be rather short range and have marked directional properties. A good example of a reaction of this type is $F+H_2 \rightarrow HF+H$ for which very detailed data is available, both from molecular beam and chemiluminescence methods. The total reaction cross-section is 2 Å^2 at thermal energies and since the reduced mass is comparatively small the orbital angular momentum associated with those trajectories which react is quite small $\sim 30\hbar$ (cf. $J \simeq 700\hbar$ for $K+I_2$). The initial internal angular momentum of H_2 at thermal energies is also small and since the exit H atom can carry away only a small amount of orbital angular momentum the product HF cannot be rotationally very hot.

The scattering distribution, fig. 14, reflects this effect in the small islands of intensity corresponding to product formation in particular vibrational states. The width of each island being a measure of the rotational excitation in the product—the distribution is sufficiently narrow that the various vibrational state contributions do not merge (as in KI from $K+I_2$). The $v=4$ state of the HF is the dominant product so that this reaction produces a large vibrational population inversion and is in fact the basis for a chemical laser system. Even more detailed information can be obtained from chemiluminescence experiments, in which the i.r. radiation from the products in a time short with respect to any relaxation effects is used to determine the vibrational and rotational distribution of the product. This information on product state distribution is conveniently summarized in a triangle plot, fig. 15, in which each vertex represents total release of the reaction energy into

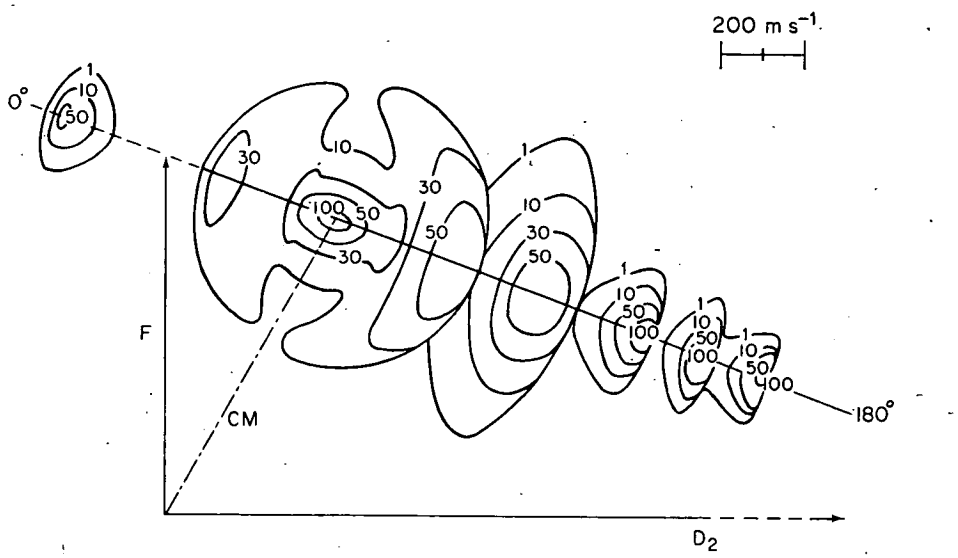

Fig. 14. Flux map for DF product from the reaction $F+D_2 \rightarrow DF+D$, laboratory distribution. The different vibrational states in the product are easily distinguished. (Schafer 1970.)

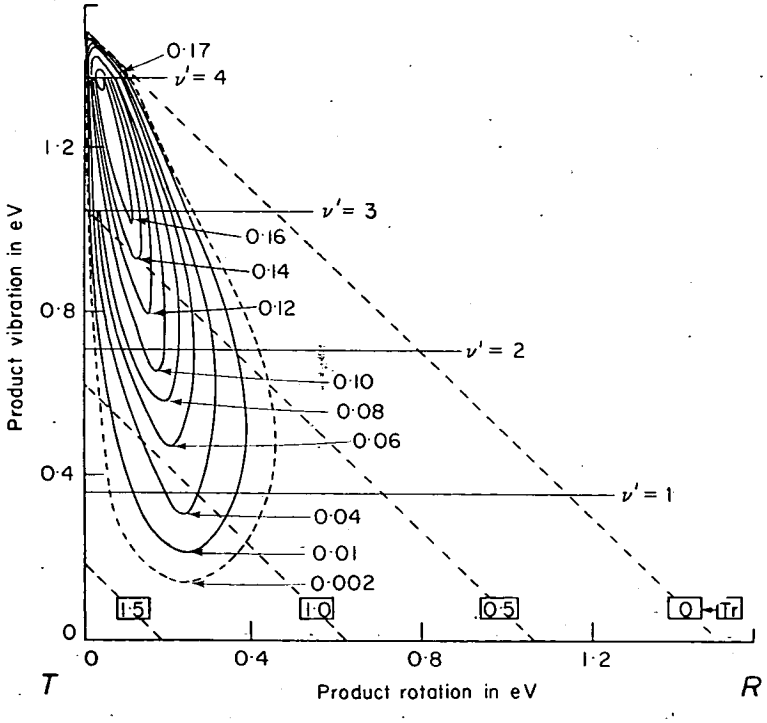

Fig. 15. Triangle plot for DF product from $F+D_2 \rightarrow DF+D$. (Polanyi 1972.)

either translational, vibrational or rotational energy. The figure shows that the product is rotationally quite cold with most of the reaction energy ending in vibrational excitation. Somewhat surprisingly, the observed vibrational distribution can be represented by a single temperature like parameter of -2700 K (as can the reaction $F+D_2 \rightarrow DF$ and a number of others). The significance of this apparently statistical distribution embedded in a direct collision process with very non-statistical overall behaviour is not clear. A potential surface has been calculated for this reaction though trajectory studies on it show the features of the reaction to be very sensitive to its details.

Reactions of the type $H+Cl_2$, Br_2, $I_2 \rightarrow HCl+Cl$, etc., are also of the direct type with the energy release into translation closely similar to that found in photodissociation, fig. 16, suggesting that the same electronic structure is

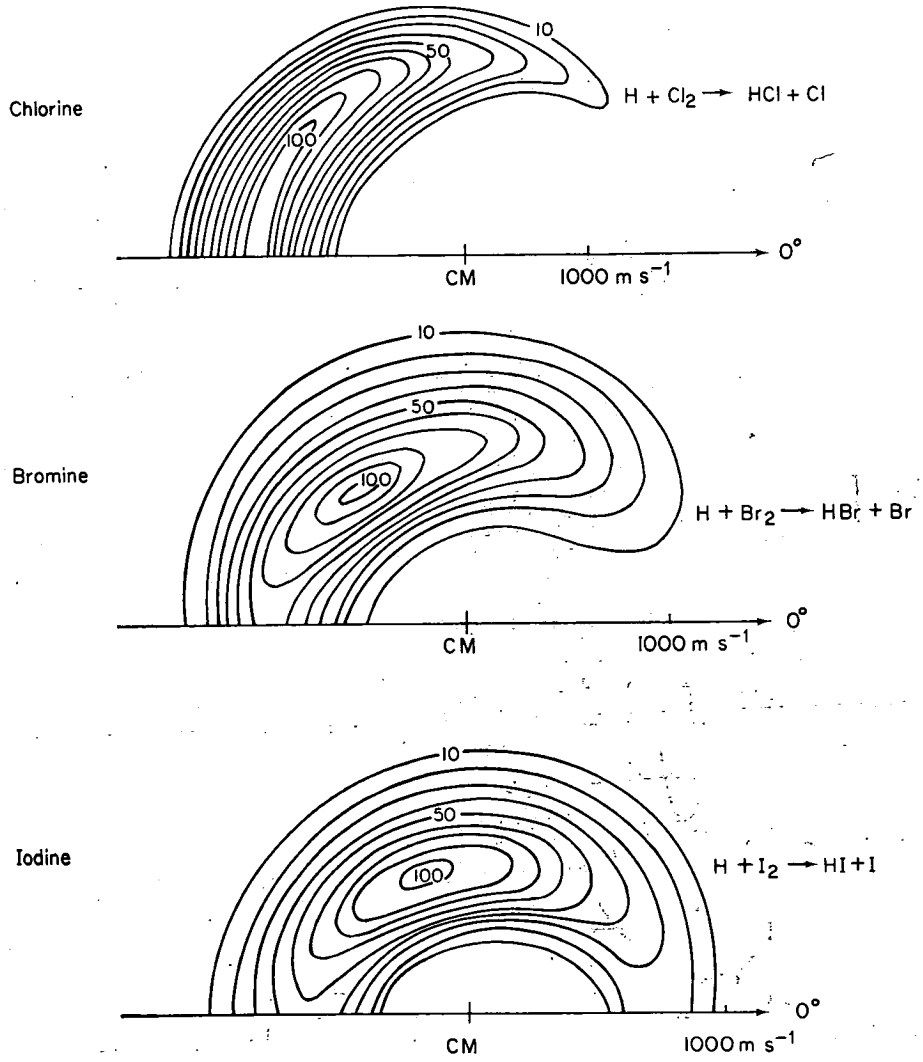

Fig. 16. Flux map for product from reaction of $H+Cl_2, Br_2, I_2$. Note the steady forward shift in the peak scattering as the electronegativity of the halogen decreases, $Cl_2 > Br_2 > I_2$. (Herschbach 1973.)

involved in the transition state as in the photo excited halogen (cf. CH_3I in which a similar parallel is observed). The observed shift in the angular distribution from directly backwards for the chlorine reaction to 110° for the iodine also correlates with this view. Since the attacking atom is so light in comparison with the target halogen the angular distribution is primarily dependent on the orientation of the target and H atom when reaction occurs. In accordance with Walsh's rules, we might expect the H – X – X transition state to become more bent as the central atom becomes less electronegative and the 2σ orbital acquires more p character along the Cl, Br, I sequence.

Finally as an example of a reaction on a covalent surface involving a collision complex we cite the process:

$$O(^3P) + Br_2(^1\Sigma_g^+) \rightarrow BrO(^2\Pi) + Br(^2P)$$

which appears to fit well statistical predictions based on O – Br – Br structures for the complex (Parrish 1973).

The few examples that could be discussed here do not do justice to the number of reactions that are now beginning to be understood in the detail described. In future work, the experimental range will be further extended, particularly in the direction of the more complicated reactions typical of synthetic chemistry where even quite crude measurements would be informative, as well as to reactions of wider scientific importance such as those mentioned in the introduction. In simpler systems measurements will be extended in energy range and resolution so that the region in which the transition from complex to direct dynamics occurs can be probed and the inevitable failure of statistical models explored in detail. Experiments with even more detailed channel specificity to study for example the role of reagent orientation, a murky area in chemical kinetics, and the vector distribution of angular momentum in the product will also be increasingly important, while the non-adiabatic effects in potential surface crossing will also be of interest. In short, much more detail can be expected and will tax our models for the chemical reaction process, particularly if associated with some *a priori* information as to the potential surface involved. Indeed, in the medium term, it is the computation of potential surfaces with sufficient precision to allow useful comparison with experiment that may prove the major obstacle to our further understanding of the dynamics of chemical change.

References

General references for further reading:

Faraday Discussions, *Molecular Beam Scattering*, 1973, **55**.

Fluendy, M. A. D., and Lawley, K. P., 1974, *Chemical Applications of Molecular Beam Scattering* (London: Chapman-Hall).

Levine, R. D., and Bernstein, R. B., 1974, *Molecular Reaction Dynamics* (New York: Oxford University Press).

Massey, H. S. W., 1971, *Contemporary Phys.*, **12**, 537.

Massey, H. S. W., 1972, *Contemporary Phys.*, **13**, 375.

Massey, H. S. W., 1973, *Contemporary Phys.*, **14**, 497.

Mott, N. F., and Massey, H. S. W., 1965, *Theory of Atomic Collisions* (3rd Edn.) (Oxford University Press).

Other references:

BRUMER, P., and KARPLUS, M., 1973, *Disc. Farad. Soc.*, **55,** 80.
BUNKER, D. L., and BLAIS, N. C., 1964, *J. Chem. Phys.*, **41,** 2377.
GILLEN, K. T., RULIS, A. M., and BERNSTEIN, R. B., 1970, *J. Chem. Phys.*, **54,** 2831.
HERSCHBACH, D. R., 1973, *Disc. Farad. Soc.*, **55,** 233.
KARPLUS, M., 1970, *Molecular Beams and Reaction Kinetics*, 382 (New York: Academic Press).
KARPLUS, M., and WOLKEN, G., 1974, *J. Chem. Phys.*, **60,** 351.
MCCULLOUGH, E. A., and WYATT, R. E., 1971, *J. Chem. Phys.*, **54,** 3578.
MCDONALD, J. D., LEBRETON, P. R., LEE, Y. T., and HERSCHBACH, D. R., 1972, *J. Chem. Phys.*, **56,** 769.
PARRISH, D. D., and HERSCHBACH, D. R., 1973, *J. Amer. Chem. Soc.*, **95,** 6133.
POLANYI, J. C., and WOODALL, K. B., 1972, *J. Chem. Phys.*, **57,** 1574.
PORTER, R. N., and KARPLUS, M., 1964, *J. Chem. Phys.*, **40,** 1105.
RULIS, A. M., and BERNSTEIN, R. B., 1972, *J. Chem. Phys.*, **57,** 5497.
SCHAFER, T. P., SISKA, P. E., PARSON, J. M., TULLY, F. F., WONG, W. C., and LEE, Y. T., 1970, *J. Chem. Phys.*, **53,** 3385.

The Author:

Dr. M. A. D. Fluendy received a B.A. degree in chemistry from the University of Oxford in 1960 and researched there under Professor R. P. Bell to obtain a D.Phil. in 1962. He then went to America to work with Professor D. R. Herschbach at Berkeley and at Harvard University. He returned to become a lecturer in chemistry at the University of Edinburgh in 1964.

Dr. M. A. D. Fluendy, Dr. K. P. Lawley, Mr. J. M. McCall and Dr. C. Sholeen (*Edinburgh University*) said: Elastic and inelastic differential cross sections for molecular collisions in the 100–300 eV range have been measured using a time-of-flight technique. A typical measurement of the system K + CH_3I at an impact energy of 164 eV is shown in fig. 1. The main features observed in this system are:

(i) Large losses in the elastic channel with an onset at 95 eV°.

(ii) Substantial cross sections for electronic excitation of scattered K atoms, dominantly to the 4*p* level but with a minor fraction exiting in the 5*s* or 3*d* configuration. These processes also onset at small $E\theta$ values close to the onset of losses in the elastic channel.

(iii) Energy losses corresponding to electronic excitation of the CH_3I are also seen but have much smaller cross sections and onset at considerably larger $E\theta$'s than for the K* excitation process.

(iv) At still larger $E\theta$'s an excitation process at 12 eV—possibly the excitation of an autoionising state of CH_3I is seen. Measurements at different impact energies show similar onsets at the same $E\theta$'s.

These qualitative features are interpreted on the basis of the following simple model.

(i) The potentials are assumed to be spherically symmetric. A cut through the surfaces evolving from the various states involved in the collision is shown in fig. 2. These diabatic surfaces are based loosely upon those used by Raff and Karplus[5] and LaBudde *et al.*[6]

(ii) At the collision velocities $>2 \times 10^4$ m s^{-1} and the small scattering angles

[1] R. N. Dixon and J. M. V. Hugo, *Mol. Phys.*, 1975, 29, 953.
[2] P. W. Tasker, G. G. Balint-Kurti and R. N. Dixon, *Mol. Phys.*, 1976, 32, 1651.
[3] A. M. Stoneham, *Theory of defects in solids* (Clarendon Press, Oxford, 1975).
[4] T. Shida, Y. Takahashi, H. Hatano and M. Imamura, *Chem. Phys. Letters*, 1975, 33, 491.
[5] L. M. Raff and M. Karplus, *J. Chem. Phys.*, 1966, 44, 1212.
[6] R. A. LaBudde, P. J. Kuntz, R. B. Bernstein and R. D. Levine, *J. Chem. Phys.*, 1973, 59, 6286.
* In solution.[4]

$<5°$, used in these measurements the internal motion of the CH_3I target is effectively frozen during the collision.

(iii) The Landau-Zener approximation is used.

Comparison of fig. 1 and 2 then suggests that the distinction between the small $E\theta$

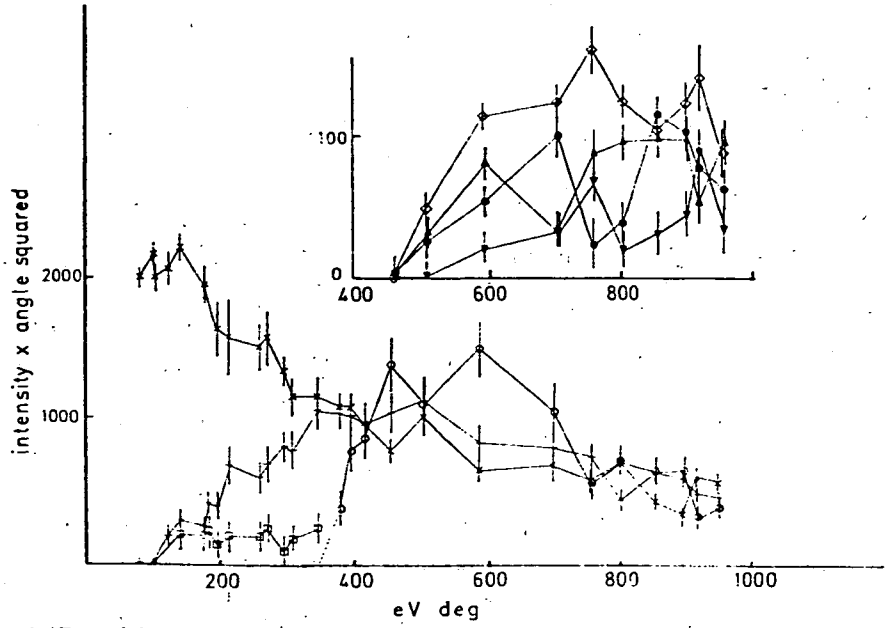

FIG. 1.—Differential scattering cross sections for K + CH_3I at centre of mass energy 164 eV impact energy. The cross sections are normalised to the ground state neutral potential, V_{11}, of LaBudde *et al.*[6] The spectroscopic states of CH_3I are labelled as in Herzberg.[4] Energy losses (eV) ×0.0; +1.6; □2.6; ○3.5; ◇6.2; ●7.3; ▲9.6; ▼12.0.

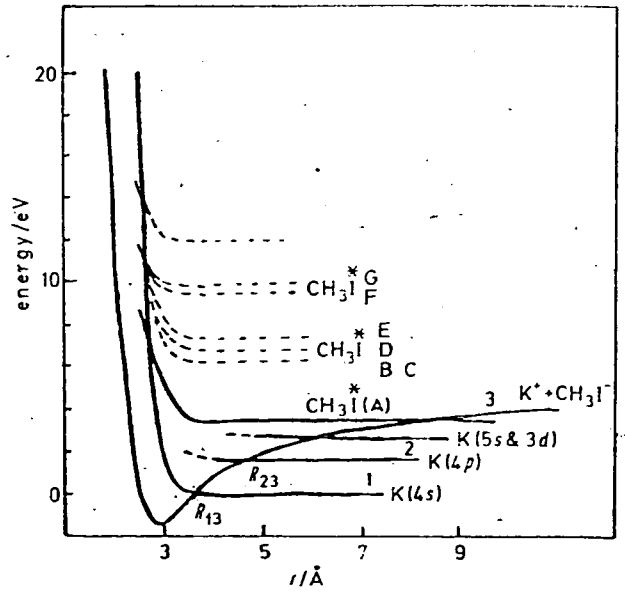

FIG. 2.—Diabatic potential surfaces for K + CH_3I.

[4] G. Herzberg, *Electronic Spectra of Polyatomic Molecules* (Van Nostrand, N.Y., 1966).

processes leading to K excitation and the larger $E\theta$ collisions required to excite the CH_3I originate in the diabatic ionic potential which crosses all the K* states on its outer branch. In contrast the CH_3I^* states interact only at shorter distances on the repulsive wall. (The dissociative A state of CH_3I which lies asymptotically just below the energy of the separate ions will interact at long distances where the matrix element is small, though some contribution perhaps 30% of that of K(5s 3d) from this process cannot be excluded on the basis of these experiments.)

The excited K states thus feed from the ionic surface and onset when the incident collisions can reach R_{13}. K ionisation and excitation will thus have a common onset, though successive leakage of flux to excited states via crossings such as R_{23} will reduce the ion production cross section.

The $E\theta$ onsets associated with the various crossings can yield estimates for the crossing radius via the small angle approximation

$$E\theta_{\text{onset}} = R_c \int_{R_c}^{\infty} \left(\frac{dV_{11}}{dR}\right) (R^2 - b^2)^{-\frac{1}{2}}\, dR$$

Thus if V_{11} is assumed R_{13} can be calculated. Under this analysis the surface of LaBudde *et al.* yields $R_{13} = 3.05$ Å in good agreement with the value 3.1 Å chosen by them on other grounds. The LaBudde neutral potential also provided a good fit to the elastic cross section below 95 eV°, though the angular range where data are available is not large. This potential thus seems a good approximation to reality so that the observed cross sections can be placed on an absolute scale by comparison with calculations from this surface. Extrapolation of the elastic neutral surface cross section to larger $E\theta$'s enables the total (all channels) inelastic scattering to be estimated and hence by difference the probability of ionisation for trajectories in this region of impact parameter space. Application of the L-Z approximation then provides an estimate for $V_{13} = 0.28$ eV the matrix element for crossing from the neutral to the ionic surface.

The excited state crossing radius R_{23} lies in a region where the ionic potential is essentially coulombic while the neutral K^*/CH_3I potential is expected to be small so that R_{23} can be estimated directly as 4.7 Å. Application of the L-Z approximation at R_{23} to those trajectories which have already crossed to the ionic surface at R_{13} then yields $V_{23} = 0.09$ eV for the corresponding matrix element.

These observations support the arguments of Lacmann and Herschbach[1] concerning the role of the ionic surface in producing electronic excitation. In the high velocity region of these experiments the dynamics are essentially two body. The suggestion of Balint-Kurti *et al.* concerning the mechanism for ionisation in M + HF should thus be accessible to test by examining the velocity dependence of the inelastic differential cross sections so as to establish the location of the line of intersection between the ionic and incident potential surfaces. As the interaction moves from the incident to the reactive exit region of the surface we expect the dynamics to change from 2 to 3 body.

J. Phys. E: Sci. Instrum., Vol. 11, 1978. Printed in Great Britain

29

Signal enhancement by velocity modulation in time-of-flight analysis of atomic and molecular beam scattering

J M McCall and M A D Fluendy
Department of Chemistry, University of Edinburgh, West Mains Road, Edinburgh EH9 3JJ, UK

Received 20 December 1977, in final form 17 February 1978

Abstract The use of velocity modulation techniques to enhance signal-to-noise ratios in time-of-flight analysis of molecular beam scattering is discussed. The design, construction and performance of such a device for use in experiments with charge-exchanged beams are described.

1 Introduction

Atomic and molecular collision processes are normally described by interaction potentials between the colliding atoms together with terms representing coupling which induce transitions between the accessible quantum states of the colliding species. Except in very favourable circumstances, these potentials and coupling coefficients are not available from theory with any accuracy. Measurements of the elastic and inelastic differential scattering cross-sections can, however, be interpreted to yield interaction potential and coupling coefficient data for comparison with theory (Smith 1969).

If the atomic states excited during the collision involve exchange of energy between the relative motion of the atoms and their internal modes, measurement of the velocity change produced by a collision is sufficient to specify the excitation process. Measurements of the inelastic differential cross-section at a specified initial relative kinetic energy thus require the scattered atomic flux to be determined as a function of the velocity change and deflection angle produced by the atomic collision. Such velocity changes can conveniently be measured by pulsing one of the beams and recording, at a fixed distance, the resulting scattered flux from the beam pulse as a function of time. In this way each exit channel is distinguished.

In the most direct realisation of this approach a single narrow pulse is transmitted at well spaced intervals; the disadvantage is then the very low beam utilisation, and hence signal-to-noise ratio, that results as the transmitted pulse is narrowed to achieve the required energy resolution. This limitation can be circumvented by the use of a cross-correlation technique in which the source is modulated on–off by a suitable pseudo-random sequence. Cross-correlation of the resultant detector signal with the random code then produces an approximation to the required impulse response. This technique allows up to 50% beam utilisation but spreads the statistical noise evenly through the arrival-time spectrum so that regions of low intensity are measured with lower accuracy. Pseudo-random modulation is thus not suited to spectra dominated by a large peak yet having important information in weaker subsidiary peaks, as in this work. Both methods are also limited by the difficulty of producing the narrow pulses (less than 100 ns) of neutral atoms required (Fowler and Good 1960, Secrest and Meyer 1972). The merits of both techniques have been discussed in detail by Beijerinck (1975).

In this paper an alternative approach to beam modulation for time-of-flight measurements is described. In this system the beam is pulsed and accelerated simultaneously so that particles near the trailing edge of the beam pulse are accelerated to catch up with those near the leading edge by the time the detector is reached. The extra energy spread introduced by this acceleration can be substantial, but does not usually exceed 5%, a figure comparable to the angular resolution achieved. At the same time the beam pulse at the detector is compressed so that a substantial increase in the duty cycle can be achieved without loss in the resolution of the energy loss produced in the collision.

The use of sinusoidal bunching fields is of course well established, for example, in the klystron (Farago 1970) and in accelerators (Lefevre *et al* 1962).

2 Velocity modulation

2.1 *Requirements*

The cross-sections of interest, $\sigma(\chi, E, \Delta E)$, are functions of scattering angle χ, collision energy E and energy loss ΔE, as revealed by changes in flight time. The resolution required in energy loss depends upon considerations such as the need to distinguish between collisions leading to different final exit states. The resolution in flight time required is

$$\delta t/t = 2\delta(\Delta E)/E \qquad (1)$$

where $\delta(\Delta E)$ is the energy loss resolution needed and E is the primary-beam energy. The achievable resolution is limited by the final energy spread δE in the primary neutral beam. In the present experiments this spread is about 0·2 eV, corresponding to $\delta t/t$ in the range 10^{-2}–10^{-4} for $E = 10$–1000 eV and it is desirable to work close to this limit.

In collision scattering at small angles it is easily shown that the impact parameter is a function of the product $E\chi = \tau$, so that the precision with which a process may be located in impact parameter space depends upon the resolution:

$$\delta\tau/\tau = \delta E/E + \delta\chi/\chi \qquad (2)$$

where $\delta E/E$ and $\delta\chi/\chi$ are the relative FWHM resolutions in collision energy and scattering angle, and it is natural to choose $\delta E/E \approx \delta\chi/\chi$ when designing an experiment. In principle, to obtain maximum detail from an experiment $\delta\tau/\tau$ should be set to the quantum limit. In practice, intensity restrictions which vary approximately inversely as the resolution set a limit to the usable resolution. In this work $\delta\chi/\chi \approx 0{\cdot}03$ so that $\delta E/E$ should be similar. Comparison with the limiting energy loss requirement, 0·2 eV, suggests that a much better beam energy resolution will be required, with a corresponding decrease in beam intensity below that which might be suitable for measurements in τ.

Contrary to these expectations, however, a time-focusing velocity modulation technique will allow both these conditions to be met simultaneously. By deliberately increasing $\delta E/E$ in such a way as to decrease $\delta t/t$ we can tailor the shape of the phase space distribution available in the primary beam to suit the experimental requirements.

0022-3735/78/0007–0631 $01.00

If an initial beam pulse of duration $\delta t'$ and energy spread $\delta E'$ is modulated in such a fashion as to produce a pulse of duration $\delta t''$ (satisfying the $\delta t/t$ requirement) and an increased energy spread $\delta E''$ (satisfying the $\delta E/E$ requirement) then the Liouville theorem requires $\delta E'\delta t' = \delta E''\delta t''$. Since $\delta E'' > \delta E'$, then $\delta t' > \delta t''$, i.e. we obtain the required time resolution with an enhanced utilisation of the beam and consequent improvement in signal.

2.2 *Design*

In this experiment the primary neutral-atom beam is formed by charge neutralisation of an ion beam so that the beam energy and any required modulation can be impressed by suitable electric fields. The modulation scheme is shown in figure 1.

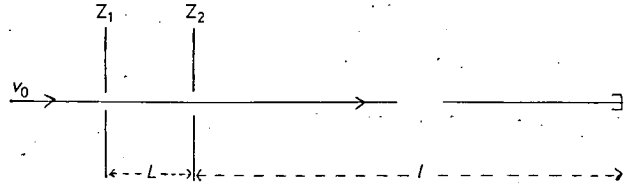

Figure 1 Diagram showing compression zone and flight path to the detector.

Ions of mass m with a well defined velocity v_0 enter the pulser at Z_1; the requirement is to apply such a time-dependent field between plates Z_1 and Z_2 as to 'focus' all the ions in this region so that they arrive nearly simultaneously at the detector distant l from Z_2.

Consider an element of beam located between Z_1 and Z_2 at the start of the modulation sequence at time $t=0$. After modulation this element will have its initial energy $E(=\frac{1}{2}mv_0^2)$ incremented by an amount $\epsilon(t_a)$, where t_a is the time of flight in the field, i.e. Z_1 to Z_2. The velocity of the element will now be Rv_0, where

$$R^2 = 1 + \epsilon(t_a)/E,$$

and this element will arrive at the detector at a time

$$t(t_a) = l/Rv_0 + t_a.$$

For an element at Z_2 at $t=0$, $t_a=0$ so that

$$t(0) = l/v_0,$$

and we require $\epsilon(t_a)$ to be such as to bring the other elements to the detector at the same time, i.e.

$$l/Rv_0 + t_a = l/v_0 = t(0),$$

so that

$$R = \frac{l/v_0}{l/v_0 - t_a},$$

and the required energy modulation is

$$\epsilon(t_a) = E(R^2 - 1) = E\left(\frac{l/v_0}{l/v_0 - t_a}\right)^2 - 1. \qquad (3)$$

$\epsilon(t_a)$ is closely linear with t_a when $t_a/t(0) \ll 1$ and this is the interesting region since the resolution requirement for $\delta E/E \approx \epsilon(t_a)/E$ restricts our interest to situations where the distribution produced by the modulation is only a few per cent, so that the required modulation function can readily be implemented.

Since the pulse length is small compared to the total flight path l, equation (3) yields

$$\epsilon(t_a) = 2Et_av_0/l$$

while, since $\epsilon(t_a) \ll E$, $t_a \approx x/v_0$ where x is the distance of the element from Z_2 at $t=0$ and e is the electron charge:

$$E(t_a) \approx 2Ex/l \approx exF.$$

A steady electric field F applied at $t=0$ between Z_1 and Z_2 will thus 'time-focus' ions in this region if

$$F = 2E/le. \qquad (4)$$

The duration t_z of this pulse and hence the required length of the pulser L are ultimately limited by the nonlinearity of equation (3) but in practice the energy resolution required will determine them as

$$t_z = (l/v_0)\,\delta E/E \text{ and so } L = l(\delta E/E). \qquad (5)$$

The enhancement in signal intensity in each pulse as a result of this compression will be, as expected,

$$\text{Enhancement} = \frac{\delta E/E \text{ after modulation}}{\delta E/E \text{ before modulation}}.$$

For the present system a final value of $\delta E/E = 0{\cdot}05$ should yield an enhancement of 25, considering the known energy spread (0·2 eV) at 100 eV.

The possible pulse repetition rate will depend upon the structure of the signal but in some cases beam utilisation could approach 100% if the information is contained in the period t_z after the arrival of the main pulse. It is interesting to note that the signal-to-noise ratio with this technique is considerably better than in the unmodulated DC beam experiment, the reverse of the usual situation in which additional state or energy analysis decreases the signal.

Since inelastic collision processes alter the flight time in the apparatus, some defocusing of these inelastic peaks occurs. For large-energy-loss processes it may be necessary to alter the focusing voltage F so as to focus these peaks specifically. The magnitude of this effect can be seen in figure 2.

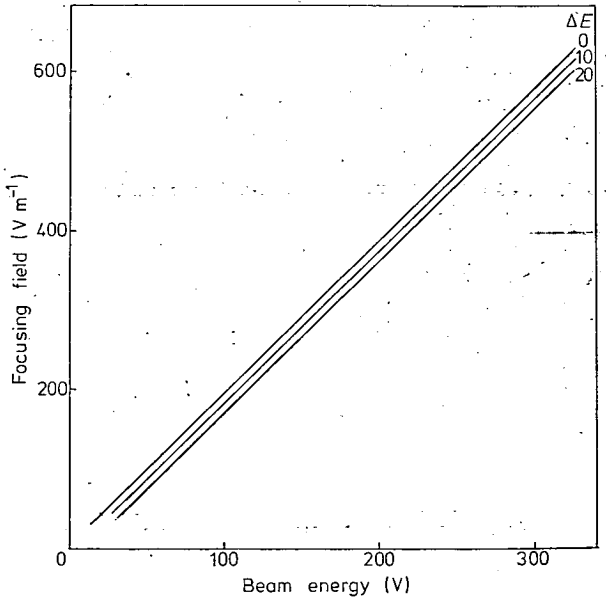

Figure 2 Focusing field for a flight path of 1 m for a range of beam energies. The two lower lines show the focusing fields required for energy losses of 10 and 20 V in collisions 60 cm from the detector.

More detailed computations including the effect of the initial internal energy spread in the beam have been made numerically as an aid to design. The results of these calculations are compared with the experimental performance in a subsequent section.

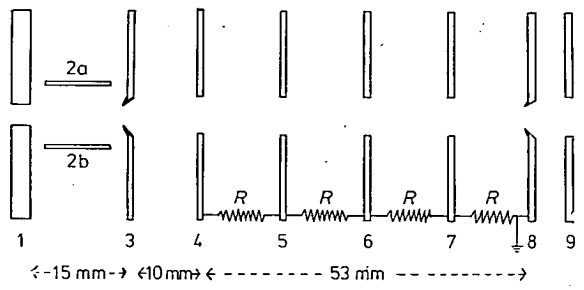

Figure 3 View of the modulation showing the X-pulse plates 2a and b, the Z-modulation system, plates 4–8 ($R = 12{\cdot}5\ \Omega$) and the final refocusing and steering plate 9.

3 Construction

The pulser device constructed is shown schematically in figure 3. The entrance (1) and exit apertures (8) are at earth potential. The X-modulation plates (2a, b) in conjunction with the aperture (8) turn the beam on and off. Modulation applied to these plates is used to fill plates (4) to (8) of the pulser region with ion beam; the open time of the X modulation, $1{\cdot}2\ t_z$, is timed in advance of the Z modulation so that the leading edge of the transmitted beam pulse reaches (8) as the Z-focus pulse is applied. The Z modulation is applied between plates 4 and 8; the intermediate plates operated at linearly interpolated voltages help to preserve field uniformity in the pulser. These lens plates are shunted with resistors to form a 50 Ω termination to the coaxial pulser drive line.

The X modulation is arranged symmetrically about ground potential so that during beam-on periods both plates are at 0 V. Nevertheless, during the switching period of these potentials the finite thickness of the beam results in some undesired energy modulation in the leading and trailing edges of the beam pulse in the compression region. Effects of this type produce a broadening in the far wings of the detected atom pulse. Since this region is where the possibly weak inelastic scattering events are found, such broadening can sharply reduce the signal-to-noise ratio in an experiment. The trailing edge of the atom pulse can be sharpened and this effect overcome by applying a second step voltage to the Z plates immediately after the focusing pulse. The amplitude of this 'clearing' pulse is chosen so as to accelerate any ions in the trailing edge of the X pulse so that they reach

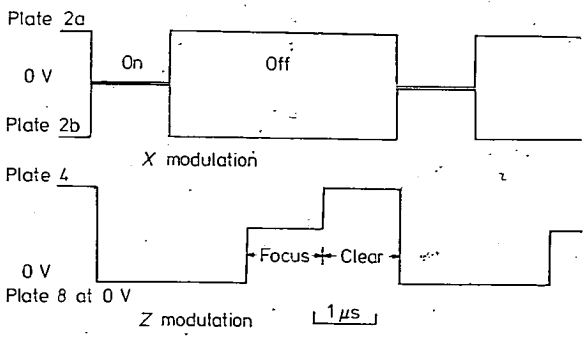

Figure 4 Pulse timings are illustrated for 200 V beam energy. The delay between the X- and Z-pulse trains corresponds to the beam flight time between plates 2 and 4.

the detector at a time of no physical interest, e.g. for forward centre-of-mass scattering they can be dumped into times before the arrival of the main elastic peak. The appropriate pulse timings are shown in figure 4 and table 1. The on-line computer system and interface arrangements used in these measurements are described elsewhere (Fluendy *et al* 1975).

4 Performance

The atom arrival pulses obtained using this technique are shown in figure 5. The results of calculations assuming a beam energy spread equivalent to the source temperature (1700 K) are shown dotted in comparison. The additional width seen in the histograms arises in part from time spreads in the electronics which account for perhaps 20 ns of the

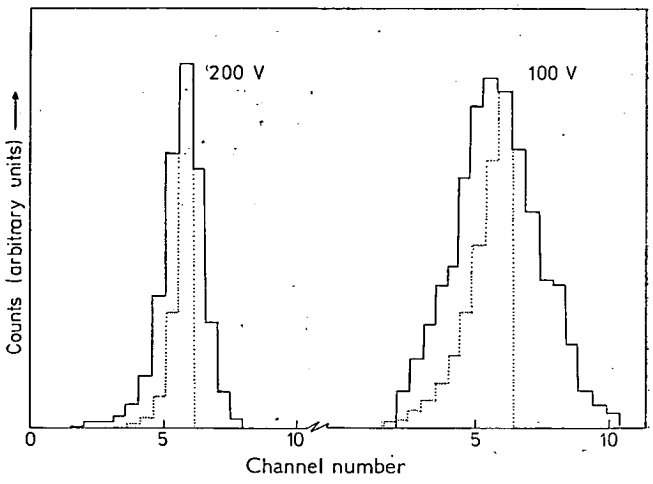

Figure 5 Comparison of calculated and observed performance at 200 V and 100 V. Calculated values are dotted lines (each channel is 20 ns wide).

Table 1 Pulse timings.

Beam energy (V)	X width (ns)	Delay front X to Focus (ns)	Focus		Clear		Duty cycle (%)	Energy resolution $\delta E/E$
			Width (ns)	Amplitude (V)	Width (ns)	Amplitude (V)		
100	1600	3200	1280	9·6	640	15	25	0·04
200	1280	2560	1280	19·2	1280	30	25	0·07

extra width. The remaining discrepancy may arise from time spreads in the detector itself or in space charge effects in the beam source. At beam energies of 200 V or more the former effects are dominant, while at lower energies the energy spread in the beam, fluctuations in contact potentials, and space charge effects play the most important role.

Experience has shown that the performance of the system depends as expected upon the cleanliness and careful alignment of the lens assemblies. Additionally it is found that setting the lens potentials for maximum transmission does not necessarily produce the optimum pulse shape and that some experimentation is usually required in setting up.

References

Beijerinck H C W 1975 *PhD Thesis* Eindhoven University

Farago P S 1970 *Free-Electron Physics* (London: Penguin) p 131

Fluendy M A D, Kerr J H, McCall J M and Munro D 1975 Atomic and molecular beam collision measurements using an on-line computer
On-line Computing in the Laboratory ed R A Rosner, B K Penney and P N Clout (London: Advance)

Fowler T K and Good W M 1960 A theory on obtaining short bursts of ions from a beam of ions
Nucl. Instrum. Meth. **7** 245

Lefevre H W, Borchers R R and Poppe C H 1962 Fast neutron time-of-flight spectrometer
Rev. Sci. Instrum. **33** 1231

Secrest D and Meyer H D 1972 Time-of-flight modulation
Max Planck Institut fur Stromingforschung Report No. 137/1972

Smith K 1969 Atom–atom scattering
Scattering Theory ed A O Barut (New York: Gordon and Breach) p 249

30

Electronic Excitation in Potentially Reactive Atom–Molecule Collisions

By Malcolm A. D. Fluendy, Kenneth P. Lawley, John McCall, Charlotte Sholeen and David Sutton

Department of Chemistry, University of Edinburgh, Edinburgh EH9 3JJ

Reprinted from

FARADAY DISCUSSIONS
OF
THE CHEMICAL SOCIETY

No. 67

FARADAY SYMPOSIUM 67

1979

Electronic Excitation in Potentially Reactive Atom–Molecule Collisions

By Malcolm A. D. Fluendy, Kenneth P. Lawley, John McCall, Charlotte Sholeen and David Sutton

Department of Chemistry, University of Edinburgh, Edinburgh EH9 3JJ

Received 11*th December*, 1978

Inelastic differential scattering cross sections for the system potassium + alkyl halide have been measured in the small angle region for $E\chi$ between 20-1000 eV°. Electronic excitation of both collision partners is seen together with vibrational excitation of the alkyl halide.

Evidence is adduced suggesting that excitation occurs by either of two paths corresponding to the preliminary transfer of an electron in the entrance channel or as the colliding pair recedes. A harpooning model incorporating bond stretching in the negative molecular ion is developed that agrees well with most of the observations.

A large number of exit channels are open in the collision system alkali atom + alkyl halide at higher energies. They include:

$M + RX \rightarrow M + RX(RX^{\dagger})$	elastic (inelastic)	(i)
$\rightarrow MX + R$	reaction	(ii)
$\rightarrow M^{+} + RX^{-}$	chemi-ionisation	(iii)
$\rightarrow M^{*} + RX$ $\quad M + RX^{*}$	electronic excitation	(iv)
$\rightarrow M + R + X$	dissociation.	(v)

The first two processes have been extensively investigated at thermal collision energies[1,2] and are well known examples of the electronic harpooning mechanism, subsequent chemical reaction occurring at thermal energies by ionic combination.

The chemi-ionisation channel is less well explored[3] but provides direct evidence for non-adiabatic behaviour at the ionic/covalent surface crossing. The importance of an ionic surface in coupling ground and excited electronic states of the atom is confirmed by collision-induced fluorescence studies.[4]

In the work described here continuing the programme outlined in a previous Faraday Discussion,[5] we have eliminated the reaction channel by working at high relative kinetic energies and choosing a heavy halogen atom, iodine. Equally important from the point of view of analysis, by confining scattering observations to very small angles ($\lesssim 5°$) the K atom trajectories are essentially rectilinear and of constant velocity. Nevertheless, because the forward momentum is high, interesting regions of the potential inside the harpooning radius can be probed by these small deflections. Electronic excitation of several eV is readily observed.

EXPERIMENTAL

APPARATUS

The apparatus used in this work is shown schematically in fig. 1. The beam of fast alkali atoms was produced initially as ions by surface ionization and electrostatic focusing. The ion beam was then pulse modulated, using a velocity compression technique described elsewhere,[6] so that the energy loss resulting from a collision could be recorded by measurement of the flight time of the scattered atom and hence the post-collision states of the atom and molecule inferred. After modulation the ion beam was neutralised in a vapour cell and any remaining ions deflected away.

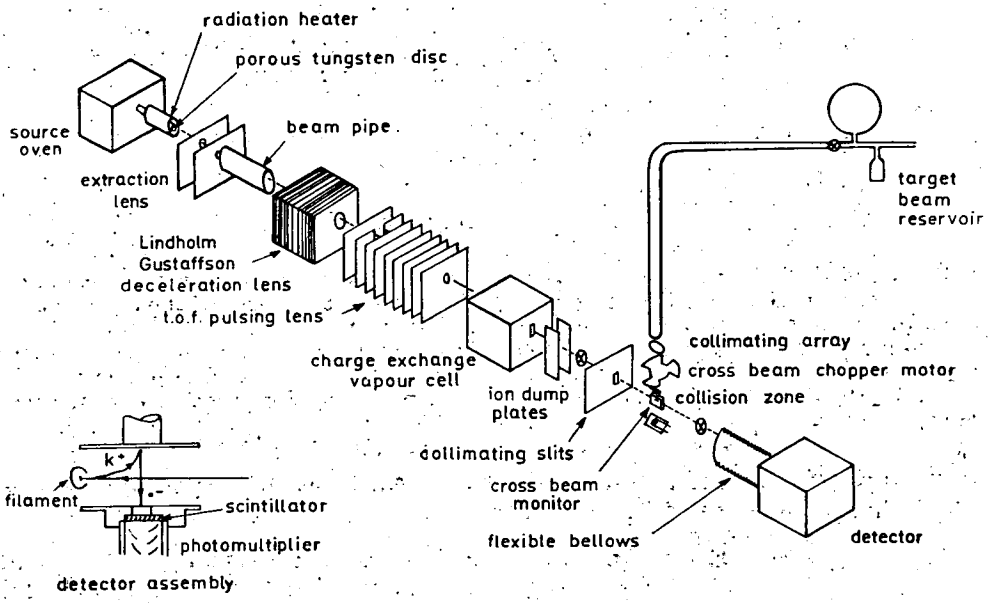

FIG. 1.—Schematic representation of apparatus.

The fast neutral beam then intercepted a slow target beam of molecules formed by effusion from a capillary array in a well defined collision zone. This beam was also modulated (at 47 Hz) and the target flux continuously monitored by a gauge placed directly below the collision zone.

Potassium atoms scattered from this region were ionised on a cool W wire and detected *via* a scintillator and photomultiplier. The detector could be varied in angle with a precision of $\pm 0.002°$. Atom arrivals located in angle by the detector position were arranged to stop a 50 MHz clock running in synchronism with the pulse modulation so that the flight time could be recorded.

The collection of data and the operation of the experiment were controlled by an on-line computer.[7] The signal collection and experimental control arrangement are shown schematically in fig. 2. Hard copy log and graphical output facilities were provided to allow operator intervention.

DATA COLLECTION AND ANALYSIS

Count rates are very low in this experiment (<0.01 counts s^{-1}) and periods of ≈ 12 h were required to collect sufficient counts at the widest angles. Data collection thus took place over periods of about five days. During this time the main beam arrival time profile was checked at intervals under program control and data collection suspended and the operator

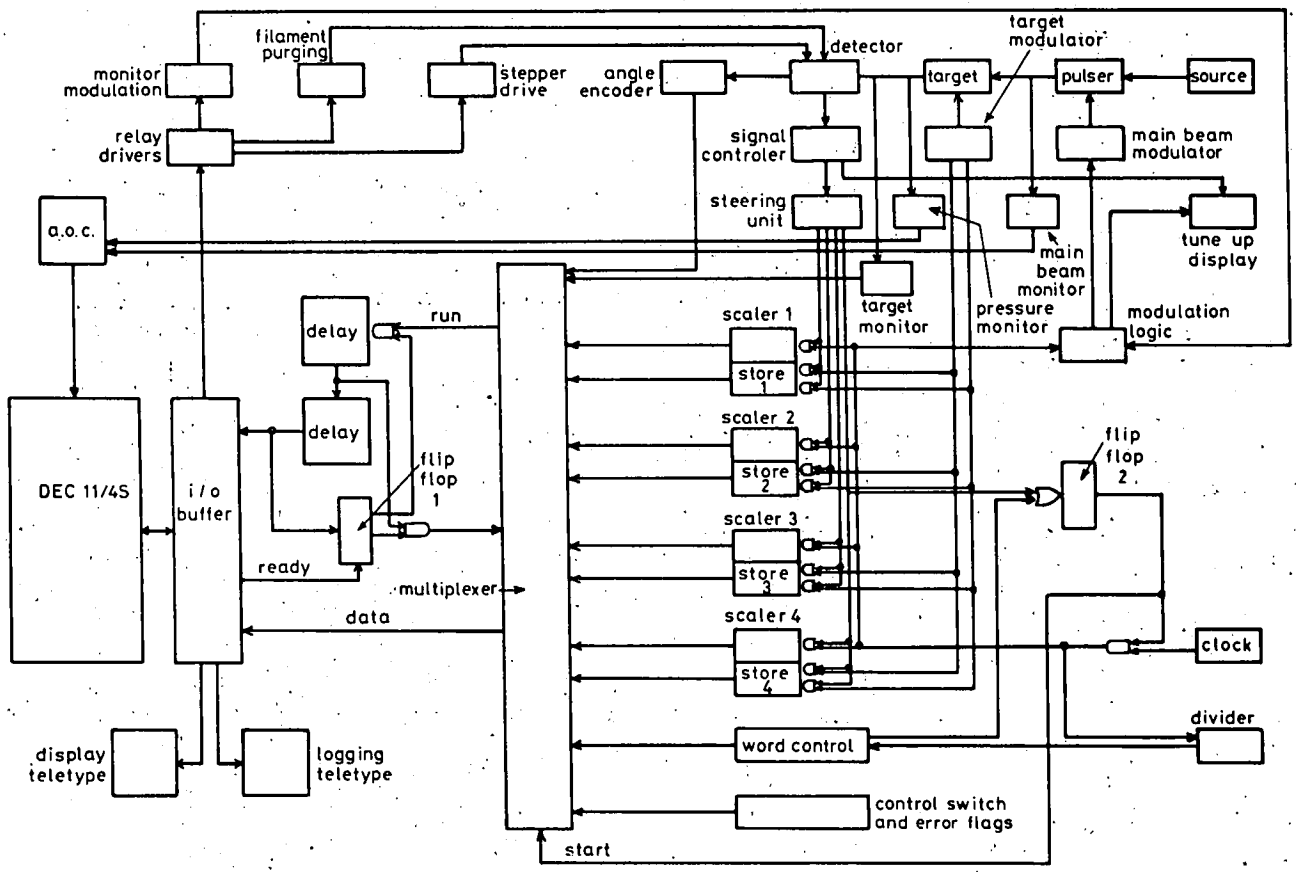

FIG. 2.—Schematic representation of data collection.

alerted if any significant changes in the beam fluxes or other operating conditions took place. The angular scan was made automatically to a predetermined sequence, angle changes being initiated automatically when a set precision had been reached.

The data reported in this paper were accumulated over a period of about eighteen months during which time the equipment was removed from one building to another and a number of small changes made. Partly as a result the time location of the primary beam pulse varied by as much as 30 ns between different experiments. The data were therefore adjusted in time so as to be relative to the unscattered beam arrival as measured in each experiment. Any accompanying variation in the pulse width was corrected by a process of deconvolution and reconvolution to a standard pulse width, the stability of these operations being checked by trials with synthesised noisy data. Inconsistencies of this type between different experimental runs rather than counting statistics account for most of the noise seen in the results.

After these adjustments had been made in the laboratory frame the data were transformed into the c.m. frame using the most probable laboratory velocities.

RESULTS

These results are most compactly presented as c.m. contour maps showing the variation in the product of the scattered intensity and the square of the scattering angle, $I(\chi)\chi^2$, as a function of the variable τ (τ = collision energy × scattering angle, $E\chi$) and the post-collision velocity.

The contour map in fig. 3 shows such a plot for K + Ar and illustrates the energy

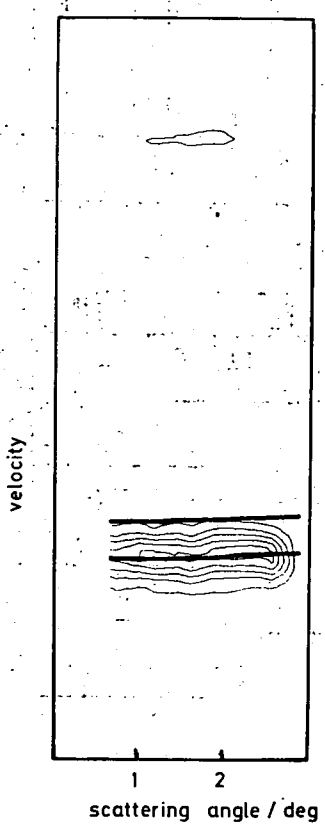

FIG. 3.—K + Ar scattering at 108 eV c.m. collision energy. The thick lines indicate energy losses of 0.0 and 1.6 eV (centre of mass frame).

resolution since in this E region the scattering is at least 98 % elastic. The island of intensity at slow exit velocities is due to the K^{41} isotope present at ≈ 6 % abundance. The other contour maps in fig. 4-6 show similar plots for methyl and propyl iodide at various initial collision energies. In comparison with the K + Ar data considerable inelasticity, particularly at the wider angles, is immediately apparent and can be seen to onset at specific $E\chi$.

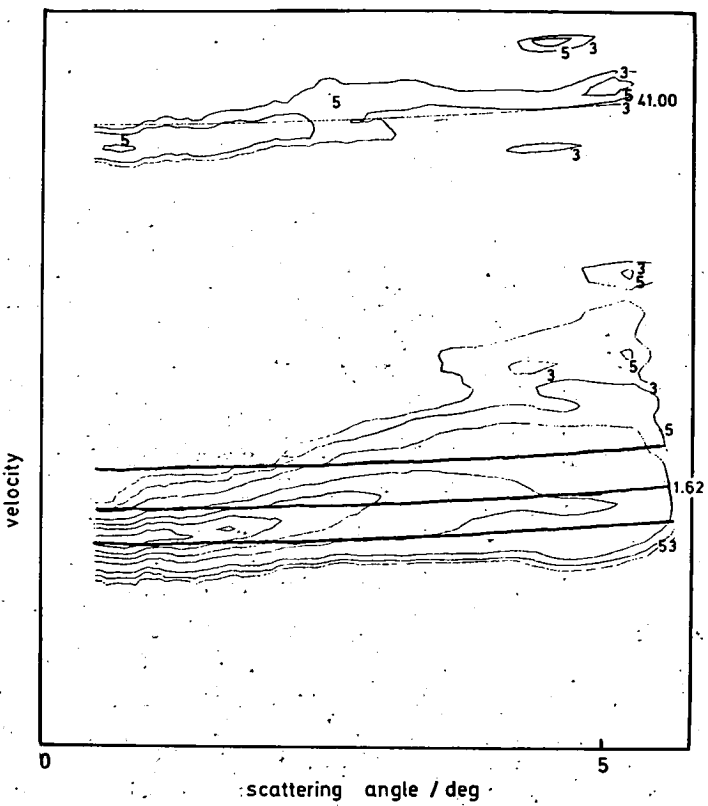

FIG. 4.—K + CH_3I scattering at 164 eV collision energy. The thick lines indicate energy losses of 0.0, 1.6 and 3.47 eV (centre of mass frame).

Cuts through the surface show the intensity of scattered K atoms as a function of the energy lost by them in collision are perhaps more suggestive. A number of examples computed by averaging together several sets of independent observations in a narrow range of angle are shown in fig. 7 and 8. The solid curves on these figures show the results of a deconvolution procedure using the 0° profile as a reference profile. The peaks are sharpened by this process but can already be distinguished in the unprocessed data; moreover, independent angular scans yield peaks which move smoothly with angle as in fig. 9-11. The enhanced scattering profiles prepared in this way are combined to yield similarly sharpened contour maps as shown in fig. 12 and 13.

Time of flight data of this type are of limited value in molecular systems because it is not possible to associate a given velocity change in the K atom with a specific exit channel, owing to the number of closely spaced energy states. Thus, in the K + RI system the K ionisation continuum starts at 4.34 eV and there is a near con-

tinuum of vibration–rotation states in each electronic level of RI. Table 1 summarises the relevant information for K and CH_3I (C_3H_7I is similar).

In view of this continuum of vibronic levels, it is remarkable that discrete energy losses are observed at least up to 10 eV at the largest angles of scattering.

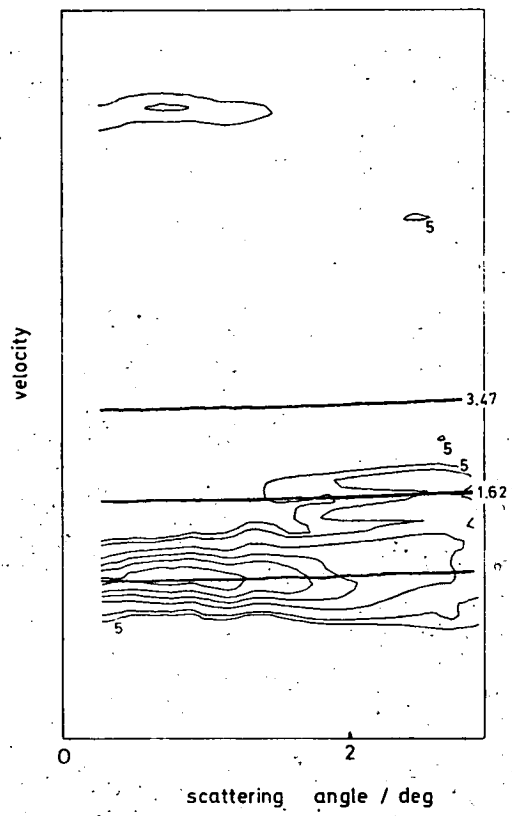

FIG. 5.—K + CH_3I scattering at 81 eV collision. The thick lines indicate energy losses of 0.0, 1.6 and 3.47 eV (centre of mass frame).

DISCUSSION

At scattering angles $\chi \lesssim 5°$, the momentum transfer perpendicular to the incident velocity is small (χ = final transverse momentum/incident forward momentum).

The various small-angle approximations are valid and the momentum changes in the forward direction cancel on the incoming and outgoing halves of the trajectory. Under these conditions the maximum energy transferable to vibration/rotation of the molecular partner is

$$\Delta E = \left(\frac{M_R M_I}{M_R + M_I}\right)\left(\frac{M_K}{M_X^2}\right)E_i\chi^2 \qquad (1)$$

where X = I or R, the end struck, and a "forceless" oscillator has been assumed. The maximum energy thus transferred at the angles of observation will be <0.5 eV, far smaller than most of the observed energy loss channels. The extensive vibronic energy transfer that is observed can only occur if the potential energy surfaces are

profoundly modified in the course of the collision. The source of this alteration is clearly the crossing onto the ionic state.

The harpoon model, equivalent to adiabatic behaviour at the ionic/covalent crossing, is well established as the mechanism for chemical reaction in many alkali metal systems at thermal energies. At the collision energies of the present experiments the reactive channel is essentially closed because the fast K^+ ion cannot accelerate the

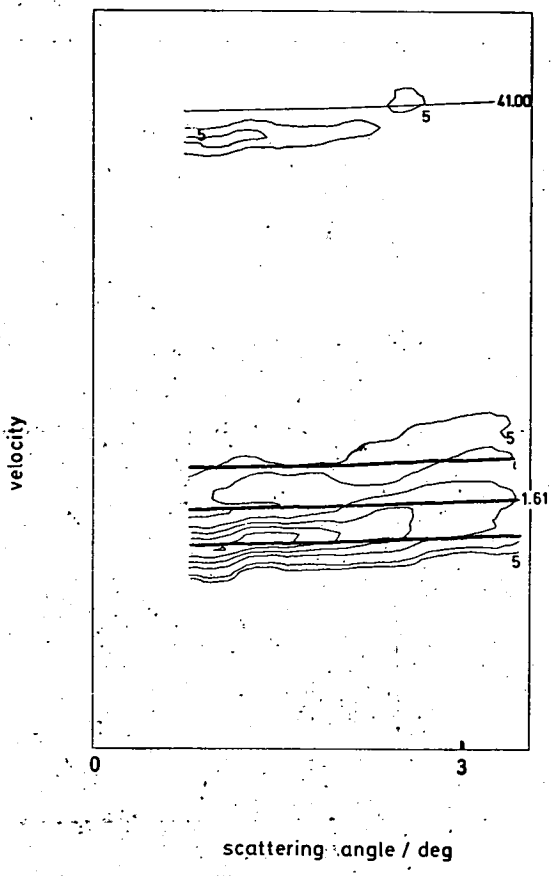

FIG. 6.—K + C_3H_7I scattering at 166 eV collision. The thick lines indicate energy losses of 0.0, 1.6 and 3.47 eV (centre of mass frame).

I^- ion sufficiently rapidly to capture it before leaving the ionic surface. The residual electronic excitation is like the grin on the face of the Cheshire Cat, the aftermath of a much more profound electronic rearrangement.

We develop a model to account for the broad features of the observed scattering in two stages. As a first approximation, the collision is assumed to be isotropic and sudden with respect to the R–I motion, *i.e.*, the R–I bond is clamped at its equilibrium value throughout the collision. The behaviour of the various diabatic potential surfaces can then be displayed solely as a function of the K–I coordinate, fig. 14(*a*). The vertical electron affinity of the alkyl iodides is sufficiently small (−0.9 eV) for the ionic state to intersect all the K* channels (including the ionised continuum) and thus to provide a route for populating these states. Excited electronic states of RI, except the *A* state, lie above the dissociation limit of K^+RI^- (5 eV) and must then be populated

by a different mechanism. We speculate that an excited charge transfer state is involved but the mechanism will not be discussed here.

The only important adjustable parameter in these potentials is the short range repulsion behaviour of the ionic state and the coupling matrix elements at the various crossings. Whatever the values of the parameters, some simple consequences arise because any exit channel can be reached *via* two paths, according to whether or not the electron is transferred on the first passage of the ionic/covalent crossing.

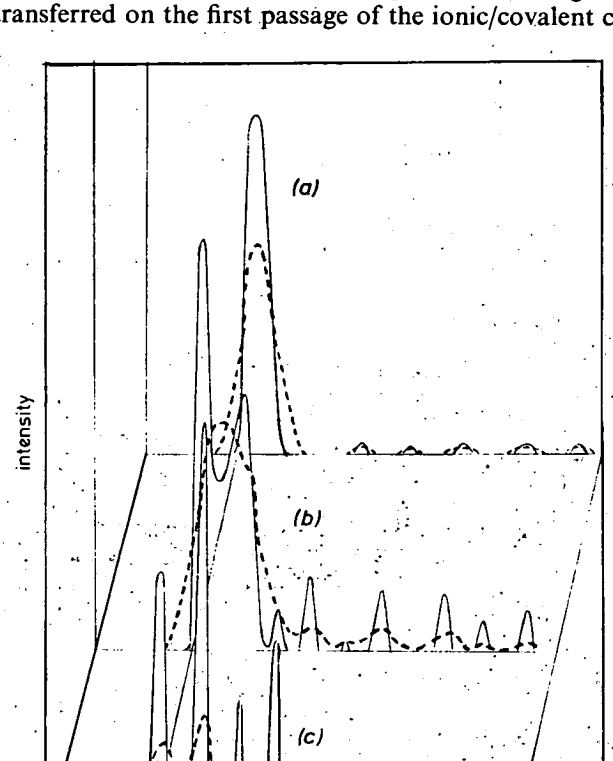

FIG. 7.—Energy loss profiles observed at various scattering angles for K + CH_3I at 81 eV collision energy. The dashed curves are observed values and the solid lines their deconvolution. (*a*) 61, (*b*) 122 and (*c*) 203 eV°.

The predictions of this model (using the potentials shown, the Landau–Zener approximation and the classical small-angle formulae to evaluate the cross-sections) are compared with experiment at 164 eV in fig. 15, the energy loss data being partitioned in accord with the asymptotic energy losses assuming only electronic excitation.

The model is partially successful, especially in predicting the narrow angle thresholds of K* and CH_3I^* (*A*) state onsets. If the route to these states involved a crossing on the respulsive wall of the potential, the angular threshold would appear at much larger angles and the intervention of a strongly attractive surface is unambiguous.

The model is less satisfactory in predicting the change in angular onsets of the various channels with incident energy. These thresholds are seen to occur at lower E values in the 81 eV data, whereas the basic model necessarily predicts constant $E\chi$ values (assuming straight line trajectories). More important differences are seen in

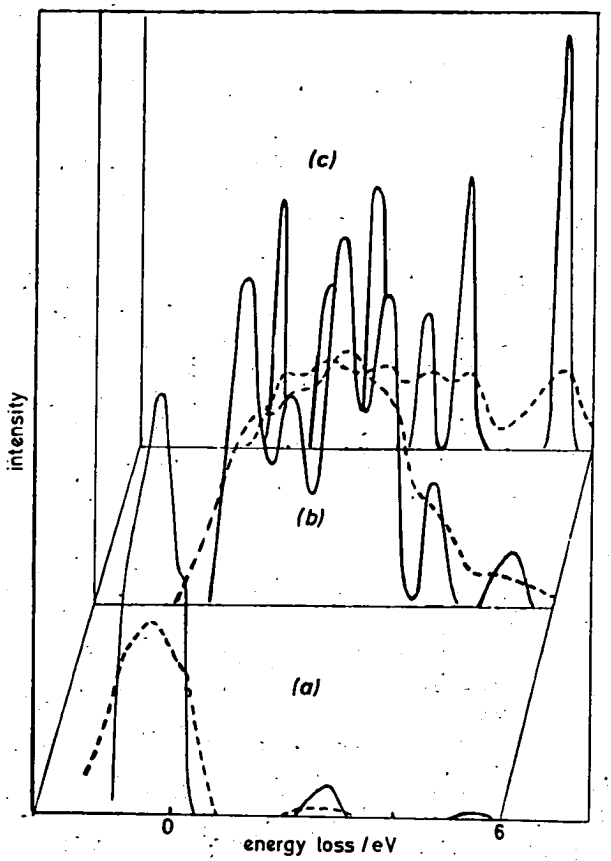

FIG. 8.—Energy loss profiles observed at various scattering angles for K + CH_3I at 164 eV collision energy. The dashed curves are observed values and the solid line their deconvolution. (*a*) 75, (*b*) 450 and (*c*) 900 eV°.

the energy loss spectrum where the model only permits energy losses corresponding to the electronic states of the separated species. The observations (*e.g.*, fig. 7 and 8) show a much larger number of discrete energy loss processes, some of them (those <1.6 eV) not being assignable at all to electronic excitation. The most serious assumption of the basic model lies in the neglect of the internal motion of the target molecule. During the collision lifetime, typically 10^{-14} s, changes in the C–I bond distance can occur which greatly alter the vertical electron affinity and hence the position of the ionic/covalent crossing. Such effects have been discussed by other workers[8] in connection with chemical reaction and chemi-ionisation. The initial crossing at R_1 yields CH_3I^- in a strongly repulsive state [fig. 14(*b*)], assuming a vertical transition. As the C–I bond stretches on the ionic surface, the ionic/covalent crossing moves to larger R values (fig. 16) and on the return of the electron a large amount of energy can be dumped in the Me–I vibration. The extent of such energy transfer clearly depends on the time spent on the ionic surface and ranges from zero if the motion at R_1 is diabatic (electron not transferred) to actual dissociation of the Me–I bond if the MeI^- surface is sufficiently repulsive. Since there are in general two classical paths leading to a particular angle of deflection (if $b < R_1$), corresponding to diabatic or adiabatic motion at R_1, each electronic exit channel should be accompanied by two distinct peaks in the time of arrival spectrum.

Our second model, then, is to permit relaxation of the C–I bond in the ionic state by introducing a term

$$V^{\text{ion}}(R_{\text{R-I}}) = A \exp\left[-\alpha(R_{\text{RI}} - R_{\text{RI}}^{(0)})\right] \quad (2)$$

into the total potential energy. The I–K interaction remains coulombic and there is no K–R interaction. One result emerges immediately from this model. If the parameters in $V^{\text{ion}}(R_{\text{RI}})$ are taken to be those of the isolated ion,[9] far too much vibrational excitation is predicted even in the ground electronic exit state. In fact, we would have a runaway situation with extensive bond dissociation (and probably chemi-ionisation). In practice (fig. 9-11) the vibrational energy gain in both the ionic K and K* channels is quite small (≈ 1 eV) and almost constant with $E\chi$ after the threshold.

The CH_3I^- ion is thus perturbed by the passing K^+ ion and we can very crudely incorporate this effect in the model by making α adjustable. However, even this degree of freedom is not sufficient for the data to be fitted; if the vibrational energy gain in the K* (ionic) channel is fitted, too little energy loss occurs in the ground state channel. In qualitative terms, the initial acceleration of the methyl group after

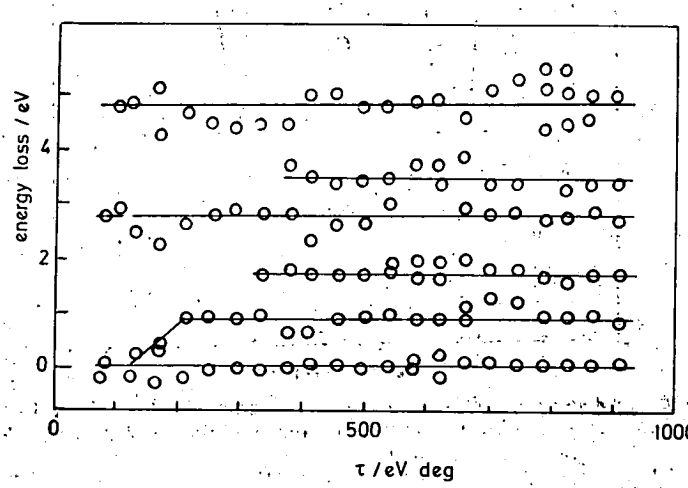

FIG. 9.—Plot showing the location of the peaks observed in the energy loss measurements as a function of the reduced scattering angle, τ. CH_3I + K 164 eV collision energy.

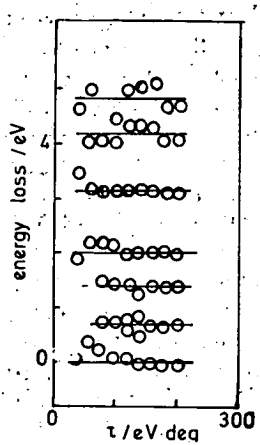

FIG. 10.—Plot showing the location of peaks observed in the energy loss measurements. CH_3I + K at 81 eV collision energy.

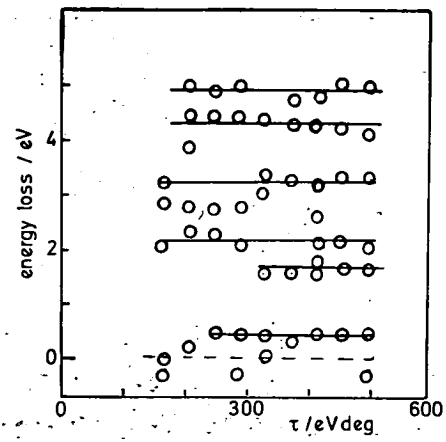

FIG. 11.—Plot showing the location of peaks observed in the energy loss measurements. $C_3H_7I + K$ at 166 eV collision energy.

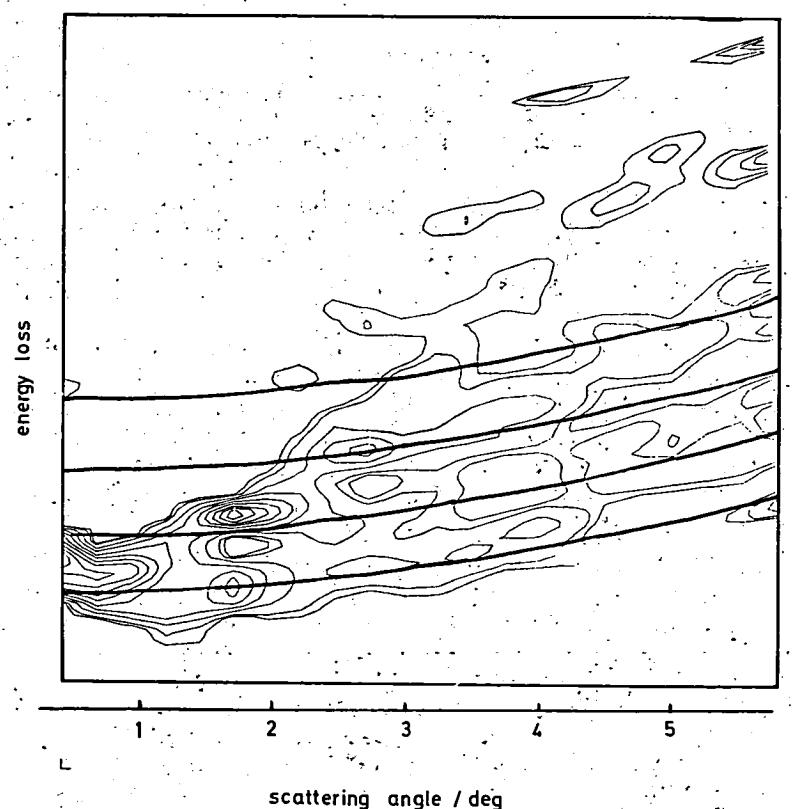

FIG. 12.—Contour plot showing $CH_3I + K$ scattering as a function of energy loss and c.m. scattering angle at a collision energy of 164 eV and after enhancement by deconvolution. Thick lines are drawn at energy losses of 0.0, 0.86, 1.6 and 2.8 eV.

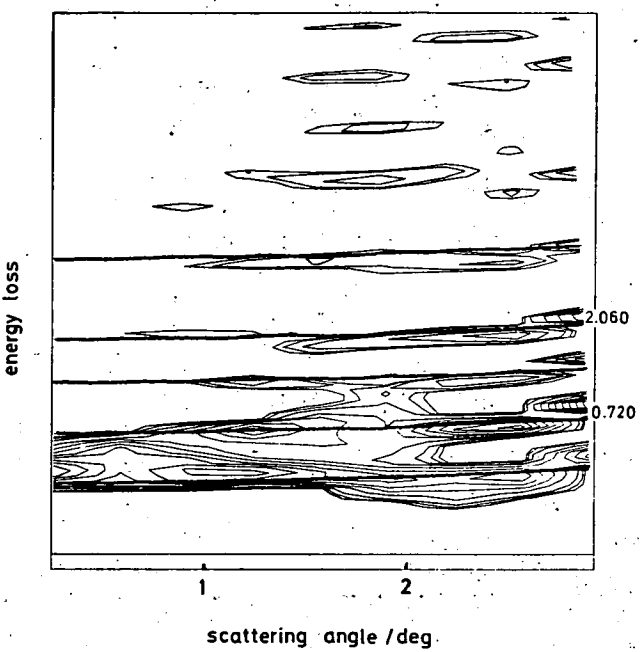

FIG. 13.—Contour plot showing CH_3I + K scattering as a function of energy loss and scattering angle at a collision energy of 81 eV and after enhancement by deconvolution. Thick lines are drawn at energy losses of 0.0, 0.72, 1.4, 2.0 and 3.2 eV.

electron transfer seems to be rapid, but the repulsion soon drops almost to zero. The functional form of eqn (2) must be wrong and the dependence of V^{ion} on R_{MeK} should be introduced. This could be interpreted as due to the repulsion of the departing Me group by the K^+ ion, or the change in bond order of MeI^- due to partial back transfer of the electron to K^+.

Nevertheless, relaxation of the Me–I bond on the ionic surface is a key step in the collision process. Besides leading to extensive vibrational excitation, the deflection of trajectories sampling the ionic surface will depend on the extent of R–I relaxation during the collision. The angular thresholds for all electronic processes fed by the ionic surface will not thus scale with $E\chi$, and will also depend upon the reduced mass of RI. These effects can be seen in fig. 17, where the energy losses calculated from this

TABLE 1.—EXCITED STATES OF K AND CH_3I

K	energy/eV	CH_3I	energy/eV
$4^2S_{\frac{1}{2}}$	0.0	$X(^1A_1)$	0.0
$4^2P_{\frac{1}{2},\frac{3}{2}}$	1.62	A^*	3.47*
$5^2S_{\frac{1}{2}}$	2.61	B, $C(E)$	6.10, 6.16
$3^2D_{\frac{3}{2},\frac{5}{2}}$	2.67	D, (E)	6.77
$5^2P_{\frac{1}{2},\frac{3}{2}}$	3.06	E,	7.30
Rydberg states		F, G	9.4, 9.8
I.P.	4.34	Rydberg states	
		I.P.	9.54

* Onset of continuous adsorption; peak at 4.5 eV.

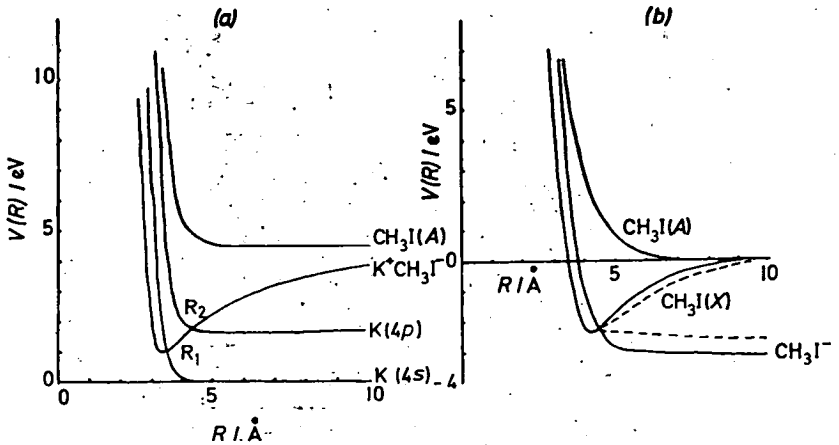

FIG. 14.—(*a*) Isotropic diabatic potential model for K + RI interaction. (*b*) CH_3I and CH_3I^* potentials. Dashed curves show the perturbation used to obtain the approximate fit described.

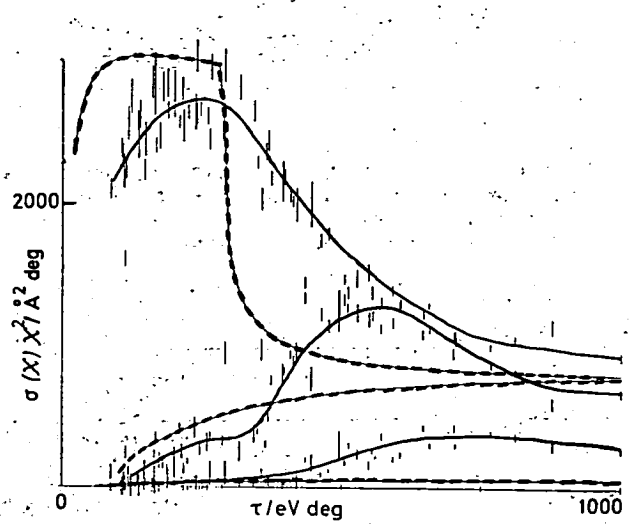

FIG. 15.—Isotropic sudden model; comparison with observations for CH_3I + K at 164 eV.

model are displayed against the corresponding scattering angle. In the $E\chi$ region around 150 eV°, particularly at 81 eV collision energy, a rainbow feature can be seen where two branches for the ionic ground state scattering coalesce.

The invariance of vibrational excitation with angle of scattering is a remarkable feature of the plots and again points to a relatively small shift of the ionic/covalent seam with changing transit time over the surface.

Finally, the differential cross sections for the channels identified are displayed, together with the model predictions, in fig. 18 and 19. The observed very narrow angle elastic scattering is normalised to the model.

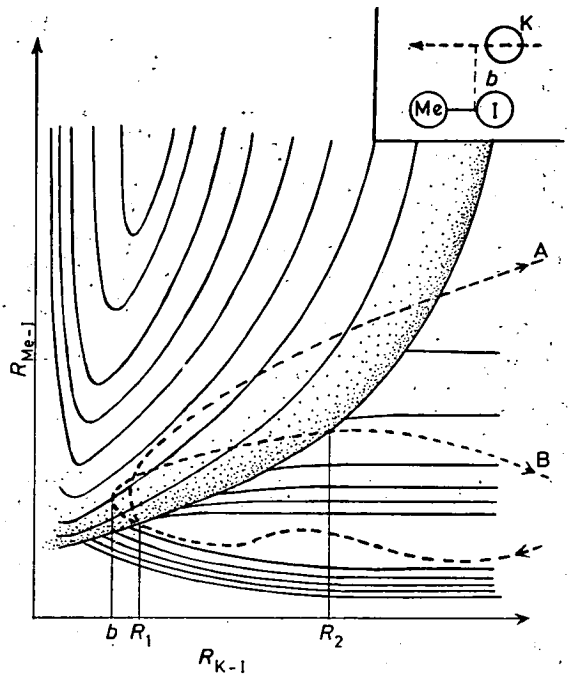

FIG. 16.—High energy trajectories on an ionic/covalent surface. Two trajectories are shown, corresponding to different initial kinetic energies ($E_A < E_B$). The crossing point on the outward path (R_2) is very sensitive to E. In case A, R_2 is so large that dissociation or ionisation would result. The K trajectory in real space is inset.

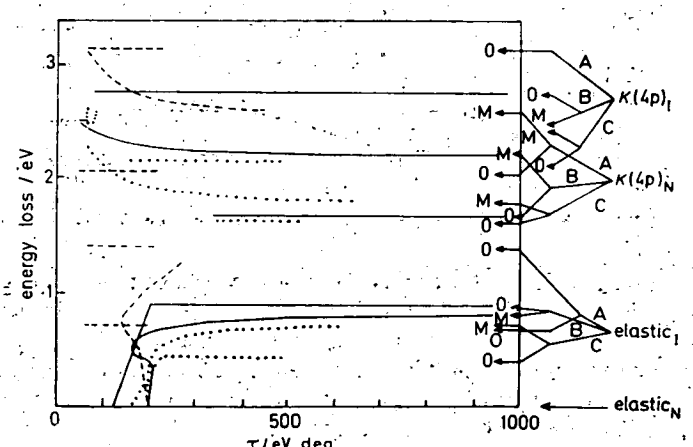

FIG. 17.—Comparison of observed (O) and bond stretching model predictions (M) for the energy loss as a function of reduced scattering angle. The subscript I indicates motion on the neutral surface. Model and experiment are in accord in predicting an increasing energy loss as the mass of R decreases and as the collision lifetime increases. Dashed curve, 81 eV MeI; solid curve, 164 eV MeI; dotted curve, 166 eV PrI.

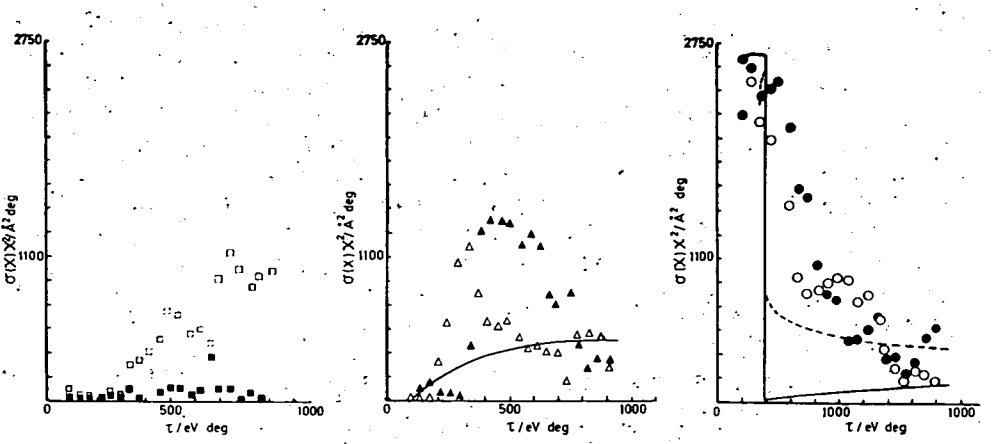

FIG. 18.—Differential cross-sections for K + CH_3I at 164 eV. (○, ●) ground state N, I; (△, ▲) K* (4*p*) N, I; (□, ■) CH_3I^* (*A*) N, I. Lines are the model fit (——) N and (– – – –) I.

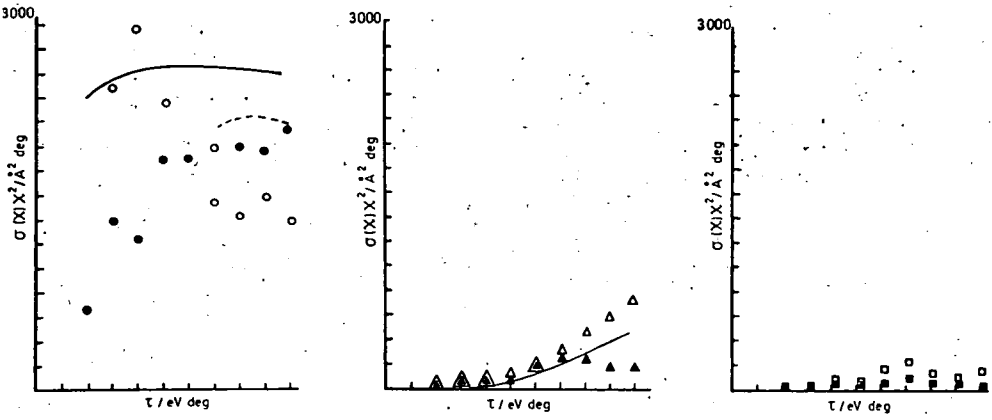

FIG. 19.—As for fig. 18, but at 81 eV.

CONCLUSIONS

Our conclusions as to the processes involved may be summarised with reference to fig. 14(*a*) as follows:

(*a*) Each electronic exit channel is accompanied by two vibrational channels, one with small or zero internal energy change, the other with substantial vibrational excitation. These two channels correspond to, respectively, diabatic or adiabatic (harpooning) behaviour at the first crossing R_1. Both channels are important in the experimental energy range.

(*b*) The negative ion state involved is a repulsive state, but with rather different characteristics from the isolated RI^- ion. In particular, the amount of bond stretching is less than expected (at least in the configuration probed in the bound state exit channels) and points to some containment of the alkyl group.

(*c*) The differential cross section summed over all discrete exit channels (ground plus excited states) is approximately constant over the χ range from 0.5 to 5° (LAB). This strongly suggests that continuum processes (bond dissociation and ionisation), unless they onset at very small angles of deflection, play a negligible role at impact parameters $\lesssim \sigma_{LJ}$.

(*d*) The excitation of the *A* state of CH_3I is observed to have two energy loss contributions and angular thresholds, but these have less intensity than in the K* channel. An ionic surface again probably intervenes because of the small angular thresholds. But even without bond stretching, the ground state $K^+CH_3I^-$ surface would lead to a crossing at ≈ 50 Å on the outward branch, at which point the coupling matrix element between the two states would be essentially zero. Some electronic excitation of the negative ion may be involved, *i.e.*, harpooning to a different empty orbital.

(*e*) Discrete energy losses >5 eV are observed and these must correspond to electronic excitation of the alkyl iodide. Since these energy levels are above the energy of the separated K^+RI^- ion pair, the ground state ionic surface cannot be involved in their coupling.

[1] J. L. Kinsey, *Molecular Beam Reactions* (M.T.P. Int. Rev. Sci., Physical Chemistry, 1972) ser. 1, vol. 9.
[2] M. E. Gersh and R. B. Bernstein, *J. Chem. Phys.*, 1972, **56**, 6131.
[3] A. P. M. Baede, *Charge Transfer between Neutrals at Hyperthermal Energies, Adv. Chem. Phys.*, (Wiley, Chichester, 1975), vol. 30.
[4] V. Kempter, *Electronic Excitation in Collisions between Neutrals, Adv. Chem. Phys.*, (Wiley, Chichester, 1975), vol. 30.
[5] M. A. D. Fluendy, K. P. Lawley, J. M. McCall and C. Sholeen, *Faraday Disc. Chem. Soc.*, 1977, **62**, 149.
[6] J. M. McCall and M. A. D. Fluendy, *J. Phys. E*, 1978, **11**, 631.
[7] M. A. D. Fluendy, J. H. Kerr, J. M. McCall and D. Munro, *On-line Computing in the Laboratory*, ed. R. A. Rosner, B. K. Penney and P. N. Clout (Advance, London, 1975).
[8] J. A. Aten, G. A. H. Lanting and J. Los, *Chem. Phys.*, 1977, **19**, 241.
[9] W. E. Wentworth, R. George and H. Keith, *J. Chem. Phys.*, 1969, **51**, 1791.

Dr. M. A. D. Fluendy, Dr. K. P. Lawley and Mr. D. Sutton (*Edinburgh*) said: In the paper presented at this meeting Fluendy *et al.*[2] discussed energy losses in the 0.5-5 eV region observed in K/CH_3I collisions. The same data showed a number of inelastic processes with energy losses in the 5-12 eV region (fig. 3).

The points to be noted about these results are as follows. (1) There is a relative sparsity of states compared with optical spectra taken in this region. (2) The energy losses are discrete and with the exception of process (7)[2] constant with increasing scattering angle. (3) The processes are observed to onset at very narrow scattering angles.

The combination of small scattering angles and large energy losses is evidence for the involvement of strong attractive potentials and suggests that these processes proceed *via* transient excited ionic states.

Fig. 4 shows a possible set of potential energy curves allowing access to highly excited molecular states and leading to only small angles of deflection.

If the intermediate negative molecular ion potential is different from the ground state potential, changes in the CH_3I geometry would be expected to occur during the collision. Thus process (7) may be associated with harpooning into the σ^*(C—H)

[1] R. Wolfgang and R. Cross, *J. Phys. Chem.*, 1969, 73, 743.
[2] M. A. D. Fluendy, K. P. Lawley, J. McCall, C. Sholeen and D. Sutton, *Faraday Disc. Chem. Soc.*, 1979, 67, 41.

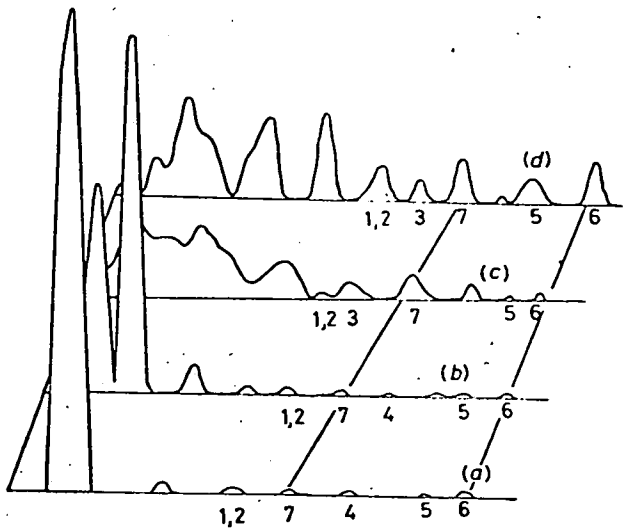

FIG. 3.—Observed energy loss profiles K/CH_3I at c.m. collision energy 164 eV, E_χ in eV: (*a*) 97, (*b*) 287, (*c*) 656 and (*d*) 861.

orbital (fig. 5) followed by recapture from the iodine lone pairs. This transient ionic potential would be repulsive in the C—H coordinate. The time spent in this repulsive state varies with the impact parameter and scattering angle so that, in view of the light mass of the H atom, quite rapid variation in geometry and energy deposition can be expected, in accord with these observations.

In general electronic excitation will take place if donation into a high lying, normally vacant orbital is followed by recapture from a lower, normally filled orbital.

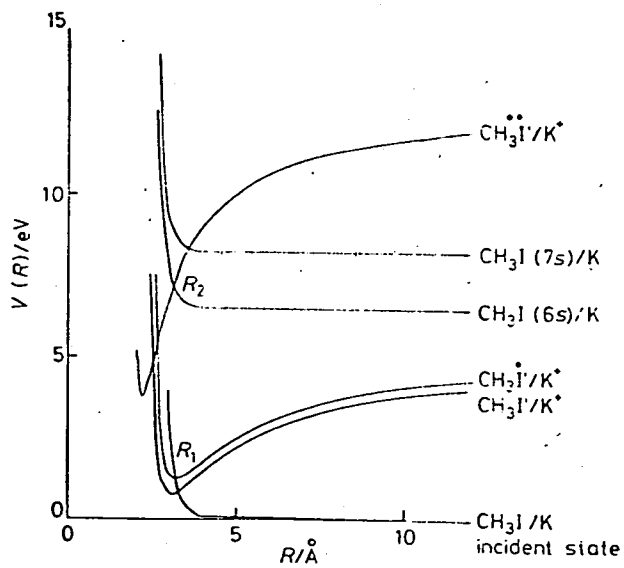

FIG. 4.—Diabatic potentials illustrating incident channel and the electron capture and recapture processes at R_1 and R_2 leading to excited states.

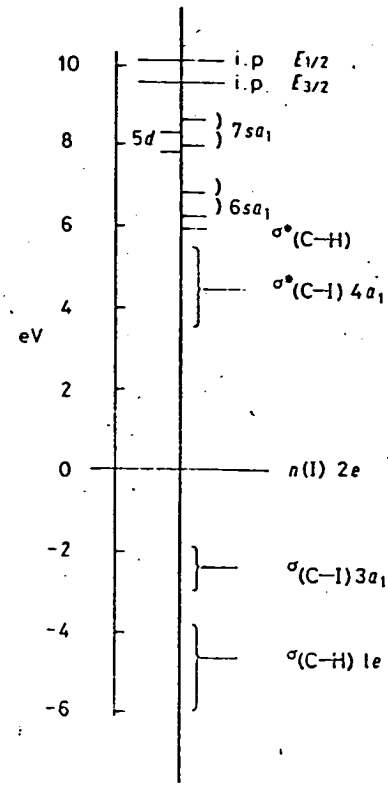

FIG. 5.—Schematic orbital energy diagram for CH_3I.

Possible energy losses arising from such a mechanism have been calculated, allowing us to make tentative assignments to the processes observed.

Dr. M. A. D. Fluendy and Mr. D. Sutton (*Edinburgh*) said: The results presented by Setser *et al.* in which they observed substantial production of electronically excited bromine molecules in collisions with rare gas metastables provide yet another contrast to the behaviour of the analogous alkali metal/halogen molecule systems. Preliminary measurements of the excitation produced in K/Br_2 collisions using the time of flight crossed beam technique described earlier in this Discussion[1] are shown in fig. 1.

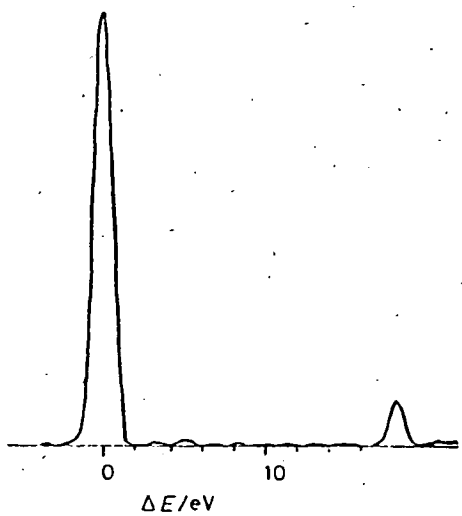

FIG. 1.—K/Br_2 Energy loss profile at a collision energy of 164 eV (centre of mass).

The results are the average of 27 separate observations at angles between 0.45 and 1.78°. The main peak at $\Delta E \simeq 0$ is broadened, presumably by vibrational excitation of the Br_2, but possible electronic transitions with $\Delta E > 1.4$ eV account for $<2\%$ of the observed scattering. The second main feature is due to the K^{41} isotope which occurs with 6% abundance and provides a useful magnitude comparison. In these

[1] M. A. D. Fluendy, K. P. Lawley, J. McCall, C. Sholeen and D. Sutton, *Faraday Disc. Chem. Soc.*, 1979, **67**, 41.

alkali metal/halogen systems, interactions between the ion pair potential surface and the surface leading asymptotically to the excited halogen molecule occur at extremely large distances and cannot therefore be an important route to these excited states. In contrast, as suggested, in the rare gas metastable analogue systems the same $V(RG^+, Br_2^-)/V(RG, Br_2^*)$ interaction lies inside the initial electron transfer radius $[V(RG^*, Br_2)/V(RG^+, Br_2^-)]$.

Dr. M. A. D. Fluendy, Dr. K. P. Lawley and Mr. G. W. Black (*Edinburgh*) said: We have carried out Monte Carlo trajectory surface hopping calculations on the potassium–methyl-iodide system incorporating surfaces corresponding asymptotically to excited potassium atom and methyl iodide molecular states. The potential surfaces used were based upon those developed by Blais and Bunker[1] which correctly describe the individual pair interactions and incorporate a switching function important in the close encounter region. The ionic CH_3I^- potential used was that described by Wentworth *et al.*[2]

Though satisfactory in describing most features of reactive scattering at thermal energies, this potential system was unsatisfactory at high velocities. Only limited access to the ionic surface crossing could be achieved and of those trajectories which crossed to the ionic surface on entrance the majority lead to dissociation rather than to electronic excitation, in contrast to the experimental results.[3]

The difficulty in accessing the ionic surface on entrance arises from the potassium–methyl repulsion, which becomes a dominant feature in the sudden collision, since there is little opportunity for movement within the methyl iodide before harpooning.

[1] D. L. Bunker and N. C. Blais, *J. Chem. Phys.*, 1964, **41**, 2377.
[2] W. E. Wentworth, R. George and H. Teeth, *J. Chem. Phys.*, 1969, **51**, 1791.
[3] M. A. D. Fluendy, K. P. Lawley, J. McCall, C. Sholeen and D. Sutton, *Faraday Disc. Chem. Soc.*, 1979, **67**, 41.

With these surfaces reaction occurs *via* a concerted pre-stretching in the methyl iodide bond as the potassium atom approaches. At high velocities this process is not available and the size of the access window to the ionic surface is correspondingly limited.

After harpooning, these surfaces predict rapid stretching in the CI coordinate and the exit crossing seams to the excited potassium and excited methyl iodide states move to wide internuclear distances. The crossing probability is then small and little electronic excitation can be produced. Comparison of these trajectory results with experiment thus suggests that the isolated pair-wise interactions must be substantially modified in the interaction region.

Volume 65, number 1 CHEMICAL PHYSICS LETTERS 1 August 1979

ELECTRONIC EXCITATION IN POTASSIUM ALKYL IODIDE COLLISIONS

F. CASTANO ‡, M.A.D. FLUENDY, K.P. LAWLEY, C. SHOLEEN ‡ and D. SUTTON
Department of Chemistry, University of Edinburgh, Edinburgh EH9 3JJ, UK

Received 23 April 1979; in final form 7 June 1979

The production of highly excited states of the alkyl iodides by collision with fast potassium atoms has been studied by a time of flight molecular beam technique. A simple electron capture and recapture mechanism is advanced to account for the observations.

The manifold of electronically excited states available in the alkyl iodides falls into three classes corresponding to valence transitions in the C–I band of $n \rightarrow \sigma^*$ type, Rydberg transitions to high *nl* states similar to those of the iodine atom and valence $\sigma \rightarrow \sigma^*$ transitions in the C–H bond. Transitions corresponding to all these three classes are observed in the optical spectrum though the C–H transitions are seen only as a continuum background to the other processes [1–3]. Photodissociation of the alkyl iodides with radiation in the 3.5–5.5 eV region occurs via the continuum A state ($n \rightarrow \sigma^*$) and produces both ground, $I_{3/2}$, and excited, $I_{1/2}$ atoms [4] while the same σ^* orbital occupied in the molecular negative ion is responsible for the substantial translational excitation seen in the reaction [5]

$$K + RI \rightarrow KI + R, \qquad (1)$$

which are classic examples of electron harpooning.

In this work inelastic differential scattering cross sections have been measured for this system in the high energy (50–200 eV) small angle (0–5°) region in which the collision trajectory is approximately rectilinear and explores the potential surfaces inside the harpooning radius. The reaction channel itself is closed in this regime due to momentum constraints on the I capture so that the electronic transitions can be studied in isolation from the capture dynamics.

The measurements described were made by a time of flight method in which the potassium atom beam was pulse modulated and the energy loss in the collision inferred from the change in the measured flight time. In this way a contour map was built up showing the scattered K atom flux versus scattering angle and energy loss at various initial collision energies [6,7].

Very considerable inelasticity is observed in these measurements with energy losses ranging from 0.5 to ≈12 eV. The lower energy processes, < 5 eV which include the electronically elastic, K(4p) and CH_3I (A) state as exit channels have been discussed elsewhere [8] and shown to involve an ionic intermediate repulsive in the C–I bond. This paper discusses the higher energy loss processes corresponding to Rydberg and C–H transitions, which are also seen, though with smaller cross sections.

Typical energy loss profiles are shown in fig. 1 for several reduced scattering angles ($E\chi$, eV°). The optical spectrum in the same energy region shows a very large number of discrete features associated with transitions from n(I) to various Rydberg states (n, l) having $n > 5$, l = s, d, p and core terms of $E_{1/2}$ and $E_{3/2}$. Continuum absorption from C–H transitions is seen as a background to these discrete features. In comparison, the relative sparsity of the collision induced transitions is immediately apparent and at each angle of scattering or impact parameter only discrete energy losses are seen. The observed features occur systemati-

‡ Present address: Departamento de Quimica Fisica, Facultad de Ciencas, University de Bilbao, Bilbao, Spain.
‡ Present address: Argonne National Laboratory, Argonne, Illinois, USA.

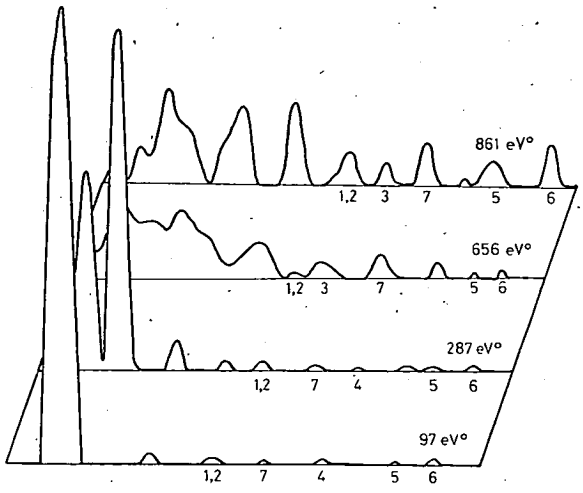

Fig. 1. Observed energy loss profiles K/CH_3I at centre of mass collision energy of 164 eV, $E\chi$ in eV°. Peak numbers refer to table 1.

cally as the scattering angle is varied, though the intensity varies considerably; their behaviour is summarised in table 1. The observed energy losses are independent of reduced scattering angle with one exception, process 7 for which the energy loss observed increases approximately linearly with $E\chi$. The angular dependence of the differential cross sections is illustrated in fig. 2 where the results have been approximately scaled by normalising the very small angle elastic scattering (arising from outside the harpooning radius) to model potentials for this region developed in molecular dynamic studies [12].

The energy loss processes reported are seen in fig. 2 to onset at small $E\chi$ values, This combination of a substantial energy exchange coupled with a small reduced deflection is good evidence for the involvement of strong attractive potentials during the collision and suggests that processes of interest may also occur via a transient negative ion.

Table 1
Observed energy losses

Process number	Observed energy loss (eV)			Proposed assignment (see table 2)	
	MeI		PrI		
	c.m. collision energy = 81 eV	c.m. collision energy = 164 eV	c.m. collision energy = 166 eV	effective transition	predicted energy loss (eV)
1	5.2	5.5	6	$n(I) \rightarrow \sigma^*_{(C-I)}$	3.5 a)
2	5.7				5.5
3	6.4	6.4	6.6	$n(I) \rightarrow$ 6s Rydberg	6.5
4	8	8.4	8.5	$n(I) \rightarrow$ 7s Rydberg	8.2
5	higher energy loss process	10.4	10.8	$\sigma_{p(C-H)} \rightarrow$ 6s Rydberg	11.0
6	obscured by ^{41}K isotope	12.4	13.2	$\sigma_{p(C-H)} \rightarrow$ 7s Rydberg	12.9
7	6–7.2 in $E\chi$ range 40–220 eV°	6.4–9.0 in $E\chi$ range 60–900 eV°	11–12.8 in $E\chi$ range 160–550 eV°	$n(I) \rightarrow \sigma^*_{(C-H)}$	internal energy internal energy b)

a) This transition is to the dissociative A state of CH_3I.
b) The equivalent $\sigma^*_{(C-H)}$ orbital in propyl iodide cannot be identified unambiguously but is likely to be considerably higher in energy.

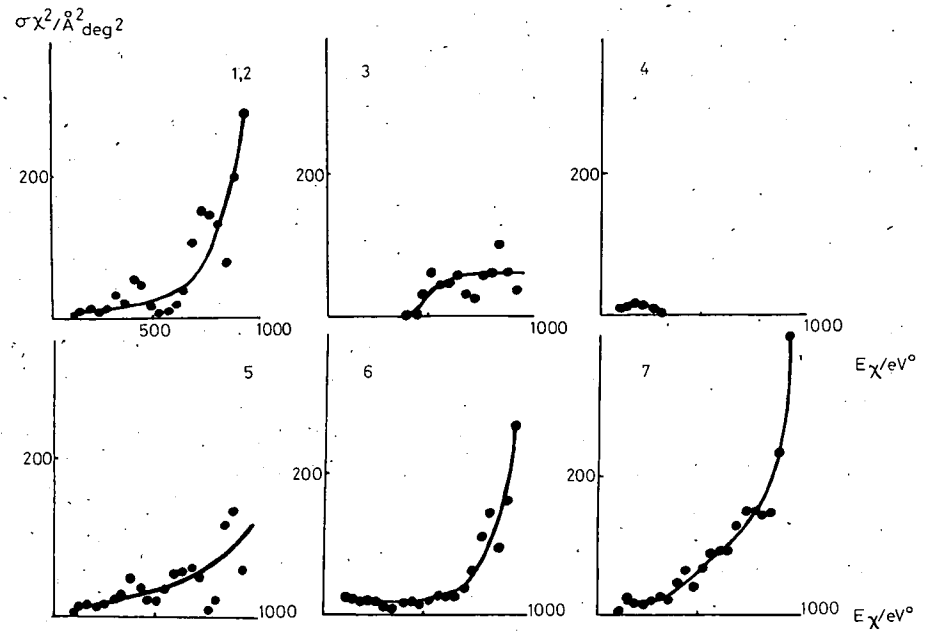

Fig. 2. Differential scattering cross sections for K/CH_3I at 164 eV (c.m.). The processes are identified in table 1.

A schematic energy diagram showing the location of the lower orbitals in CH_3I is drawn in fig. 3. The lowest unoccupied orbitals include the $\sigma^*_{(C-I)}$ (the electron receptor orbital of importance in the reactive and smaller energy loss processes) and the $\sigma^*_{(C-H)}$, which are both antibonding in the C–I and C–H respectively, together with the Rydberg levels 6sa, 7sa and $5da_1$ + 2e. These are all possible receptor levels – higher Rydberg states though available in principle will have considerably smaller coupling matrix elements due to the large size of these orbitals and are thus unlikely to be important.

Since these measurements are confined to the neutral exit channel, electron capture must be followed by the recapture of an electron by the K^+ ion on exit from the collision. Electronic excitation will now take place if an electron is recaptured from a lower, normally filled orbital leaving the receptor orbital occupied and a lower lying vacancy. Possible energy losses arising from this mechanism are shown in table 2; the spin orbit splitting is comparable to the energy resolution of the measurements at the 164 eV collision energy while the 7s and 5d Rydberg states are also too close to be resolved and the energies of these states are averaged together in table 2. Comparison with the observa-

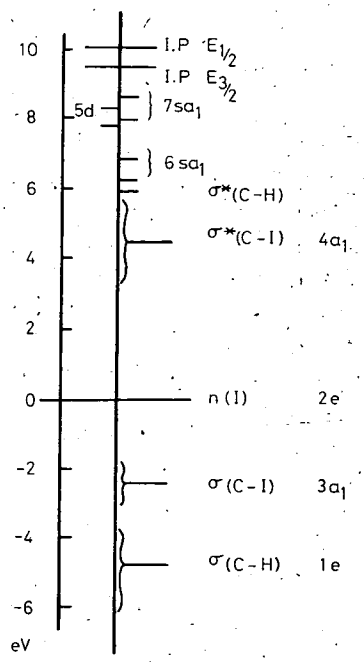

Fig. 3. Schematic orbital energy diagram for CH_3I. The orbitals n(I), $\sigma_{(C-I)}$ and $\sigma_{(C-H)}$ are located from photoelectron spectra [9,10]. The $\sigma^*_{(C-I)}$ and Rydberg levels form optical spectra [1–3]. The $\sigma^*_{(C-H)}$ is derived with rather less certainty from the optical spectra of the alkanes [11].

Table 2
Transitions and energy losses expected from electron harpooning and subsequent recapture in CH_3I

Exit process: Orbitals from which electron is recaptured	Highest occupied orbital	Incident process: Lowest unoccupied orbital: Orbital into which electron is captured — $\sigma^*_{(C-I)}$ $4a_1$	6s Rydberg $6sa_1$	$\sigma^*_{(C-H)}$	$\left.\begin{matrix}5d\\7s\end{matrix}\right\}$ Rydberg $7sa_1$ $5da_2$ + 2e	Energy losses in eV
	n(I) 2e	3.5–5.5	6.18 and 6.77 6.5	≈6.0	7.84 8.30 8.03 8.65 8.2	
	$\sigma_{(C-I)}$ $3a_1$	≈7	8.6 and 9.2 8.9	8.4		
	σ_p (C–H) 1e	9.2	10.9 and 11.1 11.0	10.7	12.5 13.0 12.7 13.4 12.9	

tions in table 1 is immediately suggestive and leads to the tentative assignment shown in table 1. The model thus suggests that electron capture into the lower empty Rydberg or valence levels is possible. The relative probability being at least partly determined by the orientation of the CH_3I during the collision. Thus process 7, n(I) → $\sigma^*_{(C-H)}$, involving capture into the $\sigma^*_{(C-H)}$ followed by recapture of an electron from the iodine lone pairs would presumably be favourable for trajectories in which the K moves first past the CH_3 and then the I groups. Similarly processes 5 and 6, $\sigma_{(C-H)}$ → 6s and 7s, would involve trajectories moving in the reverse direction while the other transitions occur at the iodine atom only. It is notable that with this model process 7 which was unique in showing an energy loss increasing with $E\chi$, is seen to arise from an intermediate ion state which is antibonding and repulsive in the C–H coordinate. Since $E\chi$ is inversely related to the impact parameter, itself inversely related to the time between the capture and recapture episodes on the trajectory, the time spent in this repulsive state increases with $E\chi$. The increasing energy loss can now arise as a result of the substantial changes in geometry which occur during the collision.

Similar effects as a result of populating the $\sigma^*_{(C-I)}$ orbital can be distinguished in the lower energy losses but because of the much greater mass of the ejected group (CH_3 as compared to H in the case of the $\sigma^*_{(C-H)}$ orbital) the effect is much smaller and cannot be distinguished in the $E\chi$ range discussed here. The dynamics leading to this dissociative state are further complicated since it may be accessed on either the inward or outward branches of the trajectory [8]. It is possible that the two channels observed at 81 eV, where the resolution is better (≈ 0.25 eV), correspond to dissociative states leading to either the $I_{1/2}$ or $I_{3/2}$ states of iodine with considerable translational energy; the spin orbit splitting is not resolved experimentally at the higher collision energies.

The C–I force constant is essentially unchanged by population of Rydberg states so that transitions to these states would be expected at a fixed energy in accordance with these observations. Finally it is worth noting that all the capture transitions can be assigned to s or σ orbitals (though the 5d and 6p $E_{1/2}$ levels at 8.30 and 7.99 eV could not be distinguished from the 7s levels) suggesting that electron orbital angular momentum is conserved in these collisions.

Considerable mixing of the various orbitals will take place under the time dependent perturbation of the K^+ ion and the precise description of the orbital from which recapture finally occurs is unclear. A simplified diabatic potential scheme illustrating a possible mechanism is shown in fig. 4 where the doubly starred

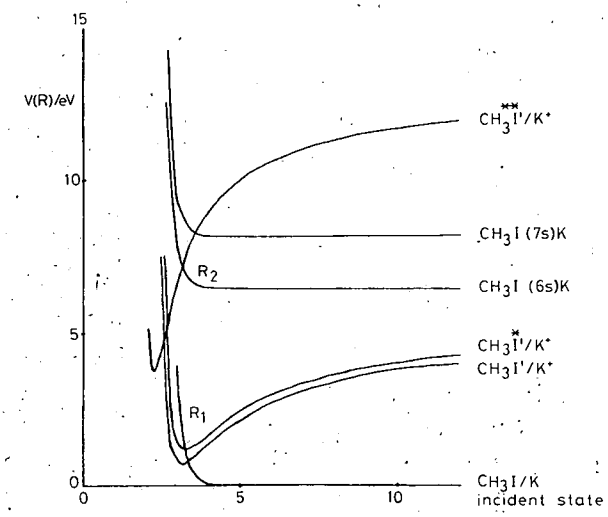

Fig. 4. Diabatic potentials illustrating the incident channel and the electron capture and recapture processes at R_1 and R_2 leading to excited RI states.

curve represents the state of the CH_3I under perturbation by K^+. The most significant features of this model are the two electron transfers at R_1 and R_2 on entry and exit and the strong attractive exit potential which will produce scattering at small $E\chi$.

The authors are glad to acknowledge helpful discussions with Dr. Stephen Cradock.

References

[1] G. Herzberg, Electronic spectra and electronic structure of polyatomic molecules (Van Nostrand, Princeton, 1966).
[2] R.A. Boschi and D.R. Salahub, Mol. Phys. 24 (1972) 289.
[3] H.T. Wang, W.S. Felps, G.L. Findley, A.R.P. Rau and S.P. McGlynn, J. Chem. Phys. 67 (1977) 3940.
[4] S.J. Riley and K.R. Wilson, Faraday Discussions Chem. Soc. 53 (1972) 132.
[5] D.R. Herschbach, Faraday Discussions 55 (1973) 233.
[6] M.A.D. Fluendy, J.H. Kerr, J.M. McCall and D. Munro, in: On-line computing in the laboratory, eds. A. Rosner, B.K. Penney and P.N. Clout (Advance, London, 1975).
[7] J.M. McCall and M.A.D. Fluendy, J. Phys. E 11 (1978) 631.
[8] M.A.D. Fluendy, K.P. Lawley, J.M. McCall, C. Sholeen and D. Sutton, Faraday Discussions 67 (1979), to be published.
[9] D.W. Turner, C. Baker, A.D. Baker and C.R. Brundle, Molecular photoelectron spectroscopy (Wiley, New York, 1970).
[10] A.D. Baker and D. Betteridge, Photoelectron spectroscopy (Pergamon, Oxford, 1972).
[11] J.W. Raymonda and W.T. Simpson, J. Chem. Phys. 47 (1967) 430.
[12] L.M. Raff and M. Karplus, J. Chem. Phys. 44 (1966) 1212.

ELECTRONIC EXCITATION AND ENERGY TRANSFER IN K–N_2 COLLISIONS

G.W. BLACK, M.A.D. FLUENDY and D. SUTTON
Department of Chemistry, University of Edinburgh, Edinburgh EH9 3JJ, UK

Received 15 October 1979; in final form 1 November 1979

Inelastic differential scattering cross sections for the system K/N_2 have been measured in the small-angle regime for E_X in the range 80–600 eV deg. A cross beam time-of-flight technique was used to measure energy transfer effects occurring in the collision. The dominant inelastic process in the region explored was production of the $K(4\,^2P)$ state together with simultaneous vibrational excitation of the N_2 molecule. The observations are in excellent agreement with published potentials and a simple classical model involving an intermediate with considerable negative-ion character.

1. Introduction

The quenching of alkali atoms as a result of collisions with diatomic molecules has been of interest for a considerable time [1]; the system Na/N_2 has been of particular interest both experimentally [2] and theoretically [3,4]. The inverse process, atomic excitation as a result of energetic collisions with diatomic molecules, has also been studied [5]. More recently the system of interest here, K/N_2, has been studied by a novel coincidence technique [6] in which the differential cross section for the process $K(4\,^2S) + N_2 \rightarrow K(4\,^2P) + N_2$ was determined, the final state of the molecule not being measured in this experiment. All this work is consistent with an early suggestion that an ion-pair (K^+/N_2') state is an important intermediate.

In the present experiments the time-of-flight technique provides additional information on the excitation of other states, vibrational excitation of N_2 and elastic scattering. The combination of this data with Kempter's observations is consistent with significant ionic character in the description of the collision system both in the angular distributions and now in the vibrational excitation of the N_2.

2. Experimental

2.1. Apparatus

A schematic of the apparatus is shown in fig. 1. The beam of fast alkali atoms is produced initially as ions by surface ionisation on a porous tungsten disc heated radiatively to ≈1500 K. The ions are accelerated to the required collision energy and electrostatically focused. The beam is then pulse-modulated, using a velocity compression technique [7], so that the time-of-flight analysis of the scattered atoms may be carried out. After modulation, the ion beam is neutralised by charge exchange in a vapour cell, and any residual ions are deflected away.

The fast neutral beam enters the collision zone where it intercepts the orthogonally introduced slow target beam, formed by effusion through a capillary array, and modulated at 47 Hz. The scattered potassium atoms are ionised on a cool tungsten wire at the detector, and arrivals are counted via a scintillator and a photomultiplier. The detector can be varied in angle with a precision of ±0.002 deg. The arrivals at the detector stop a 50 MHz crystal clock running in synchronism with the pulse modulation, and so their flight time is recorded. The data collection and experimental operation are controlled by an on-line computer [8], which also monitors important experimental conditions, such as beam fluxes, throughout the run. Due to

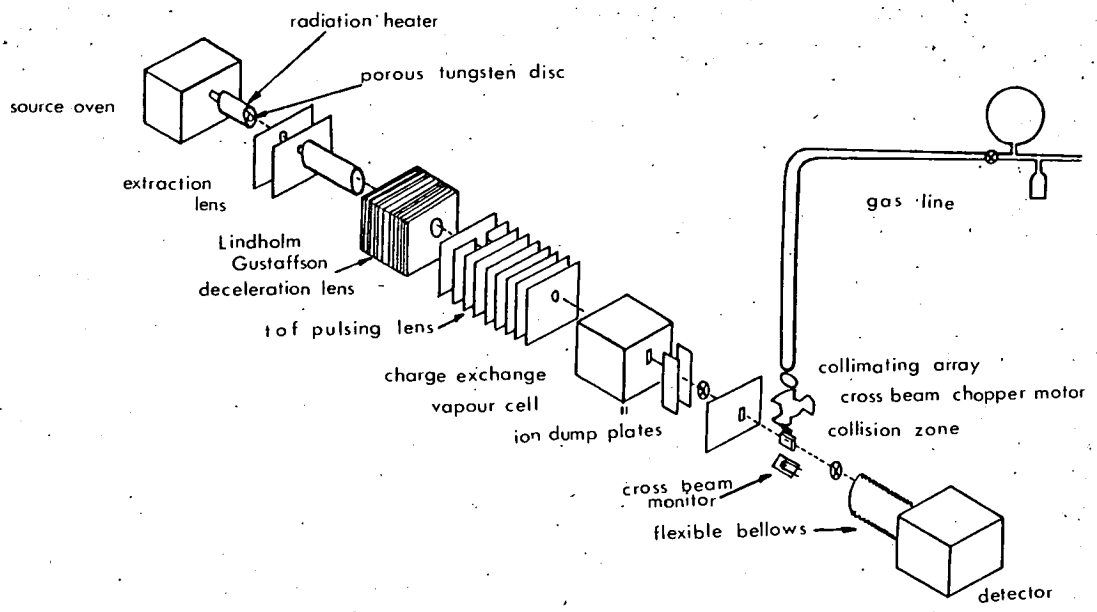

Fig. 1. Schematic of the apparatus.

the very low count rates associated with experiments of this type, less than 0.01 s^{-1} at wide angles, an experiment takes about five days. In these experiments the resolution in $E\chi$, the reduced scattering angle, was ≈35 eV deg and the energy loss could be determined to ±0.15 eV.

2.2. Results

The results were collected over two separate experimental runs, and are presented after transformation to the c.m. reference frame. A c.m. contour map showing the variation in the product of the scattered intensity and the square of the scattering angle, $I(\chi)\chi^2$, as a function of scattering angle and post-collision velocity, is presented in fig. 2.

Such contour plots are highly information-intensive but the grosser features are more easily displayed in a time-of-flight profile. Fig. 3 shows such a profile averaged over all the angles of observation. It is immediately apparent that the elastic channel dominates the collision while an inelastic process with a most probable energy loss of 2.8 eV arises in ≈16% of collisions. A number of very much smaller processes are seen at greater energy losses. The ^{41}K isotope with 6% abundance provides a useful marker.

Measurements of this type do not unambiguously identify the exit channel; however, the lowest excited state of N_2, $A\,^3\Sigma_u^+$, is 6.2 eV above the incident channel, while fluorescence measurements [10] on this system revealed predominantly K(4 ^{2}P) excitation, the K(5 ^{2}P) and (6 ^{2}S), states being populated to ≈2% and 0.6% in comparison. The inelastic channel observed in this experiment onsetting at 1.6 eV and having a maximum at 2.8 eV is therefore assigned to K(4 ^{2}P) excitation with, by elimination, concurrent vibrational excitation of the N_2. A very weak inelastic peak with an energy loss of 4.7 eV and ≈10% of the intensity of the K(4 ^{2}P) scattering can also be seen. This may be associated with similar excitation of the K atom to K(5 ^{2}S) or (5 ^{2}P) states and again concurrent vibrational excitation of the N_2, but will not be further discussed here. The proposed assignment is supported by the success of the model based upon this interpretation of the energy loss data.

Previous time-of-flight measurements by Gersing et al. [11] on this system show similar loss profiles to those observed in this work but were interpreted solely as K excitation and led to the conclusion that production of K (5s) and (3d) states was the main inelastic channel – an unsafe conclusion in view of the fluorescence experiments [10].

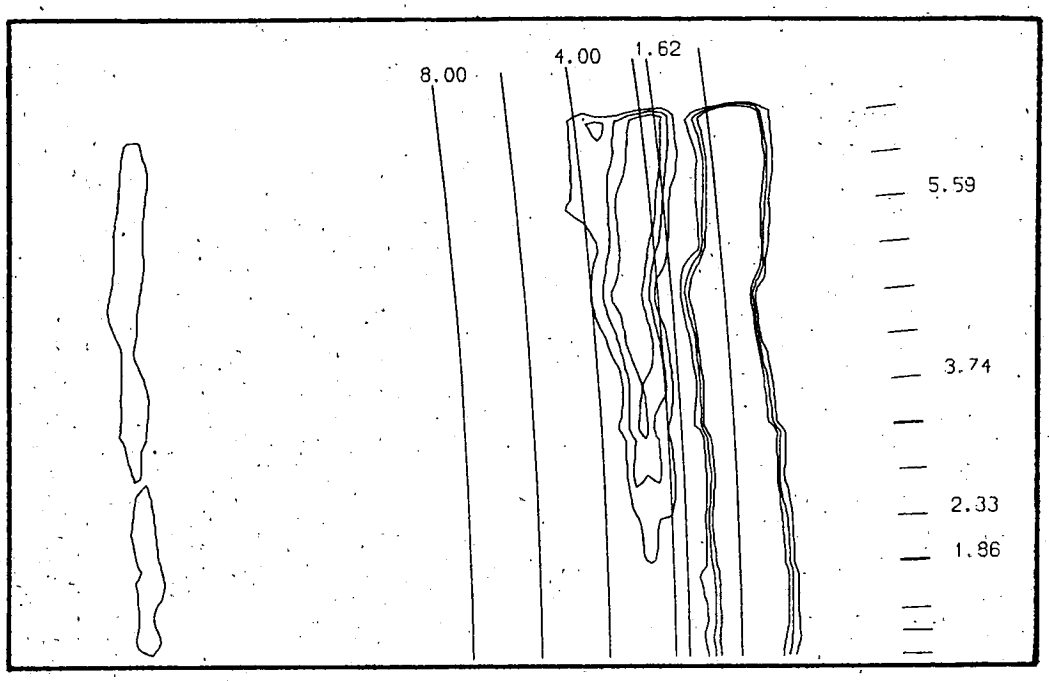

Fig. 2. Polar contour plot showing $I(\chi)\chi^2$ as a function of c.m. scattering angle, χ, and energy loss. The K/N_2 collision energy was 85.5 eV (c.m.). Contours are drawn at 5, 10 and 15%. The angles at which observations were taken are indicated together with an energy-loss graticule. Two distinct peaks can be seen; the lowest shows an energy loss < 0.6 eV, the higher (a rather weaker one) a loss ≈ 2.8 eV. The feature at the top of the figure arises from the ^{41}K isotope.

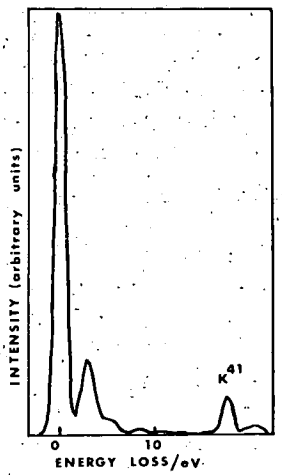

Fig. 3. Energy-loss profile averaged over all angles of observation (0.9–7.5 c.m.). Collision energy 85.5 eV.

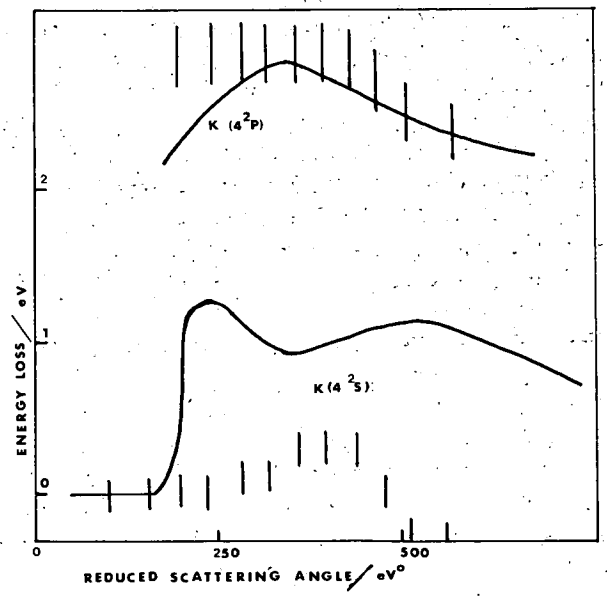

Fig. 4. Most-probable energy loss associated with $K(4\,^2S)$ and $K(4\,^2P)$ scattering. Experimental observations are shown as bars, two standard deviations long. Continuous curve is model prediction. Collision energy 85.5 eV.

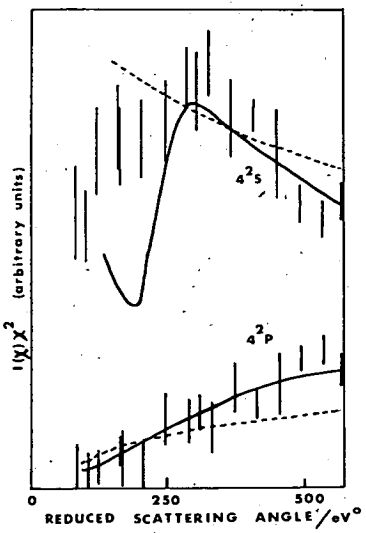

Fig. 5. Differential scattering cross sections, $I(\chi)\chi^2$, in arbitrary units for K(4 ^{2}S) and K(4 ^{2}P) scattering. Model predictions using the Kempter potentials are dashed, approximately adjusted potentials solid line. Collision energy 85.5 eV.

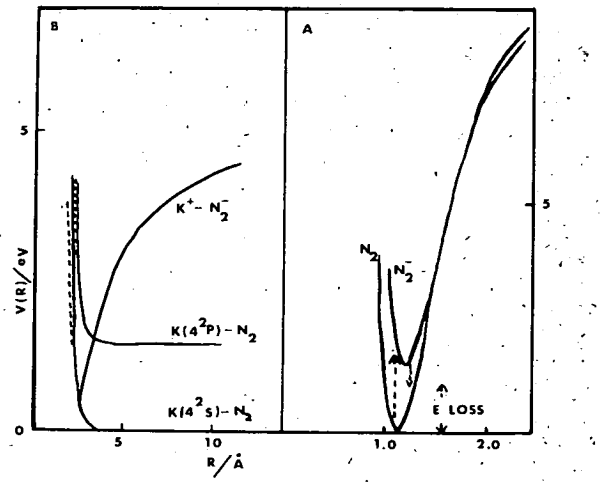

Fig. 6. (a) Potentials [10] for N_2 and N_2'; vertical electron transitions are shown arrowed. (b) Diabatic potentials for K/N_2. The potentials adjusted to accord with the results are shown in solid line, the Kempter potentials are dashed.

In the coincidence experiments of Kempter et al. [6], only K(4 ^{2}P) excitation was reported. However the flight-time resolution of their experiment, as estimated from the reported apparatus dimensions, was insufficient to distinguish the additional energy loss associated with N_2 vibrational excitation and the two experiments are thus not in contention.

The differential cross sections for the electronically elastic and inelastic channels, calculated by summing appropriate regions of the individual energy loss profiles are plotted in fig. 5. They are similar to those reported by Kempter et al. In fig. 4, the most probable loss for these two channels is plotted against scattering angle.

3. Discussion

The measurements reported are confined to the narrow angle region in which the trajectories are approximately rectilinear and of constant velocity so that the deflection angle, collision lifetime and impact parameter can be simply related by small-angle formulae [12]. The collision lifetime is dependent upon the impact parameter but is of the order 10^{-14} s and so is comparable to the vibrational period of N_2 and N_2'.

The potentials relevant to this system are displayed in fig. 6, 6a illustrating the potentials for N_2 and N_2' derived by Gilmore [13], while 6b shows a very simplified set of diabatic potentials for the K–N_2 interaction. It can be seen that both the ground and excited K atom scattering can arise by two routes according to whether the crossing to the surface with ionic character occurs on the ingoing or outgoing phases of the collision. The electron transfer corresponding, in this simple picture, to the formation of the negative ion and the subsequent recapture of an electron to reform neutral potassium in either a ground or excited state are illustrated in fig. 6a. The transitions are assumed vertical in position and to conserve momentum. Since the potential curves for N_2 and N_2' are mutually displaced, the period spent as a negative ion results in vibrational excitation of the N_2 molecule on exit from the collision.

A simple classical model based on this picture using the Landau–Zener approximation to compute the crossing probability and assuming independent motion in the N–N and (N_2)–K dimensions was developed. (The model is very similar to that successfully used to describe similar processes in systems of the type K/RI [14].) In this model the only interaction permitted between these separate motions was via vertical electron transitions and changes in R_c occurring as a result

of the variation in electron affinity as the N–N bond stretched. The model calculations were performed in a simple iterative fashion; the initial estimates of cross section, scattering angle and lifetime on the ionic surface (and hence N_2 vibrational excitation) were computed using the small-angle formulae based on the $v = 0$ N_2 electron affinity. Numerical computation of the N_2' motion during the collision lifetime produced a revised vertical electron affinity and R_c that were used to update the small-angle scattering calculation. Iteration of this process yielded very rapid convergence.

The potentials used in this model for N_2 and N_2' were of Morse form fitted to the well-established Gilmore potentials [13] in their bowl region of importance in the calculation:

$$V_{N_2} = D_1\{1 - \exp[-\beta_1(R - R_{01})]\}^2 - D_1, \quad (1)$$

where

$$D_1 = 9.8 \text{ eV}, \quad \beta_1 = 2.5, \quad R_{01} = 1.10 \text{ Å};$$

$$V_{N_2'} = D_2\{1 - \exp[-\beta_2(R - R_{02})]\}^2 - D_2 + 0.3, \quad (2)$$

where

$$D_2 = 8.5 \text{ eV}, \quad \beta_2 = 2.2, \quad R_{02} = 1.185 \text{ Å}$$

corresponding to a vertical electron affinity of 1.9 eV at the N_2 equilibrium distance.

The K/N_2 potentials were initially chosen to be identical to those used by Kempter et al. to fit the $K(4\,^2P)$ scattering. These were later modified to provide better agreement particularly with the angular distribution of $K(4\,^2S)$ scattering observed here, and the forms finally chosen are

$$V_{K/N_2} = \epsilon(\sigma/R)^s, \quad (3)$$

where

$$s = 6.4 \quad (R > R_c),$$
$$= 9.0 \quad (R < R_c),$$
$$\epsilon = 0.05 \text{ eV}, \quad \sigma = 4.03 \text{ Å},$$

$$V_{K/N_2'} = V_{K/N_2} - 62.2/R^4$$
$$- 14.394/R + 6.25 \text{ eV} \quad (R > R_c),$$
$$= V_{K/N_2} \quad (R < R_c).$$

The crossing probability was of the usual Landau–Zener form with $V_{12} = 0.7$ eV.

The vibrational excitation predicted by this model is largely determined by, and is rather sensitive to, the difference in the N_2 and N_2' potentials, while the angular dependence is similarly primarily a function of the K/N_2 potential. This separation results from the bounded motion of the N_2' ion and the limited changes in R_c which occur as the N_2' vibrates.

The predictions for energy loss are shown in fig. 4. The agreement in the $K(4\,^2P)$ channel is particularly satisfying and is certainly well within the available precision of the N_2' potential. The observed energy loss for $K(4\,^2S)$ scattering is in less satisfactory agreement – possibly as a result of changes in V_{12} with the N–N distance which are not included in the present model. Increasingly diabatic behaviour can be expected as R_{N_2} increases, diminishing the contribution of the ionic surface, with its attendant vibrational excitation, to scattering in the $K(4\,^2S)$ state, and so decreasing the average energy loss actually observed. Incorporation of such a V_{12} dependence in the model would improve agreement with the observations but observations over a wider collision energy range would be required to establish its validity.

Interestingly, the model predicts that the vibrational excitation oscillates with scattering angle (i.e. collision lifetime) as the N_2' ion itself oscillates. A similar mechanism has been advanced to account for maxima in the total ionization cross section observed in Cs/O_2 collisions [15]. In the present experiments, since the early and late crossing contributions to the scattering are in an approximately random phase relation, this oscillation would be difficult to resolve. Experiments at lower collision velocities, where the energy loss resolution is substantially improved and probably adequate to resolve the predicted separate early and late crossing contributions, will be particularly interesting in testing the detailed success of this primitive classical model.

Finally, in distinction to systems of the K/RI type where the RI negative ion was found to be substantially perturbed by the K^+ ion, the N_2' pair potential (within the limited precision with which it is known) accounts for the present results rather well.

The differential cross sections computed from the model are compared with experiment in fig. 5. The agreement is satisfactory considering the simple analytic forms used to represent the K/N_2 potentials. The maxima and minima calculated in the $K(4\,^2S)$ channel,

which is the sum of early and late crossing contributions, arises from the operation of the LZ terms in the model.

References

[1] H.S.W. Massey and E.H.S. Burhop, Electronic and ionic impact phenomena, Vol. 3 (Oxford Univ. Press, London, 1973).

[2] I.V. Hertel, H. Hofmann and K.A. Rost, Chem. Phys. Letters 47 (1977) 163.

[3] C. Bottcher, Chem. Phys. Letters 35 (1975) 367.

[4] E. Bauer, E.R. Fisher and F.R. Gilmore, J. Chem. Phys. 51 (1969) 4173.

[5] V. Kempter, Advan. Chem. Phys. 80 (1975) 417.

[6] P.J. Martin, E. Clemens, L. Zehnle and V. Kempter, Z. Physik A289 (1979) 373.

[7] J.M. McCall and M.A.D. Fluendy, J. Phys. E11 (1978) 631.

[8] M.A.D. Fluendy, J.H. Kerr, J.M. McCall and D. Munro, in: On line computing in the laboratory, eds. A. Rosner, B.K. Penney and P.N. Clout (Adv., London, 1975).

[9] K. Lacmann and D.R. Herschbach, Chem. Phys. Letters 6 (1970) 106.

[10] V. Kempter, B. Kübler, P. LeBreton, J. Lorek and W. Mecklenbrauck, Chem. Phys. Letters 21 (1973) 164.

[11] E. Gersing, H. Pauly, E. Schadlich and M. Vonderschen, Faraday Discussions Chem. Soc. 55 (1973) 211.

[12] M.A.D. Fluendy and K.P. Lawley, Chemical applications of molecular beams (Chapman and Hall, London, 1973).

[13] F.R. Gilmore, J. Quant. Spectry. Radiative Transfer 5 (1965) 369.

[14] M.A.D. Fluendy, K.P. Lawley, J. McCall, C. Sholeen and D. Sutton, Faraday Discussions Chem. Soc. 67 (1979), to be published.

[15] A.W. Kleyn, M.M. Hubers and J. Los, Chem. Phys. 34 (1978) 55.

MOLECULAR PHYSICS, 1981, VOL. 42, NO. 1, 1–20

36

Electronic excitation in potassium/alkyl halide collisions—The electron harpoon

by MALCOLM A. D. FLUENDY, KENNETH P. LAWLEY, CHARLOTTE SHOLEEN† and DAVID SUTTON‡

Department of Chemistry, University of Edinburgh, West Mains Road, Edinburgh EH9 3JJ, Scotland

(*Received* 10 *July* 1980 ; *accepted* 24 *July* 1980)

Inelastic differential scattering cross sections for collisions between potassium atoms and CH_3I, C_3H_7I, CH_3Cl, CF_3I and HI are reported for the reduced scattering angle range from 20–1000 eV °. The measurements were made in the quasi-rectilinear trajectory regime using a velocity change method. Electronic excitation of the K atom accompanied by substantial vibronic excitation of the target molecule extending to the lower Rydberg states is seen in all the systems studied. The results are in accord with an electron harpoon model involving successive donation and recapture of an electron by the potassium atom. In the case of collisions leading to the ground electronic state of the molecule a doorway state similar, but not identical, to the molecular negative ion is involved and a model incorporating the effects of bond stretching—analogous to that advanced to interpret collision induced ionization in alkali metal + halogen molecule collisions—is in excellent agreement with the observations. Excited electronic states of the molecular target are believed to be populated by a similar mechanism involving excited ionic doorway states including one leading to C–H dissociation.

1. INTRODUCTION

The alkali metal–alkyl halide family of reactions has played a key role in the development of chemical reaction dynamics [1–3] and a very considerable body of data concerning the reaction channel is available, presenting a significant challenge to theory [4–6]. The basic understanding of the reaction process as an example of electron harpooning is secure but the relatively short range encounters required for harpooning in these systems destroys the simplicity of near spectator stripping dynamics found in the otherwise analogous alkali metal–halogen molecule reactions. The description of the reactive process is thus particularly dependent upon the potential surfaces and non-adiabatic effects at short ranges, where information on these properties is scant. Progress in understanding the more intimate details of this reaction will thus require a direct study of the harpoon mechanism.

Information relevant to the harpoon itself can be obtained by studying a wide range of possible exit channels from these collisions : the differential cross sections for elastic scattering [7] ion production [8] and electronic excitation [9]

† Now at : Argonne National Laboratory, Argonne, Illinois, U.S.A.
‡ Now at : ICI Corporate Laboratory, Runcorn, Cheshire, England.

0026–8976/81/4201 0001 $02·00

being especially interesting. Total cross sections for ion production in alkali metal–methyl halide systems over a range of collision energies have been reported by Los and other workers [10–12]. Much more detailed results are however, available from their studies of ion production in alkali metal–halogen molecule systems which have much larger cross sections for ionization than those studied here. This elegant work has recently been reviewed [13]; the effects of bond stretching in the target molecule revealed in these measurements will be relevant to the discussion later in this paper.

The electronic excitation channel was originally studied in alkali metal collisions with a range of halogen containing molecules by Polanyi using the famous diffusion flame technique [14]. Interestingly, these experiments at thermal energies showed no emission from sodium in the systems $Na + CH_3I$, CH_3Cl. More recent work exploiting modern techniques and covering a wide energy range has recently been reviewed [15, 16] but alkali metal–alkyl halide systems have not yet apparently been studied by these techniques.

Alkyl halide molecules have a small electron affinity so that the harpooning radius is small and the ion exit channel can only be reached after avoiding crossings at short range with excited state potential surfaces. The ion production cross section (in distinction to the analogous halogen molecule systems) are thus likely to be smaller and perhaps less informative than measurements of the neutral excited state differential cross sections. In exploring non-adiabatic effects via the neutral channels, measurements over a considerable velocity range are especially valuable since the state coupling probabilities are velocity dependent; while the collision lifetime may similarly be varied with respect to the vibrational periods in the target molecule so that the effects of internal molecular motion on the harpoon can be studied. To sample the relevant regions of the potential surface it is also necessary to make these observations in appropriate ranges of the reduced scattering angle, EX. These various requirements can be met most satisfactorily by operating in the high velocity—small scattering angle regime in which the trajectories become almost linear and of approximately constant velocity. In the work described here measurements of this type using a time of flight technique to distinguish the various excited exit states have been made. The present paper extends the results and the discussion presented previously in a preliminary fashion [17, 18].

2. Experimental

The apparatus has been described previously [17]. The fast alkali beam was produced by charge exchange and pulse modulated for time of flight purposes using a velocity compression technique [19]. The molecular target beam was formed by effusive flow from a capillary array and modulated at 47 Hz. The scattered alkali atoms were detected by surface ionization using a cool W ribbon and detected via a scintillator and photomultiplier. Each atom arrival was arranged to stop a 50 MHz clock so that the flight time could be recorded. Data was collected and the angular position of the detector etc. controlled by an on-line computer [20]. The angular resolution of the apparatus in this work was $\sim 0{\cdot}2°$ and the resolution in energy loss (at the highest collision energy used) $\sim 0{\cdot}2$ eV. The effective resolution in EX, $\delta(EX)/EX \approx 0{\cdot}08$.

The signals recorded in the weakest inelastic channels were very small ($\sim 0{\cdot}01$ c s^{-1}) and counting times of ~ 12 h were required at the largest scattering angles. The major experimental difficulty in this work arose from fluctuations in the primary beam energy probably associated with the contact potential or space charge effects reported by other workers [21]. These effects were partially controlled by measuring the 0° flight time at regular intervals and appropriately normalizing the time dependencies observed after scattering.

3. Results

Inelastic scattering measurements have been made in the small deflection angle region for potassium atoms colliding with a range of target molecules. Energy transfer from translational to internal modes of the collision species extending up to 12 eV with significant probability was observed. The molecular targets studied were CH_3I, C_3H_7I, CH_3Cl, CF_3I and HI, these molecules being chosen so as to explore a range of reduced masses in R–X but to retain similar electronic structures and intramolecular potentials.

A contour map showing the scattered intensity of K atoms, $I(\chi)$ multiplied by the square of the centre of mass scattering angle, χ, as a function of the scattering angle and the post collision relative velocity for the system $K+CH_3I$ is shown in figure 1. This map is typical of those observed in this work, considerable inelasticity is visible (up to 12 eV in this case) and a number of rather sharp onsets for specific energy loss channels can be distinguished. Closer examination of the surface displayed in figure 1 reveals considerable structure which is most easily displayed by cuts through the surface at constant scattering

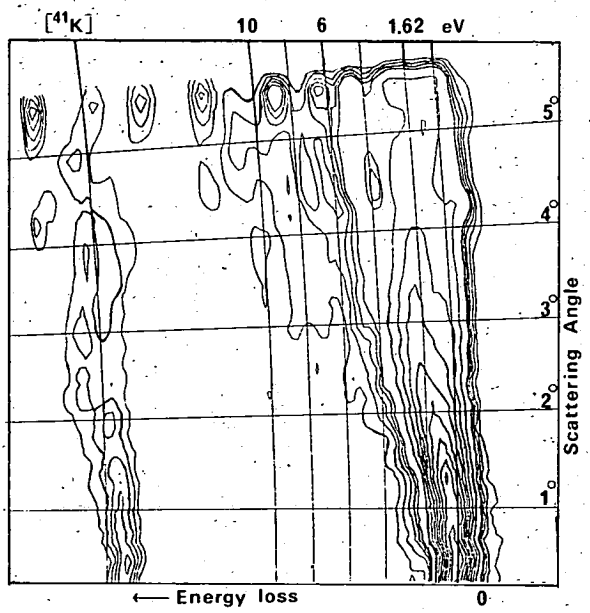

Figure 1. Typical contour diagram showing $I(\chi)\chi^2$ for the scattered K atoms as a function of energy loss and deflection angle. This example is for K/CH_3I at a collision energy of 164 eV (centre of mass). The growth of inelastic scattering with increasing angle together with a drop in elastic scattering is apparent.

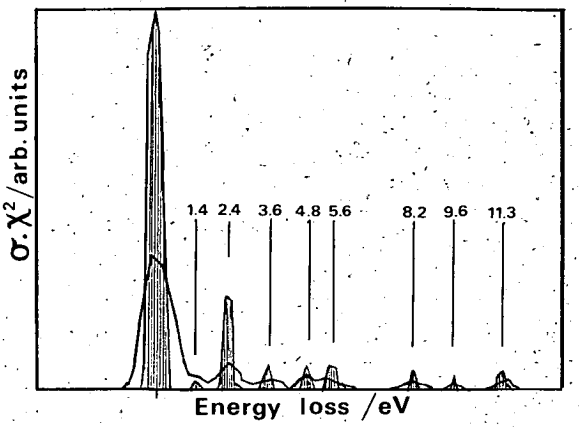

Figure 2. Cut through a contour diagram at constant deflection angle. The example is for the system K/CH_3Cl at 2·75° and 115 eV (centre of mass).

angle. Examples of such cuts are displayed in figure 2 and represent the mean of several independent measurements in a narrow angular range. The experimental data is shown after application of any necessary shift in time origin based upon the observed arrival time of the 0° reference profile. The shaded curve shows the result of a partial deconvolution procedure using the 0° profile as a reference. The peaks are sharpened by this process so that the relative intensity in each loss channel can be estimated more easily, but can already be distinguished in the unprocessed data. This treatment was applied to all the data obtained in this work and the position of every peak in the energy loss profile, regardless of its amplitude, plotted against scattering angle to produce collision process maps for the various systems, figures 3–6. These collision maps provide a much better visualization of the topography of the scattering, though they contain no information of the size or importance of the process illustrated.

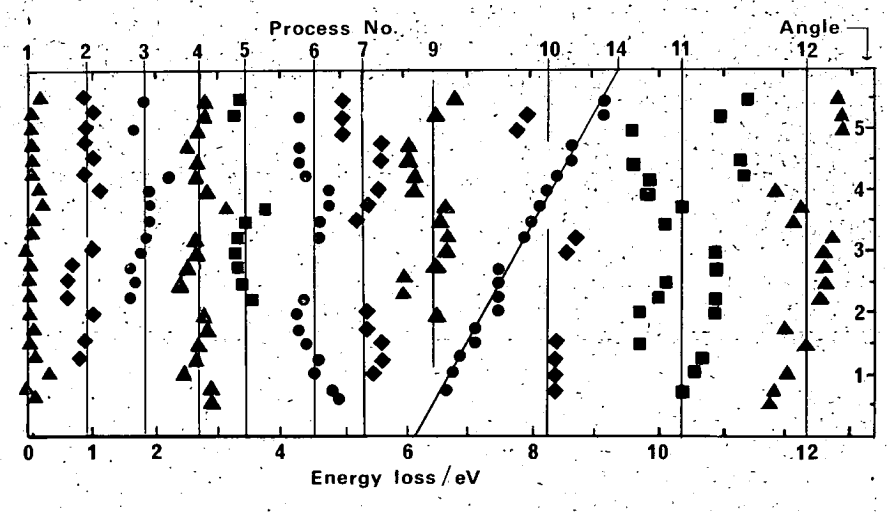

Figure 3. Collision process map for K/CH_3I 164 eV(CM). The CM scattering angle is on the vertical scale and a sequentially assigned process number is shown at the top of the figure.

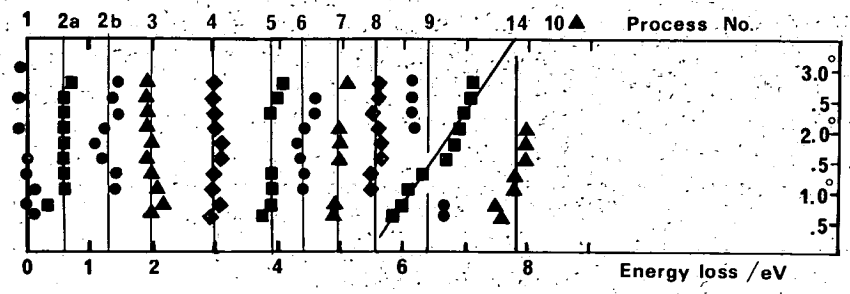

Figure 4. Collision process map for K/CH_3I 81 eV. The CM scattering angle is on the vertical scale and a sequentially assigned process number is shown at the top of the figure.

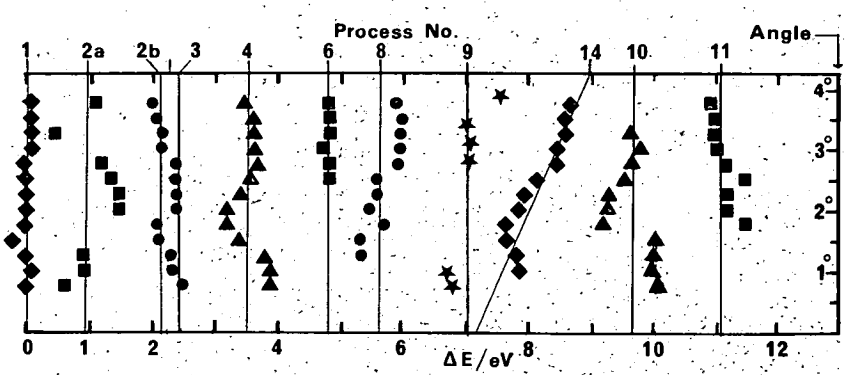

Figure 5. Collision process map for K/CH_3Cl 115 eV. The CM scattering angle is on the vertical scale and a sequentially assigned process number is shown at the top of the figure.

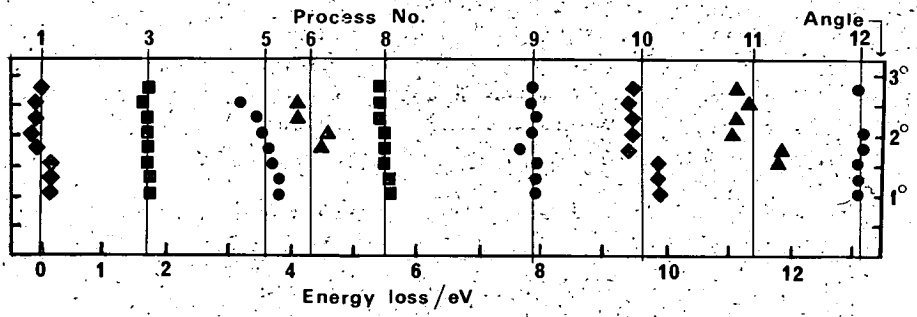

Figure 6. Collision process map for K/CF_3I 170 eV. The CM scattering angle is on the vertical scale and a sequentially assigned process number is shown at the top of the figure.

In general, a fairly clear pattern emerges in these collision maps though in some regions ambiguity arises, for example, where two processes with similar energy losses merge or cross within the effective energy resolution of the apparatus. It is apparent from these collision maps that with one or two possible (and interesting) exceptions the observed processes have energy losses that are

independent of scattering angle. In some cases the observed energy losses change with the initial collision energy while in others the energy loss remains constant. The observed channels are summarized for all the systems and collision energies in table 1.

Table 1. Observed energy loss channels.

Process number		System and collision energy MeI 81 eV	MeI 164 eV	PrI 166 eV	MeCl 115 eV	Losses in eV CF_3I 86 eV	CF_3I 170 eV	HI 157 eV
1		0·0	0·0	0·0	0·0	0·0	0·0	0·0
2‡	K° + vibn and K^* + vibn	0·6	1·0	0·4	1·0	0·7	—	—
		1·3			(2·2)‡			
3		2·0	1·7	1·6	2·5	2·0	1·7	1·6
4		3·1	2·8	2·2	3·7	2·6		
5	Valence transitions	4·0	3·6	3·3		2·9	3·7	3·0
6		4·6	4·8	4·4	4·8	3·9	4·5	—
7		5·0						
8		5·7	5·5	5·1	6·0	6·2	5·4	5·3
9	Rydberg and transitions from deeper levels	6·4	6·4	6·6	7	7·5	7·8	7·4
10		8·0	8·4	8·5	9·7	†	9·7	—
11		†	10·4	10·8	11·2	†	11·3	11·0
12		†	12·4	13·2	†	†	13·1	—
13		†	—	—	†	†	14·8	—
14		6 →7·2 increasing in E_χ range 40–220 eV°	6·4 →9·0 increasing in E_χ range 60–900 eV°	11 →12·8 increasing in E_χ range 160–550 eV°	7·5 →8·7 increasing in E_χ range 90–430 eV°			

† Process not observable since ^{41}K isotope peak obscures this region.
— Process not seen
‡ Model fits suggest two channels, the upper almost coincident with three and only partially resolved in the data.

Differential cross sections were extracted from the deconvoluted data for each process in the collision map by summing the scattered intensity in a narrow band of energy loss centred on the appropriate loss peak. Small changes in the location of peaks in energy loss can produce large variations in the size of the differential cross section estimated in this way and it is necessary to make a large number of measurements. Most extensive data is available for the CH_3I/K system and differential cross sections derived in the way described are shown in figures 7, 8 and 9. In figure 10 the total (all channels) neutral scattering differential cross section for this system is compared with that for HI which displays a very rapid fall off in neutral scattering as the angle increases.

Figure 7

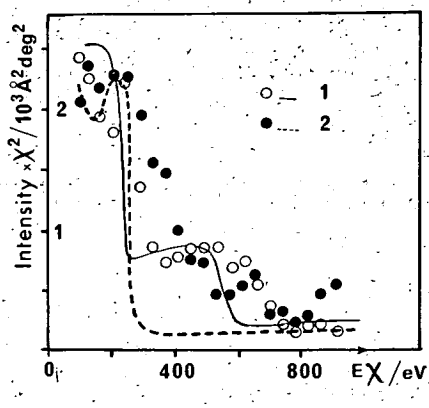

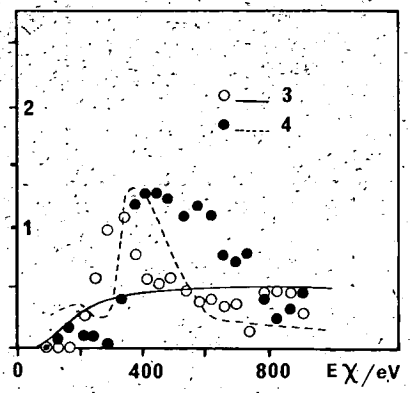

Figure 8

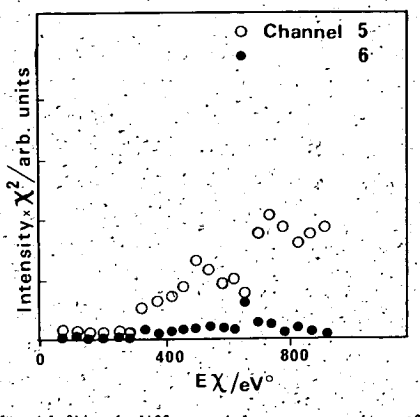

Figure 9

Figures 7 to 9. Observed and fitted differential cross sections for the smaller energy loss processes in the K/CH_3I system at 164 eV. The solid fitted curves are based on the model defined by equations (3)–(9), the observed cross sections are normalized to these curves. The numerals in each plot refer to the process number.

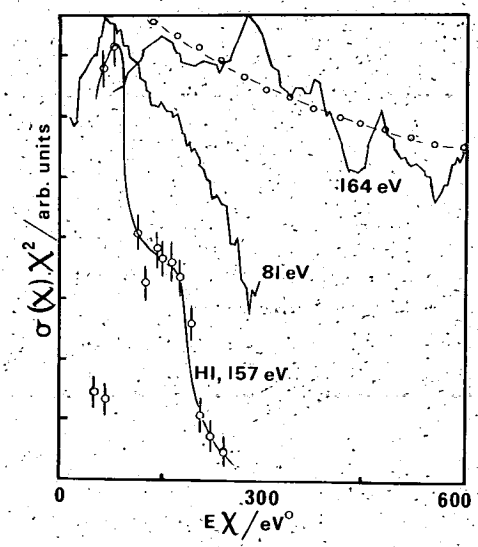

Figure 10. The total differential cross section obtained by summing over all the neutral exit channels for the K/CH_3I system at 164 and 81 eV and HI at 157 eV are shown. The relative position of each curve is arbitrary but for comparison the cross section computed from the ground state potential of the model for CH_3I at 164 eV is also shown (–O–O–O–).

4. Discussion

The energy losses observed are clearly vibronic in character ; the possibilities are

$$M+RX \rightarrow M+RX, \quad (1)$$
$$\rightarrow M+RX^{\dagger} \rightarrow (\text{or } M+R+X), \quad (2)$$
$$\rightarrow M^{*}+RX, \quad (3)$$
$$\rightarrow M^{*}+RX^{\dagger}, \quad (4)$$
$$\rightarrow M+RX^{*}(RX^{*\dagger}), \quad (5)$$
$$\rightarrow M^{+}+RX^{-}, \quad \text{(not measured in this experiment)}$$

where (*) indicates electronic and (†) vibrational excitation. The doubly excited channels, $M^{*}+RX^{*}$, are energetically open, but we have not found it necessary to invoke them in interpreting the small angle scattering.

The quasi-linear trajectories explored in these measurements are not only advantageous in simplifying the trajectories themselves but also in limiting the momentum transfer available to produce inelastic processes by direct collision on the repulsive potential wall. The *maximum* energy, ΔE, transferable in this way by quasi-linear trajectories can be estimated by assuming the molecule RX to be a forceless oscillator, for which

$$\Delta E_{\max}=\frac{M_R M_X}{M_R+M_X}\frac{M_K}{M_Z^2}E\chi^2, \quad (1)$$

where the M_s represent the masses of the various groups and M_Z is the mass of either R or X according to which end is struck. For the onset angles of the processes observed here χ is typically $< 2°$ and the maximum energy transferable is $< 0{\cdot}5$ eV. This still leaves open the possibility of much larger vibrational energy gain via head-on collisions with the CH_3 or H end of RI. We discount this possibility, firstly, because of its inherently low probability as a small impact parameter effect and, secondly, because the accompanying energy transfer would be strongly angle dependent (as can be seen from equation (1) or the corresponding equation for $M_K > M_X$). It is one of the striking characteristics of the observations under discussion that the energy loss is nearly always independent of scattering angle.

There is a natural division between the channels, (1), (2) and (3) which necessarily lie below the ionization energy of potassium (4·3 eV) plus a vibrational component and the remaining channels which can extend up to the ionization potential of the target molecule and beyond. The elastic and K* scattering are thus discussed in § 4.1, the lowest excited molecular states (the $\tilde{A}$ states) in § 4.2 and the higher excited states in § 4.3.

4.1. *Vibrational and alkali atom excitation*

These processes can extend up to 4·3 eV, the ionization potential for potassium, however, the highly excited states of K (> 3·5 eV) are unlikely to be important since geometric factors will ensure that the crossing probabilities to these levels will be very small. In the collision energy range used in this work the reactive channel associated with the electron harpoon mechanism is closed,

because the K^+ ion formed in the collision cannot accelerate and capture the halide negative ion before leaving the ionic surface or escaping from the collision. Nevertheless, it is reasonable to speculate that similar electronic rearrangements will occur although the actual dynamics of the nuclear motion will be different. This speculation is confirmed at least partly by the small values of reduced scattering angles at which the processes are observed to onset, a factor suggesting the operation of both strong attractive potentials and relatively long range interactions in producing the observed inelasticity. Following in the spirit of the harpoon model we postulate that the large energy losses, both vibrational and electronic, result from a substantial change in the potential surface during close encounters. An essential feature of this change is a switch to a much more repulsive state in the R–X coordinate. In contrast, no strong repulsion force is experienced along the K–X coordinate and the angle of deflection remains small even in the presence of substantial energy transfer.

The nature of this intermediate R–X repulsive surface is clear. Because of the low ionization potential of the K atom, charge transfer (CT) states become important as the K atom approaches and in a diabatic representation even cross the non-bonding states correlating with the neutral partners. This same intermediate state, since it is attractive in the K–RX coordinate, can act as a doorway for passing from the entrance channel to states correlating with $K(4^2P)$. Normally, e.g. in K/Ar, states correlating with $K(4^2S)$ only cross those correlating with $K(4^2P)$ far up the repulsive wall of the potential and K* would not be expected to appear at small scattering angles. The intervention of a CT state over which $(dV/dR_{K-X}$ is predominantly positive, scatters the K* into the forward direction.

The ingredients of our basic model are now complete. Referring to figure 11 the system enters along the K–RX coordinate from the right with the RX coordinate at its equilibrium distance R_e. At the crossing, when $R_{K-RX} = R_C$, the motion may either continue diabatically along the potential (A) or a transition made to the CT state (B) in which case the RX^- ion starts to extend rapidly. The motion in the K–RX dimension meanwhile unwinds to a second crossing of the two surfaces. The location of this second crossing at R'_c corresponding to electron recapture, is very sensitive to the length of the R–X bond. If the electron returns at this first attempt the system exits as $K(4^2S) + CH_3I$ which may be vibrationally excited (2) if the collision sampled the CT state or vibrationally cold (1) via the alternative neutral surface (A). If the motion continues on past R'_c on potential (B) a second chance for the electron to return occurs at R'_1, the crossing with a K* state, and the system exits at K* in channels (3) and (4). The R–X bond has meanwhile continued to stretch so that R'_1 progressively moves to larger R as the electron affinity of RX increases towards that of the free halide atom. The probability of electron recapture falls rapidly as R'_1 increases so that the likelihood of the system exiting as ions increases as the RX bond stretches. The key features of this model are thus the two successive electron transfers with changes in the molecular geometry occurring during the CT phase of the motion.

The validity of this model is explored under the following assumptions :

(i) a constant velocity rectilinear trajectory ;

(ii) electron transfer is vertical at each crossing ;

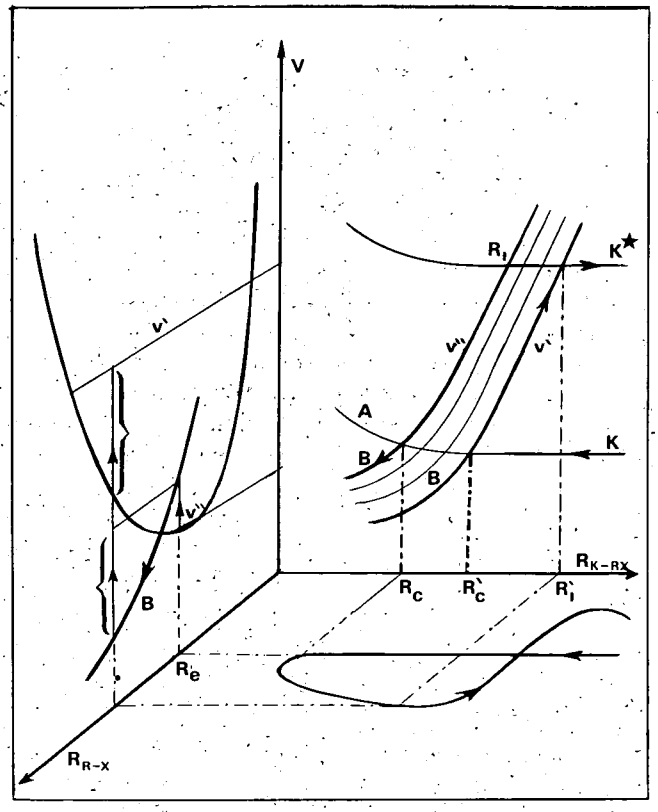

Figure 11. Schematic cuts through the K–CH_3I potential surface. A typical section along the K–RX coordinate is projected onto the $V(R_{K\text{-}RX})$ wall, where successive cuts through the CT surface (B) are shown as the R–X coordinate expands and the crossing on the return path, R'_c is pushed out. The actual path of motion in this coordinate system for an impact parameter slightly less than R_c is projected onto the base plane of the diagram and illustrates the considerable vibrational energy transfer that can result.

(iii) the motion in the R–X coordinate is uninfluenced by the K^+ ion ;

(iv) the repulsive potential in RX^- is linear i.e. $(dV/dR_{R-X}) = k$ (where k can be obtained from electron attachment data) ;

(v) the crossing points R_c, R'_c, R_I, R'_I are independent of the stretch in the R–X bond.

Under these conditions we find :

$$\Delta E'_{T-V} = \tfrac{1}{4} k^2 M_K d^2/(\mu_{RX} E_{LAB}) + \Delta V_{RX}, \qquad (2)$$

where μ_{RX} is the reduced mass of the oscillator, d the distance along the K^+ path between the two crossings at R_c and R'_c and ΔV_{RX} is the change in potential energy of the neutral RX arising from the bond extension. Although this last term is important for large extensions of the oscillator we can obtain a reference parametrization by neglecting it. Thus in figure 12 we plot the measured energy loss (in the 0–4 eV region) against $\beta = k^2 M_K/\mu_{RX} E$).

While it is hardly to be expected that these plots would be linear (in accord with this simple model) they show a clear ordering. In the limit of fast collisions, i.e. no molecular geometry change involved, the observed losses are seen to converge on 0 and 1·6 eV, K(4^2S) and (4^2P), production respectively. The behaviour of the two vibrational branches associated with each electronic channel is clearly differentiated and can readily be explained by the mechanism outlined above. Channel (2) arises from a crossing onto the CT state at the first opportunity on the incoming path, R_c, leaving again at the first opportunity on the outward path, R'_c. Channel (3) arises from a late crossing on the outward path onto potential (B) in figure 11 and channel (4) from an early crossing onto the CT state (B) on the inward path and continuing on (B) to R'_1. A pattern can also be discerned in the deviations from linearity of these plots. The initial slope of the plot is always greater than the mean slope for a particular process and the energy transfer for large values of β correspondingly less than the value predicted by the simple model.

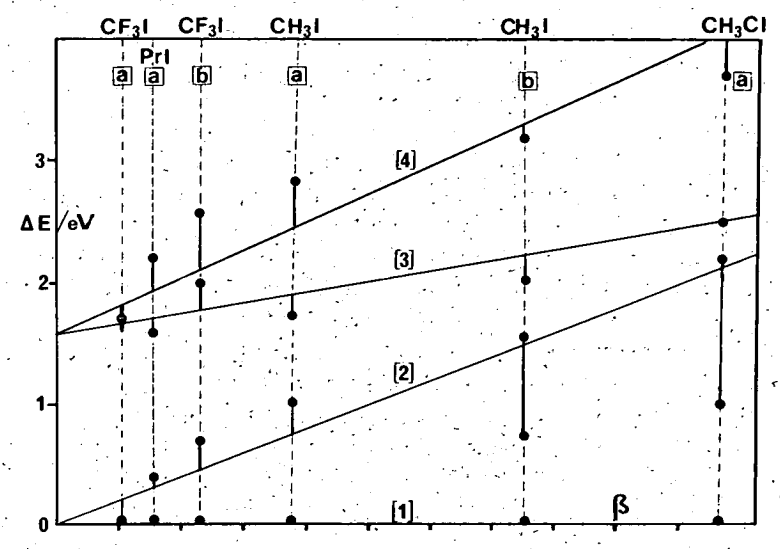

Figure 12. Plot of energy loss in the first four channels of all the systems as a function of the reduced parameter β (equation 2). Systems labelled (a) are at 200 eV LAB and (b) at 100 eV.

Inclusion of the omitted term, ΔV_{RX}, would increase the amount of vibrational energy predicted by this model. But it is clear that the assumption of a constant repulsive force in the negative ion cannot hold for larger bond extensions (final values of R_{RX} are typically 0·2 Å greater than the equilibrium value).

Trajectories behaving adiabatically at only one avoided crossing i.e. transferring an electron only once, will exit as ions. The importance of the ion production channel depends upon the extent to which the C–X bond stretches in the negative ion state. As this bond stretches the electron affinity increases and the crossing points, R'_1 and R'_c, between the neutral and ion pair surface move

rapidly to larger radii and the probability of electron recapture decreases rapidly, approaching that for the free halogen atom/potassium system which is known to be small [22].

This pattern of behaviour is demonstrated most clearly in the HI system (figure 10) where the very light reduced mass of the oscillator results in the rapid departure of the H atom when the negative ion state is formed. In measurements on this system only the late crossing branches for K (4^2S) and (4^2P) could be observed and the total differential cross section falls off extremely rapidly with angle. Similar, though much less marked behaviour can also be seen in the CH_3I/K differential cross sections. For this system a cross section computed from the fitted neutral potential (A) is also shown for comparison. Computations using this potential to obtain the $b(\chi)$ dependence yield an estimate for the total ion production cross section of 12 Å^2 at a collision energy of 81 eV.

A more detailed analysis of the proposed sequential electron transfer model was made by developing a computer algorithm to model the collision dynamics for particles moving in the potential scheme of figure 11. The potentials (as for almost all systems of chemical interest) are not well known and it was appropriate to develop a simple classical picture using Landau–Zener probabilities to describe the non-adiabatic electron transfers. Since the trajectories are closely linear and of almost constant velocity considerable simplification can be made in the dynamical calculations.

In the initial realization of the model the motion of the potassium atom and the expansion of the negative ion were assumed to be entirely independent except that the lifetime of the ion pair was determined by the period spent between the curve crossings in the K–I dimension. The location of these crossings was adjusted iteratively during the computation of the trajectory as the negative ion expanded and its electron affinity changed. The small angle formula was used to compute the deflection along each section of potential and appropriate Landau–Zener probabilities applied to calculate the differential cross section. The energy loss was evaluated by summing the internal kinetic energy of the negative ion and assuming vertical electron transitions, i.e. the construction shown in figure 11.

The results obtained from this model with the initial set of potentials (solid lines in figures 13 (a) and (b) could not be brought into agreement with the observed energy losses. Particularly severe difficulties arose with trajectories having an early electron transfer, i.e. on the incoming leg of the motion which sampled the ion pair potential most exhaustively. The uniformly repulsive nature of the C–X^- potential assumed in this model almost inevitably led to dissociative ion production in complete disagreement with the rather striking experimental observation of a substantial neutral channel with a constant energy loss. The RX potential used in this calculation is derived from electron attachment experiments which yield information primarily about the isolated negative ion in a configuration close to that of the stable neutral molecule. In contrast, in the dynamical situation pictured in the present model a positive ion, K^+, is always in close proximity during the important phases of the motion. Very substantial polarization effects are certain to occur and a considerable reduction in the effective population of the $\sigma^*(C$–$X)$ orbital can be expected. Effects of this type modifying the repulsive C–X^- potential in the close 3 body collision region can be incorporated into the model by including an appropriate 3 body term into

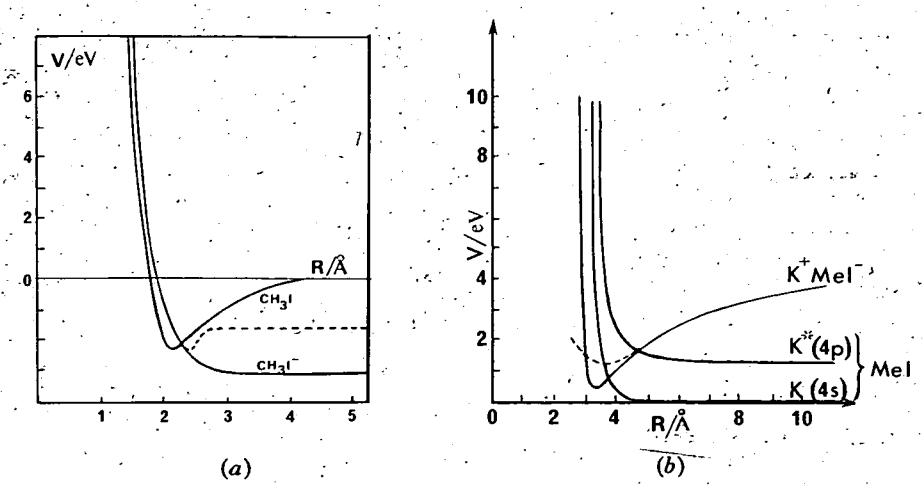

Figure 13. (*a*) The CH_3I potentials. Two negative ion potentials are shown, that of the free ion and (dashed) the modified form found necessary in fitting the present data. (*b*) The K–MeI potentials. Two CT potentials are shown, corresponding to the two limiting orientations of the alkyl halide and given by equations (5) and (6) (dashed), respectively.

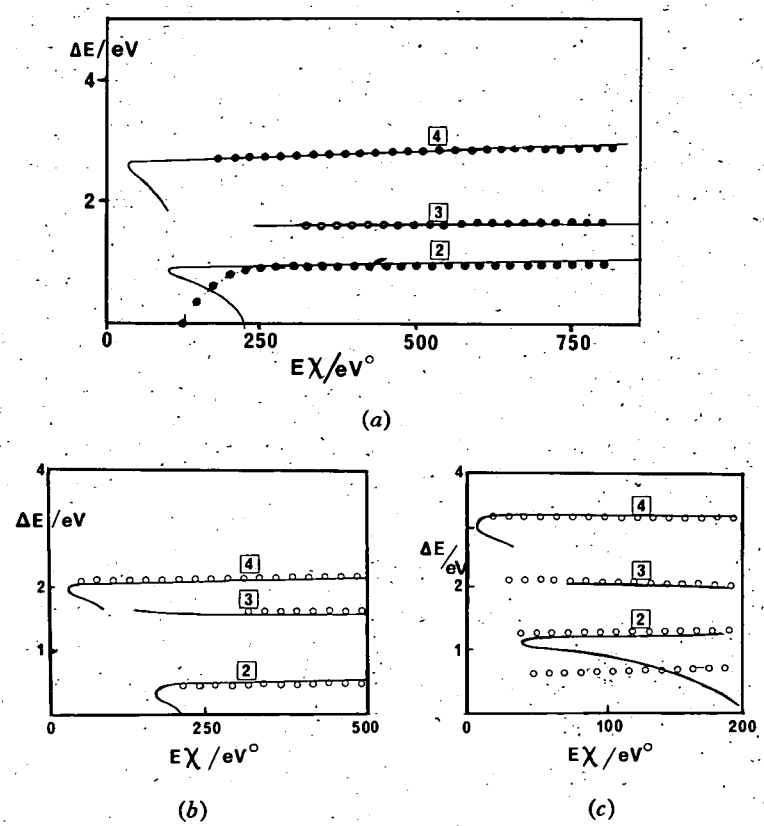

Figure 14. Detailed fitting of the angular dependence of the energy loss (ΔE in eV) in K–CH_3I. (*a*), K–CH_3I at 164 eV CM ; (*b*), K–C_3H_7I at 166 eV CM ; (*c*), K–CH_3I at 81 eV. The first three inelastic channels are shown. The circles show the location of the inelastic peaks obtained by smoothing the contour maps.

the negative ion potential—a term which will be sizeable only when the K^+ ion is in close proximity.

This modification was qualitatively immediately successful in providing, for example, an explanation of the additional energy loss channel seen at low collision energies in the CH_3I scattering. This is now seen (cf. figure 14 (*c*) to rise from a rainbow effect in which scattering at the same angle arises from two different impact parameters corresponding in their turn to different periods spent in the ion pair state. No attempt via extensive parametrization has been made to obtain a quantitative fit but the excellent agreement, seen in figures 14 (*a*), (*b*), and (*c*) is obtained with simple potentials and confirms the validity of this picture of the collision.

The angular variation in the differential cross sections for the process under discussion depends largely upon the $K–CH_3I$ and $K^+–CH_3I^-$ potentials, the interaction in the C–I dimension (which largely determined the energy loss behaviour) now being involved less directly in fixing the exit crossing radii. Inspection of the cross sections (cf. figures 7–9) reveals a number of features which can be interpreted fairly directly. In the ground state elastic channel (process 1) the expected sharp fall off in intensity as the first crossing becomes accessible is visible at 200 eV ° implying a curve crossing at $\sim 3{\cdot}3$ Å. The second fall off at wider angles implying a further onset is discussed later. The vibrationally hot ground electronic scattering (process 2) shows a rainbow peak at narrow angles as expected for trajectories sampling the ionic bowl—the fall off to low angles is visible in 81 eV data and to wide angles in the 164 eV measurements. Processes 3 and 4 leading to $K(4^2P)$ excitation also show the expected narrow angle onsets, process 4, involving a crossing to the ionic surface on entry, onsetting at the lowest angle. The peaks seen in both channels are probably associated with rainbow phenomena as in the ground electronic state scattering.

These observations are in accord with the model proposed with the exception of the second wide angle fall off in process 1 and the two peaks seen in process 4. These features might be reproduced by modifying the form of the potentials used in the model rather substantially, though there would be little physical basis for the changes required. A more plausible explanation can be obtained by considering the probable anisotropy of the potentials. Estimates of this behaviour have been made previously in molecular dynamics computations [23] and suggest that the initial curve crossing radius diminishes in the region of the methyl group, i.e. that the ionic potential becomes more repulsive. Since the various angular features are fairly sharp it is probable that the potential variations occur over a fairly small range of orientations. In the spirit of the present model the molecule could then be represented as the sum of two separate isotropic contributions representing the CH_3 and I groups. Two suitable potentials are shown in figure 13 (*b*), the potential associated with the CH_3 group being shown dashed. The second wider angle peak in process 4 and the wider angle fall off in the elastic scattering then arise naturally as a result of collisions with the methyl group. Adjustment of the relative contribution of the two potentials to obtain agreement with the observations leads to a ratio of 70 per cent iodine/30 per cent CH_3, a ratio in accord with the orientation experiments of Brooks [24] which yielded 60 : 40.

Computations with this model are compared with the observations in figures 7, 8 and 14. The agreement is rather good, particularly in view of the restricted

parametrization used. The most significant deviations from the model are seen close to the onset angles for the various processes possibly reflecting the inadequacy of the diabatic potential forms in this region.

The potentials used in these model computations, shown in figure 13, are as follows :

(1) K–RX relative motion governed by

$$V^{K}(R)/\text{eV} = 0{\cdot}24[(3{\cdot}8/R)^{12} - (3{\cdot}8/R)^{6}], \quad (3)$$

$$V^{K^*}(R)/\text{eV} = V^{K}(R) + 1{\cdot}61, \quad (4)$$

$V^{K^+}(R)$ iodine orientation/eV

$$= 0{\cdot}1(3{\cdot}36/R)^{12} - 120/R^4 - 14{\cdot}4/R + (\text{I.P.} - E_A), \quad (5)$$

$V^{K^+}(R)$ methyl orientation

$$= 0{\cdot}1(5{\cdot}4/R)^{5} - 120/R^4 - 14{\cdot}4/R + (\text{I.P.} - E_A), \quad (6)$$

(with trajectories sampling the two alternative orientations in the ratio 7 : 3)

(2) RX interaction

$$V^{RX}(R_1)/\text{eV} = D_0[\exp(-1{\cdot}7\ R_1(R_1 - 2{\cdot}14)) - 2\exp(-1{\cdot}7(R_1 - 2{\cdot}14)] \quad (7)$$

and

$$V^{RX'}(R_1)/\text{eV} = 1{\cdot}65\exp(-4{\cdot}65(R_1 - 2{\cdot}14)) + V^{(3)}(R_1, R), \quad (8)$$

where the 3 body term which serves to constrain the C–I expansion when the K^+ ion is in close proximity is parametrized, rather crudely as

$$V^{(3)}(R_1, R) = 0{\cdot}8\ (\tanh 4(R_c - R)) \times (\tanh 2(R_1 - 2{\cdot}3)). \quad (9)$$

(3) The crossing probabilities are calculated by the standard Landau–Zener formula.

For crossings from the entrance channel to the CT state

$$H_{12} = 0{\cdot}28\ \text{eV}$$

with the difference in gradient, ΔF, given by

$$\Delta F = e^2/R^2.$$

Similarly, exit from the CT surface is determined by another application of the Landau–Zener formula with the *same* value of H_{12} (despite the different position of the crossing) if the crossing is to the $K(4^2S)$ channel and with the value

$$H_{23} = 0{\cdot}20\ \text{eV}$$

if the crossing is to the $K(4P)$ channel.

We conclude that the sequential electron transfer model accounts well for all the systems studied and that there is clear evidence of a substantial modification of the molecular negative ion potential in the close encounter situation with a K^+ ion acting so as to contain the expansion. The data also suggests that the K^+ CH_3I^- potential is less strongly attractive in the region of the methyl group with approximately 30 per cent of the trajectories sampling this region of the molecule.

4.2. *$\tilde{A}$ state excitation*

In the systems studied transitions to the C–X antibonding levels occur in the 4–6 eV range. Spectroscopically the six molecular states arising from this electronic configuration (cf. figure 15) are seen as continua. Only in the case of CH_3I can transitions to the $^3\Pi_0^+$ and $^3\Pi_1$ states be unfolded from the observed band. Otherwise little information is available to guide the assignment of the observed processes to the production of specific molecular states. In general, the number of available states exceeds the number of peaks observed while the possibility of accompanying vibrational excitation is a further complication.

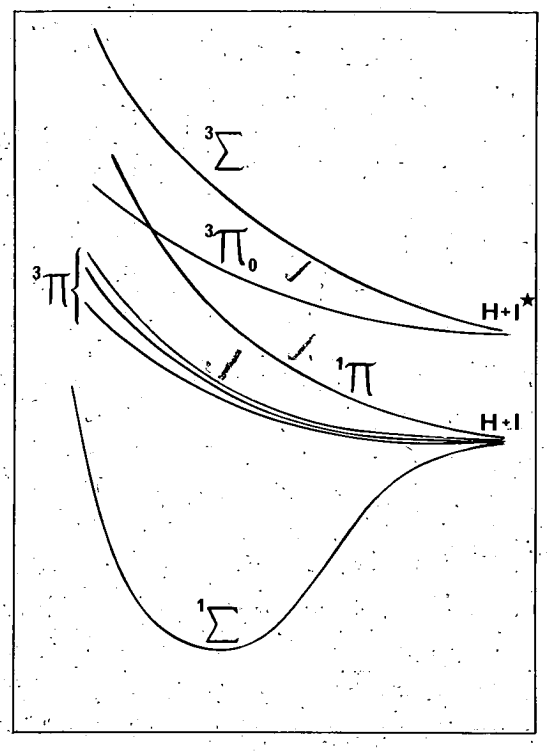

Figure 15. Schematic of the probable relative position of the $\tilde{A}$ states of RI. The spectroscopic designations are strictly only applicable to HI in Hund's cases (*a*) or (*b*).

As in the lower energy processes channels in this region are seen to onset at quite small $E\chi$ values suggesting once again the involvement of charge transfer states in the dynamics. It is unlikely, however, that this could involve the ground state of the molecular ion since the crossing with the $\tilde{A}$ states would then be at large distances where the probability would be small. The peaks observed in this region are shown in table 2, in general the systems containing iodine show three transitions though in CH_3I at 81 eV four peaks are seen and HI yields only two peaks. CH_3Cl, with a much smaller spin–orbit splitting, is seen to produce only two peaks. Comparison of these results with the states expected in figure 15 leads to the very tentative assignment of these peaks to transitions to the $^3\Pi_{1,2}$, $^3\Pi_0$ and $^3\Sigma$ states with the $^3\Pi_{1,2}$ and $^3\Pi_0$ states merging in CH_3Cl because of the

References

[1] Herschbach, D. R., 1973, *Faraday Discuss. chem. Soc.*, **55**, 233.

[2] Kinsey, J. L., 1972, *M.T.P. Int. Rev. Phys. Chem. Series* 1, **9**, 213, edited by J. C. Polanyi (Butterworth).

[3] Herm, R. R., 1979, *Alkali Halide Vapours*, edited by P. Davidovits and D. L. McFadden (Academic Press), p. 189.

[4] Bunker, D. L., and Goring, E. A., 1972, *Chem. Phys. Lett.*, **15**, 521.

[5] Bunker, D. L., and Goring-Simpson, E. A., 1973, *Faraday Discuss. chem. Soc.*, **55**, 93.

[6] Gislason, E. A., 1979, *Alkali Halide Vapours*, edited by P. Davidovits and D. L. McFadden (Academic Press), p. 416.

[7] Harris, R. M., and Wilson, J. F., 1971, *J. chem. Phys.*, **54**, 2088.

[8] Lacmann, K., 1980, *Potential Energy Surfaces*, edited by K. P. Lawley (*Adv. Chem. Phys.*, Vol. 42), (Wiley), p. 513.

[9] McFadden, D. L., 1979, *Alkali Halide Vapours*, edited by P. Davidovits and D. L. McFadden (Academic Press), p. 361.

[10] Moutinho, A. M. C., Aten, J. A., and Los, J., 1974, *Chem. Phys.*, **5**, 84.

[11] Kleyn, A. W., Hubers, M. M., and Los, J., 1978, *Chem. Phys.*, **34**, 55.

[12] McNamee, P. E., Lacmann, K., and Herschbach, D. R., 1973, *Faraday Discuss. chem. Soc.*, **55**, 318.

[13] Los, J., and Kleyn, A. W., 1979, *Alkali Halide Vapours*, edited by P. Davidovits and D. L. McFadden (Academic Press p. 275.)

[14] Polanyi, M., 1932, *Atomic Reactions* (Williams & Norgate).

[15] Kempter, V., 1975, *Molecular Scattering*, edited by K. P. Lawley (*Adv. Chem. Phys.*, Vol. 30), (Wiley), p. 417.

[16] Menzinger, M., 1975, *Potential Energy Surfaces*, edited by K. P. Lawley (*Adv. Chem. Phys.*, Vol. 30), (Wiley), p. 1.

[17] Fluendy, M. A. D., Lawley, K. P., McCall, J., Sholeen, C., and Sutton, D., 1979, *Faraday Discuss. chem. Soc.*, **67**, 41.

[18] Castano, F., Fluendy, M. A. D., Lawley, K. P., Sholeen, C., and Sutton, D., 1979, *Chem. Phys. Lett.*, **65**, 26.

[19] McCall, J. M., and Fluendy, M. A. D., 1978, *J. Phys. E*, **11**, 631.

[20] Fluendy, M. A. D., Kerr, J. H., McCall, J. M., and Munro, D., 1975, *On line Computing in the Laboratory*, edited by R. A. Rosner, B. K. Penney and P. N. Clout (Advance Publications).

[21] Aten, J. A., and Los, J., 1975, *J. Phys. E*, **8**, 408.

[22] Moutinho, A. M. C., Aten, J. A., and Los, J., 1971, *Physica*, **53**, 471.

[23] La Budde, R. A., Kuntz, P. J., Bernstein, R. B., and Levine, R. D., 1973, *J. chem. Phys.*, **59**, 6286.

[24] Brooks, P. R., and Jones, E. M., 1966, *J. chem. Phys.*, **45**, 3449.

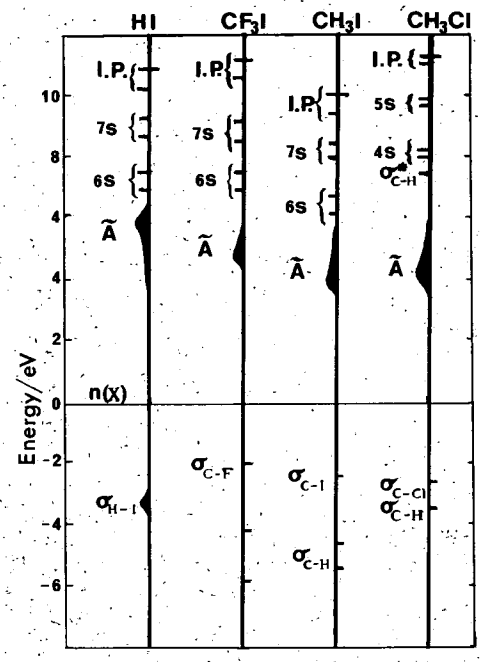

Figure 16. The arrangement of empty and filled orbitals in the various target molecules. The position of any level depends upon the R–X coordinate and in the case of the anti-bonding orbitals populated in the $\tilde{A}$ states the spread of energies covered by the $X \rightarrow \tilde{A}$ continuum is indicated.

previously published preliminary account [18]. The additional data presented here is in accord with the original assignment except in the case $n(I) \rightarrow 7s$ transition in HI which is not observed (possibly because of the very rapid changes in geometry which can occur in this molecule). However, the large number of states which occur in this energy region make an unequivocal assignment difficult. Nevertheless, it is interesting to note the absence of any peaks that could be associated with transitions to other than Rydberg s states.

The mechanism by which these transitions can proceed with relatively little deflection of the K atom will be discussed elsewhere. Here we only note that all the observed states differ from the ground state by the promotion of only one electron. That is, the final states are characterized by a hole in a previously doubly occupied orbital and an electron in a previously empty orbital. In the spirit of our model for the excitation of the K* states, this suggests a sequential two step electron capture/removal mechanism using new intermediate charge transfer states.

Support for this work by the Science Research Council is gratefully acknowledged.

Table 3. Energy losses >6 eV, proposed assignment and predicted energy loss.

Process number	Proposed assignment	System and collision energy: MeI 81 eV	MeI 164 eV	PrI 166 eV	MeCl 115 eV	Observed energy loss eV/predicted energy loss eV: CF_3I 170 eV	CF_3I 86 eV	HI 157 eV
9	$n(X) \rightarrow (n+1)s$	6·4/6·5	6·4/6·5	6·6/6·5	7† /7·7	7·8/7·4	7·5/7·4	7·4/7·4
10	$n(X) \rightarrow (n+2)s$	8·0/8·3	8·4/8·3	8·5/8·3	9·7/9·8	9·7/9·2	†/9·2	—/9·1
11	σ(C–H) $\rightarrow (n+1)s$	†/11·0	10·4§/11·0	10·8/11·0	11·2/11·3	—/—	—/—	—/—
12	σ(C–H) $\rightarrow (n+2)s$	†/12·9	12·4/12·9	13·2/12·9	†/13·4	—/—	—/—	—/—
11	σ(H–I) $\rightarrow (n+1)s$							11·0/10·7
11	$n'(F) \rightarrow (n+1)s$ $n'(F) \rightarrow (n+2)s$	—/—	—/—	—/—	—/—	11·3/11·2	†/11·2	—/—
12	or $n''(F) \rightarrow (n+1)s$	—/—	—/—	—/—	—/—	13·1/13·1	†/13·1	—/—
13	$n''(F) \rightarrow (n+2)s$	—/—	—/—	—/—	—/—	14·8/15·0	†/15·0	—/—
14	$n(I) \rightarrow \sigma^*$(C–H)	6–7·2 in $E\chi$ range 40–220 eV°/ 6 + internal energy	6·4–9·0 in $E\chi$ range 60–900 eV°/ 6 + internal energy	11–12·8 in $E\chi$ range 160–550 eV°/‖	7·5–8·7 in $E\chi$ range 90–430 eV°/ 7 + internal energy	—	—	—

† ^{41}K isotope peak prevents observation in this region.
‡ Process moves through this region making resolution of the peak difficult.
§ There is evidence of two peaks in this region at 10·0 and 10·8.
‖ The $\sigma^*_{C\text{-}H}$ can not be deduced unambiguously from the optical spectra but are likely to be much higher in CH_2 of the C_3H_7 group.

smaller spin–orbit splitting. In HI the possible effects of non-vertical electron transitions are likely to be much larger.

Table 2. Observed energy losses and proposed assignment in the molecular $\tilde{A}$ state region.

Process number	Proposed assignment	System and collision energy MeI 81 eV	MeI 164 eV	PrI 166 eV	MeCl 115 eV	Observed energy losses/eV CF_3I 86 eV	CF_3I 170 eV	HI 157 eV
5	$^3\Pi_{1,2}$	4·0	3·6	3·3	4·8	2·9	3·7	3·0
6	$^3\Pi_0$	4·6	4·8	4·4		3·9	4·5	—
7		5·0						
8	$^3\Sigma$	5·7	5·5	5·1	6·0	6·2	5·4	5·3

4.3. *Excited molecular states above the $\tilde{A}$ states*

The energies of the most important excited molecular states are displayed in figure 16. There are several series of excited states converging on different ionization limits, but the only secure set of levels are those obtained from U.V. spectroscopy. These correspond to the promotion of a halogen lone pair electron to progressively higher orbitals of increasingly Rydberg character. However, there are other series of levels arising from the promotion of a C–H bonding electron (from one of the σ_{C-H} orbitals, neglecting the splitting under C_{3v} symmetry) or from the C–X bonding orbital. The ionization potentials of these processes are known from photoelectron spectroscopy. We have included these deeper lying orbitals in the diagram by assigning the various ionized states of the molecule a common energy, that of the ground state ion and placing the deeper filled orbitals so as to give their observed ionization energy. Within the framework of Koopman's theorem we can now read off the approximate excitation energy for say, promoting a σ_{C-H} bonding electron to the 6s Rydberg level as simply the difference between the relevant orbital energies in the diagram.

All the molecular energy levels vary with the molecular geometry, though this is particularly important in the case of the purely repulsive $\tilde{A}$ states and the energy range observed spectroscopically for the $X \rightarrow \tilde{A}$ continuum is indicated.

The lower lying members of the various progressions that are obtained in this way are given in table 3. The first series, $n(X) \rightarrow (n+1)$s converges on the ground state ion RX^+. The next series, $\sigma_{C-H} \rightarrow (n+1)$s converges on the first excited state of the alkyl halide ion. The analogous excitation in CF_3I, $\sigma_{C-F} \rightarrow (n+1)$s, lies at a higher energy than the process $n'(F) \rightarrow (n+1)$s, involving the F atom lone pairs. The final process, with an electron promoted to a σ_{C-H} anti-bonding orbital really belongs in the first progression since it involves removing an electron from the iodine lone pairs.

Comparison of the possible transition energies between the levels in figure 16 and those observed experimentally is also made in table 3, which supplements a

37

ELECTRONIC AND VIBRATIONAL EXCITATION IN $K+SF_6$ COLLISIONS

G.W. Black and M.A.D. Fluendy

Department of Chemistry, University of Edinburgh

Measurements of the inelastic differential scattering cross sections for $K+SF_6$ have been made using a time of flight technique described elsewhere (1). At a centre of mass collision energy of 162 eV the observed neutral K atom scattering is dominated by an almost elastic process which falls off more rapidly with angle than expected for typical repulsive inter-molecular potentials. A number of weak but discrete processes are also observed and listed in the Table.

Process No.	Energy loss /eV	% of Elastic Peak	Assignment	SF_6 Vibn Extn.
1	0	100	$K(4^2S)$	0
2	2.4	3.5	$K(4^2S)$	2.4
3	4.3	0.3	$K(4^2P)$	2.7
4	5.3	0.2	SF6(A)?	Dissoc. Te= 5.7eV
5	6.7-8.4	1.5	SF6(B)	Dissoc. Te= 7.9eV
6	10.4	0.2	SF6(C)??	Dissoc. Te=11.2eV

A number of workers (2)(3)(4) have investigated ion production in these collisions. Ionisation is found to be an important channel increasing rapidly from onset at the adiabatic threshold and rising more slowly thereafter. The vibrational motion of the SF_6 is strongly coupled as evidenced by the production of fragment ions and the effectiveness of target vibration in promoting ionisation.

The process is interpreted as proceeding via a vertical electron transition to a compressed configuration of the SF_6 ion, Fig. 1.

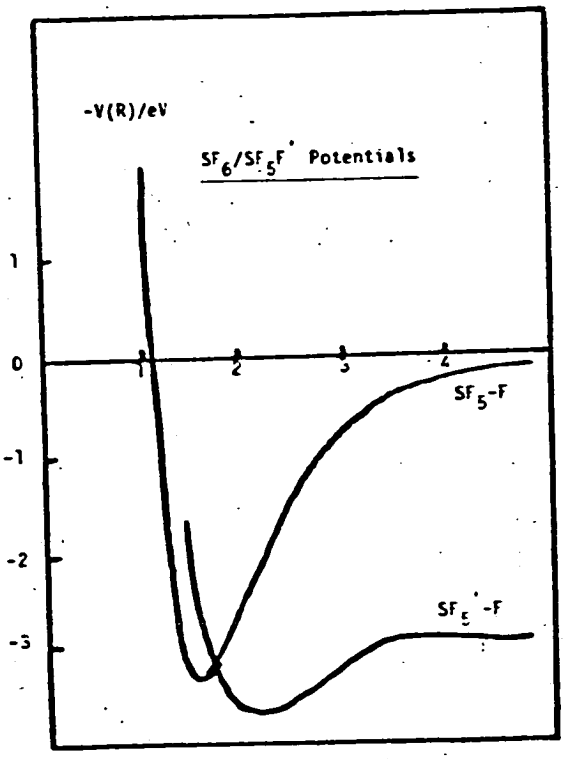

In these measurements the angular dependence of the elastic cross section, corresponding to diabatic behaviour at the ingoing crossing, is distorted by the substantial adiabatic process. This usually leads to ionisation as a result of the S-F bond stretch in the negative ion. A small fraction is seen, however to behave adiabatically at the outgoing crossing with either the $K(4^2S)$ potential to produce vibrationally hot SF_6 (process 2) or with the $K(4^2P)$ potential to produce both an excited alkali atom and hot SF_6 (process 3).

Simple classical calculations (as described elsewhere (1)) using the potentials shown in the figure yield good agreement with the observed energy losses, Fig. 2. The calculated energy losses are particularly sensitive to the form of the SF_6 potential, which is not well known and must have a slightly narrower bowl than that drawn by previous workers. The two branches contributing to the $K(4^2P)$ scattering originating from early or late crossings to the ionic surface are found to have similar energy losses in the model and are averaged together in Fig. 2.

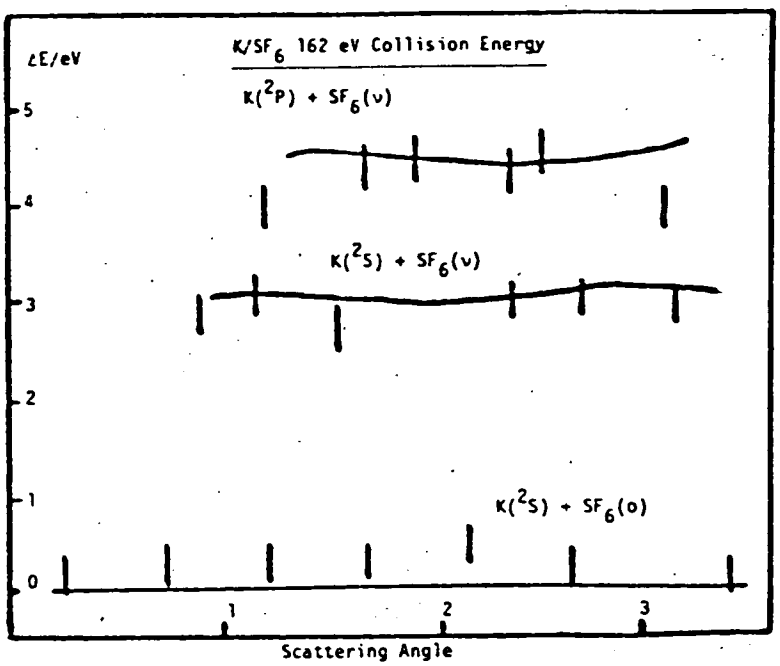

Fig. 2 Energy loss
as observed and co
puted using the
potentials shown

Potentials:

V K/SF_6

$V(\text{neutral}) = (2.3 \times 107/R)13.7\ \text{eVA}^{\circ}$

$V(\text{ionic}) = (3.44 \times 106/R)13.7\text{-}14.394/R + 4.86$

V SF_6

$V(\text{neutral}) = 3.38(1-\exp(-1.58(r-1.56)))^2\text{-}3.38$ eV

$V(\text{ionic}) = 1.00(1-\exp(-1.25(r-2.12)))^2\text{-}1.00$
$+ 0.4(1-\tanh^2(r-3.25)) - 2.9\ \text{eVA}^{\circ}$

(corresponds to a vertical Ea of -0.56eV)

References

1. G.W. Black, M.A.D. Fluendy and D. Sutton, Chem.Phys.Letts. 69, 260(1980).

2. M.M. Hubers and J. Los, Chem.Phys. 10, 235, (1975).

3. R.N. Compton and C.D. Cooper, J.Chem.Phys. 59, 4140, (1973)

4. C.B. Leffert, S.Y. Tang, E.W. Rothe and T.C. Cheng, J.Chem.Phys. 61, 4949, (1974).

5. S. Okada, Chem.Phys.Letts., 70, 45, (1980).